Journal of
Geophysics
Zeitschrift für
Geophysik
Volume 41 1975

Springer-Verlag Berlin Heidelberg New York

Printed in Germany by Univ.-Druckerei H. Stürtz AG, Würzburg

Author Index

Subject Index

Journal of Geophysics Zeitschrift für Geophysik

Volume 41 · Number 1 · 1975

Contents

Original Investigations

Indexed in Current Contents

Springer-Verlag
Berlin · Heidelberg · New York

J. Geophys. – ZEGEA7 41(1) 1–134 – 3. | 1975

Journal of Geophysics - Zeitschrift für Geophysik

Edited for the Deutsche Geophysikalische Gesellschaft by

W. Dieminger and J. Untiedt

The "Journal of Geophysics" accepts Review Articles (invited by the Editors), Original Papers, Short Communications, Letters to the Editors and Book Reviews concerned with the entire field of Geophysics and related fields.

Manuscripts may be addressed to any of the Editors. For addresses see last cover page. Manuscripts should conform with the Journal's accepted practice as described in the Instructions to Authors.

The journal is published bimonthly. One volume will be published in 1975. The price is DM 168.– per volume plus postage and handling. Members of the Deutsche Geophysikalische Gesellschaft are entitled to purchase the Journal for their own use at a privilege price of DM 65.– payable with the Membership dues. Orders should be sent to the Society's office at the following address: 2 Hamburg 13, Binderstr. 22.

50 offprints of each paper are provided free of charge. Additional copies may be ordered at cost price.

All business correspondence except orders at the membership price should be directed to

Springer-Verlag

D-6900 Heidelberg 1, Postfach 105 280, Telephone (0 62 21) 487·1, Telex 04-61 690
D-1000 Berlin 33, Heidelberger Platz 3, Telephone (0 30) 82 20 01, Telex 01-83 319
Springer-Verlag New York Inc., 175 Fifth Avenue, New York, N.Y. 10010

Responsible for advertisements: L. Siegel, W. Pehla, D-1000 Berlin 15, Kurfürstendamm 237, Telephone: (0 30) 8 82 10 31, Telex: 01-85 411. Printed in Germany by Hans Meister KG, Kassel.

J. Geophys. 41, 1–12, 1975

Original Investigations

Statistical Behaviour of Elastic Waves in a Reverberating Solid

J. Drisler and P. Antony-Spies

Institute of Meteorology and Geophysics,
University Frankfurt am Main

Received May 3, 1974

Abstract. A reverberation method of measuring the Q-value of a rock sample of arbitrary size and shape is investigated theoretically on the basis of randomly travelling shear and compressional waves. Formulae are derived for the mean attenuation of these waves, their energy ratios and the energy conversion rates of the two types into each other. The evaluation for a spherical sample with an isotropic and a sine distribution of the wave intensity incident on the sample surface gives energy ratios E_P/E_S between 0.35 and 0.60 depending on the wave velocities. The influence of size and shape of the sample is found to be rather weak generally for typical laboratory samples with dimensions from about 2 to 20 cm.

Key words: Elastic Waves-Attenuation — Q-value — Reverberation — Energy-Statistics — Wave Conversion — Wave Mixture.

1. Introduction

One of the most striking results of the first seismic experiments on the moon was the discovery that elastic waves have an extremely small attenuation compared with the values obtained for the solid earth. Therefore much work has been done in the last few years in order to find out the reasons. Most of the investigations were laboratory measurements of elastic wave absorption in rock under various lunar environmental conditions.

In this paper we want to point out some interesting theoretical aspects of the absorption measurements of Herminghaus and Berckhemer (1974). They applied the reverberation techniques well known in architectural acoustics using a rock sample as the reverberation chamber. Applications to ultrasonic absorption measurements in liquids are described by Kurtze and Tamm (1953), Bergmann (1954) and Ohsawa and Wada (1967). Reverberation is the persistence of sound in an enclosure as the result of continuous reflections at the walls after the sound source has been turned off. The sample surface which is usually irregular and other inhomogeneities serve as reflective sources and cause the sound energy distribution to become uniform. The reverberation time at a specific frequency is a reciprocal measure for the absorption and proportional to the Q-value of the sample.

There are two important features which distinguish the reverberation method applied to solid samples from its analogue in architectural acoustics. First, in addition to compressional waves also shear waves have to be considered and second, the measured attenuation is taken to be a characteristic material property and should be independent of the shape and the size of the sample. The difference between the present method and the conventional methods of elastic wave absorption measurements (Truell *et al.*, 1969) is, that in the latter scattering by inhomogeneities and reflections by surface irregularities must be prevented with the aid of adequately chosen samples and high precision mechanical surface preparation. In the present method the samples are not mechanically prepared. Apart from the practical advantage of this, the method simulates another important discovery in lunar seismograms: the strong multiple scattering and randomness of reflections of seismic waves. The results of our investigations might be applied in principle to other large scale multiple scattering and random reflection phenomena in seismology.

2. *Physical Model*

The problem is to describe the mean time behaviour of the elastic wave energy in a solid after a single pulse has been transmitted from a point source on the surface of the sample. The solution presented below is a statistical approach based on the following assumptions:

(1) The elastic wave energy is described by randomly travelling shear and compressional waves (S and P waves).

(2) The mean energy E_{PS} of S waves generated per unit time by P waves incident on the surface and on inhomogeneities is proportional to the total P wave energy E_P. The same is assumed for the mean energy E_{SP} of P waves generated by S waves. We write

$$E_{PS} = A \cdot E_P, \tag{1}$$

$$E_{SP} = B \cdot E_S\,, \tag{2}$$

where the factors A and B are independent of time.

The quantities E_{PS} and E_{SP} will be called "*P/S and S/P energy conversion rates*" respectively, and the factors A and B "*relative energy conversion rates*". The latter account for the material and the geometrical properties of the sample.

For illustration we use a simple ray model for a homogeneous sample. Consider a single ray from a compressional pulse emitted from the source at the time $t=0$. At the first reflection from the surface it splits up into a P

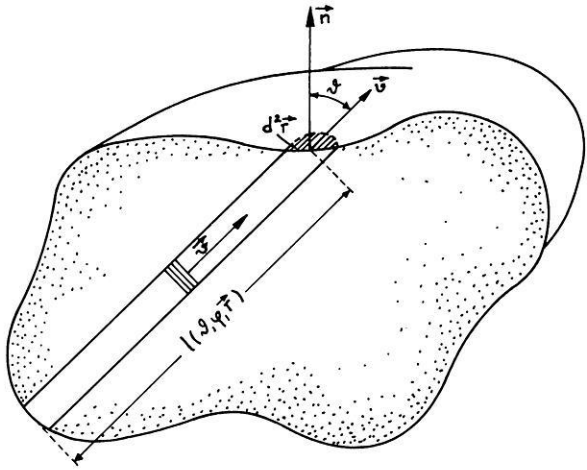

Fig. 1. Cut of the sample in the plane of incidence of an elastic wave. The azimuth φ is the angle between the cut and any reference plane containing the normal vector $\vec{n}$

and an S ray. Each of them splits up again at the second and all subsequent reflections. After n reflections there are 2^n P and S rays. At a given time t we have

$$n \approx \frac{\bar{v}}{\bar{l}}\, t\,, \tag{3}$$

where $\bar{l}$ is the mean free path and $\bar{v}$ the mean velocity of the rays. For samples with a diameter of about 10 cm the mean number of reflections $\bar{l}/\bar{v}$ suffered per second by a ray lies between 10^4 and 10^5. The number of rays increases very rapidly with time causing a corresponding fine spatial distribution of energy and an equilibrium mixture of P and S waves.

3. P/S and S/P Energy Conversion Rates

In order to calculate the energy conversion rates we use the simple model of the last section. We define local angular distribution functions $f_{\mathrm{P}}(\vartheta, \varphi, \vec{r})$ and $f_{\mathrm{S}}(\vartheta, \varphi, \psi, \vec{r})$ of mean P and S wave energy flux as follows: Consider the energy $d\varepsilon_{\mathrm{P}}$ of P waves travelling in the direction ϑ, φ towards the surface element $d^2\vec{r}$ at the point $\vec{r}$ (Fig. 1). It is contained in a thin prism of length $l(\vartheta, \varphi, \vec{r})$. The time it takes P waves with velocity v_{P} to pass the prism is the ratio $l(\vartheta, \varphi, \vec{r}) / v_{\mathrm{P}}$. Denoting the mean intensity of P waves by $I_{\mathrm{P}}(\vartheta, \varphi, \vec{r})$ and the solid angle by $d\Omega = \sin\vartheta\, d\vartheta\, d\varphi$, we have

$$d\varepsilon_{\mathrm{P}} = I_{\mathrm{P}}(\vartheta, \varphi, \vec{r})\, \frac{l(\vartheta, \varphi, \vec{r})}{v_{\mathrm{P}}} \cos\vartheta\, d^2\vec{r}\, d\Omega\,. \tag{4}$$

For S waves the analogous expression is

$$d\varepsilon_S = I_S(\vartheta, \varphi, \psi, \vec{r}) \frac{l(\vartheta, \varphi, \vec{r})}{v_S} \cos\vartheta d^2\vec{r} d\Omega d\psi , \tag{5}$$

where the angle ψ describes the polarization such that $\psi = 0$ for SV waves and $\psi = \pi/2$ for SH waves. The total P and S wave energies E_P and E_S in the sample are obtained by integration:

$$E_P = \int I_P(\vartheta, \varphi, \vec{r}) \frac{l(\vartheta, \varphi, \vec{r})}{v_P} \cos\vartheta d^2\vec{r} d\Omega \tag{6}$$

and

$$E_S = \int I_S(\vartheta, \varphi, \psi, \vec{r}) \frac{l(\vartheta, \varphi, \vec{r})}{v_S} \cos\vartheta d^2\vec{r} d\Omega d\psi . \tag{7}$$

The local angular distribution functions of the energy flux towards the surface can then be defined by

$$f_P(\vartheta, \varphi, \vec{r}) \equiv \frac{1}{E_P} I_P(\vartheta, \varphi, \vec{r}) \frac{l(\vartheta, \varphi, \vec{r})}{v_P} \cos\vartheta \tag{8}$$

and

$$f_S(\vartheta, \varphi, \psi, \vec{r}) \equiv \frac{1}{E_S} I_S(\vartheta, \varphi, \psi, \vec{r}) \frac{l(\vartheta, \varphi, \vec{r})}{v_S} \cos\vartheta . \tag{9}$$

They are normalized to 1 according to Eqs. (6) and (7). Expressing the P/S and S/P energy conversion rates in terms of these functions we have

$$\begin{aligned} E_{PS} &= \int A_{PS}(\vartheta, \varphi) I_P(\vartheta, \varphi, \vec{r}) \cos\vartheta d^2\vec{r} d\Omega \\ &= E_P v_P \int A_{PS}(\vartheta, \varphi) \frac{f_P(\vartheta, \varphi, \vec{r})}{l(\vartheta, \varphi, \vec{r})} d^2\vec{r} d\Omega = E_P A \end{aligned} \tag{10}$$

and

$$E_{SP} = E_S v_S \int A_{SP}(\vartheta, \varphi, \psi) \frac{f_S(\vartheta, \varphi, \psi, \vec{r})}{l(\vartheta, \varphi, \vec{r})} d^2\vec{r} d\Omega d\psi \equiv E_S B , \tag{11}$$

where $A_{PS}(\vartheta, \varphi)$ and $A_{SP}(\vartheta, \varphi, \psi)$ are the ratios of the S wave energy generated at a surface element to the energy of P waves incident in the direction ϑ, φ and vice versa.

In the case of incident S waves only the component in the plane of incidence is converted. We can therefore write

$$A_{SP}(\vartheta, \varphi, \psi) = A_{SP}(\vartheta, \varphi) \cdot \cos^2 \psi , \tag{12}$$

where $A_{SP}(\vartheta, \varphi)$ refers to incident S waves without regard to polarization.

According to their general form the expressions (10) and (11) are supposed to be valid also for models of scattering and diffraction including wave theory instead of simple rays. We note by inspection of the integrals that the energy conversion rates generally depend on size and shape of the sample.

The practical calculation of the relative energy conversion rates A and B from the formulas (10) and (11) requires special assumptions about the angular distribution functions. In the two following examples the sample has been chosen to be a sphere with radius R. In model I we assume the elastic wave intensity to be homogeneous and isotropic:

$$\begin{aligned} f_P(\vartheta, \varphi, \vec{r}) &= \frac{1}{8\pi^2 R^2} , \\ f_S(\vartheta, \varphi, \psi, \vec{r}) &= \frac{1}{8\pi^3 R^2} . \end{aligned} \tag{13}$$

In model II a cosine distribution is assumed:

$$\begin{aligned} f_P(\vartheta, \varphi, \vec{r}) &= \frac{1}{4\pi^2 R^2} \cos\vartheta , \\ f_S(\vartheta, \varphi, \psi, \vec{r}) &= \frac{1}{4\pi^3 R^2} \cos\vartheta . \end{aligned} \tag{14}$$

The S wave intensity is independent of polarisation in both models. The energy ratios A_{PS} and A_{SP} are given in plane wave theory by the expressions (Gutenberg, 1944):

$$A_{PS}(\vartheta) = \frac{4 L_P^2}{(L_P^2 + 1)^2} \tag{15}$$

and

$$A_{SP}(\vartheta) = \frac{4 L_S^2}{(L_S^2 + 1)^2} , \tag{16}$$

where

$$L_P^2 = \frac{\left[\left(\frac{v_P}{v_S}\right)^2 - 2\sin^2\vartheta\right]^2}{2\sin\vartheta\sin 2\vartheta\sqrt{\left(\frac{v_P}{v_S}\right)^2 - \sin^2\vartheta}} \tag{17}$$

and

$$L_S^2 = \left(\frac{v_P}{v_S}\right)^2 \frac{\cot 2\vartheta\cos 2\vartheta}{2\sin\vartheta\sqrt{\left(\frac{v_S}{v_P}\right)^2 - \sin^2\vartheta}} \tag{18}$$

They are plotted in Fig. 2 for different ratios of the wave velocities. The relative energy conversion rates have been listed in Table 1. We observe that the values are strongly effected by the angular distribution functions of the incident energy. They are greater for model I than for model II because the mean distance between two reflections is longer in model II. The influence of the velocity ratio is comparably weak.

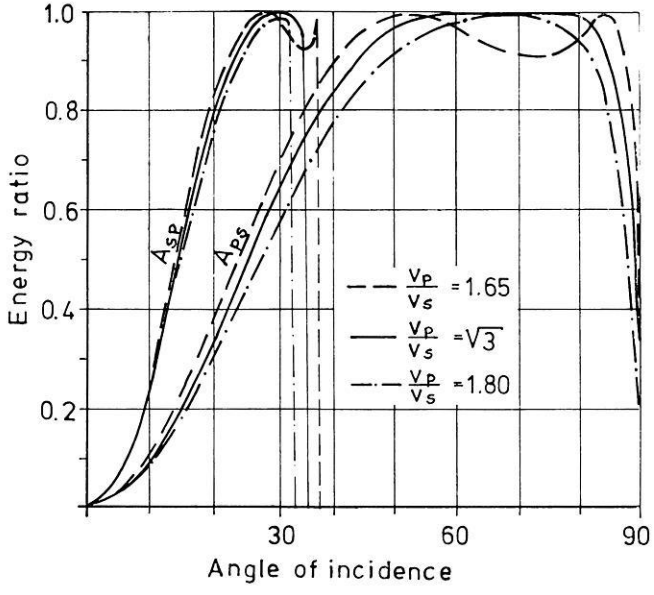

Fig. 2. Energy ratios of reflected P waves to incident S waves and vice versa as a function of the angle of incidence for various velocity ratios v_P/v_S. (after Gutenberg)

Table 1. Relative energy conversion rates A and B for various ratios v_P/v_S

model	v_P / v_S	$A \cdot \frac{R}{v_P}$	$B \cdot \frac{R}{v_S}$
I	1.65	2.04	1.68
II		0.72	0.50
I	$\sqrt{3}$	1.78	1.69
II		0.83	0.50
I	1.80	1.57	1.69
II		0.79	0.50

4. *Damping of P and S Wave Mixtures*

We shall now calculate the time dependence of elastic wave energy. The change of P wave energy in time is given by the energy increase E_{SP} per unit time by S/P conversion, the decreases $-E_{PS}$ by P/S conversion and $-D_P$ by attenuation

$$\frac{dE_P}{dt} = E_{SP} - E_{PS} - D_P \,. \tag{19}$$

For S waves we have

$$\frac{dE_S}{dt} = -E_{SP} + E_{PS} - D_S \,. \tag{20}$$

The energy losses D_P and D_S per unit time can be expressed in terms of the energy damping constants a and b

$$D_P = a \cdot E_P \,, \tag{21}$$

$$D_S = b \cdot E_S \,. \tag{22}$$

The damping constants are closely related to the well known Q-value of elastic waves defined by

$$\frac{1}{Q} = \frac{1}{2\pi} \frac{\Delta E}{E} \,, \tag{23}$$

where $\Delta E/E$ is the relative energy loss per cycle. Division of the absolute energy loss per cycle, ΔE, by the period T gives

$$D_P = \frac{\Delta E_P}{T} = \frac{2\pi}{Q_P T} E_P \equiv a E_P , \tag{24}$$

$$D_S = \frac{\Delta E_S}{T} = \frac{2\pi}{Q_S T} E_S \equiv b E_S . \tag{25}$$

Inserting the expressions for D_P, D_S, E_{PS} and E_{SP} into Eqs. (19) and (20) we obtain two coupled linear differential equations of first order in time:

$$\frac{dE_P}{dt} = E_P (-A - a) + E_S B, \tag{26}$$

$$\frac{dE_S}{dt} = E_P A + E_S (-B - b) . \tag{27}$$

They are solved by letting

$$E_P = E_{P0} \cdot e^{-ct} , \tag{28}$$

$$E_S = E_{S0} \cdot e^{-ct} , \tag{29}$$

where the constant c is given by

$$c = \frac{A+B+a+b}{2} - \sqrt{\frac{(A+B+a+b)^2}{4} - Ab - aB - ab} . \tag{30}$$

The solution shows that the decreases of the total P and S wave energies within the solid are the same, giving a constant ratio E_P/E_S.

By inserting the solutions (28) and (29) into the differential Eqs. (26) and (27) we obtain

$$\frac{E_P}{E_S} = \frac{E_{P0}}{E_{S0}} = \frac{B}{c+A+a} = \frac{c+B+b}{A} . \tag{31}$$

If the damping of P and S waves is sufficiently small the energy ratio only depends on the relative energy conversion rates:

$$\frac{E_P}{E_S} = \frac{B}{A} . \tag{32}$$

Some numerical values of E_P/E_S for the two models in the last section are given in Table 2. We note that the energy of S waves is greater than the P wave energy approximately by a factor of 2.

Table 2. Ratio of P wave to S wave energy for vanishing absorption for various ratios v_P/v_S

model	v_P / v_S	$E_P / E_S = B / A$
I	1.65	0.50
II		0.42
I	$\sqrt{3}$	0.55
II		0.35
I	1.80	0.60
II		0.35

5. *Discussion*

The previous considerations yield the theoretical background for the absorption measurements of Herminghaus and Berckhemer (1974). The quantity determined by the experiments is the mixed damping constant c. According to equation (30) it can be calculated from the damping constants a and b of pure P and S waves and the relative energy conversion rates A and B. The evaluation for a typical case of the ratio a/b is shown in Fig. 3, where the mixed damping constant is plotted against the relative energy conversion rates. For convenience the dimensionless quantities c/a, A/a, B/a and a/b are used. In Fig. 4 we have plotted the curves of constant mixed damping in the $A/a - B/a$ plane. Here the straight isolines confirm the simplicity of the relations. The mixed damping always lies between the individual damping constants. It approaches the S wave damping if the relative conversion rate A of P into S waves is high in comparison with the reverse process and vice versa.

As mentioned before the mixed damping is effected in general by the shape and the size of the sample. Because of the integrals in Eqs. (10) and (11) the influence of the shape is not sufficiently transparent for straightforward considerations. The effect of the size of the sample, however, can be easily seen. Let the relative conversion rates of a reference sample be A_0 and B_0. The free path of the rays be $l_0(\vartheta, \varphi, \vec{r})$. For a body with the same shape but a different size all lengths are multiplied by a constant δ:

$$l(\vartheta, \varphi, \vec{r}) = \delta \cdot l_0(\vartheta, \varphi, \vec{r}) . \tag{33}$$

The relative conversion rates are

$$A(\delta) = \frac{1}{\delta} A_0$$

and (34)

$$B(\delta) = \frac{1}{\delta} B_0 .$$

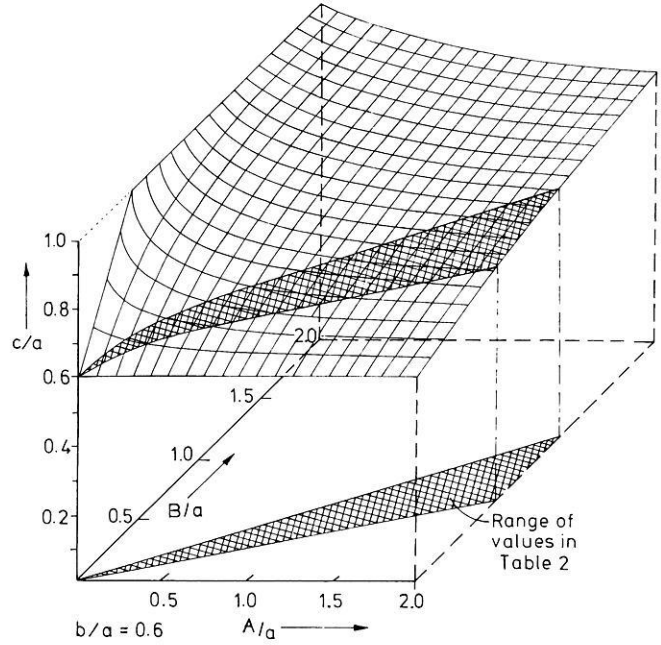

Fig. 3. Mixed damping versus the two relative energy conversion rates with the fixed ratio b/a of the damping constants due to pure S and P waves

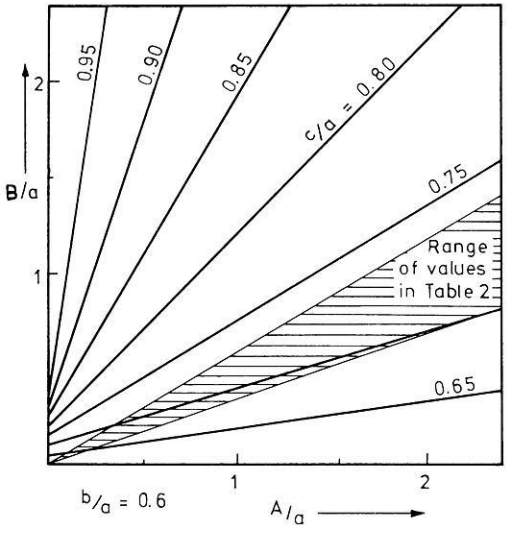

Fig. 4. Lines of constant mixed damping for variable relative energy conversion rates

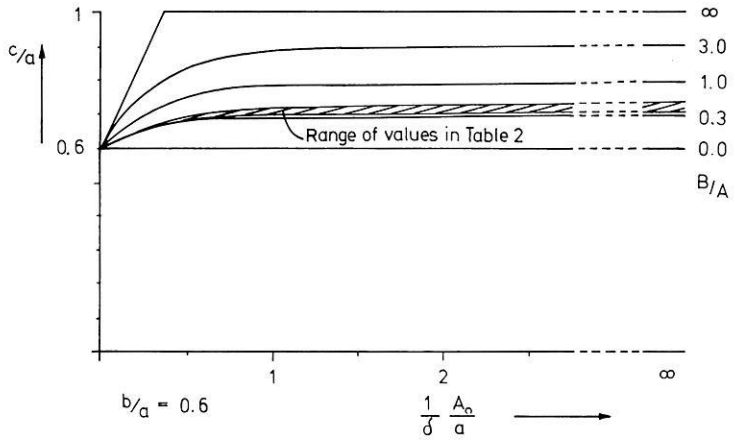

Fig. 5. Dependence of the mixed damping on the size parameter δ of the sample. The conversion rate of the reference sample is denoted by A_0

For a fixed shape which means a constant ratio B/A we get a straight line with the slope B_0/A_0 through the origin in the $A/a - B/a$ plane in Figs. 3 and 4. Inserting Eqs. (34) into the formula (30) we obtain the mixed damping as a function of the size parameter δ. It is plotted in Fig. 5 versus the quantity $A/a = A_0/a\delta$ for $b/a = 0.6$ and various shape parameters B_0/A_0. There are two limiting cases. For large bodies ($\delta \gg A/a$) the conversion rates are low and the mixed damping is near the weaker damping constant. For small bodies the conversion rates become high and the mixed damping is independent of size. Obviously this is achieved if

$$A_0/a\delta > 1.5 \,. \tag{35}$$

In the experiments of Herminghaus and Berckhemer (1974) the samples had diameters of $d = 5$ to 10 cm. The measured Q-values are in the range of 100 to 800 for frequencies between 100 and 400 kHz. The P wave velocities v_P are between 2500 and 5000 m/s. Taking the most unfavourable data from the measurements and from Table 1 for a reference sample ($\delta = 1$) we have, using Eq. (24):

$$\frac{A_0}{c} = A_0 \frac{Q\,T}{2\,\pi} \gtrsim 100 \,.$$

If we assume that $a < 5c$ we can be sure that the mixed damping measured by the reverberation method is independent of the size.

As shown by Fig. 5 the dependence on the shape is also weak, supposed that the estimates of the models I and II are realistic. This might be the case if there are no extreme deviations from a spherical shape like long

rods for example. Small shape variations are thought to be simulated to a certain amount by variation of the angular distribution functions.

Finally, we can give a rule for mixing the Q-values of pure P and S waves. From Eqs. (23) to (25) one obtains

$$\frac{1}{Q} = \frac{1}{Q_P} \frac{E_P}{E_P + E_S} + \frac{1}{Q_S} \frac{E_S}{E_P + E_S}, \tag{36}$$

giving for our special models a mixing rule:

$$\frac{1}{Q} = \alpha \frac{1}{Q_P} + (1 - \alpha) \frac{1}{Q_S}, \quad \alpha = 0.68 \pm 0.06. \tag{37}$$

For bodies larger than laboratory samples like regions of the seismic wave scattering in the outer layers of the moon fixed numbers of α might become questionable. However, one should be able to give a range of the mixed damping reaching from slightly above the smaller component to a certain considerable amount below the greater one.

Acknowledgements. The authors would like to express their appreciation to Prof. Dr. H. Berckhemer for suggesting this problem. They thank him, Prof. Dr. W. Jacoby and Ch. Herminghaus for various helpful discussions. This work was supported by the Bundesministerium für Bildung und Wissenschaft under contract no. WRK 246 and by the Deutsche Forschungsgemeinschaft under contract no. 299/36.

References

Bergmann, L.: Der Ultraschall und seine Anwendung in Wissenschaft und Technik, 6th ed., Stuttgart: S. Hirzel 1954

Gutenberg, B.: Energy ratio of reflected and refracted seismic waves. Bull. Seism. Soc. Am. *34*, 85–101, 1944

Herminghaus, Ch., Berckhemer, H.: Ultrasound absorption measurements in rock samples at low temperatures. J. Geophys. *40*, 341–354, 1974

Kurtze, G., Tamm, K.: Measurements of sound absorption in water and aqueous solutions of electrolytes. Acoustica *3*, 33–48, 1953

Ohsawa, T., Wada, Y.: Resonance reverberation method of ultrasonic measurements of liquids from 10 to 300 kc. Jap. J. Appl. Phys. *6*, 1351–1356 1967

Truell, R., Elbaum, Ch., Chick, B.: Ultrasonic methods in solid state physics. New York: Academic Press 1969

Jürgen Drisler
Peter Antony-Spies
Institut für Meteorologie
und Geophysik der Universität
D-6000 Frankfurt am Main
Feldbergstraße 47
Federal Republic of Germany

J. Geophys. 41, 13–22, 1975

A Compressed Air Gun Accelerator for Shock Magnetization and Demagnetization Experiments up to 20 kbar

U. Hornemann, J. Pohl, and U. Bleil

Institut für Angewandte Geophysik der Universität München

Received March 4, 1974

Abstract. For the investigation of the effect of stress waves on magnetic properties of rocks a non-magnetic compressed air gun accelerator was built. The stress waves are generated by planar impact of accelerated aluminium projectile plates on the rock samples. The velocity of the projectiles can be varied between about 15 m/s and 200 m/s. The stress amplitudes range from 1.5 to 20 kbar. The duration of the stress waves is of the order of several μs and can be varied by using projectiles of different thickness. The cylindrical rock samples have a maximum diameter of 2.5 cm and a length up to several cm. For basalt samples the stress is determined by using Hugoniot-data of basalt and aluminium and the impact velocity of the projectile. The stress wave profile is measured with piezo-ceramic transducers. The magnetic field at the place of the sample is controlled with a triple set of Helmholtz coils.

Key words: Rock Magnetism — Shock Magnetization — Shock Demagnetization — Piezomagnetic Effect — High Pressures.

1. Introduction

In an ambient magnetic field stress waves can produce a remanent magnetization in ferromagnetic materials (SRM, shock remanent magnetization), in zero field they can demagnetize ferromagnetic materials having a remanent magnetization (shock demagnetization).

For rocks containing ferromagnetic minerals these effects have been studied by several authors (Domen, 1961; Pohl, 1967; Hargraves and Perkins, 1969; Nagata, 1971). For the generation of the stress waves automatic hammering devices, falling masses or explosives were used. Generally the stresses did not exceed several hundred bar, exept when explosives were employed. In this case the stresses probably were of the order of tens of kilobars, but only qualitative informations could be obtained from the experiments.

It therefore seemed interesting to make quantitative measurements of the magnetizing and demagnetizing effect of stress waves in the higher stress range. For this purpose a non-magnetic compressed air gun accele-

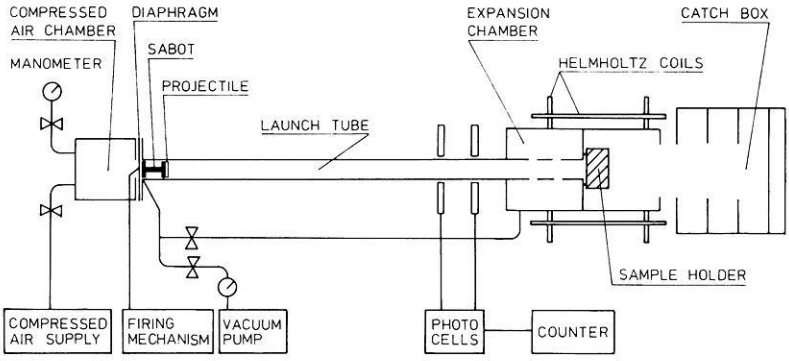

Fig. 1. Schematic view of the non-magnetic compressed air gun accelerator

rator was developed to generate stress waves of a duration of several μs with a maximum amplitude up to 20 kbar. In the following a description of the apparatus and the calibration for experiments with basaltic rocks will be given.

2. *The Compressed Air Gun Accelerator*

The apparatus consists mainly of a compressed air chamber and an evacuated launch tube separated by a diaphragm consisting of one or several thin plastic foils (Fig. 1). The launch tube has a length of 190 cm and an inner diameter of 3 cm. It is closed by the sample holder device, which adheres to the end of the evacuated tube by the atmospheric pressure. Over several slits at the end of the tube an expansion chamber is mounted to prevent compression of air in front of the accelerated projectile. At present 3 mm thick, flat grinded aluminium plates are used as projectiles. For acceleration they are pasted on a plastic sabot (Trovidur), which is designed to give an exact guidance to the projectile within the launch tube, thus providing a planar impact. The velocity of the projectile is measured with two photocells. It depends on the sabot and projectile mass and the pressure in the compressed air chamber. With a pressure of 5 bar a 50 g projectile is accelerated to a velocity of about 100 m/s at the end of the launch tube. The amplitude of the stress wave in the sample generated by the impact is determined by accelerating the projectile to an appropriate velocity. The desired velocity can be obtained with an accuracy better than 1%.

For an experiment the sabot with the projectile is placed just behind the diaphragm, the lauching tube and the expansion chamber are evacuated to a pressure less than 0.1 mbar; the compressed air chamber is filled, the diaphragm perforated with a match point and the sabot with the projectile

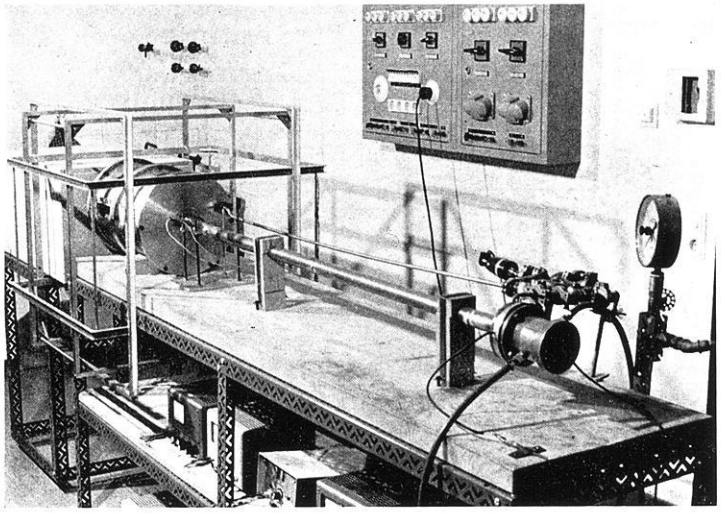

Fig. 2. The compressed air gun accelerator. To the right the compressed air chamber is shown, to the left the expansion chamber and a triple set of Helmholtz coils for the control of the magnetic environment

accelerates in the launch tube. The impact of the projectile on the sample holder device generates a stress wave in the sample. A catch box for the sample holder device filled with soft plastic material permits to avoid further shocks on the impacted sample.

In order to allow measurements of magnetic properties of the rocks, the launch tube, the expansion chamber and the sample holder device are made of non-magnetic materials (brass and aluminium). The sample holder is placed at the center of a triple set of Helmholtz coils which control the magnetic field at the place of the sample. The magnetic field in the laboratory can be compensated to ± 0.005 Oe and magnetic fields up to 10 Oe produced in various directions.

3. The Sample Holder Device

To prevent rapid crushing and demolition by the impact the basalt samples are mounted in a special sample holder device, which also provides a simple vacuum tightening of the launch tube (Fig. 3). The basalt samples have a cylindrical form 25 mm in diameter and 25 mm in length. They are pasted into a thin aluminium ring with an epoxy resin. The aluminium ring is fitted into a larger aluminium cylinder, which is closed on both sides with aluminium cover plates. After the impact the aluminium ring with the basalt sample can easily be removed from the aluminium cylinder for measure-

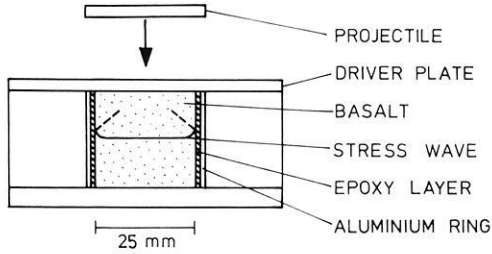

Fig. 3. Sample and sample holder device

ments of the magnetization and other magnetic experiments. The faces of the projectile, the cover plate and the basalt sample are face grinded to provide a good contact between the impacting projectile, the cover plate and the sample, which is necessary to assure a most ideal transmission of the stress wave.

4. *Determination of the Amplitude of the Stress Waves*

Stress waves generated by planar impact can be described in terms of the Rankine-Hugoniot equations for shock waves. These are obtained from the conservation laws for mass, momentum and energy across a single steady shock front in the one-dimensional case (Duvall and Fowles, 1963; for a discussion of the anisotropic stress distribution in stress waves see McQueen, *et al.* (1970)). The relation between stress σ and particle velocity u behind the stress wave front is given by:

$$\sigma = \varrho_0 \, u \, U \tag{1}$$

U — propagation velocity of the stress wave; ϱ_0 — initial density.

Experimental Hugoniot-Curves giving the relation between σ and u are known for aluminium and basalt (Fowles, 1961; Ahrens and Gregson, 1964; Ahrens, Petersen and Rosenberg, 1969). With these curves and the impact velocity v of the projectile on the driver plate it is possible to determine the stress σ in the basalt.

After the impact a stress wave runs from the interface projectile/driver plate into the driver plate and in opposite direction into the projectile. The momentum is partitionned and the particle velocity in the driver plate will be (Duvall and Fowles, 1963):

$$u = 1/2 \, v \, . \tag{2}$$

Knowing u we can determine the stress amplitude of the wave in the driver plate from the experimental Hugoniot-curve for aluminium (Fig. 4, $u_1 \rightarrow \sigma_1$).

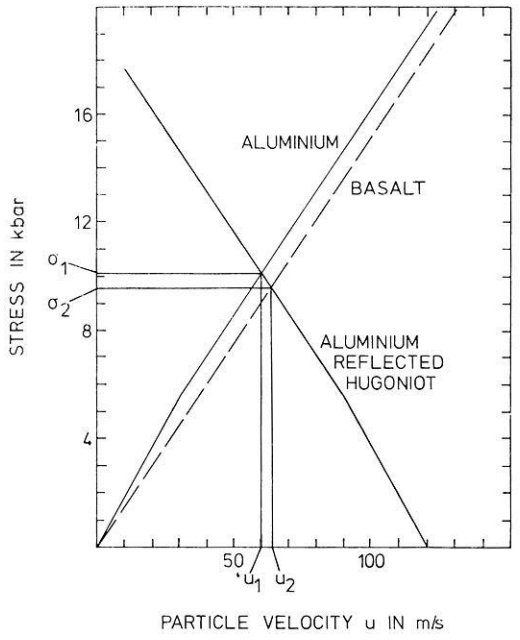

Fig. 4. Experimental Hugoniot-data for aluminium and basalt for the determination of the stress wave amplitude in basalt

At the interface driver plate/basalt the incident wave is partly transmitted and partly reflected as the basalt has a different impedance for stress waves. The relation between stress and particle velocity for the reflected wave in aluminum is given by the reflected Hugoniot-curve in Fig. 4. The amplitude σ_2 of the stress wave in the basalt is determined by the following boundary conditions: At the interface the resulting stress must be the same on both sides of the interface and the state of the interface must lie on both the reflected Hugoniot-curve for the driver plate through the point (u_1, σ_1) and on the Hugoniot curve for basalt. This yields the stress σ_2 and the particle velocity u_2 in the basalt. The graphical method to determine σ_2 is illustrated in Fig. 4. Due to the different wave impedances of aluminium and basalt the stress in the rock sample is about 0.5 kbar lower than in the aluminium driver plate.

By propagating through the basalt the amplitude of the stress wave decreases by about 20% on the distance of 25 mm (see section 5). Here only a short discussion of different mechanisms contributing to the amplitude decrease will be given. Absorption may be neglected on the short distance of 25 mm. The epoxy-resin layer acts as a side barrier for the wave energy. Divergence and thus an amplitude reduction of the initial plane stress wave

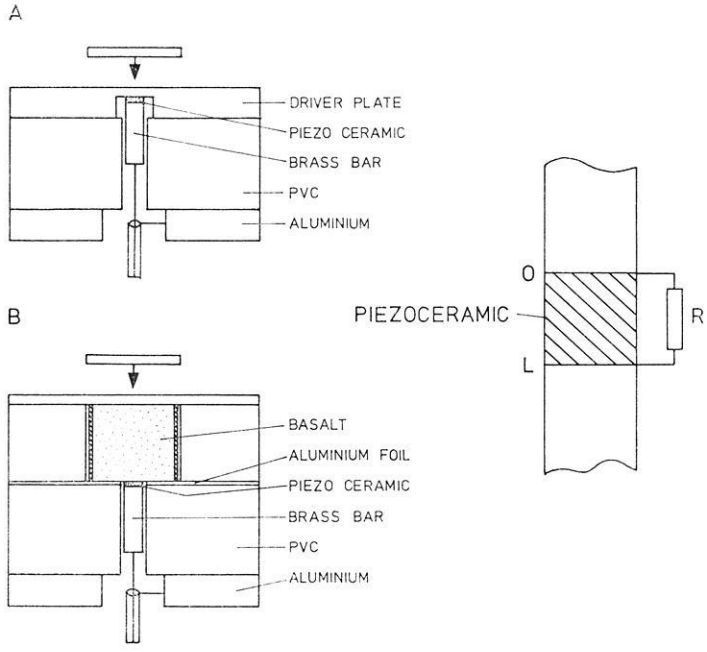

Fig. 5. Experimental devices for the measurement of stress wave forms with piezo-ceramic transducers (a) on the impact side and (b) on the back side of the basalt sample. Schematic diagram of the piezo-ceramic transducer

with increasing distance from the impacted surface is therefore highly suppressed. Only about 10% of the energy are thought to leave the sample. This causes a curvature of the wave front (Fig. 3). An additional effect may come from a weak oblique rarefaction wave reflected from the sides of the sample. A further reduction of the amplitude results from the faster moving back side rarefaction wave which overtakes the primary stress wave at a certain distance.

5. Measurement of the Wave Profile

The calculations in section 4 give only an information about the maximum amplitude of the stress wave but not on the wave profile. Therefore measurements of the stress wave form generated with the above described gun accelerator were made in the low stress range using piezoelectric ceramics with remanent polarization.

The piezoelectric element acts as a capacitor C which is charged by the stress wave travelling through. It is discharged through a resistance R connected in parallel (Fig. 5, one-dimensional case). The corresponding

voltage drop is measured with an oscilloscope. The piezoelectric polarization P is given by:

$$P = \sigma d \tag{3}$$

d — piezoelectric constant, $\sigma = \sigma(t)$ — stress.

The dielectric displacement D is

$$D = \varepsilon \varepsilon_0 E + \sigma d \tag{4}$$

ε, ε_0 — relative and absolute dielectric constant, E — electric field.

Integration over the length l of the piezo-element yields the following linear differential equation for the relation between the electric voltage $u(t)$ and the stress $\sigma(t)$ (Reibold, 1972):

$$C_0 \frac{du(t)}{dt} + \frac{u(t)}{R} - \frac{Fd}{\alpha}(\sigma(0, t) - \sigma(l, t)) = 0 \tag{5}$$

With the initial condition $u(0) = 0$ a general solution is

$$u(t) = \frac{Fd}{\alpha C_0} \int_0^t (\sigma(0, t') - \sigma(l, t'))\, e^{-\frac{T+\alpha-t'}{\tau}}\, dt' \tag{6}$$

T — signal length, α — travel time of the stress wave through the piezo-element, $\tau = R C_0$ — time constant of the measuring circuit, F — area of the piezo-element.

According to Reibold (1972) simple solutions of (6) can be obtained in special cases. For $\tau \gg T \gg \alpha$ the solution is

$$u(t) = \frac{F \cdot d}{C_0} \sigma(0, t) \tag{7}$$

This solution was used in the present case. The conditions $\tau \gg T \gg \alpha$ are satisfied with the short duration of the generated stress waves and by using thin ceramic plates. The impulse length T is of the order of 10 to 25 μs with the maximum amplitude lasting no longer than about 1 μs. The piezo-ceramic elements have a diameter of 5.7 mm and a thickness of 0.4 mm. With a sound velocity of 4.3 km/s the travel time through the plate is estimated to 0.1 μs. The total capacity C_0 of the measuring circuit system (capacities of the piezo-ceramic element, connecting cable and input of the oscilloscope) is 700 pF. With a resistance R of 1 MΩ the time constant τ is about 60 s. The piezo-ceramic material is a lead zirconate-titanate Sonox I (Stemag AG, Lauf, W.-Germany) with the following characteristics:

Density	ϱ	7.6	g/cm³
Young's modulus	E	$10.7 \cdot 10^{-10}$	N/m^2
Piezo-electric charge constant	d_{33}	$150 \cdot 10^{-12}$	C/N
Relative dielectric constant	ε	650	—
Frequency constant (thickness expansion)	N_T	2.15	kHz · m
Curie temperature	T_C	410	°C

Non-linearities are neglected.

Fig. 5 shows the two measuring arrangements for the wave profile at the front side and the back side of the sample. The piezo-ceramic discs are mounted with an electroconductive epoxy resin. In order to avoid reflections at the back side of the ceramic plate a brass bar 25 mm long is pasted on the ceramic plate with the same epoxy resin. The thickness of the epoxy film does not exceed 0.02 mm. The length of the brass bar provides about 12 μs measuring time without disturbance by a reflected wave from its free end. The capacitor electrodes of the ceramic plate are connected with coaxial cables to an oscilloscope.

Measured stress wave profiles are shown in Figs. 6a and 6b .The impact velocities are $v = 18.8$ m/s for Fig. 6a and $v = 18.2$ m/s for Fig. 6b. The stress impulse measured just behind the driver plate is thought to be similar to the impulse in the basalt near the impacted surface. In front of the basalt sample the duration T of the stress impulse is about 8 μs and the rise time about 1 μs. The secondary peak about 2 μs after the first maximum is, as travel time calculations show, due to the reflected wave from the back side of the 3 mm thick projectile. The integral $\int \sigma \, dt$ over the impulse gives the momentum per unit surface. It is in good agreement with the theoretical half momentum per unit surface of the impacting projectile.

On the back side of the basalt sample the impulse length is about 25 μs with a rise time of 10 μs. The broadening of the impulse is to a great deal due to waves reflected from the boundaries of the experimental arrangement. Thus for example the small peak observed in the broad maximum is caused by a wave reflected at the end of the brass bar. The delay time of about 12 μs corresponds to the travel time through the brass bar.

From the measured voltage the amplitude σ_{exp} of the stress wave may be estimated with relation (7). For Figs. 6a and 6b we have $\sigma_{\text{exp}} = 1.50$ kbar and $\sigma_{\text{exp}} = 1.19$ kbar respectively. The amplitudes σ_{theor} deduced from the impact velocities as described in section 4 give for the same experimental arrangements $\sigma_{\text{theor}} = 1.74$ kbar and $\sigma_{\text{theor}} = 1.50$ kbar. The stress obtained with the piezo-ceramic transducers is about 15 to 20% lower than the values deduced from the impact velocities. Several factors may account for this difference. For the calculation of the stress amplitudes in the

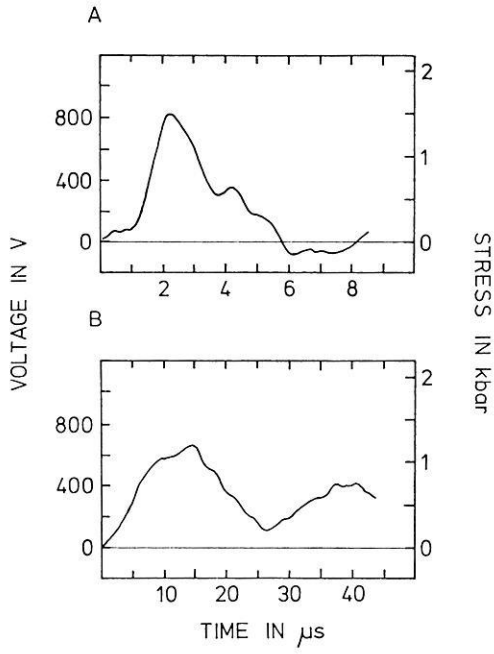

Fig. 6. Stress wave form (A) on the impact and (B) on the back side of a basalt sample

basalt a purely one-dimensional wave propagation was assumed. Especially for the back side of the basalt sample this method can only give approximate results. The boundary conditions for the interfaces aluminium/piezo-ceramic and basalt/piezo-ceramic are not considered as Hugoniot-curves for the ceramics used are not known. Furthermore it is assumed that the piezoelectric polarization is proportional to the stress although this relation is not linear in the high stress range. Finally the reciprocal piezoelectrical effect in lead zirconate-titanate also contributes to reduce the measured voltage. As a result we estimate that the stress values calculated from the impact velocities should be reduced by about 5 to 10%.

Acknowledgements. We wish to thank Prof. G. Angenheister, director of the Institut für Angewandte Geophysik, University of Munich, for his encouragement and support. We are also grateful to Dr. N. Petersen, Dr. A. Schult and Prof. H. Soffel for valuable discussions. Special thanks are due to A. Krumm and B. Nasdala, Weil, for preparation of the sample holder devices and for assistance in making the impact experiments. The financial support of the Deutsche Forschungsgemeinschaft is gratefully acknowledged.

References

Ahrens, T. J., Gregson, V. G.: Shock compression of crustal rocks: Data for quartz, calcite, and plagioclase rocks. J. Geophys. Res. *69*, 4839–4873, 1964

Ahrens, T. J., Petersen, C. F., Rosenberg, J. T.: Shock compression of feldspars. J. Geophys. Res. *74*, 2727–2746, 1969

Domen, H.: A note on remanent magnetism caused by impulsive pressure. Bull. Fac. Educ. Yamaguchi Univ. *10*, 71–76, 1961

Duvall, G. E., Fowles, G. R.: Shock waves. High pressure physics and chemistry. R. S. Bradley, ed. London: Academic Press 1963

Fowles, G. R.: Shock wave compression of hardened and annealed 2024 aluminium. J. Appl. Phys. *32*, 1475–1487, 1961

Hargraves, R. B., Perkins, W. E.: Investigations of the effect of shock on natural remanent magnetism. J. Geophys. Res. *74*, 2576–2589, 1969

McQueen, R. G., Marsh, S. P., Taylor, J. W., Fritz, J. N., Carter, W. J.: The equation of state of solids from shock wave studies. High-velocity impact phenomena, R. Kinslow, ed. New York: Academic Press 1970

Nagata, T.: Introductory notes on shock remanent magnetization and shock demagnetization of igneous rocks. Pageoph *89*, 159–177, 1971

Pohl, J.: Magnetisierung und Entmagnetisierung von Stahl und Magnetit durch Stoßwellen. Unpublished report, Institut für Angewandte Geophysik, University of Munich, 1967

Reibold, R.: Piezoelektrische Wandler zur Untersuchung mechanischer Kurzzeitbelastungen. Acustica *27*, 189–196, 1972

Dr. U. Hornemann
Arbeitsgruppe für
Ballistische Forschung
D-7858 Weil
Hauptstr. 18
Federal Republic of Germany

Dr. J. Pohl
Institut für Angewandte Geophysik
der Universität
D-8000 München 2
Theresienstr. 41
Federal Republic of Germany

Dr. U. Bleil
Institut für Geophysik
der Ruhr-Universität
D-4630 Bochum
Buscheystrasse
Federal Republic of Germany

J. Geophys. 41, 23–41, 1975

Shock Magnetization and Demagnetization of Basalt by Transient Stress up to 10 kbar

J. Pohl, U. Bleil, and U. Hornemann

Institut für Angewandte Geophysik der Universität München

Received March 4, 1974

Abstract. The effect of stress waves on the magnetization of basalt was studied. The stress waves were generated by impacting cylindrical basalt samples with aluminium projectiles. The 3 mm thick aluminium plates were accelerated in a non-magnetic compressed air gun accelerator to velocities ranging from 20 to 160 m/s, corresponding to peak stresses in the basalt between 2.5 and 10 kbar. The duration of the stress impulse was about several micro-seconds. For the experiments a basalt with well-known magnetic properties was used (Rauher Kulm, Germany). — The magnetizing effect of the stress waves was determined as a function of the number of impacts, the intensity and direction of the applied magnetic field (<10 Oe) and the peak stress amplitude. In the used stress range the measured shock remanent magnetization (SRM) tends to a final steady value after 5 or 6 impacts. This value is proportional to the intensity of the applied field and increases with the peak stress applied. The produced SRM can be erased with maximum ac-fields of about 150 to 200 Oe. Any dependance of SRM on the direction of the applied magnetic field could not be recognized within the accuracy limits of the experiments. — The demagnetizing effect of stress waves on the high-field (1000 Oe) isothermal remanent magnetization, the low-field (1 Oe) thermoremanent magnetization and the natural remanent magnetization was studied as a function of the number of impacts and the peak stress. A final steady state of magnetization is generally obtained after 4 or 5 impacts. With increasing peak stresses increasingly harder remanent magnetizations can be demagnetized, with stresses of 2.5 kbar corresponding to coercive forces of about 75 Oe, 5.5 kbar to about 125 Oe and 8 kbar to about 175 Oe.

Key words: Rock Magnetism — Piezomagnetic Effect — Dynamic Magnetization — Shock Demagnetization — High Pressures — Meteorite Impacts — Nuclear Explosions — Lunar Magnetism.

1. Introduction

Effects of static and transient stresses on magnetic properties of rocks are of importance in numerous natural and man-made phenomena such as the seismomagnetic effect (Stacey, 1964; Rikitake, 1968; Talwani and Kovach, 1972; Abdullabekov *et al.*, 1972), the volcano-magnetic effect (Stacey, Barr and Robson, 1965; Johnston and Stacey, 1969), the dam-magnetic effect (Davis and Stacey, 1972), the magnetic effects associated with chemical (Barsukov and Skovorodkin, 1969) and nuclear explosions (Short, 1966;

Hargraves and Perkins, 1969; Hasbrouck and Allen, 1972) and with meteorite impacts on Earth and on the Moon (Hargraves and Perkins, 1969; Pohl, 1971).

The effects of static uniaxial stress on magnetic properties of rocks, mainly reversible changes of susceptibility and reversible and irreversible changes of remanent magnetizations, have been studied by many authors. The remanent magnetization produced by static stresses is called piezoremanent magnetization (PRM). The demagnetizing effect of stresses is called stress demagnetization. A review on this subject was given by Nagata (1970).

The effect of transient stresses on magnetic properties of rocks has been studied much less. It is well known that shocks can change the remanent magnetization of ferromagnetic materials. Systematic investigations of the effect of repeated shocks on nickel were made for example by Gerlach (1949). The demagnetizing effect of intense stress waves on iron has been used in a technique for generating high electric current impulses of short duration (Kultermann, Neilson and Benedick, 1958). — At the beginning of rock magnetic research many investigators suspected that shocks could also change the remanent magnetization of rocks. They studied this effect by giving different types of rocks numerous consecutive shocks with automatic hammering devices, but they generally found only minor changes in remanence (e.g. Koenigsberger, 1932, 1936; Schmucker, 1957) and concluded that the effect is negligeable for paleomagnetic research.

It seems that in these early investigations rock types with quite stable remanent magnetizations were used, because more recently it was found that shocks can cause appreciable changes of magnetic properties of many rock types. Demagnetized rocks can acquire a remanent magnetization in the presence of a magnetic field under the effect of shocks. This phenomenon has been called dynamic magnetization or shock magnetization. The remanent magnetization produced by this procedure is called shock remanent magnetization (SRM, Nagata, 1971). On the other hand a remanent magnetization can also be destroyed by shocks (shock demagnetization).

The shocks or stress waves used in these experiments were generated by automated hammering devices (Shapiro and Ivanov, 1966, 1967), by falling masses (Domen, 1961; Nagata, 1971) and by explosives (Pohl, 1967; Hargraves and Perkins, 1969). The effect of shocks was measured as a function of the number of repeated shocks, of the intensity of the shock (kinetic energy of the impacting hammer, momentum of the falling mass) and of the applied magnetic field in the case of a production of remanent magnetization. Nagata (1971) gave also some information about the duration of the used stress impulse. The stability of shock remanent magnetizations was measured by Shapiro and Ivanov (1966). — In the above cited experiments either very low or very high stresses were used. Generally the stress

amplitudes did not exceed several hundred bar. In cases where explosives were used, the stresses were estimated to be of the order of several tens of kbars (Pohl, 1967; Hargraves and Perkins, 1969).

Static experiments with uniaxial stress without a confining hydrostatic pressure are limited to stresses of about 2 kbar, where the samples generally crash. With stress waves of short duration much higher stresses can be used. A limit is given also in these experiments by the pulverization of the sample.

The aim of the present study was to investigate the effect of stress waves up to about 10 kbar on a basalt with well-known magnetic properties. Different results of experiments with static uniaxial compressive stress on the same basalt, which can be usefully compared with dynamic experiments, are shown in the corresponding sections.

It should be noted that the expression "shock waves" is not appropriate to describe these experiments, although the expressions shock remanent magnetization and shock demagnetization are used. The term "shock wave" is applied to a compressional wave having an amplitude exceeding the Hugoniot elastic limit. The shock front is characterized by a discontinuity in pressure, density, energy and particle velocity. In the used stress range the compressional waves in solids have a comparatively long rise time, particularly in inhomogeneous materials such as rocks. In a first approximation the state of strain behind the wave front is uniaxial and the stress distribution is anisotropic.

2. Experimental Method

The stress waves are generated by the impact of aluminium projectiles (30 mm diameter, 3 mm thick) on an aluminium driver plate (3 mm thick) which is in contact with the cylindrical basalt sample (25 mm in diameter and 25 mm high). The projectiles are accelerated in a compressed-air gun accelerator (Hornemann, Pohl and Bleil, 1975). The peak stress is derived from the impact velocity, using Hugoniot-data for aluminium and basalt, and from direct measurements with piezo-ceramic transducers. The length of the stress pulse increases from about 8 μs at the impact side of the basalt sample to about 25 μs at its back side. The amplitude of the stress wave decreases by about 20% within the specimen. The magnetic field at the place of the sample is controlled by a triple set of Helmholtz coils. The remanent magnetization of the samples is measured with a Digico flux-gate spinner magnetometer.

The measuring procedure is as follows. For magnetizing experiments the samples are placed at the end of the launching tube, a magnetic field is applied and an impact is given to the sample. Then the remanent magnetization is measured in the Earth's magnetic field. For demagnetizing ex-

periments the sample with a remanent magnetization is impacted in magnetic zero-field. The measurement of the residual remanent magnetization is also made in the Earth's magnetic field.

Nagata (1971) has introduced the following notation for the description of static and transient stress experiments in rock magnetism: H^+ = application of a magnetic field, H^0 = removal of a magnetic field, P^+ = application of static stress, P^0 = removal of static stress, S = application of a shock. It seems convenient to add the notation H^e indicating that the Earth's magnetic field is applied and to restrict the notation H^0 to the meaning of the removal of any applied field, e.g. cancellation of the Earth's magnetic field. With these notations the remanent magnetization J_r produced in the magnetizing experiments described above after n impacts is given by

$$J_r(H^+S_1H^e,\ H^+S_2H^e,\ \ldots,\ H^+S_nH^e)$$

Similarly the demagnetizing experiments can be described by

$$J_r(\mathrm{TRM},\ H^0S_1H^e,\ H^0S_2H^e,\ \ldots,\ H^0S_nH^e)$$

where TRM means that the original remanence was a thermoremanent magnetization which must however be specified.

In order to determine the remanence it is necessary to preserve the samples after each impact in the original form. Since the used peak stresses highly exceed the breaking strength of the rock material, the samples were embedded with an epoxy resin in thin aluminium rings. At a peak stress of about 2 kbar small cracks begin to appear on the impacted surface of the samples. The number of cracks increases with higher impact velocities and repeated impacts. At a stress of about 10 kbar the sample is strongly brecciated after a few impacts. Measurements of the effect of repeated shocks are therefore limited at this stress level. However single shot experiments can be made with the available apparatus up to stresses of about 20 kbar, as the remanent magnetization can be measured as long as the sample is recovered approximately in its original form.

There is suspicion that the strong brecciation could modify the coercivity spectrum of the basalt by the development of cracks and/or lattice defects in the ferrimagnetic minerals. Therefore the coercivity spectra of the isothermal remanent magnetization (IRM) produced in a 1000 Oe field were measured before and after repeated impacts. As they were almost identical we conclude that such brecciation effects can be neglected in this study. Other macroscopic magnetic properties have not yet been investigated in this respect. It would be interesting for example to consider irreversible changes of the initial susceptibility and to measure the rotational hysteresis and the susceptibility anisotropy before and after impacting.

Table 1. Magnetic properties of the Rauher Kulm basalt

Compositional Curie point	T_c	245	°C
Measured Curie point	T_c	220	°C
Susceptibility (low field)	χ	$4 \cdot 10^{-3}$	emcgs
Saturation magnetization (20 °C)	J_s	4	G
Saturation remanent magnetization (20 °C)	J_{sr}	0.5	G

Ferrimagnetic ore: Homogeneous titanomagnetite, oxidation class I. $xFe_3O_4 \cdot (1 - x)Fe_2TiO_4$, x = 0.46.

Ore content: 4 Vol%

Grain size distribution:

Size (μm)	Vol%
30 — 50	24.5
10 — 30	60
5 — 10	12
1 — 5	3.15
< 1	0.35

The decrease of the peak stress intensity and the increase of the pulse length within the sample could produce an inhomogeneous remanent magnetization which can easily be detected by a simple flux-gate measuring arrangement (Helbig, 1965). No indications for any inhomogeneity in magnetization were however found within the accuracy limits of the method (3%). This may be due to the fact that an increase in pulse length leads to a higher remanence whereas a decrease in stress amplitude causes a lower remanence and that both effects cancel each other more or less.

3. Magnetic Properties of the Basalt from Rauher Kulm (RK), Germany

Basalts having acquired a SRM in low fields (< 10 Oe) and in the stress range lower than 10 kbar can be demagnetized with peak ac-fields of about 100 to 200 Oe. Therefore a basaltic material with a coercivity spectrum having a maximum at coercive forces below 100 Oe was selected for this study. The used basalt comes from the Tertiary "Rauher Kulm", Germany. Magnetic and mineralogical properties of this basalt have been described by Refai (1960); Petersen (1966); Soffel (1968); Creer and Petersen (1969); Creer, Petersen and Petherbridge (1970). Investigations of static uniaxial compression effects on magnetic properties of the RK-basalt have been carried out by Schmidbauer and Petersen (1968) and Zinsser (1970). Some additional measurements have been made in this study. A summary of different magnetic and mineralogical properties is given in Table 1 and in Figs. 1 and 2.

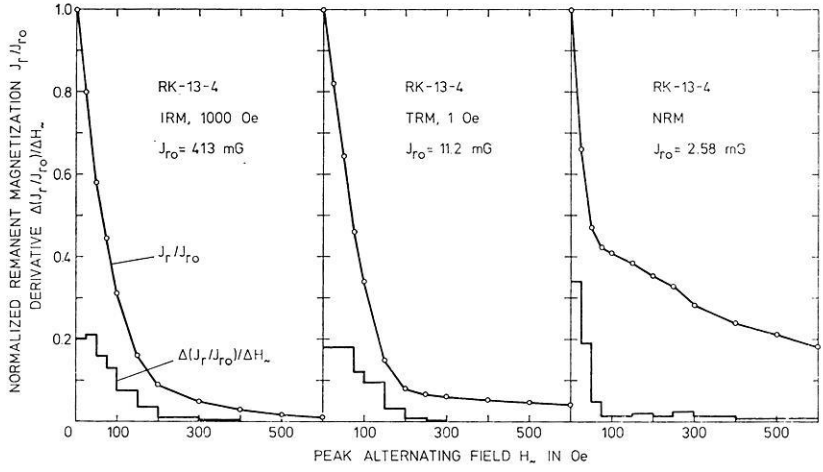

Fig. 1. Ac-demagnetization and coercivity spectra of the strong field isothermal remanent magnetization (IRM), the weak field thermoremanent magnetization (TRM) and the natural remanent magnetization (NRM, see also Fig. 11) for the Rauher Kulm (RK) basalt

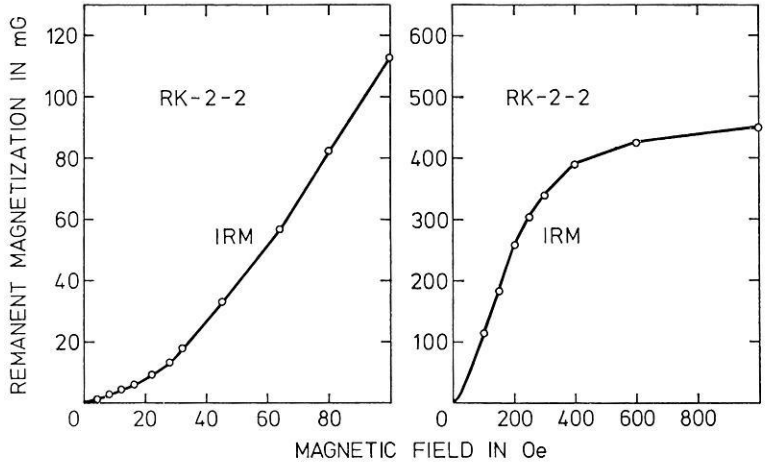

Fig. 2. Isothermal remanent magnetization (IRM) for the RK-basalt as function of the applied magnetic field

The carriers of remanence in the RK-basalt are both single domain (SD) and multi-domain (MD) grains. The mixed SD and MD behaviour was investigated by microscopic analysis of the magnetic domain structure by Soffel (1968). He showed that remanent magnetizations with coercive forces H_c smaller than about 200 Oe are located in MD grains and that

remanent magnetizations with coercive forces higher than about 200 Oe, especially the stable TRM component, are located in SD grains. The mixed SD and MD behaviour is also suggested by applying the Lowrie and Fuller (1970) criterion (see also Dunlop, Hanes and Buchan, 1973). The normalized ac-demagnetization curves of low field TRM and high field IRM (Fig. 1) are nearly identical for $H \sim < 200$ Oe. For $H \sim > 200$ Oe the TRM curve is above the IRM curve indicating a SD behaviour in this H_c-region. The ac-demagnetization of natural remanent magnetization (Figs. 1 and 11) also shows that the NRM of the RK-basalt consists both of an unstable, probably viscous component (Creer, Petersen and Petherbridge, 1970) and a stable TRM component (Soffel, 1968). The samples used in this study were taken from unoriented boulders which have probably been lying in the Earth's magnetic field with an orientation different from their original in situ orientation for several hundred years.

4. *The Effect of Repeated Impacts*

A characteristic feature of shock magnetization and demagnetization is that for a given peak stress intensity a final steady state of magnetization is not achieved by a single impact but that it is gradually approached with an increasing number of shocks. For low stresses this was shown by Gerlach (1949), Shapiro and Ivanov (1966) and Nagata (1971). The experimental results of magnetizing igneous rocks by repeated stress waves can empirically be represented in exponential laws (Shapiro and Ivanov, 1966). The remanent magnetization obtained in low magnetic fields after n impacts is given by

$$J_r(n) = J_r(\infty)\,(1 - e^{-\alpha n})\,. \tag{1}$$

$J_r(\infty)$ denotes the resulting final state of magnetization after a great number of impacts. The residual remanent magnetization after n impacts in non-magnetic space is given by

$$J_r(n) = J_r(\infty) - (J_r(\infty) - J_0)\, e^{-\alpha n} \tag{2}$$

J_0 denotes the initial remanent magnetization.

The experiments described in this study indicate that these relations can also be applied for stresses up to 10 kbar. Fig. 3 shows the remanent magnetization acquired by repeated impacts in a low field. Demagnetization curves are shown in Figs. 7 and 8.

The coefficient α indicates how rapidly the final steady state is approached. α can be estimated by comparing the normalized experimental curves with a set of standard curves. It is generally impossible to use numerical or geometrical methods because of the small number of experimental points and their rather high scatter. α depends on numerous parameters, such as

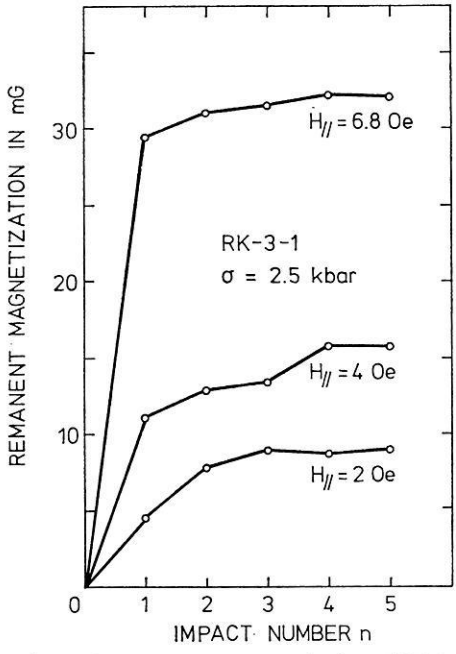

Fig. 3. Aquisition of shock remanent magnetization (SRM, $J_r(H^+S_1H^e, \ldots, H^+S_nH^e)$) and dependance on the number of impacts and the applied magnetic field

material properties, stress wave characteristics and intensity and direction of the applied magnetic field. In demagnetization experiments the particular type of initial remanence must also be considered. For the RK-basalt and stresses between 2.5 and 10.5 kbar, α varies from 0.8 to about 2. The final steady state of magnetization is generally approached to more than 95% after 3 or 4 shocks. Although no definite conclusions can be drawn due to the scatter of the experimental results, it seems that α increases with higher magnetic fields applied in magnetization experiments. No correlation was found between α and the peak stress intensity. The relations between α and the applied magnetic field and the peak stress intensity may be somewhat obscured by the fact that the determination of α strongly depends on the rate of the magnetization obtained after the first shock relative to the final state of magnetization after n shocks.

5. Shock Remanent Magnetization (SRM)

The relationship between the shock remanent magnetization $J_r(H^+S_1H^e, H^+S_2H^e, \ldots, H^+S_nH^e)$, the peak stress intensity and the intensity and direction of the applied magnetic field (<10 Oe) was investigated (Figs. 3,

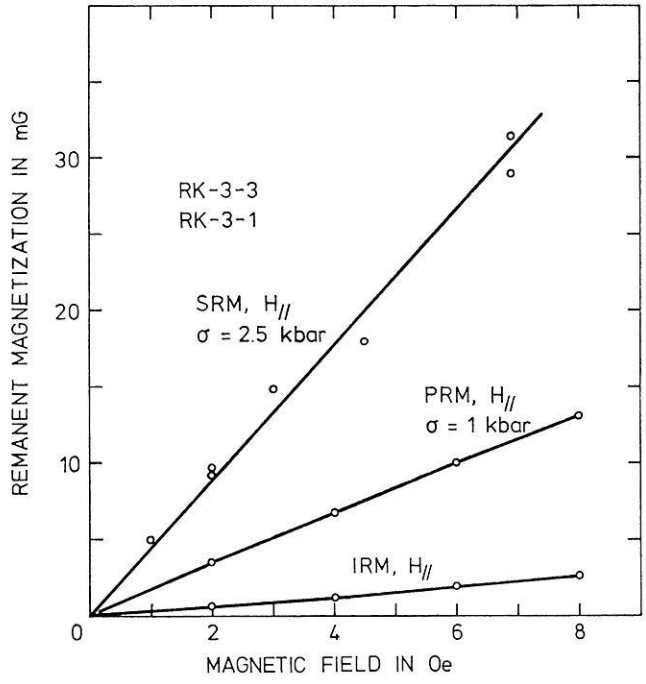

Fig. 4. Shock remanent magnetization $J_r(H^+S_1H^e, \ldots, H^+S_nH^e)$, piezo-remanent magnetization $J_r(H^+P^+P^0H^0)$ and isothermal remanent magnetization as functions of the applied magnetic field. For the SRM final steady state values obtained after several impacts are plotted

4 and 5). Prior to the magnetization experiments the samples were demagnetized in an ac-field of 1500 Oe. In the Earth's magnetic field the samples acquired a viscous magnetization of about 0.2 mG after several minutes, which is however small in comparison with the produced SRM and can therefore be neglected. The SRM is always parallel to the applied magnetic field.

Fig. 4 shows that for stresses from 2.5 to 10 kbar the SRM (final steady state values achieved after several impacts) increases almost linearly with the applied field H. These results correspond to those of Shapiro and Ivanov (1966) and of Nagata (1971) in the low stress range (<1 kbar). For comparison the dependance of a piezo-remanent magnetization J_r $(H^+P^+P^0H^e)$ and of the isothermal remanent magnetization on the applied field are also shown in Fig. 4. The PRM is proportional to H, whereas the IRM curve has a slight curvature corresponding to the Rayleigh-relationship between IRM and H ($\sim H^2$, see also Fig. 2). The magnetic field was applied parallel to the propagating direction of the stress wave (longitudinal mag-

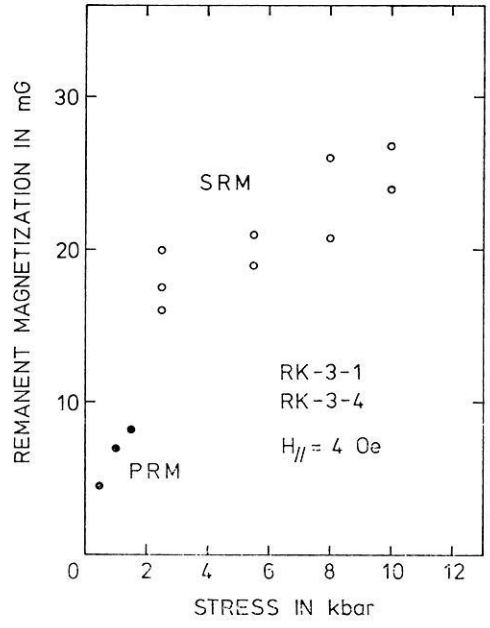

Fig. 5. Shock remanent magnetization (open circles) $J_r(H^+S_1H^e, \ldots, H^+S_nH^e)$ as dependent on the stress wave amplitude and piezo-remanent magnetization (full circles) $J_r(H^+P^+P^0H^0)$ as dependent on the applied uniaxial compressive stress. For the SRM final steady state values after several impacts are plotted

netization) and perpendicular to it (transverse magnetization). The longitudinal remanent magnetization was in most cases slightly higher than the transverse remanent magnetization, but the scatter of the intensities does not allow to determine a quantitative difference. The trend of the difference however confirms similar results for PRM and SRM in the lower stress range (Nagata, 1971).

The dependance of the final steady values of SRM on the peak stress is shown in Fig. 5. The remanent magnetization increases with increasing stress, but the rate of increase diminishes at higher stresses. The final SRM values may well be lying on the continuation of the curve obtained by experiments with static uniaxial compression, which is also shown in Fig. 5. The static experiments could only be made up to stresses of 1.8 kbar beyond which the samples crushed. The diminution of the rate of increase of the SRM at high stresses can in part be explained by the coercivity spectrum of the RK-basalt, if we assume that with increasing stress grains with increasing coercive forces can be magnetized. A quantitative analysis can not yet be made as the relation between the peak stress and the coercive forces is not well enough known.

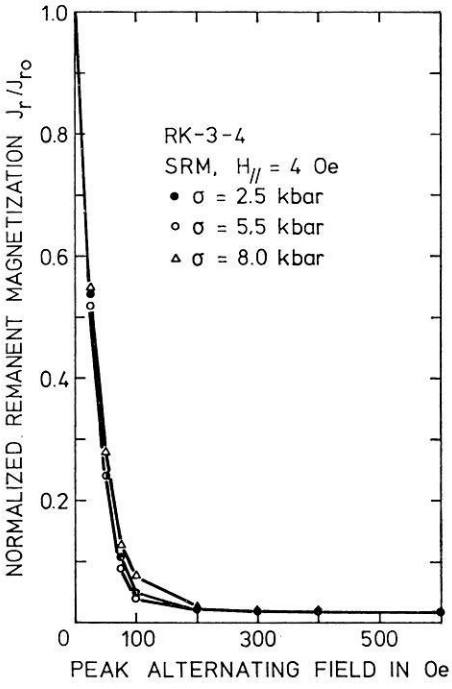

Fig. 6. Ac-demagnetization of shock remanent magnetization (normalized) acquired at different peak stress intensities

The produced SRM is not very stable against ac-demagnetization (Fig. 6). Peak ac-fields of about 100 Oe erase more than 90% of the SRM produced with stress intensities up to 10 kbar. There is only a slight indication that SRM produced at higher stresses has a greater stability. Shock demagnetization however shows clearly that with increasing stress intensity remanent magnetizations with higher coercive forces can be demagnetized (Section 6).

6. Shock Demagnetization of IRM, TRM and NRM

The demagnetizing effect of stress waves was studied for high field IRM ($\sim$ saturation remanent magnetization), low field TRM and NRM of the Rauher Kulm basalt (Figs. 7—11). The rock samples were impacted in non-magnetic space and the residual remanent magnetization was measured after each impact. Generally a final steady state of magnetization was obtained after 4 or 5 impacts. The values found for the coefficient α are in most cases slightly higher than in magnetizing experiments, but the scattering of the results does not allow to give a quantitative relationship.

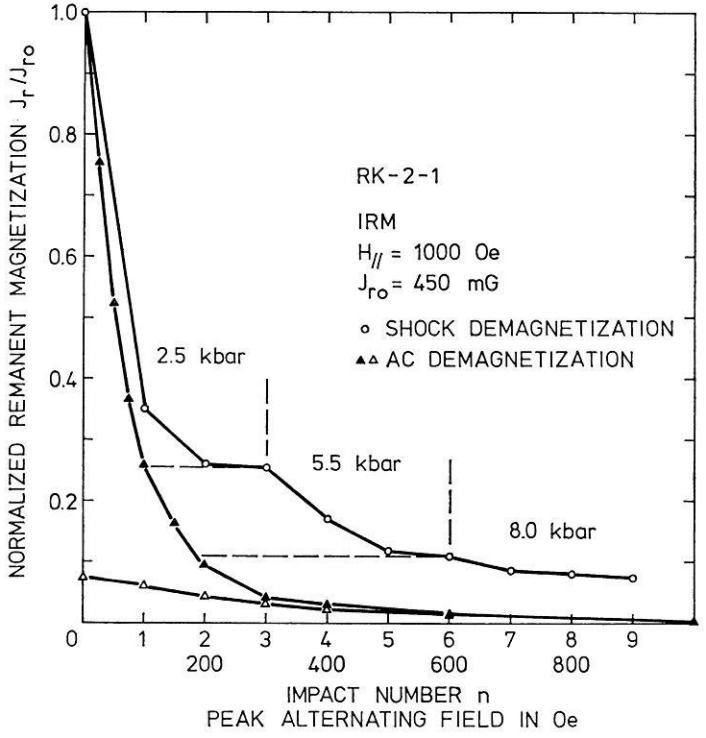

Fig. 7. Shock demagnetization (open circles) and ac-demagnetization (full triangles) of strong field isothermal remanent magnetization. Ac-demagnetization of the residual IRM (open triangles) after shock demagnetization with peak stress intensities of 8 kbar

The demagnetization by stress waves was carried out for remanent magnetizations parallel and perpendicular to the propagating direction of the stress waves, but no systematic difference could be found.

To obtain an idea about the coercive forces of the remanent magnetizations that can be erased by a certain peak stress amplitude the demagnetization by shock can be compared to the ac-demagnetization experiments. Ac-demagnetization of a residual remanent magnetization after impacting can give similar information. By applying ac-demagnetization to such a residual remanent magnetization, the remanence generally decreases only slightly until a certain peak value of the alternating field is reached, where it then decreases approximately as in ac-demagnetization of the original remanent magnetization of the same type. Because the residual remanent magnetization is not constant at low ac-fields (of the order of 100 Oe, Figs. 7 and 8), we must assume that magnetic grains with low coercive forces have not been completely demagnetized by the applied stress waves.

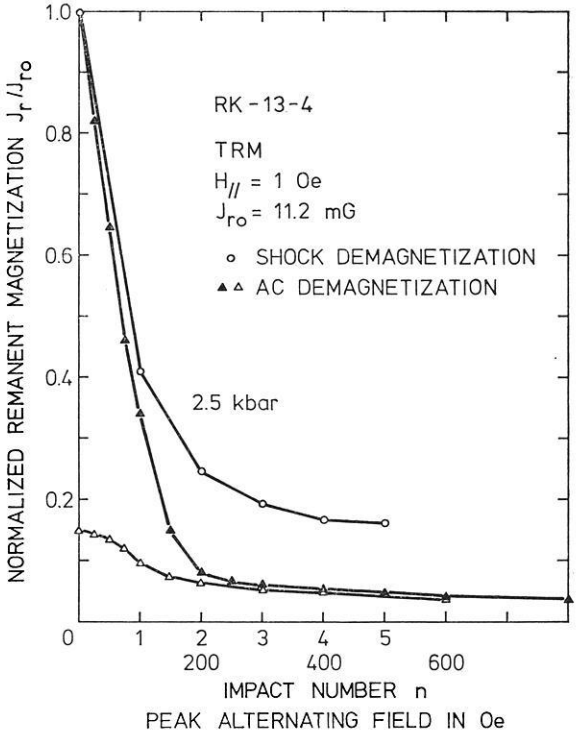

Fig. 8. Shock demagnetization (open circles) and ac-demagnetization (full triangles) of low field thermoremanent magnetization. Subsequent ac-demagnetization of the residual TRM after shock demagnetization with peak stress intensities of 2.5 kbar

On the other hand the ac-demagnetization curves of the residual remanent magnetization always lie below the ac-demagnetization curve of the original remanent magnetization. Therefore also grains with high coercive forces must have been affected by the stress waves.

The influence of the peak stress intensity was studied in two different ways. In one series of experiments the samples having the original remanent magnetization were impacted several times with the same velocity, beginning with a low velocity, until a certain final steady state was achieved. Then the sample having the residual remanent magnetization was impacted several times with a higher velocity, and so on (Fig. 7). In another series of experiments the demagnetization was made by impacting samples having always the original remanent magnetization with different velocities. Both experimental procedures gave similar results.

Fig. 7 shows shock demagnetization and ac-demagnetization of IRM produced at room temperature in a magnetic field of 1000 Oe. For com-

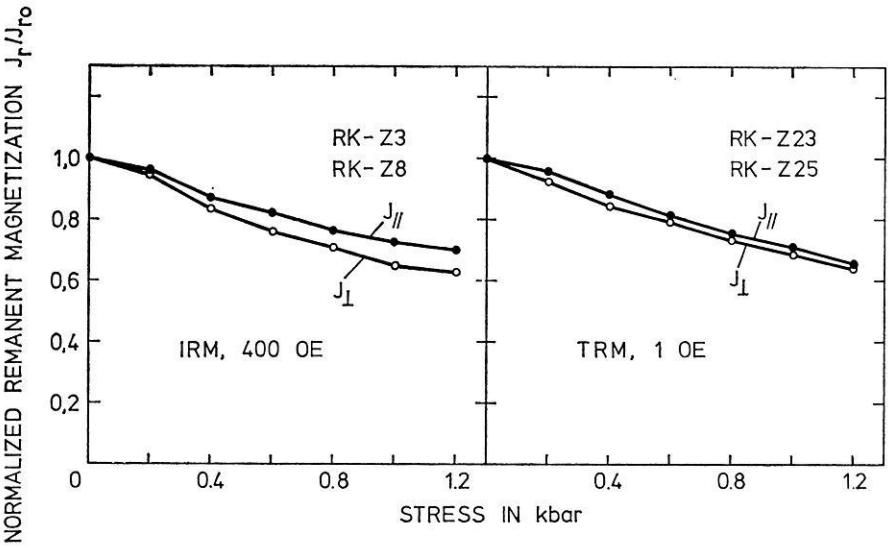

Fig. 9. Demagnetization of strong field isothermal remanent magnetization and low field thermoremanent magnetization by static uniaxial stress (after Zinsser, 1970). The residual remanence $J_r(H^0 P^+ P^0 H^0)$ is plotted as function, of the applied stress

parison the demagnetization by static uniaxial compressive stress of an IRM produced at 400 Oe in the same rock is shown (Zinsser, 1970). The difference of the magnetizing fields in both cases is not significant as in the used stress range both shock and static stress demagnetization hardly affect magnetizations of grains with coercive forces higher than 200 to 300 Oe. From Fig. 7 it can be seen that peak stresses of 2.5 kbar correspond to a demagnetizing ac-field of about 100 Oe, 5.5 kbar to about 200 Oe and 8.0 kbar to about 250 Oe. An extrapolation of the demagnetization rates obtained by static experiments to the stresses used in the dynamic experiments leads approximately to the same values (Figs. 7 and 9).

Results of shock demagnetization and ac-demagnetization of a TRM produced in a field of 1 Oe are shown in Fig. 8. Demagnetization of TRM by static uniaxial compression is shown in Fig. 9 (Zinsser, 1970). The RK-basalt has a low Curie-temperature of about 220 °C. TRM can therefore be produced several times without major alterations of the samples due to heating, provided the heating time does not exceed a few minutes (Creer, Petersen and Petherbridge, 1970). TRM produced several times in the same sample has the same value and the coercivity spectra are also identical. We can therefore assume that no important changes have occured in the homogeneous titano-magnetites by the heating operations. — The shock demagnetization of strong field IRM and weak field TRM is very similar.

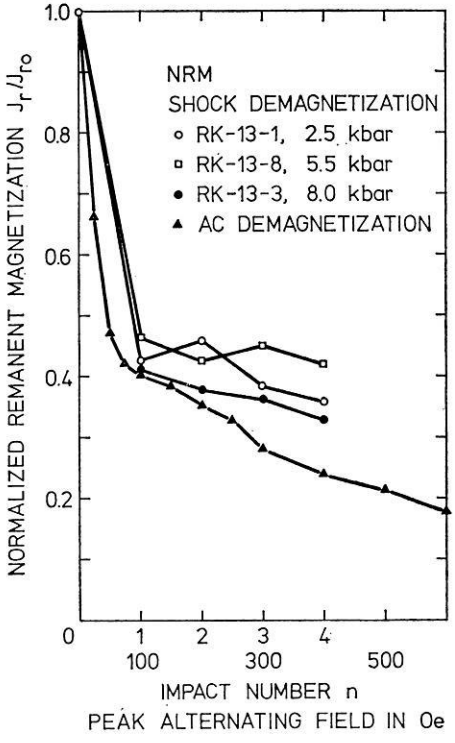

Fig. 10. Shock demagnetization and ac-demagnetization of NRM. $J_{r0,13-1} = 2.05$ mG, $J_{r0,13-3} = 2.70$ mG, $J_{r0,13-8} = 2.36$ mG

This corresponds to the similarity of the ac-demagnetization of strong field IRM and weak field TRM. As in the case of IRM, the extrapolation of static demagnetization experiments leads to the demagnetization values obtained by shock demagnetization of TRM (Figs. 8 and 9).

Shock demagnetization and ac-demagnetization of the natural remanent magnetization of the RK-basalt are shown in Fig. 10 (intensity) and Fig. 11 (direction). The NRM consists of both an unstable, viscous component and a stable TRM component (Soffel, 1968). In the demagnetization curves showing the decrease of intensity scattering is rather high. This is mainly due to a viscous magnetization of about 0.2 to 0.3 mG acquired by the samples in the Earth's field in a few minutes which is about 10% of the NRM intensity. Thus a relationship between the demagnetization effect and the peak stress used can not be obtained from these demagnetization curves. The comparison of the changes of the direction of the NRM with ac-demagnetization and shock demagnetization however shows clearly that with increasing peak stress the final stable direction is approached

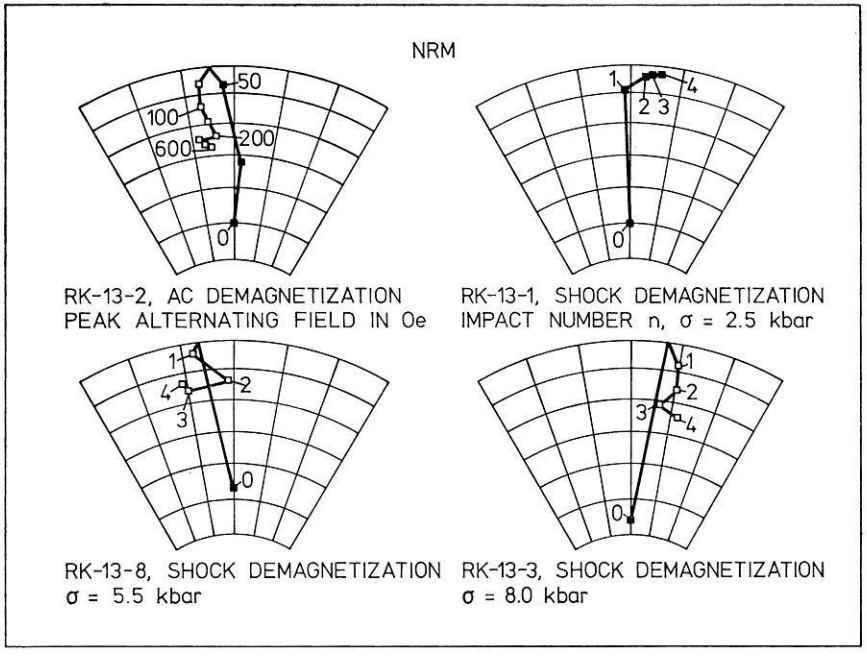

Fig. 11. Shock demagnetization and ac-demagnetization of NRM showing changes of the direction. The grid intervall is 10 degrees. A common zero original declination was chosen as the samples were not orientated. Full squares: upper hemisphere, open squares: lower hemisphere

asymptotically. From Fig. 11 it follows that 2.5 kbar correspond to a peak ac-field of about 50—75 Oe, 5.5 kbar to about 75—125 Oe and 8 kbar to about 150—200 Oe (see also Fig. 7).

7. *Conclusion*

In the preceeding sections the main features of the magnetizing and demagnetizing effect of stress waves with peak stress intensities between 2.5 and 10 kbar have been described for a basaltic rock from the Rauher Kulm. The characteristics of shock magnetization and shock demagnetization in the high stress range are similar to those in the low stress range and also to those of experiments with static uniaxial compressive stress. It is thus probable that existing theories for static experiments can be applied to dynamic experiments, taking into account the short duration of the stress impulse and the effect of repeated shocks. Nagata (1971) applied the theory of Nagata and Carleton (1969), which was established for static experiments, to his dynamic experiments in the low stress range. In this theory it is as-

sumed that the changes of remanent magnetization are due to irreversible movements of 90° domain walls. The results in the high stress range agree in general with this theory but as the RK-basalt shows both single-domain and multi-domain behaviour, it is probable that in the stress range from 2.5 to 10 kbar both irreversible displacements of 90° domain walls and irreversible rotations of spontaneous magnetization contribute to changes of the remanent magnetization (Dunlop, Ozima and Kinoshita, 1969; Nagata, 1970; Stacey and Johnston, 1972). Theories for single-domain particles must also be considered. — In the future more detailed investigations of the stability of SRM and the relation to the coercivity spectrum are desirable, using materials with selected spectra of coercive forces and remanent magnetizations within a defined coercive force intervall. The effect of the duration of the stress impulse and a possible relation with the viscous remanence properties of the material also deserve more detailed investigations. The advanced shock effect (Nagata, 1971) which is described by $J_r(SH+H^e)$ has not been investigated in this study. It will be dealt with in a further study in connection with measurements of the magnetic after-effect on the RK-basalt.

Acknowledgments. The authors wish to thank Prof. G. Angenheister, director of the Institut für Angewandte Geophysik, University of Munich, for his encouragement and support. They are also grateful to Dr. N. Petersen, Dr. E. Schmidbauer, Dr. A. Schult, Prof. H. Soffel and Dipl.-Phys. H. Zinsser for many helpful discussions. The work has been supported by the Deutsche Forschungsgemeinschaft.

References

Abdullabekov, K.N., Bezuglaya, L.S., Golovkov, V.P., Skovorodkin, Yu.P.: On the possibility of using magnetic methods to study tectonic processes. Tectonophysics *14*, 257–262, 1972

Barsukov, O.M., Skovorodkin, Y.P.: Magnetic observations in the region of the Medeo blast work. Izvestiya, Solid Earth, 310–311, 1969 (English edition)

Creer, K.M., Petersen, N.: Thermochemical magnetization in basalts. Geophys. J. *35*, 501–516, 1969

Creer, K.M., Petersen, N., Petherbridge, J.: Partial self-reversal of remanent magnetization and anisotropy of viscous magnetization in basalts. Geophys. J. *21*, 471–483, 1970

Davis, P.M., Stacey, F.D.: Geomagnetic anomalies caused by a man-made lake. Nature *240*, 348–349, 1972

Domen, H.: A note on remanent magnetism caused by impulsive pressure. Bull. Fac. Educ. Yamaguchi Univ. *10*, 71–76, 1961

Dunlop, D.J., Hanes, J.A., Buchan, K.L.: Indices of multidomain magnetic behaviour in basic igneous rocks: Alternating-field demagnetization, hysteresis and oxide petrology. J. Geophys. Res. *78*, 1387–1393, 1973

Dunlop, D. J., Ozima, M., Kinoshita, H.: Piezomagnetization of single-domain grains: A graphical approach. J. Geomagn. Geoelectr. *21*, 513–518, 1969

Gerlach, W.: Über den Erschütterungseinfluß auf die Magnetisierung und seine Temperaturabhängigkeit. Helv. Phys. Acta *22*, 142–148, 1949

Hargraves, R. B., Perkins, W. E.: Investigations of the effect of shock on natural remanent magnetism. J. Geophys. Res. *74*, 2576–2589, 1969

Hasbrouck, W. P., Allen, J. H.: Quasi-static magnetic field changes associated with the Cannikin nuclear explosion. Bull. Seismol. Soc. Am. *62*, 1479–1487, 1972

Helbig, K.: Optimum configuration for the measurements of the magnetic moment of samples of cubical shape with a flux-gate magnetometer. J. Geomagn. Geoelectr. *17*, 373–380, 1965

Hornemann, U., Pohl, J., Bleil, U.: A compressed air gun accelerator for shock magnetization and demagnetization experiments up to 20 kbar. J. Geophys. *41*, 13–22, 1975

Johnston, M. J. S., Stacey, F. D.: Transient magnetic anomalies accompanying volcanic eruptions in New Zealand. Nature *224*, 1289–1290, 1969

Koenigsberger, J. G.: Über remanenten Magnetismus von Gesteinen. Gerlands Beitr. Geophys. *35*, 204–216, 1932

Koenigsberger, J. G.: Die Abhängigkeit der natürlichen remanenten Magnetisierung bei Eruptivgesteinen von deren Alter und Zusammensetzung. Beitr. angew. Geophys. *5*, 193–246, 1936

Kulterman, R. W., Neilson, F. W., Benedick, W. B.: Pulse Generator based on high shock demagnetization of ferromagnetic material. J. Appl. Phys. *29*, 500–501, 1958

Lowrie, W., Fuller, M.: On the alternating field demagnetization characteristics of multi-domain thermoremanent magnetization in magnetite. J. Geophys. Res. *76*, 6339–6349, 1971

Nagata, T.: Effects of a uniaxial compression on remanent magnetizations of igneous rocks. Pageoph *78*, 100–109, 1970

Nagata, T.: Basic magnetic properties of rocks under the effects of mechanical stresses. Tectonophysics *9*, 167–195, 1970

Nagata, T.: Introductory notes on shock remanent magnetization and shock demagnetization of igneous rocks. Pageoph *89*, 159–177, 1971

Nagata, T., Carleton, B. J.: Notes on piezo-remanent magnetization of igneous rocks (III). J. Geomagn. Geoelectr. *21*, 623–645, 1969

Petersen, N.: Beobachtung einiger mineralogischer und magnetischer Eigenschaften dreier Basaltproben nach unterschiedlicher thermischer Behandlung. J. Geomagn. Geoelectr. *18*, 463–479, 1966

Pohl, J.: Magnetisierung und Entmagnetisierung von Stahl und Magnetit durch Stoßwellen. Unpublished report. Institut für Angewandte Geophysik, Universität München, 1967

Pohl, J.: Magnetisierung der Gesteine und Interpretation der Anomalien des Erdmagnetfeldes im Ries-Krater. Dissertation, Universität München, München 1971

Refai, E.: Magnetfeld und Magnetisierung der Basaltvorkommen im Raum von Kemnath. Z. Geophys. *27*, 175–187, 1960

Rikitake, T.: Geomagnetism and earthquake prediction. Tectonophysics *6*, 59–68, 1968

Schmidbauer, E., Petersen, N.: Some magnetic properties of two basalts under uniaxial compression measured at different temperatures. J. Geomagn. Geoelectr. *20*, 169–180, 1968

Schmucker, U.: Gesteinsmagnetische Untersuchungen und Experimente am Basalt des Steinberges bei Barlissen. Abh. Akad. Wissensch. Göttingen, Math.-Phys. Klasse, Nr. *26*, 100 S., Göttingen 1957

Shapiro, V. A., Ivanov, N. A.: The stability parameters of dynamic magnetization compared with other types of remanent magnetization. Izvestiya, Solid Earth 681–685, 1966 (English edition)

Shapiro, V. A., Ivanov, N. A.: Dynamic remanence and the effect of shocks on the remanence of strongly magnetic rock. Dokl. Akad. Nauk. USSR *173*, 1065–1068, 1967

Short, N. M.: Effects of shock pressures from a nuclear explosion on mechanical and optical properties of granodiorite. J. Geophys. Res. *71*, 1195–1215, 1966

Soffel, H.: Die Bereichsstrukturen der Titanomagnetite in zwei tertiären Basalten und die Beziehung zu makroskopisch gemessenen magnetischen Eigenschaften dieser Gesteine. Habilitationsschrift, Naturwiss. Fak. Univ. München, 1968

Stacey, F. D.: The seismomagnetic effect. Pageoph *58*, 5–22, 1964

Stacey, F. D., Barr, K. G., Robson, G. R.: The volcano-magnetic effect. Pageoph *62*, 96–104, 1965

Stacey, F. D., Johnston, M. J. S.: Theory of the piezomagnetic effect in titanomagnetite-bearing rocks. Pageoph *97*, 146–155, 1972

Talwani, P., Kovach, R. L.: Geomagnetic observations and fault creep in California. Tectonophysics *14*, 245–256, 1972

Zinsser, H.: Induzierte und remanente, insbesonders thermoremanente Magnetisierung von Proben zweier Basaltvorkommen (Rauher Kulm und Parkstein, Oberpfalz) in Abhängigkeit von einaxialer Druckspannung. Diplomarbeit, Institut für Angewandte Geophysik, Universität München, 1970

Dr. J. Pohl
Institut für Angewandte Geophysik
der Universität
D-8000 München 2
Theresienstr. 41
Federal Republic of Germany

Dr. U. Bleil
Institut für Geophysik
der Ruhr-Universität
D-4630 Bochum
Buscheystrasse
Federal Republic of Germany

Dr. U. Hornemann
Arbeitsgruppe für
Ballistische Forschung
D-7858 Weil
Hauptstr. 18
Federal Republic of Germany

J. Geophys. 41, 43–61, 1975

K-Ar-Altersbestimmungen an Vulkaniten bekannter paläomagnetischer Feldrichtung.

I. Oberpfalz und Oberfranken

W. Todt und H. J. Lippolt

Laboratorium für Geochronologie der Universität, Heidelberg

Eingegangen am 17. Juli 1974

K-Ar Age Determinations on Volcanics with Known Paleomagnetic Field Parameters.

I. Oberpfalz and Oberfranken

Abstract. Potassium-argon age determinations on 18 basaltic rocks from Oberpfalz and Oberfranken (Germany) and on a lava from western Bohemia have been made.

The ages cover the interval from 24 to 19 m.y., which corresponds to Aquitanian – Helvetian times. The basalt from Steinwitzhügel and the lava from Kammerbühl are exceptions (29 m.y., Upper Oligocene; <2 m.y., Pleistocene respectively). The alleged occurrence of Pliocene volcanics in this area is thus excluded. The coal deposits of Klausen considered to be slightly older than this volcanism are consequently of Lower Miocene age.

These age determinations together with paleomagnetic data taken from the literature date two reversals of the terrestrial magnetic field: one from reverse to normal at 23.0 ± 1.4 m.y., the other from normal to reverse at 20.7 ± 1.0 m.y. ago.

Key words: Potassium-Argon Dating – Upper Tertiary Volcanics – Paleomagnetism.

Einführung

Die Basaltvorkommen der Oberpfalz und von Oberfranken lassen sich stratigraphisch nur sehr ungenau als Tertiär datieren (Schröder, 1962; Schröder und Siegling, 1966). Die genauere zeitliche Einstufung kann nur mit Hilfe von isotopischen Altersbestimmungen gelöst werden.

An Basalten dieses Gebietes sind von Seiten des Instituts für Angewandte Geophysik, München, paläomagnetische Untersuchungen durchgeführt worden. Dabei fanden sich sowohl normal magnetisierte Vorkommen als auch solche mit inverser Magnetisierungsrichtung. Diese Vulkanite haben demnach zu verschiedenen Zeiten den Curiepunkt unterschritten.

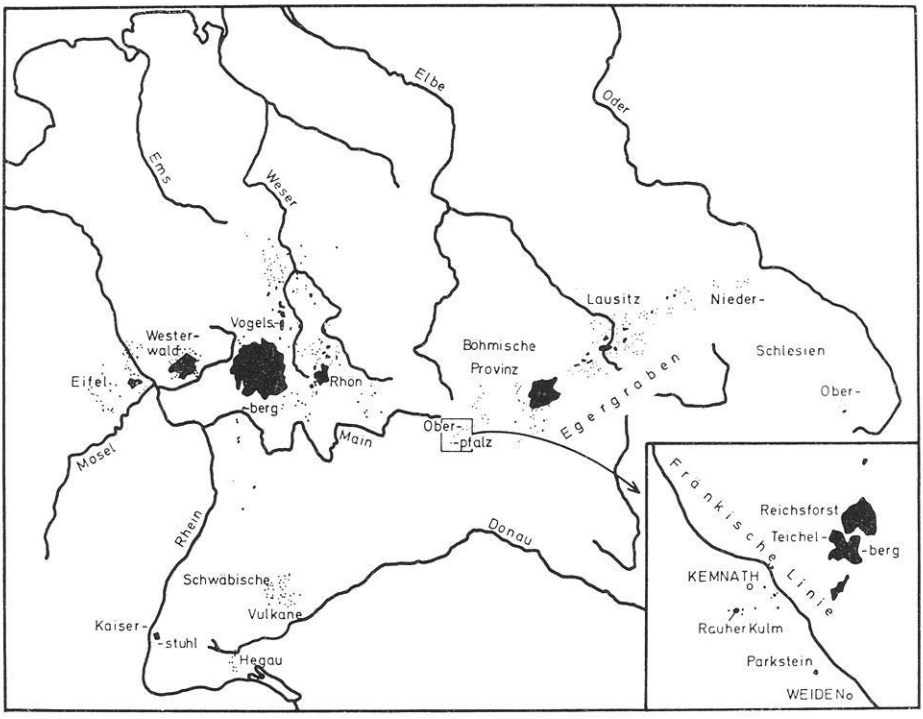

Abb. 1. Karte der tertiären Vulkanite Mitteleuropas (nach Soffel und Supalak, 1968) mit Lage des Gebietes der datierten Vulkanite

Es war zu hoffen, mittels Kalium-Argon-Altersbestimmungen an diesen Basalten die Unsicherheit bezüglich ihrer Alter beseitigen zu können. Außerdem sollten die Altersbeziehungen des Vulkanismus dieses Gebietes zu dem der Nachbargebiete aufgeklärt und mindestens eine im Tertiär aufgetretene Umkehrung der Richtung des Erdmagnetfeldes zeitlich festgelegt werden. Zu diesem Zweck wurden neunzehn vulkanische Gesteine der Oberpfalz, von Oberfranken und von Böhmen untersucht.

Geologische Grundlagen

Die untersuchten Basaltvorkommen stellen die westlichsten Ausläufer einer Zone von Vulkaniten dar, die im benachbarten, tertiär angelegten Eger-Graben aufgedrungen sind (Abb. 1). Im Osten des Eger-Grabens bilden die vulkanischen Durchbrüche zwei große und einheitliche Gebirge, das Böhmische bzw. das Duppauer Gebirge. In Richtung Westen sind die Vulkanit-Vorkommen in Form kleinerer Eruptionszentren räumlich

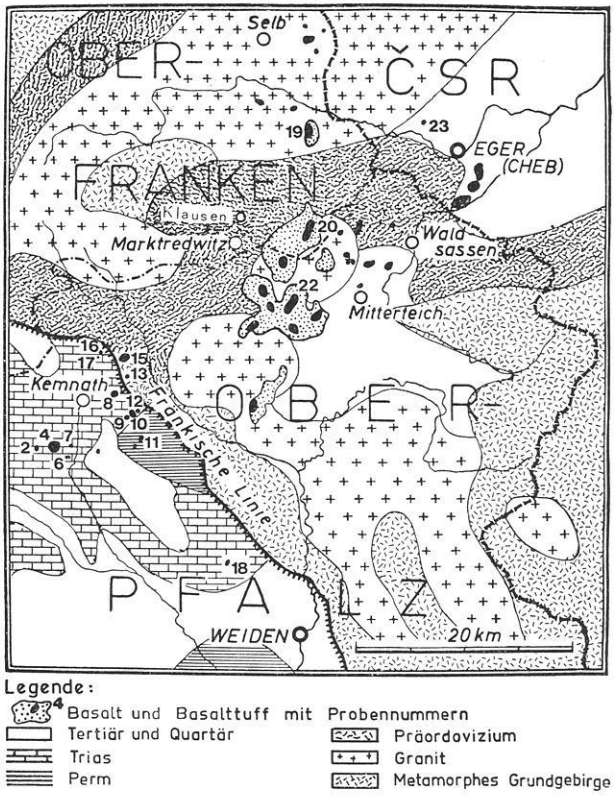

Abb. 2. Geol. Karte (nach Wurm, 1961 vereinfacht) der tertiären Vulkanite Oberfrankens, der Oberpfalz und Westböhmens mit den Proben-Nummern (Nr. 2 bis Nr. 23) der datierten Gesteine

getrennt (Abb. 2). Der Reichsforst (Nr. 20) und der Teichelberg (Nr. 22) bilden noch relativ große zusammenhängende Eruptionsgebiete. Weiter westlich im Bereich der Fränkischen Linie, dem Verwerfungssystem zwischen dem sogenannten Alten Gebirge und dem mesozoischen Sedimentbecken, finden sich nur noch sehr kleine Basaltvorkommen. Es gibt sowohl gangförmige Eruptionen, wie z. B. am Parkstein (Nr. 18), als auch auf Spalten aufsitzende Vorkommen mit voneinander getrennten Durchbrüchen. Beispiele sind die drei Vorkommen Kusch (Nr. 9), Schloßberg (Nr. 10) und Galgenberg (Nr. 12) bei Waldeck. Die Spalten streichen NE—SW, also parallel dem Streichen der Vulkanzone, die sich von der Oberpfalz bis zur Niederlausitz erstreckt, und parallel dem Streichen des tertiären Egergrabens. Daneben kommen deckenförmige Oberflächenergüsse vor. Diese sind aber nur in Form von Denudationsresten wie z. B. den

Basaltvorkommen Großer Teichelberg (Nr. 22) und Reichsforst (Nr. 20) vorhanden. Die Basalte der Oberpfalz befinden sich heute in einem fortgeschrittenen Abtragungsstadium. Das Auftreten von Tuffen und Laven deutet auf Eruptionen mit Explosions- und Effusionsphasen hin.

In den meisten Fällen ist der ganze vulkanische Oberbau zerstört und bis auf den Magmenzufuhrkanal abgetragen. Der Rauhe Kulm (Nr. 4) und der Parkstein (Nr. 18) stellen solche aus ihrer Umhüllung herauspräparierte Schlotfüllungen dar. Der Parkstein (Nr. 18) trägt noch einen Kranz tertiärer Sande und Konglomerate. Das Auftreten von Tuffen bei einigen Basaltvorkommen zeigt, daß es sich um Effusiv-Gesteine handelt. Die Eruptionen haben im Nebengestein keine oder nur geringe Störungen hervorgerufen, die nicht weiter als ca. einen Meter vom Kontakt reichen (Küh-Hübel, Nr. 7, Wurm, 1961, S. 320). Die Umwandlung an den Fremdeinschlüssen, die aus dem Untergrund mitgerissen wurden, sind dagegen wesentlich stärker als die des Nebengesteins.

Nach geologischen Kriterien begannen die vulkanischen Eruptionen im Böhmischen Mittelgebirge im Oligozän und reichten bis ins Miozän, im Dubbauer Gebirge haben sie im Aquitan begonnen (Wurm, 1961; Schröder, 1962; Schröder und Siegling, 1966). Für die stratigraphische Einstufung der Basalte der Oberpfalz und von Oberfranken liegen nur wenige Indizien vor. So findet man örtliche Verknüpfungen der Basalte mit tertiären Ablagerungen, zum Teil mit Braunkohlen. Gümbel (1868) stellte die Basalteruptionen der Oberpfalz und Oberfrankens kurz vor oder spätestens in die Zeit der Bildung der tertiären Braunkohlenschichten. Die Braunkohlenflöze wurden von Kirchheimer (1937) und Gothan (1941) hauptsächlich aufgrund von Fossilfunden im Klausener Vorkommen mit den Rheinischen Braunkohlen parallelisiert. Das Rheinische Hauptflöz wird ins untere bis mittlere Miozän gestellt (Anderson, 1966), so daß auch für die hier untersuchten Basalte miozäne oder jüngere Alter zu erwarten wären. Da man in den tertiären Schichten nirgends Basaltgerölle gefunden hat, ist es jedoch wahrscheinlich, daß der Basaltvulkanismus jünger als die tertiären Sedimente ist (Wurm, 1932). Ausführliche Darstellungen weiterer Argumente finden sich bei Wurm (1961, S. 313). Eine weitere zeitliche Festlegung der Basalte ist mit Hilfe von Gesteinseinschlüssen denkbar, deren Alter bekannt sind. Die meisten gefundenen Einschlüsse stammen aus dem Keuper oder aus der Oberkreide. Schröder (1962) fand in zwei Schloten Sedimenteinschlüsse, die eventuell auf ein jungpliozänes bis pleistozänes Alter der Schlote hindeuten. Allerdings ist das pliozäne Alter der fraglichen Schottereinschlüsse nicht sicher. Tillmann (1956) hatte diese Schotter an das Tertiär der miozänen Braunkohle des Naab-Raumes angeknüpft, doch das Alter dieser etwa 30 km von dem Basaltgebiet entfernt liegenden Braunkohlen ist nicht gut durch Fossilien gestützt. Einzelne Eruptionen (z. B. Kammerbühl und Eisenbühl bei Eger) erfolgten erst im

Pleistozän, was man aus der lockeren Aufschüttung ihrer Förderprodukte bzw. aus deren Lage zum Fluß-Terrassensystem ableitet (vgl. z. B. Lochmann, 1961). Aufgrund dieser geologischen Hinweise allein kann daher nicht eindeutig geschlossen werden, daß sich die vulkanische Aktivität im Raum Oberpfalz und Oberfranken vom Tertiär bis ins Pleistozän fortgesetzt hat.

Die untersuchten Proben

Die Gesteine der Oberpfalz und Oberfrankens sind dichte, dunkelgraue Gesteine und gehören ausschließlich in die Basalt-Gruppe, im Gegensatz zu der Vielfalt der Magmen-Differentiate im Osten des Eger-Grabens (Wurm, 1961, S. 317). Einzelne Vorkommen sind außerordentlich reich an endogenen Einschlüssen, z. B. Peridotit und Pyroxenit. Der mikroskopische Befund der Basalte zeigt meist eine sehr feinkörnige Grundmasse aus Augit, Magnetit, Plagioklas, meist auch Biotit und in ihr Einsprenglinge von Olivin und Augit. In einigen Basalten ist Glas in der Grundmasse vorhanden. Der Feldspat kann durch Nephelin ganz oder teilweise vertreten sein. Nach Richarz (1920) werden die Basalte der Oberpfalz in die Gesteinsgruppen Feldspatbasalt, Nephelinbasalt und Nephelinführender Feldspatbasalt unterteilt. Nach der Definition von Wimmenauer, (1972) sind von den 18 untersuchten Gesteinen dieses Gebietes 15 Olivin-Nephelinite und 3 Alkali-Olivin-Basalte. Die Lava vom Kammerbühl/Eger ist als Olivin-Nephelinit anzusprechen. Refai (1960) teilte die Olivin-Nephelinite der Oberpfalz in zwei Typen ein: 1. Basalte vom Schloßbergtyp, mittel- bis feinkörnig, die sich durch Einschlüsse von Olivinknollen auszeichnen. Dazu zählte sie neben den Gesteinen vom Schloßberg (Nr. 10) die vom Rauhen Kulm (Nr. 4). 2. Basalte des Kuschbergtyps, die eine porphyrische Struktur zeigen und als Einsprenglinge idiomorphe Olivine enthalten. Dieser Typ führt sehr viele, zumeist weitgehend assimilierte Nebengesteinseinschlüsse. Neben dem Gestein vom Kuschberg (Nr. 11) rechnete Refai (1960) zu dieser Gruppe diejenigen vom Küh-Hübel (Nr. 7), vom Lerchenbühl (Nr. 6) und von den beiden Aigner Kuppen (Nr. 16 und Nr. 17).

Im folgenden sind die datierten Gesteine aufgeführt. Angegeben sind jeweils Lab.-Nr., Lokalität, Meßtischblatt, Koordinaten sowie die Gesteinbezeichnungen (nach Wimmenauer, 1972; in Klammern nach Richarz, 1920) mit Angabe des Erhaltungsgrades (Definition nach Horn *et al.*, 1972).

Angaben über Einschlüsse (exogene Einschlüsse) beziehen sich naturgemäß nur auf die untersuchten Dünnschliffe; es ist nicht gesagt, jedoch auch nicht auszuschließen, daß solche Einschlüsse auch im Probenmaterial waren.

Oberpfalz

Probennummer	
2	Kleiner Kulm bei Neustadt, Blatt Kemnath 6137 r 448800, h 552115; Olivin-Nephelinit (Feldspatbasalt), sehr frisch, wenig braungelbes Glas.
4	Rauher Kulm bei Neustadt, Blatt Kemnath, r 448918, h 552125. Olivin-Nephelinit (Nephelinbasalt), frisch.
6	Lerchenbühl bei Weha, Blatt Kemnath, r 449055, h 552089. Olivin-Nephelinit, sehr frisch.
7	Küh-Hübel bei Weha, Blatt Kemnath, r 449070, h 552127. Olivin-Nephelinit (Nephelin-Basalt), unfrisch, Quarz als Einschluß mit Reaktionssaum, Sanidin als Neubildung?
8	Anzenberg bei Kemnath, Blatt Kemnath, r 449430, h 552577. Olivin-Nephelinit, frisch, Glas (geschmolzene Quarze), Einschlüsse.
9	Kusch, SW vom Schloßberg bei Waldeck. Blatt Kemnath, r 449590, h 552420. Olivin-Nephelinit, unfrisch, sehr wenig Biotit.
10	Schloßberg bei Waldeck, Blatt Kemnath, r 449630, h 552455. Olivin-Nephelinit, frisch. Glasbutzen bis zur Größe der Augiteinsprenglinge, Entglasungserscheinungen.
11	Kuschberg bei Atzmannsberg, Blatt Kemnath, r 449745, h 552210. Olivin-Nephelinit, unfrisch, keine Augiteinsprenglinge, Glas, (Grundgebirgs-?) Einschlüsse.
12	Galgenberg (Kalvarienberg) bei Waldeck. Blatt Kemnath, r 449680, h 552495. Olivin-Nephelinit, sehr frisch, sehr wenig Biotit.
13	Armesberg (Armannsberg) bei Zisst. Blatt Kemnath, r 449632, h 552830. Alkali-Olivin-Basalt, frisch. Erz als Einsprenglinge, Rhönit, Biotit?.
13M2	Mineralpräparat: ca. 60% Augit, $\geqslant$ 25% Plagioklas, wenig Olivin und Matrix, hergestellt aus Probe 13.
14	Aigner Kuppe-Nord, Lesestein, Blatt Ebnath 6037. Olivin-Nephelinit, unfrisch, keine Einschlüsse.
15	Steinwitzhügel bei Wunschenberg, Blatt Ebnath, r 449575, h 552925. Alkali-Olivin-Basalt (Nephelin-führender Feldspatbasalt), frisch.
16	Aigner Kuppe — Nord, Blatt Ebnath, r 449410, h 553015. Olivin-Nephelinit, unfrisch, mit Feldspat -Nestern.
17	Aigner Kuppe — Süd, Blatt Ebnath, r 449400, h 553000. Olivin-Nephelinit, unfrisch.
18	Parkstein, Blatt Parkstein 6238, r 450520, h 551063. Olivin-Nephelinit (Feldspat-Basalt), frisch, als Einschlüsse korrodierte Quarze mit Pyroxenkränzen.
22	Großer Teichelberg bei Großschlattengrün, Blatt Waldershof 6038, r 451190, h 553590. Olivin-Nephelinit (Nephelin-Basalt), frisch.

Oberfranken

19	Steinberg bei Hohenberg, Blatt Waldsassen 5939, r 451312, h 555065, Olivin-Nephelinit, frisch.
20	Reichsforst bei Brand, Blatt Marktredwitz 5938. 20E: r 451116, h 554120 Alkali-Olivin-Basalt, unfrisch. 20C: r 451154, h 554212 Alkali-Olivin-Basalt, unfrisch, abgerundeter Feldspat-Einschluß.

Böhmen

Probennummer

23 Kammerbühl bei Eger (verlassener Steinbruch ca 4 km NW von Eger auf tschechoslowakischem Gebiet).
Limburgitischer Olivin-Nephelinit, blasig; im Handstück große Einschlüsse sichtbar (ca. mm-groß); im Dünnschliff ein granitischer Einschluß mit Reaktionssaum aus basischem Glas.

Paläomagnetismus

Von den datierten Basalten der Oberpfalz und von Oberfranken sind paläomagnetische Messungen an orientiert entnommenen Handstücken oder Bohrkernen durchgeführt worden (Refai, 1960/1961; Soffel und Supalak, 1968; private Mitteilung Pohl und Soffel).

In der Tabelle 1 sind die paläomagnetische Polarität der untersuchten Vorkommen und die jeweiligen Autoren angegeben.

Das Vorkommen Großer Teichelberg (Nr. 22) hat nach magnetischen Feld-Untersuchungen von Söllner (1960) normal gerichtete Magnetisierung.

Unveröffentlichte Messungen an Basaltproben von Pohl und Soffel (private Mitteilung) deuten aber darauf hin, daß das Vorkommen invers magnetisiert ist.

Tabelle 1. Paläomagnetische Polarität der untersuchten Proben. N: normale Magnetisierung, R: inverse Magnetisierung

Proben-Nr.	Vorkommen	Polarität	Autoren
2	Kleiner Kulm	N	Refai, 1960; Refai, 1961
4	Rauher Kulm	N	Refai, 1960; Refai, 1961
6	Lerchenbühl	R	Refai, 1960; Refai, 1961
7	Küh-Hübel	R	Refai, 1960; Refai, 1961
8	Anzenberg	N	Refai, 1960; Refai, 1961
9	Kusch	N	Refai, 1960; Refai, 1961
10	Schloßberg	N	Refai, 1960; Refai, 1961
11	Kuschberg	R	Refai, 1960; Refai, 1961
12	Galgenberg	N	Refai, 1960; Refai, 1961
13	Armesberg	N	Refai, 1960; Refai, 1961
15	Steinwitzhügel	N	Refai, 1960; Refai, 1961
16	Aigner Kuppe N	R	Refai, 1960; Refai, 1961
17	Aigner Kuppe S	R	Refai, 1960; Refai, 1961
18	Parkstein	R	Soffel und Supalak, 1968
19	Steinberg	nicht untersucht	
20	Reichsforst	R	priv. Mitt. Pohl und Soffel
22	Gr. Teichelberg	R N	priv. Mitt. Pohl und Soffel Söllner, 1960

Experimentelle Arbeiten

Probennahme. Bei der Probennahme im Gelände und der Auswahl der Proben im Labor wurde darauf geachtet, möglichst Material ohne Fremdeinschlüsse zu erhalten. Von allen gesammelten Proben wurden Dünnschliffe untersucht, um zu klären, ob und wie gut sich diese Gesteine für eine K-Ar-Datierung eignen. Es zeigte sich, daß alle Gesteine ausreichend frisch waren, d.h. der primäre Mineralbestand unverändert war oder die feststellbaren Veränderungen nur die kaliumfreien Minerale betrafen. Auch zeigten die Untersuchungen, daß die gelegentlich auftretenden Fremdeinschlüsse in den Gesteinen so weit umgewandelt waren, daß kein wesentlicher Beitrag von ererbtem Argon zu erwarten war. Von den Basalt-Proben wurden Gesamtgesteinsalter bestimmt. Von den Vorkommen Armesberg (Nr. 13) wurden zusätzlich Augite zusammen mit Plagioklasen abgetrennt und daran das Mineralalter bestimmt.

Probenaufbereitung. Es wurden frische, von Verwitterungskrusten freie Stücke zerkleinert und aus dem Zerkleinerungsgut eine Konfraktion von 200—500 μ abgesiebt. Die Proben wurden anschließend im Ultraschallbad in destilliertem Wasser gewaschen. Zeolithe und Karbonate wurden teils durch Handauslesen, teils magnetisch entfernt. Zum Teil wurden sie mit HF weggelöst. Die Proben wurden geteilt und auf Kalium und Argon analysiert.

Kalium-Bestimmung. Das Kalium wurde mit Hilfe eines Zeiss-Flammenspektralphotometer in Emmission gemessen. Die Meßlösungen und die Vergleichslösungen wurden zur Beseitigung von Querbeeinflussungen mit Na und Ca gepuffert (Cooper, 1963). Der 1-σ-Fehler des Einzelwertes der Messungen liegt bei 0,5% (Horn *et al.*, 1972). Alle Bestimmungen wurden mindestens doppelt durchgeführt und aus den jeweiligen Ergebnissen wurden die Mittelwerte gebildet.

Argon-Bestimmung. Die in Nickelfolie eingepackten Proben von ca. 1/2 g wurden vor dem Aufschließen ca. 12 Std. lang bei 220° C im Vakuum ausgeheizt, um den Luftargonbeitrag zu reduzieren.

Der Verlust an radiogenem Argon liegt dabei nach Messungen von Lippolt *et al.* (1963) und Amaral *et al.* (1966) unter 1%. Danach wurden die Proben in einem Molybdäntiegel induktiv bei mehr als 1700 °C geschmolzen. Die Extraktion und die Reinigung der Gase aus den Gesteinen erfolgte in einer Glasapparatur mit Hg-Sperren. Das Argon wurde an einem ausheizbaren 180°-Sektorfeld-Massenspektrometer mit 5 cm Ablenkradius statisch gemessen. Für den Massendurchlauf wurde die Beschleunigungsspannung variiert. Die Auflösung $M/\Delta M$ betrug etwa 130 (5% Taldefinition).

Der Argon-Blank betrug bei diesen Messungen etwa 10^{-8} cm³. Als Spike wurde $2{,}1 \cdot 10^{-6}$ cm³STP ^{38}Ar zugegeben. Die Fehler für die Argon-

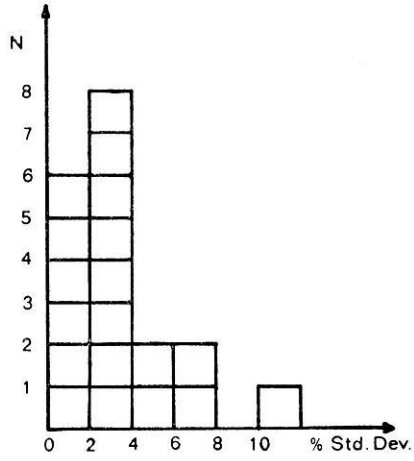

Abb. 3. Darstellung der Reproduzierbarkeit der vorliegenden Argon-Analysen in einem Histogramm. Aufgetragen ist die Häufigkeit der Standard-Abweichung (N) der Einzelwerte (aus jeweils 2–5 Messungen) gegen die Standard-Abweichungen (%)

Bestimmungen waren im Mittel ca. 4%. Die Häufigkeit der Standard-Abweichung der Einzelwerte ist im Histogramm Abb. 3 dargestellt. Von jeder Probe wurden zwei bis fünf Ar-Analysen durchgeführt und die Mittelwerte gebildet. Zwei der Vorkommen (Aigner Kuppe/Nord Nr. 16 und Nr. 17 und Reichsforst Nr. 20E und C) wurden anhand zweier verschiedener Proben datiert. Die Mittelwerte für die beiden jeweiligen Proben liegen einmal ca. 1,5%, im anderen Fall ca. 0,4% auseinander. Dies kann als Maß für die Reproduzierbarkeit der Mittelwerte angesehen werden.

Standards. Messungen an den internationalen Standards Bern 4M und USGS P-207 zeigten Übereinstimmung innerhalb von 5% (Horn *et al.*, 1972) mit den als Bestwert für diese Proben angesehenen Ergebnissen (Dalrymple und Lauphere, 1969). Messungen an dem Biotit-Standard LP-6 Bio des U.S. Geological Survey ergaben einen K-Gehalt von 8.37% und einen Argon-Gehalt von $4.32 \cdot 10^{-5}$ cm³ STP/g. Das Alter wurde zu 126.5 Ma berechnet.

Datierungsergebnisse und Diskussion

Die Ergebnisse der Kalium- und Argon-Analysen und die aus ihnen errechneten K-Ar-Alter sind in Tab. 2 aufgeführt und in Abb. 4 mit den Ergebnissen der paläomagnetischen Messungen korreliert. Einige vorläufige Ergebnisse dieser Untersuchungen wurden als Kurzfassung an anderer Stelle vorgestellt (Todt und Lippolt, 1972). Die Alterswerte sind

Tabelle 2. Analysenwerte der datierten Vulkanite. Die einzelnen Argon-Messungen einer Probe wurden innerhalb verschiedener Serien analysiert. Die radiogene Argonmenge (Mittelwert) ist in Spalte 4 in cm^3 STP/g Material angegeben. Der Anteil des Luftargonbeitrages ist je nach dem Ausheizungsgrad der jeweiligen Probe verschieden; die Extremwerte sind in der Spalte 5 in % angegeben. Die 7. Spalte gibt den quadratisch addierten Fehler der Argon- und Kaliumbestimmungen (1%-Fehler) an. Die verwendeten Konstanten sind: $\lambda = 0{,}532 \cdot 10^{-9} a^{-1}$; $R = 0{,}123$; $^{40}K = 0{,}0118\%$ des K_{gesamt}

Proben-Nr.	Lokalität	Kalium in Gew.-%	^{40}Ar rad in 10^{-6} cm^3 STP/g	Luftargon in %	Zahl der Ar-Messungen	Alter in Ma
		Oberpfalz				
2	Kleiner Kulm bei Neustadt	0,780	0,6777	16–66	5	21,9 ± 0,7
4	Rauher Kulm bei Neustadt	0,975	0,7999	18–64	3	20,7 ± 0,8
6	Lerchenbühl bei Weha	1,415	1,1494	39–53	4	20,5 ± 0,6
7	Küh-Hübel bei Weha	0,861	0,6905	36–56	3	20,2 ± 0,9
8	Anzenberg bei Kemnath	1,008	0,8903	30–54	4	22,3 ± 0,8
9	Kusch SW vom Schloßberg	0,803	0,7211	26–49	4	22,6 ± 0,6
10	Schloßberg bei Waldeck	1,213	0,9994	11–40	4	20,8 ± 0,7
11	Kuschberg	0,505	0,3849	24–60	3	19,2 ± 0,9

12	Galgenberg bei Waldeck	0,888	0,7782	18–58	3	22,1 ± 0,7
13	Armesberg	0,869	0,8021	26–55	4	23,3 ± 0,9
13M	Augit und Plag. aus 13	1,060	0,52591	38–77	2	23,2 ± 1,7
14	Aigner Kuppe Nord Lesestein	0,774	0,7028	51–76	3	22,9 ± 1,2
15	Steinwitzhügel bei Wunschenberg	0,526	0,6032	49–59	3	28,8 ± 1,8
16	Aigner Kuppe Nord	0,728	0,6705	62–70	3	23,2 ± 2,5
17	Aigner Kuppe Süd	0,688	0,5657	55–64	3	20,7 ± 1,2
18	Parkstein	0,793	0,7493	39–44	2	23,8 ± 1,1
22	Gr. Teichelberg	0,959	0,8126	57–60	2	21,4 ± 1,1
		Oberfranken				
19	Steinberg	0,799	0,7295	57–66	2	23,0 ± 1,3
20E	Reichsforst bei Brandt/Süd	1,060	0,9641	52–40	2	22,9 ± 1,0
20C	Reichsforst bei Brandt/Nord	0,872	0,7874	41–49	2	22,8 ± 1,8
		Westböhmen				
23	Kammerbühl bei Eger	1,450	0,1113	95	1	2,0 ± 1,8

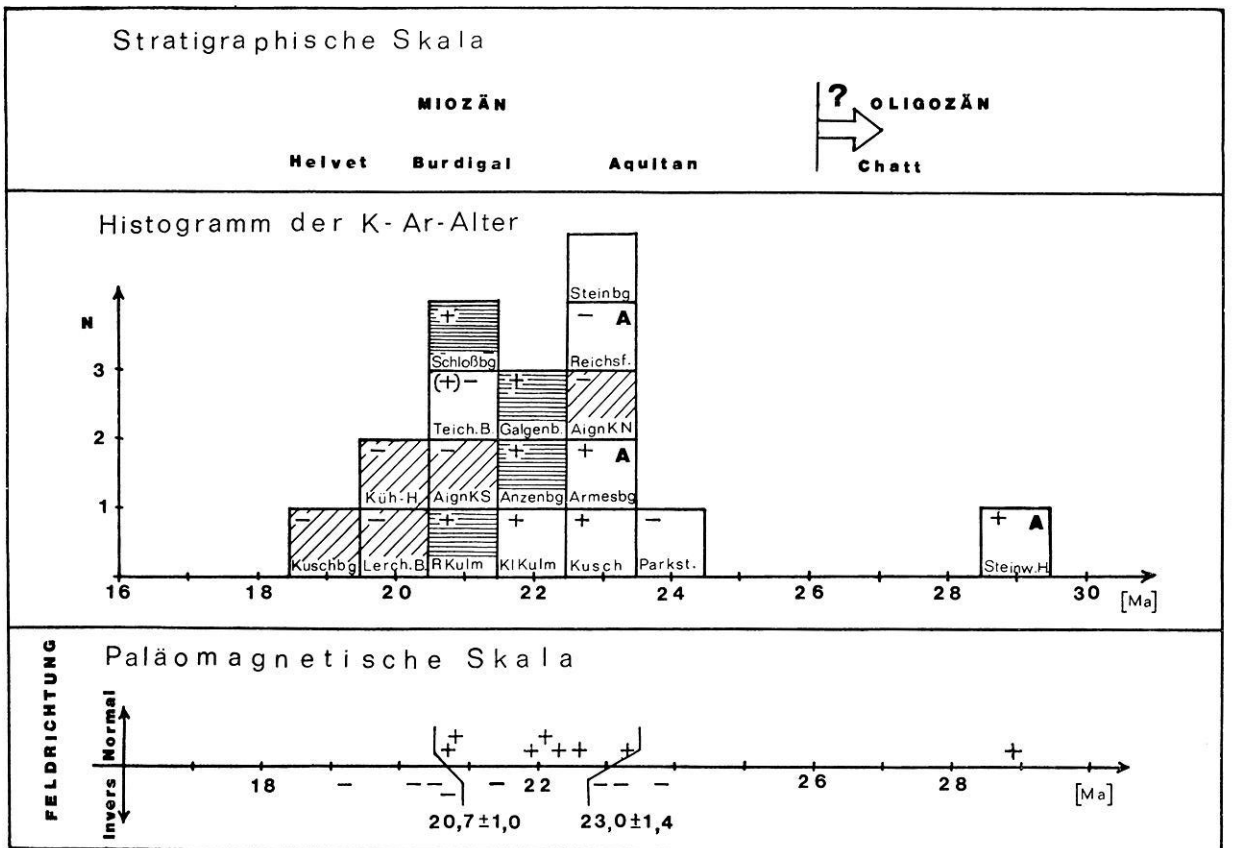

Abb. 4. Zusammenfassung der Ergebnisse: Oben: Stratigraphische Skala nach Funnel (1964). Mitte: Histogramm der K—Ar-Altersergebnisse. Waagrechte Schraffur: Typ Schloßberg, schräge Schraffur: Typ Kuschberg (nach Refai, 1960); — inverse Magnetisierung, + positive Magnetisierung. A—Alkali-Olivin-Basalte, alle anderen: Olivin-Nephelinite. Unten: Ausschnitt der paläomagnetischen Skala nach den hier verwendeten Daten

Modellalter, die unter den folgenden zwei Voraussetzungen aus den Analysenergebnissen errechnet wurden:

1. Es lagen geschlossene Systeme für Kalium und Argon vom Zeitpunkt der Eruption an bis heute vor.

2. Zur Zeit der Bildung enthielten die Gesteine nur Argon das der heutigen Zusammensetzung des Luftargons entspricht.

Aus den Alterswerten ergibt sich, daß die Aktivität einer ersten tertiären Eruptionsphase in Oberpfalz und in Oberfranken ca. 10 Ma gedauert hat. Alle untersuchten Vorkommen bis auf Kammerbühl haben Modellalter zwischen 19 Ma und 29 Ma mit einem deutlichen Schwerpunkt bei 22 Ma. Neun der 19 untersuchten Vorkommen liegen zwischen ca. 21 und 23 Ma. Der Höhepunkt der vulkanischen Tätigkeit in diesem Gebiet lag damit im Unteren Miozän, der Beginn spätestens an der Wende Oligozän/Miozän (nach Funnel, 1964). Falls man das Modellalter des Steinwitzhügels (Nr. 15) mit 29 Ma als Eruptionsalter deutet (siehe folgende Diskussion), begann die vulkanische Aktivität im unteren Ober-Oligozän. Die Probe Kuschberg (Nr. 11) zeigt das jüngste Modellalter mit 19,2 Ma — etwa die Grenze Unter-/Mittel-Miozän. Die Eruptionen dieser Phase müssen mindestens bis in diese Zeit fortgedauert haben. Die vulkanische Aktivität in der Oberpfalz und in Oberfranken fällt demnach in denselben Zeitabschnitt, der für das Böhmische bzw. das Duppauer Gebirge aufgrund stratigraphischer Beobachtungen angenommen wird.

Die Probe (Nr. 15) vom Vorkommen Steinwitzhügel ergab ein Modellalter von 29 Ma. Die Eruption dieses Basaltes fand somit im Oligozän statt, wenn man nach Funnel (1964) die Grenze Oligozän/Miozän bei $\geqslant$26 Ma annimmt. Da dieses Alter deutlich von den Altern der übrigen Basalte abweicht, liegt der Verdacht nahe, daß das hohe Alter auf Überschuß-Argon zurückzuführen ist. Einmal könnte der Basalt beim Auskristallisieren radiogenes Argon aus dem umgebenden Gestein und/oder aus Einschlüssen aufgenommen und eingebaut haben, zum anderen könnten unvollständig entgaste Einschlüsse im Probenmaterial zu einer Erhöhung des gemessenen Alters führen (Horn *et al.*, 1972). Um einen Hinweis hinsichtlich der zweiten Fehlermöglichkeit zu bekommen, haben wir Dünnschliffe von dem zur Analyse verwendeten Körnermaterial hergestellt. Untersuchungen dieser Dünnschliffe gaben keinen Hinweis auf derartige Einschlüsse. Ganz ausgeschlossen könnte Exzess-Argon nur durch Analysen an mehreren Mineralseparaten werden, die aber bei diesen feinkörnigen Basalten nur mit großem Aufwand hätten gewonnen werden können. Die von uns analysierten Proben waren frisch, d.h. K-haltige Mineralien waren nicht angegriffen. Daher ist ein durch K-Verlust erhöhtes Alter der Probe vom Steinwitzhügel sehr unwahrscheinlich. Obwohl wir keine Anzeichen für Exzess-Argon verdächtige Einschlüsse unmittelbar

im untersuchten Material haben, kann das Vorhandensein von Überschuß-Argon nicht ausgeschlossen werden. Der zum Steinwitzhügel direkt benachbarte Armesberg (Nr. 13) ist mit einem Modellalter von 23 Ma fast um 6 Ma jünger als dieser. Ein Mineralseparat aus Augit und Plagioklas aus dem Gestein vom Armesberg ergab ein zum Gesamtgesteinsalter konkordantes Ergebnis. Bei dieser Probe dürfte daher kein Exzess-Argon aufgetreten sein. Beide Vorkommen bestehen aus Alkali-Olivin-Basalten. Es muß daher offenbleiben, ob zwischen den Eruptionen dieser beiden benachbarten Basalte eine Zeitspanne von 6 Ma liegt oder ob der Alterswert des Vorkommens Steinwitzhügel überhöht ist.

Der Kammerbühl bei Eger (Nr. 23) ergab wegen des hohen Anteils von atmosphärischem Argon ($>95\%$) nur ein ungenaues K-Ar-Ergebnis von 2 ± 1 Ma. Dieser Alterswert bestätigt, daß im Quartär eine zweite Phase des jungen Vulkanismus auflebte. Das gefundene Alter sollte jedoch wegen des makroskopischen und mikroskopischen Auftretens von Einschlüssen in diesem Basalt und des eventuellen Vorhandenseins von ererbtem Argon im Analysenmaterial nur als Maximalalter verstanden werden. Die vorgenommene Altersabschätzung ordnet dem Kammerbühl also ein Alter jünger (oder gleich) 3 Ma zu.

Geologische Schlußfolgerungen

Schröder (1962) hatte aufgrund von Schottereinschlüssen für die Vorkommen Lerchenbühl (Nr. 6), Küh-Hübel (Nr. 7) pliozäne bis pleistozäne Alter abgeleitet. Soellner (1960) vermutete für das Gestein vom Teichelberg (Nr. 22) pliozänes Alter. Nach den Ergebnissen dieser Arbeit sind alle diese Vorkommen ins untere Miozän zu stellen. Die von Schröder gefundenen Schottereinschlüsse können deshalb nicht pliozänen Alters sein, sondern müssen aus älteren, vermutlich kretazischen Schottern stammen.

Betrachtet man als erwiesen, daß die oberfränkischen Braunkohlenflöze erst kurz vor oder während der Zeit der Basalteruptionen gebildet wurden, so stufen unsere K—Ar-Altersbestimmungen diese Braunkohlenflöze in das untere Miozän bzw. in das obere Oligozän ein. Die mehr oder weniger zeitliche Gleichstellung der oberfänkischen Braunkohlen mit dem Rheinischen Hauptflöz (Kirchheimer, 1937; Gothan, 1941) ist somit zurecht erfolgt. Unveröffentlichte Altersbestimmungen zum Alter des Rheinischen Hauptflözes (Todt, 1971) sowie dessen stratigraphische Einordnung in das untere bis mittlere Miozän (Anderson, 1966) belegen ebenfalls die Altersübereinstimmung.

Die Vulkanitvorkommen, die längs einer NE—SW gerichteten Spalte aufgereiht sind, weisen untereinander kein einheitliches Alter auf. Bei den Vorkommen Kusch-Schloßberg-Galgenberg sind unter Berücksichtigung der 1σ-Fehler die beiden äußeren, kleineren Eruptionen gleich alt ($22{,}6 \pm 0{,}6$

und 22,1 ± 0,7), die zentrale Eruption des Schloßberges fand nicht ganz 2 Ma später statt (20,8 ± 0,7). Ein zweites Beispiel sind die Aigner Kuppen. Die hohen Fehler lassen aber keinen eindeutigen Schluß zu. Es kann aus der Verteilung der Vulkanitalter am Kusch-Schoßberg-Galgenberg geschlossen werden, daß die Tektonik, welche die Zufuhrwege für diese Basalte öffnete, über einen Zeitraum von ca. 2 Ma aktiv war.

Die Zeit vor dem Basaltvulkanismus war in diesem Gebiet durch starke Abtragung und Einebnung gekennzeichnet, der eine Heraushebung des Gebirges vorausgegangen war (Wurm, 1961, S. 473). Die Basalte der Oberpfalz und von Oberfranken sind also nach dem Schema Hebung — Spaltung — Vulkanismus entstanden. Die Eruptionen werden als Zeitmarken zwischen der vorbasaltischen und einer nachbasaltischen Einebnung dieses Gebietes angesehen. Nach den Ergebnissen der vorliegenden Datierungen erscheint es möglich, daß die nachbasaltische Einebnung nicht erst im Pliozän (Wurm, 1961, S. 474), sondern bereits im mittleren bis oberen Miozän begonnen hat.

Ein strenger Zusammenhang zwischen K—Ar-Altern und Gesteinstyp ist nicht erkennbar. Die drei untersuchten Alkali-Olivin-Basalte (Nr. 15; Nr. 13; Nr. 20) gehören zu den älteren der analysierten Gesteine. Refai (1960) hatte einige Olivin-Nephelinite der Oberpfalz in die Gesteinstypen „Schloßberg" und „Kuschberg" unterschieden. Die Gesteine des Kuschberg-Typs sollen u. a. häufiger meist assimilierte Fremdgesteinseinschlüsse führen. Da alle Vorkommen des Gesteinstyps Kuschberg invers magnetisiert sind, während dem Schloßbergtyp nur Gesteine mit normaler Feldrichtung angehören, kann man schließen, daß diese Gesteine nicht zum selben Zeitpunkt gebildet worden sind. Nach den K—Ar-Altersbestimmungen kann man aber nicht jedem Typ einen eigenen Altersbereich zuordnen, vielmehr überlappen sich die Altersverteilungen beider Typen (Abb. 4 Mitte). Das von Refai (1960) beobachtete häufige Auftreten von Nebengesteinseinschlüssen in den Gesteinen des Kuschbergtyps ist nicht mit einem höheren Modellalter korreliert.

Geophysikalische Schlußfolgerungen

Trägt man die Altersergebnisse zusammen mit der jeweiligen paläomagnetischen Polarität der einzelnen Vorkommen in ein Diagramm auf, so erhält man eine Zeitskala für die Richtung des Erdmagnetfeldes (Abb. 4 unten). Die paläomagnetische Skala, die sich auf die Alter und die paläomagnetische Polarität der Oberpfälzer und der Oberfränkischen Basalte gründet, zeigt mindestens zwei Umklappungen des Magnetfeldes. Dabei wurden die Umklappzeitpunkte in Anlehnung an Cox und Dalrymple (1967) bestimmt. Im Altersbereich von 23,8 Ma bis 22,8 Ma haben drei untersuchte Proben inverse Polarität. Zwischen 23,3 Ma und 20,7 Ma

haben sieben untersuchten Vorkommen normale Polarität und im Bereich jünger als 20,7 Ma sind 4 Proben invers magnetisiert.

Das Vorkommen Großer Teichelberg (Nr. 22), das nach Söllner (1960) normal magnetisiert ist, fällt mit einem Alter von 21,4 Ma in einen Bereich mit Proben normaler Polarität. Nach neueren Messungen von Pohl und Soffel (private Mitteilung) ist das Gestein invers magnetisiert. Durch die Fehler der Altersbestimmung ist nicht zu entscheiden, ob dieses Vorkommen bereits in den Bereich jünger als 20,7 Ma mit inverser Feldrichtung fällt oder ob zwischen ca. 22 Ma und 21 Ma zwei weitere Umklappungen liegen.

Für den Altersbereich der letzten 70 Ma haben Heirtzler *et al.* (1968) eine paläomagnetische Skala auf der Grundlage der Paläomagnetisierung der Meeresbodengesteine aus dem Indischen, Pazifischen und Atlantischen Ozean aufgestellt. Bisher ist diese Skala nur durch wenige Altersbestimmungen geeicht. Zwischenwerte wurden unter der Annahme einer konstanten "sea-floor-spreading-rate" bestimmt. Das bedeutet, daß sowohl die Dauer als auch die zeitliche Einstufung der einzelnen Epochen einheitlicher Feldrichtung noch nicht befriedigend bestimmt sind. Nach dieser Heirtzler-Skala sollen in den Zeitraum von 29 Ma bis 18 Ma mehr als 30 Umklappungen des Erdmagnetfeldes fallen. Die durchschnittliche Länge einer Epoche einheitlicher Feldrichtung war demnach kleiner als 0,5 Ma.

Weitere Eichpunkte für diese Skala können grundsätzlich durch die Datierung von solchen Umklappungen des Erdfeldes gewonnen werden, die in kontinentalen Eruptivgesteinen konserviert sind.

Wegen der geringen Dauer einer Epoche mit einheitlicher Feldrichtung im Vergleich zu den Fehlern der K—Ar-Altersbestimmungen an den Vulkaniten der Oberpfalz und von Oberfranken ist eine Zuordnung der beiden Feldumklappungen zu einer bestimmten Feldumkehr nach der Heirtzler-Skala jedoch nicht möglich.

Unter der Annahme, daß die Heirtzler-Skala keiner wesentlichen Revision bedarf, ist anzunehmen, daß zwischen die beiden datierten Umklappungen noch weitere einzuordnen sind.

Nach der Heirtzler-Skala war die Zeitdauer einer Epoche mit einheitlicher Feldrichtung im Durchschnitt kleiner als 0,5 Ma. Der Vulkanismus im Raum Oberfranken und Oberpfalz dauerte über einen wesentlich längeren Zeitraum (4,6 Ma: Parkstein Nr. 18 bis Kuschberg Nr. 11). Bei kontinuierlichem Auftreten der Eruptionen würde man auf der paläomagnetischen Zeitskala (Abb. 4 unten) eine statistische Verteilung der normalen und inversen Feldrichtungen erwarten. Da dies nicht der Fall ist, sondern sich deutlich drei Gruppen einheitlicher Feldrichtung abzeichnen, muß man schließen, daß die Vulkanite in dem betrachteten Gebiet nicht zeitlich statistisch verteilt gefördert wurden. Es müssen wenige (evtl. drei) nur kurz anhaltende Schübe ($\leqslant 1$ Ma) gewesen sein, in denen zeitlich nacheinander

die einzelnen Eruptionen stattgefunden haben. Unter der Annahme, daß zwischen Tektonik und Vulkanismus ein enger Zusammenhang besteht, ist dieser Schluß auch auf die Bruchtektonik übertragbar.

Für den hier interessierenden Altersbereich von etwa 30 bis 16 Ma gibt es weitere an Eruptivgesteinen ermittelte paläomagnetische Daten. So haben York *et al.* (1971) in Zentralcolorado 26 tertiäre Basaltströme paläomagnetisch vermessen und K—Ar-Alter bestimmt. Die K—Ar-Alter der normal magnetisierten Bereiche und der Basalt-Lagen in einer Übergangszone waren ca. 24,0 $\pm$ 1,0 Ma, die invers magnetisierten Lagen waren 21,5 $\pm$ 1,0 Ma alt.

Gromme *et al.* (1972) bestimmten die Richtung des paläomagnetischen Feldes und die Zeitpunkte der Eruptionen von mitteltertiären Tuffen in Nevada und Utah. Innerhalb des uns hier interessierenden Altersbereichs fanden sie an Tufflagen mit inverser Magnetisierung K—Ar-Mineral-Alter um 30 Ma. Eine Lage mit normaler Magnetisierung datierten sie zu 23,1 $\pm$ 0,6 Ma und eine weitere mit inverser Magnetisierung zu 22,1 $\pm$ 0,6 Ma.

K—Ar-Altersergebnisse an miozänen Basalten Südfrankreichs haben Bout *et al.* (1966) vorgelegt. Vor 18 $\pm$ 1 Ma (Gergovie-Intrusion) erwies sich die paläomagnetische Feldrichtung als invers und vor 16 $\pm$ 1 Ma (Gergovie coulée supérieure) als normal.

Die Messungen dieser Autoren belegen mehrere Umklappungen des Erdmagnetfeldes innerhalb des genannten Zeitraumes. Die eine oder andere der zitierten Umklappungen könnte mit einer der von uns gefundenen identisch sein.

Wegen der relativ großen Fehler der Altersbestimmung läßt sich aber in keinem Fall ein exakter Nachweis führen.

Lage des magnetischen Poles

Außer der Richtung des paläomagnetischen Feldes kann aus den paläomagnetischen Daten der Gesteine auch die Lage des virtuellen Poles bestimmt werden. Von den untersuchten Gesteinen können dazu nur die Daten des Parksteins verwendet werden, da die Ergebnisse aller anderen Proben nicht durch Entmagnetisierungstests gesichert sind. Soffel und Supalak (1968) bestimmten die Lage des virtuellen geomagnetischen Poles auf der Nordhalbkugel zu $\varphi = 72°$ und $\lambda = 199°$ E. Das Ergebnis liegt im Vergleich zu den Ergebnissen tertiärer Gesteine anderer Gebiete am Rande der Verteilung. Während die meisten virtuellen Pole der Tertiär-Zeit in der Nähe des heutigen Poles liegen (Irving 1964), befindet sich der aus den Gesteinen des Parksteins bestimmte Pol im Nord-Polarmeer in der Nähe der NW-Spitze Alaskas. Diese abweichende Lage wird von Soffel und Supalak (1968) mit der fehlenden zeitlichen Mittelung erklärt, weil bei der raschen Abkühlung des Parksteins nur die momentane Lage des magneti-

schen Poles innerhalb der Schwankungsbreite der Säkularvariation konserviert wurde. Das in dieser Arbeit bestimmte Alter für die Eruption des Parkstein beträgt $23{,}8 \pm 1{,}1$ Ma.

Anerkennung. Die Dünnschliffuntersuchungen wurden von den Herren Dr. P. Horn und Dr. I. Baranyi durchgeführt, wofür wir an dieser Stelle danken. Den Herren Dipl. Geol. V. v. Drach und Dr. F.-P. Oesterle sind wir für kritisches Lesen unseres Manuskripts und Verbesserungsvorschläge zu Dank verpflichtet. Den Herren H. I. Funke und A. Lutz danken wir für sorgfältige Mitarbeit bei den Analysen. Die vorliegende Arbeit wurde dankenswerter Weise partiell durch die DFG unterstützt.

Literatur

Amaral, G., Cordani, U. G., Kawashita, K., Reynolds, J. H.: Potassium-argon dates of basaltic rocks from southern Brazil. Geochim. Cosmochim. Acta *30*, 159–189, 1966

Anderson, H.-J.: Die Schichtenfolge des Tertiär und Quartär. in: Geologische und bergbauliche Übersicht des rheinischen Braunkohlenreviers. Herausgegeb. v. d. Deutschen Geol. Ges., Frühjahrstagung Köln 1966: 2–5, Krefeld 1966

Bout, P., Frechen, J., Lippolt, H.-J.: Datations stratigraphique et radiochronologique de quelques culées basaltiques de Limagne. Rev. d'Auvergne. *80*, 208–231, 1966

Cooper, J. A.: The flame photometric determination of potassium in geological materials used for potassium argon dating. Geochim. Cosmochim. Acta. *27*, 525–546, 1963

Cox, A., Dalrymple, G. B.: Statistical analysis of geomagnetic reversal data and the precision of potassium-argon dating. J. Geophys. Res. *72*, 2603–2614, 1967

Dalrymple, G. B., Lauphere, M. A.: Potassium-argon dating, W. H. Freeman and Company, 110–120, 1969

Funnel, B. M.: The tertiary period. The Phanerozoic time-scale. A Symposium dedicated to Arthur Holmes. Quart. J. Geol. Soc. (London). *120*, Suppl., 179–191, 1964

Gothan, W.: Über eine kleine Oberkreide-Flora von Friedersreuth bei Neustadt a. d. Waldnaab (Opf.). Jahrb. Reichsst. f. Bodenf. f. d. Jahr 1939, *60*, 240–274, 1941

Grommé, C. S., McKee, E. H., Blake, Jr., M. C.: Paleomagnetic correlations and potassium-argon dating of middle tertiary ash-flow sheets in the eastern great basin, Nevada and Utah. Geol. Soc. Am. Bull. *83*, 1619–1638, 1972

Gümbel, C. W.: Geognostische Beschreibung des Ostbayerischen Grenzgebirges. Gotha 1868

Heirtzler, J. R., Dickson, G. O., Herron, E. M., Pitman III, W. C., Le Pichony, X.: Marine magnetic anomalies, geomagnetic field reversals, and motions of the ocean floor and continents. J. Geophys. Res. *73*, 2119–2136, 1968

Horn, P., Lippolt, H. J., Todt, W.: Kalium-Argon-Altersbestimmungen an tertiären Vulkaniten des Oberrheingrabens. I. Gesamtgesteinsalter. Ecol. Geol. Helv. *65/1*, 131–156, 1972

Irving, E.: Paleomagnetism, and its application to geological and geophysical problems. New York: Wiley 1964

Kirchheimer, F.: Grundzüge einer Pflanzenkunde der deutschen Braunkohlen (S. 102–103). Halle: Knapp 1937
Lippolt, H. J., Gentner, W., Wimmenauer, W.: Altersbestimmungen nach der Kalium-Argon-Methode an tertiären Eruptivgesteinen Südwestdeutschlands. Jahrb. Geol. Landesamt Baden-Württemberg *6*, 507–538, 1963
Lochmann, Z.: Železná Hůrka (Eisenbühl). Anthropozoikum *11*, 69–88, 1961
Refai, E.: Magnetfeld und Magnetisierung der Basaltvorkommen im Raum von Kemnath (Oberpfalz). Diss. Univ. München 1960
Refai, E.: Magnetic anomalies and magnetisation of basalts in the area around Kemnath (Oberpfalz). Z. Geophysik, *27*, 175–187, 1961
Richarz, St.: Die Basalte der Oberpfalz. Z. deutsch. geol. Ges. *72*, 1–100, 1920
Schröder, B.: Zur Altersstellung der oberpfälzer Vorlandsbasalte. – Geol. Bl. NO-Bayern *12*, 1–15, 1962
Schröder, B., Siegling, M.: Erläuterung zur geologischen Karte von Bayern, 1:25000, Blatt Nr. 6137 Kemnath, München 1966
Söllner, K.: Das Basaltvorkommen vom Teichelberg bei Großschlattengrün. Aufschluß-Sonderheft: Fichtelgebirge, 90–103, 1960
Soffel, H., Supalak, P.: Paläomagnetische Messungen am Basalt des Parkstein bei Weiden (Bayern). Geophys., *34*, 287–296, 1968
Tillmann, H.: Zur Geologie des Oberpfälzer Tertiärs und seiner Lagerstätten. Festschrift der Bayer. Braunkohlen-Ind. AG Schwandorf, Schwandorf 1956
Todt, W.: Kalium-Argon-Altersbestimmungen an mitteleuropäischen miozänen Vulkaniten bekannter paläomagnetischer Feldrichtung. Diss. Univ. Heidelberg 1971
Todt, W., Lippolt, H.-J.: Kalium-Argon-Altersbestimmungen an Basalten der Oberpfalz. Fortschr. Miner. *50*, Beih. 3, 8–9, 1963
Wimmenauer, W.: Charakteristische Gesteine des tertiären u. quartären Vulkanismus in Mitteleuropa. Zitiert von v. Gehlen. In: DFG Forschungsbericht: Unternehmen Erdmantel, 248. Wiesbaden 1972
Wurm, A.: Erläuterungen zur Geol. Karte von Bayern, Blatt Wunsiedel, 1932
Wurm, A.: Geologie von Bayern: Frankenwald, Münchberger Gneismasse, Fichtelgebirge, Nördlicher Oberpfälzer Wald. Berlin: Borntraeger 1961
York, D., Strangway, D. W., Larson, E. E.: Preliminary Study of a Tertiary Magnetic Transition in Colorado. Earth Plan. Sci. Letters *11*, 333–338, 1971

Dr. Wolfgang Todt
Prof. Dr. Hans Joachim Lippolt
Laboratorium für Geochronologie
der Universität Heidelberg
D-6900 Heidelberg 1
Berliner Str. 17
Bundesrepublik Deutschland

J. Geophys. 41, 63–70, 1975

Dispersed Shots at Optimum Depth - An Efficient Seismic Source for Lithospheric Studies

A. W. B. Jacob

Institute of Geological Sciences, Edinburgh

Received July 21, 1974

Abstract. The case for dispersing charges fired at sea into a number of packages fired simultaneously at optimum depth is outlined and an experiment, carried out to check that linear addition of the signals from separate sources does occur, is described. The advantages of this system for lithospheric studies are demonstrated.

Key words: Dispersed Underwater Explosions — Seismic Source — Seismic Long Range Profiles.

Introduction

It has been known for some time that there are considerable advantages to be gained from firing underwater explosions at "optimum depth" (O'Brien, 1967a; Jacob, 1970, Jacob and Willmore, 1972). In the third paper it was reported that this method, of firing at the depth where the bubble pulse and the surface reflection are in phase, had been used to produce teleseismic signals from an explosion of only 10 tons TNT. Other 10 ton shots have since been fired in 1972 and in 1973. In all cases teleseismic signals were observed.

These 10 ton explosions have also been used to provide observations at shorter range (Hirn *et al.*, 1974, Bonjer *et al.*, 1974) and further work has been carried out using optimum depth explosions of up to 5 or 10 tonnes to investigate the lithosphere in Europe.

An alternative system which could be used for this type of work, i.e. up to ranges of the order of 1000 km, is considered here. It generates rather higher frequencies but the lithosphere is a region of relatively high Q and losses due to absorption are not serious up to the frequencies considered here (about 4 Hz).

If the explosion is to be fired in one package, the optimum depth system is the most efficient way to generate seismic waves for investigating the Earth's structure, but there are a number of limiting factors:

1. It has been theoretically calculated that the particle velocity generated in the far-field increases only as $W^{0.47}$ (Wielandt, 1972) where Q is infinite and W is the weight of the charge. The effect of finite Q is considered

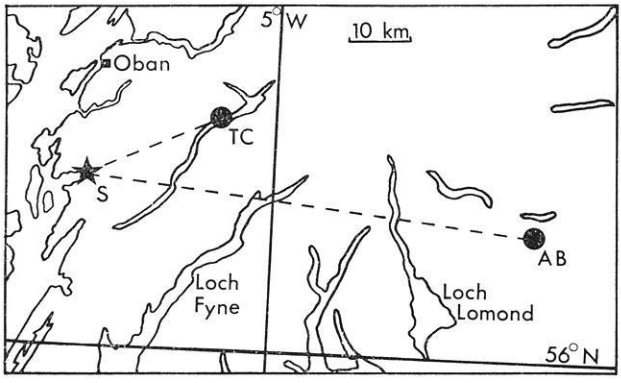

Fig. 1. The positions of the shot-point (S) and the two recording stations. TC is Taycreggan and AB is Aberfoyle

later but in practice a square root law may be a good approximation in the 2 to 4 Hz range when 1 Hz seismometers are used.

2. As the charge size is increased the water depth required increases. If the shot is to be kept clear of the bottom then depths of about 90 metres are required for a 0.1 tonne shot, 140 metres for a 1 tonne and 220 metres for a 10 tonne one. This considerably reduces the number of available shot sites near to land.

3. Large single charges are difficult to handle at sea, calm conditions are necessary and to wait for these is expensive.

4. When charge size is increased both amplitudes and predominant frequencies are changed.

A logical step is thus to split the explosive into a number of smaller packages. If there is linear addition of the signals generated by N packages, then the summed signal should be N times that generated by one package. The water depth required should only be that necessary to accomodate an individual package and, as these would be smaller, they should be easier to handle though the shot pattern as a whole may present difficulties of a different kind. Finally, the source waveform should be unchanged as the number of packages is increased. The dispersal of charges when firing in boreholes on land is quite common practice if the shot totals more than a few hundred pounds (O'Brien, 1967b), but seems not to have been used for optimum depth firing in water.

Experimental Test of Linear Addition

We have recently carried out an experiment to check that linear addition does occur. If $A = kN^X$ for a given shot/station pair where A is the trace amplitude observed, k is a constant, N is the number of packages, and the

Table 1

(a)

No. of packages N	No. of shots	Average V at TC (μms^{-1})	Average V at AB (μms^{-1})
1	1	0.57	0.073
2	1	1.43	0.142
3	4	2.26	0.183
4	4	3.42	0.274
5	2	3.72	0.312

(b) N = 3 for all shots

Shot	Separation (m)	V at TC (μms^{-1})	V at AB (μms^{-1})
1	24	2.42	0.205
2	18	2.36	0.167
3	12	2.19	0.182
4	6	2.08	0.178

index X is to be measured, then factors that might cause X to be less than 1 include interference between the individual bubbles, and inhomogenietites in the structure under the shot pattern, which would reduce coherence.

The experiment was carried out in Loch Melfort in the West of Scotland (Fig. 1, point S). The Loch has an area of very sheltered water deep enough (about 40 metres) to allow optimum depth shooting with 1.36 Kg (3 lb) packages of TNT. There is a possible fault in the Precambrian basement running NE/SW through the Loch, but the shots were all fired on the SE side of its likely position. They were fired in North/South strings of up to 5 packages and the shot area extended about 250 metres from North to South. Most of the shots were fired with a separation of 24 metres between charges (this is equivalent to separating 0.2 tonne charges by about 90 metres) though three were fired at separations of 18 metres, 12 metres, and 6 metres to test for any loss of signal when the bubbles are closer together. The maximum bubble radius for these charges at optimum depth is about 1.1 metres.

The packages were suspended by the firing cable below small buoys and they were fired electrically using two N79 detonators in each package. The N79 detonators normally explode between 1 and 5 msec. after the onset of the firing current, giving a scatter of sources within only $\pm 2\%$ of the dominant period of the waveform (about 100 msec.).

Results are shown in Table 1(a) for two recording stations at Taycreggan (TC) and Aberfoyle (AB), at distances of 23.6 and 72.9 km respectively (Fig. 1). The figures in columns 3 and 4 of Table 1(a) give an average ground

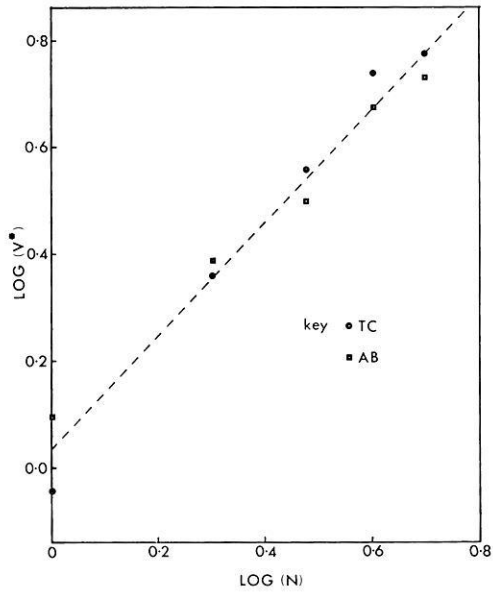

Fig. 2. Plot of Log (V*) against Log (N) demonstrating the linearity of the relationship between them

velocity V (proportional to the trace amplitude) within a window of 0.25 second around the maximum observed in the first phase. This was calculated by taking the average of 5 swings on the seismogram centred around the largest swing. The velocity response of the system at that frequency then gives an average ground velocity for that window.

Table 1(b) shows the results obtained from 4 shots fired with $N = 3$ but various shot separations. Shot 1 was at a slightly different position from shots 2, 3, and 4, but there is no clear loss of amplitude due to the compression of the pattern. Fig. 2 shows a plot of log (N) against log (V*) for both stations. V* is the ground velocity V normalized so that the average value of V for each set (TC and AB) becomes 3. The slope of 1.06 (standard error 0.06) demonstrated experimentally that the relationship is linear.

The radiation will be noticeably directional for linear shot patterns whose length is comparable to the wavelength λ of the seismic signal. The trace amplitude of the dominant frequency component in the far-field at an angle ϕ to the perpendicular to the array is given by:

$$A = A_0 \frac{\sin\left(\frac{N\psi}{2}\right)}{\sin\left(\frac{\psi}{2}\right)} \quad \text{where} \quad \psi = \frac{2\pi d \sin\phi}{\lambda}$$

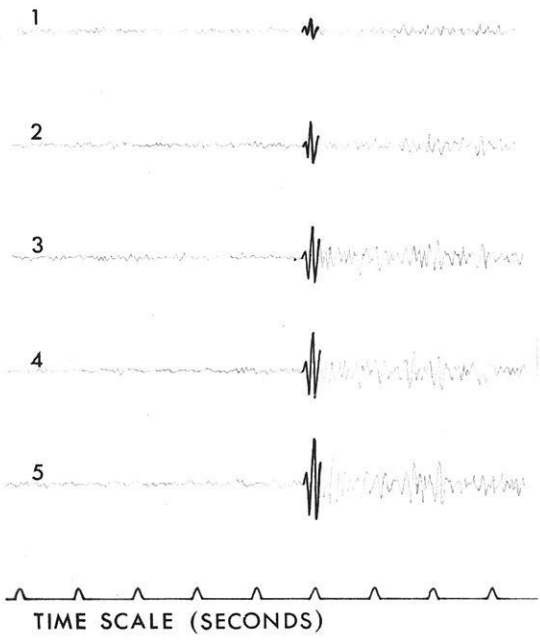

Fig. 3. Records from AB band-pass filtered 2–32 Hz. The coherence of the addition is very clear

A_0 is the trace amplitude from one charge and d is the spacing between charges.

The Effect of Absorption

We have not so far considered losses in the transmission path due to absorption, scattering, etc. For a station at distance r from the source we may write (see, for instance, Berg *et al.*, 1971).

$$A(f,r) = V(f)\, I(f)\, F(r) \exp(-\pi f t/Q) \qquad (1)$$

Where A is the amplitude spectrum of the seismogram, $V(f)$ is the source velocity spectrum, $I(f)$ is the velocity response of the recording system, $F(r)$ is the geometrical spreading factor. The factor F can be considered to be frequency-independent for the narrow band of frequencies considered here. t is the travel time and Q is an average value over the path. There may be losses due to scattering by heterogeneities in the structure along the ray path. However, it is precisely this structure that is under investigation when seismic profiling is carried out, amplitude variations

are part of the information gained from an experiment and they should be used in its interpretation. As these factors are unpredictable before the structure is known and as there may even be preferential transmission of some higher frequencies in certain structures, these factors may be ignored for the purposes of source comparison. Treating the sources as nearly monochromatic, we can deduce from Eq. (1) that the ratio R of the trace amplitudes generated for a given shot/station path is

$$R = \frac{A_1}{A_2} = \frac{V_1(f_1)}{V_2(f_2)} \exp\left[\frac{\pi t}{Q}\left(f_2 - f_1\right)\right]$$

Where A_1 and A_2 are the trace amplitudes generated in a particular phase by two sources of weight W_1 and W_2 which produce at optimum depth a dominant frequency of f_1 and f_2. The recording system velocity response is assumed constant in the frequency band including f_1 and f_2. Given that the peak value of the source velocity spectrum varies as $W^{0.47}$ we can write

$$R = \left(\frac{W_1}{W_2}\right)^{0.47} \exp\left(\frac{\pi t}{Q}\left(f_2 - f_1\right)\right] \tag{2}$$

f can be deduced from the charge weight W (in kilograms) using the relation (derived from Willis, 1941)

$$W = \left[\frac{d(d+10)^{\frac{5}{6}}}{803}\right]^3 \tag{3}$$

which gives d, the optimum depth in metres, and f is then given by $f = 380/d$ where the assumed velocity of sound in water is 1520 metres/sec. Eq. (3) applies to TNT and if a different explosive is used, the equivalent weight in TNT should be calculated.

Use of the Dispersed Shot System in Practice

We can now consider a particular case. In the summer of 1974, an experiment to investigate the structure of the lithosphere in Britain (LISPB) was carried out. The maximum shot to station distance planned for this experiment was about 1000 km. The explosives available were in the form of Minol depth charges and these are equivalent to 0.2 tonne TNT. Depth charges are a convenient size to use in a dispersed charge pattern. They can be manhandled while larger charges demand power assistance with a consequent slowing down in the process of setting up the pattern

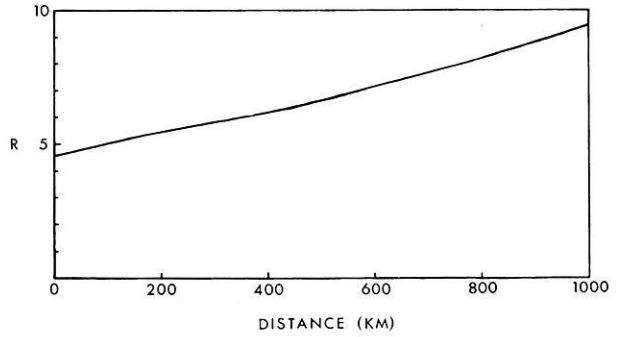

Fig. 4. Dominant period trace amplitude ratios between 5 tonne and 0.2 tonne TNT explosions (Q = 1000). Use of this diagram is explained in the text

and a more critical need for calm sea conditions. To produce useful seismograms out to a range of 1000 km one would normally use a charge of about 5 tonnes. We can use the equation (2) to calculate the relative seismogram amplitudes which would be generated by a 5 tonne and a 0.2 tonne charge if we calculate $f_1 = 2.16$ Hz and $f_2 = 3.97$ Hz and substitute values for Q and a travel time t appropriate to the distance at which we are making the comparison. At a distance of 1000 km, t is about 130 seconds for the first arrival and if we assume Q to be 1000, then R is found to be 9.5. This means that a dispersed shot with 10×0.2 tonne charges ($N = 10$) could be used to produce a signal 5% greater in amplitude than that produced by a 5 tonne shot. At a shorter range, Q has less effect, R is smaller, and the number of packages needed is correspondingly less. Fig. 4 shows how R and therefore, the required N will vary if we want to equal a 5 tonne shot at ranges between 0 and 1000 km. The LISPB experiment has only just finished but the indications are that the dispersed shots have produced signals out to the required range of about 1000 km.

While the dispersed charge system should be very effective in regions of reasonably high Q, there is no substitute for large single charges generating low frequency waves if the seismic work is to be carried out in, for instance, a low-Q volcanic area. In the case of LISPB it enabled us to bring the northern shot point well onto the shelf and nearer the Scottish mainland and in the south it enabled us to generate large seismic signals in an area where there is not enough depth of water to allow optimum depth firing of large charges.

Acknowledgement. I thank P. L. Willmore (Edinburgh) and E. Wielandt (Zurich) for discussions and also those who assisted in the experimental work in mid-winter. The work was supported by the Natural Environment Research Council and is published by permission of the Director of I. G. S.

References

Berg, J. W., Long, L. T., Sarmah, S. K., Trembly, L. D.: Crustal and Mantle Inhomogenieties as Defined by Attenuation of Short-Period P waves. A. G. U. Monograph *14*, 51–57, 1971

Bonjer, K. P., Kaminski, W., Kind, R.: Seismic Observations in Germany of a 10 ton Explosion off Scotland. J. Geophys. *40*, 259–264, 1974

Hirn, A., Perrier, G., Steinmetz, L.: 10 Ton Explosion off Scotland 1972 observed in the distance range 900 to 1500 km in France. Compt. rend. In press (1974)

Jacob, A. W. B.: Long range observations of underwater explosions. Proc. Geol. Soc. (London) *1662*, 82–83, 1970

Jacob, A. W. B., Willmore, P. L.: Teleseismic P Waves from a 10 Ton Explosion. Nature *236*, 305–306, 1972

O'Brien, P. N. S.: Quantitative Discussion on Seismic Amplitudes produced by explosions in Lake Superior. J. Geophys. Res. *72*, 2569–2575, 1967a

O'Brien, P. N. S.: The Efficient use of large charges, in Seismic Refraction Prospecting. In: Seismic Refraction Prospecting. A. W. Musgrave, ed., pp. 152–170. S. E. G., Tulsa, Oklahoma 1967b

Wielandt, E.: Anregung seismischer Wellen durch Unterwasserexplosionen. PhD. thesis, University of Karlsruhe, 1972

Willis, H. F.: Underwater explosions, time interval between successive explosions. British Report WA-47-21, 1941

A. W. B. Jacob
Institute of Geological Sciences
Geophysical Laboratories
6 South Oswald Road
Edinburgh EH9 2HX, Scotland

J. Geophys. 41, 71–84, 1975

Crustal Structure and *P*-Wave Travel Time Anomalies at NORSAR

K. A. Berteussen

NORSAR, Kjeller

Received July 12, 1974

Abstract. Deviations from theoretical, expected travel times are observed for *P* signals crossing the array. These anomalies are presented, and some concern is given to the effect of these on the event detection and location capability of the array. Tests are made in order to find out whether or not these anomalies can be explained as the effect of a depth varying Moho-discontinuity. It is found that a dipping plane is able to explain 18% of the total variance of these anomalies. A second degree polynomial interface may explain 21% of the variance, while a third degree interface may explain 24%. The conclusion is thus that more complicated models will have to be introduced in order to explain the bulk of these anomalies.

Key words: Time Anomalies — Location Calibration — Crustal Structure — Least Square Interface.

Introduction

It is well known that the observed time delays for signals crossing a seismic array exhibit considerable deviations from the theoretically expected values. Especially for LASA (Large Aperture Seismic Array, Montana, USA) several studies have been made of slowness and travel time anomalies for the purpose of determining the local structure, as well as inhomogeneities in the lower mantle, f.ex., Chinnery and Toksöz (1967); Greenfield and Sheppard (1969); Glover and Alexander (1969); Mack (1969); Zengeni (1970); Iyer (1971); Engdahl and Felix (1971); Davies and Sheppard (1972).

Also for other arrays there have been similar analyses, f.ex., Niazi (1966); Otsuka (1966); Otsuka (1966a); Johnson (1967); Jonson (1969); Corbishley (1970); Husebye *et al.* (1971); Brown (1973); Brown (1973a). At NORSAR few studies of this type have been made: Noponen (1971); Gjøystdal *et al.* (1973). Recently a crustal model has been introduced where wave scattering is caused by small variations in the index of refraction. It is shown that this model is able to explain the large variation in the array data (Aki, 1973; Capon 1974; Dahle, Husebye, Berteussen, and Christofferson, paper in preparation).

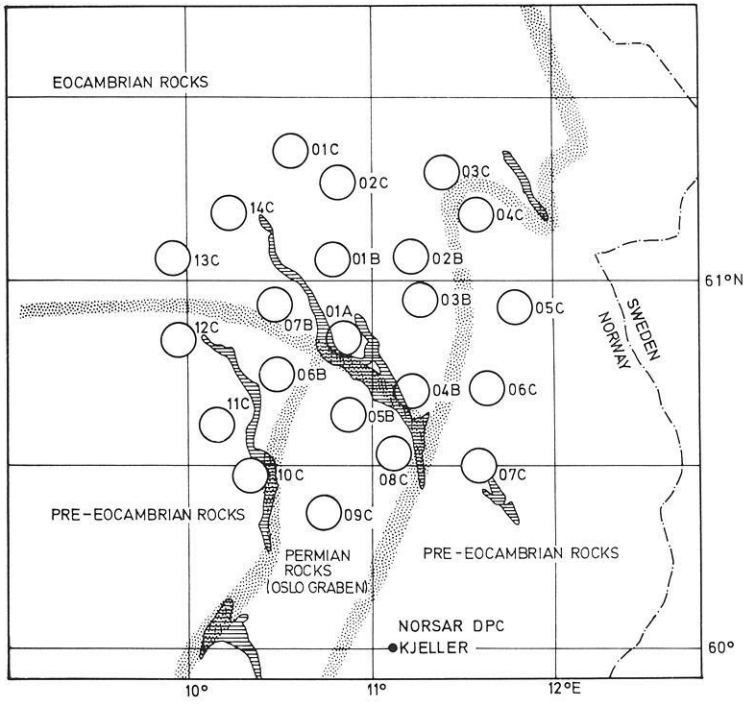

Fig. 1. NORSAR Array configuration. The geological structures in the siting area are briefly outlined

In this paper the *P*-wave travel time and slowness anomalies observed at NORSAR (60.82 N, 10.83 E) will be presented, and some attention will be given to the effect of these on the event location and detection capability of the array.

From other types of data the mantle-crust interface is found to exhibit large elevation differences in this area (Kanestrøm, 1973). The main objective of this paper is therefore to test whether or not the observed anomalies can be explained by either a plane dipping Moho-discontinuity or a Moho which is a curved interface.

DATA

NORSAR has 22 subarrays, each with 6 SP (short period) instruments. The array configuration is shown in Fig. 1. For a more complete description of the array, the reader is referred to Bungum *et al.* (1971).

Because of the time anomalies observed, extensive calibration files had to be established in order to ensure good event location and detection capabilities at the array. The data used in this study is the data which

currently is used for this purpose at NORSAR. The data base has been established by measuring subarray delays on a total of 149 events, all with good signal-to-noise ratio. The delays are found by an iterative cross-correlation procedure (Bungum and Husebye, 1971). Usually a 1.0–3.0 Hz bandpass (third order recursive Butterworth) filter has been applied, but on some of the events a 0.8–2.5 Hz bandpass filter is used. The difference is, however, not believed to be significant in this context (Bungum and Husebye, 1971). A good test of the stability of this method is to measure delays on several events with the same epicenter. For example, for explosions from the same test site it is found that the difference in measured delays is of the order ± 0.02 seconds. For some areas where several events are found close together, the anomalies have been averaged over 2–6 events in order to increase the stability further. The final data set consists of 93 data points, where each point represents one single event or an average over several events.

The anomalies are available in the form:

$$d_{ij} = (\tau_{0_{ij}} - \tau_{c_{ij}}) - (\tau_{0_{rj}} - \tau_{c_{rj}}) \tag{1}$$

$\tau_{0_{ij}}$ is observed delay for subarray i and seismic region j.

$\tau_{c_{ij}}$ is calculated delay for subarray i and seismic region j. The calculated delay is based on NOAA (National Oceanic and Atmospheric Administration) epicenter solutions and a smoothed version of Herrins (1968) tables.

$\tau_{0_{rj}}$ ($\tau_{c_{rj}}$) is observed (calculated) delay at the reference point. In our case we use the average of the delays for this region.

Some of this data is shown as a function of azimuth in Fig. 2. Here as in the rest of the paper only data from *P*-phases have been used. The smooth curves are the sine approximations of the data and will be commented upon later.

The values of the deviations are up to ± 0.7 seconds. When beamforming the array such deviations would have a serious degrading effect on the event detection capability if not corrected for. At NORSAR an interpolation routine is used in order to find the correct delays for each point in slowness space. The SNR (signal-to-noise ratio) gain from applying these corrections has been calculated by analyzing 479 events randomly selected in the period November 1972 until September 1973. It is found that 10% of the events have a gain of 1.5 dB or less, 10% have a gain of 12.5 dB or more, while the median is 6.8 dB. A median of 6.8 dB implies an improvement of 0.34 M_B units in detection capability.

In the calibration system at NORSAR these anomalies are actually split in two. That is, through the 22 subarray delays is fit, in a least square sense, a plane wavefront. This procedure does give a slowness and a direc-

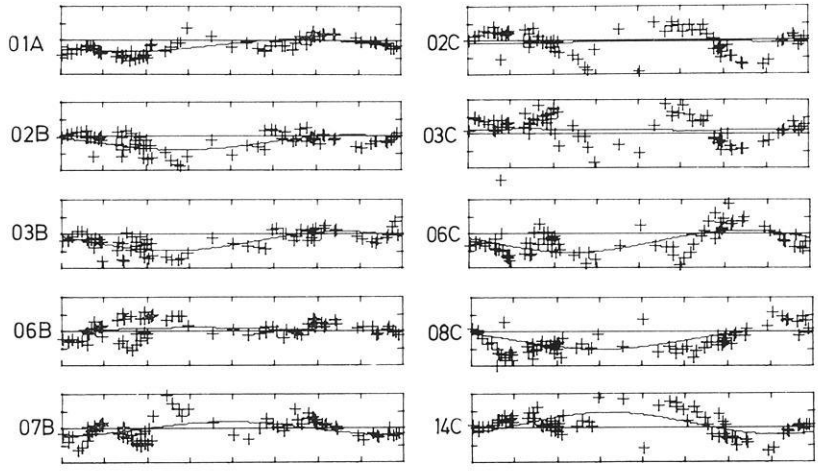

Fig. 2. Observed P wave travel anomalies as a function of (NOAA) azimuth. The vertical axis goes from —0.5 to +0.5 seconds, while the horizontal axis goes from 0 to 360 degrees azimuth. The smooth curve represents the best fit to the sine approximation (Eq. (6)). Only values for 10 of the 22 subarrays are included

tion of approach (azimuth) for the particular event. The location calibration is now defined as the difference in slowness and azimuth between the NORSAR solution and that predicted from the NOAA epicenter location. On Fig. 3 the location calibration vectors for the 93 data points are plotted in slowness space. That is, the tail of the arrow represents the slowness and angle of approach measured at NORSAR, while the head of the arrow represents the corresponding expected values based on the NOAA epicenter solution. The effect of the calibration vectors on the location capability of the array has also been measured, and it is found that for P-phases 10% of the calibrations are greater than 1100 km and the median is 450 km. For the period from April 1972 until March 1973 Bungum and Husebye (1974) have reported a median location difference between NOAA and NORSAR epicenter solutions of 145 km for P-phases, while the 90% level was 490 km. It should also be noted that until 30 November 1972 an older and less complete correction data base was in use. It thus is a safe statement that without the calibrations the event location performance of the array would have been 3 times worse.

Data Interpretation

As mentioned in the introduction, several hypotheses have been put forward in order to explain the types of deviations described here. Mainly they have been interpreted as the single or combined effect of lateral in-

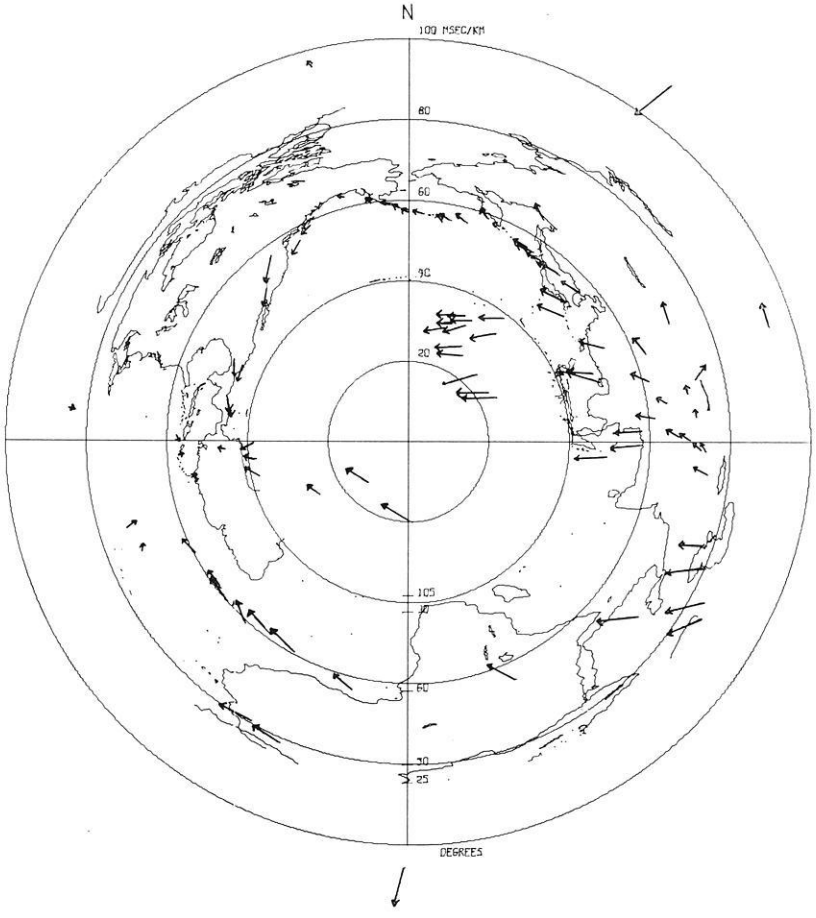

Fig. 3. Location calibration vectors plotted in slowness space. The tail of the arrow represents the observed point, while the head represents the NOAA solution. The contours drawn represent the world map as seen in slowness-space at NORSAR

homogeneities at three different locations along the ray path. One, bending of the ray at the source side of the path, explained as the effect of down-dipping tectonic plates, two, bending of the ray at its deepest (turning) point, and three, inhomogeneities in the crust and upper mantle at the receiver side of the ray path. These last inhomogeneities have usually been interpreted as a Moho interface which deviates from the horizontal plane. More recently scattering caused by small random variations in the index of refraction have been found to be able to explain a large part of the anomalies observed at LASA (Aki, 1973; Capon, 1974). Such studies

have also been performed at NORSAR (Capon and Berteussen, 1973), where the conclusion so far is that the scattering in the upper mantle and crust under NORSAR is too strong to be explained by the Chernov theory (Chernov, 1960). Further studies on this subject are in progress (Dahle *et al.*, paper in preparation).

The mantle-crust interface has been found to exhibit considerable variations in this area (Kanestrøm, 1973). An experiment has therefore been made in order to find out how much of the deviations can possibly be explained by a depth-varying interface located somewhere in the crust or upper mantle beneath NORSAR. To be more specific, this interface will be given a reference depth of 33 km and the *P*-velocities below and above this interface are set to 8.2 and 6.6 km/sec respectively. The aim is then to find the depth varying interface which can explain as much as possible of the deviations which are observed.

Only data from *P*-phases will be used. The deviations will be used as presented in Eq. (1), except that the data will be averaged in intervals of 10 degrees in azimuth. This is to avoid that the cluster of events between azimuth 0 and 90 degrees will have too much influence.

First we will test how much of these anomalies can possibly be explained by a plane dipping interface. A plane wavefront crossing such an interface may change slowness and angle of approach, but will still be a plane wavefront. Therefore such an interface cannot explain any of the wavefront deviations. Using the formulae developed by Niazi (1966) it is possible to calculate the change in slowness and azimuth on a given wavefront when the parameters of the dipping plane are known. Note that in Niazi's paper $\cos(r')$ on page 494 should be replaced by $-\cos(r')$ once in Eq. (6) and two times in Eq. (7) (in the equation for n and the equation for m).

For a certain dipping plane, let dp_{ij} be the travel time anomaly this plane would cause at subarray i for seismic region j. The best plane is then defined as the plane where the parameter

$$R = \sum_{j=1}^{N} \sum_{i=1}^{M} (d_{ij} - dp_{ij})^2 \tag{2}$$

has its minimum. $N = 36$, is number of seismic regions. (The data has been averaged in intervals of 10 degrees spacing in azimuth.) $M = 22$, is number of subarrays d_{ij} is observed travel time anomalies, dp_{ij} is predicted travel time anomalies.

By varying the dip angle and up-dip direction, the plane which gives the minimum value of R has been found. This plane has an up-dip direction of 94 degrees clockwise from north and the dip is 6 degrees. With another velocity contrast the dip angle would of course change. (A contrast of 6.2/8.2 gives for example a dip angle of 4 degrees.) This dipping plane is

Table 1. Table of coefficients for best plane, second degree interface and third degree interface. Per cent reduction in mean squared deviations is also listed for the three models

Model A	$B \cdot 10^3$	$C \cdot 10^3$	$D \cdot 10^3$	$E \cdot 10^3$	$F \cdot 10^3$	$G \cdot 10^6$	$H \cdot 10^6$	$I \cdot 10^6$	$J \cdot 10^6$	% Gain
Plane	−33.0	90.4	22							17.9
2nd degree	−33.0	99.3	−7.9	0.47	−2.0	0.3				21.4
3rd degree	−33.0	222.9	13.1	0.003	−1.55	0.17	33.	−13.5	−51.0	−3.9	24.3

able to explain 17.9% of the squared deviations (Row 1, Table 1). That is, the parameter R (Eq. (2)) is reduced with 17.9% relative to the case where dp_{ij} is uniformly zero.

In this example the interface has been located at the crust-mantle boundary. One is, however, completely free to locate it wherever one should prefer. If, for example, for some reasons the upper mantle is found to be the most likely place the velocity contrast would have to be changed, this would change the dip of the plane, but the updip direction would still be the same. What is most important is, however, that it is not possible to explain more than 17.9% of the variance of the deviations wherever the plane is located.

The equation for the plane used may be written

$$Z = A + B \cdot X + C \cdot Y \tag{3}$$

The values for A, B and C are given in row 1 on Table 1. Our coordinate system is then centered in the array's center with X-axis towards east, Y-axis towards north and Z-axis upwards.

Since a dipping plane cannot satisfactorily explain the deviations, we will go further and try a second degree interface. The equation for this is:

$$Z = A + BX + CY + DX^2 + EXY + FY^2 \tag{4}$$

When the interface can be described in this way, ray-tracing is especially simple and not very time-consuming on a computer. The procedure has therefore been to vary all the coefficients in Eq. (4) systematically. For each set of coefficients conventional ray-tracing has been applied in order to find the deviationas this particular interface would give for our data points. The best interface is then as in the preceding case defined as the interface

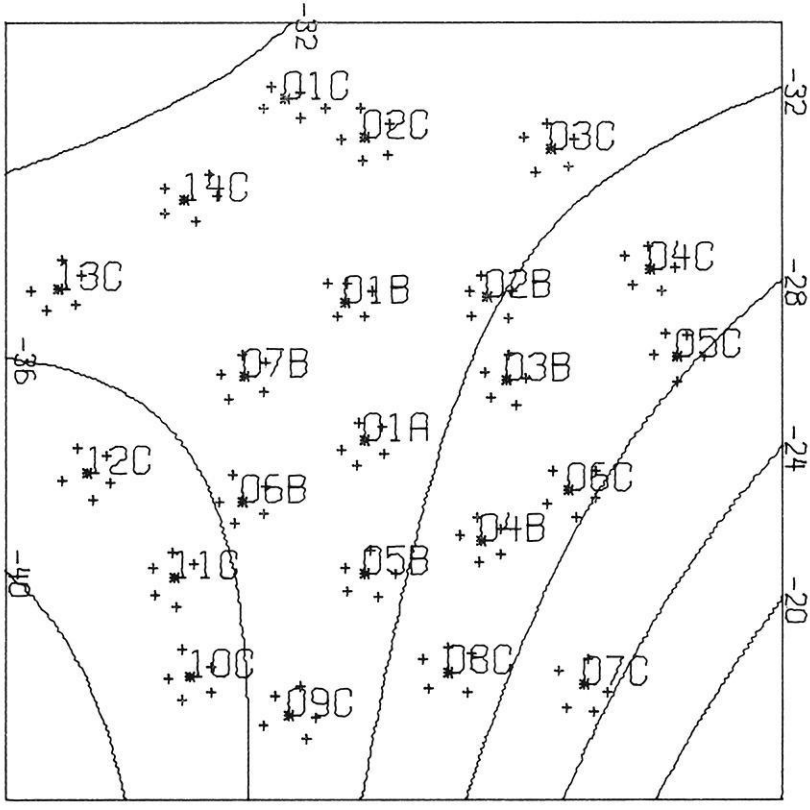

Fig. 4. Depth contours for best 2nd degree interface. $V_C = 6.6$ km/sec, $V_M = 8.2$ km/sec. The NORSAR array configuration is also included

where the sum of the squared differences between predicted and observed deviations has been reduced to a minimum. The coefficients for this surface are listed in row 2, Table 1. As also can be seen from Table 1, this interface is able to explain only 21.4% of the squared deviations. The depth contours for this interface are plotted in Fig. 4. Actually the parameter R in Eq. 2 showed up to be a very well behaved parameter with regard to the coefficients $A, B, \ldots, F$. Some other more efficient minimization procedures could therefore probably have been used with benefit.

The next step was to repeat the above procedure except that this time a polynomial of third order was used. The equation for this is:

$$Z = A + BX + CY + DX^2 + EXY + FY^2 + GX^3 + HX^2Y + IXY^2 + JY^3 \tag{5}$$

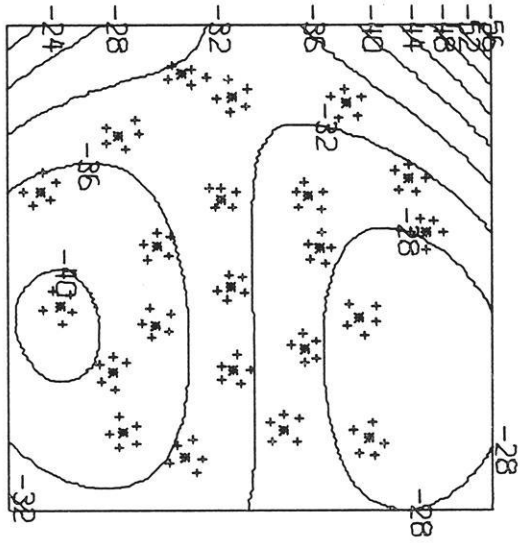

Fig. 5. Depth contours for best 3rd degree interface. $V_C = 6.6$ km/sec, $V_M = 8.2$ km/sec

The coefficients for this interface are listed in row 3 of Table 1. This interface is able to explain 24.3% of the observed squared deviations. The contours for this are drawn in Fig. 5.

Travel time residuals for ordinary stations are commonly approximated with the equation (Bolt and Nuttli, 1966; Nuttli and Bolt, 1969; Lilwall and Douglys, 1969; Payo, 1971).

$$d = A + B \cdot \sin(\sigma + \phi) \tag{6}$$

where σ is station azimuth and the 'early direction' is $(3/4\ \pi - \phi)$. This has been done also for the NORSAR travel time anomalies. The difference from the more common situation is of course that we here are talking of residual between stations instead of absolute travel time residuals. On Fig. 2 the smooth curve is the least squares approximation of the data to Eq. (6). Before performing the approximation, the data as before was grouped and averaged in intervals of 10 degrees in azimuth in order to avoid that the cluster of data between 0 and 90 degrees in azimuth should have too much influence.

The values obtained for A, B and the 'early direction' are listed in Table 2 for the case where only *P*-phase data have been used. In the table are also listed the percentage reduction in mean square deviations by just

Table 2. A, B and early direction for each subarray (see Eq. (6)). Only P-phase data used. Model 1 gives reduction in mean square deviations by using only A, that is, by just subtracting the normalized mean deviations for each subarry. Model 2 gives reduction mean square deviations by using the whole Eq. (6)

Sub. No.	Name	A	B	Early Direction	Model 1 Improvement (%)	Model 2 Improvement (%)
1	01A	—0.07	0.09 ± 0.03	73 ± 23	31.3	56.4
2	01B	—0.05	0.06 ± 0.03	98 ± 32	16.7	27.6
3	02B	—0.09	0.11 ± 0.03	129 ± 18	39.0	61.7
4	03B	—0.10	0.14 ± 0.04	117 ± 16	42.0	77.8
5	04B	—0.08	0.16 ± 0.06	98 ± 23	13.6	39.2
6	05B	—0.10	0.06 ± 0.03	107 ± 35	42.0	48.2
7	06B	0.02	0.03 ± 0.02	320 ± 54	6.9	10.5
8	07B	—0.01	0.10 ± 0.04	356 ± 24	0.2	24.3
9	01C	—0.06	0.10 ± 0.06	308 ± 38	5.9	13.0
10	02C	—0.03	0.01 ± 0.05	26 ± 320	2.2	2.3
11	03C	0.06	0.01 ± 0.05	243 ± 297	8.3	8.5
12	04C	—0.05	0.11 ± 0.04	184 ± 21	9.5	27.9
13	05C	—0.08	0.09 ± 0.04	184 ± 27	14.8	26.0
14	06C	—0.11	0.16 ± 0.05	110 ± 20	28.4	55.8
15	07C	—0.14	0.06 ± 0.05	101 ± 58	31.2	33.8
16	08C	—0.13	0.13 ± 0.04	137 ± 20	36.2	53.8
17	09C	0.07	0.07 ± 0.04	171 ± 35	16.4	23.2
18	10C	0.22	0.12 ± 0.04	242 ± 22	59.3	68.7
19	11C	0.28	0.11 ± 0.03	274 ± 18	77.6	83.6
20	12C	0.26	0.24 ± 0.03	297 ± 8	66.7	91.4
21	13C	0.13	0.32 ± 0.06	313 ± 12	22.9	79.6
22	14C	0.06	0.16 ± 0.05	324 ± 20	8.7	37.7
Total effect					33.8	51.4

subtracting the mean, corresponding to using only A in Eq. (6) (Model 1). The next columns (Model 2) give the percentage reduction in variance by using the whole Eq. (6).

Since the variance of the anomalies changes somewhat from one subarray to another, the total effect of these two models is somewhat different from the average effect on each subarray. From the last row (Table 2) it is seen that by using the whole Eq. (6), the variance may be reduced by 51.4%. This model (2) is the one which best fits the data. For single stations there are several ways to interpret such a model (Nuttli and Bolt, 1969; Lilwall and Douglas, 1969; Payo, 1971). In this case with 22 stations so close together it is difficult to invert the mathematical model into physically reliable structures. For each single subarray the deviations could for example be interpreted as being caused by a plane dipping interface with depth, dip and updip direction given from A, B, and the

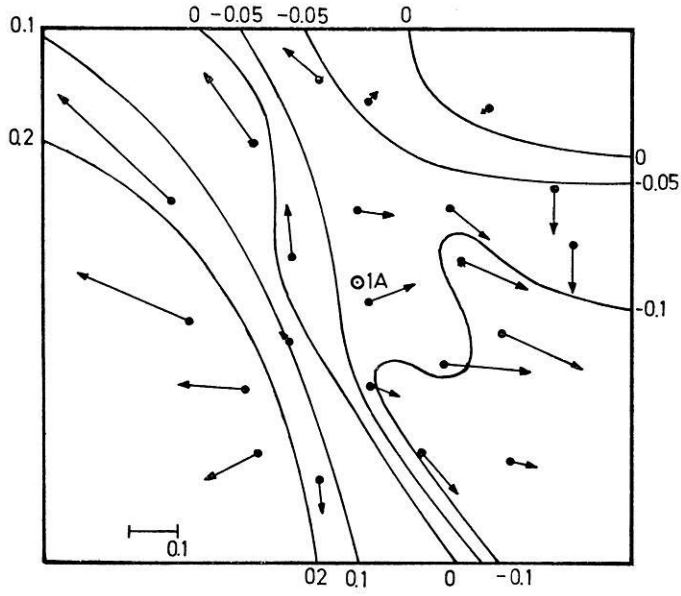

Fig. 6. Contours for average deviations relative to NOAA wavefronts (sec). Only *P*-phase data has been used. The length of the arrow is proportional to B in Eq. (6), while the direction gives the early direction

'early direction'. However, it is quite impossible to combine these planes in a way such that all the 22 equations could be satisfied. It should be noted that model 1, that is, just subtracting a fixed mean value for each subarray, shows a better fit performance than any of the polynomial interfaces tested previously. This model, which has been considered earlier by Gjøystdal *et al.* (1973), may be thought of as representing structural inhomogeneities in the array site area. On Fig. 6 contours for average deviations for *P*-phases are plotted. The arrows on the figure give the 'early direction' and the length of the arrow is proportional to B in Eq. (6).

Discussion

As seen from Figs. 4 and 5, the interfaces found do exhibit such large elevation differences that their geophysical reality is questionable. To increase the order of the polynomial to higher degrees than 3 cannot be done because we then will end up with such a detailed map that simple ray theory may not be used. If the velocity in the crust above the interface is set to 6.2 km/sec, a second degree polynomial found in the same way as described in the above section will be able to explain 24.9% of the squared deviations. The contours for this interface are shown in Fig. 7. The conclu-

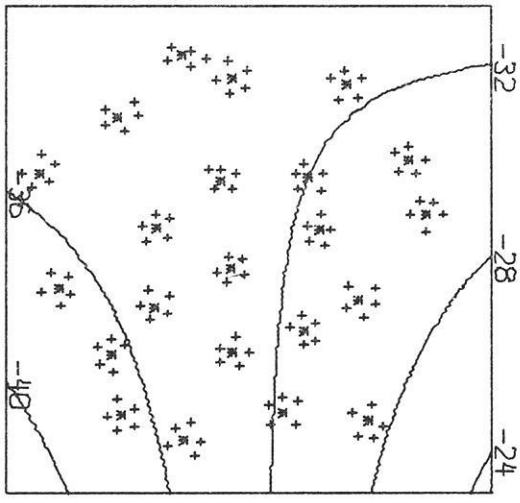

Fig. 7. Depth contours for best 2nd degree interface $V_C = 6.2$ km/sec, $V_M = 8.2$ km/sec

sion is that it is not possible to construct a physically trustworthy interface which is able to explain more than say 25% of the sum of the squared deviations observed at NORSAR. It thus seems that in order to explain the bulk of the deviations observed, other types of models have to be introduced; for example, models where wave scattering and possibly multipathing take a more important part.

To make it quite clear, the Figs. 4, 5 and 7 are not thought of as representing a real interface. The intention with these figures and the section above is to show that the kind of deviations observed exhibit such large variations that they cannot be explained satisfactorily by simple smooth interfaces. Thus, the effect of varying Moho depth cannot be dominant in this data base. In order to say something about the shape of the Moho interface, other types of data therefore have to be used.

Acknowledgement. The NORSAR project is sponsored by the United States Air Force and monitored by the European Office of Aerospace Research and Development, Air Force Systems Command, under Contract Number F-44620-74-C-0001 with the Royal Norwegian Council for Scientific and Industrial Research.

References

Aki, K.: Scattering of P-waves under the Montana LASA. J. Geophys. Res. *78*, 1334–1346, 1973

Bolt, B. A., Nuttli, O.: P-wave residuals as a function of azimuth, I, Observations. J. Geophys. Res. *71*, 5977–5985, 1966

Brown, R. J.: Slowness and azimuth at the Uppsala array. Part 1: Array Calibration and Event Location. Pure Appl. Geophys. *105*, 759–769, (1973)

Brown, R. J.: Slowness and azimuth at the Uppsala array. Part 2: Structural studies. Pure Appl. Geophys. *109*, 1623–1637, 1973a

Bungum, H., Husebye, E. S.: Errors in time delay measurements. Pure Appl. Geophys. *91*, 56–70, 1971.

Bungum, H., Husebye, E. S., Ringdal, F.: The NORSAR array and preliminary results of data analysis. Geophys. J. *25*, 115–126, 1971

Bungum, H., Husebye, E. S.: Analysis of the operational capabilities for detection and location of seismic events at NORSAR, Bull. Seism. Soc. Am., in press, 1974

Engdahl, E. R., Felix, C. P.: Nature of travel time anomalies at LASA. H. Geophys. Res. *76*, 2706–2715, 1971.

Gjøystdal, H., Husebye, E. S., Rieber-Mohn, D.: One-array and two-array location capabilities, Bull. Seism. Soc. Am. *63*, 549–569, 1973

Glover, P., Alexander, S. S.: Lateral variations in crustal structure beneath the Montana LASA. J. Geophys. Res. *74*, 505–531, 1969

Greenfield, R. J., Sheppard, R. M.: The Moho depth variations under the LASA and their effect on $DT/d\Delta$ measurements. Bull. Seism. Soc. Am. *59*, 409–420, 1969

Herrin, E., (Chairman) Seismological table for P-phases, Bull. Seism. Soc. Am. *58*, 1193–1241, 1968

Husebye, E. S., Kanestrøm, R., Rud, R.: Observations of vertical and lateral P-velocity anomalies in the earth's mantle using the Fennoscandinavian continental array. Geophys. J. *25*, 3–16, 1971

Iyer, H. M.: Variation of apparent velocity of teleseismic P-waves across the Large Aperture Seismic Array (LASA), Montana, J. Geophys. Res. *76*, 8554–8567, 1971

Capon, J.: Characterization of crust and upper mantle structure under LASA as a random medium, Bull. Seism. Soc. Am., in press, 1974

Capon, J., Berteussen, K. A.: Semiannual Technical Summary Report to the Advanced Research Projects Agency, Mass. Inst. Tech., Lincoln Lab., Cambridge, Mass., USA, December 1973

Chernov, L. A.: Wave Propagation in a Random Medium, Translated by R. A. Silverman. New York: McGraw-Hill Book Company 1960

Chinnery, M. A., Toksöz, M. N.: P-wave velocities in the mantle below 700 km. Bull. Seism. Soc. Am. *57*, 199–226, 1967

Corbishley, P. J.: Multiple array measurements of the P-wave travel time derivative. Geophys. J. *19*, 1–14, 1970

Davies, D., Sheppard, R. M.: Lateral heterogeneity in the earth's mantle. Nature *239*, 318–323, 1972

Iyer, H. M., Healy, J. H.: Teleseismic residuals at the LASA USGS extended array and their interpretation in terms of crust and upper mantle structure. J. Geophys. Res. *77*, 1503–1527, 1972

Johnson, L. R.: Array measurements of P velocities in the upper mantle. J. Geophys. Res. *72*, 6309–6324, 1967

Johnson, L. R.: Array measurements of P velocities in the lower mantle, Bull. Seism. Soc. Am. *59*, 973–1008, 1969

Kanestrøm, R.: A crust-mantle model for the NORSAR area. Pure Appl. Geophys. *105*, 729–740, 1973

Lilwall, R. C., Douglas, A.: Estimation of P-wave travel times using the joint epicenter method. Geophys. J. *19*, 165–181, 1970

Mack, H.: Nature of short-lived P-wave signal variations at LASA. J. Geophys. Res. *74*, 3161–3170, 1969

Niazi, M.: Corrections to apparent azimuths and travel time gradients for a dipping Mohorovicic discontinuity. Bull. Seism. Soc. Am. *56*, 491–509, 1966

Noponen, I.: Analysis of event location errors using arrays in Scandinavia. Proc. from the seminar on seismology and seismic arrays. NTNF/NORSAR, Kjeller, Norway, 1971

Nuttli, O. W., Bolt, B. A.: P-wave residuals as a function of azimuth, 2, Undulations of the mantle low-velocity layer as an explanation. J. Geophys. Res. *74*, 6594–6602, 1969

Otsuka, M.: Azimuth and slowness anomalies of seismic waves measured on the central California seismographic array, Part 1, Observations. Bull. Seism. Soc. Am. *56*, 223–239, 1966

Otsuka, M.: Azimuth and slowness anomalies of seismic waves measured on the central California seismographic array, Part 2, Interpretation. Bull. Seism. Soc. Am., *56*, 655–675, 1966a

Payo, G.: P-wave resicuals at some Iberic stations and deep structure of South-Western Europe. Geophys. J. *26*, 481–497, 1971

Zengeni, T. G.: A note on azimuthal correction for $dT/d\Delta$ for a single dipping plane interface. Bull. Seism. Soc. Am., *60*, 299–306, 1970

K. A. Berteussen
NTNF/NORSAR
Post Box 51
N-2007 Kjeller
Norway

J. Geophys. 41, 85–109, 1975

Electromagnetic Induction in Three-Dimensional Structures

P. Weidelt

Institut für Geophysik der Universität, Göttingen

Received August 14, 1974

Abstract. The treatment of electromagnetic induction in three-dimensional structures is simplified by converting Maxwell's equations to a linear inhomogeneous vector integral equation over the domain where the electrical conductivity deviates from a horizontally layered structure. An algorithm for the calculation of the (tensor) kernel is given. The integral equation is solved either by an iterative method or by matrix inversion. In an application the complete electromagnetic surface field of a simple conductivity anomaly and induction arrow maps are given. The gradual transition from three to two dimensions is investigated for a particular model.

Key words: Electromagnetic Induction — Electrical Conductivity — Conductivity Anomalies.

1. Introduction

Numerical solutions of the three-dimensional modelling problem of electromagnetic induction are only scarcely encountered in the current literature (e.g. Jones and Pascoe, 1972; Lines and Jones, 1973). This is not due to mathematical difficulties, but results from the fact that the usual reduction of Maxwell's equations to finite differences, including into the domain under consideration the air half-space, requires large computer storage and is time consuming as well.

A reduction of computer time and storage is achieved by applying surface and volume integral techniques based on Green's tensor. Consider for example an anomalous three-dimensional conductivity structure of finite extent embedded in a normal conductivity structure consisting of a horizontally stratified half-space. Then given an external source field, Maxwell's equations have to be solved under the condition of vanishing anomalous field at infinity. At least three approaches to a numerical solution of this problem are possible. Approach A is to choose a basic domain (including the air layer) as large as possible and to solve within this domain Maxwell's equations by finite differences, subject either to the now only approximate boundary condition of zero anomalous field or to a more refined impedance boundary condition (Fig. 1, top). This is the approach

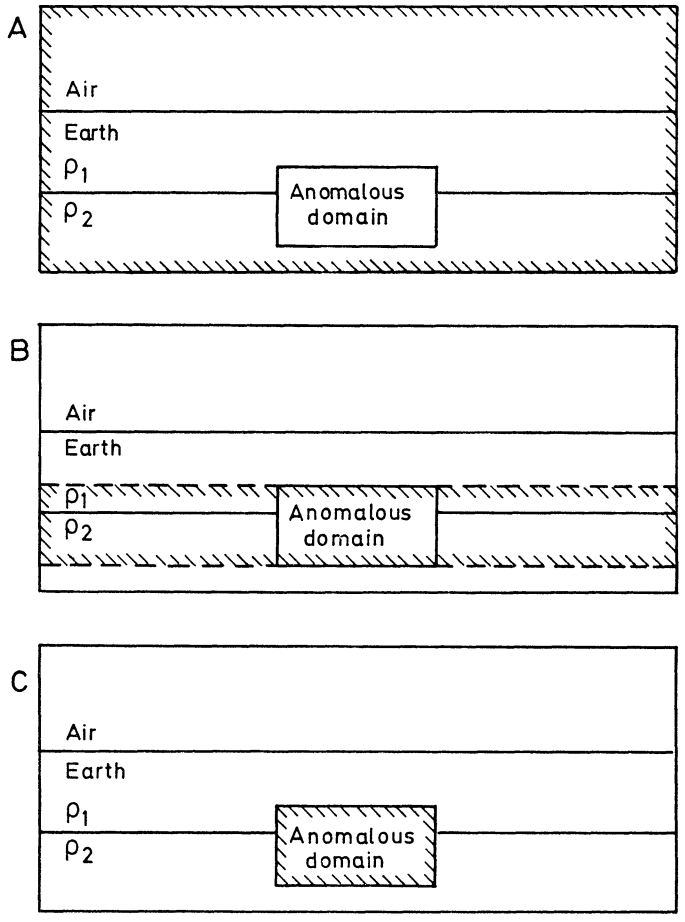

Fig. 1. The three different choices of a basic domain (boundary hatched) for model calculations

of Jones and co-workers. A first reduction of the basic domain is achieved by considering only the anomalous slab which contains the conductivity anomaly (Fig. 1, centre). Within this slab, Maxwell's equations are solved by finite differences as before, but now all field values outside the anomalous slab are expressed by a surface integral in terms of the tangential component of the anomalous electric field at the horizontal boundaries of the slab. At the vertical boundaries of the anomalous slab approximate boundary conditions analogous to those of approach A are applied. This is approach B. A modified version of it for two dimensions is used by Schmucker (1971). In approach C the basic domain is reduced

still further by deriving from Maxwell's equations by a Green's tensor an integral equation for the electric field involving volume integrals only over the anomalous field vector within the anomalous domain (Fig. 1, bottom). The boundary conditions are incorporated in the kernel of the integral equation, and hence are satisfied automatically by the solution. This method has been applied in two dimensions by Hohmann (1972) and has been formulated in three dimensions by Raiche (1974).

From approach A to C the gradual reduction of the basic domain must be paid by increasing expenses for calculating the required kernels. Approach C is of particular advantage if the anomalous domain is small. If the domain extends appreciably in horizontal direction (e.g. different conductivities at the left and the right of the anomalous slab), approach B is appropriate. Approach A can be avoided in any case.

This paper presents a short outline of approach B and a detailed description of approach C, thereby reformulating the method of Raiche (1974) in a slightly different way. The basic equations are stated in Sec. 2, general formulae for Green's tensor for an earth with an arbitrary number of layers are given in Sec. 3, and a few numerical problems encountered in applying approach C are treated in Sec. 4. The final Sec. 5 presents some results.

2. Green's Tensor Approaches to the Modelling Problem

2.1. Definitions, Basic Equations

$\boldsymbol{r}$ denotes the position vector and x, y, z (z positive downwards) are cartesian coordinates, which for the sake of convenience are sometimes also denoted by x_1, x_2, x_3. Let the conductor with conductivity $\sigma(\boldsymbol{r})$ occupy the half-space $z > 0$. Neglecting the displacement current, assuming vacuum permeability and a harmonic time factor $e^{i\omega t}$ throughout, the complex amplitudes $\boldsymbol{E}$ and $\boldsymbol{H}$ of the electric and magnetic field vector are related by

$$\operatorname{curl} \boldsymbol{H}(\boldsymbol{r}) = \sigma(\boldsymbol{r})\, \boldsymbol{E}(\boldsymbol{r}) + \boldsymbol{j}_e(\boldsymbol{r}), \tag{2.1}$$

$$\operatorname{curl} \boldsymbol{E}(\boldsymbol{r}) = -i\omega\mu_0 \boldsymbol{H}(\boldsymbol{r}), \tag{2.2}$$

or combined

$$\operatorname{curl}^2 \boldsymbol{E}(\boldsymbol{r}) + k^2(\boldsymbol{r})\, \boldsymbol{E}(\boldsymbol{r}) = -i\omega\mu_0 \boldsymbol{j}_e(\boldsymbol{r}), \tag{2.3}$$

SI units being used. $\boldsymbol{j}_e(\boldsymbol{r})$ is the current density of the external source field, $\operatorname{curl}^2 = \operatorname{curl} \operatorname{curl}$, and

$$k^2(\boldsymbol{r}) = i\omega\mu_0\sigma(\boldsymbol{r}). \tag{2.4}$$

Split $\sigma(\boldsymbol{r})$ into a normal and anomalous part, the former consisting of a set of horizontal uniform layers. (For simplicity, within the earth all layer conductivities are assumed to be non-zero.) Hence,

$$\sigma = \sigma_n + \sigma_a,\ k^2 = k_n^2 + k_a^2,\ \boldsymbol{E} = \boldsymbol{E}_n + \boldsymbol{E}_a, \tag{2.5}$$

$\boldsymbol{E}_n$ being defined as the solution of

$$\text{curl}\ {}^2\boldsymbol{E}_n(\boldsymbol{r}) + k_n^2(\boldsymbol{r})\,\boldsymbol{E}_n(\boldsymbol{r}) = -\,i\omega\mu_0\,\boldsymbol{j}_e(\boldsymbol{r}), \tag{2.6}$$

vanishing for $z \to \infty$. Methods for the computation of $\boldsymbol{E}_n$ are well-known (e.g. Schmucker, 1970; Weaver, 1970).

2.2. The Volume Integral Method (Approach C)

From (2.3), (2.5), and (2.6) follows

$$\text{curl}\ {}^2\boldsymbol{E}_a(\boldsymbol{r}) + k_n^2(\boldsymbol{r})\,\boldsymbol{E}_a(\boldsymbol{r}) = -\,k_a^2(\boldsymbol{r})\boldsymbol{E}(\boldsymbol{r}). \tag{2.7}$$

Let $\boldsymbol{G}_i(\boldsymbol{r}_0|\boldsymbol{r})$, $i = 1,2,3$, be the solution of

$$\text{curl}\ {}^2\boldsymbol{G}_i(\boldsymbol{r}_0|\boldsymbol{r}) + k_n^2(\boldsymbol{r})\,\boldsymbol{G}_i(\boldsymbol{r}_0|\boldsymbol{r}) = \hat{\boldsymbol{x}}_i\,\delta(\boldsymbol{r}-\boldsymbol{r}_0), \tag{2.8}$$

vanishing at infinity. In (2.8) and in the sequel, $\hat{}$ denotes a unit vector. Multiply (2.8) by $\boldsymbol{E}_a(\boldsymbol{r})$ and (2.7) by $\boldsymbol{G}_i(\boldsymbol{r}_0|\boldsymbol{r})$ and integrate the difference with respect to $\boldsymbol{r}$ over the whole space. Green's vector theorem (e.g. Morse and Feshbach, 1953, p. 1768)

$$\begin{aligned}&\int\{\boldsymbol{U}\cdot\text{curl}\ {}^2\boldsymbol{V} - \boldsymbol{V}\cdot\text{curl}\ {}^2\boldsymbol{U}\}d\tau\\ &= \oint\{\hat{\boldsymbol{n}}\times\boldsymbol{V})\cdot\text{curl}\ \boldsymbol{U} - (\hat{\boldsymbol{n}}\times\boldsymbol{U})\cdot\text{curl}\ \boldsymbol{V}\}dA,\end{aligned} \tag{2.9}$$

where $d\tau$ is a volume element, dA a surface element, and $\hat{\boldsymbol{n}}$ the outward normal vector, yields

$$E_{ai}(\boldsymbol{r}_0) = -\int k_a^2\,\boldsymbol{G}_i(\boldsymbol{r}_0|\boldsymbol{r})\cdot\boldsymbol{E}(\boldsymbol{r})d\tau, \quad i = 1,2,3, \tag{2.10}$$

since $\boldsymbol{E}_a$ and $\boldsymbol{G}_i$ vanish at infinity. After combining all three components and introducing $\boldsymbol{E}$ instead of $\boldsymbol{E}_a$, the vector integral equation

$$\boldsymbol{E}(\boldsymbol{r}_0) = \boldsymbol{E}_n(\boldsymbol{r}_0) - \int k_a^2(\boldsymbol{r})\,\mathfrak{G}(\boldsymbol{r}_0|\boldsymbol{r})\cdot\boldsymbol{E}(\boldsymbol{r})d\tau \tag{2.11}$$

is obtained. Here $\mathfrak{G}$ is the Green's tensor (using dyadic notation)

$$\mathfrak{G}(\boldsymbol{r}_0|\boldsymbol{r}) = \sum_{i=1}^{3} \hat{\boldsymbol{x}}_i \boldsymbol{G}_i(\boldsymbol{r}_0|\boldsymbol{r}) = \sum_{i,\,j=1}^{3} G_{ij}(\boldsymbol{r}_0|\boldsymbol{r})\, \hat{\boldsymbol{x}}_i\, \hat{\boldsymbol{x}}_j. \tag{2.12}$$

The tensor elements G_{ij} admit a simple physical interpretation: $G_{ij}(\boldsymbol{r}_0|\boldsymbol{r})$ is the j-th electric field component of an oscillating electric dipole of unit moment pointing in x_i-direction, placed in the *normal* conductivity structure at $\boldsymbol{r}_0$; the point of observation is $\boldsymbol{r}$. Note that the first index and argument refer to the source, the second index and argument to the observer. Because of the fundamental reciprocity in electromagnetism, observer and source parameters are interchangeable, i.e.

$$G_{ij}(\boldsymbol{r}_0|\boldsymbol{r}) = G_{ji}(\boldsymbol{r}|\boldsymbol{r}_0). \tag{2.13}$$

For a proof replace in (2.8) $\boldsymbol{r}$ by $\boldsymbol{r}'$, write an analogous equation for $\boldsymbol{G}_j(\boldsymbol{r}|\boldsymbol{r}')$, multiply cross-wise by $\boldsymbol{G}_j$ and $\boldsymbol{G}_i$, integrate the difference with respect to $\boldsymbol{r}'$ over the whole space, and obtain (2.13) on using (2.9). Due to (2.13), (2.11) is alternatively written

$$\boldsymbol{E}(\boldsymbol{r}_0) = \boldsymbol{E}_n(\boldsymbol{r}_0) - \int k_a^2(\boldsymbol{r})\, \boldsymbol{E}(\boldsymbol{r}) \cdot \mathfrak{G}(\boldsymbol{r}|\boldsymbol{r}_0) d\tau. \tag{2.14}$$

Eq. (2.11) or (2.14) is a vector Fredholm integral equation of the second kind for the electric field $\boldsymbol{E}$. The kernel $\mathfrak{G}$ and inhomogeneous term $\boldsymbol{E}_n$ depend only on the normal conductivity structure. The domain of integration is the anomalous domain. To determine the kernel $\mathfrak{G}$ replace first the conductivity within the anomalous domain by its normal values. Then place at each point of the domain two mutually perpendicular horizontal dipoles and one vertical dipole and calculate the resulting vector fields at each point of this domain. At a first glance the work involved appears to be prohibitive, but it is sharply reduced by the reciprocity (2.13) and the isotropy of the normal conductor in horizontal direction. In particular, only one horizontal dipole is required. Since the kernels are independent of σ_a and $\boldsymbol{E}_n$, the same kernels apply if the conductivity within the anomalous domain is changed and/or the external field is altered (e.g. different polarization).

In the simplest, though physically not very interesting case of a uniform whole space with conductivity σ_0 the tensor elements are simply

$$\begin{aligned} k_0^2 G_{ij}(\boldsymbol{r}_0|\boldsymbol{r}) &= (k_0^2 \delta_{ij} - \partial^2/\partial x_i\, \partial x_j) e^{-k_0 R}/(4\pi R) \\ &= \{(1+u+u^2)\delta_{ij} - (3+3u+u^2)\,(x_i - x_{i0})\,(x_j - x_{j0})/R^2\} e^{-u}/(4\pi R^3) \end{aligned} \tag{2.15}$$

(e.g. Morse and Feshbach, 1953, p. 1781). Here, $R=|\boldsymbol{r}-\boldsymbol{r}_0|$, $k_0^2=i\omega\mu_0\sigma_0$, $u=k_0R$, and δ_{ij} is the Kronecker symbol. For a uniform half-space the elements are given in the appendix. A method for calculating the elements for an arbitrary number of layers is presented in Sec. 3.

The integral equation (2.11) or (2.14) is decomposed into a set of linear equations, which are solved either by iterative techniques or by matrix inversion. Suggestions for the use of either of these techniques are given in Sec. 4. When the electric field within the anomaly is known, a second set of kernels is required, which transform the field via (2.11) or (2.14) into the surface field. The kernels for the magnetic field are obtained by considering the curl of (2.11) or (2.14) with respect to $\boldsymbol{r}_0$.

2.3. The Surface Integral Method (Approach B)

Let the anomalous slab be confined to the depth range $z_1\leq z\leq z_2$. Approach B is to solve within the anomalous slab the inhomogeneous equation

$$\text{curl}\ {}^2\boldsymbol{E}_a(\boldsymbol{r})+k^2(\boldsymbol{r})\,\boldsymbol{E}_a(\boldsymbol{r})=-k_a^2(\boldsymbol{r})\,\boldsymbol{E}_n(\boldsymbol{r}) \tag{2.16}$$

(from (2.3), (2.5), and (2.6)) subject to two homogeneous boundary conditions at $z=z_1$ and $z=z_2$, which involve σ_n for $z<z_1$ and $z>z_2$ respectively, and account for the vanishing anomalous field for $z\to\pm\infty$. When (2.16) is solved by finite differences, the discretization involves also the field values one grid point width above and below the anomalous slab. The surface integral method is simply to express these values by a surface integral in terms of the tangential component of $\boldsymbol{E}_a$ at z_1 and z_2, respectively.

Let V_1 and V_2 be the half-spaces $z<z_1$ and $z>z_2$, respectively, and let S_m, $m=1,2$, be the planes $z=z_m$. Let $\boldsymbol{G}_i^{(m)}(\boldsymbol{r}_0|\boldsymbol{r})$, $\boldsymbol{r}_0\in V_m$, $\boldsymbol{r}\in V_m\cup S_m$, be a solution of

$$\text{curl}\ {}^2\boldsymbol{G}_i^{(V)}(\boldsymbol{r}_0|\boldsymbol{r})+k_n^2(\boldsymbol{r})\boldsymbol{G}_i^{(m)}(\boldsymbol{r}_0|\boldsymbol{r})=\hat{\boldsymbol{x}}_i\delta(\boldsymbol{r}-\boldsymbol{r}_0) \tag{2.17}$$

($i=1,2,3$; $m=1,2$) satisfying for $\boldsymbol{r}\in S_m$ the boundary condition

$$\hat{\boldsymbol{z}}\times\boldsymbol{G}_i^{(m)}(\boldsymbol{r}_0|\boldsymbol{r})=0. \tag{2.18}$$

In V_1 and V_2, $\boldsymbol{E}_a$ is a solution of

$$\text{curl}\ {}^2\boldsymbol{E}_a(\boldsymbol{r})+k_n^2(\boldsymbol{r})\,\boldsymbol{E}_a(\boldsymbol{r})=0. \tag{2.19}$$

Multiply (2.19) by $\boldsymbol{G}_i^{(m)}$, (2.17) by $\boldsymbol{E}_a$, integrate the difference with respect to $\boldsymbol{r}$ over V_m, and obtain on using (2.9), (2.18) and $\boldsymbol{E}_a \to 0$ for $\boldsymbol{r} \to \infty$

$$E_{ai}(\boldsymbol{r}_0) = (-1)^m \int_{S_m} \{\hat{\boldsymbol{z}} \times \boldsymbol{E}_a(\boldsymbol{r})\} \cdot \operatorname{curl} \boldsymbol{G}_i^{(m)}(\boldsymbol{r}_0|\boldsymbol{r})\, dA, \tag{2.20}$$

$r_0 \in V_m$, or in tensor notation

$$\boldsymbol{E}_a(I_0) = (-1)^m \int_{S_m} \operatorname{curl} \mathfrak{G}^{(m)}(\boldsymbol{r}_0|\boldsymbol{r})\, \{\hat{\boldsymbol{z}} \times \boldsymbol{E}_a(\boldsymbol{r})\}\, dA,$$

where $\operatorname{curl} \mathfrak{G}^{(m)} = \sum_i \hat{\boldsymbol{x}}_i \operatorname{curl} \boldsymbol{G}_i^{(m)}$.

This is the required mapping, which admits the representation of the field values outside the anomalous layer in terms of the boundary values of the (continuous) tangential component of $\boldsymbol{E}_a$.

A physical interpretation of Green's vector $\boldsymbol{G}_i^{(m)}(\boldsymbol{r}_0|\boldsymbol{r})$ subject to (2.18) is as follows: Reflect the normal conductivity structure for $z < z_1$ and $z > z_2$ at the planes $z = z_1$ and $z = z_2$ respectively, place a unit dipole in x_i-direction at $r_0 \in V_m$ and an image dipole at $\boldsymbol{r}_0' = \boldsymbol{r}_0 + 2\,(z_m - z_0)\hat{\boldsymbol{z}}$, the moment being the opposite for the two horizontal dipoles and the same for the vertical dipole. Then the tangential component of $\boldsymbol{G}_i^{(m)}$ vanishes at $z = z_m$.

Hence, if V_m is a uniform half-space, $\boldsymbol{G}_i^{(m)}$ is constructed from the whole space formula (2.15). Eq. (2.20) then reads

$$E_{ax}(\boldsymbol{r}_0) = |z_0 - z_m| \int_{S_m} F(R) E_{ax}(\boldsymbol{r})\, dA, \tag{2.21a}$$

$$E_{ay}(\boldsymbol{r}_0) = |z_0 - z_m| \int_{S_m} F(R) E_{ay}(\boldsymbol{r})\, dA, \tag{2.21b}$$

$$E_{az}(\boldsymbol{r}_0) = (-1)^m \int_{S_m} F(R)\{(x - x_0) E_{ax}(\boldsymbol{r}) + (y - y_0) E_{ay}(\boldsymbol{r})\}\, dA, \tag{2.21c}$$

where $R = |\boldsymbol{r} - \boldsymbol{r}_0|$, $k_0^2 = i\omega\mu_0\sigma_0$, and

$$F(R) = -\frac{1}{2\pi R} \frac{d}{dR} (e^{-k_0 R}/R) = (1 + k_0 R) e^{-k_0 R}/(2\pi R^3).$$

Eqs. (2.21a–c) contain as important subcase the condition at the air-earth interface ($z_1 = 0$, $k_0 = 0$).

Because of the limited range of the kernels, in applications of the surface integral only a small portion of S_m is considered. For E_{ax} and E_{ay} the contribution of the region nearest to $\boldsymbol{r}_0$ is most important. Assuming E_{ax} and E_{ay} to be constant within a small disc of radius ϱ centered perpendicularly over $\boldsymbol{r}_0$, the weight from (2.21a, b) is simply

$$e^{-k_0\lambda} - (\lambda/\sqrt{\lambda^2 + \varrho^2}) e^{-k_0\sqrt{\lambda^2+\varrho^2}},$$

where $\lambda = |z_m - z_0|$ is the vertical grid point width. Under the same conditions the disc does not contribute to E_{az}.

At the vertical boundaries of the anomalous layer the condition $\boldsymbol{E}_a = 0$ might be a very crude approximation, in particular for a small grid. Here, an impedance boundary condition for the tangential component $\boldsymbol{E}_{at}$ of the anomalous electric field,

$$k\,\boldsymbol{E}_{at} = \hat{\boldsymbol{n}} \times \operatorname{curl} \boldsymbol{E}_a,$$

$\hat{\boldsymbol{n}}$ = outward normal, $k^2(\boldsymbol{r}) = i\omega\mu_0\sigma(\boldsymbol{r})$, performs substantially better (Jones, 1964, p. 325).

3. Computation of Green's Tensor

Consider a normal conductivity structure consisting of a non-conducting air half-space (index 0) and M uniform conducting layers with conductivities σ_m, $m = 1,2, \ldots, M$, all different from zero. Let the interfaces be placed at the depths $h_1 = 0, h_2, \ldots, h_M$. To calculate Green's tensor for approach C, two mutually perpendicular horizontal electric dipoles and one vertical electric dipole of unit moment have to be placed at each point, which will be occupied by the anomalous domain, and the three components of each resulting field have to be determined for each interior point of the domain. Because of the horizontal isotropy, in practice one horizontal dipole is sufficient.

The calculation of dipole source fields within a layered structure is a classical problem (e.g. Sommerfeld, 1935; Wait, 1970). In the applications (e.g. electromagnetic sounding, antenna theory), however, only the position of a dipole *above and on* the structure is of interest. Largely referring to the above studies, only the modifications due to the position of the dipole *within* the structure are stated.

Let the dipole with moment in x_i-direction be placed in the μ-th layer at $\boldsymbol{r}_0$, and let $\boldsymbol{G}_i^m(\boldsymbol{r}_0|\boldsymbol{r})$ be the resulting field in the m-th layer at point $\boldsymbol{r}$. The continuity of the tangential components of the electric and magnetic field at interfaces leads to the conditions

$$\hat{\boldsymbol{z}} \times (\boldsymbol{G}_i^{m-1} - \boldsymbol{G}_i^m) = 0,\ \hat{\boldsymbol{z}} \times \operatorname{curl} (\boldsymbol{G}_i^{m-1} - \boldsymbol{G}_i^m) = 0, \qquad z = h_m,\ m = 1,\ldots,M. \tag{3.1}$$

$\boldsymbol{G}_i$ is represented with the aid of a Hertz vector $\boldsymbol{\pi}_i$:

$$\boldsymbol{G}_i^m(\boldsymbol{r}_0|\boldsymbol{r}) = k_m^2\,\boldsymbol{\pi}_i^m(\boldsymbol{r}) - \operatorname{grad} \operatorname{div} \boldsymbol{\pi}_i^m(\boldsymbol{r}), \tag{3.2}$$

where $k_m^2 = i\omega\mu_0\sigma_m$ and $\boldsymbol{\pi}_i^m$ satisfies

$$\Delta\boldsymbol{\pi}_i^m(\boldsymbol{r}) = k_m^2\,\boldsymbol{\pi}_i^m(\boldsymbol{r}) - \hat{\boldsymbol{x}}_i\,\delta(\boldsymbol{r} - \boldsymbol{r}_0)/k_m^2. \tag{3.3}$$

For the sequel a cylindrical co-ordinate system (r,ϕ,z) is adopted and the dipole is placed at $r=0$, $z=z_0$. The vertical and horizontal dipole require different treatment.

α) *Vertical Dipole*

$\boldsymbol{\pi}_z^m$ has a vertical component only,

$$\boldsymbol{\pi}_z^m(\boldsymbol{r}) = \pi_{zz}^m(\boldsymbol{r})\hat{\boldsymbol{z}}, \tag{3.4}$$

where π_{zz}^m satisfies

$$\Delta\pi_{zz}^m(\boldsymbol{r}) = k_m^2\pi_{zz}^m(\boldsymbol{r}) - \delta(\boldsymbol{r}-\boldsymbol{r}_0)/k_m^2. \tag{3.5}$$

Eq. (3.1) implies the boundary conditions

$$\sigma_{m-1}\pi_{zz}^{m-1} - \sigma_m\pi_{zz}^m = 0,\ \frac{\partial}{\partial z}(\pi_{zz}^{m-1} - \pi_{zz}^m) = 0,\ z = h_m. \tag{3.6}$$

The general solution of circular symmetry of the homogeneous version of (3.5) can be built up from terms of the form

$$f_m^{\pm}(z)J_0(sr),\ \text{where } f_m^{\pm} = e^{\pm\alpha_m(z-h_m)},\ \alpha_m^2 = s^2 + k_m^2,\ m = 0,\ldots,M \tag{3.7a-c}$$

with $h_0=0$; s is the constant of separation and J_0 the zero order Bessel function of the first kind. The plus and minus sign denote upward and downward travelling waves, respectively. The solution of (3.5) for a uniform whole-space with $\sigma=\sigma_\mu$ is

$$\frac{e^{-k_\mu R}}{4\pi k_\mu^2 R} = \frac{1}{4\pi k_\mu^2}\int_0^\infty \frac{s}{\alpha_\mu} e^{-\alpha_\mu|z-z_0|}J_0(sr)ds,\ R = |\boldsymbol{r}-\boldsymbol{r}_0|. \tag{3.8}$$

Now let for $0\leq m\leq M$

$$\pi_{zz}^m = \int_0^\infty (P_m^+ + P_m^-)J_0\,ds,\ \text{where } P_m^{\pm} = \begin{cases}\gamma_0 A_m^{\pm} f_m^{\pm}, & z\leq z_0\\ \gamma_M B_m^{\pm} f_m^{\pm}, & z\geq z_0\end{cases}. \tag{3.9}$$

$A_m^{\pm}$, $B_m^{\pm}$, γ_0 and γ_M are also functions of s; γ_0 and γ_M being so adjusted that $A_0^+ = B_M^- = 1$. The absence of downgoing waves for $z\leq 0$ and upgoing waves for $z\geq z_0$, if z_0 is in the M-th layer, yields $A_0^- = B_M^+ = 0$.

Starting with $A_0^+ = 1$, $A_0^- = 0$, the boundary conditions imply for $1 \leq m \leq \mu$ the recurrence relations

$$\begin{aligned} A_m^\pm = &\left(\frac{\sigma_{m-1}}{\sigma_m} \pm \frac{\alpha_{m-1}}{\alpha_m}\right) g_{m-1}^+ A_{m-1}^+ \\ &+ \left(\frac{\sigma_{m-1}}{\sigma_m} \mp \frac{\alpha_{m-1}}{\alpha_m}\right) g_{m-1}^- A_{m-1}^- , \end{aligned} \tag{3.10}$$

where

$$g_m^\pm = \frac{1}{2} e^{\pm a_m (h_{m+1} - h_m)}, \quad m = 0, \ldots, M-1. \tag{3.11}$$

Similarly starting with $B_M^+ = 0$, $B_M^- = 1$, Eq. (3.6) yields for $M-1 \geq m \geq \mu$ the backward recurrence relations

$$B_m^\pm = \left(\frac{\sigma_{m+1}}{\sigma_m} \pm \frac{\alpha_{m+1}}{\alpha_m}\right) g_m^\mp B_{m+1}^+ + \left(\frac{\sigma_{m+1}}{\sigma_m} \mp \frac{\alpha_{m+1}}{\alpha_m}\right) g_m^\mp B_{m+1}^- . \tag{3.12}$$

In the case $\mu = M$ no recurrence is required for $B_m^\pm$. Having computed $A_\mu^\pm$ and $B_\mu^\pm$ via (3.10) and (3.12), γ_0 and γ_M are determined from

$$(\gamma_0 A_\mu^- - \gamma_M B_\mu^-) f_\mu^- (z_0) = (\gamma_M B_\mu^+ - \gamma_0 A_\mu^+) f_\mu^+ (z_0) = \frac{-s}{4\pi \alpha_\mu k_\mu^2} . \tag{3.13}$$

The first equality results from (3.9) for $z = z_0$, the second from the fact that the difference in the upgoing (downgoing) waves for $z > z_0$ and $z < z_0$ is due to the primary excitation, given by (3.8). Hence,

$$\begin{aligned} \gamma_0 &= \frac{s}{4\pi \alpha_\mu k_\mu^2} \cdot \frac{B_\mu^- f_\mu^- + B_\mu^+ f_\mu^+}{\Delta (A,B)} , \\ \gamma_M &= \frac{s}{4\pi \alpha_\mu k_\mu^2} \cdot \frac{A_\mu^- f_\mu^- + A_\mu^+ f_\mu^+}{\Delta (A,B)} , \end{aligned} \tag{3.14}$$

where $f_\mu^\pm = f_\mu^\pm (z_0)$ and

$$\Delta(A,B) = A_\mu^+ B_\mu^- - A_\mu^- B_\mu^+ . \tag{3.15}$$

When π_{zz}^m is determined, the tensor elements G_{zx}, G_{zy}, G_{zz} are calculated via (3.4) from (3.2). The field in $z \leq 0$ is simply

$$\boldsymbol{G}_z^0 = -\operatorname{grad} \left(\int_0^\infty \gamma_0 e^{sz} J_0 s ds \right) \tag{3.16}$$

β) Horizontal Dipole

Let the dipole be directed along the x-axis. The Hertz vector has two components now:

$$\boldsymbol{\pi}_x^m(\boldsymbol{r}) = \pi_{xx}^m(\boldsymbol{r})\,\hat{\boldsymbol{x}} + \pi_{xz}^m(\boldsymbol{r})\,\hat{\boldsymbol{z}}. \tag{3.17}$$

From (3.3) follow the differential equations

$$\Delta\,\pi_{xx}^m = k_m^2\,\pi_{xx}^m - \delta(\boldsymbol{r}-\boldsymbol{r}_0)/k_m^2, \quad \Delta\,\pi_{xz}^m = k_m^2\,\pi_{xz}^m. \tag{3.18a,b}$$

Eq. (3.1) yields four boundary conditions at $z = h_m$:

$$\sigma_{m-1}\,\pi_{xx}^{m-1} - \sigma_m\,\pi_{xx}^m = 0, \quad \frac{\partial}{\partial z}(\sigma_{m-1}\,\pi_{xx}^{m-1} - \sigma_m\,\pi_{xx}^m) = 0, \tag{3.19a,b}$$

$$\sigma_{m-1}\,\pi_{xz}^{m-1} - \sigma_m\,\pi_{xz}^m = 0\,, \ \operatorname{div}(\boldsymbol{\pi}_x^{m-1} - \boldsymbol{\pi}_x^m) = 0\,. \tag{3.19c,d}$$

Condition (3.19d) couples π_{xx} and π_{xz}. — Particular solutions of the homogeneous versions of (3.18a,b) are

$$f_m^{\pm}(z)\,J_n(sr)\cos n\phi \ \text{ and } \ f_m^{\pm}(z)\,J_n(sr)\sin n\phi\,,$$

where J_n is the n-th order Bessel function and $f_m^{\pm}$ is given by (3.7b). Since the excitation is expressed by (3.8), J_0 is appropriate for π_{xx}. Condition (3.19d) then shows that $J_1\cos\phi$ is the correct choice for π_{xz} (ϕ reckoned positive from the x-axis in direction to the y-axis). Let for $0 \le m \le M$

$$k_m^2\,\pi_{xx}^m = \int_0^\infty (\mathcal{Q}_m^+ + \mathcal{Q}_m^-) J_0\,ds, \text{ where } \mathcal{Q}_m^{\pm} = \begin{cases} \delta_0 C_m^{\pm} f_m^{\pm}, & z \le z_0 \\ \delta_M D_m^{\pm} f_m^{\pm}, & z \ge z_0 \end{cases}. \tag{3.20}$$

Then the determination of $C_m^{\pm}$, $D_m^{\pm}$, δ_0, and δ_M is quite similar to that of $A_m^{\pm}$, $B_m^{\pm}$, γ_0, and γ_M, respectively. Thus the boundary conditions (3.19a,b) yield for $1 \le m \le \mu$ starting with $C_0^+ = 1$, $C_0^- = 0$:

$$C_m^{\pm} = \left(1 \pm \frac{\alpha_{m-1}}{\alpha_m}\right) g_{m-1}^{+}\,C_{m-1}^{+} + \left(1 \mp \frac{\alpha_{m-1}}{\alpha_m}\right) g_{m-1}^{-}\,C_{m-1}^{-}, \tag{3.21}$$

and starting with $D_M^+ = 0$, $D_M^- = 1$ for $M-1 \ge m \ge \mu$:

$$D_m^{\pm} = \left(1 \pm \frac{\alpha_{m+1}}{\alpha_m}\right) g_m^{\mp}\,D_{m+1}^{+} + \left(1 \mp \frac{\alpha_{m+1}}{\alpha_m}\right) g_m^{\mp}\,D_{m+1}^{-}. \tag{3.22}$$

Again, there is no recurrence required for $\mu = M$. The unknowns δ_0 and δ_M are determined similarly to (3.13) and (3.14):

$$\begin{aligned} \delta_0 &= \frac{s}{4\pi\alpha_\mu \Delta(C,D)} (D_\mu^+ f_\mu^+ + D_\mu^- f_\mu^-), \\ \delta_M &= \frac{s}{4\pi\alpha_\mu \Delta(C,D)} (C_\mu^+ f_\mu^+ + C_\mu^- f_\mu^-), \end{aligned} \tag{3.23}$$

where $f_\mu^\pm = f_\mu^\pm(z_0)$, and the Δ-symbol is defined in (3.15). The computation of π_{xz} is slightly more complicated. Let

$$k_m^2 \pi_{xz}^m = \int_0^\infty (R_m^+ + R_m^-) J_1 \cos\phi \, ds,$$

where

$$R_m^\pm = \begin{cases} (\varepsilon_0 E_m^\pm + \delta_0 F_m^\pm) f_m^\pm, & z \leq z_0 \\ (\varepsilon_M G_m^\pm + \delta_M H_m^\pm) f_m^\pm, & z \geq z_0 \end{cases} \tag{3.24}$$

Since at each interface four new coefficients are introduced, whereas there are only the two boundary conditions (3.19c,d), two additional conditions are imposed by equating at each interface the coefficients of ε_0 and δ_0 (or ε_M and δ_M) separately, thus obtaining four pairs of decoupled recurrence relations (using (3.21 and (3.22) to remove $C_{m-1}^\pm$ and $D_m^\pm$):

$$E_m^\pm = \left(1 \pm \frac{\beta_{m-1}}{\beta_m}\right) g_{m-1}^+ E_{m-1}^+ + \left(1 \mp \frac{\beta_{m-1}}{\beta_m}\right) g_{m-1}^- E_{m-1}^-, \tag{3.25}$$

$$\begin{aligned} F_m^\pm = &\left(1 \pm \frac{\beta_{m-1}}{\beta_m}\right) g_{m-1}^+ F_{m-1}^+ + \left(1 \mp \frac{\beta_{m-1}}{\beta_m}\right) g_{m-1}^- F_{m-1}^- \\ &\pm \frac{s}{2\alpha_m} \left(1 - \frac{\sigma_m}{\sigma_{m-1}}\right) (C_m^+ + C_m^-), \end{aligned} \tag{3.26}$$

$$G_m^\pm = \left(1 \pm \frac{\beta_{m+1}}{\beta_m}\right) g_m^\mp G_{m+1}^+ + \left(1 \mp \frac{\beta_{m+1}}{\beta_m}\right) g_m^\mp G_{m+1}^-, \tag{3.27}$$

$$\begin{aligned} H_m^\pm = &\left(1 \pm \frac{\beta_{m+1}}{\beta_m}\right) g_m^\mp H_{m+1}^+ + \left(1 \mp \frac{\beta_{m+1}}{\beta_m}\right) g_m^\mp H_{m+1}^- \\ &\pm \frac{s}{\alpha_m} \left(1 - \frac{\sigma_m}{\sigma_{m+1}}\right) g_m^\mp (D_{m+1}^+ + D_{m+1}^-), \end{aligned} \tag{3.28}$$

where $\beta_m = \alpha_m / \sigma_m$.

To determine ε_0 and ε_M, Eq. (3.24) is considered at $z = z_0$. Since π_{xz} has no singularity, upward and downward travelling waves agree. Hence,

$$\varepsilon_0 E_\mu^\pm + \delta_0 F_\mu^\pm = \varepsilon_M G_\mu^\pm + \delta_M H_\mu^\pm,$$

or

$$\varepsilon_0 = \{\Delta(F, G)\,\delta_0 + \Delta(G, H)\,\delta_M\} / \Delta(G, E), \tag{3.29a}$$

$$\varepsilon_M = \{\Delta(F, E)\,\delta_0 + \Delta(E, H)\,\delta_M\} / \Delta(G, E). \tag{3.29b}$$

So far, the starting values for the recurrence (3.25)—(3.28) have not been specified. Since in the last layer there is no upward travelling wave below the source,

$$G_M^- = 1,\ G_M^+ = H_M^+ = H_M^- = 0 \tag{3.30a}$$

is a correct choice of the initial values of (3.27) and (3.28). For the air layer, a corresponding choice of $E_0^+ = 1$, $E_0^- = F_0^- = F_0^+ = 0$ would be appropriate, if the air had non-zero conductivity. In the case of $\sigma_0 = 0$, (3.25) and (3.26) break down. As a remede recurrence has to start at $m = 2$ and the coefficients for $m = 1$ must be specified. Assume for the moment that the air half-space is slightly conducting, i.e. $k_0^2 \neq 0$. Whereas $\boldsymbol{\pi}_x$ is only an auxiliary function, the quantities $k_0^2 \boldsymbol{\pi}_x^0$ and $\operatorname{div} \boldsymbol{\pi}_x^0$, entering in (3.2), have a physical meaning and must be finite for $z < 0$. Let

$$k_0^2 \pi^0{}_{xz} = \int_0^\infty \tilde{\varepsilon}_0\, e^{sz} J_1 \cos\phi\, ds.$$

Then $\operatorname{div} \pi_x^0$ is finite if $(\tilde{\varepsilon}_0 - \delta_0)/k_0^2$ is finite for $\sigma_0 \to 0$. Hence, $\tilde{\varepsilon}_0 = \delta_0$. Satisfying the boundary condition (3.19c) at $z = 0$ by equating the coefficients of ε_0 and δ_0 separately, yields $E_1^- + E_1^+ = 0$, $F_1^- + F_1^+ = 1$. Specifying ε_0 as the amplitude of the upward propagating wave in the first layer, the final starting values

$$E_1^- = -1,\ E_1^+ = 1,\ F_1^- = 1,\ F_1^+ = 0 \tag{3.30b}$$

are obtained. This completes the treatment of the horizontal dipole.

Now, on using (3.2), (3.9), (3.20), and (3.24) all tensor elements can be given explicitly. Let

$$U_1 = \int_0^\infty \{Q_m^+ + Q_m^-\} J_0\, ds + \frac{1}{k_m^2 r} \int_0^\infty \{s(Q_m^+ + Q_m^-) - \alpha_m(R_m^+ - R_m^-)\} J_1\, ds,$$

$$U_2 = -\frac{1}{k_m^2} \int_0^\infty \{s(Q_m^+ + Q_m^-) - \alpha_m(R_m^+ - R_m^-)\} J_2\, s\, ds,$$

$$U_3 = -\int_0^\infty \{P_m^+ + P_m^-\} J_0\, s^2\, ds,$$

$$U_4 = -\int_0^\infty \{P_m^+ - P_m^-\} J_1\, \alpha_m\, s\, ds,$$

where $U_i = U_i(z_0, z, r)$, $i = 1, \ldots, 4$. Then

$G_{xx}^m = U_1 + U_2 \cos^2\phi$, $G_{xy}^m = G_{yx}^m = U_2 \sin\phi \cos\phi$, $G_{yy}^m = U_1 + U_2 \sin^2\phi$

$G_{zx}^m = U_4 \cos\phi$, $G_{zy}^m = U_4 \sin\phi$, $G_{zz}^m = U_3$.

The missing elements G_{xz}^m, G_{yz}^m can also be expressed by Q and R terms, or simpler on using the reciprocity (2.13), as

$G_{xz}^m = -U_4(z, z_0, r) \cos\phi$, $G_{yz}^m = -U_4(z, z_0, r) \sin\phi$.

The sign is reversed, since the interchange of source and receiver changes ϕ by π. The nine elements of $\mathfrak{G}$ can be expressed in terms of the four auxiliary functions U_1 to U_4. For $i = 1, 2, 3$ reciprocity requires $U_i(z_0, z, r) = U_i(z, z_0, r)$. Hence, these functions have to be determined for $z \leq z_0$ only.

The tensor elements which transform the electric field within the anomalous domain into the surface field, become particularly simple. Eqs. (3.19 d) and (3.20) yield

$$k_1^2 \operatorname{div} \boldsymbol{\pi}_x^0 = \int_0^\infty \{2\,\alpha_1\,\varepsilon_0 - (\alpha_1 + s)\delta_0\}\, e^{sz} J_1 \cos\phi\, ds\,. \tag{3.31}$$

Hence, defining

$$V_1 = \int_0^\infty \delta_0 J_0\, ds + \frac{1}{k_1^2 r} \int_0^\infty \{(s + \alpha_1)\,\delta_0 - 2\,\alpha_1\,\varepsilon_0\} J_1\, ds,$$

$$V_2 = -\frac{1}{k_1^2} \int_0^\infty \{(s + \alpha_1)\,\delta_0 - 2\,\alpha_1 \varepsilon_0\} J_2\, s\, ds,$$

$$V_3 = -\int_0^\infty \gamma_0 J_0\, s^2\, ds, \quad V_4 = \int_0^\infty \gamma_0 J_1\, s^2\, ds,$$

$$V_5 = \int_0^\infty \delta_0 J_1\, ds + \frac{1}{k_1^2} \int_0^\infty \{(s + \alpha_1)\,\delta_0 - 2\,\alpha_1\,\varepsilon_0\} J_1\, s\, ds,$$

where $V_i = V_i(z_0, r)$, Eq. (3.2) yields as tensor elements for $z = -0$:

$G_{xx}^0 = V_1 + V_2 \cos^2\phi$, $G_{xy}^0 = V_2 \sin\phi \cos\phi$, $G_{xz}^0 = V_5 \cos\phi$

$G_{yx}^0 = G_{xy}^0$, $G_{yy}^0 = V_1 + V_2 \sin^2\phi$, $G_{yz}^0 = V_5 \sin\phi$

$G_{zx}^0 = V_4 \cos\phi$, $G_{zy}^0 = V_4 \sin\phi$, $G_{zz}^0 = V_3$.

In $z \leq 0$, the electric field of a dipole in x-direction (say),

$$\boldsymbol{G}_x^0 = \int_0^\infty \delta_0(\hat{\boldsymbol{x}} J_0 + \hat{\boldsymbol{z}} J_1 \cos\phi)\, e^{sz}\, ds - \text{grad div}\, \boldsymbol{\pi}_x^0, \tag{3.32}$$

where $\text{div}\boldsymbol{\pi}_x^0$ is given by (3.31), can be split uniquely into a toroidal part $\boldsymbol{T}$ (purely tangential) and a poloidal part $\boldsymbol{S}$,

$$\boldsymbol{G}_x^0 = \boldsymbol{T} + \boldsymbol{S},\ \boldsymbol{T} = \text{curl}\,(\hat{\boldsymbol{z}}\, \psi_T)\,,\ \boldsymbol{S} = \text{grad}\, \psi_S\,. \tag{3.33}$$

The poloidal part is due to surface charges at $z = 0$. Since the z-component of the first term of (3.32) is poloidal per definition, ψ_S and ψ_T are given by

$$\psi_S = \int_0^\infty \delta_0\, s^{-1} J_1 \cos\phi\, e^{sz}\, ds - \text{div}\, \boldsymbol{\pi}_x^0,\quad \psi_T = \int_0^\infty \delta_0\, s^{-1} J_1 \sin\phi\, e^{sz}\, ds. \tag{3.34}$$

The electric field of a vertical dipole is purely poloidal in $z \leq 0$ (cf. (3.16)). When the kernels for the toroidal part are calculated by (3.33) and (3.34), the electric surface field obtained by (2.14) is easily decomposed into its poloidal and toroidal part. For an elongated anomaly and a toroidal external electric field, the resulting anomalous field is either almost toroidal or poloidal, according whether the external field is parallel or perpendicular to the strike.

In $z \leq 0$ only the toroidal part of the surface electric field gives rise to a magnetic field. Let $\boldsymbol{F}_i^0(\boldsymbol{r}_0|\boldsymbol{r})$, $i = 1, 2$, be the magnetic field at $\boldsymbol{r}$ due to a horizontal dipole in x_i-direction at $\boldsymbol{r}_0$. Then from (2.2)

$$i\omega\mu_0\, \boldsymbol{F}_i^0(\boldsymbol{r}_0|\boldsymbol{r}) = -\,\text{curl}\, \boldsymbol{G}_i^0(\boldsymbol{r}_0|\boldsymbol{r})\,,\ i = 1,2\,.$$

Defining

$$i\omega\mu_0\, W_1 = \int_0^\infty \delta_0 \left(\frac{1}{sr} J_1 - J_0\right) s\, ds,\ i\omega\mu_0\, W_2 = \int_0^\infty \delta_0 J_2\, s\, ds,$$

$$i\omega\mu_0\, W_3 = -\int \delta_0 J_1\, s\, ds,$$

the magnetic field kernels are

$$F_{xx}^0 = -\,W_2 \sin\phi\cos\phi,\quad F_{xy}^0 = W_1 + W_2 \cos^2\phi,\ F_{xz}^0 = W_3 \sin\phi,$$
$$F_{yx}^0 = -\,W_1 - W_2 \sin^2\phi,\ F_{yy}^0 = W_2 \sin\phi\cos\phi,\quad F_{yz}^0 = -\,W_3 \cos\phi.$$

Hence, the determination of the electric and magnetic surface field requires the tabulation of eight additional functions (V_1 to V_5 and W_1 to W_3), all functions of z_0 and r. The range of r depends on the surface domain, where the anomalous field is to be evaluated.

4. *Numerical Considerations*

The integral equation (2.11) or (2.14) is solved by the simple approximate approach of Hohmann (1971). It consists in decomposing the anomalous domain into a set of equal rectangular cells, assuming a constant electric field within each cell. For N cells results a linear system of $3N$ equations and unknowns. The coefficients are essentially the tensor kernels integrated with respect to source coordinates (Eq. (2.14)) or observer coordinates (Eq. (2.11)) over a cell. Care must be exercised in evaluating the contribution of the singular cell and of its neighbourhood. In general, the most important contribution arises from the primary excitation in direction of its moment. Let the dimensions of a cell be λ_x, λ_y, λ_z, and let

$$G^p_{xx} = (k^2 - \partial^2/\partial x^2)\, e^{-kR}/(4\pi k^2 R)$$

be the excitation in x-direction. For an approximate evaluation, the singular cell C_S is replaced in the first term by a sphere of the same volume and in the second term by a circular cylinder with axis in x-direction, length λ_x and cross-section $\lambda_y \cdot \lambda_z$. It results

$$k^2 \int_{C_S} G^p_{xx}\, d\tau = e^{-kR1} - (R_1/R_2)\, e^{-kR2} - (1 + kR_3)\, e^{-kR3} + 1,$$

where $R_1 = \lambda_x/2$, $R_2^2 = \lambda_x^2/4 + \lambda_y \lambda_z/\pi$, $R_3^3 = 3\, \lambda_x \lambda_y \lambda_z/(4\pi)$.

For symmetry reasons, there is no contribution from G^p_{xy} and G^p_{xz}. The integrals over the adjacent cells can be effected in a similar way. In the numerical evaluation of the kernels given in Sec. 3, the integration with respect to z is easily included by adding in the integrand the factor

$$2 \sinh(\alpha_\mu \lambda_z/2)/\alpha_\mu,$$

by which $\exp(\pm \alpha_\mu z_0)$ is multiplied when integrated over the thickness of the cell centered at z_0.

The system of equations is solved either iteratively (e.g. by means of the Gauß-Seidel method) or by matrix inversion. Because of the large storage required, the latter method is attractive only for small anomalous domains. It is of great advantage to exploit all symmetries. For structures with two vertical symmetry planes, the number of unknowns is reduced to almost 25%, and hence, the storage for matrix inversion is only 1/16 of the original storage. For iterative methods, both the computer time for one iteration and the number of iterations is reduced.

The Gauß-Seidel iterative scheme converges only for moderate conductivity contrasts. In numerical experiments it was found that a good convergence can be obtained for conductivity contrasts up to 1:100 only; $\boldsymbol{E}_n$ was used as initial guess for $\boldsymbol{E}$. If for higher contrasts matrix inversion is not possible, the best remede might be to apply the powerful method of shifting the spectrum as described by Hutson *et al.* (1972, 1973).

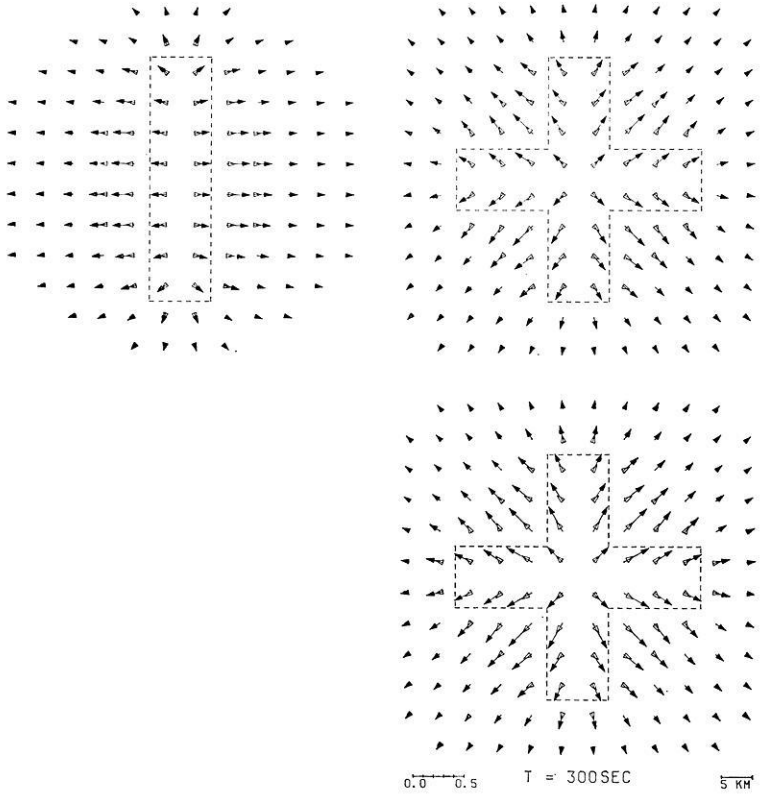

Fig. 2. Induction arrow maps for two different configurations of the anomalous domain (top). Vectorial addition of the arrow of the left structure and of a similar structure rotated through 90° (bottom). Only arrows longer than one half of the length of an arrow head are shown

5. Results

The feasibility of the integral equation approach has been tested for simple cases. Some of the results are presented below. A complete and concise presentation of the anomalous field vectors for a three-dimensional model poses a difficult problem. For a quasiuniform external field, 24 displays of a function over a two-dimensional array are required to give a complete description of the in-phase and out-of-phase part of the electric and magnetic field vector for the two mutually perpendicular polarizations of the external field. Four of these displays (in-phase and out-of-phase part of H_z for both polarizations) can be combined to yield an induction arrow map. Examples of such maps are shown in the upper half of Fig. 2 for two different configurations of the anomalous domain. The bodies of

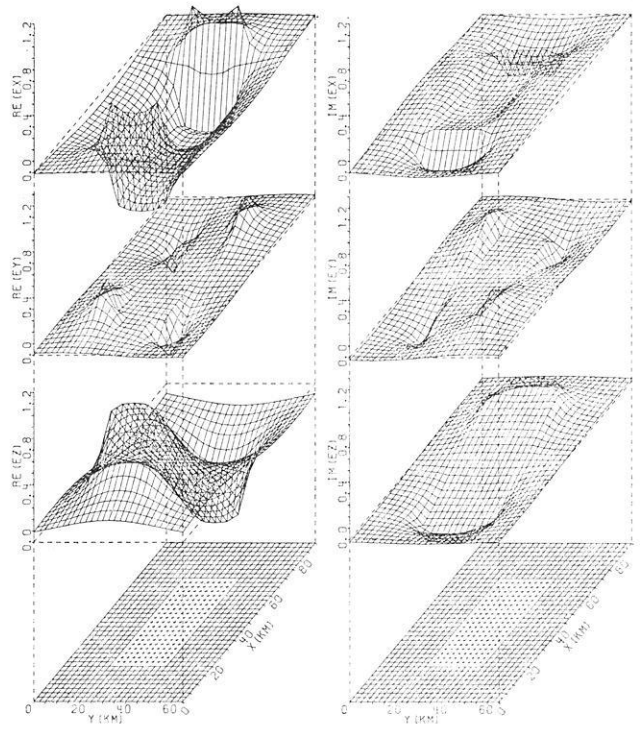

Fig. 3. In-phase and out-of-phase part of the anomalous electric field vector for a uniform external field in x-direction serving as reference field. The associated normal magnetic field points in y-direction. A rectangular anomalous domain, 50 km × 25 km × 10 km of $\varrho = 1\,\Omega$ m, embedded in a uniform half-space with $\varrho = 10\,\Omega$ m just below the surface is chosen. The period of the inducing field is 120 sec

$\varrho = 1$ Ωm are 10 km thick and are placed immediately below the surface of a uniform substratum of $\varrho = 10$ Ωm. In-phase and out-of-phase arrows are marked by black and white heads, respectively. Only arrows longer than one half of the arrow head are shown. It has been proved by Siebert (1971) that the induction arrows for a complex structure, consisting of two elongated, mutually perpendicular anomalies can be obtained approximately by vectorial superposition of the individual arrows. Along this line, the lower map of Fig. 2 has been obtained by adding to the arrows of the left map the arrows of the same structure, rotated through 90°. Since mutual induction is neglected, the induction effect is slightly overestimated.

The complete set of 24 displays for a different high conducting intrusion is illustrated in Figs. 3–6. The plots are thought to provide a qualitative idea of the fields, although quantitative results can be extracted by a some-

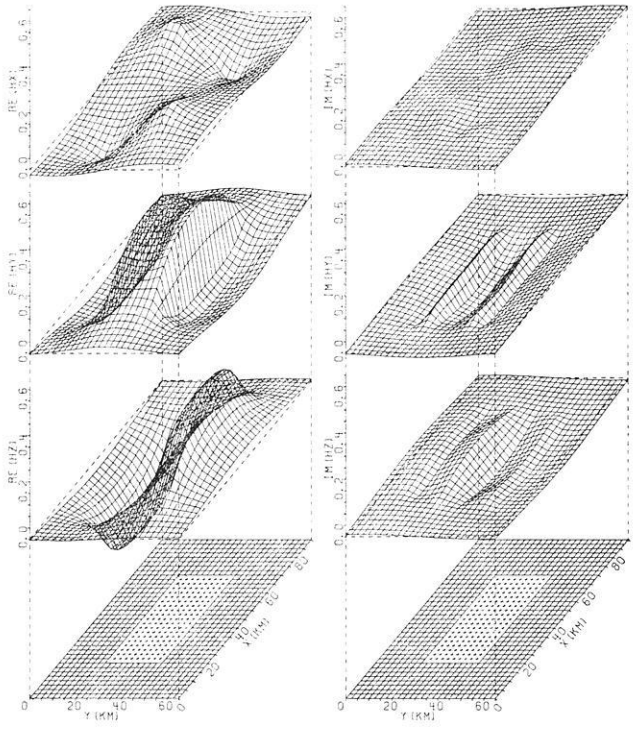

Fig. 4. The anomalous magnetic field of the model described in the caption to Fig. 3. The normal magnetic field serves as reference field

what awkward procedure. The disturbing body is decomposed into cubes with 5 km edges. There are 10, 5, and 2 cubes in x, y, z-direction, respectively. The complete surface field has been evaluated on a 18×13 grid. On a UNIVAC 1108 computer the determination of all kernels took 70 sec, the solution of the integral equation and the evaluation of the surface field required additional 50 sec for each polarization, the Gauß-Seidel iterative scheme being convergent after 10 iterations.

In all subsequent figures, only the anomalous fields are shown. The modulus of the corresponding normal field serves as reference. Fig. 3 presents the electric field for a uniform external electric field in x-direction. The associated normal magnetic field points in y-direction. Within the good conductor, the E_x-component breaks down. It exhibits a discontinuity at the front and rear surface since the normal component of the current density is continuous there. The E_y-component differs appreciably from zero only near the corners. The signs are easily understood using the idea of the electric currents being sucked into the good conductor. The

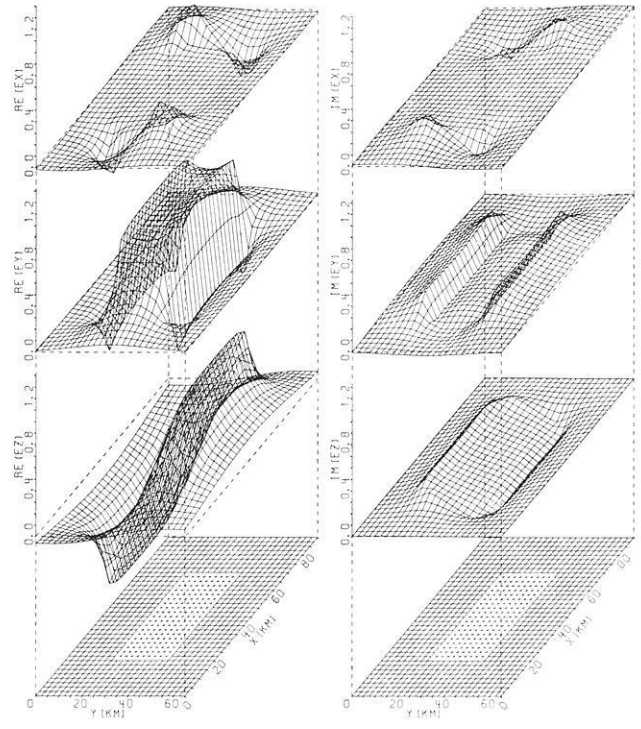

Fig. 5. In-phase and out-of-phase part of the anomalous electric field vector for a uniform external field in $-y$-direction associated with a normal magnetic field in x-direction. The same anomalous domain and period as in Fig. 3

magnitude of the E_z-component is of the order of E_x. Its origin are surface charges: negative charges at the front bending the current lines towards the surface and positive charges at the rear reflecting the lines from the surface. Fig. 4 shows the corresponding magnetic field. The signs are understood using the idea of magnetic field lines expelled from the good conductor.

Figs. 5 and 6 display the electric and magnetic field for an external magnetic field in x-direction associated with an electric field in $-y$-direction. With the present choice of the dimensions of the disturbing body, this polarization resembles the two-dimensional H-polarization, i.e. the anomalous magnetic field vanishes if the anomaly is extended to infinity at both ends. In the same limit the former polarization degenerates into the E-polarization case.

After decomposing the kernels $\boldsymbol{G}_{\mathrm{x}}^{0}$ and $\boldsymbol{G}_{\mathrm{y}}^{0}$ according to (3.33) and (3.34), the poloidal and toroidal part of the electric surface field can be obtained

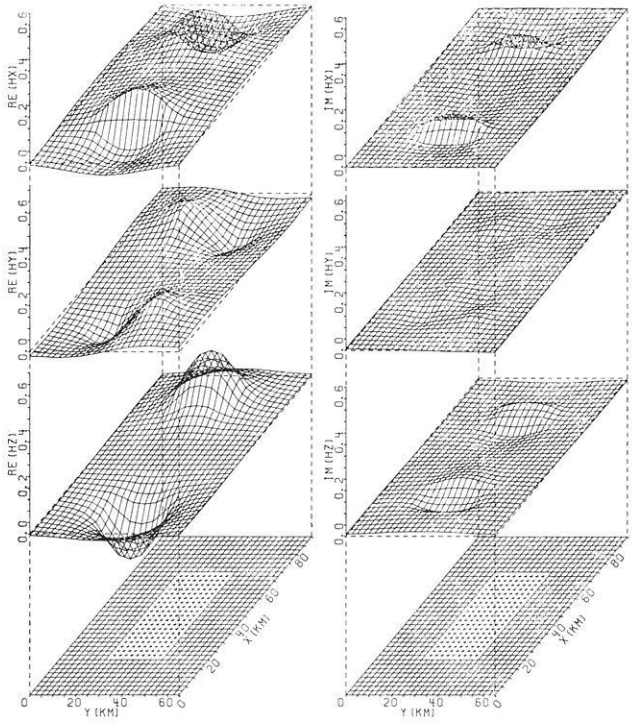

Fig. 6. The anomalous magnetic field vector of the model of Fig. 5

separately. For the E_x and E_y component of Fig. 3 this is done in Figs. 7a and 7b.

Finally, the transition from three to two dimensions has been investigated for a particular model. Fig. 8 illustrates that on a central profile a two-dimensional description is adequate if the length of the disturbing body exceeds three times its width.

6. Conclusion

The integral equation technique based on Green's tensor turns out to be a useful tool in treating three-dimensional induction problems.

It is suitable for small anomalous domains, and here it is of particular advantage if the anomalous field is required for a set of different conductivities within the anomalous domain and/or different external fields, for the time consuming computation of the pertinent kernels has to be carried out once only. Work is still necessary to develop effective iterative methods if the conductivity contrast is large ($>100:1$). For large anomalous domains, a finite difference technique combined with a surface integral boundary condition appears to be the most promising approach.

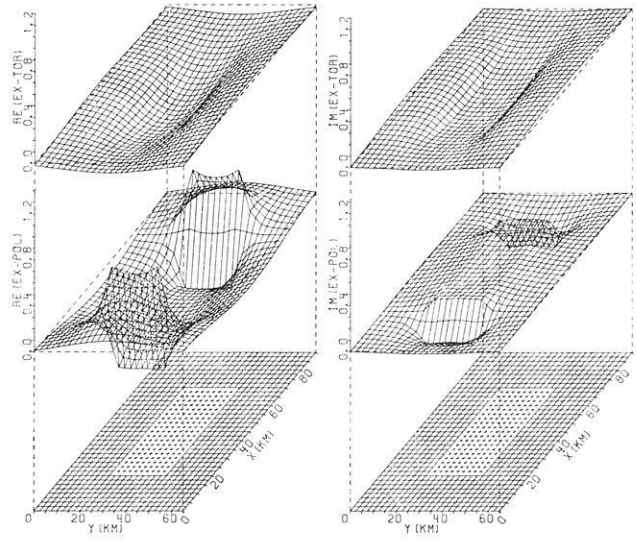

Fig. 7a. Toroidal and poloidal part of the E_x-component of Fig. 3

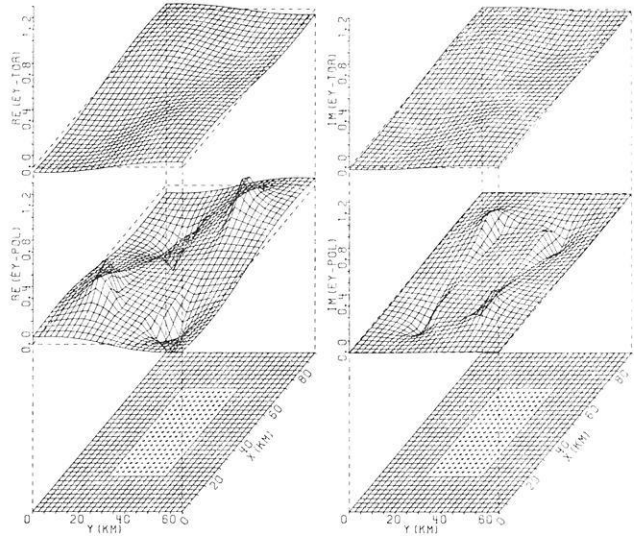

Fig. 7b. Toroidal and anomalous part of the E_y-component of Fig. 3

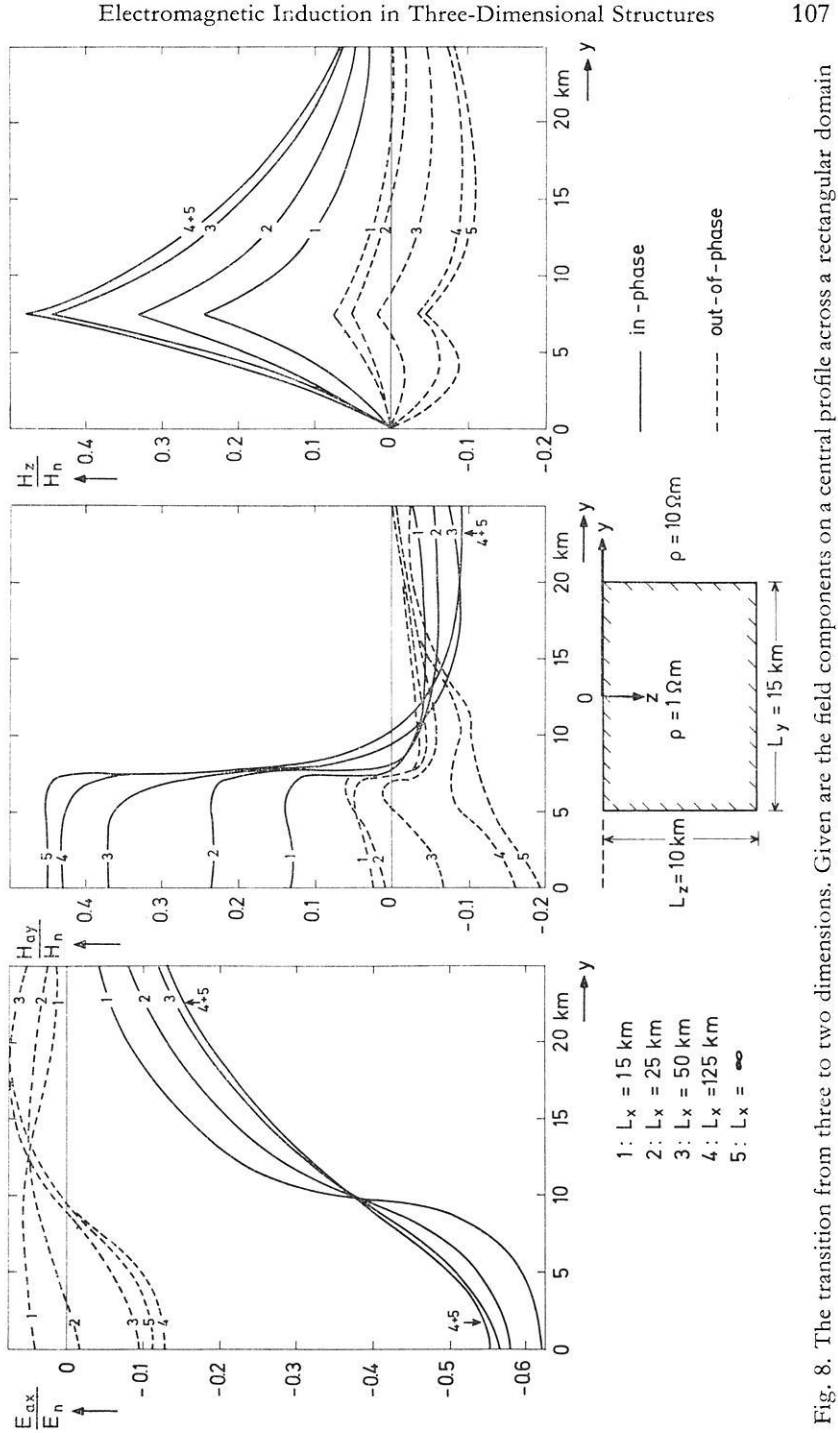

Fig. 8. The transition from three to two dimensions. Given are the field components on a central profile across a rectangular domain with dimensions L_x, L_y, L_z

Appendix

The Tensor Elements for a Uniform Half-Space

For a uniform half-space with $\sigma_n(z) = \sigma_0$ these elements have already been given by Raiche (1974) in terms of integrals. However, all integrations can be carried out explicitly. Using source coordinates x_0, y_0, z_0 and the abbreviations.

$$R_\pm^2 = (x - x_0)^2 + (y - y_0)^2 + (z \pm z_0)^2,$$

$$g_\pm = \exp(-k_0 R_\pm)/(4\pi R_\pm), \quad \alpha_\pm = g_- \pm g_+, \quad k_0^2 = i\omega\mu_0\sigma_0,$$

$$\beta = \alpha_- - (\partial/\partial z)\left\{I_0\left(\frac{1}{2}k_0[R_+ - z - z_0]\right) \cdot K_0\left(\frac{1}{2}k_0[R_+ + z + z_0]\right)\right\}/(2\pi),$$

where I_0 and K_0 are modified Bessel functions of order zero, first and second kind, it results for z, $z_0 > 0$

$$k_0^2 G_{xx} = (k_0^2 - \partial^2/\partial x^2)\beta + (\partial^2/\partial z^2)(\alpha_+ - \beta),$$
$$k_0^2 G_{xy} = k_0^2 G_{yx} = -(\partial^2/\partial x\, \partial y)\beta,$$
$$k_0^2 G_{xz} = -(\partial^2/\partial x\, \partial z)\alpha_+,$$
$$k_0^2 G_{yy} = (k_0^2 - \partial^2/\partial y^2)\beta + (\partial^2/\partial z^2)(\alpha_+ - \beta),$$
$$k_0^2 G_{yz} = -(\partial^2/\partial y \partial z)\alpha_+,$$
$$k_0^2 G_{zx} = -(\partial^2/\partial z \partial x)\alpha_-,$$
$$k_0^2 G_{zy} = -(\partial^2/\partial z \partial y)\alpha_-,$$
$$k_0^2 G_{zz} = (k_0^2 - \partial^2/\partial z^2)\alpha_-.$$

The vertical components G_{xz}, G_{yz}, G_{zz}, vanishing for $z \to +0$, tend for $z \to -0$ to the limiting values

$$k_0^2 G_{xz} = -(\partial^2/\partial x\, \partial z_0)\gamma, \quad k_0^2 G_{yz} = -(\partial^2/\partial y \partial z_0)\gamma,$$
$$k_0^2 G_{zz} = -(\partial^2/\partial z_0^2)\gamma,$$

where

$$\gamma = (\partial/\partial z_0)\left\{I_0\left(\frac{1}{2}k_0[R_0 - z_0]\right) \cdot K_0\left(\frac{1}{2}k_0[R_0 + z_0]\right)\right\}/(2\pi),$$

$$R_0^2 = (x - x_0)^2 + (y - y_0)^2 + z_0^2.$$

Since in applications an integration over the source or observer coordinates (Eqs. (2.14) and (2.11), respectively) is involved, most of the above differentiations need not to be carried out. (Use $\partial/\partial x = -\partial/\partial x_0$, $\partial/\partial y = -\partial/\partial y_0$, and e.g. $\partial\alpha_-/\partial z = -\partial\alpha_+/\partial z_0$, $\partial\alpha_+/\partial z = -\partial\alpha_-/\partial z_0$.)

References

Hohmann, G.W.: Electromagnetic scattering by conductors in the earth near a line source of current, Geophysics *36*, 101–131, 1971

Hutson, V.C.L., Kendall, P.C., Malin, S.R.C.: Computation of the solution of geomagnetic induction problems: a general method, with applications. Geophys. J. *28*, 489–498, 1972

Hutson, V.C.L., Kendall, P.C., Malin, S.R.C.: The modelling of oceans by spherical caps. Geophys. J. *33*, 377–387, 1973

Jones, D.S.: The theory of electromagnetism. Oxford: Pergamon Press 1964

Jones, F.W., Pascoe, L.J.: The perturbation of alternating geomagnetic fields by three-dimensional conductivity inhomogeneities. Geophys. J. *27*, 479–485, 1972

Lines, L.R., Jones, F.W.: The perturbation of alternating geomagnetic fields by three-dimensional island structures. Geophys. J. *32*, 133–154, 1973

Morse, P.M., Feshbach, H.: Methods of theoretical physics. New York: McGraw-Hill 1953

Raiche, A.P.: An integral equation approach to three-dimensional modelling. Geophys. J. *36*, 363–376, 1974

Schmucker, U.: Anomalies of geomagnetic variations in the south-western United States. Bull. Scripps Inst. Ocean. Univ. Calif. *13*, 1970

Schmucker, U.: Neue Rechenmethoden zur Tiefensondierung. In: Protokoll Kolloquium Erdmagn. Tiefensondierung 14.–16. Sept. 1971, Rothenberge/Westf., 1971

Siebert, M.: Zur Deutung von Induktionspfeilen bei schmalen langgestreckten orthogonalen Leitfähigkeitsanomalien. In: Protokoll Kolloquium Erdmagn. Tiefensondierung 14.–16. Sept. 1971, Rothenberge/Westf., 1971

Sommerfeld, A.: Elektromagnetische Schwingungen. In: Frank- v. Mises: Differentialgleichungen der Physik, vol. 2. Braunschweig: Vieweg 1935

Wait, J.R.: Electromagnetic waves in stratified media, 2nd ed. Oxford: Pergamon Press 1970

Weaver, J.T.: The general theory of electromagnetic induction in a conducting half-space. Geophys. J. *22*, 83–100, 1970

Dr. P. Weidelt
Institut für Geophysik der Universität
D-3400 Göttingen
Herzberger Landstraße 180
Federal Republic of Germany

J. Geophys. 41, 111–122, 1975

Acoustic Normal Modes Generated by Explosive Sources

H.-H. Essen, H.-W. Kebe, J. Siebert

Institut für Geophysik, Universität Hamburg

Received May 30, 1974; Revised Version September 10, 1974

Abstract. The theory of normal modes is applied to sound-propagation data from a shallow-water area of the North Sea. The signals generated by explosives have been recorded by a vertical array of hydrophones. In order to resolve the different modes the time series are filtered by narrow bandpass filters. In general, observed propagation velocities and vertical amplitude distributions are in good agreement with values computed from a simple wave-guide model consisting of a liquid layer (water) above a liquid halfspace (sediments). However, observed amplitudes of higher modes are smaller than predicted by theory, which probably is due to mode-dependent reflection and scattering losses at the boundaries. An observed splitting of wave groups seems to be caused by bubbles.

Key words: Acoustic Normal Modes — Propagation Velocities — Vertical Amplitude Functions.

1. Introduction

In order to study the interaction of underwater sound with random oceanographic wave fields simultaneous measurements are planned in an experimental site westward of the island of Sylt in the North Sea. Acoustic investigations using explosive and CW (continuous wave) sources have been started.

For acoustic propagation within a shallow water area the most important perturbations result from the boundaries, especially from surface waves. Surface waves have been studied intensively at the Sylt site along a profile with different wave recorders yielding both the wave heights and the directional distributions (Hasselmann *et al.*, 1973). When proceeding from the assumption that acoustic and surface wavelengths are of the same order, the interaction processes can be described by the theory of resonant wave-wave interaction (Essen and Hasselmann, 1970). According to this theory the attenuation of the direct signal as well as the distribution of the scattered field may be computed.

In this paper only acoustic measurements are presented. The underwater sound is generated by explosive sources. A vertical array of eight hydrophones is used in order to resolve the structure of the acoustic wave

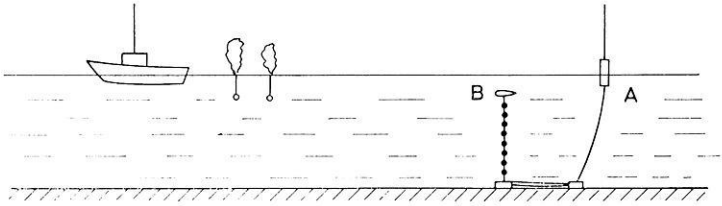

Fig. 1. Experimental configuration (schematic): A = Telemetry buoy, B = Vertical array of eight hydrophones

field, which in the case of shallow water is given by a superposition of discrete modes. The purpose of this experiment is to verify an acoustic waveguide model for the Sylt site.

Normal-mode investigations in shallow water areas were made by various authors. It turned out that the two-layered fluid model, first treated by Pekeris (1948), yields good agreement between theory and measurements. Kind (1970) worked with explosives and analysed the seismogram of one hydrophone by narrow bandpass filters and found the mode group velocities. Tolstoy (1958) used a CW source and compared the measured and theoretically-predicted horizontal structure of the acoustic pressure field. The group velocities as well as the vertical amplitude functions of the different modes were experimentally determined by Ferris (1972). Short pulses were produced by a CW source (400 and 750 cps) and recorded by a vertical array of hydrophones.

The measurements presented in this paper differ from those of Ferris (1972) with respect to the acoustic source and the analysed frequencies (50–300 cps). These low frequencies are of interest in the theory of acoustic-surface wave interaction.

2. *Method of Measurements*

Experiments with explosive sources were carried out during a test cruise with the vessel "Uthörn" at the Sylt site in December 1972. The method of measurements is illustrated in Fig. 1 (Kebe, 1973). The telemetry buoy (*A*) on the surface is moored and connected to a vertical chain of eight hydrophones (*B*) by cable. This cable is also part of the mooring system and connects the hydrophones with an eight-channel FM-FM-Multiplex-Equipment inside the telemetry buoy. A streamlined subsurface floatation element maintains the hydrophone chain in the vertical position. This position of the hydrophone array is verified by the simultaneous onset times of the signals at all hydrophones (cf. Fig. 3). The received FM-Multiplex-signal from the telemetry buoy is recorded on tape. The signal is also demodulated and simultaneously recorded on strip charts.

The explosion points were located at intervals of 300—500 m along a profile of 6.3 km in length. Separate detonations were made with exploders and bursting charges of various types.

3. Theoretical Wave-Guide Model

Sound propagation in shallow water is best represented by normal modes. Shallow implies here that the depth of water is of the order of a few acoustic wavelengths. The normal modes are free wave solutions of a layered halfspace, with the ocean as the uppermost layer. It is assumed that the sound velocity increases with depth. Due to the resulting angle of total reflection at the layer boundaries only a finite (frequency-dependent) number of modes is trapped within the overlying layers. The different modes are characterised by their propagation velocities and amplitude dependence on depth.

For distances r much larger than the water depth h_1 the acoustic pressure generated by a point source ($r=0$, $x_3=d$) can be described by a Fourier integral (Pekeris, 1948),

$$p(t, r, x_3) = r^{-\frac{1}{2}} \int_0^\infty \sum_{n=1}^{N(\omega)} a_n(\omega)\, \varphi_n(d)\, \varphi_n(x_3) \cdot \exp\left(i\left(\omega t - k_n r + \frac{\pi}{4}\right)\right) d\omega \tag{1}$$

where $a_n(\omega)$ depends on the source characteristics and waveguide model, $\varphi_n(x_3)$ is a vertical amplitude function which is a solution of an eigenvalue problem, and k_n are eigenvalues given by a dispersion relation,

$$f_n(\omega, k_n) = 0 \tag{2}$$

The acoustic energy propagates with the group velocity,

$$v_n = \frac{d\omega}{dk_n} = -\frac{\partial f_n}{\partial k_n} \Big/ \frac{\partial f_n}{\partial \omega} \tag{3}$$

Computed group velocities for different wave-guide models are shown as a function of frequency and mode number n in Fig. 2. The parameters of the sedimental layering are taken from former seismic refraction investigations (Essen *et al.*, 1973).

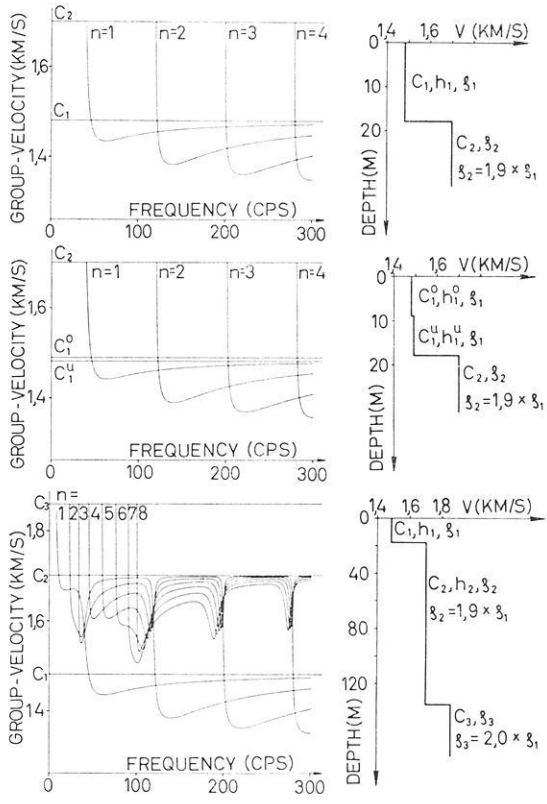

Fig. 2. Group velocities calculated as function of frequency and mode number (n) for different wave-guide models

c_i = sound velocity
h_i = thickness
ϱ_i = density
} of layer $i = 1, 2, 3$

The vertical sound-velocity profile of the water layer was not measured during the experiment but can be considered constant, because measurements made during the same season showed fluctuations of less than 1 ms^{-1} varying randomly with depth. This is due to homogeneous mixing by tides and waves during the winter months.

The first panel of Fig. 2 shows the group velocities of the simplest model, a water layer of constant sound velocity overlying a homogeneous sediment halfspace. The second model includes a weak discontinuity in the centre of the water layer. The resulting change of group velocities is negligible. (For higher frequencies and greater water depths the influence of discontinuities becomes more important. Ferris (1972) shows a case of a

second-mode arrival before the first-mode arrival.) The third panel applies to a model with a two-layered sediment halfspace. The uppermost sediment layer thickness is 6.5 times the water depth (Essen *et al.*, 1973). The group velocities of modes trapped within both the water and sediment layer show a complicated dependence on frequency. However, for modes which are trapped in the water layer only, there is almost no influence of the sediment layering, as being expected.

Numerical computations were also made for a model with non-zero gradients of sound velocity of the water and sediment layer. The differences compared with the simplest model of Fig. 2 (first panel) were found to be small. In the following only this simple two-layer model is used.

In accordance with other authors (Pekeris, 1948; Kind, 1970; Ferris, 1972) shear waves in the sediment halfspace have been neglected. Possible shear-wave velocities are less than the sound velocity of water, and in consequence there are no trapped modes within the water layer. Only in the limit of small shear-wave velocities (some 100 ms^{-1}) does the approximation of normal modes become valid. From different methods shear-wave velocities of 100—500 ms^{-1} were measured in fully saturated sediments (Hamilton, 1971).

In the case of Fig. 2 (first panel) the following relations are found,

$$\varphi_n(x_3) = \sin\left(\sqrt{\frac{\omega^2}{{c_1}^2} - k_n^2}\cdot x_3\right) \tag{4}$$

(arbitrarily normalized)

$$f_n(\omega, k_n) = \sqrt{k_n^2 - \frac{\omega^2}{{c_2}^2}}\,\varphi_n(h_1) + \frac{\varrho_2}{\varrho_1}\,\varphi_n'(h_1) = 0 \tag{5}$$

$$a_n(\omega) = G(\omega)\sqrt{k_n}\left(\varphi_n(h_1)\,\frac{\partial f_n(\omega, k_n)}{\partial k_n}\right)^{-1} \tag{6}$$

where $G(\omega)$ depends on the frequency spectrum of the source only.

4. *Experimental Results*

During this test experiment acoustic signals from different charges were recorded along one vertical array of eight hydrophones at varying distances between the array and the explosion points. Explosive sources yield a broad frequency spectrum. Computed normal mode group velocities and vertical amplitude functions, however, are valid for fixed frequencies only. In order

to resolve modes by travel times the received pressure signals have to be filtered by narrow bandpass filters designed from the following considerations:

For a fixed range r (= distance source-receiver) and a fixed frequency $\nu\left(\nu = \frac{\omega}{2\pi}\right)$ the time difference of the arrivals of wave groups of mode m and n is given by,

$$\tau_{nm} = \frac{r}{v_m} - \frac{r}{v_n} \tag{7}$$

where v_n, v_m are the respective group velocities, cf. (3).

The relation (7) applies in the theoretical limit of sharply defined frequencies. This is incompatible with a finite-duration signal, which is necessary for separation of modes by travel times. In order to obtain a finite pulse length Δt one has to consider a finite frequency interval $\Delta\nu$ determined by the uncertainty relation,

$$\Delta\nu \approx \frac{1}{\Delta t} \tag{8}$$

Therefore two conditions must be satisfied in order to resolve the modes by travel times. First,

$$\tau_{nm} > \Delta t \tag{9}$$

where τ_{nm} can be increased by increasing the distance r of sources and receiver, cf. (7), and secondly, the change of group velocity of an individual mode within the interval $\Delta\nu$ must be small compared with the difference between the group velocities v_n and v_m in the relation (7). This condition can be most easily satisfied by bandpass filters of bandwidth $\Delta\nu$ smaller than the frequency interval between two adjacent modes and centre frequencies approximately in the centres of these intervals. From the model of Fig. 2 (first panel) it is found,

$$\Delta\nu \lesssim 80 \text{ cps} \tag{10}$$

and:

central frequency (cps):	85	170	255
number of modes:	1	2	3

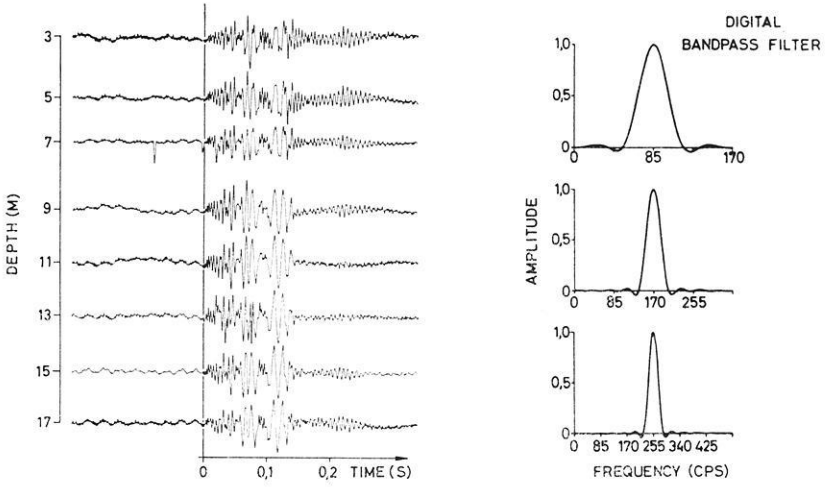

Fig. 3. Left: Original recordings of the vertical hydrophone array (normalized to same maximum amplitude); Right: Digital bandpass filter curves

Substituting (10) into (8), a requirement for the propagation distance r is obtained from condition (9) and the computed group velocities, cf. (7) and Fig. 2 (first panel):

$$r \gtrsim 1 \text{ km} \tag{11}$$

Modes simultaneously trapped within the water and at least one sediment layer can be neglected. Due to the depth of the first sediment layer (6.5 times the water depth) the energy density of those modes is small. As seen in Fig. 2 these modes propagate with velocities higher than the sound velocity of water (as opposed to modes trapped within the water layer only). In fact, no modes with velocities higher than the sound velocity of water were observed.

An original recording of the vertical hydrophone array is shown in the left panel of Fig. 3. The distance r from the source was 4.1 km and the water depth was nearly constant within the range of propagation ($h_1 = 18 \pm 0.5$ m). The positions of the hydrophones are marked on the ordinate scale. The zero point of the time scale coincides with the first signal onset.

The right panel of Fig. 3 shows the filter curves chosen to satisfy the conditions given above. Fig. 4 shows the filtered time series of the received pressure signals. The time scales are the same as in the original seismograms, but the signal amplitudes are normalized to have the same maximum amplitude. The vertical lines indicated by mode numbers n

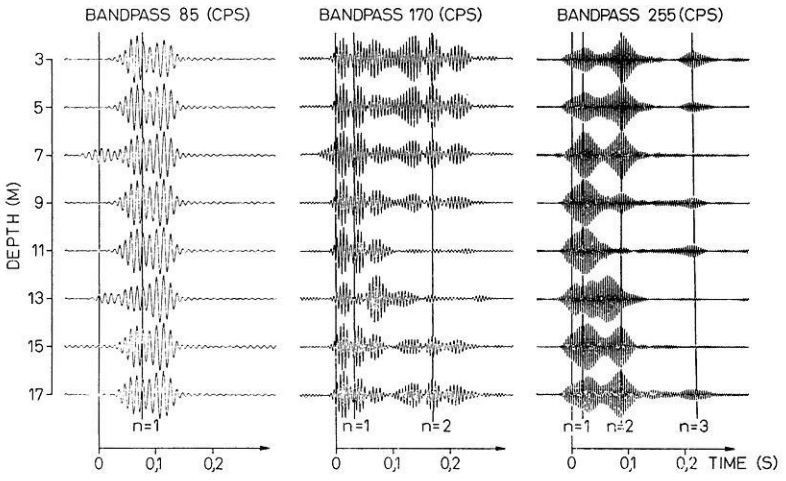

Fig. 4. Bandpass-filtered recordings at the central frequencies: 85, 170, 255 cps (normalized to same maximum amplitude)

mark the theoretical arrival times of the normal modes. They are computed from the group velocity curves of Fig. 2 (first panel) at the central frequencies of the bandpass filters. Because of the uncertainty relation the arrival times are not defined exactly but only within a limited interval. An additional broadening of this interval results from the variation of the group velocity within the frequency interval of the bandpass filters.

The single modes can be identified by their amplitude dependence on depth. In the case of the simplest two-layer model this is given by a sine-function, cf. (4). The number of nodes of this function in the water column is equal to the mode number n. The nodes are clearly identifiable in Fig. 4, as well as the phase reversal on either side of a node ($n = 2,3$). The positions of the nodes agree well with theoretical prediction. The observed and theoretical arrival times are also in good agreement. The "splitting" of wave groups belonging to one mode probably results from bubbles (see below). It should be mentioned that the signal of the hydrophone at 13 m depth obviously is disturbed.

Fig. 5 shows a more detailed analysis of the vertical amplitude function of the modes. The theoretical amplitudes are computed from the central frequencies, and it is assumed that they are nearly constant within the frequency interval of the bandpass filters, which is in fact fulfilled. The theoretical curves are matched to the measured points by the method of least squares. The depth dependence of the hydrophone sensitivity was corrected for this analysis.

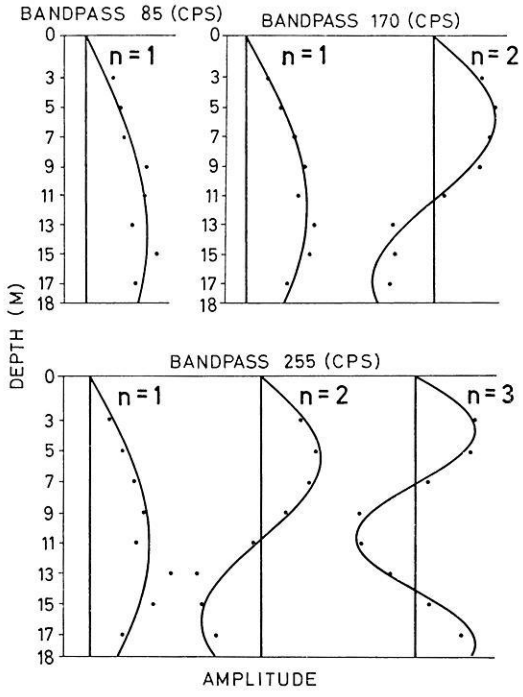

Fig. 5. Theoretical (lines) and observed (dots) vertical amplitude functions for various modes n (mode amplitude in arbitrary units)

Table 1. Comparison of observed and theoretical normal-mode amplitudes

Bandpass filter 170 (cps)	measured	theoretical
$\frac{\{a_n \varphi_n(d)\}\ n=2}{\{a_n \varphi_n(d)\}\ n=1}$	0.52	0.79

Bandpass filter 255 (cps)	measured	theoretical
$\frac{\{a_n \varphi_n(d)\}\ n=2}{\{a_n \varphi_n(d)\}\ n=1}$	0.95	1.1
$\frac{\{a_n \varphi_n(d)\}\ n=3}{\{a_n \varphi_n(d)\}\ n=2}$	0.22	0.44

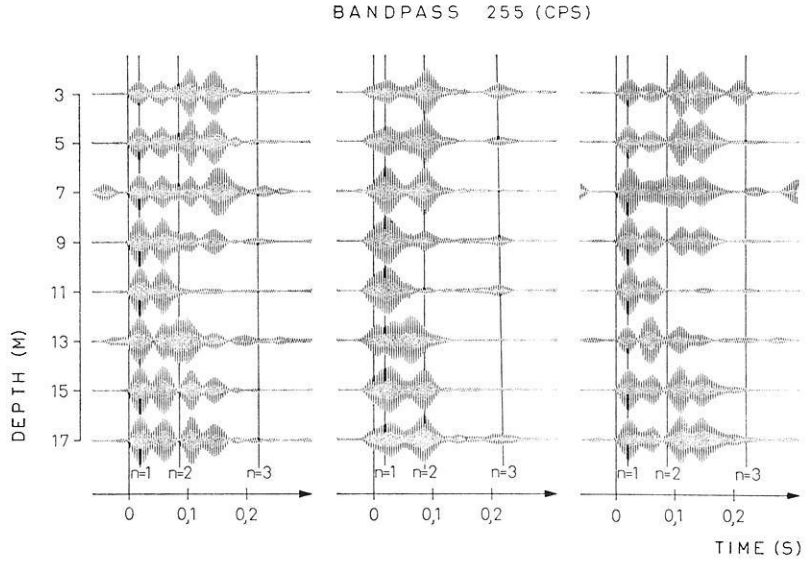

Fig. 6. Bandpass-filtered recordings for different charges (normalized to same maximum amplitude), from left to right: 1) bursting charge (cylindric, 15 g, mainly $Ba(NO_3)_2$), 2) exploder, 3) bursting charge (cubic, 27 g, mainly gun powder)

Relative maximum amplitudes of different modes at the same frequency are compared in Table 1. The theoretical values for a point source apply for the central frequencies of the bandpass filters. The charge depth was $d = 5$ m.

The measured amplitudes of the higher modes $n = 2,3$ are considerably smaller than expected from theory. Most probably this can be explained by the mode-dependent attenuation from reflection losses at the bottom (Ingenito, 1973) or scattering processes at the boundaries (Essen and Hasselmann, 1970).

Up to this point only results from one special explosion have been discussed. Fig. 6 shows three bandpass-filtered recordings from the same position of source and receiver, obtained, however, from different charges. The second column in Fig. 6 represents the recordings which have been discussed in detail above. The first and third column represent bandpass-filtered registrations, which are very similar but different from the second one. Thus, it is apparent that the main influence results from the brisance of the charges. Our interpretation is that the splitting of the wave groups belonging to the same mode is generated by bubbles. There are two reasons for this: The observed periods agree with those computed according to

the formula of Willis (1951) and the periods are independent of the distance from the source (not shown in this paper).

The bursting charges mainly differ in two respects from the exploder: The travel times of the mode $n=2$ do not agree with the theoretical value, and the mode $n=3$ is not observed. Whereas the first effect probably results from an interference of first-mode bubbles with the second mode, the second effect is not yet understood. In spite of the divergence of the propagation velocities, the theoretical and measured vertical amplitude functions show nearly the same good agreement as in Fig. 5.

About 20 explosions have been analysed. Because of the bubbles, the smaller distances from the source, i.e. smaller than $r=4.1$ km, allow no clear separation of the modes. At distances greater than this value the signal was lost in the telemetry noise, so that all data shown in this paper were analysed for the one favourable shot distance of 4.1 km.

In spite of these experimental limitations, it is concluded that the measured data agree well with the theoretical values obtained from the simple two-fluid layer model.

Acknowledgements. Thanks are due to all our colleagues who helped in gathering the data. This work was supported by the Deutsche Forschungsgemeinschaft, Sonderforschungsbereich 94, Meeresforschung Hamburg.

References

Essen, H.-H., Hasselmann, K.: Scattering of low-frequency sound in the ocean, Z. Geophys. *36*, 655–678, 1970

Essen, H.-H., Hirschleber, H. B., Siebert, J.: Geschwindigkeits- und Dämpfungsmessungen an Sedimenten der Nordsee. Z. Geophys. *39*, 833–854, 1973

Ferris, R. H.: Comparison of measured and calculated normal-mode amplitude functions for acoustic waves in shallow water. J. Acoust. Soc. Am. *48*, 981–988, 1972

Hamilton, E. L.: Elastic Properties of Marine Sediments. J. Geophys. Res. *76*, 579–604, 1961

Hasselmann, K., Barnett, T. P., Bouws, E., Carlson, H., Cartwright, D. E. Enke, K., Ewing, J. A., Gienapp, H., Hasselmann, D. E., Kruseman, P., Meerburg, A., Müller, P., Olbers, D. J., Richter, K., Sell, W., Walden, H.: Measurements of Wind-Wave Growth and Swell Decay during the Joint North Sea Wave Project. Ergänzungsheft zur Dt. Hydrogr. Z. (8°) Nr. *12*, 1–95, 1973

Ingenito, F.: Measurements of mode attenuation coefficients in shallow water. J. Acoust. Soc. Am. *53*, 858–863, 1973

Kebe, H.-W.: Ein Meßverfahren zur Untersuchung von akustischen Streuprozessen im Flachwasser. Kongreßberichtswerk der Interocean, 849–860, 1973

Kind, R.: Auswertung seeseismischer Messungen mit einer digitalen Methode unter Anwendung der Theorie der Schallwellenausbreitung im Flachwasser. Z. Geophys. *36*, 549–567, 1970

Pekeris, C. L.: Theory of propagation of explosive sound in shallow water, Geol. Soc. Am. Mem. *27*, 43–70, 1948

Tolstoy, I.: Shallow water test of the theory of layered wave guides. J. Acoust. Soc. Am. *30*, 348–361, 1958
Willis, H. F.: Underwater explosions, time interval between successive explosions. British Report Wa-47-21, 1941

Dipl.-Phys. Heinz-Hermann Essen
Phys.-Ing. Hans-Werner Kebe
Dipl.-Phys. Jürgen Siebert
Institut für Geophysik der Universität
D-2000 Hamburg 13
Binderstraße 22
Federal Republic of Germany

J. Geophys. 41, 123–126, 1975

Hydromagnetic Waves in a Non-Uniform Plasma

E. Kupfer

Lehrstuhl B für Theoretische Physik der Technischen Universität
Braunschweig

Received June 4, 1974

Abstract. It is shown, that a small δ-like density perturbation in a cold uniform plasma cannot explain the latitude dependence of the poloidal mode of geomagnetic micropulsations.

Key words: Micropulsations – Hydromagnetic Waves.

Observations of geomagnetic micropulsations of typ Pc3 show a pronounced latitude dependence of the frequency of the north-south component of the perturbed earth's magnetic field (Voelker, 1963; Zelwer and Morrison, 1972). Assuming that non-interacting density lamellae along the field lines exist, Siebert (1965) attributes these observations to the poloidal mode of hydromagnetic waves in the magnetosphere. Abandoning the assumption of absolute density decoupling the influence of a density perturbation on the poloidal mode is considered in the present paper. Below we discuss in more detail the connection of the present treatment to Siebert's model.

The propagation of hydromagnetic disturbances in a column of a cold perfectly conducting plasma possessing a nonuniform mass density distribution:

$$\varrho = \varrho_0 \cdot \left[1 + \lambda \cdot \delta\left(\frac{r}{r_a} - \frac{r_0}{r_a}\right)\right] \tag{1}$$

(ϱ_0: unperturbed mass density, λ: parameter of the δ-like mass density disturbance at radius r_0, r_a: radius of the cylindrical column) is investigated. The plasma column of length L is subject to a uniform axial magnetic field $\mathbf{H}_0$.

The fundamental equations used are Maxwell's equations omitting the displacement current, the equation of motion and Ohm's law. The equations are linearized by assuming the wave field to be small compared to the steady magnetic field.

Under the assumption of axial symmetry the wave equation decomposes into two independent equations for the field components E_ϕ and E_r,

both of which are of the form $R(r) \cdot \exp[i(\omega t - kz)]$. Only the isotropic mode is considered below. The equation for the azimuthal electric field E_ϕ is:

$$\frac{\mu_0 \varrho}{B_0^2} \cdot \frac{\partial^2 E_\phi}{\partial t^2} = \frac{\partial^2 E_\phi}{\partial z^2} + \frac{1}{r} \cdot \frac{\partial}{\partial r}(r \cdot E_\phi) . \tag{2}$$

For a uniform plasma in a column with perfectly conducting walls the solution of the radial part of (2) can be reduced to an eigenvalue problem by expanding $R(r)$ in terms of first-order Bessel functions J_1:

$$R = \sum_m R_m^{(0)} = \sum_{m=1}^{\infty} A_m^{(0)} \cdot J_1\left(j_m \frac{r}{r_a}\right) \tag{3}$$

where j_m is the m-th zero of J_1.

The eigenvalues are given by

$$\omega_{mk}^{(0)2} = \frac{B_0^2}{\mu_0 \varrho_0} \cdot \left[k^2 + \frac{j_m^2}{r_a^2}\right] . \tag{4}$$

For a parabolic density distribution the solutions are confluent hypergeometric functions (Pneuman, 1965; Cross and Lehane, 1968).

In the model just described meridional planes correspond to planes $\phi = \text{const}$. Assuming axial symmetry the equation of motion for the poloidal modes is given by (2) and corresponds to Siebert's Eq. (5.17). Lamellae are defined by decomposing the meridian plane parallel to the z axis into a discontinuous sequence of strips of zero and nonzero density. Siebert's assumption (5.20a) that the field parameters do not significantly change over a given lamella-cross section would read $\partial E_\phi / \partial r = 0$ in our model. In order to investigate the effect of incomplete density decoupling on the poloidal modes we have introduced the density distribution (1).

In this case we have to solve the following equation

$$\left\{r^2 \frac{d^2}{dr^2} + r \frac{d}{dr} - 1 - k^2 r^2 + r^2 \cdot \frac{\omega^2 \mu_0 \varrho_0}{B_0^2} \cdot \left[1 + \lambda \cdot \delta\left(\frac{r}{r_a} - \frac{r_0}{r_a}\right)\right]\right\} R = 0 . \tag{5}$$

If the density $\varrho_0 \lambda \delta(r/r_a - r_0/r_a)$ is sufficently small the solution of (5) can be found by first-order perturbation theory yielding

$$R = \sum_m R_m \tag{6}$$

$$R_m = A_m^{(0)} \cdot \left[J_1\left(j_m \frac{r}{r_a}\right) - \lambda \omega_{km}^{(0)2} \cdot \frac{\mu_0 \varrho_0}{B_0^2} \cdot 2 r_0 r_a \right.$$
$$\left. \times J_1\left(j_m \frac{r_0}{r_a}\right) \sum_{l \neq m} \frac{J_1\left(j_l \frac{r_0}{r_a}\right)}{J_1'^2(j_l)} \cdot \frac{J_1\left(j_l \frac{r_0}{r_a}\right)}{j_m^2 - j_l^2} \right] + 0(\lambda^2) \tag{7}$$

$$\omega_{mk}^2 = \omega_{mk}^{(0)2} \cdot \left[1 - 2\lambda \frac{r_0}{r_a} \frac{J_1^2\left(j_m \frac{r_0}{r_a}\right)}{J_1'^2(j_m)} \right] + 0(\lambda^2) . \tag{8}$$

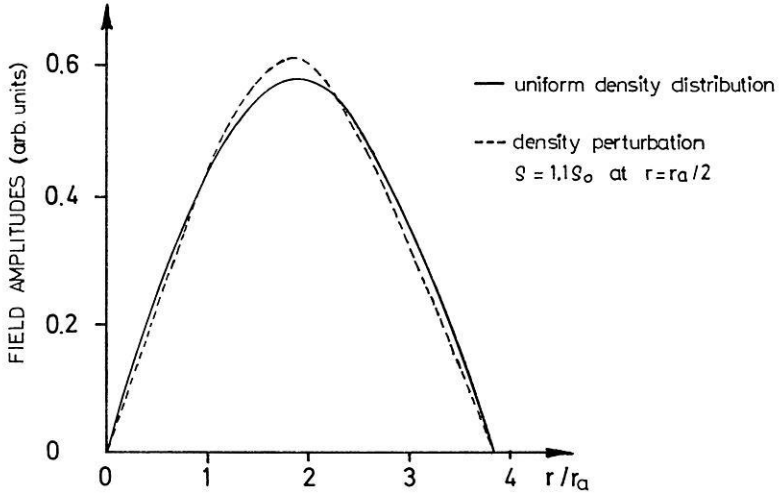

Fig. 1. Radial distribution of the azimuthal electric field E_ϕ in a plasma column of radius r_a and length L

Let us assume that fundamental mode excitation is dominant. Fig. 1 then shows the influence of the density perturbation on the radial part of the field for reasonable parameter values ($r_a = 3 \cdot 10^3$ km, $L = 6 \cdot 10^4$ km, $V_A = (B_0^2/\mu_0 \varrho_0)^{1/2} = 10^3$ km s^{-1}, density enhancement 10% of ϱ_0 at $r_0 = r_a/2$). The frequency is shifted to $\omega_{11} = 0.89\ \omega_{11}^{(0)}$. Only a small increase of R_1 compared to $R_1^{(0)}$ is observed. We thus conclude that the observed latitude dependence of the poloidal mode of the micropulsations at the surface of the earth cannot be explained by a small density variation.

Acknowledgement. I would like to thank Prof. E. Richter for many valuable discussions.

References

Cross, R.C., Lehane, J.A.: Hydromagnetic waves in a nonuniform hydrogen plasma. Phys. Fluids *11*, 2621–2626, 1968

Pneuman, G.W.: Hydromagnetic waves in a current carrying plasma column. Phys. Fluids. *8*, 507–516, 1965

Siebert, M.: Zur Theorie erdmagnetischer Pulsationen mit breitenabhängigen Perioden. Mitt. Max-Planck-Institut f. Aeronomie Nr. 21, 1965

Voelker, H.: Zur Breitenabhängigkeit erdmagnetischer Pulsationen. Mitt. Max-Planck-Institut f. Aeronomie Nr. 11, 1963

Zelwer, R., Morrison, H.F.: Spatial characteristics of midlatitude geomagnetic micropulsations, J. Geophys. Res. *77*, 674–694, 1972

Dr. E. Kupfer
Institut für Atom- und Festkörperphysik der Freien Universität
D-1000 Berlin 33
Boltzmannstr. 20

J. Geophys. 41, 127–133, 1975

Time-Domain Electromagnetic INPUT* Response of a Conducting Horizontal Thin Sheet

K. Mallick and S. C. Jain

National Geophysical Research Institute, Hyderabad, India

Received September 4, 1973; Revised Version August 13, 1974

Abstract. The time-domain response of a conducting horizontal thin sheet to the airborne electromagnetic INPUT system is obtained from the corresponding step-function response. In the INPUT system the primary signal is generated by a large horizontal loop antenna mounted on the aircraft as a series of alternate half-sine wave pulses. The thin sheet model will be useful for the interpretation of conducting overburden, swamps and thin clay covers overlying a highly resistive substratum. As an aid to interpretation, the channel amplitudes and the channel amplitude ratios are illustrated.

Key words: INPUT System — Electromagnetic Response — Conducting Thin Sheet.

1. Introduction

In airborne electromagnetics the conducting overburden poses serious problems. This is particularly true in the Indian subcontinent where the resistivity of the top layer, consisting of sedimentary rocks, alluvial soil or even weathered granitic and basaltic rocks, varies between 10 ohm-m to about 100 ohm-m. While working in electromagnetic models, Braekken and Sakshang (1973) have reported that "in various pyrite fields, and outspokenly those of Norway, it is rather common situation that ores are occuring in connection with extensive sheet-like formations of conducting material. That may be graphite sheets or disseminated ore layers of presumably sedimentary origin. This makes it of considerable importance to know the effect of such conductive sheets". With this view in mind, an earlier simple model of single — turn conductive horizontal circuit (Mallick, 1972) has been improved to include a conducting thin horizontal infinite sheet. Homogeneous half-space, layered half-space and thin sheets have been described from various view points by Morrison, Phillips and

* INPUT (*IN*duced *PU*lse *T*ransient) is the registered trade name of an airborne electromagnetic system used by Barringer Research Ltd., Canada.

O'Brien (1969); Nelson and Morris (1969); and Becker (1969). In the present analysis, the time-domain response of the conducting and thin infinite sheet to the INPUT system is derived by the method of superposition from the step-function response.

2. *Primary INPUT Signal*

In the Barringer's INPUT system, the primary signal is sent from a large horizontal loop antenna mounted on an aircraft as a series of alternate half-sine wave pulses. The pulse width is 1.5 msec, and the quiet period between two pulses is 2.0 msec. During this quiet period, sampling is made (Mark V version of Barringer's INPUT system) for a duration of 200 μsec at mean delays of 300, 500, 700, 1100, 1500 and 1900 μsec. These six points in time are termed channels. A complete description of the system is given by Ward (1967). The primary INPUT signal has the following form:

$$\begin{aligned} F(t) &= H_0 \sin \omega t && 0 < t < 1.5 \text{ msec} \\ &= 0 && 1.5 < t < 3.5 \text{ msec} \\ &= -H_0 \sin \omega t && 3.5 < t < 5.0 \text{ msec} \\ &= 0, && 5.0 < t < 7.0 \text{ msec} \end{aligned} \tag{1}$$

with $\omega = 2\pi/T$. $T = 3.0$ msec is the period of the continuous sine wave. Fig. 1 shows the transmitting coil mounted on the aircraft, the receiver bird towed behind, the excitation pulse, and the position of the sheet.

3. *Principle of Superposition*

Any continuous function can be assumed to be made up of a number of step-functions. The pulse, defined in Eq. (1), can therefore be replaced by several step-functions. Once the response of a step-function is known, the response of the continuous pulse can conveniently be evaluated by the method of superposition described below:

Let $F(t)$ be the continuous pulse and $H(t)$ the step-function response. The response in the INPUT system, i.e. the response due to the continuous pulse will be

$$H_i(t) = H(t)\, F(O^+) + \int_0^t H(t-\tau) \frac{\delta F(\tau)}{\delta \tau}\, d\tau \,. \tag{2}$$

This is referred to as Duhamel Integral (Weber, 1957). For the half-sine pulse given by Eq. (1), $F(O^+) = F(T/2) = 0$. From Eq. (2) the response is then obtained as

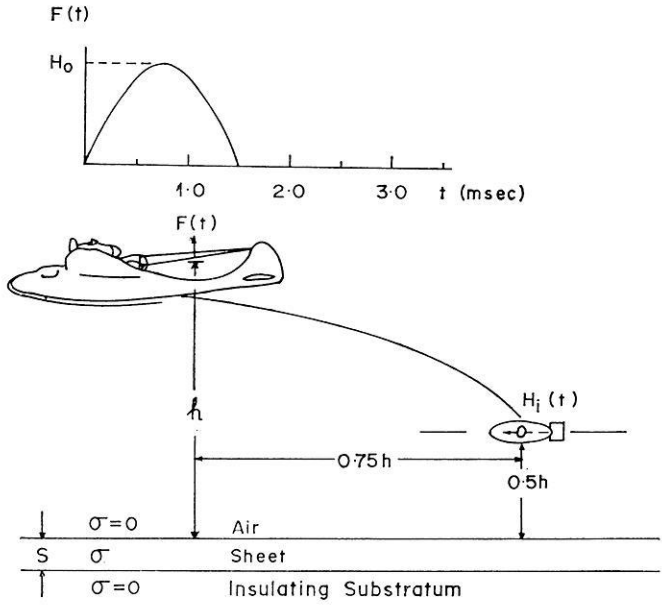

Fig. 1. Schematic diagram of the airborne electromagnetic INPUT system together with thin sheet model (bottom) and primary (exciting) signal (top). σ is the conductivity of the sheet

$$H_i(t) = \int_0^t H(t-\tau)\,\frac{\delta F(\tau)}{\delta \tau}\,d\tau \qquad \text{for } 0 < t < T/2 \tag{3a}$$

in the presence of the primary field, and

$$H_{\text{INPUT}}(t) = \int_0^{\frac{T}{2}} H(t-\tau)\,\frac{\delta F(\tau)}{\delta \tau}\,d\tau \qquad \text{for } T/2 < t \tag{3b}$$

when the primary field is taken off.

4. Step-Function Response of the Infinite Sheet

Induction currents in a thin, conducting infinite sheet and their decay under the influence of resistance and selfinductance are described by Jeans (1963). Grant and West (1965) have derived the same results in greater detail and have illustrated the response of different coil systems for a continuous sinusoidal source field.

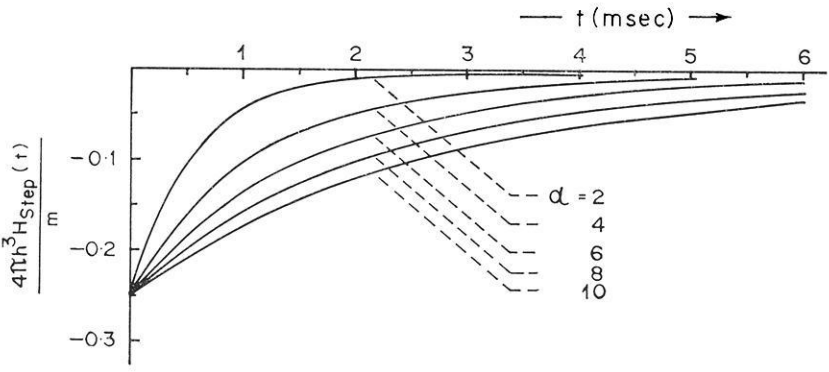

Fig. 2. Step-function response of a thin horizontal infinite sheet. $\alpha = \mu_0 \sigma s h$ is given in msec

Suppose a very thin sheet of conductance σs (σ = conductivity and s = thickness of the sheet) lies in the plane z = O, above an insulating half-space as shown in Fig. 1. If the primary source is an oscillating magnetic dipole, which varies step-wise in time and is oriented in an arbitrary direction at (x_0, y_0, h), the secondary field at another point (x, y, z) is (Grant and West, 1965)

$$\vec{H}^{(s)} = -\frac{1}{4\pi}\left[\nabla\left\{\vec{m}.\nabla_0\left((x-x_0)^2+(y-y_0)^2+\left(z+h+\frac{2t}{\sigma\mu_0 s}\right)^2\right)^{-\frac{1}{2}}\right\}\right] \quad (4)$$

where m is the magnetic dipole moment, and the operators ∇_0 and ∇ operate at the source and the observer respectively. μ_0 is the magnetic permeability of the air and equals to that of the sheet and the insulating substratum.

For the Barringer INPUT system, the transmitting magnetic dipole is vertical and the secondary field is recorded by a vertical coil in the bird towed behind the aircraft as shown in Fig. 1. The axis of the receiver coil is horizontal and along the flight direction. For such a transmitter-receiver combination $H_{step}(t)$, the step-function response, can be obtained from Eq. (4):

$$\frac{4\pi h^3}{3m} H_{step}(t) = -\left[\beta^2 + \left(1+\eta+\frac{2t}{\alpha}\right)^2\right]^{-5/2}\left(1+\eta+\frac{2t}{\alpha}\right), \quad (5)$$

where $\beta = (x - x_0)/z$, $\eta = z/h$ and $\alpha = \sigma\mu_0 sh$.

Fig. 2 shows the response due to step-function excitation for a system with transmitter at a height h, the receiver at 0.5 h and the transmitter-receiver horizontal separation 0.75 h for several values of α.

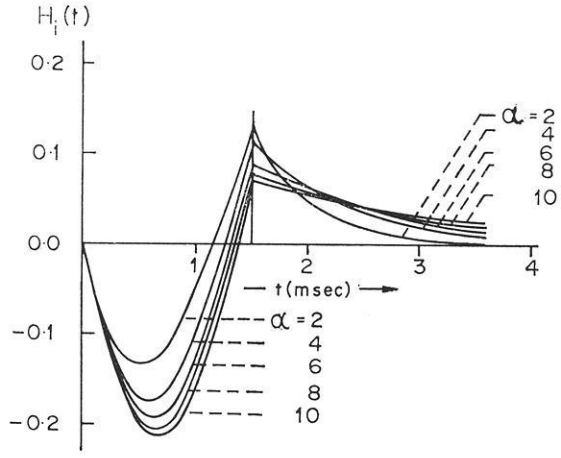

Fig. 3. INPUT response of the sheet. The values of α are the same as in Fig. 2

It can be observed from Fig. 2 that the conductance is inversely related to the decay constant of the transient field.

5. INPUT Response

The INPUT response of the sheet is obtained from the step-function response given in Eq. (5) by applying the principle of superposition (for example, see Mallick, 1973a and 1973b):

$$H_{\text{INPUT}}(t) = -\frac{3m}{4\pi b^3}\left[\int_0^t \left\{\beta^2 + \left(1+\eta+\frac{2(t-\tau)}{\alpha}\right)^2\right\}^{-5/2} \cdot \beta\left(1+\eta+\frac{2(t-\tau)}{\alpha}\right) \cdot \omega \cos \omega\tau \, d\tau\right] \left\{1+u(t-T/2)\right\}, \tag{6}$$

where $u(t-T/2)$ is the delayed unit step-function.

$H_{\text{INPUT}}(t)$, from now on to be written as $H_i(t)$, has been computed and in being shown in Fig. 3 for the same geometry of transmitter, receiving bird and the sheet, and for the same values of α as in Fig. 2. Similar to the step-function response, the INPUT response decays more rapidly for smaller values of α.

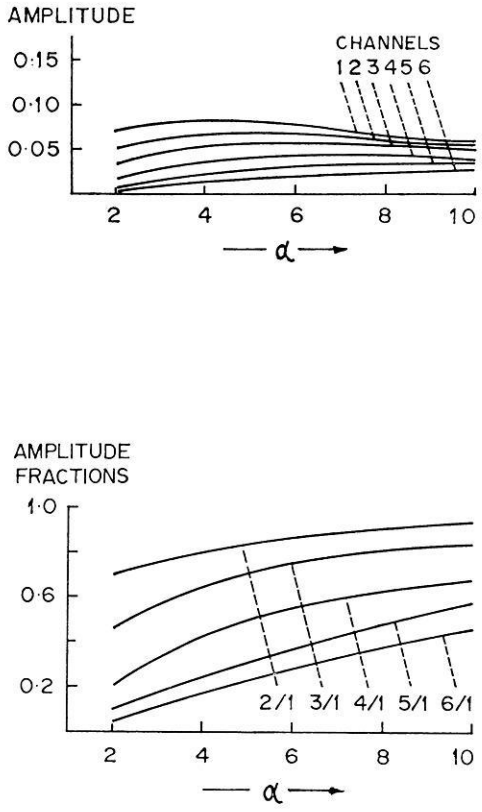

Fig. 4. The channel amplitudes in units of $\frac{3m}{4\pi b^3}$ (top) and the channel amplitude ratios as fractions of the first channel amplitude (bottom)

6. Channel Amplitudes and Channel Aplitude Ratios

As a possible aid to interpretation of field data, the channel amplitudes in units of $\frac{4\pi b^3}{3m}$ and the channel amplitude ratios (as fractions of the first channel amplitude and indicated by 2/1, 3/1 etc.) are illustrated at the top and the bottom of Fig. 4 respectively. The range of α is chosen between 2.0 and 10.0 msec, as in Figs. 2 and 3, since the response reaches its resistive limit for $\alpha < 2.0$ msec and its inductive limit for $\alpha > 10.0$ msec (Grant and West 1965, p. 502). The analysis of Grant and West has, however, been made for a continuous sinusoidal field.

The amplitude ratios can be matched with the field data for a system where the magnetic field is recorded. The NGRI version of the INPUT system is such a system; it records the field and its time-derivative (voltage developed in the receiver coil) as well.

Acknowledgements. We record our deep gratitude to Dr. A. Roy for his interest in this problem. For some useful discussion we thank Mr. D. Guptasarma of the National Geophysical Research Institute. One of the authors (K.M.) thanks his wife for her help in the preparation of the manuscript. The publication is authorised by the Director, National Geophysical Research Institute.

References

Becker, A.: Simulations of Time-Domain, Airborne Electromagnetic System Response. Geophysics *34*, 739–752, 1969

Braekken, H., Sakshaug, G.F.: EM Anomalies of Conductor Overlain or Underlain by Conducting Sheet like Formations – A Model Study (Abstract). Paper read at 35th Meeting of EAEG held at Brighton, England, 5th–8th June 1973

Grant, F.S., West, G.F.: Interpretation Theory in Applied Geophysics. New York: MacGraw Hill 1965

Jeans, J.: The Mathematical Theory of Electricity and Magnetism, 5th Ed., Cambridge Univ. Press 1963

Mallick, K.: INPUT Response to Single-Turn Conductive Circuit, Geoexploration *10*, 255–259, 1972

Mallick, K.: Conducting Infinite Horizontal Cylinder in Electromagnetic INPUT Field, Geophys. Prospecting, *21*, 102–108, 1973a

Mallick, K.: Effect of Magnetic Permeability on INPUT Response of a Spherical Ore Body. Geoexploration *11*, 183–186, 1973b

Morrison, H.F., Phillips, R.J., O'Brien, D.P.: Quantitative Interpretation of Transient Electromagnetic Field over a Layered Halfspace. Geophys. Prospecting *17*, 82–101, 1969

Nelson, P.H., Morris, D.B.: Theoretical Response of a Time-Domain, Airborne, Electromagnetic system. Geophysics *34*, 729–739, 1969

Ward, S.H.: The Electromagnetic Methods. In: Society of Exploration Geophysicist's Mining Geophysics, Tulsa, Oklahoma, Vol. 2, 1967

Weber, E.: Linear Transient Analysis, Vol. I. New York: Wiley 1957

Kumarendra Mallick
Sheel C. Jain
National Geophysical Research Institute
Hyderabad 500007, India

Book Reviews

Handbuch der Physik. S. Flügge, Hrsg. Band XLIX/3, *Geophysik* III/3, Bandherausgeber: K. Rawer.
Berlin–Heidelberg–New York: Springer 1971. Preis: DM 188,–, Subskriptionspreis: DM 150,40.

Der Band behandelt den Erdmagnetismus und dessen Beobachtungs- und Meßmethoden. Die einzelnen Abschnitte können für sich als kleine Lehrbücher aufgefaßt werden. Dazu muß der Leser einige Voraussetzungen in theoretischer und experimenteller Physik mitbringen, um den Inhalt gut verarbeiten zu können. Die Erkenntnisse wurden bis ca. 1970 berücksichtigt.

Im einzelnen sind die Kapitel: Morphology of Magnetic Disturbance. Theoretical Aspects of the Worldwide Magnetic Storm Phenomenon. Maßzahlen der erdmagnetischen Aktivität. Classical Methods of Geomagnetic Observations. Neuere Meßmethoden der Geomagnetik. Three-Component Airborne Magnetometers. Aeromagnetic Surveying with the Fluxgate Magnetometer. Geophysical Applications of High Resolution Magnetometers. Phénomènes T.B.F. d'origine magnétosherique. Ein Sachverzeichnis in Deutsch, Englisch und Französisch schließt an.

Das Buch sollte in jeder Bibliothek von Einrichtungen stehen, deren Mitarbeiter sich mit Erdmagnetismus beschäftigen. O. Walk, Karlsruhe

Handbuch der Physik. S. Flügge, Hrsg. Band XLIX/4, *Geophysik* III/4, Bandherausgeber: K. Rawer.
Berlin–Heidelberg–New York: Springer 1972. Preis DM 198,–, Subskriptionspreis: DM 158,40.

Diesen Band kann man als Weiterführung von Geophysik III/3 sehen. Er befaßt sich mit der Magnetosphäre und deren Erscheinungen. Der Aufbau ist dem vorhergehenden Band analog.

Die Kapitel sind folgende: The Earth's Magnetosphere. The Earth's Radiation Belt. Variations repides du champ magnétique terrestre. Waves and Resonances in Magnetoactive Plasma.

Zu diesem Buch kann man das Gleiche sagen wie zu Geophysik III/3, daß er für Bibliotheken von Einrichtungen empfehlenswert ist, deren Mitarbeiter sich mit diesem Fachgebiet befassen. O. Walk, Karlsruhe

Studienhefte der Physik des Erdkörpers, Heft 1: G. Angenheister und H. Soffel: *Gesteinsmagnetismus und Paläomagnetismus.*
Berlin–Stuttgart: Gebrüder Borntraeger, 1972. Preis: DM 22,–.

Das Studienheft bietet dem etwas physikalisch vorgebildeten Leser eine vorzügliche Einführung in den Gesteinsmagnetismus und den sich daraus ergebenden Schlüssen für die Erdgeschichte. Es ist klar und gut verständlich aufgebaut. Die Kapitel dieses Studienheftes sind: Grundlagen zur Theorie des Gesteins-Magnetismus. Diamagnetismus, Paramagnetismus, Ferromagnetismus. Die Eigenschaften der magnetischen Minerale. Die remanente Magnetisierung von Gesteinen. Instrumente des Gesteinsmagnetismus. Paläomagnetismus. Ergänzungen. Dieses Studienheft kann jedem Studenten, der sich für Geophysik interessiert, empfohlen werden. O. Walk, Karlsruhe

J. Geophys. 41, 135–148, 1975

Originals Investigations

Seismic Investigations along the Scandinavian "Blue Road" Traverse

H. B. Hirschleber
Institut für Geophysik, Hamburg

C.-E. Lund
Department of Solid Earth Physics, Uppsala

R. Meissner
Institut für Geophysik, Kiel

A. Vogel*
Department of Solid Earth Physics, University of Uppsala

W. Weinrebe
Institut für Geophysik, Kiel

Received May 2, 1974; Revised Version June 27, 1974

Abstract. At the end of July and the beginning of August 1972 seismic studies were carried out along the Scandinavian "Blue Road" traverse, an area of interdisciplinary geoscientific research. Geographically, it runs from the Norwegian coast, near the arctic circle, through Sweden into southern Finland, having a total length of about 600 km, passing through the Caledonian mountain chain and extending into the Baltic Shield within its central area of land uplift.

Velocity models of the crust and upper mantle were computed, based on very clear arrivals of refracted P-waves. The crust mantle boundary, which was mapped along the whole profile, shows only minor undulations. Reaching a depth of about 40 km on the Baltic Shield the Moho shows no distinct roots below the Caledonian mountains. A constant mantle velocity is derived, to depths of about 80 km, from parallel P_n-branches. Apart from different geological structures near the surface, the overall distribution of seismic velocities appears to be very similar within the Caledonides and the Baltic Shield.

Key words: Deep Seismic Sounding – Crustal Structure of Baltic Shield and the Caledonides.

Introduction

The Caledonian mountain range and the Baltic Shield form the northern part of the European continent. The Caledonides represent the remnants of an orogeny which took place between 700 and 400 m.y. B. P. (Lundegård *et al.*, 1970). The structure of the Caledonides indicates lateral compression and overthrust of nappes, eastward, on to the Baltic Shield, processes which probably took place on the col-

* Present Address: Institut für Meteorologie und Geophysik, FU Berlin.

lision or the subduction zone of drifting plates in accordance with the theory of plate tectonics. The Baltic Shield represents a very old tectonic unit and consists of remnants of ancient orogenies which took place in several cycles: the Svecofennian folding, covering the greater part of Sweden and southern Finland, took place between 2100 and 1500 m.y., the adjacent units to the north show increasing ages up to about 3000 m.y. (the Cola massiv, Welin, 1966, 1970), whereas the southern parts of Sweden are "only" 1400 to 860 m.y. old. There is considerable evidence that the Baltic Shield has been uplifted almost continuously since Caledonian times; the present and more recent land uplift is explained by isostatic compensation after the last ice-age (Haskell, 1935; Penttilä, 1969b).

About 18 seismic explosion investigations have already been carried out in Fennoscandia (Penttilä, 1969a, 1972). Most of the profiles were only about 200 km long and stayed in the same tectonic unit. Average *P*-wave velocities of 6.0 to 6.2 km/s for the "granitic" layer, values of 6.4 to 6.6 km/s for an intermediate crustal refractor, and 8.0 to 8.3 km/s for the mantle, have been found in different areas of Scandinavia. (Dahlman, 1967; Sellevoll and Pomeroy, 1968; Penttilä, 1969a, 1972; Båth, 1971; Kanestrøm, 1971; Vogel and Lund, 1971). The scatter of these data was small suggesting a rather uniform structure of the whole crust.

Following a recommendation of the European Seismological Commission in Luxembourg 1970, the Department of Solid Earth Physics at the University of Uppsala set out plans for an interdisciplinary investigation along a traverse, including a seismic profile from the Norwegian coast through Sweden, across the Gulf of Bothnia and into Finland. Starting at Mo i Rana the profile crosses the Caledonides, runs along the river Ume Älv, goes across the Gulf of Bothnia between Umea and Vaasa, and continues for 100 km inside the Svecofennian Shield of Finland. In Sweden, the profile follows the well known tourist route called the "Blue Road". Five shot points, with an average distance of 100 km, were planned for this 600 km long "lithospheric profile". At first, a multiple coverage of refractors was arranged by a system of reversed shots in order to obtain accurate physical parameters of crust and upper mantle over a longer range, and in two fundamentally different areas: the Caledonides in the north-west, and the Baltic Shield in the south-east, including the zone of maximum land uplift (Fig. 1).

Seismic Field Work

Seismic field work was carried out between July 28th and August 4th, 1972. Explosive charges equivalent to 700 kg TNT were fired, in the ocean at shot point 1, in small lakes at shot points 2, 3 and 4, and in the Gulf of Bothnia at shot point 5. Explosions at shot point 2—5 were prepared by the Research Institute of the Swedish National Defence, and those at shot point 1 were arranged by the Seismological Institute in Bergen. 42 recording units, MARS 66, for land stations were collected from geophysical institutes in Berlin, Bochum, Clausthal, Frankfurt, Görttingen, Hamburg, Hannover, Karlsruhe, Kiel, München, Münster, Stuttgart und Uppsala, one additional land station from the Institute of Seismology in Helsinki and three sea stations from the Geophysical Institute in Hamburg. Two series of four shots per night were recorded at 46 field stations along the profile. 42 MARS stations were equipped with multiplex FM modulators, three 2 Hz geophones, and a radio receiver.

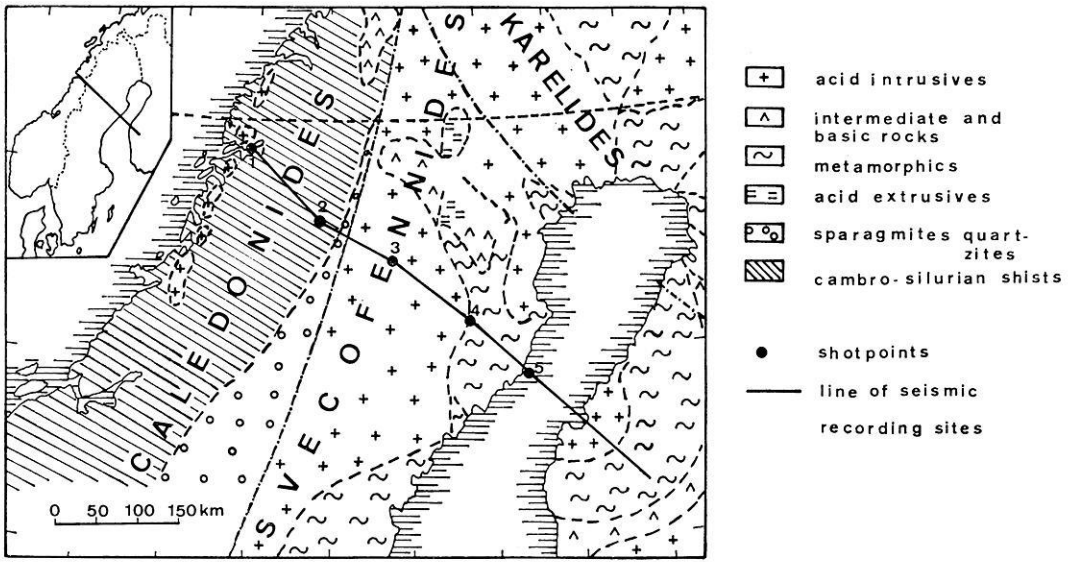

Fig. 1. Simplified geological map with profile and location of shot points; geologic data after Bundesanstalt für Bodenforschung and Unesco (1966)

Every third station was set up as a three component geophone array, the others with vertical geophones, about 400 m apart. The average spacing between stations was about 4 km. The whole field arrangement may be seen in Fig. 2. The sea stations were equipped with hydrophones on the seafloor. The seismic FM signals were transmitted from anchored sono-buoys to receivers on a nearby island. Time signals and radio announcements were provided by the Swedish radio network from a communication centre maintained by the Research Institute of Swedish National Defence. Two series of four shots each were fired within two nights of recording. During the first night of operation (spread A in Fig. 2) 36 land stations were arranged with equal spacing between shot points 3 and 5 (in the Swedish part of the Baltic Shield), two sea stations and one land station in the Gulf of Bothnia and five land stations in Finland, recording signals from shot points 1, 3, 4, 5, using 1400 kg TNT at shot point 3. In the second night of recording (spread B in Fig. 2) 37 land stations were arranged between shot points 1 and 3; one station remained on an island in the Gulf of Bothnia and one sea station remained on its former position; two sea stations and five land stations in Finland moved to greater distances. In this second night of operation shots at shotpoints 1, 2, 3 and 5 were fired, using 1400 kg TNT at shotpoint 5. After each night of recording field crews working in Sweden and Norway met at the operational centre at Storuman for the play-back of recorded data and for further information on the operations. A total of four reversed sections, each about 100 km in length, two reversed, each about 200 km in length, and one of about 400 km were obtained. In addition, several unreversed sections of 200 km and more were observed by the stations operating in Finland and the Gulf of Bothnia; the largest recording distance was about 600 km. The quality of the data, due to low noise level and favourable weather, was extremely good.

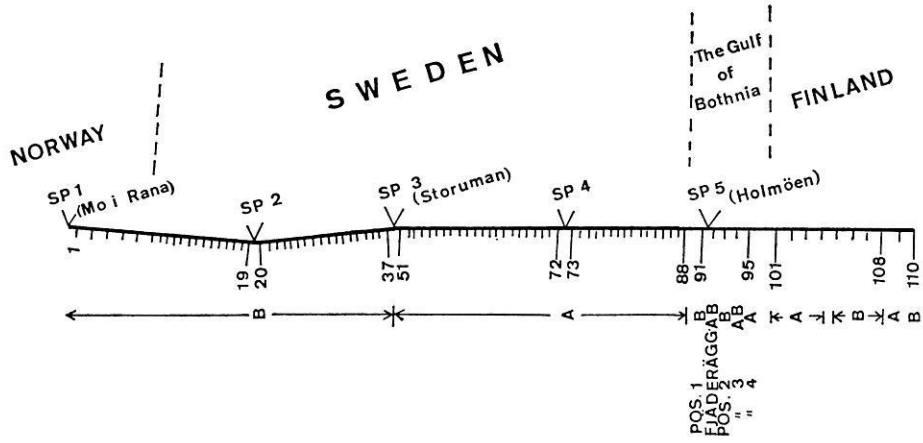

Fig. 2. Arrangement of shotpoints and recording stations along the profile

Interpretation

Analog or digital processing was applied to the data. This information was then compiled into seismogram sections after being filtered by a band pass of 1 to 20 Hz. Fig. 3 to 7 show nine sections, each reduced with a velocity of 8.0 km/s in order to draw attention to the P_n-waves. Although excellent first arrivals were found along the whole profile, secondary arrivals were generally weak. No clear wide angle reflections have been detected although some indications were observed at distances of 120—250 km on profiles 1-East, 3-East and 5-West. Thus, reflection observations could not be used in converting travel-time curves into velocity-depth functions.

In general, only first arrivals were evaluated, and a ray tracing program after G. Mueller (1971, unpublished) was used in order to calculate theoretical traveltime curves. Velocities were considered as a function of depth. In general, velocities in the upper part of the crust increase continuously, or discontinuously, from 5.7 to about 6.2 km/s. Velocities between 6.0 and 6.2 km/s characterize the layers down to about 15 to 20 km. Below these depths velocities around 6.5 to 6.8 km/s are found for the deeper crust below all shot points. The Mohorovičić discontinuity (= Moho) is found between 37 and 40 km in the region surrounding the five shot points (Fig. 8).

The theoretical travel-time curves of these velocity-depth functions are in close agreement with the observed first arrivals. As a consequence of these velocity models, however, one should expect secondary arrivals, such as reflected and refracted waves from the first order boundaries. As definitely only small cusps in the travel time behaviour are observed, one has to look for more refined models. Secondary arrivals on seismogram sections 1-East and 5 West forming a cusp do not show apparent velocities (v_a) larger than 8 km/s. This means that no subcritical reflections from the Moho with $v_a > 8$ km/s are observed, and hence, most probably, no first order interface with a considerable increase of velocity values exists at the crust-mantle boundary. Velocity-depth models without a significant first order disconti-

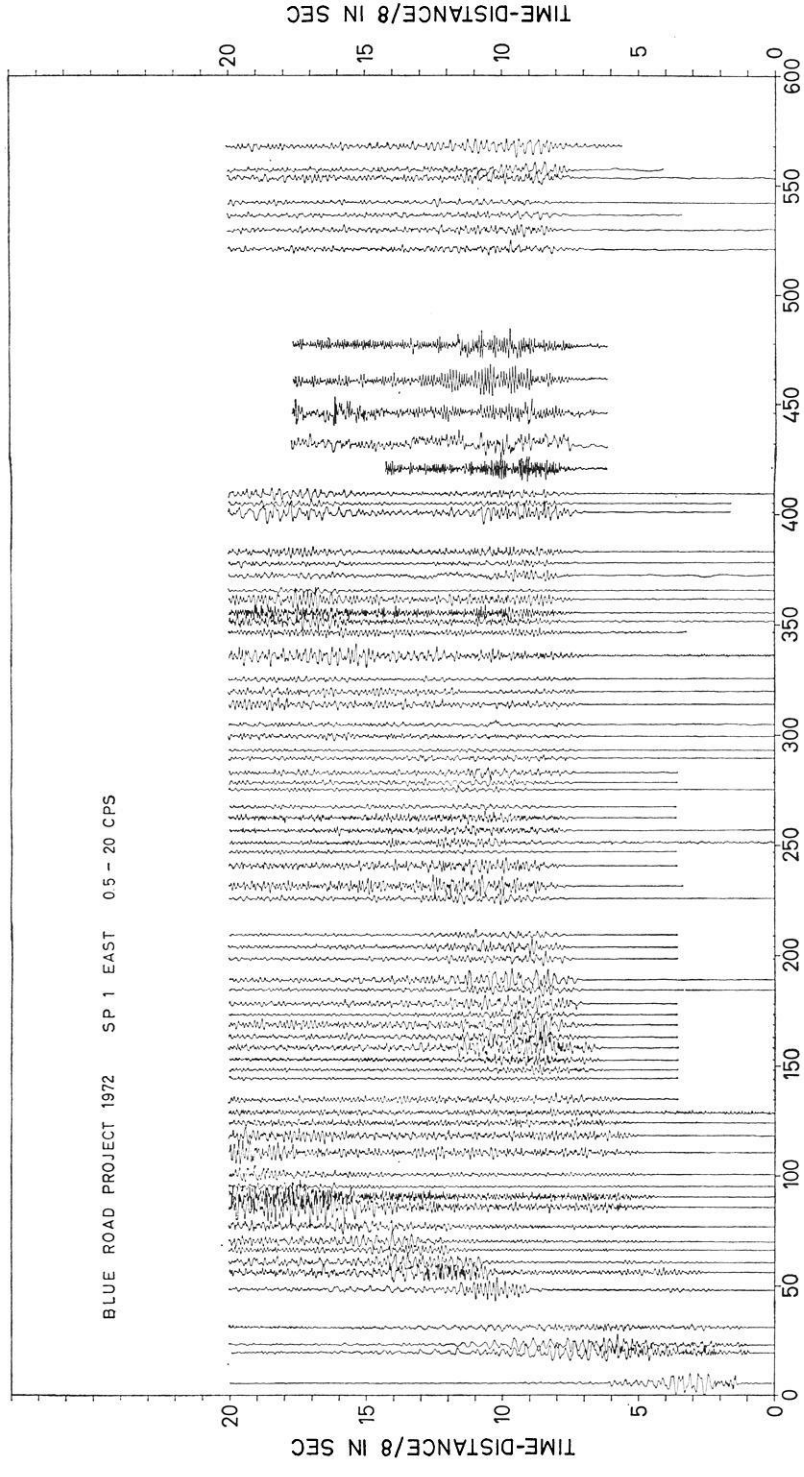

Figs. 3–7. Record sections

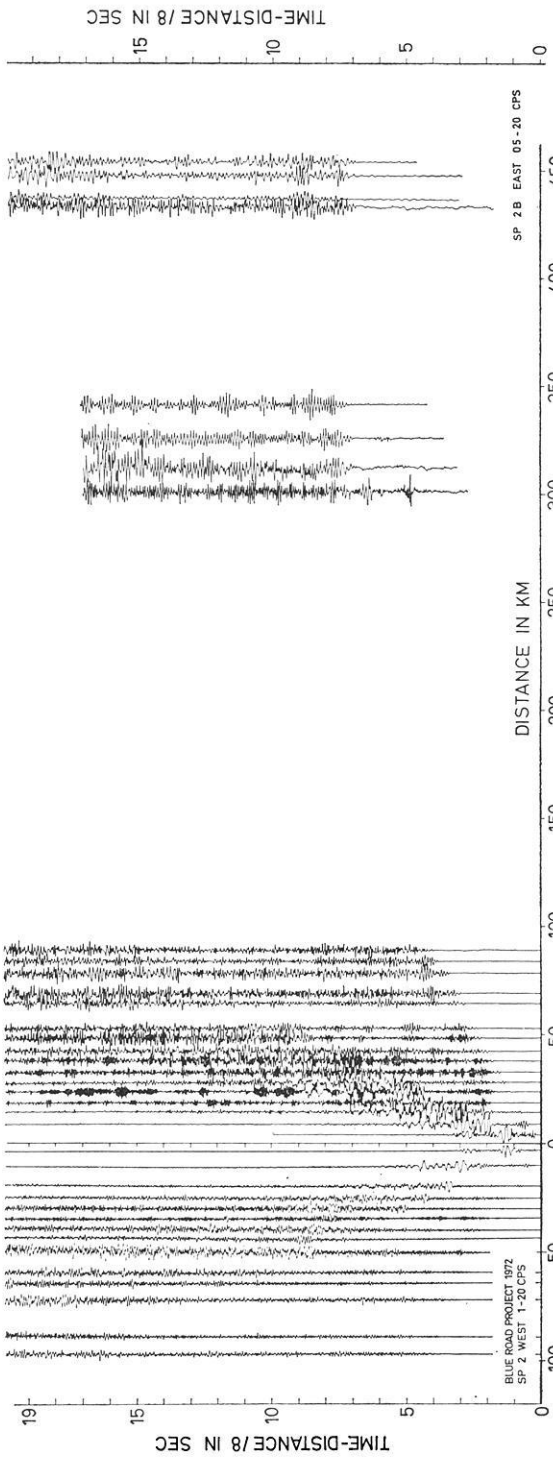
TIME-DISTANCE / 8 IN SEC
0
5
10
15
SP 2 B EAST 05-20 CPS
DISTANCE IN KM
0
50
100
150
200
250
300
350
400
450
BLUE ROAD PROJECT 1972
SP 2 WEST 1-20 CPS
TIME-DISTANCE / 8 IN SEC
19
15
10
5
0

Fig. 4

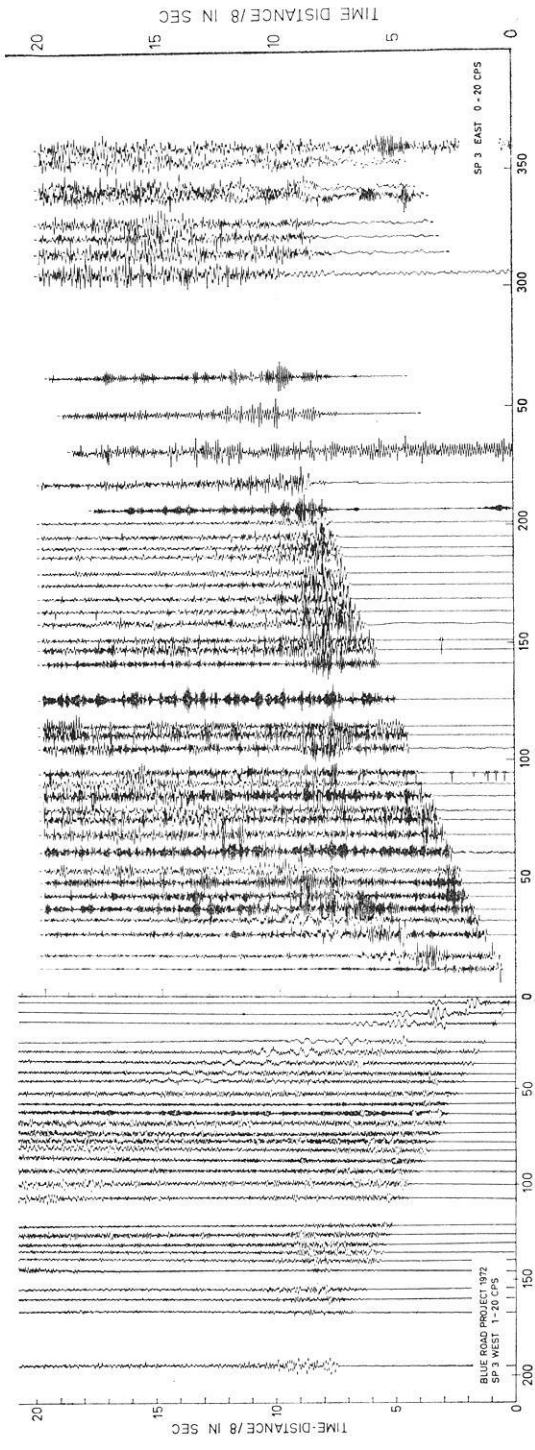
TIME DISTANCE / 8 IN SEC
20
15
10
5
0
SP 3 EAST 0 - 20 CPS
350
300
50
200
150
100
50
0
50
100
150
200
DISTANCE IN KM
BLUE ROAD PROJECT 1972
SP 3 WEST 1 - 20 CPS
TIME-DISTANCE / 8 IN SEC

Fig. 5

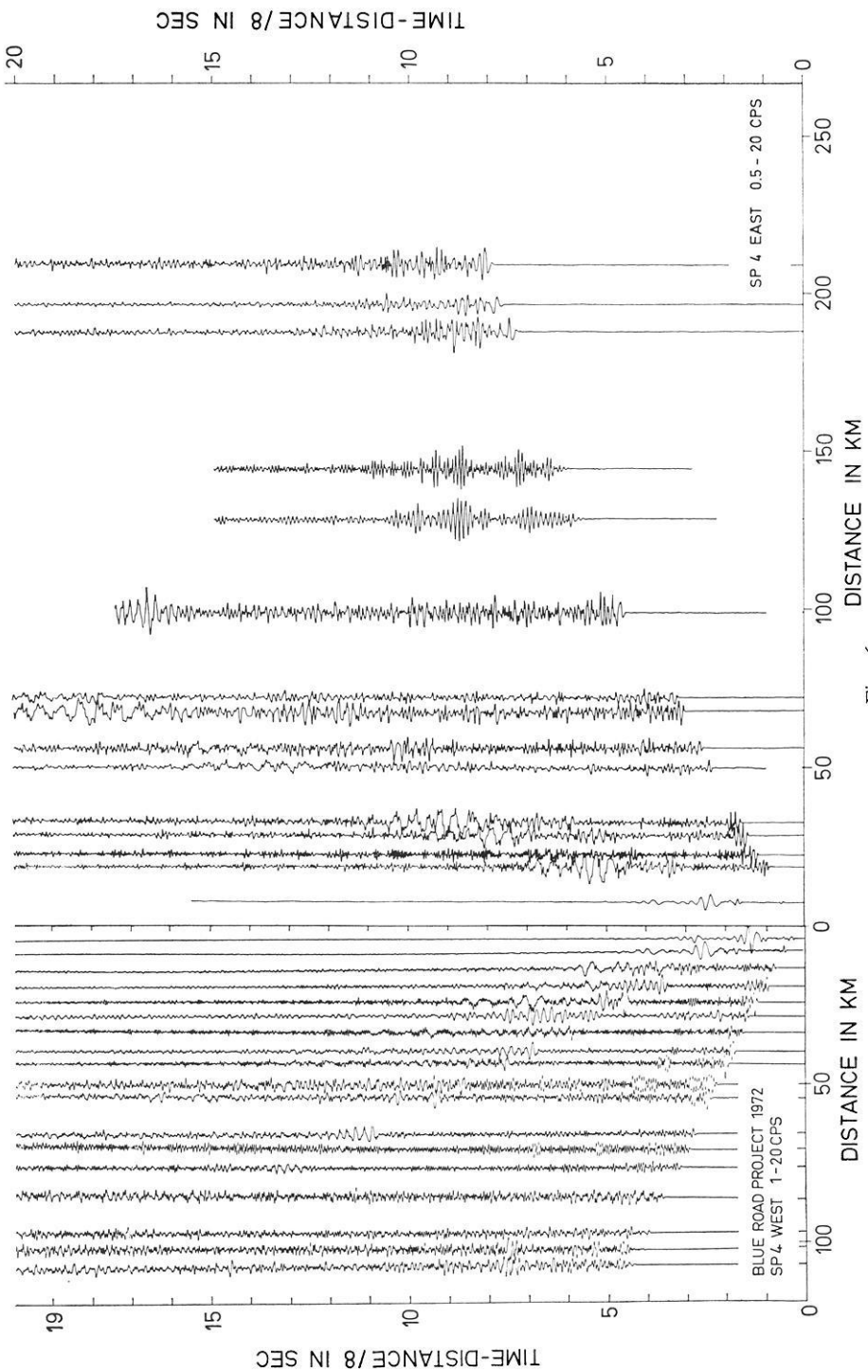
TIME-DISTANCE/8 IN SEC
20
15
10
5
0
SP 4 EAST 0.5 - 20 CPS
250
200
150
100
50
0
DISTANCE IN KM
BLUE ROAD PROJECT 1972
SP 4 WEST 1-20 CPS
100
50
0
DISTANCE IN KM
19
15
10
5
0
TIME-DISTANCE/8 IN SEC

Fig. 6

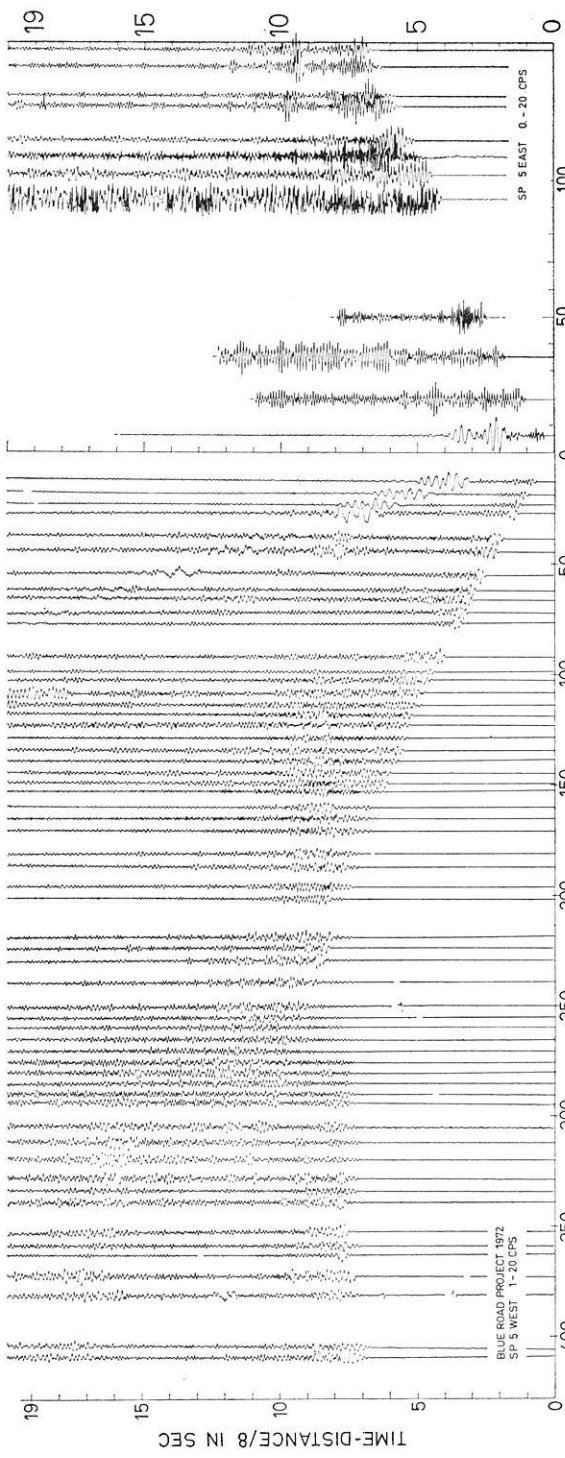
SP 5 EAST 0.-20 CPS
BLUE ROAD PROJECT 1972
SP 5 WEST 1-20 CPS
DISTANCE IN KM
TIME-DISTANCE/8 IN SEC

Fig. 7

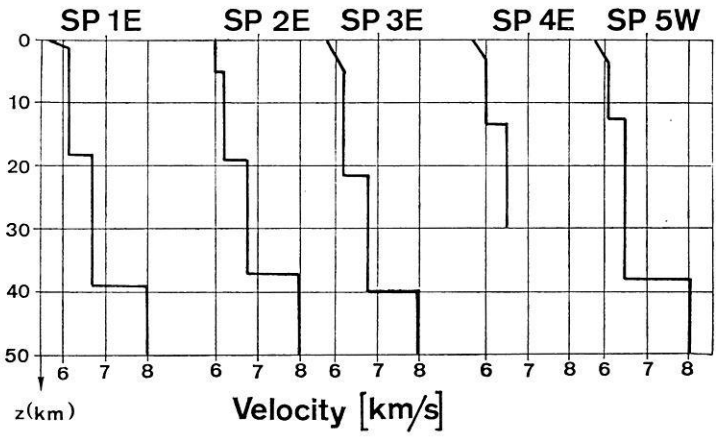

Fig. 8. Velocity-depth functions with best fit of theoretical to observed travel-time curves along the profile

nuity should certainly be given preference. Fig. 9 shows the seismogram section 5-West with the theoretical travel-time curves of a best fitting gradient model with only a small first order boundary at the base of the crust; (note the cusp between 130 and 260 km). In general crustal thickness is increased by a model including gradients. From first arrivals only weak indications are found for the existence of a Conrad boundary in the depth range between 12 and 20 km. It cannot be decided whether they represent a small first order discontinuity or a general smooth increase to velocity values of 6.6 to 6.8 km/s.

There is no indication for a low velocity channel in the crust. The P_n-arrivals from the Moho particularly show many variations of the apparent velocity along the profile. In most cases, recordings of additional P_n-arrivals from the same part of the profile permit a direct correlation between these velocity variations and the dip of the Moho. This is especially reliable for the area between 170 and 280 km south-east of shot point 1, where a complete coverage of the Moho surface by reversed-profiles has been achieved. As there is a twofold of threefold coverage of the Moho by refracted arrivals from different shot points, the apparent velocities of these arrivals can be controlled. It was a surprise that apparent P_n-velocities from various distances, such as 500 to 600 km and 150 to 250 km turned out to be exactly the same. This means that there is no positive velocity gradient in the first 50 km of the upper mantle[1].

With the continuous coverage of the Moho a cross section along the whole profile was obtained. The velocity models mentioned before were used in order to apply wave-front methods for the calculation (Meissner, 1965). Wave-fronts and depths were plotted by a computer program based on well known ray equations for media with constant velocities and continuous series with constant velocity gradients. Generally, Moho depths coincide with those of the ray tracing models. At some

1 One of us (C.-E. Lund) does not agree with these conclusions and plans to publish a separate paper on this subject.

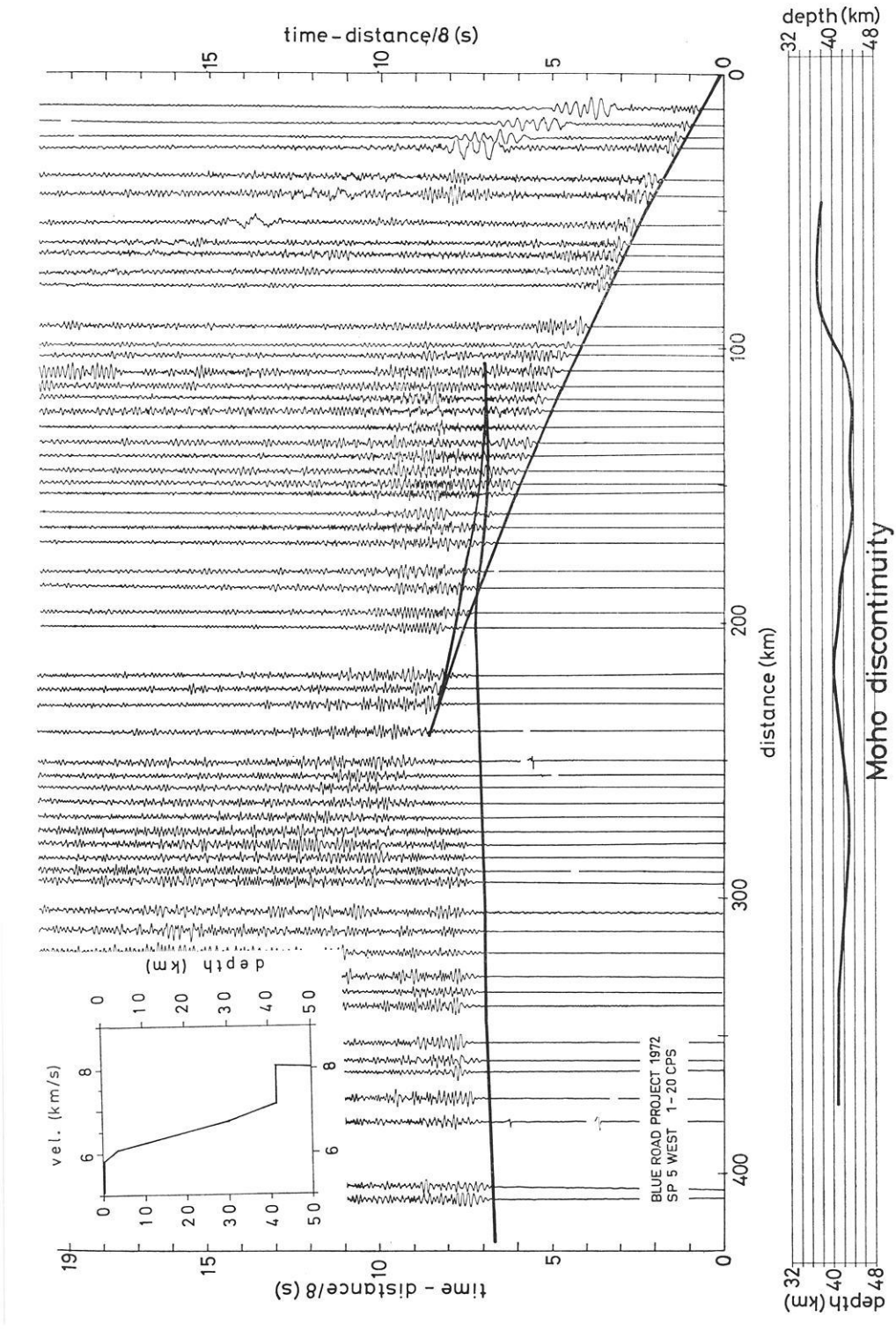

Fig. 9. Seismogram section 5-West with the theoretical travel time curves of a gradient model

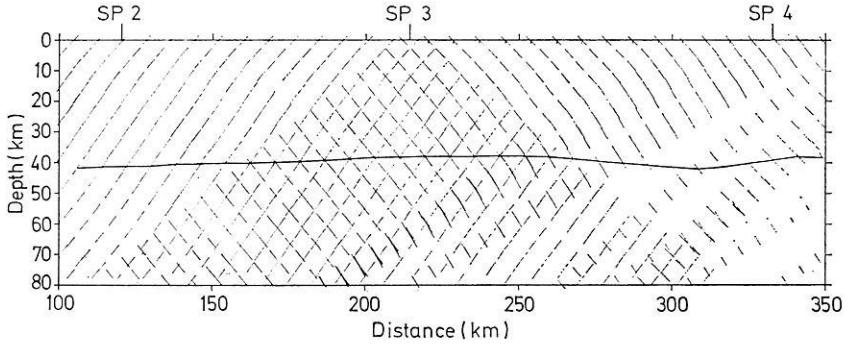

Fig. 10. Computer plot of wave-front diagram and construction of the Moho between 150 and 260 km

single points, however, small differences of about one km occurred, because the depth data from the models are based on average travel time curves, neglecting dips and being accurate only at a certain distance from the shot point. Wave-front constructions, on the other hand, are most reliable for the area between 170 and 280 km where a reversed coverage was achieved. The true upper mantle velocity obtained here is 8.15 ± 0.02 km/s. Fig. 10 shows an example of wave-fronts and Moho depths in this area. In the other regions of the profile this velocity was used in fitting segments of length $\Delta s = V_n \Delta t$ between plotted wave-fronts. Assuming slightly different V_n-velocities in these areas, some small deviations in depth might arise. They are limited, however, by the model calculations mentioned above and by the small amount of scatter of available P_n-velocity values in Scandinavia.

The best wave-front construction of the Moho for the whole profile is presented in Fig. 11. This section also shows the mean topographic heights along the profile. Large crustal depths were found on the south-east slope of the Caledonian mountain system, the Moho being 42 km deep. Depths stay quite constant along the transition to the Baltic Shield in Sweden with a small anticline bringing the Moho to a depth of 37 km about 60 km north-west of the shore of the Gulf of Bothnia. Below the south-eastern part of the Gulf of Bothnia a maximum depth of 44 km is found.

Whereas depths and undulations of the Moho could accurately be mapped, those of other boundaries, inside the crust, could not be plotted with the same reliability. They have, however, been included as dashed lines in Fig. 11, in order to give a general idea of possible changes in seismic parameters at the indicated depth levels. General geological data are also plotted along the profile. No significant lateral changes of velocity or other physical parameters were detected.

Conclusions

The crust-mantle boundary appears as a smooth, unfaulted discontinuity, crossing various tectonic areas which seem to be welded together. Seismic models from shot points 1, 2, and 3 show no basic difference. The seismic structure of the crust and the crust-mantle boundary do not indicate isostatic compensation of the Caledonian mountains. Negative Bouguer anomalies in the mountain area, however,

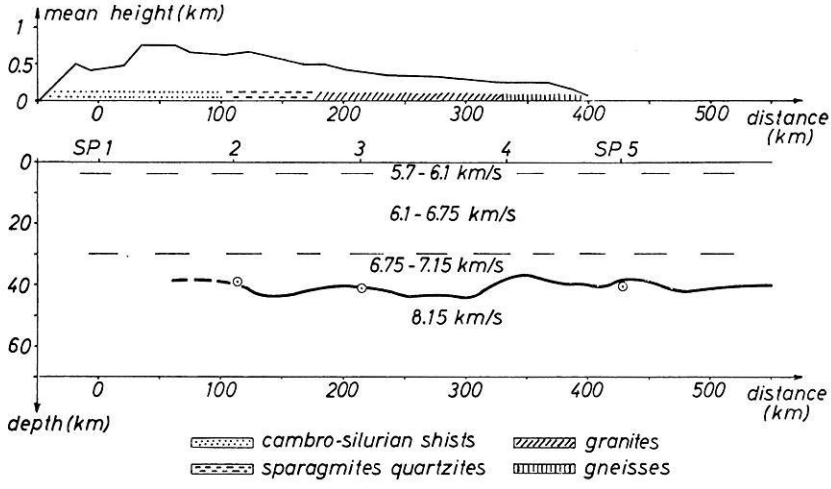

Fig. 11. Crustal cross-section along the profile Upper part: Topographic profile, exaggerated 1:60, with main geologic structures Lower part: Seismic boundaries, exaggerated 1:1,5, with velocity values in km/s

point to compensating mass deficiencies. It seems that the mass distribution in the asthenosphere contributes significantly to the isostatic compensation of the Caledonian mountain range.

There is no positive velocity gradient in the upper mantle. P_n-arrivals from various distances are exactly parallel. This means that, at least down to depths of 80 km, the same velocity and hence most probably the same density and material are found in the upper mantle[2]. A kind of Conrad discontinuity may be mapped by introducing a first order boundary in the north eastern part of the Gulf of Bothnia. Preference is given, however, to velocity-depth functions indicating a smooth transition zone in the crust between 20 and 25 km in depth, as shown in Fig. 9. No crustal low velocity layer is observed. Neither have continuous reflected waves P_m along the profile been found. Only some secondary arrivals have been detected consisting of supercritical reflections and diving waves. No subcritical reflections with $V_a > 8$ km/s have been found, which supports the idea of gradient zones instead of strong first order boundaries. This nearly complete absence of good P_M-arrivals in the Caledonides and the shield areas during these and previous investigations is hard to understand in view of the excellent signal to noise conditions. It is tentatively suggested that the reflection coefficient at the Moho must be rather small owing to i.) a concentration of grabboic and denser material in the lower crust, and/or ii.) and extended zone of small velocity gradients, similar to the model shown in Fig. 9, at the base of the crust, or/and iii.) low velocity zones and lamelles being absent in this area.

Only slight seismic evidence has been found for the nearly continuous uplift of the Fennoscandian Shield since the Palaeozoic. One indication is that sediments are

2 See footnote page 144.

missing. Another indication is the presence of rather high velocities, such as 6.6 to 6.8 km/sec, at comparatively shallow depths, around 20 km. Assuming the Moho as a chemical boundary, it seems probable that it, too, has been uplifted during the last 400 m.y., a process which apparently has not resulted in overthrusting or strong faulting, but only in gentle undulations. Apart from structures near the surface, the earth's crust along the profile seems to represent a uniform tectonic unit.

Acknowledgements. The "Blue Road" seismic experiments were mainly supported by the Swedish Natural Science Research Council and the Deutsche Forschungsgemeinschaft. Also funds from Norwegian and Finnish sources have been contributed to the project.

References

Båth, M.: Average crustal structure of Sweden. Pageoph. *88*, 75–91, 1971

Bundesanstalt für Bodenforschung and Unesco: Carte géologique internationale de l'Europe, Feuille C2 and D2, Hannover: Bundesanstalt für Bodenforschung 1966

Dahlmann, O.: On Scandinavian crustal travel times. FOA 4 report C 4295–23, April 1967

Haskell, N. A.: The motion of a viscous fluid under a surface load. Physics *6*, 265–269, 1935

Kanestrøm, R.: Seismic investigations of the crust and upper mantle in Norway. In: Deep seismic sounding in Northern Europe (A. Vogel, ed.), pp. 17–27. Stockholm: Swedish Natural Science Research Council 1971

Lundegård, P. H., Lundequist, J., Lindström, M.: Berg och Jord i Sverige, 2nd ed., Stockholm: Almqvist & Wiksell 1970

Meissner, R.: Wellenfrontverfahren für die Refraktionsseismik. Berichte des Instituts für Meteorologie und Geophysik der Universität Frankfurt/Main *9*, 1–81, 1965

Penttilä, E.: A report summarizing on the velocity of earth-quake waves and the structure of the Earth's crust in the Baltic Shield. Geophysica *10*, 11–23, 1969a

Penttilä, E.: On the influence of the structure of the Earth's crust and the ice age on isostatic equilibrium and land uplift in the Baltic Shield. Geophysica *10*, 24–34, 1969b

Penttilä, E.: Crustal structure in Fennoscandia from seismological and gravimetric observations. Annales Adadémiae Scientiarum Fennicae, Series A, III. Geologica-Geographica, Nr. 110 Helsinki: Suomalainen Tiedeakatemia 1972

Sellevoll, M. A., Pomeroy, P.: A travel time study for Fennoscandia. Årbok for Universitetet i Bergen, Mat.-Naturv. Serie *9*, 1–29, 1968

Vogel, A., Lund, C.-E.: The Trans-Scandinavian seismic profile of 1969, profile section 2–3. In: Deep seismic sounding in Northern Europe (A. Vogel, ed.), pp. 62–75. Stockholm: Swedish Natural Science Research Council 1971

Welin, E.: The absolute time scale and the classification of precambrian rocks in Sweden. Geol. Fören. Stockholm Förh. *88*, 29–33, 1966

Welin, E.: Den Svekofenniska orogena zonen. Geol. Fören. Stockholm Förh. *92*, 433–451, 1970

Dipl.-Geophys. H. B. Hirschleber
Institut für Geophysik
D-2000 Hamburg 13
Binderstr. 22
Federal Republic of Germany

C.-E. Lund, Fil. Lic.
Department of Solid Earth Physics
Vasagatan 1A
S-751 22 Uppsala, Sweden

Prof. Dr. R. Meissner
Dipl.-Geophys. W. Weinrebe
Institut für Geophysik
D-2300 Kiel
Olshausenstr. 40–60, Neue Universität
Federal Republic of Germany

Prof. Dr. A. Vogel
Institut für Geophysikalische Wissenschaften
D-1000 Berlin 33
Rheinbabenallee 49

J. Geophys. 41, 149–172, 1975

Computations of *SV* Waves in Realistic Earth Models*

R. Kind and G. Müller

Geophysical Institute, University of Karlsruhe

Received October 14, 1974

Abstract. The reflectivity method for the calculation of theoretical body-wave seismograms is extended to include a double-couple point source. Theoretical seismograms of *SV* waves from this type of source are presented for models of the earth's crust and the crust-mantle boundary, and for models of the whole earth. In the models of the crust-mantle boundary, there are up to four *SV* head waves, depending on the sharpness of the transition. The most remarkable one is slightly slower and later than S_n and has unusually low frequencies. Theoretical *SV*-wave seismograms for models of the whole earth for periods from 15 s to 60 s and in the epicentral distance range from 10° to 160° show as prominent phases *S*, *ScS*, *SKS* and *SKKS*. *SKS* and *SKKS* are different in wave form, in agreement with observations from long-period *WWNSS* stations. A diffracted wave $SP_{diff}KS + SKP_{diff}S$ is found in the theoretical seismograms whose travel-time curve is tangential to that of *SKS* at a distance of 107°. The resulting interference causes the wave form of *SKS* to change markedly around 120°. Since the theoretical seismograms are the complete response of the earth models from the crust-mantle boundary down to the inner core, they also include many multiple and converted phases. Besides those associated with the crust-mantle boundary there are phases related to the transition zones in the upper mantle. Their amplitudes depend strongly on the sharpness of these zones.

Key words: Theoretical Seismograms — Wave Theory — Earth Structure.

Introduction

The interest of seismologists in seismic body waves seems to have increased during the last years not only due to the new possibilities that are offered by arrays but also because methods are now available to investigate, with conventional stations, the *dynamic* properties of these waves. Seismologists have always expressed the view that these properties, i.e. amplitude and wave form, contain information about the wave velocities and density within the earth which supplements and in some important cases *exceeds* the information from the kinematic properties, i.e. travel times and ray parameters. Only recently, however, methods for body wave computations in earth models with arbitrary depth dependence of velocities and density have been developed to the stage of allowing their more or less routine application to observations. High quality data, i.e records from well-calibrated, identical stations with sufficiently close spacing, are a basic condition for quantitative interpretations. They are now routinely obtained in explosion seismological experiments like that described by Hirn *et al.* (1973) and Kind (1974). In earthquake seismology, such data are available since about 10 years from the Worldwide Network of Standardized Seismographs (WWNSS) and from the Canadian Seismic Network (CSN).

---

* Contribution No. 117, Geophysical Institute, University of Karlsruhe.

We consider the *long-period* records from the approximately 150 stations of these two networks as an especially abundant source of information about the elastic and also anelastic properties of the earth. Up to now, only a few quantitative interpretations of long-period data have been published. Examples are papers by Mitchell and Helmberger (1973) on the *SH* components of *S* and *ScS*, by Müller (1973a) on *PKP*, and by Helmberger and Engen (1974) on the *SH* component of *S* travelling through the upper mantle. Our present work is mainly directed towards an investigation of the core-mantle boundary using the *SV* component of *ScS* together with *SKS* and *SKKS*. Our calculations of theoretical *SV*-wave seismograms for both simple and realistic models gave a number of interesting results which are compiled in this paper. Data analysis and interpretation in terms of earth structure are under way and will be published separately.

Two different methods are presently being used for the calculation of theoretical seismograms for point sources in vertically inhomogeneous half spaces or spheres, generalized ray theory and the reflectivity method. By now, generalized ray theory is relatively well known and used by various authors. The same is not yet true for the reflectivity method which was introduced by Fuchs (1968b) and developed further by Fuchs and Müller (1971). However, this method deserves wider distribution since it is more exact than generalized ray theory in that it includes *all* wave types in the reflecting medium–primary reflections, multiple reflections and converted waves. By contrast, when using generalized ray theory one normally has to restrict the calculation to primary reflections. Multiples and conversions can be included only in special cases. For instance, it would be quite hard to calculate theoretical seismograms for *SKKS* or *SKKKS* with generalized ray theory whereas these phases are automatically included in computations with the reflectivity method, as can be seen later in this paper.

Both generalized ray theory and the reflectivity method are methods for layered half spaces. In computations for spherical earth models, an earth flattening approximation (EFA) is usually applied beforehand. There are derivations of the EFA from a comparison of both geometric ray theory (Müller, 1971, 1973b) and wave theory (Hill, 1972; Chapman, 1973) for a sphere and a half space. Both approaches give almost the same results for the transformation of the sphere into a half space, but it seems that the simple approach, based on geometric ray theory, gives a more complete EFA since it also includes the possibility that the point source and the receiver are at different depths. The range of applicability of the EFA has been discussed by Müller (1973b) with the aid of a numerical experiment and found to include waves with periods of up to 30 s, propagating as deep as several hundred kilometers below the boundary of the inner core. The similarity of observed and theoretical seismograms for core phases in Müller (1973a) is in itself a qualitative proof that the EFA has a wide range of applications. Buchbinder (1974) recently noted this similarity in the case of the diffraction at the caustic of *PKP* which produces a very low frequent and dispersed precursor to *PKIKP* in long-period records. Another example is given in Fig. 18 of the present paper for *SKS* and *SKKS*. In this case, the theoretical seismogram shows the same difference in pulse form between the two phases as the observed records.

The following section gives a brief account of the reflectivity method for a double-couple point source in a layered half space. The introduction of this source type is

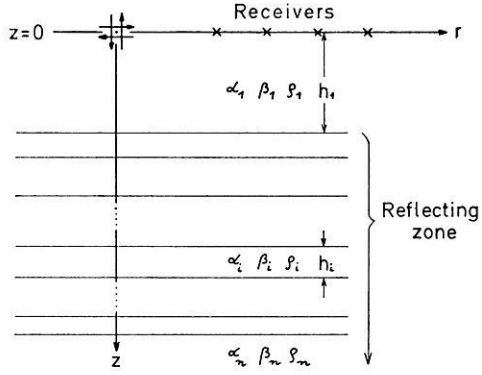

Fig. 1. Double-couple point source with special orientation in a layered medium

necessary, since the final aim of our work is the investigation of waves from earthquakes. Details of the derivation and formulas are given in the appendices A and B. First examples of theoretical SV-wave seismograms for two half spaces, separated by a first-order discontinuity or a transition zone, are then discussed. The system of head waves in these models is particularly interesting from a theoretical point of view. A seismogram section is also given for a realistic model of the earth's crust, derived from recent refraction experiments. The main part of this paper gives results for the propagation of SV waves in different models of the whole earth. One P-wave seismogram section is also included. The SV sections show, besides the main body-wave phases S, ScS, SKS and $SKKS$, a surprising number of additional, mostly weaker, phases. Most of them are multiples and converted wave types which are produced at discontinuities and transition zones of the models; one is a wave, diffracted at the earth's core and related to SKS. The identification of these phases was mainly made with the aid of their travel times. The investigation of these minor phases is necessary for our work on the main SV phases, since there may be interference. Some of these phases may also be of interest in the study of the fine structure of the earth's mantle.

Basic Formulas

Fig. 1. shows the geometry of the double-couple point source and the layered medium that is assumed in all calculations of this paper. This is a special and simple case of the more general geometry treated in Appendix A. The model consists of a reflecting zone below a homogeneous half space. The half space contains source and receivers and is characterized by the P velocity α_1, the S velocity β_1 and the density ϱ_1. The distance of source and receivers from the reflecting zone is h_1. The reflecting zone consists of n-2 layers and a half space; n is the total number of different media. The force system of the double couple is located in a vertical plane, and the receivers are assumed to lie in this plane along a horizontal profile through the source. As Fig. 2 shows, the SV radiation of the double couple is maximum along the z-axis whereas the P radiation vanishes in this direction. There is no SH motion at the receivers, and SV and P waves are polarized in the vertical plane through the receivers.

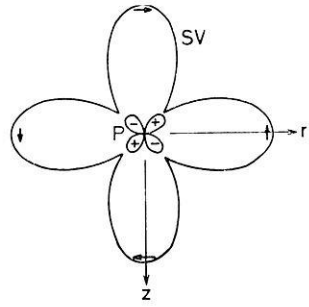

Fig. 2. Far-field radiation characteristics of the double couple in the vertical plane, containing the receivers. The SV motion is transversal, the P motion longitudinal. It has been assumed that the velocity ratio α_1/β_1 is $\sqrt{3}$

This is true for both the direct waves and the reflections from the reflecting zone. The usual description of the time dependence of a double couple is by the moment function $M(t)$. In the far field, all displacements of the direct waves have the form of the derivative $M'(t)$.

If $\bar{M}(\omega)$ ($\omega =$ circular frequency) is the Fourier transform of $M(t)$, then the Fourier transform of the horizontal and vertical displacements of the reflected SV wave at the reveivers, due to the incident SV wave, are (see Appendix A):

$$\bar{u}_r = -\frac{\omega^2 \bar{M}(\omega)}{4\pi\varrho_1\beta_1^4} \int_{\gamma_1}^{\gamma_2} (2\sin^2\gamma - 1)\sin\gamma\cos\gamma\, R_{ss}(\omega,\gamma)\, J_0\left(\frac{\omega r}{\beta_1}\sin\gamma\right) \exp\left(-i\frac{2b_1\omega}{\beta_1}\cos\gamma\right) d\gamma \tag{1}$$

$$\bar{u}_z = \frac{i\omega^2 \bar{M}(\omega)}{4\pi\varrho_1\beta_1^4} \int_{\gamma_1}^{\gamma_2} (2\sin^2\gamma - 1)\sin^2\gamma R_{ss}(\omega,\gamma)\, J_1\left(\frac{\omega r}{\beta_1}\sin\gamma\right) \exp\left(-i\frac{2b_1\omega}{\beta_1}\cos\gamma\right) d\gamma \tag{2}$$

In the following, these displacements are called the SS response of the medium. Analogously, the PP response is:

$$\bar{u}_r = -\frac{\omega^2 \bar{M}(\omega)}{2\pi\varrho_1\alpha_1^4} \int_{\gamma_1}^{\gamma_2} \sin^3\gamma\cos\gamma\, R_{pp}(\omega,\gamma)\, J_0\left(\frac{\omega r}{\alpha_1}\sin\gamma\right) \exp\left(-i\frac{2b_1\omega}{\alpha_1}\cos\gamma\right) d\gamma \tag{3}$$

$$\bar{u}_z = -\frac{i\omega^2 \bar{M}(\omega)}{2\pi\varrho_1\alpha_1^4} \int_{\gamma_1}^{\gamma_2} \sin^2\gamma\cos^2\gamma\, R_{pp}(\omega_1\gamma)\, J_1\left(\frac{\omega r}{\alpha_1}\sin\gamma\right) \exp\left(-i\frac{2b_1\omega}{\alpha_1}\cos\gamma\right) d\gamma \tag{4}$$

In these expressions, i is the imaginary unit, γ is the real angle of incidence at the top of the reflecting zone, γ_1 and γ_2 are the limits of γ and are chosen according to the waves of interest. $R_{ss}(\omega,\gamma)$ and $R_{pp}(\omega,\gamma)$ are the plane-wave reflection coefficients (or reflectivities) of the reflecting zone which normally depend both on ω and γ. Some explanations, concerning the calculation of $R_{ss}(\omega,\gamma)$, are given in Appendix B. J_0 and J_1 are Bessel functions of the first kind. Details of the calculation of theoretical seismograms with the aid of formulas such as (1) through (4) have been given by Fuchs and Müller (1971).

For the calculations of this paper, the following assumption has been made about the spectrum of the double-couple moment function:

$$\bar{M}(\omega) = \frac{1}{2}\left(1 + \cos\frac{\pi\omega}{\omega_0}\right), \quad -\omega_0 \leq \omega \leq \omega_0$$

ω_0 is the (circular) cutoff frequency. $M'(t)$, the derivative of the moment function, is approximately one sine period with duration $T \approx 15/\omega_0$. This pulse, and therefore also the direct wave from the double couple, are acausal, i.e., they are nonzero for negative times. The essential acausality can be removed by a shift to greater times by $T/2$. This time shift is applied to all theoretical seismograms.

Theoretical Seismograms for SV Waves in Crustal Models

In this section, theoretical seismograms for a few models of the earth's crust will be presented.

Figs. 3 and 4 show plots of the horizontal displacement component of the SS response of a 30 km thick homogeneous crust, overlying a homogeneous mantle. The crust-mantle boundary (Moho) is a first-order discontinuity. The free surface is not included in the model, neither at the source nor at the receiver. The main frequency of the input signal is 7 Hz. The main phase in Fig. 3 is the reflection from the Moho. The same seismograms as in Fig. 3 are plotted in Fig. 4 on a ten times larger amplitude scale. Now, three weak head waves are visible in addition to the Moho reflection, one with the P velocity of the mantle, one with the P velocity of the crust, and one with the S velocity of the mantle, the last type-being the S_n wave of our model. The head wave $S_1P_2S_1$ originates from S-P and P-S conversions at the Moho and is expected to exist. A head wave of the type $S_1P_1S_1$, travelling with the P velocity of the crust, is less familiar although not unexpected (cf. Fig. 2–13 of Ewing *et al.*, 1957). Another pecularity is the shape of the S_n wave. The short period onset of this wave is followed by a signal with much larger period. It is not clear whether this is a second arrival or due to dispersion of the S_n wave. Professor F. Gilbert has drawn our attention to the possibility that this long-period signal is due to a pseudo-Rayleigh wave at the top of the lower half space, which radiates S body waves to the surface. (Roever *et al.*, 1959; Gilbert and Laster, 1962). This suggestion is supported by the fact that the phase velocity of this signal is slightly less than the velocity of the S_n arrival.

In Fig. 5, the first-order discontinuity in the models of Figs. 3 and 4 is replaced by a 1 km thick transition zone. Now, the onset of S_n has larger amplitudes than in Fig. 4, and the long-period later arrival is reduced in amplitude. This shows that this feature of the S_n wave depends on the thickness of the transition zone. Up to now,

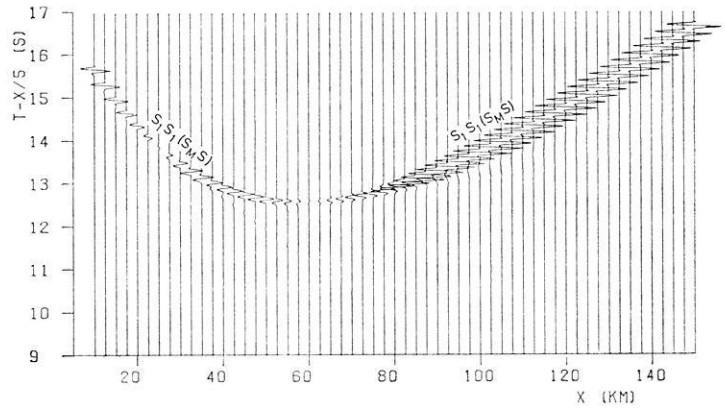

Fig. 3. Theoretical SV-wave seismograms for a model, consisting of two homogeneous half spaces. The properties of the two media roughly correspond to average velocities and densities of crustal and upper mantle material, respectively ($\alpha_1 = 6.0$ km/s, $\beta_1 = 3.46$ km/s, $\varrho_1 = 2.53$ g/cm^3, $\alpha_2 = 8.0$ km/s, $\beta_2 = 4.62$ km/s, $\varrho_2 = 3.28$ g/cm^3). The double-couple point source and the receivers are located 30 km above the interface between the two media (Moho). The duration of the source signal is 0.15 s. The seismograms are shown on a reduced time scale and correspond to the horizontal displacement in profile direction which is of SV type alone. On the amplitude scale used, the Moho reflection S_1S_1 (in usual nomenclature S_MS) is practically the only arrival that is visible. The amplitudes in Figs. 3–7 should be divided by $\sqrt{x}$ in order to obtain the true amplitudes

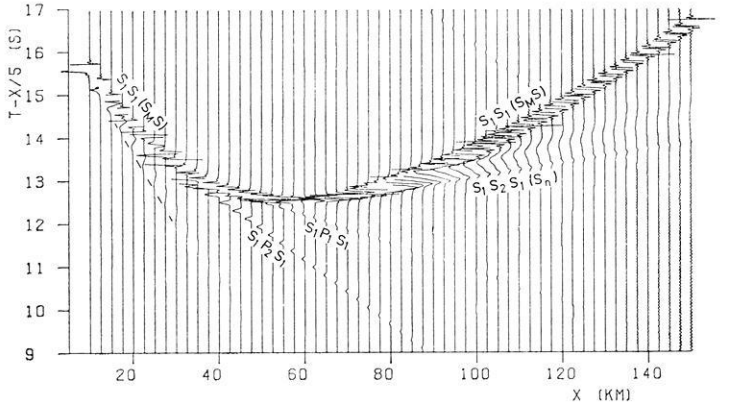

Fig. 4. The same as Fig. 3, but with a tenfold increase in amplitude scale. The amplitudes of the Moho reflection are clipped. Now, three head waves are visible, travelling, respectively, with the P and the S velocity of the lower half space ($S_1P_2S_1$, $S_1S_2S_1$ or S_n) and with the P velocity of the upper half space ($S_1P_1S_1$). The long-period arrival between S_n and S_MS is probably due to a pseudo-Rayleigh wave at the top of the lower half space. The arrival marked by the dashed line is a purely numerical effect and travels with the highest phase velocity that is used in the seismogram calculation. Arrivals of this sort are also visible in other seismogram sections of this paper, and they travel with either the highest or the lowest phase velocity

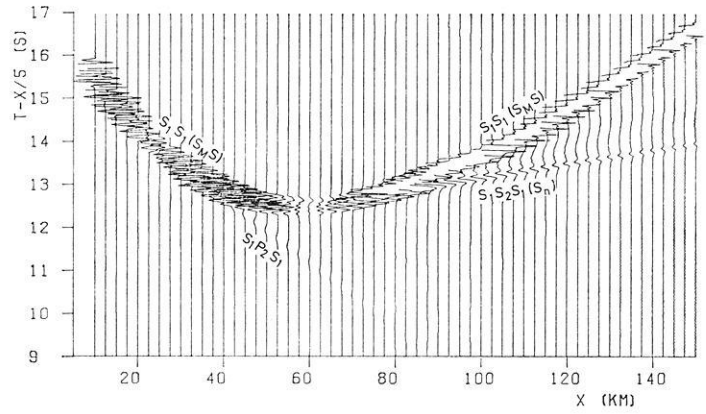

Fig. 5. The same as Fig. 4 for a transition zone with thickness 1 km between the two half spaces. The transition zone is approximated by 4 thin homogeneous layers. The corresponding fine structure determines the Moho reflection for distances up to about 80 km. Beyond, the seismograms resemble those for a linear transition zone

this long-period tail of S_n has, to our knowledge, not yet been found in observations. The head wave $S_1P_1S_1$ has disappeared in Fig. 5, indicating that this wave is also closely connected to the sharpness of the crust-mantle transition. The head wave $S_1P_2S_1$ is reduced in amplitude and has longer periods. This shows that only those long-period parts of the signal are converted into P waves at the transition zone, for which this zone is still close to a first-order discontinuity.

In Figs. 6 and 7, theoretical S-wave seismograms for a realistic crustal model of the Rhinegraben area are plotted. The P-velocity model is taken from Edel *et al.* (1974), and the S-velocity distribution has the same form. The most prominent phases in Fig. 6 are the reflection S_MS from the broad crust-mantle transition zone and the head wave S_n. S_n is not followed by a long-period signal. This emphasizes that in fact this peculiarity of S_n is closely related to the sharpness of the crust-mantle transition. At later times and larger distances, there is a multiple reflection between the crust-mantle transition and the top of the basement. A relatively strong phase, ${}^sP_M\,P^s$, appears at earlier times and with higher apparent velocity. This is a wave which travels in the sedimentary layer as an S wave, is then converted at the top of the basement into a P wave which is reflected at the crust-mantle transition zone and converted back into an S wave at the top of the basement. (The occurrence of this wavetype is due to the use of the SS reflection coefficient. If, for example, the SP reflection coefficient would be used in order to calculate the SP response of the model, an even stronger phase ${}^sP_M\,P^p$ would be observed.) The same seismograms as in Fig. 6 are plotted in Fig. 7 on a ten times larger amplitude scale. Many more weak multiples and converted phases are now visible. This figure emphasizes the real power of the reflectivity method in that the *complete* response of the model is obtained. In this respect, the reflectivity method is superior to ray-theoretical methods, based on generalized ray theory, where it is not always easy to know which multiples and converted waves should be taken into account. Computed sections like the one in Fig. 7 sometimes pose difficult problems with regard to the interpretation of

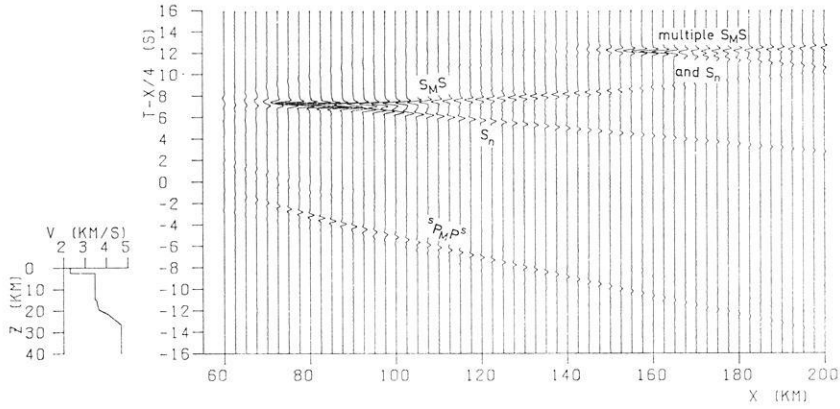

Fig. 6. Theoretical SV-wave seismograms for a realistic crustal model. The S-velocity distribution is shown on the left. The seismograms are the complete S response from the structure below the sedimentary layer due to the S wave from the double-couple point source. The gradient zones are approximated by homogeneous layers whose thickness is about 1 km. The duration of the source signal is 0.3 s. The main phases are described in the text

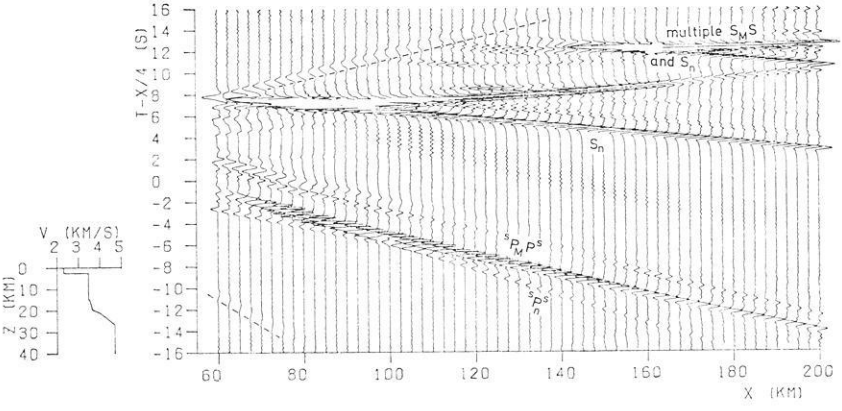

Fig. 7. The same as Fig. 6, but with a tenfold increase in amplitude scale. The amplitudes of the most prominent phases are clipped. Many weak phases due to multiples and conversions in the reflecting zone below the sedimentary layer are now visible. The arrivals along the dashed lines are numerical effects. They are explained in the caption of Fig. 4

multiple and converted waves. We have not studied this question for the section of Fig. 7. The problem will, however, be discussed in greater detail in the next section for models of the whole earth.

Our results for S_n in different models suggest a simple and perhaps useful way of investigating the thickness of the crust-mantle transition in the real earth. Comparative studies of the frequency content of P_n and S_n from near earthquakes with foci in the crust or from explosions could be made, and if substantially more low frequencies are found in S_n than in P_n (after correction for the influence of attenuation), then this would point to a relatively sharp transition. If, on the other hand, no essential

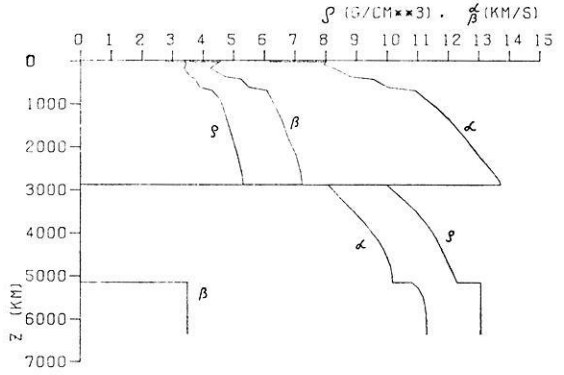

Fig. 8. Earth model A that is used in most calculations of this paper ($\alpha = P$-wave velocity, $\beta = S$-wave velocity, $\varrho =$ density)

difference in frequency content is found, then, according to our preliminary calculations, the transition should be thicker than roughly the S wavelength, corresponding to the main frequency of the source pulse. This method could supplement the more obvious method of investigating the Moho reflection P_MP around the critical point in refraction data.

Theoretical Seismograms for Realistic Earth Models

In this section, synthetic seismograms for P and SV phases in realistic earth models will be discussed. The model that is mainly used is based on several recent seismological investigations of the earth's mantle and core (Johnson, 1969; Buchbinder, 1971; Dziewonski and Gilbert, 1971; Press, 1972; Müller, 1973a; Qamar, 1973; Wiggins *et al.*, 1973). This model, called model A in the following, is listed in Table 1 along with a modified version wherein the upper mantle is replaced by the smoother Jeffreys-Bullen upper mantle (Bullen, 1963). Model A is also plotted in Fig. 8. In some cases, the calculations have been performed for models without a crust, i.e., the upper mantle material extends to the earth's surface. Table 2 contains information about all models investigated. The layer thickness given there is the thickness of the homogeneous layers by which the inhomogeneous earth model is approximated. The ratio of S wavelength to layer thickness varies, in the lower mantle, from about 2 to about 7. The appropriate ratio for modelling an inhomogeneous structure depends on the wave type under investigation and has to be determined by numerical experiments.

The double-couple point source is oriented as in Fig. 1. For rays propagating towards the lower mantle and the core, its SV radiation is approximately independent of the radiation angle (see Fig. 2). The P radiation, however, depends strongly on this angle since one of the two nodal planes for P is vertical. Different values of the main period of the source pulse have been used, as given in Table 2. Source and receivers are located at the same level, corresponding to the earth's surface. The influence of the surface is, however, not taken into account, neither at the source nor at the receivers.

Table 1. Velocity-density distribution

Depth (km)	P velocity (km/s)	S velocity (km/s)	Density (g/cm^3)
(a) Earth model A			
0	6.20	3.58	2.80
33	6.20	3.58	2.80
33	8.05	4.60	3.45
100	7.95	4.40	3.45
200	8.32	4.25	3.40
380	8.83	4.75	3.60
430	9.56	5.25	3.75
620	10.04	5.50	3.90
700	10.94	6.10	4.30
900	11.29	6.25	4.57
1100	11.64	6.38	4.67
1400	12.07	6.60	4.80
1800	12.56	6.78	4.97
2200	12.99	7.05	5.14
2600	13.48	7.20	5.27
2800	13.69	7.24	5.32
2890	13.73	7.25	5.32
2890	8.10	0	10.00
3200	8.50	0	10.50
3500	8.92	0	10.95
3800	9.31	0	11.30
4000	9.52	0	11.50
4200	9.74	0	11.66
4400	9.91	0	11.80
4600	10.03	0	11.93
4800	10.14	0	12.07
5000	10.19	0	12.21
5162	10.20	0	12.30
5162	10.83	3.50	13.08
5300	11.05	3.50	13.08
5500	11.20	3.50	13.08
5700	11.26	3.50	13.08
5900	11.30	3.50	13.08
6100	11.31	3.50	13.08
6300	11.32	3.50	13.08
6371	11.32	3.50	13.08
(b) Jeffreys Bullen upper mantle			
0	6.20	3.58	2.80
33	6.20	3.58	2.80
33	7.76	4.36	3.32
413	8.97	4.96	3.64
600	10.25	5.66	4.13
800	11.00	6.13	4.49
900	11.29	6.25	4.57

Table 2. Earth models, parameters and computing times

Fig. No.	Earth model	Average layer thickness in km	Main period of source signal in s	Computing time on a UNIVAC 1108
9	model A	100	54	4 h 23 min
10	model A	100	54	2 h 06 min
11	model A	100	30	4 h 04 min
12	model A with JB upper mantle	100	54	2 h 06 min
13 and 14	model A without crust	50	54	6 h 59 min
15	model A with JB upper mantle, without crust	50	17	2 h 12 min

The theoretical record sections in Fig. 9, and Figs. 11 through 15, show the horizontal displacement component in profile direction for the SS response of the earth models. Fig. 10 is a display of the vertical displacement component of the PP response. These record sections will be described in some detail in the following. The main point of the discussion will be that besides the main body wave phases such as S, ScS, SKS, $SKKS$, P, PKP etc. many additional phases are visible. We have been able to identify most of them, and even with regard to the unidentified phases we are sure that they correspond to a physical wave path. Some of these phases may possibly help to determine earth structure in certain depth ranges, provided that they are observed, but most of them only contribute to the background noise for the main phases. Figs. 16 and 17 are schematic diagrams of some of the ray paths associated with the arrivals in the theoretical record sections.

The most energetic phases in Fig. 9 are S and ScS at shorter epicentral distances, and SKS and $SKKS$ at larger distances. Many additional phases may be detected in this section. They arrive earlier or later than the main phases, and in most cases they have less energy. These phases are due to multiple reflections and converted wave types at various discontinuities and transition zones of the model. The crust-mantle boundary (Moho) and the core-mantle boundary are the two major discontinuities of the model. One multiple between these boundaries may be recognized. It is marked $ScSmScS$. The letter m stands for reflection at the Moho and was introduced to distinguish this phase from the multiple at the free surface, $ScSScS$, which would arrive a few seconds later with larger amplitudes. $ScSScS$ does not appear in the seismograms since in the present version of our computer program there is no possibility to include reflectors above the source. Similarly, a phase SmS is seen in the synthetic seismograms with travel times close to those of SS. Phases arriving earlier than S and SKS and phases arriving between $SKKS$ and SmS will be discussed later in connection with Fig. 11.

The prominent phases in the P-wave seismogram section of Fig. 10 are P, P_{diff} and PKP. PcP has very small amplitudes at short distances and is therefore difficult to detect on the amplitude scale used. At larger distances, it interferes with other

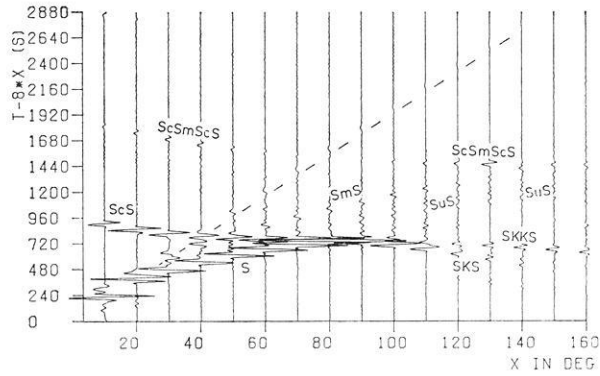

Fig. 9. *SS* response of model A (horizontal displacement in profile direction). The main period of the source pulse is 54 s. For an explanation of the various phases, see the text and Figs. 16 and 17. The arrival along the dashed line is a numerical effect and is explained in the caption of Fig. 4. The amplitudes in Figs. 9–15 should be divided by $\sqrt{\sin x}$ in order to obtain the true amplitudes

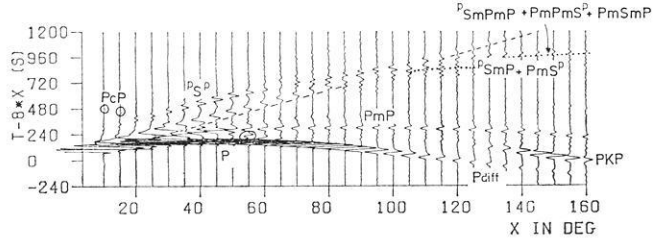

Fig. 10. *PP* response of model A (vertical displacement). The main period of the source pulse is 54 s. The encircled arrival in the seismogram at 55° is *PcP*. After division by 4, the amplitudes are on the same scale as the *S*-wave amplitudes in Fig. 9

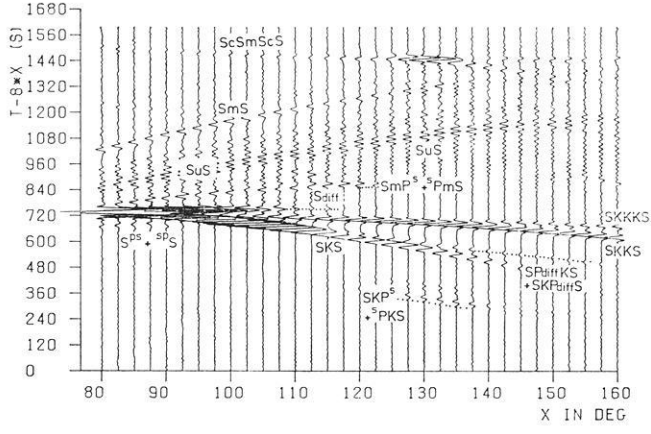

Fig. 11. *SS* response of model A for a source pulse with main period 30 s (horizontal displacement in profile direction)

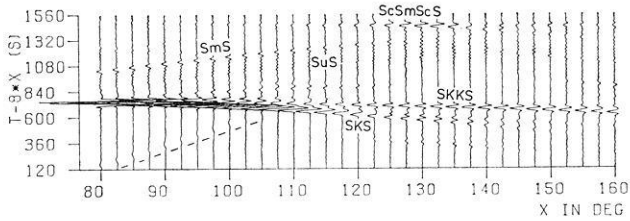

Fig. 12. *SS* response of model A with a smooth upper mantle, corresponding to the Jeffreys-Bullen earth model. The source pulse has a length of 54 s. *SuS* is much weaker than in Fig. 11 where model A has been used throughout

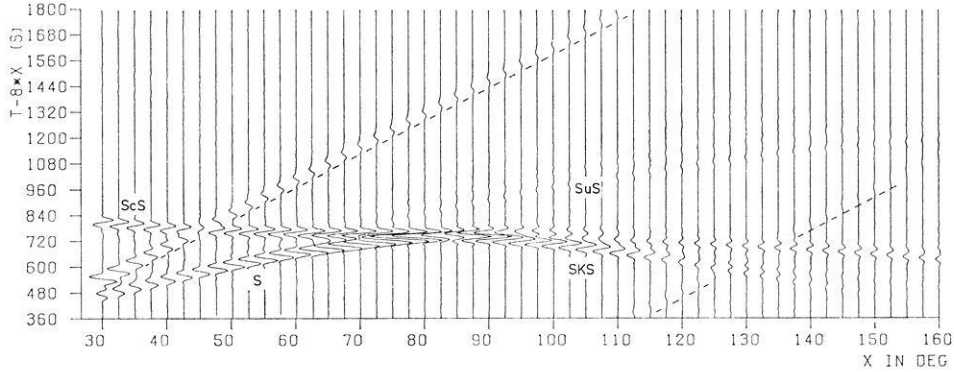

Fig. 13. *SS* response of model A with the crust removed. The average layer thickness is 50 km, and the source-pulse length is 54 s. Since the model has no Moho, multiples such as *SmS* and *ScSmScS* are missing. Because of the small layer thickness, compared to the wavelength, *SuS* is a good approximation of the true pulse

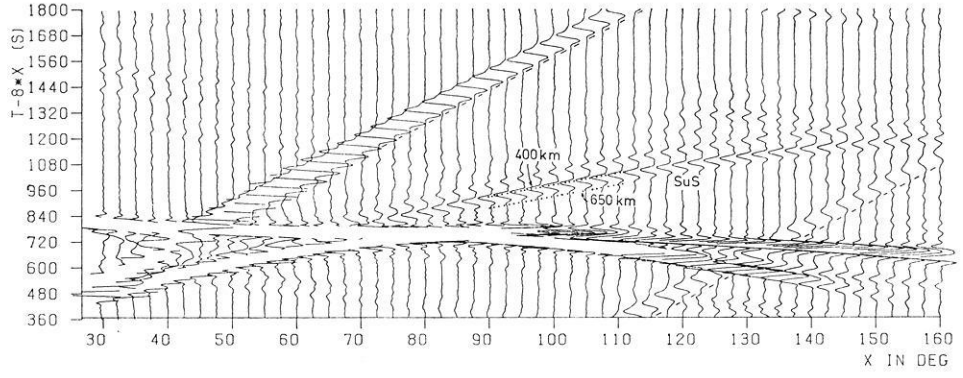

Fig. 14. The same as Fig. 13, but on a ten times larger amplitude scale. The two dotted lines approximately give the theoretical travel times of the *SuS* contribution from the 400 km and the 650 km transition zone. respectively. They are based on the Jeffreys-Bullen travel time tables for *S* waves from deep-focus earthquakes. The shift of some arrivals from the end of the seismograms to the beginning and vice versa beyond 110° is due to aliasing in the time domain

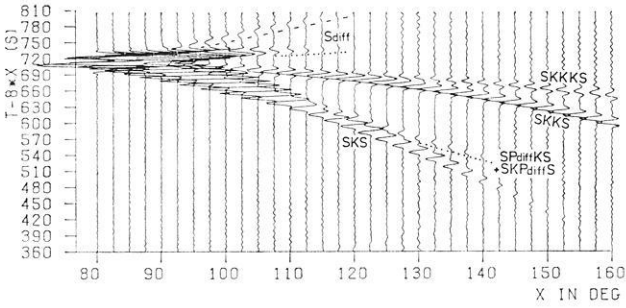

Fig. 15. *SS* response of model A with a smooth upper mantle and no crust, including mainly *SKS*, *SKKS* and *SKKKS*, for a relatively short duration of the source pulse, namely 17 s. The forms of *SKS*, *SKKS* and *SKKKS* are quite different. The causes are discussed in the text

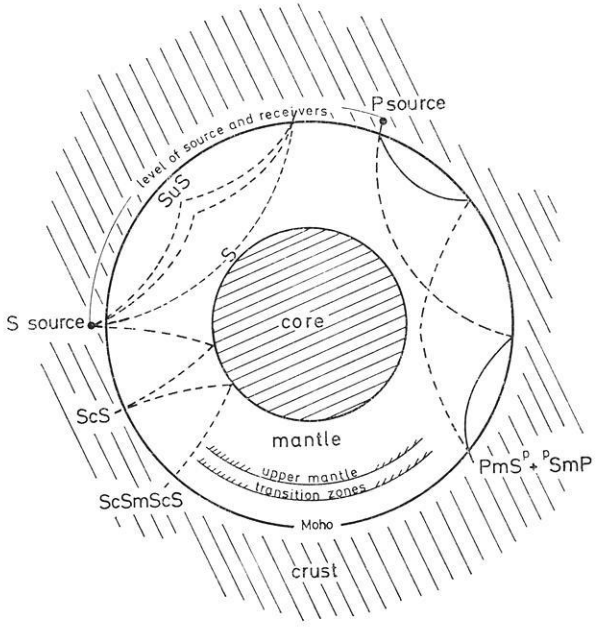

Fig. 16. Ray-path diagrams of some of the phases, appearing in Figs. 9 through 15. *S*-wave segments are dashed, *P*-wave segments are full lines

arrivals except at 55° where it is clearly visible. *PmP*, which is analogous to *SmS* in Fig. 9, can be recognized instead of *PP*. Another wave train at later times and with lower apparent velocity can be seen. This wave train consists of various converted and multiple wave types such as ^{p}SS, ^{p}SmP, PmS^{p}, $^{p}SmPmP$, $PmPmS^{p}$ and *PmSmP*. The superscript p stands for a wave travelling in the crust as a *P* wave with conversion into or from *S* at the Moho. These waves are close in travel time, but not in amplitude, to *S*, *SP*, *PS*, *SPP*, *PPS* and *PSP*, respectively. Examples of these phases are illustrated in the ray-path diagram of Fig. 16.

Fig. 11 shows an *SV*-wave seismogram section for model A and for a source pulse with duration 30 s. This duration is shorter than that used in the calculation

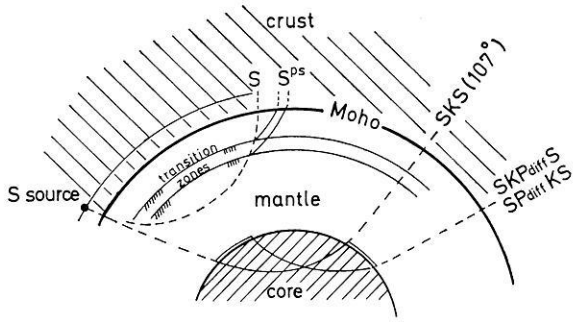

Fig. 17. Some more ray paths

for Fig. 9 and thus gives a better time resolution. In addition, the receiver spacing has been decreased which makes it easier to follow phases. The phases $SmP^s + {}^sPmS$ and $SKP^s + {}^sPKS$ arrive close to the onset times of $SP + PS$ and $SKP + PKS$, respectively, but have different amplitudes. The superscript s denotes a crustal S-wave segment of the ray either before or after conversion at the Moho. In addition to these phases, a very quickly decaying S_{diff}, and $SKKKS$ are visible in Fig. 11. The influence of the structure in the upper mantle also becomes very obvious. Most of the energy between S, S_{diff} and $SmP^s + {}^sPmS$ on the one hand and SmS on the other is due to reflections from the transition zones in the upper mantle. These phases are called SuS in Fig. 11, and their rays are illustrated in Fig. 16. The ringing character of SuS is explained by the fact that the average layer thickness in the mantle of model A is, for these phases, not small enough relative to the dominant wavelength of the signal. Thus, SuS does not correspond to the inhomogeneous model A, but only to its approximation by discrete layers. However, the large amplitude wave group in the middle of the ringing wave train which corresponds to reflections from the two transition zones centered around depths of 400 km and 650 km, respectively, indicates that SuS for the inhomogeneous model is not negligibly small. This will later be confirmed in connection with Figs. 13 and 14. The transition zones in the upper mantle cause further phases. For example, forerunners to S between 80° and 90° epicentral distance are due to the conversion of portions of the energy of S into P waves at these transition zones. These forerunners travel through the crust as S waves once more, since only S waves in the crust are included in the calculations. They may therefore be called S^{ps}, and forerunners of the type ${}^{sp}S$ are likewise included. The ray path of S^{ps} is illustrated in Fig. 17. Similarly, the arrivals about 50 s after $SKP^s + {}^sPKS$ are caused by the conversion of P waves into S waves and vice versa at the upper mantle transition zones. However, perhaps the most interesting aspect of Fig. 11 is the phase labelled $SP_{diff}KS + SKP_{diff}S$ which has, to our knowledge, not yet been reported from observations. The two ray paths of this phase are shown in Fig. 17. Both of them include a P-wave portion diffracted along the core-mantle boundary. The travel-time curve of this phase is a straight line with the slope of P_{diff} and tangential to the travel-time curve of SKS at a distance of 107°. This diffracted wave produces strong pulse deformations of SKS in the distance range around 120° where it separates from SKS.

Figs. 12 to 14 show further investigations of *SuS*. The model used for Fig. 12 has a smooth upper mantle with Jeffreys' velocity distributions and Bullen's density distribution A (Bullen, 1963). As shown in Table 2, the average layer thickness is the same as that used for Fig. 11, but the dominant period of the source pulse, 54 s, is almost twice the value for that figure. Because of the greater wavelength to layer thickness ratio the ringing character of *SuS* is reduced, but its generally smaller amplitudes are mainly due to the smoothness of the upper mantle model used. In order to determine *SuS* correctly for model A, a calculation with an average layer thickness of 50 km was performed (Figs. 13 and 14). For a source pulse with main period 54 s this is, in the transition region of the upper mantle, about one sixth of the *S* wavelength. Ringing has now disappeared, and *SuS* is close to the true reflection from the upper mantle transition zones, i.e., further reduction of the layer thickness would not change it essentially. At epicentral distances up to 110°, *SuS* consists mainly of the reflections from the two transition zones at depths of 400 and 650 km. At larger distances, there are some more oscillations in *SuS* which are reflections from the depth range of the pronounced low-velocity zone in the *S*-velocity distribution (see Fig. 8).

An interesting feature of the phases *SKS*, *SKKS* and *SKKKS* is their strong difference in wave form. This is especially evident from Fig. 15 where the shortest of all pulse lengths, 17 s, has been used, thus giving clearly separated arrivals. The reasons for the differences in pulse form are that the rays of *SKKS* and *SKKKS* touch caustics in the outer core whereas the rays of *SKS* do not, and that there are partly phase shifts upon transmission and reflection at the coremantle boundary. Choy and Richards (1975) have discussed these effects in general and given approximate transformations which relate the shapes of phases such as *sS* and *SS* from deep focus earthquakes, or *SKS* and *SKKS*. They assume that *sS* and *SKS* have not suffered essential wave-form changes along their paths. For *SKS* at distances around 120°, however, the diffracted wave $SP_{\text{diff}}KS + SKP_{\text{diff}}S$ actually produces severe deformations in *SKS*, as is seen in Figs. 11 and 15, and it is just in this distance range that Choy and Richards apply their transformation method to longperiod *WWNSS* records of *SKS* and *SKKS*. Besides noise of different origin in the data, this is probably a major reason why this method, which certainly takes correct account of the main causes of pulse deformation, does not give particularly satisfactory results. From the seismograms in Fig. 15, more suitable distance ranges for this method appear to be the interval from 100° to 110° approximately and distances around 140° where $SP_{\text{diff}}KS + SKP_{\text{diff}}S$ has separated from *SKS*, and *SKKKS* from *SKKS*. Two of the observed seismograms in Choy's and Richards' paper resemble so closely the theoretical seismogram at the distance 117.5° in Fig. 15 that we have drawn them on the same time scale in Fig. 18 in order to demonstrate the agreement between observation and theory that can be achieved.

Summary and Conclusions

The reflectivity method for the calculation of theoretical seismograms has been extended to include a double-couple point source and to compute *SV*-wave seismograms, using the *SS* reflection coefficient of a layered medium. Synthetic seismograms of *SV* waves have been computed for crustal models and for models of the whole

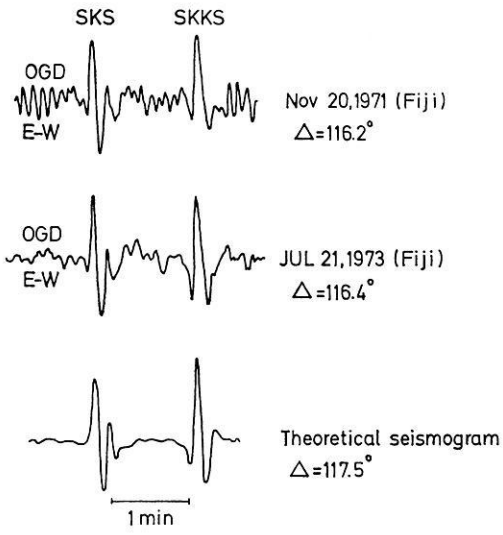

Fig. 18. Comparison of observed and theoretical seismograms for SKS and $SKKS$. The observed seismograms are from a paper by Choy and Richards (1975) and represent the long-period E—W component at the *WWNSS* station Odgensburg, New Jersey, U.S.A. With respect to the epicenters, this component is practically radial and therefore directly comparable with the theoretical seismogram which was taken from Fig. 15. Correcting the epicentral distances of OGD for the effect of focal depth gives an increase of 0.8° to 1° and thus values close to 117.5°. The data of the two earthquakes are: (1) November 20, 1971, 07:28:01.1; 23.4 S, 179.9 W; depth 551 km; $m_b = 6.0$. (2) July 21, 1973, 04:19:17.1, 24.8 S, 179.2 W; depth 411 km; $m_b = 5.9$

earth. These calculations gave the complete SV-wave response of the models, including multiple reflections and conversions. Since such phases, for instance $SKKS$ and $SKKKS$, are sometimes of considerable interest in seismology, the reflectivity method has a broader field of applications in seismic body-wave studies than generalized ray theory. This advantage is, however, accompanied by the requirement of relatively long computing times.

For a model of two half spaces, separated by a first-order discontinuity and having average proporties of the earth's crust and upper mantle, respectively, we found two unfamiliar types of SV head waves, one travelling with the P velocity of the upper half space, and one which is slightly slower than the head wave travelling with the S velocity of the lower half space. The second of these head waves has unusually low frequencies and is probably caused by a pseudo-Rayleigh wave at the top of the lower half space. Both head waves eventually disappear if the discontinuity between the half spaces is replaced by transition zones of increasing thickness. Models of the whole earth also produce SV phases that are not always expected. One is the diffracted wave $SP_{\mathrm{diff}}KS + SKP_{\mathrm{diff}}S$ whose travel-time curve is a straight line tangential to the travel-time curve of SKS. It interferes stongly with SKS in the distance range around 120°.

Another result of our calculations is that the structure of the upper mantle is quite important for various types of multiples and converted waves. We have identified reflections SuS from the transition zone region of our earth model A,

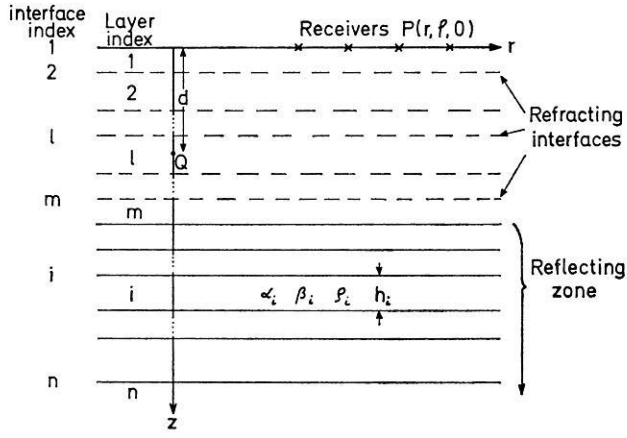

Fig. A-1. The layered medium with the double-couple point source

produced by S waves incident from below, and forming forerunners to SS. Moreover, there are forerunners to S due to conversions from S to P waves in this region. The existence of these various forerunners depends strongly on the sharpness of the transition zones in the upper mantle, and therefore they might be used in checking proposed velocity and density distributions.

The main S-wave phases, S, ScS, SKS and $SKKS$, are the prominent arrivals in our S-wave seismogram sections, and the phases mentioned in the preceding paragraphs, as interesting as they are, are almost all quite weak in comparison. The final purpose of the present work is to compare observed long-period and theoretical seismograms for the main S phases. This comparison should show whether or not present earth models are, in their lower mantle and outer core part, compatible with the amplitudes and signal shapes of these phases. Besides that, it will be of interest to search in data for some of the minor phases mentioned above.

Acknowledgements. This research was supported by a grant from the Deutsche Forschungsgemeinschaft. The extensive calculations were performed at the computing center of the University of Karlsruhe and on the computer of the Geophysical Institute. Our work on the latter was greatly supported by Werner Kaminski. We are grateful to David Bamford and Karl Fuchs for reading the manuscript and for discussions, and to George Choy and Paul Richards for a preprint of their paper. The manuscript was typed by Ingrid Hörnchen.

Appendix A: Reflectivity Method for a Double-Couple Point Source

In this appendix, a compact description of the reflectivity method for a double-couple point source is given, including all necessary formulas. Fig. A-1 shows the geometry of the layered medium. It is subdivided into the reflecting zone and a stack of m surficial layers which produce only time shifts and elastic transmission losses. The source Q is assumed to lie inside one of the layers 1 through m. Two coordinate systems are used; cylindrical coordinates r, φ, z for the receivers and the displacement components u_r, u_φ, u_z, and cartesian coordinates x_1, x_2, x_3 for describing the orientation of the double couple (Fig. A-2). The unit vectors $\boldsymbol{f} = (f_1, f_2, f_3)$ and $\boldsymbol{n} = (n_1, n_2, n_3)$ are those normals to the P nodal planes that have between them one of

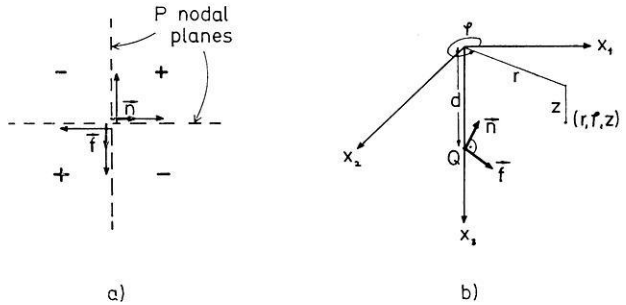

Fig. A-2. a) Unit vectors $\boldsymbol{f}$ and $\boldsymbol{n}$, describing the double couple. The plus and minus signs denote first P motions away and towards the source, respectively. b) Cylindrical and cartesian coordinates that are used, and the unit vectors $\boldsymbol{f}$ and $\boldsymbol{n}$ of the double couple

the quadrants with first P motions *towards* the source. (Instead of $\boldsymbol{f}$ and $\boldsymbol{n}$, $-\boldsymbol{f}$ and $-\boldsymbol{n}$ can also be used.) In practical applications, these vectors can be derived from fault-plane solutions of earthquakes.

The starting point of the derivation is a paper by Müller (1969) on generalized ray theory for single-force and dipole point sources. The expressions (13) of that paper give the complete displacements, corresponding to an arbitrary generalized ray from a harmonic single-force point source to the receiver. We have used these expressions and the transformation formulas (19) in the same paper to derive the displacements due to a single couple. Superposing the displacements due to a second single couple gives the displacements due to a harmonic double couple. In the whole derivation, near-field terms are dropped which essentially means that P and SV waves have no azimuthal displacement u_φ, and SH waves no radial displacement u_r. This neglection is fully justified in view of practical applications. The resulting displacements are then specialized for the following generalized rays:

a) SH ray from the source Q to the top of the reflecting zone (RZ) and from RZ to the receiver P (SH response)
b) P ray from Q to RZ and from RZ to P (PP response)
c) P ray from Q to RZ, SV ray from RZ to P (PS response)
d) SV ray from Q to RZ and from RZ to P (SS response)
e) SV ray from Q to RZ, P ray from RZ to P (SP response)

These displacements contain the generalized reflection coefficients, in the sense of generalized ray theory, of the interface on top of the reflecting zone. Replacing these interface reflection coefficients by the reflection coefficients (or reflectivities) of the *whole reflecting zone* gives the displacements according to the reflectivity method. They are given in the following in the form of Fourier transforms for an arbitrary double-couple moment function $M(t)$. Because of their derivation from generalized ray theory, they are integrals over the apparent slowness u. The angle of incidence at the top of the reflecting zone, γ, is introduced at the end.

The following abbreviations are used in the displacement formulas:

$$\gamma_1 = f_1 \cos\varphi + f_2 \sin\varphi \qquad \gamma_2 = -f_1 \sin\varphi + f_2 \cos\varphi \qquad \gamma_3 = f_3$$

$$\delta_1 = n_1 \cos\varphi + n_2 \sin\varphi \qquad \delta_2 = -n_1 \sin\varphi + n_2 \cos\varphi \qquad \delta_3 = n_3$$

$$q_j = (u^2 - \alpha_j^{-2})^{\frac{1}{2}} \qquad q_j' = (u^2 - \beta_j^{-2})^{\frac{1}{2}}$$

Table A-1. The functions $F_1(u)$, $F_2(u)$, $F_3(u)$

Type of wave at receiver	Free surface included?	$F_1(u)$	$F_2(u)$	$F_3(u)$
SH	no	1	—	—
	yes	2	—	—
P	no	—	1	$-\frac{q_1}{u}$
	yes	—	$\frac{4\beta_1^2 q_1 q_1'}{D(u)}$	$-\frac{q_1}{u}\cdot\frac{4\beta_1^2 u^2-2}{D(u)}$
SV	no	—	$\frac{q_1'}{u}$	-1
	yes	—	$\frac{q_1'}{u}\cdot\frac{4\beta_1^2 u^2-2}{D(u)}$	$-\frac{4\beta_1^2 q_1 q_1'}{D(u)}$

$$D(u) = 4\beta_1^4 u^2 q_1 q_1' - (2\beta_1^2 u^2 - 1)^2$$

The radicals q_j and q_j' are positive imaginary for real u from $u=0$ to $u=\alpha_j^{-1}$ and $u=\beta_j^{-1}$, respectively.

SH Wave at Receiver

$$\bar{u}_r = 0$$

$$\bar{u}_\varphi = -\frac{\omega^2 \bar{M}(\omega)}{4\pi\varrho_1\beta_1^2}\int_0^\infty \Big[(\delta_3\gamma_2+\delta_2\gamma_3)\, u J_0(u\omega r) + (\delta_1\gamma_2+\delta_2\gamma_1)\frac{u^2}{q_1'} J_1(u\omega r)\Big] P'(\omega,u)\, F_1(u)\, e^{g(u)\omega}\, du \qquad (A-1)$$

$$\bar{u}_z = 0$$

Here we have:

$$P'(\omega,u) = \prod_{l+1}^{m} t_j^+(u) \times \prod_{2}^{m} t_j^-(u) \times r_{ss}(\omega,\gamma(u))$$

$t_j^+(u)$ and $t_j^-(u)$ are plane-wave transmission coefficients for the j-th interface, corresponding to downward and upward propagation, respectively:

$$t_j^+(u) = 2\varrho_{j-1}\beta_{j-1}^2 q_{j-1}'/N(u) \qquad t_j^-(u) = 2\varrho_j\beta_j^2 q_j'/N(u)$$
$$N(u) = \varrho_{j-1}\beta_{j-1}^2 q_{j-1}' + \varrho_j\beta_j^2 q_j'$$

$r_{ss}(\omega,\gamma(u))$ is the *SH* reflectivity of the reflecting zone and depends on both frequency and apparent velocity or angle of incidence. It can be calculated by matrix

Table A-2. The functions $A(u)$ and $B(u)$

Type of wave at receiver	$A(u)$	$B(u)$
P	$\dfrac{\delta_1 \gamma_3 + \delta_3 \gamma_1}{2\pi \varrho_l} u^3$	$\dfrac{\delta_3 \gamma_3 - \delta_1 \gamma_1}{2\pi \varrho_l} \cdot \dfrac{u^4}{q_l} - \dfrac{\delta_3 \gamma_3}{2\pi \varrho_l \alpha_l^2} \cdot \dfrac{u^2}{q_l}$
SV	$\dfrac{\delta_1 \gamma_3 + \delta_3 \gamma_1}{4\pi \varrho_l} \cdot \dfrac{(2u^2 - \beta_l^{-2})\, u^2}{q_l'}$	$\dfrac{\delta_3 \gamma_3 - \delta_1 \gamma_1}{2\pi \varrho_l} u^3$

Table A-3. The functions $P(\omega, u)$ and $g(u)$

Response	$P(\omega, u)$	$g(u)$
PP	$\prod_{l+1}^{m} T_j^+(u) \times \prod_{2}^{m} T_j^-(u) \times R_{pp}(\omega, \gamma(u))$	$H q_l - \sum_{1}^{m} h_j q_j - \sum_{l+1}^{m} h_j q_j$
PS	$\prod_{l+1}^{m} T_j^+(u) \times \prod_{2}^{m} U_j^-(u) \times R_{ps}(\omega, \gamma(u))$	$H q_l - \sum_{1}^{m} h_j q_j' - \sum_{l+1}^{m} h_j q_j$
SS	$\prod_{l+1}^{m} U_j^+(u) \times \prod_{2}^{m} U_j^-(u) \times R_{ss}(\omega, \gamma(u))$	$H q_l' - \sum_{1}^{m} h_j q_j' - \sum_{l+1}^{m} h_j q_j'$
SP	$\prod_{l+1}^{m} U_j^+(u) \times \prod_{2}^{m} T_j^-(u) \times R_{sp}(\omega, \gamma(u))$	$H q_l' - \sum_{1}^{m} h_j q_j - \sum_{l+1}^{m} h_j q_j'$

$$H = d - \sum_{1}^{l} h_j$$

methods. The function $F_1(u)$ depends on whether or not the influence of the free surface is to be taken into account at the receivers. It is given in Table A-1. The function $g(u)$ is the same as that for the SS response in Table A-3.

P or SV Wave at the Receiver

$$\bar{u}_r = \omega^2 \bar{M}(\omega) \int_0^\infty [-A(u) J_0(u\omega r) + B(u) J_1(u\omega r)]\, P(\omega, u)\, F_2(u)\, e^{g(u)\omega}\, du \quad \text{(A-2)}$$

$$\bar{u}_\varphi = 0$$

$$\bar{u}_z = \omega^2 \bar{M}(\omega) \int_0^\infty [A(u) J_1(u\omega r) + B(u) J_0(u\omega r)]\, P(\omega, u)\, F_3(u)\, e^{g(u)\omega}\, du \quad \text{(A-3)}$$

The functions $A(u)$ and $B(u)$ depend on whether P or SV radiation at the source is considered. They are given in Table A-2. The functions $F_2(u)$ and $F_3(u)$ are analogous to $F_1(u)$ in the case of SH waves. They are given in Table A-1. The functions $P(\omega, u)$ and $g(u)$ depend on the type of interaction with the reflecting zone and are compiled in Table A-3. The functions $T_j^+(u)$ and $T_j^-(u)$ are plane-wave transmission

coefficients for P waves and for downward and upward propagation, respectively, $U_j^+(u)$ and $U_j^-(u)$ are the corresponding SV transmission coefficients. These coefficients are as follows:

$$T_j^+(u) = 2\,\varrho_{j-1}\,q_{j-1}\,[(cu^2-\varrho_{j-1})\,q_j' - (cu^2+\varrho_j)\,q_{j-1}']/O(u)$$

$$U_j^+(u) = 2\,\varrho_{j-1}\,q_{j-1}'\,[(cu^2-\varrho_{j-1})\,q_j - (cu^2+\varrho_j)\,q_{j-1}]/O(u)$$

$$T_j^-(u) = \frac{\varrho_j\,q_j}{\varrho_{j-1}\,q_{j-1}}\,T_j^+(u) \qquad U_j^-(u) = \frac{\varrho_j\,q_j'}{\varrho_{j-1}\,q_{j-1}'}\,U_j^+(u)$$

$$O(u) = u^2(cu^2-\varrho_{j-1}+\varrho_j)^2 - q_j\,q_j'(cu^2-\varrho_{j-1})^2 - q_{j-1}\,q_{j-1}'(cu^2+\varrho_j)^2$$
$$- \varrho_{j-1}\,\varrho_j(q_j\,q_{j-1}'+q_{j-1}\,q_j') + c^2\,u^2\,q_{j-1}\,q_j\,q_{j-1}'\,q_j'$$

$$c = 2\,(\varrho_{j-1}\,\beta_{j-1}^2 - \varrho_j\,\beta_j^2)$$

The P-SV reflectivities R_{pp}, R_{ps}, R_{ss} and R_{sp} of the reflecting zone are calculated by matrix methods. Appendix B gives some details.

For the numerical integration of expressions such as (A-2), the angle of incidence at the top of the reflecting zone, γ, is introduced by the relation

$$u = \frac{\sin\gamma}{c} \tag{A-4}$$

where $c = \alpha_m$ for the PP and PS response, and $c = \beta_m$ for the SH, SS and SP response. The numerical integration is performed, using equidistant and real values of γ. The restriction to real γ gives the body-wave response in the corresponding range of apparent velocities. More details about the numerical calculation can be found in Fuchs and Müller (1971). For the special orientation of the double couple, used in the main part of this paper, and for $m = 1$, formulas (A-2) and (A-3) reduce, after introduction of (A-4), to expressions (1) through (4).

Appendix B: Calculation of SS and SP Reflection Coefficients

Reflection and transmission coefficients of plane elastic waves for a horizontally layered medium between two half spaces have been calculated, among others, by Fuchs (1968a) and Červený (1974), using the methods of Haskell (1953) and Dunkin (1965). The desired SS and SP reflection coefficients, R_{ss} and R_{sp}, may be calculated directly from the elements of the Haskell matrix M. This matrix is given by Fuchs (1968a) in the following form:

$$M = T_n^{-1} \cdot G_{n-1} \cdot \ldots \cdot G_1 \cdot T_0$$

where T_n^{-1}, G_i and T_0 are the matrices of the lower half space, the i-th layer and the upper half space, respectively. The elements of these matrices are also given by Fuchs (1968a). However, since numerical difficulties may arise from a direct application of the Haskell matrix, Dunkin's matrix method which avoids these difficulties is usually used. The elements of Dunkin's 6×6 matrix $\hat{M}$ are all possible 2×2 subdeterminants of the 4×4 Haskell matrix M. $\hat{M}$ is called the delta matrix of M

(Červený, 1974). The construction of delta matrices is described in detail by Fuchs (1968a) and Červený (1974). Since the delta matrix of a product of matrices is equal to the product of their delta matrices, the delta matrices $\hat{T}_n^{-1}$, $\hat{G}_i$ and $\hat{T}_0$ of T_n^{-1}, G_i and T_0 may be used instead of these matrices themselves. Červený (1974) has calculated R_{ss} and R_{sp} in terms of the elements $\hat{M}_{ij}$ of the Dunkin matrix $\hat{M}$:

$$R_{sp} = \hat{M}_{15}/\hat{M}_{11} \qquad R_{ss} = -\hat{M}_{13}/\hat{M}_{11}$$

For the calculation of $\hat{M}_{11}$, $\hat{M}_{13}$ and $\hat{M}_{15}$, only the first row of $\hat{T}_n^{-1}$, the complete delta matrices $\hat{G}_i$, and the first, third and fifth column of $\hat{T}_0$ are needed. Most of these quantities, i.e. all but the third and fifth column of $\hat{T}_0$, are given by Fuchs (1968a). The elements of the third and fifth column of $\hat{T}_0$ are:

$$(\hat{T}_0)_{13} = -k^2 + \nu_0 \nu_0' \qquad (\hat{T}_0)_{15} = 2\nu_0' k$$
$$(\hat{T}_0)_{23} = i\nu_0' \mu_0 (2k^2 - l_0) \qquad (\hat{T}_0)_{25} = 0$$
$$(\hat{T}_0)_{33} = -ik\mu_0 (l_0 - 2\nu_0 \nu_0') \qquad (\hat{T}_0)_{35} = 2i\nu_0' \mu_0 l_0$$
$$(\hat{T}_0)_{43} = (\hat{T}_0)_{33} \qquad (\hat{T}_0)_{45} = 4i\nu_0' \mu_0 k^2$$
$$(\hat{T}_0)_{53} = i\nu_0 \mu_0 (2k^2 - l_0) \qquad (\hat{T}_0)_{55} = 0$$
$$(\hat{T}_0)_{63} = \mu_0^2 (4k^2 \nu_0 \nu_0' - l_0^2) \qquad (\hat{T}_0)_{65} = 4\mu_0^2 \nu_0' k l_0$$

with

$$\mu_0 = \beta_0^2 \varrho_0 \qquad \nu_0 = \begin{cases} (k_{\alpha_0}^2 - k^2)^{\frac{1}{2}}, & k_{\alpha_0} \geq k \\ -i(|k_{\alpha_0}^2 - k^2|)^{\frac{1}{2}}, & k_{\alpha_0} < k \end{cases}$$
$$l_0 = 2k^2 - k_{\beta_0}^2$$
$$k_{\beta_0} = \omega/\beta_0 \qquad \nu_0' = \begin{cases} (k_{\beta_0}^2 - k^2)^{\frac{1}{2}}, & k_{\beta_0} \geq k \\ -i(|k_{\beta_0}^2 - k^2|)^{\frac{1}{2}}, & k_{\beta_0} < k \end{cases}$$
$$k_{\alpha_0} = \omega/\alpha_0$$

and wavenumber k, circular frequency ω, and density ϱ_0, P velocity α_0 and S velocity β_0 in the upper half space. In these formulas, we have retained the original numbering of the layers, used by Fuchs (1968a), which differs from the numbering in this paper. In applications, the index zero above has to be replaced by the index m of the layer immediately on top of the reflecting zone. The relation between wavenumber k and apparent slowness u, as used in this paper, is $k = u\omega$.

References

Buchbinder, G.G.R.: A velocity structure of the earth's core. Bull. Seism. Soc. Am. *61*, 429–456, 1971

Buchbinder, G.G.R.: Diffraction from the PKP caustic B. Bull. Seism. Soc. Am. *64*, 33–43, 1974

Bullen, K.E.: An introduction to the theory of seismology. Third ed. London: Cambridge University Press 1963

Červený, V.: Reflection and transmission coefficients for transition layers. Studia geoph. et geod. *18*, 59–68, 1974

Chapman, C.H.: The earth flattening transformation in body wave theory. Geoph. J. R. A. S. *35*, 55–70, 1973

Choy, G.L., Richards, P.G.: Pulse distortion and Hilbert transformation in multiply reflected and refracted body waves. Bull. Seism. Soc. Am. *65*, 1975 (in press)

Dunkin, J.W.: Computation of modal solutions in layered media at high frequencies. Bull. Seism. Soc. Am. *55*, 335–358, 1965

Dziewonski, A.M., Gilbert, F.: Solidity of the inner core of the earth inferred from normal mode observations. Nature *234*, 465–466, 1971

Edel, J.-B., Fuchs, K., Gelbke, C., Prodehl, C.: Deep structure of the southern Rhinegraben area from seismic refraction measurements. Submitted to J. Geophys., 1974

Ewing, W.M., Jardetzky, W.S., Press, F.: Elastic waves in layered media. New York: McGraw-Hill Book Comp. 1957

Fuchs, K.: Das Reflexions- und Transmissionsvermögen eines geschichteten Mediums mit beliebiger Tiefen-Verteilung der elastischen Moduln und der Dichte für schrägen Einfall ebener Wellen. Z. Geophys. *34*, 389–413, 1968a

Fuchs, K.: The reflection of spherical waves from transition zones with arbitrary depth-dependent elastic moduli and density. J. Phys. Earth *16*, Special Issue, 27–41, 1968b

Fuchs, K., Müller, G.: Computation of synthetic seismograms with the reflectivity method and comparison with observations. Geophys. J. R. A. S. *23*, 417–433, 1971

Gilbert, F., Laster, S. J.: Excitation and propagation of pulses on an interface. Bull. Seism. Soc. Am. *52*, 299–319, 1962

Haskell, N.A.: The dispersion of surface waves in multi-layered media. Bull. Seism. Soc. Am. *43*, 17–34, 1953

Helmberger, D.V., Engen, G.: Upper mantle shear structure, J. Geophys. Res. *79*, 4017–4028, 1974

Hill, D.P.: An earth-flattening transformation for waves from a point source. Bull. Seism. Soc. Am. *62*, 1195–1210, 1972

Hirn, A., Steinmetz, L., Kind, R., Fuchs, K.: Long range profiles in Western Europe: II. Fine structure of the lower lithosphere in France (southern Bretagne). Z. Geophys. *39*, 363–384, 1973

Johnson, L.R.: Array measurements of P velocities in the lower mantle. Bull. Seism. Soc. Am. *59*, 973–1008, 1969

Kind, R.: Long range propagation of seismic energy in the lower lithosphere. J. Geophys. *40*, 189–202, 1974

Mitchell, B.J., Helmberger, D.V.: Shear velocities at the base of the mantle from observations of S and ScS. J. Geophys. Res. *78*, 6009–6020, 1973

Müller, G.: Theoretical seismograms for some types of point-sources in layered media. Part III: Single force and dipole sources of arbitrary orientation. Z. Geophys. *35*, 347–371, 1969

Müller, G.: Approximate treatment of body waves in media with spherical symmetry. Geophys. J. R. A. S. *23*, 435–449, 1971

Müller, G.: Amplitude studies of core phases. J. Geophys. Res. *78*, 3469–3490, 1973a

Müller, G.: Theoretical body wave seismograms for media with spherical symmetry—discussion and comparison of approximate methods. Z. Geophys. *39*, 229–246, 1973b

Press, F.: The earth's interior as inferred from a familiy of models. In: The nature of the solid earth (E. C. Robertson, ed.), 147–171. New York: McGraw-Hill Book Comp. 1972

Qamar, A.: Revised velocities in the earth's core. Bull. Seism. Soc. Am. *63*, 1073–1105, 1973

Roever, W.L., Vining, T.F., Strick, E.: Propagation of elastic wave motion from an impulse source along a fluid-solid interface, I, II, III. Phil. Trans. Roy. Soc. London, Ser. A, *251*, 455–523, 1959

Wiggins, R.A., McMechan, G.A., Toksöz, M.N.: Range of earth structure nonuniqueness implied by body wave observations. Rev. Geophys. Space Phys. *11*, 87–113, 1973

Rainer Kind
Gerhard Müller
Geophysical Institute
University of Karlsruhe
D-7500 Karlsruhe
Federal Republic of Germany

J. Geophys. 41, 173–177, 1975

On Tracing Seismic Rays with Specified End Points

Ramesh Chander

Department of Physics, University of Zambia

Received April 9, 1974

Abstract. A method for tracing seismic rays with specified end points is described. It is based on a technique due to Euler in which integrals of variational problems are replaced by sums to be minimized. Thus ray tracing is reduced to solution of a system of algebraic equations. Application of the method is illustrated by tracing a ray between two given points in a medium in which the seismic velocity varies linearly with distance from a plane.

Key words: Seismic Ray Defermination — Numerical Methods

1. Introduction

A little used technique due to Euler (Courant and Hilbert, 1953; Elsgolc, 1962) for direct solution of variational problems provides a method of constructing seismic rays. Attention is confined in this initial paper to flat-earth models in which seismic velocity varies only with depth below the free surface in an arbitrary but known way.

An important feature of the present method is that the starting and termination points of the ray to be traced are specified. This is in contrast to other methods of seismic ray tracing in current use (Jackson, 1970) in which the starting point and the direction of the ray at the start are specified. However, as in the other numerical methods of ray tracing, when the seismic velocity varies continuously in the medium, the present method also yields only polygonal approximations to actual rays.

Conceptually, the method adopted in many optics books (Jenkins and White, 1957) to show that Snell's law is a consequence of Fermat's principle may be regarded as a particularly simple application of the present method.

2. Statement of the Problem

Let S (Fig. 1) be the source and R the receiver of seismic waves in an isotropic elastic medium in which the wave velocity v(y) varies with the y-coordinate only in a prescribed manner. It is required to construct the refracted ray between S and R.

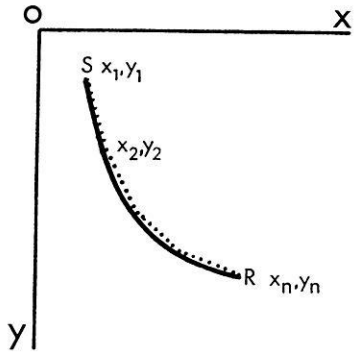

Fig. 1. Actual seismic ray (full line) between source S and receiver R and its polygonal approximation (dotted line) to be determined

2.1. Solution of the Problem by the Euler Technique

By Fermat's principle, the ray SR will be a path of minimum time; i.e., the integral representing the total travel time (t_{SR}) along the ray

$$t_{SR} = \int_S^R ds/v(y) = \int_S^R (1 + x'^2)^{\frac{1}{2}}\, dy/v(y) \qquad (1)$$

will be a minimum for small variations of the ray path. Here, $ds = (1 + x'^2)^{\frac{1}{2}} dy$ is the length of an element of arc along the ray and $x' = dx/dy$.

The idea of the Euler technique is that the integrals of variational problems, such as the present, are replaced by sums to be minimized. To this end, the continuous ray of Fig. 1 is replaced by a polygonal curve (dotted line in Fig. 1), along each linear segment of which the wave velocity is assumed constant. Let (x_1, y_1) and (x_n, y_n) be the specified coordinates of S and R. Let $(x_p, y_p; p = 2, 3, \ldots, n-1)$ be the coordinates of the $n-2$ intervening vertices of the polygonal curve. Let $V_p = (v_{p-1} + v_p)/2$ be the mean velocity along the segment connecting the $(p-1)$—st and p—th vertices. Then, with $dy_p = y_p - y_{p-1}$ and $x'_p = (x_p - x_{p-1})/(y_p - y_{p-1})$,

$$t_{SR} = \int_S^R (1 + x'^2)^{\frac{1}{2}}\, dy/v(y) \approx \sum_{p=1}^{n} [(y_p - y_{p-1})^2 + (x_p - x_{p-1})^2]^{\frac{1}{2}}\, V_p^{-1} \qquad (2)$$

The next step is to fix the y-coordinates $(y_2, y_3, \ldots, y_{n-1})$ of the $n-2$ vertices. The corresponding x-coordinates $(x_2, x_3, \ldots, x_{n-1})$ of these vertices will render the above sum a minimum for small variations in the values of each x_p individually when the following $n-2$ equations are satisfied simultaneously.

$$\frac{\partial t_{SR}}{\partial x_p} = (x_p - x_{p-1})\,[(y_p - y_{p-1})^2 + (x_p - x_{p-1})^2]^{-\frac{1}{2}} V_p^{-1} - (x_{p+1} - x_p)\,[(y_{p+1} - y_p)^2 + (x_{p+1} - x_p)^2]^{-\frac{1}{2}} V_{p+1}^{-1} = 0; \quad p = 2, 3, \ldots, n-1 . \tag{3}$$

The $x_2, x_3, \ldots x_{n-1}$ which are solutions to these equations along with the pre-assigned $y_2, y_3, \ldots, y_{n-1}$ enable the minimum-time polygonal curve approximating the ray SR to be traced.

3. Application of the Method of Ray Tracing

The applicability of the above method of ray tracing was tested in several cases for which the results could also be obtained by other methods. Details of one of these tests are given below in Section 3.2.

3.1 Scheme for Numerical Solution of the Simultaneous Equations

The modified Newton-Raphson iterative scheme for solution of a system of non-linear equations (Stark, 1970) was adopted for the present purpose. The $(k+1)$-st iterated values of the x-coordinates of the polygonal curve are obtained from the k-th iterated values by the relations

$$(x_p)_{k+1} = (x_p)_k - [(\partial t_{SR}/\partial x_p)\,(\partial^2 t_{SR}/\partial x_p^2)^{-1}]_k , \; p = 2, 3, \ldots, n-1; \tag{4}$$

or,

$$(x_p)_{k+1} = (x_p)_k - \{[(x_p)_k - (x_{p-1})_{k+1}]\, l_p^{-1} V_p^{-1} - [(x_{p+1})_k - (x_p)_k]\, l_{p+1}^{-1} V_{p+1}^{-1}\} \div \{(y_p - y_{p-1})^2 l_p^{-3} V_p^{-1} + (y_{p+1} - y_p)^2 l_{p+1}^{-3} V_{p+1}^{-1}\}, \; p = 2, 3, \ldots, n-1; \tag{5}$$

where,

$$l_p^2 = (y_p - y_{p-1})^2 + [(x_p)_k - (x_{p-1})_{k+1}]^2$$

and

$$l_{p+1}^2 = (y_{p+1} - y_p)^2 + [(x_{p+1})_k - (x_p)_k]^2$$

Convergence to the required set of values is accelerated by using the latest available values of x-coordinates at each stage of the computation. This is why the subscript indicating the iteration number is $k+1$ for x_{p-1} and k for x_p and x_{p+1} on the right hand sides of the above equations.

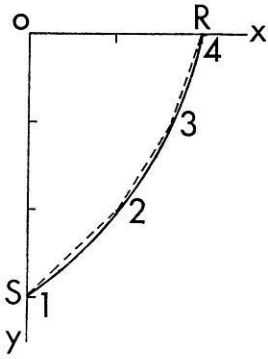

Fig. 2. Comparison of the actual seismic ray (full line) and the minimum-time four-cornered polygonal approximation (dotted line) between source S and receiver R in a medium in which velocity is given by the relation $v(y) = 2 + 2y$. The actual ray is an arc of a circle with centre at $-2 \cdot 75$, -1)

A Compucorp 425/44 desk calculator was programmed to accept numerical values of $(x_p)_k$, $(x_p)_k - (x_{p-1})_{k+1}$, $(x_{p+1})_k - (x_p)_k$, $y_p - y_{p-1}$, $y_{p+1} - y_p$, V_p, V_{p+1} and yield a new estimate $(x_p)_{k+1}$ using Eq. 5. A straight forward programme of 135 steps required 3 seconds for execution after the 7 input data were entered from the key board. The process was repeated for each p $(=2, 3, \ldots, n-1)$ to complete one iteration.

3.2 An Example

A medium with the following velocity depth relation was chosen for constructing a seismic ray in one of the tests.

$$v(y) = 2 + 2\,y \quad (\text{km s}^{-1}) \tag{6}$$

The source S (Fig. 2) was assumed to be at a depth of 3 km and the receiver R at the surface at a point removed 2 km from the vertical line through S. Choosing the y-axis to coincide with this line, and x-axis through R, the coordinates of these points are (0,3) and (2,0) respectively. The exact ray path in this case is an arc of a circle with its centre on a line 1 km above the x-axis and parallel to it (Nettleton, 1940). An approximation to it was sought with a polygonal curve of 4 vertices, with the two extreme vertices (1 and 4) coinciding with S and R. The depths of the intervening vertices (2 and 3) were fixed at $y_2 = 2$ km and $y_3 = 1$ km. The mean velocities V_2, V_3, and V_4 are 7, 5, and 3 kms^{-1} respectively. Starting with $(x_2)_0 = 0.7$ km and $(x_3)_0 = 1.5$ km the successive iterated values shown in Table 1 were obtained.

Table 1

k	$(x_2)_k$ km	$(x_3)_k$ km
0	0.7	1.5
1	0.948	1.641
2	1.042	1.665
3	1.058	1.670
4	1.062	1.671
5	1.062	1.671
	iteration stopped	

Thus the vertices 2 and 3 of the minimum-time four-cornered polygonal curve approximating the ray have coordinates (1.062, 2) and (1.671, 1). For comparison, the exact ray passes through points (1.066, 2) and (1.673, 1).

4. *Conclusion*

A seismic ray tracing method inspired by a little used variational technique due to Euler has been described. Positions of both the end points of the ray to be traced are specified in this method, in contrast to other current methods of seismic ray tracing in which the position of the starting point and the direction of the ray at the start are specified When the seismic velocity of the medium varies with a single space-coordinate only, the computations are simple enough to be carried out on programmable desk-top computers. Thus rapid tracing of rays with specified and points becomes a practicable proposition even for quite complicated seismic velocity variations in situations where large digital computers may not be available.

References

Courant, R., Hilbert, D.: Methods of Mathematical Physics. Vol. 1. New York: Interscience 1953

Elsgolc, L. E.: Calculus of Variation. London: Pergamon 1962

Jackson, P. L.: Digital Simulation of Seismic Rays. Ph. D. dissertation, Department of Geology and Mineralogy, University of Michigan, Ann Arbor, Mi. 1970

Jenkins, F. A., White, H. E.: Fundamentals of Optics. New York: McGraw-Hill 1957

Nettleton, L. L.: Geophysical prospecting for Oil. New York: McGraw-Hill 1940

Stark, P. A.: Introduction to Numerical Methods. London: MacMillan 1970

Dr. Ramesh Chander
Department of Physics
University of Zambia
Box 2379
Lusaka, Zambia

J. Geophys. 41, 179–187, 1975

Geothermal Models of the Ivrea-Zone

A. Höhndorf, R. Haenel, and W. Giesel

Niedersächsisches Landesamt und Bundesanstalt für Bodenforschung, Hannover,

Received September 17, 1974

Abstract. Stationary thermal models of the Ivrea-Zone have been developed on the basis of new data for the terrestrial heat flow and the heat production of rocks with the aid of finite difference methods.

Moderate variations in the spatial extend of the Ivrea body and the distribution of heat sources in its neighbourhood have a relatively minor influence on the temperature distribution. The major source of possible errors in the calculated temperature field of the crust results from the lack of knowledge of the thermal conductivity of the underground.

For λ-values between 6 and $4 \cdot 10^{-3}$ cal $\cdot$ cm$^{-1} \cdot$ s$^{-1} \cdot$ deg^{-1} the temperatures at the Mohorovičić discontinuity at 50 km depth (west of Ivrea-Zone) range between 900 and 1300 °C and at 30 km depth (east of Ivrea-Zone) between 500 and 800 °C. The calculated temperature fields show that in the west of the Ivrea body in the region of the low velocity layer a complete or partial melting is possible if wet granitic material is assumed.

Key words: Geothermal Models – Finite Difference Method – Temperature Field – Rock Melting.

1. Introduction

Under the International Upper Mantle Project a number of geological and geophysical investigations in the Ivrea region have been carried out which led to new structure models of the crust in this region (Giese, 1968; Berckhemer, 1968, Makris, 1971; Ahrendt, 1972).

During the above investigations no attempt was made to calculate the temperature field in the crust which is of importance for the interpretation of the low velocity layer determined under the Ivrea-zone by seismic investigations.

Based on new data for the heat production of rock samples collected from the Ivrea formation and surface heat flow measurements, model calculations have been carried out to obtain an insight into possible temperature distributions at depth.

2. Basis of Geothermal Models

The heat transport in the crust is caused essentially by heat conduction such that the temperature field is given by

$$\frac{\partial T}{\partial t} = \frac{1}{\varrho c}(-\operatorname{div} q + A) \tag{1}$$

with:

T = temperature (°C)
t = time (s)
ϱ = density (gcm^{-3})

c = specific heat (cal g^{-1} deg^{-1})
q = $-\lambda \cdot \text{grad}\ T$ = heat flow (cal cm^{-2} s^{-1}), 1 HFU = 10^{-6} cal cm^{-2} s^{-1}
λ = thermal conductivity (cal $cm^{-1}s^{-1}deg^{-1}$)
A = heat production (cal $cm^{-3}s^{-1}$), 1 HGU = 10^{-13} cal $cm^{-3}s^{-1}$

In the stationary case, $\partial T/\partial t = 0$ the equation is simplified to

$$-\operatorname{div} q + A = 0 \tag{2}$$

The equations were solved numerically with the aid of finite difference methods (Smith, 1971).

For the solution of (2) temperature or heat flow on the surface enclosing the considered volume, heat production and thermal conductivity λ within the considered volume are required. For solution of (1) initial temperature data must also be given.

In the application to heat conduction in the Earth's crust known values of q at the Earth's surface provide an effective control for the proper choice of the model parameter A and the heat flow, entering into the crust from the upper mantle.

The parameters A and λ cannot easily be determined. Heat production data were taken from surface samples which are used for the spatial distribution of heat sources in the whole geological structural model.

The heat production is generated essentially by the radioactive decay of Uranium, Thorium and Potassium. The distribution of the heat sources is controlled by the distribution of these radioactive elements in the crust. By chemical and magmatic differentiation the concentrations of these elements could have in- or decreased in different parts of the crust. However, there is a positive correlation with the SiO_2 content of the rocks. For areas within the USA in three large regions a linear correlation was established between heat flow and the heat production of rocks collected at the surface of plutons (Birch *et al.*, 1968). Two explanations for this correlation have been offered (Blackwell, 1971):

a) a constant heat production in a layer with constant thickness

b) an exponential decrease of heat production with depth.

These assumptions, however, can only be used in areas with uniform rock complexes. In thoroughly folded areas like the Alps we ought to expect much more complex distributions of heat sources.

The estimation of the thermal conductivity causes another problem, since its value is dependent on rock type as well as on temperature. A discussion of the considerable range of variations of the values of λ is given in Kappelmeyer and Haenel (1974), which shows that generally λ-values within $4 - 6 \cdot 10^{-3}$ cal/cm sec °C ought to be expected in crustal material of temperatures between 100 to 1000 °C.

3. Model Calculations

3.1. Model Parameters

The profile of the crustal structure of the Ivrea-Zone (Fig. 1) which runs south of Lago Maggiore in a west-east direction was assumed according to a model of Berckhemer (1968) based on seismic and gravitational data.

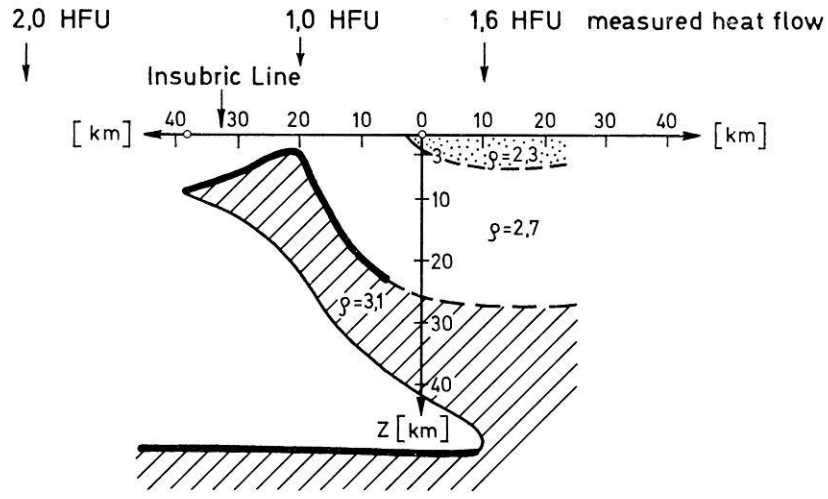

Fig. 1. The structure model of the 200 km-fan (after Berckhemer, 1968). Thick lines show boundaries proved by seismic results, ϱ = density assumed by Berckhemer

The position of the Ivrea body in this profile, which runs perpendicular to the strike, gave us reason to construct a 2-dimensional grid for our model calculations. The horizontal and vertical extent of the grid represent a total distance of 200 km each. Boundary conditions are: a given constant heat flow at depth of 200 km and purely vertical heat flow at the vertical boundaries of the grid point system.

No reliable data on the heat flow from the mantle into the crust under the Alps are available. Estimations on the heat production in the crust west and east of the Ivrea body let us expect that the heat flow from the mantle in this area can assumed to be 0.7 HFU.

The distribution of heat sources in the crust west of the Ivrea body can be inferred from the structure model which is based on the results of seismic investigations (Giese, 1968). The calculations rest on the assumption that the true heat source distribution can be represented by 3 layers (Rybach, 1973)

11 km granite $A = 7.0$ HGU
20 km diorite $A = 2.0$ HGU
19 km gabbro $A = 1.2$ HGU

For the area east of the Ivrea body new data for the heat production of rocks collected from the Ivrea-zone have been used in the calculations (Höhndorf, in press). The values are shown in Fig. 3, Model 2. The nearly vertically dipping layers of the Ivrea complex in the Toce Valley are considered in our model to continue with decreasing inclination towards the east (Giese *et al.*, 1970). The presumably ultramafic Ivrea body is given zero heat production.

First for the thermal conductivity we used constant values for λ between $4-6 \cdot 10^{-3}$ cal/cm sec °C throughout the calculations. Then, temperature dependent λ, as discussed by Haenel (1973), was used in a separate model.

The results of these model calculations can be compared with available heat flow data (Haenel, 1974).

East of the Ivrea body (Lago Maggiore)	1.6 HFU
On top of the Ivrea body (Ivrea)	1.0 HFU
West of the Ivrea body (NW Italy)	2.0 HFU

No corrections due to uplift of the Alps are included in these data. The values are projected on Fig. 1.

The low heat flow measured on top of the Ivrea body does not directly lie on the profile of the 200 km-fan. The similarity of the seismic response of the 200 km-fan north and a 120 km-fan south of Ivrea suggest a fairly uniform structure of this body. Analogously we might expect fairly low heat flow along the ridge of the whole Ivrea body.

3.2. Instationary Model

To gain an insight, whether stationary thermal conditions can be expected in the Ivrea region today, the development of the thermal balance of a suddenly ascending Ivrea body with a temperature of 630 °C from depth was analysed. From the temperature change at different depths (Fig. 2) it is obvious that the thermal perturbation has essentially disappeared after approximately 10 m.y. Because there is no evidence that the structure of the Ivrea-zone was formed less than 10 m.y. ago, the following investigations concerning the temperature field can be dealt with as a stationary problem without appreciable error.

3.3. Stationary Models

Fig. 3 shows the essential sections of the structural models under consideration.

As seen from the calculated curves for the terrestrial heat flow it appears that a distinct minimum on the ridge of the Ivrea body exists. The heat flow in the minimum depends on the accepted thickness of the Ivrea body and has a value of 1.24 HFU for a 25 km thick intrusive body. This value is clearly higher than the value measured near the town of Ivrea. The assumption of greater thickness would cause discrepancy with the results from the seismic and gravimetric investigations. The adoption of greater thickness in the deep region of the pertubate Ivrea body causes only minor influence on the heat flow at the surface.

No assertions about the exact depth of the top of the Ivrea body can be made by seismic and gravimetric data. It is only certain that near the surface a considerable contrast of density exists (Makris, 1971). In another model, therefore, the Ivrea body was continued to the surface. The terrestrial heat flow is reduced on the ridge of the body to 1.19 HFU in this case.

A further deepening of the heat flow minimum will only result from the adoption of a smaller heat flow out of the mantle. In order to preserve the heat flow balance for this case in the East and West of the Ivrea body acid rocks of greater thickness must be postulated, i.e. the heat production in the crust regions must be increased.

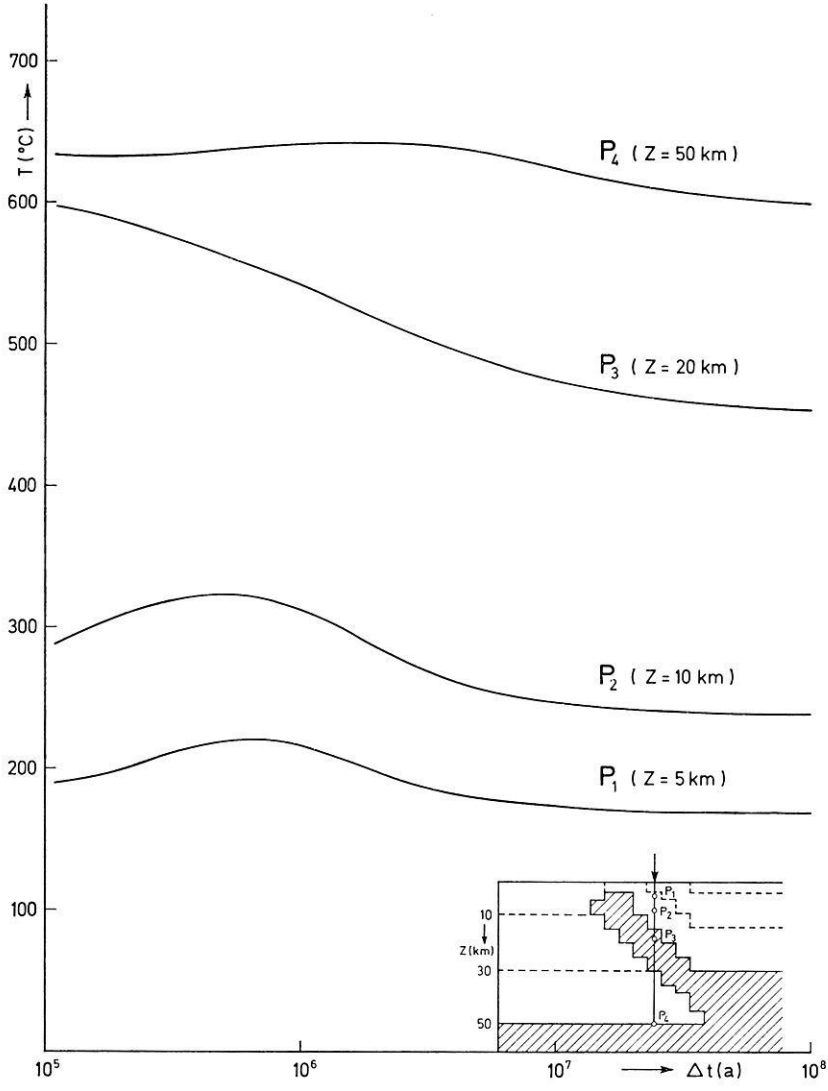

Fig. 2. Temperature as function of time Δt after intrusion of the Ivrea body for selected points marked in the model sketch. The temperature curves are calculated from Eq. (1) with the following parameters: $\lambda = 6 \cdot 10^{-3}$ cal·cm^{-1}·s^{-1}·deg^{-1}, $\varrho \cdot c = 0.5$ cal·cm^{-3}·deg^{-1}, heat flow from the mantle = 0.3 HFU, and heat source distribution as in model 2 (Fig. 3)

Considering a heat flow out of the mantle of 0.5 HFU and a thickness of 16 km granite in the West, 17.5 km "gneiss" (5.5 HFU) in the East respectively the heat flow above the Ivrea body decreases to 1.08 HFU.

The heat flow profile which, unfortunately, is only be defined be three points, does not give justification to conclude that the value of the heat flow out of the mantle is so low.

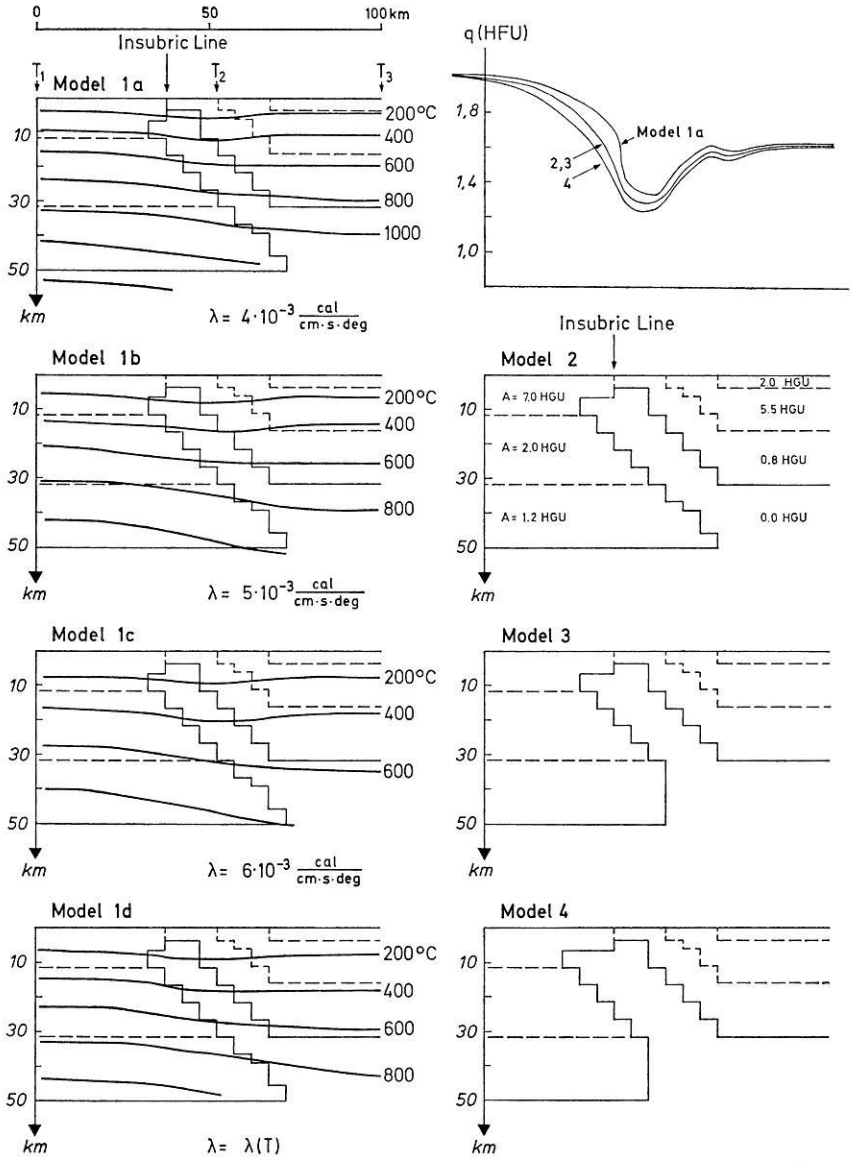

Fig. 3. Models used for calculation of the temperature field. Heat generation as indicated in model 2 is taken the same for all models. Left side: the temperature distribution of models 1a–1d was calculated with indicated thermal conductivities T_1, T_2, T_3 = localities of temperature profiles drawn in Fig. 5. Right side: calculated heat flow above the Ivrea body for the given models

3.4. The Temperature Field

The temperature-depth-curve in the western part of the Ivrea body is of great interest for the interpretation of the observed velocity-inversion of seismic waves in this part of the crust.

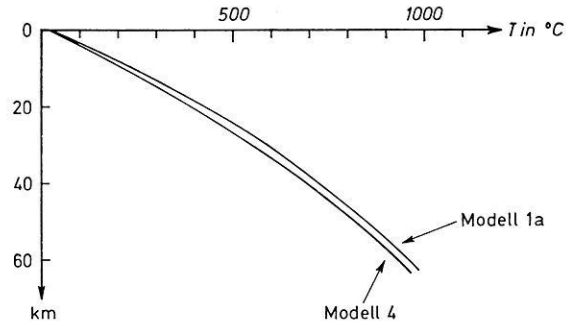

Fig. 4. Temperature profiles for models 1a and 4 below the Insubric Line

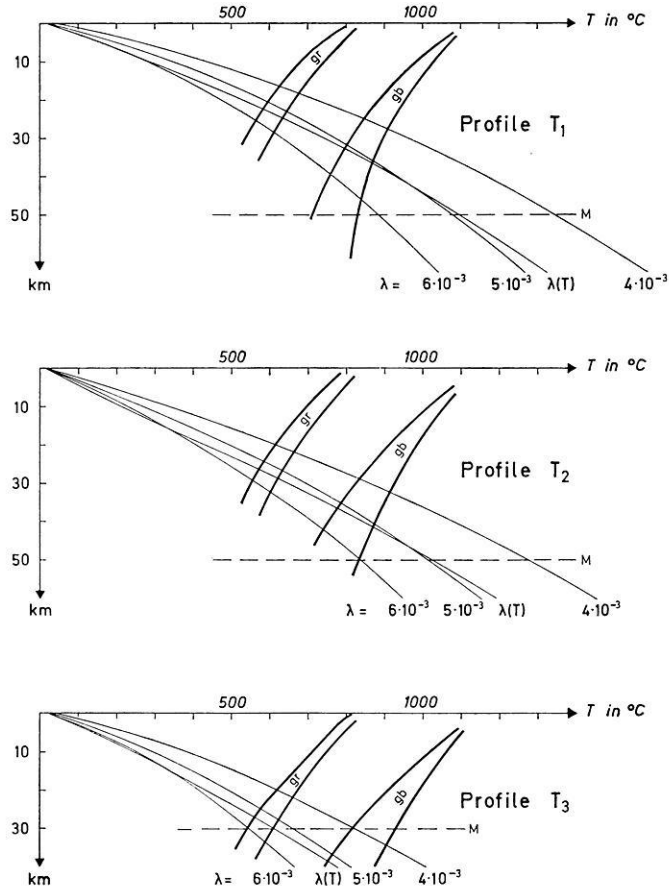

Fig. 5. Temperature profiles at T_1, T_2, T_3 (cf. Fig. 3 models 1a–1d) and range of melting points of granitic rocks (gr) and gabbroic rocks (gb) after Meissner (1974).
M = Mohorovičić discontinuity, λ in cal·cm^{-1}·s^{-1}·deg^{-1}

It turns out that the temperature distribution in this part of the crust depends only slightly upon the choice of the model body. Fig. 4 shows the temperature-depth-curve below the Insubric line for models 1a and 4 which differ only in the form of the model bodies. The temperature differences amount to 35 °C at the most.

The inaccuracy of the measured heat flow data which are considered to have an error of about $\pm 20\%$ produces a uncertainty in the temperature field of ± 200 °C at the depth of 50 km.

The distribution of the heat sources has a comparatively minor effect on the temperature field if the overall heat production in the crust is held constant.

Contrary to this the distribution of the temperature depends to a great extent upon the value of the assumed thermal conductivity of the rocks. Fig. 5 shows the temperature curves, which result for models 1a to 1c at the points T_1, T_2 and T_3 (s. Fig. 3). A dependence of the thermal conductivity on the rock type was not taken into consideration in the models because for most crustal rocks λ-values are in the range considered here. Therefore, no matter what rock types are assumed, the temperature distribution should lie within the range of variation found here.

As one can see, the difference of the calculated temperature curves immediately grow to several hundred degrees with increasing depth. Herewith the lack of knowledge of the thermal conductivity of deeper subsurface proves to be the main factor for possible errors of the calculated distribution of temperature.

In the western region of the intrusive body (T_1) a possible temperature interval of 480 °C to 950 °C results in depths of 20—30 km, i.e. in the region of the seismic inversion zone. The melting zones for granitic and gabbroic rocks with water inincluded are also drawn in the temperature profiles (Meissner, 1974). According to this the geotherms cross the melting point-curve of the wet granite in depths of 20—30 km for all adopted thermal conductivities so that a complete or partial melting seems to be possible.

In the eastern region of the Ivrea body at depths below 20 km exist possibly more basic rocks. Therefore, no melting would be possible considering the calculated temperature curves.

Acknowledgements. The measurements of the heat flow and the heat production are financially supported by the Deutsche Forschungsgemeinschaft (German Scientific Research Foundation). Further it should be noted that the heat flow values were determined by joint cooperation of Italy, Switzerland and Germany (Prof. O. Vecchia, Prof. E. Niggli, Prof. H. Closs, Prof. A. Hahn). The authors also thank Mr. J. Scheuch, Dipl.-Phys., Mr. G. Delisle, M. A., Mr. W. Grote and Mr. G. Zoth, engineer, for their helpful cooperation.

References

Ahrendt, H.: Zur Stratigraphie, Petrographie und zum tektonischen Aufbau der Canavese Zone und ihrer Lage zur Insubrischen Linie zwischen Biella und Cuorgné (Norditalien). Göttinger Arb. Geol. Paläont. *11*, 1972

Berckhemer, H.: Topographie des "Ivrea-Körpers" abgeleitet aus seismischen und gravimetrischen Daten. Schweiz. Min. Petr. Mitt. *48*, 235—246, 1968

Birch, F., Roy, R.F., Blackwell, D.D.: Heat generation of plutonic rocks and continental heat flow provinces. Earth Planet. Sci. Lett. *5*, 1—12, 1968

Blackwell, D.D.: The thermal structure of the continental crust. In: The structure and physical properties of the earth's crust. Geophys. Monogr. Ser. *14*, (J. G. Heacock, ed.), AGU, 1971

Giese, P., Günther, K., Reuter, K. J.: Vergleichende geologische und geophysikalische Betrachtungen der Westalpen und des Nordapennins. Z. Deut. Geol. Ges., Jg. 1968, *120*, 151–195, 1970

Giese, P.: Die Struktur der Erdkruste im Bereich der Ivrea-Zone. Schweiz. Min. Petr. Mitt. *48*, 261–284, 1968

Haenel, R., Zoth, G.: Heat flow measurements in Austria and heat flow maps of Central Europe. Z. Geophys. *39*, 425–439, 1973

Haenel, R.: Heat flow measurements in Northern Italy and heat flow map of Europe. J. Geophys. *42*, 367–380 1974

Höhndorf, A.: Radioaktive Wärmeproduktion in Gesteinen der Ivrea-Zone. Schweiz. Min. Petr. Mitt. *55*, in press

Kappelmeyer, O., Haenel, R.: Geothermics with special reference to application. Geoexploration Monographs. Ser. 1, No. 4. Berlin–Stuttgart: Gebr. Bornträger 1974

Makris, J.: Aufbau der Kruste in den Ostalpen aus Schweremessungen und die Ergebnisse der Refraktionsseismik. Hamburger Geophys. Einzelschriften 15, 1971

Meissner, R.: Viscosity-depth-structure of different tectonic units and possible consequences for the upper part of converging plates. Z. Geophys. *40*, 57–73, 1974

Rybach, L.: Wärmeproduktionsbestimmungen an Gesteinen der Schweizer Alpen. – Beitr. Geol. Schweiz, Geotechn. Ser. 51, Mitt. 82, Inst. Geoph. ETH Zürich, Bern 1973

Smith, G. D.: Numerical solutions of partial differential equations. London: Oxford University Press 1971

Dr. Axel Höhndorf
Dr. Wilfried Giesel
Bundesanstalt für Bodenforschung
D-3000 Hannover-Buchholz
Stilleweg 2
Federal Republic of Germany

Dr. Ralph Haenel
Niedersächsiches Landesamt
für Bodenforschung
D-3000 Hannover-Buchholz
Stilleweg 2
Federal Republic of Germany

J. Geophys. 41, 189–200, 1975

A Note on the Palaeomagnetism of the Late Precambrian Malani Rhyolites near Jodhpur - India

C. T. Klootwijk

Geological Institute, State University of Utrecht, Utrecht

Received September 23, 1974

Abstract. Palaeomagnetic properties from a series of mainly rhyolitic lava flows from the Malani volcanic suite in Rajasthan-India, dated at 745 ± 10 my, were studied by means of alternating fields and thermal demagnetization methods.

The mean direction of the characteristic magnetization component, of both normal and reversed polarity: $D = 354.5°$, $I = +53.5°$, $\alpha_{95} = 8°$, $N = 10$, (Pole: 80.5° N, 43.5° E, $dp = 8°$, $dm = 11.5°$) is in good agreement with earlier results obtained by Athavale *et al.* (1963). The fold test gives a positive result and the above mentioned mean direction from the Malani rhyolites is in agreement with other Precambrian data from the Indian subcontinent. Therefore, this mean direction is interpreted to represent the primary magnetization direction. The position and orientation of the Indian subcontinent about 745 my ago was more or less alike its present-day orientation, however, at that time India was situated at a slightly higher latitude.

Key words: Palaeomagnetism — Precambrian Malani Rhyolites — Malani Rhyolites — India.

Introduction

The Malani igneous suite, formed predominantly by rhyolites and some later intrusive granites, covers an area of several thousands of square miles in Western Rajasthan (India). The rhyolites, dated at 745 ± 10 my by Crawford and Compston (1970) are locally seen to overly unconformably Early Precambrian rocks of the Aravalli System. When the two are present together, the Malani rhyolites are covered with erosional disconformity by the probably Late Precambrian Jodhpur sandstones. Locally the Malani rhyolites are in a tilted position with dips, sometimes up to 70 degrees, assigned either to blockfaulting (Rutten, 1965) or to folding on a regional scale (Mukherjee, 1966).

Rutten has studied the Malani rhyolites in the area near Jodhpur (26 °N 73 °E), and found that the rhyolites in this area predominantly showed typical ignimbritic field characters. However, his conclusion was disputed by Mukherjee (1966).

A previous palaeomagnetic study of the Malani rhyolites was undertaken by Athavale *et al.* (1963) who collected their samples (60 in all) from subhorizontal flows only. Their results, obtained after alternating field demagnetization up to 200 Oe peak value and thermal demagnetization studies, showed a reasonably dense distribution of directions grouped around a mean direction $D = 353°$, $I = +56°$. The inclination of this mean direction is somewhat higher than the present local field direction in the sampling area ($D = 360°$, $I = +38°$). Athavale's *et al.* data seem to favour a counterclockwise rotational movement of the Indian subcontinent during Middle and Late Precambrian times as has been tentatively concluded from radiometrically dated palaeomagnetic results available (Klootwijk, 1974). However, in view of the slight variance between the palaeomagnetic direction of the Malani rhyolites, ob-

tained by Athavale *et al.*, and the present local field direction it seemed appropriate to confirm the stability of the palaeomagnetic direction by means of some further tests, for instance the fold test not applied by Athavale *et al.* (1963). For this purpose a collection of oriented samples from the Malani rhyolites, sampled by the late Prof. Rutten from both subhorizontal and tilted flows in the Jodhpur area, was studied. In addition a study was made of the magnetic susceptibility anisotropy mainly in order to attribute some additional pro or contra arguments for the ignimbritic nature of the flows. These data will be discussed elsewhere.

Sampling and Laboratory Treatment

Altogether 45 handsamples (Table 1) were taken by Rutten (Fig. 1, 1965), from mainly rhyolites (11 sites) and in addition from a felsitic dyke (1 site) and a basaltic dyke (1 site). The samples were collected over the total height of the rhyolites each, some of which showed a tuffaceous top and a massive centre. Orientation of the samples was done in the field by means of a normal compass.

Initial natural remanent magnetization measurements were made with the samples cast in paraffine wax. For demagnetization treatment, a total of 106 cores of 1 inch diameter and 2.2 cm in heigt were drilled from these samples.

All remanent magnetization measurements were carried out on the astatic magnetometers of the Palaeomagnetic Laboratory, State University of Utrecht. From each site at least one specimen was progressively demagnetized by means of alternating fields in 11 to 18 steps up to 3000 Oe peak value. In addition at least one specimen from each site was progressively demagnetized by thermal methods in 23 steps up to zero intensity. The remaining specimens were partially progressively demagnetized in alternating fields (9 to 13 steps) or by thermal methods (11 to 18 steps). Directional analysis of the data was made according to standard techniques described elsewhere (Zijderveld, 1967). For data processing and map plotting, the CDC-6500 computer of the Academic Computer Centre Utrecht was programmed in Algol-60.

Results

The intensity of initial remanence ranged between 10^{-6} to 10^{-3} emu/cm^3 with a mean around 2.10^{-4} emu/cm^3. Q-values generally exceeded unity with the exception of samples from site 14 which showed Q-values between 0.3 and 0.7 (Table 1).

The initial specimen directions reveal a prominent northern concentration with moderate downward dips (Fig. 1A, 2A2). A minor concentration of initial directions, pointing south-southwest and upwards, was made up by the two reversely magnetized sites 15 and 16 (Fig. 1A, 2A1). In general the initial specimen directions grouped rather well within each site, with site 13 showing a much larger initial scatter.

AF-Demagnetization

Upon alternating field demagnetization it appeared that in most sites mainly one single component was present (Fig. 3A). However, pilot specimens especially from sites 13 and 16 showed a more or less distinct local field component of rather small intensity, i.e. 10 to 20% of the initial intensity which could be eliminated at 250 to 400 Oe peak value (Fig. 3G, 3K). Sample 13A reveals a notable behaviour (Fig.

Table 1. Initial measurements

Site	Constitution	Samples	Specimens	Mean direction (degrees)		α_{95} (degrees)	k	Intensity[b]	Q-value	Anisotropy % (K_{max}/K_{min}^{-1}) $\times 100\%$
RI– 2	rhyolite (26°18′N 73° 1′E)	7	15	359	+61.5	8.5	54	1– 48	0.4–23	1.5–3.3
RI– 3	rhyolite (26°18′N 73° 1′E)	4	14	20	+51	15	39.5	84–234	9.7–40	0.6–1.9
RI– 4	rhyolite (26°18′N 73° 1′E)	3	13	57	+60.5	—	—	1.4–27	1.1–21	3.3
RI– 5	rhyolite (26°18′N 73° 1′E)	1	3	14	+61.5	—	—	116–117	14–22	1.2
RI– 7	rhyolite (25°48′N 72° 10′E)	4	9	344	+35	20.5	20.5	79– 82	0.9–1.2	2.2–3.2
RI– 8	felsitic dyke (25°48′N 72° 10′E)	2	4	341	+41.5	—	109	50– 53	0.7	2.7–2.9
RI–10	rhyolite (25°48′N 72° 10′E)	5	10	349.5	+47.5	11	71.5	77–148	1.2–3.5	0.9–2
RI–11	basaltic dyke (25°48′N 72° 10′E)	2	6	341.5	+24.5	—	4	77–177	0.9–1.6	1.2–1.7
RI–12	rhyolite (25°48′N 72° 10′E)	3	9	340.5	+53.5	22.5	30.5	204–254	1.8–2.1	1.9–3.7
RI–13	rhyolite (25°40′N 73° 9′E)	5	17	51	+46	45	4	83–488[a]	0.9–3.2	1.5–2.5
RI–14	rhyolite? (26°7′N 73° 3′E)	4	6	6	+53.5	27	12.5	9– 26	0.3–0.7	3.1–6.3
RI–15	rhyolite (26°7′N 73° 3′E)	3	8	227	—25	23	30	673–944	5.5–7.6	3.2–3.6
RI–16	rhyolite (26°7′N 73° 3′E)	2	3	211	—16	—	14	66–325	0.9–3.5	2.2–3.6

[a] Specimens of sample RI13A showed much higher initial intensities, between 2827 and 3405 $\times 10^{-6}$ emu/cm^3 and Q-values between 18.6 and 20.6.

[b] In units of 10^{-6} emu/cm^3.

Table 1 (continued). After alternating field or thermal demagnetization

Site	Samples[a]	Specimens[b]	Mean direction (degrees)		α_{95} (degrees)	k	Strike and dip (degrees)	Site mean direction after dip correction (degrees)	
RI— 2	6 (1)	14 (4)	3.9	+62.5	6.5	133	subhorizontal		
RI— 3	4	13 (4)	23.5	+52.5	5.3	297.5	subhorizontal		
RI— 4	2	2 (1)	3.2	+65.2	—	23.5	subhorizontal		
RI— 5	1	3 (2)	16.5	+62.5	1.5[c]	5070	subhorizontal		
RI— 7	4	8 (3)	340	+45	12.5	55	subhorizontal		
RI— 8	2	3 (1)	339	+48	—	14	intruded into RI7		
RI—10	5	9 (2)	346.5	+52	6	162	subhorizontal		
RI—11	2	5 (3)	342.5	+46	—	47	intruded into RI10		
RI—12	3	6 (3)	353	+61	7	316	200E/12W	337	+54.5
RI—13	4	13 (6)	87	+42	4	490.5	188E/51W	345	+81
RI—14	4	6 (3)	356	+57	12.5	54	195E/46W	320	+27.5
RI—15	3 (1)	6 (3)	213	—30.5	12	430.5	195E/46W	182	—33
RI—16	2	2 (1)	211	—25.5	—	207	210E/65W	189	—11.5

[a] Between brackets number of samples rejected, because of uninterpretable demagnetization graphs.
[b] Between brackets number of specimens treated by thermal methods, all other specimens were demagnetized in alternating fields.
[c] Unit weight given to specimen directions.

Table 1 (continued). Mean direction after cleaning

Number of sites (degrees)	Mean direction (degrees)		α_{95}	k	Pole position (degrees)		dp (degrees)	dm (degrees)
Before dip corr: 10[a]	0.5	+54.4	9.5	26				
after dip corr: 10[a]	354.5	+53.5	8	35.3	80.5°N	43.5°E	8°	11.5°

[a] Sites 13, 14 and 16 are excluded.

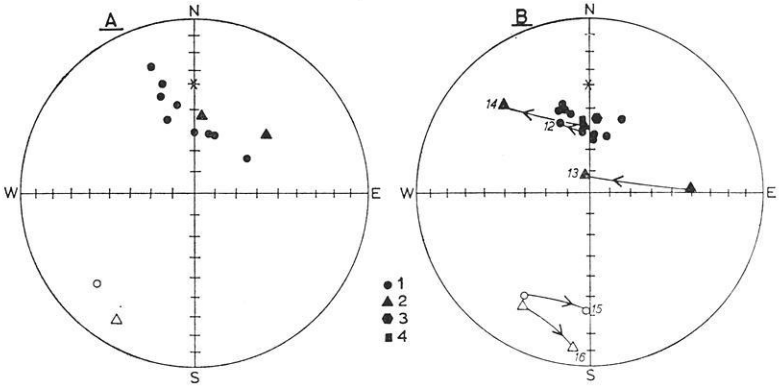

Fig. 1. Stereographic projection of site-mean directions: A initial directions: B after demagnetization treatment. Site-mean directions from sites 12 to 16 are shown before and after correction for the local dip of the strata, both directions combined by arrowed full lines. Dots denote directions pointing downwards, Circles denote directions pointing upwards. The asterisk denotes the present local field direction at the sampling locality, dipping downwards

Legend: 1. Accepted site-mean directions.
2. Site-mean directions excluded for computation of the mean-site direction (sites 13, 14 and 16).
3. Mean-site direction before application of a correction for local dip of the strata.
4. Idem after correction for the local dip of the strata

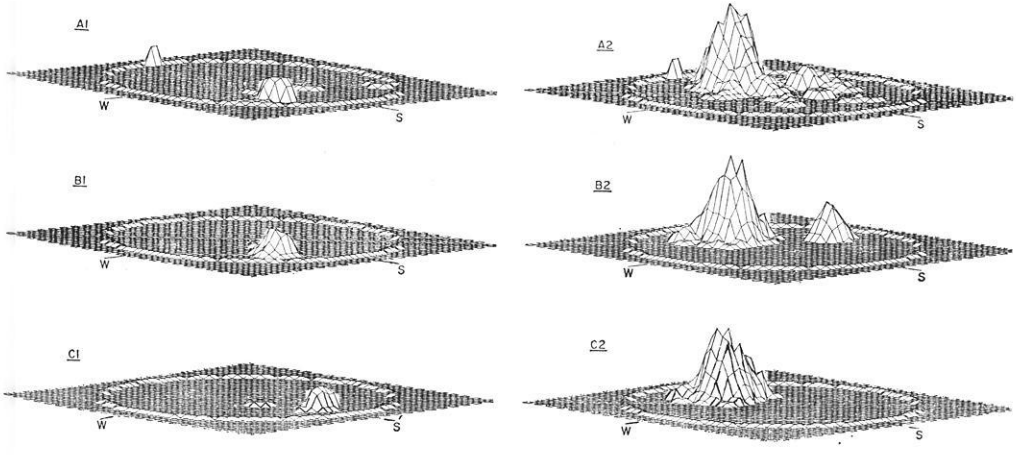

Fig. 2. Density distribution of remanent magnetization directions, represented as a three dimensional perspective view of an equal area projection. The view is taken from the southwest. The rim on the figures represents the outline of the equal-area projection

A1: Initial specimen directions, upper hemisphere.
A2: Idem, lower hemisphere.
B1: Specimen directions after demagnetization treatment, upper hemisphere.
B2: Idem, lower hemisphere.
C1: Specimen directions after demagnetization treatment, and correction for local dip of the strata. Specimens from the rejected sites excluded, upper hemisphere.
C2: Idem, lower hemisphere

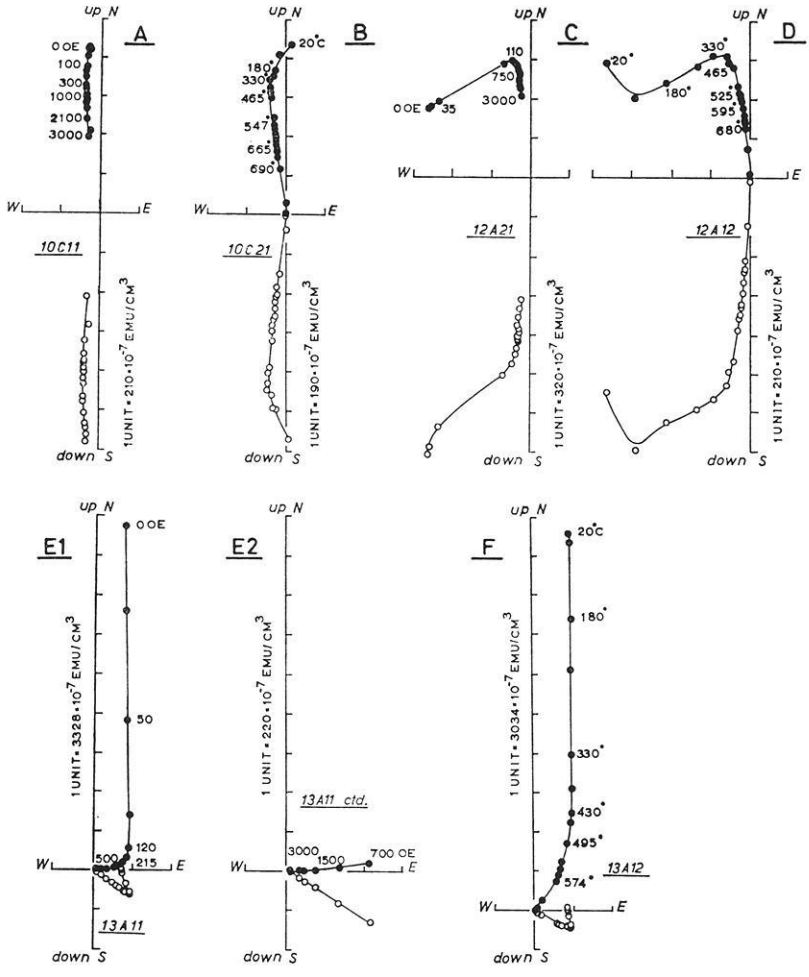

Fig. 3. Demagnetization diagram of specimens cleaned in alternating fields (A, C, E1, E2, G, I, K) or by thermal methods (B, D, F, H, J), The points represent successive positions — in orthogonal projectional — of the end of the resultant magnetization vector during progressive demagnetization. Circles denote projections on the vertical east-west plane. Dots denote projections on the horizontal plane. Numbers denote successive oersted peak values of the applied alternating fields or successive peak values of the applied temperatures. Compare the alternating field and thermal results from both specimens (in most cases specimens from the same sample) from the same site

3E1, 3E2). In this sample the initial intensity of remanence was about 10 times higher than that of the other samples from this site, mainly due to a very large present field like component which constituted about 85% of the initial intensity. The characteristic direction, determined after removal of this present field like component, is of the same intensity and nicely groups with similar characteristic directions from the other samples of this site (Table 1).

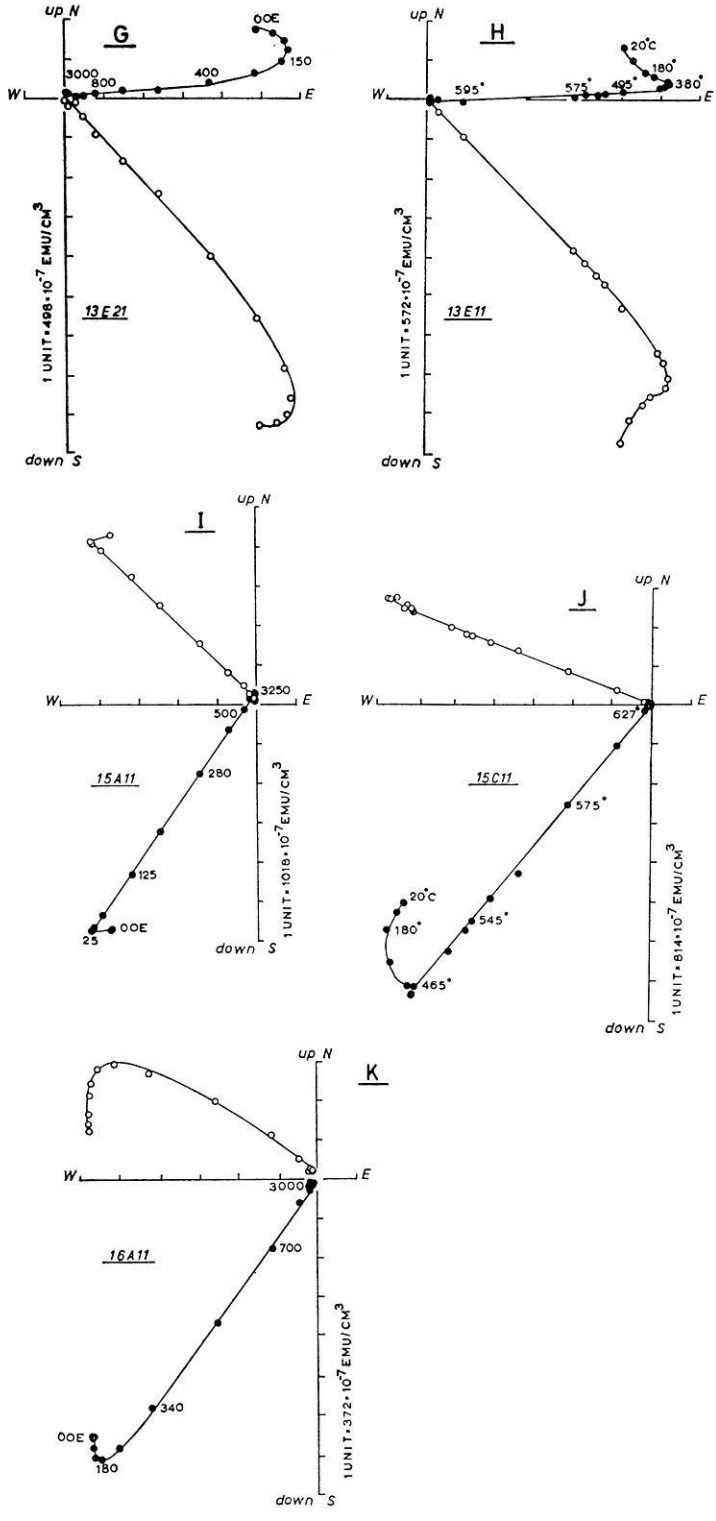
G
up N
W
E
down S
00E
150
400
800
3000
13 E 21
1 UNIT = 498 · 10⁻⁷ EMU/CM³
H
20°C
180°
380°
595°
575°
495°
13 E 11
1 UNIT = 572 · 10⁻⁷ EMU/CM³
I
3250
500
280
125
25
00E
15 A 11
1 UNIT = 1018 · 10⁻⁷ EMU/CM³
J
627°
575°
545°
465°
20°C
180°
15 C 11
1 UNIT = 814 · 10⁻⁷ EMU/CM³
K
3000
700
340
00E
180
16 A 11
1 UNIT = 372 · 10⁻⁷ EMU/CM³

Fig. 3. G-K

In some specimens from sites 7, 12, 14 and 15 dispersed components of slight intensity and probably of viscous origin could be removed up to 50 to 200 Oe peak value (Fig. 3C, 3I). Sites 7, 8 and 14 specimens showed a very fast intensity decrease of the characteristic component (Fig. 4A, 4B). In all studied specimens from the Malani rhyolites an accurate characteristic component could be determined. In case of sites 2, 3, 4, 5, 10, 11 and 12, this component had a rather high coercivity spectrum so that it could not become eliminated completely at 3000 Oe peak value (Fig. 3A, 3C, 3E2, 3G, 3I, 3K), the highest alternating magnetic field available at our laboratory.

Thermal Demagnetization

The normalized thermal intensity decay curves in sites 2, 3, 4, 5, 7, 10, 11 and 12 specimens (Fig. 4C) reveal the existence of a thermally discrete component (Irving and Opdyke, 1965) of great stability which disappears above 650 °C (Fig. 4C). The

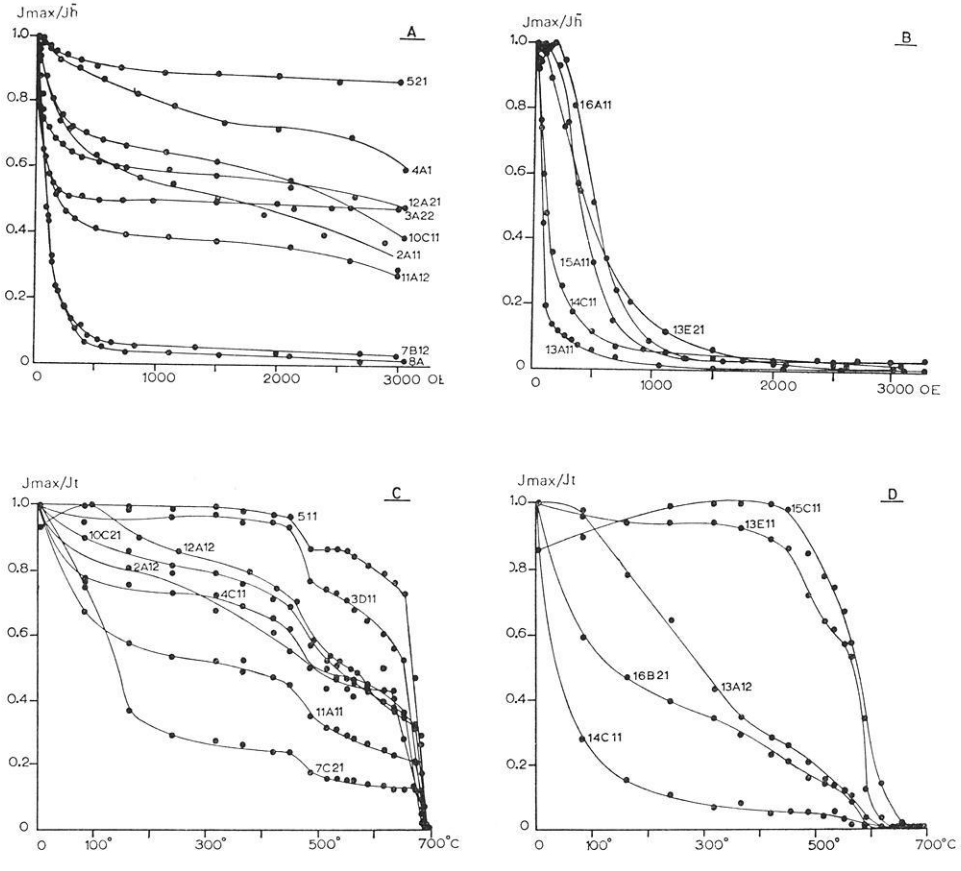

Fig. 4. Normalized intensity decay curves of total remanent magnetization during treatment in alternating fields (A, B) or by thermal methods (C, D). The notable change around 480 °C does not reflect a real magnetization property, but results from inappropriate operation of the temperature registration apparatus

blocking temperature range indicates that hematite is the characteristic magnetization carrier as was to be expected from the high coercivity values for this component as deduced during alternating field studies (Fig. 4A). Pilot specimens from sites 13, 15 and 16 reveal a thermally discrete component with blocking temperatures between 500 °C and 600 °C (Fig. 4D). In accordance with the alternating field results (Fig. 4B) this suggests that in these sites magnetite is probably the characteristic magnetization carrier. Pilot specimens from most of both groups of sites also reveal the existence of a thermally distributed component with a series of blocking temperatures varying between room temperature and 650 °C (Fig. 4C) or 500 °C (Fig. 4D) respectively. The orthogonal demagnetization graphs in analogy with the AF-results reveal that this thermally distributed component can be assigned either to a distinct local field component as shown for a site 13 pilot specimen (Fig. 3F, 3E1, 3E2) or to dispersed components, probably of viscous origin (Fig. 3D, 3C).

The magnetic properties of site 14 specimens form a notable exception. The thermal analysis of specimen 14C11 (Fig. 4D) reveals the existence of a thermally distributed component only, which is easily eliminated during thermal demagnetization or alternating field demagnetization (Fig. 4A). Upon storage in the earth magnetic field this pilot specimen quickly acquires a considerable magnetization component. After alternating field treatment up to 3000 Oe, the intensity of remanent magnetization of this pilot specimen 14C11 was diminished from an initial intensity of 220.10^{-7} emu/cm^3 to 7.10^{-7} emu/cm^3. However, after storage in the earth magnetic field for about 1 month, the intensity of remanent magnetization was increased again up to 140.10^{-7} emu/cm^3. Therefore, the results of the thermal analysis in accordance with the low Q-value (Table 1) and the low stability of magnetic remanence suggest that the characteristic magnetization component in site 14 samples might be of secondary origin as will be discussed later on.

Discussion

The characteristic directions obtained after demagnetization in alternating fields or by thermal methods are in very good agreement with each other as can be seen from the comparable graphs of pilot specimens (Fig. 3) and from the three-dimensional density distribution representation of specimen directions (Fig. 2B1, 2B2). Note the distinctly improved grouping of sample directions after demagnetization treatment (Fig. 2B1, 2B2, Table 1).

Before dip correction the site-mean directions, obtained by giving unit-weight to sample-mean directions, for sites 2 to 12 show a fairly good concentration of normal polarity directions, pointing northwards with a downward dip of about 50 degrees (Fig. 1B). Sites 15 and 16 show mean directions of reversed polarity which, before application of a moderate dip (Table 1) are not exactly opposite to the normal polarity concentration. Note the mean direction of site 13. In this site the internal consistency of the characteristic directions is greatly improved after elimination of a secondary present field component of variable intensity, but before correction for the considerable dip of the strata (Table 1), this mean direction is distinctly aberrant from one of the concentrations mentioned above.

The tectonic position of the flows has been measured by Rutten (1965) from "the parallel, vague, fluidal structure", supposed to be originally subhorizontal in ignim-

brites, and from columnar structures in the flows standing at right angles to the fluidal structure. According to Rutten's field studies, most of the flows were in a subhorizontal position but the flows from sites 12 to 16 appeared to be tilted sometimes up to 70 degrees (Table 1). Therefore, the fold test could be applied to the mean directions from these sites and the resultant configuration is shown in Fig. 1 B. A slight correction only had to be applied for site 12, but after a moderate correction for sites 13, 15 and 16 the concentration and opposite alignment of the normal and reversed groups is decidedly improved (Fig. 1). However, in case of sites 13 and 16 it must be concluded from Fig. 1 B that the tectonic control is not sufficiently accurate. Dip measurements of these flows range between 50 and 70 degrees. So it is clear that slight errors in strike measurements after dip correction will result in considerable deflections of inclination of the palaeomagnetic vector. (Fig. 1 B). Nevertheless, the distinct tendency for improved grouping of site-mean directions after dip correction plainly indicates the fold test to be positive.

It was discussed before that the characteristic magnetization component of site 14 specimens was of very low stability. For this site, the fold test gives a negative result (Fig. 1 B). It must be concluded that the magnetization of this particular site presumably is of secondary origin.

The site-mean directions from sites 13, 14 and 16 are not included in the computation of the mean-site direction. The data from all accepted sites together (Table 1, Fig. 1 B) result in a mean-site direction: $D = 354.5°$, $I = +53.5°$, $\alpha_{95} = 8°$, $N = 10$, which is in very good agreement with the data from Athavale *et al.* (1963): $D = 353°$, $I = +56°$, $\alpha_{95} = 10°$, $N = 9$. The positive fold test result as obtained in the present study, indicates that the characteristic magnetization direction is definitely of pretectonic origin and most probably of primary origin as can be concluded from the agreement with other Precambrian data from the Indian subcontinent (Klootwijk 1974, Fig. 5, Athavale *et al.* 1963, 1970).

Rutten's (1965) field evidence in favour of a general ignimbritic origin of the Malani rhyolites near Jodhpur has been disputed by Mukherjee (1966). It was found by Ellwood and Watkins (1974) that the susceptibility anisotropy data of ignimbrites constitute a notable exception among extrusives. According to their preliminary data, ignimbrites are exceptional in that they are characterized by well grouping principal susceptibility axes. In the present collection of the Malani rhyolite samples, very well grouping principal susceptibility axes were found also. So, following Ellwood and Watkins, these data can be interpreted as further evidence for the ignimbritic nature of the Malani rhyolites in the Jodhpur area. These susceptibility anisotropy data were obtained by means of a rotating sample susceptibility anisotropy bridge, recently constructed at the Palaeomagnetic Laboratory (Mullender and Van den Berg, in preparation: A rotating sample susceptibility bridge), and will be discussed in greater detail elsewhere (Klootwijk *et al.*, in preparation).

Some deflection of the NRM direction due to planar fabric of the Malani rhyolites might be expected. In view of the presumably ignimbritic nature of the Malani rhyolites, we may apply the conclusion reached by Grommé *et al.* (1972) on NRM deflections in the Bishop Tuff ash flow in California (Dalrymple *et al.*, 1965; Grommé *et al.*, 1972). From the uniformity of NRM directions throughout the variably welded Bishop Tuff and its xenolithic inclusions, Grommé *et al.* have concluded that a deflection of NRM due to compaction or welding, does not seem to occur in general

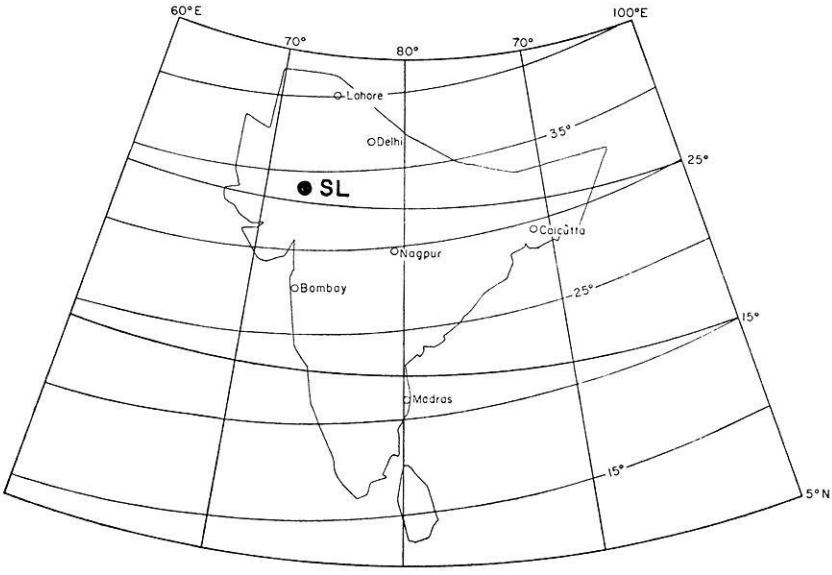

Fig. 5. Palaeolatitude map for the Indian subcontinent as deduced from the Malani rhyolite palaeomagnetic data. The pattern is computed according to the central axial dipole field formulae. SL denotes sampling locality

in ash flows. Welding and compaction in normal ash flows obviously takes place at temperatures above the blocking temperature of the magnetic constituents. This is supported by experimental data from Ross and Smith (1961) who have found welding temperatures between 580° and 750 °C or perhaps 900 °C.

The low value of the susceptibility anisotropy in the Malani rhyolites (generally less than 3%, Table 1) seems to exclude a significant deflection of the NRM direction due to anisotropy effects as well. So the obtained mean-site direction can be taken to represent the ambient magnetic field direction during the time of extrusion.

Interpreted in accordance with other Indian Precambrian data (Klootwijk, 1974), the present result reveals a position and orientation of the Indian subcontinent about 745 my ago, more or less like its present-day orientation. However, at that time, India was situated at a slightly higher latitude, as shown by the palaeolatitude map (Fig. 5).

References

Athavale, R.N., Radhakrishnamurty, C., Sahasrabudhe, P.W.: Palaeomagnetism of some Indian rocks. Geophys. J. *7*, 304–313, 1963

Athavale, R.N., Verma, R.K., Bhalla, M.S., Pullaiah, G.: Drift of the Indian subcontinent since Precambrian times. In: S.K. Runcorn (Ed.) Palaeogeophysics. pp. 291–305, London: Academic Press 1970

Crawford, A.R., Compston, W.: The age of the Vindhyan System of Peninsular India. Quart. J. Geol. Soc. London *125*, 351–372, 1970

Dalrymple, C.B., Cox, A., Doell, R.R.: Potassium-Argon age and Palaeomagnetism of the Bishop Tuff, California. Geol. Soc. Am. Bull. *76*, 665–674, 1965

Ellwood, B. B., Watkins, N. D.: Anistropy of magnetic susceptibility and emplacement modes of submarine igneous rocks. EOS (Trans. Am. Geophys. Union) *54*, 985–986 (Abstract), 1974

Grommé, C. S., McKee, E. H., Blake, M. C.: Palaeomagnetic correlations and Potassium-Argon dating of Middle Tertiary Ash-flow sheets in the Eastern Great Basin, Nevada and Utah. Geol. Soc. Am. Bull. *83*, 1619–1638, 1972

Irving, E., Opdyke, N. D.: The palaeomagnetism of the Bloomsburg red beds and possible application to the tectonic history of the Appalachians. Geophys. J. *9*, 153–167, 1965

Klootwijk, C. T.: Palaeomagnetic data from the Precambrian Gwalior Traps, Central India. Tectonophysics *21*, 181–197, 1974

Mukherjee, A.: Tectonics of Late Precambrian ignimbrites in Western Rajasthan (India)-Discussion. Geol. Mijnbouw *45*, 193–196, 1966

Ross, C. S., Smith, R. L.: Ash-flow tuffs. Their origin, geologic relation and identification. U. S. Geol. Survey. Prof. Paper. 366, 81 p., 1961

Rutten, M. G.: Tectonics of Late Precambrian ignimbrites in Western Rajasthan (India). Geol. Mijnbouw *44*, 316–319, 1965

Zijderveld, J. D. A.: AC-demagnetization of rocks. Analysis of results. In: D. W. Collinson, K. M. Creer, S. K. Runcorn (Eds.): Methods in palaeomagnetism. pp. 254–286 Amsterdam: Elsevier, 1967

C. T. Klootwijk
Geological Institute
State University of Utrecht
Oude Gracht 320
Utrecht, The Netherlands

J. Geophys. 41, 201–213, 1975

An Evaluation Method Combining the Differential Doppler Measurements from Two Stations that Enables the Calculation of the Electron Content of the Ionosphere

R. Leitinger

Institut für Meteorologie und Geophysik, University of Graz, and Institut für Weltraumforschung der Österreichischen Akademie der Wissenschaften

G. Schmidt

Max-Planck-Institut für Aeronomie, Lindau/Harz

A. Tauriainen

University Oulu

Received August 18, 1974

Abstract. Differential Doppler measurements of signals from NNSS Navigational Satellites can be used to give the electron content of the ionosphere. Measurements carried out up to now using data from one station provide limited information about the structure of the ionosphere, since the method relies on an assumption being made about the prevailing ionospheric conditions. If these conditions are not fulfilled, this method can lead to large errors in the predicted electron content. In the method described in this paper, Differential Doppler data from two stations are combined, resulting in considerably more reliable results, particularly when there is strong horizontal structure in the ionosphere, as is often the case in Polar regions. Examples of model calculations and experimental measurements are also included.

Key words: Ionospheric Electron Content – Differential Doppler Effect – Two Station Evaluation – Horizontal Structure.

1. Outline of the Evaluation Method

The satellites of the Navy Navigational Satellite System (NNSS) allow Differential Doppler observations using two coherent signals (nominal frequencies 150 MHz and 400 MHz). The receiving system produces the phase difference between the 150 MHz-signal phase divided by 3 and the 400 MHz-signal phase divided by 8.

For the frequencies of the NNSS beacons, the slant electron content I_s can be considered as a linear function of the measured phase difference ψ (Ebel *et al.*, 1969):

$$\psi + \phi_0 = C_D I_s$$

where ϕ_0 is an unknown initial value, C_D combines all constants, $I_s = \int_B^S N\,ds$, N is the

number density of free electrons, ds is the differential of the straight line B—S from the receiving station B to the satellite S (Fig. 1).

If it is assumed that the ionosphere does not change during the pass of an NNSS satellite, the time can be used as a parameter for the position of the satellite. Then I_s and ψ can be considered to be functions of time. To be able to convert $\psi(t)$ into electron content one first has to find a value for ϕ_0. For this purpose it is necessary to make assumptions on the state of the ionosphere or to use additional measurements.

In both cases one has to use the vertical electron content $I_v = \int_0^{h_s} N\,dh$ (dh: small increment in height above ground; h_s: height of the satellite). Let i be the angle between B—S and the vertical height h (Fig. 1). Then one can write

$$I_s = \int_0^{h_s} \frac{N}{\cos i}\,dh, \text{ where } i = i(h)\,.$$

To convert slant content into vertical content, one has to divide I_s by a factor

$$D' = \frac{\int_0^{h_s} (N/\cos i)\,dh}{\int_0^{h_s} N\,dh}$$

D' can be calculated only if the distribution of electrons along B—S is known. Generally this is not the case and one has to make a reasonable guess at a value for D'. This is done by choosing a "mean ionospheric height" h_i, some tens of kilometers above the height of the maximum of the electron density, h_m (compare among others, references [2], [3]). It can be shown by means of model calculations, that for various realistic electron distributions $(h_i - h_m) = 50$ km is a good choice. In practice it is not necessary to change h_i as a fixed value is good enough for most purposes. The guessed geometrical factor is denoted by the letter D, to distinguish it from the "true" conversion factor D'. D is given by the expression $D = 1/\cos\chi$, where $\chi = i(h_i)$. (Fig. 1).

Once a mean ionospheric height has been assumed, D is calculated for each measured ψ-value, using only the geometrical relations involving the position of the observing station and the position of the satellite.

For the vertical electron content obtained from D, the letter I is used to distinguish it from the "true" electron content I_v over P'; $I_v = \left(\int_0^{h_s} N\,dh\right)_{P'} \cdot P'$ is the "subionospheric point" (projection of the ionospheric point P onto the ground; P is found at the height h_i, on the line B—S. For an undisturbed ionosphere during the daytime, I and I_v will differ by not more than a few percent if the zenithal distance of the satellite, ξ, is not too large. The best agreement will be reached when the shape of the height distribution of electrons is nearly independent of both latitude and longitude, as can easily be shown by model calculations.

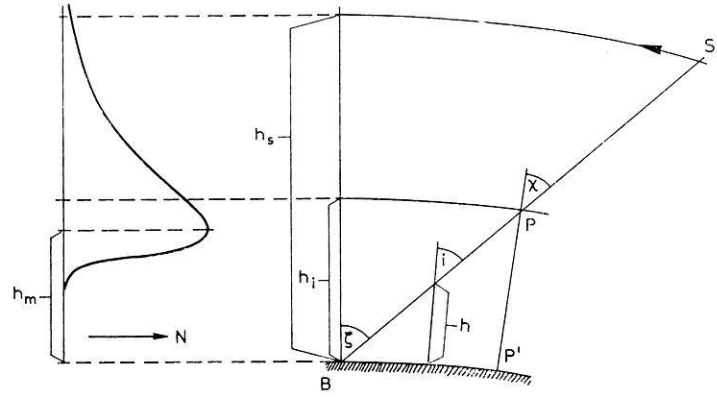

Fig. 1. Geometry receiving station (B) — position of the satellite (S) — ionospheric point (P) — subionospheric point (P'). (h_i: mean ionospheric height, h_m: height of the maximum of the electron density, h_s: height of the satellite)

If no other independent measurements are available then the assumption of a nearly linear "time" — dependence of vertical electron content is the only practicable way of obtaining a solution (time as a parameter for the position of the satellite!). As the NNSS satellites have orbits with a nearly constant longitude (except in the polar region) this means a nearly linear latitude dependence on the (vertical) electron content: $I_v = I_{v0}\ (1 + a\,(\phi - \phi_0))$ (ϕ: geogr. latitude, I_{v0}, a and ϕ_0 are constant). As no physical reasoning can be applied, it makes no sense to base the calculation of ϕ_0 upon a more complicated state of the ionosphere. Some of the restrictions imposed by our assumption can be overcome by using curve fitting methods that include all measured ψ-values in the calculation. By this means, reasonable values can still be obtained provided there is some mean linearity in the time dependence of the electron content in the latitude region under consideration. Several different methods of fitting should be applied simultaneously to check the validity of the basic assumption: if the difference between the results exceeds a few percent, then the ϕ_0-values obtained are certainly not good enough for some purposes, e.g. for the calibration of electron content measurements made with geostationary satellites. If the differences are in excess of 30%, one cannot contribute any significance to the results except for statistical purposes. During nighttime, the evaluation can even give negative values of electron content, which have no meaning at all.

It is impossible to distinguish which fitting method gives the best results if the assumption of a nearly linear latitude dependence of vertical electron content is not fulfilled: no criteria exist to qualify the results. Model calculations show that the "true" results can even be outside the range given by the lowest and the highest values obtained by different fitting methods. In one peculiar situation, all methods give identical wrong results, that is if $I_v = I_{v0}\ (1 + a\,(\phi - \phi_0) + b\cos\chi))$ ($b = \text{const.}$, all other symbols used as above). All fitting methods then give $I_{v0}\ (1 + a\,(\phi - \phi_0))$ neglecting the term $b\cos\chi$. This case can only be recognized when $I_{v0}\ (1 + a\,(\phi - \phi_0))$ reaches negative values in the observed interval of latitudes (s. Fig. 9). One has to draw the conclusion that even results obtained by several fitting methods which show a linear latitude dependence are not always reliable.

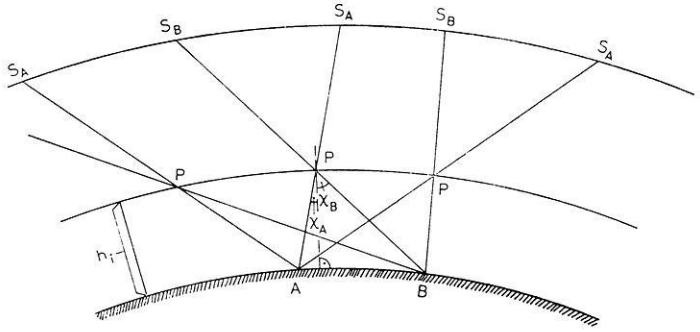

Fig. 2. Geometry for two stations. For simplicity of drawing, it is assumed that the orbit of the satellite and the centre of the earth define a plane, and that the stations A and B are in this plane

The best way to improve the situation is to use additional measurements. As in general no values of vertical electron content from the ground to the height of the satellite, derived from other observations than satellite beacon measurements are available, this can be done by operating a second Differential Doppler station. The combination of the observations is possible if a region in the mean ionospheric height can be seen from both stations (region of overlap).

The method we will describe also has to rely upon the conversion of slant into vertical electron content, but no assumptions are necessary concerning the state of the ionosphere.

In a given subionospheric latitude within the region of overlap, the ionospheric points of the two stations should be as close together as possible. For NNSS satellites this means that the longitude difference of the stations should be as small as possible.

The geometry for the combined evaluation is shown in Fig. 2. For simplicity in the figure, it is assumed that the orbit of the satellite and the centre of the earth define a plane, and that both stations are in this plane. If rays are drawn from the two stations A and B, one can see that a latitude dependence of the electron content introduces an error since

$$\left(\int_A^{S_A} N\,ds_1\right)\cos\chi_1 \neq \left(\int_0^{h_s} N\,dh\right)_{P'} \neq \left(\int_B^{S_B} N\,ds_2\right)\cos\chi_2\,.$$

It can be shown that the differences between the three values are small if the latitude dependence of $\int_0^{h_s} N\,dh$ is not too large and if the shape of the height distribution of electrons is nearly independent of latitude (compare ch. 2). The results of the evaluations will show any serious differences between the three values quite clearly.

For the purpose of outlining our method, it is assumed that both stations give the same electron content. Then for a given subionospheric latitude (index i) the following equations hold

$$\phi_{01} + \psi_{1i} = C_D D_{1i} I_i$$
$$\phi_{02} + \psi_{2i} = C_D D_{2i} I_i$$

The indices 1 and 2 refer to the two stations A and B respectively. For another subionospheric latitude (index j) one has

$$\phi_{01} + \psi_{1j} = C_D D_{1j} I_j$$
$$\phi_{02} + \psi_{2j} = C_D D_{2j} I_j$$

The system of four equations can be solved to give the unknowns ϕ_{01}, ϕ_{02}, I_i, I_j.

Since it cannot be expected that using other pairs of subionospheric latitudes would give exactly the same ϕ_{01} — and ϕ_{02} — values it is advisable to use n subionospheric latitudes simultaneously. One gets n equations for each station:

$$\begin{aligned} \phi_{01} + \psi_{1k} &= C_D D_{1k} I_k \\ \phi_{02} + \psi_{2k} &= C_D D_{2k} I_k \end{aligned} \qquad k = 1, 2, \ldots n$$

A combination of the two equations with index k leads to

$$\frac{\phi_{01}}{D_{1k}} + \frac{\psi_{1k}}{D_{1k}} - \frac{\phi_{02}}{D_{2k}} - \frac{\psi_{2k}}{D_{2k}} = 0$$

The use of all n equations allows to calculate ϕ_{01} and ϕ_{02} when the expression

$$\sum_{k=1}^{n} \left(\frac{\phi_{01}}{D_{1k}} + \frac{\psi_1}{D_{1k}} - \frac{\phi_{02}}{D_{2k}} - \frac{\psi_{2k}}{D_{2k}} \right)^2 \text{ has a minimum value.}$$

This gives a best fit (in the sense of the method of least squares) for ϕ_{01} and ϕ_{02} in the region of overlap. The inevitable scatter of data and some of the effects which arise from the differences in slant electron contents for the two stations are compensated for.

The vertical electron content is calculated with ϕ_{01} and the ψ-values of station A and with ϕ_{02} and the ψ-values of station B for a set of subionospheric latitudes. A comparison of the I-curves for the two stations provides a check on the accuracy of the results.

2. Check by Model Calculations

Model calculations can be used to construct ψ-values for a pass of an NNSS satellite from a given three dimensional distribution of electrons. First the coordinates of the satellite are calculated for a set of n subionospheric latitudes (the difference in latitudes between adjacent subionospheric points is chosen to be 0.5°) and for two

observing stations. Then the slant electron content I_s for each position is calculated by means of numerical integration. I_s is converted into ψ-values using the expressions

$$\begin{aligned} \psi_{1k} &= C_D\, I_{sk} - \bar{\phi}_{01} \\ \psi_{2k} &= C_D\, I_{sk} - \bar{\phi}_{02} \end{aligned} \qquad k = 1, 2, \ldots n$$

Appropriate values for $\bar{\phi}_{01}$ and $\bar{\phi}_{02}$ are assumed. The index k designates the sub-ionospheric latitude. The two sets of ψ-values are then used to calculate ϕ_{01} and ϕ_{02}, using the combination method described above.

With ϕ_{01} and ϕ_{02} and the two sets of ψ-values, one can easily express the results in terms of slant electron content I_s' or of projected vertical electron content $I' = I_s'/D$. (I_s' and I' are used to distinguish the results of the evaluation from the given model values I_s and I).

In the following, only results for one type of model are shown: A Chapman-Elias profile of constant shape was used for the height distribution of electrons, a sinusoidal latitude dependence of electron density was assumed and the longitude dependence was neglected. This gave the following expression for the electron number density

$$N = N_0\,(1 - a\cos[b(\phi - \phi_0])\exp({}^1\!/_2[1 - \zeta - \exp(-\zeta)])$$

with $\zeta = (h - h_m)/H$.

N_0: undisturbed value of the maximal electron density

ϕ : geographical latitude

ϕ_0 : reference latitude

a : amplitude of the disturbance

b : scale factor for the spatial frequency of the disturbance

h : height

h_m : height of the maximum of the electron density

H : scale height

For the examples given in Fig. 3 and in Fig. 4 the following values have been used: $N_0 = 1.0 \times 10^{11}$ m^{-3}, $h_m = 350$ km, $H = 50$ km, $\phi_0 = 51.75°$ N, $a = 0.5$, $b = 100$ (Fig. 3), $b = 25$ (Fig. 4).
Height of the satellite: 1097 km. Position of the stations: station 1: 55.5° N, station 2: 40.5° N.

The orbit of an NNSS satellite was assumed but the excentricity was set to zero (circular orbit). The longitude of the satellite was chosen to be very close to the longitude of the stations. Since the stations have the same longitude, the neglection of any longitude dependence of electron density does not matter. For the model calculations, a mean ionospheric height $h_i = 400$ km was used. The amplitude of the sinusoidal disturbance was exaggerated to demonstrate the following effect: in the projected vertical electron content I, the disturbance is seen nearly unchanged

only in the vicinity of the point of closest approach of the satellite (PCA). If one goes away from PCA, the amplitude of the disturbance appears attenuated and the phase of the disturbance appears shifted. This is an effect resulting from the integration along the line B—S from the receiver to the satellite, which leads to I_s (remember: $I = I_s/D$).

The characteristic scale for this effect is the spatial period of the disturbance. In the region of latitudes seen from the receiving stations, the integration effect is important only for disturbances of small scale. This can be seen clearly by comparing Fig. 3 and Fig. 4: in Fig. 3, a disturbance of comparatively small scale has been used (spatial period: 3.6° of latitude), for Fig. 4, the scale was four times larger (spatial period 14.4° of latitude). The figures show the projected vertical content I vs. subionospheric latitude. In Fig. 3 one period of the given sinusoidal I_v is shown on the right margin. The minima of the given I_v are indicated in Figs. 3 and 4 by vertical bars below the I-curves. The location of each station is also indicated.

The comparison of more material from model calculations leads to the conclusion that the large scale component of the latitude dependence of true vertical electron content is seen in the converted slant electron content to be nearly unaffected by the integration effect. Therefore, the large scale structure of the vertical electron content from Differential Doppler observations is realistic, if the evaluation process produces good ϕ_0-values. The small scale structure can be seen only in the vicinity of the PCA. The results from two stations should show the same large scale structure, but will have differences in the small and medium scale structure, when such a structure exists.

Some of the results of our model calculations in respect to the accuracy of ϕ_0-values obtained by the combination method are briefly summarized: In the case of Fig. 3 (sinusoidal structure of the ionosphere, spatial period 3.6°, relative amplitude of the disturbance: 0.5) our method of combined evaluation for two stations gives for the PCA, a relative error $(I' - I)/I$ of 5.4% for the minimum, and of 1.8% for the maximum of the disturbance. In the case of Fig. 4 (sinusoidal structure of the ionosphere, spatial period 14.4°, relative amplitude of the disturbance 0.5) the values are 5.9% and 2.9%. The relative error is reduced if the amplitude of the disturbance is smaller.

3. Some Results

To illustrate the use of our method of combined evaluation for two receiving stations, some results are shown in the following figures. The stations are Graz (47.08° N, 15.49° E), Lindau (51.62° N, 10.09° E) and Oulu (65.11° N, 25.48° E). There is a difference in longitudes between the stations and in interpreting the results this fact must be taken into account. If a significant longitude dependence of electron content exists, the values along the traces of the subionospheric points of the two stations are different. Our method will then give average values.

Fig. 5 shows very good agreement between the I-curves obtained by the combination method north of 48° N. A small scale structure exists, and can be seen a bit south of the PCA of the corresponding station. The large scale structure is nearly linear and therefore the results for single station evaluations (indicated by vertical bars in the figure) agree very well, and are very close to the results of the combined evaluation. Fig. 6 shows a map with the projection of the orbit of the satellite and

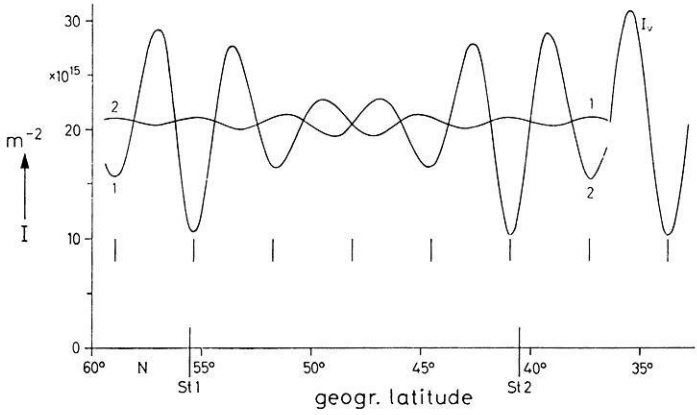

Fig. 3. Results of model calculations: vertical electron content I converted from slant content vs. subionospheric latitude for a sinusoidal disturbance of the ionosphere. Spatial period of the disturbance: 3.6°. On the right margin one period of the given (true) vertical content I_v is shown. The minima of I_v are indicated by vertical bars below the I — curves. The location of the two receiving stations is indicated (St 1, St 2). Curve 1 belongs to station 1, curve 2 to station 2

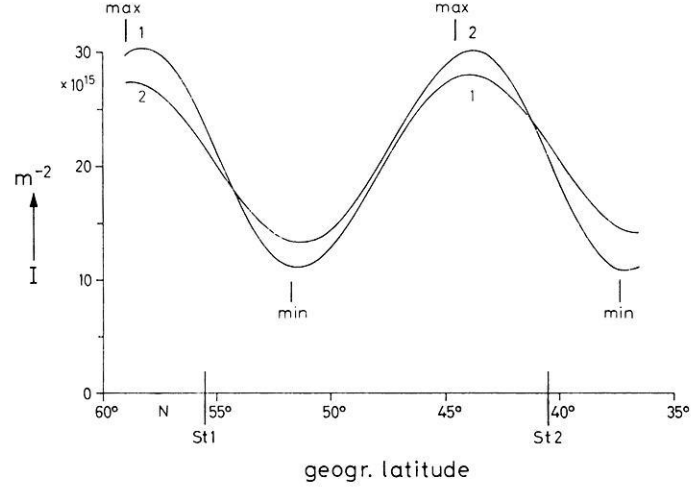

Fig. 4. Results of model calculations as in Fig. 3 but spatial period of the disturbance 14.4°. Again, the minima of the given vertical content I_v are indicated by vertical bars

with the traces for the subionospheric points for Graz (IG) and for Lindau (IL). Another example with a clear small scale structure is shown in Fig. 7. The deviation from a nearly linear large scale structure leads to greater differences between the single station evaluations for Lindau, but the agreement is still quite good.

Figure 8 shows the results obtained from 5 passes of NNSS satellites on the same day. It should be noted that during nighttime, the single station evaluations for Lindau cannot give reliable values: there is a strong deviation from a nearly linear latitude dependence. (For simplicity of drawing, no single station results are shown).

A very interesting case is shown in Fig. 9: there is no significant small scale structure, but the large scale structure has a distinct maximum in 47.5° N and a distinct minimum in 64° N. For Graz, the formula $I = I_0\,(1 + a\,(\phi - \phi_0) + b \cdot \cos\chi)$ would fit the results very well. Therefore, the single station evaluations give completely wrong values, since they neglect the term $b \cdot \cos\chi$. In this case, the situation can be guessed because the (wrong) straight line fitted by the single station evaluations gives negative values of electron content north of 55° N. For Lindau too, the large scale structure does not allow good single station evaluations.

In Fig. 10, an example is shown for the combination of measurements from Oulu, Lindau and Graz. Agreement between Lindau and Oulu and between Graz and Lindau is quite good but the combination Graz—Oulu gives significantly higher values. This could be an effect of the difference in longitudes (c. Fig. 11) but one should also bear in mind that the region of overlap between Graz and Oulu is only short and that the combination Lindau—Oulu shows medium scale differences of considerable amplitude. These differences could again be the result of the different subionospheric longitudes. The single station evaluations do not help in the interpretation of results: the differences between the results for Oulu are by far too large to allow any conclusions to be made, and the single station evaluations for Graz and for Lindau agree very well with the results of the combinations Lindau—Oulu and Graz—Lindau. It can be seen from the map in Fig. 11 that the geographical situation for the three stations is complex.

4. Conclusion

In many cases the accuracy of Differential Doppler evaluations can be considerably improved if the measurements from two stations are combined. This method does not depend on the assumption of a nearly linear latitude dependence of the vertical electron content (or on the a priori assumption of another special structure of the ionosphere). To give the best results, the difference in the longitudes of the two stations should be as small as possible in the case where NNSS satellites, which have polar orbits, are used. The difference in latitudes can range from about 2 to 20 degrees. If it is too small, there is some danger of numerical instability. If it is too large, the region of overlap may be too small to provide a good fit.

One important advantage of NNSS observations should be mentioned: the Differential Doppler results can give a very good representation of the latitude dependence of the electron content in the large scale, if a good value for the constant ϕ_0 can be found. In general we have found that the described combination method gives results which are much better than the results which can be achieved when the data from only one station are used.

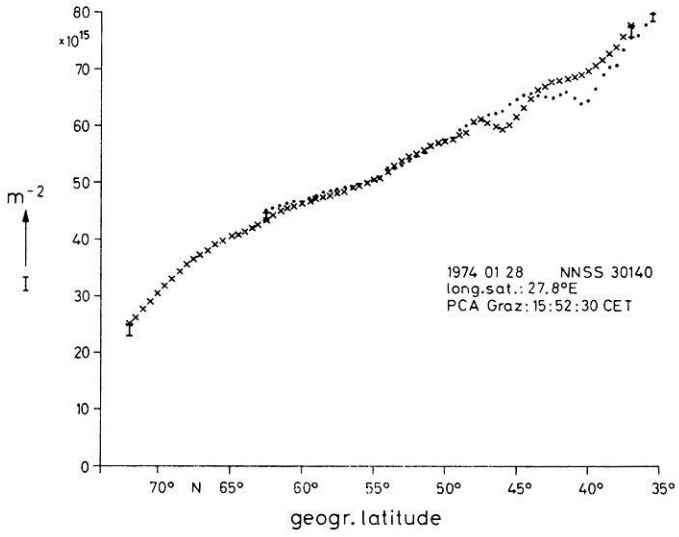

Fig. 5. Results of the combined evaluation for Graz (47.08° N, 15.49° E) and Lindau (51.62° N, 10.09° E). The characteristics of the pass of the NNSS-satellite used, are given in the drawing. (Date in year, month, day; number of the satellite; longitude of the satellite for 50° N; time, when the point of closest approach for Graz was reached in hours, minutes, seconds [UT + 1 hour]). Electron content vs. subionospheric latitude. Values from the combined evaluation: crosses for Lindau, dots for Graz. The range of values from single station evaluations, by means of three different methods, are indicated by vertical bars at the ends of each trace

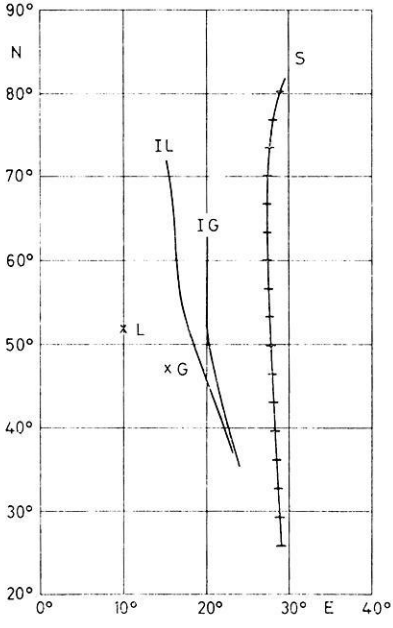

Fig. 6. Map showing the projection of the satellite orbit (*S*), the stations Lindau and Graz (L, G), the traces of the subionospheric points for Lindau (IL) and Graz (IG). Time marks on the satellite orbit every minute, beginning at 15:46 CET (south-north pass)

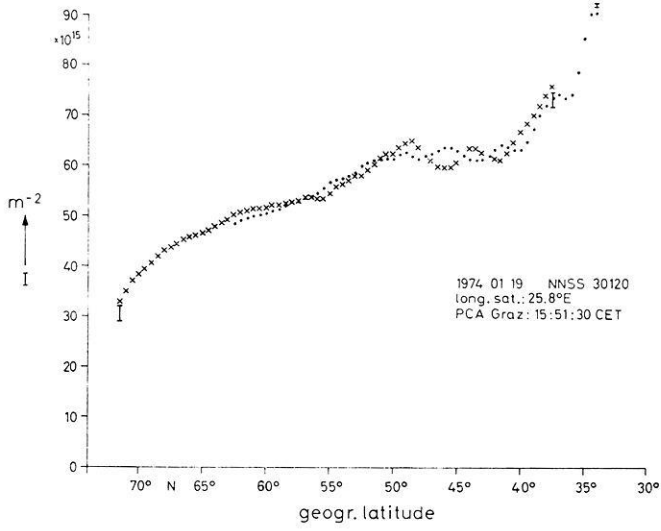

Fig. 7. Results of combined evaluation Graz — Lindau. Symbols as in Fig. 5

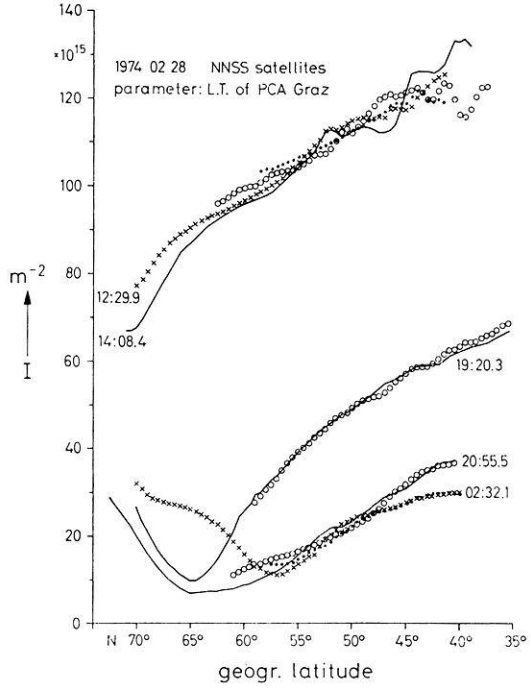

Fig. 8. Results obtained from 5 passes of NNSS satellites on the same day. Combined evaluation Graz — Lindau. Electron content vs. subionospheric latitude. Crosses or solid lines for Lindau, dots or circle for Graz. The local time (L.T.) (hours and minutes) is given for a subionospheric latitude of 50° N (station Graz)

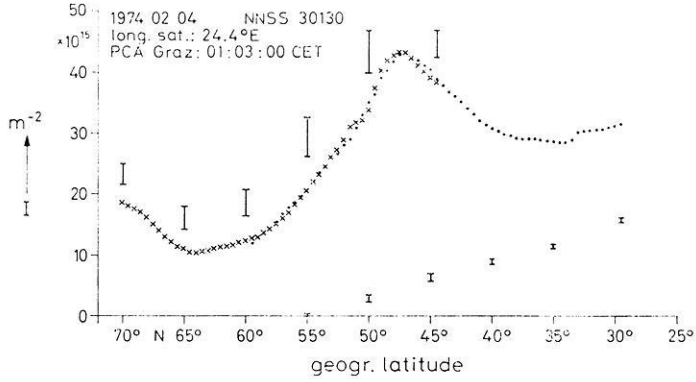

Fig. 9. Results of combined evaluation Graz — Lindau. Symbols as in Fig. 5. Bars above the curves for single station results from Lindau. Bars below the curves for single station results from Graz

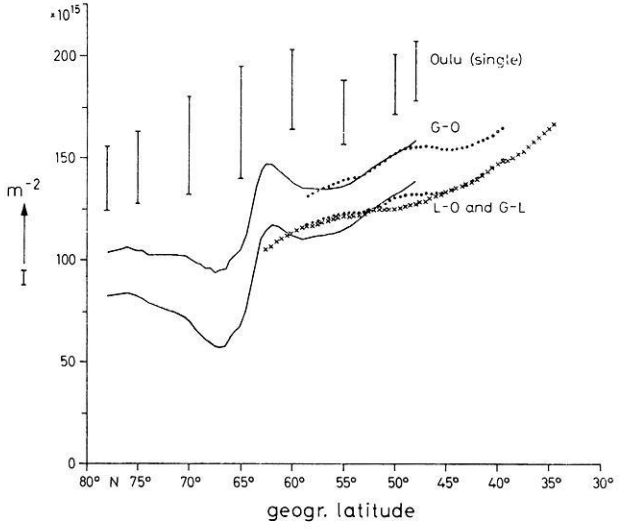

Fig. 10. Results of the combined evaluation for Lindau — Oulu (L—O, crosses for Lindau, solid line for Oulu), for Graz — Lindau (G—L, dots for Graz; the results for Lindau are not shown, as they were only slightly above the crosses of L—O), for Graz — Oulu (G—O, dots for Graz, solid line for Oulu). Electron content vs. subionospheric latitude. Bars above the curves correspond to single station results from Oulu. Characteristics of the satellite: NNSS 30190 on April 11, 1974. PCA Graz: 16:03:30, PCA Lindau: 16:02:20, PCA Oulu: 15:58:00 (all in hours:minutes:seconds CET). The geometry is shown in Fig. 11

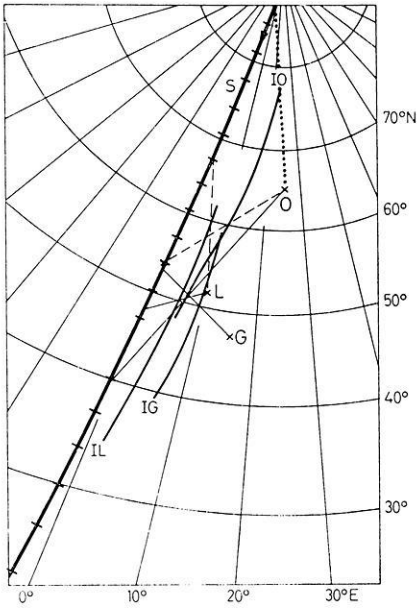

Fig. 11. Map showing the projection of the satellite orbit (*S*), the stations Oulu (O), Lindau (L) and Graz (G), and the traces of the subionospheric points for Oulu (IO), for Lindau (IL) and for Graz (IG). The characteristics of the satellite are given in the caption of Fig. 10. Timemarks on the orbit of the satellite are shown for each minute, beginning at 15:53 CET. Projections of the straight line from a receiving station to the satellite are shown for a subionospheric latitude of 50° N (all three stations, solid lines) and for a subionospheric latitude of 60° N (stations Oulu and Lindau, dashed lines). The projection for the map is gnomonic, centered on Oulu

Acknowledgement. We wish to thank Mag. rer. nat. E. Putz for the reading of the registrations made in Graz and in Oulu and for his help in preparing computer programs.

The support of the Fonds zur Förderung der wissenschaftlichen Forschung in Österreich who financed the construction of the measuring equipment used in Graz is gratefully acknowledged.

All calculations have been made on the UNIVAC 494 of the Rechenzentrum Graz.

References

Ebel, A., Hartmann, G., Leitinger, R., Schmidt, G., Schödel, J. P.: Vergleichende Auswertung von Faraday-Effekt-Beobachtungen zweier Empfangsstationen. Z. Geophys. *35*, 373–411, 1969

de Mendonça, F.: Ionospheric electron content and variations measured by doppler shifts in satellite transmissions. J. Geophys. Res. *67*, 2315–2337, 1962

Ross, W. J.: Second-order effects in high-frequency transionospheric propagation. J. Geophys. Res. *70*, 597–612, 1965

Dr. R. Leitinger
Institut für Meteorologie
und Geophysik der Universität
A-8010 Graz/Austria

Dr. G. Schmidt
Max-Planck-Institut für Aeronomie
D-3411 Lindau/Harz
Federal Republic of Germany

A. Tauriainen
University of Oulu
Oulu/Finland

J. Geophys. 41, 215–218, 1975

Short Communications

Measured and Calculated Secondary Electron Energy Spectra (20 - 1500 eV) above 120 km

A. Loidl and K. Schlegel

Max-Planck-Institut für Aeronomie
Lindau/Harz

Received September 10, 1974

Key words: Photoelectrons — Energy Spectra — Rocket Measurements — Monte Carlo Simulation.

In February and May 1973 three sounding rockets were launched in the scope of the "AEROS-Support-Rocket-Program" which carried a combined payload of 5 (in one case 6) experiments to record vertical profiles of aeronomical parameters. Besides neutral and ion composition, electron density, airglow and thermal electron flux, the energy spectrum of electrons in the range of 20 to 1500 eV was measured by a cylindrical plate analyzer device developed by the authors. Whilst an integrated data evaluation of all the experiments of these flights will be presented in a future paper, a special aspect of the electron energy spectra measurements — the comparison with Monte-Carlo calculations — should be reported here.

The data presented here were measured during two of the three flights, from one flight the data could not be evaluated because of a defect in the payload-system. Some characteristics of the successful flights are summarized in Table 1.

The cylindrical plate analyzer as an energy filter is widely used to measure energy spectra of charged particles and should not be described here in detail therefore (c. f. Hughes and Rojansky, 1929). In the range from 20 to 1500 eV the electron flux

Table 1. Data of the rocket flights

Flight	NATAL	ANDOYA I
Range Place	Natal (Brazil)	Andoya (Norway)
Latitude	5° 55′ 19″ S	69° 17′ 33″ N
Rocket Name	Black Brant Vc	Black Brant Vc
Apogee	308 km	306 km
Date	Feb. 1, 1973	May 12, 1973
Time	14.33 LT	13.42 LT
Solar zenith angle	39°	52.8°
Solar activity (F 10.7)	91	85
Magnetic activity Kp	3+	2
local (ΔB_Z)	—	$< 20\,\gamma$

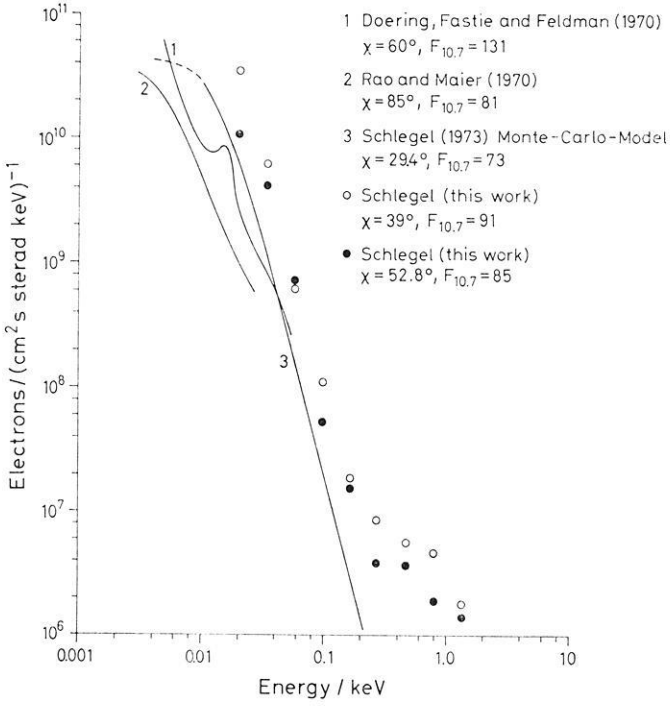

Fig. 1. Comparison of electron energy spectra measured and calculated by these authors and results of other authors.
○ flight NATAL, 306 km altitude
● flight ANDOYA I, 298 km altitude

was recorded in 9 logarithmicaly spaced energy channels with a width of $\frac{\Delta E}{E} = \pm 6\%$. The electrons having passed the analyzer were detected with a continuous channel electron multiplier (channeltron). Details of the experiment are described in an internal report (Loidl and Schlegel, 1972). The experiment was looking perpendicular to the rocket spin axis and the sample time of one energy interval was matched to the spin frequency of the rocket providing an integration over an azimuth angle of 2π. It took 2.56 s to record one energy spectrum consisting of 9 counting rates of 9 energy channels and a reference value.

Typical energy spectra for the flights ANDOYA I and NATAL are shown in Fig. 1 (full and open dots). The shapes of the spectra were remarkably constant over the hight range from about 180 km to the apogee and the counting rates exhibit few scatter in the energy range from 20 to about 400 eV. The slope of the energy spectra in this range in a double logarithmical scale was $-(3.78 \pm 0.08)$ for the flight NATAL and $-(3.0 \pm 0.1)$ for the flight ANDOYA I. Below 180 km the slopes decreased in both cases. At 130 km (the minimum measuring altitude) it was approximately -2.4 for the flight NATAL and approximately -1.9 for the flight ANDOYA I.

The different slopes of the energy spectra for the two flights are probably a consequence of the different solar zenith angles at the flight time (c. f. Table 1). That means the electrons of this energy range are mainly photoelectrons or secondaries produced

by photoelectrons. For comparison the photoelectron spectra measured by other authors (Doering, Fastie and Feldman, 1970; Rao and Maier, 1970) are plottet in Fig. 1. The agreement is reasonably good taking into account the different solar activities (characterized by $F_{10.7}$) and solar zenith angles. Recent measurements of photoelectron energy spectra are also in the same order of magnitude (Hays and Sharp, 1973; Mukai and Hirao, 1973).

The solid curve in Fig. 1 represents a special result of a Monte-Carlo simulation of a model ionosphere (Schlegel, 1974). Since this Monte-Carlo model is described elsewhere in detail (Schlegel, 1971; Schlegel, 1973) only its input parameters should be mentioned here again. Besides solar activity and the solar zenith angle these are density profiles of O, O_2, N_2, the electron density profile, the solar UV and EUV spectrum, the earth magnetic field and several reaction rate cross sections. Comparing the calculated curve with our measured values yields that the slope of the Monte-Carlo curve (-3.7) is in very good accordance with the slope of the measured energy spectra, but the absolute values are too low by a factor of 5. Since the solar activity and the solar zenith angle are not too much different in the case of the Monte-Carlo simulation and at the time of the rocket flights, the factor 5 hardly could be a sole consequence of this small difference. That means that either the input parameters of the Monte-Carlo model are too far away from the real atmospheric conditions during the rocket flights or that the absolute values of the measured energy spectra are too high. Probably both is true. On the one hand the exact calibration of an electron energy analyzer in this energy range is very difficult and thus the absolute values of the electron flux may be wrong by a factor of 2. On the other hand the fact that the input parameter of the model do not fit the atmospheric conditions at the flight time could led to considerable errors in the calculated energy spectra. Specially the density profiles of O, O_2 and N_2 and the solar UV und EUV spectrum have a great influence on the photoelectron spectrum. The model itself could not be too far from reality because of the reliable results with respect to other ionospheric parameters (Schlegel, 1971; Schlegel, 1973). Possibly the integrated data evaluation of all experiments of the flights could provide some data to improve the input parameter set of the model.

Acknowledgements. The authors thank Mr. Kellner for his assistance in building the equipment. The paper is published by permission of Prof. Dieminger, the director of the Max-Planck-Institut für Aeronomie.

References

Doering, J.P., Fastie, W.G., Feldman, P.D.: Photoelectron excitation of N_2 in the day airglow. J. Geophys. Res. *75*, 4787, 1970

Hays, P.B., Sharp, W.E.: Twilight airglow, 1. Photoelectrons and [OI] 5577 — angstrom radiation. J. Geophys. Res. *78*, 1153, 1973

Hughes, A.L., Rojansky, V.: On the analysis of electronic velocities by electrostatic means. Phys. Rev. *34*, 284, 1929

Mukai, T., Hirao, K.: Rocket measurement of the differential energy spectrum of the photoelectrons. J. Geophys. Res. *78*, 8395, 1973

Narasinga Rao, B.C., Maier, E.J.R.: Photoelectron flux and protonospheric heating during the conjugate point sunrise. J. Geophys. Res. *75*, 816, 1970

Schlegel, K.: Photoionization yields of O, O_2 and N_2 for high and low solar activity. J. Atmospheric Terrest. Phys. *33*, 1923, 1971

Schlegel, K.: Monte Carlo simulation of a model ionosphere — II. Energy flow and energy dissipation. J. Atmospheric Terrest. Phys. *35*, 415, 1973
Schlegel, K.: Monte Carlo simulation of a model ionosphere — III. Photoelectron and escape electron spectra. J. Atmospheric Terrest. Phys. *36*, 183, 1974

Dr. Alfred Loidl
Dr. Kristian Schlegel
Max-Planck-Institut für Aeronomie
D-3411 Katlenburg-Lindau 3
Postfach 20
Federal Republic of Germany

Book Reviews

Cospar Space Research XII
Berlin: Akademie-Verlag 1972, 2 Bände, insgesamt 1815 Seiten, 260.00 M.

Die 12. Ausgabe von Space Research enthält 193 Vorträge, die auf der 14. Plenartagung von COSPAR (The Committee on Space Research) gehalten worden sind; diese Tagung fand vom 21. Juni 1971 bis zum 2. Juli 1971 in Seattle, Washington, USA, statt. In dieser großen Zahl von Beiträgen sind auch Arbeiten eingeschlossen, über die am gleichen Ort auf dem „Symposium on dynamics of the thermosphere and ionosphere above 120 km" (24. bis 26. Juni 1971) und dem „Symposium on high angular resolution astronomical observations from space" (28. Juni bis 1. Juli 1971) referiert worden ist.

Space Research XII, das S. A. Bowhill, L. D. Jaffe und M. J. Rycroft herausgeben, gliedert sich in zwei Bände. Der erste Band umfaßt alle Beiträge über den Mond, die Venus und den Mars, den kosmischen Staub, die vom Weltraum aus beobachtete Erde und die neutrale Atmosphäre der Erde. Im zweiten Band sind alle Referate zusammengestellt, die die Dynamik der Thermo- und Ionosphäre oberhalb 120 km, die Ionosphäre, die polare Ionosphäre und das Ausfallen von „low energy charged particles", die solar-terrestrischen Beziehungen, die Astronomie und astronomische Beobachtungen vom Weltraum aus mit großer Winkelauflösung betreffen.

Die großen Kapitel sind jeweils in mehrere Abschnitte unterteilt; dadurch wirkt dieser Tagungsbericht sehr übersichtlich. Er enthält sehr viele interessante Vorträge, die klar und verständlich geschrieben sind. Wenn man aber einigermaßen gerecht urteilen will, kann man keinen einzelnen hervorheben; alle stellen nämlich äußerst wertvolle Beiträge über den Stand der Weltraumforschung im Jahr 1971 dar. Space Research XII sollte deshalb in keiner naturwissenschaftlichen Bibliothek fehlen.

H. Mayer, Karlsruhe

Cospar Space Research XIII
Berlin: Akademie-Verlag, 1973, 2 Bände, insgesamt 1198 Seiten.

Space Research XIII wird von M. J. Rycroft und S. K. Runcorn herausgegeben und enthält Vorträge über Probleme der Weltraumforschung und der damit zusammenhängenden Physik; sie sind auf der 15. Plenartagung von COSPAR (The Committee on Space Research) in Madrid (10. bis 24. Mai 1972) gehalten worden. Space Research XIII beschäftigt sich neben der Erforschung des äußeren Weltraums auch mit der Verwendung von Raumfahrzeugen und „Remote Sounding"-Plänen zur Erkundung von verschiedenen Teilen der Erdatmosphäre und -oberfläche.

Space Research XIII besteht, wie auch schon früher XI und XII, aus zwei Bänden. Im ersten Band sind alle Vorträge der Themenkreise „Tracking of Artifical Earth Satellits", „Remote Sensing of the Earth", „The Neutral Atmosphere", „Dynamics of the Thermosphere and Ionosphere" und „The Ionosphere" zusammengefaßt. Der zweite Band enthält Referate aus den Gebieten „The Magnetosphere", „The Sun", „Astronomical Measurements", „The Moon" und „Cosmic Dust".

Wie bei den zwei anderen, aus dem Akademie-Verlag stammenden Ausgaben von Space Research (XI und XII), sind auch bei Space Research XIII die großen Abschnitte mehrmals unterteilt. Die einzelnen Beiträge setzen zwar gewisse Kenntnisse voraus; aufgrund ihrer klaren Form können sie aber ohne große Schwierigkeiten verstanden werden. Die ausgezeichneten Literaturverzeichnisse ermöglichen es u. a., die abgedruckten Vorträge als Ausgangspunkte neuer Arbeiten zu verwenden. Der Akademie-Verlag hat den wertvollen Inhalt der zwei Bände von Space Research XIII wieder so gut dargestellt, daß man sie auch deshalb nur empfehlen kann. Space Research XIII ist ein Tagungsbericht, von dem man mit gutem Gewissen behaupten kann, es lohne sich, ihn zu lesen und in der Nähe zu wissen.

H. Mayer, Karlsruhe

J. Frisius: *Vektorrechnung — kurz und bündig.* Kamprath-Reihe Grundwissen. Würzburg: Vogel 1973, 176 Seiten, 66 Abb. (2farbig), kartoniert DM 22,80.

Dieses Buch ist hauptsächlich für Studierende der Naturwissenschaften gedacht und soll ihnen den Übergang von der elementaren Mathematik zu den Methoden der theoretischen Physik erleichtern. Vorausgesetzt werden nur die mathematischen Grundkenntnisse, die an Gymnasien vermittelt werden, wie z. B. elementare Algebra, elementare Geometrie und ebene Trigonometrie, analytische Geometrie und Grundbegriffe der Differential- und Integralrechnung. „Vektorrechnung — kurz und bündig" baut auf geometrischer Anschauung auf und ist an physikalischen Anwendungen orientiert; deshalb sollte der Leser auch Kenntnisse in der elementaren Experimentalphysik besitzen.

Das Buch ist in neun große Kapitel eingeteilt: 1. Darstellung von Punkten durch Koordinatensysteme, 2. Darstellung von Vektoren in kartesischen Koordinatensystemen, 3. Produktartige Verknüpfung zwischen Vektoren, 4. Matrizen, 5. Orthogonale Transformationen, 6. Veranschaulichung von Tensoren durch Kurven und Flächen zweiter Ordnung, 7. Differentiation von Vektoren und Einheitsvektorsystemen nach einer skalaren Variablen, 8. Räumliche Differentialoperationen an Skalar- und Vektorfeldern in kartesischen Koordinaten und 9. Differentialoperationen in krummlinigen, orthogonalen Koordinaten. In den jeweils zahlreichen Unterabschnitten enthält das Buch die wesentlichen Grundzüge der Vektorrechnung. Es muß nicht in der Reihenfolge der Kapitel sondern kann auch in abgekürzter Form durchgearbeitet werden; dazu gibt der Autor im Vorwort einige Anweisungen.

Die Darstellungsart des Buches ist sehr ansprechend; die inhaltlichen Schwerpunkte sind durch Fettdruck oder Umrandung hervorgehoben, dadurch wirkt das Buch sehr klar und verständlich. Es erfüllt vollständig den zu Beginn genannten Zweck und stellt wegen seiner übersichtlichen Form auch ein wertvolles, kleines Nachschlagewerk über die Vektorrechnung dar. Das Buch kann deshalb sowohl den angehenden als auch den ausgebildeten Naturwissenschaftlern sehr empfohlen werden.

H. Mayer, Karlsruhe

J. Geophys. 41, 221–232, 1975

Original Investigations

The Behaviour of Minor Species in the Solar Wind*

J. M. Ryan

Physics Dept., University of California, Riverside

W. I. Axford

Max-Planck-Institute for Aeronomy, Lindau/Harz

Received January 2, 1975

Abstract. The flow of minor species in the solar wind is considered on the basis of a model in which all species are heated in an arbitrary manner as they leave the Sun and the minor species interact with the background proton-electron plasma through the radial electric field associated with the latter and by means of Coulomb collisions. In order to produce satisfactory results in which the ions all move at more or less the same speed at the orbit of the Earth, it is necessary to introduce heating functions such that each species is given energy in proportion to its mass. Coulomb collisions are found to be important as a means of removing energy from the heavier species close to the Sun and bringing all species closer to thermal equilibrium at great distances from the Sun. Substantial velocity differences can occur between species, especially close to the Sun. Furthermore it is not difficult to construct solutions in which the bulk velocity of the helium ions exceeds that of the solar wind, as is often observed.

Key words: Coronal Heating – Solar Wind – Minor Species.

1. Introduction

The solar wind is a fully ionized plasma comprised mainly of protons, electrons and alpha particles, but also containing small amounts (less than about 0.1% by mass) of hevier elements which in most cases are not fully ionized. The relative abundance of helium to hydrogen ions varies from $<1\%$ to $>25\%$ by number, being on the average about 4%, which is significantly different from the photospheric ratio (Neugebauer and Snyder, 1966; Wolfe *et al.*, 1966; Hundhausen *et al.*, 1967a; Bame *et al.*, 1968; Ogilvie and Wilkerson, 1969; Robbins *et al.*, 1970; Formisano *et al.*, 1970; Danziger, 1970; Formisano and Moreno, 1971; Bame, 1972; Hirshberg, 1972, 1973; Hirshberg *et al.*, 1972, 1974). The relative abundances of heavier ions are also variable and differ from the expected photospheric abundances (Bame *et al.*, 1968, 1970; Bühler *et al.*, 1969; Geiss *et al.*, 1970a; Hundhausen, 1970; Bame, 1972).

In the vicinity of the Earth's orbit the plasma is usually not in thermal equilibrium. For example the electron temperature is typically of the order of $1–2 \times 10^5$ °K whereas the proton temperature is typically $10^4–10^5$ °K and on the average is about 4×10^4 °K (Strong *et al.*, 1966; Neugebauer and Snyder, 1966; Hundhausen *et al.*, 1967abc, 1970; Coon, 1968). Furthermore the proton thermal distribution is usually anisotropic with the parallel temperature generally exceeding the perpendicular

* Dedicated to Professor Georg Pfotzer with best wishes for his 65th anniversary.

temperature. There is evidence that the thermal velocities of different species are often comparable, so the temperatures of the species are then roughly proportional to their atomic mass (Neugebauer and Snyder, 1966; Wolfe *et al.*, 1966; Hundhausen *et al.*, 1967; Ogilvie and Wilkerson, 1969; Robbins *et al.*, 1970; Formisano *et al.*, 1970). Furthermore it has recently been confirmed that the bulk velocity of the helium component commonly exceeds that of the protons by as much as 5—10% (Formisano *et al.*, 1970; Bollea *et al.*, 1972; Asbridge *et al.*, 1973; Ogilvie and Zwally, 1972; Hirshberg *et al.*, 1974). There is no reason not to expect that similar velocity differences are prevalent in the case of other species.

In this paper we describe the results of calculations based on a model for a multi-fluid solar wind designed to elucidate some of the phenomena outlined above. The model differs in some essential aspects from previous models discussed by Jokipii (1966), Geiss *et al.* (1970b); Nakada (1970) and Alloucherie (1970). In contrast to the earlier work we make no assumptions concerning the temperatures of the different components of the solar wind, but instead use complete equations of motion for each species, including an energy equation. Heat sources are invoked as a means of simulating the presumed heating of the corona resulting from the damping of hydromagnetic or other waves (e.g. Konyukov, 1967; Holzer and Axford, 1969, 1970; Hartle and Barnes, 1970). We have also taken into account the effects of Coulomb collisions between protons and heavier ions which lead to an exchange of energy as well as momentum.

We have been forced to make several simplifying assumptions, which will need to be considered more carefully in future work. Firstly, we assume (as have most other workers) that the solar wind is essentially a proton-electron plasma and that the concentration of heavier ions is sufficiently small for them to have no significant effect on the flow of the protons. This approach is advisable in view of the complexity of the self-consistent multi-fluid problem (see for example, the three-fluid model considered by Yeh, 1970). Each species is therefore considered to be a separate fluid satisfying conservation equations for mass, momentum and energy, and interacting with the dominant proton-electron plasma only as a consequence of the electric field associated with the latter and of Coulomb collisions between protons and heavier ions. The fact that the treatment is not self-consistent may lead to substantial errors, although it is difficult to estimate these at the present time.

The effects of viscosity and of heat conduction by the protons and heavier ions are ignored, but these are probably not important. The state of ionization of heavier ions is assumed to be constant; however since this must depend on the electron temperature (which as a consequence of thermal conduction should be fairly uniform close to the Sun), the neglect of possible changes in the state of ionization of heavier ions should not be serious. We have neglected for the present the effects of a non-radial magnetic field and of solar rotation, although these may be important especially as far as the heavy ions are concerned. Our treatment of the process(es) by which hydromagnetic or other waves heat the solar wind is also rather arbitrary, and we have neglected to take into account the effects of momentum absorption which should in fact be related in a self-consistent way to the absorption of energy. Finally, although we have assumed that only Coulomb collisions and the large scale electric field couple the minor species with the dominant proton-electron plasma, it is certainly possible that turbulence generated by instabilities may play an important role in this respect.

2. *The Background Solar Wind*

In order to determine the behaviour of minor species, it is necessary to know the flow speed (u), the density (ρ) and the temperature (T) of the background proton-electron plasma and also the radial electric field (E). For convenience we make use of the simple solution for a single-fluid solar wind flow with heat addition discussed by Holzer and Axford (1970). [However it should be noted that a two-fluid treatment allowing for heat addition (e.g. Leer and Axford, 1972) would not be a great deal more difficult to handle.] The appropriate equations for steady, spherically-symmetric, radial flow are as follows:

$$\varrho\, u\, r^2 = F\,, \tag{1}$$

$$u\frac{du}{dr} + \frac{1}{\varrho}\frac{dp}{dr} + \frac{G\mu}{r^2} = 0\,, \tag{2}$$

$$\frac{1}{r^2}\frac{d}{dr}\left[\varrho\, u\, r^2\left(\frac{1}{2}u^2 + \frac{5}{2}\frac{p}{\varrho} - \frac{G\mu}{r}\right)\right] = \mathcal{Q}(r)\,, \tag{3}$$

where r is the radial distance from the center of the sun, p is the plasma pressure, G is the gravitational constant, μ is the mass of the sun, F is the mass flux per steradian and $\mathcal{Q}(r)$ is a term representing addition of energy to the flow resulting from the damping of hydromagnetic or other waves. The radial electric field $E(r)$, assuming the proton and electron temperatures are equal, is given by

$$E = \frac{m}{2e}\left(u\frac{du}{dr} + \frac{G\mu}{r^2}\right), \tag{4}$$

where m is the mass and e the charge of a proton.

It is convenient to express these equations in terms of the Mach number $M = u/\sqrt{(5p/3\varrho)}$ and a dimensionless form of the radial distance $\xi = r/r_o$, where r_o is the radius of the sun. By this means it is possible to reduce Eqs. (1), (2) and (3) to a single first order differential equation for M^2:

$$(M^2-1)\frac{dM^2}{d\xi} = \frac{2\,M^2(M^2+3)}{3\,H(\xi)}\left\{\frac{2\,\mathscr{E}_o}{\xi} + \frac{2}{\xi}\int_1^{\xi} P(\xi')\,d\xi' - \frac{1}{6}(5\,M^2+3)\,P(\xi)\right\}. \tag{5}$$

Here $P(\xi) = r_o^3\,\xi^2\,\mathcal{Q}(\xi)/F$ and $H(\xi)$ is the stagnation enthalpy per unit mass:

$$H(\xi) = \frac{1}{2}u^2 + 5p/2\varrho = \mathscr{E}_o + \int_1^{\xi} P(\xi')\,d\xi' + G\mu/r_o\,\xi\,, \tag{6}$$

and $\mathscr{E}(\xi)$ is the total energy per unit mass:

$$\mathscr{E}(\xi) = \mathscr{E}_o + \int_1^{\xi} P(\xi')\,d\xi' = \frac{1}{2}u_o^2 + 5p_o/2\varrho_o - G\mu/r_o + \int_1^{\xi} P(\xi')\,d\xi'\,. \tag{7}$$

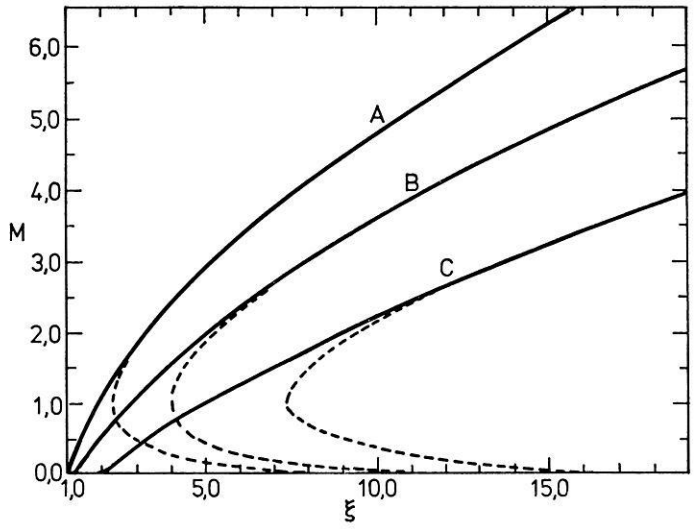

Fig. 1. Mach number versus radial distance for parameters representative of typical solar wind conditions. For curve A, $\mathscr{E}_o = -1.2 \times 10^{27}$ eV g^{-1}, $F = 1.6 \times 10^{11}$ g sec^{-1}, $Q = 1.23 \times 10^{8}$ eV cm^{-3}sec^{-1}, and $\beta = 4$. For curves B and C, $\mathscr{E}_o$ and F have the same values as for curve A, but Q has the values 5.41×10^{6} eV cm^{-3}sec^{-1} and 4.51×10^{5} eV cm^{-3}sec^{-1}, and β the values 2.0 and 1.0, respectively. The dashed curves represent solutions of the corresponding equations without heat addition but with total energies equal to the asymptotic energies obtained in the three cases considered. (See Holzer and Axford, 1970)

The subscript o refers to conditions at $r = r_o$ (i.e. $\xi = 1$). Eq. (5) has a singular point at $M^2 = 1$, $\xi = \xi_c$ where ξ_c is obtained from the condition that the term in braces on the right hand side should vanish:

$$\mathscr{E}_o + \int_1^{\xi_c} P(\xi')\, d\xi' + \frac{2}{3}\, \xi_c\, P(\xi_c) = 0\,. \tag{8}$$

We choose $Q = Q_o \exp(-\beta\xi)$ as a suitable form for the heating function, in which case it can be shown that the relation (8) defines a unique value $\xi = \xi_c > 1$ provided

$$\mathscr{E}(\infty) = \mathscr{E}_o + \int_1^{\infty} P(\xi')\, d\xi' > 0\,, \tag{9}$$

i.e. the total energy per unit mass at infinity is positive. It should be noted that under normal conditions in the solar corona $\mathscr{E}_o < 0$ and hence it is essential that energy should be given to the fluid by some means in order to permit it to escape from the Sun.

Examples of solutions of Eq. (5) are shown in Fig. 1 for various values of β and Q_o and with values of F and $\mathscr{E}_o$ corresponding to quiet solar conditions. These solutions pass through the singular point $M^2 = 1$, $\xi = \xi_c$ in each case, and are such that $M^2 = 0$ at $\xi = 1$ and $M^2 \to \infty$ as $\xi \to \infty$. They satisfy the requirement that $(p + \varrho u^2) \to 0$ as $r \to \infty$, which is appropriate to expansion of the solar corona into

the relative vacuum of interstellar space. For the purpose of this paper, these solutions have been fitted by sixth degree polynomials, from which it is a simple matter to compute the speed, density and temperature of the proton-electron plasma and the electric field for use in treating the problem of the flow of minor species.

3. Equations of Motion for Minor Species

We treat each minor species as a separate fluid which interacts with the proton-electron plasma via Coulomb collisions and the radial electric field defined in Eq. (4), and which is heated as a result of wave damping in an arbitrary manner. With the same assumptions as made for the background solar wind flow and described in section 2 the equations governing the behaviour of a minor species (denoted by subscript i), having ionic charge Ze and mass Am are as follows:

$$\varrho_i u_i r^2 = F\,, \tag{10}$$

$$u_i \frac{du_i}{dr} + \frac{1}{\varrho_i}\frac{dp_i}{dr} + \frac{G\mu}{r^2} = \frac{Ze\,\mathrm{E}}{Am} + C_i\,, \tag{11}$$

$$\frac{1}{r^2}\frac{d}{dr}\left\{\varrho_i u_i r^2\left(\frac{1}{2}u_i^2 + \frac{5p_i}{2\varrho_i} - \frac{G\mu}{r} + \frac{Ze\,\phi}{Am}\right)\right\} = Q_i + Q_i' + \varrho_i u_i C_i\,, \tag{12}$$

where $\phi = -\int_{r_o}^{r} E(r')\,dr'$ and Q_i is the rate of heating of the i-species by wave damping.

The term C_i on the right of Eq. (11) represents the effects of friction (i.e. bulk momentum exchange) due to Coulomb interactions between the proton gas and the i-species. Q_i' is the corresponding rate at which energy is exchanged. According to Burgers (1969), for Maxwellian fluids

$$C_i = \left(\frac{8\pi e^4 \ln\Lambda}{m^3}\right)\frac{Z^2}{A^2}(A+1)\,\varrho\,\frac{\Phi(v/\alpha)}{\alpha}\,, \tag{13}$$

$$Q_i' = \left(\frac{16\pi^{\frac{1}{2}} e^4 \ln\Lambda}{m^4}\right)\frac{Z^2}{A^2}\varrho_i\,\varrho\,\frac{\exp(-v^2/\alpha^2)}{\alpha^3}\,k(T - T_i)\,, \tag{14}$$

where $\alpha^2 = 2k(T_i/A + T_p)/m$, k is Boltzmann's constant, $v = (u - u_i)$, $\ln\Lambda \approx 22$ and $\Phi(\varkappa) = \{\psi(\varkappa) - \varkappa\psi'(\varkappa)\}/2\varkappa^2$ with $\psi(\varkappa)$ being the error function. T_p and T_i are the temperatures of the protons and the i-species ions, respectively.

As before, we express the equations of motion in terms of the Mach number for the species concerned, viz. $M_i = u_i/\sqrt{(5p_i/3\varrho_i)}$:

$$\begin{aligned}(M_i^2 - 1)\frac{dM_i^2}{d\xi} = \frac{2M_i^2(M_i^2+3)}{3H_i(\xi)}\Bigg[\frac{2}{\xi}\Bigg\{\mathscr{E}_{oi} + \int_1^{\xi}(P_i(\xi') + P_i'(\xi') + C_i(\xi'))\,d\xi' \\ - \frac{Ze\,\phi(\xi)}{Am}\Bigg\} + 2r_o\left\{\frac{Ze\,E(\xi)}{Am} + C_i(\xi)\right\} \\ - \frac{1}{6}(5M_i^2 + 3)\{P_i(\xi) + P_i'(\xi)\}\Bigg]\,,\end{aligned} \tag{15}$$

where

$$H_i(\xi) = \mathscr{E}_{oi} + \int_1^{\xi} (P_i(\xi') + P_i'(\xi') + C_i(\xi'))\, d\xi' - \frac{Ze\,\phi(\xi)}{Am} + \frac{G\mu}{r_o\,\xi}, \quad (16)$$

and $P_i(\xi) = r_o^3 \xi^2 \mathcal{Q}_i(\xi)/F_i$, $P_i' = r_o^3 \xi^2 \mathcal{Q}_i'(\xi)/F_i$. The quantity $\mathscr{E}_{oi}$ is the total energy per unit mass at $r = r_o$:

$$\mathscr{E}_{oi} = \frac{1}{2} u_{oi}^2 + \frac{5}{2} p_{oi}/\varrho_{oi} - G\mu(r_o)\,. \quad (17)$$

Eq. (15) has a singular point where $M_i^2 = 1$ and $\xi = \xi_{ci}$, ξ_{ci} being determined from the condition that the term on the right in square brackets should vanish:

$$\frac{2}{\xi_{ci}} \left\{ H_i(\xi_{ci}) - \frac{G\mu}{r_o\,\xi_{ci}} \right\} + 2 r_o \left\{ \frac{Ze\,E(\xi_{ci})}{Am} + C_i(\xi_{ci}) \right\} = \frac{4}{3} \{ P_i(\xi_{ci}) + P_i'(\xi_{ci}) \}. \quad (18)$$

This condition is effectively a relationship between the values of T_i and ξ at the point where $M_i = 1$ since $H_i(\xi) = \frac{5}{6} (M_i^2 + 3) k T_i$ and all the other quantities can be regarded as being functions of ξ, M_i^2 and T_i only. The relationship has the property that $dT_i/d\xi < 0$ for the simple exponential heating functions we have assumed, and its intersections with the actual temperature profiles are possible singular points. It is difficult to determine how many such singular points there are in general., however in the cases we have examined only one singular point (a saddle point permitting a subsonic-supersonic transition) appears to exist at relatively small values of ξ.

Solutions of Eq. (15) can be obtained by integrating towards $\xi = 1$ from a trial sonic point with the initial conditions determined from (18). It is found that in general a narrow range of values of ξ_c exists such that the integration proceeds smoothly towards $\xi = 1$, and for one value only, $\frac{1}{2} u^2 + 5p/2\varrho - G\mu/r \to \mathscr{E}_{oi}$ as $\xi \to 1$.

4. *Discussion of Solutions*

Our calculations have been limited to situations involving $^4He^{+2}$, $^{16}O^{+6}$, $^{20}Ne^{+8}$ and $^{56}Fe^{+12}$ as minor species. We have considered cases with $\beta = 1$ and $\beta = 2$, and with heat addition proportional to particle mass, to particle charge, and the same for all species. The proton flux at the orbit of Earth was usually taken to be 4.4×10^8 cm^{-2}sec^{-1}, corresponding to a number density of 10 cm^{-3} and a speed of 440 km sec^{-1}, but in addition some calculations were carried out with fluxes both larger and smaller than this value.

The results obtained were generally similar for $\beta = 1$ and $\beta = 2$, although in the latter case more solutions were "acceptable" in the sense that the speeds of all species were comparable to the speed of the background solar wind at large distances from

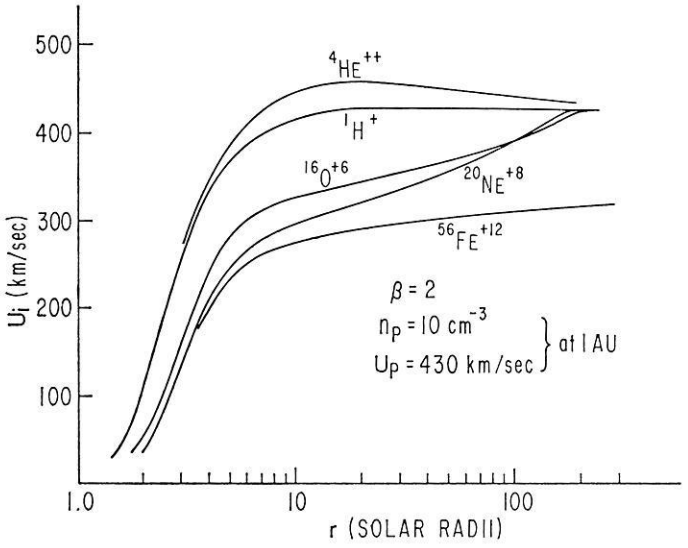

Fig. 2. Bulk speed of various species versus distance from the Sun for a case in which the solar wind flux is 4.3×10^8 cm^{-2}sec^{-1} and species are heated in proportion to their mass. Note that the bulk speed of the helium ions exceeds that of the background solar wind, whereas the $^{56}Fe^{+12}$ ions move considerably more slowly than the solar wind at 1 a.u. As a consequence of Coulomb collisions, $^{16}O^{+6}$ and $^{20}Ne^{+8}$ reach equilibrium with the background solar wind at the orbit of the Earth

the Sun. It is perhaps not surprising that the results are most sensitive to the form of the term representing heat addition. Indeed acceptable solutions were obtained only in cases where Q_i was taken to be proportional to A, so that if *all* interaction effects were neglected, each ion would behave more-or-less like an equivalent group of A protons moving together. Note however that the effect of the electric field is not the same for all species, and hence with $Q_i \propto Z$ it was found that the $^4He^{+2}$ gas attains a bulk speed of 360 km sec^{-1} at 1 a.u., while the speed of the $^{16}O^{+6}$ gas is 150 km sec^{-1} at the same distance. With $Q_i \propto A$, $\beta = 2$ and a proton flux of 4.4×10^8 cm^{-2} sec^{-1} at 1 a.u., the minor ions mostly move at about the same speed as the protons at 1 a.u., although the $^4He^{+2}$ speed is slightly greater and the $^{56}Fe^{+12}$ speed considerably smaller (see Fig. 2). The temperatures of the minor species are very large close to the sun in these circumstances (see Fig. 3), but except in the case of $^{56}Fe^{+12}$ they tend to approach the proton temperature at large distances from the Sun.

If the proton number density (and flux) is increased, thus increasing the importance of Coulomb collisions, it is found that the $^4He^{+2}$ speed no longer exceeds the proton speed at 1 a.u., and that the $^{56}Fe^{+12}$ speed is even further reduced (see Fig. 4). In contrast, if the proton flux is decreased, as shown in Fig. 5, the $^4He^{+2}$ gas moves considerably faster than the background solar wind at 1 a.u., while the heavier species (including $^{56}Fe^{+12}$) move essentially at the solar wind speed at 1 a.u. In general the temperatures of the minor species at 1 a.u. approach that of the protons if the speeds also approach the solar wind speed. Otherwise the minor species are much hotter than the protons.

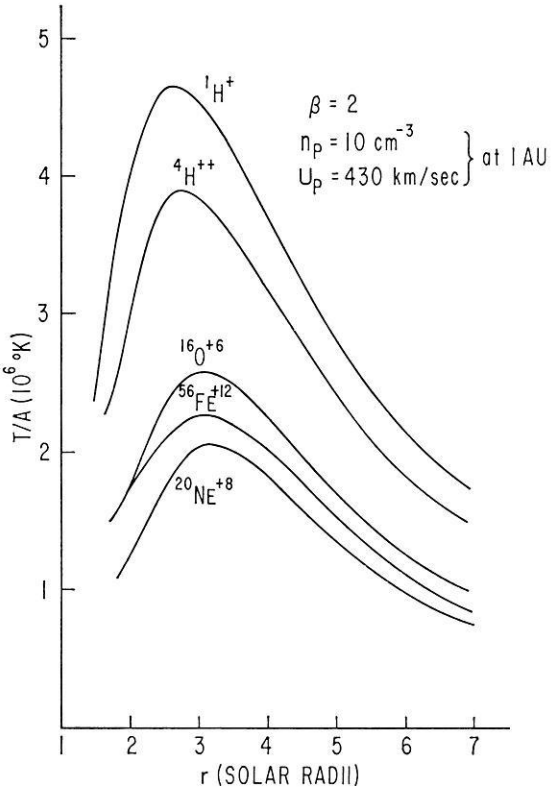

Fig. 3. Temperature distributions for various species as a function of distance from the Sun under the same conditions as described for Fig. 2

Unfortunately, due to the relative complexity of our model, we are unable to present any results in analytic form, as have Geiss *et al.* (1970b). However, as a consequence of our inclusion of (admittedly arbitrary) heat sources for minor species as well as protons and electrons, it must be expected that our results should differ from those obtained from a model in which the minor species escape from the Sun's gravitational field mainly as a result of friction due to Coulomb collisions (i.e. the term C_i on the right of Eq. (11)).

5. Conclusions

It is evident from the results described in the previous section that the nature of the heating mechanism is likely to play a very important role in determining the flow of minor species in the solar wind. Furthermore, in order to permit the heavier ions to escape from the Sun with reasonable speeds energy must be given preferentially to these species by whatever processes are involved in heating the corona. Our conclusion that the heating should be roughly proportional to particle mass is likely to remain valid even if we make more detailed calculations on the basis of refined models.

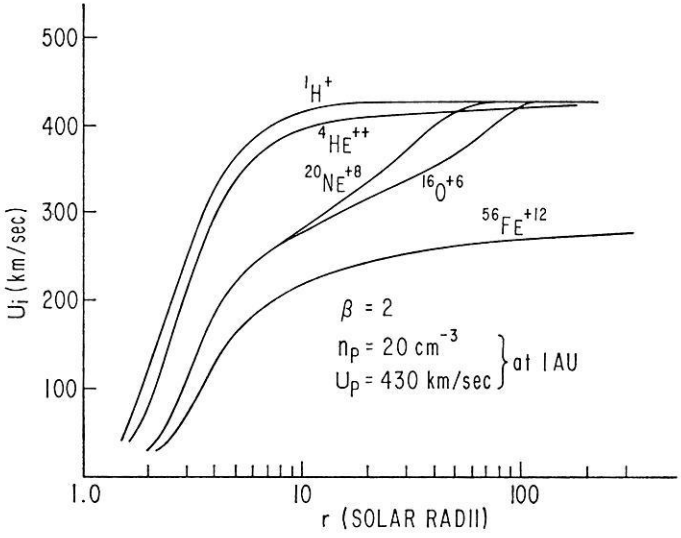

Fig. 4. Bulk speeds of various species versus distance from the Sun for a case in which the solar wind flux is 8.6×10^8 cm^{-2}sec^{-1}, and all ions are heated in proportion to their mass. In this case the bulk speed of the helium ions remains below that of the background solar wind but rapidly approaches it at the orbit of Earth and beyond. The bulk velocity of $^{56}Fe^{+12}$ is everywhere well below that of the background solar wind

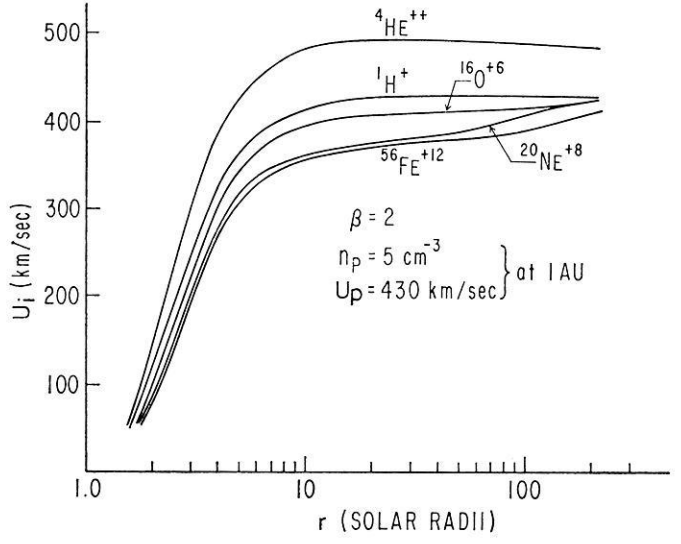

Fig. 5. Bulk speeds of various species versus distance from the Sun for a case in which the solar wind flux is 2.15×10^8 cm^{-2}sec^{-1} and all species are heated in proportion to their mass. In this case the bulk speed of the helium ions exceeds that of the background solar wind everywhere, being about 15% greater at the orbit of the Earth. As a consequence of reduced energy losses close to the Sun the $^{56}Fe^{+12}$ ions retain sufficient energy at large distances for their bulk velocity to remain close to that of the background solar wind; hence Coulomb collisions are sufficient to make the speeds approximately equal at a heliocentric distance of about 2 a.u.

As a consequence of preferential heating, the temperatures of heavy ions should in general exceed the solar wind proton temperature except perhaps at great distances from the Sun where Coulomb collisions may permit some species to come into thermal equilibrium with the protons.

In fact, it should be expected that different species should be heated differently although one cannot predict the nature of the differences without knowing the details of the mechanism(s) involved. For example, if heating results from the damping of hydromagnetic or other waves by resonant acceleration of particles, species with differing charge to mass ratios should certainly absorb different amounts of energy since they will resonate with different regions of the wave spectrum. The problem is extremely complicated however, since one must know, in addition to the wave spectrum, how each species moves relative to the background solar wind in order to determine which frequency range is important at any given location.

Our calculations serve to illustrate the effects of Coulomb collisions fairly clearly. The most important effect appears to be associated with heat transfer from heavy ions to the relatively cool proton gas close to the Sun. This is evident from the fact that the iron escapes more readily from the Sun when the proton flux is reduced (compare Fig. 2, 4 and 5). Secondly, it appears that species with velocities and temperatures that are not too different from those of the background protons approach thermal equilibrium and move together with the proton gas at large heliocentric distances purely as a result of Coulomb collisions. This is also evident in the Figures, especially with regard to the species $^{16}O^{+6}$ and $^{20}Ne^{+8}$.

The results described here suggest that there may be large velocity differences between minor ion species and the background solar wind, especially within a few tens of solar radii of the Sun. If this is indeed the case then it is essential that further calculations should take the presence of interplanetary electric and magnetic fields into account. Since all particles must move along magnetic field lines (considered to be co-rotating with the Sun), species which do not move at exactly the same speed as the protons cannot move radially (even if we neglect any tendency of the protons themselves to co-rotate). Accordingly, centrifugal effects must be important, especially for the heavier species. This should lead to some variation in the nature of the solar wind with heliolatitude as far as minor species are concerned.

Finally, we wish to draw attention to a basic shortcoming of the model we have used here, both with regard to the background solar wind and the minor species. If wave energy is absorbed as we have assumed, and if the source of the waves is the Sun, then the wave momentum which is absorbed must also be taken into account. That is, there should be terms in Eqs. (2) and (11) representing the wave momentum absorbed by the fluids, and having forms which are consistent with the energy absorption terms in Eqs. (3) and (12).

We intend to extend this work, taking into account the effects of the interplanetary magnetic field and of momentum absorption in addition to heating. However, we expect that our general conclusions with regard to the effects of Coulomb collisions and the need for differential heating for minor species will not be drastically changed.

It should be noted that although a model such as this can suggest reasons for differences of velocity and temperature between various species in the solar wind it contains no mechanism by which the ratios of particle fluxes can be made to differ

from the equivalent concentration ratios in the photosphere. Such effects can be explained only by invoking processes such as mixing at the corona-chromosphere interface (e.g. Delache, 1967; Jokipii, 1966; Nakada, 1969).

Acknowledgements. This work was carried out at the University of California, San Diego, and was supported by NASA under contract NGR-05-009-081.

References

Alloucherie, Y.: Diffusion of heavy ions in the solar corona. J. Geophys. Res. *75*, 6899–6914, 1970

Asbridge, J.R., Bame S.J., Feldman, W.C.: Variations in the helium component in the solar wind. Trans. Am. Geophys. Union *54*, 440, 1973

Bame, S.J.: Spacecraft observations of the solar wind composition. Proc. Asilomar Solar Wind Conf., NASA SP-308, 535, 1972

Bame, S.J., Asbridge, J.R., Hundhausen, A.J., and Montgomery, M.D.: Solar wind ions: $^{56}Fe^{+8}$ to $^{56}Fe^{+12}$, $^{28}Si^{+7}$, $^{28}Si^{+8}$, $^{28}Si^{+9}$, and $^{16}O^{+6}$. J. Geophys. Res. *75*, 6360, 1970

Bame, S.J., Hundhausen, A.J., Asbridge, J.R., Strong, I.B.: Solar wind ion composition. Phys. Rev. Letters *20*, 393, 1968

Bollea, D., Formisano, V., Hedgecock, D.C., Moreno, G., Palmiotto, F.: HEOS-1 helium observations in the solar wind. Pro. Asilomar Solar Wind Conf. NASA SP-308, 588, 1972

Bühler, F., Eberhardt, P., Geiss, J., Meister, J.: Apollo-11 solar wind composition experiments: First results. Sci. *166*, 1502, 1969

Burgers, J.M.: Flow equations for composite gases. New York and London: Academic Press 1969

Coon, J.H.: Solar wind observations. In Earth's Particles and Fields, ed. B. M. McCormac, 359, New York: Reinhold 1968

Danziger, I.J.: The cosmic abundance of helium. Ann. Rev. Astron. Astrophys. *8*, 161, 1970

Delache, P.: Contribution à l'étude de la zone de transition chromosphère-couronne. Ann. Astrophys. *30*, 827–860, 1967

Formisano, V., Moreno, G.: Helium and heavy ions in the solar wind. Riv. Nuovo Cim. *1*, 365 ,1971

Formisano, V., Palmiotto, F., Moreno, G.: Particle observations in the solar wind. Solar Phys. *15*, 479, 1970

Geiss, J., Eberhardt, P., Bühler, F., Meister, J., and Signer, P.: Apollo-11 and 12 solar wind composition experiments: fluxes of He and Ne isotopes. J. Geophys. Res. *75*, 5972, 1970a

Geiss, J., Hirt, P., Leutwyler, H.: On acceleration and motion of ions in corona and solar wind. Solar Phys. *12*, 458–483, 1970b

Hartle, R.E., Barnes, A.: Nonthermal heating in the two-fluid solar wind model. J. Geophys. Res. *75*, 6915–6931, 1970

Hirshberg, J.: Solar wind helium enhancements following major solar flares. Proc. Asilomar Solar Wind Conf. NASA SP-308, 582, 1972

Hirshberg, J.: Helium abundance of the Sun. Rev. Geophys. Space Phys. *11*, 115, 1973

Hirshberg, J., Asbridge, J.R., Robbins, D.E.: Velocity and flux dependence of the solar wind helium abundance. J. Geophys. Res. *77*, 3583, 1972

Hirshberg, J., Asbridge, J.R., Robbins, D.E.: The helium component of solar wind velocity streams. J. Geophys. Res. *79*, 934–938, 1974

Holzer, T.E., Axford, W.I.: The theory of stellar winds and related flows. Ann. Rev. Astron. Astrophys. *8*, 31–60, 1970

Hundhausen, A.J.: Composition and dynamics of the solar wind plasma, Rev. Geophys. Space Phys. *8*, 729–812, 1970

Hundhausen, A.J., Asbridge, J.R., Bame, S.J., Gilbert, H.E., Strong, I.B.: Vela-3 satellite observations of solar wind ions: a preliminary report. J. Geophys. Res. *72*, 87, 1967a

Hundhausen, A. J., Asbridge, J. R., Bame, S. J., and Strong, I. B.: Vela satellite observations of solar wind ions. J. Geophys. Res. *72*, 1979, 1967b

Hundhausen, A. J., Bame, S. J., Ness, N. F.: Solar wind thermal anisotropies, Vela-3 and Imp-3. J. Geophys. Res. *72*, 5265, 1967c

Hundhausen, A. J., Bame, S. J., Asbridge, J. R., Sydoriak, S. J.: Solar wind proton properties: Vela-3 observations from July 1965 to June 1967. J. Geophys. Res. *75*, 4643, 1970a

Jokipii, J. R.: Effects of diffusion on the composition of the solar corona and the solar wind. In: The solar wind, ch. XIV, ed. R. J. Mackin and M. Neugebauer, 215–218, New York: Pergamon Press 1966

Konyukov, M. V.: Parker's solar wind theory, II. Flow with a heat source depending on a point. Geomagnetizm: Aeronomiya *7*, 469–475, 1967

Leer, E., Axford, W. I.: A two-fluid solar wind model with anisotropic proton temperatures. Solar Phys. *23*, 238–250, 1972

Nakada, M. P.: A study of the composition of the solar corona and solar wind. Solar Phys. *14*, 457–479, 1970

Neugebauer, M., Snyder, C. W.: Mariner-2 observations of the solar wind, average properties. J. Geophys. Res. *71*, 4469, 1966

Ogilvie, K. W., Wilkerson, T. D.: Helium abundance in the solar wind. Solar Phys. *8*, 435, 1969

Ogilvie, K. W., Zwally, H. J.: Hydrogen and helium velocities in the solar wind. Solar Phys. *24*, 236, 1972

Robbins, D. E., Hundhausen, A. J., Bame, S. J.: Helium in the solar wind. J. Geophys. Res. *75*, 1178, 1970

Strong, I. B., Asbridge, J. R., Bame, S. J., Heckman, H. H., Hundhausen, A. J.: Measurements of proton temperatures in the solar wind. Phys. Rev. Letters *16*, 628, 1966

Wolfe, J. H., Silva, R. W., McKibbin, D. D., Mason, R. H.: The compositional, anisotropic and non-radial flow characteristics of the solar wind. J. Geophys. Res. *71*, 3329, 1966

Yeh, T.: A three-fluid model of the solar wind. Planetary Space Sci. *18*, 199, 1970

J. M. Ryan
Physics Department
University of California
Riverside, Calif. 92 502, USA

W. I. Axford
Max-Planck-Institute for Aeronomy
D-3411 Lindau/Harz
Federal Republic of Germany

J. Geophys. 41, 233–242, 1975

The Effect of Low Energetic Electrons in the Polar Ionosphere*

G. K. Hartmann

Max-Planck-Institut für Aeronomie, Lindau/Harz

Received June 25, 1974

Abstract. Measurements of the dispersive Doppler effect of the 150/400 MHz signals of the five orbiting US-NNSS satellites provide with good accuracy, the integral electron content I of the ionosphere as a function of geographic latitude φ. The research reported here was based on I (φ)-curves calculated at Oulu, Finland and such from Lindau/Harz. They enable to study the behaviour of the main trough in I. Data from winter 1972 were compared with relevant *FoF2* data measured at Freiburg, FRG; Lindau, FRG; Juliusruh, GDR; Uppsala and Lycksele, Sweden; and Sodankylä, Finland. On November 11th 1971 an effect was observable which was not reported yet. The electron content I showed in the latitude range 60° to 65° N in the time interval from 1600 UT to 1700 UT a strong increase towards north. The relevant *FoF2* curve at 1700 UT showed a *reverse* behaviour. At earliest one hour later the *FoF2* showed again a trend similar to that of I. If the increase of I was caused by precipitating low energetic particles the above mentioned time delay of at least one hour leads to the conclusion that the increase was caused by precipitating electrons with energies less than 100 eV.

Key words: Precipitation — Electrons — Electron Content — Dispersive Doppler Effect — Satellite Beacons — Gradients — Critical Frequencies — Dayside Plasma Trough — Subpolar Ionosphere.

Introduction

The 150 and 400 MHz signals of the five orbiting US-NNSS satellites have been recorded at Lindau/Harz (FRG) since 1970 and at Oulu (Finland) since 1971. Identical measuring equipment has been used. The satellites have an almost circular polar orbit, the altitude is approximately 1100 km above the surface of the earth. The evaluation of the Dispersive Doppler Effect (DD) (Schmidt, Tauriainen, 1970; Ebel, Hartmann, Leitinger, Schmidt, Schödel, 1969; Hartmann, Oberländer, Schmidt, Schödel, 1972; Hartmann Tauriainen, 1973; Tyagi, 1973) yields with good accuracy the total electron content (TEC) I as a function of geographic latitude φ of the subionospheric point. The results presented here are based on total electron content data from Lindau and Oulu. They were selected thus that the geographic longitudes of the subionospheric points were located between 10° east and 25° east. The I (φ)-curves from winter 1971 are compared with the relevant *FoF2* data from Freiburg (FRG), Lindau (FRG), Juliusruh (GDR), Uppsala (Sweden), Lycksele (Sweden) and Sodankylä (Finland). A phenomenon which has not yet been observed is reported here.

*To Prof. G. Pfotzer in honor of his 65th birthday.

1. Negative Horizontal Gradient

Due to the nearly circular polar orbits of the NNSS-satellites the horizontal gradient of the total electron content I can be defined as follows.

$$G_R \stackrel{!}{=} \mathrm{d}I/\mathrm{d}\varphi \neq O \tag{1}$$

where φ represents the geographic latitude of the relevant subionospheric point. If there would be a clear dependance from the zenith distance χ of the sun there should be observable a decrease in I with decreasing χ, e.g.

$$\mathrm{d}I/\mathrm{d}\varphi > O \quad \text{if} \quad \mathrm{d}\chi/\mathrm{d}\varphi < O \tag{2}$$

$$\mathrm{d}I/\mathrm{d}\varphi < O \quad \text{if} \quad \mathrm{d}\chi/\mathrm{d}\varphi > O \tag{2a}$$

Data which did not satisfy these conditions were selected for the following investigation. This phenomenon was defined "Negative horizontal gradient of the total electron content I".

Rai and Hook (1967) and Liszka (1969) reported variations of I during winter months. On magnetic quiet days as well as on disturbed days I (φ) displayed temporarily "unusual" behaviour. The recent detailed comparison between the negative horizontal gradient of I and *FoF2* data revealed an additional yet unknown effect.

2. Results

a) Data from November 11th, 1971

Fig. 1 shows the electron contents I and critical frequencies *FoF2* as functions of the geographic latitude, respectively invariant latitude Λ. The I (φ)-curves represent data which were continuously measured therefore the lines are drawn fat. The critical frequencies were only available for Freiburg (FR), Lindau (LI), Juliusruh (JU), Uppsala (UP), Lycksele (LY), and Sodankylä (SO). This data was connected by a thin line in order to indicate that the thus drawn curve may deviate considerably from the actual continuous unknown *FoF2* (φ)-curve. If in the following the *FoF2* (φ)-curve is mentioned this special graphical representation is under consideration. The abscissa in the lower part of the figure represents the geographic latitude φ that in the upper part the invariant latitude Λ. The ordinate to the right displays the critical frequency *FoF2* in MHz, that to the left indicates the electron content I per m^2 [el/m^2] times 10^{-16}. Eight *FoF2* (φ)-curves between 1500 UT and 2200 UT and five I (φ)-curves are given. The first (fat dotted) was calculated from Lindau data of the NNSS satellite 30180 during its passage at 1600 UT. The second (solid line) was calculated from data of the satellite 30120, recorded in Oulu at 1700 UT. The last three curves were calculated from Lindau data of the satellites 30130—1932 UT —; 30130—2120 UT —; and 30140—2341 UT. This day had slight magnetic activity. During the measuring period the following *Kp*-indices were reported. 1) 12—15 UT $Kp = 3-$; 2) 15—18 UT $Kp = 2$; 3) 18—21 UT $Kp = 4+$; 4) 21—24 UT $Kp = 3-$. *Ap* was 16 that day. Rai and Hook (1967) defined similar observations

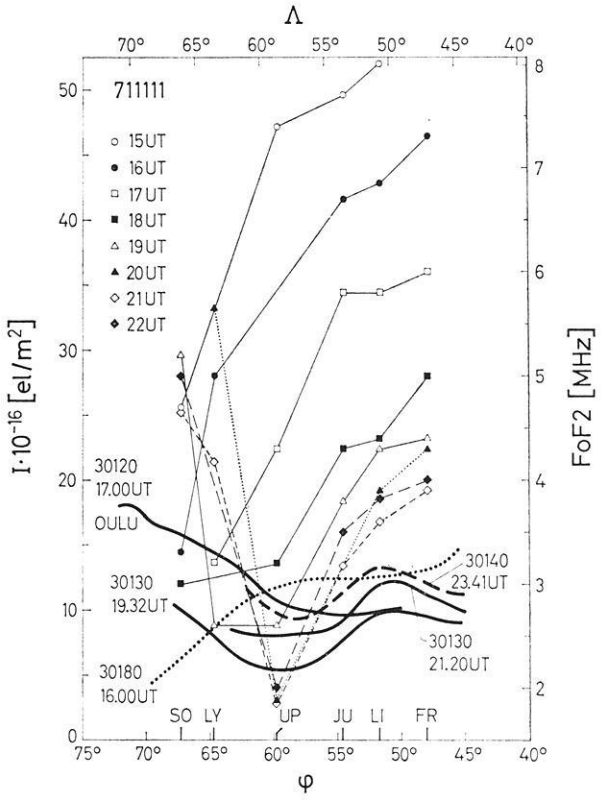

Fig. 1. Electron content I and critical frequency $FoF2$ as a function of geographic latitude φ, respectively invariant latitude Λ within the latitude range 10° east and 25° east, calculated for Nov. 11th, 1971, in the time interval 1500 UT to 2400 UT. The ordinate to the right displays the critical frequency $FoF2$ [MHz], that to the left indicates the electron content I per m² [el/m²] times 10^{-16}. $I(\varphi)$-curves denoted with Oulu were calculated with data measured in Oulu. Those without denotation were calculated with data measured in Lindau. The numbers 30120, 30130, 30140, 30180 and 30190 give the international nomenclature of the five US NNSS satellites. Time is given in Universal Time (UT). Local time in Lindau is Central European Time (CET) = UT + 1 hour. Local time in Oulu is Eastern Eropean Time (EET) = UT + 2 hours

"quiet" as long as Ap was less than 15 and the K index of College, Alaska, as well as Kp were less than 2.

The two most important curves are the first and second $I(\varphi)$-curve. At 1600 UT $I(\varphi)$ shows in the latitude range 60° to 65° N a strong decrease. At 1700 UT $I(\varphi)$ shows a strong increase in this range. Sodankylä displays an increase in I from 6×10^{16} el/m² to 16×10^{16} el/m², e.g. by a factor of three. Stations further north exhibit an even stronger increase.

Similar increases of I were reported by Liszka (1966) in northern Scandinavia, by Rai and Hook (1967) in Alaska, and by Stuart (1972) in New Zealand. Liszka as well as Rai and Hook assumed that precipitating low energetic particles were the cause of this unusual increase. They had available only data from a single low orbiting

satellite. Hence a denser time sequence of $I(\varphi)$ data was impossible and thus comparisons with other ionosphere data like *FoF2* were very difficult. Due to the now orbiting five satellites these comparisons can be carried out more efficiently.

A comparison between the $I(\varphi)$-curves and the *FoF2* (φ)-curves reveals the following: The *FoF2*-curve at 1600 UT (black circles) decreases towards north like the relevant $I(\varphi)$-curve (dotted). The *FoF2*-curve at 1700 (open squares) *decreases* up to 65° N, the station Lycksele. The data from Sodankylä is missing, so there is no clear statement possible whether the curve is decreasing even further north. On some other days in November, magnetically quiet and disturbed ones, at 1700 the minimum of the trough was observed already overhead Lycksele, that means that at that time there is already an increase of the *FoF2*-curve from Lycksele towards Sodankylä. These increases of the critical frequencies were reported by several authors (Möller, 1967). The relevant $I(\varphi)$-curve at 1700 UT however *increases* within the whole measuring range (solid curve). The *FoF2* curve at 1800 UT (solid squares) shows in the range 60° to 70° latitude a very weak decrease. Recent new reductions of ionograms kindly supplied on request by Mr. A. Hedberg. (Uppsala) revealed that the *FoF2* data from Lycksele — which was missing at the time when the figure was drawn — was smaller than that from Sodankylä and Uppsala. This means that the actual *FoF2* curve decreases up to Lycksele and then starts again increasing towards north. The *FoF2*-curve at 1900 UT as well as the following three ones show clearly the well known trough. The third $I(\varphi)$-curve (1932 UT), the fourth (2120 UT), and the fifth (2141 UT) clearly reveal the trough in electron content I.

b) Discussion

The comparison of the $I(\varphi)$- and *FoF2* (φ)-curves yielded the following:

I) The electron content showed in the latitude range 60° to 65° N in the time interval from 1600 UT to 1700 UT a strong increase towards north. The relevant *FoF2* (φ)-curve at 1700 UT showed a *reverse* behaviour. At the earliest one hour later the *FoF2* showed again a trend similar to that of $I(\varphi)$.

II) Overhead the station Lycksele the electron content I increased during this time interval by a factor of 1.7, however the cirtical frequency *FoF2* decreased by a factor of 1.5. There are no statements possible for the time interval 1700—1800 since there were no I and *FoF2* data available.

I and II lead to the conclusion that the behaviour of the $I(\varphi)$-curves and the *FoF2* (φ)-curves show a time delay of approximately *one* hour in the early evening. Roughly spoken *FoF2* lags behind I about one hour. If the increase of $I(\varphi)$ was caused by precipitating low energetic particles the above mentioned time delay of at least one hour leads to the suggestion that the increase was caused by precipitating electrons with energies less than 100 eV. Electrons with higher energies would penetrate at least to the maximum of the *F2*-layer, e.g. the increase in I and *FoF2* should occur simultaneously. The increase of I towards north during early evening hours in winter was reported also by other authors, however this time delay between I and *FoF2* is reported the first time. Whether this phenomenon is only observable during medium or stronger magnetic activity or whether it is generally related with the formation phase of the trough cannot be decided yet due to the few data available for comparisons. However the first statement seems to be more likely. This is

supported by statements presented by Chappell (1972) about regions of detached plasma in the dayside plasma trough. Mass spectrometers on board both OGO 3 and OGO 5 have measured masses of ambient plasma enhanced density levels that are detached from the main body of the plasmasphere. These masses of plasma are present across the dayside of the plasma trough, with particular concentration in the afternoon-dusk local time sector. Approximately 70% of the total number of detached plasma instances occurred following periods of moderate to high magnetic activity. ($Kp > 3^-$ in the previous 24 hours). Whether these regions of detached plasma can explain at least partially the above mentioned effect is not clear yet and needs further investigations.

Tyagi (1974) used Stubbe's (1973) modified model to calculate I and $FoF2$ up to about 60°. Beyond that the ion- and heat-production due to precipitated electrons has been added to that program. The observed effect could not be explained satisfactorily by these model calculations. The model seems to be not very much suited for the study of transient phenomena. However if the EUV model which is used as the background for the calculation of ionization due to low energy precipitating electrons can be improved so as to reproduce the observed latitudinal gradients in the EUV ionization zone ($\leqslant 60°$ N), then it may be possible to reproduce both the trough and gradient reversal at the beginning and ending of trough formation using appropriate precipitating flux. The application of another model (Mayr *et al.*, 1972) was not taken into consideration due to a statement given by the authors that disagreement with experiment above 60° is to be expected. Above 60°, at the plasmapause and beyond, H^+ is depleted by electric field convection and polar wind escape which is not included in that study. A review on plasmapause — plasmasphere problems (Carpenter; Park, 1973) gave no indication that an applicable theoretical model of the plasmapause — trough region is available. This was supported by a very recent review about exospheric models of the topside ionosphere. (Lemaire, Scherer, 1974). Even if there are mainly the applications of kinetic theory to the collision-free domains of the terrestrial atmosphere are reviewed. Thus it seems fairly unlikely that an unambiguous theoretical explanation of this effect will be available in the near future.

c) Difficulties by Comparing the I and $FoF2$ Data

The fact that in many cases the ionogram reductions from Uppsala, Lycksele and Sodankylä were not possible — mainly due to spread F-limited the number of comparisons drastically. Thus only this one clear effect could be presented. In cooperation with colleagues from Finland (University Oulu) and from Sweden (Uppsala) a coordinated measuring program of I and $FoF2$ has been started this winter to obtain more data. The problem of ionogram reduction however is still present. Nichol (1973) showed the close relation between the trough phenomenon in subpolar latitudes and the occurrence of spread F. This also explains the simultaneous observation of satellite scintillations which can be investigated also by using the signals of the NNSS satellites (Hartmann, 1972; Schmidt, 1972). During very strong scintillation cases the reduction of the dispersive Doppler effect (DD) for calculating I is also impossible. Due to the fairly high observing frequencies (150 MHz/400 MHz) the "I reduction" fails in much fewer cases than the "$FoF2$ reduction".

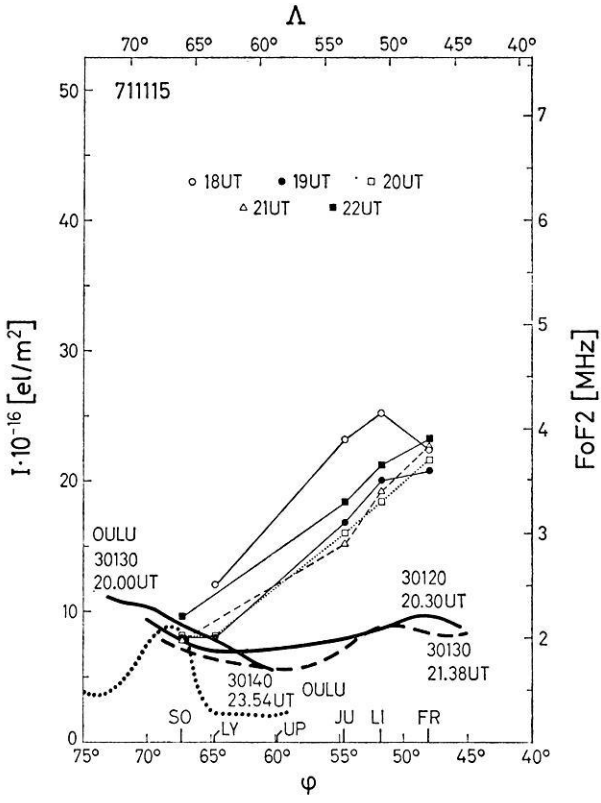

Fig. 2. Same nomenclature as for Fig. 1, however the I (φ)- and $FoF2$ (φ)-curves were displayed for Nov. 15th, 1971, in the time interval 1800 UT–2400 UT

A comparison with other satellite data, especially particle measurements was not possible since there were no such data available for the relevant time period. The following example may briefly show the difficulties of such comparisons. There were available particle data from INJUN 5 from February to June 1971 which should be compared with electron content data from the NNSS satellites. There were 42 cases, for which satellite INJUN 5 and one of the five NNSS satellites were observable — with respect to our station Lindau — in the range 10° longitude (east) $\pm 15°$ and 52° latitude (north) $\pm 10°$, simultaneously within one hour time interval. Data are referred to the subsatellite points. The final comparison revealed that only for *one* day (Feb. 25) a true comparison of I data from the NNSS satellites and the particle data from INJUN 5 was possible. Further comparisons of the I (φ) data with bottom side data were also impossible.

Fig. 2 displays the electron content I and the critical frequency $FoF2$ calculated for Nov. 15th, 1971 for the time interval 1800 UT to 2400 UT as a function of geographic latitude φ, respectively invariant latitude Λ. ($Ap = 2$). This is another example for an increase of I towards north (2000 UT) and a subsequent formation of the trough. Since $FoF2$ data from Uppsala are missing for the time intervall 1800 UT

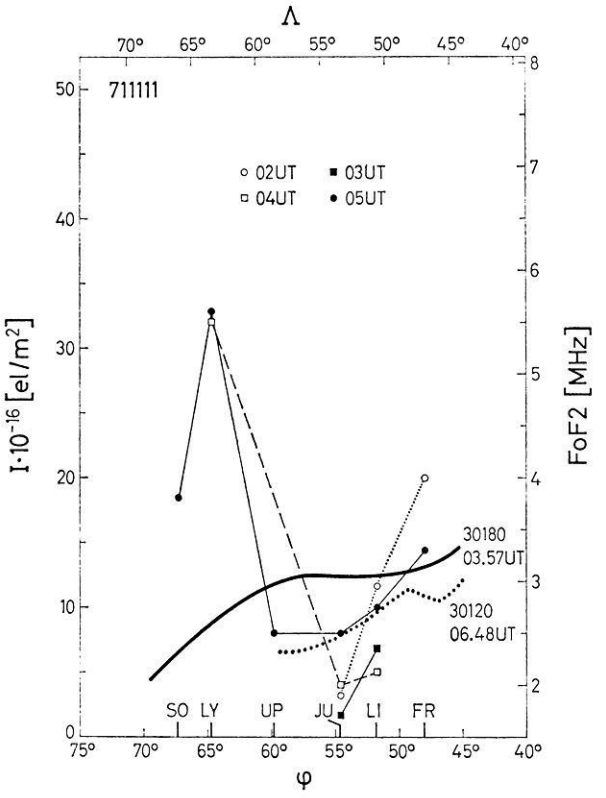

Fig. 3. Same nomenclature as for Fig. 1, however the I (φ)- and $FoF2$ (φ)-curves were displayed for Nov. 11th, 1971, in the time interval 0200 UT—0700 UT

—2200 UT and those from Lycksele for 2100 UT and 2200 UT no statement about a time lag between I and $FoF2$ is possible. This is just one example out of many similar cases.

Fig. 3 displays the electron content I and the critical frequency $FoF2$ again calculated for Nov. 11th, 1971 ($Ap = 16$) for the time interval 0200 UT to 0700 UT as a function of latitude. Both I (φ)-curves show a decrease towards north. The few $FoF2$ data available for this time period enable no reasonable comparison between I and $FoF2$. If the $FoF2$ (φ)-curve drawn for 0400 UT should represent to a first approximation the actual continuous $FoF2$ (φ) behaviour then we would have an increase in $FoF2$ in the range 60° to 65° N latitude but a decreasing I-curve. This would be a behaviour reverse to that observed in the early evening (Fig. 1).

Fig. 4 displays the electron content I and the critical frequency $FoF2$ calculated for Dec. 3rd, 1971 ($Ap = 4$) for the time interval 0900 UT—1500 UT as a function of latitude. I (φ) shows a behaviour which is abnormal for that time of day. It displays an increase towards north. $FoF2$ reveals very strong variations. The general tendency of the I (φ) and $FoF2$ (φ)-curve is pretty much the same.

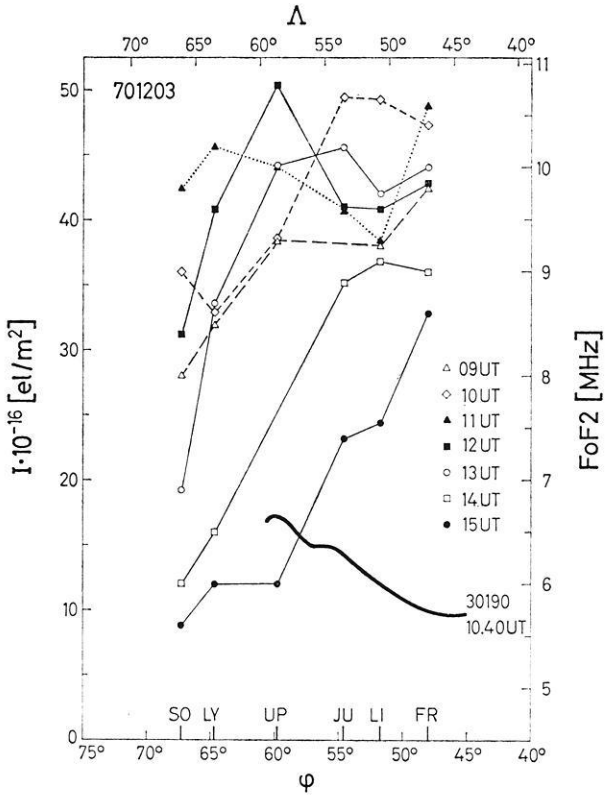

Fig. 4: Same nomenclature as for Fig. 1, however the I (φ)- and $FoF2$ (φ)-curves were displayed for Dec. 3rd, 1971, in the time interval 0900 UT–1500 UT

d) Final Remarks

If, by the just planned coordinated measuring program, further data might be obtained which give further support of this pretented one hour time delay between I and $FoF2$ during early evening hours in winter and if there will be a satisfactory theoretical explanation, then it seems to be possible to measure the effect of low energetic electrons (<100 eV) in subpolar regions by the described procedure. In our specific case the following data are required.

a) I (φ)-curves from Oulu and Lindau

b) $FoF2$ data from Freiburg, Lindau, Juliusruh, Uppsala, Lycksele and Sodankylä.

Even if finally there will be not sufficient relevant data for this proposed comparison — due to spread F, satellite scintillations or other distortions — already the calculated I (φ)-curves may reveal new useful informations, especially if it is possible to gather data in a dense time sequence during the formation phase of the trough or also during its deformation phase. This seems to be very valuable for an improvement of the various theories about the trough formation and its relation to the plasmapause which are not yet in agreement.

The recently started investigations of irregularities in the polar ionosphere by means of holography (Schmidt, 1972), which are also based on observations of the 150 MHz and 400 MHz signals of the NNSS satellites should be carried out simultaneously. A cooperation with colleagues from Oulu has been already started.

These measurements should be supplemented by radar echoes measurements like those carried out by Hagfors *et al.* (1970). They showed that strong radar echoes occurred in the absence of observable electron precipitation but were in close time and spatial coincidence with proton precipitation, although the proton contribution to the ionization at the scattering height at 112 km was computed to be negligible compared with the solar ionization.

Acknowledgement. The author thanks Prof. Dr. J. Oksman and his coworker, Dr. A. Tauriainen, (University Oulu) for supplying the electron content data from Oulu. He thanks his colleague, Dr. G. Schmidt, for supplying those data from Lindau, further Mr. A. Hedberg (Uppsala) for a refined ionogram reduction of *FoF2* data from Uppsala and Lycksele. Finally he values the critical comments and cooperation of his colleagues, Dr. W. Becker, Dr. H. Kohl, Dr. R. Pilkington, Dr. P. Stubbe and Dr. T. R. Tyagi.

References

Carpenter, D. L., Park, C. G.: On what Ionospheric workers should know about plasmapause – plasmasphere. Rev. Geophys. Space Phys. *11*, 133–154, 1973

Chappell, C. R.: Recent Satellite measurements of the morphology and dynamics of the plasmasphere. Rev. Geophys. Space Phys. *10*, 951–979, 1972

Ebel, A., *et al.*: Vergleichende Auswertung von Faraday-Effekt-Beobachtungen zweier Empfangsstationen. Z. Geophys. *35*, 363–411, 1969

Hagfors, T., *et al.*: Simultaneous observation of proton precipitation and auroral radar echoes. J. Geophys. Res. *76*, 6093–6098, 1971

Hartmann, G. K., *et al.*: Satellite beacon observations from 1964 to 1970. Mitteilungen aus dem MPI f. Aeronomie Nr. 48 Berlin–Heidelberg–New York: Springer 1972

Hartmann, G. K.: Brief review of scintillation studies. Space Research *XII*, 1221–1228, 1972

Hartmann, G. K., Tauriainen, A.: Negative Horizontalgradienten des integralen Elektroneninhaltes *I* der Ionosphäre. Kleinheubacher Berichte, Bd. Nr. *16*, 359–370, 1973

Lemaire, J., Scherer, M.: Exospheric models of the topside ionosphere. Space Sci. Rev. *15*, 591–640, 1974

Liszka, L.: Latitudinal and diurnal variations of the ionospheric electron content near the auroral zone in winter. In: Electron density profiles in ionosphere and exosphere, ed. J. Frihagen. Amsterdam: North Holland Publishing Company 1966

Mayr, H. G., Fontheim, E. G., Brace, L. H., Brinton, H. C., Taylor, H. A. Jr.: A theoretical model of the ionosphere dynamics with interhemisphere coupling. J. Atmosph. Terr. Phys. *34*, 1659–1680, 1972

Möller, H. G.: Oblique sweep frequency experiments over a 2000 km north-south subauroral path. Radio Science *2*, 77, 1967

Nichol, D. G.: Spread *F* in the midlatitude ionospheric trough zone. J. Atmosph. Terr. Phys. *35*, 1869–1879, 1973

Rai, D. B., Hook, J. L.: The total electron content and its variation in the auroral zone during winter. J. Geophys. Res. *72*, 5319–24, 1967

Schmidt, G., Tauriainen, A.: Bestimmung des Elektroneninhaltes der Ionosphäre über Oulu/Finnland mit Hilfe des Satelliten Explorer 22 (S-66) nach dem Faraday-Doppler-Hybrid Verfahren und Vergleich mit Lindauer Ergebnissen. BMBW, Forschungsbericht W 70–50, 1970

Schmidt, G.: Determination of the height of ionospheric irregularities with the holographic method. Z. Geophys. *38*, 891–913, 1972

Stuart, G. F.: Characteristics of the abrupt scintillation boundary. J. Atmosph. Terr. Phys. *34*, 1455–1468, 1972
Stubbe, P.: The thermosphere and *F*-region. A reconciliation of theory with observations. The Pennsylvania State University. Sc. Rep. No 148, 1973
Tyagi, T. R.: Electron content and its variations over Lindau. J. Atmosph. Terr. Phys. *36*, 475–487, 1973
Tyagi, T. R.: Some aspects of satellite radio beacon studies of the ionosphere. Sc. Rep. Max-Planck-Institut f. Aeronomie, June 1974

Dr. G. Hartmann
Max-Planck-Institut für Aeronomie
D-3411 Katlenburg-Lindau 3
Postfach 20
Federal Republic of Germany

J. Geophys. 41, 243–263, 1975

Transmission of Electric Fields and Photoelectron Fluxes between Conjugate Ionospheric F2-Regions*

E. F. Petelski

Dornier System, Space Division, Friedrichshafen

Received February 26, 1974; Revised Version December 8, 1974

Abstract. The dynamic behaviour of the ionospheric F2-layer requires considerable vertical transport of ionization. Possible causes of such transport are ambipolar diffusion, neutral air winds and electric fields. Here mid-latitude electric fields are investigated. Real height variations of the F2-layer indicate that the phases and amplitudes of these fields are similar at well conjugate points and that the field strengths can become unexpectedly high. It is further shown that photoelectrons can migrate between the two hemispheres along the geomagnetic field lines.

Key words: Ionospheric F2-layer — Real Heights — Critical Frequencies — Conjugate Points — Electric Fields — Neutral Winds — Declination Effect — Photoelectron Fluxes — Numerical Filtering — Correlation Coefficients.

1. Introduction

Even at magnetically quiet times the mid-latitude ionospheric F2-layer undergoes large height and density fluctuations. These variations cannot be due to photochemical processes only but require considerable vertical transport of ionization. Possible causes of such transport are ambipolar diffusion, neutral air winds and electric fields.

So far, experimental results do not provide a detailed and reliable picture of the winds and the electric fields in the upper atmosphere. Therefore, attempts to theoretically understand the dynamic peculiarities of the ionosphere have to proceed from models. In this way numerous authors have come to the conclusion that wind effects predominate in middle and high latitudes whereas electric fields have some importance in equatorial latitudes, at most. However, there does exist experimental evidence indicating that wind and field models are insufficient and that electric fields may exert appreciable influence on the mid-latitude ionosphere, too. Regrettably, effects of this kind cannot easily be identified by conventional methods of ionospheric sounding. That is why an attempt was made to take advantage of the geomagnetic coupling of conjugate ionospheric regions with a view to distinguish wind- and electric field induced effects in the F2-layer. Another intention was to assess the strength of the involved fields and to derive information about photoelectron fluxes between the two hemispheres.

---

* This publication is the shortened version of a doctor thesis which was prepared at the Max-Planck-Institute for Aeronomy, D-3411 Lindau/Harz.

2. *Background and Method*

From measurements of the orbital periods of earth satellites, atmospheric density variations within the F2-layer can be deduced which stem from the daily succession of heating and cooling of the air. These data render feasible the preparation of atmospheric models giving information on the global distribution of pressures as well as temperatures. According to King and Kohl (1965), the pressure gradients drive large systems of horizontal winds within the F2-layer. Many papers have already been dedicated to the calculation of such winds from the world-wide pressure distribution. A typical result is that by Challinor (1970).

Evidently, models of this kind are of limited validity because they are not derived from direct measurements but calculated indirectly from satellite observations. Moreover, geophysical models usually represent space and time averages which exclude predictions of local or irregular effects.

The influence of neutral winds on charged particles is exerted by air drag, i.e. by frictional forces. Within the F2-layer, the resulting movements of the ionization are restricted to directions corresponding those of the earth's magnetic field. Analytically, this means

$$\mathbf{V} = (\mathbf{U} \cdot \mathbf{B})\, \mathbf{B}/B^2 \; ; \tag{1}$$

V: velocity of electrons and ions, **U**: velocity of neutral air, **B**: geomagnetic field. Although the neutral gas moves horizontally, the magnetic inclination introduces vertical components in the ionization velocity:

$$V_z = U_x \sin I \cos I \; ; \tag{2}$$

V_z: vertical velocity component of **V**, U_x: north-south component of **U**, I: geomagnetic inclination.

To estimate the effects of ionization drifts on the F2-layer, continuity equations for all plasma components have to be solved. For example, the concentration N_i of one kind of ions in a certain height z behaves like

$$\left.\frac{\partial N_i}{\partial t}\right|_z = q - \beta N_i^2 - \operatorname{div}(N_i \boldsymbol{V}_i), \tag{3}$$

where q is the ionization rate, β the recombination coefficient and t the time. To be sure, the ionization is not exclusively accelerated by winds. It also diffuses under the influence of gravity and its own partial pressure and it is exposed to Lorentz forces as well as to electric fields. In order to account for all these parameters, the equations of motion for ions, electrons and the neutral gas have to be taken into consideration. In case of charged particles, these equations are of the following kind:

$$m_i \frac{d\mathbf{V}}{dt} = m_i \mathbf{g} - \frac{1}{N_i} \nabla p_i + e\mathbf{E} + e(\mathbf{V} \times \mathbf{B}) - m_i \nu_{in} (\mathbf{V} - \mathbf{U}) \; ; \tag{4}$$

p_i: partial pressure of ions
E: electric field
ν_{in}: collision frequency ions-neutral particles
m_i: ion mass
g: gravitational acceleration
e: elementary charge
B: geomagnetic field
U: neutral wind velocity

For neutral particles one gets:

$$m\frac{d\mathbf{U}}{dt} + 2m\boldsymbol{\Omega}\times\mathbf{U} = m\mathbf{g} - \frac{1}{N}\nabla p - m\nabla\psi + \frac{\mu}{N}\nabla^2\mathbf{U} - m\nu_{ni}(\mathbf{U}-\mathbf{V})\,; \quad (5)$$

m: mass of single particle
N: density of particles
ψ: scalar potential of tidal forces
ν_{ni}: collision frequency neutral particles-ions
$\boldsymbol{\Omega}$: earth's angular velocity
p: pressure
μ: molecular coefficient of viscosity

By simultaneously solving the complete set of Eqs. (3) to (5), one can show that vertical motions of the F2-layer ionization finally result in two effects: they change the height of the ionization density maximum, the "layer height", and they alter the maximum ionization density itself. The latter effect is a consequence of the fact that in different heights different recombination rates apply: an upward drift increases both the layer height and the ionization density and a downward drift acts in the opposite way.

A lot of research has already been done concerning wind induced effects of the above kind. Mostly, the authors have solved the system of coupled equations twice, once inserting and once omitting neutral air winds, and compared the results with experimental ionospheric data. In this way it could be demonstrated that winds do act a vital part among those factors which determine the F2-layer dynamics. In particular, it was established that winds are the reason for the well-known evening enhancement of the F2-layer height. However, most of these studies suffer from an essential drawback in that the theoretical values are compared to averaged experimental results which do no more contain short-time, individual events. Moreover, only a few stations have been brought into play so far.

When calculating the variations of ionospheric parameters, most authors neglected electric fields. This somewhat perfunctory treatment of a potentially important parameter has its roots in current field models. A famed one is that by Matsushita (1969) which has been computed from geomagnetic Sq-variations (Sq for solar quiet) and reasonable assumptions on winds and conductivities in the ionospheric E-layer. Matsushita's starting point was a theory according to which thermal and gravitational "tides" within the E-layer produce dynamo electric fields. Owing to the low resistivity along the geomagnetic field lines, these fields are supposedly projected up to the F2-layer without attenuation. There the strength as well as the direction of the "Sq-field" change continuously, having a period of 24 hours and typical amplitudes of 2 V/km in middle latitudes.

Electric fields in the F2-layer must basically have the same effects as winds in that they induce ionization drifts and thus change the height and the density of the layer. Ions as well as electrons will achieve velocities $\mathbf{V}$ given by

$$\mathbf{V} = \mathbf{E}\times\mathbf{B}/B^2\,. \quad (6)$$

Their vertical velocity components will depend on the azimuthal field E_y and the geomagnetic inclination I:

$$V_z = E_y\cos I/B. \quad (7)$$

Presupposing electric fields of uniform strength, the vertical drift should be largest about the equator because there the inclination vanishes. In fact, successful attempts have already been made to explain the equator anomaly of the F2-layer in terms of electric fields. According to Hanson and Moffet (1966) west-east electric fields of less than 1 V/km make the ionization rise at the equator and fall down along the magnetic field lines elsewhere. So the characteristic meridional distribution comes about with humps in middle latitudes and a groove at the equator. On the other hand, the Sq-field seems to be unsuited for the explanation of ionospheric properties in higher latitudes. From his own calculations Rüster (1971a) concluded that the effects of Matsushita's dynamo fields may well be ignored in relation to those of the neutral air winds. According to Stubbe and Chandra (1970) the dynamo electric fields would have to be augmented by a factor of 3 to 5 in order to match the winds.

At this point, the validity of models must be queried once again. As is commonly known, strong electric perturbation fields occur during magnetically disturbed periods. It is therefore conceivable that at quiet times supplementary fields have to be reckoned with, too. Regrettably, a definite solution to this problem has not yet been found. Though one now disposes of a bunch of methods for measuring electric fields, experimental data are still sparse. This is essentially due to the fact that most methods are either inexact, or restricted to certain times (dawn, dusk), or too expensive or delicate for large scale, routine application. Nevertheless, considerable evidence has been accumulated that even at magnetically quiet intervals the dynamo field can be superimposed with additional fields of remarkable strength. These may be fields of magnetospheric origin which have protruded into the plasmasphere and there been guided down along the magnetic field lines into the ionosphere.

Some supporting evidence has been collected by Mühleisen *et al.* (1971). From potential measurements on balloons, they inferred fields of up to 8 V/km in middle latitudes, i.e. the dynamo values times four. Other balloon flights were done by Mozer (1971) in auroral latitudes. Here fields were encountered of up to 100 V/km. These values by far exceed all dynamo estimates. Carpenter and Bowhill (1971) also hit upon large electric fields. They made use of the incoherent backscatter facilities at Millstone Hill ($\varphi = 43\,°\mathrm{N}$, $I = 72\,°\mathrm{N}$) and compared the experimental results with theoretical ones which were deduced from Cho and Yeh's (1970) wind model. The resulting velocity differences were treated as being caused by electric fields. In this way they ascertained field amplitudes of 9.6 to 15 V/km.

To be sure, Carpenter and Bowhill's result is not fully convincing, since wind models were used to determine the electric fields. It would be more satisfactory if wind- and field induced motions within the F2-layer could be discriminated directly. At first sight this could be achieved most easily by simultaneously watching vertical and horizontal ionization drifts. As can easily be shown, an electric field induced vertical drift is accompanied by a northward horizontal component, whereas in the wind case a southward horizontal component will appear. Deplorably, this method necessitates sophisticated incoherent backscatter sounders which were not at hand for the study in question. As a consequence, it was tried to find out whether the magnetic coupling of conjugate points can be utilized to discriminate wind- and field induced effects.

Now, what is the meaning of "conjugate?" It refers to pairs of points on the earth's surface which are linked by a magnetic field line. The geographic positions of

such points can be roughly estimated from dipole approximations of the geomagnetic field. More exact calculations, however, must take into account the distortions of the magnetic field lines caused by the solar wind and by the magnetospheric current systems. For this end, multipole models have been prepared by Cain *et al.* (1971). They incorporate magnetic field data gathered on the earth's surface as well as in satellite heights.

Since magnetic field lines may serve as ducts for charged particles and waves, close relationships should exist between geophysical phenomena at their nadirs. Presumably, "conjugate events" might set in simultaneously or alternately and they might pass off similarly or adversely. If they were coupled, the degree of correlation should vary in time and space following the shape and the position of the field lines. That is why observations at conjugate points give promise of new insight into the generation and transmission of various effects as well as into the exact configuration, and its variation, of the geomagnetic field lines. Accordingly, the number of conjugate experiments has increased sharply after the IGY.

A somewhat peculiar conjugate effect has been suggested by Gold (1959): The Geomagnetic field lines being near equipotentials, electric potentials in and above conjugate F2-regions should be balanced. Since this would also apply to the corresponding electric fields, good correlation should exist for those ionospheric motions which are exclusively caused by electric fields. In contrast to electrodynamic movements, wind induced drifts will be subject to differing geographical and/or seasonal conditions. Hence, the similarity of conjugate ionospheric motions is a criterion for the identification of electric field effects.

Starting from these considerations, real height variations of the ionospheric F2-layer were examined above several pairs of conjugate stations. They were deduced from ionograms using a method by Becker (1967). This method comprises the necessary apparatus and software for the digitization of ionograms as well as an extensive program for the final computation of real heights and ionization densities.

Instead of doing own soundings, ionograms were procured from routinely operated stations. This procedure posed formidable problems in that it was difficult to find near conjugate stations which produced suitable data. As a first step, the few stations in the southern hemisphere were selected which could be roughly associated with a northern counterpart. Then Lenhart (1969) calculated the exact coordinates of the conjugate points in order to refine the selection. Finally, the number of pairs was reduced by applying the following requirements:

As conjugate points should be connected by closed field lines, high latitude stations were to be ignored.

To avert geographically induced correlations, the geographical latitudes of any two stations had to be different.

The declination effect had to be allowed for.

The latter effect, which has been discovered by Eyfrig (1963), denotes the control of the F2-layer behaviour by the declination of the earth's magnetic field. This effect was interpreted in terms of the daily variation of the neutral air winds by Kohl *et al.* (1969) and will become evident from Fig. 1.

The upper part of this sketch applies to the northern hemisphere. For the sake of simplicity the wind velocity is considered a vector of unity length rotating clock-

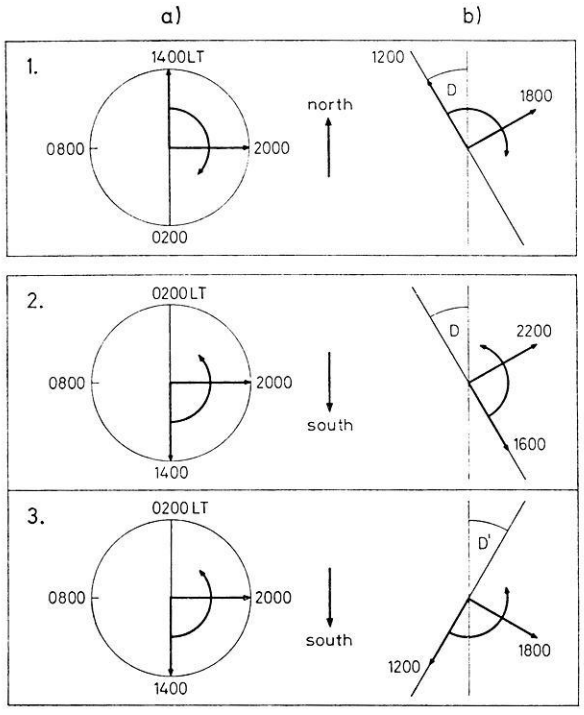

Fig. 1. Declination effects in different hemispheres. 1. Northern hemisphere, a) $D = 0°$, b) $D = 30°$ W. 2. Southern hemisphere, a) $D = 0°$, b) $D = 30°$ W. 3. Southern hemisphere, a) $D = 0°$, b) $D' = 30°$ E. The daily variation of the wind velocity vector as computed by Challinor (1970) is indicated by the left hand "clocks"

wise once within 24 hours and pointing northwards at 2 p.m. In the case of zero declination this time coincides with the maximum downward drift of the ionization. Six hours later the drift vanishes since the wind vector is now perpendicular to the magnetic field. In the second case a declination of 30° west has been assumed. Now the extremes of the ionization transport come about 2 hours earlier. On the other hand, an easterly declination would shift the phase in the opposite sense. Obviously, this explanation of the declination effect is not confined to winds but might as well proceed from dynamo electric fields which also rotate. The southern hemisphere is referred to in the lower section of Fig. 1. Here the wind vector's sense of rotation reverses and so does the declination effect. As different declination effects may conceal the correlation of ionospheric motions at conjugate points, stations with equal declination effects should be preferred for conjugate studies. To meet this requisition the sum of the declinations must vanish. However, only a few appropriate pairs of stations exist in the world.

Eventually, 9 combinations of conjugate stations were sorted out (Table 1). Among them Canberra and Petropavlovsk were deemed preferable because of the following attractions: The distance between each of these stations and the exact conjugate point of its counterpart is less than 65 km, the geographical latitudes are quite different and the sum of the declinations amounts to only 5°.

Table 1. Names, positions and geomagnetic data of conjugate stations

pair of stations	abbreviation	geographic latitude	geographic longitude	geomagnetic declination	geomagnetic inclination
Argentine Island-	AI	65,3°S	64,3°W	17,5°O	57,9°S
Wallops Island	WI	37,9°N	75,5°W	8,5°W	69,6°N
Canberra-	CB	35,3°S	149,2°O	11,3°O	66,1°S
Petropavlovsk	PE	53,0°N	158,7°O	5,8°W	64,0°N
Capetown-	CT	34,1°S	18,3°O	24,2°W	64,2°S
Poitiers	PO	46,6°N	0,3°O	6,8°W	62,6°N
Garchy	GA	47,3°N	3,1°O	5,6°W	63,3°N
Hobart-	HO	42,9°S	147,3°O	13,6°O	72,8°S
Magadan	MD	59,5°N	150,8°O	10,8°W	70,7°N
Kerguelen-	KE	49,4°S	70,3°O	50,8°W	67,0°S
Archangelsk	AR	64,6°N	40,5°O	13,0°O	76,3°N
Gorki	GO	56,2°N	44,3°O	10,3°O	71,6°N
Sogra	SO	62,8°N	46,3°O	14,5°O	75,3°N
Marion Island-	MI	46,9°S	37,9°O	35,1°W	62,3°S
Lindau	LI	51,7°N	10,1°O	2,3°W	66,6°N
Rarotonga-	RA	21,2°S	159,8°W	13,0°O	38,2°S
Maui	MA	20,8°N	156,5°W	11,0°O	38,3°N
Townsville-	TO	19,3°S	146,7°O	7,3°O	48,4°S
Kokubunji	KO	35,7°N	139,5°O	6,0°W	48,9°N
Tsumeb-	TS	19,2°S	17,7°O	15,4°W	56,8°S
Capo San Lorenzo	CS	39,5°N	9,6°O	3,8°W	55,0°N

3. Results

At first, it was aimed to confirm the equivalence of electrodynamic ionization drifts above conjugate points. For this purpose, periods with geomagnetic bays were analyzed. According to Rüster (1969), disturbances of this kind are accompanied by strong electric fields which force drastic height variations upon the F2-layer. The presence of such fields has been confirmed by Maynard *et al.* (1973).

The next drawing, Fig. 2, presents information about two bays which occurred in October 1959. Magnetograms for Hermanus (near Capetown) and Chambon-la Forêt (near Garchy) are presented in the lower left. Both the H- and D-components show the typical bay disturbances. Above, height variations of the F2-layer are given for the conjugate pair Capetown and Garchy as well as for the non-conjugate combination Tsumeb and Lindau. The straight lines indicate the occurrence of sunset as a function of height. Obviously, the vertical motions above Canberra and Garchy are in much better agreement than those above Tsumeb and Lindau. This finding is in favour of Gold's (1959) concept of a potential equilibrium at conjugate points.

It could be objected that the conformity of electric fields at conjugate points and during magnetic bay disturbances be given a priori, superseding any equalizing influence of the magnetic field lines. This argument could be refuted by detection of similar motions of the F2-layer during asymmetric disturbances. In this context solar eclipses are of great importance. Carlson and Walker (1972) forecasted fluctuations of the ionospheric electric field during sunrise and sunset which would induce motions of the F2-layer. Correspondingly, field variations should occur during eclipses. If these variations could also be established for the non-eclipse conjugate regions, this would mean a direct proof for the transmission of electric fields along the geomagnetic field lines.

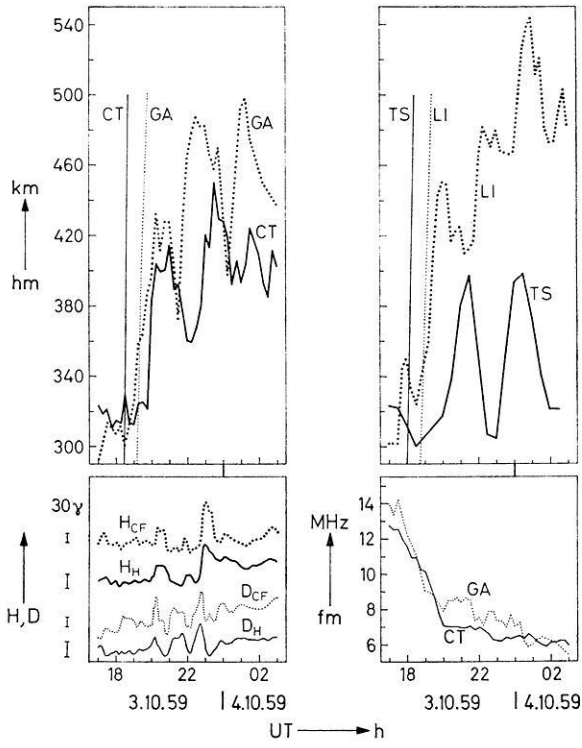

Fig. 2. F2-layer behaviour at Capetown-Garchy (CT—GA) and Tsumeb-Lindau (TS—LI) during two bay disturbances; magnetograms from Chambon-la-Forêt (CF) and Hermanus (H)

In Fig. 3 real height variations of the F2-layer are pictured for Argentine Island and Wallops Island, and during an eclipse. The event took place in the northern hemisphere on March 7, 1970, and its onset and termination are marked by short vertical bars in the drawing. It was excepted that, within this interval, vertical motions should occur at both stations. However, no such movement can be discerned above Wallops Island, whilst there is a sharp rise of approximately 65 km at Argentine Island. Although the ascent of the F2-layer at the southern station may well be a conjugate effect a more viable explanation is in terms of magnetic disturbances since *Kp* was rather high about that time. Generally speaking, the transmission of electric fields between the two hemispheres could not be substantiated in this direct way. On the other hand, it was shown in the previous section that during geomagnetic bays the correlation of F2-motions is confined to well conjugate points. This fact may suffice as an indirect proof of the coupling concept.

We now turn to the normal behaviour of the F2-layer, i.e. its behaviour during magnetically quiet times. In Fig. 4 the jagged curves represent measured height variations of this layer at Canberra and Petropavlovsk in March and September 1969. The smooth curves are appropriate theoretical values which were calculated using a program by Kohl (1972). This program took into account solar as well as neutral

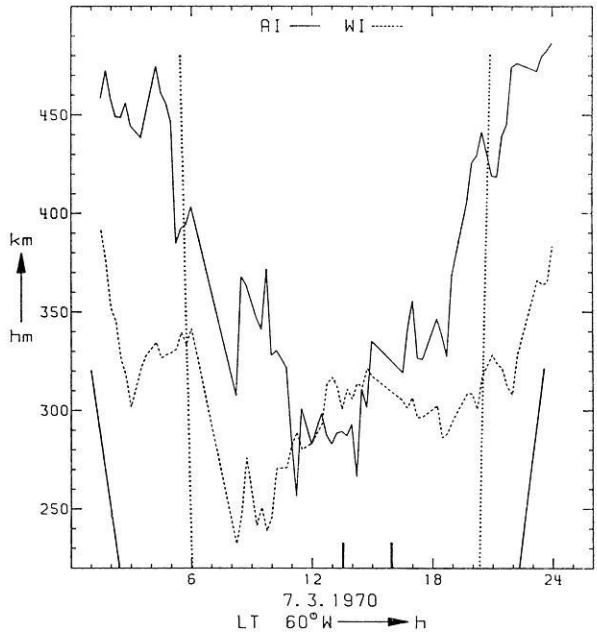

Fig. 3. Height variations of the F2-layer above Argentine Island (AI) and Wallops Island (WI) during an eclipse. Magnetic indices: 4+ 30 40 4+ 5— 6— 4+

wind effects but ignored electric fields. One again notices straight lines denoting the occurrence of sunrise and sunset for each station as a function of height. The experimental results almost exactly match each other but slightly deviate from the theoretical values. Phase differences between the morning drops of the layers are considerably smaller in the experimental case than in the theoretical one. Furthermore, there are striking similarities between the experimental minima which are not reflected by theory.

Surprisingly, the accord of the empirical height variations above Canberra and Petropavlovsk is well maintained in June (Fig. 5), a solsticial month, when the seasonal conditions are different in the two hemispheres (difference of solar elevation angles for CB and PE = 28°).

For this period, theoretical predictions neglecting electric fields postulate phase differences of up to 3 hours. Admittedly, the plot reveals some small scale deviations from conjugacy but the envelopes of the traces are quite similar. Most of the jitter stems from ionospheric disturbances like spread-F which gave rise to random errors in the evaluation of the ionograms. It should be stressed, however, that the morning peaks of the layer height above Canberra correspond to real motions.

In December (difference of the solar elevation angles for CB and PE = 64°), the phase coincidence of the experimental data is still better than that of the theoretical values, although the phase difference has now shrunk to 1.5 hours (Fig. 6). About midnight peculiar depressions occur at both stations which are well-nigh simultaneous, have amplitudes of up to 100 km and do not show up in the theoretical forecasts.

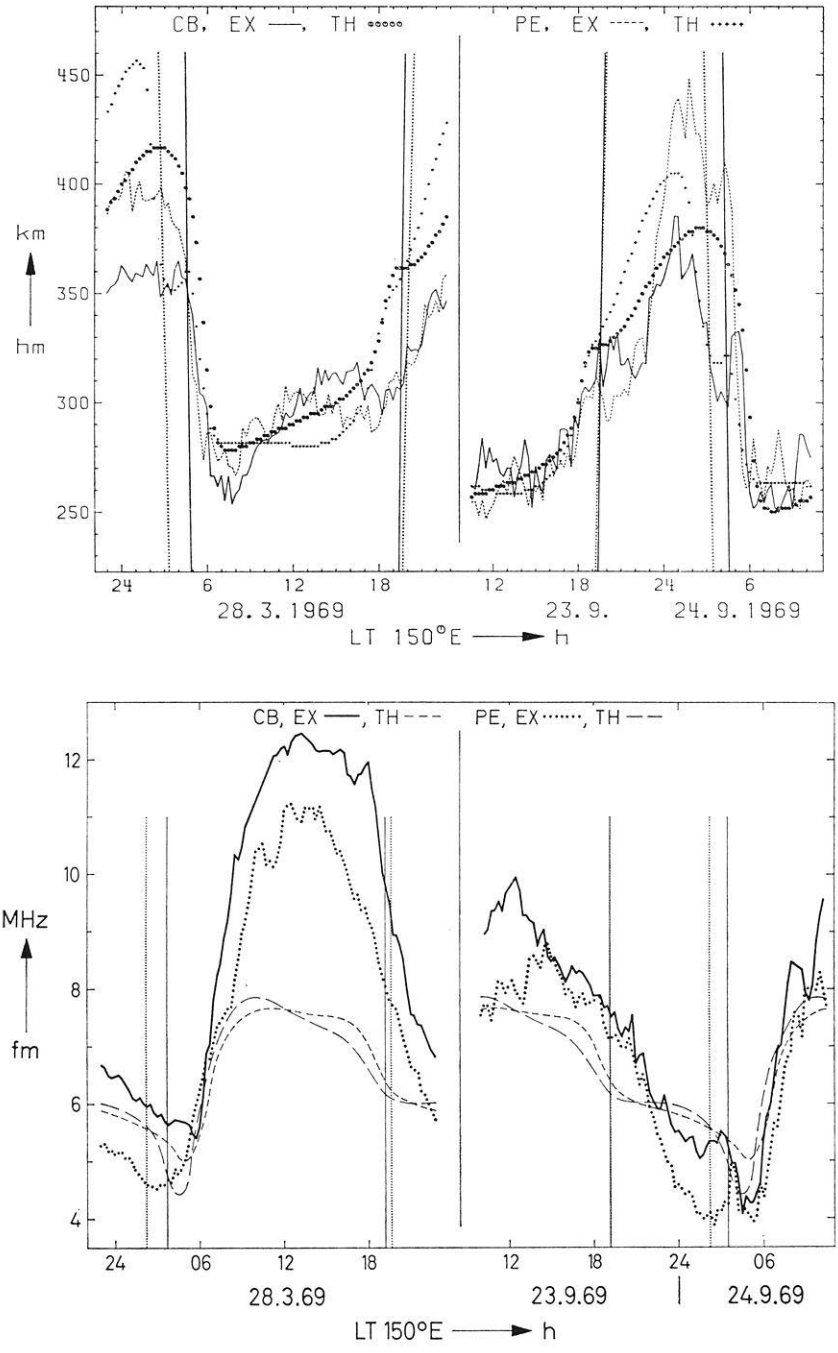

Fig. 4. Above: height variations; below: critical frequency variations of the F2-layer at Canberra (CB) and Petropavlovsk (PE) in March and September. EX: experimental values, TH: theoretical values. Sounding intervals: 15 minutes. Sunrise, sunset: CB --------, PE..... Magnetic Kp-indices: March: 20 10 0+ 0+ 10 2— 2— 1+; September: 0+ 0+ 0+ 1— 30 20 2+ 3+

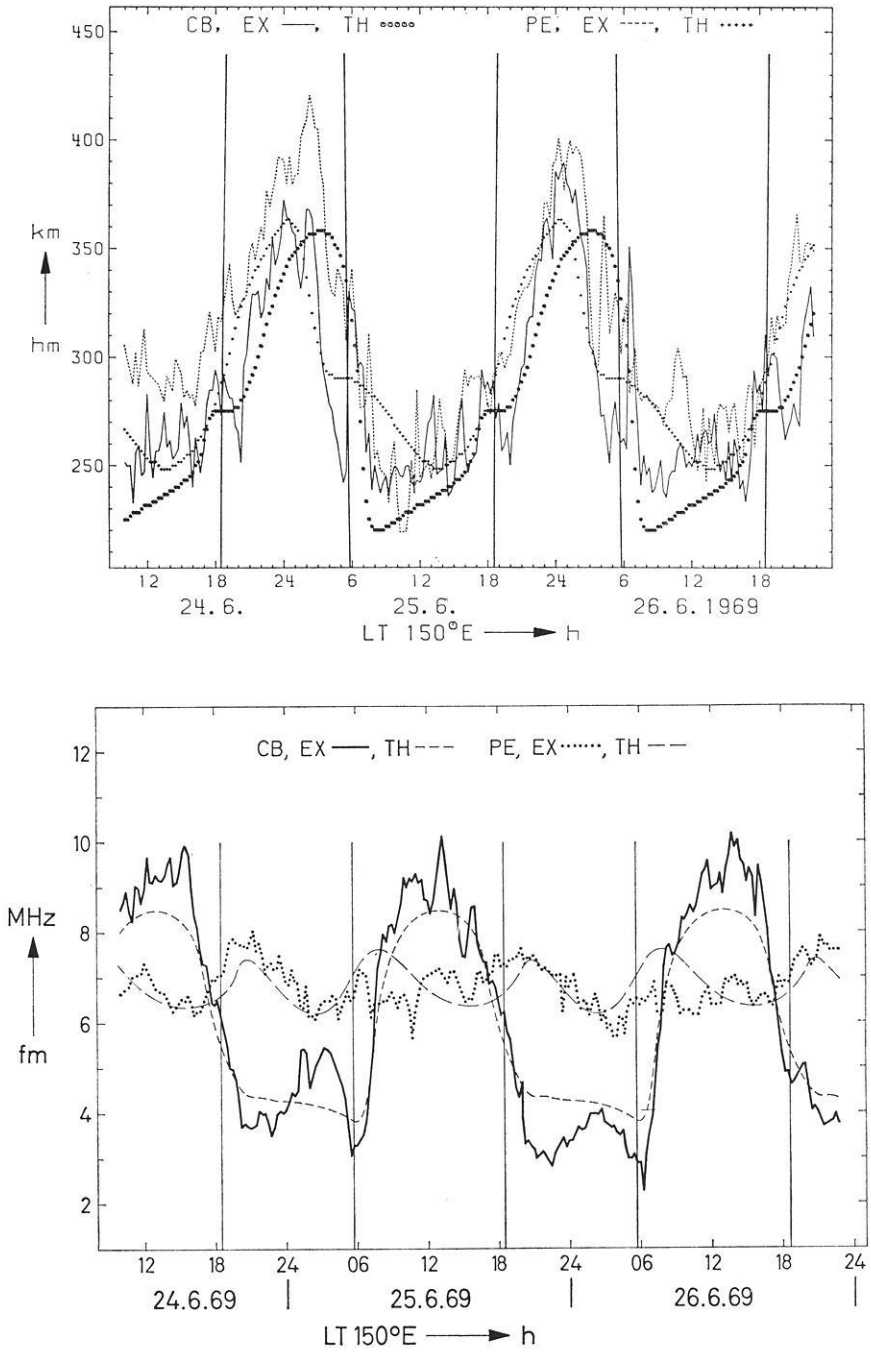

Fig. 5. Above: height variations; below: critical frequency variations of the F2-layer at Canberra (CB) and Petropavlovsk (PE) in June. EX: experimental values, TH: theoretical values. Sounding intervals: 15 minutes. Sunrise, sunset: CB --------, PE..... Magnetic Kp-indices: 30 30 2+ 20 3+ 2+ 20 3— 1+ 2— 2+ 1+ 20 30 30 30 20 2— 1+ 2+

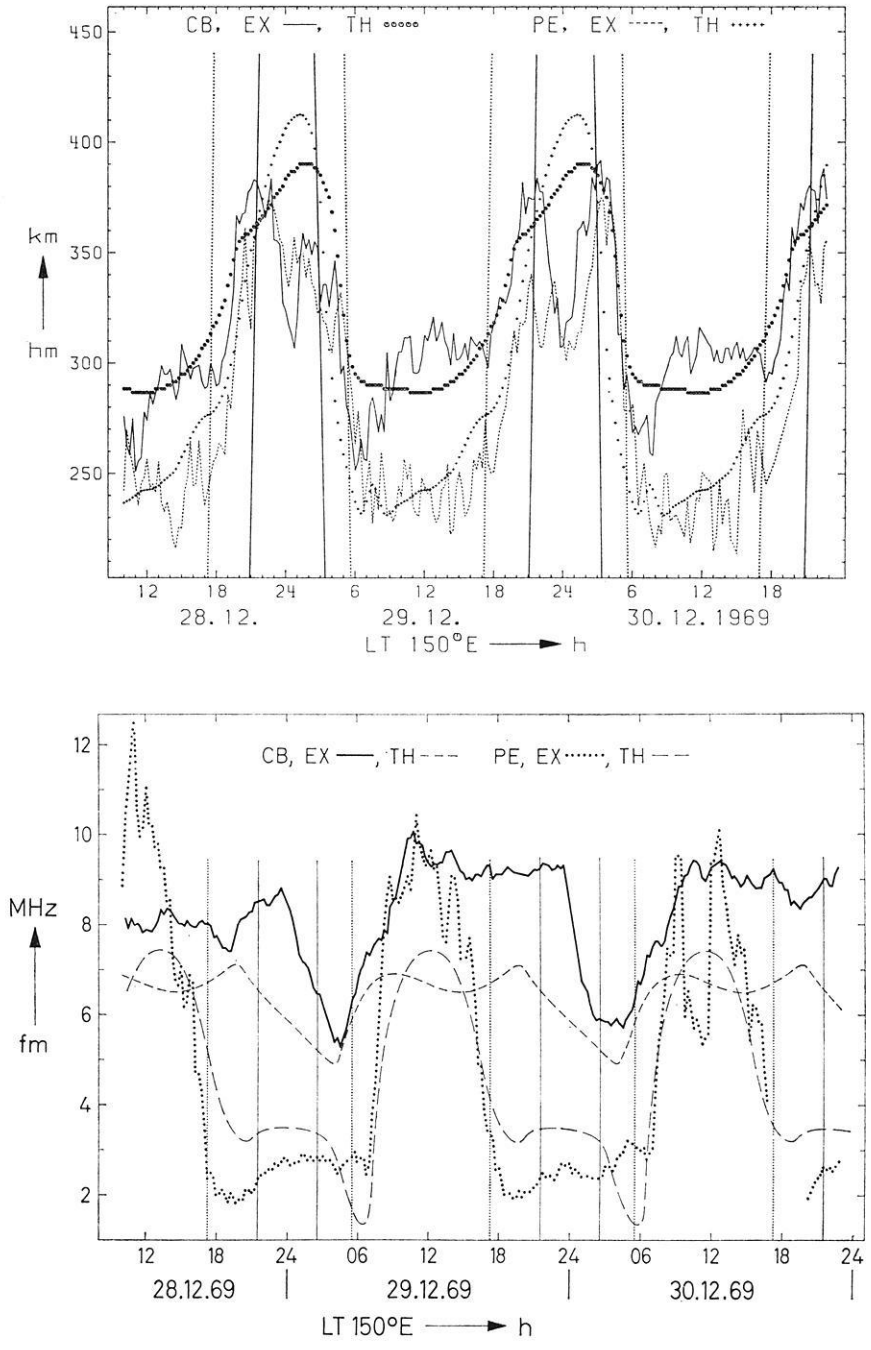

Fig. 6. Above: height variations; below: critical frequency variations of the F2-layer at Canberra (CB) and Petropavlovsk (PE) in December. EX: experimental values, TH: theoretical values. Sounding intervals: 15 minutes. Sunrise and sunset: CB --------, PE..... Magnetic Kp-indices: 0+ 0+ 0+ 10 0+ 2+ 10 1+ 2— 10 1+ 1+ 1+ 1+ 1+ 1— 0+ 0+ 10 00 1—

They certainly result from electric fields. Other mechanisms must be involved in the enhancement of the layer height between 6 a.m. and 1 p.m. at Canberra because there are no corresponding motions at the conjugate point.

It is worth mentioning that midnight depressions are far from being rare or exceptional events. Rather, Nelson and Cogger (1971) have found a multitude of similar variations at single stations. These facts are at variance with a theory by Stubbe and Chandra (1970), according to which nighttime height variations of the ionization are inexistent above 300 km.

Along with real F2-layer heights critical frequencies f_0 were calculated. They are related to the maximum electron densities n_e by the relation

$$n_e = 12400 \; f_0^2 \,. \tag{8}$$

The aim was to check the influence of photoelectron fluxes on the ionosphere which was claimed by Shawhan *et al.* (1970) to consist in significant increases of the electron density by impact ionization.

In the lower half of Fig. 4 critical frequencies were shown for equinoctial conditions. Their excellent agreement indicates that during these times geographic asymmetries of conjugate points may be offset by particle fluxes along the magnetic field lines. Similar results have been published by e.g. Benkova *et al.* (1969). In June, however, the two curves do no longer concur (see Fig. 5, below). Obviously, large differences of the solar flux go beyond any compensational mechanism. This also applies to December (see Fig. 6, below); yet, at second sight, pre-dawn enhancements. are perceptible in the Petropavlovsk plot which are apparently related to sunrise at Canberra. Bukin *et al.* (1968) have found corresponding humps and attributed them to photoelectron transport from the sunlit into the dark hemisphere.

According to the results mentioned so far height variations of the F2-layer at Canberra and Petropavlovsk are almost identical in all seasons (whereas the critical frequencies differ widely in the solstices). It is concluded that electric fields are among the most important parameters bearing on the ionospheric dynamics. One might protest that nothing has been said as yet about the situation at less or non-conjugate stations. Possibly, the ionosphere behaves uniformly everywhere and the above inference is not justified.

This conjecture is impaired by Fig. 7. It shows real height variations of the F2-layer above Tsumeb and Capo San Lorenzo. Either station is situated approximately 350 km from the exactly conjugate point of its counterpart and the declinations sum up to 19.2 degrees. Although this is not so very bad a conjugacy the height variations do no more reveal any correlation. One may therefore lend confidence to the assumption that identical motions at well conjugate points are indicatory of electric fields.

Now what about the amplitudes of these fields? This problem was tackled in the following way: The nighttime height depressions above Canberra and Petropavlovsk in December being the most conspicuous individual conjugate effects, the electric field was estimated which could have produced them. To this end a program by Rüster (1971 b) was used for model calculations, the results of which are pictured in Fig. 8. First the behaviour of the F2-layer height was computed from the variation

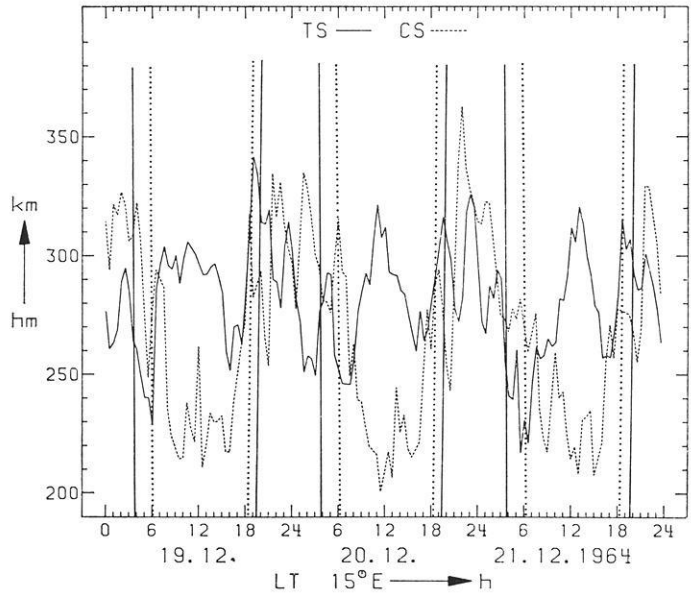

Fig. 7. Height variations of the ionospheric F2-layer at Tsumeb (TS) and Capo San Lorenzo (CS). Sounding intervals: 30 minutes. Sunrise and sunset: TS --------, CS..... Magnetic Kp-indices: 2— 20 1+ 1+ 20 30 3+ 20 0+ 00 00 20 1— 1— 20 20 10 0+ 2— 10 10 20 1— 0+

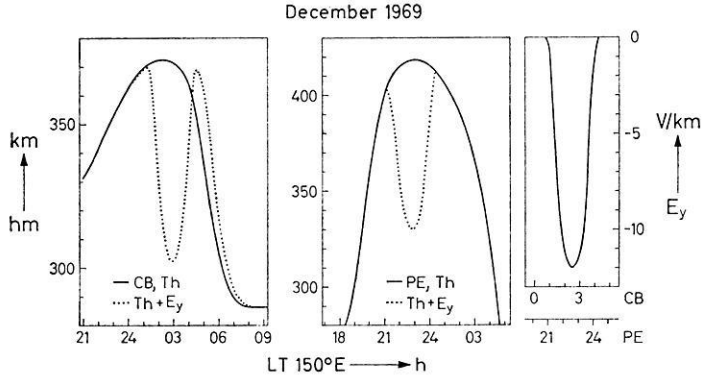

Fig. 8. Theoretical simulation of the F2-layer nighttime behaviour at Canberra and Petropavlovsk in December

of the usual parameters, i.e. the solar elevation angle and neutral winds. In this way the continuous curves (Th) were obtained. Then reasonable model fields were included in the calculation with a view to reconstruct the nighttime depressions.

The best fitting field is plotted on the right hand. It caused variations of the streaked kind (Th + Ey) which closely resemble the actual behaviour of the F2-layer. The amplitude of these fields was 12 V/km, compared to less than 3 V/km as predicted by Matsushita (1969). That is, the dynamo electric field model does not ad-

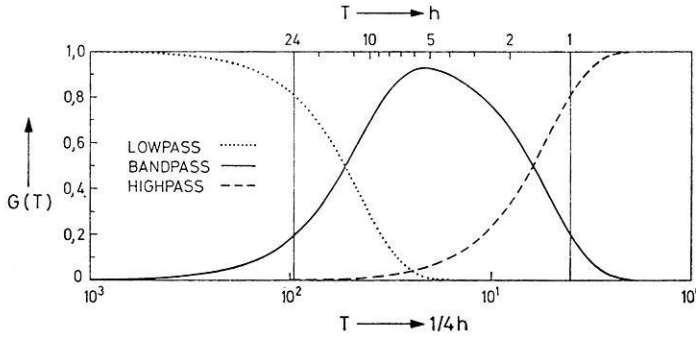

Fig. 9. Filter characteristics G as a function of period T

equately describe the situation at magnetically quiet times. This finding is consistent with the results of measurements which were performed by Mozer (1973) at slightly higher latitudes.

Daily variations of the F2-layer height encompass a large range of frequencies, amplitudes and phases. As various components may differ with regard to their conjugate behaviour, the Canberra and Petropavlovsk data were subjected to numerical filtering. It was aimed to separately correlate individual groups of spectral components. Three filters were prepared whose characteristics are reproduced in Fig. 9. They were conceived to facilitate the separation of a 24-hour basic period, of short oscillations at the sounding frequency (once a quarter hour) and of fluctuations in an intermediate wavelength range centered at about six hours.

In Fig. 10 original as well as filtered data are grouped for equinox conditions. The drawing is self-explanatory in so far as it emphasizes the conformity of the long and medium term variations and the complete lack of correlation for the high frequency oscillations.

In June (Fig. 11) the long period variations are still parallel. This accordance is noteworthy because seasons as well as neutral winds are different now, and electrodynamic drifts with periods as long as a full day were expected to be severely damped (cf. Jones, 1971). The band pass results do show several *in*-phase peaks but also include some uncorrelated sinusoidal variations which might correspond to gravity waves. December height variations (Fig. 12) are characterized by an increased similarity of the intermediate wavelength components. The low pass curves, however, diverge in the daytime. Possibly this digression reflects the extraordinarily high difference between the solar elevation angles in December (64° instead of 28° in June). Summing up, it appears that the fundamental wave ($T = 24$ h) is largely governed by the solar radiation, whilst shorter oscillations with periods of a few hours are dominated by electric fields.

In order to quantitatively compare height variations at different pairs of conjugate stations, correlation coefficients were calculated (Table 2). Though not fully compatible due to a lack of appropriate data they do permit the following conclusions: The correlation coefficients decrease rapidly with increasingly different declination effects and with growing distance between a given station and the conjugate point of its counterpart. This distance is a maximum for Townsville and Kokubunji, a pair of stations with almost identical declination effects. Here the correlation coef-

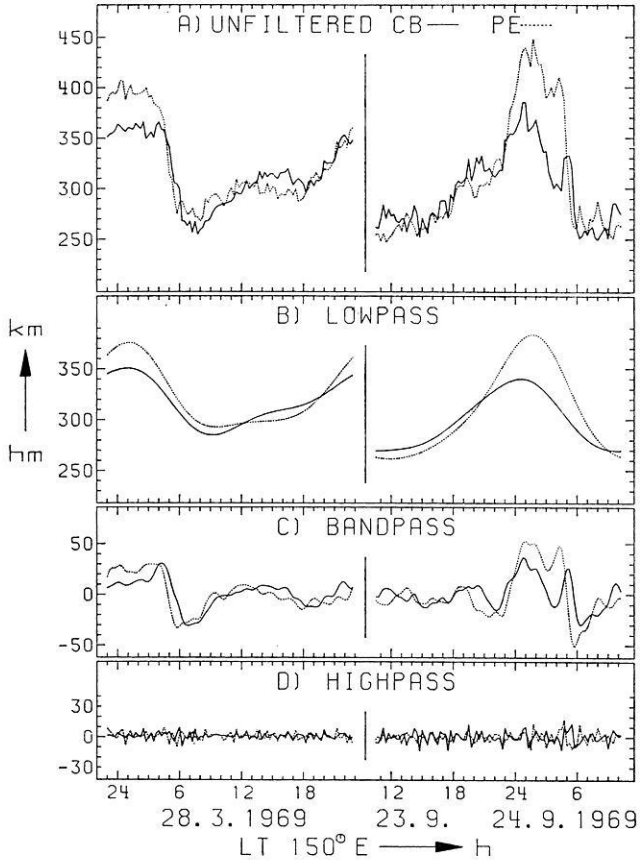

Fig. 10. Measured and filtered height variations of the F2-layer for Canberra and Petropavlovsk in March and September

ficient has fallen to 0.15. It is comparably small for Kerguelen and Sogra, which are closely conjugate but suffer from extremely different declination effects. The smallest correlation coefficient, i.e. —0.1, has been calculated for Tsumeb and Capo San Lorenzo which are poorly conjugate and have rather different declination effects. Considering the high quality and the great number of the respective ionograms, this value is of outstanding significance. Special attention was paid to Hobart and Magadan because these stations are situated almost on the same meridian. They have similar declination effects but are weakly conjugate. From the resulting correlation coefficient of only 0.35 one may infer that simultaneity of ionospheric height variations at Canberra and Petropavlovsk cannot be attributed to local time coincidence.

These observations demonstrate that high correlation coefficients are not a trivial feature of the ionospheric behaviour in different hemispheres but are confined to near conjugates with approximately equal declination effects. This evidence confirms the concept of a coupling mechanism for ionospheric motions above conjugate points. It appears that east-west electric fields of the order of magnitude 10 V/km are responsible for this effect.

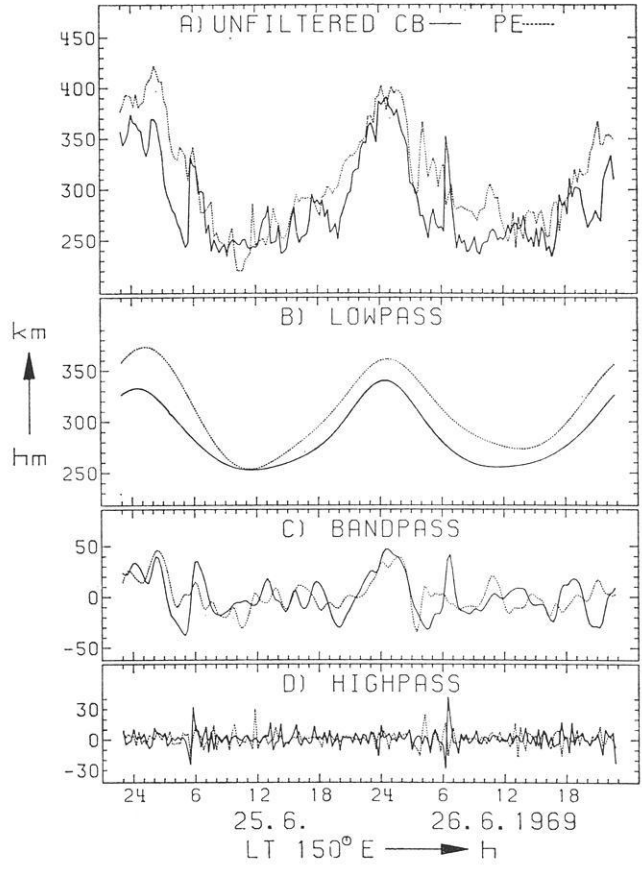

Fig. 11. Measured and filtered height variations of the F2-layer for Canberra and Petropavlovsk in June

Ordinary correlation coefficients being of limited value, a more refined analysis was performed employing correlation functions. It was aspired to find out whether defined phase lags exist between ionospheric events at weakly conjugate stations. The point was that a difference in geographical longitude or magnetic declination could possibly be compensated for by commensurate displacements of the conjugate height sequences relative to each other. However, no clear-cut relationship could be detected between discrepancies of the local times or the declination effects on the one hand and mutual phase shifts of the daily hight variations on the other hand (cf. Petelski, 1973).

4. Outlook

In conclusion, it ought to be stressed that the results of this study are preliminary and demand elaboration in many respects:

At least one pair of exactly conjugate stations with identical declination effects should be established and furnished with high performance ionosondes of the same kind.

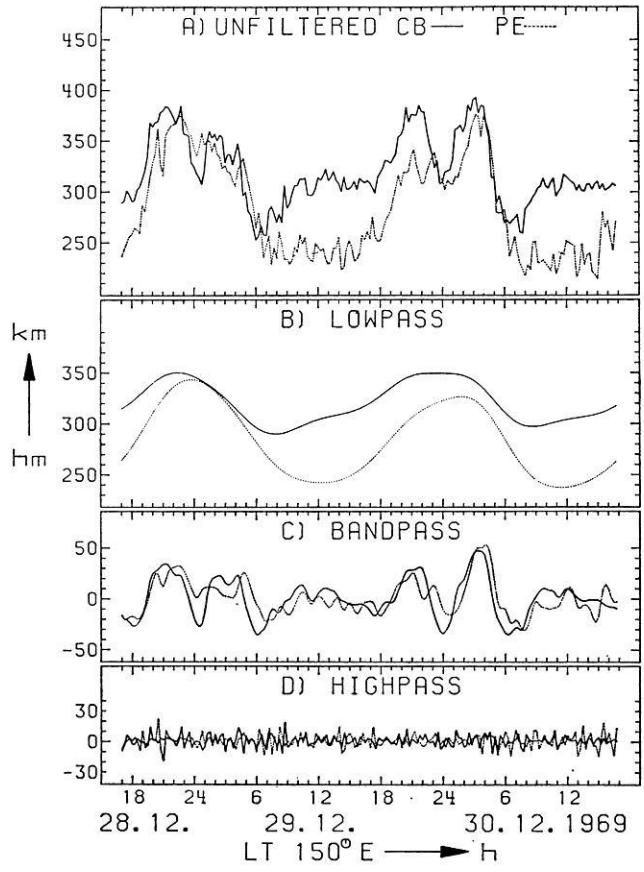

Fig. 12. Measured and filtered height variations of the F2-layer for Canberra and Petropavlovsk in December

Australia/north-east Asia and Argentine/Carribbean Islands are considered most suitable for this undertaking.

Shorter sounding intervals and longer periods of observation would be desirable to promote reliability and temporal resolution.

It is recommended that the geomagnetic conditions be supervised by magnetometers at both stations.

Theoretical investigations would have to be implemented concerning the generation of electric fields during magnetically quiet periods and the velocity of transmission of such fields along the geomagnetic field lines. The latter problem may turn out to be a messy one since the field line conductivity appears to be complicated by plasma turbulence. Coarse estimates by Boström (1973) come out to a time constant of about eight minutes which is a reasonably short time.

In order to check magnetic field models and to trace magnetospheric phenomena, an idea by Roederer (1969) should be caught on. He suggested to inject high energy protons (some GeV would do) into a magnetic flux tube and to watch the effects of the resulting cascades at the conjugate point. Geneva with its CERN proton-syn-

Table 2. Correlation coefficients

pair of stations	local time difference (hours)	angular sum of declinations÷	distance (km) †	interval (month/ year)	length of interval (hours)	number of soundings	correlation coefficient for hmF2 (and fmF2 solstice	equinox
			a) solar eclipse					
Argentine Island-Wallops Island	+0,75	+ 9,0°	820	3/70	23	64		0,609
			b) bay disturbance					
Capetown-Garchy	+1,01	-29,8°	280	10/59	10	41	0,802	
Tsumeb-Lindau	+0,51	-18,0°	1700	10/59	10	19	0,424	
			c) magnetically quiet days[x]					
Canberra-Petropavlovsk	-0,63	+ 5,5°	60	3/69	24	90		0,900(0,977)
				6/69	48	186	0,825(-0,176)	
				9/69	24	96		0,838(0,932)
				12/69	48	191	0,758(0,509)	
Capetown Poitiers	+1,20	-31,0°	155	12/58	24	92	-0,035	
				3/65	24	64		0,460
Hobart-Magadan	-0,23	+ 2,8°	600	12/68	24	86	0,354	
Kerguelen-Archangelsk	+1,99	-37,8°	280	6/68	24	92	0,611	
Gorki	+1,73	-40,6°	750	9/58	22	23		0,670
				12/65	8	26	0,219	
Sogra	+1,60	-36,3°	55	7/66	10	35	0,208	
				9/66	17	64		0,421
Marion Island-Lindau	+1,85	-37,4°	430	7/57	20	62	0,599	
				12/57	12	50	0,266	
Rarotonga-Maui	-0,22	+24,0°	490	1/58	23	48	-0,072	
				6/58	17	33	0,343	
				9/58	22	44		0,591
				3/64	21	43		0,508
				6/64	24	89	0,058	
Townsville-Kokubunji	+0,48	+ 1,3°	900	3/64	24	77		0,359
				12/65	24	67	0,153	
Tsumeb-Capo San Lorenzo	+0,54	+19,2°	350	12/64	72	144	-0,084	
				3/70	48	50		0,275
			d) comparison of stations					
Lindau-Gorki	-2,28	+12,6	2200	9/58	48	132		0,721

÷ the angular sum of the declinations measures the difference of the declination effects
† distance between the northern station and the conjugate point of the southern station
x $Kp \leq 3+$

chrotron and Mossel Bay in South Africa would be an optimum combination of conjugate stations for this purpose.

Generally speaking, conjugate ionospheric observations are means of cheaply and continuously controlling electric fields in the higher atmosphere, particle fluxes between the two hemispheres, distortions of the geomagnetic field lines, and the ionospheric behaviour in remote or inaccessible regions of the earth. In the light of these options the present study is a mere beginning which is hoped to stimulate further investigations.

Acknowledgements. The author is grateful to Prof. Dr. W. Dieminger for having sponsored this investigation. He thanks Dr. W. Becker who suggested to do conjugate research and provided the apparatus and computer-software required for the evaluation of electron density profiles. He is indebted to the directors of several ionosphere sounding stations and of the World Data Centres in Boulder, Moscow, Slough and Tokyo who supplied the ionograms. Thanks are also due to Drs. H. Kohl and R. Rüster for theoretical computer programs and to Dr. K. G. Lenhart for the calculation of conjugate coordinates. The support of Mr. and Mrs. Böker in the ionogram analysis as well as the assistance rendered by Mr. H. Benecke in the control and compilation of the results are highly appreciated. Most of the data processing was done at the GWDG computer facility in Göttingen.

References

Becker, W.: On the manual and digital computer methods used at Lindau for the conversion of multifrequency ionograms to electron density-height profiles. Radio Sci. *2*, 1205–1232, 1967

Benkova, N.P., Bukin, G.V., Kolokolov, L.Y., Lafeille, M., Taieb, C., Faynot, G.M.: Dynamics of magnetically conjugate regions in the F2-layer of the ionosphere. Geomagn. Aeron. *9*, 742–744, 1969

Boström, R.: Ionosphere-Magnetosphere Coupling. Magnetospheric Physics, B.M. McCormack, ed., pp. 45–59, Dordrecht-Holland: D. Reidel 1974

Bukin, G.V., Yevzovich, N.P., Katsenelson, I.B., Sukhorukova, E.V., Yelizaryev, Y.N., Shatkhin, K.Z.: Predawn effect in f_0F2 variations caused by sunrise at a magnetically conjugate point. Geomagn. Aeron. *8*, 752–754, 1968

Cain, J.C., Hendricks, S.J., Langel, R.A., Hudson, W.V.: A proposed model for the international geomagnetic reference field 1965. J. Geomagnetism Geoelectricity *19*, 335–355, 1967

Carlson, Jr., H.C., Walker, J.C.G.: Electrodynamic drift in the nocturnal F-region ionosphere caused by conjugate point sunrise. Planetary Space Sci. *20*, 141–148, 1972

Carpenter, L.A., Bowhill, S.A.: $E \times B$ drifts at midlatitudes. Radio Sci. *6*, 203–207, 1971

Challinor, R.A.: Neutral-air winds in the ionospheric F-region for an asymmetric global pressure system. Planetary Space Sci. *18*, 1485–1487, 1970

Cho, H.R., Yeh, K.C.: Neutral winds and the behaviour of the ionospheric F2-region. Radio Sci. *5*, 881–894, 1970

Eyfrig, R.W.: The effect of the magnetic declination on the F2-layer. J. Geophys. Res. *68*, 2529–2530, 1963

Gold, T.: Motions in the magnetosphere of the earth. J. Geophys. Res. *64*, 1219–1224, 1959

Hanson, W.B., Moffet, R.J.: Ionization transport effects in the equatorial F-region. J. Geophys. Res. *71*, 5559–5572, 1966

Jones, K.L.: Electrodynamic drift effects in mid-latitude F-region storm phenomena. J. Atmospheric Terrest. Phys. *33*, 1311–1319, 1971

King, J.W., Kohl, H.: Upper atmospheric winds and ionospheric drifts caused by neutral air pressure gradients. Nature *206*, 699–701, 1965

Kohl, H.: The calculation of winds from thermospheric models. Space Res. *12*, 1069–1078, 1972

Kohl, H., King, J.W., Eccles, D.: An explanation of the magnetic declination effect in the ionospheric F-layer. J. Atmospheric Terrest. Phys. *31*, 1011–1016, 1969

Lenhart, K.G.: private communication, 1969

Matsushita, S.: Dynamo currents, winds, and electric fields. Radio Sci. *4*, 771–780, 1969

Maynard, N.C., Bahnsen, A., Christophersen, P., Egeland, A., Lundin, R.: An example of anticorrelation of auroral particles and electric fields. J. Geophys. Res. *78*, 3976–3980, 1973

Mozer, F.S.: Power spectra of the magnetospheric electric field. J. Geophys. Res. *76*, 3651–3667, 1971

Mozer, F.S.: Electric fields and plasma convection in the plasmasphere. Rev. Geophys. Space Phys. *11*, 755–765, 1973

Mühleisen, R., Fischer, H.-J., Hofmann, H.: Horizontal electric fields in the ionosphere derived from air electric measurements. Z. Geophys. *37*, 1055–1059, 1971

Nelson, G.J., Cogger, L.L.: Dynamical behaviour of the night time ionosphere at Arecibo. J. Atmospheric Terrest. Phys. *33*, 1711–1726, 1971

Petelski, E.F.: Dynamik der ionosphärischen F2-Schicht mittlerer Breiten über erdmagnetisch konjugierten Punkten – Meßergebnisse. Doktorarbeit, Universität Göttingen, 1973

Roederer, J.G.: Conjugate point phenomena. Solar-Terr. Phys.: Terr. Aspects. M.I.T. Press, Ann. IQSY *5*, 397–416, 1969

Rüster, R.: Theoretical treatment of the dynamical behaviour of the F-region during geomagnetic bay disturbances. J. Atmospheric Terrest. Phys. *31*, 765–780, 1969

Rüster, R.: The relative effects of electric fields and atmospheric composition changes on the electron concentration in the mid-latitude F-layer. J. Atmospheric Terrest. Phys. *33*, 275–280, 1971a

Rüster, R.: Solution of the coupled ionospheric continuity equations and the equations of motion for the ions, electrons and neutral particles. J. Atmospheric Terrest. Phys. *33* 134–147, 1971b

Shawhan, S.D., Block, L.P., Fälthammar, C.-G.: Conjugate photoelectron impact ionization J. Atmospheric Terrest. Phys. *32*, 1885–1900, 1970

Stubbe, P., Chandra, S.: The effect of electric fields on the F-region behaviour as compared with neutral wind effects. J. Atmospheric Terrest. Phys. *32*, 1909–1919, 1970

Dr. E. F. Petelski
Dornier System, Space Division
D-7990 Friedrichshafen
Federal Republic of Germany

J. Geophys. 41, 265–279, 1975

Characteristics of Azimuth Independent Optimum Velocity Filters Designed for Two-Dimensional Arrays

P. Hubral

Bundesanstalt für Bodenforschung, Hannover

Received April 11, 1974; Revised Version August 19, 1974

Abstract. The design of azimuth independent optimum velocity filters for arbitrary two-dimensional arrays is simplified with zero-order Bessel functions. Similarities with optimum velocity filters for one-dimensional arrays are discussed. An adequate choice of the array origin is recommended as it results in minimum length filter components. Simplifications for the computation and analysis of optimum velocity filters are provided for centre-symmetric array patterns. Computational experiments are performed on filters to characterize their performance on a large class of likely input signals. Features which can be related to the twodimensional wavenumber response of the array are described. The filters permit a control of the signal-to-noise ratio in the filtered output. It is shown that an increase in this ratio is only obtained at the expense of basically two types of signal distortion.

Key words: Optimum Multichannel Wiener Filters — Optimum Velocity Filters — Array Geometry — Frequency-Wavenumbers Domain — Filter Characteristics.

1. Introduction

The particular type of velocity filters investigated in this work is based on the theory of optimum multichannel Wiener filters. Such a theory exists for continuous (Wiener, 1949; Robinson, 1962) and discrete filters (Robinson, 1967; Treitel, 1970). Velocity filters designed for two-dimensional arrays with the use of the continuous multichannel Wiener theory were first described by Burg (1964). Suboptimum velocity filters for one-dimensional arrays are discussed by Foster, Sengbush and Watson (1964). Optimum velocity filters for one-dimensional arrays are treated by Sengbush and Foster (1968), who compare their superior characteristics with various other velocity filters as suboptimum doublet filters (Foster *et al.*, 1964) and pie-slice filters (Embree, Burg and Backus, 1963). A critical analysis of optimum velocity filters with regard to their successful application to two-dimensional marine reflection data is given by Cassano and Rocca (1974). Superior characteristics of optimum velocity filters and the possibility to control the signal-to-noise ratio of the filtered output are the main reasons which led to the design of three-dimensional optimum velocity filters (Hubral, 1972). In the three-dimensional case various velocity filter designs are possible. It is the azimuth independent type which is shortly reviewed and subsequently characterized here. Examples are given to describe transfer characteristics and resolution of computed filters. An approximate relationship between the wavenumber response (Krey and Toth, 1973) of an array and the threedimensional Fourier transform of velocity filters for the same array is established. The control which can be exercised on the signal-to-noise ratio of the filtered output is investigated with the help of computational experiments. Some general rules for the use of the filters are established, which should be considered in their application.

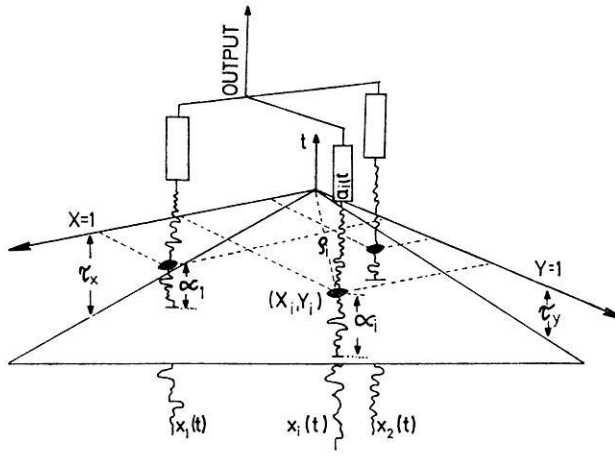

Fig. 1. Array pattern in (x,y) plane and recorded traces indicating the moveout plane $t = -\tau_x x - \tau_y y$

2. *Theory*

The following stochastic model for actual seismic traces recorded at N arbitrary detector locations (X_i, Y_i), $(i=1,\ldots,N)$ is assumed to be the input for the desired filter:

$$\begin{gathered} x_i(t) = s(t-\alpha_i) + c(t-\bar{\alpha}_i) + n_i(t);\ (i=1,\ldots,N) \\ \alpha_i = \tau_x X_i + \tau_y Y_i;\ \bar{\alpha}_i = \bar{\tau}_x X_i + \bar{\tau}_y Y_i \end{gathered} \tag{1}$$

$s(t)$ is the common signal in each trace, $c(t)$ the coherent noise and $n_i(t)$, $(i=1,\ldots,N)$ some uncorrelated noise, which may vary from trace to trace. The values α_i, $(i=1,\ldots,N)$ are the relative moveouts of a desired plane wave with signal waveform $s(t)$. The values $\bar{\alpha}_i$, $(i=1,\ldots,N)$ are respectively the moveouts of an undesired coherent noise plane wave with signal $c(t)$. Rather than designing a filter $a_i(t)$, $(i=1,\ldots,N)$, (Fig. 1) for just one stochastic input model of form (1) it is assumed that an ensemble of input traces is to be optimally filtered into the signal $s(t)$. To achieve this, each ensemble member is allowed to differ only in the values τ_x, τ_y (Fig. 1) and $\bar{\tau}_x$, $\bar{\tau}_y$ in such a way that all permitted plane waves from all azimuths fall into two apparent velocity ranges. The ensemble of signal plane waves is expected to fall into a velocity range refered to as the pass region, the ensemble of coherent noise waves into a range refered to as the reject region. The filter $a_i(t)$, $(i=1,\ldots,N)$ which is obtained with the assumption that all signals are broad band and all waves within pass and reject region may arrive at the array with equal likelihood is specified by the following normal equations (Hubral, 1972):

$$\sum_{i=1}^{N} A_i(f)[\Phi_{s_i s_j}(f) + \eta \Phi_{c_i c_j}(f) + \nu \Phi_{n_i n_j}(f)\,\delta_{ij}] = \Phi_{ss_j}(f);\ (j=1,\ldots,N) \tag{2}$$

$$\Phi_{s_i s_j}(f) = (1/2\pi \Delta r_0) \int_0^{2\pi} \int_{r_0-\Delta r_0/2}^{r_0+\Delta r_0/2} \exp\left(-2\pi i f r(\varrho_i \cos(\alpha-\xi_i) - \varrho_j \cos(\alpha-\xi_j))\right) d\alpha\, dr$$

$$\Phi_{c_i c_j}(f) = (1/2\pi \Delta r_0) \int_0^{2\pi} \int_{\bar{r}_0 - \Delta \bar{r}_0/2}^{\bar{r}_0 + \Delta \bar{r}_0/2} \exp\left(-2\pi i f r(\varrho_i \cos(\alpha - \xi_i) - \varrho_j \cos(\alpha - \xi_j))\right) d\alpha\, dr$$

$$\Phi_{s s_j}(f) = (1/2\pi \Delta r_0) \int_0^{2\pi} \int_{r_0 - \Delta r_0/2}^{r_0 + \Delta r_0/2} \exp\left(2\pi i f r \varrho_j \cos(\alpha - \xi_j)\right) d\alpha\, dr$$

$$\Phi_{n_i n_j}(f) = 1$$

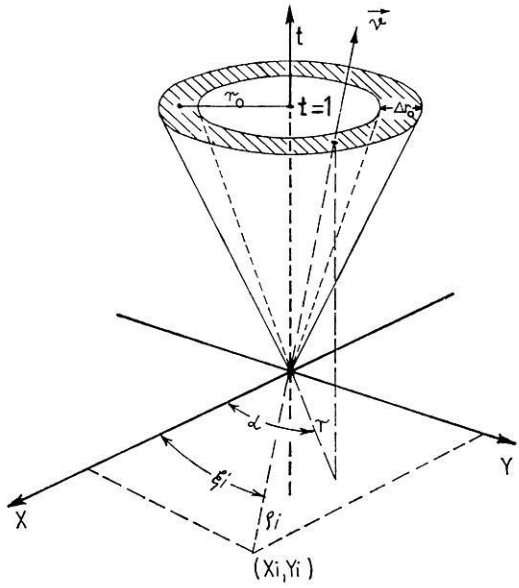

Fig. 2. Time domain cone featuring the limits of normal vectors of permitted moveout planes

$A_i(f)$, $(i = 1, \ldots, N)$ are the Fourier transforms of the wanted components $a_i(t)$, $(i = 1, \ldots, N)$ of the velocity filter. ϱ_i, ξ_i are polar coordinates of the detector location i in respect to some as yet unknown coordinate origin within or outside the array. r_0 and Δr_0 are the moveout limits of the pass region. They are explained with the help of Fig. 2. Both values describe two inverted cones between which all normal vectors $\mathbf{v} = (\tau_x, \tau_y, 1)$ of the permitted input signal plane waves fall. r in Fig. 2 is connected with τ_x and τ_y by the expression $r = \sqrt{\tau_x^2 + \tau_y^2}$. $\bar{r}_0$ and $\Delta \bar{r}_0$ define the corresponding reject region for the coherent noise. Both, reject and pass region should not overlap with each other. η and ν in (2) are arbitrary weighting factors influencing the signal-to-noise ratio of the filtered output. Noise weighting factors have been used in the context of various filter designs (Deregowski, 1971) with very good success. Their presence in optimum filter designs is justified by the fact that large noise weights cause increased rejection of the respective noise (Sengbush and Foster, 1968). Some negative side effects due to increasing η and ν however exist and will be discussed later on. The solution of Eq. (2) is simplified with the help of zero-order Bessel functions as shown in the Appendix.

The (f, k_x, k_y) transform is an ideal means of analysis (Burg,1964) to characterize a computed filter with regard to its performance on expected plane waves. It is used in this work to show the influence of various design parameters, as for instance the noise weighting factors and the recording patterns, on the filtered output. The (f, k_x, k_y) domain of a computed filter is established as follows. The N arbitrarily placed filter components $a_i(t)$, $(i=1,\ldots,N)$ at locations X_i, Y_i, $(i=1,\ldots,N)$ are used to define the following threedimensional operator:

$$a(t, x, y) = \sum_{i=1}^{N} a_i(t)\, \delta(x - X_i)\, \delta(y - Y_i)$$

Its Fourier transform is (Hubral, 1972)

$$A(f, k_x, k_y) = \sum_{i=1}^{N} A_i(f) \exp\left[-2\pi i(k_x X_i + k_y Y_i)\right] \tag{3}$$

This three-dimensional transform is periodic in k_x and k_y if detector locations fall onto a rectangular grid. The frequency response of any δ-plane wave with the moveouts

$$\alpha_i = \tau_x X_i + \tau_y Y_i,\ (i = 1,\ldots,N;\ -\infty < \tau_x, \tau_y < +\infty)$$

can be expressed as:

$$R(f) = \sum_{i=1}^{N} A_i(f) \exp\left[-2\pi i f(\tau_x X_i + \tau_y Y_i)\right] \tag{4}$$

This function is obtained from (3) along the line $k_x = \tau_x f$, $k_y = \tau_y f$. If no filters are applied to the detector locations, the array acts only as a wavenumber filter (Krey and Toth, 1973). The function which is obtained by substituting $A_i(f) = 1$, $(i=1,\ldots,N)$ into (3) is commonly refered to as the wavenumber response of the array. It is shown with the help of an example that the wavenumber response, which is only determined by the array configuration, can strongly effect the characteristics one wants to force upon the array by designing a specific optimum velocity filter for it.

3. Array Geometry

For any array and a specific pass and reject region the (x,y) origin for the filter design can be chosen in such a way that the resulting filter length is small. This is of practical importance as it reduces the amount of computations for the design as well as the actual filtering process. The real input traces need then only approximate stationarity over a shorter time interval. Particular array symmetries can in addition reduce the size of the normal equations, speed up the filter computations and cause a zero-phase response for any plane wave arriving at the array. As many of the subsequent observations apply to most other velocity filters they are only briefly reviewed.

3.1. Choice of Origin

For a given array an infinite number of velocity filters can be computed for one and the same pass and reject region. This is achieved by just changing the (x,y) origin in the filter design. Only one filter is optimum optimorum. Its origin should be selected in such a way that the largest of all resulting detector distances ϱ_i, $(i=1, \ldots, N)$ is at its minimum. This results in the shortest overall moveoutwidth of the pass and reject region within the array. It is easily seen in Fig. 1 that moving the (x,y) origin to a place within the detectors reduces the moveouts $\alpha_i (i=1,\ldots,N)$. Filters should be as long as the largest moveout difference in the input. This has been shown by Galbraith and Wiggins (1968) for optimum stacking filters. These filters are in fact closely related to optimum velocity filters as shown by Hubral (1974). The choice of origin recommended here leads in the case of two-dimensional optimum velocity filters to the so-called 'centre-trace estimate' filter (Sengbush *et al.*, 1968). The maximum moveout difference for velocity filters in this work is $t_M = 2 r_{\max} \varrho_{\max}$, $r_{\max} = \mathrm{Max}(r_0 + \Delta r_0/2, \bar{r}_0 + \overline{\Delta r}_0/2)$. $r_{\max}$ is the maximum moveout value and $\varrho_{\max}$ the maximum detector distance of $\varrho_i (i=1,\ldots,N)$ from the origin. The choice of origin also affects the phase response of filters. This is shown in the next subsection.

3.2. Phase Response

The velocity filter transfer function for a specific broad band plane wave is given in expression (4). For an arbitrary array configuration and plane wave this is generally a complex function, thus indicating that both the amplitude of a plane wave signal and its phase is modified by the filter. As every increase in the phase of a signal affects a delay, plane waves arriving from various azimuths with even the same velocity may pass with different delays. This is generally undesired and can often be avoided by ensuring a zerophase response of the array for all possible plane waves. The velocity filter is then entirely characterized by the modulus of $A(f, k_x, k_y)$ as the phase of this transform is zero everywhere. This particular advantage is offered by centre-symmetric arrays. It is easily verified that the function (4) is real for any array configuration where for each detector location (X_i, Y_i) another location $(-X_i, -Y_i)$ exists and both have the same symmetric filter component applied to it. That all filter components obtained from (2) are symmetric and the same for centre-symmetric pairs is verified by substitution.

3.3. Array Symmetry and Normal Equations

Centre-symmetric arrays not only provide simple phase relations, they also reduce the number of normal Eq. (2) and thus speed up the computation of filters considerably. For any centre-symmetric pair of detectors, the number of normal equations can be reduced by one. This can again be verified by substitution. Consequently those arrays may easily be computed where many detector positions fall centre-symmetrically on few concentric circles. In this case the number of normal equations corresponds then only to the number of circles.

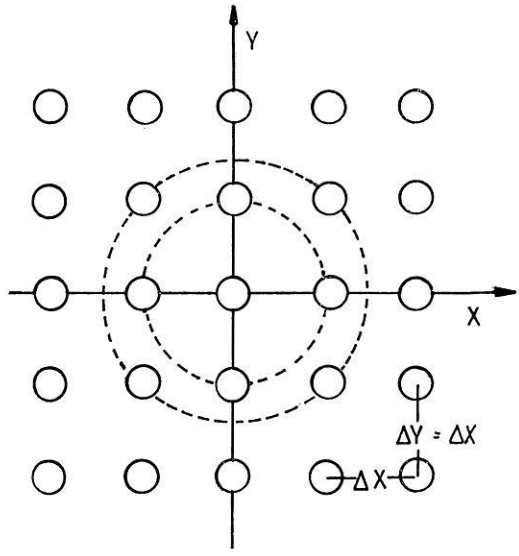

Fig. 3. Array pattern

4. *Computational Experiments*

Although filters are designed to possess azimuth independent transfer characteristics, the actual filter properties for certain array patterns are nevertheless often azimuth dependent. One example is subsequently discussed, where desired characteristics are well approximated. Another example is presented to point out a generally existing relationship between velocity filter characteristics and the wavenumber response of the array. The expected least square error as a function of the filter length (Treitel, 1970) is shown to be also useful in providing some indication about how well desired velocity filter characteristics are approximated by the actual filter. An investigation of the noise weighting factors η and ν is done on some representative examples. Increasing the weighting factors reveals that increased attenuation of the noise has to be paid for with a deterioration of signal transfer characteristics. Increasing ν depresses the high frequency content of the filtered signals. Increasing η causes a 'pushing effect' in the characteristics of the (f, k_x, k_y) domain, which is explained below.

4.1. Example

The array pattern is the rectangular $N \times N$ grid ($N=5$) of Fig. 3. As the 25 detectors can be considered to fall onto six concentric circles, the normal Eqs. (2) can be reduced to the sixth order. Additional design parameters are chosen as: $r_0=0.5$, $\Delta r_0=1.0$, $\nu=0.08$ and $\eta=0$. The time sampling period of the computed digital filter is $\Delta t=1$. The first quadrant of the three-dimensional (f, k_x, k_y) diagram is shown in Fig. 4 at different levels of frequencies: $f=0, f=f_N/4, f=f_N/2, f=3f_N/4$ and $f=f_N$. $f_N=1/2\,\Delta t$ is the Nyquist frequency. The three-dimensional transform is periodic with the periods $k_x=1/\Delta x$, $k_y=1/\Delta y$ and $f=1/\Delta t$. Fig. 4 (lower right

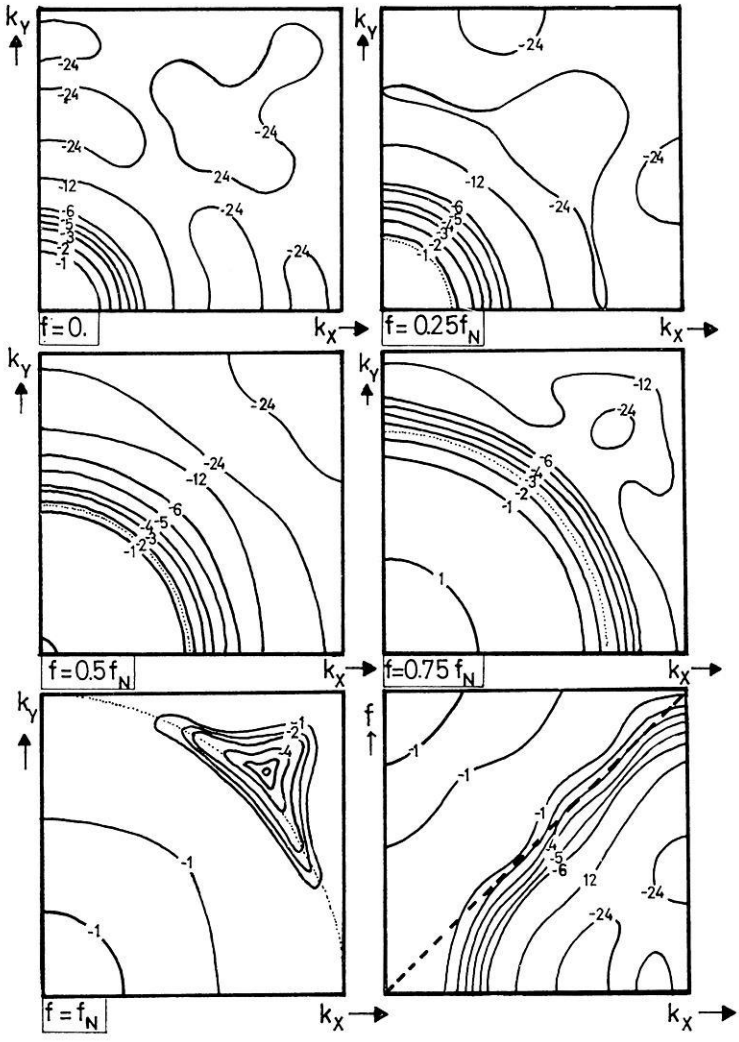

Fig. 4. Contours of the function $20 \log|A(f, k_x, k_y)/A_{\max}(f, k_x, k_y)|$ in the first quadrant $(0 \leq k_x \leq 1/2\,\Delta x, 0 \leq k_y \leq 1/2\,\Delta y, 0 \leq f \leq 1/2\Delta t)$ at different frequency levels

corner) shows the first quadrant in the plane $k_y = 0$. The limit of the circular cone is indicated as a straight dotted line. The area inside the cone represents the desired pass region in the (f, k_x, k_y) domain in which all function values are expected to approximate $A(f, k_x, k_y) = 1$. Outside the cone is the reject region which should hopefully approach $A(f, k_x, k_y) = 0$.

The desired characteristics of this example are reasonably well approximated apart from frequencies near $f = 0$. This is typical for optimum velocity filters and has already been observed on one-dimensional arrays (Sengbush *et al.*, 1968). The desired circular shape of the characteristics is reasonably well maintained. If for instance the width between the —3 dB and —12 dB contours is defined as the resolution of the

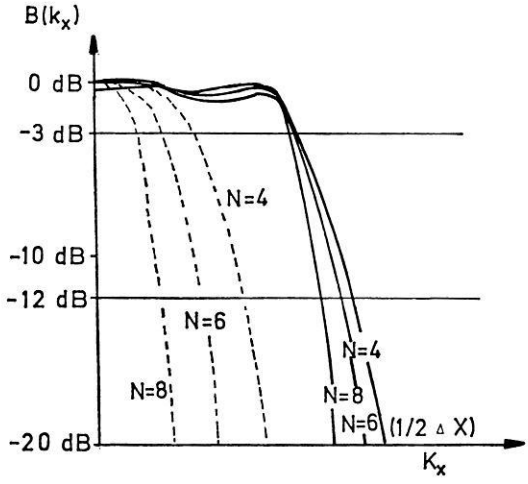

Fig. 5. Graphs of $B(k_x) = 20 \log |A(f_N/2, k_x, 0)/A_{\max}|$ for velocity filters (full lines) and straightforward stacks (dashed lines) as a function of the array size N

filter, one can state that this resolution is very much independent of frequencies and azimuths. To give some indication on how the resolution of the filter changes as a function of N, the values $A(f_N/2, k_x, 0)$ are displayed in Fig. 5 as a function of k_x for $N=4$, $N=6$ and $N=8$. Fig. 5 also includes the corresponding function $A(f_N/2, k_x, 0)$ for the straight-forward stack. It can be seen that for the same N the resolution of the filter is of the same order as for the straight stack. To verify this one only has to shift the respective curves for the same value of N in Fig. 5 parallel to the k_x-axis to have their downward sloping part overlapped with each other.

4.2. Reluctance Tendancy

Certain arrays show a larger or smaller degree of reluctance towards approximating desired velocity filter characteristics. Some relationship can however be established between actually observed characteristics in the (f, k_x, k_y) domain and the wave number response of the array. As seen by their wavenumber responses L-shaped and cross shaped arrays favour very much the directions of the array legs, while triangular or circular arrays reveal far less azimuth dependent characteristics. A summary of the characteristics of basic array patterns is given by Harjes and Henger (1973). As various computational experiments have shown, it is not possible to design azimuth independent optimum velocity filters for L-shaped or cross-shaped arrays as their wavenumber responses only favour specific directions. The following example elucidates this point. A velocity filter was designed for the cross array of Fig. 6 with all other design parameters being equal to the previous example. The first quadrant of $A(f, k_x, k_y)$ of the computed filter is shown in Fig. 7 for the frequencies $f=0$, $f=f_N/4$, $f=f_N/2$ and $f=3f_N/4$. Rather than the desired circular conic pass-region of the previous example, it is this time an inverted pyramidic pass region which is approximated by the actual filter of this example.

This shows that obviously a strong dependence of the characteristics exists on the directions of the cross-legs. A good understanding of wavenumber responses of

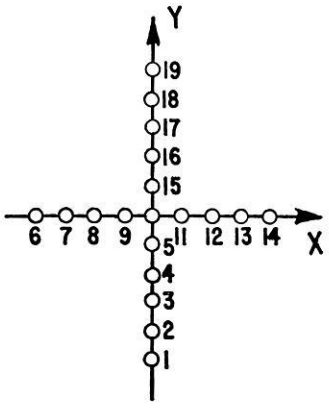

Fig. 6. Cross array

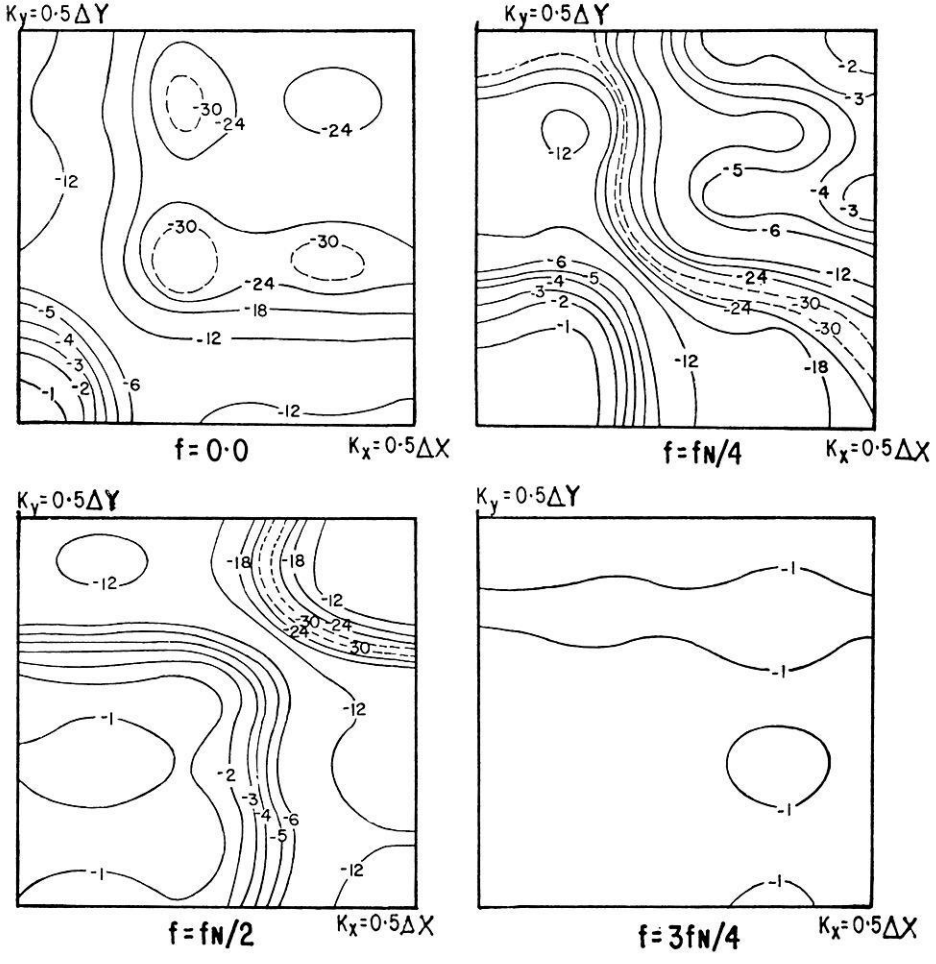

Fig. 7. Contours of $20 \log |A(f, k_x, k_y)/A_{\max}(f, k_x, k_y)|$ at different frequency levels

arrays can therefore be used to predict already to some extent the actually resulting but certainly more complex velocity filter characteristics. It is consequently not only the array size and the number of detectors, but also an inherent reluctance towards certain directions as already indicated by the wavenumber response which prevent actual characteristics of computed velocity filters from approximating desired ones. The (f, k_x, k_y) transform is a useful means of analysis of a velocity filter as one can obtain from it the array response for all possible plane waves. It can however still not provide any information with regard to the filter performance on uncorrelated noise nor can it be used to describe the signal-to-uncorrelated noise ratio of the filtered output. Other functions are equally useful to characterize velocity filters in this respect. This is shown in the next subsection.

4.3. Expected Errors

The expected error can provide some general qualitative indications about the performance of a computed filter. The basic operation which leads to the design of a filter, where the N traces (1) are to be optimally filtered into the signal trace $s(t)$, is the minimization of the following least-square expression (Robinson, 1962):

$$E = \lim_{T\to\infty} \frac{1}{2T} \int_{-T}^{T} \left(s(t) - \sum_{i=1}^{N} a_i(t)^* x_i(t) \right)^2 dt \tag{5}$$

Substituting the computed filter together with the assumed model traces (1) into this expression provides the expected error (Treitel, 1972). The smaller this error, the better is the performance of the computed filter on the model traces.

The expected error can thus be investigated as a function of any filter design parameter (i.e. (x,y) origin, detector locations, noise weighting factors, etc.). To demonstrate the usefulness of an expected error analysis, the first example of subsection 4.1 was again used and the normalized errors $E/E_{\max}$ were plotted as a function of the filter length and $r_{\max} = r_0 + \Delta r_0/2$. The results are shown in Fig. 8. They indicate that for all values $r_{\max}$ less than Δt the expected errors approximate small values when increasing the filter length. From a certain length onwards there is no further reduction possible of the errors and computed filters perform from then on equally well on the specified ensemble of plane waves. It is obvious that for instance an increase of the incoherent noise enlarges the expected error. It is however not so obvious that increasing $r_{\max}$ to be greater than Δt causes a similar effect (Fig. 8). The explanation for this is easily found as for $r_{\max} > \Delta t$ the conic pass region no longer fits into the basic period of the (f, k_x, k_y) domain. Overlapping and partial cancellation of pass regions due to spatial periodicity of the (f, k_x, k_y) transform cause then tremendous complexities which are commonly known as frequency and space aliasing effects. An indication of what can happen to optimum velocity filters for one-dimensional arrays due to space aliasing is provided by Sengbush and Foster (1968) and Cassano and Rocca (1974). The complexities they describe for one-dimensional arrays are larger in the case of two-dimensional arrays, particulary then, when array locations dont fall onto a rectangular recording grid and

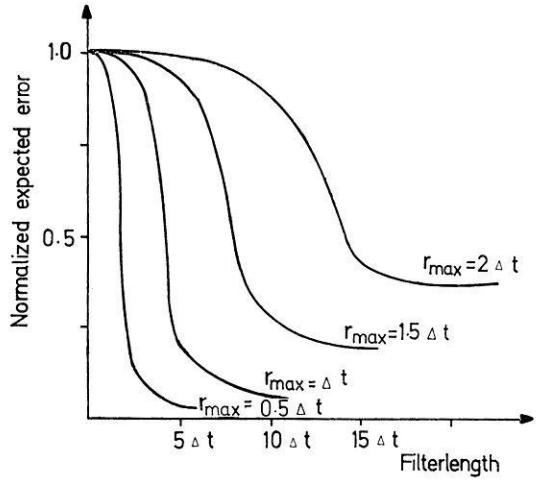

Fig. 8. Normalized expected errors as a function of the filter length

$A(f, k_x, k_y)$ is consequently not strictly periodic in k_x and k_y. To avoid problems of wavenumber or space aliasing in the design, $r_{\max}$ should never be chosen to be larger than Δt if detectors fall onto a grid with the spacing Δx. This is in correspondence with the conclusions arrived at by Sengbush and Foster (1968) for one-dimensional arrays.

4.4. The Noise Influence

It is assumed that the following random functions represent the ensemble of plane waves which arrive at the array locations (X_i, Y_i), $(i=1,\ldots,N)$

$$x_j(t) = s(t-(\tau_x X_i + \tau_y Y_i)) + n_j(t)\ ;\ (j=1,\ldots,N)$$

The values τ_x and τ_y satisfy the condition $\sqrt{\tau_x^2+\tau_y^2}=r$. In addition the following equations are true for the power spectra of $s(t)$ and $n_i(t)$, $(i=1,\ldots,N)$

$$\Phi_{ss}(f) = \mathrm{rec}\,(f),\ \Phi_{n_i n_j}(f) = \mathrm{rec}\,(f)\,\delta_{ij},\ (i,j=1,\ldots,N)$$

$$\mathrm{rec}\,(f) = \begin{cases} 1 \text{ for } |f| \leq 1/2 \\ 0 \text{ for } |f| > 1/2 \end{cases}$$

The array locations are given by the array of Fig. 3. The velocity filter applied to the array is the one computed in subsection 4.1 for $N=6$.

The output power of the signals as a function of r is subsequently refered to as $P(r)$ and the output power of the uncorrelated noise as P_n. The signal-to-uncorrelated noise ratio $P(r)/P_n$ as a function of the moveout r for various weighting factors ν of the filter is shown in Fig. 9a. It is seen that the signal-to-uncorrelated noise ratio of the optimum velocity filter can be improved by as much as a factor of 2 for $\nu=300$. This improvement however decreases with increasing the moveout r. For

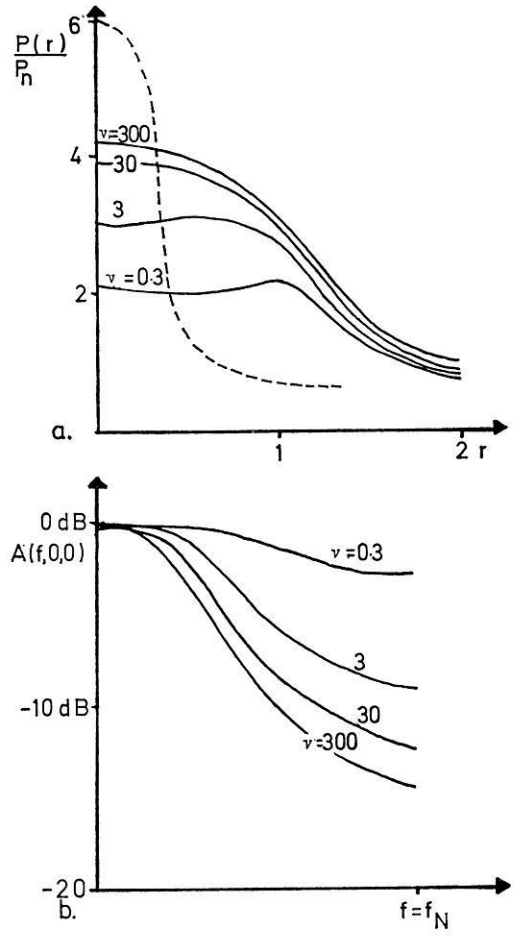

Fig. 9. a Signal-to-uncorrelated noise ratio as a function of moveout r. Dashed line corresponds to straight stack. b Values of $20 \log |A(f, k_x, k_y)/A_{\max}(f, k_x, k_y)|$ along the line $k_x = k_y = 0$

small moveouts r the signal-to-noise ratio is never as good as in the straightforward stack, which is known to be the best incoherent noise rejector. The corresponding function representing a straight-forward addition is the dotted curve in Fig. 9a. From the graphs one can draw the interesting conclusion that one can obviously not have an optimum incoherent noise rejector and an optimum velocity filter (i. e. coherent signal pass- or reject filter) at the same time. A compromise between both extremes must and can be found by changing ν. The optimum value of ν depends on the type of traces to be filtered. The increased rejection of uncorrelated noise has to be paid for with a loss in the high frequency content of the passed signals. This is shown in Fig. 9b for the same examples however only for $r = 0$. To complete the investigation of noise weighting factors, the influence of η on the transfer characteristics is demonstrated with the help of one more example. A significant improvement of the signal-to-correlated noise ratio for broad band signals was observed by increasing η. The

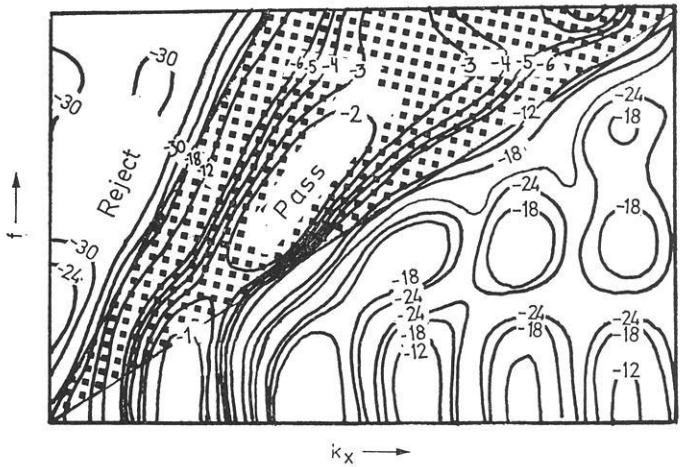

Fig. 10. Cross section of $20 \log |A(f, k_x, k_y)/A_{\max}(f, k_x, k_y)|$ of a pass-reject filter in the plane $k_y = 0$ for $0 \leq f \leq f_N$ and $0 \leq k_x \leq 1/2\Delta x$

improvement can be as much as a factor of 10. For marine reflection data and optimum velocity filters for one-dimensional arrays the optimum value of η was found to fall between 0.5 and 2.0 (Cassano *et al.*, 1974). The increased rejection is again achieved at the expense of distorted signal characteristics. In particular it was observed that actual pass regions in the (f, k_x, k_y) domain of a filter are increasingly pushed away from reject regions by enlarging η. This happens mainly at low frequencies and only up to a certain value of η. The low left corner in Fig. 10 gives a demonstration for this. The specific design parameters of the pass-reject filter are not given as they are not needed to explain the effect. For small values of η and low frequencies the actual pass region moves towards the left and for large values of η to the right. This interesting result which was constantly observed on various computed filters should by all means be considered, when applying computed filters to actual traces. Pass and reject signals for low frequencies which fall close to each other at the pass and reject limits are mostly influenced by the pushing effect and can cause an appreciable change of quality of the filtered traces.

Appendix

Expression $\Phi_{s_i s_j}(f)$ can be simplified to

$$\Phi_{s_i s_j}(f) = (1/2\pi\Delta r) \int_0^{2\pi} \int_{r_0 - \Delta r_0/2}^{r_0 + \Delta r_0/2} \exp\left(2\pi i f r \, Rij \cos(\alpha - \lambda)\right) d\alpha \, dr$$

with

$$R_{ij}^2 = \varrho_i^2 + \varrho_j^2 - 2\,\varrho_i\,\varrho_j \cos(\xi_i - \xi_j)$$

and

$$\tan\lambda = (\varrho_i \sin\xi_i - \varrho_j \sin\xi_j)/(\varrho_i \cos\xi_i - \varrho_i \cos\xi_j)$$

This in turn can be written as

$$\Phi_{s_i s_j}(f) = \frac{1}{\Delta r_0} \int_{r_0 - \Delta r_0/2}^{r_0 + \Delta r_0/2} I_0(2\pi f r\, R_{ij})\, dr$$

$I_0(r)$ is the zero-order Bessel function.

Substituting $p_0 = 2\pi f R_{ij}(r_0 - \Delta r_0/2)$ and $p_1 = 2\pi f R_{ij}(r_0 + \Delta r_0/2)$ leads to the further simplified expression:

$$\Phi_{s_i s_j}(f) = (1/2\pi R_{ij} f \Delta r_0) \cdot [\mathrm{Int}\,(p_1) - \mathrm{Int}\,(p_0)]$$

The zero-order Bessel function $I_0(r)$ and even its integral are often available as mathematical subroutines in a computer software library. If this is not the case one can expand $\mathrm{Int}(r)$ into a sufficiently long series of the form

$$\mathrm{Int}(r) = 2 \sum_{n=0}^{\infty} (-1)^n (r/2)^{2n+1} / ((2n+1) \cdot (n!)^2)$$

For expressions $\Phi_{c_i c_j}(f)$ and $\Phi_{s s_j}(f)$ one correspondingly can obtain the appropriate expressions:

$$\Phi_{c_i c_j}(f) = \frac{1}{\Delta \bar{r}_0} \int_{\bar{r}_0 - \Delta \bar{r}_0/2}^{\bar{r}_0 + \Delta \bar{r}_0/2} I_0(2\pi f r\, R_{ij})\, dr$$

$$\Phi_{s s_j}(f) = \frac{1}{\Delta r} \int_{r_0 - \Delta r_0/2}^{r_0 + \Delta r_0/2} I_0(2\pi f r\, \varrho_j)\, dr$$

References

Burg, J. B.: The application of the Wiener filter theory to the design of seismic arrays, S.E.G. Yearbook, p. 269, 1962

Burg, J. B.: Three-dimensional filtering with an array of seismometers. Geophysics *29,* 693–713, 1964

Cassano, E., Rocca, F.: After stack multichannel filters without mixing effects. Geophys. Prospecting *22,* 330–344, 1974

Deregowski, S. M.: Optimum digital filtering and inverse filtering in the frequency domain. Geophys. Prospecting *19,* 729–768, 1971

Embree, P., Burg, J. P., Backus, M. M.: Wide-band velocity filtering – the pie-slice process. Geophysics *28,* 948–974, 1963

Foster, M. R., Sengbush, R. L., Watson, R. J.: Design of suboptimum filter systems for multitrace seismic data processing. Geophys. Prospecting *12,* 173–191, 1964

Galbraith, J. N., Wiggins, R. A.: Characteristics of optimum multichannel stacking filters. Geophysics *33,* 36–48, 1968

Harjes, H. P., Henger, M.: Array – Seismologie. J. Geophys. *39,* 865–905, 1973

Hubral, P.: Three-dimensional optimum multichannel velocity filters, Geophys. Prospecting *21,* 29–45, 1972

Hubral, P.: Stacking filters and their characterisation in the (f–k) domain. Geophys. Prospecting *22,* 722–735, 1974
Krey, Th., Toth, F.: Remarks on wavenumber filtering in the field. Geophysics *38,* 959–970, 1973
Robinson, E. A.: Random wavelets and cybernetic systems. London: Griffin 1962
Robinson, E. A.: Statistical communication and detection with special reference to digital data processing of radar and seismic signals. London: Griffin 1967
Sengbush, R. L., Foster, M. R.: Optimum multichannel velocity filters. Geophysics *33,* 11–35, 1968
Treitel, S.: Digital multichannel filtering. Geophysics *35,* 785–811, 1970
Wiener, N.: Extrapolation, interpolation and smoothing of stationary time series. Technology Press of Mass. Inst. Techn., Cambridge, Mass., 1949

Dr. Peter Hubral
Bundesanstalt für Bodenforschung
D-3000 Hannover-Buchholz
Stilleweg 2
Federal Republic of Germany

J. Geophys. 41, 281–288, 1975

Travel Time Residuals in the Iranian Plateau

B. Akasheh

Institute of Geophysics, Tehran University

Received April 9, 1974; Revised Version January 9, 1975

Abstract. Travel time residuals with respect to the Herrin 1968 tables have been calculated for about 120 events ($45° < \Delta < 100°$), recorded at 5 Iranian Stations (Shiraz, Tehran, Tabriz, Kermanshah and Meshed). The residuals do not show a significant variation with respect to epicentral distance, azimuth (except Shiraz), magnitude of events, but show a variation with depth of events. To minimize source effects, residuals relative to Tehran have also been computed. The residuals are positive and suggest crustal and/or upper mantle velocity anisotropy. The crustal and/or upper mantle velocity anisotropy is different under stations on the Iranian Plateau. The stations are underlain by an unusual low velocity material or different crustal thickness. The residual at the Shiraz Station is +0.3 s in NE direction but +1.7 s in the SE direction. This phenomenon can be explained by the existence of a high velocity zone under the Zagros Mountains which dips towards NE. The Bouguer gravity anomalies and crustal thickness contour are calculated for about 70 points and they have been compared with *P* wave travel time residuals.

The absolute anomalies are expressed in terms of variations of the thickness of the crust, difference in velocity in the low velocity channel, and the velocity variations in the crust under the stations.

Key words: Travel Time — Residual — Iranian Plateau — Crust — Upper Mantle — Low-Velocity Channel.

1. Introduction

Travel time of seismic *P* waves from earthquakes and nuclear explosions determined at many stations indicate certain deviations from Jeffreys-Bullen and Herrin Tables. Part of the deviation is systematic, varying as a function of epicentral distance, part is station dependent. Seismic travel times and their residuals (observed travel time minus theoretical travel time) have been extensively analyzed statistically by Herrin (1968) and Herrin and Taggart (1968), who have determined residuals at many stations and by Lomnitz (1969). The *P* travel time residuals, with respect to the 1968 Herrin tables have been calculated for about 120 events ($45° < \Delta < 100°$), recorded at 5 Iranian Stations to determine the anomalies in the crust and in the upper mantle and to estimate the crustal thickness variation under the stations on the Iranian Plateau. The next attempt is to correlate the travel time anomalies with the Bouguer gravity anomalies and to make some models. Values of the Bouguer anomaly in the Iranian Plateau are used to deduce some regional thickness.

2. Seismicity and Tectonics of the Region

The Iranian Plateau is made primarily of sediments accumulated over geological time in the Tethys. The main folding of this sea area into the Zagros and Elburz

Mountains began during the passage from the Cretaceous to the Eocene periods. The Zagros thrust zone extends about 1400 km and has a straight alignment, extending westward, where it joins the Taurus ranges in Turkey. At its southern extension it goes toward Pakistan and Oman. Southwest of the Zagros thrust zone lie the foothills and the foreland. The foreland extends from the Red Sea to the Persian Gulf. The folded zone is characterized by a long parallel pattern of asymetric synclines with axes, generally parallel to the Zagros trend, indicating a northeast-southwest compression, (Stöcklin, 1968; Pilger, 1971). The width of the Zagros seismic zone extends from the northern shore of the Persian Gulf to the southern boundary of the Zagros thrust. This zone is the most active seismic zone in Iran. The focal depths increase with a dip about 15° toward the northeast (Niazi and Basford, 1968; Gansser, 1969; Akasheh 1971, 1972a, 1973; Nowroozi, 1971). The Elburz Mountain Range extends from north-west to the nort-east and appears to be linked with the Hindu-Kush ranges. This range is geologically a continuation of Central Iran but with a decrease of folding.

3. Data, Method, Results and Discussion

For about 120 events the epicentral distance and azimuth have been computed. The epicentral location, depth, origin time and magnitude of events published in the Bulletins of the USCGS and their *P* wave arrival times are given in the Bulletin of the Institute of Geophysics, Tehran University.

The location of the 5 stations used in this study are:

Shiraz	29° 48′ 39″ N	52° 51′ 34″ E	Height 1595 m
Tehran	35° 44′ 16″ N	51° 23′ 09″ E	Height 1360 m
Kermanshah	34° 21′ 08″ N	47° 06′ 21″ E	Height 1310 m
Tabriz	38° 04′ 03″ N	46° 19′ 36″ E	Height 1430 m
Mesheh	36° 18′ 40″ N	59° 35′ 16″ E	Height 830 m

Observed travel time and theoretical travel time according to 1968 Herrin tables have been calculated. Fig. 1a is a plot of the travel time residuals at 5 stations. The residuals are corrected with regard to station elevation. Each data point is the average of a 10° azimuth sector. The circle around each station shows zero residual. Fig. 1b is a plot of the travel time residual versus epicentral distance. Each data point is the average for 10° distance interval. The average residual for all data is about +0.5 s at the Shiraz Station, +1.6 s at the Tehran and Kermanshah Stations, +2.1 s at the Tabriz Station and +2.8 s at the Meshed Station. The residuals do not show a significant variation with azimuth (except Shiraz) and epicentral distance. The residuals at the Shiraz Station are +0.3 s in the N and NE direction but are +1.7 s in the SE direction. This phenomenon can be explained by the existence of a high velocity zone under the Zagros Mountains which dips toward NE. Nowroozi (1972) discussed independentely the existence of a slab under the Zagros Mountains. To minimize the source region effects, residuals relative to Tehran Station have also calculated. The residual relative to Tehran is at the Shiraz Station about —0.9 s, at the Kermanshah Station —0.1 s, at the Tabriz Station +0.4 s and at the Meshed Station about +1.4 s.

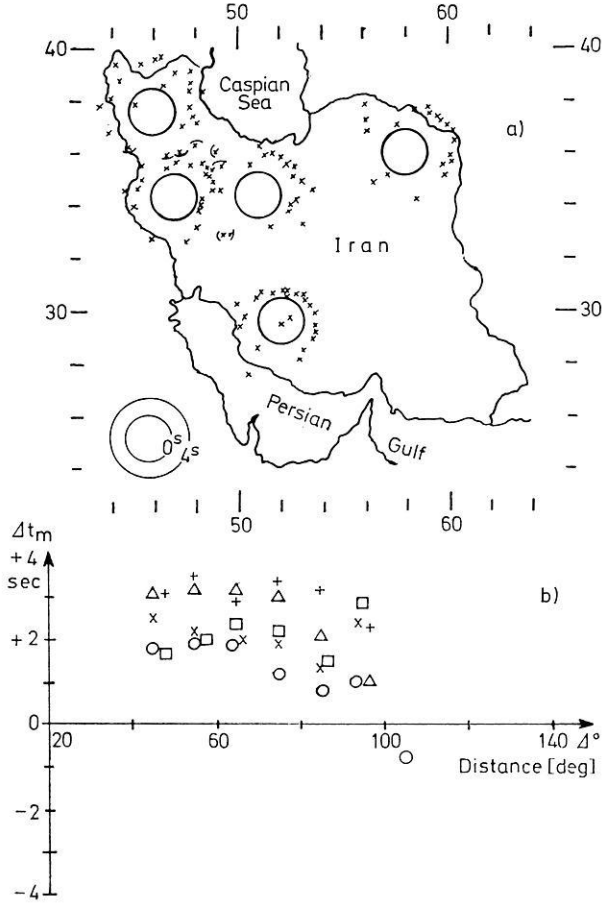

Fig. 1. Travel time residuals at 5 Iranian Stations. The circle around each station means the zero residual. Each data point is the average residual a) for a 10° sector, b) for 10° epicentral distance interval. O: Shiraz Station, □: Tehran Station, Δ : Tabriz Station, x: Kermanshah Station, +: Meshed Station

The residuals do not show regular variation according to the angle of incidence i_0 at the station, the angle of incidence i_d in the focus and the magnitude of events but show a regular variation according to the depth of events. Fig. 2 shows the travel time residuals at the Tehran Station according to d, depth of events. The circles represent the averages for 10, 20, and 100 km depth intervals. It is to seen from Fig. 2 that the residuals vary with depth of event. Residuals of events deeper than about 140 km are about one second less than the mean.

The residuals are positive and suggest crustal and/or upper mantle velocity difference and anisotropy. The crustal and/or upper mantle velocity variation and anisotropy may be different under station on Iranian Plateau. The stations on Iranian Plateau may be underlain by different crustal thickness or an unusual low-velocity material. If we assume that the anomalies (Δt) are caused by the variations in the crustal thickness (ΔH_0) we can calculate (for the mean angle of incidence at the station

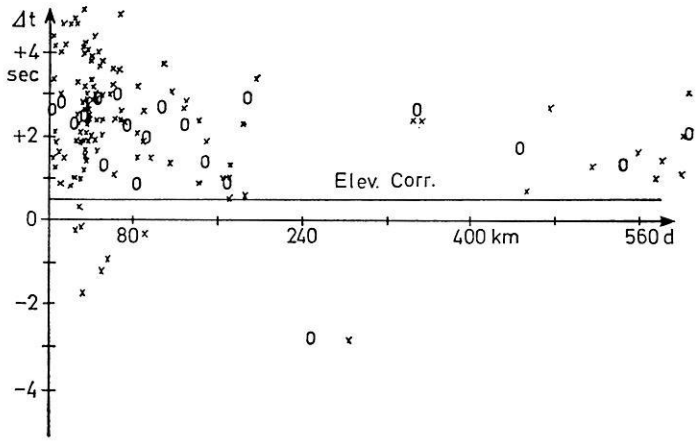

Fig. 2. Plot of the travel time residuals at the Tehran Station versus the angle of incidence in the focus. The station correction is shown with line parallel with d axis. The circles are the mean values

i_0 about 20°, mean crustal velocity $v_0 = 6.37$ km/s, velocity in the upper mantle $v_1 = 8.05$ km/s (Herrin *et al.*, 1968) the rate of change of crustal thickness H_0 for corresponding change in t by the relation $\Delta H_0 = \frac{v_0 \cdot v_1 \cos i_0}{v_1 - v_0} \Delta t$. To explain the absolute anomalies (+0.5 s at the Shiraz Station, +1.6 s at the Tehran and Kermanshah Stations, +2.1 s at the Tabriz Station and +2.8 s at the Meshed Station) we have to assume crustal thickness under Shiraz to be about 14 km thicker than the Herrin *et al.* model 1968 (40 km), under Tehran and Kermanshah about 46 km thicker, under Tabriz about 60 km thicker and under Meshed about 80 km thicker than the value of H_0 in the model.

Deep refraction seismic work in the region has not been done, but attempts have been made from body wave studies of earthquakes to determine the crustal structure and the thickness of the crust in Iran. From these studies it is quoted that the southern regions have a crustal thickness of 49 ± 6 km, whereas crustal thickness in the western and central regions is 55 ± 6 km (Akasheh, 1972b; Akasheh and Nasseri, 1972). Goudarzi *et al.* (1970) give a thickness of 39 ± 5 km for the crust in the Shiraz region. Eslami (1972) gives a thickness of 48 ± 4 km for region Shiraz, 42 ± 4 km for the south and south east region of Shiraz, 48 ± 6 km for the region Kermanshah and 53 ± 3 km for the region north and north west of Kermanshah and 57 ± 6 km for the south and south east region of Kermanshah.

We know that crustal thickness varies with respect to the Bouguer anomaly and surface elevation. For a continental type of crustal structure Heiskanen and Vening Meinesz (1958) have given a linear relationship between the surface elevation and the depth to the Mohorovicic discontinuity. Demenitskaja (1958) and Woollard (1959) have shown empirically in their works that the thickness of the crust varies with respect to Bouguer anomaly and elevation.

Gravity measurements are made since 1960 by the Institute of Geophysics, Tehran University (1960, 1962, 1970) and by Zomorrodian (1971, 1972). For about 70 points the Bouguer gravity anomaly is calculated for a simple model, using a

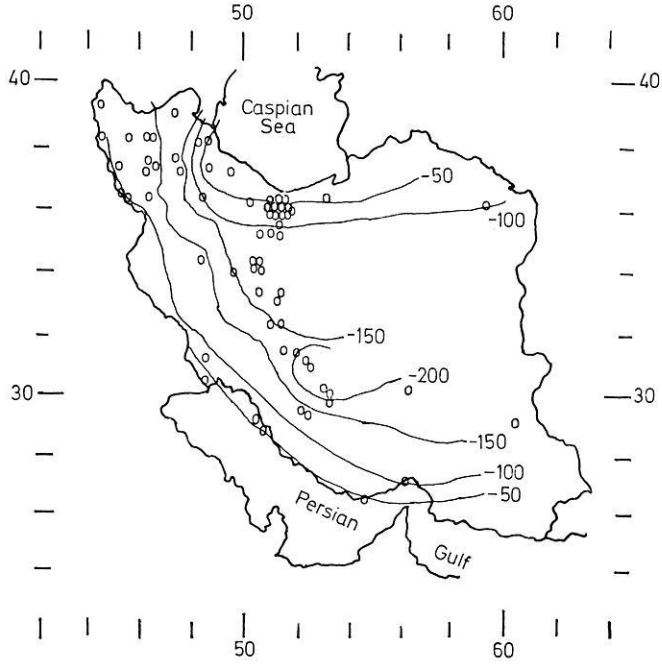

Fig. 3. Simple Bouguer gravity map of Iran (in mgal)

density of 2.67 g cm^{-3} (Schick and Schneider, 1973), Fig. 3. The gravity anomaly values display trends that are related to the major relief. The axis of regional Bouguer gravity anomalies is parallel with the Zagros chains. The gravity fields in the Iranian Plateau are characterized by large negative Bouguer anomalies (about —200 mgal) in the Zagros zone and about —150 mgal in the Elburz zone, but it seems that the Bouguer gravity anomalies are about zero in the Caspian Sea and Persian Gulf. That means that the Zagros and Elburz zones are associated with a large mass deficiency, a mechanism involving underthrusting of light continental crust into higher density mantle in the Zagros and Elburz zones. This mechanism is consistent with regional seismicity, focal mechanism, depth of the foci and crustal thickness variation.

An estimate of the crustal thickness is made from Demenitskaja's formula. Fig. 4 shows the contours of crustal thickness based on the Bouguer anomaly. The crustal thickness in Fig. 4 delineate the Zagros and Elburz zones, which seem to have an average depth to the Moho of the order of 50 km. The crustal model used in travel time studies by Herrin *et al.*, 1968, has a thickness of 40 km for the crust. That is of the order of crustal Thickness under the 5 Iranian Stations.

We assume now that the travel time absolute anomalies at the stations are caused within a depth of 300 km, we can calculate the velocity in the low-velocity channel. On the basis of a reference model:

Crustal thickness $H_0 = 35$ km, crustal velocity $v_0 = 6.1$ km/s. Thickness Moho-Low Velocity Upper Interface $H_1 = 85$ km with a velocity $v_1 = 8.2$ km/s.

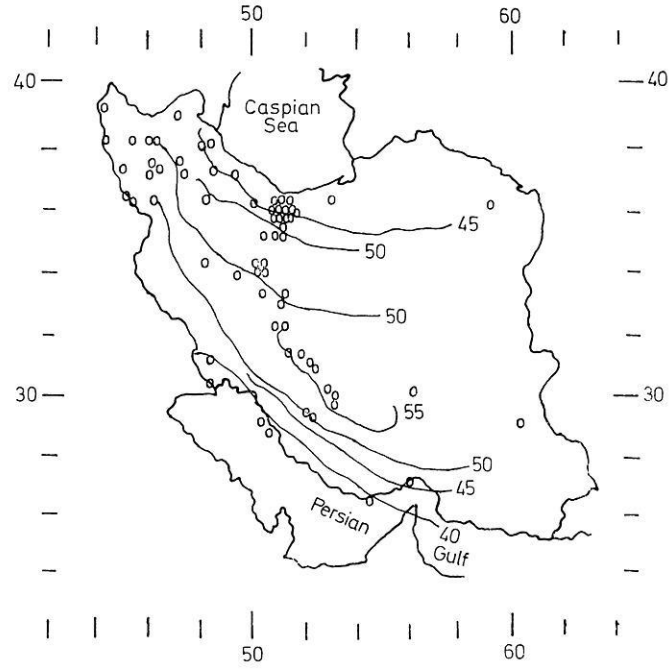

Fig. 4. Contours of crustal thickness (in km) based on the Bouguer anomaly

Thickness Low Velocity Upper Interface and 300 km depth, $H_2 = 180$ km with a velocity $v_2 = 8.13$ km/s.

Which is consistent with results from Jacob, 1971, we have calculated several models to explain the travel time anomalies at the stations. For $v_0 = 6.1$ km/s $H_0 = 45$ km, $H_1 = 75$ km and $v_1 = 8.2$ km/s under all stations, we can express the anomalies in terms of low-velocity channel. We find that:

$v_2 = 8.10$ km/s for the Shiraz Station
$v_2 = 7.75$ km/s for the Tehran and Kermanshah Stations
$v_2 = 7.56$ km/s for the Tabriz Station
$v_2 = 7.34$ km/s for the Meshed Station

We assume but now that the travel time absolute anomalies are caused within the crust and we calculate the velocity in the crust under the stations. On the basis of the same reference model and for $H_0 = 45$ km, $v_1 = 8.2$ km/s, $v_2 = 8.13$ km/s beneath all stations, we can explain the anomalies at the stations in terms of different crustal velocity v_0 as:

$v_0 = 6.03$ km/s for the Shiraz Station
$v_0 = 5.26$ km/s for the Tehran and Kermanshah Stations
$v_0 = 4.97$ km/s for the Tabriz Station
$v_0 = 4.61$ km/s for the Meshed Station

The $+0.7$ to $+1.9$ s smaller travel time residual at Shiraz Station means that the reason of smaller residual at Shiraz Station can be the different crustal velocity or the different upper mantle velocity under stations. The Shiraz Station indicates higher velocity with respect to other stations.

Acknowledgements. The author is greatly indebted to Prof. Dr. H. Berckhemer for the critically reviewing the manuscript, to Prof. Dr. H. K.-Afshar, Director of Institute for Geophysics Tehran University for his support and to Dr. A. A. Nowroozi (from Pahlawi University Shiraz) for the fruitful discussions. Dipl.-Phys. S. M. Arastoo and Mrs. F. Blouri assisted me in this work.

References

Akasheh, B.: A mathematical model of earthquakes and its comparison with the tectonics. Bull. Fac. Sci., Teheran Uni. *3*, 15–21, 1971

Akasheh, B.: Seismizität und Tektonik von Iran. J. Earth Space Phys. *1*, 8–24, 1972a

Akasheh, B.: The thickness of the crust in Iran. Bull. Fac. Sci. Tehran Uni. *4*, 63–69, 1972b

Akasheh, B.: Mechanismus des Bebens vom 10. April 1972. Z. Geophys. *39*, 1055–1061, 1973

Akasheh, B., Nasseri, S.: Die Mächtigkeit der Erdkruste in Iran. J. Earth Space Phys. *1*, 1–6, 1972

Demenitskaja, R. M.: cited by E. D. Korjakin. In: Dokl. Akad. Nauk *129*, 1287, 1958

Eslami, A. A.: Velocity of P_n and depth of Moho discontinuity in western Iran. J. Earth Space Phys. *1*, 1–12, 1972

Gansser, A.: The large earthquakes of Iran and their geological frame. Eclogae Geol. Helv. *62/2*, 443–466, 1969

Heiskanen, W. A., Vening Meinesz, F. A.: The earth and its gravity field. p. 204. New York: Mc Graw-Hill 1958

Herrin, E.: Introduction to "1968 seismological tables for P phases". Bull. Seism. Soc. Am. *58*, 1193–1241, 1968

Herrin, E., Taggart, J. N.: Regional variations in P travel times. Bull. Seism. Soc. Am. *58*, 1325–1337, 1968

Herrin, E., Tucker, W., Taggart, J. N., Gordon, D. W., Lobdell, J. L.: Estimation of surface focus P travel times. Bull. Seism. Soc. Am. *58*, 1273–1291, 1968

Institute of Geophysics Tehran University: Gravity measurements in Iran. Iranian national report. XII General Assembly of the international union of geophysics and geodesy in Helsinki. 1960

Institute of Geophysics Tehran University: Gravity measurements in Iran. Publication No. 9, 1962

Institute of Geophysics Tehran University: The measurements and the adjustments of the first order gravity network in Iran. Publication No. 48, 1970

Jacob, K. H.: Global Tectonic Implications of Anomalous Seismic P Traveltimes from the Nuclear Explosion Longshot. J. Geophys. Res. *77*, 2556–2573, 1972

Lomnitz, C.: A definition of travel time anomalies. Bull. Seism. Soc. Am. *59*, 421–425, 1969

Moazami-Goudarzi, K., Soltanian, R., Mozafari, N.: Etude de la Croute Terrestre a Chiraz. Bull. Fac. Sci., Tehran Uni. *2*, 1970

Niazi, M., Basford, J. R.: Seismicity of iranian plateau and Hindu-Kush region. Bull. Seism. Soc. Am. *58*, 417–426, 1968

Nowroozi, A. A.: Seismo-tectonics of the Persian Plateau, Eastern Turkey, Caucasus and Hindu-Kush Region. Bull. Seism. Soc. Am. *61*, 317–341, 1971

Nowroozi, A. A.: Focal mechanism of earthquakes in Persia, Turkey, West Pakistan and Afghanistan and plate tectonics of the Middle East. Bull. Seism. Soc. Am. *62*, 823–850, 1972

Pilger, A.: Die zeitlich-tektonische Entwicklung der iranischen Gebirge. Clausthaler Geol. Abh., *8*, 1971

Schick, R., Schneider, G.: Physik des Erdkörpers. S. 138–144. Stuttgart: Enke 1973

Stöcklin, J.: Structural history and tectonics of Iran. A Review. Bull. Am. Assoc. Petrol. Geologists *52*, 1229–1258, 1968

Woollard, G. P.: Crustal structure from gravity and seismic measurements. J. Geophys. Res. *64*, 1521–1544, 1959

Zomorrodian, H.: The measurements and the adjustments of the second order gravity network in Iran. Institute of Geophysics, Tehran University, Publ. No. 53, 1971

Zomorrodian, H.: The establishment of the iranian national gravity line. Institute of Geophysics, Tehran University, Publ. No. 58, 1972

Dr. B. Akasheh
Institute of Geophysics
Tehran University
Amir-Abad-Bala
Tehran/Iran

J. Geophys. 41, 289–302, 1975

Noise Variance Fluctuations and Earthquake Detectability

O. Steinert, S. Husebye, H. Gjøystdal

NORSAR, Kjeller

Received October 14, 1974; Revised Version February 3, 1975

Abstract. Shimshoni (1972) observed diurnal variations in earthquake occurrence as reported by NOAA. This effect, which is generally explained in terms of noise level fluctuations, manifests itself at the NORSAR array in Norway. However, large diurnal variations are also observed in the number of pure noise detections (false alarms) reported by the NORSAR on-line detector. This has to be attributed to changes in the statistical properties of the noise, as the detector, having a fixed detection threshold, is insensitive to fluctuations in the noise level. Such changes are not likely to be reflected accurately in the inherently subjective detectability based on visual inspection of seismograms.

Two indicators for estimating the false alarm rate have been considered; the most successful, called the noise stability, is defined as the ratio between squared noise average and noise variance. A relation between detection threshold, stability and false alarm rate has been established which makes it possible to fix the false alarm rate and let the threshold 'float', i.e., vary as function of the noise stability. It is shown that implementation of a floating detection threshold will generally improve signal detectability by about 4% relative to a fixed threshold operation. Other advantages are avoidance of system saturation during extremely noisy time intervals and a more economical use of the computer capacity with respect to load caused by diurnal false alarm rate. The treatment presented is applicable to other types of on-line signal detection problems.

Key words: Noise Variance Fluctuations – Earthquake Detection – NORSAR Array – Fixed and Floating Event Detector Threshold.

Introduction

Earthquake occurrence has been thought to be a response of the earth to periodic stresses connected with orbital frequencies of the sun-earth-moon system. Recently, in a statistical analysis of three years of NOAA (U.S. National Oceanic and Atmospheric Administration) earthquake data, Shimshoni (1971) found that the earthquake activity was highest during local night time, and in consequence postulated that the sun has an effect on seismicity. However, according to Davis (1972), Flinn *et al.* (1972) and Knopoff and Garder (1972) this conjecture is based on an incorrect interpretation of the raw NOAA data, as the effect on diurnal noise level fluctuations on the global network seismic event detection capability is not taken into account. It is well-established that short period seismic noise is significantly greater during day than night, the effect being more pronounced where cultural sources contribute significantly to the noise background. In a reply to the critical analyses, Shimshoni (1972) concedes that the diurnal noise fluctuations are very important for the interpretation of his original results, but he expresses doubt as to whether this effect could explain all the observed diurnal variation in earthquake occurrence. Not unexpectedly, Bungum and Ringdal (1973) found that the seismicity as observed by

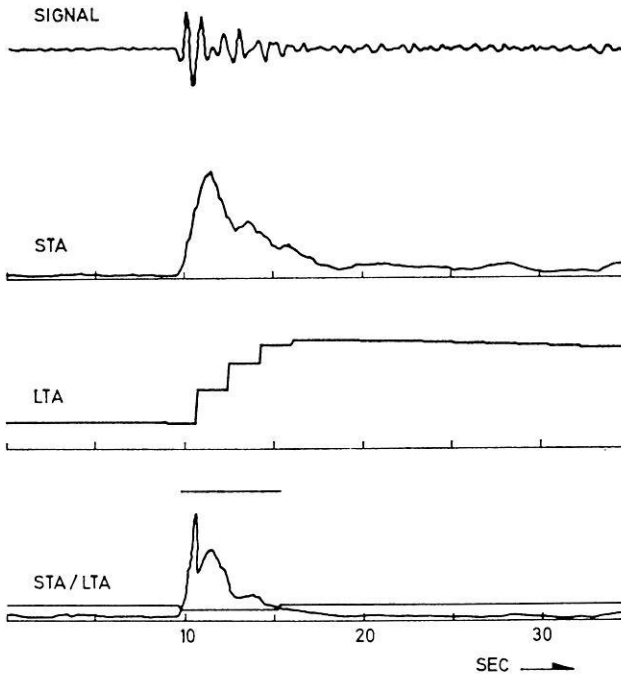

Fig. 1. Beam, STA, LTA and STA/LTA for earthquake from Tsinghai, China; arrival time Jan 27 1970, 10.59.40.1 filtered 1.0–3.0 Hz. STA integration time is 1.8 s, and LTA computation rate is 5/9 Hz. The short line above the STA/LTA curve indicates detection state, and the line crossing the curve is the threshold

the NORSAR array exhibits a clear diurnal variation. However, they also found that the number of times the array's automatic event detector was triggered was much larger during local night time than day time (see Fig. 1). The latter result indicates that not only the noise level but also the noise variance or noise field variations must be considered when discussing the detectability of small earthquakes.

The aim of this study is to investigate the effect of noise field variations on the earthquake-reporting performance of the NORSAR array. Also, ways to improve its event detectability will be considered. The reasons for using the NORSAR installation are numerical convenience and, more importantly, to avoid the subjectivity involved in visual seismogram readings. We remark, however, that the problems and principles involved are of a general type, and are relevant in a variety of on-line signal detectors.

Seismic Array Detector Design and Noise Characteristics

The large arrays LASA and NORSAR represent in general the most efficient tool available for detecting small seismic events. The basic operational principle of the array is beamforming; the array is regularly steered towards a large number of predetermined points distributed throughout the active seismic regions. Due to the large amount of data generated by NORSAR's 132 short period seismometers,

an on-line detector is required for the surveillance task of the array. The most commonly used detector is based on a continuous comparison between a certain parameter η and a present detection threshold, η being the ratio between the linear array beam power measured in a short (STA) and a long (LTA) time window. (The NORSAR array and its operational procedures are described by Bungum *et al.* (1971) and Bungum and Husebye (1974).

The problem of declaring a signal detection represents a hypothesis test based on the test statistic η: declare a detection whenever η is equal to or exceeds a present detection threshold (TH), i.e., choose hypothesis H_1. Otherwise, decide that H_1 is false, i.e., hypothesis H_0 is chosen. Symbolically,

$$\eta \underset{H_0}{\overset{H_1}{\gtrless}} \mathrm{TH} \tag{1}$$

This binary decision model has two error conditions; the false alarm (FA) or choosing H_1 when H_0 is true, and the missed detection (MD) or choosing H_0 when H_1 is true. The test statistic itself is given in Eq. (1), while the definitions of the STA and LTA parameters are

$$\mathrm{STA}(t) = \sum_{i=t}^{t+L-1} |a(i)| \tag{2}$$

$$\mathrm{LTA}(t') = (1-2^{-5}) \cdot \mathrm{LTA}(t'-\mathrm{L}) + \mathrm{STA}(t'-\mathrm{L})/2 \tag{3}$$

Here t and t' are STA and LTA sampling times, $a(i)$ is array beam amplitude, and L is STA integration window length, typically 1.5 sec. The η and STA sampling rate is 2 Hz while the much more slowly varying parameter LTA has a 2/3 Hz sampling rate. A schematic representation of the array detector is shown in Fig. 1. The STA operation is equivalent to time domain filtering of the rectified beam, and its frequency response is shown in Fig. 2. Additional noise suppression beside that of beamforming is obtained by prefiltering with a 3rd order Butterworth bandpass filter. The possibility of seismic signal recording is tested around $50 \cdot 10^6$ times every day, although only one third of these tests can be considered independent due to time and/or spatial overlaps of the STA parameter. It is important to note that the detector is working on the very tail of the η or STA distribution function, as the TH-value is roughly the mean value plus 6—8 times the standard deviation of the STA samples.

The design of the NORSAR detector is not derived from any optimum criteria (Helstrøm, 1968) because the noise amplitude probability function is not exactly known and the noise exhibits both diurnal and seasonal fluctuations. This means that the test statistic η is unstable, which implies a variable false alarm probability for a given threshold. An example of the non-stationarity of the noise field is given in Fig. 3. During local night time the noise decreases, thus explaining why the number of events reported increases. Flinn *et al.* (1972) have obtained similar results for the

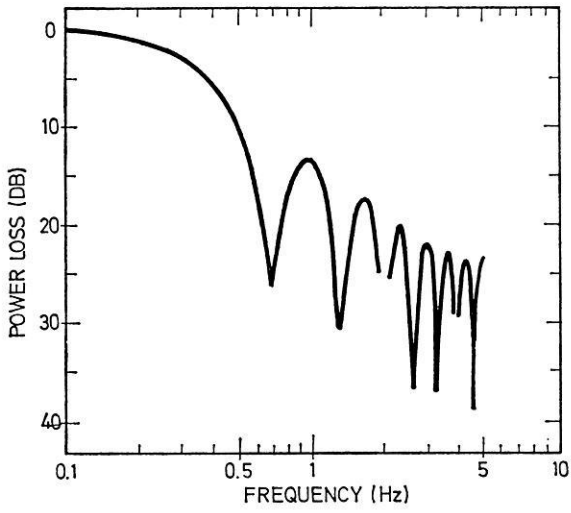

Fig. 2. Response curve for the STA-operator. Filter length is 1.5 sec

LASA array. However, during night the number of false alarms also increases (see Fig. 4), and this phenomenon must be attributed to changes in the noise character. The reason is that the false alarm rate is independent of the noise level or the STA-value itself, but does depend on its variance. In terms of the binary decision model incorporated in the array's detector, this means also that the probability of a missed detection is larger during day time. The above phenomenon is fairly easy to explain in terms of noise spectra fluctuations. During night time the relatively low frequency microseismic noise dominates, while high frequency cultural noise is added during day time (see Fig. 3). From the theoretical studies of Rice (1944) and Cartwright and Longuet-Higgins (1956) the probability density distribution of noise maxima is expected to vary accordingly, i.e., between Rayleigh and Gaussian distributions. Also during heavy microseismic storms the noise spectra change. A theoretical explanation of the corresponding variations in the false alarm rate has been given. by Lacoss (1972).

Data Analysis and Results

In the previous sections it was demonstrated that an array's event detectability, i.e., its ability to report 'true' seismic signals, does depend both on the noise level and the noise character or, in other words, the unstable noise probability function. Moreover, when a fixed detection threshold is used, the probability of a missed detection is higher during day time than night time. One possible way to improve the event detectability is to exercise a better control with the false alarm rate, i.e., to use a floating threshold value in the automatic signal detector. This point will be discussed in detail in a later section.

Two different false alarm indicators have been analyzed. The first, here denoted ε, was suggested by Cartwright and Longuet-Higgins (1956) in their study of distribution functions of ocean wave maxima. In general, ε is a measure of the RMS

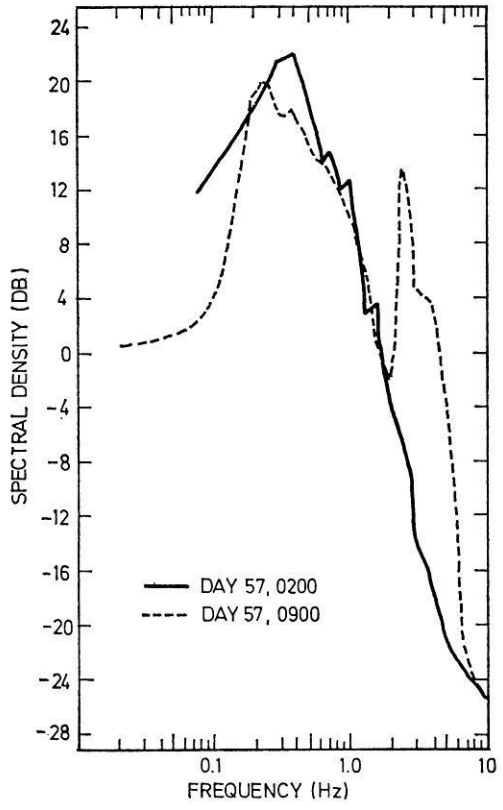

Fig. 3. Power spectral densities for two single sensor noise samples showing the difference between typical night- and daytime situations in 1973

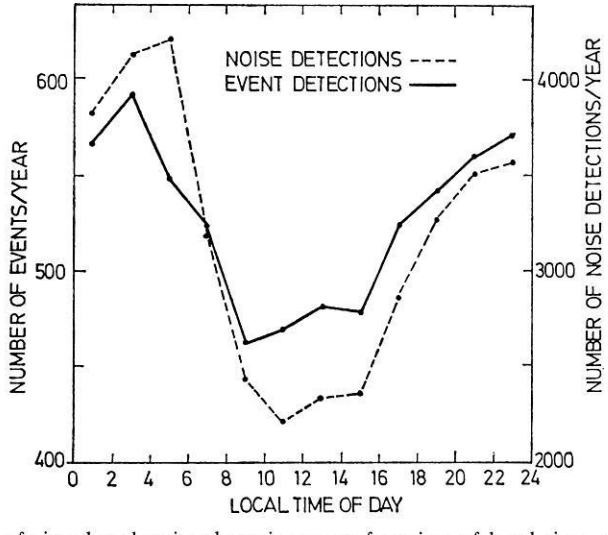

Fig. 4. Number of signal and noise detections as a function of local time of day, obtained by Bungum and Ringdal, 1974

width of the energy spectrum, and was found to vary between zero and one as the probability density function of the waveform maxima changed from Rayleigh to Gaussian. ε is defined as

$$\varepsilon^2 = \frac{m_0 m_4 - m_2^2}{m_0 m_4} \tag{4}$$

or

$$\varepsilon^2 = 1 - \frac{N_0^{+2}}{N_1} \tag{5}$$

where m_i is the spectral moment of i-th order, N_0^+ is the density of zero line upcrossings, and N_1 the density of maxima in a certain time window. Due to its computational simplicity, Eq. (5) was used in the analysis.

The other false alarm indicator considered, in the following called the noise stability, is defined as:

$$S = \frac{\eta^2}{\sigma^2(\eta)} \approx \frac{\overline{STA}^2}{\sigma^2(\overline{STA})} \tag{6}$$

where $\eta = STA/LTA$ and the bar indicates averaging. The S-term approximation used above will not introduce significant errors as the LTA-term varies very slowly. The stability S is a generalized measure of the spread in the η observations and is likely to be a sensitive indicator for phenomena of the type investigated here (Lacoss, 1972).

The signal detector at NORSAR comprises 318 array beams, of which a subset of 63 beams distributed evenly in geographic space were chosen for this analysis. The ε and S indicators were estimated over subwindows of approximately 12 minutes, or equivalently approx. 500 independent STA samples. Different types of noise conditions were analyzed; quiet, normal and noisy (Table 1). Artificial coloring of the noise was obtained by using different types of bandpass filters. Although the calculation performed is simple, it is very time-consuming as we had to utilize a modified, off-line version of the on-line signal detector. For example, the analysis of one hour of real-time data required approx. six hours of computer time.

Table 1. Data used in the analysis

Data set	Time intervals (Year 1972)	Typical LTA within freq.band 1.2–3.2 Hz	Bandpass filtering[a]
1	276/17/15 – 276/18/05	80	A, B, C
	278/21/55 – 278/22/45	200	A, B, C
	279/16/45 – 279/17/30	140	A, B, C
2	239/23/00 – 240/01/45	77	A, B, D
	240/04/00 – 240/07/16	80–110	A, B, D
3	271/09/00 – 271/12/50	230	A, B, D

[a] Bandpass filters (Hz): 1.2–3.2 (A), 1.4–3.4 (B), 1.6–3.6 (C), 2.0–4.0 (D)

In Table 2 the ε-values which were measured from the STA time traces are presented. The variation in ε is very small and discloses little or no dependence on the noise conditions, filters used and the indicator. Cartwright and Longuet-Higgins (1956) assume a Gaussian distribution function for the waveform amplitudes in their model. The importance of this assumption is not known, but it is certainly violated by the distribution function of the STA-values. A Kolmogorov-Smirnov test here gave mostly Rayleigh or lognormal distributions in different STA-trace intervals. Further evidence for the skewness in the STA-distribution is the fact that the threshold value TH is far out on the tail of the STA distribution function, as indicated earlier.

Table 2. Cartwright and Longuet-Higgins (1956) ε-parameter observations for different noise situations and different bandpass filters

Time interval (1972) (day/hour/min)	Bandpass filter (Hz)					
	1.2–3.2		1.6–3.6		2.0–4.0	
	min	max	min	max	min	max
239/23/00 – 240/01/45	0.812	0.826	0.822	0.830	0.711	0.767
240/04/00 – 240/07/16	0.812	0.836	0.806	0.830	0.687	0.716
271/09/00 – 271/12/50	0.822	0.840	0.835	0.871	0.788	0.832

The results of the stability measurements for the data analyzed for different noise conditions are shown in Fig. 5. The effect of bandpass filtering on the noise stability is striking, but not unexpected from physical considerations. The point is that the probability of constructive interference between randomly phased and amplitude-modulated waves is smaller for high frequency than for low frequency wave trains. Fig. 6 shows the false alarm rate as function of the stability parameter for four different detection threshold values. The false alarm rate is defined as the sum of all detections reported to have an STA/LTA ratio larger than 8.5, 9.0, 9.5 and 10.0 dB respectively. To safeguard against weak signals in the noise samples, values of STA/LTA larger than 10.5 dB were assumed to be 'true' signal detections and henceforth removed from the sample population. It is noteworthy that the noise stability-false alarm relationship is apparently independent of whether the noise field varies artificially, using bandpass filters, or naturally.

The results of Fig. 6 may be used to find a mathematical relation between detection threshold (TH), false alarm rate (FA) and noise stability (S). A reasonable approach would be to apply a two-dimensional linear regression analysis, considering TH as a linear function of log FA and S. The reason for choosing FA and S as independent variables is that in practical application, the question of interest is what value of TH would correspond to a predetermined false alarm rate for a certain value of S. The least square fit gave:

$$\mathrm{TH(dB)} = 12.08 - (0.89 \pm 0.01) \cdot \log \mathrm{FA} - (0.18 \pm 0.02) \cdot \mathrm{S} \qquad (7)$$

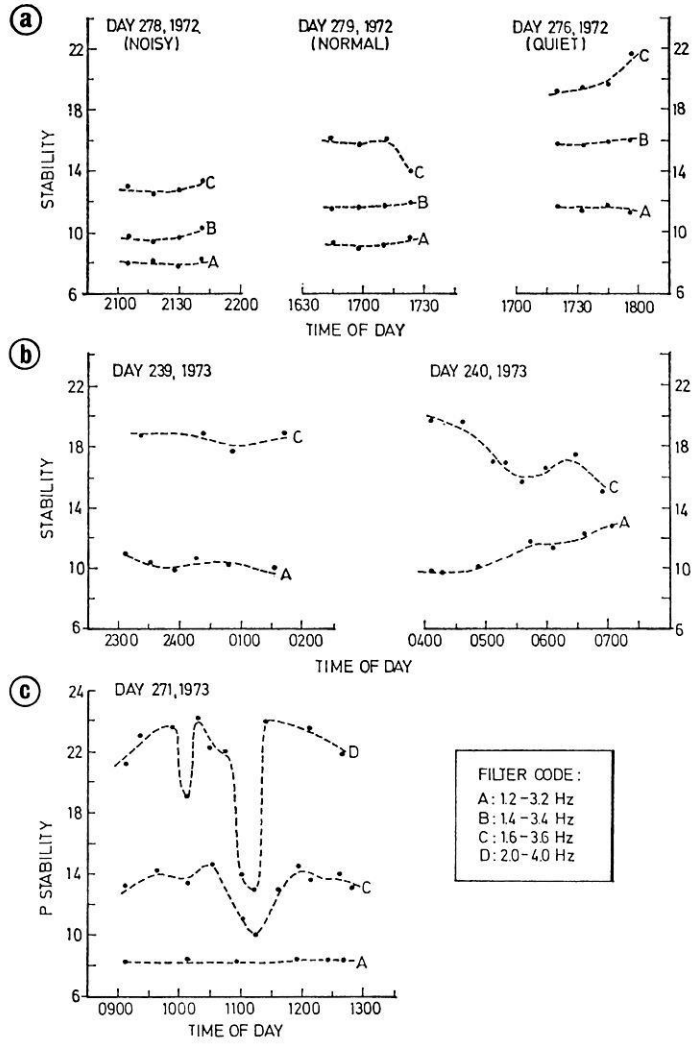

Fig. 5. Variation of stability with local time of day for different noise situations and different bandpass filters

This relation makes it possible to fix the false alarm rate and let the threshold vary as a function of noise stability. In the Appendix it is shown that the expected signal detectability R of a floating threshold procedure, relative to one with a fixed threshold, is given by

$$R = \frac{\sum_{i=1}^{M} (N_{si} \cdot N_{ni}^{-k}) \left(\sum_{i=1}^{M} N_{ni} \right)^k}{M^k \cdot \sum_{i=1}^{M} N_{si}} \tag{8}$$

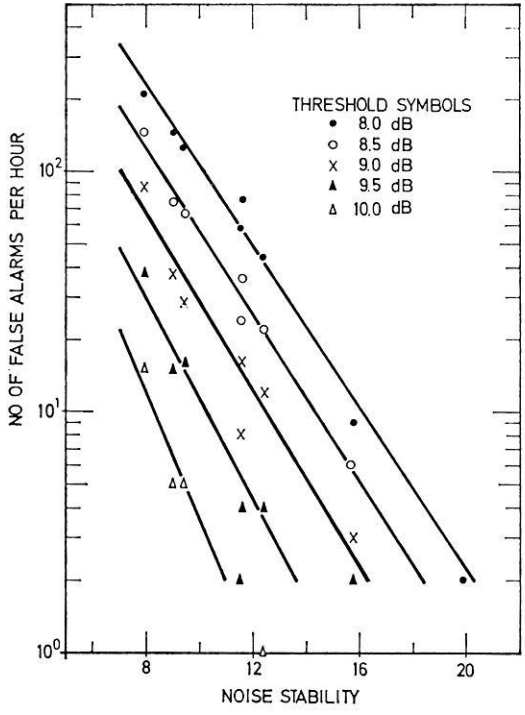

Fig. 6. False alarm rate as a function of noise stability for different values of detection threshold

where N_{si} and N_{ni} are samples of the signal and noise detection frequencies in a time interval with M samples, and k is the ratio of the slopes of the lines describing the signal and noise detection frequencies.

In order to estimate the coefficient R, we need models giving typical variations of N_s and N_n with time. Roughly, the noise variation may be divided into two parts, namely, the seasonal variation due to microseismic storm activity and the short-term variation due to diurnal fluctuations of the cultural noise. These two phenomena will have totally different effects on the noise stability. In the first case the energy increases in the low frequency range (decreasing stability) and in the second one energy increases in the high frequency range (increasing stability). In the latter case, the diurnal components of the signal and noise detection rates (N_s and N_n) will be approximately in phase (see Fig. 4), while the seasonal variations involving significant fluctuations in the LTA-level imply a phase difference of 180 degrees (Bungum and Ringdal, 1974). We use the following simple models for the variations of N_s and N_n for the i-th sample:

$$\begin{aligned} N_{si} &= A_s + B_s \cos\left(2\pi \frac{i}{M} + \phi_s\right) \\ N_{ni} &= A_n + B_n \cos\left(2\pi \frac{i}{M} + \phi_n\right) \end{aligned} \tag{9}$$

For simplicity the diurnal and seasonal noise effects on R are estimated separately. In the first case the two cosine functions are in phase (see Eq. (9)) and thus $\phi_s = \phi_n = 0$. In the second case we have $\phi_s = 0$, $\phi_n = \pi$. To estimate the coefficients A_s, B_s, A_n and B_n we need to know the relative fluctuations of signal and noise detection rates. This information may be deduced directly from Fig. 4. As to the seasonal variations, similar results are available from rough studies of signal and noise detection rates during noisy and quiet time intervals. The relative fluctuations of N_s and N_n together with the corresponding coefficients A_s, B_s, A_n and B_n are given in Table 3. From Eq. (9), N_{st} and N_{nt} were calculated and substituted into Eq. (8) to get final estimates of R for different values of k-parameter. The results obtained (see Table 4) indicate a small but significant improvement in the average signal detectability when using a floating threshold as compared to a fixed threshold detector of the type considered here. This is especially true when considering the seasonal variations in noise level, as in this case the threshold value is set too high in order to avoid system saturation during extreme noise conditions. In practice, this means that the false alarm rate is approximately zero during day time over an extended period of time. A value of k of the order 0.1 is reasonable (Bungum and Ringdal, 1974) and gives an R factor equal to about 1.04. As expected the floating threshold is especially favorable in the seasonal case, sinde these variations cause high stability (and thereby allow for low thresholds) when the LTA-level is low, whereas the opposite is true for the diurnal variations.

Table 3. Table showing typical relative variations in signal and noise detection rates, together with coefficients A_s, B_s, A_n and B_n of Eq. (9). For simplicity, A_s and A_n are set equal to 1

Quantity	Diurnal variation	Seasonal variation
$N_{s,\max}/N_{s,\min}$	1.3	3.0
$N_{n,\max}/N_{n,\min}$	1.9	6.0
A_s, B_s	1.0, 0.13	1.0, 0.5
A_n, B_n	1.0, 0.33	1.0, 0.7

Table 4. Table showing the relative gain factor R for different values of the ratio k. Values are obtained separately for a typical diurnal and a typical long term variation

k	Diurnal variation	Seasonal variation
1.0	1.04	1.7
0.5	1.01	1.2
0.1	1.001	1.04
0.05	1.0004	1.02
0.01	1.00006	1.004

Discussion

The physical operations involved in the NORSAR event detection processing are bandpass filtering for removal of low-frequency noise, then rectification which is roughly equivalent to a doubling of the signal frequency, and finally, the STA-estimation which removes most of the highfrequency signal components (see Fig. 2). The STA operation is not a perfect lowpass filter, so the high-frequency componente would be folded into the STA-spectrum (aliasing effects) as the STA sampling rate is 2 Hz. Moreover, the bandpass filter will allow low-frequency energy to leak into the filter passband. The latter effect is most pronounced during microseismic storms but in general seems to be less important than the cultural noise generated during the daily working hours. In short, variations in the ambient noise field would change the STA-spectra and henceforth its variance, as quantitatively demonstrated in Fig. 5. The removal of low-frequency noise gives better stability values, i.e., a smaller false alarm rate. However, for the extremely high-frequency filters, the stability parameter becomes less stable again, probably due to short time fluctuations in the cultural noise and the narrowness of the corresponding noise spectra.

A large data base covering time periods where the change in cultural background noise has been observed to be largest, i.e., early morning and evening during work days, would have been advantageous, but only one such period is presented. For Day 240, Fig. 5 shows that the noise stability increases with time for the 1.2—3.2 Hz filter. This filter is currently used in the NORSAR detection processor, and the time of day analyzed is that for which Fig. 4 shows the most rapid decrease in the false alarm rate.

From the above discussion we conclude that the stability parameter represents a useful false alarm rate indicator. On the other hand, the ε-parameter seems to be for all practical purposes independent of changes in the noise field and/or the bandpass filter in use, and in consequence is not useful as a false alarm rate indicator.

It is appropriate to comment on the potential gain when the false alarm rate of the detector is kept approximately constant by using a floating threshold value. The false alarm indicator and the associated threshold value estimator defined in Eqs. (6) and (7) have not yet been implemented in the NORSAR on-line detector. However, as a first approximation to control the false alarm rate on a diurnal basis we have implemented a predefined, sinusoidal TH-parameter variation as a function of local time of day. The amplitude of this function, determined on the basis of the noise character of the five work days of the week, is 0.075 units, corresponding to a maximum value of TH at night time of around 3.70 and a minimum value of TH at day time of around 3.55. Preliminary analysis of the false alarm rate after implementation of the above TH-function shows that it has been successful in removing a large part of the diurnal effect.

We remark that the floating threshold procedure has advantages besides that of controlling the false alarm rate and the expected increase in signal detectability. For example, Bungum and Ringdal (1974) pointed out that the considerable diurnal variation in signal detection rate (see Fig. 4) could not be fully explained by the modest fluctuation in noise level (see also Shimshoni, 1972). They proposed that a possible explanation might be a tendency to accept more noise detections as signals when the false alarm rate is high and vice versa, accounting for the good correlation between

the two curves of Fig. 4. Obviously, using a floating threshold would tend to eliminate such an unwanted effect, as the false alarm rate would not be subject to diurnal fluctuations. The underlying assumption is, of course, that earthquake occurrence is independent of local time of day (e.g., see Davis, 1972; Flinn *et al.*, 1972; and Knopoff and Gardner, 1972).

Finally, it is not clear whether the result presented above is valid for signal detections based on visual inspections of ordinary seismograms. However, noise spectra variations would, if not accounted for, significantly affect the global network detectability of small earthquakes because large seismic arrays NORSAR and LASA contribute significantly to the seismicity of the earth as reported by NOAA and similar agencies.

Conclusions

In this paper it is demonstrated that noise variance fluctuations besides those of noise level fluctuations also affect our capability to detect small earthquakes when an automatic seismic signal detector is utilized. The importance of maximizing this detectability in surveillance and other seismological studies needs no further emphasis here. The advantages of a floating threshold detector as compared to a fixed threshold detector are an increase in the average signal detectability, an approximately constant number of false alarms per unit time in the detector system, and avoidance of system saturation during extremely noisy periods which otherwise could only be obtained by using an overly conservative threshold level.

Acknowledgement. This research was supported by the Advanced Research Projects Agency of the U. S. Department of Defense and was monitored by AFTAC/VSC, Patrick AFB FL 32925, under Contract No. F 0860674C0049.

Appendix

Evaluation of Signal Detectability Using Fixed and Floating Detection Thresholds

The earthquake frequency-magnitude distribution of NORSAR may be described by a straight line as shown in Fig. 7 (Bungum and Husebye, 1974). Thus, the signal detection rate of NORSAR, N_s, may be tied directly to this functional relationship, namely,

$$\log N_s = b_s \cdot \mathrm{TH} + a_s \tag{A1}$$

where the slope b_s is approximately —1.

The relationship between the noise detection frequency, N_n, and the detection threshold is given by Eq. (7):

$$\log N_n = b_n \cdot \mathrm{TH} + a_n \text{ where } a_n = c_n \cdot \mathrm{S} + d_n \tag{A2}$$

The above signal-noise detection model is demonstrated in Fig. 7, and will be used for a functional comparison of the signal detection performance of the STA/LTA-detector using fixed and floating threshold values. It is required that N_{tot},

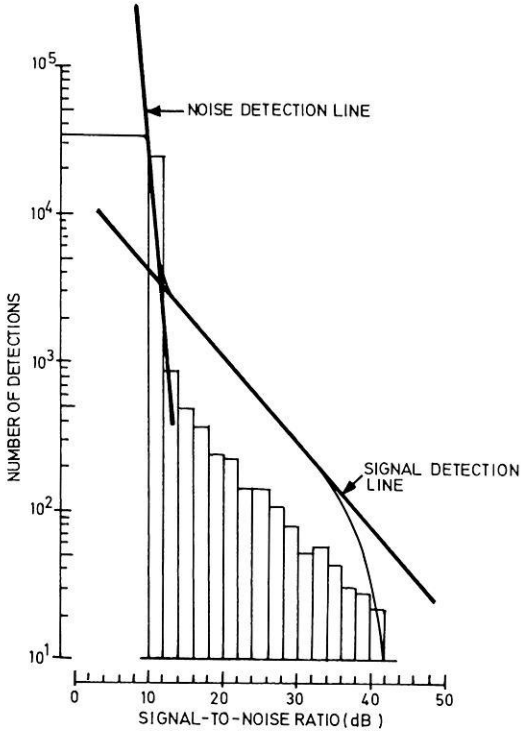

Fig. 7. Incremental and cumulative distribution of number of detections as a function of SNR. The data is from the time period July-December 1972. (After Bungum and Ringdal 1974)

i.e., the total number of acceptable false alarms within an interval T, is the same for the two threshold settings considered.

The number of signal detections N_{fix} and N_{fl} for fixed and floating threshold values in the interval T can be estimated from Eqs. (A1) and (A2). For fixed threshold values we have:

$$N_{\text{fix}} = N_{\text{tot}}^k \left(\int_0^T 10^{a_s(t)}\, dt \right) \left(\int_0^T 10^{a_n(t)}\, dt \right)^{-k} \quad k = b_s/b_n \tag{A3}$$

and for floating threshold values:

$$N_{\text{fl}} = \left(\frac{N_{\text{tot}}}{T} \right)^k \cdot \int_0^T 10^{a_s(t) - k \cdot a_n(t)} dt \tag{A4}$$

If N_s and N_n were known for a certain fixed threshold, the functions a_s and a_n can be estimated from (A1) and (A3). From (A3) and (A4), we get

$$N_{\text{fix}} = N_{\text{tot}}^k \left(\int_0^T N_s(t)\, dt \right) \cdot \left(\int_0^T N_n(t)\, dt \right)^{-k} \tag{A5}$$

$$N_{\mathrm{fl}} = \left(\frac{N_{\mathrm{tot}}}{T}\right)^{k} \cdot \int_{0}^{T} N_s(t)\, N_n(t)^{-k}\, dt \tag{A6}$$

Considering N_s and N_n as discrete functions of time, and choosing the number of false alarm rate samples in the time interval T equal to M we may write:

$$R = \frac{N_{\mathrm{fl}}}{N_{\mathrm{fix}}} = \frac{\sum_{i=1}^{M} (N_{si} N_{ni}{}^{-k}) \left(\sum_{i=1}^{M} N_{ni}\right)^{k}}{M^{k} \sum_{i=1}^{M} N_{si}} \tag{A7}$$

Note that only the relative variation of N_s and N_n with time must be known, as any constant multiplication factor from Eqs. (A5) and (A6) will vanish in Eq. (A7). For this reason, when estimating the N_s and N_n functions, it is not necessary to refer to the same threshold.

References

Bungum, H., Husebye, E. S., Ringdal, F.: The NORSAR array and preliminary results of data analysis. Geophys. J. *25*, 115–126, 1971

Bungum, H., Husebye, E. S.: Analysis of the operational capabilities for detection and location of seismic events at NORSAR. Bull. Seism. Soc. Am. *64*, 637–656, 1974

Bungum, H., Ringdal, F.: Diurnal variation of seismic noise and its effect on detectability. NORSAR Scientific Report No. 5–73/74, NTNF/NORSAR, Kjeller, Norway, 1974

Cartwright, D. E., Longuet-Higgins, M. S.: The statistical distribution of the maxima of a random function. Proc. Roy. Soc. (London) Ser. A. *237*, 212–232, 1956

Davies, D.: Nocturnal earthquakes. Geophys. J. *28*, 305, 1972

Flinn, E. A., Blandford, R. R., Mack, H.: Comments on 'Evidence for higher seismic activity during the night', by Michael Shimshoni. Geophys. J. *28*, 307–309, 1972

Helstrom, C. W.: Statistical theory of signal detection. Oxford: Pergamon Press 1968

Knopoff, L., Gardner, J. K.: Higher seismic activity during local night on the raw worldwide earthquake catalogue. Geophys. J. *28*, 311–313, 1972

Lacoss, R. T.: Variation of false alarm rates at NORSAR. Semiannual Technical Summary. Seismic Discrimination, M.I.T. Lincoln Lab, Mass. Inst. of Tech., Cambridge, Mass., June 1972, 53–57, 1972

Rice, S. O.: Mathematical analysis of random noise. Bell System Tech. J., *23*, 282–332, 1944

Shimshoni, M.: Evidence for higher seismic activity during the night. Geophys. J. *24*, 97–99, 1971

Shimshoni, M.: Response to comments by Davies, by Flinn *et al.* and by Knopoff *et al.* on the 'Evidence for higher seismic activity during the night'. Geophys. J. *28*, 315, 1972

Ole Steinert
Eystein S. Husebye
Håvar Gjøystdal
NTNF/NORSAR
Post Box 51
N-2007 Kjeller, Norway

J. Geophys. 41, 303–310, 1975

An Electronic Filter and Damping System for the Askania Borehole Tiltmeter

D. Flach and W. Große-Brauckmann

Institut für Geophysik der Technischen Universität Clausthal

Received June 25, 1974; Revised Version January 23, 1975

Abstract. A Butterworth-Bessel low-pass filter is described which filters the output signal of the Askania borehole tiltmeter. The frequency and time-domain properties of the filter characteristics have been adapted optimally for using the tiltmeter as an earth tide recording instrument. Furthermore, a damping system of the instrument is described. This device prevents the linear range of the electronic recording system from being exceeded under extreme conditions, e.g. strong microseisms. Due to the improvements achieved the accuracy of the records has been raised substantially.

Key words: Tilt and Solid Earth Tidal Measurements – Borehole Tiltmeter – Vertical Pendulum – Electronic Filters.

1. Introduction

The Askania borehole tiltmeter (vertical pendulum) is an instrument which is suitable for recording low-frequency tilts and horizontal accelerations. For the reduction of surface influences, especially meteorological effects, it is installed in 30 m deep boreholes (Flach and Rosenbach, 1971). In common with nearly all recordings of geophysical data, the problem has to be considered that the atcual signal, e.g. tides, is accompanied by undesirable noise, e.g. microseisms. If the noise covers another frequency range than the signal its separation and elimination is practicable. In the present case low-pass filtering must be used, since the noise frequencies (microseisms, natural period of the pendulum) are much higher than the signal frequencies (tides). Originally a passive two-pole low-pass filter has been used by the manufacturer. But for the following reasons, this type of filter does not meet the requirements based on the present state of electronics:

1. Passive low-pass filters with very low cutoff frequencies of 4×10^{-4} Hz can technically only be realized with electrolytic capacitors depending to a high degree on time, temperature and input voltage. Furthermore, passive networks are not independent of load.

2. The step response of such a filter is very poor because of the high time lag of 40 min. This property particularly causes problems of the transfer of the calibration pulse (Flach, Jentzsch, Rosenbach and Wilhelm, 1971).

An active filtering and damping system will be described in the following. In the case of tidal recordings it mainly filters the noise (microseisms, natural period of the pendulum) superimposed on the signal and is optimally adjusted to the conditions at the station Zellerfeld-Mühlenhöhe (51.82 °N, 10.34 °E).

2. *Specifications of the Filter*

The signal generated by the recording system of the tiltmeter contains frequencies between 0 Hz and the natural frequency of the pendulum (0.7 Hz). Above the tidal frequencies it mainly consists of the frequencies of the oceanic microseisms (0.15—0.25 Hz) and the natural frequency of the measuring pendulum (0.7 Hz). The maximum amplitude of the microseisms at the station Zellerfeld-Mühlenhöhe is about 30 mV_{pp} at 0.15 Hz, corresponding to the 1.5-fold tidal maximum amplitude.

A suitable low-pass filter has to attenuate the amplitudes of the microseisms in such a way, that they do not appear in the tidal records any longer. In order to be sure that the microseisms under no circumstances affect the recordings a damping of —80 dB is necessary. Such an attenuation can be realized by filters of different constructions and specifications. The following conditions should however be complied with as far as possible.

(a) flat amplitude response in the band-pass of the filter,

(b) high attenuation beyond the cutoff frequency,

(c) small phase shift at tidal frequencies,

(d) good step response properties,

(e) high input impedance, low output impedance,

(f) simple design,

(g) good possibility of realization with regard to the properties of the construction elements.

From these conditions it follows that only active filters are in consideration, since (e) and (d) require the use of amplifiers.

2.1. Choice of Filter Type

Active filters allow complicated amplitude and phase responses which are optimally designed with regard to different aspects (Tietze and Schenk, 1971). The most important filter types are Butterworth, Bessel and Teschebyscheff. Conditions (a), (b) and (c), for example, are very well met by a Butterworth filter, while for condition (d) the Bessel filter is particularly suitable. Conditions (e), (f) and (g) apply to all active filters in like manner and are of no importance in selecting the type of filter.

A Butterworth filter however is ruled out for filtering the signal in question because of its disadvantageous step response.

During the calibration of the tiltmeter by the ball calibration method, square wave impulses are superimposed on the tidal signal. These are due to the shift of a small ball inside the measuring pendulum by an exactly defined amount (Jacoby, 1966). As the accuracy of the calibration strongly depends on the number of calibration pulses in a fixed time interval (Flach, Jentzsch, Rosenbach and Wilhelm, 1971), it is desirable to carry out the calibration pulses as quickly as possible (Große-Brauckmann, 1973). As a fast step response allows more calibration cycles in a fixed time interval a Butterworth-Bessel low-pass filter was chosen. This is a compromise between the good amplitude response of the Butterworth filter and the advantageous step response of the Bessel filter. The poles of such a filter are located in the complex frequency plane between those of the Butterworth and Bessel filters (Al Nasser, 1972).

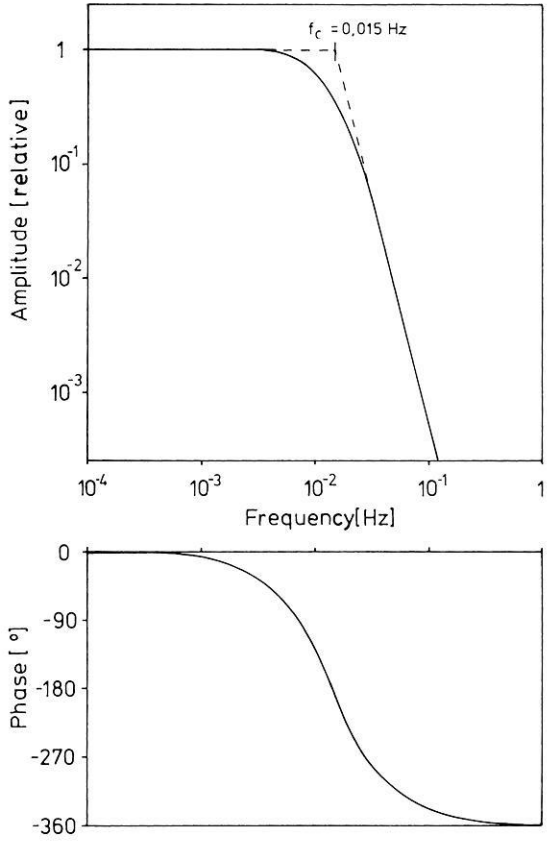

Fig. 1. Frequency response of the four-pole Butterworth-Bessel low-pass filter (amplitude above, phase below). Cutoff frequency 0.015 Hz

For the required damping of —80 dB at 0.15 Hz a four-pole Butterworth-Bessel low-pass was chosen. The number of poles n of a filter determines the attenuation of the gain m^+ beyond the cutoff frequency f_c according to

$$m^+ = -n\ 20\ \text{dB/decade for}\ f > f_c \tag{1}$$

The less the number of poles of the filter, the lower must be its cutoff frequency to achieve the same attenuation at a fixed frequency.

A four-pole filter is constructed by using 2 two-pole filter elements in series. The capacitances and resistances can easily be calculated by the aid of tables (Al Nasser, 1972).

2.2. Characteristics of the Filter

In case of high resistance signal sources it is advisable to connect the filter with a differential amplifier in series, since otherwise the output resistance of the signal source is added to the input resistance of the filter circuit and the filter characteristic

will be changed. Furthermore, with the amplifier in series an additional gain can easily be obtained. A further advantage of the differential amplifier is the suppression of common mode noise which is capacitively superimposed on circuits.

A graph of the amplitude and phase responses is given in Fig. 1.

The step response of the filter shows an overshoot of 3%. After 130 sec the deviation from full deflection lies within 0.1%.

2.3. Test of the Filter

A critical point of active filters is the constancy of zero setting of the output voltage depending on the offset voltage drift of the operational amplifiers used in filter circuits. In Table 1 all data of the filter are given with regard to the drift and noise properties of the operational amplifiers.

Table 1. Drift and noise properties of the filter

Zero drift (dependent on time)	Zero drift (dependent on temperature)	Noise (0.001–10 Hz
4 μV / day	2 μV / degree centigrade	1 μV_{pp}

As 1 bit of the digital recording system represents a voltage of 50 μV, it is obvious that these values do not affect the accuracy of the records. The increase of the zero drift is non-linear in time. After x days the total drift is about $\sqrt{x}$ times the drift per day. This dependence was empirically derived from long-term measurements (Analog Devices, 1971).

Fig. 2 shows a record of 2 days. For a better control two identical filters have been connected in parallel with the same channel of the borehole tiltmeter. These have now been operating successfully for more than 18 months. Besides tidal waves surface waves of a distant earthquake can be recognized in the record. As these waves can have periods of some 100 sec and very large amplitudes, they are not suppressed by the low-pass filters.

3. Damping of the Pendulum by an Electronic Feedback System

3.1. Mechanical Properties of the Pendulum

Examinations of the mechanical behaviour of the Askania borehole tiltmeter revealed a very small damping of the pendulum, the damping factor being about 0.01. Strong microseisms in the frequency range of the pendulum's natural frequency of 0.7 Hz result in resonant oscillations and therefore the unfiltered signal shows very large amplitudes. In extreme cases the amplitudes may exceed the linear amplification range of the recording system. Then the integration of the falsified signal by the lowpass filter yields a measuring signal which is distorted considerably without any possibility of recognizing this distortion afterwards.

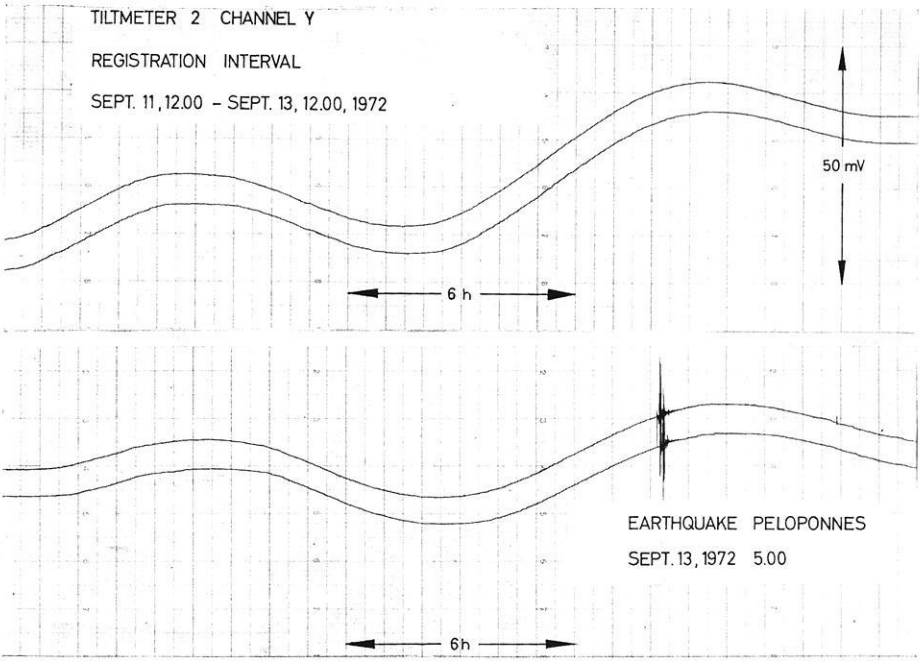

Fig. 2. Original record of 2 days; synchronous filtering of the same signal component with two identical filters in parallel.
Time shift of the traces due to the pen position of the recorder: 3 min
Continuous record from 11 Sept, 1972 / 12 00 EMT to 13 Sept., 1972 / 12 00 EMT

Short-time accelerations which may occur in seismic areas are able to overexcite the undamped measuring system as well. However, it is very important to get correct recordings during and immediately after earthquakes in order to detect possible sudden tilts of the earth's crust due to the earthquake mechanism.

The reasons mentioned above speak for a stronger damping of the pendulum. Two methods of damping can be considered:

mechanical damping by dipping the pendulum in a viscous fluid,

damping by electronic feedback of the pendulum's movement.

Fluid damping has not been planned by the constructors of the tiltmeter and would only be realizable by fundamental alterations of the instrument.

3.2. Damping by Differentiating Feedback

Damping by electronic feedback can be achieved by translatory forces at the pendulum's lower end which are proportional, but with a phase shift of 180 , to the velocity of the pendulum. Such forces can be generated by the device provided for continuous calibration of the tiltmeter (Jacoby, 1966). This device consists of a small permanent magnet mounted on the pendulum's lower end and a Helmholtz coil attached to the pendulum carrier. A current through the coil creates a homogeneous magnetic field which produces a certain force upon the pendulum. The strength of the magnetic field and consequently the deflection of the pendulum is proportional

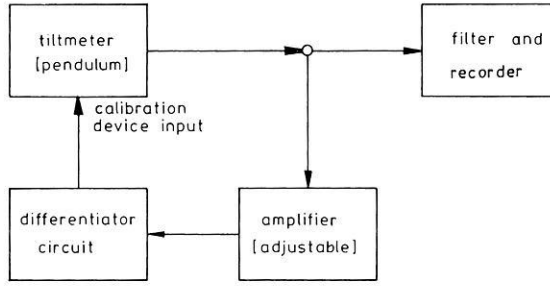

Fig. 3. Block diagram of the complete damping system

to the current in the coil. By the aid of a suitable feedback circuit and the calibration device just described a damping system was built which makes possible damping factors up to $\alpha \approx 1$ without any reconstruction of the tiltmeter.

The output voltage of the recording system is proportional to the angular deflection of the pendulum. A signal corresponding to the velocity of the pendulum can be obtained by differentiating this voltage with respect to time. The operation d/dt is achieved by an electronical differentiator, which contains operational amplifiers for the improvement of the differentiating properties of this circuit. In order to adjust the gain of the feedback system G_F a preamplifier is connected in series with the differentiator circuit. A block diagram of the complete damping system is shown in Fig. 3.

The feedback is applied to both components X and Y of the pendulum's movements in order to achieve a total damping of the tiltmeter.

3.3. Samples of Results

Investigations of the pendulum showed that by the aid of the feedback circuit damping coefficients up to $\alpha = 1$ can be realized depending on the gain G_F of the feedback voltage. As the gain of the differentiator decreases at low frequencies by -20 dB/dec G_F is always related to 1 Hz. The relation between the damping coefficient and G_F is linear but the mechanical damping α_M of the pendulum has to be added to the damping by feedback, i.e.

$$\alpha = \alpha_F + \alpha_M \tag{2}$$

with $\alpha_F = D\, G_F \qquad D = \text{const} = 0.031$

and $\alpha_M = 0.01$

In practice it is most advantageous to use gains of $G_F \approx 23$ dB which result in a damping coefficient of $\alpha = 0.5$ so that at 0.7 Hz the resonant increase of the pendulum's amplitude is about 1.15 (compared with a resonant increase of 55 of the undamped pendulum). An undesired heating of the Helmholtz coils is largely avoided in this case. The loss of heat is about 10 μW as an average while the preamplifiers of the capacitive transducer system have a power loss of 60 mW. These values demonstrate the small contribution of the feedback system to the total power loss.

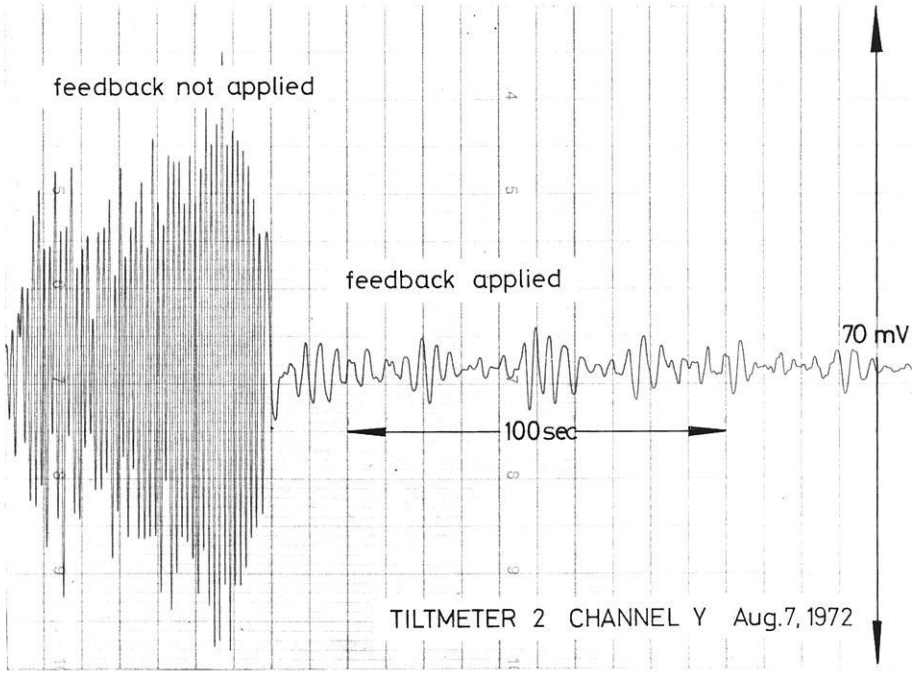

Fig. 4. Unfiltered signal without and with damping of the measuring pendulum

If the feedback voltage is increased very much, i.e. the gain G_F at 1 Hz is higher than 30 dB, resonant rises of the pendulum appear. They are caused by the non-ideal features of the differentiator circuit and a certain amount of cross coupling between both components.

In Fig. 4 the effect of the damping system is shown by means of an original record of the unfiltered signal. Without feedback the signal contains amplitudes up to 70 mV_{pp} mainly caused by the natural oscillations of the pendulum. After the damping device has been applied, the amplitudes are greatly reduced to about 10 mV_{pp}.

The influence of the damping system on tidal amplitudes is very small. Due to the small gain of the differentiator circuit at tidal frequencies (—93 dB compared with the gain at 1 Hz) this influence is less than 0.005% of the maximum semidiurnal tides at the station Zellerfeld-Mühlenhöhe.

A long-term record of the constancy of the zero setting of the damping circuit revealed a drift of 14 μV in 16 days. Such a direct voltage is superimposed on the feedback voltage and causes a deflection of the pendulum of 0.006% of the maximum tides. Thus a serious effect of this drift on the long-term stability of the tiltmeter can be excluded.

4. *Conclusions*

By means of modern operational amplifiers it is possible to construct active filters which are substantially superior to the passive filters originally used by the manufacturer of the Askania borehole tiltmeter. This superiority covers the frequency response as well as the long-term and temperature stability.

Furthermore, the Butterworth-Bessel filters with a cutoff frequency $f_c = 0.015$ Hz especially reconciled with the requirements of the recording system of the Askania borehole tiltmeter enable a more accurate performance of the ball calibration (Große-Brauckmann, 1973).

The electronic damping device makes it possible to operate the tiltmeter even in regions of strong microseisms since it prevents resonant oscillations which could exceed the linear range of the recording system. By a special design of the differentiator circuit of the damping device an undesirable heating of the Helmholtz coils due to high-frequency influences is avoided. The damping device has no significant effect on tidal recordings.

Acknowledgement. We wish to thank Prof. Dr.-Ing. Rosenbach for the encouragement to our work. Furthermore, we are grateful to the German Research Society (Deutsche Forschungsgemeinschaft) for the financial support of the measurements with the Askania borehole tiltmeter.

References

Al-Nasser. F : Tables shorten design time for active filters. Electronics *23*, 113–118, 1972

Analog Devices: Long-term drift measurements on op amps. Analog Dialogue *5*, 13, 1971

Flach, D., Jentzsch, G., Rosenbach, O., Wilhelm, H.: Ball-calibration of the Askania borehole tiltmeter (Earth tide pendulum). Z. Geophys. *38*, 1005–1011, 1971

Flach, D., Rosenbach, O.: Der Askania Bohrloch-Neigungsmesser (Gezeitenpendel) nach A. Graf auf der Test-Station Zellerfeld-Mühlenhöhe. Bull. Inform. Marèes Terrestres *60*, 2934–2943, 1971

Große-Brauckmann, W.: High precision ball calibration of the Askania borehole tiltmeter (Earth tide pendulum). 7th Int. Symp. on Earth Tides, Sopron (Hungary) 1973

Jacoby, H.-D.: Das neue Bohrloch-Gezeitenpendel nach Graf. Askania Warte *67*, 12–17, 1966

Tietze, U., Schenk, C.: Halbleiter-Schaltungstechnik. Berlin-Heidelberg-New York: Springer 1971

Dr. D. Flach
Dipl.-Geophys. W. Große-Brauckmann
Institut für Geophysik der Technischen
Universität Clausthal
D-3392 Clausthal-Zellerfeld
Adolf-Römer-Straße 2A
Federal Republic of Germany

J. Geophys. 41, 311—319, 1975

Two-Dimensional Magnetotelluric Model Calculations for Overhanging, High-Resistivity Structures *

W. Losecke and W. Müller

Bundesanstalt für Geowissenschaften und Rohstoffe, Hannover

Received September 9, 1974; Revised Version January 7, 1975

Abstract. Apparent resistivitiy and phase curves across the profiles of highly resistive overhanging and non-overhanging theoretical two-dimensional models as they may be realized by salt domes, mushroom-shaped intrusions etc. are compared with each other. The finite difference approach with a grid of about 8000 points allowed a very fine contouring of the structures' boundaries. The influence of rough and fine contouring is investigated. For the presented models the surface values of the overhanging structure are very different from those of the non-overhanging one if the resistivity of the structure is not of the same order of magnitude as the surrounding layers or if the basement is not too thick. In such cases fine contouring should be applied.

Key words: Finite Difference Method – Grid Spacing – Two-Dimensional Modelling – Salt Domes – Overhanging Structures – Resolving Power of Magnetotellurics.

Introduction

The determination of boundary surfaces of large scale geological structures or bodies is one important aim of applied geophysics. Of special interest are structures of the overhanging type such as mushroom-shaped intrusions, salt domes, overthrusts, overturned folds etc. The more complicate a structure is the more geophysical methods we generally need in order to obtain a good approximation of its shape. Thus, from the point of view of the theoretical geophysicist it is well worth to ask what magnetotellurics could probably contribute to the solution of such problems.

In 1972 magnetotelluric measurements were carried out across a longitudinal salt dome in the North German basin (Losecke, 1972). The apparent resistivities were represented in pseudo cross sections. The shape of the isolines was a clearly recognizable non-linear image of the contours of the salt dome's cross section. This result gave rise to calculations of the magnetotelluric field across certain theoretical two-dimensional geometries which in practice may be realized more or less by geological structures of the types mentioned above.

The governing aim was to get some ideas on the resolving power of magnetotellurics especially if we compare an overhanging structure to a non-overhanging one. It is the question which effects we have to expect if a measurement shall be carried

* Paper read at the 2nd Workshop on Electromagnetic Induction in the Earth, Ottawa, August 1974.

out across one of those structures. This includes the problem of how good a geological boundary has to be mathematically approximated in order not to introduce effects due to mathematical errors.

Apart from some modifications the numerical treatment of the present work is applied as proposed by Neves (1957) or Jones and Pascoe (1971). Boundaries between areas of different conductivity follow grid lines; thus, a complicate shape is approximated by a rectangular step curve. The quality of this approximation depends on the number of grid points; the more grid points, the better a boundary may be represented. Moreover, increasing the number of grid points improves accuracy when solving the differential equation. Thus, refining of the grid permits a refined contouring of the two-dimensional structure. When keeping the number of grid points constant it is possible to calculate effects on surface field values which are only due to differences between rough and fine contouring. In other words, we obtain statements on the resolving power of magnetotellurics in the two-dimensional case which allow a decision whether at all or to what degree refining is necessary.

Model Results

For all models the number of grid points was kept constant to 7200 for H-polarization and 8600 for E-polarization. Grids of such a size need a lot of computer time and their field values tend to instability. Therefore, three special acceleration techniques had to be applied. First the fine contoured model was roughly approximated by a pre-model with larger grid spacings and the well iterated field matrix of this pre-model was then spread out over the fine grid. So the iterations of the fine model started with good initial field values. Secondly successive over-relaxation as described by Smith (1965) was used with overrelaxation factors up to 1.9. Thirdly the field values obtained for one period in a special manner were used for initializing the next case with a new period not too different from the previous one. Calculations were carried out on a CDC-CYBER 76—14.

The main model for which computation was done is a fine-contoured, overhanging, 1000 Ohm · m perturbation contained in "sedimentary" rock of 10 Ohm · m resistivity (model A, Fig. 1). Its cross section has an extent of about 2.6 km in the vertical and 2 km in the horizontal direction. It is underlain by a 37 km thick layer of high resistivity basement. This model only is a mathematical one to study its magnetotelluric effects but not a representation of a really existing geological structure. On the other hand, the model parameters are chosen as for models which really could exist. The grid spacing increases with increasing depth and towards the external boundaries. The smallest grid spacing is 50 m and it is kept constant within and near the perturbation (between 12.9 km and 16.5 km on the horizontal scale and up to a depth of 3.4 km).

In order to analyse effects caused by contour differences only, we have to avoid effects which could be introduced by a grid spacing which is too large. Neves (1957) derived from calculations over an uniform earth an actual error of 0.6% when comparing differential with finite difference solution obtained by a grid spacing of $^1/_4$ of the skin depth. In order not to exceed this error the grid spacing must fall below this limit. Our calculations were carried out in a period range of 1 to 1000 sec. For the most disadvantageous conditions $\varrho = 10$ Ohm · m and $T = 1$ sec, the skin

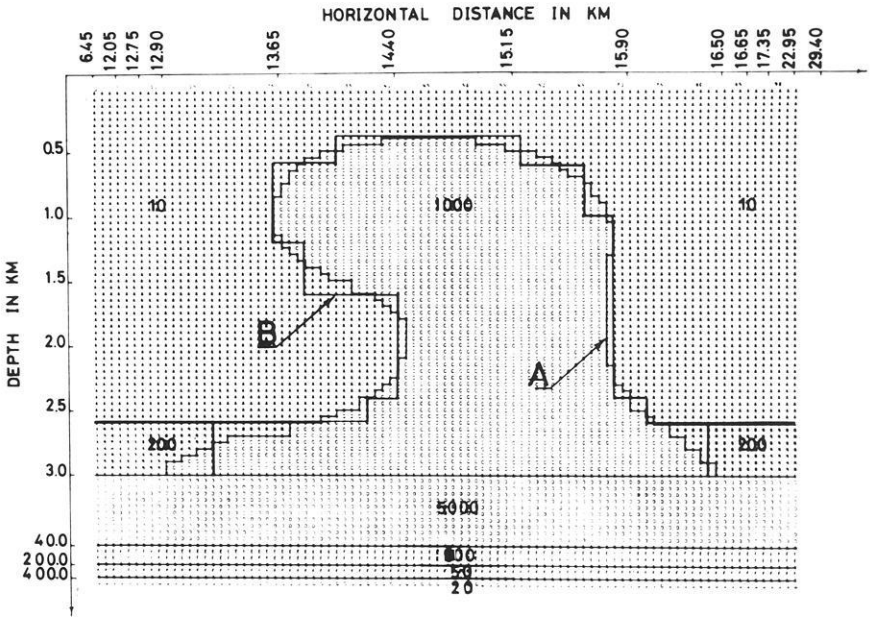

Fig. 1. Vertical cross section of two-dimensional models A and B (resistivity in Ohm · m)

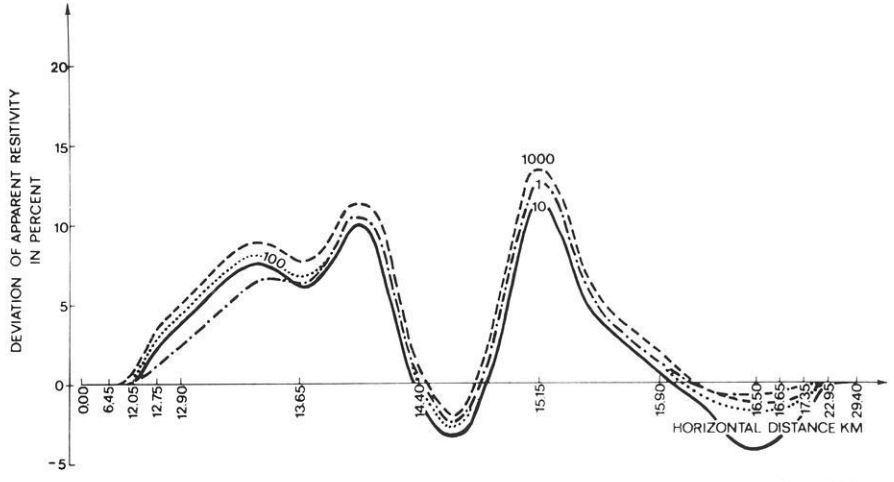

Fig. 2. Deviation of apparent resistivity of model B compared to model A for different periods across profile (H-polarization, the numbers indicate the period in seconds)

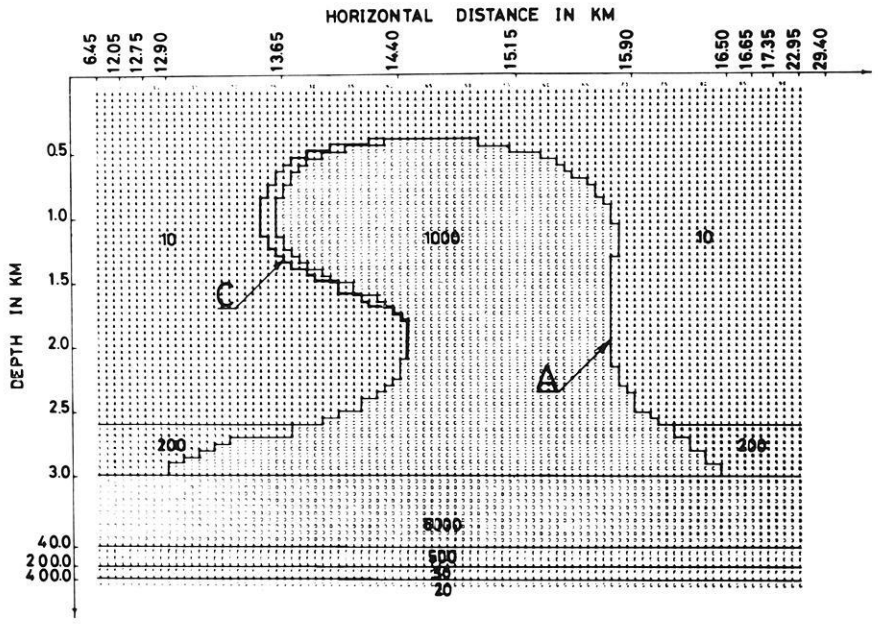

Fig. 3. Vertical cross section of two-dimensional models A and C (resistivity in Ohm · m)

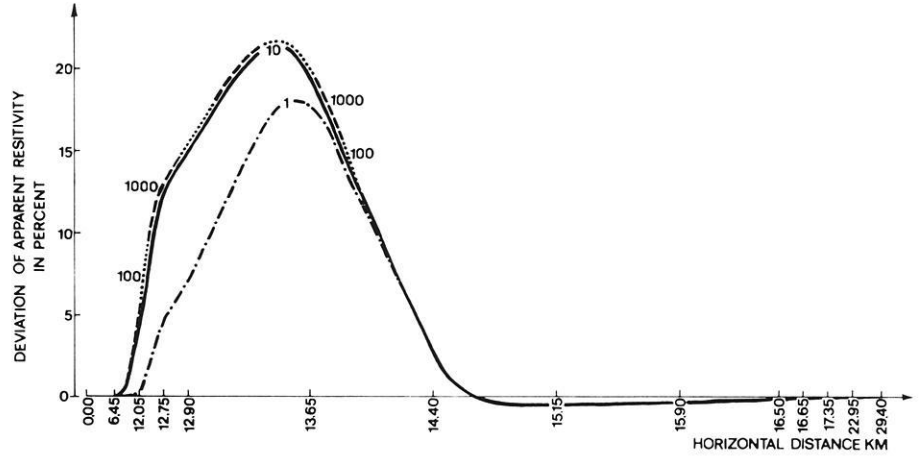

Fig. 4. Deviation of apparent resistivity of model C compared to model A for different periods across profile (H-polarization, the numbers indicate the period in seconds)

depth is about 1.6k m and therefore, the maximum grid size as proposed by Neves is 400 m. For two-dimensional structures this limit might not be small enough but the 50 m ($^1/_{32}$ skin depth) grid spacing of the fine-contouring is so far from this limit that it should guarantee a good accuracy.

Model B in Fig. 1 corresponds to model A but it is more roughly contoured though it is based on the same grid. Both the models were iterated for the periods 1, 10, 100 and 1000 sec for H- and E-polarization and the surface values of apparent resistivity and phase were calculated. Moreover, the relative deviation of apparent resistivity between the two models $((\varrho_\alpha(A)-\varrho_\alpha(B))/\varrho_\alpha(A))$ was computed for each surface point. The maximum deviation for H-polarization is about 13.5% (Fig. 2), whereas for E-polarization it is only 2%, too low to warrant a figure. This smaller rate was to be expected because of the continuity of the apparent resistivity when crossing a vertical boundary. If the resistivity of the perturbation is increased from 1000 to 10.000 Ohm · m, the maximum deviation in the case of H-polarization becomes about 17%. Consequently, it is clear that, in the present case, the H-polarization values react noticably to slight modification of the contours.

In order to obtain further information on the resolving power of H-polarization, calculations for the models shown in Fig. 3 were carried out. Model C is the result of a shifting of the overhanging part of model A by 100 m. The relative deviation of surface values for the above mentioned four periods is given in Fig. 4. The maximum deviation reaches 22% and is located almost exactly above the shifted boundaries. If the resistivity of the structure is assumed to be 10.000 Ohm · m the maximum deviation turns out to be nearly the same. We may conclude that rather small translations of vertical boundaries have considerable effect even if they are overlain by a low resistivity layer. Regarding d'Erceville and Kunetz's (1962) calculations on a fault, this effect is not surprising. Since in our case it is due to only 100 m of translation, it would not have been recognized with a grid spacing larger than 100 m.

The sensitivity of surface values to differences in contour was the reason for comparing apparent resistivities of the far overhanging structure E (Fig. 5) with those of the non-overhanging structure D. Calculations were executed for perturbation resistivities of 10.000, 1000 and 100 Ohm · m. For 10.000 Ohm · m the maximum deviation is less than 2% in H-polarization and 14% in E-polarization. For 1000 Ohm · m the results are presented in Fig. 6 and Fig. 7. If the resistivity is decreased to 100 Ohm · m, maximum deviation is about 14% for E-polarization and 60% for H-polarization. Though the perturbation of 100 Ohm · m has the smallest resistivity contrast with the surrounding "sediments", the surface apparent resistivity deviation of 60% shows the greatest effect. This result seems to be explainable when we note that the rather thick 5000 Ohm · m basement and the relatively thin and small 1000 or 10.000 Ohm · m perturbation have resistivities of the same order of magnitude. If we modify the boundaries, the effect on the surface values remains small. However, if we use 100 Ohm · m for the perturbation, this resistivity differs by at least one order of magnitude from the resistivities of both the basement and the surrounding "sediments". Consequently, a modified contour may cause a larger deviation of the surface values.

The deviation of phase differences between surface electric and magnetic fields were calculated for all models but they react only slightly to changes in contour.

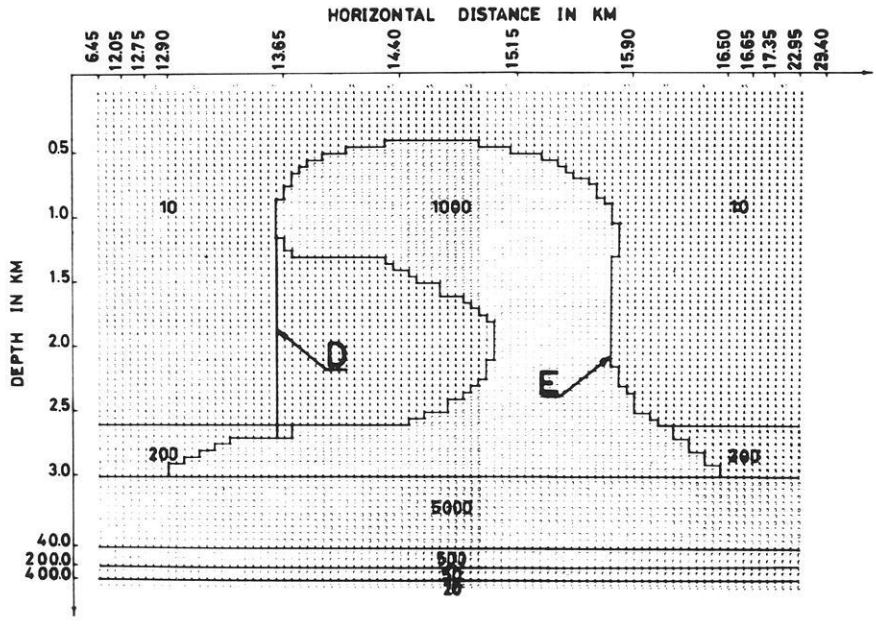

Fig. 5. Vertical cross section of two-dimensional models D and E (resistivity in Ohm · m)

For model A with a perturbation resistivity of 1000 Ohm · m, apparent resistivity and phase curves for 16 periods in the range 1 to 1000 sec in both the modes were calculated at each surface point of the profile. By means of the results the pseudo cross sections of apparent resistivity similar to those from Losecke (1972) were drawn in Fig. 8 and 9. In this case the asymmetric shape of the model is not or only slightly indicated by an asymmetric shape of the isolines for reasons given above, i.e. the dimensions of the basement and the comparatively small difference between the basements and the perturbations resistivities.

Conclusions

The influence of two-dimensional contouring on the surface values of apparent resistivity has been investigated. General statements on the effects of an arbitrary two-dimensional model cannot be given because they depend too much on the shapes and resistivities of the surrounding layers, but from the model results we may conclude:

1. Fine contouring, i.e. using a grid spacing much smaller than $^1/_4$ of a skin depth should be applied in cases where the "basement" layer either is not too thick compared to the height of the perturbation or the perturbation's resistivity is not of the same order of magnitude as the surrounding layers. Apart from that, fine contouring in every case improves the accuracy.

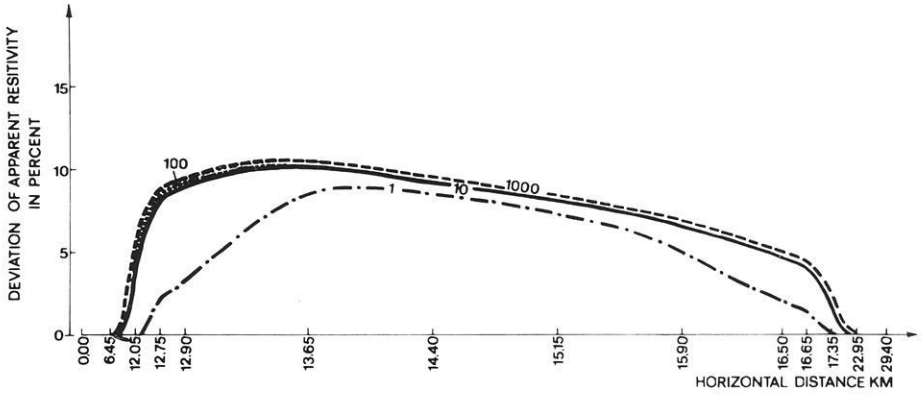

Fig. 6. Deviation of apparent resistivity of model E compared to model D for different periods across profile (H-polarization, the numbers indicate the period in seconds)

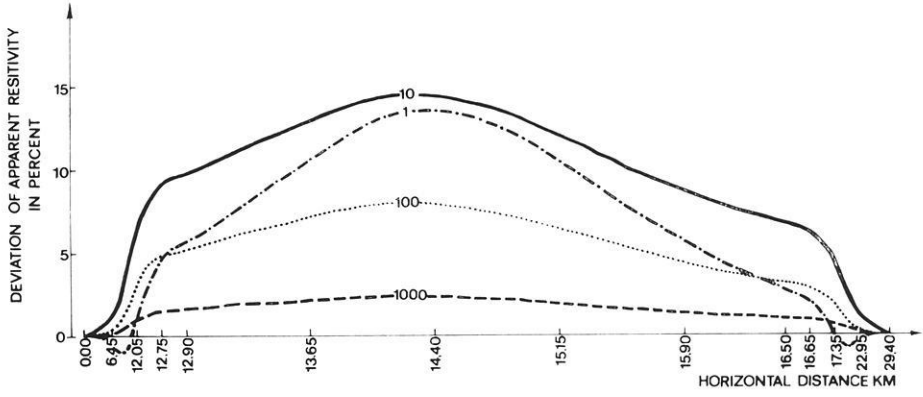

Fig. 7. Deviation of apparent resistivity of model E compared to model D for different periods across profile (E-polarization, the numbers indicate the period in seconds)

2. For cases given under 1. the calculated surface values of an overhanging structure of the modelled type are clearly distinguishable from a non-overhanging one (60% deviation). The question whether or not quite another configuration could produce the same surface values is not subject of the present papre.

3. From the figures we see that the surface effects caused by contour differences are not sharply localized to the area of the modified contour but spread out more or less along the profile. The best localized effects can be expected if a vertical part of a boundary is shifted (Fig. 3).

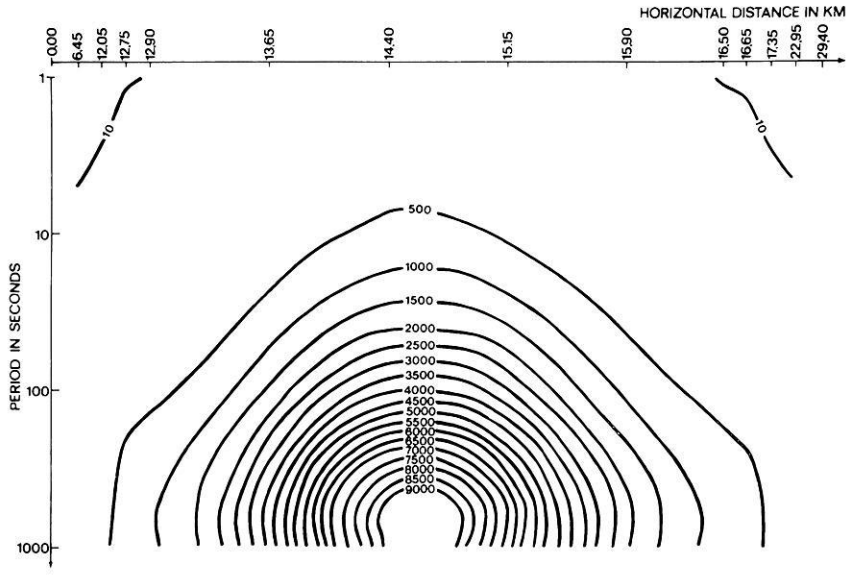

Fig. 8. Magnetotelluric pseudo cross section of model A (H-polarization), isolines of apparent resistivity (numbers in Ohm · m)

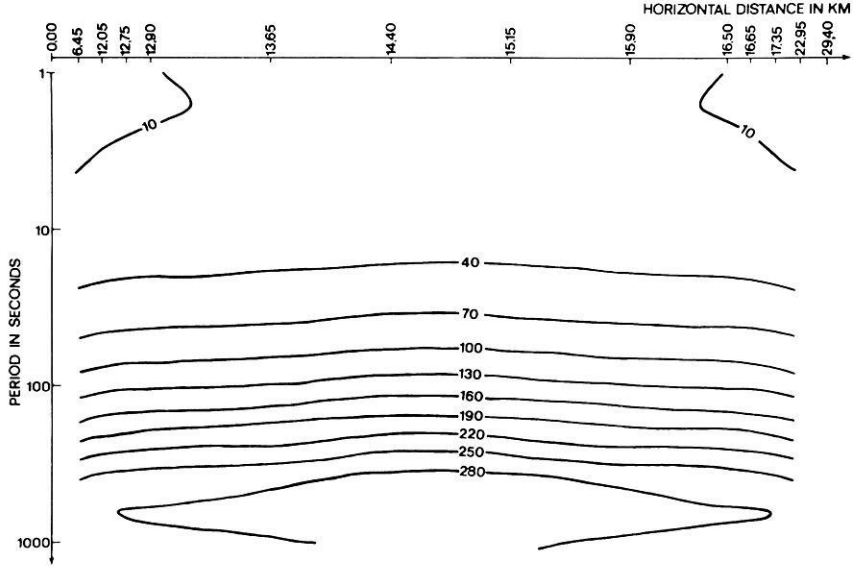

Fig. 9. Magnetotelluric pseudo cross section of model A (E-polarization), isolines of apparent resistivity (numbers in Ohm · m)

References

D'Erceville, I., Kunetz, G.: The effect of a fault on the earth's natural electromagnetic field. Geophysics *27*, 651–665, 1962

Jones, F. W., Pascoe, L. J.: A general computer program to determine the perturbaton of alternating electric currents in a two-dimensional model of a region of uniform conductivity with an embedded inhomogeneity. Geophys. J. R. Astron. Soc. *23*, 3–30, 1971

Losecke, W.: On the determination of boundary surfaces of salt domes by the magnetotelluric method. Z. Geophys. *38*, 959–962, 1972

Neves, A. S.: The magnetotelluric method in two-dimensional structures. Ph. D. thesis, Dept. of Geology and Geophysics, M. I. T., Cambridge, Mass., 1957

Smith, G. D.: Numerical solution of partial differential equations. London, U. K.: Oxford University Press 1965

Dr. W. Losecke
Dipl. Phys. W. Müller
Bundesanstalt für Geowissenschaften
und Rohstoffe
D-3000 Hannover 23
Stilleweg 2
Federal Republic of Germany

J. Geophys. 41, 321–324, 1975

Short Communications

A New Type of Vertical Gravity Gradiometer

E. Groten

Technical University Darmstadt

Received August 14, 1974; Revised Version January 9, 1975

Key words: Gravimetry — Gradiometry — Vertical Gradient — Earth's Figure — Electronic Microbalance — Geophysical Prospecting.

Gravity gradiometry on moving platforms has found recent interest since airborne gravimetry failed to give satisfactory results. In contrast to such sophisticated instrumentation (Ames *et al.*, 1973) where mainly dynamical measuring principles are applied static measuring principles are well adapted to less sophisticated instruments which can be used for geophysical and geodetic field work at the earth's surface. The construction of such vertical gradiometers is an idea which has incited in vain the numerous attempts of physicists and technologists for more than a century. Since ten years high precision gravity meters which yielded relative accuracy of $\pm 10^{-9}$ or, in absolute terms, $\pm 10^{-9}$ g gave way to measuring vertical gravity differences so approximations for $\partial g/\partial h$ were available. Even though the ultimate limit of accuracy for static instruments seems to be of the order of $\pm 10^{-13}$ depending on Brownion motion and *stationary* gravimeters yield accuracy of better than $\pm 10^{-10}$ under favorable conditions gravimeter systems on *moving* platforms might have reached their ultimate accuracy in field work between $\pm 10^{-9}$ to $\pm 10^{-10}$ because of transportation drift and small jumps in the drift curve when the meter is clamped.

A previous attempt to use an electronic microbalance for vertical gradiometry failed mainly because of deficiencies of the read-out-systems at that time (Kibler, 1969). By the balance using the well known principle after Gast (for description see, e.g., (Gardner and Smith, 1972)) having an inductive read-out-system previous deficiencies have been overcome so that a highly sensitive vertical gradiometer based on this principle became available. A torsion tape suspension of the balance system together with zero reading instead of deflections measurements gives way to relatively high accuracy.

There are several advantages of such an ultramicrobalance system in comparison to spring balances like gravimeters where the measuring systems are directly affected by temperature effects etc.

Some details of the new gradiometer as well as the first experiments have been described in Groten (1974). In order to measure the gravity difference along the plumb line the balance is mounted on a steel rack (Fig. 1). A small mass ($\approx$20 grams) is suspended in an evacuated tube on a thin platinum iridium fiber at two different levels having a separation of about 80 or 30 centimeters. The weight difference corresponding to the difference in gravity along the plumb line is compensated by the

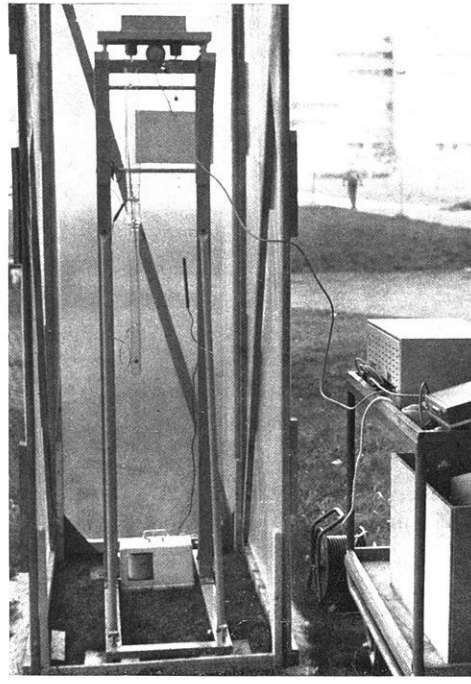

Fig. 1. Measuring system (after removal of insulating material, tube of evacuation etc.) with glass tubes, control box and additional electronics (strip chart recorder, digital voltmeter, additional filtering equipment etc.)

feed-back-system of the balance. The inductive read-out-system used for nulling the measuring system yields relative accuracy of the order of $\pm 10^{-9}$ when the temperature is kept constant within ± 0.01 °C which is easily achieved by modern thermistors and electric heating as used in gravimeters. In a well sealed or evacuated tube within a well insulated box variations of buyoancy, fiber length, volume of small masses (of gold etc.) etc. are negligible so that field work is feasible.

Perturbations by thermodiffusion as, e.g., the Knudsen effect, as well as corresponding disturbances are dodged whenever instead of perfect vacuum a constant slight air (or CO_2)-pressure exists in the tube. Absolute gradiometry is feasible when the weighted mass is determined with a relative accuracy of the order of $\pm 10^{-4}$ or $\pm 10^{-5}$. Relative gradiometry is feasible when the unknown mass is kept constant and the apparatus is calibrated against a laboratory instrument. As the vertical gravity gradient is of the order of

$$-0.31 \text{ mgal/m}$$

(where 1 mgal $= 10^{-3}$ cm/sec^2) measuring weight differences of about $\pm 10^{-7}$ grams yields the above mentioned accuracy in vertical gradients. Using the damping effect of the "not perfect" vacuum slight centrifugal and similar forces are checked by precise observations of the damped fiber-oscillations through a window in the tube. Presently available electronics do permit output of sufficient linearity for those measurements. Electrostatic perturbations are avoided by using metallic tubes instead of glass tubes. The shift of the mass from one level to the other is done auto-

matically by a fork-system. By recording the output of the balance for a time span of about 20 to 30 minutes random perturbations can be averaged out. Wind and other environmental effects can be dodged by setting up the apparatus in a tent. In general, the balance was found to behave in field work like a long-period seismograph. The whole electronics are operated by battery power so geodetic and geophysical field work in open air is indeed feasible. The time necessary for observing at one station is less than the time necessary for observing the horizontal gradients by torsion balances. Potentialities of balance gradiometers are within the 3 Eötvös accuracy or even better.

Moore and Farrell (1970) have described difficulties and improvement of a capacitance transducer used together with an electrostatic force transducer (Weber *et al.*, 1966, Block *et al.*, 1961) in a LaCoste and Romberg feed-back gravimeter where quadratic terms arise. With inductive read-out-system where the torque of a magnetic coil is used in the feed-back-system serious linearization problems do not arise. As the measured quantities do not depend on time the dynamic behavior is not of basic interest.

As the resonance frequency of the apparatus is outside of the main frequency range of microseism and since we are only interested in the zero frequency part the electronic read-out-system with low time constant does not imply any technical difficulties. The accuracy of the feed-back-system and of the electronic output is basicly a problem of costs; a relatively simple system yields ± 1 microgram. The inductive read-out-system where variation of output voltage is proportional to the weight difference and to the torque of the magnetic coil is consequently simpler than feed-back-systems having capacitance transducers with electrostatic forces (Weber *et al.*, 1966; Block *et al.*, 1966; Moore *et al.*, 1971) where quadratic terms are dominant as applied in gravimeters.

Mechanical vibrations imply one-sided centrifugal forces which are, however, less disturbing than was first anticipated. One sided electronic effects due to nonlinear output in case of large amplitudes were not found to be remarkable. Fig. 2 gives damped vibrations showing mainly mechanical one-sided effect where the mechanical part can be separated from any electronic one-sided disturbance. Fig. 3. shows the output as recorded on a strip chart recorder.

As the torque needed for "nulling" the measuring system is relatively small, temperature variations around the magnetic coil are not disturbing with quartz beam. Long term variations of the output as seen in Fig. 3 are partly correlated with temperature variations and partly (not fully explained) reversible features of the order of ± 0.5 μgrams.

The tape suspension used in the microbalance applied by us seems to be a reliable tool in field equipment. On the other hand, knife edge and similar supports which have long been considered as a primary error source in pendulum measurements have found partial rehabilitation by recent experiments (Graf, 1973). As the position of the knife edge does not vary much in case of feed-back measuring systems used in laboratories very high accuracy ($\pm 10^{-9}$) is now achieved with knife edge supported balances (Kochsiek, private communication).

Acknowledgement. Helpful suggestions by Dr. Thyssen-Bornemisza are appreciated. Thanks are due to Dr. Brein for reading the paper; H. Vahlbruch and H. Schaab assisted in doing the experiments.

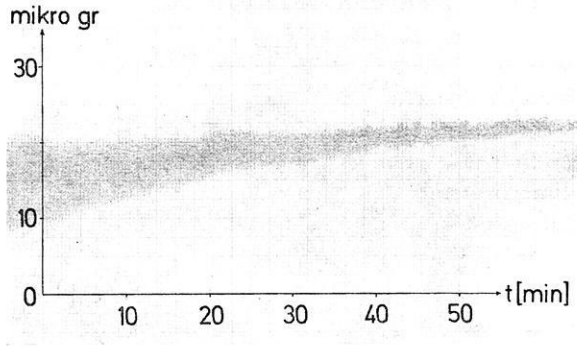

Fig. 2. One sided effect due to centrifugal force

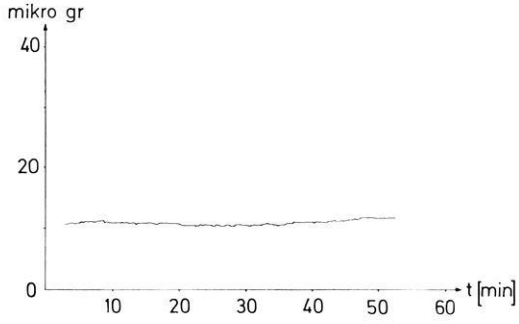

Fig. 3. Example of strip chart record

References

Ames, C. B., Forward, R. L., LaHue, P. M., Pettersson, R. W., Rouse, D. W.: Prototype moving base gravity gradiometer, AFCRL-73-TR-73-0141, P3961, Hughes Res. Lab. Malibu, 1973

Block, B., Moore, R. D.: Measurements in the earth mode frequency range by an electrostatic sensing and feedback gravimeter. J. Geophys. Res. *71*, 4361–4325, 1966

Gardner, W. E., Smith, T. F.: A Sartorius microbalance and superconducting magnet apparatus for the accurate measurement of magnetization and differential magnetization in high fields. In: T. Gast and E. Robens (eds.) Progress in vacuum microbalance techniques, pp. 155–180. London: Heyden 1972

Graf, A.: Messung der Schwingungszeit von Pendeln mit einer modernen Zeitmeßeinrichtung. Neues von Rohde & Schwarz *58*, 5–8, Dez./Jan. 1972/73

Groten, E.: Microgravimetry. Report presented at the meeting of the International Gravimetric Commission, Paris 1974

Kibler, K. G.: Techniques for gravity measurements, General Dynamics, Res. and Engn. Dept ERR-FW-969, 43 pp., Fort Worth, 1969

Moore, R. D., Farrell, W. E.: Linearization and calibration of electrostatically feedback gravity meters. J. Geophys. Res. *75*, 928–938, 1971

Weber, J., Carson, J. V.: Operation of LaCoste and Romberg gravimeter at sensitivity approaching the thermal fluctuation limits. J. Geophys. Res. *71*, 6005–6009, 1966

Prof. Dr.-Ing. E. Groten
Technische Hochschule, Fachbereich 12
Fachgebiet Astronomische Geodäsie und Satellitengeodäsie
D-6100 Darmstadt, Petersenstraße 13
Federal Republic of Germany

J. Geophys. 41, 325–327, 1975

Letters to the Editors

Comment on

Hydromagnetic Waves in a Non-Uniform Plasma by E. Kupfer

J. Geophys. *41*, 123–126, 1975

M. Siebert

Institut für Geophysik der Universität Göttingen

Received February 3, 1975

In a recently published paper Kupfer (1975) reconsiders the problem of geomagnetic pulsations with periods systematically depending on geomagnetic latitude. The existence of simultaneous pulsations showing this characteristic was first demonstrated by Voelker (1962, 1963, 1965). Subsequently other authors have described observations where the dominant pulsation period increases with increasing latitude (see e.g. Stuart and Usher, 1966; Münch, 1968; Miletits, 1971; Orr and Matthew, 1971; Rostoker and Samson, 1972; Zelwer and Morrison, 1972). The effect can be seen from a special class of pc 3–5 events and most distinctly from a pi 2-type of pulsations having the shape of a damped oscillation and appearing only in the daytime with an occurrence maximum about noon (Voelker, 1966, 1967). These comparatively rare events which, moreover, are found almost exclusively in the H-component, were named pulsation single effects (pse's). In my opinion their characteristic features are most typical for the effect under consideration.

In spite of the extreme simplifications of Kupfer's model I agree with the conclusion that a small δ-shaped spatial deviation of the undisturbed plasma density from an otherwise smooth distribution cannot explain the observed latitude dependence in terms of poloidal hydromagnetic oscillations. The reason for publishing this comment is that Kupfer's result is inconclusive without detailed discussion. At least the following annotations should be added:

1. Much of the difficulty of interpretation arises from the restriction to poloidal oscillation modes that are required by the predominant H-polarization of pulsations with latitude-dependent periods, unless very complex propagation conditions in the ionosphere are involved. It is this observed H-polarization that makes it impossible to apply the well known theory of magnetospheric oscillations by Dungey (1954) having predicted an equal effect, but for D-polarized pulsations only.

2. Insisting on the general conception that these pulsations are caused by poloidal field-aligned hydromagnetic oscillations, I was led to the idea of a partly lamellar structure of the magnetospheric plasma (Siebert, 1964, 1965). As a crude model this means that the plasma distribution is continuous along the field lines and

discontinuous in direction of their principal normals, i.e. between adjacent L-shells. The azimuthal behaviour of the plasma is of less importance here. This lamellar structure hinders the plasma of a region from oscillating as a whole with a uniform period; instead, eigenoscillations of non-interacting lamellae are possible and lead to an easy interpretation of the observational facts. When the rigorous assumption of lamellar discontinuities is replaced by that of small δ-shaped changes in the plasma density, the effect under consideration can no longer be explained. Thus, the result obtained by Kupfer supports the idea of separately oscillating lamellae.

3. There is no question that the model described above and used in this crude form because of its mathematical practicability, is not realistic. Actually, the term "discontinuity" must not be understood in a severe mathematical sense but rather as the appearance of steep gradients in the plasma density. While estimations yielded already ten years ago that such a magnetospheric structure is sufficiently stable when it comes to exist, there remained the open question whether it will exist at all. Since then, Chappell *et al.* (1971) and Bewersdorff and Sagalyn (1972) discovered a phenomenon which might correspond to the predicted lamellar structure. By analysing satellite data of the magnetospheric plasma density they found large spatial density fluctuations over very narrow L-ranges at or near the plasmapause. Especially Bewersdorff and Sagalyn report cases of multiple splitting of the plasmapause. The phenomenon is most pronounced when this outer boundary of the plasmasphere is situated in $2 < L < 3$ or about $L = 3$. Then, there are density changes of over an order of magnitude in less than 0.1 L. According to these results it can be taken for proved that the lamellar structure is an idealized but reasonable and physically admissible model to study the effect in a first approximation. Unfortunately, no observations of this kind are available as yet which could allow a direct comparison between satellite and ground-based records belonging together.

References

Bewersdorff, A. B., Sagalyn, R. C.: Spatial and temporal variations of the thermal plasma between 3000 and 5000 kilometers at L = 2 to 4. J. Geophys. Res. *77*, 4734–4745, 1972

Chappell, C. R., Harris, K. K., Sharp, G. W.: The dayside of the plasmasphere. J. Geophys. Res. *76*, 7632–7647, 1971

Dungey, J. W.: Electrodynamics of the outer atmosphere. Penn. State Univ. Ionosph. Res. Lab. Sci. Rep. No. *69*, 1–52, 1954

Kupfer, E.: Hydromagnetic waves in a non-uniform plasma. J. Geophys. *41*, 123–126, 1975

Miletits, J. Cz.: On the latitude dependence of pc-type pulsations. Acta Geodaet. Geophys. Montan. Hung. *6*, 141–153, 1971

Münch, J.: Statistische Frequenzanalyse von erdmagnetischen Pulsationen. Mitteil. Max-Planck-Inst. Aeronomie *34*, 1–66, 1968

Orr, D., Matthew, J. A. D.: The variation of geomagnetic micropulsation period with latitude and the plasmapause. Planetary Space Sci. *19*, 897–905, 1971

Rostoker, G., Samson, J. C.: Pc micropulsations with discrete, latitude-dependent frequencies. J. Geophys. Res. *77*, 6249–6253, 1972

Siebert, M.: Geomagnetic pulsations with latitude-dependent periods and their relation to the structure of the magnetosphere. Planetary Space Sci. *12*, 137–147, 1964

Siebert, M.: Zur Theorie erdmagnetischer Pulsationen mit breitenabhängigen Perioden. Mitteil. Max-Planck-Inst. Aeronomie *21*, 1–106, 1965

Stuart, W. F., Usher, M. J.: An investigation of micropulsations at middle latitudes. Geophys. J. *12*, 71–86, 1966

Voelker, H.: Zur Breitenabhängigkeit der Perioden erdmagnetischer Pulsationen. Naturwissenschaften *49*, 8–9, 1962
Voelker. H.: Zur Breitenabhängigkeit erdmagnetischer Pulsationen. Mitteil. Max-Planck-Inst. Aeronomie *11*, 1–55, 1963
Voelker, H.: Göttinger Untersuchungen über erdmagnetische Pulsationen und ihre Beziehungen zur Magnetosphäre. Kleinheubacher Ber. *10*, 237–243, 1965
Voelker, H.: On geomagnetic pulsations accompanying storm sudden commencements and sudden impulses. Earth. Planet. Sci. Lett. *1*, 383–386, 1966
Voelker, H.: Zur Feinstruktur erdmagnetischer ssc's und si's duch überlagerte Pulsationen. Kleinheubacher Ber. *12*, 45–51, 1967
Zelwer, R., Morrison, H. F.: Spatial characteristics of midlatitude geomagnetic micropulsations. J. Geophys. Res. *77*, 674–694, 1972

Prof. M. Siebert
Institut für Geophysik
Postfach 876
D–3400 Göttingen
Federal Republic of Germany

Book Reviews

Jeffreys, H.: *Collected Papers of Sir Harold Jeffreys on Geophysics and Other Sciences.* Vol. 1, Theoretical and Observational Seismology. London–Paris–New York; Gordon and Breach Science Publishers, 1971, £ 11.45.

The first volume of the *Collected Papers* consists of papers concerning the mechanical properties of solids, the theory of elastic waves, and observational seismology. These topics are chosen according to the corresponding chapters of Sir Harold's text-book *The Earth* which contains many geophysical results of these papers. Thus, this volume of the *Collected Papers* is a valuable aid for the reader of *The Earth* who wants to know the scientific background.

Section I contains fundamental papers on the elastic and inelastic properties of solids. Therefore, a short summary of their contents shall be given. In the first paper it is shown that the irregular distribution of mass on strings has marked effects on the propagation of elastic waves. The elastic properties of liquids and vitreous solids are discussed in the following paper. Their structure is compared with the structure of solids and gases. The next paper points out that the velocity of elastic waves in the earth's crust is almost not affected by the difference between the isothermal elastic moduli and the adiabatic ones which are actually involved in wave propagation. Inelastic properties of solids are discussed in a paper on plasticity and creep: In non-homogeneous solids, probably any law of imperfection of elasticity including elasticoviscosity or exponential afterworking is possible, according to the spatial distribution of weak places. A paper on the relation between fusion and strength discusses the suggestion that the elastic failure of a solid can be ascribed to local melting under stress. With an assumed law relating the strength to the actual temperature and the melting temperature, the strength in the interior of the earth is determined. The condition for elastic instability which is generally described by the assumption that large displacements can be accompanied by small strains, is formulated more precisely. In a paper on initial stress and instability, it is shown that elastic instability occurs when in some possible displacements the rotations are much larger than the strains. The problem of an elliptical ridgid inclusion in an elastic solid with homogeneous stress at large distance is solved in the last paper dealing with elastic properties of solids. The last paper of Section I gives a completeness theorem for expansions of a vector function in spherical harmonics. According to the title of this paper, it should belong to a purely mathematical section, but as the theorem is of special interest for problems involving spherical boundary values it is important for studying the elastic properties of the earth.

In section II there are 17 papers concerning problems of the theory of elastic waves. Only four of them are not cited in *The Earth*. Together with the 17 papers of section III on observational seismology they are of special interest for seismologists. But some of them are also of general importance, e.g. the Reflexion of a Pulse Within a Sphere, Elastic Waves in a Continuously Stratified Medium, The Rigidity of the Earth's Central Core, and the State of the Earth's Central Core.

This volume of the *Collected Papers* is valuable for everyone who is studying the elastic properties of the earth's interior and who cannot get these papers in their original context. The intention of Gordon and Breach Science Publishers to present a review of Sir Harold's work cannot be appreciated high enough.

H. Wilhelm, Göttingen

W. Bitterlich und H. Wöbking: *Geoelektronik*
289 Abbildungen, 349 Seiten, Wien–New York: Springer 1972, DM 129,–.

„Die Beschreibung elektronischer Meßverfahren zur Lösung von geophysikalischen, lagerstättenkundlichen und montanistischen Problemen ist das Hauptanliegen dieses Buches". Mit diesem Satz beginnt der Klappentext. Die elektrische Meßtechnik mit den Mitteln der modernen Elektronik ist heute dominierend bei der Lösung von Meßaufgaben. Für den Geowissenschaftler ist diese Technik jedoch nur Mittel zum Zweck, und er möchte für seine Meßprobleme wenn möglich auf kommerziell hergestellte Fertiggeräte oder zumindest auf Bausteine, wie Operationsverstärker und integrierte Schaltkreise zurückgreifen. Wichtig ist deshalb speziell die Frage, mit welchem Gerät oder mit welcher Zusammenstellung von Bausteinen eine optimale Lösung von Meßaufgaben erreicht werden kann.

Hierbei spielen Fragen über Störspannungen, Störabstand, Dynamikumfang, Gleichtaktunterdrückung, Nullpunktstabilität, lineare und nichtlineare Verzerrungen, Intermodulation und Datenspeicherung die herausragende Rolle.

Begriffe dieser Art findet man allerdings in dem vorliegenden Buch nicht oder nur ganz am Rande erwähnt. Statt dessen wird auf den ersten 38 Seiten eine Einführung in die Grundlagen der Elektrotechnik gegeben, wie man sie praktisch in jedem elementaren Lehrbuch der elektrischen Meßtechnik nachlesen kann.

Die in dem Buch zahlreich angegebenen Schaltungsbeispiele entsprechen zum größten Teil dem Stand der Elektronik bis vor etwa 15 Jahren. Operationsverstärker, integrierte Schaltungen und Funktionsmodule, heute die zentralen Bauelemente bei der Entwicklung einer preisgünstigen und funktionsgerechten elektronischen Schaltung, werden in keiner der angegebenen Schaltungen eingesetzt, das Stichwortverzeichnis enthält diese Begriffe nicht. Das Schaltbild des in Abb. 4.17 auf Seite 164 gezeigten Langwellensenders enthält Senderöhrentypen, welche seit Ende des 2. Weltkrieges nicht mehr gefertigt werden und heute nur noch als Rarität zu erhalten sind. Die heute gefertigten Senderöhren sind nicht unbedingt besser. Wenn jedoch ein Schaltbild mit genauer Bestückung angegeben wird, so sollten die angegebenen Bauteile dafür nicht schon seit vielen Jahren vergriffen sein. Um nur noch ein Beispiel dieser Art herauszugreifen: In der Seismik dürfte der Röhrenverstärker seit etlichen Jahren ausgedient haben. Nicht jedoch in dem Buch „Geoelektronik", wo auf den Seiten 305, 306 und 307 Röhrenschaltungen zur Verstärkung seismischer Signale angegeben werden. Daneben werden aber auch mit Transistoren arbeitende Schaltungen diskutiert.

Nimmt man jedoch die zum größten Teil veralteten Schaltungsentwürfe in Kauf, so erhält das Buch einige recht interessante Kapitel über Gebiete, die sonst in der Literatur nur schwer zu finden sind.

So wird von Seite 147–188 die Ausbreitung elektromagnetischer Wellen durch Gesteine ausführlich behandelt, mit einer für den Praktiker sehr nützlichen Beschreibung der bei Längstwellen auftretenden Antennenprobleme. Ebenso lehrreich ist der Abschnitt über die Prospektion mit Hilfe elektromagnetischer Wellen, in welchem Theorie und Praxis gut aufeinander abgestimmt sind.

Andere Kapitel beschäftigen sich mit den Messungen von mechanischen und elektrischen Gesteinsparametern. Besondere Berücksichtigung finden dabei die im alpinen Gebirge vorkommenden Gesteine. Ein Abschnitt beschreibt die elektrischen Eigenschaften von Bergwasser.

Kapitel 7 beschäftigt sich mit dem Einsatz elektronischer Hilfsmittel bei Vermessungsarbeiten im Bergbau, wie zum Beispiel bei der Ortung eines Bohrloches. Hier wird ein Problemkreis angesprochen, der auch dem Geophysiker für seine Praxis gute Anregungen vermittelt.

Zusammenfassend kann gesagt werden, daß das Buch dem Geowissenschaftler und dem im Bergbau tätigen Ingenieur auf speziellen Gebieten einen guten Einblick in praxisnahe Probleme gibt. Die angegebenen Schaltungsentwürfe sind jedoch häufig veraltet, und für einen Nachbau nicht geeignet. Man wünscht sich

deshalb für die 2. Auflage eine gründliche Überarbeitung der Gerätebeschreibungen, um das lesenswerte Buch ohne Vorbehalt empfehlen zu können.

R. Schick, Stuttgart

R. Schick, G. Schneider: *Physik des Erdkörpers.* Eine Einführung für Naturwissenschaftler und Ingenieure. (*Physics of the Earth.* An introduction for scientists and engineers.) 267 pages, 127 figures and 14 tables.
Stuttgart: Ferdinand Enke 1973. Price: DM 59,00.

Introductory texts in branches of science, which, like the physics of the earth are covering a broad variety of different themes, have, as is well-known, always to cope with numerous difficulties and the authors have to draw compromises, mainly due to the limited size of the book. Each author will solve the resulting selection problems in a different manner, depending objectively on the prospective circle of readers and their background and subjectively on his own ideas of the matter, his preferences and his personal field of research. These shortcomings are in my opinion inherent ones, but are in most cases compensated by the didactic advantages of a uniform treatment of the material.

As indicated in the subtitle, the present book, written in german, is designed as an introduction to the physics of the earth for scientists and engineers with special regard to graduate students of neighbouring disciplines.

The general concept of the book follows the classical division of earth physics: seismology (3 chapters), gravimetry (2 chapters), magnetic field of the earth (2 chapters) and terrestrial heat flow (2 chapters). For each of these four main branches one chapter is devoted to the respective instruments and measuring techniques. This valuable consideration makes allowance for the fact, that the rapid progress in geophysics is not at last due to recent improvements in instrumentation.

In the final chapter there is a short description of some of the problems pertaining to the physical constitution of the earth's interior and to physical earth models. An extensive bibliography, well balanced between general text-books and special articles in scientific journals, supplements the clear presentation of the subject matter.

The treatment is elementary throughout and in most cases emphasis is laid upon physical rather than mathematical comprehension; long mathematical deductions are omitted. The illustrating examples of results are up to date, the quality of the numerous figures is excellent. Together with the numerous tables of data they give good informations about the present state of knowledge.

Special mention has to be made of chapter 3, giving a very detailed description of modern aspects of seismic source mechanisms and its tectonic implications. Compared to the relative completeness of this chapter, some other sections are rather concise, especially with regard to mutual connexions of the different results. The authors obviously decided to concentrate on the basic physical principles of the different methods, which could only be achieved at the expense of other topics. So, only brief mention is given to important modern research fields like the combined application of petrology, solid state physics and geophysics to the problems of composition, equation of state of matter and internal constitution of the earth's interior or the basic concept of global tectonics and geodynamics, which could only be established by cooperation of all earth sciences. Completely omitted is the field of geochronology and the problem of age and development of the earth.

Apart from these minor objections, the book in general is an excellent introduction to the physical background of earth physics for students of neighbouring disciplines. Moreover, due to the lucidity of the text and the elementary treatment it is equally well suited for all, who are interested in geophysics and who want to have informations beyond the level of popular scientific magazines.

H. Burkhardt, Clausthal-Zellerfeld

The Upper Mantle. Proceedings of the final UMP Review-Symposium, Moscow, 9–13 August 1971.

Upper Mantle Project; Scientific Report No. 41, edited by A. R. Ritsema.
Developments in Geotectonics, No. 4, 644 S., 284 Figuren. Elsevier Publ. Co., Amsterdam 1972. Dfl. 57,50

Im Vorwort des Upper-Mantle Committee (U.M.C.) wird auf die von Tuzo Wilson eingebrachte Empfehlung hingewiesen, daß ein Hauptanliegen des Upper Mantle Project (U.M.P.) sein sollte zu prüfen, ob Kontinentaldrift existiere oder ob nicht. Während des U.M.P. wurde das Konzept der Plattentektonik geboren; die gegenwärtigen Beobachtungsdaten sprächen für dieses Konzept, heißt es im Vorwort weiter, doch würde die endgültige Entscheidung erst aufgrund direkter Bohrergebnisse aus der ozeanischen Kruste fallen. Die zur Zeit vorliegenden Beobachtungen sprächen für einen jungen Ozeanboden, doch sei die Verbindung zwischen der kontinentalen Entwicklung und der Plattentektonik weniger klar und verbleibe als das wichtigste Problem künftiger Forschung. Ihr Stand, wie er sich bis 1971 abzeichnete, ist in den 32 Einzeldarstellungen von Übersichtsvorträgen niedergelegt, die auf dem „Final Symposium of the Upper Mantle Project" vom 9.–13. August 1971 in Moskau von international renommierten Fachvertretern der verschiedenen Disziplinen gehalten wurden. Im allgemeinen wird von den Autoren neben eigenen Ergebnissen ein guter Überblick über den Erkenntnisstand ihres Arbeitsgebietes vermittelt einschließlich umfangreicher Literaturangaben (insgesamt rd. 1700 Titel). Hinsichtlich der Informationsfülle ist das von Gelfand *et al.* im Zusammenhang mit ihren Untersuchungen über Kriterien hoher Seismizität im östlichen Zentralasien gebrachte Zitat von T. S. Eliot des Nachdenkens wert (Seite 422): „Where is the wisdom we have lost in knowledge? Where is the knowledge we have lost in information"?

Will man aus den Einzeldarstellungen des Buches ein Gesamtbild unseres heutigen Wissens vom oberen Erdmantel gewinnen, so muß man dieses Zitat von hinten nach vorn verifizieren. Ein Buch wie dieses enthält implizit mehr Wissen über die Erde als explizit darstellbar ist mangels eines in alle Details eingeweihten Synoptikers.

Das Buch umfaßt, zusammengefaßt und etwa in der Reihenfolge der Artikel, folgende Themen: Entstehung der Erde, Entwicklung von Erdkruste und Erdmantel, Vulkanologie, Mineralogie des Erdmantels, Temperatur des Erdmantels, Wärmefluß, Geomagnetische Tiefensondierung, Binnen- und Randmeere, Sprengseismik, Paläomagnetismus, Schwerefeld und Mantelkonvektion, Erdgezeiten und Polbewegungen, rezente Krustenbewegungen, Seismizität und Globale Tektonik, Erdbebenherdmechanismen, Struktur des oberen Erdmantels aus P-Laufzeiten und aus der Dispersion von Oberflächenwellen, experimentelle Untersuchungen zur Schallgeschwindigkeit bei hohen Drucken, Bruch- und Fließverhalten von Gesteinen, Kriechprozesse in der Erde, Hochtemperatur-Rheologie, Anelastizität des Mantels und dynamische Prozesse im tieferen Mantel.

Hieraus seien nur einige Details hervorgehoben. Das Konzept der Plattentektonik wird von den meisten Autoren vertreten, wenn auch Jeffreys durch Anwendung des modifizierten Gesetzes von Lomnitz zu dem Schluß gelangt, daß Konvektion im Erdmantel nicht möglich sei. Die für die Plattentektonik wichtige Frage, ob die Asthenosphäre überall vorhanden sei, untersucht Knopoff mittels Dispersionskurven von Oberflächenwellen für 5 geologische Provinzen (Ozeane, Riftsysteme, aseismische Kontinentaltafeln, Gebirge und Schilde): Sie existiert überall mit Ausnahme der alten Schilde, wo sie nur schwach oder gar nicht ausgebildet ist. Hier müßte nach Knopoff die Lithosphärenbewegung einen merklichen Widerstand erfahren. Auch im Bericht von Schmucker und Jankowsky über Ergebnisse der geomagnetischen Tiefensondierung wird die Existenz der Asthenosphäre als Schicht mit einem spezifischen Widerstand von 50 Ω m bestätigt.

Im Widerspruch zur Plattentektonik vermutet Beloussov intermittierende Aufheizungen von Mantelschichten mit der Folge von periodischen Aufwärtsbewegungen der Asthenosphäre. Hauptsächlich auf die Asthenosphäre konzentrieren sich nach St. W. Smith die mechanisch dämpfenden Eigenschaften des Mantels: Beispielsweise kann hier Q_β bis auf 60 abnehmen. Ab 300 bis 400 km Tiefe erfolgt ein schneller Anstieg von Q auf 1000 bis 2000, was unabhängig aus Raumwellen, Oberflächenwellen und Eigenschwingungen folgt. Der Dämpfungsmechanismus beruhe vermutlich auf intergranularer thermo-elastischer

Relaxation, Korngrenzendiffusion und partiellem Schmelzen. Nach Ahrens ist die Asthenosphäre eine Schicht partiell geschmolzener Gesteine mit basaltischer Zusammensetzung der geschmolzenen Fraktion; bis 365 km Tiefe liegt Olivin mit f_{o80}—f_{o90} vor, geht hier in die Spinellstruktur über und bei 620 km in gemischte Oxyde wie MgO (Periklas) und SiO_2 (Stishovit). Kennedy und Higgins betrachten die Schmelztemperaturen im Mantel und leiten einen Aufbau (bis 400 km Tiefe) aus 65% Olivin, 30% Pyroxen und 5% Granat ab. Akimoto behandelt das System MgO–FeO–SiO_2 bei hohen Drucken und Temperaturen bezüglich der Phasengleichgewichte und elastischen Eigenschaften. Die Systeme Mg_2SiO_4–Fe_2SiO_4 (Olivin), $MgSiO_3$–$FeSiO_3$ (Klinopyroxen) und SiO_2 (Quartz) und deren Übergänge in Spinellstrukturen bei etwa 400 km Tiefe und Postspinellstrukturen ab etwa 650 km, bei Quartz in Coesit bzw. Stishovit, verhalten sich im Einklang mit den aus seismischen Daten folgenden Strukturen des oberen Erdmantels, d.h. den z.B. im Beitrag von Hales diskutierten, aus dem Early-rise-Experiment und anderen sprengseismischen Untersuchungen bestätigten Diskontinuitäten bei rd. 400 und 600 km Tiefe.

Runcorn („... real science, like faith, is the evidence of things not seen!") diskutiert hinsichtlich der nichthydrostatischen Erdfigur die Möglichkeit von Konvektion auch im unteren Mantel und bringt, wie Kaula in seinem Beitrag über Schwerefeld und Mantelkonvektion, die Aufrechterhaltung der Geoidundulationen mit den viskosen Kräften der konvektiven Bewegungen in Verbindung. Er weist auf den Mangel der bisher diskutierten Antriebsmechanismen der Platten hin (Zug durch abtauchende Zunge oder/und Druck aus der Rückenachse): Es fehle hier die Erklärung, wie die Platten ursprünglich gestartet wurden. Aus dem Geoid läßt sich das Spannungsfeld berechnen, das die Konvektionsströme den rigiden Platten aufprägen; es reicht aus, um die Festigkeit der Kruste gegen Deformationen zu überwinden; eine Theorie der Tektonik ließe sich hierauf gründen.

Auch die Archäologie kann offensichtlich Daten über rezente Krustenbewegungen beisteuern: Wellmann erwähnt eine Azimutdrehung der Cheops-Pyramide um 2,5 Bogenminuten in 4500 Jahren, was einer rezenten Drehgeschwindigkeit Nordafrikas von $25 \cdot 10^{-9}$ rad/Jahr entsprechen würde.

Das Buch enthält nicht alles, was im Laufe des U.M.P. an Erkenntnissen gewonnen wurde, doch kommen die außerordentlichen Fortschritte, welche die Geowissenschaften durch dieses großangelegte internationale Programm erzielen konnten, klar zum Ausdruck.

K. Strobach, Stuttgart

J. Geophys. 41, 333–356, 1975

Original Investigations

Deep Structure of the Southern Rhinegraben Area from Seismic Refraction Investigations*

J. B. Edel**

Institut de Physique du Globe, Strasbourg

K. Fuchs, C. Gelbke, C. Prodehl

Geophysikalisches Institut der Universität Karlsruhe

Received December 6, 1974

Abstract. A joint interpretation of all seismic-refraction profiles in the southern part of the Rhinegraben area is presented. A time-term analysis of all P_g-arrivals reveals the topography of the crystalline basement and provides an average velocity of 6.0 km/s for the uppermost crust. The crust-mantle boundary is clearly elevated in the Rhinegraben rift system forming an arch with a span of 150–180 km and reaching a depth of only 25 km at the flanks of the graben proper. The velocity of P-waves in the uppermost mantle is 8.0–8.1 km/s. Below the flanks of the graben, the crust-mantle boundary is formed by a first-order discontinuity. Within the graben proper it is replaced by a transition zone of 4 km thickness with the strongest velocity gradient at a depth of 21 km. This transition zone is regarded as region of crust-mantle interaction and seems to be confined to the graben proper.

Key words: Seismic-Refraction Profiles — Rhinegraben — Time-Term Analysis — Elevation of Crust-Mantle Boundary — Crust-Mantle Transition

Introduction

Since the large explosions near Haslach in the Black Forest in 1948 (HA in Fig. 1) the Rhinegraben, especially its southern part, has been the site of a large number of explosion-seismic experiments (Fig. 1 and Table 1). Also deep-reflection profiles were recorded in some areas of the Rhinegraben (Dohr, 1957, 1967, 1970; Schulz, 1957). The explosions during one of these experiments (near Rastatt, 1971) could be used for seismic-refraction observations (profile RA-250). These investigations culminated in a large-scale refraction survey in September 1972 in the southern part of the Rhinegraben when a dense network of seismic-refraction profiles was established (Rhinegraben Research Group, 1974; Fig. 1).

It is the purpose of this paper to present a unified interpretation of all available deep-seismic sounding data in the southern part of the Rhinegraben. Strong lateral variations in the uppermost crust cause difficulties in their interpretation. The geological and tectonic structure of the area under investigation is extremely complex. Three main tectonic events have influenced the area: The Variscan orogeny mainly in

---

* Contribution no. 175 within a joint research program of the Geophysical Institutes in Germany sponsored by the Deutsche Forschungsgemeinschaft (German Research Association). Contribution no. 108, Geophysical Institute, University of Karlsruhe.

** Also Geophysikalisches Institut der Universität Karlsruhe.

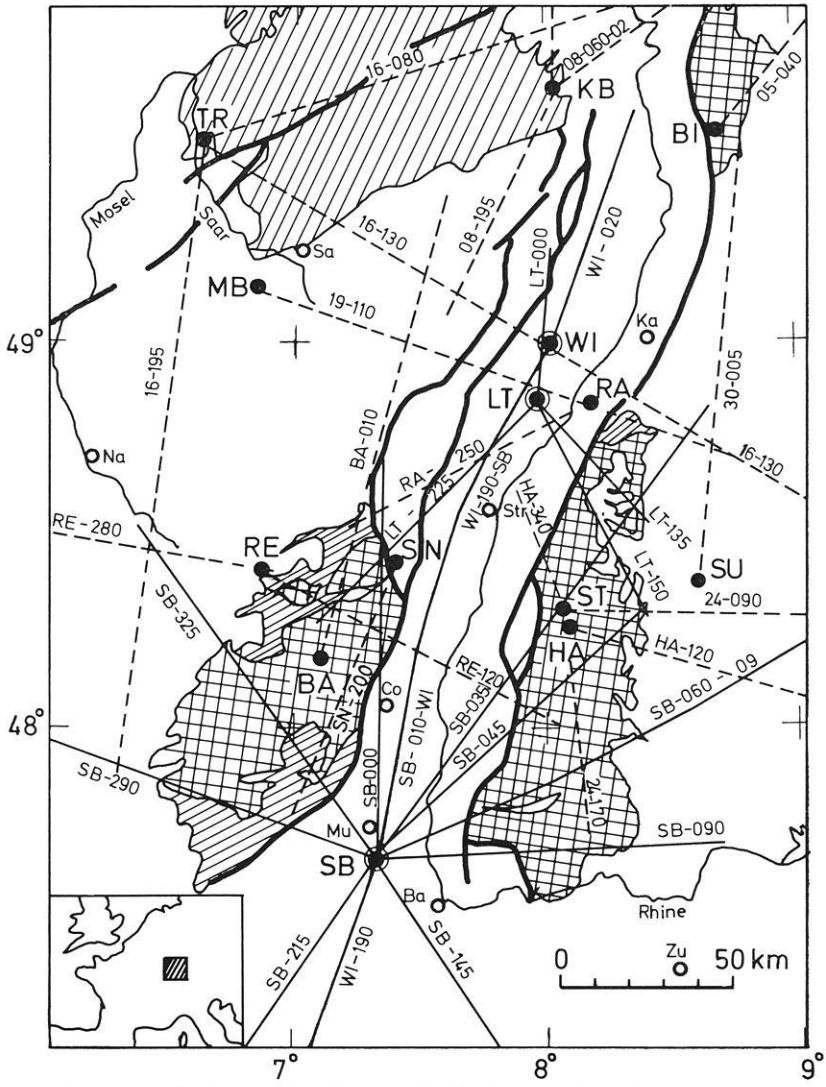

Fig. 1. Location map of seismic-refraction profiles in the central and southern Rhinegraben until 1974

Explanations:

profiles recorded in September 1972

other profiles

Each profile is denoted by: shotpoint code — azimuth (—reversed shotpoint code)

faults

crystalline outcrops

Paleozoic outcrops

Fig. 1. Explanations: (continued)

⊙ ● Shotpoints:

LT	Leutenheim,	SB	Steinbrunn,
WI	Wissembourg,	BA	Col des Bagenelles,
HA	Haslach,	BI	Birkenau (05[a]),
MB	Merlebach,	KB	Kirchheim-bolanden (08),
RE	Raon l'Étape,		
ST	Steinach (24),	SN	Saint Nabor,
TR	Taben Rodt (16)	SU	Sulz (30)

○ Cities:

Ba	Basel	Na	Nancy
Co	Colmar	Sa	Saarbrücken
Ka	Karlsruhe	Str	Strasbourg
Mu	Mulhouse	Zu	Zürich

[a] The numbers refer to the denotations used for shotpoints (quarries) within western Germany (Bamford, 1973; Giese and Stein, 1971).

Table 1. Profiles observed prior to 1972 and references

Shotpoint	Azimuth	Profile[a]	Authors of Interpretations[b]
Haslach (HA)	120	HA-120	1, 2, 3, 4, 5, 6, 7, 12, 14, 15, 16, 17, 18, 19
Haslach (HA)	340	HA-340	2, 5, 12, 16, 17, 18, 19
Taben-Rodt (TR)	080	16-080	6, 9, 10, 11, 17
Taben-Rodt (TR)	130	16-130	1, 2, 3, 6, 12, 13, 14, 17
Taben-Rodt (TR)	195	16-195	2, 14, 17
Merlebach (MB)	110	19-110	1, 2, 6, 12, 13, 14, 17
Kirchheimbolanden (KB)	195	08-195	2, 17
Saint Nabor (SN)	200	SN-200	1, 2, 3, 6, 8, 13, 14, 17
Col des Bagenelles (BA)	010	BA-010	1, 2, 3, 6, 8, 13, 14, 17
Raon l'Étape (RE)	120	RE-120	2, 14, 17
Raon l'Étape (RE)	280	RE-280	2, 14, 17
Birkenau (BI)	040	05-040-02	3, 5, 6, 11, 17
Rastatt (RA)	250	RA-250	2, 17
Steinach (ST)	090	24-090	2, 3, 14, 17
Steinach (ST)	170	24-170	1, 2, 3, 14, 17

[a] The denotation corresponds to that by Giese and Stein (1971).

[b] 1 Ansorge *et al.* (1970), 2 Edel *et al.* (this report), 3 Emter (1971), 4 Förtsch (1951), 5 German Research Group (1964), 6 Giese and Stein (1971), 7 Landisman and Mueller (1966), 8 Lauer and Peterschmitt (1970), 9 Meissner and Berckhemer (1967), 10 Meissner *et al.* (1970), 11 Meissner and Vetter (1974), 12 Mueller *et al.* (1967), 13 Mueller *et al.* (1969), 14 Mueller *et al.* (1973), 15 Prodehl (1965), 16 Reich *et al.* (1948), 17 Rhinegraben Research Group (1974), 18 Rothé (1958), 19 Rothé and Peterschmitt (1950).

NE-SW direction, the Alpine orogeny causing a general uplift and block faulting of the Variscan area, and the formation of the graben. In consequence, the sedimentary covers show variable thicknesses: reaching 6000 m in the "Saar-Nahe-Trog" in the NW, 2000—4000 m in the graben, while in other areas (Vosges, Black Forest, Odenwald) the crystalline basement is exposed. — Special explosions in drill holes are expensive and could be arranged only in a few cases. Otherwise, available quarry blasts had to be used as energy sources. Therefore, the position of the profiles is not always optimal with regard to geologic and tectonic settings of the area.

In spite of these complications the record sections of the numerous profiles exhibit a similar pattern of traveltime branches which permit a classification of the observed record sections in relation to the graben. Conventional flat-layer methods of interpretation had to be applied with care. They were supplemented by a time-term analysis for the top of the basement.

Correlation of Phases

Most of the data obtained in the area of investigation are presented in record sections (Figs. 2—6). The correlated traveltime curves are shown in the record sections by thin dashed lines. Lateral heterogeneities are expressed clearly in breaks and sudden delays of the traveltime curves which can be correlated frequently with tectonic and petrographic changes. This makes the correlation sometimes very difficult. The size of the relative amplitudes varies considerably within one profile as well as from one profile to the other. In some cases, multiple phases can be identified in the distance range from 0 to 60 km (e.g. profile WI-190-SB).

The general pattern of traveltime curves of all record sections (Fig. 7) corresponds to a general velocity-depth model (see Fig. 11), the variations of which do not only cause traveltime delays but also significant changes of relative amplitudes.

First Arrivals. Only within the first 10 km the direct wave travelling in the sediments (P_s) is visible. The P_g-arrivals can be followed in the distance range from 10 to 60 km and for some profiles up to 90 km. The P_n-phase can be correlated only on part of the profiles as first arrival at distances greater than 90 km (Table 2). The only reversed profile in the area under investigation is that between Steinbrunn (SB) and Wissembourg (WI). The scatter of P_n-arrivals on the record sections of this line causes difficulties in the exact determination of the true velocity within the uppermost mantle. Nevertheless, the data indicate that the true P_n-velocity is about 8.0—8.1 km/s.

Reflected Phases. On the profiles in the central part of the Rhinegraben (16—130, 16—195, 19—110, 08—195, WI—120) reflections within the upper crust are well developed (phases 3, 4). The relative amplitudes of phase 1 (P_MP-reflection) and phase 2 (intermediate reflection from the lower crust) seem to vary from region to region. In the southern graben proper (profiles SB-035, SB-010-WI, SB-000, WI-190-SB, RA-250) phase 2 is dominant. Here the P_MP-reflection is either hidden within the coda of the high-amplitude phase 2 or is too weak. On the profiles crossing the flanks of the graben, however, mostly the P_MP-reflection shows the strongest amplitudes (phase 1), while the reflected phase 2 is less well developed (SB-060-09, SB-045, 24-090, 24-170, 05-140-02, LT-225, BA-010, SN-200, RE-280). On some profiles (RE-120, SB-290) crustal reflections (phase 2, 3) and P_MP (phase 1) are both well

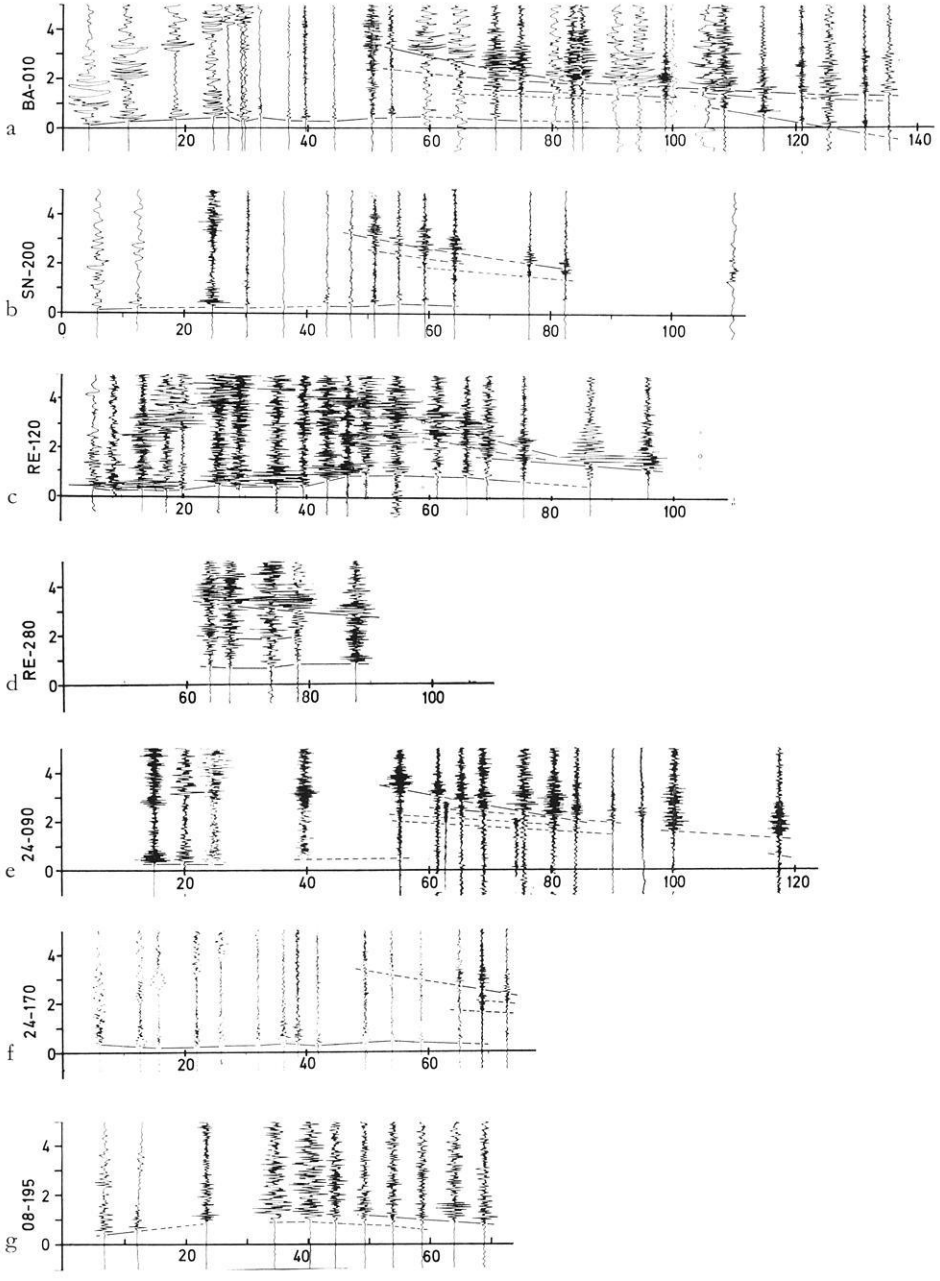

Fig. 2a–g. Record sections. From top to bottom: Bagenelles-N (BA-010), Saint Nabor-S (SN-200), Raon l'Étape-ESE (RE-120), Raon l'Étape-W (RE-280), Steinach-E (24-090), Steinach-S (24-170), Kirchheimbolanden-S (08-195)

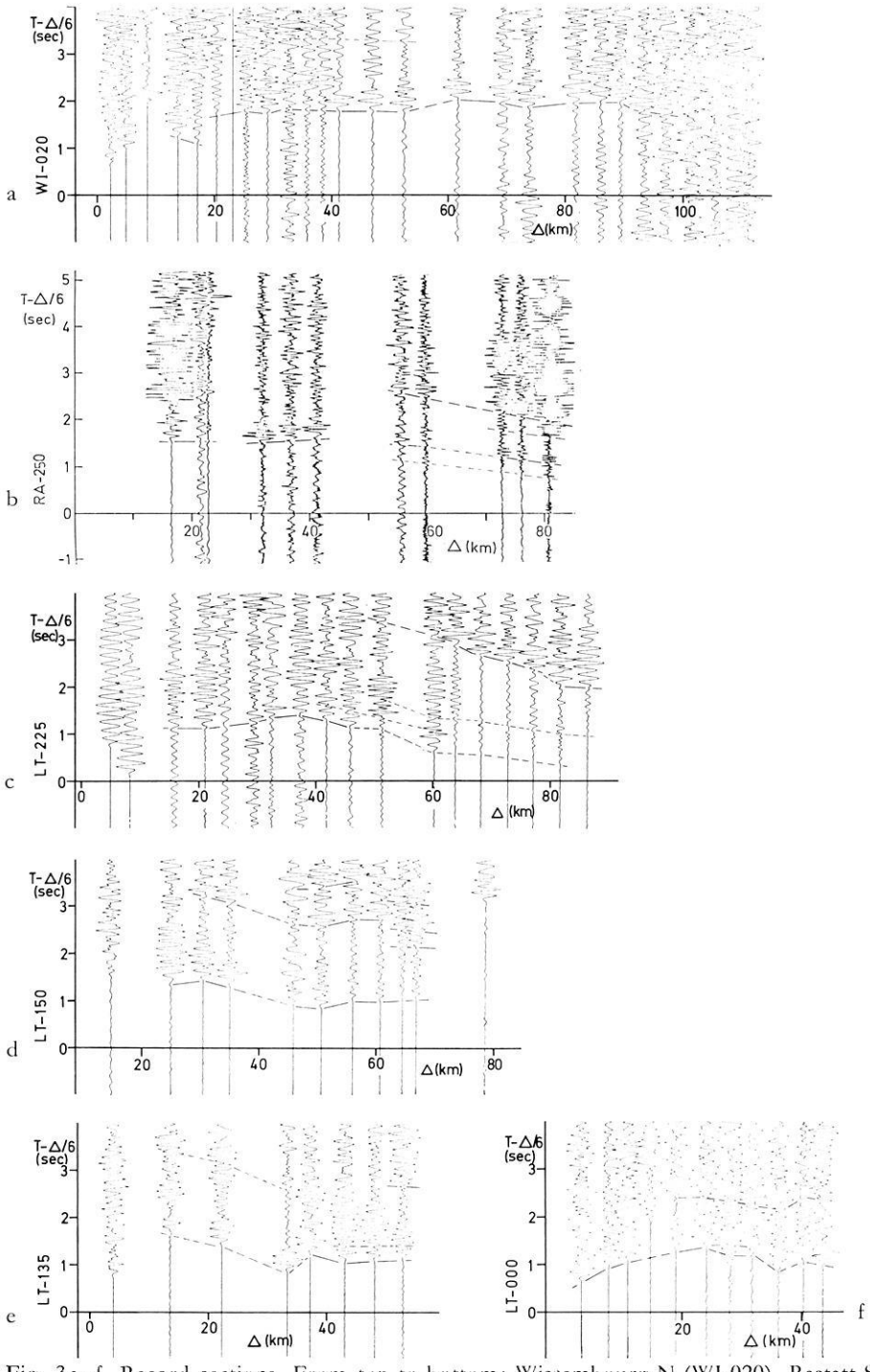

Fig. 3a–f. Record sections. From top to bottom: Wissembourg-N (WI-020), Rastatt-SW (RA-250), Leutenheim-SW (LT-225), Leutenheim-SSE (LT-150), Leutenheim-SE (LT-135), Leutenheim-N (LT-000)

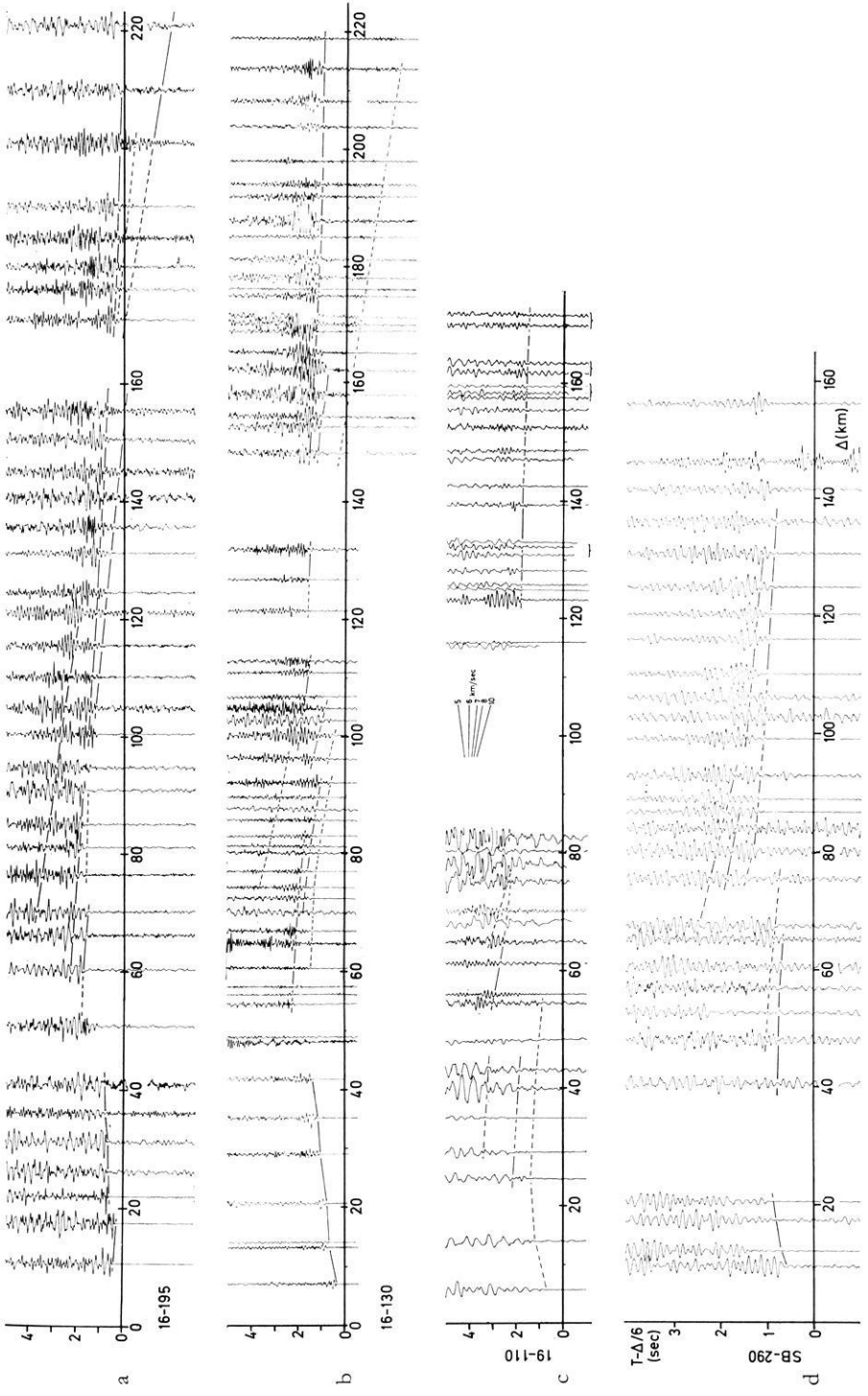

Fig. 4a–d. Record sections. From left to right: Taben Rodt-S (16-195), Taben Rodt-ESE (16-130), Merlebach-E (19-110), Steinbrunn-W (SB-290)

Fig. 5a–c. Record sections. From left to right: Wissembourg-S (WI-190-SB), Steinbrunn-N (SB-010-WI), Steinbrunn-NNE SB-035)

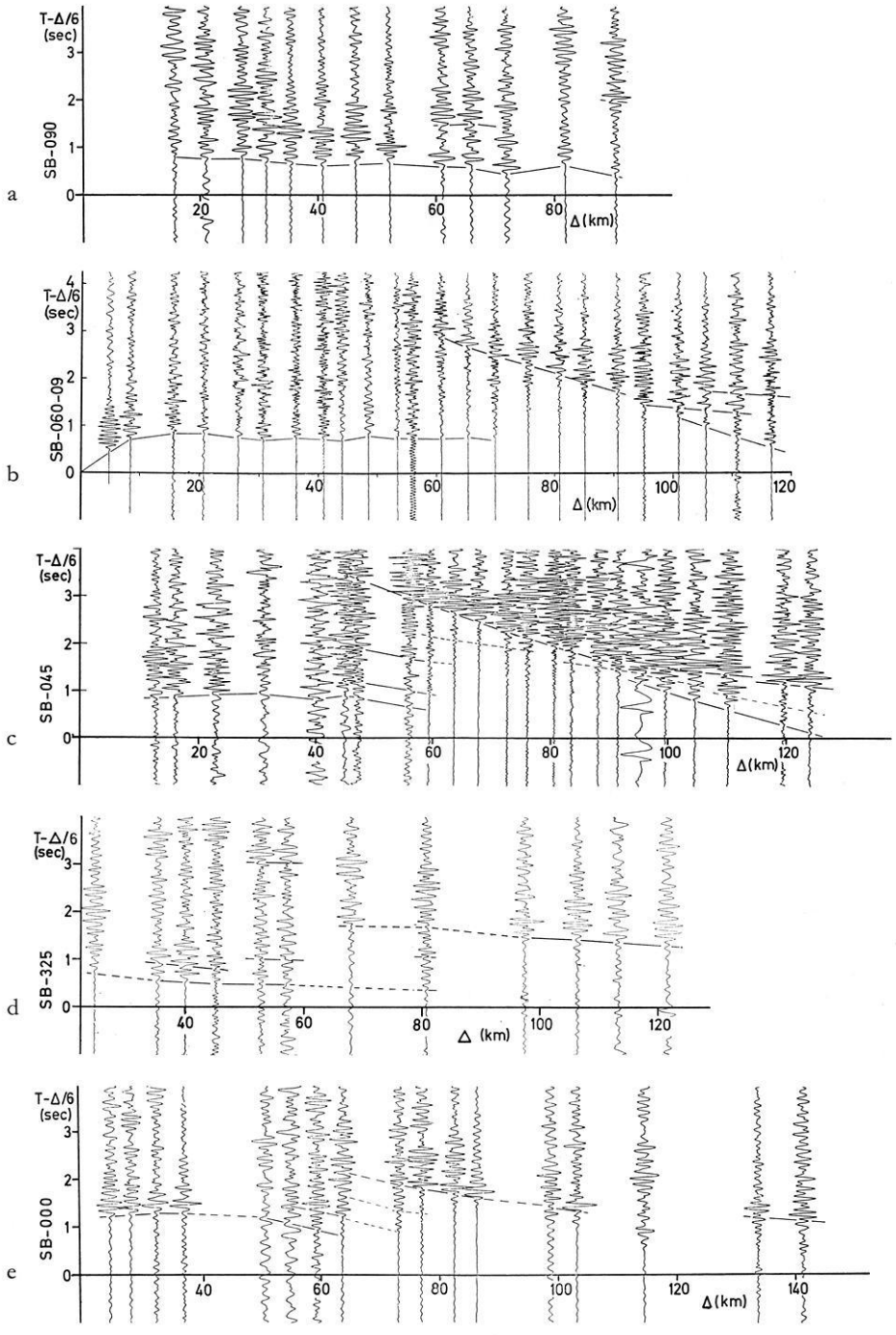

Fig. 6a—e. Record sections. From top to bottom: Steinbrunn-E (SB-090), Steinbrunn-ENE (SB-060-09), Steinbrunn-NE (SB-045), Steinbrunn-NW (SB-325), Steinbrunn-NNW (SB-000)

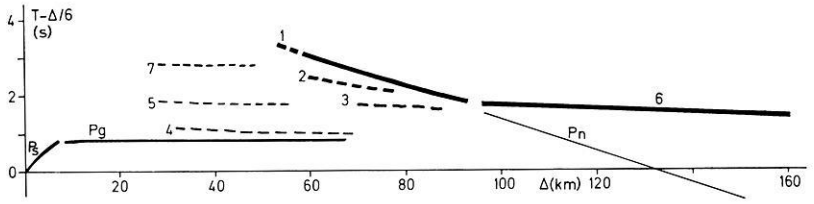

Fig. 7. Basic traveltime diagram of the profiles recorded in the Rhinegraben area

Table 2. P_n observations

Profile	apparent P_n velocity (km/s)	distance range (km)
SB-060-09	7.8	95–125
	8.3	125–150
SB-045	7.9	95–125
SB-035	8.0	110–140
SB-010-WI	8.05	105–130
WI-190-SB	8.1	100–130
16-130	7.8	160–195
16-195	7.8	170–210

expressed. Phase 6 in Fig. 7 denotes strong arrivals which are observed beyond 100 km distance. In the preliminary interpretation by Rhinegraben Research Group (1974) these arrivals were erroneously interpreted as $P_M P$ phase. However, in a more detailed analysis that correlation had to be modified to take into account the existence of phases 2 and/or 3 and a sharp bend in the traveltime curve with an abrupt change in apparent velocity (SB-045, BA-010, RE-120, SB-290): The phase 6 has rather to be interpreted as formed by supercritically reflected energy of the phases 2 and/or 3. The record sections also show that not only supercritically reflected energy is recorded, but also energy is visible in the subcritical distance ranges. In some cases, phases denoted as 4, 5, and 7 can be recognized between 20 and 60 km which apparently continue phases 2 or 3 to smaller distances. While phases 5 and 7 could be identified as multiple reflections from the free surface, phase 4 is probably caused by a heterogeneity in the upper part of the crystalline basement. These phases have not been included in the determination of the velocity-depth model.

Inversion of Observations

The strong lateral heterogeneities in the area under investigation complicate the determination of a detailed velocity-depth distribution, since most of the existing inversion methods require the absence of lateral variations.

The basement delays in the sediments and the velocity in the crystalline basement can be estimated by applying a time-term method (Bamford, 1973) to the numerous P_g-observations. Taking the velocity in the bottom layer as constant this "refractor" velocity is 6.00 ± 0.02 km/s. Fig. 8 shows the contours of the delay times in the area

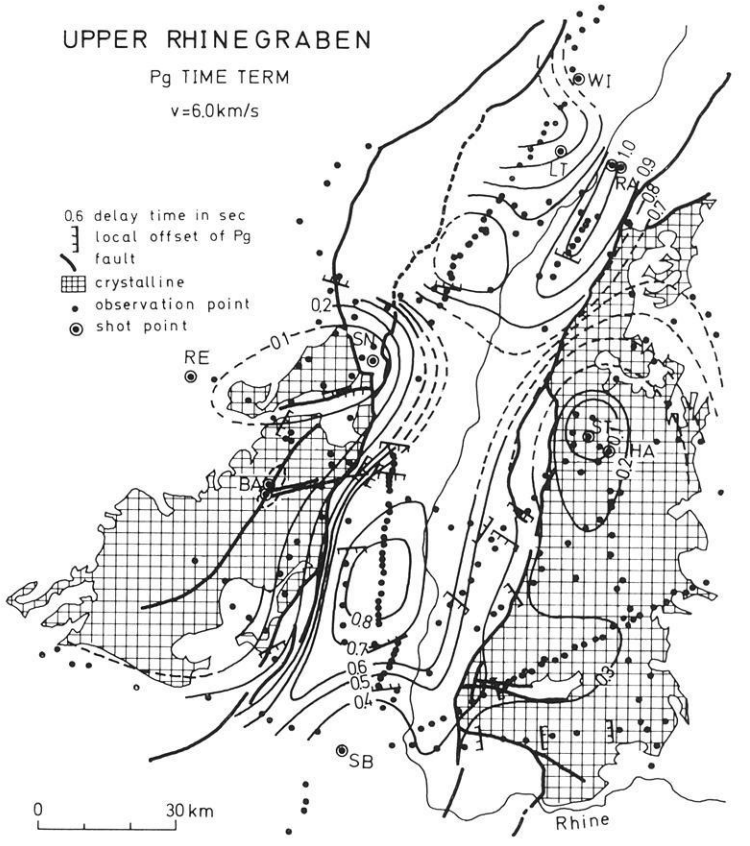

Fig. 8. Delay-time map of the 6.0 km/s surface for the upper Rhinegraben based on fourth order Fourier series solutions. Cross-hatched areas represent crystalline and Paleozoic outcrops. Shotpoint codes see Fig. 1

as computed for a surface formed by a first-order polynomial and fourth-order Fourier series. The conversion of these delay times into depths of the top of the 6 km/s-layer was not performed because the large variations of the overburden velocity are not known sufficiently.

The contour lines in the graben reflect in a first approximation the variations of the depth to the basement. Two great depressions are evident: the southern one between Mulhouse and Colmar in the potash basin of Alsace, the northern one in the so-called "Rastatter Loch" between Baden-Baden and Karlsruhe. Relatively low values of delay times are obtained in the south on the horst of Mulhouse and in the middle of the map on the swells of Colmar and Erstein. The delay times in the areas of outcropping basement are small, but vary slightly, possibly due to the fact that the influence of weathering and fracturing changes from one area of the basement to the other. Sudden delays in the P_g-traveltime curves, possibly caused by vertical displacements of the basement, are also indicated in the map.

Contour Map of the Crust-Mantle Boundary. The depth of the crust-mantle boundary is derived from all observed data of phase 1 in the distance range from 50—90 km.

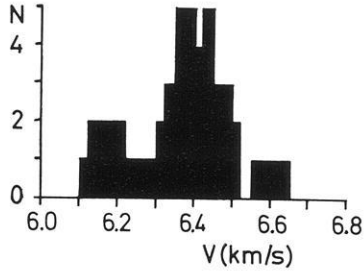

Fig. 9. Histogram showing average crustal velocity vs. frequency of occurrence (number N of profiles) as determined by the T^2, Δ^2 method for the southern and central Rhinegraben

The average crustal velocity on each profile is estimated by the T^2, Δ^2 method. The observations have been corrected to a reference level at a depth of 3 km taking into account sediments or basement rocks as described in detail by Rhinegraben Research Group (1974). From the histogram of the average crustal velocities of all profiles (Fig. 9) 6.4 km/s appears to be a representative velocity. To take into account the effect of ray refraction (e.g., Dix, 1955; Stewart, 1966) the smaller value of 6.25 km/s was then chosen for depth-calculations in a single-layer crust as mean crustal velocity below the reference depth of 3 km. Even then the average velocity is relatively high. It must partly be attributed to the elimination of the uppermost 3 km; but may also be partly connected with the existence of high velocities (about 7 km/s) in the lower crust as will be shown below. Depth values derived from seismic-reflection data (Demnati and Dohr, 1965; Dohr, 1967, 1970) with the same mean crustal velocity have been included in the contour map (Fig. 10) showing depths below sea level. Assuming 8.0—8.1 km/s as true velocity, the dip deduced from the observed apparent P_n-velocities (Table 2) is concordant with the topography of the crust-mantle boundary based on the reflected phase 1 (P_MP).

Slight differences between this contour map and the one presented earlier by Rhinegraben Research Group (1974) are due to the restriction on the reliable observations of phase 1 in this paper. The crust-mantle boundary is clearly elevated in the area of the Rhinegraben rift system reaching a minimum depth of 24–25 km in its southern part. The dome-like elevation displays slight asymmetry: its slope towards the east is rather gentle while towards the northwest and south it is rather steep.

Detailed Velocity-Depth Models. From the main phases shown in Figs. 2—6, for each profile a starting model is derived applying the T^2, Δ^2 method or intercept-time formulas, etc. In a second stage this model is improved by comparison of theoretical and observed traveltimes and position of critical points. This step is done iteratively until the best fit is reached. Then the observations are compared with theoretical seismograms in order to obtain not only the best fit of traveltimes but also of relative amplitudes of the different phases.

The generalized traveltime correlation of Fig. 7 is concordant with the following generalized velocity-depth model depicted in Fig. 11. The velocity in the surface layer (sediments and weathered basement rocks) has been roughly estimated as 4.0 km/s, for the depth range AB a constant average velocity of 6.0 km/s is taken from the time-

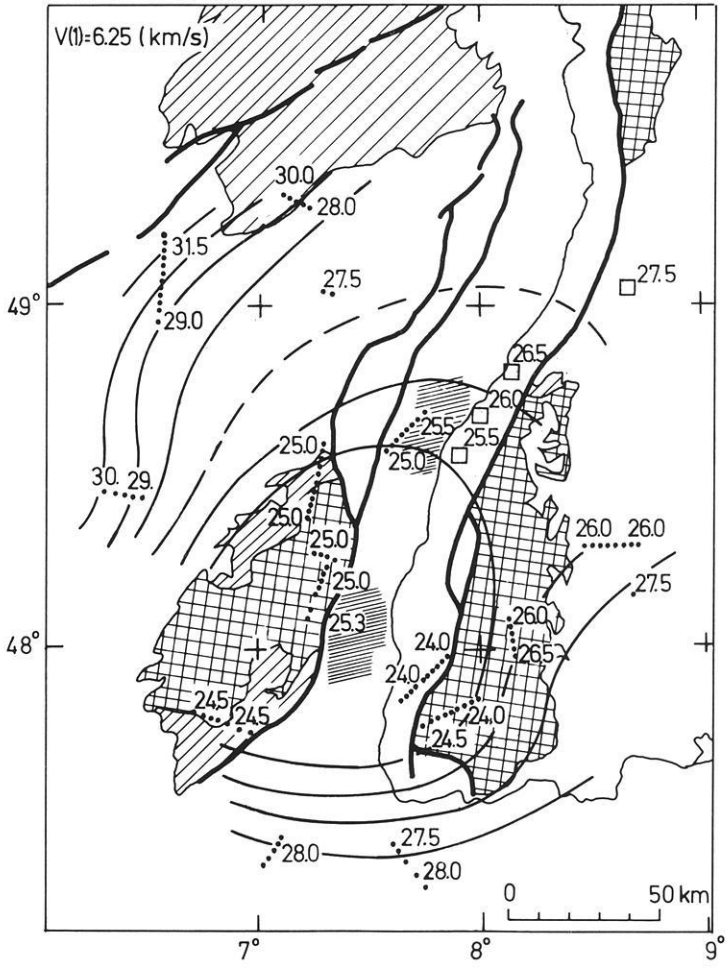

Fig. 10. Contour map of the depth to the crust-mantle boundary below sea-level for the area of the southern Rhinegraben (based on phase 1). The depths are calculated with a mean crustal velocity V(1) = 6.25 km/s below a reference depth of 3 km

28.8	depth in km
• • • • • • • •	positions for which depths were calculated from seismic-refraction data
□	positions for which depths were calculated from seismic-reflection data
////	areas where phase 1 is not observed

Further explanations see Fig. 1

term method. It is difficult to deduce details of the velocity-depth structure in this depth range, though, locally, the true P_g-velocity may be higher or lower than 6.0 km/s. Especially, a zone of low velocity has not been included in the generalized velocity-depth distribution between A and B. Such a velocity inversion had been deduced in the area of the Rhinegraben from previous observations by a number of

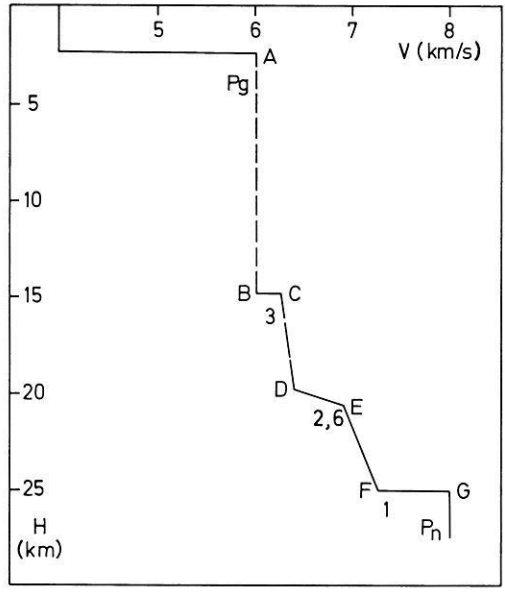

Fig. 11. Generalized velocity-depth model for the area of the Rhinegraben. Explanations of A, B, C, ... see text. P_g, P_n, 1, 2, 3: denotation of depth ranges from which the corresponding phases in the traveltime diagram (see Fig. 7) originate

authors (Ansorge *et al.*, 1970; Meissner *et al.*, 1970; Meissner and Vetter, 1974; Mueller *et al.*, 1967, 1969, 1973). The phase corresponding to the reflection from the bottom of such a low-velocity zone was termed P_c by Mueller and Landisman (1966). Although such a phase can be found on some profiles it is often impossible to follow it to neighbouring profiles and map it on a regional scale. The new observations of 1972 furnished no further information concerning the low-velocity zone. The explosions within the graben proper generated strong multiple reflections and reverberations within the sediments which completely mask the distance range important for the detection of P_c. Therefore, no fine structure was included in the upper part AB of the crustal model, and only its average velocity was taken into account. The presence of considerable vertical and horizontal heterogeneities in this zone is quite likely, and is indicated by the dashed line. A more complicated velocity-depth distribution in this range, however, would only little affect the model derived for the structure of the middle and lower crust (see Fig. 14).

The reflections from the transition zones BC, DE, FG are formed by phases 3, 2, and 1, respectively. Their relative amplitudes are governed by the velocity increase and the thickness of the transition zone which are found to be different inside and outside of the graben. The following examples demonstrate clearly this important difference.

On the record section of the profile SB-010-WI (Steinbrunn to Wissembourg) in Fig. 12, completely located in the graben proper, phases 1 and 3 are absent, and P_n is intersecting phase 2 reflected from zone DE at a depth of about 20 km. In the graben proper this zone has the strongest velocity gradient and produces the predominant reflection from the lower crust. The first-order discontinuity at FG has

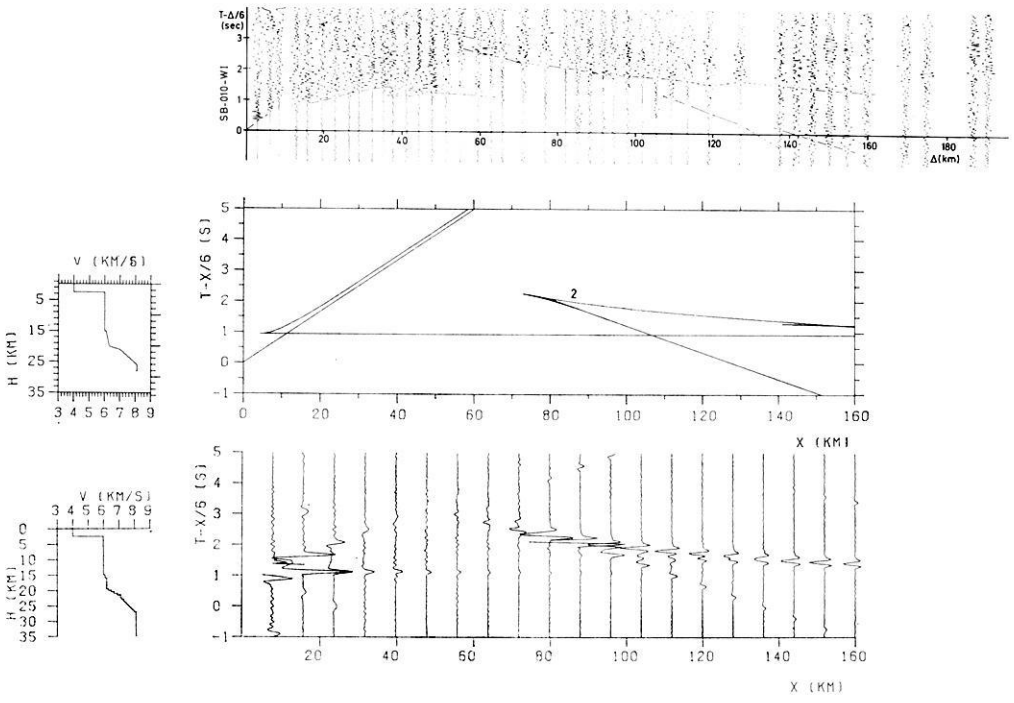

Fig. 12. Observed record section, traveltime interpretation, and synthetic record section of profile SB-010-WI with the corresponding velocity-depth functions

disappeared. The transition zone EF merges continuously into the upper mantle generating the relatively strong P_n-amplitudes. The velocity step at BC is also smaller than outside the graben proper.

The profile SB-045 (Steinbrunn-NE) crosses the eastern flank of the Rhinegraben. On the record section of this profile (Fig. 13) P_n is tangential to phase 1 which here provides the prominent arrivals. The reflecting zone FG is formed by a first-order discontinuity. Phase 2 is best recognized by the abrupt change of the apparent velocity of the large-amplitude reflections at 90 km distance, its critical point being located close to the intersection of phases 1 and 2.

The record section of profile BA-010 (Bagenelles-N) in Fig. 14 (top) displays a very similar amplitude pattern of the phases 1 to 3 compared with profile SB-045. P_n is again tangential to phase 1 and phases 1 and 2 are intersecting close to the critical point of phase 2. On this profile phase 3 can be traced backwards to a distance of at least 70 km. It must be regarded as phase P_c reflected from the bottom of a low-velocity zone within the upper crust. For comparison, Fig. 14 contains synthetic record sections for two crustal models which differ in the presence of a low-velocity zone in the upper crust. Phases 1 and 2 duplicate the observations satisfactorily and are little influenced by the different structure of the upper crust. Phase 3 is better explained by the presence of a low-velocity zone.

It should be pointed out that the observed and the synthetic record sections indicate the existence not only of supercritically but also of subcritically reflected energy which is already visible 10—20 km prior to the critical distance.

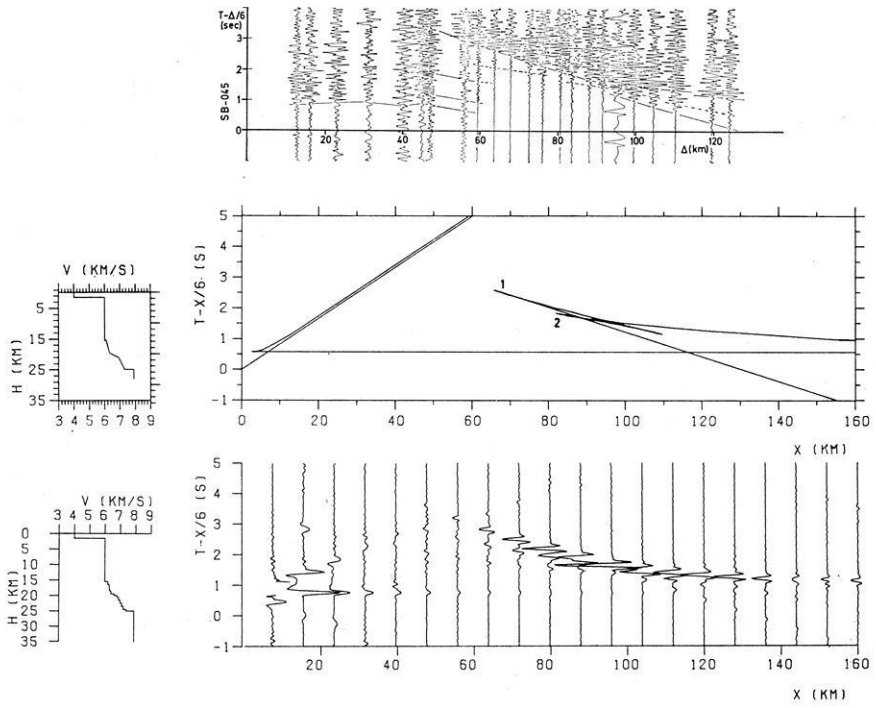

Fig. 13. Observed record section, traveltime interpretation, and synthetic record section of profile SB-045 with the corresponding velocity-depth functions

Detailed velocity-depth models are also derived for all other profiles in the southern part of the Rhinegraben rift system wherever an interpretation in terms of negligible lateral heterogeneity is justified. A compilation of these models is discussed in the next section.

Crustal Structure in the Southern Part of the Rhinegraben Rift System

In Fig. 15 an attempt has been made to compile selected crustal models (Table 3) derived in various parts of the southern Rhinegraben. The inlets with the models are placed as close as possible into the regions of which they are typical. As pointed out already a systematic regional variation related to the graben proper can be recognized.

Outside the graben proper all models are characterized by zone FG as a first-order discontinuity at a depth of 25—26 km where the velocity increases abruptly from about 7.3 to 8.0 km/s. Since zone FG is also the zone of the strongest gradient, there should be no dispute that it represents the crust-mantle boundary. In the graben proper the strongest gradient is encountered in zone DE at a depth of about 21 km where the velocity starts to increase rapidly from 6.3 to 7.1 km/s. Below E, there is a continuous increase of velocity to 8.1 km/s, the velocity of the upper mantle. The discontinuity at FG has disappeared. In the graben proper, it is a matter of definition whether the crust-mantle boundary is placed at the depth of the strongest gradient at about 21 km (see, e. g. Giese and Stein, 1971) or at the depth between 24 and 26 km where a velocity of 8.0 km/s is reached. The authors are inclined to consider the whole

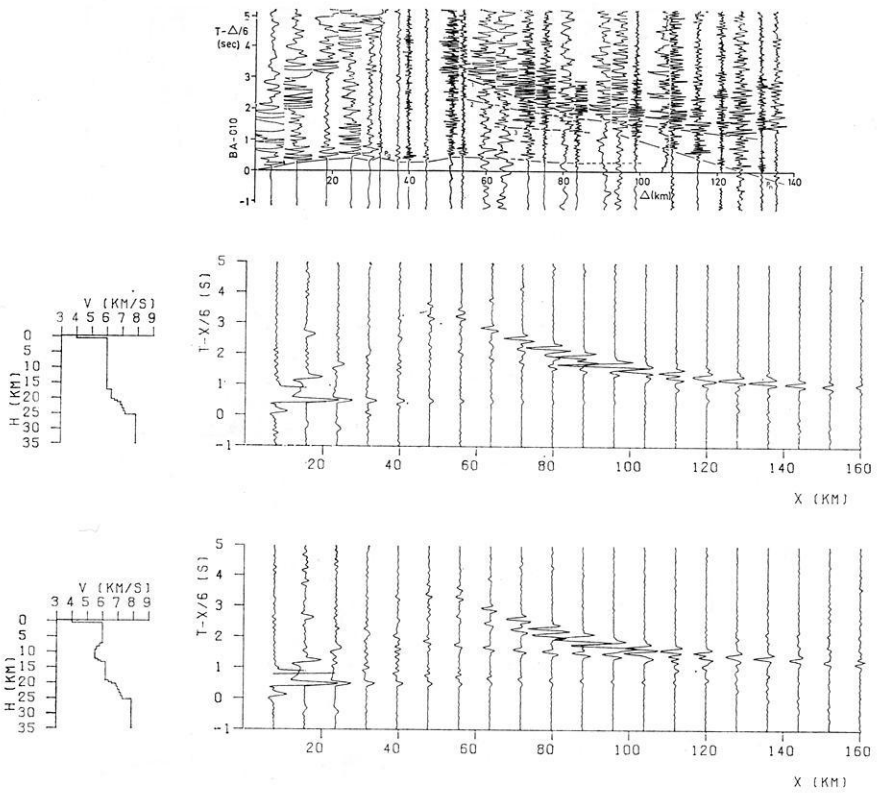

Fig. 14. Observed and synthetic record sections as determined for profile BA-010 with the corresponding velocity-depth functions

depth range between 21 and 26 km as a zone of crust-mantle interaction. This transition zone seems to be confined rather strictly to the graben proper since the first-order discontinuity FG appears as soon as profiles — originating in the graben — enter the crystalline areas of the flanks at about 60—80 km recording distance (LT-225 and SB-035). The zone DE which forms the zone of strongest gradient in the graben proper is well expressed in the neighbouring regions and separates the lower crust into two parts. Its gradient is slightly weaker outside than within the graben. In the whole area the zone BC with a velocity increase from 6.0 to about 6.2 km/s at a depth between 15 and 18 km marks the transition from the upper to the middle crust.

Two cross-sections through crust and uppermost mantle in the stripes AB and CB in the southern part of the Rhinegraben are displayed in Fig. 16. The cross-sections show lines of equal velocity (thin lines) and the depth of the main crustal boundaries (thick dashed lines) as defined by the points B, D, and F of the velocity-depth models (see Fig. 11).

The following features deserve special attention. Outside the graben proper the crust-mantle boundary is a first-order discontinuity into which the velocity isolines from 7.4—8.0 km/s converge. This boundary forms a wide arch with a span of 150—180 km rising from the west towards the graben where the 8.0 km/s-isoline reaches

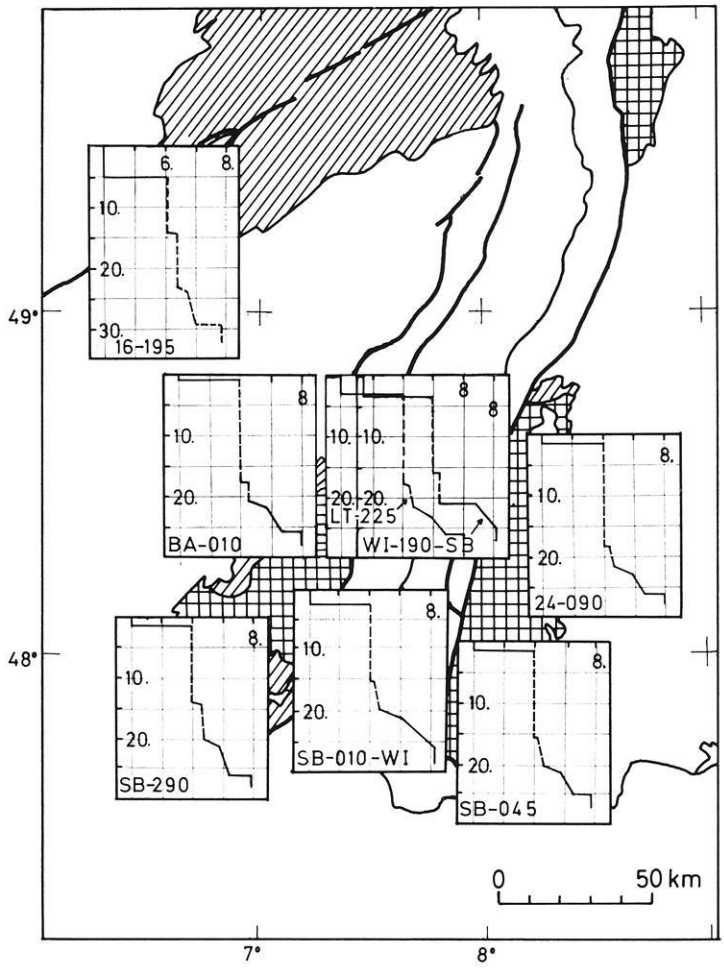

Fig. 15. Map of the area of the central and southern Rhinegraben showing velocity-depth distributions for the corresponding profiles (position see Fig. 1). The velocity-depth functions are representative for the area into which they have been placed

a depth of about 25 km. On the other side of the graben, the crust-mantle boundary dips gently towards the east. Beneath the graben proper, the first-order discontinuity near the 8.0 km/s-isoline has disappeared, here the isolines 7.2—7.8 km/s are warped upward steeply, producing a new zone of strongest velocity gradient at the shallower depth of only 21 km.

Discussion

Fig. 17 presents a compilation of the contour map for the southern Rhinegraben (Fig. 10) and the one for the northern part (Meissner and Vetter, 1974, Fig. 5). Although the number of seismic profiles in the northern part is much smaller, some common features of crustal structure can be outlined. The updoming of the mantle

Table 3. Velocity-depth models

SB-290		SB-010-WI		SB-045	
depth (km)	velocity (km/s)	depth (km)	velocity (km/s)	depth (km)	velocity (km/s)
0.0	4.0	0.0	4.0	0.0	4.0
1.5	4.0	2.5	4.0	1.5	4.0
1.5	6.0	2.5	6.0	1.5	6.0
14.0	6.0	15.0	6.0	15.5	6.0
14.5	6.3	15.0	6.1	15.5	6.1
20.0	6.4	19.5	6.3	20.0	6.3
21.0	6.9	21.0	7.0	21.0	6.9
26.0	7.2	26.0	8.1	25.0	7.4
26.0	7.9			25.0	7.9

SB-060-09		24-090		WI-190-SB	
depth (km)	velocity (km/s)	depth (km)	velocity (km/s)	depth (km)	velocity (km/s)
0.0	4.0	0.0	4.0	0.0	3.7
2.0	4.0	1.5	4.0	3.5	3.7
2.0	6.0	1.5	6.0	3.5	6.0
17.0	6.0	18.5	6.0	16.0	6.0
17.0	6.1	18.5	6.2	16.0	6.1
19.5	6.3	21.5	6.3	21.0	6.1
21.0	6.9	23.0	6.9	21.0	7.2
25.0	7.4	26.0	7.3	25.0	8.1
25.0	8.0	26.0	8.0		

		BA-010					
LT-225		model 1		model 2		16-195	
depth (km)	velocity (km/s)	depth (km)	velocity (km/s)	depth (km)	velocity (km/s)	depth (km)	velocity (km/s)
0.0	4.0	0.0	4.0	0.0	4.0	0.0	4.0
3.0	4.0	0.8	4.0	0.8	4.0	5.0	4.0
3.0	6.0	0.8	6.0	0.8	6.0	5.0	6.1
17.5	6.0	17.5	6.0	7.0	6.0	14.0	6.1
17.5	6.1	17.5	6.3	9.5	5.5	14.0	6.4
21.5	6.3	21.0	6.3	12.5	5.5	23.0	6.4
22.5	6.8	21.5	6.9	13.5	6.2	24.0	6.75
26.0	7.4	25.5	7.3	19.5	6.2	29.0	7.0
26.0	8.0	25.5	7.9	20.5	6.9	29.0	7.9
				25.5	7.4		
				25.5	7.9		

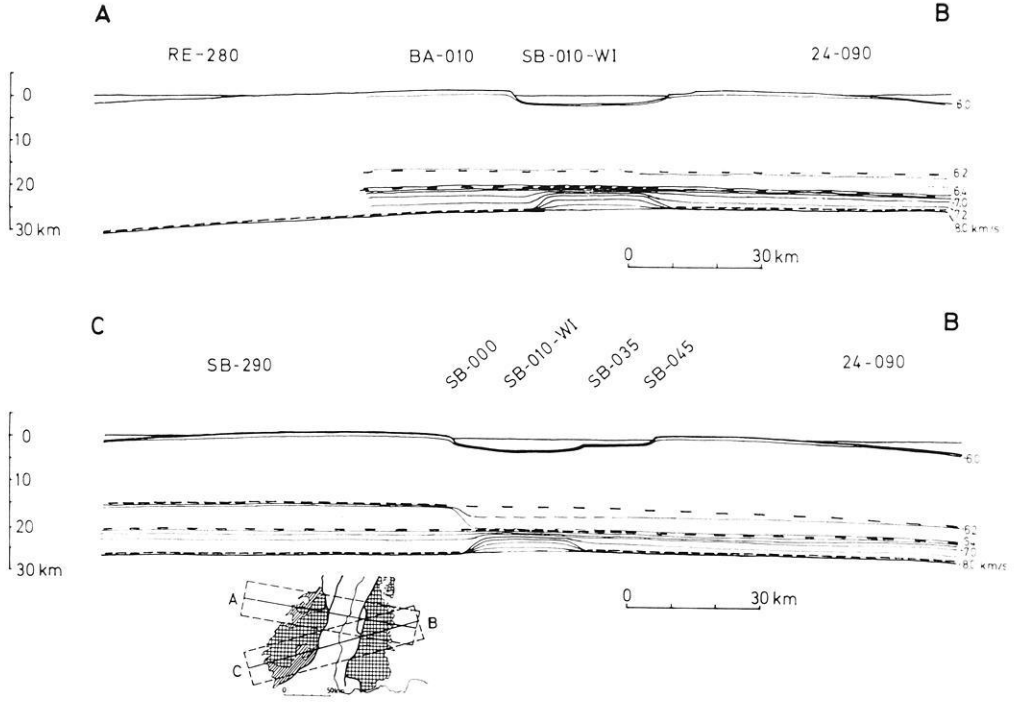

Fig. 16. Crustal sections through the southern part of the Rhinegraben. Thin lines: lines of equal velocity, contour interval 0.2 km/s. Thick continuous line: surface of the crystalline basement. Thick dashed lines: mean depth of the main crustal boundaries

which apparently represents a fairly active stage of epeirogeny (Menard, 1973) is culminating in the southernmost part of the Rhinegraben from where the elevation of the apex is slightly dipping towards the north. For the northern part of the graben proper Meissner and Vetter (1974) deduce a similar structure of the lower crust. They find a velocity of 7.2—7.4 km/s and a strong velocity gradient at a depth of 24 to 25 km in the graben proper. Here $P_M P$-reflections (our phase 1) are also not observed, while the phase with 7.2—7.4 km/s (our phase 2) evidently is absent outside the graben.

A P_n-velocity of 8.2 km/s is reported by Hirn and Perrier (1974) on reversed profiles in the Limagne graben parallel to its strike at a depth of 40 km. They also find a velocity range of 7.2—7.4 km/s between a depth of 20 to 25 km from where the velocity increases continuously to that of the upper mantle.

From seismic reflection measurements, Dohr (1967, 1970) reports reflections with traveltimes of 7 s and 8.5 to 9.0 s which can be attributed to the zone of strong velocity gradient at about 21 km depth and to the depth range at about 25 km. The reflections observed with traveltimes of 13.5 s and about 17.5 s may indicate zones of strong heterogeneities within the upper mantle. Recent long-range observations in France (Hirn *et al.*, 1973) and similar observations by Emter (1971) under the Swabian Jura about 80 to 100 km east of the graben proper have shown the existence of pronounced heterogeneities in the lower lithosphere. However, as already mentioned by Rhine-

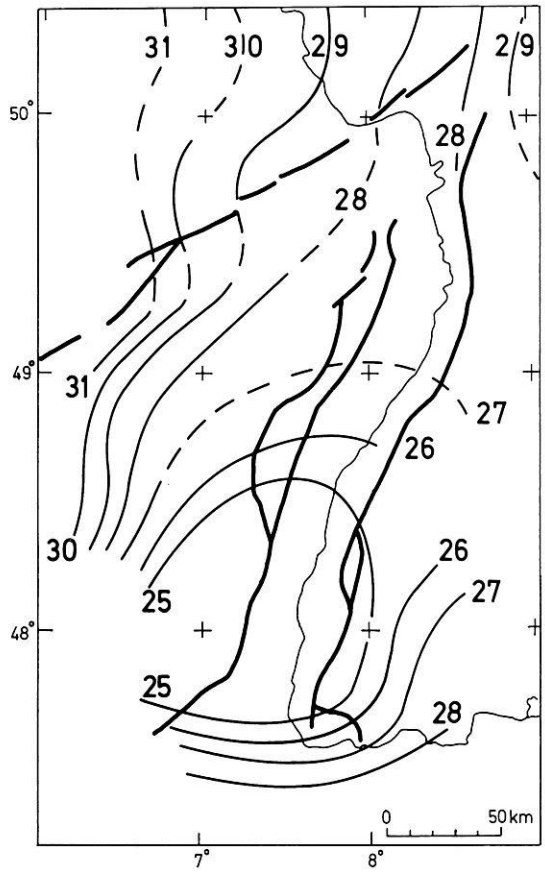

Fig. 17. Contour map of the depth to the crust-mantle boundary combining the map of Fig. 10 and the map shown by Meissner and Vetter (1974, Fig. 5). 28 depth in km

graben Research Group (1974), at present no long-range data in the graben area are available which would allow a statement about the deeper structure below the crust-mantle boundary.

The contour map of the heat-flow anomaly (Haenel, 1971) and the geoid undulations (Groten and Rummel, 1974) reflect the elevated and anomalous crust-mantle transition in the southern part of the Rhinegraben. A low-resistivity layer of 25—30 Ωm is deduced inside the graben from geomagnetic (Winter, 1973, 1974) and magnetotelluric (Scheelke, 1974) observations at a depth of about 25 km which is not encountered at a distance of 45 km outside the graben (Haak and Reitmayr, 1974). These findings are supported by estimates of temperatures at a depth of 25 km in the Rhinegraben area (Mueller and Rybach, 1974). Values of 660 °C are found below the graben proper which exceed the temperatures below the Black Forest by 200 °C at the same depth. These results suggest again that the anomalous crust-mantle transition is confined to the graben proper.

In conclusion, the seismic investigations of the Rhinegraben rift system have established a detailed model of the crust and upper mantle in this area which differs

specificly from the neighbouring normal continental crust. A highly anomalous crust-mantle transition confined to the graben proper is superimposed on a regional uplift of the crust-mantle boundary.

The difference of velocity-depth models at the crust-mantle boundary within the graben proper and below the flanks suggests strongly that the lower crust and upper mantle below the Rhinegraben proper have a different composition than below the adjacent areas. The disappearance of the first-order discontinuity and the modification of the velocity gradient in the lower crust, both phenomena strictly confined to the graben, cannot be explained by heating and/or depressurization from local uplift. Mass intrusion from the upper mantle, differentiation, or phase transformations can be considered as possible causes for the observed phenomena.

Acknowledgements. The authors are indebted to R. Kind and G. Müller for critical comments and stimulating advice. Helpful discussions with J. Ansorge, A. Hirn, St. Müller, and L. Steinmetz are gratefully acknowledged. D. Bamford kindly provided the computer program for the time-term analysis. D. Emter and E. Peterschmitt kindly permitted the publication of unpublished record sections. Computation facilities were made available by the computer center of Karlsruhe University. The record sections were plotted at the Institut de Physique du Globe, Paris, and at the Computer Center of the Kernforschungszentrum Karlsruhe. During the interpretation J. B. Edel received a DAAD (Deutscher Akademischer Austauschdienst) fellowship at the University of Karlsruhe. The fieldwork was enabled by the support of the Institut National d'Astronomie et Géophysique of France, the German Research Association, and the Fond National Suisse de la Recherche Scientifique.

References

Ansorge, J., Emter, D., Fuchs, K., Lauer, J. P., Mueller, St., Peterschmitt, E.: Structure of the crust and upper mantle in the rift system around the Rhinegraben. In: Illies, H., Mueller, St. (eds.): Graben Problems, pp. 190–197. Stuttgart: Schweizerbart 1970

Bamford, D.: Refraction data in western Germany — a time-term interpretation. Z. Geophys. *39*, 907–927, 1973

Demnati, A., Dohr, G.: Reflexionsseismische Tiefensondierungen im Bereich des Oberrheintalgrabens und des Kraichgaues. Z. Geophys. *31*, 229–245, 1965

Dix, C. H.: Seismic velocities from surface measurements. Geophysics *20*, 68–86, 1955

Dohr, G.: Zur reflexionsseismischen Erfassung sehr tiefer Unstetigkeitsflächen. Erdöl, Kohle *10*, 278–281, 1957

Dohr, G.: Beobachtungen von Tiefenreflexionen im Oberrheingraben. Abh. Geol. Landesamt Baden-Württemberg *6*, 94–95, 1967

Dohr, G.: Reflexionsseismische Messungen im Oberrheingraben mit digitaler Aufzeichnungstechnik und Bearbeitung. In: Illies, H., Mueller, St. (eds.): Graben Problems, pp. 207–218. Stuttgart: Schweizerbart 1970

Emter, D.: Ergebnisse seismischer Untersuchungen der Erdkruste und des obersten Erdmantels in Südwestdeutschland. Dissertation, Univ. Stuttgart, 108 p., 1971

Förtsch, O.: Analyse der seismischen Registrierungen der Großsprengung bei Haslach im Schwarzwald am 28. April 1948. Geol. Jahrb. *66*, 65–80, 1951

German Research Group for Explosion Seismology: Crustal structure in western Germany. Z. Geophys. *30*, 209–234, 1964

Giese, P., Stein, A.: Versuch einer einheitlichen Auswertung tiefenseismischer Messungen aus dem Bereich zwischen der Nordsee und den Alpen. Z. Geophys. *37*, 237–272, 1971

Groten, E., Rummel, R.: Improved gravimetric geoid for $7° \leq \lambda \leq 12°$ (E) and $48° \leq \phi \leq 54°$ (N). Allgem. Vermessungsnachr., in press, 1974

Haak, V., Reitmayr, G.: The distribution of electrical resistivity in the Rhinegraben area as determined by telluric and magnetotelluric methods. In: Illies, H., Fuchs, K. (eds.): Approaches to Taphrogenesis, pp. 366–369. Stuttgart: Schweizerbart 1974

Haenel, R.: Bestimmungen der terrestrischen Wärmestromdichte in Deutschland. Z. Geophys. *37*, 119–134, 1971

Hirn, A., Perrier, G.: Deep seismic sounding in the Limagne graben. In: Illies, H., Fuchs, K. (eds.).: Approaches to Taphrogenesis, pp. 329–340. Stuttgart: Schweizerbart 1974

Hirn, A., Steinmetz, L., Kind, R., Fuchs, K.: Long range profiles in western Europe: II. Fine structure of the lower lithosphere in France (southern Bretagne). Z. Geophys. *39*, 363–384, 1973

Landisman, M., Mueller, S.: Seismic studies of the earth's crust in continents. II.: Analysis of wave propagation in continents and adjacent shelf areas. Geophys. J. *10*, 539–554, 1966

Lauer, J. P., Peterschmitt, E.: Ondes réfléchies des explosions des Bagenelles et de St. Nabor (Vosges, France). Proc. 10th Gen. Ass. Europ. Seismol. Comm. (Leningrad 1968) Acad. Sciences USSR, Moscow, 444–453, 1970

Meissner, R., Berckhemer, H.: Seismic refraction measurements in the northern Rhinegraben. Abh. Geol. Landesamt Baden-Württemberg *6*, 105–108, 1967

Meissner, R., Berckhemer, H., Wilde, R., Poursadeg, M.: Interpretation of seismic refraction measurements in the northern part of the Rhinegraben. In: Illies, H., Mueller, St. (eds.): Graben Problems. pp. 184–190. Stuttgart: Schweizerbart 1970

Meissner, R., Vetter, U.: The northern end of the Rhinegraben due to some geophysical measurements. In: Illies, H., Fuchs, K. (eds.): Approaches to Taphrogenesis, pp. 236–243. Stuttgart: Schweizerbart 1974

Menard, H. W.: Epeirogeny and plate tectonics. EOS Trans. AGU *54*, 1244–1255, 1973

Mueller, St., Landisman, M.: Seismic studies of the earth's crust in continents. I.: Evidence for a low-velocity zone in the upper part of the lithosphere. Geophys. J. *10*, 525–538, 1966

Mueller, St., Peterschmitt, E., Fuchs, K., Ansorge, J.: The rift structure of the crust and the upper mantle beneath the Rhinegraben. Abh. Geol. Landesamt Baden-Württemberg *6*, 108–113, 1967

Mueller, St., Peterschmitt, E., Fuchs, K., Ansorge, J:. Crustal structure beneath the Rhinegraben from seismic refraction and reflection measurements. Tectonophysics *8*, 529–542, 1969

Mueller, St., Peterschmitt, E., Fuchs, K., Emter, D., Ansorge, J.: Crustal structure of the Rhinegraben area. In: Mueller, St. (ed.): Crustal structure based on seismic data. Tectonophysics *20*, 381–392, 1973

Mueller, St., Rybach, L.: Crustal dynamics in the central part of the Rhinegraben. In: Illies, H., Fuchs, K. (eds.): Approaches to Taphrogenesis, pp. 379–388. Stuttgart: Schweizerbart 1974

Prodehl, C.: Struktur der tieferen Erdkruste in Südbayern und längs eines Querprofiles durch die Ostalpen, abgeleitet aus refraktionsseismischen Messungen bis 1964. Boll. Geofis. Teor. Appl. *7*, 35–88, 1965

Reich, H., Schulz, G. A., Förtsch, O.: Das geophysikalische Ergebnis der Sprengung von Haslach im südlichen Schwarzwald. Geol. Rundschau *36*, 85–96, 1948

Rhinegraben Research Group for Explosion Seismology: The 1972 seismic refraction experiment in the Rhinegraben. – First results. In: Illies, H., Fuchs, K. (eds.): Approaches to Taphrogenesis, pp. 122–137. Stuttgart: Schweizerbart 1974

Rothé, J. P.: Quelques expériences sur la structure de la croûte terrestre en Europe occidentale. In: Ingerson, E.: (ed.) Contributions in Geophysics in Honor of Beno Gutenberg, pp. 135–151. Oxford: Pergamon Press 1958

Rothé, J. P., Peterschmitt, E.: Étude sismique des explosions d'Haslach. Ann. Inst. Phys. Globe Strasbourg *5,3*, 3–28, 1950

Scheelke, I.: Models for the resistivity distribution from magneto-telluric soundings. – In: Illies, H., Fuchs, K. (eds.): Approaches to Taphrogenesis, pp. 362–365, Stuttgart: Schweizerbart 1974

Schulz, G.: Reflexionen aus dem kristallinen Untergrund des Pfälzer Berglandes. Z. Geophys. *23*, 225–235, 1957

Stewart, S. W.: Seismic ray theory applied to refraction surveys of the earth's crust in Missouri. Ph. D. Thesis, St. Louis University, St. Louis, Missouri, USA, 189 p., 1966

Winter, R.: Der Oberrheingraben als Anomalie der elektrischen Leitfähigkeit, untersucht nit Methoden der erdmagnetischen Tiefensondierung. Diss., Univ. Göttingen, 117 p., 1973

Winter, R.: A model for the resistivity distribution from geomagnetic depth soundings. In: Illies, H., Fuchs, K. (eds.): Approaches to Taphrogenesis, pp. 369–375. Stuttgart: Schweizerbart 1974

J. B. Edel
Institut de Physique du Globe
5, rue René Descartes
F-67 Strasbourg
France

K. Fuchs
C. Gelbke
C. Prodehl
Geophysikalisches Institut
der Universität
D-7500 Karlsruhe, Hertzstr. 16
Federal Republic of Germany

J. Geophys. 41, 357–366, 1975

Faeroe Islands - a Microcontinental Fragment?

U. Casten

Ruhr-University of Bochum

P. Hedebol Nielsen

University of Aarhus

Received February 11, 1975

Abstract. The crust between the continental blocks of Europe and Greenland has a complex structure. Ridges, banks and abyssal plains in between are the dominant features, and different types of crustal structure have been investigated.

During summer 1972 the North Atlantic Seismic Project has been carried out with the aim to investigate the oceanic area between Scotland and Iceland. Thereby the results of refraction experiments on the Faeroe shelf show that the crust beneath the Faeroes essentially differs in two respects from the typical oceanic crust under deep sea basins and the anomalous crust beneath Iceland and the Iceland-Faeroe Ridge: (i) Two P_g-phases with velocities of 5.3 km/s and 6.1 km/s are typical for a metamorphic and granitic basement. (ii) Submoho P_n phases have apparent velocities from 7.1 km/s to 8.3 km/s and time terms of more than 3 s giving a depth to moho of more than 30 km. This means the crust is more like the continental type.

The Faeroes may be interpreted as a continental fragment like Rockall Bank and the western part of Vøring Plateau being left behind during the opening of the North Altantic in Tertiary.

Key words: Continental Fragments – North Atlantic Seismic Project – Time Term Analysis – Continental Type of Crust.

1. Introduction

The opening of the north-eastern part of the North Atlantic in Tertiary has left behind a crust between the continental blocks of Europe and Greenland, which shows a complex structure. The dominant features are expressed in the topography of the ocean floor and are determined by ridges and banks with abyssal plains in between. Fig. 1 shows the bathymetric contours of the sea between Northern Europe and Greenland.

Lying perpendicular to the Midatlantic Ridge and more or less parallel to the fracture zone of Jan Mayen the Iceland-Faeroe Ridge connects the plateau of Iceland with the Faeroe Bank. The velocity-depth distribution of the ridge corresponds partly to that of Iceland and is neither of the oceanic nor the continental type (Bott *et al.*, 1971).

The results of gravity surveys between Iceland and the Faeroes show lateral changes in crustal density. The Bouguer anomalies on the ridge have values up to 100 mgal and on the Faeroe shelf about 30 mgal. According to Bott *et al.* (1971) the crust under the Faeroes is less dense and thicker than the crust of the ridge. A half circular shaped anomaly north-west of the Faeroes with high positive values is supposed to be effected by the existence of a continental margin.

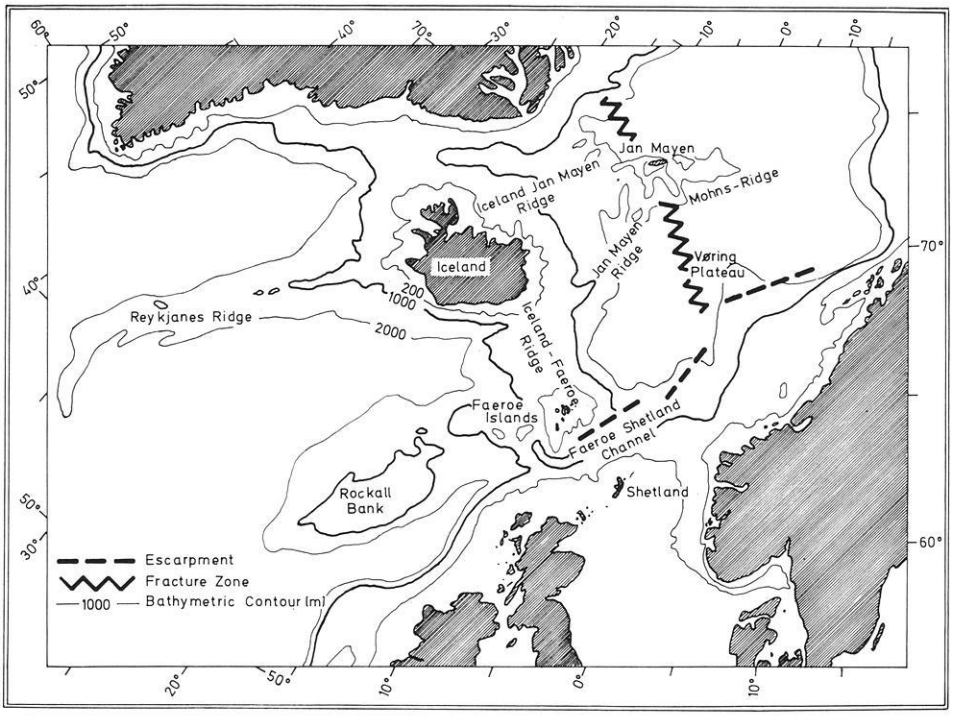

Fig. 1. The Atlantic ocean between Northern Europe and Greenland illustrating the complex structure of the ocean floor

The uppermost structure of the Faeroe Islands has a similarity with Iceland (Pálmason, 1965). Thick layers of basaltic lavas, radiometrically dated at 50 to 60 m. y. (Tarling and Gale, 1968), cover the substratum. Moreover the observation of refracted waves travelling with a velocity of about 6 km/s in a depth of 4 to 6 km has given reason for the supposition that sialic material underlies the basalts of the islands (Casten, 1970, 1973). Schrøder (1971) has interpreted low values of gravity by the presence of material with lower density.

Geophysical investigations (Talwani and Eldholm, 1972) have traced a burried marginal escarpment from Voring Plateau in the Norwegian Sea down to the Faeroe-Shetland Channel. Its basement dips towards the continental shelf. Seismic soundings on the Vøring Plateau show parallel to it an uplift of lower crust (Hinz, 1972). Thus the part of the Vøring Plateau west of the escarpment is supposed to be a continental fragment. Rockall Bank south of the Faeroes shows a crustal thickness of more than 30 km. The structure of this part of the crust can be interpreted as typical for the continental type (Bott and Watts, 1970).

2. Deep Seismic Sounding

During summer 1972 the international North Atlantic Seismic Project has been carried out to investigate the deeper structure of the water covered area between Scotland and Iceland. The project was proposed, planned, and organized by the

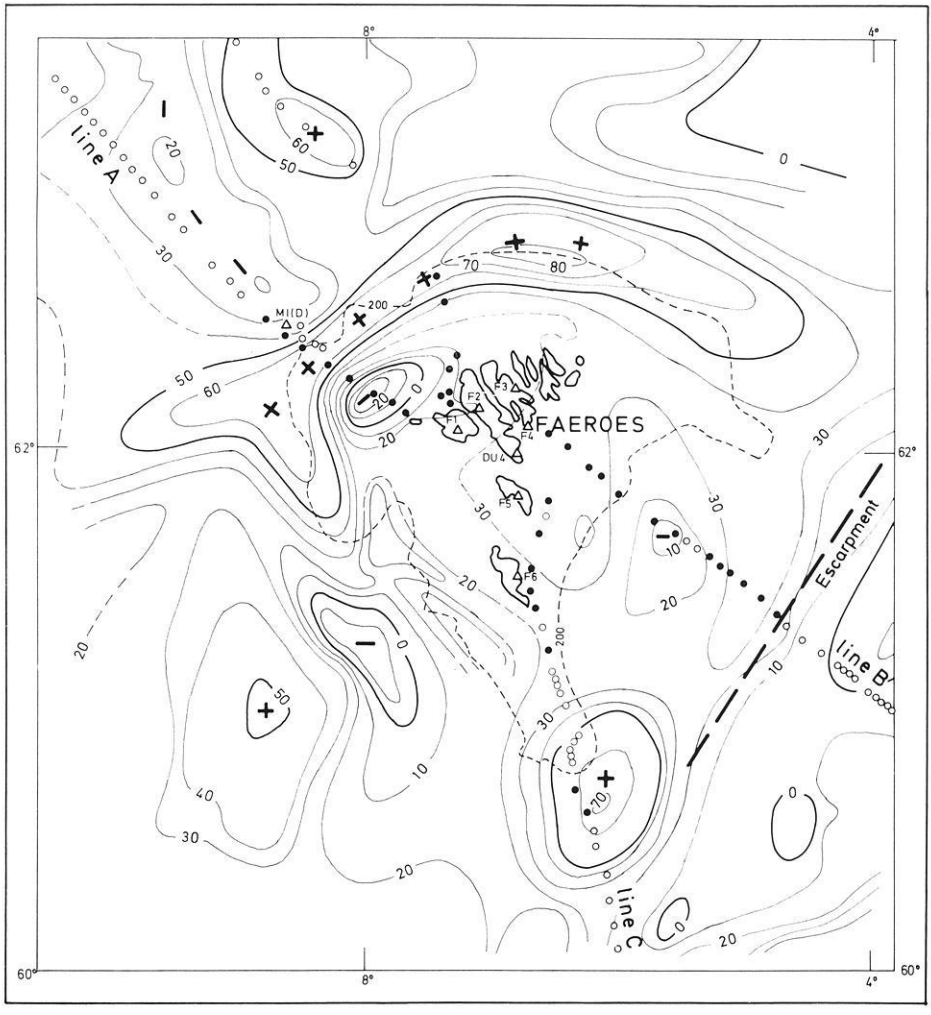

Fig. 2. Map showing the free-air anomalies (in mgal) from the area around the Faeroe Islands together with the shotpoints and stations of the North Atlantic Seismic Project

Department of Geological Sciences, University of Durham, including the participation of institutes from several countries. Shots with charges of 300 lbs, 600 lbs, and in some cases of 1200 lbs, were fired at sea and the seismic signals recorded by stations on land and additionally by two marine stations. Three of the shotlines were connected with the Faeroe Islands (Fig. 2). Line A was fired from the Faeroes to Iceland, line B from the Faeroes to Shetland, and line C from Scotland to the Faeroes and north of the islands.

The position of shots near the islands has been chosen with respect to the gravity anomalies of interest. So line A runs over a local minimum of about —20 mgal near the islands and then crosses the above mentioned maximum of more than +60 mgal. Line B runs over a minimum which is effected by sediments, and line C crosses a maximum of unknown origin.

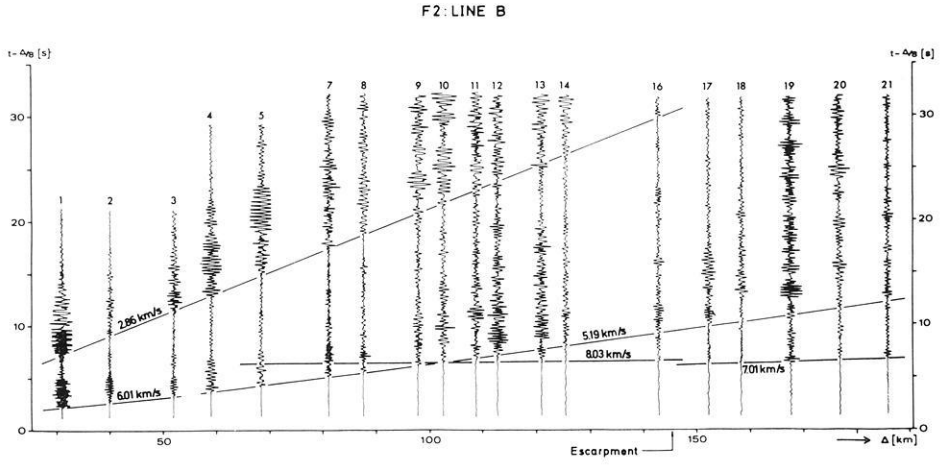

Fig. 3. Seismogram section from line B in reduced time scale (reducing velocity is 8 km/s) with straight line correlations. Signal numbers are the shotpoints

Altogether seven recording stations were placed on the Faeroes. Six stations (F1 to F6) using MARS 66 equipment were provided by the Aarhus University in cooperation with the Universities of Copenhagen, Hamburg and Kiel. One station (DU4) was provided by the Durham University. A hydrophone station (MI(D)) was placed north-west of the islands. The stations on the Faeroes and also on Iceland and Shetland successfully recorded signals from shots on the Faeroe shelf (bold dots on map of Fig. 2). The hydrophone station recorded signals only from shots on line A.

The inspection of seismograms showed that valuable information is given in most cases by first arrivals. Later ones with strong amplitudes are due to shear waves. As an example Fig. 3 shows the seismogram section with a reduced time scale containing signals from shotline B recorded at station F2. Correlating the P-arrivals four apparent velocities are derived: 6.01 km/s, 5.19 km/s, 8.03 km/s, and 7.01 km/s. By correlation of the *S*-arrivals a velocity of 2.86 km/s is derived. In a preliminary paper (Bott *et al.*, 1974) a velocity of 8.87 km/s instead of 8.03 was reported.

The change in velocity between shot 3 and 4 from a higher *P*-velocity to a lower one has been observed also in the seismogram sections from other stations. A second change in velocity occurs between shot 16 and 17. Shot 16 is located west of the escarpment and shot 17 east of it. The escarpment forms the edge of the Faeroe shelf in this part of the sea.

3. *Velocity Distribution*

The histogram in Fig. 4 shows the distribution of apparent *P*-wave velocities according to all the measurements on the Faeroe shelf and on the islands made up to now and including the results of the North Atlantic Seismic Project. The velocities have been calculated from distances and traveltimes using a least square method. Together five phases from different layers can be separated:

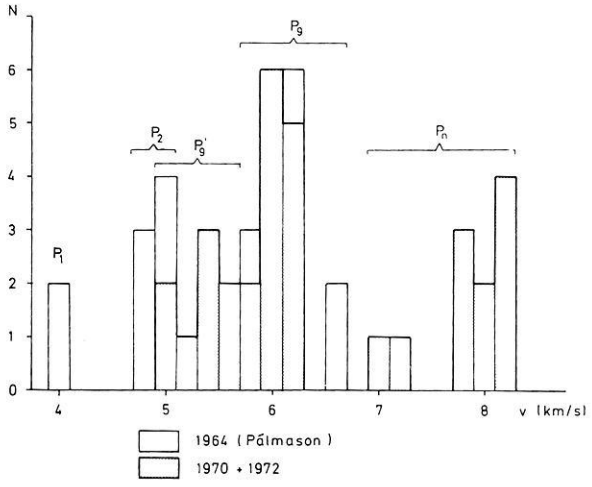

Fig. 4. Histogram of apparent P-velocities for the Faeroe Islands and the shelf. Pálmason's values have been obtained on land and the others on profiles at sea. The distribution is separated into phases from different layers

P_1, velocity 4.0 km/s, corresponds to the upper basalt layer being found only on the Faeroe islands above sea level.

P_2, velocity 4.9 km/s, corresponds to the middle and lower basalt layer and is found only on the islands. Due to a corresponding. S_2-phase,velocity 2.86 km/s, observed on line B and a S_2-phase, velocity 2.57 km/s, observed on an earlier profile north of the islands (Casten, 1974) it is supposed that the middle and lower layer – or at least the lower – are present in the shelf area around the islands.

P_g', average velocity 5.3 km/s, is observed on line B and on the south-eastern part of line C (C_{SE}). This phase corresponds to a layer below the known basalts.

P_g, velocity 6.1 km/s, is observed on line A, on the north-western part of line C (C_{NW}), and on the first part of line B. The corresponding layer also is situated beneath the basalts.

P_n, observed on line A, B, C_{NW}, and C_{SE}, is separated into two groups – 7.1 km/s and 8.0 km/s – yet it corresponds to one layer as it is controlled by two-way observation. This layer is situated in greater depth and has a downdip towards the centre of the Faeroes.

The P_1- and P_2-phase are known also from Iceland. The phases in the histogram with a velocity of 6.6 km/s are observed on short profiles on land only and therefore are quite uncertain. They correspond to a layer with the velocity of 6.4 km/s on Iceland (Pálmason, 1971). This has given reason for the assumption that the crustal structure of the Faeroes is similar to that of Iceland. However, this statement seems to hold only for the uppermost part of the crust built up by the Tertiary flood basalts. The lower crust beneath the Faeroes and the lower crust beneath Iceland differ essentially from one another because a 6.4 km/s or 6.6 km/s has not been observed in the shelf area of the Faeroes.

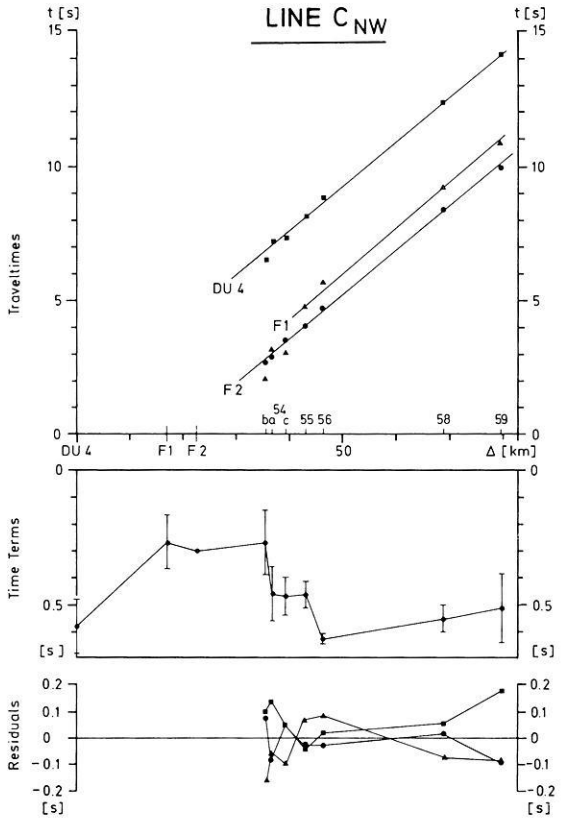

Fig. 5. P_g-traveltimes (upper part) from line C_{NW} observed at the stations DU4, F1 and F2 together with time terms and residuals (lower part). Least square calculation of apparent velocities yield: 5.93 ± 0.08 km/s (DU4), 5.96 ± 0.12 km/s (F1), and 6.04 ± 0.09 km/s (F2)

4. *Time Term Analysis and Crustal Model*

Traveltimes (corrected for water depth) of the phases P_g', P_g and P_n together with distances have been analysed using the time term method described among others by Willmore and Bancroft (1960) and Berry and West (1966).

The results for the P_g'-data from the southern shelf area give velocities in the range from 5.3 km/s to 5.5 km/s. This is distinctly more than 4.9 km/s of P_2 and distinctly less than the 6.1 km/s of P_g. That means, there must be a difference in the structure of the upper crust between the southern and northern part of the Faeroe shelf. It is to be seen from the change in velocity between shot 3 and 4 on line B. The calculation of P_g'-time terms has not been possible because of the too large error in velocity.

The analysis of P_g-data from the northern shelf region (line A and line C_{NW}) results in a velocity of 6.12 ± 0.14 km/s and time terms varying from 0.3 s to 0.9 s. Fig. 5 contains traveltimes, time terms, and residuals for line C_{NW} and Fig. 6 the same for line A. The comparatively high time term of 0.9 s belongs to shot 3 on line A, beeing situated in the centre of the gravity minimum west of the islands.

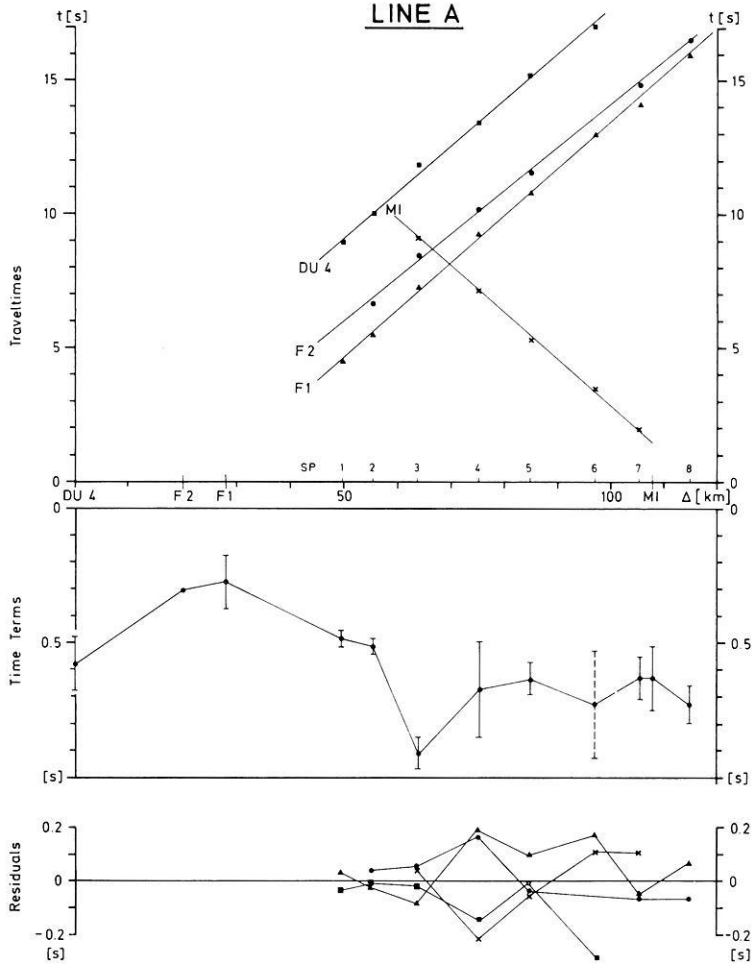

Fig. 6. P_g-traveltimes (upper part) from line A observed at the stations DU4, F2, F1 and MI together with time terms and residuals (lower part). Apparent velocities are: 6.13 ± 0.17 km/s (DU4), 6.18 ± 0.12 km/s (F2), 5.98 ± 0.08 km/s (F1), and 6.11 ± 0.26 km/s (MI)

It can be shown by calculation of gravity models that the delay in travel time is caused by a trough filled with sediments (Fleischer, 1971; Casten, 1974). A connection between time terms and the gravity maximum cannot be revealed. Due to the P-wave velocity of 4.9 km/s in the upper layer the time terms give values for the depth varying between 2 km under the stations and 5 km under the shotpoints.

Assuming a constant P_n-velocity in the shelf area around the islands the analysis of P_n-data from shot lines A, B and C yields values of 7.61 ± 0.22 km/s for P_n. Fig. 7 contains the time term values for the different lines. In the northern shelf area (line C_{NW} and line A) the values vary between 2 s and 3 s. In the southern area (line C_{SE} and line B) the time terms have values between 3 s and 4 s. Assuming a constant average velocity for the crust the refractor on these lines will be situated at a greater depth than north of the islands but be at the same depth when assuming a higher

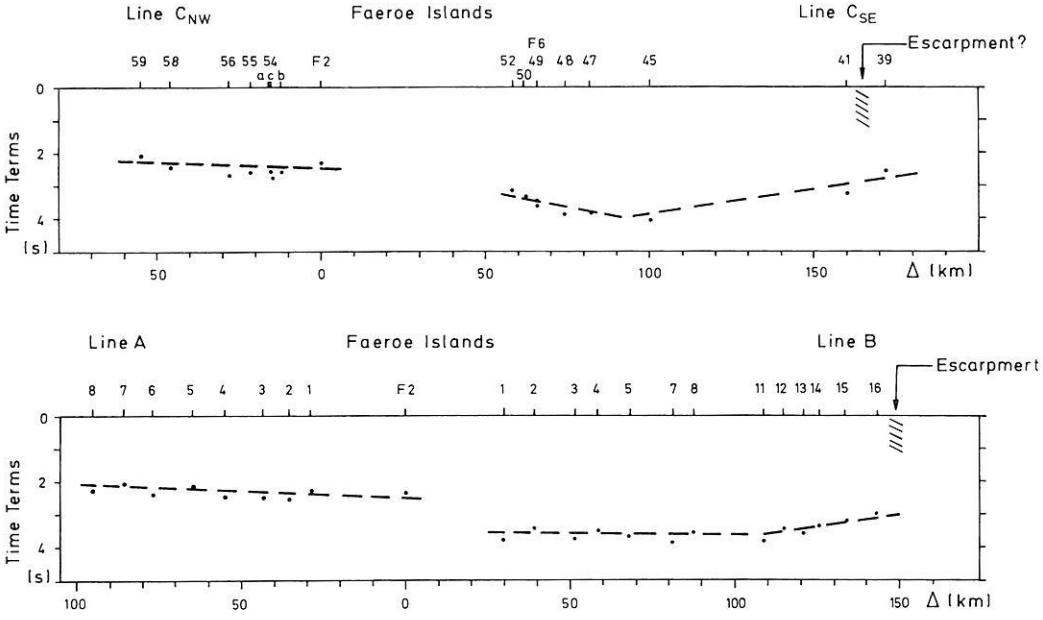

Fig. 7. P_n-time terms from the lines C_{NW}, C_{SE}, A and B arranged in two sections with station F2 as center point. Traveltimes have been used from stations on Iceland, the Faeroes and Shetland

average velocity. Taking into account the lateral change in P_g-velocities a lateral change in average velocity for the crust is very probable. In any case the refractor shows a raise towards the Iceland-Faeroe Ridge in the north-west and towards the Faeroe-Shetland Channel in the south-east. There it may be connected with the escarpment at the edge of the shelf. Line B crosses the escarpment between shot 16 and 17 and line C_{SE} possibly between shot 41 and 39.

A model of the crust showing a good fit between calculated and observed traveltimes is the following one: A surface layer with a thickness of 6 km and a velocity of 4.9 km/s covers the basement. This basement has a velocity of 6.1 km/s beneath the islands and northern shelf and a velocity of 5.3 km/s beneath the southern shelf. The average value for the crust beneath line B and line C_{SE} is 6.0 km/s and it is 6.5 km/s for the crust beneath line A and line C_{NW}. With these values the crust-mantle boundary is at a depth of more than 30 km beneath the islands and at about 20 km beneath the ridge and the escarpment.

5. Discussion

Two results give reason for the assumption that the properties of the crust beneath the Faeroes may be similar to those of a continental one:

The two P_g-phases with velocities of 5.3 km/s and 6.1 km/s, which are typical for a metamorphic and a granitic basement.

The sub-moho phase has apparent velocities from 7.1 km/s to 8.3 km/s which are results of a raise of 'moho' from about 30 km under the islands to about 20 km under the ridge and the escarpment.

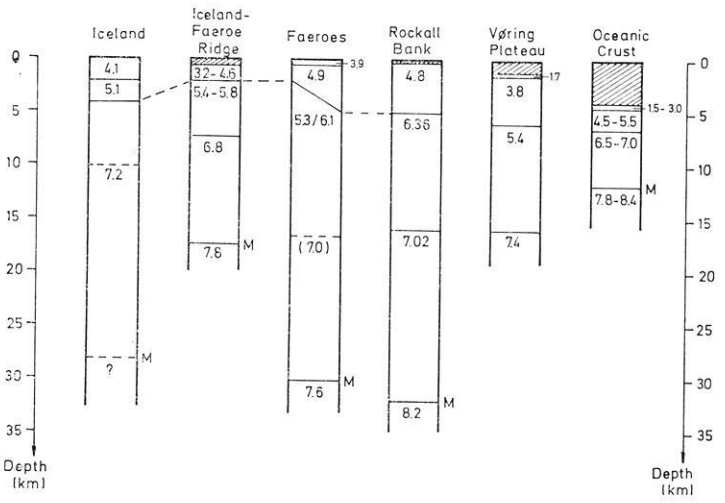

Fig. 8. Crustal structure of the Faeroes in comparison with results of deep seismic soundings in the North Atlantic. The Oceanic Crust is an average of results from different positions (Ewing and Ewing, 1959)

As the P_n-velocity of 7.6 km/s is less than normally observed on continents a classification of the Faeroe's crust as typical continental is not correct. Assuming this crustal element being a continental one before the opening of the North Atlantic ocean in Tertiary we find that the split up and then following drift of the continental blocks of Europe and Greenland must have effected a change of properties mostly in the transition zone between crust and upper mantle. This possibly explains the lower P_n-velocity. The conception of a continental fragment is in accordance with the gravity anomalies. The lower density of crust is effected by sialic material, and the greater thickness of crust beneath the Faeroes has been demonstrated clearly by the refraction measurements.

Another argument for the continental fragment is given by the Pre-tertiary distribution of continents in the area of the present North Atlantic ocean. Trying to achieve a best fit of the continental margins of Europe and Greenland, as it is done by Bott and Watts (1970), a continental crust is required under the Faeroes and also under Rockall Bank, because both together remain as a gap between the margins.

When comparing seismic results from different areas in the North Atlantic, as it is shown in Fig. 8, one may get the following picture: Neglecting the overlying water and sediments Iceland, the Iceland-Faeroe Ridge, the Faeroes, Rockall Bank, and the typical oceanic crust have near the surface of the crust basaltic material. The deeper crust is different. There is on one side the oceanic crust of deep sea basins, the continental crust of Rockall Bank, and the seaward fragment of Vøring Plateau, and on the other side the anomalous crust of Iceland and the Iceland-Faeroe Ridge. Clearly the structure of the Faeroe's crust corresponds to that of Rockall Bank and Vøring Plateau.

An apparent velocity of 7.0 km/s for the Faeroes, shown in Fig. 8, was observed at the stations F1 and F2 only from shot line A, on a profile section of the ridge (100 to 180 km). Using the calculated intercept time for the Faeroes the corresponding

refractor is to be placed at a depth between 15 and 20 km. Its existence under the Faeroe shelf could not be proofed, yet similar refractors are present under Rockall Bank and Vøring Plateau.

The final conclusion is, that the deep seismic sounding in the area of the Faeroe Islands have made it possible to consider the crust beneath the islands as a micro-continental fragment left behind under the opening of the North Atlantic in Tertiary.

Acknowledgements. Financial support was given by the Natural Environment Research Council to the UK contribution, by the Statens Naturvidenskabelige Forskningsråd to the Danish contribution, and by the Deutsche Forschungsgemeinschaft to the German contribution. We are grateful to all the colleagues who took part in the project, to Prof. S. Saxov for organizing the field campaign on the Faeroe Islands, and to Prof. M. H. P. Bott for placing material at our disposal.

References

Berry, M. J., West, G. F.: A time-term interpretation of the first-arrival data of the 1963 Lake Superiour experiment. In: The earth beneath the continents. Steinhart, J. S., Smith, T. J. eds. Am. Geophys. Un., Geophys. Monograph *10*, 166–180, 1966

Bott, M. H. P., Sunderland, J., Smith, P. J., Casten, U., Saxov, S.: Evidence for continental crust beneath the Faeroe Islands. Nature *248*, 202–204, 1974

Bott, M. H. P., Browitt, C. W. A., Stacey, A. P.: The deep structure of the Iceland-Faeroe Ridge. Marine Geophys. Res. *1*, 328–351, 1971

Bott, M. H. P., Watts, A. B.: Deep structure of the continental margin adjacent to the British Isles. In: Delany, F. M. (Ed.), ICSU/SCOR Working Party 31 Symposium, Cambridge 1970: The geology of the East Atlantic continental margin. 2. Europe. Rept. No. 70/14, Inst. geol. Sci., 90–109, 1971

Casten, U.: Eine Analyse seismischer Registrierungen von den Färöer Inseln. Hamburger Geophysikalische Einzelschriften, Heft 21, 1974

Casten, U.: The crust beneath the Faeroe Islands. Nature Phys. Sci. *241*, 83–84, 1973

Ewing, J., Ewing, M.: Seismic refraction measurements in the Atlantic Ocean basins, in the Mediterranean Sea, on the Midatlantic Ridge, and in the Norwegian Sea. Bull. Geol. Soc. Am. *70*, 291–318, 1959

Fleischer, U.: Gravity surveys over the Reykjanes Ridge and between Iceland and the Faeroe Islands. Marine Geophys. Res. *1*, 314–327, 1971

Hinz, K.: Der Krustenaufbau des Norwegischen Kontinentalrandes (Vøring Plateau) und der Norwegischen Tiefsee zwischen 66° und 68° N nach seismischen Untersuchungen. Meteor Forsch.-Ergebnisse C, 10, 1–16, 1972

Pálmason, G.: Crustal structure of Iceland from explosion seismology. Soc. Sci. Islandica, Reykjavik 1971

Pálmason, G.: Seismic refraction measurements of the basalt lavas of the Faeroe Islands. Tectonophysics *2*, 475–482, 1965

Schrøder, N. F.: Magnetic anomalies around the Faeroe Islands. Ann. Soc. Sci. Faeroensis *19*, 20–29, 1971

Talwani, M., Eldholm, O.: Continental margin off Norway: A geophysical study. Bull. Geol. Soc. Am. *83*, 3575–3606, 1972

Tarling, D. H., Gale, N. H.: Isotopic dating and paleomagnetic polarity in the Faeroe Islands. Nature *218*, 1043–1044, 1968

Willmore, P. L., Bancroft, A. M.: The time-term approach to refraction seismology. Geophys. J. *3*, 419–432, 1960

Dr. U. Casten
Institute for Geophysics
Ruhr-University of Bochum
D-4630 Bochum-Querenburg
Universitätsstraße 150
Federal Republic of Germany

P. Hedebol Nielsen
Laboratory for Geophysics
University of Aarhus
Finlandsgade 6
DK-8200 Aarhus N, Denmark

J. Geophys. 41, 367–384, 1975

A Seismic Reflection Method for Solving Engineering Problems

R. Schepers

Institut für Geophysik der Ruhr-Universität Bochum

Received November 15, 1974

Abstract. In this paper a seismic reflection technique capable of resolving thin near surface layers is described. The theoretical discussion is accompanied by a case history demonstrating the identification of four reflections within a time interval of 15 ms corresponding to a total depth of 8 m.

Body waves are generated by means of a thumber on the bottom of a small borehole thus suppressing the coherent noise in the reflection seismograms (*S*-waves and surface waves). The described digital recording system provides efficient suppression of the incoherent noise by means of an on-line averaging process. Its high dynamic range has enabled a successful application of processing techniques with the following features: The deconvolution of one-channel seismograms and the suppression of multiples are achieved by means of homomorphic filtering. Equally the wavelet emitted by the seismic source can be separated from an one-channel seismogram by means of homomorphic filtering. This wavelet can be used to yield the deconvolution of multi-channel seismograms by means of optimum inverse filtering.

Key words: Engineering Seismics – Reflection Method – Seismic Field Technique – Noise Suppression – Homomorphic Filtering – Deconvolution – Suppression of Multiples.

1. Introduction

In engineering geophysics seismic measurements can help to determine the physical and lithological properties of the uppermost part of the crust including depths of a few meters to at least 100 meters. These seismic measurements are generally carried out for civil engineering purposes, for the location of subsurface cavities and for hydrogeological and rock mechanical investigations. In case of delineating interfaces or locating faults and cavities these investigations are labelled 'structural'.

Until now for structural investigations the seismic refraction technique is commonly used. Certainly the refraction technique provides not only the depths of the different interfaces but also the velocities in each of the layers yet there are some cases where it fails:

i) The length of the geophone spread has to be about 5 times greater than the depth of the deepest refractor. Hence measurements within urban areas are difficult or rather impossible. Moreover, the interpretation of refraction measurements carried out by means of long geophone spreads leads to rough models of the subsurface or, supposing the geological situation is complicated, completely fails. This problem can partly be overcome by shooting overlapping profiles.

ii) A necessary assumption for the use of the refraction technique are velocities increasing with depth. If this assumption is not valid the interpretation will be erroneous to a great extent.

iii) Supposing only first arrivals are used for interpretation 'overshooting' of layers can occur (blind zone problem).

iv) Locating a subsurface cavity by means of the refraction technique may only be possible for the special case the refractor intersecting the cavity or passing closely underneath.

There are few attempts to make use of the seismic reflection technique (Meidav, 1969; Stoll, 1971) though it has many advantages and has proven to be a powerful tool in exploration geophysics. The reflection technique can be applied to all the problems mentioned above. This is partly due to the short geophone spread used in the reflection technique. A further advantage is the more detailed image yielded by means of the seismic reflection technique.

The difficulties in using the reflection technique for problems of engineering geophysics can be described as follows:

In exploration geophysics both the depth to the deepest reflector and the thickness of the thinnest layer are about 40 times greater than in engineering geophysics. Assuming the same layer thickness-to-wavelength ratio for both exploration and engineering geophysics means for the latter case the use of signals with dominant frequencies of about 1000 Hz. Supposing the use of a hammer or a thumber as source of the seismic signal the mentioned high frequencies cannot be produced in soil. As our experiments with different types of a hammer or a thumber and an electrical sparker buried in a water-filled borehole showed seismic signals received in a distance of 2 meters to the source contained frequencies in the range of 50 Hz to 800 Hz with dominant frequencies about 150 Hz. Furthermore the duration of the source pulses came to about 15 ms.

For very many cases this means that the two-way traveltime of the seismic waves concerning the near surface layers is shorter than the duration of the source pulse. Let us e.g. assume a depth of 50 meters for the deepest reflector and a spread length of 25 meters we then find all reflected *P*- and *S*-waves recorded within a time of 50 to 100 ms depending on the velocity distribution. Hence a reflection technique that takes into account only *P*-wave arrivals has to solve three problems. It is necessary:

i) to suppress the unwanted parts of the seismic signal, e.g. the arrivals of *S*-waves and surface-waves,

ii) to compress the source pulse,

iii) to be able to distinguish primaries from multiples.

The field technique and the digital recording facilities described in the first part of this paper provide an efficient tool for suppressing unwanted seismic signals. The second part of this paper describes a digital process for the deconvolution of the near-surface reflection seismograms and the suppression of multiples. This is illustrated by a case history at the end of each chapter.

2. Field Technique

2.1. The Digital Recording System

Among all possible processes of signal enhancement in near-surface reflection seismic the application of a deconvolution filter is essential. Provided the seismic signal has a broad frequency range and the signal-to-noise ratio is high this filter will

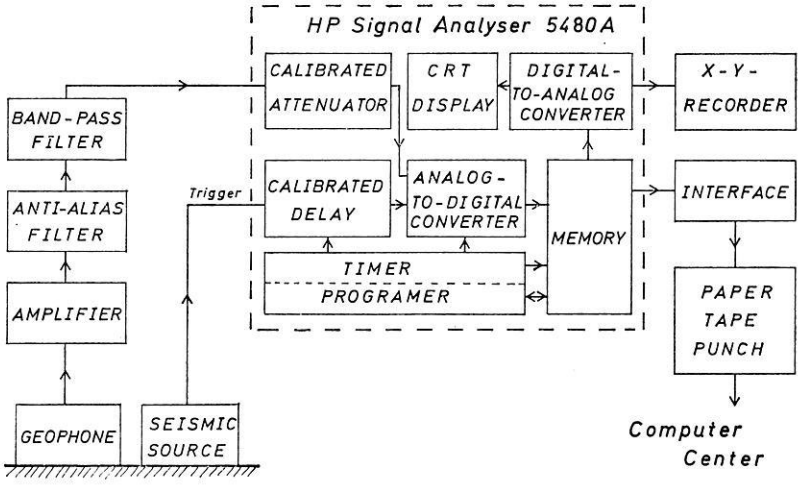

Fig. 1. Block diagram of the seismic recording system

be most effective. Consequently a highly resolved record is an essential condition for a broad frequency range used for the deconvolution process. Since no qualified recording system for near-surface reflection measurements is available Rüter[1] and Schepers designed a digital recording system which embodies further advantages beyond the great dynamic range of its stored data. This recording system improves the signal-to-noise ratio by means of an on-line averaging process. Fig. 1 shows a block diagram of the system. The recorded seismic signal is converted to digital data and stored in a magnetic core memory. Part of the hardware yields the averaging of repetitive signals and hence improves the signal-to-noise ratio and the resolution of the analogue-to-digital conversion. The resolution due to one process cycle is 54 dB. Doubling the number of process cycles improves the resolution for 6 dB and the signal-to-noise ratio for 3 dB. Hence the dynamic range of the digitally stored data is improved for 3 dB. Performing 16 process cycles means a dynamic range of 66 dB and an improvement of the signal-to-noise ratio for 12 dB. The digital-to-analogue converter provides a continuous display of the data on a CRT without flickering. So a signal improvement can be visually controlled. This holds during the run-down process of a cycle too. As the averaging process is executed in real-time this recording system provides an immense data reduction.

The memory of the used signal analyser allows the storage of 1000 24-bit words. It can be divided into quarters so that four different input signals can be processed simultaneously. In this case the minimum sampling rate of the used apparatus is 0.04 ms corresponding to a Nyquist frequency of 12.5 kHz being sufficient even for measurements in solid rock.

The final data can be plotted on an X-Y-recorder and punched on a tape. Further processing of the data is carried out in a computer center. In the final stage of system

1 Dipl. Geophys. H. Rüter, Institut für Geophysik, Schwingungs- und Schalltechnik der Westfälischen Berggewerkschaftskasse, Bochum, Herner Straße 45.

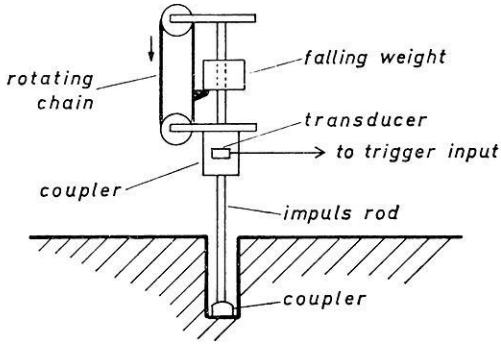

Fig. 2. Scheme of the seismic source

development all processes of signal enhancement should be done immediately in the field by means of a processor.

2.2. The Seismic Source

A thumber was designed to be employed either in vertical boreholes or on the surface. Fig. 2 shows a scheme of its construction. An electric motor drives a rotating chain lifting the weight. The dropping weight strikes a coupler on top of a rod causing a displacement of another coupler on the bottom of the borehole. Hence the second coupler emits body waves. As we want to produce an averaged seismic signal based on several weight-drops a reliable trigger signal is essential. After failure of many experiments we came to using a piezoelectric transducer shaped like a disc and cemented into the first coupler on top of the rod. The weight drop generated compressional wave in this coupler gives rise to a trigger pulse having an amplitude of roughly 1 V and a rise time of a few microseconds. The repetition rate of the weight drops is variable from 1 Hz to 0.2 Hz. The shape of the seismic pulse emitted by this source is reproduced very well.

2.3. Case History

2.3.1. The Test Site. Our first field experiments have taken place in the neighbourhood of the Bochum University within the 'Ruhrtal'. We generally shall refer to this site with the abbreviation 'BRT'. There are several arguments for choosing BRT as test site:

i) A few boreholes exist being drilled in connection with a survey for drinking-water. Hence the lithological sequence at some points of the area is well known. The data supplied by boreholes are given in Table 1.

ii) From the data given in Table 1 we can infer a sharp separation of the different layers and fairly flat reflectors.

iii) There exist three reflectors within a depth of 8 m. The two-way traveltime of *P*-waves within the different layers comes to only 5 ms on an average. However if the reflection technique will successfully be applied within the scope of engineering geophysics it should be possible to resolve reflections separated only a few milliseconds.

Table 1. Data supplied by boreholes

lithology	BRT1	BRT2	BRT3
sandy clay	0. −1.2 m	0. −2.0 m	0. −1.6 m
sand with fine gravel (dry)			1.6 −3.9 m
sand with fine gravel (wet)			3.9 −6.1 m
coarse gravel (dry)	1.2 −3.2 m	2.0−4.1 m	
coarse gravel (wet)	3.2 −8.1 m	4.1−7.0 m	6.1 −8.5 m
bedrock (shale, sandstone)	8.1 m−		8.5 m−

Table 2. *P*-wave velocities derived from refraction surveys

lithology	profile 1, 3 (BRT1,2)	profile 2	profile 4, 6	profile 5 (BRT3)
sandy clay	430 m/s	400 m/s	360 m/s	390 m/s
sand with fine gravel (dry)			690 m/s	
sand with fine gravel (wet)				1150 m/s
coarse gravel (dry)		850 m/s		
coarse gravel (wet)	1670 m/s			
bedrock (shale, sandstone)	3100 m/s	3200 m/s	3050 m/s	2950 m/s

On BRT test site six refraction surveys were carried out to yield information about the *P*-wave velocities in the different layers. The layers identified by means of drilling holes (c.f. Table 1) and their corresponding velocities are listed in Table 2. The results indicate that all refraction surveys contain the effect of 'overshooting' one layer causing an erroneous calculation of the depth to the bedrock. So e.g. a straigthforward interpretation of the refraction data on site BRT1 results in a depth of 6.3 m to the bedrock instead of 8.1 m derived from the drilling survey.

2.3.2. Field Procedure and Results. For a model corresponding to site BRT1 theoretical traveltime curves were computed. Fig. 3 depicts the traveltime curves of the direct *P*- and *S*-wave, the reflected *P*-primaries and a surface wave having a velocity of 230 m/s. Supposing the length of the source pulse comes to at least 10 ms, the traveltime curves in Fig. 3 indicate that there is no favorable shot-to-geophone distance yielding a separation of the reflected primaries from one another or from other signal generated arrivals. For small shot-to-geophone distances the direct *P*-wave and the *S*-waves disturb the reflection arrivals. At a distance of 5 m the traveltime curves of the first two reflection arrivals cross over and refraction arrivals begin to emerge.

Supposing very shallow reflectors efficient attenuation of the surface wave seems to be important producing interpretable seismograms. Our field experiments have shown that a seismic source coupled to the soil on the bottom of a shallow borehole as described above has the advantage of diminishing the amplitude of the surface wave to a great extent. E.g. a reflection seismogram section containing 30 traces is given in Fig. 4. The source was at a depth of 2 m just on top of the gravel (c.f. Table 2). The geophones have been placed on the surface with distances between 0.2 m and 6 m to the epicentre. As site BRT2 lies 30 m apart a motor-road the on-line

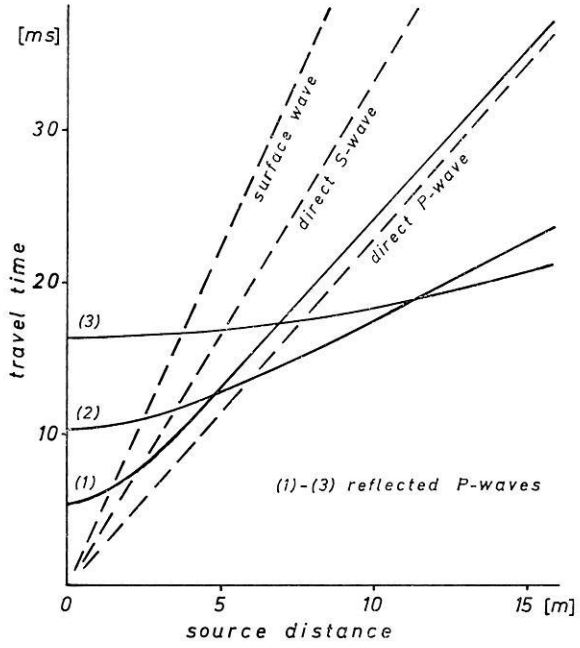

Fig. 3. Theoretical traveltime curves for site BRT1

averaging process of the recording system was used to suppress the traffic generated noise. As the amplitude of the surface wave in Fig. 4 is low for distances less than 3 m we can clearly correlate two reflected arrivals at different shot-to-geophone distances. The one found at distances between 0.2 m and 2.0 m is due to the *P*-wave reflected by the ground water surface; the other one existing at distances between 1.6 m and 3.8 m is due to the reflection by the bedrock. Though the reflected arrivals can clearly be separated the determination of the traveltime differences between the direct arrival and the reflected ones — being essential for computing layer thickness — is difficult. Despite of this traveltime estimations for the two reflected pulses agree well with the traveltimes computed from the available data at site BRT2.

Summarizing the results of our measurements we can say: Unprocessed reflection seismograms with clearly distinguishable reflection arrivals can be obtained even in cases where the two-way traveltime comes to only few milliseconds. Yet data processing seems to be necessary improving the resolution and making an exact interpretation possible.

3. Deconvolution and the Suppression of Multiples

Using a weight-drop on the bottom of a borehole is advantageous in so far as a geophone placed close to the epicentre receives only *P*-waves travelled upwards. (This statement is exactly valid in case of horizontally layered sequences). Hence the output of this geophone is a comparatively simple seismic signal and we expect signal enhancement processes to be less complicated and in due course more effective. E.g.

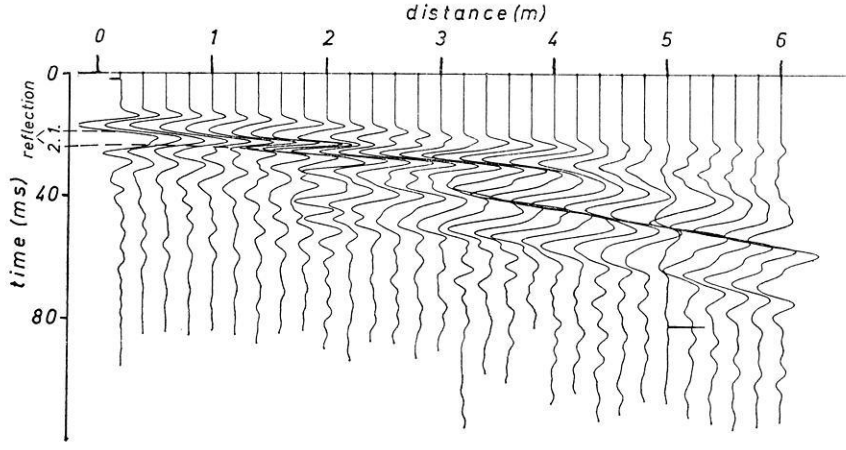

Fig. 4. Reflection seismogram recorded at site BRT2

in Fig. 4 the trace at the distance of 0.2 m should only contain vertically travelled *P*- waves. For the main part of this chapter we will discuss how to filter such one-channel reflection seismograms. The assumptions the filter design is based on are given in the first part of this chapter.

3.1. Synthetic Seismograms

Assuming the behaviour of the earth is describable as a linear system a seismic signal generally represents the convolution of a wavelet representing the source pulse with the unit impulse response of an elastic earth model. Furthermore perfect elasticity yields linear systems containing constant parameters. Given the case of vertically travelling *P*- waves in a horizontally layered subsurface computer programs for numerical solutions of the unit impulse response are simple (Robinson,1967; Schepers, 1972). Synthetic seismograms for such a model of the lithological sequence are derived from the convolution of a wavelet with the unit impulse response.

The computation of the synthetic seismogram is entirely based on plane-wave theory yet a correction of the spherical divergence of the wavefront can easily be included into the program. For practical applications we have to consider additional noise. Hence the synthetic seismogram $s(n)$ reads:

$$s(n) = w(n) * r(n) + v(n) * u(n)$$

where $w(n)$ represents the seismic wavelet, $r(n)$ represents the unit impulse response, $u(n)$ represents a white time series, and $v(n)$ represents the noise wavelet. It ought to be stressed that this representation of a seismic signal is not unique. Yet its usefulness will be appreciated by the degree of success in interpretating field seismograms. Two processes of signal enhancement shall be considered:

i) The separation of the unit impulse response from the wavelet, commonly termed as deconvolution.

ii) The suppression of multiples.

3.2. Homomorphic Deconvolution

Deconvolution can be performed by inverse filtering or by Wiener filtering, provided the shape of the seismic wavelet to be removed is known or the wavelet is a minimum-delay one and the unit impulse response of the subsurface layering is a white series (this means the autocorrelation $\Phi(\tau)=0$ except for $\tau=0$) (Robinson, 1967; Robinson and Treitel, 1967). Using predictive deconvolution (Peacock and Treitel, 1969) the only assumption is the unit impulse response to be a white series.

As in most cases we have at least one thin surface layer and hence the individual wavelets will overlap to a great extent we cannot expect to know the shape of the wavelet in near-surface reflection work. This is demonstrated by the reflection seismogram in Fig. 4. On the other hand the unit impulse response is far from being a white series because in near-surface reflection surveys we typically find a few reflectors with great reflection coefficients. Together with the reflection coefficient equal to 1 at the surface this leads to strong multiples. E.g. in the unit impulse response of Fig. 7 the only arrivals to be regarded as random ones are the three primary arrivals. All other arrivals mainly shaping the unit impulse response are deterministic.

Oppenheim (1965) has formulated the general theory for the synthesis of nonlinear filters for signals which can be expressed as a convolution of components. Known as homomorphic filtering this method has been applied by Oppenheim, Schafer and Stockham (1968) to image enhancement, echo removal and speech waveform processing. Ulrych (1971, 1972) has presented the application of homomorphic filters for the recovery of the seismic wavelet out of a time series formed by the convolution of this wavelet with a spike series. He used this method known as homomorphic deconvolution separating the seismic wavelet in earthquake seismograms.

Concerning our problem homomorphic filters have the considerable advantage that no assumption about the unit impulse response and the delay properties of the wavelet needs to be made. The theory and the principles of applying homomorphic filters have fully been dealt with by Oppenheim (1965) and Oppenheim *et al.* (1968) and considerations concerning their realisation on digital computers are given by Oppenheim *et al.* (1968) and Ulrych (1971). Here only a brief summary of the principles of homomorphic filtering shall be given.

The general principle of homomorphic filtering corresponds to transforming the original problem to a space where the components are added, and — after linear filtering — transforming the results back to the original space of inputs. According to this principle a homomorphic filter represents a cascade of three systems as shown in Fig. 5. The system D in Fig. 5 called the characteristic system is a nonlinear system transforming the input sequence $x(n)$ from a convolutional space to an additive space. The function $\hat{x}(n)$ being the output of the system D and the input of the system L is called the complex cepstrum. The system L is a linear system. The system D^{-1} shown in Fig. 5 is the inverse system to D, D^{-1} transforms the output $\hat{y}(n)$ of the

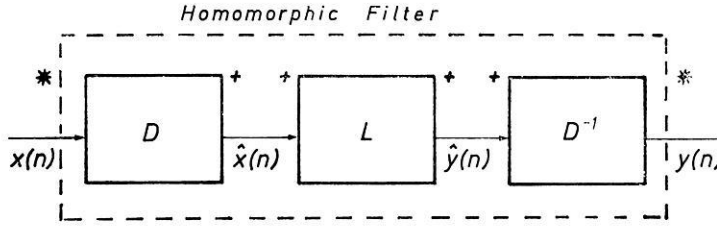

Fig. 5. Representation of homomorphic filtering as a cascade of three systems

system L from an additive space into a convolutional space. The characteristic system D remains the same for all filtering problems, only the linear system L has to be adapted. We find the system D successively consisting of the z-transform, the natural logarithm and the inverse z-transform. The system D^{-1} successively consists of the z-transform, the exponential function and the inverse z-transform.

Practical applications involve the use of finite time series. Each finite time series $s(n)$ is to be considered as the convolution of a minimum delay time series $s_1(n)$ with a maximum delay time series $s_2(n)$

$$s(n) = s_1(n) * s_2(n)$$

The complex cepstrum $\hat{s}_1(n)$ of $s_1(n)$ is zero for $n<0$ and the complex cepstrum $\hat{s}_2(n)$ of $s_2(n)$ is zero for $n>0$ (Oppenheim *et al.*, 1968; Schepers, 1972). Hence follows that the maximum delay and the minimum delay components of a signal are completely separated in the complex cepstrum.

How the actual separation of convolved components is carried out by the system L of Fig. 5, is illustrated by means of a simple example in Fig. 6. Time series (1) in Fig. 6 consists of two spikes separated only by four samples. This spike series represents a minimum delay time series whereas the wavelet (2) is a mixed delay one. The complex cepstrum (4) of the spike series (1) only contains non-vanishing amplitudes for $n \geqslant 4$. The value $n=4$ is due to the time difference between the two spikes in time series (1). On the other hand the main contribution of the wavelet (2) to the complex cepstrum (5) consists of values in the neighbourhood of $n=0$ and the amplitudes of the complex cepstrum decrease rapidly with increasing n. The system L separating the two components — spike series and wavelet — of time series (3) from the complex cepstrum (6) simply consists of multiplying the complex cepstrum (6) with two rectangular time windows I and W as indicated in Fig. 6. The two time windows are fully defined by the time t_c stating the latest time of the window W and the first time of the window I. Furtheron the time t_c shall be labelled 'cut-off time'.

In our example of Fig. 6 we have chosen a cut-off time $t_c = 3 \cdot \Delta t$ for separating the wavelet and the spike series. The outputs of the two different systems L are transformed back to the time domain by the system D^{-1}. The results are shown in Fig. 6. As some contribution of the wavelet (2) to the complex cepstrum (3) occurs for values $n \geqslant 4$ time series (7) does not reproduce perfectly the wavelet (2). Yet time series (8) is very much similar to the spike series (1).

Though the example given in Fig. 6 is simple the reflection response of the subsurface may be a very complex spike series. Nevertheless the wavelet $w(n)$ and the

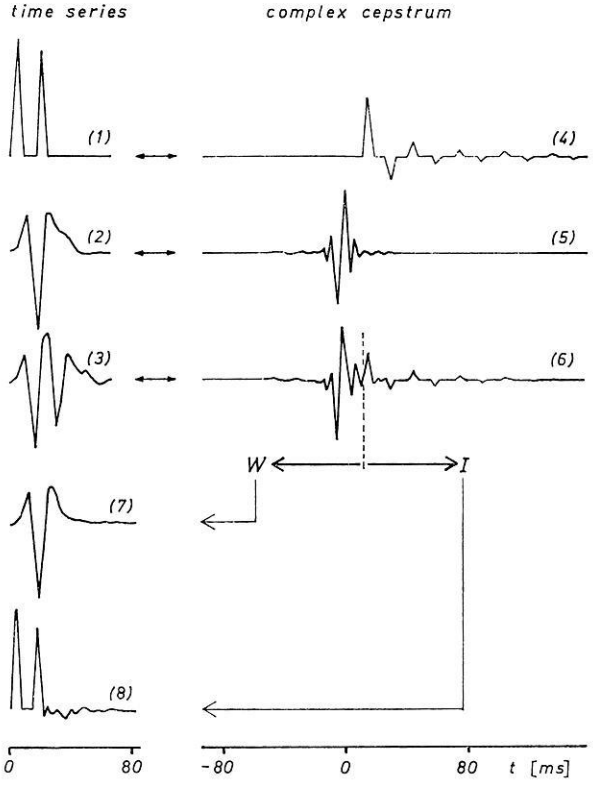

Fig. 6. The concept of the complex cepstrum as applied to homomorphic deconvolution. (1) impulse series with one echo, (2) wavelet, (3) convolution of (1) and (3), (4) (5) (6) complex cepstra of (1) (2) (3), (7) wavelet reconstructed from part W of (6), (8) impulse series reconstructed from part I of (6)

unit impulse response $i(n)$ of a real seismogram $x(n) = w(n) * i(n)$ are separable in the same way as illustrated above. Necessary conditions are the series $i(n)$ to be a minimum delay one and the time difference between the first two spikes to be sufficently great. The first condition can easily be fullfilled in seismic reflection surveys as spherical divergence causes the unit impulse response to be minimum delay in most cases. If this is not true the series $i(n)$ can be made into a minimum delay one by exponential weighting (Ulrych, 1971). The second assumption is more severe, because the lithological sequence often contains a thin surface layer with a reflection time of a few milliseconds. In these cases the separation of the wavelet may be impossible, but the identification of deeper reflection is not affected at all.

3.3. Suppression of Multiples

In the case of one layer over a halfspace the z-transform of the unit impulse response $r(n)$ can be written as follows (Robinson, 1967):

$$R(z) = (1 + cz^{-1}) / (1 - cz^{-1}) \tag{1}$$

where c is the reflection coefficient between the layer and the halfspace, and the two-way traveltime through the layer has been assumed to be one sampling rate. To compute the complex cepstrum $\hat{r}(n)$ of $r(n)$ we have to take the natural logarithm of $R(z)$:

$$\begin{aligned}
\ln R(z) &= \ln(1 + cz^{-1}) - \ln(1 - cz^{-1}) \\
&= cz^{-1} - (c^2/2)z^{-2} + (c^3/3)z^{-3} - (c^4/4)z^{-4} + (c^5/5)z^{-5} + \ldots \\
&+ cz^{-1} + (c^2/2)z^{-2} + (c^3/3)z^{-3} + (c^4/4)z^{-4} + (c^5/5)z^{-5} + \ldots \\
&= 2cz^{-1} + 2(c^3/3)z^{-3} + 2(c^5/5)z^{-5} + \ldots
\end{aligned}$$

The complex cepstrum, therefore, is the time series $\hat{r}(n) = (0,\ 2c,\ 0,\ 2c^3/3,\ 0,\ 2c^5/5, \ldots)$ whereas the reflection response according to Eq. (1) is the time series $r(n) = (1,\ 2c,\ 2c^2,\ 2c^3,\ 2c^4,\ 2c^5, \ldots)$. Taking the complex cepstrum $\hat{r}(n)$ as the final result we find that in comparison with the series $r(n)$ the multiple events are suppressed to a great extent. The complex cepstrum $\hat{r}(n)$ essentially displays the primary reflection. A numerical example will illustrate this statement. Assuming $c = -0.5$ we find the two series

$$r(n) = (1.,\ -1.,\ 0.5,\ -0.25,\ 0.125,\ -0.0625, \ldots)$$
$$\hat{r}(n) = (0,\ -1,\ 0,\ -0.0833,\ 0,\ -0.0125, \ldots)$$

In the complex cepstrum the first multiple completely has vanished and the amplitude of the second multiple is one third of the amplitude of the second multiple in the unit impulse response.

Further analytical computations concerning the multilayer case are given by Schepers (1972). It turns out that the complex cepstrum as final result instead of the deconvolved signal can give a good image of the layered subsurface. Yet it ought to be stressed that considerable errors can occur if the reflection coefficient does vary too much with depth.

The efficiency of suppressing multiples by homomorphic filtering will be illustrated by a synthetic example. For the example in Fig. 7 a model was chosen of two thin surface layers producing strong multiples as the unit impulse response (2) in Fig. 7 demonstrates. A deep interface with a considerable smaller reflection coefficient is masked by these multiples. Time series (4) is the complex cepstrum of the seismogram (3) for values of $t \geqslant 10$ ms. The deconvolution — no noise has been added in this synthetic seismogram — is perfect and the suppression of the multiples is satisfactory. The third reflection can be identified clearly. The signal enhancement yielded by means of homomorphic filtering can be concluded from the input signal (3) in Fig. 7 and from comparing the output signal (4) with the wanted signal (1).

From this it follows that the use of the complex cepstrum instead of the unit impulse response leads directly to a good image of the subsurface. Besides computing time is saved and as long as we do not intend to extract the shape of the wavelet from the seismogram the choice of the cut-off time is not critical, because the cut-off time only determines the two-way traveltime to the first reflector we are interested in.

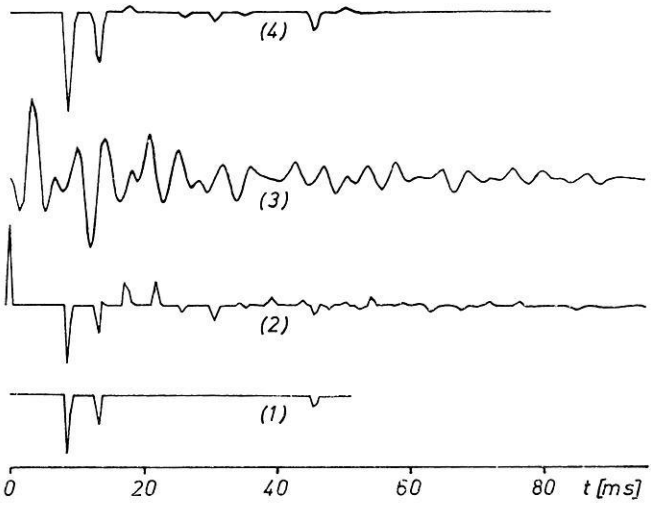

Fig. 7. Suppression of multiples. (1) series of primary reflections, (2) unit impulse response, (3) synthetic seismogram, (4) complex cepstrum of (3) for $t \geqslant 10$ ms

3.4. Computational Considerations

There are some important considerations in the computation of the complex cepstrum fully described by Oppenheim *et al.* (1968) and Ulrych (1971). So only those aspects shall be emphasized that have not been discussed so far.

We assume that the seismogram can be written in the form $s(n) = w(n) * r(n) + u(n)$ where $u(n)$ is a white series. It is preferable to use the Fast Fourier Transform for the numerical computation of the complex cepstrum instead of the z-transform (Oppenheim *et al.*, 1968). The natural logarithm of the complex spectrum can be computed via the amplitude and the phase spectrum. Special care has to be taken in the computation of the amplitude and phase spectra. This means:

i) A noisy signal has to be considered as an infinite time series. Before processing, therefore, the seismogram is multiplied with a 'hamming' window having a length of 2—3 times the two-way traveltime to the deepest reflector. Multiplying a time series with a window corresponds to a filter process in the frequency domain.

The curve (1) in Fig. 8 is the amplitude spectrum of a unit impulse response $r(n)$. The amplitude spectrum (2) is computed from a seismogram $s(n) = r(n) * w(n)$. The amplitude spectrum (3) of a seismogram $s(n) = r(n) * w(n) + u(n)$ is computed without using a time window. The result yielded by multiplying with a hamming window is the amplitude spectrum (4), which is an acceptable approximation of the noise-free spectrum (2).

ii) If noise is present difficulties will arise for the computation of the phase spectrum. The phase spectrum (7) of the noisy seismogram in Fig. 8 shows great deviations with respect to the phase spectrum (6). Considering the phase curves as time series we can classify the deviations as low-frequency noise that can be filtered out by high pass filter.

The result after applying this process is the phase spectrum (8) in Fig. 8. The low-frequency component of the phase spectrum (6) of the seismic wavelet is also filtered

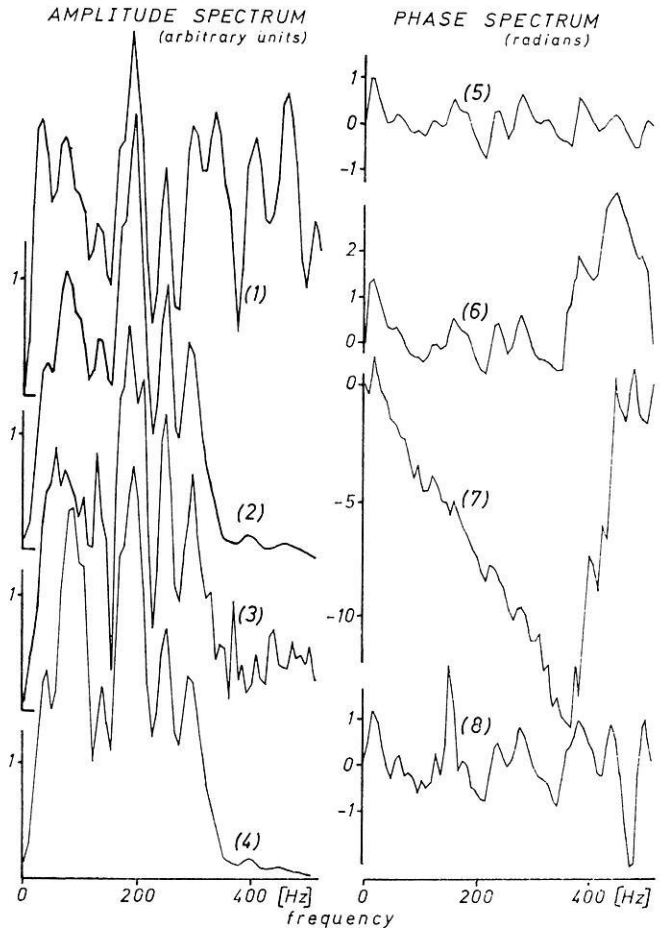

Fig. 8. The computation of the amplitude and the phase spectrum. (1) amplitude spectrum of the unit impulse response of the model shown in Fig. 10, (2) amplitude spectrum of the synthetic seismogram (1) in Fig. 10, (3) amplitude spectrum of the synthetic seismogram (2) in Fig. 10, (4) amplitude spectrum gained by filtering of the amplitude spectrum (3), (5) (6) (7) phase spectra corresponding to (1) (2) (3), (8) phase spectrum gained by filtering of the phase spectrum (7)

out and the phase spectrum (8) resembles more the phase spectrum (5) of the unit impulse response than the phase spectrum (6) of the seismogram. This means: If we want to extract the shape of the wavelet from the seismogram we must use the original phase curve.

3.5. Application of the Processing Technique to One-Channel Seismograms

Using a source at the bottom of a borehole we have to distinguish between reflections due to energy being emitted upwards and downwards. This situation is depicted in Fig. 9 for a two-layer case: The first multiple reflection from the first interface (3) arrives at the surface after the primary reflection from the second inter-

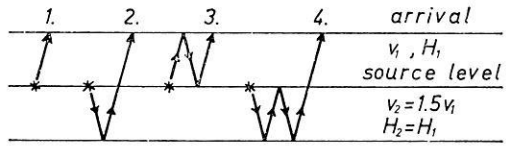

Fig. 9. The sequence of reflection arrivals for a source at the bottom of a borehole

face (2). This means reflections from deeper interfaces can be disturbed. Concerning the Ruhrtal test site we may expect the two-way traveltime through the first layer to be greater than the two-way traveltime from the source to the deepest reflector. Hence, the interpretation will be simple. It is important to note that this will not be true in most cases. Preliminary considerations must be made about the optimal depth of the source. Computation of the unit impulse response can help to solve this problem.

Assuming a source at the bottom of a borehole homomorphic filtering of synthetic seismograms for BRT was carried out to decide whether the complex cepstrum can be a good approximation to the series of the primary reflections. The results are shown in Fig. 10. The source was assumed to be 2 m deep just on top of the third layer. The time series (5) contains the primary reflections. They are labelled by numbers corresponding to the interfaces causing the reflections. The reflections labelled 3, 4 and 5 are due to a wave initially travelling downward from the source. The wave initially travelling upwards is reflected at the surface before giving rise to the reflections 1 and 2. The wavelet (6) in Fig. 10 was used to establish the seismogram (1). The corresponding unit impulse response was corrected for spherical divergence. The seismogram (2) is the same as (1) except for additive noise $u(n) * v(n)$, where $u(n)$ is a white series and $v(n)$ is the wavelet (6) in Fig. 10. The signal-to-noise ratio amounts to 2. The complex cepstrum (3) of the seismogram (1) sufficiently reproduces the primary reflections. The reflections for traveltimes greater than 15 ms are suppressed by the filtering process. The complex cepstrum (4) of the noisy seismogram (2) is worst, but the three reflections from beneath the source can be identified. The wavelets (7) and (8) in Fig. 10 were separated by homomorphic filtering using a cut-off time of 4.5 ms. Only the wavelet (7) is an acceptable approximation of the original wavelet (6). Considering the unfavourable signal-to-noise ratio of 2 this result is not unexpected.

Between site BRT2 and BRT3 8 one-channel reflection seismograms were recorded. The source was on the bottom of a borehole at a depth varying from 2.1 m to 2.7 m. To be sure that only vertically travelled *P*-waves are recorded one geophone — GEO SPACE GSC-11D — was placed at the surface directly besides the borehole. Each recorded seismogram represents the averaged signal of 16 weight drops. The sampling rate was 0.6 ms corresponding to a Nyquist frequency of 835 Hz. The results obtained by processing of these field seismograms are shown in Fig. 11. In the upper part of Fig. 11 the 8 complex cepstra of the field seismograms are plotted for times greater than 4.2 ms. Deflections of the traces to the left denote an increase of *P*-wave velocity. A multi-channel seismogram recorded at site BRT2 was already shown in Fig. 4. There were two reflections — the first from the ground water surface, the second from the bedrock — to be seen on this multi-channel

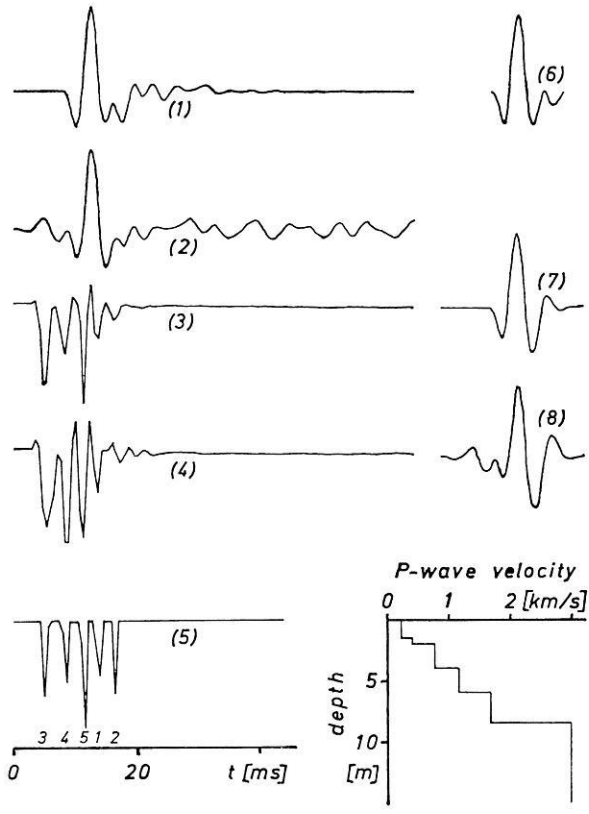

Fig. 10. Recovery of the primary reflections and the wavelet from synthetic seismograms for the Ruhrtal test site. (1) synthetic seismogram without noise, (2) synthetic seismogram with noise, (3) complex cepstrum of (1), (4) complex cepstrum of (2), (5) series of primary reflections, (6) wavelet used to construct the synthetic seismograms (1) and (2), (7) and (8) are the wavelets separated from synthetic seismogram (1) resp. (2) by homomorphic filtering

seismogram. These two reflections can be easily identified on the two traces for distances of 0. m and 20. m in Fig. 11. The other six traces in Fig. 11 display three reflections. The quality of the reflections is not satisfactory in all cases but it should be imagined the two-way traveltime between different reflections to be 5.5 ms at best. The interpretation of the 8 complex cepstra yielded the structure of the subsurface shown in the lower part of Fig. 11. The velocities the computation of the depth to the interfaces is based on are chosen according to the results of the refraction survey (Table 2). The data supplied by the borehole at site BRT3 (Table 1) is depicted in Fig. 11 for comparison.

The usefulness of the described processing technique depends on the assumptions given at the beginning of chapter 3. To test the validity of these assumptions for our field measurements synthetic seismograms were computed and compared with field seismograms. The velocity log for computing the unit impulse response was derived from the subsurface structure in the lower part of Fig. 11, the density log was estimated. The wavelet the unit impulse response was convolved with has been separated

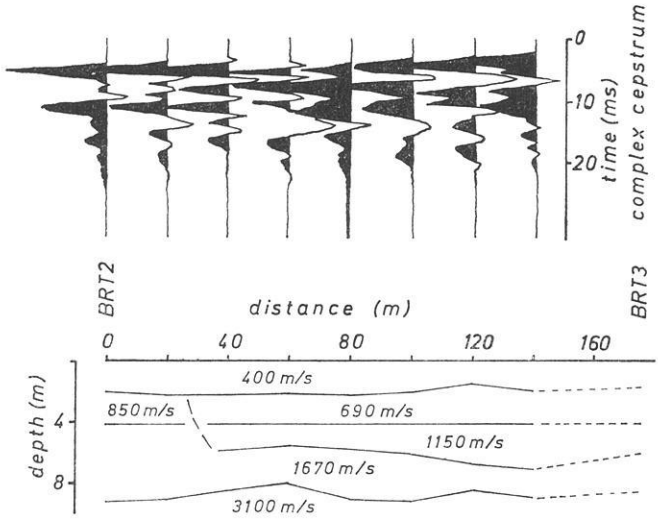

Fig. 11. The complex cepstra of field seismograms recorded between site BRT2 and BRT3, and the subsurface structure derived from the complex cepstra (the velocities are derived from refraction surveys)

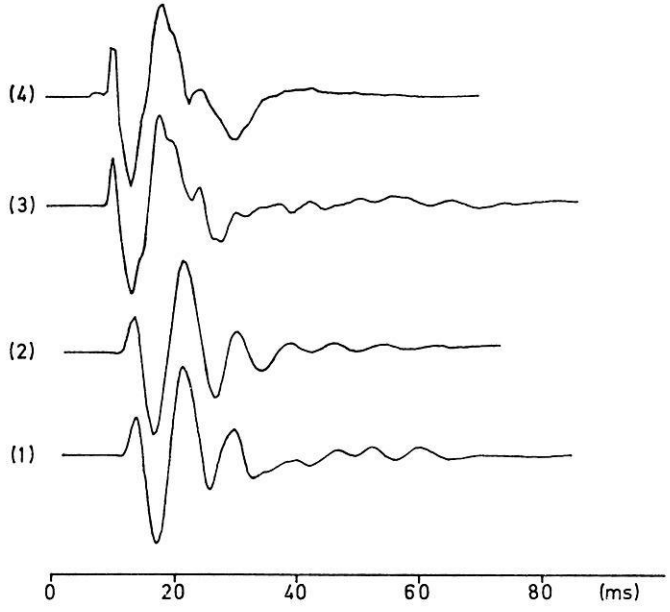

Fig. 12. Comparison of synthetic seismograms and field seismograms. (1) field seismogram for the distance of 0 m in Fig. 11, (2) synthetic seismogram for the distance of 0 m, (3) field seismogram for the distance of 40 m in Fig. 11, (4) synthetic seismogram for the distance of 40 m

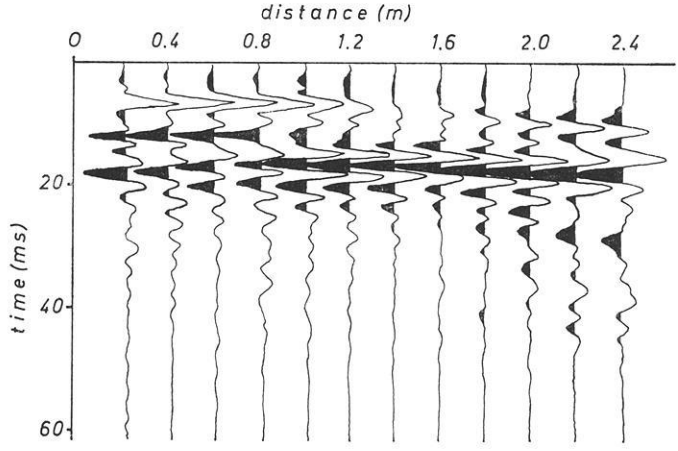

Fig. 13. Deconvolution of the first 12 traces of the seismograms shown in Fig. 4

from the corresponding field seismogram by homomorphic filtering. Two examples are given in Fig. 12: one for the case of two reflecting interfaces and one for the case of three reflecting interfaces beneath the source.

3.6. Improved Results for Multi-Channel Seismograms

As described in chapter 3.2. the wavelet emitted by the seismic source can be separated from the seismogram by homomorphic filtering. If the shape of the wavelet is known deconvolution can be achieved by optimum inverse filtering. One trace of the multi-channel seismogram shown in Fig. 4 was used to determine the wavelet of the emitted *P*-wave by homomorphic filtering. The optimum inverse operator of this wavelet was computed and each trace of the multi-channel seismogram was convolved with the inverse operator. The same procedure was carried out using different traces to determine the shape of the wavelet. The best result was obtained using the first trace recorded at the distance of 0.2 m.

E. g. Fig. 13 shows the results obtained by deconvolution of the first 12 traces of the seismogram shown in Fig. 4. The reflection from the ground water surface can be identified only on four traces, whereas the reflection from the bedrock correlates well for all 12 traces. Traces recorded at distances greater than 2.4 m are not shown as they increasingly display coherent noise. This is due to the arrival of S-waves and surface waves.

Acknowledgements. I am indebted to Prof. Dr. H. Baule for supporting this project. Thanks are expressed to Dipl.-Geoph. H. Rüter for stimulating discussions and to Prof. Dr. L. Dresen for critically reading the manuscript. The support of Dr. S. Freystätter for translating this paper is kindly appreciated. Part of this investigation has been carried out under DFG contract no. Dr 110/1.

References

Meidav, T.: Hammer reflection seismic in engineering geophysics. Geophysics *34*, 383–395, 1969

Oppenheim, A.V.: Superposition in a class of non-linear systems. Research Lab. of Electronics MIT, Tech. Rep. *432*, 1965

Oppenheim, A.V., Schafer, R.W., Stockham, T.G.: Nonlinear filtering of multiplied and convolved signals. Proc. IEEE *65*, 1264–1291, 1968

Peacock, K.L., Treitel, S.: Predictive deconvolution: theory and practise. Geophysics *34*, 155–169, 1969

Robinson, E.A.: Multichannel time series analysis with digital computer programs, 1rst ed. San Francisco: Holden-Day 1967

Robinson, E.A., Treitel, S.: Principles of Wiener filtering. Geophys. Prosp. *15*, 311–333, 1967

Schepers, R.: Bearbeitungsverfahren zur Bestimmung oberflächennaher Strukturen aus Einkanal-Reflexionsseismogrammen bei senkrechtem Einfall. Diss., University of Bochum, 1972. In: Berichte des Instituts für Geophysik der Ruhr-Universität Bochum, Nr. 2, Bochum 1972

Stoll, R.: Vibratorseismische Untersuchungen in realen Medien zur Nahortung und Kennwertbestimmung für ingenieurgeophysikalische Belange. Freiberger Forschungsh. *C 274*, 1971

Ulrych, T.J.: Application of homomorphic deconvolution to seismology. Geophysics *36*, 650–660, 1971

Ulrych, T.J.: Homomorphic deconvolution of some teleseismic events. Bull. Seism. Soc. Am. *62*, 1253–1265, 1972

Dr. Reinhard Schepers
Institut für Geophysik
der Ruhr-Universität Bochum
D-4630 Bochum
Postfach 2148
Federal Republic of Germany

J. Geophys. 41, 385–400, 1975

The Palaeomagnetism of Age Dated Tertiary Volcanites of the Monti Lessini (Northern Italy) and Its Implication to the Rotation of Northern Italy

H. Soffel

Institut für Allgemeine und Angewandte Geophysik der Universität München

Received January 30, 1975

Abstract. In the Monti Lessini and Monte Berici in Northern Italy ($\lambda = 11.5$ °E, $\varphi = 45.5$ °N) 37 lava flows of Oligocene to Eocene age have been sampled for palaeomagnetic measurements. For some of the flows radiometric ages between 33.0 and 47.2 m.y. have been determined. Alternating field demagnetization in fields up to 500 Oe were necessary for the removal of unstable secondary magnetization components. Rock magnetic and ore microscopic studies (Soffel, 1975) showed that the characteristic remanence is a primary one acquired by the rocks at the time of their formation. 15 lava flows of Oligocene age gave the following mean direction of characteristic remanence: $D = 204.1°$, $I = -34.8°$, with $N = 15$, $k = 17.6$, $\alpha_{95} = 8.6°$. The corresponding values of 18 lava flows of Eocene age are: $D = 156.5°$, $I = -38.1°$, $N = 18$, $k = 13.6$, $\alpha_{95} = 9.0°$. The difference in declination between the two groups is 47.6°. The pole position of the Oligocene lavas is at $\lambda = 146.4$ °E, $\varphi = 56.9$ °N. Its longitude is in good agreement with Lower to Middle Tertiary pole positions for Central Europe, while the latitude is about 20° too small. The pole position of the Eocene lavas is at $\lambda = 237.9$ °E, $\varphi = 59.1$ °N and is in the vicinity of the Eocene pole position of the Colli Euganei and of other Triassic and Permian rocks from the Southern Alps. The palaeomagnetic data of the Monti Lessini therefore confirm the result obtained by Soffel (1972, 1974a) for the Colli Euganei volcanites. They indicate that the anticlockwise rotation of Northern Italy of about 50° started in Upper Eocene (45 to 40 m.y.) and came to an end in Middle Oligocene (35 m.y.). The too low latitude which has been determined for the Oligocene rocks from the Southern Alps suggests that this area has drifted towards the North in times later than Middle Oligocene. There are also indications that the Colli Euganei have suffered an anticlockwise rotation of about 10° with respect to the Monti Lessini after Middle Oligocene.

Key words: Palaeomagnetism — Geodynamics in the Mediterranean — Italy.

1. Introduction

The time of rotation of Northern Italy has been determined by Soffel (1972, 1974a) by studying the palaeomagnetism of the Colli Euganei volcanites. According to these measurements the rotation through about 50° in an anticlockwise sense happened between 45 m.y. (Upper Eocene) and 35 m.y. (Middle Oligocene). The absolute time of rotation could be linked to radiometric age determinations carried out by Borsi, Ferrara and Piccoli (1969) and to biostratigraphic age determinations (Schiavinato 1950, Riedel 1950, Piccoli 1966) on some Colli Euganei volcanites.

Most radiometric age determinations by Borsi *et al.* (1969) refer to rocks of the younger volcanic cycle in the Colli Euganei which happened in Middle Oligocene and for which an average age of 33 m.y. was determined. Most of the informations about

Table 1. Site number, locality name, description of the site and age of the volcanic units which have been sampled in the Monti Lessini and Monte Berici. The radiometric ages have been provided by Piccoli (private communication, 1973). The other ages were taken from the Carta Geologica d'Italia (scale: 1:100000) and from Piccoli (1964)

Site No.	Locality name	Description of the site	Age	
1	Valle	vent, 1 km N of Valle	37.0	m.y.
2	Sarego	road cut, 1 km N of Sarego	Ol.	
3	Montebello	1,5 km NW of M., Villa Crosara	Ol.	
4	Sorio	0,5 km E of S., road cut	Ol.	
5	Brentone	road cut, 1 km W of B.	46.8	m.y.
6/1	M. Calvarina/1	road cut, 1 km W of M. C.	46.8	m.y.
6/2	M. Calvarina/2	road cut, 1 km W of M. C.	46.8	m.y.
7	Fazzi	1 km W of M. C., hamlet Fazzi	46.8	m.y.
8	Cortivo	1 km W of M. C., hamlet Cortivo	46.8	m.y.
9	S. Bortolo	road cut, leaving S. B. to Ronca	Eo.	
10	Vittori	1 km E of Ronca, hamlet Vittori	Ol.	
11	Cracchi	churchyard, hamlet of Cracchi	47.2	m.y.
12	S. Giovanni/1	0,5 km N of S. G.	Ol.	
13	Castelcerino	road intersection, 0,5 km S of C.	Eo.	
14	C. Tribbia	2 km E of Chiuppano	Eo.	
15	Togarelli	road cut, hamlet of Togarelli	Ol.	
16	Galvari	road cut, 1,5 km S of Salcedo	Ol.	
17	Arzignano	Arzignano, exit to Tezze	Eo	
18	Brognolio	road to Fitta, 0,5 km W of B.	Eo.	
19	M. Castellaro	0,5 km W of site No. 18	Eo.	
20	Fitta	0,5 km E of Fitta	Eo.	
21	S. Valentino	4 km SW of Bretonico	Eo.	
22	Torbole	1 km NE of Torbole	Ol.	
23	Besagno	road cut, 0,5 km N of Besagno	Ol.	
24/1	S. Briccio/1	old quarry, 0,5 km S of S. B.	Ol.	
24/2	S. Briccio/2	old quarry, 0,5 km S of S. B.	Ol.	
25	Colognola	0,5 km SE of Colognola ai Colli	Eo.	
26	Portinari/1	1 km NE hamlet of Portinari	Eo.	
27	Portinari/2	0,5 km NE hamlet of Portinari	Ol.	
28	Bolca	Purga di Bolca	36.2	m.y.
29	Vestananuova	0,5 km S of Vestananuova	Eo.	
30	S. Giovanni/2	0,5 km NW S. G., W of F. Alpone	Eo.	
31/1	S. Giovanni/3	1 km S of S. G., hamlet Salgaroli	Ol.	
31/2	S. Giovanni/4	1 km S of S. G., hamlet Salgaroli	Ol.	
32/1	Gambellara/1	0,5 km S of Gambellara	Eo.	
32/2	Gambellara/2	0,5 km S of Gambellara	Eo.	
33	Grancona	road cut, 2,5 km NE of Sarego	Ol.	
	Marolla	SW of Caltrano, no outcrop, not sampled	33.0	m.y.
	Fiume Famollo	between Laverda and Lavarda no outcrop, not sampled	33.5	m.y.

the age of the older cycle of volcanic activity come from palaeontological investigations yielding a Priabonian or Lutetian (Middle to Upper Eocene) age.

However a number of new radiometrically determined ages from the Monti Lessini and Monte Berici have been made available to the author by Prof. Piccoli (private communication 1973) from the Geological Institute of the University of

Padova (Italy). These two volcanic areas are situated about 50 km northwest of the Colli Euganei on the southern edge of Southern Alps. The radiometrically determined ages in these two areas vary between 33.0 and 47.2 m.y. thus covering a time span which has been considered by Soffel (1972, 1974a) for the time of rotation of Northern Italy.

2. Geology and Radiometric Ages of the Monti Lessini and Monte Berici Volcanites

Among the many papers about the geology and petrography of the Monti Lessini and Monte Berici only a few publications by Piccoli (1964, 1966, 1969) shall be mentioned. They summarize his own results as well as those obtained by others. The K/Ar ages (33.0, 33.5, 36.2, 37.0, 46.8, 47.2 m.y., see Table 1) are unpublished data provided to the author by Piccoli in 1973.

According to Piccoli (1964) volcanism in the Monti Lessini and Monte Berici lasted from about Middle Cretaceous to Miocene with a main activity in Eocene and Oligocene. This has been confirmed by the radiometric age determinations. All sites with known radiometric age have also been sampled for a palaeomagnetic study. However two radiometric ages (33.0 and 33.5 m.y.) originate from sites without suitable outcrops for such kind of research.

Fig. 1 is a simplified geological map of the investigated area showing the places of outcropping Tertiary volcanism. The places where the samples for this study have been taken are shown in Fig. 2. Numbers refer to site numbers. Table 1 contains the site number, locality name and description of the site, radiometrically determined age (if available) and/or biostratigraphic age either according to the geological map of the area (Carta Geologica d'Italia) or according to Piccoli (1964).

37 different volcanic units have been sampled, in most cases 8—12 cores have been drilled from each unit.

According to Piccoli (1966) most of the basic eruptions on the Monti Lessini and Monte Berici took place under marine environment. In these cases the flows are intercalated between limestones thus facilitating tectonic corrections. Others have been extruded under subaerial conditions and some are large intrusive bodies which have cooled slowly forming large masses of columnar basalts.

According to the kind of deposition of the basalts, subaqueous, subaerial und intrusive units show distinct rockmagnetic properties which are discussed in a different paper (Soffel, 1975) in this volume.

3. Palaeomagnetic Measurements

3.1. Natural Remanent Magnetization (NRM)

All measurements of remanent magnetization have been made with a DIGICO spinner magnetometer. The NRM of the individual sites showing sample means are plotted in Fig. 3 in equal area projection. Open symbols: negative inclinations, closed symbols: positive inclinations. The mean NRM data of the individual sites are listed in Table 2 a together with the parameters chracterizing their scatter. Some sites show extremely small scatter already for the NRM irrespective of their polarity (site number 1, 12, 14, 19, 20, 21, 24/2, 29, 31/1, 31/2, 32/1, 32/2, 33), others have considerable

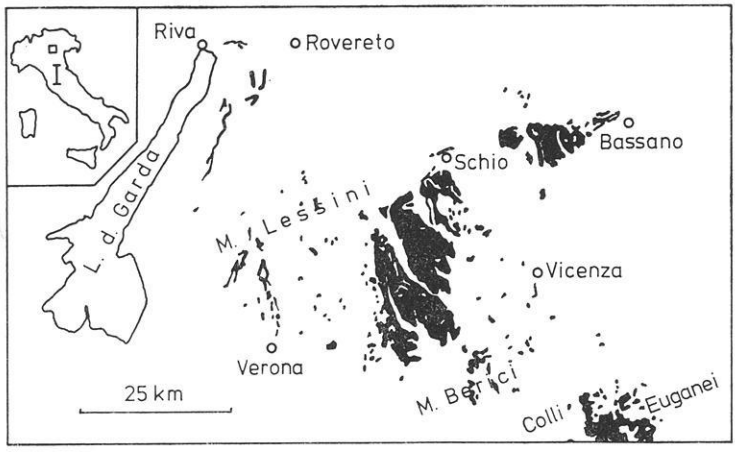

Fig. 1. Areas (in black) of Tertiary volcanism in the Monti Lessini in Northern Italy. (Redrawn from the geological map of Austria, issued by H. Vetters (1968))

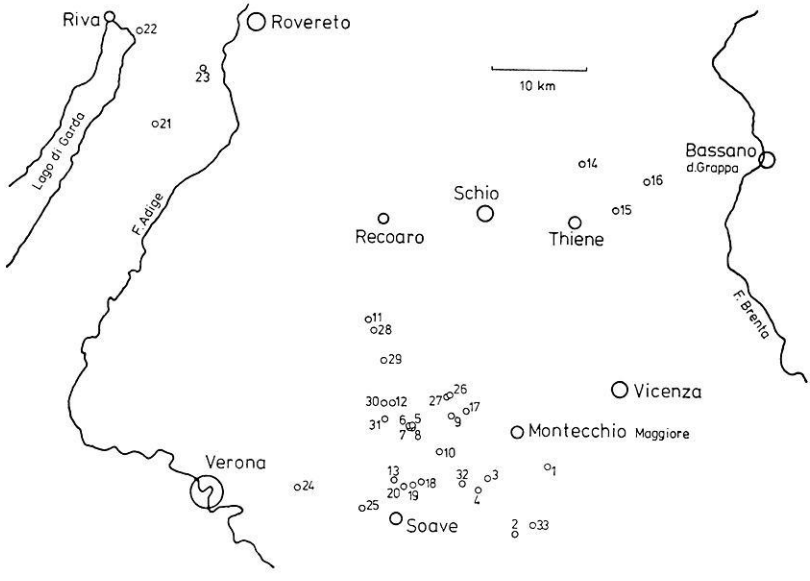

Fig. 2. Map of the sampling localities. Numbers refer to site numbers

scatter (site numbers 2—5, 15—18, 27, 28). The computation of a mean NRM direction of all sites (Fig. 4) does not seem to be reasonable. The mean intensities of NRM of the sites are also listed in Table 2a. The values vary between 600 and $26000 \cdot 10^{-6}$ Gauss. They are normal for basic volcanic rocks.

3.2. Alternating Field Demagnetization

The large scatter of the mean NRM directions of many sites suggests the presence of considerably large components of secondary magnetization in these rocks. Only

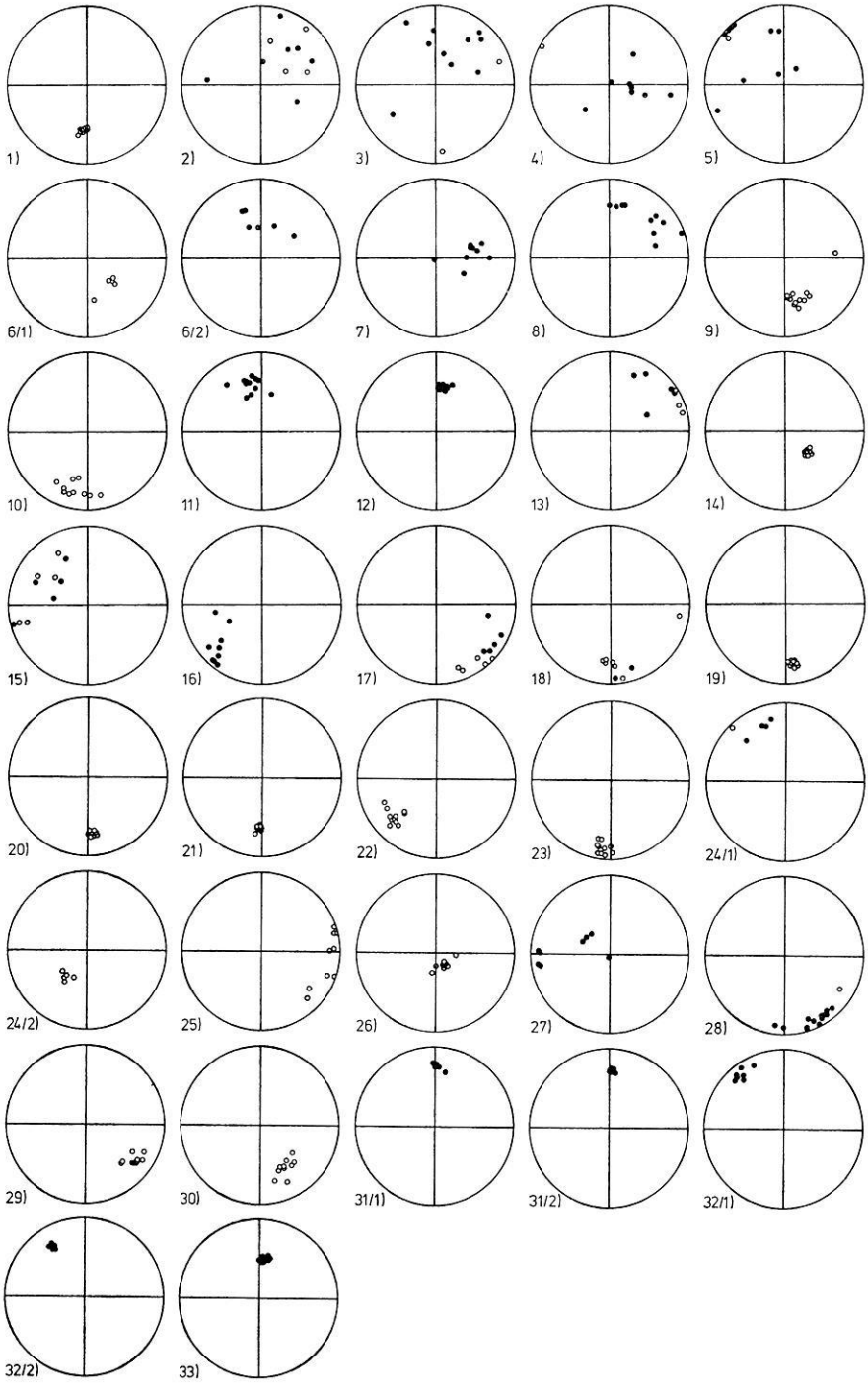

Fig. 3. Mean directions of natural remanent magnetization (sample means) of all sites. Open symbols: negative inclination, closed symbols: positive inclinations. Equal area projection

Table 2. Palaeomagnetic data for the Natural remanent magnetization (a) and for the Characteristic magnetization (b). Meaning of the different columns:
1: site number, 2: number of samples (N) and specimens (n), 3: mean declination of NRM, 4: mean inclination of NRM, 5: α_{95} value of NRM, 6: precision parameter of NRM, 7:

a) Natural remanent magnetization (NRM)

1 Nr.	2 N/n	3 $D(°)$	4 $I(°)$	5 $\alpha_{95}(°)$	6 k	7 NRM(μG)
1	10/30	185.5	−41.5	2.3	416.6	2309
2	11/24	41.6	+16.5	43.1	2.0	796
3	12/27	32.7	+44.4	37.2	2.3	2029
4	9/18	77.6	+74.6	32.4	3.4	1093
5	13/25	316.0	+37.6	26.6	3.3	5000
6/1	5/7	141.7	−54.3	9.3	45.7	1081
6/2	6/11	359.2	+51.7	15.8	13.0	1621
7	10/19	84.9	+51.7	11.6	18.0	1565
8	10/22	42.1	+31.4	14.0	10.1	3513
9	13/30	159.0	−45.7	8.5	21.1	2944
10	10/26	193.5	−26.8	7.6	33.6	1962
11	12/23	347.7	+38.6	6.2	42.5	1947
12	12/37	10.1	+42.1	2.3	299.0	23011
13	9/19	56.2	+ 9.4	13.8	11.4	8205
14	9/22	133.6	−58.3	1.6	832.2	2761
15	10/20	292.2	+ 4.4	24.6	3.2	922
16	9/24	229.9	+22.5	13.1	16.3	5146
17	10/32	136.1	+ 3.4	14.4	12.0	2699
18	9/25	171.8	−16.3	20.9	7.0	921
19	12/32	175.2	−24.6	1.8	546.6	2539
20	11/33	175.2	−30.3	1.8	636.9	2260
21	11/22	183.4	−37.1	1.8	626.1	600
22	11/22	230.1	−29.7	5.4	72.1	864
23	10/21	188.4	−15.4	5.1	89.7	774
24/1	5/10	332.6	+19.5	18.8	17.4	2129
24/2	6/11	219.2	−56.1	5.5	193.4	2598
25	10/21	97.8	−10.8	14.0	12.7	3983
26	13/23	151.9	−75.6	3.5	137.7	863
27	8/14	277.5	+39.3	25.8	5.5	5909
28	15/22	154.8	+ 8.8	8.7	20.0	26200
29	10/30	128.0	−25.1	5.2	86.1	3220
30	10/20	150.0	−37.3	6.3	58.0	2385
31/1	6/12	3.8	+26.4	4.1	263.7	1964
31/2	7/14	4.3	+29.2	1.6	1367.7	785
32/1	7/15	322.9	+13.9	5.7	110.9	3014
32/2	6/12	327.9	+27.4	3.0	472.0	1864
33	10/19	8.5	+49.6	2.7	301.1	4736

mean intensity of NRM in μG ($1\mu G = 10^{-6}$ Gauss), 8: peak field for alternating field demagnetization in Oe, 9: mean declination of CARM, 10: mean inclination of CARM, 11: α_{95} value of CARM, 12: precision parameter of CARM, 13: mean intensity of CARM in μG ($1\mu G = 10^{-6}$ Gauss), 14: type of demagnetization curve according to Fig. 5

b) Characteristic remanent magnetization (CARM)

1 Nr.	8 H_{peak}	9 D(°)	10 I(°)	11 α_{95}(°)	12 k	13 CARM (μG)	14 Demagn.
1	150	184.1	−45.6	2.8	282.3	1287	c
2	—	unstable remanence					b
3	350	180.9	−41.2	6.7	42.2	739	h
4	300	209.4	−26.8	8.9	39.2	88	e
5	10	322.2	+27.3	29.0	4.1	3605	b
6/1	200	130.5	−55.1	4.7	380.6	961	c
6/2	50	3.8	+46.4	26.9	2.5	1498	b
7	300	80.9	+34.0	9.7	25.4	506	e
8	500	353.7	+38.1	4.2	129.5	278	a
9	200	175.6	−50.4	1.7	538.0	3752	f
10	200	192.4	−34.6	4.2	112.2	2468	f
11	50	351.5	+40.0	4.5	90.1	1366	e
12	50	12.4	+39.0	2.8	225.1	6390	a
13	200	135.1	−43.5	7.0	63.4	1344	a
14	100	134.1	−57.7	1.9	712.7	2446	c
15	500	228.6	−40.1	7.2	59.5	163	g
16	400	265.7	+59.0	13.3	15.7	1451	a
17	200	149.9	− 7.7	5.2	86.3	450	a
18	100	180.2	−29.7	3.9	173.0	856	c
19	200	175.8	−24.6	2.0	436.2	1980	c
20	200	174.0	−29.7	1.7	694.4	1676	c
21	300	175.9	−21.5	1.8	579.1	332	c
22	200	211.1	−31.2	3.7	149.5	606	f
23	200	190.2	−11.7	4.7	104.9	255	c
24/1	200	215.7	−60.9	6.5	136.6	497	b
24/2	200	196.3	−46.5	5.9	126.6	1502	e
25	150	139.7	−37.0	8.8	30.6	803	a
26	200	151.6	−73.2	1.6	657.0	801	c
27	200	239.9	−21.2	16.0	15.0	369	a
28	200	227.5	− 4.2	4.5	70.7	5126	a
29	200	131.9	−41.5	2.7	340.4	1428	b
30	100	174.5	−50.0	2.3	417.6	1850	b
31/1	100	4.3	+25.9	4.3	242.9	1771	d
31/2	100	5.7	+28.6	1.4	1649.0	767	d
32/1	100	322.5	+12.3	5.5	117.8	3046	c
32/2	100	324.3	+22.3	1.5	1867.4	1657	c
33	100	6.1	+49.6	3.6	172.6	3424	e

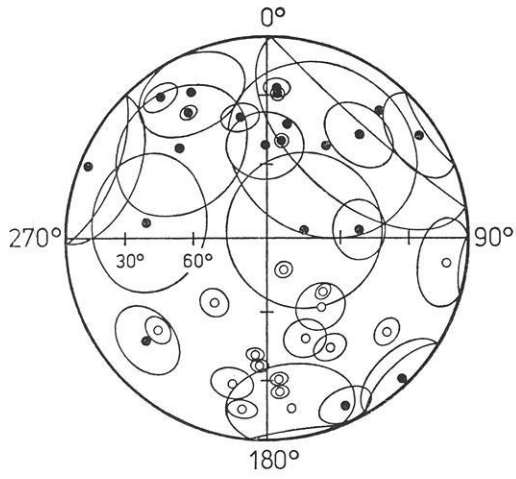

Fig. 4. Mean directions of natural remanent magnetization (NRM) together with their α_{95} cones of confidence. For legend see Fig. 3

alternating field demagnetization was applied to remove these components starting with the stepwise demagnetization of test samples from each site. The most suitable demagnetizing field for the specimens of one site was chosen according to their rock magnetic properties (Soffel, 1975) and statistical criteria (minimum of scatter). The peak fields in Oe are listed in Table 2b. The drop of intensity of remanence during alternating field demagnetization was not uniform. Eight different types could be distinguished which are shown in Fig. 5 for demagnetizing fields up to 1000 Oe. However many of the test samples have been treated with fields up to 1500 Oe. Type a) shows a large drop of intensity combined with a change in remanence direction at alternating fields between 50 and 100 Oe. The remanence remained constant up to 1000 Oe and more without essential change in direction and intensity, which was less than 10% of the NRM. Type b) showed similar behaviour as type a). However the intensity of remanence did not drop below 25% of NRM. Type c) is similar to type b), showing the drop of intensity between 200 and 400 Oe combined with a more or less sudden convergence towards a stable remanence direction. Type d) shows only a small drop of intensity in alternating fields up to 1000 Oe without a change in remanence direction. Type e) shows a slight increase of remanence in fields between 0 and 50 Oe followed by a sharp drop of intensity between 50 and 100 Oe similar to type a). Large variations of direction of remanence occur only between 0 and 150 Oe. Type f) is similar to type c), showing a slight increase of remanence combined with moderate variations of the direction of remanence between 0 and 150 Oe. A peculiar curve is type g) showing an increase of remanence between 0 and 50 Oe followed by a sharp drop between 50 and 100 Oe, a further increase between 100 and 300 Oe and a gentle decrease for still higher intensities of the alternating field. Large variations of the direction of remanence occur between 0 and 300 Oe until a final reversed direction with stable remanence is obtained. A similar behaviour (without the initial increase between 0 and 50 Oe) has the curve of type h). Rocks

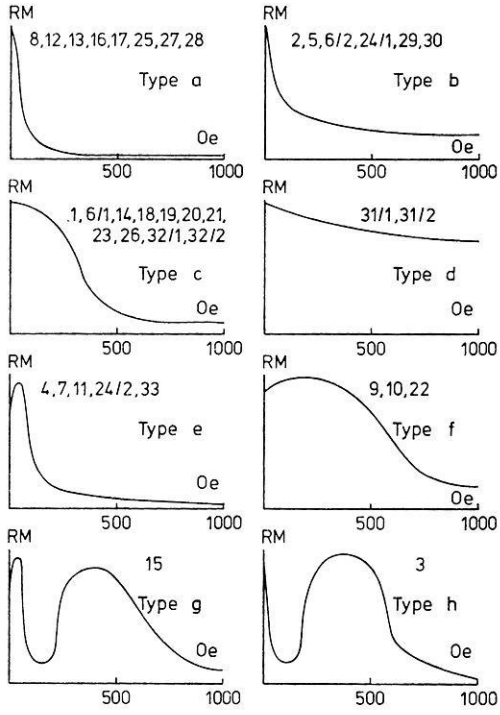

Fig. 5. Behaviour of typical test samples during alternating field demagnetization in fields up to 1000 Oe. Intensities are shown in arbitrary units. Numbers refer to site numbers

belonging to types g) and h) have unstable magnetization components more or less in the direction of the present field in the sampling area which are stronger than the primary reversed direction of remanence but (fortunately) connected with smaller coercive forces.

3.3. Characteristic Remanent Magnetization (CARM)

The directions of the stable remanence after alternating field demagnetization of all sites (sample means) are shown in Fig. 6 in equal area projection. For site number 2 no stable remanence with a grouping better than for the NRM could be obtained. The CARM data of the individual sites are also listed in Table 2b together with the parameters characterizing their scatter. The data of site 6/2 were omitted because of too large internal scatter ($\alpha_{95} = 26.9°$). Intermediate directions have been obtained for site 7 and 16. These data were also omitted for the computation of mean CARM directions.

Fig. 7 shows the mean CARM directions of all sites (minus site numbers 2, 6/2, 7 and 16) together with their cones of confidence in equal area projection. The scatter of the directions is much smaller than that for the NRM. With exception of site numbers 5 and 27 all α_{95} values are much smaller than 10°. The data plotted in Fig. 7 and listed in Table 2b already include tectonic corrections which were especially necessary in the northwestern part of the sampling area.

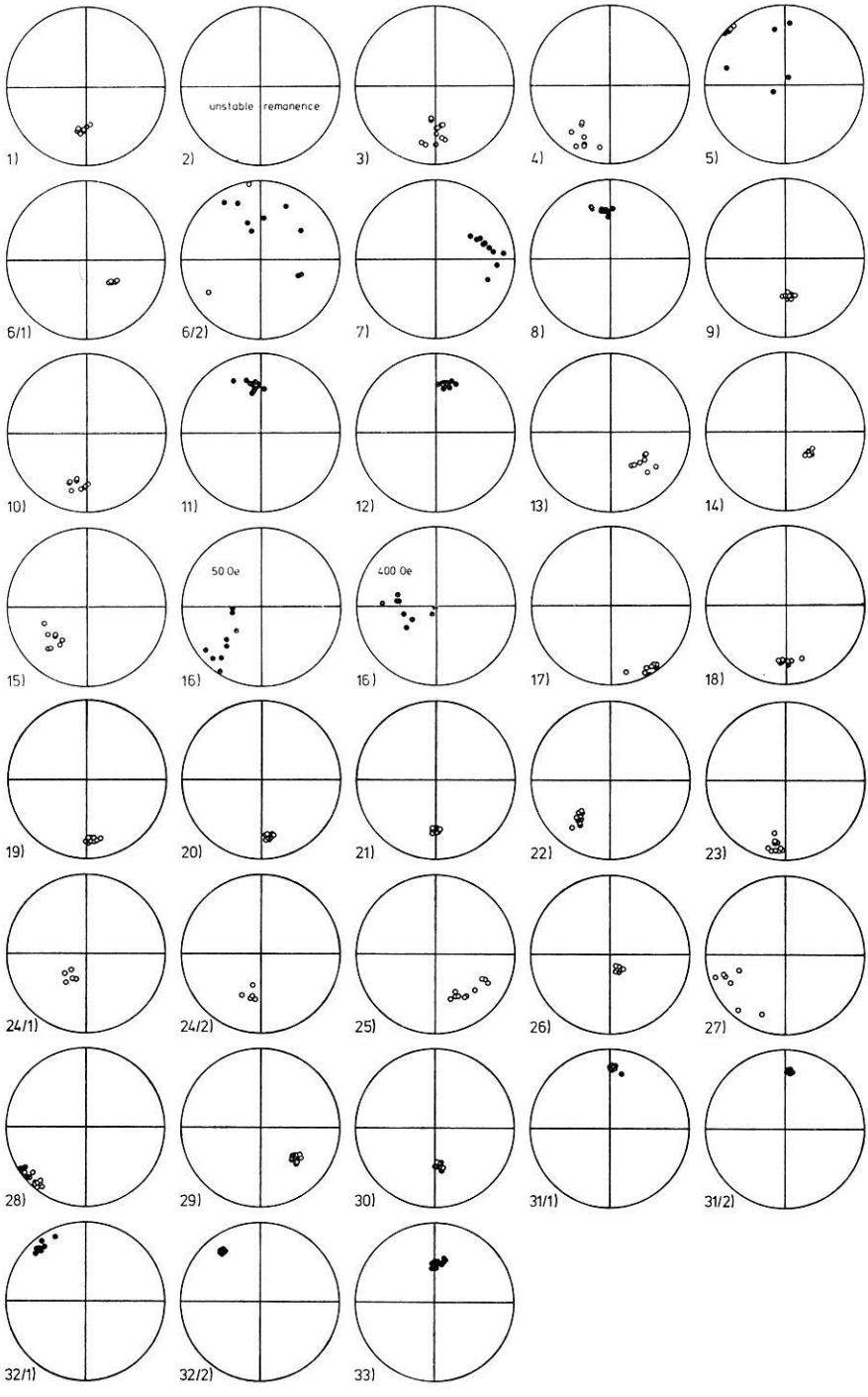

Fig. 6. Mean directions of characteristic remanent magnetization (CARM, sample means) of all sites. For legend see Fig. 3

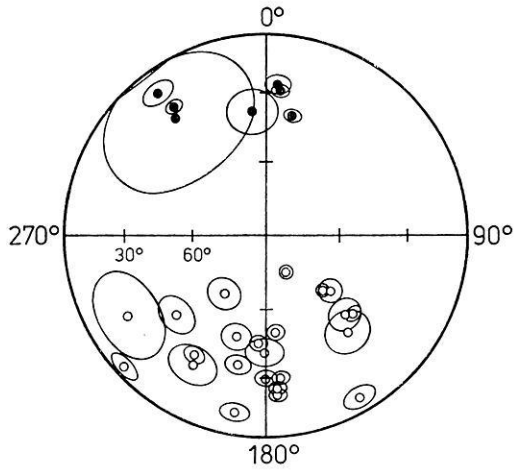

Fig. 7. Mean direction of characteristic remanent magnetization (CARM) of all sites together with their α_{95} cones of confidence. The data of site numbers 2, 6/2, 7 and 16 are not plotted

The radiometric age determinations according to Piccoli (private communication, 1973) together with data taken from the geological map of the sampling area (Carta Geologica d'Italia) and from Piccoli (1966) permitted to divide the sites into two main groups with respect to their ages. One group (group I) includes ages younger than 40 m.y. and volcanics classified as Lower and Middle Oligocene. The other group (group II) comprises rocks with ages between 40 and 50 m.y. and volcanics classified as Middle and Upper Eocene. The mean CARM directions of sites from group I (Lower and Middle Oligocene) are plotted in Fig. 8. The mean direction of this group is plotted as a square together with its α_{95} cone of confidence using equal area projection. Only reversed polarities are plotted (open symbols), the CARM direction of sites with normal polarity was projected to the other hemisphere. The mean direction of sites from group I is: $D=204.1°$, $I=-34.8°$, with $N=15$, $k=17.6$, $\alpha_{95}=8.6°$. Fig. 9 shows the mean CARM directions of sites from group II (Middle and Upper Eocene) in equal area projection together with the mean direction of all sites (square) and its α_{95} cone of confidence. Again only reversed polarities are shown, normal polarities were projected to the other hemisphere. The mean direction of sites from group II is: $D=156.5°$, $I=-38.1°$, with $N=18$, $k=13.6$, $\alpha_{95}=9.0°$. In both cases unit weight was given to each site for the computation of the mean direction. The difference in declination between the two groups is 47.6°. A declination difference of about the same amount (51.2° and 55.3° respectively, depending on the scheme of subdivision into two groups of different age) has been obtained by Soffel (1972, 1974a) from the study of the palaeomagnetism of the Tertiary Colli Euganei volcanites. As both sampling areas (Colli Euganei, Monti Lessini and Monte Berici) are only 60 km apart, their mean CARM directions of all sites can be combined for a better and more reliable determination of the mean CARM direction of Middle and Upper Eocene as well as Lower and Middle Oligocene for Northern Italy. The combined data for group I (Lower and Middle Oligocene, group I') are: $D=197.1°$, $I=-42.1°$,

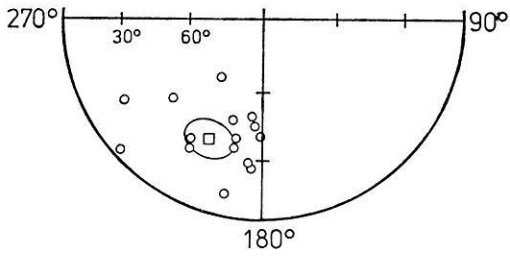

Fig. 8. Mean directions of characteristic remanent magnetization of all volcanic units of Oligocene age. Square: mean of all sites together with the α_{95} cone of confidence. Only reversed polarites are shown. The directions of sites with normal polarity were projected to the other hemisphere

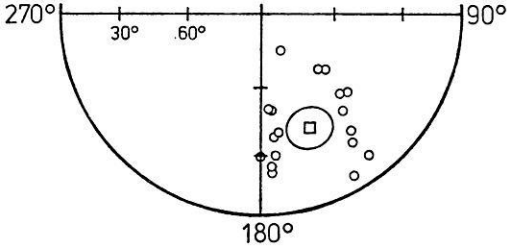

Fig. 9. Mean directions of characteristic remanent magnetization of all volcanic units of Eocene age. Square: mean of all sites together with the α_{95} cone of confidence. Only reversed polarities are shown. The directions of sites with normal polarity were projected to the other hemisphere

$N=31$, $k=13.3$, $\alpha_{95}=6.9°$, giving unit weight to each site. The combined data from both sampling areas for group II (Middle and Upper Eocene, group II') are: $D=150.3°$, $I=-37.3°$, $N=25$, $k=12.1$, $\alpha_{95}=8.0°$. The declination difference between the groups of the combined data is 46.8°.

As can be seen from Fig. 10 there seems to be a systematic difference between the mean directions of remanence of the Monti Lessini (squares) and Colli Euganei (circles) for both Eocene and Oligocene rocks. The declinations obtained for the Colli Euganei rocks are in average about 10° smaller than those obtained for the Monti Lessini rocks while the inclinations are in better agreement. This suggests an anticlockwise rotation of the Colli Euganei with respect to the Monti Lessini of about 10° since Middle Oligocene. However this conclusion is not very reliable as the mean directions of the two sampling areas, though being different systematically to some extent, are in general agreement within the possible limits of error. The eventual anticlockwise rotation of the Colli Euganei with respect to the Monti Lessini could possibly be related to the post Oligocene rotation of the Corso-Sardinian block (De Jong *et al.*, 1973) and its tectonic consequences in the area of the Apennine and Po basin.

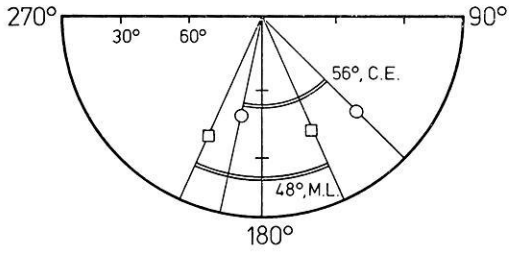

Fig. 10. Mean directions of characteristic remanent magnetization of both Oligocene and Eocene age according to Fig. 8 and Fig. 9 for the Monti Lessini (squares) and for the Colli Euganei (circles) according to Soffel (1974a). The angles of rotation are shown (48° and 56° respectively) as well as the systematic difference in declination between the two areas

3.4. Virtual Geomagnetic Pole Positions (VGP)

The mean geographic coordinates of the sampling area are: $\lambda = 11.5°$ E, $\varphi = 45.5$ °N. Within a few tenth of a degree these values are correct for both Monti Lessini and Colli Euganei area. For the group I of the Monti Lessini (Lower and Middle Oligocene) the following VGP position is obtained: $\lambda = 146.4$ °E, $\varphi = 56.9$ °N. The corresponding VGP position for the group II of the Monti Lessini (Middle and Upper Eocene) is: $\lambda = 237.9$ °E, $\varphi = 59.1$ °N. The pole positions for the combined data of the Monti Lessini and Colli Euganei are for group I′ (Lower and Middle Oligocene): $\lambda = 152.6$ °E, $\varphi = 64.7$ °N and for group II′ (Middle and Upper Eocene): $\lambda = 246.0$ °E, $\varphi = 55.3$ °N. These VGP positions are plotted in Fig. 11 in equal area projection. Fig. 11 also contains mean pole positions for Lower Tertiary (T_l) and Upper Tertiary (T_u) for Stable Europe according to the latest data compiled by McElhinny (1973). Fig. 11 shows that there is good agreement between the VGP positions of group I and group I′ (Lower and Middle Oligocene of the Monti Lessini and Monti Lessini combined with the Colli Euganei respectively) with the Lower Tertiary pole positions determined on rocks from Central Europe. The VGP positions of group II and group II′ (Middle and Upper Eocene of the Monti Lessini and Monti Lessini combined with the Colli Euganei respectively) are far apart from the Tertiary pole positions for Central Europe and in the vicinity of pole positions of Permian and Triassic rocks from the Southern Alps according to Zijderveld and Van der Voo (1973) and Manzoni (1970). These pole positions are marked with P and Tr respectively in Fig. 11. Fig. 11 also contains the pole position of paleozoic dykes from within the Ötztal Massive according to Förster, Soffel and Zinsser (1975), the pole position of Permian quartz porphyries in Vorarlberg (Austria, Va) according to Soffel (1975a) and the pole position (Tosc.) determined by Lowrie and Alvarez (1975) for the Upper Cretaceous to Lower Tertiary Scaglia Rossa formation in the Toscana in Central Italy. The data suggest an anticlockwise rotation of Northern Italy (and eventually also the remaining part of Italy) with respect to Central through an angle of rougly 50°. At least for the Southern Alps it can be assumed that the rotation took place between 45 m.y. and 35 m.y. This time interval seems to be sufficiently well confirmed by the latest radiometric age determinations by Piccoli (private communication, 1973).

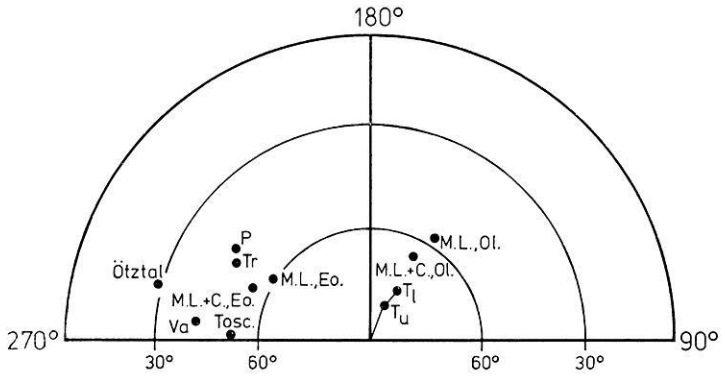

Fig. 11. Virtual geomagnetic pole positions in equal area projection. T_u and T_l: mean pole positions of Upper and Lower Tertiary respectively according to McElhinny (1973) for Central Europe. M.L., Ol. and M.L.+C., Ol.: Oligocene pole positions for the Monti Lessini area and a combined pole position for the Monti Lessini and Colli Euganei areas respectively. M.L., Eo. and M.L.+C., Eo.: same meaning, but refering to rocks of Eocene age from both sampling areas. P.: Permian pole position of the Southern Alps according to Zijderveld and Van der Voo (1973) and Tr: Triassic pole position of the same area according to Manzoni (1970). Va: Pole position of the Permian quartz porphyries in Vorarlberg according to Soffel (1975a). Ötztal: pole position of paleozoic dykes from the Ötztal massive according to Förster, Soffel and Zinsser (1975). Tosc.: Cretaceous to Lower Eocene pole position of Central Italy according to Lowrie and Alvarez (1974)

4. Conclusions

The characteristic remanent magnetization of 37 volcanic units has been investigated with standard measuring and alternating field demagnetization techniques. For two out of 37 volcanic units no stable characteristic remanence could be determined, the data of 2 other lava flows had to be omitted because of intermediate remanence directions. The mean declination of 15 Oligocene lava flows is 47.6° greater than the mean declination of 18 Eocene lava flows, while the inclinations of both groups are the same within the limits of error. The mean remanence directions of the Oligocene as well as the Eocene lava flows in the Monti Lessini are quite close to the corresponding data of the Oligocene and Eocene rocks of the Colli Euganei (Soffel, 1972, 1974a). The pole positions derived from the palaeomagnetic data are shown in Fig. 11 in comparison with the pole positions obtained for rocks of corresponding age in Central Europe. The Oligocene pole positions of both the Monti Lessini and the Colli Euganei rocks are in quite good agreement with the Lower Tertiary pole position of Central Europe. However their latitudes are somewhat lower. The Eocene pole positions of both areas are in the vicinity of the Triassic and Permian pole positions of the Southern Alps. This confirms the result obtained by Soffel (1972, 1974a) indicating that the rotation of Northern Italy in an anticlockwise sense of about 50° took place between Eocene and Oligocene.

The radiometric age determinations in the Monti Lessini (Piccoli, private communication, 1973) suggest that the rotation started between 45 and 40 m.y. and has come to an end at around 35 m.y. The too low latitude for the Oligocene pole positions of the Monti Lessini and the Colli Euganei compared with Central Europe

suggests a drift of the Southern Alps to the North in times after Middle Oligocene. A small but systematic difference between the declinations of rocks from the Monti Lessini and Colli Euganei (Fig. 10) suggests an anticlockwise rotation of the Colli Euganei with respect to the Monti Lessini after Middle Oligocene. This could eventually be related to the post Oligocene rotation of the Corso-Sardinian block and its tectonic consequences in the area of the Apennine and the Po basin.

Acknowledgement. The investigations have been made in the Institut für Angewandte Geophysik, University of Munich. Thanks are due to Prof. Dr. G. Angenheister and Dr. N. Petersen for their interest and support. Dr. Bögel from the Geological Institute of the Technical University in Munich suggested the measurements in the Monti Lessini as a check for the previously obtained Colli Euganei results. His current interest in the work is gratefully acknowledged. Prof. Piccoli from the Geological Institute of the University of Padova kindly provided some unpublished radiometric age determinations and gave valuable hints for suitable sampling localities. Dipl. Geophys. H. Becker kindly helped to collect part of the samples. Special thanks are due to the two refereees for their help to improve the manuscript.

The financial support of the Deutsche Forschungsgemeinschaft is gratefully acknowledged.

References

Borsi, S., Ferrara, G., Piccoli, G.: Determinazione col metodo K/Ar dell'età delle eruzioni Euganee. Rend. Soc. Ital. Mineral. Petr. *25*, 3–10, 1969

De Jong, K. A., Manzoni, M., Stavenga, T., Van Dijk, F., Van der Voo, R., Zijderveld, J. D. A.: Palaeomagnetic evidence for rotation of Sardinia during Early Miocene. Nature *243*, 281–283, 1973

Förster, H., Soffel, H., Zinsser, H.: Palaeomagnetism of rocks from the Eastern Alps from north and south of the Insubrian line. N. Jb. Geol. Palaeont., in press, 1975

Lowrie, W., Alvarez, W.: Rotation of the Italian peninsula. Nature *251*, 285–288, 1974

Manzoni, M.: Paleomagnetic data of Middle and Upper Triassic age from the Dolomites (Eastern Alps, Italy). Tectonophysics *10*, 411–424, 1970

McElhinny, M. W.: Palaeomagnetism and plate tectonics. Cambridge: The University Press 1973

Piccoli, G.: Tettonica e attività vulcanica nel paleogene dei Lessini (Alpi meridionali, Italia). Proc. Intern. Geol. Congr. India, Part *11*, 497–513, 1964

Piccoli, G.: Subaqueous and subaerial basic volcanic eruptions in the Paleogene of the Lessinian Alps (Southern Alps, Italy). Bull. Volcanol. *29*, 253–270, 1966

Piccoli, G.: Le conoscenze attuali sulle manifestazioni eruttive neogeniche nel Veneto. Giorn. Geol. *35*, 359–366, 1969

Riedel, A.: Geologia degli Euganei nord-occidentali. Mem. Museo Civico St. Nat. Verona *2*, 107–124, 1950

Schiavinato, G.: La provincia magmatica del Veneto sud-occidentale Mem. Ist. Geol. Mineral. Univ. Padova *17*, 1–38, 1950

Soffel, H.: Anticlockwise rotation of Italy between the Eocene and Miocene: palaeomagnetic evidence from the Colli Euganei, Italy. Earth Planet. Sci. Lett. *17*, 207–210, 1972

Soffel, H.: Palaeomagnetism and rock magnetism of the Colli Euganei volcanites and the rotation of Northern Italy between Eocene and Oligocene. Boll. Geofis. Teor. Appl. *16*, 333–355, 1974a

Soffel, H.: The palaeomagnetism of the Permian effusives near St. Anton, Vorarlberg (Austria) and the anticlockwise rotation of the Northern Calcareous Alps through 60°. Jb. Geol. Palaeont., in press, 1975a

Soffel, H.: Rock magnetism of the Monti Lessini and Monte Berici Volcanites and age of volcanism deduced from the Heirtzler polarity time scale. J. Geophys. *41*, 401–411, 1975
Zijderveld, J. D. A., Van der Voo, R.: Palaeomagnetism in the Mediterranean area. Implications of continental drift to the Earth Sciences. Vol. 1. New York: Academic Press 1973

Prof. Dr. Heinrich Soffel
Institut für Allgemeine und
Angewandte Geophysik der Universität
D-8000 München 2, Theresienstraße 41
Federal Republic of Germany

J. Geophys. 41, 401–411, 1975

Rock Magnetism of the Monti Lessini and Monte Berici Volcanites and Age of Volcanism Deduced from the Heirtzler Polarity Time Scale

H. Soffel

Institut für Allgemeine und Angewandte Geophysik der Universität München

Received January 30, 1975

Abstract. In order to support the palaeomagnetic measurements (Soffel, 1975) on Tertiary volcanites from the Monti Lessini and Monte Berici, additional rock magnetic studies have been made. They show that the carriers of remanent magnetization of the basalts are members of the Titanomagnetite solid solution series. Intrusive bodies have homogeneous Titanomagnetites with Curie temperatures between 80° and 300 °C corresponding to phases richer in Ulvöspinel than in Magnetite. Subaqueous and subaerial basalts show features of high termperature oxidation with exsolution lamellae of Hemoilmenite within a spinel phase close to Magnetite (Curie temperatures between 470° and 520 °C). Also in the subaqueous and subaerial basalts, the primary ore phase before high temperature oxidation has been a member of the Titanomagnetite solid solution series with a high Titanium content. The ores in the basalts show almost no indications of a secondary low temperature oxidation. It can therefore be concluded that the investigated basalts possess a primary remanent magnetization acquired at the time of their formation.

Several rock magnetic properties have been correlated such as saturation magnetization and susceptibility ($K = 0.845$), coercive force and ratio between saturation remanence and saturation magnetization ($K = 0.800$), reciprocal coercive force and normalized susceptibility ($K = 0.646$), Curie temperature and density ($K = -0.609$). No correlation ($K = 0.03$) could be found between coercive force and Q ratio.

A comparison of the polarity of the lavas (Soffel, 1975) with the Heirtzler *et al.* (1968) polarity time scale of the geomagnetic field suggests that in the Monti Lessini two separate cycles of volcanic activity are present. An older cycle mainly between 52 and 46 m.y. and a younger cycle mainly between 40 and 32 m.y. Such two cycles of volcanic activity are also discussed for the adjacent Colli Euganei.

Key words: Rock Magnetism – Heirtzler Polarity Time Scale.

1. Introduction

This paper should be regarded as complementary to the previous paper by Soffel (1975) which contains the results of palaeomagnetic measurements on the Monti Lessini and Monte Berici volcanites of Tertiary age in Northern Italy. It has been disconnected from it and published as a separate paper within the same volume of Journal of Geophysics because of technical reasons.

The rock-magnetic and ore microscopic studies have been made in order to determine the nature and origin of the remanent magnetization of the rocks and to support the palaeomagnetic data. The aim was further to investigate whether the natural remanent magnetization is a primary one acquired by the rocks at the time of their formation or has been altered due to secondary processes like wheathering or other chemical changes at a later time of their history.

Table 1. Rock magnetic and mineralogical data. Meaning of the different columns: 1: site number, 2: susceptibility in 10^{-6} cgs units, 3: mean intensity of induced magnetization in μG ($1\ \mu G = 10^{-6}$ Gauss), assuming a field of 0.48 Oe, 4: Q ratio for NRM, 5: saturation magnetization at room temperature in Gauss before heating, 6: saturation magnetization at room temperature in Gauss after heating, 7: type of J_s/T curve according to Fig. 1, 8: saturation remanence in 10^{-3} Gauss, 9: ratio between saturation remanence and

1 Nr.	2 $\chi(10^{-6})$	3 $J_i(\mu G)$	4 Q_{NRM}	5 $J_s(G)$	6 $J_s(G)$	7 J_s/T	8 $Rm_s(mG)$
1	865	415	5,56	0,534	0,569	10	67.2
2	4946	2374	0,33	4,164	3,768	3	923,1
3	4940	2371	0,85	3,173	3,125	6	313,5
4	3819	1833	0,59	2,117	3,472	9	411,0
5	2131	1023	4,88	1,473	3,001	8	331,5
6/1	1906	915	1,18	2,305	1,619	3	866,7
6/2	4955	2378	0,68	3,747	3,995	5	311,8
7	4596	2206	0,70	3,554	3,844	5	371,6
8	1954	938	3,74	1,825	3,160	8	364,6
9	3150	1512	1,94	1,052	1,635	7	161,9
10	6205	2979	0,65	3,025	2,847	3	386,2
11	2126	1021	1,90	1,010	1,284	8	147,0
12	3698	1775	12,96	0,523	2,077	7	100,3
13	3032	1455	5,63	1,252	2,133	7	258,3
14	354	170	16,24	0,209	0,278	7	83,4
15	3105	1491	0,61	1,940	2,720	8	336,4
16	2442	1172	4,39	1,360	2,060	8	160,5
17	2636	1266	2,13	1,480	2,310	7	218,9
18	924	443	2,07	0,750	0,810	2	127,6
19	773	371	6,84	0,540	0,330	3	171,8
20	838	402	5,62	0,360	0,320	3	106,2
21	217	104	5,76	0,210	0,210	1	43,1
22	1044	501	1,72	0,690	0,590	3	95,0
23	825	396	1,95	0,517	0,505	1	45,7
24/1	5315	2551	0,83	2,519	2,924	11	263,6
24/2	1220	586	4,43	0,417	1,545	7	93,9
25	523	251	15,86	0,285	0,949	9	30,3
26	1693	813	1,06	1,926	1,915	3	406,3
27	2455	1778	5,01	1,154	1,867	7	170,8
28	1637	786	33,33	1,185	1,768	9	316,9
29	2882	1383	2,32	1,221	2,131	7	136,6
30	2143	1029	2,31	1,099	1,773	7	158,9
31/1	802	385	5,10	1,337	0,739	3	704,3
31/2	338	162	4,84	0,289	0,251	3	98,6
32/1	1030	496	6,10	0,430	0,306	3	107,3
32/2	3090	1483	1,25	1,377	0,505	4	86,7
33	433	208	22,76	0,274	1,219	7	69,4

saturation magnetization at room temperature before heating in percent, 10: net coercive force in Oe, 11: Curie temperatures of the heating cycle. +: Pseudo Curie temperature of a Maghemite phase. 12: Curie temperatures of the cooling cycle, 13: class of high temperature oxidation according to Wilson and Haggerty (1966), 14: presence of primary Ilmenite. −: absent, +: traces, ++: rare. 15: presence of Maghemite. +: yes, −: no. 16: bulk rock density

9 Rm_s/J_s	10 H_c(Oe)	11 T_c(up)	12 T_c(down)	13 Oxid,	14 Ilm.	15 Magh.	16 σ(gcm^{-3})
12.6	70.0	500	520	3	++	−	2,76
22,2	167.2	530	500	1	++	+	2,90
9,9	43.0	200, 470	170, 470	1	+	+	2,96
19,4	61.7	300, 490	490	1	+	−	2,90
22,5	60.4	270, 480	490	1	−	−	2,90
37,6	340.0	560	530	4	++	−	2,72
8,3	48.4	530	520	1	+	+	2,83
10,5	56.8	520	490	1	+	+	2,90
20,0	58.8	250, 490	500	1	+	−	2,97
15,4	39.0	90	90, 430	1	−	−	2,99
12,8	30.3	510	480	1	+	−	3,02
14,6	48.1	320, 500	280, 520	1	++	−	2,68
19,2	22.0	80	80, 480	1	−	−	2,97
20,6	44.4	100	120, 470	1	−	−	2,93
39,9	80.0	290	540	1	++	−	2,65
17,3	63.2	250, 500	520	1	+	−	2,84
11,8	38.4	200, 480	510	1	+	−	2,58
14,8	42.0	220	470	1	−	+	2,83
17,0	82.4	530	530	4	++	−	2,65
31,8	244.0	580	560	4	++	−	2,34
29,5	266.0	580	560	4	++	−	2,39
20,5	200.0	540	530	5	++	−	2,72
13,8	86.0	540	530	2	++	−	2,72
8,8	59.6	530	520	2	++	−	2,75
10,5	51.2	350	490, 250	1	−	−	3,02
20,0	69.2	90	470	1	−	−	3,02
10,6	57.2	90, 490	90, 490	1	++	−	2,90
21,1	179.2	540	510	2	+	−	2,67
14,8	31.2	190	490	1	−	−	3,01
26,7	73.2	250, 490	490	1	−	−	2,84
11,2	27.6	190	500	1	−	−	2,94
14,5	32.0	160	500	1	+	−	2,93
52,7	543.6	560	530	4	++	−	2,67
34,1	397.2	570	540	4	++	−	2,31
25,0	164.0	550	550	4	++	−	2,32
6,5	57.2	350+, 520	500	4	++	+	2,67
25,3	64.8	80	100, 480	1	+	−	2,84

An attempt was also made to get more precise data of the age of volcanism in the Monti Lessini and Monte Berici with the observed polarity distribution of the volcanic units and the Heirtzler, Dickson, Herron, Pitman and Le Pichon (1968) polarity time scale of the geomagnetic field.

37 volcanic units have been sampled in the Monti Lessini and Monte Berici. The sampling localities and the ages of the rocks can be taken from Soffel (1975) and the site numbers are the same as in that paper in order to facilitate the correlation between the rock magnetic data of this paper and the palaeomagnetic data of the above mentioned publication.

2. Rock Magnetic Investigations and Ore Microscopic Studies

Most of the rock magnetic data are listed in Table 1. The parameters which have been measured are: susceptibility χ in cgs units, induced magnetization J_i assuming an ambient field of 0.48 Oe (which is typical for the sampling area), Q ratio, saturation magnetization J_s of the natural sample in Gauss, saturation magnetization J_s after heating the sample up to 600 °C for the determination of the Curie temperature, saturation remanence Rm_s in 10^{-3} Gauss after saturation in a field of 8000 Oe, ratio Rm_s and J_s of the natural sample in percent, net coercive force H_c in Oe, Curie temperatures of the heating cycle, Curie temperatures of the cooling cycle (after heating up to 600 °C), degree of deuteric oxidation of the ore phase according to the nomenclature introduced by Wilson and Haggerty (1966), presence of Ilmenite and/or Maghemite, bulk density in g/cm³.

2.1. Ore Microscopic Studies and Determination of Curie Temperatures

Ore microscopic studies revealed that the prevalent carriers of remanence are in general members of the Titanomagnetite solid solution series with variable Titanium content.

In some cases primary Ilmenite was found to be coexistent with primary unexsolved Titanomagnetite within the same ore grain or in the form of separate fine needles. Secondary Ilmenite is present in samples where the primary Titanomagnetite has been exsolved by deuteric oxidation of class 2—5 according to the nomenclature introduced by Wilson and Haggerty (1966). In general the ores are fresh and show no indications of subsequent low temperature oxidation due to wheathering or hydrothermal alteration. Some results of the ore microscopic studies have also been listed in Table 1. Information is given about the class of deuteric oxidation (class 1—5), the abundance of Ilmenite (++: rare, +: traces) and signs of subsequent low temperature oxidation (+: yes, −: no) leading to Titanomaghemite.

The Curie temperatures have been determined by measuring the saturation magnetization of a pulverized rock sample as dependent on temperature with a Forrer type horizontal balance as described by Petersen (1961, 1965). Measurement was made in air by heating the sample up to 600.°C and cooling it back to room temperature at a rate of about 15—20 °C per minute for each cycle. The saturation magnetization was measured digitally every 10—20° depending on the gradient of the curve. The Curie temperatures thus obtained for the heating and the cooling cycle are listed in Table 1.

Among the J_s/T curves of samples from the 37 sites 11 different types could be distinguished (Fig. 1). Their type is listed in Table 1 and will be discussed briefly with

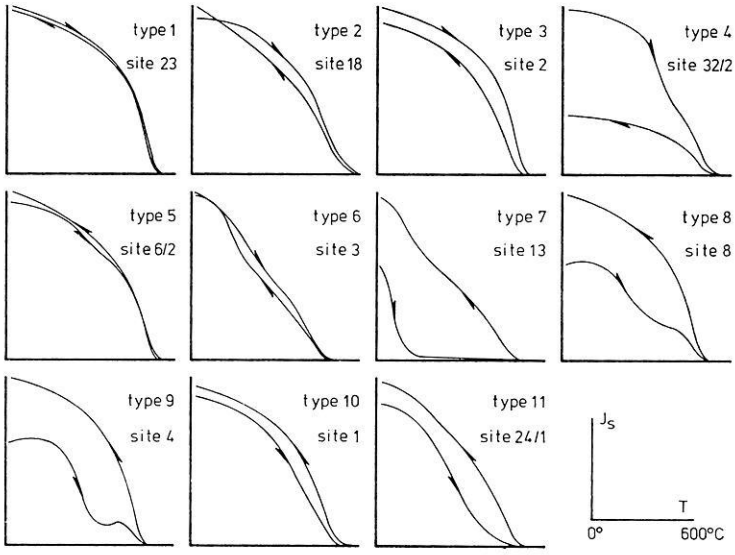

Fig. 1. Dependence of saturation magnetization (in arbitrary units) on temperature. Both heating and cooling cycle are shown and indicated by arrows. For absolute values see Table 1

respect to their main characteristics. Interpretation of the J_s/T curves has been combined with ore microscopic observation and rock magnetic properties (see Table 1) for the determination of the carrier of characteristic remanence in the rocks.

Type 1 (sites 21, 23): Exsolved Titanomagnetite due to deuteric oxidation of class 5 and 2 respectively. The slight drop of the Curie temperature and saturation magnetization of the cooling cycle may be due to a migration of Titanium back into the lattice of the cubic phase.

Type 2 (site 18): Exsolved Titanomagnetite and exsolved needles of Hemoilmenite due to deuteric oxidation of class 4. Change of Curie temperature and type of J_s/T curve due to diffusion of Titanium within the ores.

Type 3 (sites 2,6/1, 10, 19, 20, 22, 26, 31/1, 31/2, 32/1): Titanomagnetite with high Curie temperature either due to deuteric oxidation or due to primary low Titanium content. The large drop of Curie temperature and intensity of saturation magnetization of the cooling cycle is a consequence of Titanium diffusion and oxidation during the exderiment. Type 4 (site 32/2): Exsolved Titanomagnetite due to deuteric oxidation showing signs of subsequent low temperature oxidation (Titanomaghemite). Pseudo Curie temperature at around 350 °C is actually the temperature of desintegration of secondary metastable Titanomaghemite into stable Ilmohematite. Drop of the Curie temperature and intensity of saturation magnetization is a consequence of diffusion of Titanium and disappearance of metastable Titanomaghemite. Type 5 (sites 6/2, 7): Unexsolved Titanomagnetite with small Titanium content showing slight indications of a beginning low temperature oxidation. Almost reversible J_s/T curve. Small differences between heating and cooling curve are due to diffusion of Titanium.

Type 6 (site 3): Unexsolved Titanomagnetite with small Titanium content together with an anisotropic phase, possibly a member of the Ilmenite-Hematite solid

solutions series. The Titanomagnetites show no indications of a beginning low temperature oxidation.

Type 7 (sites 9, 12—14, 17, 24/2, 27, 29, 30, 33): Unexsolved Titanomagnetite with high Titanium content, sometimes coexisting with Ilmenite, showing no signs of deuteric oxidation. Irreversible J_s/T curve due to oxidation of the Titanomagnetites during the experiment forming phases closer to Magnetite.

Type 8 (sites 5, 8, 11, 15, 16): Unexsolved Titanomaghemite with medium Titanium content. Desintegration (exsolution) of the primary ore phase by heating above 300 °C results in the production of a phase close to Magnetite with a Curie temperature of about 500 °C and a correspondingly large saturation magnetization.

Type 9 (sites 4, 25, 28): Similar properties as for type 8 but with a secondary maximum of saturation magnetization at around 400 °C. Material of such properties of the J_s/T curve is capable of a partial or complete self reversal of remanence when heated under certain conditions (Petersen and Bleil, 1973; Creer and Petersen, 1969).

Type 10 (site 10): Exsolved members of the Ilmenite-Hematite and Titanomagnetite, solid solution series as a result of exsolution. Cooling curve shows increased Curie temperature and saturation magnetization probably due to formation of new phases belonging to the Titanomagnetite solid solution series. Type 11 (site 24/1): Unexsolved Titanomagnetite with medium Titanium content, probably decomposing into two phases (one with $T_c = 490$ °C, another with $T_c = 250$ °C) after heating up to 600 °C in air.

The analyses of the ore phase indicates that the primary ore phase of the volcanites of the Monti Lessini and Monte Berici area is in most cases a member of the Titanomagnetite solid solution series with a high Titanium content. This is evident from the many sites with Curie temperatures below 300 °C. Predominantly the intrusive basalts of the investigated area fall into this group. Exsolved Titanomagnetites with higher Curie temperatures of the secondary phase of around 500 °C can clearly derived from primary low Curie temperature Titanomagnetites as a consequence of deuteric oxidation under subaqueous or subaerial conditions. The high Curie temperatures observed for some apparently homogeneous and unexsolved Titanomagnetites can be due to unobservable submicroscopic exsolutions. Low temperature oxidation due to wheathering or hydrothermal alteration immediately after the formation of the rocks is rare. Such features have been found to be much more abundant among the more acid volcanics of the Colli Euganei (Soffel, 1974) which had in general a much lower Titanium content in the Titanomagnetites. This suggests that the Colli Euganei magmas have assimilated much more crustal material than the Monti Lessini and Monte Berici volcanites during their way to the earth's surface.

According to the rock magnetic and ore microscopic studies the characteristic remanent magnetization (CARM) of all sites from the Monti Lessini and Monte Berici is a primary magnetization acquired by the rocks at the time of their formation. Only the samples from site number 32/2 seem to have suffered subsequent low temperature oxidation. As the characteristic remanent magnetization of this site groups very well (and so does already the natural remanent magnetization) and has the same direction as the subjacent flow it can be assumed that the slight mineralogical changes of the ore minerals are due to hydrothermal alteration immediately during or after the formation of the rock. In this case the palaeomagnetic result of site number 32/2 can be regarded as a reliable data (Ade—Hall *et al.*, 1971).

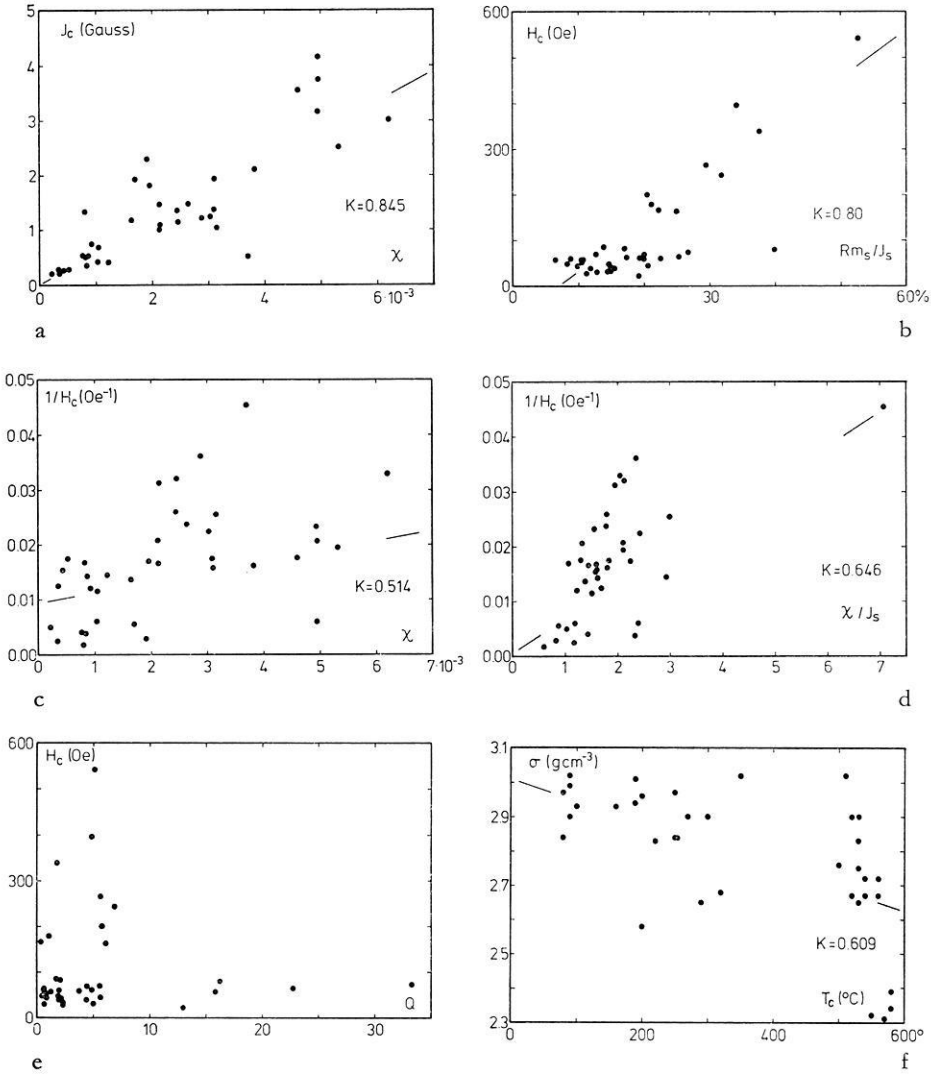

Fig. 2. Correlation between different rock magnetic parameters. a) Saturation magnetization J_s (in Gauss) versus susceptibility χ in cgs units. b) Coercive force in Oe versus the ratio between saturation remanence Rm_s and saturation magnetization J_s in percent. c) Reciprocal coercive force (in 1/Oe) versus susceptibility χ in cgs units. d) reciprocal coercive force (in 1/Oe) versus the ratio between susceptibility in cgs units and saturation magnetization J_s in arbitrary units. e) Coercive force in Oe versus Q ratio. f) Bulk density (in g cm^{-3}) versus Curie temperature

2.2. Correlation of Rock Magnetic Parameters

Some of the rock magnetic parameters which are listed in Table 1 and for which linear relationships are expected from the theory of ferro(i)magnetism have been correlated and plotted in Fig. 2. A good (Fig. 2a) correlation (correlation coefficient

$K=0.845$) could be found between saturation magnetization and susceptibility. An even better correlation between these two parameters ($K=0.917$) has been found for the Colli Euganei volcanites (Soffel, 1974). This indicates that the ore content of the Monti Lessini and Monte Berici volcanites is less homogeneous than in the Colli Euganei with respect to the chemical composition and grain size distribution. This is in fact the case. In the Colli Euganei (Soffel, 1974) there are in general acid volcanites with Titanomagnetites (exsolved as well as unexsolved) with low Titanium content. In the basic rocks of the Monti Lessini and Monte Berici Titanomagnetites with very low and very high Titanium content are present. Another good correlation ($K=0.8$) could be found between the net coercive force and the ratio between saturation remanence (produced in a field of 8400 Oe) and the saturation magnetization at room temperature. For the Colli Euganei volcanites a value of $K=0.84$ has been determined as correlation coefficient between these two parameters. All lava flows with unexsolved and large Titanomagnetite grains are found in the lower left part of this diagram (Fig. 2b) while the exsolved Titanomagnetites and the rocks with small Titanomagnetite particles are found in the upper right part of Fig. 2b. This is consistent with the idea that single domain and pseudo single domain particles have much larger coercive forces and Rm_s/J_s ratios than the large multidomain grains. A pretty bad correlation ($K=0.514$) could be found between the reciprocal coercive force ($1/H_c$) and the susceptibility although a linear relationship should be expected between these two quantities (Fig. 2c) from the theory of ferro(i)magnetism based on the model of domain wall friction. However the correlation between the two parameters is disturbed by the variable ore content of the rocks which influences the susceptibility but not the coercive force. An improvement for the correlation between $1/H_c$ and χ could be obtained by plotting $1/H_c$ versus χ/J_s in arbitraty units. The diagram is shown in Fig. 2d. The correlation coefficient is now $K=0.646$. No correlation ($K=0.03$) could be found between the coercive force H_c and the Q ratio for the natural remanent magnetization (see Fig. 2e). This is surprising because for ore grains with large coercive forces a large remanent magnetization J_r and a small induced magnetization J_i is expected from theory of ferro(i)magnetism. $Q=J_r/J_i$ should therefore correlate to some extent with H_c. A good linear (and positive) correlation between H_c and Q has been reported by Kropacek (1974, private communication) for Tertiary basalts in northern CSSR. The bad correlation between H_c and Q for the Monti Lessini and Monte Berici basalts is probably due to the different polarity of the rocks and their different acquisition capacity for viscous magnetization components. The degree of deuteric oxidation, by which the Curie temperature of the ore minerals is increased, is expected to influence also the bulk density of the rocks. Intrusive basalts with low Curie temperatures are supposed to have higher densities than basalts formed under subaerial or subaqueous conditions with high Curie temperatures due to oxidation and/or exsolution. The density versus Curie temperature is plotted in Fig. 2f. The correlation between the two parameters is not very good ($K=0.609$) but a tendency in the above mentioned sense is present.

3. Relations to the Heirtzler Polarity Time Scale of the Geomagnetic Field

A polarity time scale of the geomagnetic field for the past 80 m.y. has been determined by Heirtzler, Dickson, Herron, Pitman and Le Pichon (1968) with the help of the

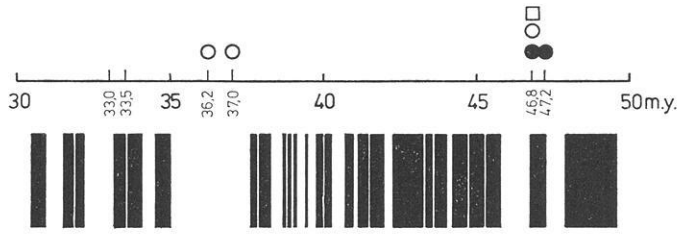

Fig. 3. Heirtzler *et al.* (1968) polarity time scale of the geomagnetic field in the time interval between 30 and 50 m.y. Radiometric age determinations in the Monti Lessini and Monte Berici are indicated as well as the polarities of remanent magnetization of rocks. Black areas and dots: normal polarity, white areas and open circles: reversed polarities. Square: intermediate remanence direction

pattern of marine magnetic anomalies in combination with radiometric and paleontological data. The polarity time scale for the time interval from 30 to 50 m.y. is shown in Fig. 3. Black areas mean times of normal polarity, white areas are times of reversed polarity. The polarity of remanent magnetization of 6 lava flows (Soffel, 1975) are also shown together with their radiometric ages according to Piccoli (private communication, 1973). Two lava flows (36.2 and 37.0 m.y.) show reversed polarity (open circles) in agreement with the Heirtzler *et al.* (1968) polarity time scale. Good agreement could also be obtained for a flow with an age of 47.2 m.y. having normal polarity (closed circle). Among three lava flows aged 46.8 m.y. one has normal, another reversed and a third intermediate polarity (open square). This age seems to represent a time of transition from a reversed to a normal polarity, again in agreement with the Heirtzler polarity time scale. Two other age determinations (33.0 and 33.5 m.y.) were made on rocks not suitable for palaeomagnetic measurements.

4. *Tentative Age Determination of the Monti Lessini Volcanism with the Heirtzler et al. (1968) Polarity Time Scale*

Regarding the polarity time scale of Heirtzler *et al.* (1968) for the time interval between 30 and 50 m.y. (see Fig. 3) it can be seen that the times of normal and reversed polarity of the geomagnetic field are not equally distributed. Between 35 and 38 m.y. a reversed polarity is prevalent, while between 42 and 45 m.y. a normal polarity is predominant. The curve shown in Fig. 4 represents the average abundance of normal polarity in percent within a time interval of ± 1.5 m.y. around a given time according to the Heirtzler *et al.* (1968) polarity time scale between 25 and 60 m.y. As previously indicated there is a small abundance of normal polarity at around 36 m.y. (less than 20% of a 3 m.y. time interval) and a large abundance (almost 80% of a 3 m.y. time interval) at around 43 m.y. Assuming that the production of volcanic material happened at a more or less constant rate during several million years and that an equally well distributed sampling in the investigated area has been made, the ratio between lava flows of normal and reversed polarity should in some way reflect the polarity distribution at the time of active volcanism.

The palaeomagnetic data of the Monti Lessini volcanites (Soffel, 1975) demonstrate that almost all lava flows have reversed polarity. In an earlier section of this paper it could be shown that the CARM of the rocks is a primary magnetization acquired by

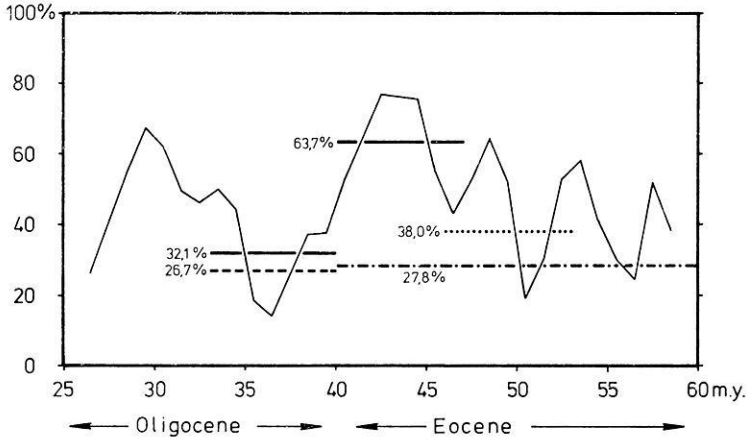

Fig. 4. Average abundance of normal polarity in percent within a time interval of ± 1.5 m. y. around a given time according to the Heirtzler *et al.* (1968) polarity time scale between 25 and 60 m.y. For the meaning of the horizontal bars: see text

the rocks at the time of their formation. Selfreversals of natural remanent magnetization have most probably not occurred. It can therefore be concluded that a reversed polarity has been acquired by the rocks at a time where the geomagnetic field had a reversed polarity.

Among 15 volcanic units in the Monti Lessini which are of Oligocene age (according to radiometric or to biostratigraphic dating), 11 (73.3%) have reversed and 4 (26.7%) have normal polarity. This value of 26.7% (abundance of lava flows with normal polarity) is shown in Fig. 4 as a dashed horizontal line covering the time interval between 33 and 40 m. y. which is supposed to be the time of volcanic activity in the Monti Lessini and Monte Berici in Lower Oligocene. From the Heirtzler *et al.* (1968) polarity time scale an abundance of 32.1% (solid horizontal line in Fig. 4) can be computed for the same time interval (33 to 40 m. y.) in agreement with observation yielding a value of 26.7%. Other intervals like 33 to 39 m. y. (34.8%), 33 to 38 m. y. (33.0%), 32 to 38 m. y. (30.3%), 32 to 39 m. y. (32.3%) and 32 to 40 m. y. (32.8%) all including the radiometrically determined ages of 33.0, 33.5, 36.2 and 37.0 m. y. (see Fig. 3) yield roughly the same value of about 30% for the abundance of normal polarity.

An abundance of 63.7% for the normal polarity (solid horizontal line in Fig. 4) should be expected if the Eocene volcanism in the Monti Lessini had occurred between 40 and 47 m. y. However among the 18 volcanic units in the Monti Lessini of Eocene age (according to radiometric or to biostratigraphic dating), 13 (72.2%) have reversed and only 5 (27.8%, dash-dotted horizontal line in Fig. 4) have normal polarity. A comparatively small abundance of normal polarities (38.0%, dotted horizontal line in Fig. 4) is only present in the time interval between 46 and 53 m. y. which contains the radiometrically determined ages of 46.8 and 47.2 m. y. (see Fig. 3). Small abundances of normal polarities can also be expected in Lower Eocene between 54 and 58 m. y. (22.5%) and between 54 and 59 m. y. (36.0%).

The abundance of lava flows with normal polarity of either Oligocene or Eocene age therefore suggests that the Oligocene volcanism occurred between 32 and 40 m. y.

and the Eocene volcanism took place between 46 and 52 m.y. or earlier. According to the small abundance of lava flows with normal polarity ages between 40 and 46 m.y. are very unlikely. This implies that in the Monti Lessini a younger (Lower to Middle Oligocene) and an older (Lower to Middle Eocene) cycle of volcanism are present, separated by a time interval of about 6 to 8 m.y. in Upper Eocene with relatively small volcanic activity. A similar situation is also discussed for the volcanism of the adjacent Colli Euganei (Schiavinato, 1950).

Acknowledgement. The investigations have been made in the Institut für Allgemeine und Angewandte Geophysik, Universität München. Thanks are due to Prof. Dr. G. Angenheister, Dr. N. Petersen, Dr. J. Pohl, Dr. E. Schmidbauer, Dr. A. Schult and Dipl. Geophys. Ch. Schweitzer for many helpful discussions. The financial support of the Deutsche Forschungsgemeinschaft is gratefully acknowledged.

References

Ade–Hall, J.M., Palmer, H.C., Hubbard, T.P.: The magnetic and opaque petrological response of basalts to regional hydrothermal alteration. Geophys. J. *24*, 137–174, 1971

Creer, K.M., Petersen, N.: Thermochemical magnetization in basalts. Z. Geophys. *35*, 501–516, 1969

Heirtzler, J.R., Dickson, G.O., Herron, E.M., Pitman, W.C. III., Le Pichon, X.: Marine magnetic anomalies, geomagnetic field reversals, and motions of the ocean floor and continents. J. Geophys. Res. *73*, 2119–2136, 1968

Petersen, N.: Untersuchungen magnetischer Eigenschaften von Titanomagnetiten im Basalt des Rauhen Kulm in Verbindung mit mikroskopischer und elektronenmikroskopischer Beobachtung. Dipl. Arbeit, Inst. f. Angew. Geophysik, Universität München, 1961

Petersen, N.: Beobachtung einiger mineralogischer und magnetischer Eigenschaften dreier Basaltproben nach unterschiedlicher thermischer Behandlung. Diss. Naturw. Fak. Universität München, 1965

Petersen, N., Bleil, U.: Self reversal of remanent magnetization in synthetic titanomagnetites. Z. Geophys. *39*, 965–977, 1973

Schiavinato, G.: La provincia magmatica del Veneto sud-occidentale. Mem. Ist. Geol. Mineral. Univ. Padova *17*, 1–38, 1950

Soffel, H.: Palaeomagnetism and rock magnetism of the Colli Euganei volcanites and the rotation of Northern Italy between Eocene and Oligocene. Boll. Geofis. Teor. Appl. *16*, 333–355, 1974

Soffel, H.: The palaeomagnetism of age dated tertiary volcanites of the Monti Lessini (Northern Italy) and its implications to the rotation of Northern Italy. J. Geophys. *41*, 385–400, 1975

Wilson, R.L., Haggerty, S.E.: Reversals of the earth's magnetic field. Endevour *25*, 104–109, 1966

Prof. Dr. Heinrich Soffel
Institut für Allgemeine und
Angewandte Geophysik der Universität
D-8000 München 2, Theresienstraße 41
Federal Republic of Germany

J. Geophys. 41, 413–439, 1975

Supersonic Plasma Flow between High Latitude Conjugate Ionospheres

G. Rösler

Max-Planck-Institut für Physik und Astrophysik,
Institut für extraterrestrische Physik, Garching bei München

Received October 3, 1974; Revised Version February 3, 1975

Abstract. The polar wind problem has been investigated for closed field lines in situations where one of the two conjugate ionospheric regions is fully illuminated by the sun and the other in darkness (solstices at high latitudes). A supersonic flow between hemispheres is possible; the magnetospheric part of this flow must be symmetric with respect to the equator. The daytime fluxes are proportional to the neutral hydrogen density (n_H). Fluxes of the order of 10^8 cm^{-2} sec^{-1} are only possible with n_H considerably higher than given by CIRA models. For stationary solutions higher flow speeds are needed on the dark side than provided from the illuminated side. It is concluded that shock waves with upward velocities of about 5 km/sec would form above the dark ionosphere. This implies a reduction by a factor of 3 to 5 of the plasma influx into the dark hemisphere, whereby F-layer densities of only up to $2 \cdot 10^4$ cm^{-3} can be maintained.

Key words: Daytime Polar Wind – Free Flow along Field Lines – Supersonic Influx – Non-Stationary Shock Waves.

I. Introduction

The stability of F-layer densities during nighttime when photoionization ceases to act as an ionization source and recombination should reduce the ion densities gave rise to many theoretical and experimental studies during the last ten years. Thermal plasma fluxes from the protonosphere have been suggested rather early as a means of maintaining nighttime F-layers for midlatidude conditions (Rishbeth, 1963; Hanson and Patterson, 1964; Yonezawa, 1965). Fluxes of the order of 10^8 cm^{-2} sec^{-1} turned out to be necessary for stationary F-layers of 10^5 cm^{-3}. Theoretical calculations of the limiting daytime fluxes into the protonosphere indicating maximum fluxes of some 10^7 cm^{-2} sec^{-1} (for example Hanson and Patterson, 1964; Geisler, 1967), however, seemed to restrict this mechanism severely and dynamical processes like upward drifts caused by neutral winds and electric fields (Hanson and Patterson, 1964; King *et al.*, 1967; Kohl *et al.*, 1968; Stubbe, Chandra, 1970) and effects of corpuscular radiation (Torr, Torr, 1970) and atmospheric composition changes (Rüster, 1971) have been favoured. Nevertheless, there is growing evidence from experimental results (Evans, 1965; Park, 1970) as well as from theoretical investigations (Nagy *et al.*, 1968; Banks, Kockarts, 1973; Park, Banks, 1974) (for instance increasing the daytime fluxes by use of more realistic atmospheric models) that the protonosphere can act efficiently as an ionization reservoir for the nighttime ionosphere at least under certain conditions.

The average electron content of a magnetic flux tube at $L = 4$, located within the plasmasphere under quiet geomagnetic conditions, is about $6 \cdot 10^{13}$ electrons/cm^2

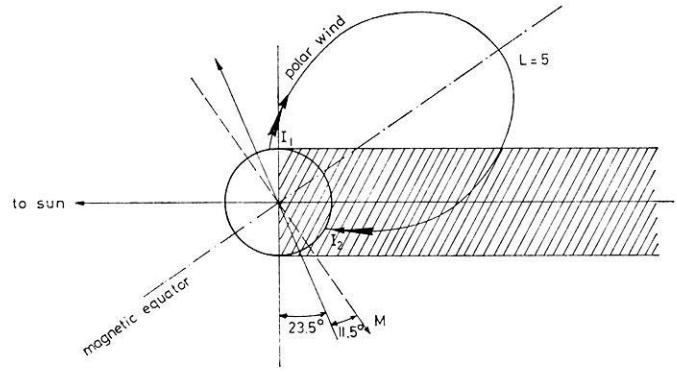

Fig. 1. Asymmetric geomagnetic configuration for solstices and magnetic midnight of the winter ionosphere I_2. The inclination of the rotation axis and the angle between geographic and magnetic axis just add. The summer ionosphere I_1 is still illuminated, the conjugate winter ionosphere I_2 in darkness

tube (e.g. Park, 1970) with an electron density of 10^3—10^4 cm^{-3}. This ionization therefore can supply nighttime fluxes for some days and does not need 'immediate' replenishment. The electron content of a closed flux tube outside the plasmasphere (with n_e of the order of 1 cm^{-3}) at for example $L = 5$—6, however, is at least two orders of magnitude less and cannot maintain downward fluxes of 10^8 cm^{-2} sec^{-1} for several hours unless the loss of ionization is balanced at the same time. Hence concerning high latitude winter conditions influx of plasma along field lines has been discounted because of the lack of a suitable source (Rishbeth, 1970). In this paper a geomagnetic configuration shall be discussed which could allow for such an influx of plasma into the winter nighttime ionosphere by a polar wind from the conjugate summer daytime ionosphere acting as a source of replenishment.

The polar wind problem for closed field lines has been studied for instance in two papers by Mayr, Grebowsky and Taylor in 1970 and by Banks, Nagy and Axford in 1971. In both papers a symmetric configuration corresponding to the magnetic axis perpendicular to the eccliptic plane is assumed with both conjugate ionospheres – which have to be nighttime ionospheres in that case – still emitting polar wind fluxes. By different arguments it is concluded that outward directed polar wind fluxes can be a rather steady phenomenon also for closed flux tubes. In contrast to these investigations of equinotial conditions the field line configuration of this paper corresponding to solstices at high latitudes is a most asymmetric one where the inclination of the magnetic axis is maximum forming an angle of 55° with respect to the eccliptic plane. This situation is shown in Fig. 1. It is evident that in this way a closed field line outside the plasmasphere with an L-value of for example 5 yields a coupling of a summer daytime ionosphere to a winter nighttime ionosphere. Diffusive plasma fluxes as a coupling between two conjugate midlatitude ionospheres have been investigated by Kohl (1966). With respect to high latitude ionospheres topside electron density and ion composition measurements only agree with high speed outward or inward plasma flow. Hence it is our objective to discuss whether a daytime polar wind can represent a mechanism of transport of ionization into the high latitude nighttime ionosphere.

There are two crucial questions connected with this model. The first one is related to the maintenance of outward directed plasma fluxes from the nighttime ionosphere. Without an effective source of ionization recombination and upward flow result in a depletion of ionization. The proton flux at great heights must be supported by an O^+-flux of equal size at lower heights through charge exchange of O^+-ions with neutral hydrogen. (For a review of ionospheric processes see for example Banks, Kockarts, 1973). This O^+-flux is fully developed at a height of about 700 km. With a mean O^+-density of $3 \cdot 10^5$ cm^{-3} and a constant recombination coefficient of $4 \cdot 10^5$ sec^{-1} an O^+-flux of $4 \cdot 10^8$ cm^{-2} sec^{-1} together with recombination would exhaust the ionospheric O^+-reservoir between 200 and 700 km height with a time scale of about 4 hours. This depletion process must be seen in the context of the high latitude convection cycle and the corresponding convection times. According to the work of Dungey (1961), Axford and Hines (1961), Nishida (1966) and Brice (1967) this cycle consists of field line merging at the front of the magnetosphere, convection across the polar caps, reconnection in the tail and migration back towards the sun along the auroral oval. Depending on the L-value of the magnetic flux tube typical convection times range from about four to ten hours. The winter ionosphere I_2 (Fig. 1) spends about three quarters of this cycle in darkness. It is therefore assumed that the nighttime fluxes at least are reduced considerably when both ionospheres I_1 and I_2 are coupled after reconnection. That is, in contrast to the above mentioned papers by Mayr *et al.* (1970) and Banks *et al.* (1971), where two polar wind flows from opposite hemispheres meet at the geomagnetic equator, we adopt for our asymmetric configuration that upward nighttime fluxes are not maintained up to reconnection. As the high latitude exospheric proton density is consistent with outward *and* inward supersonic plasma flow we conclude that the daytime polar wind flux can advance to the nighttime ionosphere at least shortly after reconnection. (It should be emphasized, however, that we do not take into account the effect of particle precipitation in this consideration. Corpuscular ionization may be very important in particular for auroral regions and could cause a much longer time scale for maintaining upward fluxes than derived above.)

The second problem is the effect of reconnection itself on the supersonic daytime fluxes. Preceding reconnection the flux tubes stretch far into the magnetic tail. The mean energy density of the plasma sheet with proton temperatures of the order of some keV, however, is much higher than the critical pressure for polar wind flow which ranges from $5 \cdot 10^{-11}$ to 10^{-10} ergs cm^{-3} (Banks, Holzer, 1969). From a pure hydrodynamic point of view one would expect the formation of shock waves preventing the supersonic flow from reaching the conjugate hemisphere irrespective of whether the nighttime ionosphere is still emitting outward fluxes or not. But clearly a hydrodynamic description is inadequate for this region. At present it appears to be very difficult to assess the effective coupling time between interpenetrating streams of cold and energetic plasmas. No attempt is therefore made to cover this problem and we neglect the presence of energetic particles at high altitudes. Nevertheless, it seems interesting to consider simply a stationary model of the configuration of Fig. 1 based on the assumption that the dominant mechanism in such a flux tube is a polar wind which can flow along closed field lines into a winter nighttime ionosphere. It is the objective of this paper to show the consequences of such a process. In section II the equations and parameters describing ionospheric processes – essentially the same as

used in previous polar wind calculations (Banks, Holzer, 1968, 1969a, 1969b) – are briefly repeated. Section III summarizes some numerical results for daytime conditions. In section IV free flow along field lines is discussed and section V concentrates on the effects of supersonic influx of plasma into the nighttime ionosphere.

II. Hydrodynamic Equations and Parameters

The theory of polar ionospheres has been extensively developed mainly in the papers by Banks and Holzer (Banks, Holzer, 1968, 1969a, 1969b; Banks, 1970, 1971; Holzer, 1970, Holzer *et al.*, 1971). High latitude conditions exhibit for example O^+ remaining the dominant ionospheric constituent up to great heights (some thousand kilometers), much lower electron densities in the topside ionosphere and large scale upward proton fluxes. It has been shown that these special features agree with a model of an expanding ion exosphere. Above F_2-heights photoionization creates an upward O^+-flux which is converted by charge exchange ($O^+ + H \rightarrow H^+ + O$) to a low speed H^+-flux of nearly equal size. Essentially owing to the electron pressure gradient the light ion species, i.e. the protons, is accelerated rather rapidly reaching supersonic speed at altitudes of several thousand kilometers. The coupling between electrons and ions is established by an outward directed polarization field. A great variety of numerical results concerning ion density distributions, escape fluxes and proton velocities for different models has been published in the above mentioned papers. In analogy to solar wind expansion the ionospheric proton flux was termed 'polar wind' as suggested by Axford. The summer daytime ionosphere I_1 (Fig. 1) supplies the boundary conditions of the plasma influx into the winter ionosphere I_2. Therefore, we will deal first with polar wind calculations for the daytime ionosphere only taking account of the appropriate field line configuration and of different atmospheric models.

The equations describing the multi-constituent plasma flow can be written for stationary conditions in the form (Banks, Holzer, 1969b):
Continuity:

$$\frac{1}{A}\frac{\partial}{\partial s}(n_i U_i A) = q_i - l_i \tag{1}$$

Momentum:

$$\begin{aligned}\frac{1}{U_i}\frac{\partial U_i}{\partial s}\left[\frac{U_i^2}{C_i^2} - 1\right] = {} & \frac{1}{C_i^2}\,\mathbf{g}\cdot\mathbf{s} + \frac{1}{A}\frac{\partial A}{\partial s} - \frac{1}{T_i}\frac{\partial T_i}{\partial s} \\ & - \frac{1}{C_i^2}\sum_k \nu_{ik}(U_i - U_k) - \frac{1}{\Phi_i}\frac{\partial \Phi_i}{\partial s} \\ & - \frac{1}{C_i^2 n_e m_i}\frac{\partial P_e}{\partial s} - \frac{q_i}{C_i^2 n_i}U_i\end{aligned} \tag{2}$$

with

$$C_i^2 = kT_i/m_i;\ \Phi_i = n_i U_i A;\ P_{e,i} = n_{e,i}\cdot k\cdot T_{e,i};$$

$n_e = \sum n_i$ and s = coordinate parallel to magnetic field, U = bulk velocity along s, n = number density, A = cross-section of magnetic flux tube, $\mathbf{g} \cdot \mathbf{s}$ = component of gravitational acceleration along s, q_i = ion production rate, l_i = ion loss rate, $T_{i,e}$ = ion, electron temperature, ν_{ik} = momentum transfer collision frequency between i and k type particle, m = particle mass, k = Boltzmann's constant.

The following we will summarize the assumptions and parameters underlying our calculations:

1. Ionospheric Constituents. Only hydrogen and oxygen ions which are the major constituents above F-region heights are considered. The presence of He-ions does not change the results in particular for the proton escape fluxes.

2. Chemical Reactions. With regard to the formation of the F-layer and the ion densities at greater heights ion production and loss is mainly caused by the following reactions (Ferguson, 1967; Mitra, 1968) with the corresponding reaction coefficients λ:

$$O + h\nu \rightarrow O^+, \lambda_1 = 5 \cdot 10^{-7} \text{sec}^{-1}$$

(Banks, Holzer, 1969a)

$$O^+ + N_2 \rightarrow NO^+ + N, \lambda_2 = 5 \cdot 10^{-13} \text{cm}^3\text{sec}^{-1}$$

(Dunkin *et al.*, 1968; Stubbe, 1969)

$$O^+ + O_2 \rightarrow O_2^+ + O, \lambda_3 = 1.6 \cdot 10^{-11} \text{cm}^3\text{sec}^{-1}$$

(Dunkin *et al.*, 1968; Stubbe, 1969)

$$O^+ + H \rightarrow H^+ + O, \lambda_4 = 4.3 \cdot 10^{-11} (T_n + T_i/16)^{1/2} \text{ cm}^3\text{sec}^{-1}$$

(Holzer, Banks, 1969)

$$H^+ + O \rightarrow O^+ + H, \lambda_5 = 3.8 \cdot 10^{-11} (T_i + T_n/16 + 1.2 \cdot 10^{-8} (U(H^+) - U(O))^2)^{1/2} \text{cm}^3\text{sec}^{-1}$$

(Holzer, Banks, 1969)

The molecular ions formed by charge exchange undergo a dissociative recombination reaction according to $AB^+ + e \rightarrow A + B$.

3. Temperatures. For daytime conditions an isothermal model with $T_e = T_i$ is adopted. This assumption may look rather poor as strong positive ion temperature gradients are known to exist between ionospheric levels and for example 3000 km (e.g. Banks, Kockarts, 1973). However, different ion temperature profiles have been inferred by Banks and Holzer (Banks, Holzer, 1969a; Holzer, 1970) in their polar wind studies. It has been shown that the magnitude of the ion temperature is far more important in determining the ion composition profile and the H^+ flow characteristics. The critical solutions (with a continuous transition from supersonic speed to subsonic speed) for the nighttime ionosphere are also calculated under this assumption which is perhaps more severe in that case as the incoming protons are heated by the collisions with the oxygen ions converting translational energy into random thermal energy. Yet these calculations serve only to illustrate the fact that the polar

wind runs into the nighttime ionosphere with a particle density and a mean velocity far from what is required by the critical solutions (see Sect. V). In the discussion of the influx of a realistic polar wind the proton temperature will be considered too.

Neglecting heat conduction the energy balance of the protons can be written as (e.g. Holzer, 1972):

$$\frac{1}{A}\frac{\partial}{\partial s}\left[\Phi_1\left(\frac{1}{2}U_1^2+\frac{\gamma}{\gamma-1}\frac{k\cdot T_1}{m_1}\right)\right]=\mathbf{g}\cdot\mathbf{s}\cdot n_1U_1+\mathcal{Q}_{\mathrm{ce}}+\mathcal{Q}_{\mathrm{coll}} \tag{3}$$

γ = adiabatic constant

(The indices 1 (2) will always refer to the hydrogen (oxygen) ions). The left hand side contains the gradient of the energy flux, the right hand side the influence of gravity and the source terms $\mathcal{Q}_{\mathrm{ce}}$ and $\mathcal{Q}_{\mathrm{coll}}$ describing the energy production per proton mass and unit volume by charge exchange (ce) $H^+ + O \leftrightarrow O^+ + H$ and the collisions (coll) of the protons with the oxygen ions and the neutral atmosphere. The oxygen ions are assumed to have a constant temperature T_i because the energy transfer from the protons is effective only up to altitudes where the O^+-ions are still the major constituent. Because of the high thermal conductivity of the electrons a constant electron temperature is accepted, too.

In the charge exchange process protons are produced which reflect the properties of the O^+-ions (that is $U \approx O$, internal energy $\frac{1}{\gamma-1}kT_i$) and protons with a mean translational energy of $\frac{1}{2}m_1U_1^2$ and internal energy $\frac{1}{\gamma-1}k\cdot T_1$ are lost. The source term $\mathcal{Q}_{\mathrm{ce}}$ therefore is given (in analogy to Holzer, 1972):

$$\mathcal{Q}_{\mathrm{ce}}=q_1\frac{1}{\gamma-1}\frac{kT_i}{m_1}-l_1\left(\frac{1}{2}U_1^2+\frac{1}{\gamma-1}\frac{kT_1}{m_1}\right) \tag{4}$$

where q_1 and l_1 are the respective production and loss rates.

The energy exchange by collisions between the constituents of a multi-component gas mixture has been derived for example by Tanenbaum (1965) from integrating the Boltzmann's equation. One gets:

$$\mathcal{Q}_{\mathrm{coll}}=\sum_i\mathcal{Q}_{\mathrm{coll}}^i$$

$$\mathcal{Q}_{\mathrm{coll}}^i=-n_1\nu'_{1j}\left[\frac{3}{2}\frac{k(T_1-T_i)}{m_1}\cdot\varepsilon-\frac{1}{2}|U_1-U_j|^2\right] \tag{5}$$

The summation extends over all kinds of H^+-collisions. ε depends on the collision cross section and approximates unity for small relative velocities. We adopt this value for all velocities in this paper. The collision frequency for energy transfer ν'_{1j} is connected with the collision frequency for momentum transfer ν_{1j} by:

$$\nu'_{1j}=\frac{2m_1}{m_1+m_j}\cdot\nu_{1j} \tag{6}$$

Eqs. (3) to (5) relate the proton temperature gradient to the velocity derivative and (1) to (5) give a closed set of differential equations for the hydrogen and oxygen ion densities and velocities and the proton temperature which can be solved numerically.

4. Earth Magnetic Field. According to Fig. 1 we consider a magnetic flux tube of a dipole model with an L-value of 5. Clearly a dipole model will be a poor description for closed field lines outside the plasmasphere and an L-value equal to 5 may look rather low for quiet time conditions. The L-value, however, is not decisive for ionospheric problems (for example regarding escape fluxes and escape velocities) where divergence of field lines $\left(\frac{1}{A}\frac{\partial A}{\partial s}\right)$ is not very important. With respect to the magnetospheric part of the polar wind flow the special field line configuration does not affect our results severely. The main point for our discussion is only the existance of a closed field line outside the plasmasphere roughly symmetric to the geomagnetic equator coupling a winter nighttime to a summer daytime ionosphere.

A dipole model yields (with β = geomagnetic latitude, $\xi = \sin\beta$, R_e = earth radius, g_0 = gravitational acceleration at the surface of the earth):

$$ds = R_e L \sqrt{1 + 3\xi^2}\, d\xi \tag{7}$$

$$\frac{1}{A}\frac{\partial A}{\partial S} = 3\xi\left(\frac{2}{1-\xi^2} + \frac{1}{1+3\xi^2}\right) \Big/ (R_e L \sqrt{1+3\xi^2}) \tag{8}$$

$$\mathbf{g}\cdot\mathbf{s} = -g_0 \cdot 2\xi/[L^2(1-\xi^2)\sqrt{1+3\xi^2}] \tag{9}$$

5. Neutral Atmosphere. Models of the neutral atmosphere still seem to involve great uncertainties especially for high latitude regions where continual loss of ionization by polar wind flow also affects the neutral composition (Banks, Kockarts, 1973). In this paper CIRA 1965-models were adopted with mod. 5, $t = 1000$ for daytime and mod. 5, $t = 0$ for nighttime conditions referring to a solar flux of $F = 150 \cdot 10^{-22}$ W/m^{2}c/sec at 10.7 cm wavelength corresponding to a mean solar activity. These models contain a neutral hydrogen density of $n(\mathrm{H}) \approx 9 \cdot 10^3 \mathrm{cm}^{-3}$ at 500 km which is very low compared to the models — especially for low neutral temperatures — used by Banks and Holzer (Banks, Kockarts, 1973). Too low neutral hydrogen densities of CIRA-models have been indicated already by Brace *et al.* (1967) and Mayr *et al.* (1967). To take account of that uncertainty results are also given for increased $n(\mathrm{H})$ in Sect. III and V. The very low proton fluxes yielded by CIRA-models seem to support the suspect that $n(\mathrm{H})_{\mathrm{CIRA}}$ is considerably too low.

6. Collision Frequencies. The collision frequencies for the various constituents are taken from Holzer (1970) and are not repeated here. These collision frequencies result from the geometric mean of the simple asymptotic limits of large and small transport speeds. In the case of the $H^+ - O^+$-collisions this approximation has been compared with the exact value arising from the integration of the Boltzmann's collision integral (Rösler, 1974). For $\nu(H^+) \approx 2 \cdot \sqrt{kT_i/m_1}$ the deviation of both formulas is maximum the actual value exceeding the approximation by about 50%.

Table 1

	neutral hydrogen density $n(H)$	$T_i = T_e$	photoionization rate
mod. I	$n(H)_{CIRA}$	1500 K	$5 \cdot 10 \cdot {}^{7}sec^{-1}$
mod. II	$10 \cdot n(H)_{CIRA}$	1500 K	$5 \cdot 10^{-7}sec^{-1}$
mod. III	$40 \cdot n(H)_{CIRA}$	1500 K	$5 \cdot 10^{-7}sec^{-1}$
mod. IV	$10 \cdot n(H)_{CIRA}$	3000 K	$5 \cdot 10^{-7}sec^{-1}$
mod. V	$40 \cdot n(H)_{CIRA}$	3000 K	$5 \cdot 10^{-7}sec^{-1}$
mod. VI	$10 \cdot n(H)_{CIRA}$	3000 K	$1.67 \cdot 10^{-7}sec^{-1}$

CIRA = CIRA, Mod. 5, $t = 1000$

III. Numerical Results for Daytime Conditions

As mentioned above the principle features of high latitude daytime ionospheres are well known from the polar wind calculations by Banks and Holzer. A brief survey of the rather similar results obtained with the assumptions of Sect. II may, therefore, be sufficient. Characteristics of the different models are listed in Table 1.

A constant photoionization rate of $5 \cdot 10^{-7}sec^{-1}$ may be representative for summer conditions ignoring the effects of optical depth. The winter ionosphere, however, will spend only a few hours at most in sunlight with a zenith angle χ not far from 90°. As shown by Thomas (1966) a change from $\chi = 0$ to $\chi = 90°$ results in a decrease of the corresponding F-maximum densities by a factor 2 to 3. This is equivalent to a reduction of the photoionization rate by the same factor. To illustrate the impact of nearly grazing incidence on the proton fluxes and velocities mod. VI (which has to be compared with mod. IV) therefore takes a lower photoionization rate of one third of the above value.

Evidently Eqs. (1) and (2) contain not only the supersonic solution which implies a unique set of boundary conditions for both ion species at high altitudes but also a variety of subsonic solutions ranging from diffusive equilibrium to a 'first' subsonic solution where the H^+-ions are accelerated to nearly speed of sound at the critical point and then decelerated again at greater heights. Hence this section summarizes numerical results for the different models both for the supersonic solution yielding the maximum proton fluxes and a 'typical' subsonic solution with diffusive H^+-velocities of the order of 100 m/sec.

Two examples of the ion density distributions are shown in Fig. 2 and 3. The profiles indicated by A refer to the subsonic solution, B and C denote the supersonic and the 'first' subsonic solution (as defined above) respectively. With the exception of mod. VI the F-layers are not affected very much by the different models and solutions with O^+-densities of 7—8 $10^5 cm^{-3}$. The lower maximum density of mod. VI is due to the reduced photoionization rate. The subsonic solution is equivalent to a low speed approximation to Eq. (2) which is representative for midlatitude ionospheres. It is characterized by a steady increase in the H^+-density up to a nearly constant value of 10^3—10^4 cm^{-3} at high altitudes according to the large scale height of the protons. On the other hand acceleration to supersonic speed in the polar iono-

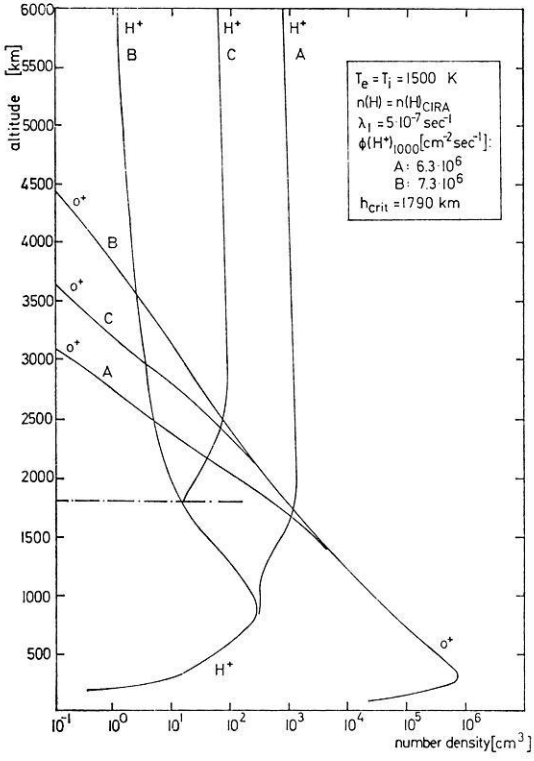

Fig. 2. Daytime ion density profiles for $T_e = T_i = 1500$ K and neutral hydrogen density according to CIRA 1965. A: low speed plasma flow (mid-latitudes), B: supersonic flow (high latitudes); C: 'first' subsonic solution

sphere has the consequence that the proton density reaches a maximum at about 1000 km and decreases after that (see Banks and Holzer). An electron pressure gradient is maintained in this way which is equivalent to an outward directed polarization field and which is mainly responsible for the acceleration of the hydrogen ions. The supersonic and 'first' subsonic profiles are clearly identical up to the critical point. Further decrease in the H^+-density and corresponding acceleration determines the supersonic flow, while an increase in the H^+-partial pressure causes the successive deceleration to lower speeds for the 'first' subsonic solution. The H^+-density range between the profiles A and C can be covered by subsonic solutions with the proton velocity reaching a maximum near the critical point. It is therefore hardly possible (especially for high ion temperature models yielding a less fast H^+-acceleration with the critical point at high altitudes, see Fig. 3) to derive from ion density measurements below the critical point whether supersonic flow really is attained (see Brinton *et al.*, 1971).

In Table 2 we summarize results for the escape fluxes $\Phi(H^+)_{1000}$ (normalized to 1000 km as usual) and the altitudes $h_=$ (defined by $n(H^+) = n(O^+)$) above which the H^+-ions become the major ion species both for the 'typical' subsonic (sb) and the supersonic (sp) solution. The critical heights h_{crit} and the H^+-bulk velocities $v(H^+)_{6000}$ and the corresponding Mach numbers $M(H^+)_{6000}$ at 600 0km height for supersonic flow are also listed there.

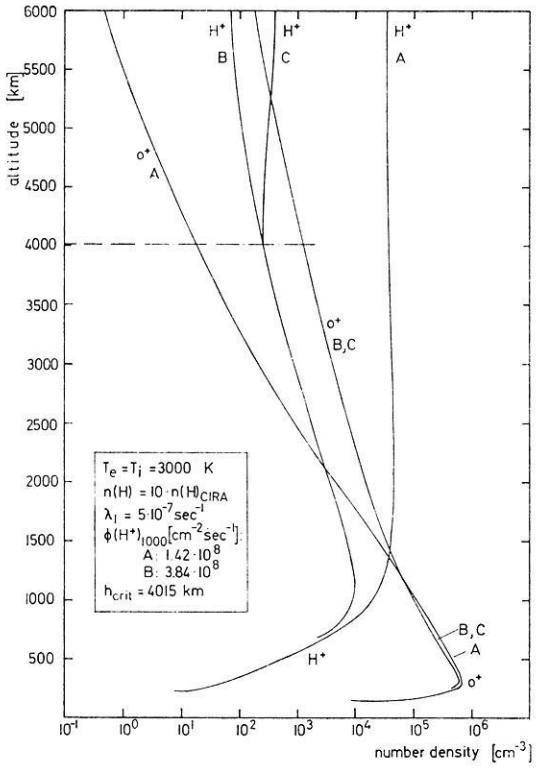

Fig. 3. Daytime ion density profiles for $T_e = T_i = 3000$ K and neutral hydrogen density ten times higher than CIRA 1965. A: low speed plasma flow (mid-latitudes); B: supersonic flow (high latitudes); C: 'first' subsonic solution

Table 2

		$\Phi(H^+)_{1000}$	h_{crit}	$v(H^+)_{6000}$	$M(H^+)_{6000}$	$h_=$
mod. I	(sb)	$6.3 \cdot 10^6$				1680
	(sp)	$7.3 \cdot 10^6$	1790	13.7	3.91	3570
mod. II	(sb)	$5.4 \cdot 10^7$				1320
	(sp)	$7.4 \cdot 10^7$	1900	11.0	3.12	2690
mod. III	(sb)	$1.27 \cdot 10^8$				1040
	(sp)	$2.88 \cdot 10^8$	2250	8.9	2.51	2360
mod. IV	(sb)	$1.42 \cdot 10^8$				1360
	(sp)	$3.84 \cdot 10^8$	4015	11.0	2.19	8400
mod. V	(sb)	$4.0 \cdot 10^8$				1085
	(sp)	$1.05 \cdot 10^9$	5000	7.5	1.51	7795
mod. VI	(sb)	$5.70 \cdot 10^7$				1480
	(sp)	$1.46 \cdot 10^8$	2642	15.0	3.02	6680
		[cm^{-2}sec^{-1}]	[km]	[km/sec]		[km]

Concerning the fluxes two points should be reemphasized: First there is no great difference between the subsonic and supersonic fluxes. That is, polar wind fluxes may be perhaps twice the diffusive midlatitude fluxes and the great discrepancy between the former subsonic calculations of, for example, Hanson and Patterson (1964) and Geisler (1967) and the polar wind fluxes given by Banks and Holzer is mainly caused by different models and not specific to subsonic and supersonic flow. The description of the plasmasphere separating midlatitude and polar ionospheres by Mayr *et al.* (1970) as a region of abrupt change not only in the H^+-density but also in the magnitude of the fluxes along the field line therefore seems doubtful at least at lower heights close to the ionospheres. Secondly, the fluxes are roughly proportional to the neutral hydrogen density (see also Banks, Kockarts, 1973). The CIRA-models with low $n(H)$ yield only fluxes of about $10^7 cm^{-2} sec^{-1}$. Fluxes of the order of $10^8 cm^{-2} sec^{-1}$ which seem to be confirmed both for high- and midlatitudes (Hoffman, 1968, 1971; Park, 1970) require a hydrogen density about ten times higher then given by CIRA. That is another reference to the fact that the neutral hydrogen density of CIRA-models seems considerably too low as stated above. An increase of the ion temperature from 1500 K to 3000 K results in a corresponding increase of the escape fluxes by a factor 4 to 5. A comparison of mod. VI and IV shows the decrease of the proton fluxes caused by a lower photoionization rate indicating that we would expect a lower polar wind flux from a winter daytime ionosphere. It should be noted, however, that this prediction is not verified at all experimentally. Hoffman (1968, 1971) derives maximum polar wind fluxes from satellite measurements for the winter morning hours which cannot be explained by photoionization and stationary models stating the efficiency of other mechanisms like for example corpuscular ionization and heating.

The proton velocity profiles are shown in Fig. 4 and 5. The results agree very well with those of the previous polar wind calculations. A higher ion temperature shifts the critical point to higher altitudes by decreasing the total electron density gradient. An increased neutral hydrogen density also yields a less rapid acceleration and higher critical points. The H^+-escape fluxes, however, are larger for a high density, slowly flowing model than for a low density, rapidly flowing model. This result differs from those of Banks and Holzer (1969). The proton velocities at 6000 km height range from 7 to 14 km/sec, the corresponding Mach numbers from 1.5 to 3.9 (referring to a speed of sound defined by $c(H^+) = \sqrt{kT_i/m(H^+)}$ which amounts to 3,52 km/sec for $T_i = 1500$ K and 4.97 km/sec for $T_i = 3000$ K).

Hence we conclude that the illuminated ionosphere of Fig. 1 will provide supersonic proton fluxes of some $10^8 cm^{-2} sec^{-1}$ with mean velocities reaching Mach numbers of 4 at most at high altitudes which will turn out to be a serious limitation in the discussion of the nighttime ionosphere.

IV. Free Flow along Field Lines

At heights exceeding several thousand kilometers the existence of oxygen ions, collisions and chemical reactions becomes neglegible. The mean velocity of the H^+-plasma is determined then by free flow along the field lines. Below the critical point the mean free path λ for the $H^+ - O^+$-collisions is less or in the order of the O^+-scale height $H(O^+)$ (Banks, Holzer, 1969). The flow therefore can be treated as

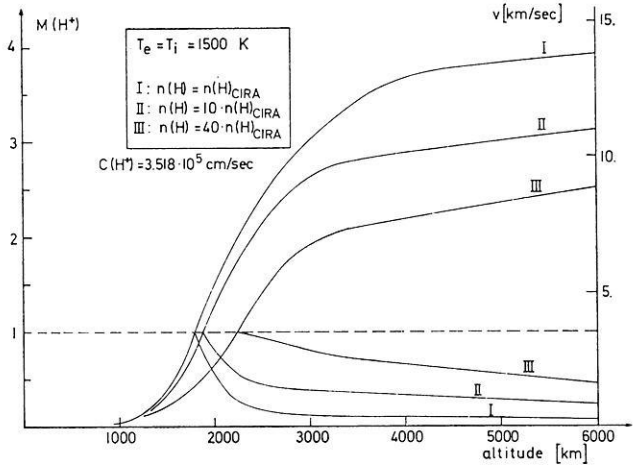

Fig. 4. Proton velocity profiles for supersonic and 'first' subsonic flow for the 1500 K models

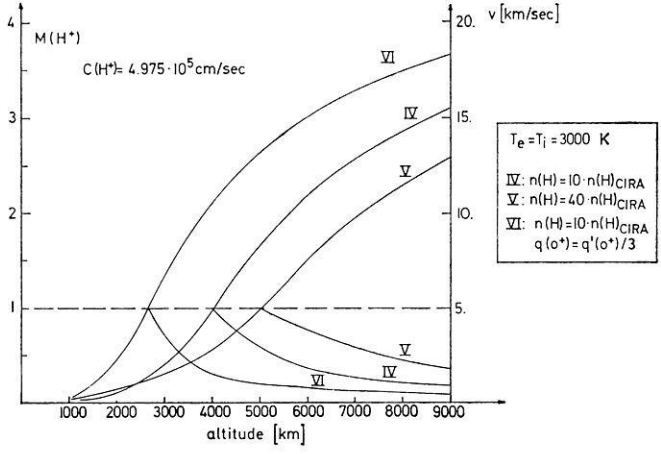

Fig. 5. Proton velocity profiles for supersonic and 'first' subsonic for the 3000 K models

collision dominated ensuring the adequacy of a hydrodynamic description with an isotropic H^+-pressure about the H^+-transport speed. As λ exceeds $H(O^+)$ the flow ceases to be collision dominated and a kinetic description would be appropriate. Decrease of the magnetic field along the flux tube and conservation of magnetic moment of the protons should establish an anisotropic pressure (Banks, Kockarts, 1973). A detailed comparison of kinetic and hydrodynamic models of an expanding ion exosphere by Holzer *et al.* (1971) has shown, however, that the results of both models essentially are the same in the region of supersonic flow. The ion density and velocity distribution is rather insensitive to the form of the proton pressure tensor and hence hydrodynamic equations with an isotropic pressure provide a good description for higher altitudes, too.

The magnetospheric part of the polar wind flow between the two hemispheres therefore is discussed also under this assumption. For isothermal conditions with $T_e = T_i = T$ Eq. (2) for the proton velocity then can be integrated from any point to the magnetic equator (e.g. Parker, 1963):

$$\frac{1}{2}(U^2 - U_e^2) - \frac{2kT}{m}\left[\ln\left(\frac{U}{U_e}\right) + \ln\left(\frac{A}{A_e}\right)\right] + \varphi - \varphi_e = 0 \tag{10}$$

with φ = gravitational potential

(The index i is omitted from now on, the index e refers to the magnetic equator). As pointed out above a dipole model of the geomagnetic configuration is adopted describing a field line by

$$r = R_e \cdot L \cos^2\beta \tag{11}$$

Hence

$$\frac{A}{A_e} = \frac{(1 - \sin^2\beta)^3}{\sqrt{1 + 3\sin^2\beta}} \tag{12}$$

and

$$\varphi = \varphi_e/(1 - \sin^2\beta) \tag{13}$$

While for a multi-constituent plasma the ion Machnumber referred to their speed of sound c_i alone (with $c_i^2 = kT_i/m_i$), an appropriate definition of the proton Machnumber for the single ion species ambipolar Eq. (10) is $M = U/c$ with $c^2 = k(T_i + T_e)/m = 2kT/m$ referring to the speed of sound in the overall proton-electron plasma. Using $\xi = \sin\beta$, $\mathrm{H} = -\varphi_e/c^2$ and (12) and (13) Eq. (10) can be written for the H^+-Machnumber:

$$\frac{1}{2}(M^2 - M_e^2) - \ln\frac{M}{M_e} - \ln\left[\frac{(1 - \xi^2)^3}{\sqrt{1 + 3\xi^2}}\right] + \mathrm{H} - \frac{\mathrm{H}}{1 - \xi^2} = 0 \tag{14}$$

The general pattern of the solutions of Eq. (14) is plotted in Fig. 6 for different values of H. This parameter represents essentially the gravitational potential of the protons at the geomagnetic equator in terms of their mean thermal energy. $\mathrm{H} = 4.5$ separates two different regimes: 1) For $\mathrm{H} > 4.5$ one asymmetric supersonic solution exists reaching the speed of sound at the geomagnetic equator with $\partial M/\partial\xi > 0$ at $\xi = 0$ corresponding to continuing acceleration. 2) For $\mathrm{H} < 4.5$ both kinds of solutions are symmetric to the geomagnetic equator. The critical point for the supersonic solutions is situated at $\xi \neq 0$, the protons are accelerated to maximum speed at the equator with successive deceleration. The subsonic velocity distribution is characterized by a small maximum at the critical height with very low equatorial velocities.

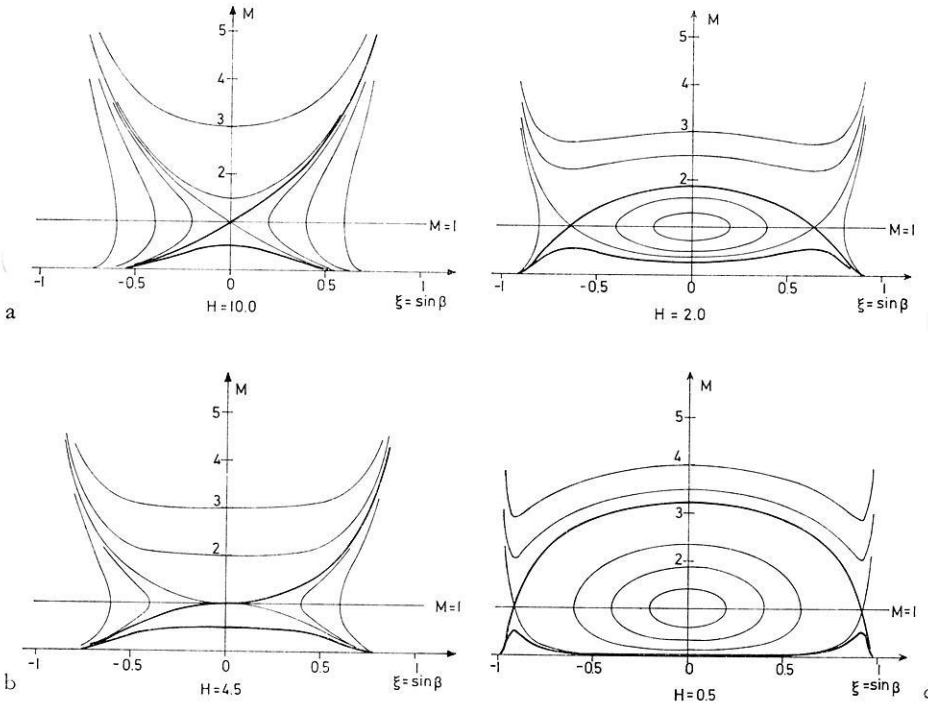

Fig. 6. Solution pattern of the H^+-Mach number as a function of geomagnetic latitude for isothermal free flow conditions. (H denotes the gravitational potential at the magnetic equator in terms of the mean thermal proton energy; $H = 0.5$ for $T_i = 1500$ K and $L = 5$)

With $\varphi_e = -\gamma M/R_e L$ (γ = gravitational constant, M = mass of earth, R_e = earth radius) one gets:

$$H = -\varphi_e \Big/ \left(\frac{2kT}{m}\right) = \frac{3.8 \cdot 10^3}{L \cdot T} \tag{15}$$

An L-value of 5 and a proton temperature of 1500 K yield $H = 0.5$. The solutions for that case are shown in Fig. 6d. Hence the symmetric solutions appear to be appropriate to out problem.

An isothermal model requires high thermal conductivity. Clearly at high altitudes with very low plasma density this assumptions no longer will be valid and the flow of the protons will be increasingly adiabatic. To check deviations of both models adiabatic flow will be discussed briefly in the following, too,

To account for finite thermal conductivity a polytropic law can be adopted:

$$\frac{P}{\varrho^\alpha} = \text{const} = \frac{P_0}{\varrho_0^\alpha} \tag{16}$$

(the index 0 indicating any fixed point, with $\alpha = 1$ for isothermal and $\alpha = 5/3$ for adiabatic conditions). In a realistic case α should vary along the field line. But as we

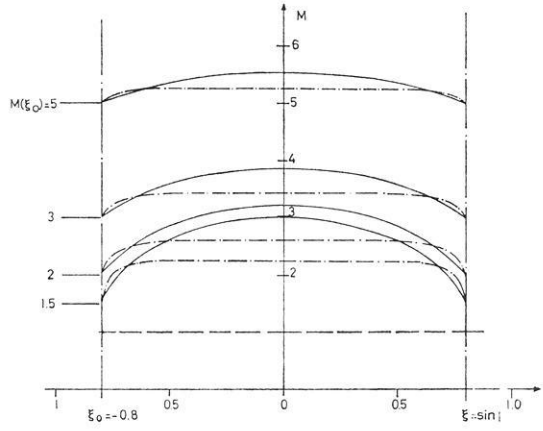

Fig. 7. Comparison of isothermal (———) and adiabatic (-·-·-) supersonic proton flow along closed field lines for H = 0.5

only intend to compare isothermal and adiabatic flow we assume it to be constant. Eq. (2) then can be integrated again to yield:

$$\frac{1}{2}(U^2 - U_0^2) + \left(\frac{2P_0}{\varrho_0}\right)\frac{\alpha}{\alpha - 1}\left[\left(\frac{U_0 A_0}{UA}\right)^{\alpha-1} - 1\right] + \varphi - \varphi_0 = 0 \qquad (17)$$

This corresponds to the integrals for the solar wind problem (Parker, 1963).

The speed of sound in the proton-electron plasma is determined by $c^2 = \partial P/\partial \varrho$ with $P = P_e + P_i$ and varies with height in the polytropic case according to the temperature variation. Accordingly the proton Machnumber should be defined by $M = U/c$. However, for easy comparison of isothermal and adiabatic conditions we introduce a formal proton Machnumber by $M = U/c_0$ where c_0 represents the isothermal speed of sound at the fixed point s_0 with $c_0^2 = 2P_0/\varrho_0$. In analogy to Eq. (14) the proton velocity distribution (17) then reads for the H^+-Mach-number:

$$\frac{1}{2}(M^2 - M_0^2) - \frac{H}{1 - \xi_0^2} - \frac{H}{1 - \xi^2} + \frac{\alpha}{\alpha - 1}\left[\left(\frac{M_0}{M}\,F(\xi^2)\right)^{\alpha-1} - 1\right] = 0 \qquad (18)$$

with

$$F(\xi^2) = \frac{(1 - \xi_0^2)^3}{\sqrt{1 + 3\xi_0^2}} \Big/ \frac{(1 - \xi^2)^3}{\sqrt{1 + 3\xi^2}} \qquad (19)$$

A complete solution pattern of (18) shall not be described here. Choosing H = 0.5 according to (15) and starting with supersonic velocities of $M(\xi_0) = 1.5$, 2.0, 3.0 and 5.0 at $\xi_0 = -0.8$ which corresponds to an altitude of 5100 km for $L = 5$ the velocity distribution along the field line up to the conjugate point is plotted in Fig. 7 both for isothermal and adiabatic flow (solid and dashed-dotted lines). Both models show a symmetric distribution with respect to the magnetic equator. For adiabatic conditions the protons are initially accelerated more rapidly than in the isothermal case, but soon

the H^+-velocity remains essentially constant, while further acceleration to a higher equatorial velocity occurs for isothermal conditions since more energy is available then. The essential features are not touched, however, and therefore from the consideration of the magnetospheric part of the flow it is concluded that the polar wind runs down into the conjugate nighttime ionosphere with the same particle density and mean velocity as produced by the daytime ionosphere. Hence the boundary conditions for the discussion of the winter nighttime ionosphere are characterized by an influx of supersonic plasma of some $10^8 cm^{-2} sec^{-1}$ with a mean velocity of 10—12 km/sec as provided by the illuminated side.

V. Supersonic Influx of Plasma into the Nighttime Ionosphere

As mentioned above diffusive influx of H^+-plasma of the order of $10^8 cm^{-2} sec^{-1}$ from the protonosphere is sufficient to maintain equilibrium F-layer densities of $10^5 cm^{-3}$ by charge exchange $H^+ + O \rightarrow O^+ + H$. In this section we discuss the question how the nighttime ionosphere is affected by a supersonic polar wind influx or vice versa for stationary conditions.

The principle structure of the hydrodynamic equations describing ionospheric processes is the same for daytime and nighttime. A critical solution also exists for supersonic influx where the speed of sound can be passed smoothly. (It should be pointed out that in contrast to daytime conditions, the nighttime critical solution does not represent a stable physical process, since this would require distinct boundary conditions for the incoming plasma. Any departure from these boundary values results in a departure from the critical solution. But if the particle density and mean velocity of the polar wind arriving at the nighttime ionosphere were close to the boundary values of the critical solution one should expect a weak stationary shock situated near the critical height.) One essential difference between outward and inward supersonic flow can be seen immediately from comparing the contributions of the various terms on the right hand side of Eq. (2). Assuming constant proton temperature Eq. (20) shows the sign of the different contributions for outward and inward flow.

$$\frac{1}{M}\frac{\partial M}{\partial s}(M^2-1) = \begin{array}{lll} & \text{out} & \text{in} \\ 1)\ \dfrac{\boldsymbol{\rho}\cdot\mathbf{s}}{c^2} & < 0 & < 0 \\ 2)\ +\dfrac{1}{A}\dfrac{\partial A}{\partial s} & > 0 & > 0 \\ 3)\ -\dfrac{1}{c^2}\displaystyle\sum_k \nu_k (U - U_k) & < 0 & > 0 \\ 4)\ -\dfrac{1}{\Phi}\dfrac{\partial \Phi}{\partial s} & < 0 & < 0 \\ 5)\ -\dfrac{T_e}{T_i}\dfrac{1}{n_e}\dfrac{\partial n_e}{\partial s} & > 0 & > 0 \\ 6)\ -q\dfrac{M^2 A}{\Phi} & < 0 & > 0 \end{array} \qquad (20)$$

Table 3

mod.	$\Phi(H^+)_{1000}$	h_{crit}	$v(H^+)_{3000}$	$M(H^+)_{3000}$	h_∞
$n(H)_{CIRA}$ $T_e = T_i = 1500$ K	$-3.49 \cdot 10^7$	385	17.2	4.90	1720
$10 \cdot n(H)_{CIRA}$ $T_e = T_i = 1500$ K	$-1.13 \cdot 10^7$	426	17.7	5.03	1670
$n(H)_{CIRA}$ $T_e = T_i = 3000$ K	$-1.54 \cdot 10^8$	383	27.9	5.61	5210
	[$cm^{-2} sec^{-1}$]	[km]	[km/sec]		[km]

CIRA = CIRA, Mod. 5, $t = 0$

The H^+-critical point is determined by vanishing of the right hand side of Eq. (20) for $M = 1$. The most important contributions arise from term 3), 4), and 5). The collision term 3) (with the $H^+ - O^+$-collisions most effective above 500 km) is < 0 (> 0) for $U > 0$ ($U < 0$). The polarization field 5) points to greater heights in both cases. The relative H^+-flux gradient $\frac{1}{\Phi}\frac{\partial \Phi}{\partial s}$ also acts in the same sense for outward and inward motion. While an outward directed proton flux ($\Phi > 0$) is built up at the expense of an O^+-flux $\left(\frac{\partial \Phi}{\partial s} > 0\right)$ for daytime conditions an inward H^+-flux ($\Phi < 0$) is converted into an O^+-flux $\left(\frac{\partial \Phi}{\partial s} < 0\right)$ in our nighttime model. The daytime critical point essentially results from a balance of the H^+-O^+-friction by the polarization field at greater heights where Φ is already nearly constant. In contrast to that the nighttime critical point must be shifted to rather low heights where chemical reactions are rapid and the relative flux gradient contribution can balance both friction and the electric field. According to the low critical height one also expects high transport speeds of the inward proton flux required by the nighttime critical solution so that supersonic flow down to the critical point is possible.

Corresponding to these considerations Table 3 lists numerical results of the nighttime critical solutions for three models with different ion temperatures and neutral hydrogen densities. The ion density and proton velocity distributions are plotted in Fig. 8 and 9.

The boundary values for the proton fluxes range from 10^7 to 10^8 cm^{-2} sec^{-1} thus maintaining equilibrium F-layer densities of only $4 \cdot 10^3$ to $5 \cdot 10^4$ cm^{-3} (Fig. 8). The critical point is located at about 400 km as compared with 2000 to 5000 km for the daytime solutions. Continuous deceleration to subsonic speed is only possible with initial velocities (at 3000 km height) as high as 17—18 km/sec for the 1500 K model and 28 km/sec for the 3000 K model. This is equivalent to Machnumbers of about 5 for all cases. The proton velocity decreases rather slowly towards lower heights. Only near the critical point a rapid deceleration to very low velocities is effective (Fig. 9).

In Sect. III results of the daytime models indicated that the sunlit polar ionosphere

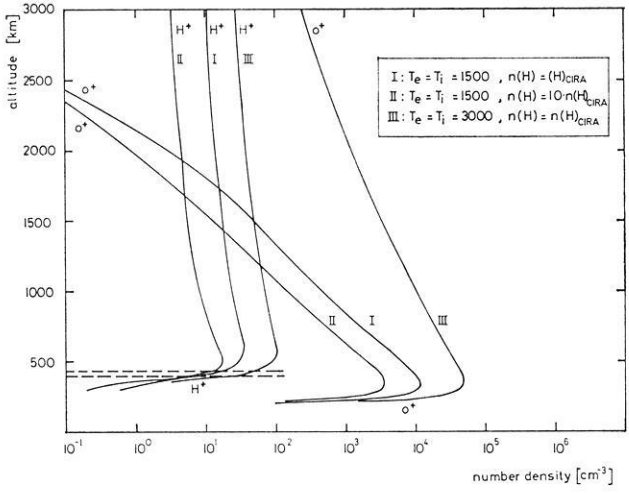

Fig. 8. Ion density profiles for the nighttime critical solution for three different models

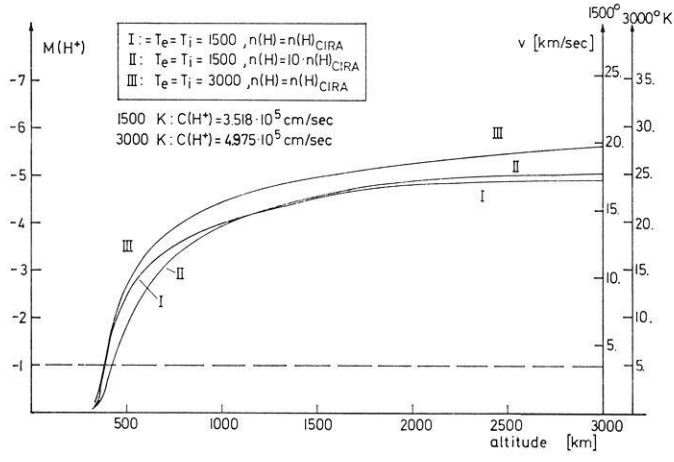

Fig. 9. Proton velocity profiles for the nighttime critical solution for three different models. The critical point lies very low as compared to daytime conditions

yields polar wind fluxes with Machnumbers not exceeding 4 at high altitudes. Since the free flow in the magnetosphere is symmetric with respect to the equator (Section IV), this implies an upper limit for the Machnumber of the plasma flow arriving at the nighttime ionosphere that is considerably less than required by the critical solutions. Consequently the realistic polar wind has to be decelerated discontinously to subsonic speed and shock waves have to be built up.

Concerning the problem of maintaining high latitude nighttime *F*-layers by a supersonic plasma influx the essential question is whether these shock waves can be stationary. The mass flux is only conserved in a coordinate system where the shock

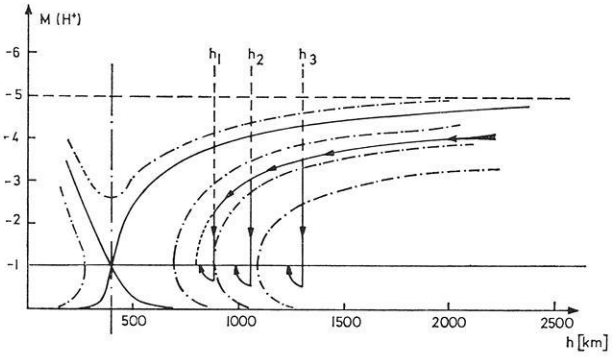

Fig. 10. Schematic solution pattern for nighttime inward plasma flow. A polar wind arriving with a Mach number of 4 cannot be decelerated strongly enough in a stationary shock wave to follow a physically reasonable subsonic solution

wave is at rest. Hence a non-stationary shock wave causes a reduction of the proton flux in a fixed coordinate system. As the equilibrium F-layer densities are proportional to the inward fluxes (e.g. Rishbeth, 1963) a non-stationary shock wave implies a reduction of the equilibrium layer.

Fig. 10 serves to illustrate that the formation of a stationary shock wave is not possible since it would decelerate the polar wind only insufficiently. A schematic solution pattern for the hydrogen ion velocities is shown. The critical solution agrees with the results plotted in Fig. 9 and accordingly has to start with a Mach number of 5 at great heights. We choose the case of a polar wind arriving with a Machnumber of 4 which proved to be an upper limit for the H^+-velocity from our dayside considerations. (Clearly the following conclusions hold as well for lower velocities than $M = 4$.) It would follow the velocity path indicated by the arrow. We try to locate a stationary shock at the heights h_1, h_2, or h_3. The compression of the H^+-plasma is, however, limited to a factor of about 4 according to the Rankine-Hugoniot-relations. Therefore, the hydrogen ions can be decelerated to a Machnumber of 0.5 to 0.6 in the shock wave and fail to reach a subsonic solution which can satisfy the boundary conditions at lower heights. They would be accelerated rather rapidly to sonic speed again. Hence the H^+-plasma must be decelerated more effectively than can be achieved by a stationary shock wave. Nonstationary shock waves will be set up propagating into the supersonic region. The limitation of the plasma discontinuity to a density ratio of 4 results from converting flow energy into thermal energy. The corresponding pressure increase prevents a stronger compression. It should be noted, however, that nonstationary shock waves are required even for an isothermal shock. (Clearly we cannot assume isothermal shocks to be set up by the incoming polar wind as the energy transfer to the oxygen ions is not effective enough. The ratio of the collision frequency for momentum transfer to the collision frequency for energy transfer is $(m(H^+) + m(O^+))/2m(H^+) = 8.5$ for the H^+-O^+-collisions (Eq. (6)). Hence the energy exchange between both ion species will not be significant within the shock that is within a few mean free paths. Nevertheless we want to consider isothermal shock conditions as an extreme case allowing maximum compression to support our conclusion that non-stationary shock waves have to originate.) Con-

servation of mass and momentum flux (the energy flux is not conserved in this case) with zero shock velocity yields $M^+ = 1/M^-$ where M^+, M^- denote the respective Machnumbers at the post- and pre-shock side (viewed from the supersonic region). As $|M^-| \leqslant 4$ one gets $|M^+| \geqslant 0.25$. This is still much to fast for reaching a physically reasonable subsonic solution in the velocity pattern of Fig. 10.

In order to extend our time-independent calculations to non-stationary shock waves we make the assumption that the only temporal dependence originates from the upward motion of the shock wave. The ion density distribution can then be described by

$$n(h, t) = n^+(h) + (n^-(h) - n^+(h)) \cdot \mathrm{H}(h - h_0) \tag{25}$$

with the step function $\mathrm{H}(x - x_0)$ defined by

$$\begin{aligned} \mathrm{H}(x - x_0) &= 0 \text{ for } x < x_0 \\ \mathrm{H}(x - x_0) &= 1 \text{ for } x > x_0 \end{aligned} \tag{26}$$

$n^+(h)$ represents a time independent solution describing the subsonic region, $n^-(h)$ the corresponding solution for the supersonic regime. h_0 denotes the momentary position of the shock wave at time t_0 and is given by

$$h_0 = h^* + \int_{t^*}^{t_0} u \, dt \tag{27}$$

(u = shock wave velocity), where h^* stands for the height where the shock wave at time t^* originally arises.

In the following numerical results of this model will be presented. We choose a supersonic proton influx of $3 \cdot 10^8 \mathrm{cm}^{-2}\mathrm{sec}^{-1}$ with $T(\mathrm{H}^+)_{3000} = 1500$ K and $M(\mathrm{H}^+)_{3000} = -4$ as boundary values at 3000 km height. The proton temperature varies, as before, with height in accordance to Eq. (3). The oxygen ions and the electrons are assumed to be isothermal with $T(\mathrm{O}^+) = T_e = 1500$ K. The O^+-flux at 3000 km is taken to be zero. Hence the O^+-density at this height and the shock velocity as a function of position have to be determined from the boundary conditions at lower heights. These boundary conditions require the vanishing of both H^+- and O^+-flux at low altitudes, and $n(\mathrm{O}^+)_{3000}$ and the shock velocity have to be adjusted until a solution is obtained having the proper characteristics. If $n(\mathrm{O}^+)_{3000}$ is chosen too low the oxygen ions follow a physically unreasonable solution and the H^+-ions still remain supersonic. With sufficiently high $n(\mathrm{O}^+)_{3000}$ the hydrogen ions reach $M(\mathrm{H}^+) = -1$ at a height h^* as sketched in Fig. 10. Now one can choose several heights h_i above h^* and adjust the shock wave velocity $u(h_i)$ so as to satisfy the boundary condition for the proton flux at low heights ($\Phi(\mathrm{H}^+) \to 0$ for $h \to 0$). After this has been achieved the O^+-flux normally will not vanish simultaneously at low altitudes. Then $n(\mathrm{O}^+)_{3000}$ must be appropriately corrected and the whole procedure has to be repeated until $n(\mathrm{O}^+)_{3000}$ is sufficiently accurate.

(It should be pointed out that the numerical results derived in that way are not fully consistent with our assumption of time-independence at both sides of the shock wave. As may be seen from Fig. 11 and 13 different locations of the shock would

cause slightly different H^+-density profiles in the subsonic region and partly even affect the O^+-density distribution too. For a non-stationary shock wave a higher shock location, however, simply corresponds to a view at the same situation at some later moment. This behaviour thus clearly reveals an explicit time-dependence which has been excluded before. But as it seems to be very difficult to perform time-dependent polar wind calculations this discrepancy must be accepted here).

Fig. 11 shows the results for an equilibrium F-layer maintained by a polar wind influx with the characteristics listed above. The oxygen and hydrogen ion densities are plotted in Fig. 11a for three different positions of the shock wave equivalent to three successive snapshots. The shock originates at a height of about 1100 km and runs upward filling the flux tube continuously with denser and hot hydrogen plasma. The proton flux is reduced by the shock wave to $6.2 \cdot 10^7 \mathrm{cm}^{-2}\mathrm{sec}^{-1}$ that is to one fifth of its original value and can therefore maintain F-layer densities of only $2.1 \cdot 10^4$ cm^{-3}. The proton velocity is shown in Fig. 11b. As already discussed the protons have to be decelerated within the shock to very low velocities. The numerical results indicate that the post-shock proton Mach-number has to be about 0.1 in order to reach a physically reasonable subsonic solution. The shock velocity u_s which turns out to be $\sim$5.5 km/sec is plotted in Fig. 11c. The protons are heated to a temperature of nearly 10^4K (Fig. 11d). The proton temperature then remains essentially constant down to about 800 km from which height the energy transfer to the oxygen ions becomes effective. The protons thereby are cooled to the background temperature within a region of less than 200 km.

Compared with the very low equilibrium F-layer density derived above experimental research of high latitude ionospheres yields a quite different picture (a synopsis of trans-polar plasma is given for example by Thomas and Andrews (1969)). With the exception of the polar cavity which is on open field lines the polar F-regions show a base level of the order of $10^5\mathrm{cm}^{-3}$ below which the maximum density does not fall even during winter night (Rishbeth, 1968).

Hence we can change our point of view and instead of calculating equilibrium F-layers consider a polar wind running into a nighttime ionosphere with an O^+-density distribution as observed. Results are shown in Fig. 12. The O^+-density profile was chosen somewhat arbitrarily as the equilibrium layer with $T(O^+) = 1500$ K provided by a diffusive proton influx of $3 \cdot 10^8 \mathrm{cm}^{-2}\mathrm{sec}^{-1}$ which just creates a maximum density of $10^5\mathrm{cm}^{-3}$. The resulting proton velocity and temperature are very similar to the previous ones. Again non-stationary shock waves are formed reducing the initial polar wind flux to a post-shock flux of $5.4 \cdot 10^7 \mathrm{cm}^{-2}\mathrm{sec}^{-1}$. The shock velocity of about 6 km/sec turns out slightly higher.

Both examples therefore indicate that only a small portion of a supersonic proton flux with the above characteristics can advance to F-region heights and that such an influx will not influence the polar F-region strongly. Fig. 13 and 14 demonstrate that this conclusion still holds for isothermal flow conditions and an isothermal shock wave which allows a higher compression. In spite of the much lower shock wave velocities of about 1.5 km/sec (for the higher shock wave positions) the post-shock fluxes are again very low. The discontinuity of the mass flux in a fixed coordinate system is given by $\varrho^+ U^+ - \varrho^- U^- = u_s(\varrho^+ - \varrho^-)$. The lower shock wave velocity u_s is balanced in this case by the higher compression by the isothermal shock wave. In the calculation of an equilibrium layer the post-shock flux is $4.4 \cdot 10^7 \mathrm{cm}^{-2}\mathrm{sec}^{-1}$

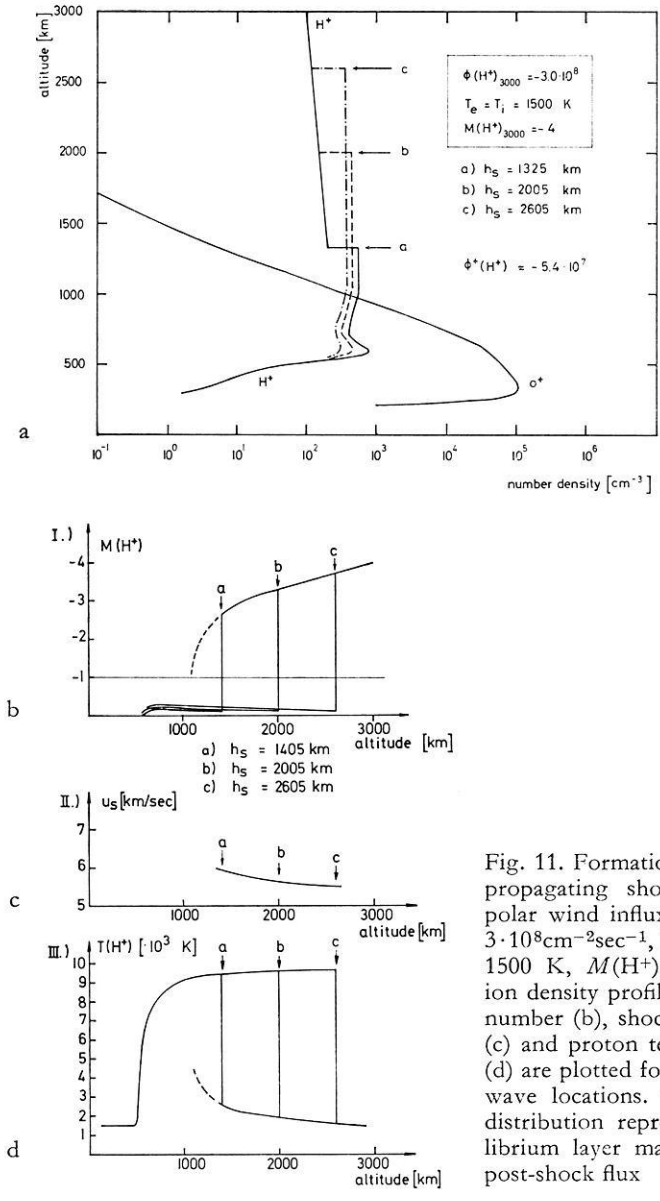

Fig. 11. Formation of an upward propagating shock wave by a polar wind influx of $3 \cdot 10^8 cm^{-2} sec^{-1}$, $T(H^+)_{3000} = 1500$ K, $M(H^+)_{3000} = -4$. The ion density profiles (a), H^+-Mach number (b), shock wave velocity (c) and proton temperature (d) are plotted for different shock wave locations. The O^+-density distribution represents the equilibrium layer maintained by the post-shock flux

maintaining a maximum density of $1.8 \cdot 10^4 cm^{-3}$ similarly to the results shown in Fig. 11. The model with a fixed O^+-density distribution yields a very high reduction of the inward flux, namely to $3.4 \cdot 10^6 cm^{-2} sec^{-1}$, i.e. to one twentieth of the initial value.

The path of the protons between both conjugate ionospheres along a dipole field line with an L-value of 5 amounts to 75000 km. If the shock wave were travelling with a constant velocity of 5 km/sec from the nighttime to the daytime ionosphere which is emitting polar wind fluxes the supersonic flow could only survive for 4.2 h.

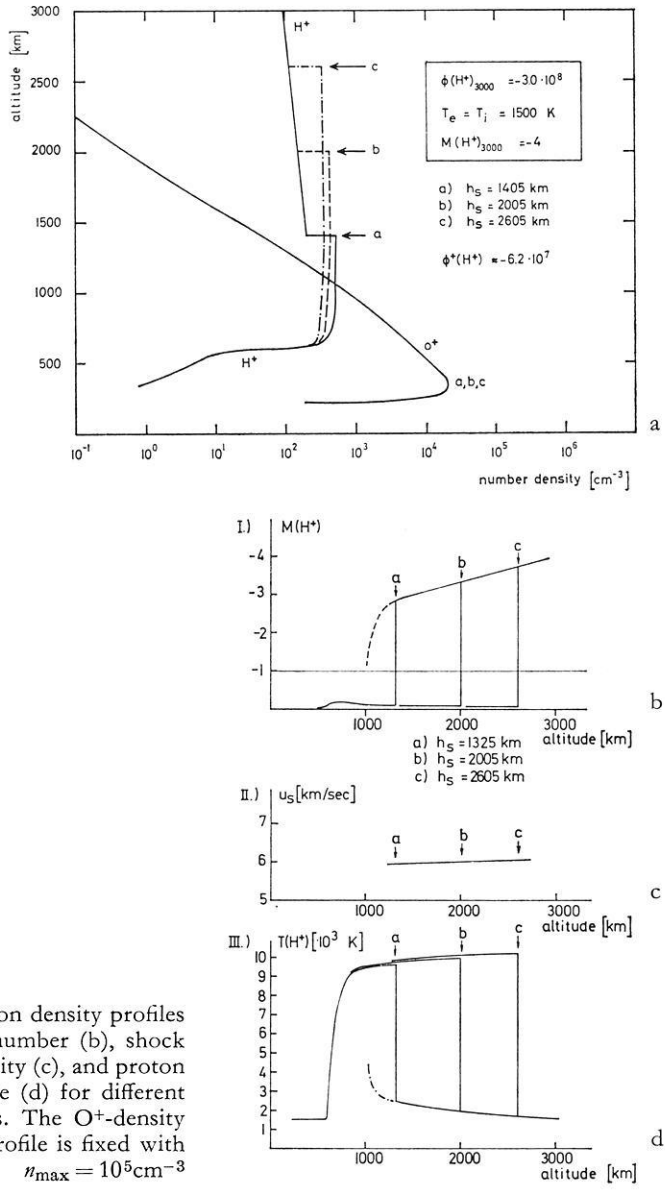

Fig. 12. Ion density profiles (a), H^+-Mach number (b), shock wave velocity (c), and proton temperature (d) for different shock locations. The O^+-density profile is fixed with $n_{max} = 10^5 cm^{-3}$

The method employed in this paper to determine the shock wave velocity, however, cannot be extended to arbitrary altitudes. It is based on performing stationary calculations implying that the protons 'know' about the boundary conditions at low altitudes at the nighttime side. Disturbances and the corresponding information are transferred in a plasma with speed of sound. If the propagation time of this information is of the same order as the time scale of temporal variations the assumption of stationary conditions no longer will be justified and the two regions essentially will be decoupled. That is, at a height of about 20000 km at most equivalent to a propaga-

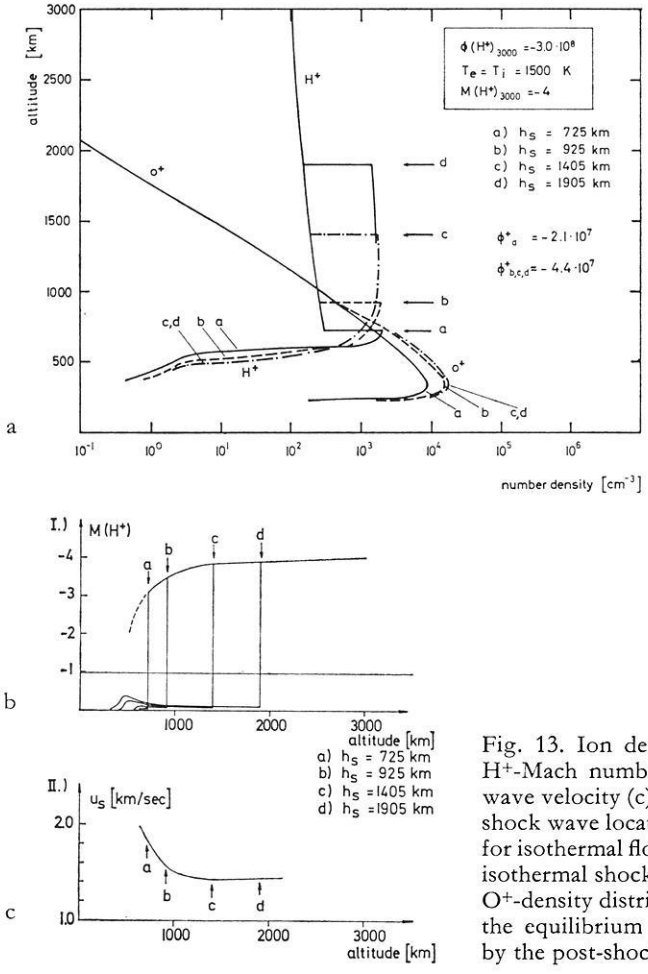

Fig. 13. Ion density profiles (a), H^+-Mach number (b) and shock wave velocity (c) for different shock wave locations computed for isothermal flow conditions and isothermal shock wave. The O^+-density distribution represents the equilibrium layer maintained by the post-shock flux

tion time of the order of one hour our calculation of the shock wave velocity from the ionospheric boundary conditions will not be reasonable any longer. The shock velocity must be determined then from similar considerations as given by Banks *et al.* (1971) in their discussion of a symmetric geomagnetic configuration. Hence their conclusion that a polar wind on closed field lines would be switched off within 22 h for $L = 5$ and (bearing in mind the time scales of the convection cycle of polar flux tubes) can represent a rather steady phenomenon also for closed flux tubes is not affected by the results described in this paper.

VI. Conclusions

The coupling of the winter nighttime ionosphere to the summer daytime ionosphere at high latitudes by a polar wind running along closed field lines has been discussed in this paper in a stationary model. It has been shown that shock waves

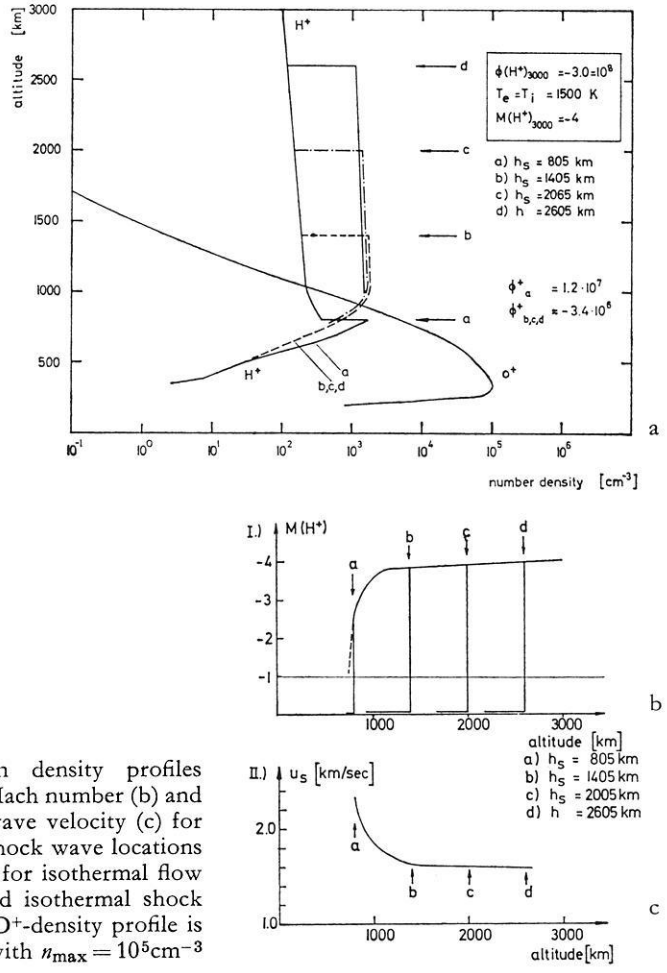

Fig. 14. Ion density profiles (a), H^+-Mach number (b) and shock wave velocity (c) for different shock wave locations computed for isothermal flow conditions and isothermal shock wave. The O^+-density profile is fixed with $n_{max} = 10^5 cm^{-3}$

with upward velocities of about 5 km/sec would form above the dark ionosphere reducing the inward fluxes considerably. Consequently such a mechanism can only be of minor influence upon polar *F*-region behaviour. However, the ionization of a polar flux tube would be changed by the passage of the shock wave at higher altitudes. If a polar orbiting satellite were traversing such a shock front the change of the plasma parameters could be easily confused with a discontinuity parallel to the magnetic field. This discussion shall emphasize the possibility of horizontal discontinuities set up by supersonic plasma influx arising from the sunlit hemisphere.

There is growing evidence that the most effective ionization source for maintaining polar winter *F*-layers and causing UT-variations (e.g. Maehlum, 1968, 1969) is corpuscular radiation with low energy electrons (50 eV–1 keV) being most important for ionization. (Many aspects of polar ionospheres are for example summarized in G. Skovli, Ed.: The polar ionosphere and magnetospheric processes). Due to plasma convection this source of ionization can extend its influence to distances quite far from the region of energetic particle influx (like the dayside polar cusp).

Acknowledgement. The author is grateful to Dr. G. Haerendel for valuable discussions and helpful advice during the preparation of this paper.

References

Axford, X.I., Hines, C.O.: A unifying theory of high-latitude geophysical phenomena and geomagnetid storms. Can. J. Phys. *39*, 1433–1464, 1961

Banks, P.M., Holzer, T.E.: The polar wind. J. Geophys. Res. *73*, 6846–6854, 1968

Banks, P.M., Holzer, T.E.: High-latitude plasma transport: the polar wind. J. Geophys. Res. *74*, 6317–6332, 1969a

Banks, P.M., Holzer, T.E.: Features of plasma transport in the upper atmosphere. J. Geophys. Res. *74*, 6304–6316, 1969b

Banks, P.M.: Plasma transport in the topside ionosphere. In: The polar ionosphere and magnetospheric processes. G. Skovli, ed., pp. 193–208, New York: Gordon & Breach 1970

Banks, P.M., Nagy, A.F., Axford, W.I.: Dynamical behaviour of thermal protons in the mid-latitude ionosphere and magnetosphere. Planetary Space Sci. *19*, 1053–1067, 1971

Banks, P.M.: Dynamical behaviour of the polar topside ionosphere, presented at the NATO Advanced Study Institute on Magnetosphere-Ionosphere Interactions. Espedalen, Norway, 1971

Banks, P.M., Kockarts, G.: Aeronomy. New York: Academic Press 1973

Brace, L.H., Reddy, B.M., Mayr, H.G.: Global behaviour of the ionosphere at 1000 km altitude. J. Geophys. Res. *72*, 265–283, 1967

Brice, N.M.: Bulk motion of the magnetosphere. J. Geophys. Res. *72*, 5193–5211, 1967

Brinton, H.C., Grebowsy, J.M., Mayr, H.G.: Altitude variation of ion composition in the mid-latitude trough region: evidence for upward plasma flow. J. Geophys. Res. *76*, 3738–3745, 1971

Dungey, J.W.: Interplanetary magnetic field and the auroral zones. Phys. Rev. Letters *6*, 47–48, 1961

Dunkin, D.B., Fehsenfeld, F.C., Schmeltekopf, A.L., Ferguson, E.E.: Ion-molecule reaction studies from 300° to 600° K in a temperature-controlled afterglow system. J. Chem. Phys. *49*, 1365–1371, 1968

Evans, J.V.: Cause of the mid-latitude winter night increase in f_0F2. J. Geophys. Res. *70*, 4331–4345, 1965

Ferguson, E.E.: Ionospheric ion-molecule reaction rates. Rev. Geophys. *5*, 305, 1967

Geisler, J.E.: On the limiting daytime flux of ionization into the protonosphere. J. Geophys. Res. *72*, 81–85, 1967

Hanson, W.B., Patterson, T.N.L.: The maintenance of the nighttime *F*-layer. Planetary Space Sci. *12*, 979–997, 1964

Hoffman, J.X.: Ion composition measurements in the polar region from the Explorer 31 Satellite. Trans. Am. Geophys. Union *49*, 253, 1968

Hoffman, J.W.: Polar wind measurements. Trans. Am. Geophys. Union *4*, 301, 1971

Holzer, T.E., Banks, P.M.: Accidentally resonant charge exchange and ion momentum transfer. Planetary Space Sci. *17*, 1074–1077, 1969

Holzer, T.E.: Effects of plasma flow on density and velocity profiles in the polar ionosphere: In: The Polar Ionosphere and Magnetospheric Processes. G. Skovli, ed. pp. 209–223. New York: Gordon & Breach

Holzer, T.E., Fedder, J.A., Banks, P.M.: A comparison of kinetic and hydrodynamic models of an expanding ion-exosphere. J. Geophys. Res. *76*, 2453–2468, 1971

Holzer, T.E.: Interaction of the solar wind with the neutral component of the interstellar gas. J. Geophys. Res. *77*, 5407–5431, 1972

King, J.W., Kohl, H., Pratt, R.: The effect of atmospheric winds on the height of the *F*2-layer peak at middle and high latitudes. J. Atmospheric Terrest. Phys. *29*, 1529–1539, 1967

Kohl, H.: The possible effect of diffusion between magnetically conjugate points on the seasonal anomaly of the *F*-layer. In: Electron density profiles in ionosphere and exosphere. J. Frihagen, ed. pp. 231–238, North-Holland, Amsterdam: Publ. Co. 1966

K ohl, H., King, J.W., Eccles, D.: Some effects of neutral winds on the ionospheric *F*-layer. J. Atmospheric Terrest. Phys. *30*, 1733–1744, 1968
Maehlum, B.N.: Universal-time control of the low-energy electron fluxes in the polar regions. J. Geophys. Res. *73*, 3459–3468, 1968
Maehlum, B.N.: On the high-latitude, universal time controlled *F*-layer. J. Atmospheric Terrest. Phys. *31*, 531–538, 1969
Mayr, H.G., Brace, L.H., Dunham, G.S.: Ion composition and temperature in the topside ionosphere. J. Geophys. Res. *72*, 4391–4404, 1967
Mayr, H.G., Grebowsy, J.M., Taylor, H.A.: Study of the thermal plasma on closed field lines outside the plasmasphere. Planetary Space Sci. *18*, 1123–1135, 1970
Mitra, A.P.: A review of D-region processes in non-polar latitudes. J. Atmospheric Terrest. Phys. *30*, 1065–1114, 1968
Nagy, A.F., Bauer, P., Fontheim, E.G.: Nighttime cooling of the protonosphere. J. Geophys. Res. *73*, 6259–6274, 1968
Nishida, A.: Formation of a plasmapause, or magnetospheric plasma knee by the combined action of magnetospheric convection and plasma escape from the tail. J. Geophys. Res. *71*, 5669–5679, 1966
Park, C.G.: Whistler observations of the interchange of ionization between the ionosphere and the protonosphere. J. Geophys. Res. *75*, 4249–4260, 1970
Park, C.G., Banks, P.M.: Influence of thermal plasma flow on the mid-latitude nighttime F_2-layer: Effects of electric fields and neutral winds inside the plasmasphere. J. Geophys. Res. *79*, 4661–4668, 1974
Parker, E.N.: Interplanetary dynamical processes. New York: Wiley 1963
Rishbeth, H.: Further analogue studies of the ionospheric *F*-layer. Proc. Phys. Soc. (London) *81*, 65–77, 1963
Rishbeth, H.: On explaining the behaviour of the ionospheric *F*-region. Rev. Geophys. *6*, 33–71, 1968
Rishbeth, H.: The polar *F*-region. In: The polar ionosphere and magnetospheric processes. G. Skovli, ed. pp. 175–192. New York: Gordon & Breach 1970
Rösler, G.: Plasmaüberschallströmung zwischen magnetisch konjugierten Ionosphären hoher Breiten. MPI-PAE/Extraterr. 97, 1974
Rüster, R.: The relative effects of electric fields and atmospheric composition changes on the electron concentration in the mid-latitude *F*-layer. J. Atmospheric Terrest. Phys. *33*, 275–280, 1971
Skovli, G., ed.: The polar ionosphere and magnetospheric processes. New York: Gordon & Breach 1970
Stubbe, P.: Temperature dependence of the rate constants for the reactions $O^+ + O_2 \rightarrow O_2^+ + O$ and $O^+ + N_2 \rightarrow NO^+ + N$. Planetary Space Sci. *17*, 1221–1231, 1969
Stubbe, P., Chandra, S.: The effects of electric fields on the *F*-region behaviour as compared with neutral wind effects. J. Atmospheric Terrest. Phys. *32*, 1909–1919, 1970
Tanenbaum, B.S.: Transport equations for a gas mixture. Phys. Fluids *8*, 683–686, 1965
Thomas, J.O., Andrews, M.K.: The trans-polar exospheric plasma, 3: a unified picture. Planetary Space Sci. *17*, 433–446, 1969
Thomas, L.: The importance of photoionization in the production of the daytime *F*-region at high latitudes during winter. Planetary Space Sci. *14*, 891–899, 1966
Torr, D.G., Torr, M.R.: A theoretical investigation of corpuscular radiation effects on the *F*-region of the ionosphere. J. Atmospheric Terrest. Phys. *32*, 15–34, 1970
Yonezawa, T.: Maintenance of ionization in the nighttime F_2-region. Space Res. *5*, 49–60, 1965.

Dr. G. Rösler
Max-Planck-Institut für Physik und Astrophysik
Institut für extraterrestrische Physik
D-8046 Garching bei München
Federal Republic of Germany

J. Geophys. 41, 441–443, 1975

Short Communications

Crustal Structure of the Aegean Sea and the Hellenides Obtained from Geophysical Surveys

J. Makris

Institut für Geophysik, Hamburg

Received April 9, 1975

Key words: Crust of Earth – Gravity Anomalies – Refraction Seismics – Greece – Aegean Sea – Hellenides.

In the period 1971 to 1974 the territory of Greece has been geophysically investigated by Greek and German Institutions. Gravity and magnetic stations have been distributed at a spacing of one station per 25 km^2. Five deep seismic sounding cross-sections have been fired and recorded along the lines: Ionian Sea – Peloponnese, Amorgos – Mikonos – Evia, Crete: East-West, Cretan Sea: North-South, Cretan Sea: East-West.

The results of the seismic programms revealed a pure continental structure of variable thickness. The most attenuated area is that of the Cretan Sea, with only 22 km depth to the Moho-Discontinuity at the Bouguer gravity maximum of +175 mgal. The very unevenly distributed sedimentary cover of the Cretan Sea is composed mainly of Neogene Sediments with thickness of 3 –3,5 km in local basins (Jonsma *et al.*, 1975). The Greek mainland along the Pindos Chains has minimum Bouguer anomalies of –120 to –140 mgal and Moho-Depths between 42–46 km. The Aegean Area builds a large dome and incorporates also a large part of the Taurides, Western Turkey (Makris, 1975).

Combining the seismic results of "Meteor" Cruises Nr. 17 and 21, from the Ionian Sea (Weigel, 1974; Hinz, 1974) with gravity and seismic data of the Hellenides (Makris, 1973; Makris *et al.*, 1973), a 2-D density model was computed (fig. 1), for the area between Turkey and the Malta Shelf. The model exhibits large lateral density variations between the deep Ionian Basin and the adjacent continental areas. These variations are not only restricted to the crust but extend also in to the Upper Mantle. A "Lithothermal" plume of low velocity and density rises from the asthenosphere into the lithosphere transporting thermal energy and causing the present tectonic activity of the Hellenides. The upward movement of the hot plume has most probably been initiated by the subduction of oceanic crust below the Hellenides. The existance of deep sitted earthquake foci (Galanopoulos, 1974, personal communication), strongly supports this supposition, though their very unequal distribution indicates that active subduction might have ceased. The mass deficiency below the Aegean Region explains approximately 100 mgal of the gravity difference of nearly 450 mgal

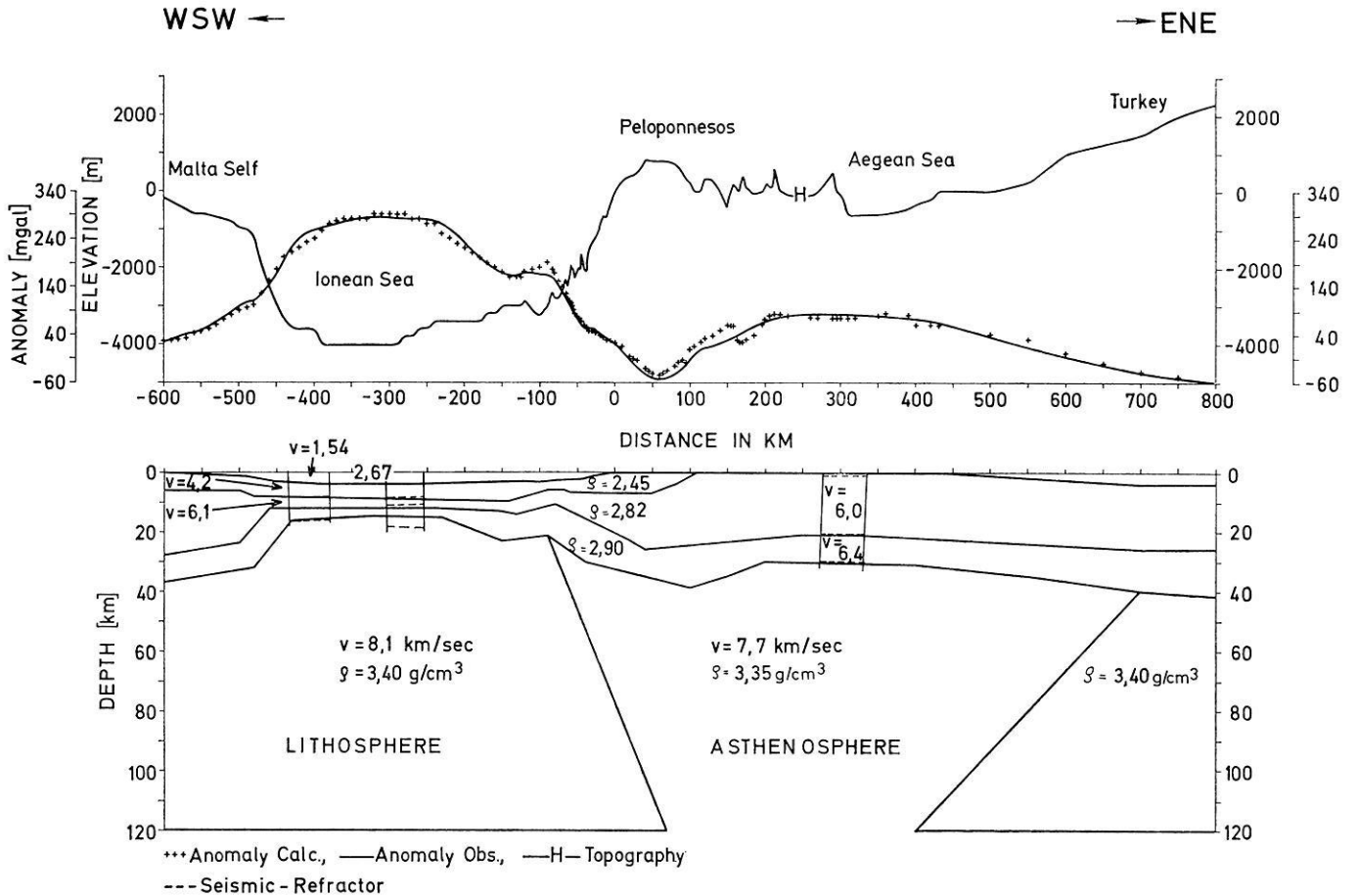

Fig. 1. 2-D crustal model between the Malta Shelf and Turkey. Seismic data in the Jonian Sea and Greece, see text. Gravity values give Bouguer anomalies

between the Hellenides and the deep Ionian Basin. The rest can be explained by the sediments and also the strong crustal attenuation of the Ionian Sea. The type of the crust in this region has not been explained satisfactorely. It seems to be of a transition type between continental and oceanic crust. More deep seismic soundings are required.

References

Jongsma, D., Wissmann, G., Hinz, K., Garde, S.: The southern aegean sea: An extensional marginal basin without spreading? Report, Bundesanstalt für Bodenforschung, Hannover, pp. 1–49, 1975

Hinz, K.: Results of seismic refraction and seismic reflection measurements in the Ionian Sea. Geol. Jahrb., E. 2, 33–65, 1974

Makris, J.: Some geophysical aspects of the evolution of the Hellenides. Bull. Geol. Soc. Greece, *X*, 206–213, 1973

Makris, J.: Geophysical investigations of the Hellenides. Hamb. Geophys. Einzelschriften, Heft 27, 1–98, 1975 (in print)

Makris, J., Mavridis, L. N., Menzel, H., Stavrou, A. and Veis, G.: The gravity field of Attika, the Peloponnese and Kithera, Greece. Z. Geophys. *39*, 929–936, 1973

Makris, J., Koschyk, K., Vees, R.: Refraction seismic measurements along the lines: Crete East-West, and Amorgos–Mikonos–Evia. In preparation

Weigel, W.: Crustal Structure under the Ionian Sea. J. Geophys. *40*, 137–140, 1974

Dr. J. Makris
Institut für Physik des Erdkörpers
D-2000 Hamburg 13
Binderstraße 22
Federal Republic of Germany

Book Reviews

J. G. Roederer, Ed. Vol. 5; A. J. Hundhausen: *Physics and Chemistry in Space. Coronal Expansion and Solar Wind.* 101 figs. XII,238 pages. Berlin–Heidelberg–New York: Springer 1972. ISBN 3-540-05875-3; DM 68,—.

The book on coronal expansion and solar wind is written by one of the most active and most successful researchers in the field of solar wind physics. It is therefore not surprising that the auther has written a book which represents an up-to-date, well written account on the state of the subject. The author has contributed himself to all the topics treated in the seven chapters of the book: It starts with the history and a phenomenological review of solar wind physics. Subsequently the "quiet" solar wind is treated as well as its chemical composition. It then treats the disturbed solar wind i.e. deviations from a quiet, homogeneous solar wind including the role of high-speed plasma streams and interplanetary shock waves. The discussion of these subjects is complete enough to give the reader an impression of the great progress made in the last decade. It also makes clear where open questions await their solution in future theoretical and observational research. The neglect of the plasma kinetic aspects of solar wind physics and the fast variations produced e.g. by discontinuities is not disturbing since the dividing line can be drawn very clearly. In conclusion, the book constitutes an excellent summary of the physics of the solar wind useful to the newcomer as well as to the researcher in this interesting field of geoastrophysical research.

F. M. Neubauer, Braunschweig

J. Geophys. 41, 445–462, 1975

Original Investigations

Synthetic Seismograms of PS-Reflections from Transition Zones Computed with the Reflectivity Method*

K. Fuchs

Geophysikalisches Institut, Universität Karlsruhe

Abstract. Expressions for the computation of synthetic seismograms of *PS*-reflections from transition zones with an arbitrary depth-dependent distribution of the elastic moduli and density are derived by the reflectivity method. Synthetic seismograms of *PS*-reflections are presented for first-order discontinuities with variable Poisson's ratio, for linear transition zones with variable thickness, and for laminas of variable thickness. The computed theoretical amplitudes show that from a crust-mantle boundary with a first-order discontinuity *PS*-reflections should be observable. However, in most crustal explosion studies *PS*-reflections are not observed, as demonstrated in a number of record sections. Both, transition zones and a reduction of *S*-wave velocity in the lower halfspace diminish the amplitudes of supercritically reflected *PS*-waves without affecting the amplitudes of the supercritical *PP*-reflection. On supercritical reflection from thin laminas both *PP* and *PS* amplitudes decrease. A transition zone is the most likely explanation of the observed absence of reflected *PS*-waves from the crust-mantle boundary. Its thickness should be at least 1 km.

Key words: *PS*-reflections – Synthetic seismograms – Reflectivity method – Crust-mantle boundary – Variable poisson's ratio – Linear transition zone – Lamina.

1. Introduction

Explosion seismology has concentrated almost exclusively on the interpretation of *P*-waves for two reasons. Firstly explosions are radiating dominantly compressional waves; and, secondly, the *P*-waves form the first arriving group, where in general arrival times can be picked much more reliably than in the case of the later arriving *S*-waves. However, there are quite a number of record sections

* Contribution No. 181 within a joint research program of the Geophysical Institutes in Germany sponsored by the Deutsche Forschungsgemeinschaft (German Research Association). Contribution No. 104, Geophysikalisches Institut Universität Karlsruhe.

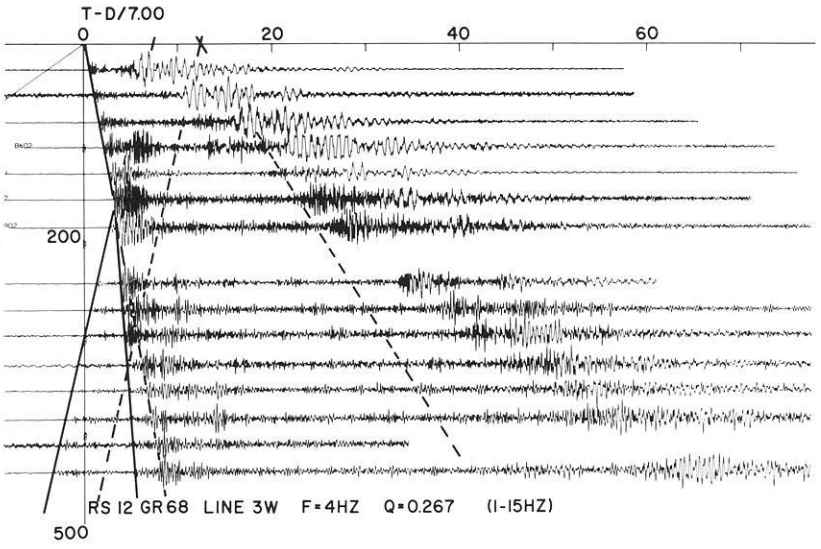

Fig. 1. Record section from profile Greenville 3 *W* in Canada. Reduction velocity 7.0 km/s. The dashed lines indicate the theoretical positions of the S_n and PPS-headwaves corresponding to the P_n-branch (adapted from Berry and Fuchs, 1973). Note the presence of the $S_M S$ phase and the absence of observable PPS- and PS-phases

available from explosion seismic experiments in various parts of the globe where *S*-phases show amplitudes comparable with the corresponding *P*-phases (Figs. 1–2). These *S*-phases must have been radiated directly from the source or converted immediately from *P*-waves in the neighbourhood of the source. These examples prove that *S*-waves are propagated with sufficient energy through the crust in the frequency range of explosion seismic experiments. Therefore, the question arises whether *PS*-reflections converted at transition zones in the crust and upper mantle can also be observed.

The reduced traveltime diagram for *PP*- and *PS*-reflections from the crust-mantle boundary of a one-layer crust is given in Fig. 4. At this first-order discontinuity the *P*-wave in the upper mantle is guiding a *P*-headwave (*PPP*) and a *S*-headwave (*PPS*). The critical distance (49.6 km) of the *PPS*-phase is nearly 20 km smaller than that for the *PPP*-phase (69.3 km). The time lag between *PPS* and *PPP* is 4.4 sec. The *PPS*-headwave is tangent to the converted $P_M S$-reflection. The asymptotic velocity of the $P_M S$-reflection at large distances becomes α_1 which is identical with the *P*-velocity of the crust, this is the same asymptotic velocity as that of the $P_M P$ reflection.

The approximate position of the *PPS*-traveltime branch is reproduced in the record sections of Figs. 1–3. It is quite evident that no energy comparable to the critical $P_M P$- or $S_M S$-reflection is present in these sections. The absence of $P_M S$-reflections appears to be a general feature of crustal record sections.

It is the purpose of this paper to investigate possible reasons for the observed absence of *PS*-reflections from the crust-mantle boundary. In the first part the reflectivity method (Fuchs, 1968b; Fuchs and Müller, 1971) is extended to include

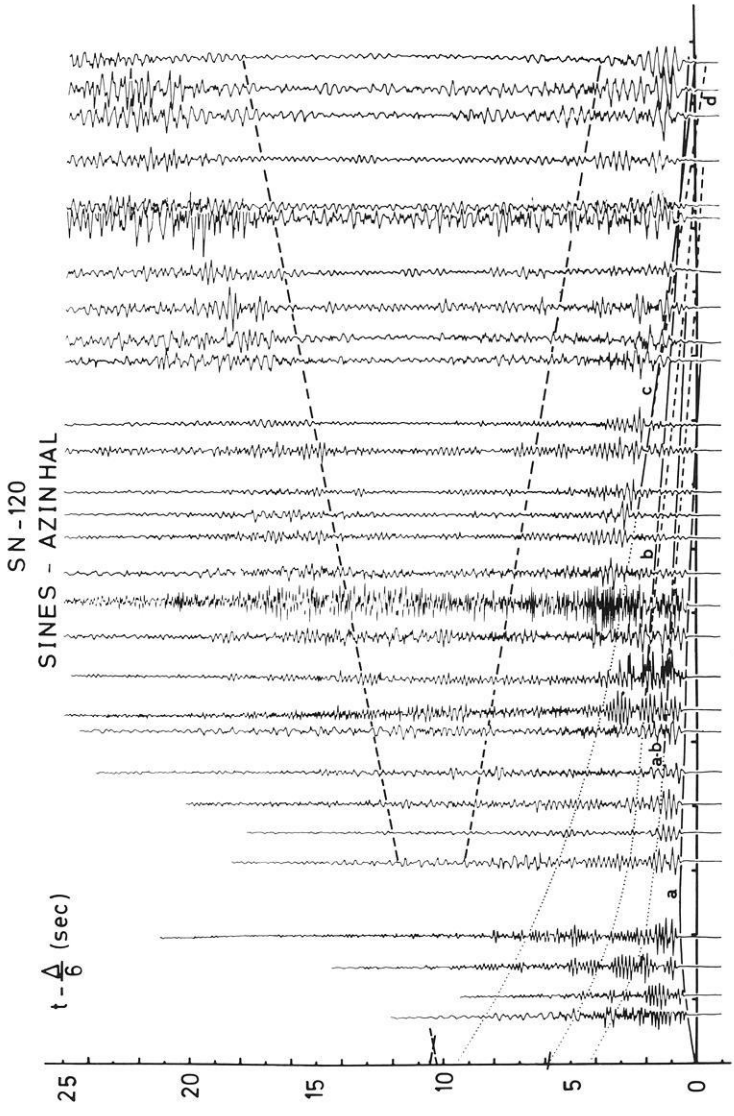

Fig. 2. Record section from profile Sines-Azinhal in Portugal. Reduction velocity 6.0 km/s. Dashed line indicates the theoretical position of the S_n and PPS headwaves corresponding to the P_n-branch (adapted from Müller *et al.*, 1973). Note the presence of the S_MS-phase and the absence of observable PPS- and PS-phases

the computation of synthetic PS-seismograms. In the second part PS-reflections from various kinds of transition zones will be presented which are likely candidates for the suppression of PS-reflections.

2. The Computation of Synthetic *PS*-Seismograms with the Reflectivity Method

The method for the computation of synthetic PP-seismograms with the reflectivity method (Fuchs, 1968 b) had been extended by Fuchs and Müller (1971) to cover the case of an arbitrary stack of horizontal layers on top of the reflecting zone. Here we will use the same notation as in this paper. The model of the layered medium is given in Fig. 5. It consists of $n-1$ plane, horizontal, homogeneous,

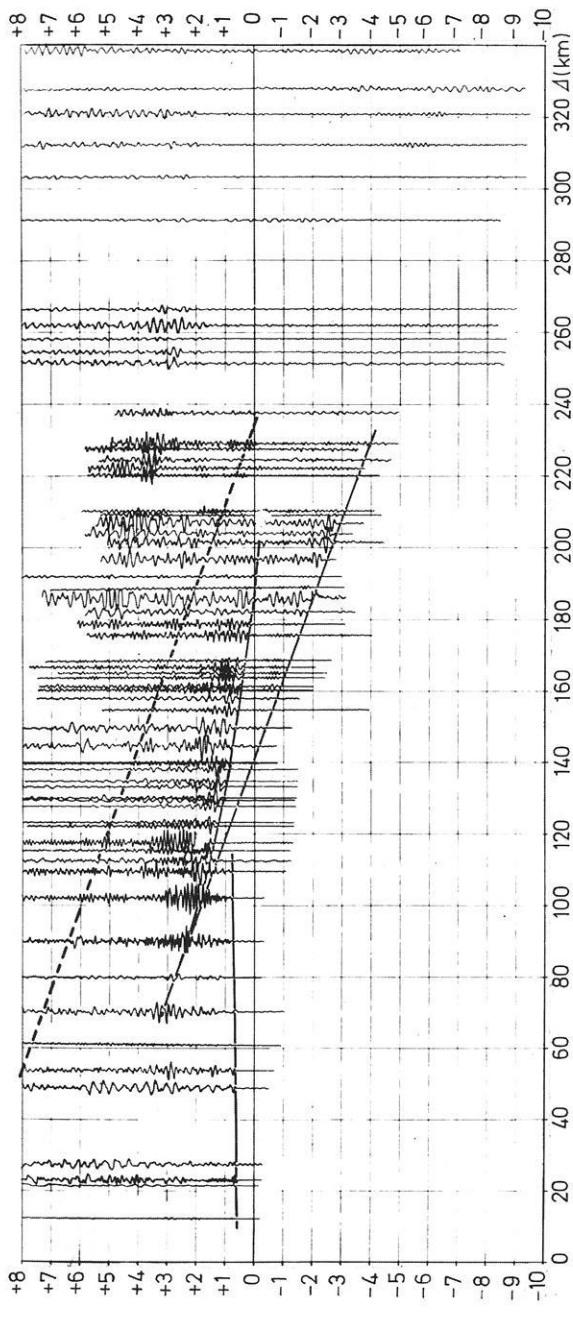

Fig. 3. Record section from profile Hilders-south in F. R. Germany. Reduction velocity 6.0 km/s. Dashed line indicates theoretical position of *PPS* headwave corresponding to the P_n-branch (adapted from Kaminski *et al.*, 1967). Note the absence of observable *PPS*- and *PS*-phases

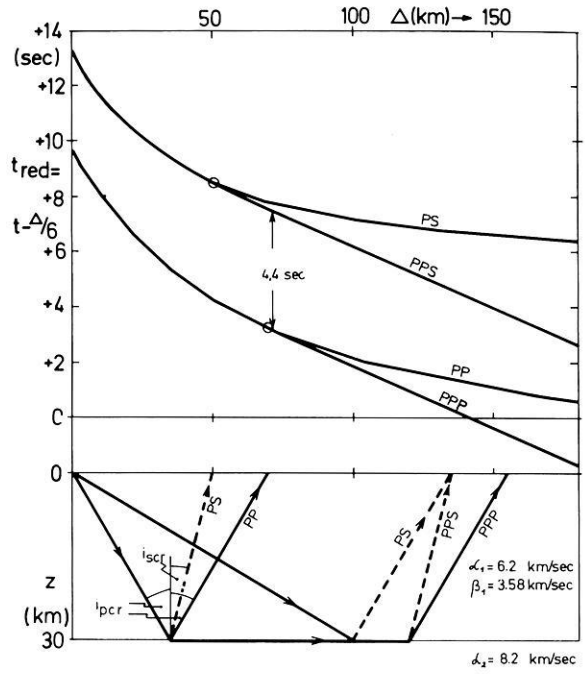

Fig. 4. Reduced traveltime diagram for *PP*- and *PS*-reflections from the base of a one-layer crust with schematic ray-paths

and isotropic layers on top of the half-space (layer n). The i-th layer is characterized by the P-velocity α_i, S-velocity β_i, density ρ_i; and thickness h_i. The explosive point source is placed in the free surface at $z=0$ without taking into account an interaction, *i.e.*, the P-waves in layer 1 are spherically symmetric and no S-waves are excited. In the layers 1 through m only transmission losses and traveltime delays of P- and S-waves are considered, multiple reflections within these m layers are neglected. The reflecting zone is formed by the layers $m+1$ through n. From the source to the top of the reflecting zone and back to the surface the exact or generalized ray theory (Müller, 1968a, b; 1970) will be followed while the reflection from the transition zone is described by the reflectivity method.

The compressional potential of the wave radiated from the explosive point source into layer 1 is:

$$\varphi_0(r, z, t)=\frac{1}{R}\cdot F\left(t-\frac{R}{\alpha_1}\right). \tag{1}$$

Where $R^2=r^2+z^2$. Its Fourier transform is in integral form:

$$\bar{\varphi}_0(r, z, \omega)=\bar{F}(\omega)\int_0^{\infty}\frac{k}{j\nu_1}\cdot J_0(kr)\exp(-j\nu_1 z)\,dk. \tag{2}$$

Here $\bar{F}(\omega)$ is the Fourier transformed source function $F(t)$, $J_0(kr)$ the Bessel function of the first kind and order zero, j the imaginary unit, k the horizontal

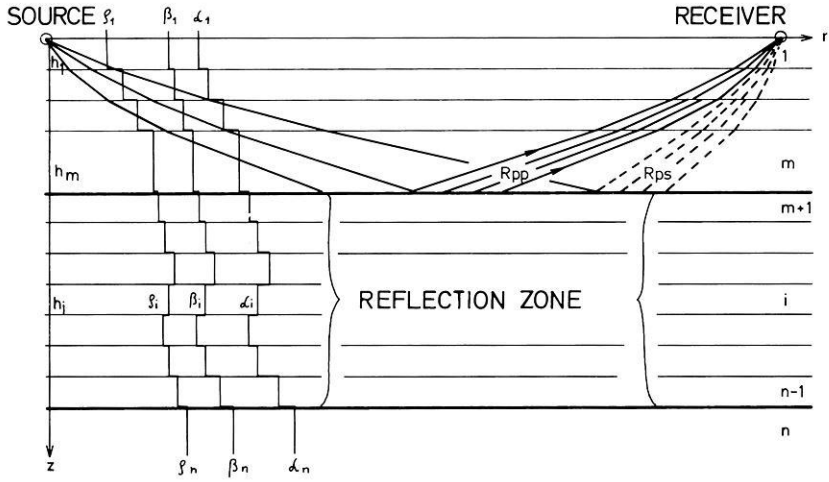

Fig. 5. Model of the layered medium with the position of the source and the receiver at the surface. The reflected *P*- and *S*-waves suffer elastic transmission losses and time delays in the layers 1 to *m*

wave number. The vertical wave numbers for *P* and *S* waves in the *i*-th layer are:

$$\nu_i=(k_{\alpha_i}^2-k^2)^{1/2}; \qquad \nu_i'=(k_{\beta_i}^2-k^2)^{1/2} \tag{3}$$

with:

$$k_{\alpha_i}=\omega/\alpha_i; \qquad k_{\beta_i}=\omega/\beta_i.$$

Transmitting this potential through the refracting layers of the overburden, the compressional potential of the *P*-wave in layer *m*, incident upon the reflecting zone, is:

$$\bar{\varphi}_1(r,z,\omega)=\bar{F}(\omega)\int_0^{\infty}\frac{k}{j\nu_1}J_0(kr)\cdot P_d(\omega,k)$$
$$\cdot\exp\left[-j\left(\sum_{i=1}^{m-1}h_i\nu_i+\left(z-\sum_{i=1}^{m-1}h_i\right)\nu_m\right)\right]dk \tag{4}$$

where $P_d(\omega,k)$ is the product of the transmission coefficients at the interfaces 2 through *m* for downward propagation of a *P*-wave.

So far we have followed the formulation of Fuchs and Müller (1971) who computed the *PP*-reflection from the transition zone. In addition to the *PP*-phase, in general, the transition zone reflects also *S*-waves whose potential in the *m*-th layer is:

$$\bar{\psi}_2(r,z,\omega)=\bar{F}(\omega)\int_0^{\infty}\frac{k}{\nu_1}J_1(kr)\cdot P_d(\omega,k)\cdot\tilde{R}_{PS}(\omega,k)$$
$$\cdot\exp\left[-j\left(\sum_{j=1}^{m}h_i\nu_i+\left(\sum_{i=1}^{m}h_i-z\right)\nu_m'\right)\right]dk. \tag{5}$$

The complex reflectivity $\tilde{R}_{PS}(\omega,k)$ of the reflecting zone is the same as defined by Fuchs (1968a), $J_1(kr)$ is the Bessel function of the first kind and first order.

The reflected wave is now propagated upwards through the interfaces m, $m-1, \ldots, 2$. Its potential in layer 1 is:

$$\bar{\psi}_3(r, z, \omega) = \bar{F}(\omega) \int_0^\infty \frac{k}{\nu_1} J_1(kr) \cdot P_d(\omega, k) \cdot S_u(\omega, k) \cdot \tilde{R}_{PS}(\omega, k) \cdot \exp\left[-j\left(\sum_{i=1}^{m} h_i(\nu_i + \nu_i') - z \cdot \nu_i'\right)\right] dk \tag{6}$$

S_u is the product of transmission coefficients of the upward travelling S-wave at the interfaces $m, m-1, \ldots, 2$.

While the effect of the free surface has been neglected at the source it will be taken into account at the receiver. At the incidence of the S-wave upon the free surface a S- and a P-wave is reflected with potentials:

$$\bar{\psi}_4(r, z, \omega) = \bar{F}(\omega) \int_0^\infty \frac{k}{\nu_1} J_1(kr)\, P_d(\omega, k) \cdot S_u(\omega, k) \cdot \tilde{R}_{PS}(\omega, k) \cdot r_{ss}(\omega, k) \cdot \exp\left[-j\left(\sum_{i=1}^{m} h_i(\nu_i + \nu_i') + z \cdot \nu_1'\right)\right] dk, \tag{7}$$

$$\bar{\varphi}(r, z, \omega) = \bar{F}(\omega) \int_0^\infty \frac{k}{j\nu_1} J_0(kr)\, P_d(\omega, k) \cdot S_u(\omega, k)\, \tilde{R}_{PS}(\omega, k) \cdot r_{sp}(\omega, k) \cdot \exp\left[-j\left(\sum_{i=1}^{m} h_i(\nu_i + \nu_i') + z \cdot \nu_1'\right)\right] dk \tag{8}$$

$r_{ss}(\omega, k)$ and $r_{sp}(\omega, k)$ are the $S-S$ and $S-P$ reflection coefficients at the free surface.

The horizontal and vertical displacement in the first layer are:

$$\bar{u} = \frac{\partial \bar{\varphi}}{\partial r} - \frac{\partial \bar{\psi}_3}{\partial z} - \frac{\partial \bar{\psi}_4}{\partial z},$$

$$\bar{w} = \frac{\partial \bar{\varphi}}{\partial z} + \frac{\partial \bar{\psi}_3}{\partial r} + \frac{\partial \bar{\psi}_4}{\partial r} + \frac{\bar{\psi}_3}{r} + \frac{\bar{\psi}_4}{r}.$$

For $z = 0$ we derive with Eqs. (6), (7) and (8):

$$\bar{u}(r, 0, \omega) = \bar{F}(\omega) \int_0^\infty \frac{jk^2}{\nu_1} J_1(kr)\, P_d(\omega, k) \cdot S_u(\omega, k) \cdot \tilde{R}_{PS}(\omega, k) \cdot \left[r_{sp} - \frac{\nu_1'}{k}(1 - r_{ss})\right] \cdot \exp\left[-j \sum_{i=1}^{m} h_i(\nu_i + \nu_i')\right] dk, \tag{9}$$

$$\bar{w}(r, 0, \omega) = \bar{F}(\omega) \int_0^\infty \frac{k^2}{\nu_1} J_0(kr) \cdot P_d(\omega, k) \cdot S_u(\omega, k) \cdot \tilde{R}_{PS}(\omega, k) \cdot \left[1 + r_{ss} - \frac{\nu_1}{k} r_{sp}\right] \cdot \exp\left[-j \sum_{i=1}^{m} h_i(\nu_i + \nu_i')\right] dk. \tag{10}$$

For numerical integration it has been found more convenient to use the angle γ as new variable, related to k by:

$$k=\frac{\omega}{\alpha_m}\sin\gamma=k_{\alpha m}\sin\gamma. \tag{11}$$

For $k\leqq k_{\alpha m}$ γ is the real angle of incidence in the m-th layer at the top of the reflecting zone. With the new variable γ the coefficients P_d, S_u, r_{ss} and r_{sp} depend only on γ. The integrals (9) and (10) become:

$$\bar{u}(r,0,\omega)=\bar{F}(\omega)\cdot k_{\alpha m}^2\int_{\gamma_1}^{\gamma_2}\sin\gamma\cos\gamma j\cdot J_1(k_{\alpha m}r\sin\gamma)\,\tilde{R}_{PS}(\omega,\gamma)\cdot A(\gamma)$$
$$\cdot\exp\left[-jk_{\alpha m}\sum_{i=1}^{m}h_i(\eta_i+\eta_i')\right]d\gamma, \tag{12}$$

$$\bar{w}(r,0,\omega)=\bar{F}(\omega)\cdot k_{\alpha m}^2\int_{\gamma_1}^{\gamma_2}\sin\gamma\cos\gamma\cdot J_0(k_{\alpha m}r\sin\gamma)\,\tilde{R}_{PS}(\omega,\gamma)\cdot B(\gamma)$$
$$\cdot\exp\left[-jk_{\alpha m}\sum_{i=1}^{m}h_i(\eta_i+\eta_i')\right]d\gamma \tag{13}$$

where

$$A(\gamma)=a(\gamma)\cdot P_d(\gamma)\cdot S_u(\gamma)\quad\text{and}\quad B(\gamma)=b(\gamma)\cdot P_d(\gamma)\cdot S_u(\gamma) \tag{14}$$

and

$$a(\gamma)=\frac{\nu_1'}{\nu_1}\left[1-r_{ss}-\frac{k}{\nu_1'}r_{sp}\right], \tag{15}$$

$$b(\gamma)=\frac{k}{\nu_1}\left[1+r_{ss}-\frac{\nu_1}{k}r_{sp}\right]. \tag{16}$$

The products of the transmission coefficients P_d and S_u are:

$$P_d=\prod_{i=2}^{m}T_{ppi}(\gamma)\quad\text{and}\quad S_u=\prod_{i=2}^{m}T_{ssi}(\gamma) \tag{17}$$

where:

$$T_{ppi}(\gamma)=-2\rho_{i-1}\cdot\eta_{i-1}\frac{C}{D},$$

$$T_{ssi}(\gamma)=-2\rho_i\eta_i'\frac{\bar{C}}{D}$$

with:

$$C=\eta_i'(d_i\sin^2\gamma-\rho_{i-1})-\eta_{i-1}'(d_i\sin^2\gamma+\rho_i),$$
$$\bar{C}=\eta_i(d_i\sin^2\gamma-\rho_{i-1})-\eta_{i-1}(d_i\sin^2\gamma+\rho_i),$$

$$D=\sin^2\gamma(d_i\sin^2\gamma+\rho_i-\rho_{i-1})^2+\eta_i\eta_i'(d_i\sin^2\gamma-\rho_{i-1})^2$$
$$+\rho_{i-1}\rho_i\eta_i\eta_{i-1}'+\eta_{i-1}[d_i^2\eta_i\eta_{i-1}'\eta_i'\sin^2\gamma$$
$$+\eta_{i-1}'(d_i\sin^2\gamma+\rho_i)^2+\rho_{i-1}\rho_i\eta_i'], \tag{18}$$
$$\eta_i=\left[\left(\frac{\alpha_m}{\alpha_i}\right)^2-\sin^2\gamma\right]^{1/2},\quad \eta_i'=\left[\left(\frac{\alpha_m}{\beta_i}\right)^2-\sin^2\gamma\right]^{1/2}.$$

The coefficients $a(\gamma)$ and $b(\gamma)$ are:

$$a(\gamma)=-\frac{1}{N}\frac{\eta_1'}{\eta_1}\cdot\frac{\alpha_m^2}{\beta_1^2}\cdot 2\left(2\sin^2\gamma-\frac{\alpha_m^2}{\beta_1^2}\right),$$
$$b(\gamma)=\frac{1}{N}\cdot 4\frac{\alpha_m^2}{\beta_1^2}\eta_1'\sin\gamma, \tag{19}$$
$$N=4\sin^2\gamma\,\eta_1\eta_1'+\left(2\sin^2\gamma-\frac{\alpha_m^2}{\beta_1^2}\right)^2.$$

Without the influence of the free surface at $z=0$ the coefficients $a(\gamma)$ and $b(\gamma)$ become:

$$a(\gamma)=\frac{\nu_1'}{\nu_1}\quad\text{and}\quad b(\gamma)=\frac{k}{\nu_1}.$$

Since we are only interested in the reflection of body waves the integration in Eqs. (12) and (13) will be restricted to real angles γ, *i.e.* $0\leqq\gamma\leqq\pi/2$ as was discussed by Fuchs and Müller (1971).

For crustal explosion studies it is convenient to replace the Bessel functions by their large distance approximations:

$$J_0(x)=\sqrt{\frac{2}{\pi x}}\cos\left(x-\frac{\pi}{4}\right)$$
$$=\frac{1}{\sqrt{2\pi x}}\left\{\exp\left[j\left(x-\frac{\pi}{4}\right)\right]+\exp\left[-j\left(x-\frac{\pi}{4}\right)\right]\right\}, \tag{20}$$
$$J_1(x)=\sqrt{\frac{2}{\pi x}}\sin\left(x-\frac{\pi}{4}\right)$$
$$=\frac{-j}{\sqrt{2\pi x}}\left\{\exp\left[j\left(x-\frac{\pi}{4}\right)\right]-\exp\left[-j\left(x-\frac{\pi}{4}\right)\right]\right\}. \tag{21}$$

The first exponential term in Eqs. (20) and (21) corresponds to waves travelling towards the source. It can be shown by numerical evaluation that the contribution of these terms to the integrals in Eqs. (12) and (13) are negligible. Neglecting these terms the two integrals become:

$$\bar{u}(r,0,\omega)=-\bar{F}(\omega)\,e^{j\pi/4}\sqrt{\frac{k_{\alpha_m}^3}{2\pi r}}\int_{\gamma_1}^{\gamma_2}\sqrt{\sin\gamma}\cos\gamma\,\tilde{R}_{PS}(\omega,\gamma)\cdot E(\gamma)$$
$$\cdot\exp\left\{-jk_{\alpha_m}\left[r\sin\gamma+\sum_{i=1}^{m}h_i(\eta_i+\eta_i')\right]\right\}d\gamma, \tag{22}$$

$$\bar{w}(r,0,\omega)=\bar{F}(\omega)\,e^{j\pi/4}\sqrt{\frac{k_{\alpha_m}^3}{2\pi r}}\int_{\gamma_1}^{\gamma_2}\sqrt{\sin\gamma}\cdot\cos\gamma\,\tilde{R}_{PS}(\omega,\gamma)\cdot B(\gamma)$$
$$\cdot\exp\left\{-jk_{\alpha_m}\left[r\sin\gamma+\sum_{i=1}^{m}h_i(\eta_i+\eta_i')\right]\right\}d\gamma. \tag{23}$$

The Fortran-program "Reflexion" has been extended to include synthetic seismograms of *PS*-reflections according to Eqs. (22) and (23).

3. *PS*-Reflections from Various Kinds of Transition Zones

In this section the extended computer-program will be applied to investigate the absence of *PS*-reflections from the crust-mantle boundary on observed record sections from crustal explosion-seismic experiments. The far-field displacement of the compressional wave from the explosive source is proportional to the derivative $F'(t)$ of the source function $F(t)$. In the following examples $F'(t)$ is:

$$F'(t)=\begin{cases}\sin 10\pi t-0.5\sin 20\pi t & \text{for } 0\leqq t\leqq 0.2\text{ sec}\\ 0 & \text{for } t<0 \quad\text{and}\quad t>0.2\text{ sec}.\end{cases}$$

This signal with a duration of 0.2 sec has a dominant frequency of about 5 Hz.

3.1. PS-Reflections from a First-Order Discontinuity

A one-layer crustal model with a first-order discontinuity as crust-mantle boundary serves as a first model (Model 1 in Table 1) for which synthetic seismograms of *PS*-reflections are computed. The traveltimes for this model had been given already in Fig. 4. The *PP*- and *PS*-section of the vertical component are given separately, both on the same amplitude scale, in Fig. 6.

The phases of the reflections $P_M P$ and $P_M S$ as well as the headwaves *PPP* and *PPS* are clearly recognized. While the $P_M P$ reflection suffers a phase change of 180° at grazing incidence, that $P_M S$ reflection shows the same phase as the subcritical $P_M S$ reflection. The most important observation is that the maximum *PS*-amplitude reaches about 0.6 of the maximum *PP*-amplitude in case of a purely compressional source. Should the source radiate *S*-waves as well, the *SP* phase would constructively interfere, with the *PS* phase, and the combined *PS* and *SP* phase could attain amplitudes larger or equal to the *PP* phase. – The maximum of the *PS*-reflection does not occur at the critical distance of 49.6 km but is displaced to larger distances (63.5 km) by the interference of the *PS*-reflection and the *PPS*-headwave. This is the same effect as discussed for supercritically reflected *P*-waves by Červený (1961).

Comparing these synthetic seismograms for *PS*-reflections from a first-order discontinuity with the observed record sections of Figs. 1–3 one clearly recognizes that the observations do not show appreciable energy of arrivals at the places where the *PS*-reflection is expected. Therefore, the question arises which models of the crust-mantle boundary may cause a suppression of the *PS*-reflections. In

Table 1. Models of Transition Zones

Model	No.	Poisson's ratio	Thickness of first layer	α_1 (km/s)	β_1 (km/s)	ρ_1 (g/cm^3)	α_2 (km/s)	β_2 (km/s)	ρ_2 (g/cm^3)
First-Order Discontinuity	1	0.25	30	6.2	3.575	2.6	8.2	4.73	3.36
	2	0.30	30	6.2	3.575	2.6	8.2	4.38	3.36
	3	0.378	30	6.2	3.575	2.6	8.2	3.575	2.6
	4	0.4	30	6.2	3.575	2.6	8.2	3.35	3.36
	5	0.5	30	6.2	3.575	2.6	8.2	0	3.36
Transition Zone		Thickness of Transition Zone d (km)							
	6	0.2	29.9	6.2	3.575	2.6	8.2	4.73	3.36
	7	0.5	29.75	6.2	3.575	2.6	8.2	4.73	3.36
	8	1.0	29.0	6.2	3.575	2.6	8.2	4.73	3.36
	9	4.0	28.0	6.2	3.575	2.6	8.2	4.73	3.36
Lamina		Thickness of Lamina h (km)							
	10	1	30	6.2	3.575	2.6	8.2	4.73	3.36
	11	0.5	30	6.2	3.575	2.6	8.2	4.73	3.36
	12	0.25	30	6.2	3.575	2.6	8.2	4.73	3.36

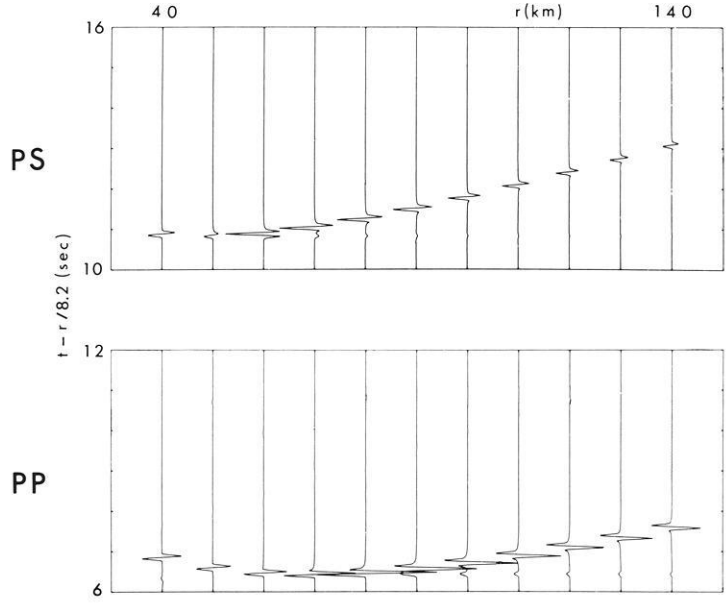

Fig. 6. Section of synthetic seismograms of *PP*- and *PS*-reflections from a first-order discontinuity at a depth of 30 km; vertical component, free surface reflection taken into account (model 1 in Table 1)

the following several possibilities for a reduction of *PS*-amplitudes are discussed. The most likely model is a transition zone, since *PS* coupling decreases in an inhomogeneous medium with decreasing gradients of the elastic properties. However, other reasons – variable Poisson's ratio in the upper mantle and reflection from a lamina – will be investigated as well.

3.2. PS-Reflections from a Linear Transition Zone

In the high-frequency limit of geometrical ray theory no converted *PS*-reflections are expected to arise from a transition zone in which the elastic parameters and the density change continuously with depth. However, for finite frequencies the equation of motion of an inhomogeneous medium does not separate completely in two wave equations for compressional and shear waves. The coupling between *P*- and *S*-waves is the stronger the larger the gradient of the elastic properties and density. Therefore, *PS*-reflections are to be expected also from continuous transition zones. Their amplitudes cannot be derived from geometrical ray theory.

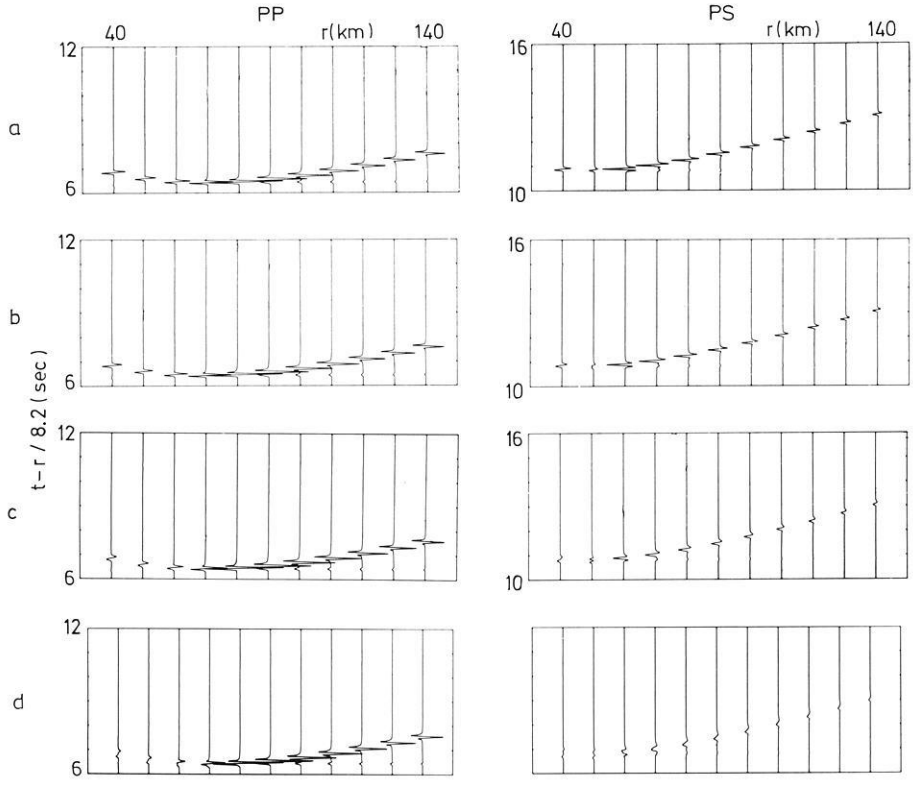

Fig. 7. Sections of synthetic seismograms of *PP*- and *PS*-reflections from linear transition zones of thickness $d = 0.2$ (b), 0.5 (c) and 1.0 km (d) (models 6 to 8 in Table 1) compared with section from first-order discontinuity (a). Vertical component, free surface accounted for

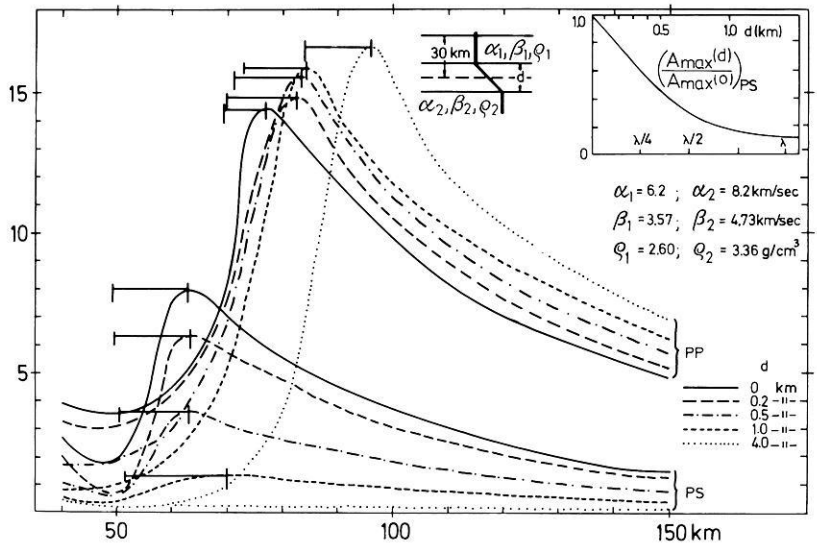

Fig. 8. Amplitude distance curves of *PP*- and *PS*-reflections from linear transition zones of thickness $d = 0$ (first-order discontinuity), 0.2, 0.5, 1.0 and 4.0 km. The displacements of the amplitude maxima from the critical distance are indicated. In the inlet the ratio of maximum *PS*-amplitudes to that from a first-order discontinuity are plotted as a function of thickness d of the transition zone and wavelength

In this section theoretical amplitudes will be computed with the aid of synthetic seismograms. The linear transition zone is approximated by a stack of 10 thin homogeneous layers. In Fig. 7 the *PP*- and *PS*-record sections of a first-order discontinuity are compared with those from transition zones of thickness 0.2 km to 1.0 km (models 6 to 8 in Table 1). As was expected, the amplitudes of supercritical *PP*-reflections are hardly changed by the introduction of the transition zone. Only the subcritical *PP*-reflections decrease strongly with increasing thickness of the transition zone. On the other hand, the *PS*-reflections diminish both in the sub- and supercritical distance range.

Amplitude-distance curves for transition models with thicknesses from 0 to 4.0 km are compiled in Fig. 8. The shift of the amplitude maxima relative to the critical points occurs also in case of transition zones and is indicated in the figure. The inlet in Fig. 8 gives the amplitude of the *PS* maxima as a function of transition thickness and *P*-wavelength ($\lambda = 1.4$ km). A rapid decrease of maximum amplitudes with growing thickness of the transition zone is to be noted. If the thickness equals about one wavelength, the maximum amplitude is only 1/10 of the maximum amplitude from a first-order discontinuity. If transition zones are considered to be responsible for the absence of *PS* phases in the observations, it suffices to replace the first-order discontinuity by transition zones of thickness of about one *P*-wavelength. – In turn it can be argued that if *PS*-reflections should be observed their presence would have to be taken as evidence of an extremely sharp transition zone of thickness less than one wavelength.

3.3. *PS-Reflections from a First-Order Discontinuity with Variable Poisson's Ratio in the Lower Half-Space*

It has been pointed out already that a transition zone is not the only possible explanation of the absence of *PS*-reflections. Even in case of a first-order discontinuity the ratio of *P*- to *S*-wave velocities may drastically change the amplitudes of the reflected *PS*-waves. In this section we will change the Poisson's ratio σ in the lower half-space from 0.25 to 0.5 keeping this ratio constantly 0.25 in the upper half-space. This range would correspond to a gradual transition from a solid through a partially molten lower half-space to a fluid medium.

In Fig. 9 a comparison of synthetic *PP*- and *PS*-record sections is given for $\sigma = 0.25$, 0.30, 0.378, 0.5 (models 1 to 5 in Table 1). While the amplitudes of the supercritical *PP*-reflections hardly change, the amplitudes of the supercritical *PS*-reflections are affected strongly. They decrease with increasing Poisson's ratio. The case $\sigma = 0.378$ and equal density in both media corresponds to equal *S*-wave velocity in which case no *PS*-waves are generated at the interface since here compressive and shear motions decouple completely (this case is a very efficient

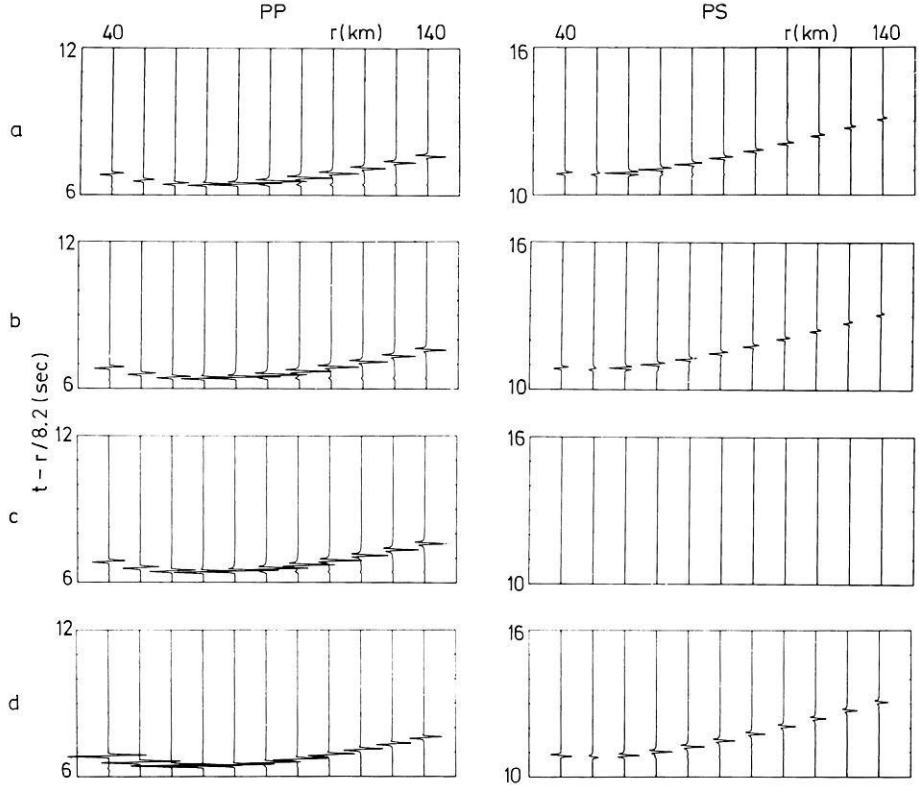

Fig. 9. Sections of synthetic seismograms of *PP*- and *PS*-reflections from a first-order discontinuity with variable Poisson's ratio in the lower halfspace ($\sigma = 0.25$ (a), 0.30 (b), 0.378 (c), 0.5 (d), models 1 to 5 in Table 1); vertical component free surface accounted for. For $\sigma = 0.378$ the density in both halfspaces has been chosen equally as 2.6 g/cm^3; complete decoupling of compressional and shear waves

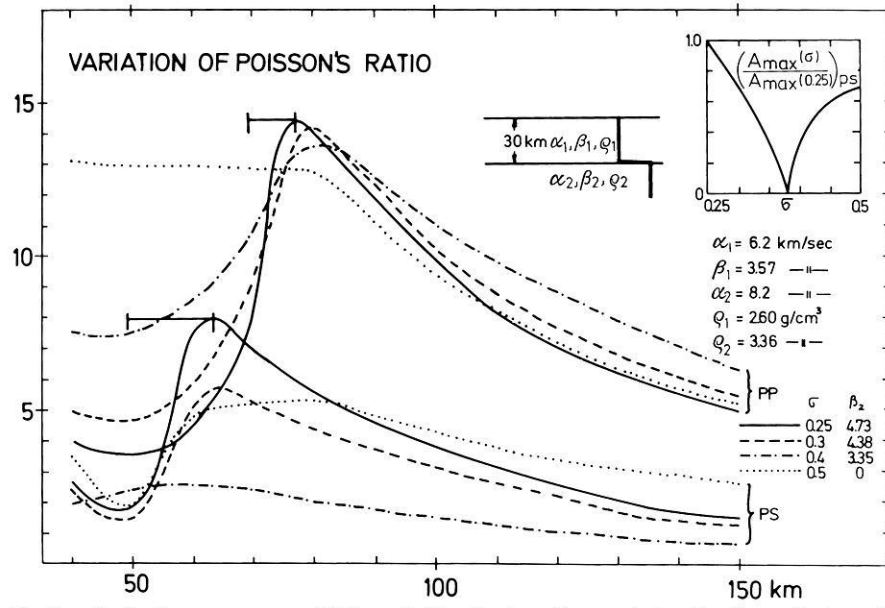

Fig. 10. Amplitude distance curves of *PP*- and *PS*-reflections from a first-order discontinuity with variable Poisson's ratio σ in the lower halfspace ($\sigma = 0.25, 0.3, 0.4, 0.5$). In the inlet the ratio of maximum *PS*-amplitudes to that for $\sigma = 0.25$ is plotted as a function of σ

test of the computer-program). For $\sigma > 0.378$ the amplitudes of the *PS*-reflections increase again but do not reach the amplitudes of the case $\sigma = 0.25$. Amplitude-distance curves for $\sigma = 0.25$, 0.3, 0.4 and 0.5 are compiled in Fig. 10. The inlet of this figure gives the ratio of the maximum *PS*-amplitude to that with $\sigma = 0.25$ as a function of σ. It is quite evident that a reduction of the *S*-wave velocity in the lower half-space can also be the cause for the disappearance of *PS*-reflections.

3.4. PS-Reflections from Single Laminas with Variable Thickness

The amplitudes of the supercritical reflection from a high velocity layer diminish substantially if the layer is thin enough and embedded between two low velocity half-spaces. For the sake of brevity, such a layer will be termed a lamina. If the lamina is sufficiently thin, the supercritical reflection looses energy since a considerable part of it is leaking through the lamina into the lower half-space. It is not known so far whether the supercritical *PS*-reflections are as strongly affected by this leakage as the *PP*-reflections.

In Fig. 11 sections of synthetic seismograms of *PP*- and *PS*-reflections from a lamina of variable thickness $d = 1.0$, 0.5 and 0.25 km are compared with the reflections from a first-order discontinuity. Both headwaves *PPP* and *PPS* have disappeared. One recognizes that the maximum amplitudes of both *PP*- and *PS*-waves diminish with decreasing thickness of the lamina. The amplitude-distance curves for these cases are presented in Fig. 12.

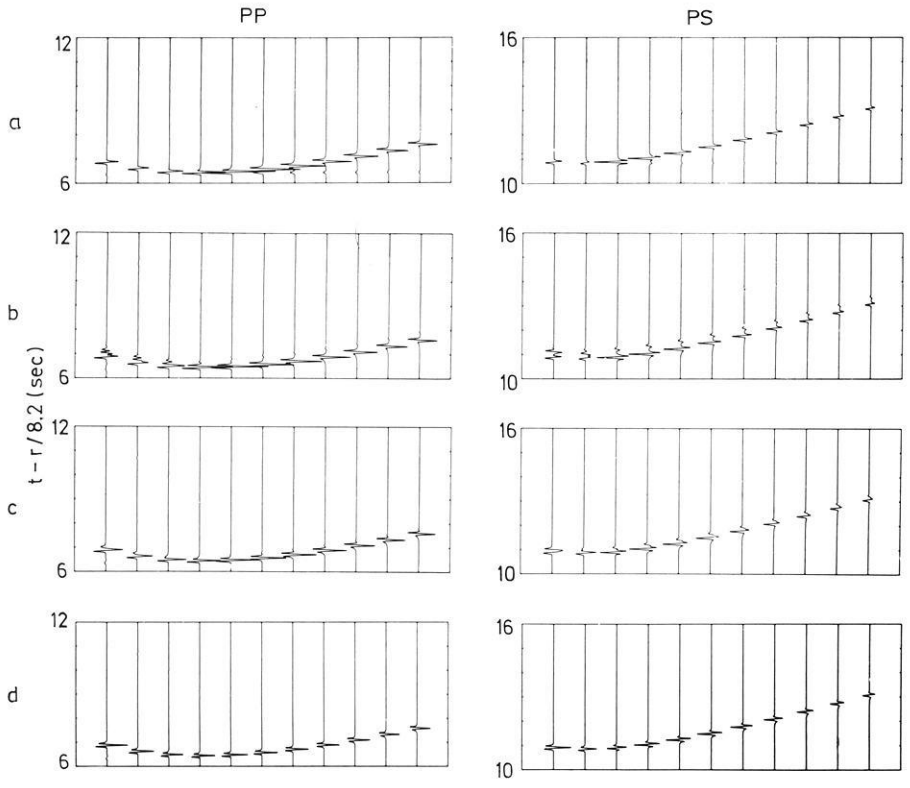

Fig. 11. Sections of synthetic seismograms of *PP*- and *PS*-reflections from a lamina with variable thickness $h = 1.0$ (b), 0.5 (c) and 0.25 km (d) (models 10 to 12 in Table 1) between two low velocity halfspaces compared with reflections from a first-order discontinuity (a); vertical component, free surface accounted for

It is obvious that the supercritical *PP*-reflections decrease much more rapidly in amplitude than the *PS*-reflections. For $d = 0.25$ km both types of reflections show nearly equal maximum amplitudes. The behaviour of the maximum amplitudes is summarized in the inlet of Fig. 12 as a function of layer thickness. It may be concluded that the *PS*-reflections from a thin lamina are less affected by the leakage of energy into the lower half-space than the *PP*-reflection. Therefore a single lamina is no suitable model for the explanation of the observed absence of *PS*-reflections from the crust-mantle boundary.

4. Discussion and Conclusions

In the first part of this paper the expressions for the *PS*-reflections from transition zones with arbitrary depth distributions of the elastic moduli and density have been derived. The program "Reflexion" described previously in detail by Fuchs and Müller (1971) has been extended to include the computation of synthetic

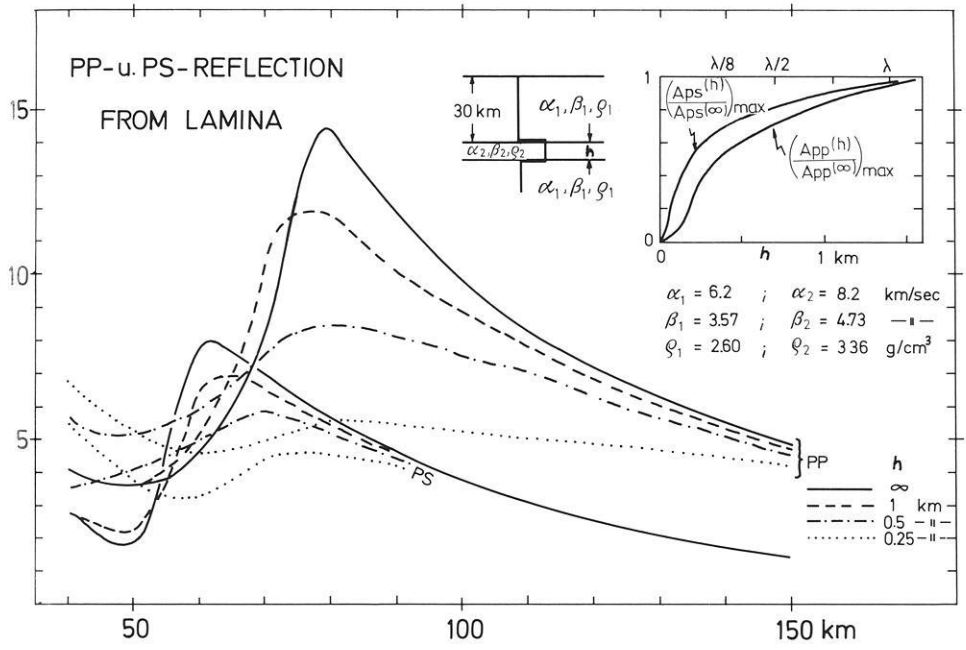

Fig. 12. Amplitude distance curves of *PP*- and *PS*-reflections from a lamina with variable thickness $h = 1.0$, 0.5 and 0.25 km. In the inlet the maximum *PP*- and *PS*-amplitudes to that for the first-order discontinuity is plotted as a function of thickness of the lamina and of the wavelength

PS-reflections. The extended program has been applied to a problem encountered in explosion seismology, *i.e.* the absence of *PS*-reflections converted at the crust-mantle boundary in the presence of strong *PP*- and *SS*-reflections.

Firstly, it could be shown that *PS*-reflections from a first-order discontinuity model of the crust-mantle boundary with Poisson's ratio $\sigma = 0.25$ should possess amplitudes comparable in size with those of the *PP*-reflection. Such a model is not in accordance with the observations. Therefore, reflections from linear transition zones have been investigated which in fact cause a strong diminution of *PS*-amplitudes with increasing thickness of the transition zone while *PP*-amplitudes show no decrease in the supercritical distance range. A thickness of about one wavelength reduces the maximum *PS*-amplitudes to 1/10 of their size for a first-order discontinuity, *i.e.* already a very thin transition zone with thickness more than 1 km will cause the *PS*-reflections to become unobservable. Therefore, supercritical *PS*-reflections are a very sensitive indication of the presence of first-order discontinuities. Wherever models with first-order discontinuities are postulated *PS*-reflections should be observable. So far, no *PS*-reflections from the crust-mantle boundary are known to the author. Should there exist regions where *PS*-reflections can be observed, the crust-mantle boundary must be extremely sharp.

A variation of Poisson's ratio in the upper mantle below the crust-mantle boundary is another possible cause for the suppression of *PS*-reflections. If, by partial melting, the *S*-velocity and density become equal to the *S*-velocity and

density in the overburden, *PS*-reflections may completely disappear. Thin Laminas diminish the amplitudes of *PP*-reflections more strongly than those of *PS*-reflections. Therefore, they do not provide an explanation of the observed phenomenon.

From the present study a variation of Poisson's ratio or the existence of a transition zone seem to be the only possible causes for the absence of *PS*-reflections. Since the variation of the Poisson's ratio would require a substantial partial melting immediately below the crust-mantle boundary, the author tends to explain the absence of *PS*-reflections by the existence of a transition zone. It must be concluded that the transition zone at the crust-mantle boundary must have a thickness of more than 1 km. From this study a search for *PS*-reflections on crustal record sections is recommended.

Acknowledgements. The author is indebted to Drs. G. Müller and C. Prodehl for many fruitful discussions and kindly reading the manuscript and to Dr. K.-O. Millahn for help in the computation. This work is sponsored by the Deutsche Forschungsgemeinschaft. Computing facilities were made available by the computer center of Karlsruhe University.

References

Berry, M.J., Fuchs, K.: Crustal structure of the Superior and Greenville provinces of the northeastern Canadian shield. Bull. Seism. Soc. Am. **63**, 1393–1432 (1973)

Červený, V.: The amplitude curves of reflected harmonic waves around the critical point. Studia geophys. geodaet. **5**, 319–351 (1961)

Fuchs, K.: Das Reflexions- und Transmissionsvermögen eines geschichteten Mediums mit beliebiger Tiefen-Verteilung der elastischen Moduln und der Dichte für schrägen Einfall ebener Wellen. Z. Geophys. **34**, 389–413 (1968a)

Fuchs, K.: The reflection of spherical waves from transition zones with arbitrary depth-dependent elastic moduli and density. J. Phys. Earth **16**, (Special Issue), 27–41 (1968b)

Fuchs, K., Müller, G.: Computation of synthetic seismograms with the reflectivity method and comparison with observations. Geophys. J.R.A.S. **23**, 417–433 (1971)

Kaminski, W., Fuchs, K., Menzel, H.: Crustal investigations along a seismic refraction line from the Harz mountains to the Alps, Paper IASPEI-166, presented at the 14th General Assembly IUGG, Zürich, 1967

Müller, G.: Theoretical seismograms for some types of pointsources in layered media, Part I: Theory. Z. Geophys. **34**, 15–35 (1968a)

Müller, G.: Theoretical seismograms for some types of pointsources in layered media, Part II: Numerical calculations. Z. Geophys. **34**, 147–162 (1968b)

Müller, G.: Exact ray theory and its application to the reflection of elastic waves from vertically inhomogeneous media. Geophys. J.R.A.S. **21**, 261–283 (1970)

Müller, S., Prodehl, C., Mendes, H.S., Moreira, V.S.: Crustal structure in the southwestern part of the Iberian peninsula. Tectonophysics **20**, 307–318 (1973)

Prof. Dr. K. Fuchs
Geophysikalisches Institut der Universität
D-7500 Karlsruhe-West
Hertzstraße 16
Federal Republic of Germany

Received March 17, 1975

J. Geophys. 41, 463–474, 1975

Explosions in Shallow Water for Deep Seismic Sounding Experiments

H. Burkhardt and R. Vees

Institut für Geophysik der Technischen Universität Clausthal

Abstract. The basic importance of underwater explosions as efficient seismic sources is due to secondary source effects, i.e. gas bubble pulsation and signal reverberation within the water, and optimum shot conditions can be defined for the case of constructive interference of both effects. In shallow water, where secondary source effect conditions are not satisfied, seismic signals are determined by the low-frequency part of the primary source signal. For very small shot depths the observed seismic signal reduction can be avoided by the use of distributed charges, which is shown to be a general means to increase the seismic source efficiency. General conditions of shot planning for deep seismic sounding experiments in deep, medium and shallow water are given, together with several examples, showing the applicability of explosions in shallow water for seismic purposes.

Key words: Underwater explosions – Deep seismic sounding – Effective shot conditions.

1. Introduction

One of the main problems of deep seismic sounding experiments is the generation of suitable seismic signals. For technical, financial and seismic reasons underwater explosions are normally preferred to underground explosions. Some advantages are: better practicability, no drilling, possibility of signal manipulation, better seismic efficiency, smaller risk of direct damages and reproducibility.

On the other hand, there is not everywhere suitable water available for this purpose or, sometimes, there are only small and shallow lakes and rivers in the region of interest. So the question arises about the necessary conditions for such waters to be suitable for efficient seismic signal generation.

With underwater explosions a general scheme for the shot-planning procedure of deep seismic sounding experiments may be compiled as shown in Fig. 1.

2. Optimum Source Conditions

It is a wellknown fact in explosion seismology, verified by theoretical calculations as well as by experimental data, that the basic importance of underwater explosions

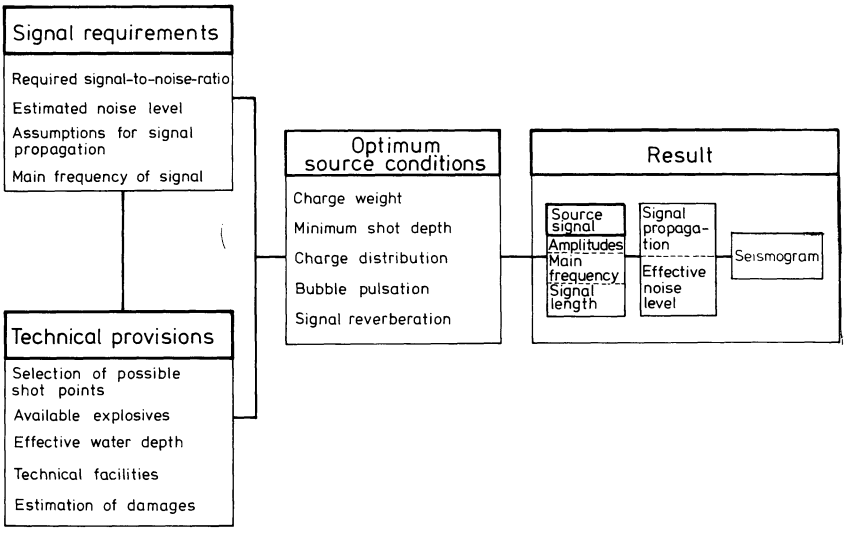

Fig. 1. Scheme for the planning procedure with underwater explosions

for seismic purposes, characterized by the relatively good efficiency in the low-frequency band of seismic signals, is mainly due to secondary source effects: gas bubble pulsation and signal reverberation within the water.[1] With these two effects it is possible, by appropriate choice of explosion conditions, to increase the seismically interesting low-frequency amplitudes of the source spectrum considerably. Further seismic signal enhancement is achieved with source conditions where constructive interference between the two effects occurs, determined by the equality of bubble pulse period and the appropriate reverberation period in the range of seismic periods; these conditions are sometimes referred to as optimum ones (*e.g.* Fuchs *et al.*, 1972; Wielandt, 1972).

Therefore, the first objective of every shot planning has to be the investigation, whether or not these optimum source conditions are possible.

The period T_B of the first bubble pulsation is given by

$$T_B = CW^{1/3}/(h+10)^{5/6} \qquad \begin{array}{l} W = \text{charge weight} \\ h = \text{shot depth} \end{array}$$

with $C \approx 2.1$ [s m$^{5/6}$ kg$^{-1/3}$] for TNT and similar explosives (Cole, 1948).

In some cases multiple bubble pulsations have to be taken into account too, with period variations due to energy radiation and vertical displacement of the pulsating gas bubble (Burkhardt, 1964). Mostly, however, it is only the first pulsation, which contributes significantly to the seismic source signal.

[1] A third secondary effect of underwater explosions in bounded media such as lakes in homogeneous surroundings is the frequently observed occurrence of resonance effects within the further surroundings of the source. This effect is also observed with some underground explosions (Burkhardt and Vees, 1974b). It should be mentioned, that even neglecting the secondary effects, underwater explosions are still more effective for seismic signal generation than underground explosions in rocks, due to the different shear strength of the surrounding medium (Wielandt, 1972).

The effective reverberation period depends on the geometry of existing boundaries, such as water surface, sea bottom, lateral boundaries, on the boundary conditions and on the location of the source with respect to the boundaries.

For suspended charges in deep water with shot depth h smaller than water depth H, *e.g.* for underwater explosions at sea with no contributing lateral boundaries, there are two periods due to surface reflections

$T_{h_n} = 4h/(2n-1)\,c_w$ (surface-source reflection)

and

$T_{H_n} = 4H/(2n-1)\,c_w$ (surface-ground reverberation)

$n = 1, 2, \ldots;$

c_w = velocity of compression wave in water.

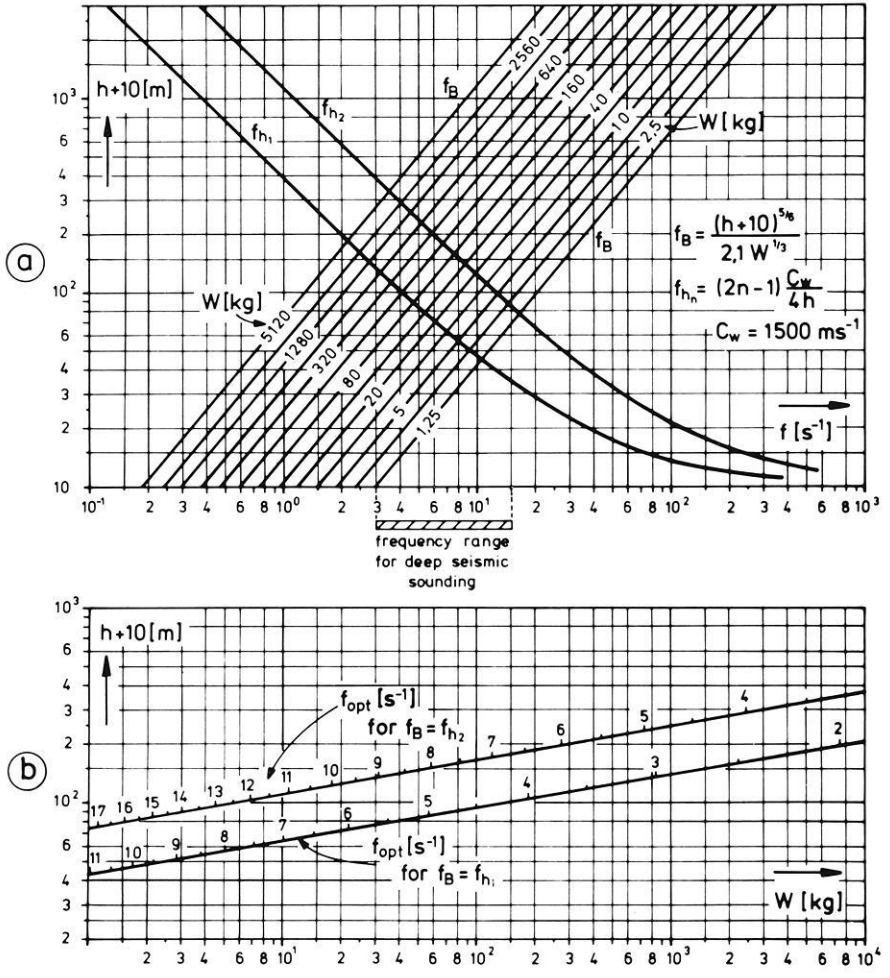

Fig. 2a and b. Optimal source conditions for underwater explosions. (a) Bubble pulse frequency f_B with parameter charge weight W, fundamental frequency f_{h_1} of surface reverberation and its first harmonic f_{h_2} as a function of shot depth h. (b) Optimal frequency f_{opt} as a function of charge weight W and shot depth h for the frequencies f_{h_1} and f_{h_2}

Then, optimal seismic source conditions occur, when

$$T_B = T_{h_n} \quad \text{or} \quad T_B = T_{H_n},$$

giving constructive interference between bubble pulse period and surface reverberation period, with n equal 1 or 2 or sometimes even 3 (Bancroft, 1966).

The only factors involved are charge weight W and shot depth h or water depth H, respectively.

The relationship between bubble pulse frequency $f_B = 1/T_B$, fundamental frequency $f_{h_1} = 1/T_{h_1}$, its first harmonic f_{h_2}, charge weight W and shot depth h is shown in Fig. 2a. The points of intersections of the two families of curves mark the optimum seismic source conditions, indicating the achievable range of appropriate pairs of charge weight and shot depth.

Fig. 2b shows the resulting optimum frequency f_{opt} as a function of shot depth and charge weight in the seismic range. With charges ranging from 1 to 10^4 kg, optimum shot depths vary between 35 m and 350 m and optimum frequencies between 17 Hz and 2 Hz for $n = 1$ and 2.

So, except for explosions at sea with sufficient water depths, optimum source conditions are normally not possible for underwater explosions in shallow water, e.g. lakes, rivers etc., which are frequently used as seismic sources for crustal investigations. In these cases underwater explosions may still be superior to underground explosions, provided that careful consideration is given to the various other factors which can influence the seismic source efficiency (see footnote p. 464). Remembering the fact, that an important contribution to the low-frequency part of the source spectrum comes from the secondary effects, the separate contributions of bubble pulsation and surface reflections have to be investigated in the frequency range for deep seismic sounding, 3 to 15 Hz approx. (Fig. 2a).

For the bubble pulsation the minimum shot depth is ca. 25 m ($W = 30$ kg, $f = 3$ Hz), this depth increasing with increasing charge weight and increasing frequency.

For the surface-source reflections there is the same minimum shot depth ($f_{h_1} = 15$ Hz) with frequency decreasing for increasing depth. The same is true for the surface-ground reverberation with regard to the water depth.

3. Explosions in Shallow Water

(a) No-Bubble Pulse Condition

If the available shot depth is smaller than this minimum depth, the secondary effects no longer improve the seismic signal, they may even tend to disturb the seismogram. In this case, in order to prevent the gas bubble from pulsating, the shot depth must be smaller than a critical depth h_c, resulting in a blowout of the bubble.

A reasonable estimation of this critical depth is given by the condition, that h_c must be equal to the maximum radius a_m of the spherical bubble during pulsation.

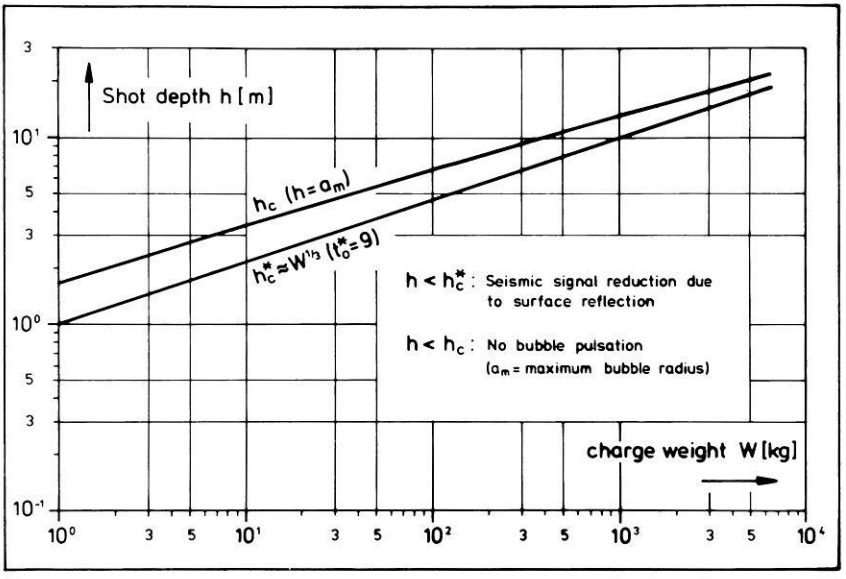

Fig. 3. Critical shot depths h_c and h_c^* for underwater explosions

In good approximation a_m is given by

$$a_m = 3.7(W/(h+10))^{1/3} \text{ [m]} \qquad W = \text{charge weight [kg]}, \quad h = \text{shot depth [m]}$$

neglecting bubble migration and boundary effects (Cole, 1948).

So, with freely suspended charges in shot depths $h < h_c = a_m$ there are no bubble pulses and the resulting seismic signals are determined only by the primary source signal (Fig. 3).

For explosions on the bottom in shallow water additional boundary forces are acting and influence the bubble expansion. In these cases the above no-bubble-condition is necessarily only a rough estimation.

(b) Minimum Shot Depth

For shallow water explosions, experiments show an influence of shot depth on seismic amplitudes, with amplitudes rapidly decreasing with the charge approaching the surface. This points out, that the main cause for this amplitude reduction is a surface effect. Due to the large pressure amplitudes, associated with an underwater explosion, the boundary conditions at the free surface will be very complicated with non-linear effects such as e.g. cavitation and spray dome. Besides these effects there is a cut-off effect for the radiated pressure wave due to the surface reflection, with the reasonable assumption, that normal water cannot sustain any tensional forces (Cole, 1948). For the primary positive pressure wave, which can be approximated by an exponentially decaying time function with a charge dependent time constant (for quantitative results with small explosives, *see* Keller,

1970), this cut-off effect leads to a reduction of the corresponding low-frequency spectral amplitudes.

Now, the distant seismic signals (e.g. particle velocity) depend on the low-frequency part of the pressure field in the water. So, a reduction of the low-frequency spectral amplitudes of the pressure wave will also lead to a reduction of the resulting seismic amplitudes.

As a minimum condition for effective seismic radiation of an underwater explosion source we require, that the cut-off effect of surface reflection must not occur before the decay of the primary pressure wave.

With

$$t_0^* = 2h/\Theta c_w \approx 9\, h/W^{1/3}$$

(h in metres, W in kg, Θ = time constant of exponentially decaying pressure wave) the minimum condition is given by the requirement, that the delay $2h/c_w$ of the surface reflection must be appreciably larger than the time constant Θ of the pressure wave, i.e. $t_0^* \gg 1$. This yields a charge dependent critical minimum shot depth h_c^*, with seismic amplitudes rapidly decreasing with smaller depths (Fig. 3).

The numerical value for t_0^* in Fig. 3 has been chosen in order to give approximate agreement with experimental evidence during the Afar experiments, where distributed charges of 20 to 60 kg in water depths of 3 metres yielded satisfactory seismic long range signals (see Fig. 6).

The rather large value for t_0^* indicates, that the cut-off effect is not the only factor involved in reducing seismic amplitudes, but that the above mentioned surface effects have to be taken into account too.

Therefore, due to its approximate nature, this condition does not necessarily mean, that seismic signals would not further increase with increasing shot depth but only determines a minimum condition, which must be satisfied for efficient seismic signal generation.

(c) Distributed Charges

For deep seismic sounding experiments with explosion generated signals the necessary charge weights are, according to experiences, in the order of several hundreds of kilograms. So, for shallow water conditions, the total charge weight has to be divided in such a way, that every single charge is fully effective in the above mentioned sense.

Furthermore, in contrast to explosions with concentrated charges, where, neglecting secondary source- and lateral boundary-effects, seismic amplitudes scale with (charge weight)$^{2/3}$, approximately (Burkhardt, 1964; Vees, 1965), we have different scaling laws for distributed charges. It is known from shockwave measurements, that in the range of linear acoustical behaviour of the pressure wave, i.e. for distances r with $r > r_x \approx 20\, kW^{1/3}$ approximately, ($k \approx 5 \cdot 10^{-2}\,\mathrm{m\,kg^{-1/3}}$) (Cole, 1948), the resulting pressure field from distributed charges is the sum of all contributing single charge pressures.

Let $W_\Sigma = n\, W_s$, where W_s = weight of single charge, n = number of charges with weight W_s. W_Σ = total charge weight.

Then the spectral amplitudes of the resulting pressure wave in the range of seismic frequencies are scaling with charge weight as

$$|P(\omega)|_n \sim n W_s^{2/3}$$

ω = frequency

provided that the distances Δx between the charges are complying with the condition

$$\Delta x \geqq 2 r_x \approx 2 W_s^{1/3}$$

(W_s in kg, Δx in metres).

In order that the gas bubbles from single charges are pulsating with a period, determined by W_s, the necessary minimum distance between the charges must be

$$\Delta x_B \gg 2 a_m \approx 7.4 \, (W_s/(h+10))^{1/3};$$

(W_s in kg, Δx_B and h in meteres),

which gives

$$\delta = \frac{\Delta x}{\Delta x_B} = \frac{(h+10)^{1/3}}{3.7} \lessapprox 1 \quad \text{for } h \lessapprox 40 \text{ [m]}.$$

For W_s = const we have

$$|P(\omega)|_n \sim n \quad \text{or} \quad |P(\omega)|_n \sim W_\Sigma^1.$$

For W_Σ = const we have for the ratio of spectral amplitudes of concentrated charges with

$$|P(\omega)|_c \sim (n W_s)^{2/3}$$

and distributed charges, the result

$$\frac{|P(\omega)|_n}{|P(\omega)|_c} = n^{1/3}$$

yielding an increasing amplitude with increasing distribution of the charge W_Σ.

If

$$W_{\Sigma_1} = n_1 W_{s_1} \quad \text{and} \quad W_{\Sigma_2} = n_2 W_{s_2},$$

the ratio of resulting spectral amplitudes is given by

$$\frac{|P(\omega)|_{n_1}}{|P(\omega)|_{n_2}} = \frac{n_1}{n_2} \left(\frac{W_{s_1}}{W_{s_2}} \right)^{2/3}.$$

Experimental verifications (within 10% approx.) of these relationships have been achieved with controlled investigations during deep seismic sounding experiments in various regions, *e.g.* Lago Bianco-experiments in the Alps (Vees, 1965) and Afar-experiments (Burkhardt and Vees, 1974a) where explosions with distributed charges were carried out in shallow lakes and rivers in shot depths as small as 2 to 3 meters and where effects from lateral boundaries were small.

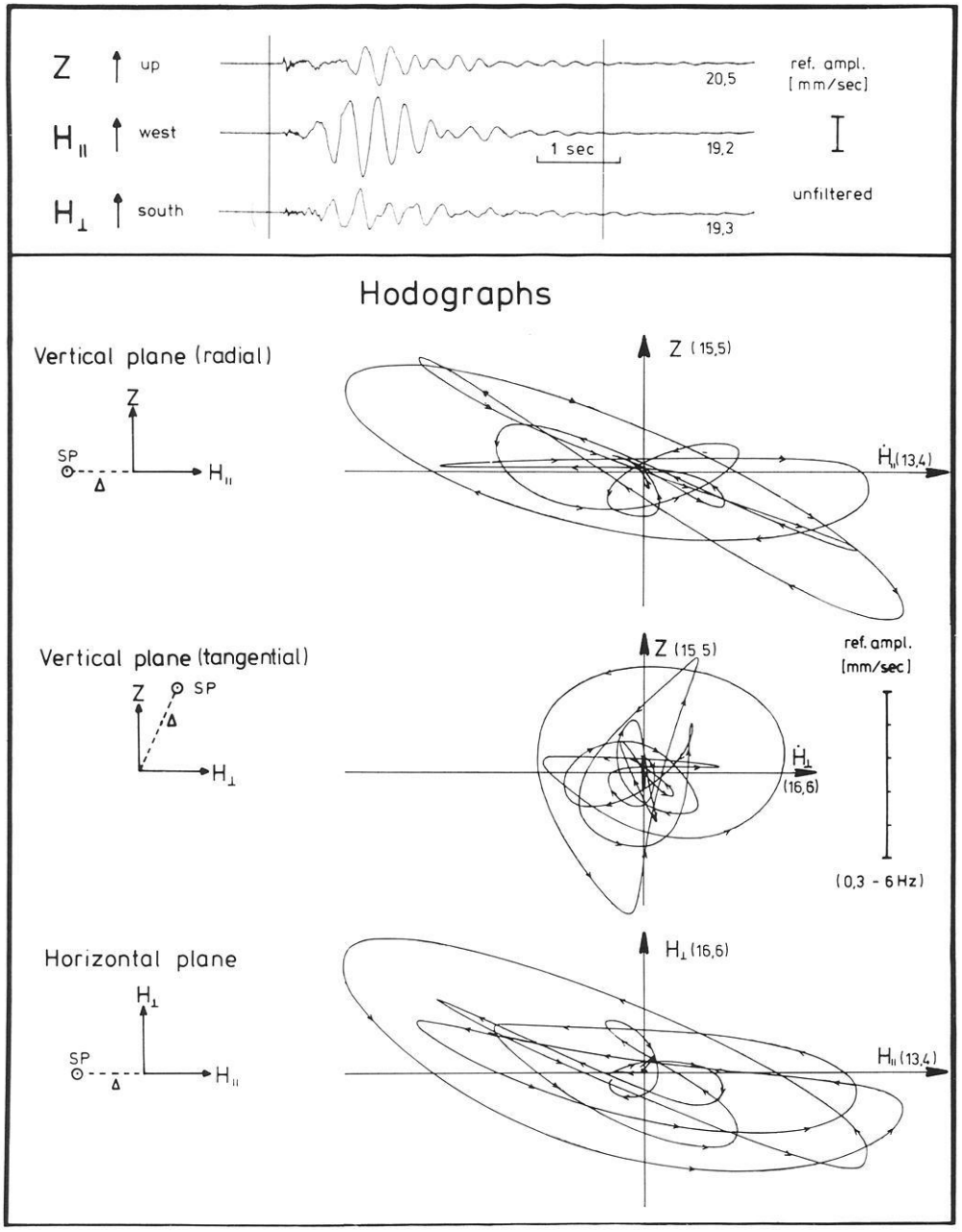

Fig. 4. Three-component seismic measurements (velocity transducer) near the source for shot point Green Lake/Ethiopia. Recording distance 300 m; charge weight $W = 10 \times 30$ kg; shot depth $h = 28$ m (bottom)

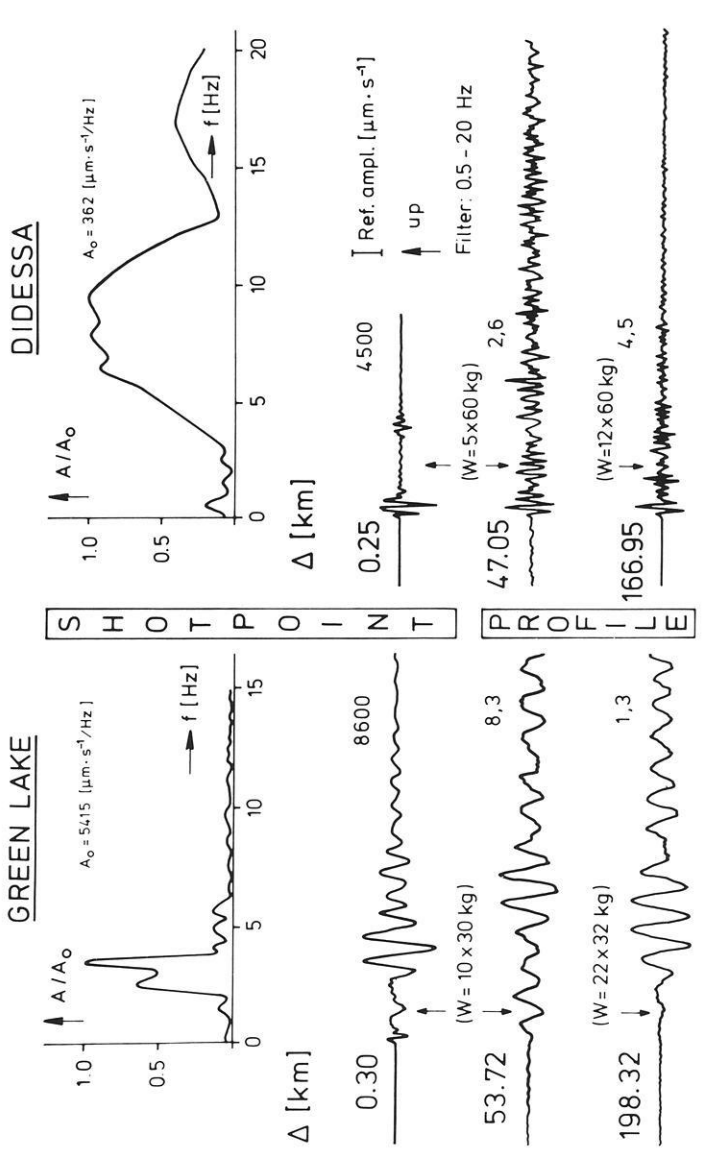

Fig. 5. Vertical components of close-by seismic records for two shot points with corresponding frequency spectra in comparison with vertical components of profile seismograms. Shot point Green Lake: see Fig. 5. Shot point Didessa: River in Ethiopia, water depth 12 metres approx. (After Burkhardt and Vees, 1947a)

4. Some Examples of Seismic Source Signals

During the deep seismic sounding experiments in the Afar region of Ethiopia in 1972 (Berckhemer, 1974; Burkhardt and Vees, 1974a) close-by seismic control measurements were carried out, which can be used as additional information for the interpretation of distant profile records.

The following examples are to demonstrate the applicability of shallow water explosions for such experiments.

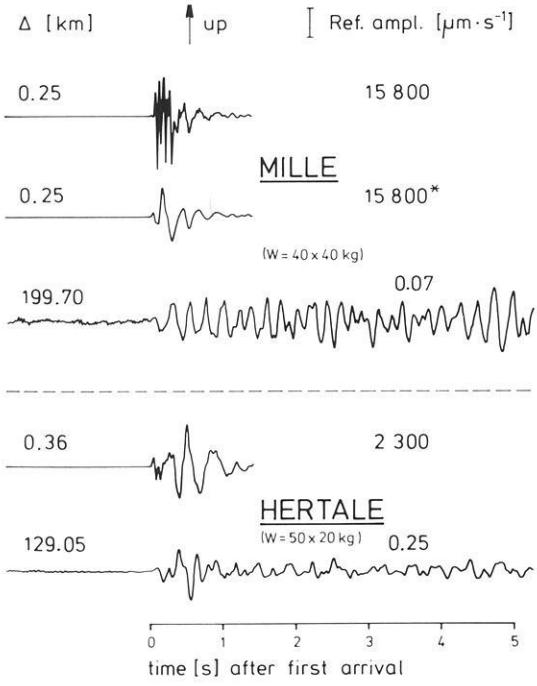

Fig. 6. Vertical components of close-by seismic records for two shot points in comparison with vertical components of profile seismograms (Afar-experiments 1972). Shot point Mille: Awash river, water depth 3 metres max. Shot point Hertale: Lake, water depth 3 metres approx. Filter settings 0.5–20 Hz. (*0.5–8 Hz)

Fig. 4 shows a three-component seismogram and the corresponding hodographs of a near-by station for the shot point Green Lake. This shot point is a crater lake in the Highlands of Ethiopia with nearly radially symmetric shape, steep side walls and a maximum depth of 25 to 28 m. The effective diameter in this depth amounts to ca. 450 m, surface diameter is approximately 800 m. The total charge weight used was divided in 10 single charges of 30 kg, which were fired on the bottom of the lake in a mutual distance of 15 m. Corresponding bubble pulse frequency of the single charges is 3.3 s^{-1}, which clearly dominates the seismograms. Due to the relative large shot depth multiple bubble pulses occur. From the hodographs it is seen, that this low-frequency part of the signal is of a radially horizontal type of motion. This fact, together with the high energy content of the signal and shape and size of the lake, led to the interpretation, that there is a constructive interference between bubble pulses and successive radial reflections within the lake with frequency $f_r = c_w/l$, where l = effective diameter of the lake. Inserting our numerical values, we get $f_r \approx 3.3\ s^{-1}$. Due to this secondary source effect we have a very effective shear-wave source with a main frequency of 3 s^{-1} (see also Fig. 5).

Figs. 5 and 6 show comparisons between close-by control seismograms and distant profile records for some shotpoints and profiles of the Afar experiments.

There is a good correspondence between respective close-by and distant signals, stressing the importance of the control measurements (Burkhardt and Vees, 1974a).

In all cases distributed charges were used because of the small available water depths. So, these examples also clearly illustrate the fact, that explosions in shallow water can be used as efficient seismic sources for long range seismic experiments, provided that the considerations given above with respect to the mechanisms of signal generation are taken into account.

5. Summary and Conclusions

1. Underwater explosions are known as efficient sources of seismic energy for deep seismic sounding experiments.

2. The basic importance of underwater explosions for seismic purposes is mainly due to secondary source effects, i.e. gas bubble pulsation and signal reverberation within the water. Optimum shot conditions occur with constructive interference of these two effects, requiring minimum water depths (35 metres approximately in the range of seismic relevant charge weights and frequencies).

3. For smaller water depths the separate contributions of the secondary source effects can be utilized to increase the seismic efficiency.

4. In shallow water conditions, where no secondary source effects occur and where the seismic signal is determined only by the low-frequency part of the primary source signal, there is a charge dependent, critical minimum shot depth due to a cut-off effect of the source signal by the surface reflection.

5. With the use of distributed charges this disadvantage can be avoided and so even explosions in shallow water can be used as efficient seismic sources. Moreover, this charge division turns out to be a general means to increase the seismic source efficiency.

6. Several examples from different experiments demonstrate the applicability of explosions in shallow water for deep seismic soundings.

Acknowledgements. The financial support of the Deutsche Forschungsgemeinschaft is gratefully acknowledged.

References

Bancroft, A.M.: Seismic spectra and detection probabilities from explosions in Lake Superior. In: The earth beneath the continents, Geophys. Monograph 10, J.S. Steinhart and T.J. Smith, ed.: pp. 234–240. Washington (D.C.): Amer. Geophys. Union, 1966

Berckhemer, H.: Deep seismic sounding in Afar and the highland of Ethiopia. In: Afar Monograph, A. Pilger, ed.: in press. Stuttgart: Schweizerbart 1974

Burkhardt, H.: Some physical aspects of seismic scaling laws for underwater explosions. Geophys. Prosp. **12**, 192–214 (1964)

Burkhardt, H., Vees, R.: The Afar 1972 seismic source signals: generation, control and comparison with profile records. In: Afar Monograph, A. Pilger, ed.: in press. Stuttgart: Schweizerbart 1974a

Burkhardt, H., Vees, R.: Seismic signals from quarry blasts. In: Results of deep seismic sounding in the Federal Republic of Germany, P. Giese, C. Prodehl and A. Stein, ed.: in press. Würzburg: Physica, 1974b

Cole, R. H.: Underwater explosions, Princeton, N.J.: Princeton University Press 1948
Fuchs, K., Hirn, A., Müller, St., Prodehl, C., Sapin, M., Steinmetz, C.: A long-range seismic profile in France from the Bretagne to the Provence. Ann. Géophys. **28**, 247–256 (1972)
Keller, F.: Druckmessungen bei Unterwassersprengungen kleiner Ladung, Clausthal: Dissertation, Technische Universität Clausthal, 1970
Vees, R.: Der seismische Impuls bei Unterwassersprengungen, Clausthal: Dissertation Bergakademie Clausthal, 1965
Wielandt, E.: Anregung seismischer Wellen durch Unterwasserexplosionen, Karlsruhe: Dissertation Universität Karlsruhe, 1972

Dr. H. Burkhardt
Dr. E. Vees
Institut für Geophysik der T. U. Clausthal
D-3392 Clausthal-Zellerfeld
Adolf-Römer-Str. 2A
Federal Republic of Germany

Received July 25, 1974; Revised Version March 24, 1975

J. Geophys. 41, 475–489, 1975

Seegangserzwungene elastische Bewegungen des Nordseebodens

P. Janle, R. Rudloff, B. Schmalfeldt und R. Szelwis

Institut für Geophysik der Universität Hamburg

Seawave-Generated Elastic Motions of the North Sea Bottom

Abstract. Simultaneously recorded time series of seawave amplitudes and of the three components of ground motion in the North Sea show high coherence in the frequency band (0.10–0.25) Hz indicating that the respective ground motion is to be interpreted as seawave-generated elastic disturbances with wavenumbers determined by the seawave dispersion relation. Source function and elastic response being known, an elastic model of the upper 30–50 meters of the North Sea ground is evaluated which is of interest in view of the little-known shear wave velocities. Directional model spectra of the elastic disturbances, identical with the directional seawave spectra, can be accounted for by the weather conditions.

Key words: Near-source elastic wave field – Transfer function – Elastic model of North Sea bottom – Directional spectrum.

Zusammenfassung. Registrierungen der Seegangsamplituden und der drei Komponenten der elatischen Bodenbewegungen in der Nordsee weisen hohe Kohärenzen im Frequenzbereich (0,10 – 0,25) Hz auf, in dem die betreffenden Bodenbewegungen durch den Seegang mitgeführte Störungen sind, deren Dispersionsverhalten durch die Seegangsdispersionsrelation bestimmt wird. Aufgrund der Kenntnis von Quellfunktion und elastischer Reaktion läßt sich ein Modell des oberen Nordseebodens bestimmen, das vor allem wegen der bisher wenig bekannten Scherwellengeschwindigkeiten von Interesse ist.
Die Richtungsspektren der elastischen Störungen, identisch mit denen des Seegangs, lassen sich gut durch die Wetterverhältnisse begründen.

I. Einleitung

Im Rahmen des „Sonderforschungsbereiches Meeresforschung“ (SFB 94), der sich mit Austauschvorgängen im System Ozean-Atmosphäre beschäftigt, steht auch die Untersuchung der seegangserzeugten Mikroseismik. Als Teil eines

Array aus seismographischen Dreikomponentenstationen, das vom Teilprojekt „Mikroseismik" im SFB 94 mit dem Ziel der Quellenidentifizierung im Ostatlantik aufgebaut wird, befindet sich eine Station auf dem Nordseegrund, etwa 30 km westlich der Insel Sylt („Meßfeld"). Im folgenden werden Auswertungen dargestellt, die aufgrund der Registrierungen dieser Dreikomponentenstation und gleichzeitiger Registrierungen des Seegangs erhalten wurden. Es erweist sich, daß ein Teil der elastischen Bodenbewegungen durch den Seegang mitgeführte Störungen sind. Diese folgen der Seegangsdispersionsrelation und liegen damit jenseits des Wellenzahl-Bereichs freier elastischer Oberflächenwellen. Sie sind also nicht als „mikroseismische Bodenunruhe" zu interpretieren, die im gleichen Frequenzbereich (ca. 0,05 – 0,25 Hz), aber mit größeren Wellenlängen auftritt und durch nichtlineare Wechselwirkung des Seegangs mit sich selbst bzw. mit dem Boden resonant angeregt wird (vgl. Hasselmann (1963)).

Bei Kenntnis der Zeitreihen des Seegangsprofils stellen sie ein Probefeld dar, mit dem ein Modell des elastischen Mediums bestimmt werden kann. Von wesentlicher Bedeutung sind Aussagen über die Scher-(*S*)Wellengeschwindigkeiten, die im Gegensatz zu den Kompressions-(*P*)Wellengeschwindigkeiten nur ungenau aus seismischen Experimenten bekannt sind.

Aus den dreikomponentigen Registrierungen der elastischen Bewegungen werden Richtungsspektralmodelle, die mit denen des Seegangs identisch sind, bestimmt und aus den Wetterverhältnissen begründet.

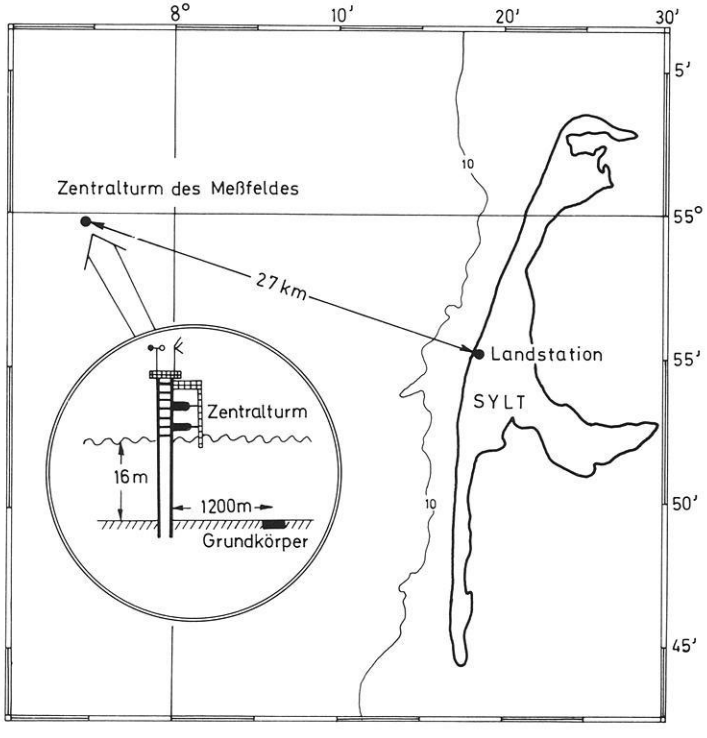

Fig. 1. Geographische Lage der Meßstation

II. Instrumentelles

Die seismischen Registrierungen im Meßfeld erfolgen durch ein Dreikomponenten-Seismometer des Typs MARK L-4-3D, das sich in kardanischer Aufhängung in einem in den Nordseeboden eingespülten Stahlgehäuse („Grundkörper") befindet. Die vorverstärkten seismischen Signale gelangen über ein Seekabel zu einem Zentralturm und werden nach Frequenzmodulation und Mischen telemetrisch zu einer Station auf der Insel übertragen und auf Magnetband aufgezeichnet (vgl. Fig. 1). Die Amplitudencharakteristik der drei registrierenden Komponenten verläuft aufgrund elektronischer Entzerrer im Bereich (0,05 – 5) Hz nahezu konstant. Die Neigung des Seismometers kann vom Zentralturm aus kontrolliert und bei Bedarf seine genaue Horizontallage wiederhergestellt werden.

III. Registrierungen

Im Oktober/November 1973 wurden an einigen Tagen gleichzeitig der Seegang und die elastischen Störungen registriert. Ein am Grundkörper befindlicher Druckmesser registrierte darüberhinaus relative Amplituden des fluktuierenden Bodendrucks. Die Registrierung der Seegangsamplituden erfolgte etwa 7 km vom Ort des Grundkörpers entfernt durch eine „Waverider-Boje". In Fig. 2 sind die Auto-(Power-)Spektren der Bodendruckvariationen und der Vertikalkomponente der elastischen Bewegungen vom 1.11.73 zusammen mit den entsprechenden Kohärenz- und Phasenspektren aufgetragen. Aufgrund der hohen Kohärenz im Frequenzbereich (0,11 – 0,23) Hz werden die elastischen Störungen überwiegend von den Bodendruckfluktuationen bestimmt. Dem Frequenzbereich entsprechen Seeganswellenlängen von ca. (110 – 30) m. Da die durchschnittliche Wassertiefe im Meßfeld etwa 20 m beträgt, handelt es sich hier um „Flachwasser". Es ist damit auch physikalisch vernünftig, die elastischen Bewegungen im hochkohärenten Bereich als seegangserzwungene Störungen des elastischen Mediums aufzufassen.

Jenseits dieses Frequenzbereichs macht dieser Anteil an den gemessenen elastischen Störungen weniger als die Hälfte aus, eine Tatsache, die sich folgendermaßen erklären läßt: Für höhere Frequenzen wirkt das Meßgebiet als „Tiefsee", d.h. der Seegang greift nicht oder nur mit schwachen Amplituden bis zum Boden durch. Für Frequenzen unterhalb des hochkohärenten Bereichs ist die Seegangsenergie gering im Vergleich zur Maximalenergie (vgl. Fig. 3). In beiden Fällen ist zu folgern, daß die freien Oberflächenwellen dominieren.

IV. Elastische Modelle

Die Berechnung der elastischen Verschiebungsgeschwindigkeiten erfolgt unter der Annahme eines Modells des elastischen Mediums, das den größten auftretenden Seegangswellenlängen entsprechend bis zu einer Tiefe von wenigen hundert Metern entscheidend ist. Es handelt sich nicht darum, ein Vielschichtenmodell zu erstellen, das den Meßergebnissen möglichst perfekt angepaßt ist, vielmehr soll die Zahl seiner Parameter überschaubar sein. Die Einbeziehung der Wasser-

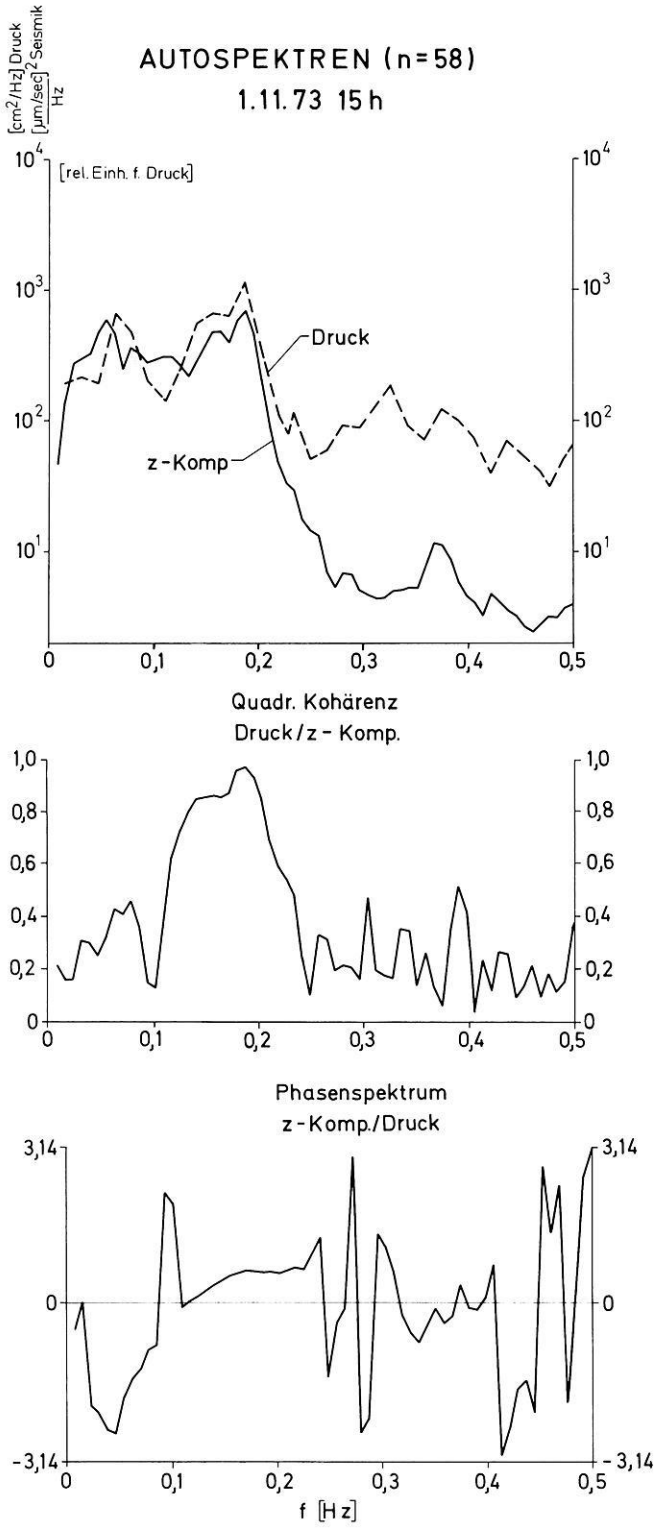

Fig. 2. Autospektren der Bodendruckfluktuationen und der Vertikalkomponente der elastischen Bodenbewegungen (oben) mit entsprechendem Kohärenz- (Mitte) und Phasenspektrum (unten) vom 1. 11. 73

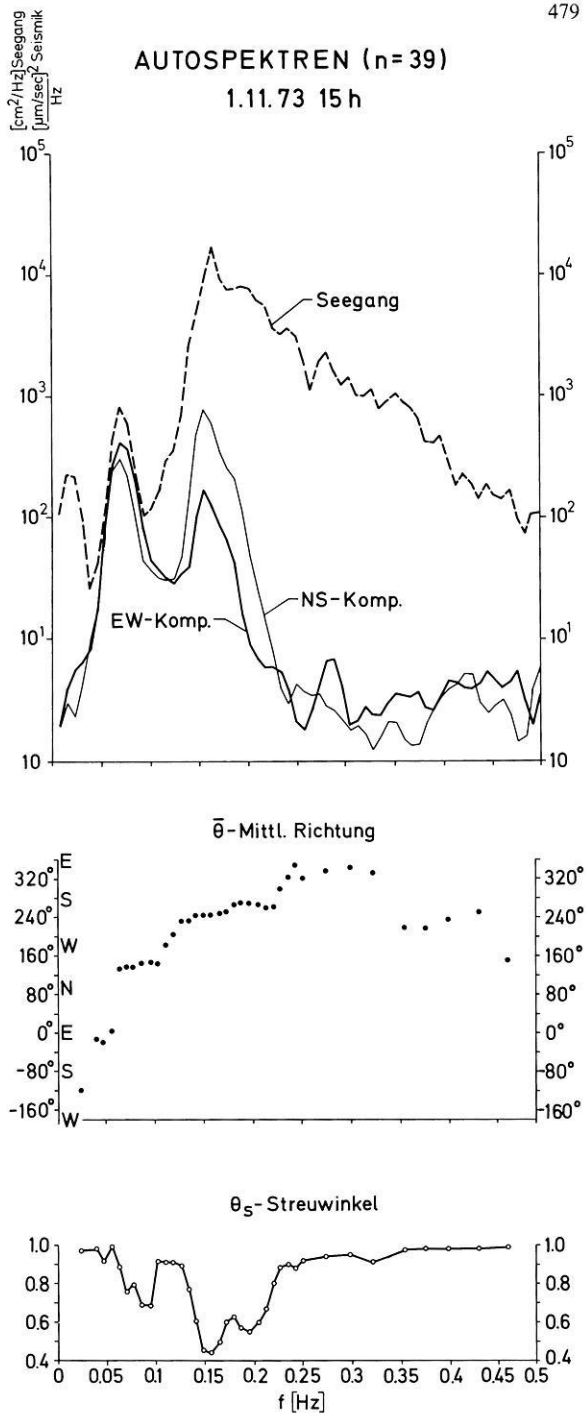

Fig. 3. Oben: Autospektren der Horizontalkomponenten der elastischen Bodenbewegung und des Seegangs. Mitte: Mittlere Einfallsrichtung des Seegangs. Unten: Dimensionslose Winkelstreubreite; für $\theta_s = \begin{pmatrix} 1 \\ 0 \end{pmatrix}$ ist die einfallende Energie $\begin{pmatrix} \text{isotrop} \\ \text{scharf gebündelt} \end{pmatrix}$

schicht über dem elastischen Medium in das Modell kann vernachlässigt werden, da die anregenden Spannungen, d.h. die Druckfluktuationen am Meeresboden, aus dem Seegang in erster Näherung als Funktion der Wassertiefe folgen.

IV. a) Das einfachste Modell stellt der homogene elastische Halbraum dar. Die freien Parameter sind die Geschwindigkeit a der P-Wellen, die der S-Wellen (b) und die Dichte ρ des Materials. In einem rechtwinklig-kartesischen Koordinatensystem mit dem Ursprung sowie der x_1- und der x_2-Achse in der ebenen Oberfläche des Halbraums ergeben sich die elastischen Verschiebungen durch Lösung der Wellengleichungen für das Kompressionspotential $\phi = \phi(\underline{\mathbf{x}}, t)$ und das Scherpotential $\underline{\psi} = \underline{\psi}(\underline{\mathbf{x}}, t)$ zusammen mit den Randbedingungen

$$\sigma_{3j} = -\tilde{p}\,\delta_{j3}, \quad j = 1, 2, 3 \quad \text{für } x_3 = 0$$

in der Form $\underline{\mathbf{u}} = \operatorname{grad}\phi + \operatorname{rot}\underline{\psi}$ (vgl. z.B. Ewing, Jardetzky und Press (1957, S, 8)). Hier sind $\sigma_{ij} = \sigma_{ij}(\underline{\mathbf{x}}, t)$ die Komponenten des Spannungstensors und $\tilde{p} = \tilde{p}(\mathbf{x}, t)$ die (vorgegebenen) Druckfluktuationen. Die dreidimensionalen Vektoren sind hier unterstrichen im Unterschied zu den Horizontalvektoren.

Nimmt man das Seegangsprofil ζ als Überlagerung ebener monochromatischer Wellen an, dann ergibt sich für die Druckfluktuationen am Meeresboden nach der linearen Seegangstheorie (vgl. z.B. Neumann *et al.*, 1966)

$$\tilde{p}(\mathbf{x}, t) = \sum_{\mathbf{k},\omega} \frac{\rho_0 g}{\cosh(k h)}\, a(\omega, \mathbf{k}) \exp[i(\mathbf{k}\,\mathbf{x} - \omega t)], \quad (x_3 = 0) \tag{1}$$

mit $\mathbf{x} = (x_1, x_2)$, $\mathbf{k} = (k_1, k_2)$, $k = |\mathbf{k}|$, $a(\omega, \mathbf{k}) =$ Spektralamplitude der Meereswellen, $h =$ Wassertiefe, $\rho_0 =$ Dichte des Wassers.

Die Beziehung zwischen k und ω wird durch die Dispersionsrelation

$$\omega^2 = g k \tanh(k h)$$

gegeben.

Mit entsprechend lautenden Ansätzen für die Potentiale ϕ und $\underline{\psi}$ folgt der Vektor der Verschiebungsgeschwindigkeit an der Oberfläche des elastischen Halbraums:

$$\underline{\mathbf{v}}(x_3 = 0) = \sum_{\mathbf{k},\omega} \frac{\rho_0 g}{\cosh(k h)} \frac{\omega\, a(\omega, \mathbf{k})}{\rho b^2 F(\omega^2, k^2)} \left\{ k_1 \left(2k^2 - \frac{\omega^2}{b^2} - 2 v v' \right), k_2(\ldots), -i v \frac{\omega^2}{b^2} \right\}$$
$$\cdot \exp[i(\mathbf{k}\,\mathbf{x} - \omega t)] \tag{2}$$

mit

$$F(\omega^2, k^2) = \left(2k^2 - \frac{\omega^2}{b^2} \right)^2 - 4k^2 v v'$$

wo

$$v = \left(k^2 - \frac{\omega^2}{a^2} \right)^{\frac{1}{2}}, \qquad v' = \left(k^2 - \frac{\omega^2}{b^2} \right)^{\frac{1}{2}}.$$

Die Wellenzahlen und damit die Ausbreitungsgeschwindigkeiten der elastischen Störungen und der Meereswellen stimmen überein. Wegen $k \gg \omega/b$, ω/a gibt es keine freien seismischen Oberflächenwellen, vielmehr handelt es sich um eine durch den Seegang erzwungene, mitgeführte Bewegung des elastischen Untergrundes. Die Amplitude der Verschiebungsgeschwindigkeit nimmt mit der Tiefe proportional zu $\exp(-k x_3)$ ab.

Um einen Vergleich mit den nach statistischen Verfahren spektralanalysierten Zeitreihen zu haben, werden die Kreuzspektren zwischen den Komponenten der elastischen Verschiebungsgeschwindigkeit berechnet. Schreibt man abkürzend

$$v_j(\mathbf{x}, t) = \sum_{\mathbf{k}, \omega} T_p T_j(\omega, \mathbf{k})\, a(\omega, \mathbf{k}) \exp[i(\mathbf{k}\mathbf{x} - \omega t)]$$

mit

$$T_p = \frac{\rho_0 g}{\cosh(kh)} \quad \text{(vgl. (1))},$$

dann lassen sie sich wie folgt in integraler Form darstellen:

$$S_{jk}(\mathbf{x}, \omega) = |S_{jk}| \exp(i\vartheta_{jk}) = \int_0^{2\pi} L_{jk}(\omega, \theta)\, S_\zeta(\omega, \theta)\, d\theta \tag{3}$$

mit $L_{ij} = T_p^2\, T_i^*\, T_j$, $\theta = \arctan(k_2/k_1)$, $S_\zeta =$ Seegangsrichtungsspektrum.

Für ein eng gebündeltes Richtungsspektrum: $S_\zeta(\omega, \theta) \approx S(\omega)\, \delta(\theta - \bar{\theta})$ folgt insbesondere

$$T_p(\omega)|T_i(\omega)| \approx \left[\frac{S_{ii}(\omega)}{S(\omega)}\right]^{\frac{1}{2}} \tag{4}$$

$$\vartheta_{ij}(\omega) \approx \arctan\left[\frac{\mathrm{Im}(L_{ij})}{\mathrm{Re}(L_{ij})}\right],$$

Beziehungen, die also gelten, falls die Fourierkomponenten des Seegangs aus wohldefinierten Richtungen eintreffen. Die Größen T_p, T_i sind die Übertragungsfunktionen (engl.: transfer functions) der Wasserschicht bzw. des elastischen Halbraums. Eine Abschätzung mit Hilfe der Näherungen

$$v \approx k\left(1 - \frac{\omega^2/a^2}{2k^2}\right), \qquad v' \approx k\left(1 - \frac{\omega^2/b^2}{2k^2}\right)$$

ergibt:

$$\frac{|T_3|}{\sqrt{T_1^2 + T_2^2}} \approx \frac{a^2}{b^2}.$$

Der Quotient der aus den Registrierungen mehrerer Tage bestimmten mittleren Übertragungsfunktionen im (hochkohärenten) Frequenzbereich (0,11 – 0,23) Hz beträgt $1{,}4 \pm 0{,}3$. Dieses Ergebnis läßt sich nicht mit dem Modell des homogenen Halbraums vereinbaren, denn einem Wert $a^2/b^2 < 2$ entspräche eine negative Poissonkonstante. Zur Illustration des Sachverhalts sind in Fig. 4 mit $a = 1{,}8$ km/s als P-Wellengeschwindigkeit, die aufgrund refraktionsseismischer Untersuchungen (Essen *et al.*, 1973) für den oberflächennahen Bereich des Nordseebodens gut bekannt ist, die Modellfunktionen $T_p|T_3|$ und $T_p(T_1^2 + T_2^2)^{\frac{1}{2}}$ für festes $f_0 = 0{,}15$ Hz (entsprechend $\lambda \approx 65$ m) in Abhängigkeit von der Scherwellengeschwindigkeit b des elastischen Halbraums aufgetragen. Demnach würden sich aus den „gemessenen" mittleren Übertragungsfunktionen der Horizontalkomponenten einerseits und der Vertikalkomponenten andererseits S-Wellengeschwindigkeiten ergeben, die sich etwa um den Faktor 10 unterscheiden. (In jedem Fall liegt die Geschwindigkeit aber außerhalb der Resonanzstelle, die durch die Wurzel der Rayleighfunktion bestimmt wird.)

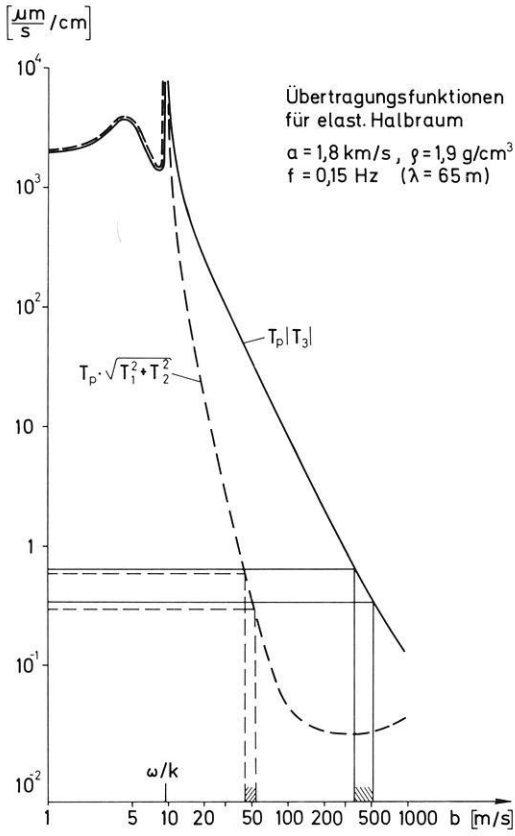

Fig. 4. Übertragungsfunktionen des homogenen elastischen Halbraums in Abhängigkeit von der Scherwellengeschwindigkeit. Der Bereich der „gemessenen" Übertragungsfunktion in einer Umgebung von $f = 0{,}15$ Hz wird durch die gestrichelten bzw. durchgezogenen Geraden gekennzeichnet

Ursache für den Unterschied könnten Abweichungen von der linearen Seegangstheorie sein: Der Ansatz (1) impliziert, daß die Vertikalverschiebung des Seegangs am Meeresboden verschwindet. Nimmt man demgegenüber an, daß der Seegang durch die Oberfläche hindurchgreift, dann ergeben sich elastische Verschiebungen in der Größenordnung der gemessenen nur für Durchgrifftiefen von einigen Millimetern. Man kann diese unrealistische Annahme ausschließen und folgern, daß unter den geltenden Voraussetzungen über den Anregungsmechanismus das Modell des homogenen Halbraums eine schlechte Näherung für den Nordseeboden darstellt.

IV. b) Das elastische Modell einer Schicht über einem Halbraum läßt sich in naheliegender Erweiterung der Beziehungen für das oben betrachtete Modell behandeln. Mit den Bezeichnungen von Ewig, Jardetzky und Press (1957, S. 189, (4−190)) folgt für die Übertragungsfunktionen: ($|T| = \sqrt{T_1^2 + T_2^2}$)

$$T_p|T| = |\omega k(A+B) - i\omega v_1'(C-D)|$$

$$T_p|T_3| = |i\omega v_1(A-B) + \omega k(C+D)|,$$

wo A, B, C, D Lösungen eines inhomogenen Systems von 6 lin. Gleichungen sind.

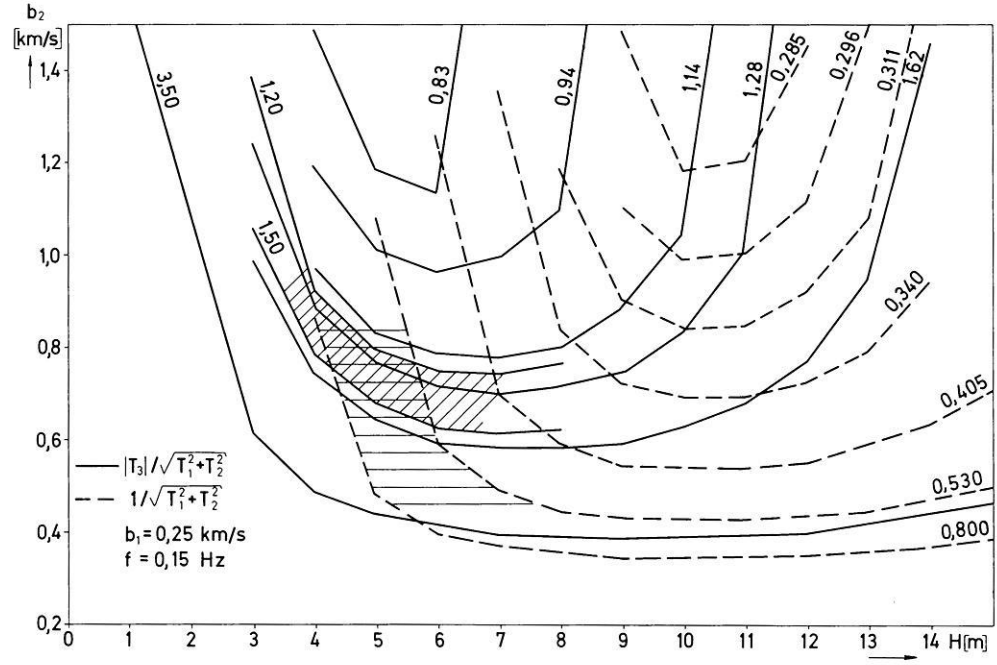

Fig. 5. Modellfunktionen $|T_3|/T$ und $1/T$ mit $T=\sqrt{T_1^2+T_2^2}$ für Zweischichtenmodell mit

$$\left.\begin{aligned} a_1&=1{,}7\\ a_2&=1{,}9\\ b_1&=0{,}25 \end{aligned}\right\}\ \text{km/s},\qquad \left.\begin{aligned} \rho_1&=1{,}9\\ \rho_2&=2{,}0 \end{aligned}\right\}\ \text{g/cm}^3$$

und variablen Parametern b_2 und H (Dicke der Deckschicht) für $f=0{,}15$ Hz. Die durch Messung ermittelten entsprechenden Größen in einer Umgebung von $f=0{,}15$ Hz liegen in den schraffiert gezeichneten Bereichen

Zur Anpassung der Modelldaten an die Meßdaten stehen 7 freie Parameter: a_i, b_i, ρ_i, $i=1,2$ und H (Dicke der Deckschicht) zur Verfügung. Aufgrund von Ergebnissen refraktionsseismischer Messungen wird von folgenden Werten ausgegangen:

$$\left.\begin{aligned} a_1&=1{,}7\\ a_2&=1{,}9 \end{aligned}\right\}\ \text{km/s},\qquad \left.\begin{aligned} \rho_1&=1{,}9\\ \rho_2&=2{,}0 \end{aligned}\right\}\ \text{g/cm}^3.$$

Die gemessenen Scherwellengeschwindigkeiten reichen von ca. 0,1 km/s (Schirmer, müdl. Mitteilung) bis ca. 1 km/s. Unter der Annahme: $b_1=0{,}25$ km/s sind in Fig. 5 die Modellfunktionen $|T_3/T|$ und $|1/T|$ für $f_0=0{,}15$ Hz in Abhängigkeit von H und b_2 aufgetragen. Da die „gemessenen" Übertragungsfunktionen in einer Umgebung von f_0 etwa $1{,}2\lesssim|T_3/T|\lesssim 1{,}5$ und $0{,}6\lesssim|1/T|\lesssim 0{,}8$ (entsprechende Einheiten) betragen, definiert die Schnittfläche beider Schwankungsbereiche (kreuz-schraffiert) einen groben Schätzwert des Modellraums:

$$\{b_1\approx 0{,}25\ \text{km/s},\ 0{,}6\lesssim b_2\lesssim 0{,}9\ [\text{km/s}],\ 4\lesssim H\lesssim 6\ [\text{m}]\}.$$

Durch Variation dieser drei Parameter wurde das den „gemessenen" mittleren Übertragungsfunktionen im hochkohärenten Frequenzbereich bestangepaßte

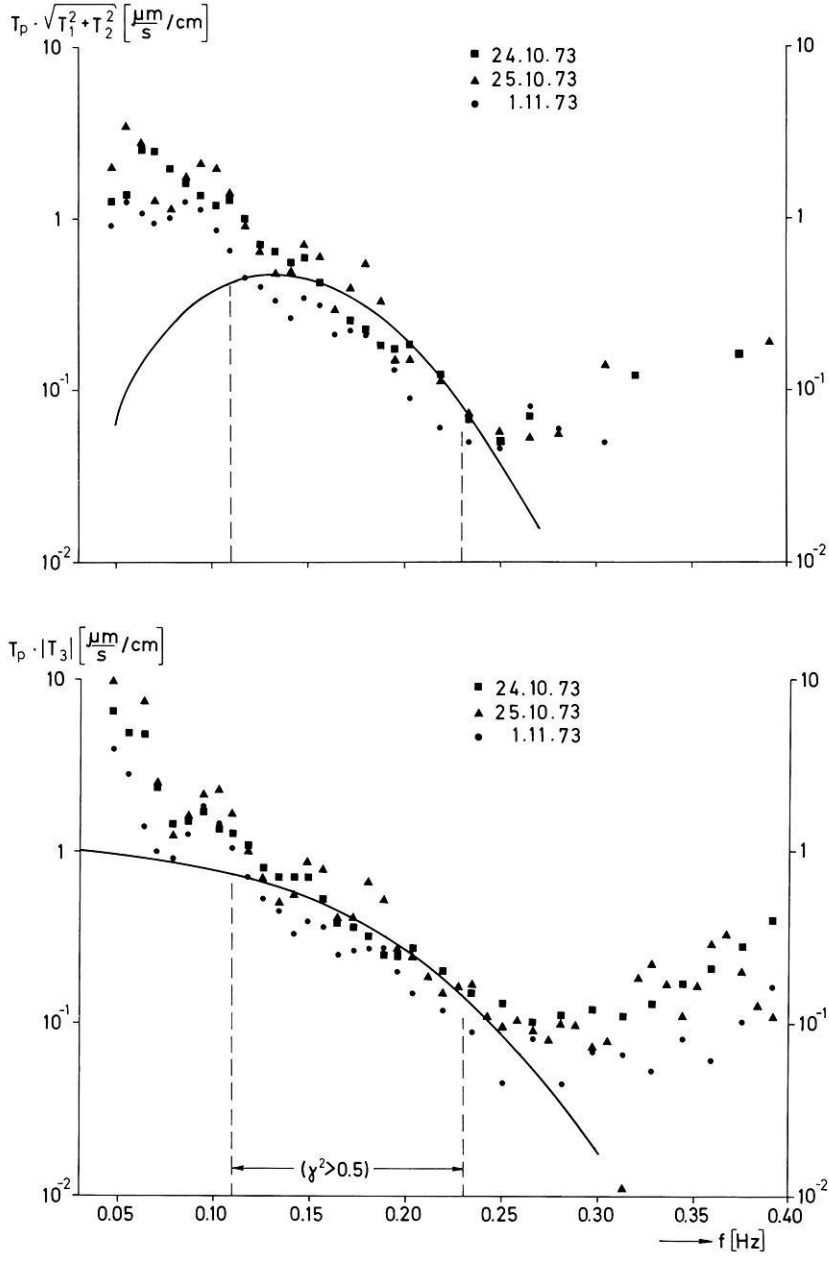

Fig. 6. Übertragungsfunktionen aus den Messungen dreier Tage (diskrete Werte) und Übertragungsfunktionen für 2-Schichten-Modell mit

$$\left.\begin{matrix} b_1 = 0{,}2 \\ b_2 = 0{,}6 \end{matrix}\right\} \text{km/s},\ H = 6\ \text{m}$$

(durchgezogene Linien). Die vertikalen, gestrichelten Geraden begrenzen den Frequenzbereich, in dem die quadrat. Kohärenz zwischen Bodenbewegungen und Bodendruckvariationen größer als 0,5 ist

Modell bestimmt (vgl. Fig. 6):

$$\left.\begin{aligned} b_1 &= 0{,}2 \\ b_2 &= 0{,}6 \end{aligned}\right\} \text{km/s}, \qquad H = 6\ \text{m}. \tag{5}$$

Eine Abschätzung der Sicherheit dieser Werte ergibt sich ebenfalls aus Fig. 5, da man voraussetzen kann, daß die Empfindlichkeit des Modells gegen Variationen von b_1 und b_2 vergleichbar ist. Die Phasenspektren zwischen den Druckfluktuationen ($\tilde{p}$) und der Vertikalkomponente (v_3) sowie zwischen den einzelnen Komponenten: v_1 (EW-Komp.), v_2 (NS-Komp.), v_3 lauten nach (4):

$$\left.\begin{aligned} \vartheta_{\tilde{p}3} &= \tfrac{\pi}{2} \\ \vartheta_{12} &= 0 \\ \vartheta_{13} = \vartheta_{23} &= \tfrac{\pi}{2} \end{aligned}\right\} 0{,}04 \leqq f \leqq 0{,}40\ [\text{Hz}].$$

Die gemessenen Phasenspektren stimmen damit im hochkohärenten Frequenzbereich gut überein (vgl. Figs. 2, 7).

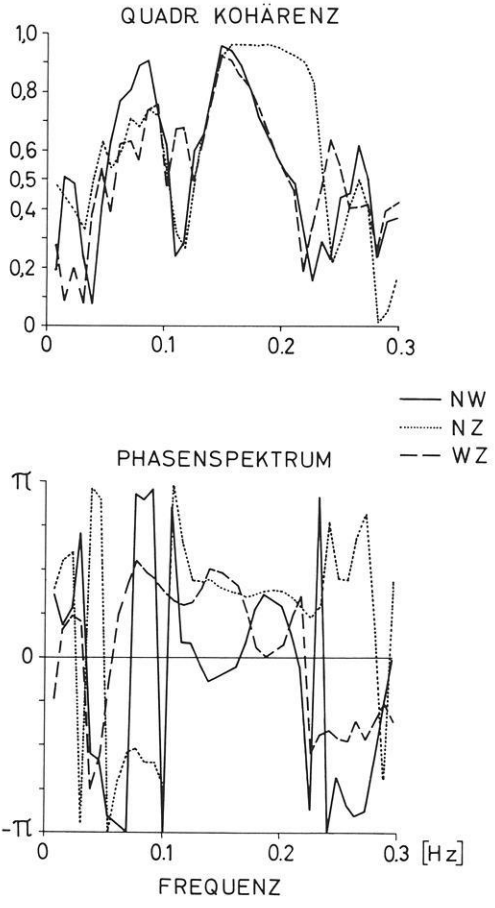

Fig. 7. Kohärenz- und Phasenspektren zwischen den Komponenten der elastischen Störungen vom 1. 11. 73

V. Richtungsmodelle

Die Beziehung (3) gestattet, aus den Kreuzspektren der gemessenen elastischen Störungen Richtungsspektralmodelle zu bestimmen, die (im betrachteten Frequenzbereich) gleichzeitig solche des Seegangs sind. Die drei seismischen Komponenten liefern vier unabhängige Elemente der Kreuzspektren $S_{ij}=C_{ij}-iQ_{ij}$, und zwar Q_{13}, Q_{23}, C_{12}, $S_{11}-S_{22}$, mit denen ein Vier-Parameter-Modell des normierten Richtungsspektrums

$$E(\theta,\omega)=\frac{S_\zeta(\theta,\omega)}{N(\omega)} \quad \text{mit} \quad \int_0^{2\pi} E(\theta,\omega)\,\mathrm{d}\theta=1$$

zu bestimmen ist. Sei $\theta_\omega=\bar{\theta}_\omega$ die mittlere Richtung eines stark gebündelten seismischen Strahls, dann gilt wegen

$$\begin{Bmatrix} T_1 \\ T_2 \end{Bmatrix}=\begin{Bmatrix} \cos\bar{\theta} \\ \sin\bar{\theta} \end{Bmatrix}\sqrt{T_1^2+T_2^2}$$

$$\frac{\sqrt{T_1^2+T_2^2}}{|T_3|}=\left(\frac{S_{11}+S_{22}}{S_{33}}\right)^{\frac{1}{2}}$$

für die mittlere Richtung und die „Varianz“:

$$\bar{\theta}=\arctan\frac{T_2}{T_1}=\arctan\frac{Q_{23}}{Q_{13}}$$

$$\theta_s^2=1-\frac{Q_{13}^2+Q_{23}^2}{S_{33}(S_{11}+S_{22})}.$$

Damit lassen sich die übrigen Parameter des Richtungsmodells

$$E(\theta,\omega)=\exp\left[-\left(\frac{\theta-\bar{\theta}}{\theta_s}\right)^2\right]\,[c+a(\theta-\bar{\theta})^2+b(\theta-\bar{\theta})^3] \tag{6}$$

eindeutig als Lösungen eines linearen Gleichungssystems bestimmen. In Fig. 3 sind $\bar{\theta}(\omega)$ und $\theta_s(\omega)$ zusammen mit den Autospektren des Seegangs und der Horizontalkomponenten der elastischen Störungen für den 1.11.73 gegeben: Im Bereich kleiner θ_s-Werte, in dem zugleich die Spitzenfrequenzen der Autospektren liegen, sind zwei Richtungen (NW und SSW) vorherrschend. Dagegen deuten die hohen θ_s-Werte auf isotrope Einstrahlung, d.h. die $\bar{\theta}$-Werte um 0° bzw. 360° (östliche Richtung) sind nicht signifikant. Richtungsspektralmodelle (6) für die Spitzenfrequenzen in den Autospektren der Zeitreihen vom 25.10. und 1.11.73 sind in Fig. 8 aufgetragen. Am 25.10. kommt die Energie des gesamten Spektrums aus NW; gegenüber der niederfrequenten Energie ($f\lesssim 0{,}12$ Hz) ist die höherfrequente ($f\gtrsim 0{,}14$ Hz) stärker gebündelt. Am 1.11. ist die Trennung zwischen der niederfrequenten Dünungsenergie und der höherfrequenten Windseeenergie zudem durch unterschiedliche Richtungsbänder gegeben.

Fign. 9a, b sind Wetterkarten, in die vom Meßort aus die den Halbwertsbreiten der Richtungsmodelle entsprechenden Strahlbreiten um die mittleren Richtungen aufgetragen sind. Die Karten zeigen die Bodenwetterlage zweiein-

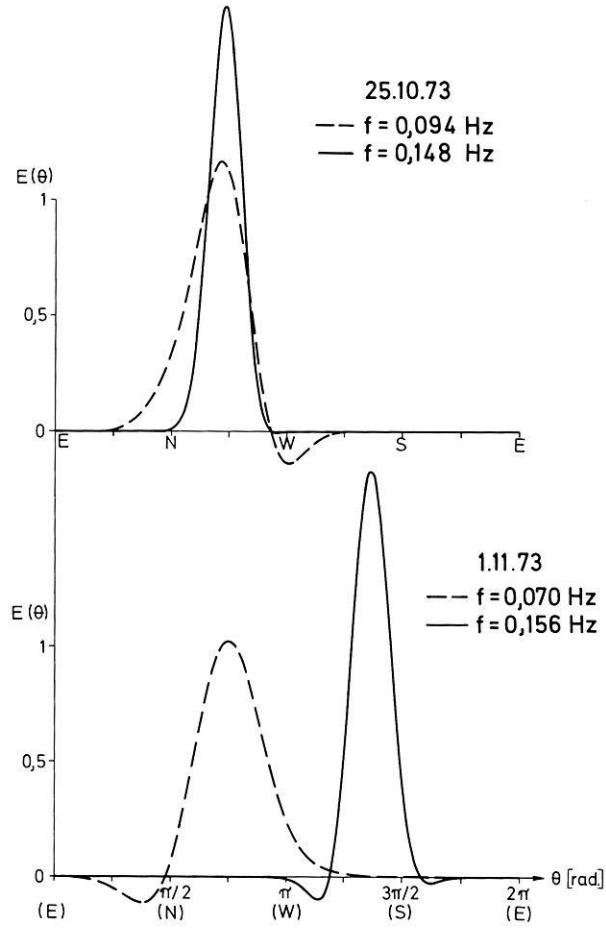

Fig. 8. Richtungsspektralmodelle für die Peak-Frequenzen der Spektren zweier Tage. Der Winkel wird von $E(\theta=0)$ ausgehend über $N(\theta=\frac{\pi}{2})$ gemessen

halb Tage vor den betreffenden Registrierungen, das entspricht etwa der Laufzeit der Dünung von Island bis Sylt. Aus diesen Darstellungen läßt sich mit Hilfe der Windgeschwindigkeit auf die Entstehungsgebiete der Seegangskomponenten schließen: Unter „idealen" Bedingungen der Seegangsentstehung ist zwischen der „charakteristischen Länge" x des Erzeugungsgebietes und der Spitzenfrequenz f_m des Seegangsspektrums folgender Zusammenhang kennzeichnend (Hasselmann *et al.*, 1973):

$$\tilde{f}_m \equiv \frac{f_m U_{10}}{g} \approx \left(\frac{U_{10}^2}{g\,x}\right)^{\frac{1}{3}} \gtrsim 0{,}14$$

(U_{10}-lokale Windgeschwindigkeit 10 m oberhalb der Wasseroberfläche).

Der untere Grenzwert entspricht dem Fall des ausgereiften Seegangs. Die Werte $\tilde{f}_m$ sind in Klammern neben den Windgeschwindigkeitsdaten angegeben,

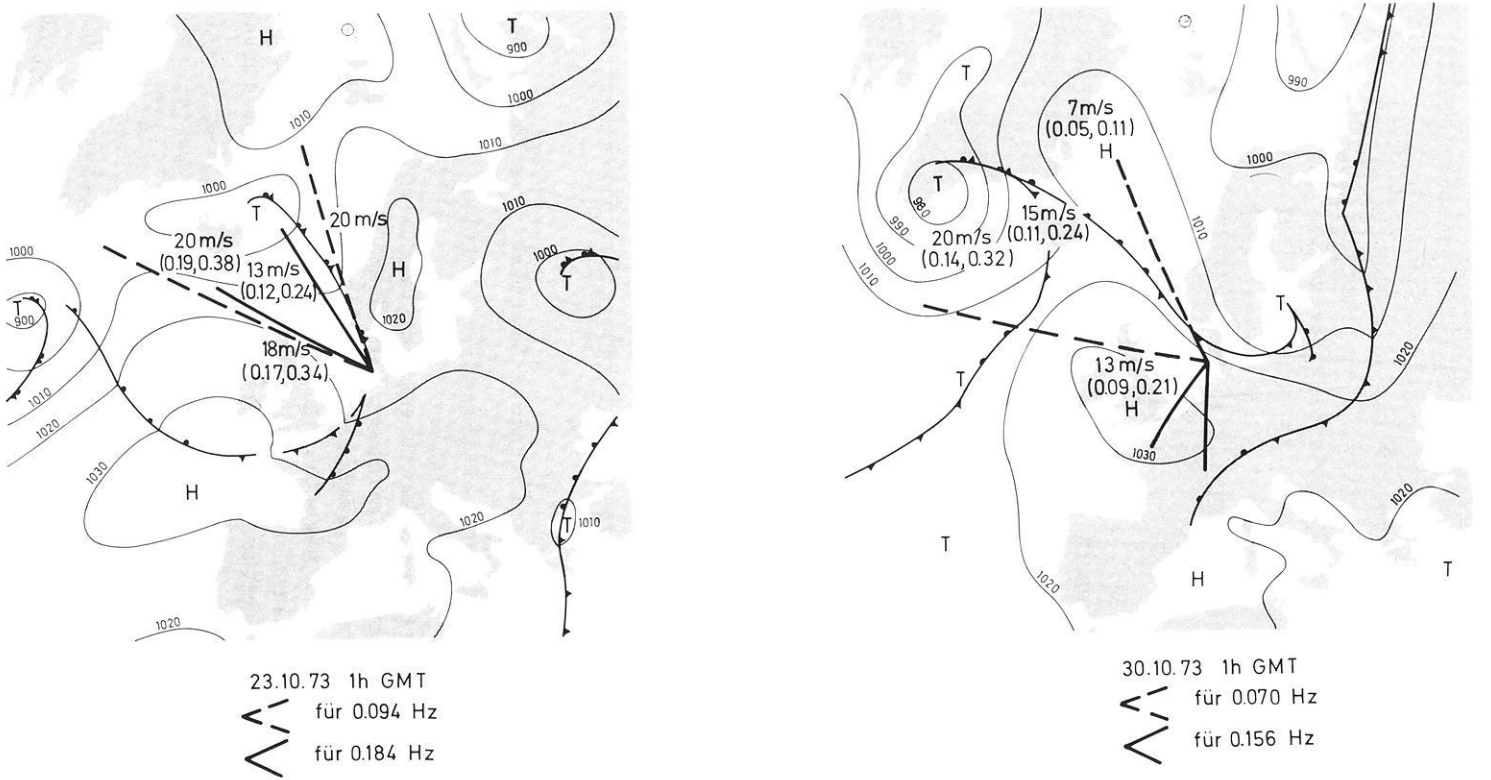

(a) (b)

Fig. 9. (a, b) Einfallsrichtungen des Seegangs in Zusammenhang mit der Wetterlage. Neben den Windgeschwindigkeiten sind (in Klammern) die Größen $\tilde{f}_m = f_m \cdot U_{10}/g$ (f_m Peakfrequenz, U_{10} lokale Windgeschwindigkeit, g Schwerebeschleunigung) angegeben, jeweils der erste Wert für die niedrigere der beiden Peak-Frequenzen

und zwar jeweils der erste Wert für die kleinere der beiden Spitzenfrequenzen. Demnach wird die Dünung vom 25.10. in einem ausgedehnten Gebiet um Island erzeugt (Entfernung ca. 1500 – 2000 km); die vom 1.11. östlich der Südspitze Grönlands (Entfernung ca. 2000 – 3000 km).

Die Entstehung der Windsee, die wesentlich geringere Reichweiten besitzt, müßte mit den lokalen Windverhältnissen am Tag der Registrierung begründet werden. So stimmt die südwestlich einfallende Energie vom 1.11., die in Fig. 9b keinen Bezug zur Wetterlage erkennen läßt, nahezu mit der Richtung des geostrophischen Windes des nach Polen gewanderten Hochdruckgebiets überein.

VI. Schluß

Die Arbeit zeigt, daß die durch den Seegang mitgeführten elastischen Bodenbewegungen ein brauchbares Probefeld darstellen, um die Scherwellengeschwindigkeiten des oberen Meeresbodens zu bestimmen. Entsprechend der Natur erzwungener Schwingungen ist das Dispersionsverhalten des elastischen Störungsfeldes vollständig durch die Quelle, d.h. den Seegang, bestimmt. Im Fall vernachlässigbarer Anregung im Registriergebiet, also nahezu glatter See, wird demgegenüber der Anteil freier elastischer Oberflächenwellen dominierend, der als „mikroseismische Bodenunruhe" (gleiches Frequenzband, jedoch größere Wellenlängen) definiert ist. In diesem Fall werden die Registrierungen des Grundkörpers in Ergänzung zu denen eines Array aus Landstationen entscheidend für die mikroseismische Energiebilanz sein.

Literatur

Essen, H.H., Hirschleber, H.B., Siebert, J.: Geschwindigkeits- und Dämpfungsmessungen an Sedimenten der Nordsee. Z. Geophys. **39**, 833 – 854, 1973

Ewing, W.M., Jardetzky, W.S., Press, F.: Elastic waves in layered media. New York: McGraw-Hill 1957

Hasselmann, K.: A statistical analysis of the generation of microseisms. Rev. Geophys. **1**, 177 – 210, 1963

Hasselmann, K., Barnett, T.P., Bouws, E., Carlson, H., Cartwright, D.E., Enke, K., Ewing, J.A., Gienapp, H., Hasselmann, D.E., Krusemann, P., Meerburg, A., Müller, P., Olbers, D.J., Richter, K., Sell, W., Walden, H.: Measurements of wind-wave growth and swell decay during the Joint North Sea Wave Project (Jonswap). Deut. Hydrograph. Z. (Ergänzungsheft), Reihe A, Nr. 12, 1973

Neumann, G., Pierson, W.J.: Principles of physical oceanography. Englewood cliffs, N.J.: Prentice-Hall 1966

P. Janle
R. Rudloff
B. Schmalfeldt
R. Szelwis
Institut für Geophysik der Universität
D-2000 Hamburg 13
Bundesstr. 55/XIV
Bundesrepublik Deutschland

Eingegangen am 18. April 1975

J. Geophys. 41, 491–499, 1975

Interpretation of a Gravity Profile across the Southern Part of the Hon Graben, Libya

H. Soffel, K. Peters* and J. Pohl

Institut für Allgemeine und Angewandte Geophysik, Universität München

Abstract. A 90 km long profile with 251 gravity stations was measured across the southern part of the Hon Graben. From a combination of a previously published ΔT anomaly (Schult, 1974) and the Bouguer anomaly $\Delta g''$, both measured along the same profile, a probable density structure for the southern part of the Hon Graben has been derived. The models show a sharp increase of thickness of Upper Cretaceous and Tertiary sediments at the graben borders. The thickness of 1800 m of these sediments, which has been obtained from geological observations, is compatible with the gravity models assuming a density contrast of 0.2 g/cm^3 with respect to older sediments. In the central part of the graben a rise of the Pre Upper Cretaceous rocks, reaching up to about 300 m below the surface, divides the Hon Graben, at least in the southern part, into two separate troughs. In the western part of the graben border basic intrusions seem to exist, which are probably connected with the adjacent Jebel Soda volcanism.

Key words: Gravimetry – Hon Graben – Libya.

1. Introduction

The tectonic structure of the Sirte Basin in Libya is characterized by a number of troughs striking NNW-SSE. They extend from the Djebel Harudji in the southeast towards the northwest into the area between Malta and Tunesia which is now covered by the Mediterranean Sea. A detailed description of the tectonic development of the Sirte Basin has been given by Klitzsch (1970). It is assumed that the formation of the troughs and rises in the Sirte Basin started in Upper Cretaceous as a consequence of east-west directed tensions. The Hon Graben, about 260 km long and between 40 and 60 km wide, is one of the most dominant structures in the western part of the Sirte Basin. It was described for the first time by Knetsch (1950). Results of field magnetic measurements in the Hon Graben were published by Schult and Soffel (1971) and Schult (1974).

The present gravity survey was made in order to obtain more detailed information about the structure of the Hon Graben.

* Now with Mobil Oil, Celle.

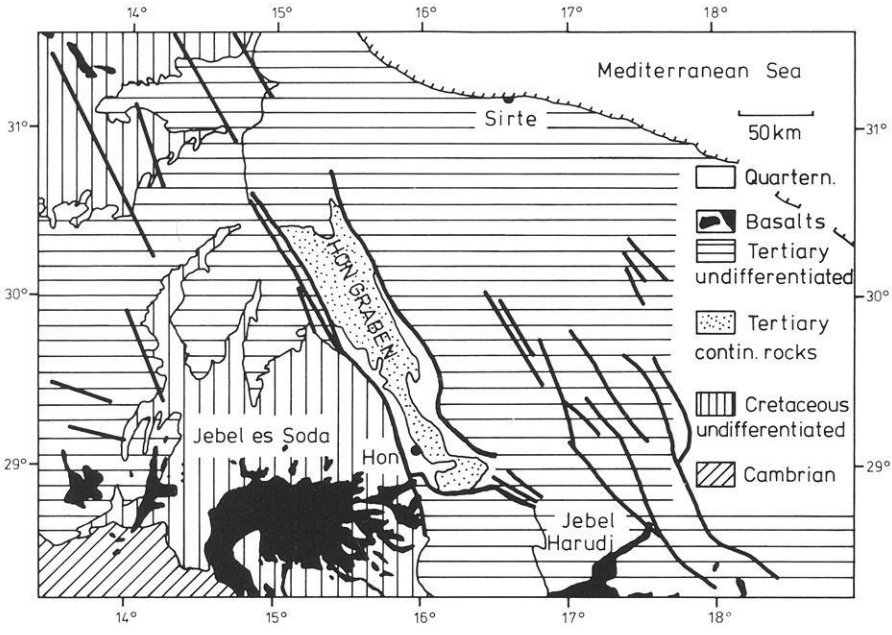

Fig. 1. Simplified geological map of the western part of the Sirte Basin in Libya. (Redrawn from the Geological map of Libya, scale 1:2000000)

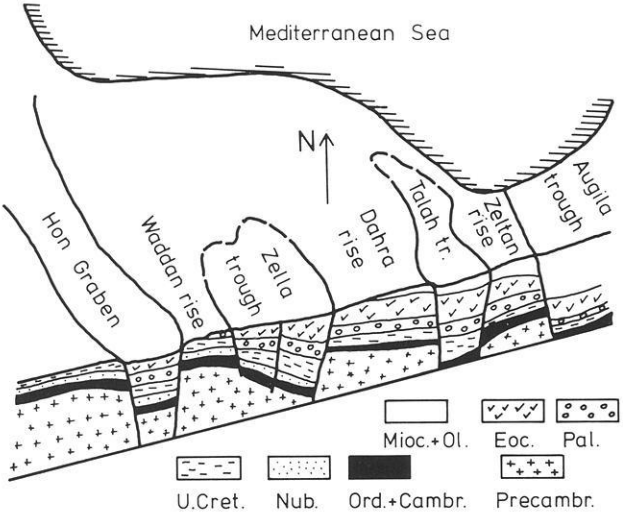

Fig. 2. Simplified cross section of the troughs and rises in the western part of the Sirte Basin. (Redrawn from Klitzsch 1970.) Conventional abbreviations for the formation names. *Nub:* Nubian sandstone, Mesozoic age

2. Geology of the Investigated Area

Fig. 1 shows the position of the Hon Graben on a simplified geological map of Libya (redrawn from the Geological map of Libya, scale 1:2000000). Accord-

ing to Klitzsch (1970), the formation of the Hon Graben was initiated in Upper Cretaceous. It has been shown by drilling about 50 km north of the profile that in the graben, at a depth of 1800 m, the Upper Cretaceous sediments lie immediately on top of the Early Mesozoic Nubian Sandstone overlaying Paleozoic series. The Upper Cretaceous sediments are supposed to have a thickness of 550 m in the graben. In the southern part of the Hon Graben they are covered by Paleocene and Eocene sediments with a thickness of about 1000 m. During the Oligocene vertical movements on both sides of the graben have continued ending in the Miocene as is revealed by further sedimentation of Oligocene and Miocene sediments. The total thickness of sediments of Upper Cretaceous and younger age is thought to be at least 1800 m in the southern part of the Hon Graben. At present the graben borders consist of Upper Cretaceous sediments which are occasionally covered by thin layers of Lower Paleocene sediments.

Fig. 2 has been redrawn from Klitzsch (1970) and shows a simplified block diagram of the troughs and rises in the southern part of the Sirte Basin.

In its present from the Hon Graben shows a marked topographic depression between 100 and 300 m only in its southern part. The fault zones on both sides are between 1 and 2 km wide in the southern part of the graben, becoming wider towards the north.

The center of the volcanic area of Jebel Soda (volcanic activity between Miocene and Pliocene) is situated about 100 – 150 km southwest of the Hon Graben. Some flows reach very close to the southwestern margin of the Hon Graben. Field magnetic investigations by Schult (1974) indicate the presence of basic intrusions near the southwestern graben border.

3. Gravity Measurements

Fig. 3 shows the position of the measured profile across the southern part of the Hon Graben. It extends from the Jebel Waddan in the east along tracks and roads through Waddan, Hon and Sokna to the small oasis Bir el Machrigh in the west. It has a length of 90 km with 251 gravity stations at an average distance of 360 m.

Altitude differences and distances between measuring stations were determined by levelling. We estimate that the altitude differences between two stations are correct within ± 0.5 cm and the distance within ± 1 m. Gravity differences were measured with a Lacoste-Romberg gravity meter, model G. At each 5th or 6th station two or three repeated measurements were carried out at intervals of 2 to 3 hrs in order to eliminate the drift of the instrument and the effect of the earth's tides.

For interpretation, the topography and the gravity data were projected on a profile perpendicular to the graben. The projected profile has a length of 78 km and is also shown in Fig. 3. The topography along the projected profile is shown in the upper part of Fig. 4. The western graben border east of Sokna (hatched area) is only poorly recognizable while the eastern border (east of Waddan, hatched area) is much more pronounced. The plateau of Jebel Waddan lies about 300 m above the inner part of the Hon Graben.

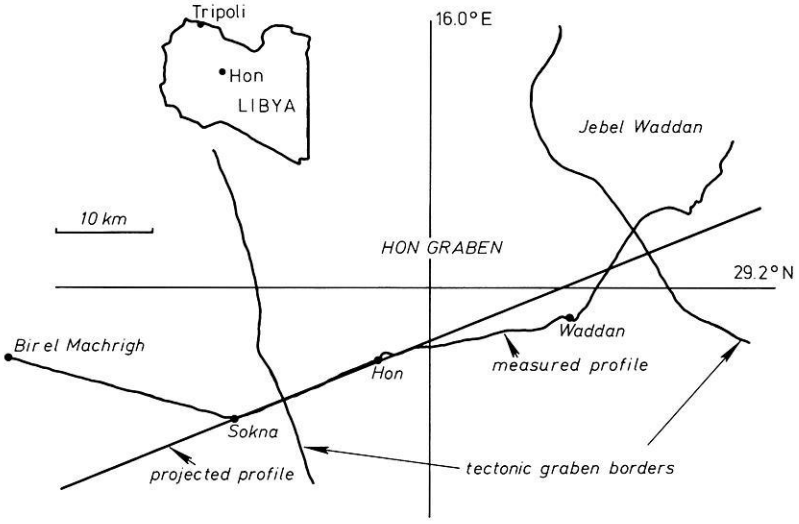

Fig. 3. Position of the measured and projected profile in the southern part of the Hon Graben

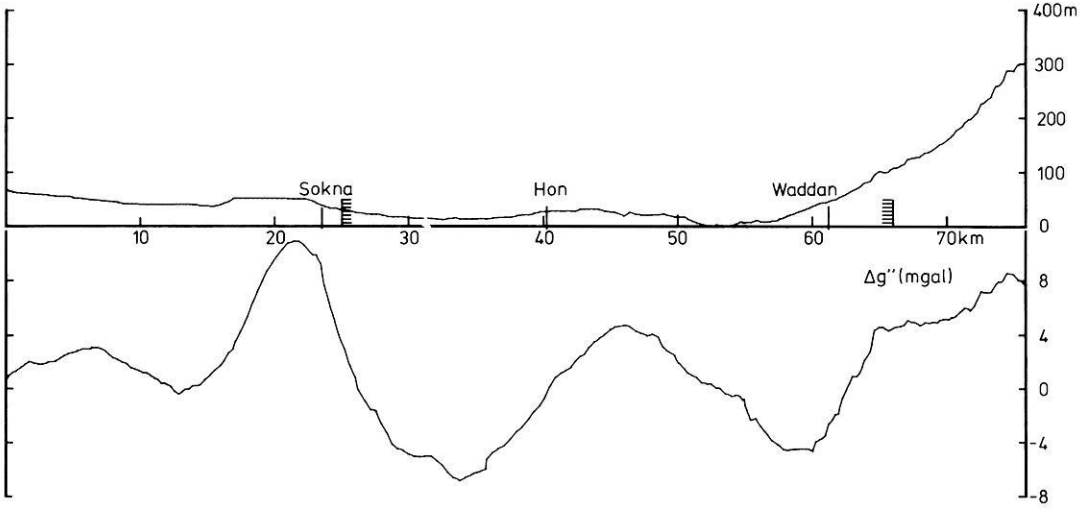

Fig. 4. Topography and Bouguer anomaly $\Delta g''$ along the projected profile

4. Determination of the Bouguer Anomaly along the Projected Profile

All gravity measurements have been referred to a base station near Waddan at the topographically lowest point of the profile. The north-south gradient of the earth's gravity field was computed from the international gravity formula. Topographic corrections, estimated on the basis of two-dimensional models (Jung, 1961), for stations within the Hon Graben were always smaller than 0.1 mgal and therefore neglected. The influence of the Jebel Soda southwest of the Hon Graben was also smaller than 0.2 mgal. Only in the eastern part of the profile

approaching the Jebel Waddan topographic corrections became necessary. An accurate determination of the topographic corrections between km 70 and km 78 of the projected profile was not possible as an exact topographic map of the Jebel Waddan was not available. From the existing large-scale maps and from our own altitude determinations the topographic corrections were estimated with two-dimensional models. The Bouguer anomaly between km 70 and km 78 of the projected profile is therefore only reliable within ± 1 mgal, in contrast to the rest of the profile where the accuracy of the Bouguer anomaly is estimated to be ± 0.2 mgal. However this part of the profile is of minor importance for the interpretation of the gravity anomaly in the Hon Graben. Within the Hon Graben a density of 2.0 g/cm^3 for near surface rocks has been used for the calculation of the Bouguer correction. For the areas outside the graben a density of 2.3 g/cm^3 was taken. Due to the small altitude differences in the Hon Graben area the choice of the density of the near surface rocks has only little influence on the Bouguer anomaly.

Fig. 4 shows the topography and the Bouguer anomaly $\Delta g''$ along the projected profile. At both margins of the graben (hatched areas) a decrease of the Bouguer anomaly of about 8 to 10 mgal with respect to the graben shoulders can be observed. In the inner part of the graben a Bouguer gravity maximum of about 8 mgal is present. The western margin of the Hon Graben is characterized by higher Bouguer anomaly values than the eastern graben border. No general trend in the Bouguer anomaly (especially no east-west trend) can be recognized which could be indicative of a strong gradient of the regional field in this direction.

5. Interpretation of the Bouguer Anomaly

The ratio between the length, width and expected depth of the Hon Graben permits to consider it as a two dimensional structure. This justifies also the projection of the gravity data on a profile perpendicular to the strike of the graben as shown in Fig. 3 and Fig. 4.

The maximum horizontal gravity gradients of 2 mgal/km (on the average 1 mgal/km) and the small half-width of the anomaly on the western margin of the graben indicate that the sources of the Bouguer anomaly are located at rather shallow depth. The good correlation between the geologically known graben borders and the Bouguer anomaly $\Delta g''$ is obvious.

Two different two dimensional models for the density distribution in the Hon Graben are discussed. It is assumed in all models that $\Delta g''$ is caused by density differences within the top 2 km of the subsurface between the Upper Cretaceous and Tertiary sediments and the Lower Mesozoic and older rocks.

For model A (Fig. 5) a density contrast of 0.2 g/cm^3 is assumed between the Upper Cretaceous and Tertiary sediments and the older rocks. In this model the graben borders are in good agreement with the fracture zones (hatched areas). For the adopted density contrast the thickness of the Upper Cretaceous and younger sediments (1.8 km) is in good agreement with geological observations. A central rise must be assumed for the explanation of the central anomaly. However a discrepancy exists on the western graben border between the model

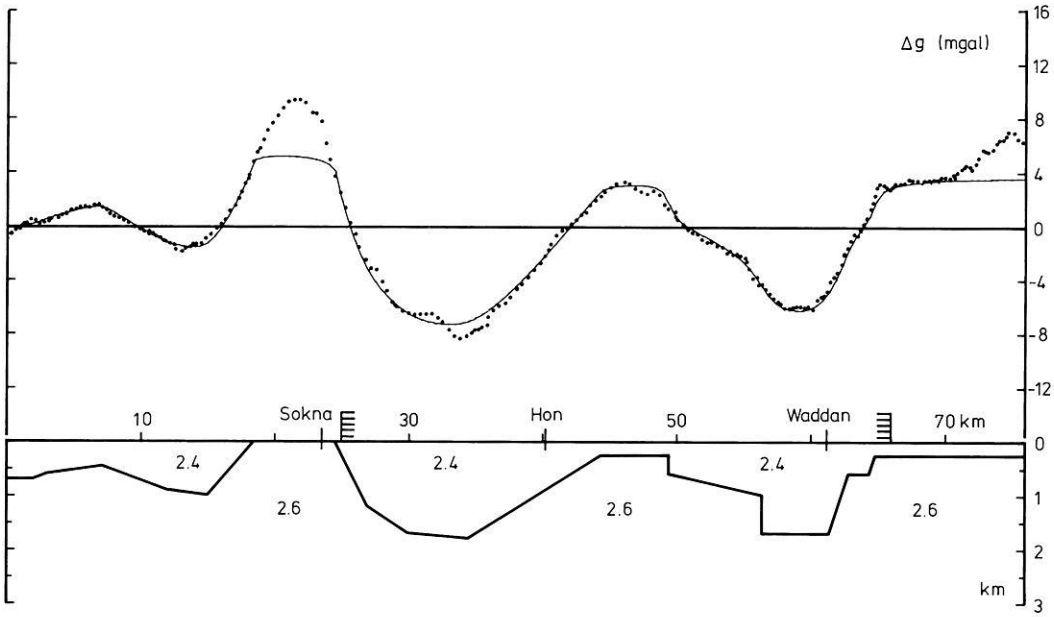

Fig. 5. Model A for the density distribution. Full line: model anomaly. Dotted line: measured $\Delta g''$

anomaly and the observed $\Delta g''$ values. Even Pre Upper Cretaceous rocks reaching to the surface (which is not in agreement with geological observation) cannot explain the observed high $\Delta g''$ values.

This discrepancy is removed by model B, shown in Fig. 6, which is the same as model A except the density distribution on the western graben border. The upper model curve (curve 1) represents Pre Upper Cretaceous rocks not reaching to the surface plus an intrusive body with a density of 2.9 g/cm^3. The presence of basic intrusives in this area has been discussed by Schult (1974). The lower model curve (curve 2) refers to the model without the intrusive body. The density distribution of model B is very probable from the presently available gravity and field magnetic data.

The presence of a central rise of the Pre Upper Cretaceous rocks not reaching to the surface has not yet been discussed in literature according to our knowledge. It implies that the Hon Graben is divided into two separate troughs at least in its southern part.

6. Comparison between Models of the Hon Graben Derived from Gravimetric and Magnetic Anomalies and Conclusion

For the same profile, Schult (1974) has published a model derived from a ΔT anomaly assuming an induced magnetization of $J_i = 1.3 \cdot 10^{-3}$ Gauss for the magnetic basement and $J_i = 0$ for the overlaying sediments. The model of the magnetic

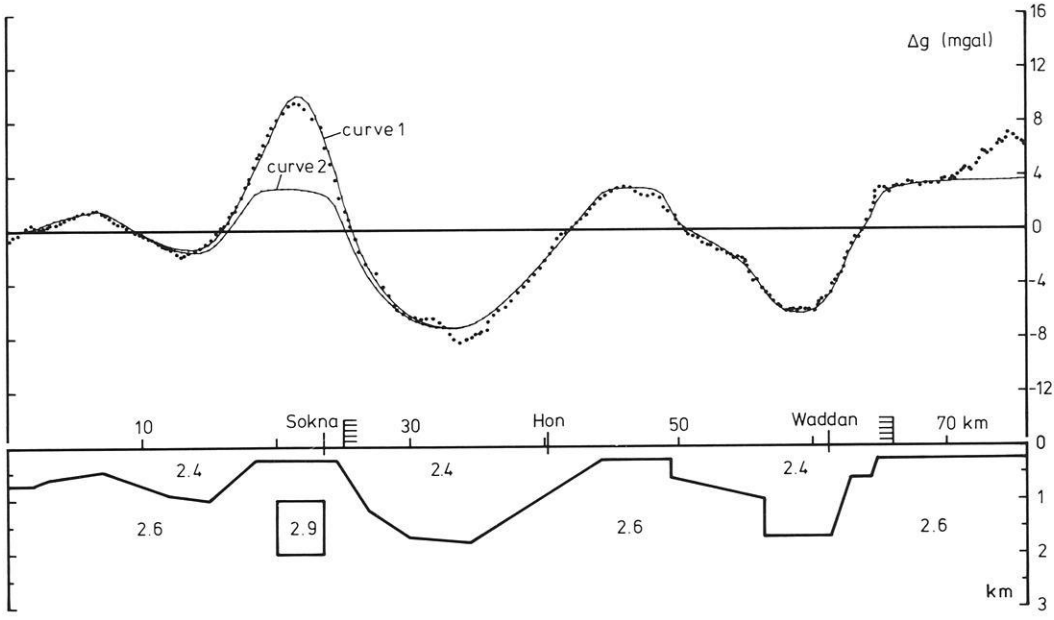

Fig. 6. Model B for the density distribution. Full lines: model anomalies. Dotted line: measured $\Delta g''$. Curve 1: whole model. Curve 2: basement alone without additional intrusive body

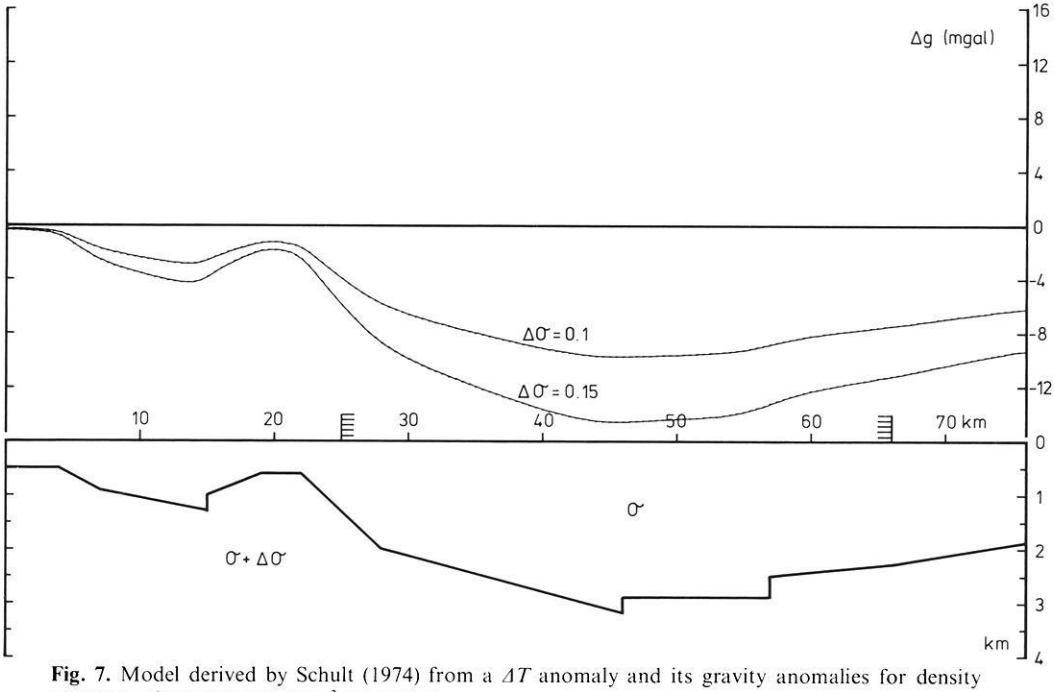

Fig. 7. Model derived by Schult (1974) from a ΔT anomaly and its gravity anomalies for density contrasts of 0.1 and 0.15 g/cm^3 respectively

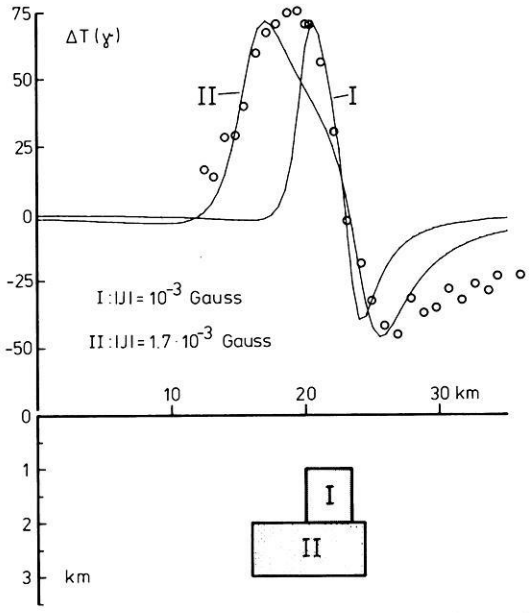

Fig. 8. ΔT anomalies of two basic intrusive bodies. Body I with an induced magnetization of 10^{-3} Gauss (curve I) corresponds to the high density body of model C (Fig. 7). Body II has an induced magnetization of $1.7 \cdot 10^{-3}$ Gauss (curve II). The strike of the two dimensional bodies is parallel to the graben borders. Dots are measured ΔT values

basement is shown in Fig. 8 together with its gravity anomaly assuming density differences between the magnetic basement and the sediments of 0.1 and 0.15 g/cm^3 respectively. A comparison of the gravity anomaly of this model with the observed $\Delta g''$ anomaly (see Fig. 4) shows a discrepancy indicating that the main sources of the gravity anomaly must be structures reaching close to the surface, as was assumed in the previous models A and B. The discrepancy favours an alternative model proposed by Schult (1974) for the interpretation of the ΔT anomaly on the western graben border. This model suggests a weakly magnetized basement with a strongly magnetized basic intrusion (in connection with the Jebel Soda volcanism) near the western margin of the Hon Graben. Fig. 8 shows that in principle intrusive bodies similar to the high density body of gravity model B (body I in Fig. 8) with plausible values for the magnetization can explain the measured ΔT anomaly on the western graben border. A complete accord between the magnetic and gravimetric interpretation in the western part of the profile cannot be expected as the western part of the magnetic profile ends a few km south of the gravity profile. The absence of a magnetic anomaly in the central part of the Hon Graben (due to the rise of the Pre Upper Cretaceous rocks as obtained from the gravimetric measurements) is a further indication for a weakly magnetized basement and also favors the interpretation of the ΔT anomaly on the western graben border by a basic intrusion.

Acknowledgement. The investigations were made in the Institut für Allgemeine und Angewandte Geophysik, Universität München. We thank its director, Prof. Dr. G. Angenheister for his kind

support. We are also grateful to the late Prof. Dr. Kneißl for his instrumental help. Special thanks are due to Prof. Dr. E. Klitzsch from the Geological Institute of the Technical University in Berlin for support and interest and Dr. A. Schult for helpful discussion. The permission of Libyan authorities for the measurements is gratefully acknowledged as well as the financial support of the Deutsche Forschungsgemeinschaft.

References

Conant, L.C., Goudarzi, G.H.: Geological map of Libya. U.S. Geol. Surv. Map I-350A, Washington 1964

Jung, K.: Schwerkraftverfahren in der angewandten Geophysik. Leipzig: Akademische Verlagsgesellschaft 1961

Klitzsch, E.: Die Strukturgeschichte der Zentralsahara. Geol. Rundschau **59**, 459–527 (1970)

Knetsch, G.: Beobachtungen in der libyschen Sahara. Geol. Rundschau **38**, 40–59 (1950)

Schult, A., Soffel, H.: Magnetic ΔZ-profile across the Hon graben, Libya. Z. Geophys. **37**, 299–301 (1971)

Schult, A.: Measurements of magnetic total field anomalies in the Hon graben, Libya. J. Geophys. **40**, 661–665 (1974)

Prof. Dr. H. Soffel
Dr. K. Peters
Dr. J. Pohl
Institut für Allgemeine und Angewandte Geophysik
D-8000 München 2
Theresienstr. 41
Federal Republic of Germany

Received April 10, 1975; Revised Version July 9, 1975

J. Geophys. 41, 501 – 511, 1975

A Comparison of Methods for Computing Surface Densities of the Geopotential from Satellite Altimetry

W. Benning

Institut für Theoretische Geodäsie der Universität Bonn

Abstract. In regard to the expected altimetry data a solution for the earth's gravity field represented by the potential of a simple layer is obtained by means of analyzing 11700 altimeter- and 500 distance-measurements. The unknown density values of the simple layer model are fitted to the given data-covering and the global gravity field is separated into several regional representations. To evaluate the data for a fine structured and global geoid resolution two methods are used and their differences and advantages are examined. First an iterative method uses a global adjustment to determine coarse structured density values. Based on this approximated solution the analysis of all data may be repeated step by step for all regional representations of fine structured density values. On the other hand a detailed resolution for a regional part of the geoid is solved directly. Thus the global solution may be kept step by step by adjusting the regional ones. As no real data is available the numerical tests have been done by means of simulated data of known accuracy.

Key words: Satellite geodesy – Altimetry data – Surface densities of the geopotential – Geoid undulations.

Introduction

The determination of the earth's gravity field from a combination of Doppler data, satellite triangulation and gravity anomalies by means of the simple layer model has been applied by Koch (1968, 1974), and gave excellent results for the gravity field. Hence this method has been proposed to represent the earth's gravity field for the analysis of satellite altimetry data (Benning, 1974).

At present the launch of the earth-satellite GEOS-C is scheduled for the end of 1975. GEOS-C will carry a radar altimeter on board to measure the shortest distance between the satellite and the surface of the ocean. With this new type of data the problem arises to analyze a huge amount of very accurate data collected over the surface of the oceans. If altimetry data will be measured within an accuracy of ± 1 m or ± 2 m this means the possibility to improve existing solutions of the geoid undulations up to this accuracy. Combining this type of data with gravimetry about all $1° \times 1°$-squares of the earth's surface will be covered with data. Here the altimeter measurements are assumed to represent the shortest distance between the satellite and the geoid, that means the surface of the oceans and the

geoid coincide. All periodic and time invariant gravitational influences of sun and moon, currents and waves have to be filtered out of the data.

To represent the gravity field the geopotential may be expressed by an expansion into spherical harmonics. But if it is asked for a detailed resolution of the unknowns, representing distances of about hundred kilometers, the spherical harmonics must be computed up to the 180-th degree and order, a task to determine nearly 32400 coefficients which yet raises some unresolved technical problems.

1. Representation of the Gravity Field

The potential W of the earth

$$W = U + T \tag{1}$$

is divided into a known potential U, which is expressed by an expansion into spherical harmonics,

$$U = \frac{kM}{r}\left[1 + \sum_{n=2}^{n_c}\sum_{m=0}^{n}\left(\frac{a}{r}\right)^n \bar{P}_{nm}(\bar{C}_{nm}\cos m\lambda + \bar{S}_{nm}\sin m\lambda)\right] + \tfrac{1}{2}\omega^2 r^2 \cos^2\beta \tag{2}$$

and into a potential T, which is unknown and represented by a potential of a simple layer distributed over the surface of the earth. In (2) r, β, λ are spherical coordinates in the usual earth-fixed coordinate system, whose 3-axis is identical with the instantaneous axis of the earth and whose 1-axis points towards the intersection of the meridian of Greenwich with the equator. k is the gravitational constant, M the mass of the earth, a is the mean equatorial radius, $\bar{P}_{nm}$ are the fully normalized associated Legendre functions of degree n and order m, and ω is the angular velocity of the earth. The fully normalized harmonic coefficients $\bar{C}_{nm}$ and $\bar{S}_{nm}$ are taken up to the 15th degree and order from Koch (1974, p. 14). The values of a and kM are

$$kM = 3.986013 \times 10^{14}\ \mathrm{m^3\,sec^{-2}}, \qquad a = 6378145\ \mathrm{m}.$$

The potential T is evaluated by numerical integration of

$$T = \sum_{i=1}^{p} \chi_i \iint_{\Delta E_i} \frac{dE}{l}, \tag{3}$$

where l is the distance between the fixed point at which T is computed and the moving point on the surface E of the earth, which is divided into p elements ΔE_i. The unknown density values χ_i are assumed to be constant in ΔE_i, which are bordered by meridians and parallels. The kernel of (3) is computed for the midpoint of each ΔE_i and is assumed to be constant over ΔE_i. To determine the coordinates of these midpoints the reference surface $U = U_0$ is introduced. The value U_0 is defined by the potential of a level ellipsoid, whose constants kM, a, C_{20} and ω are taken from (2), (Koch, 1971). Hence r is computed by the inversion of (2) iteratively.

The density values can be converted into normalized spherical harmonics by (Koch, 1974):

$$\bar{C}_{nm}=\bar{C}_{nmu}+\frac{1}{(2n+1)kM}\sum_{i=1}^{p}\chi_i\iint_{\Delta E_i}\left(\frac{r}{a}\right)^n\bar{P}_{nm}\cos m\lambda\, dE$$
$$\bar{S}_{nm}=\bar{S}_{nmu}+\frac{1}{(2n+1)kM}\sum_{i=1}^{p}\chi_i\iint_{\Delta E_i}\left(\frac{r}{a}\right)^n\bar{P}_{nm}\sin m\lambda\, dE, \tag{4}$$

where $\bar{C}_{nmu}$ and $\bar{S}_{nmu}$ are the original harmonic coefficients which define (2).

2. Computational Procedures

Satellite orbits should be computed in an inertial reference frame. In this analysis orbit computations do not exceed a time interval of 7 days. Thus an inertial system is well approximated by a geocentric coordinate system, whose 3-axis coincides with the instantaneous axis of the earth and whose 1-axis points towards a point east of the true vernal equinox which takes into account precession and nutation in right ascension.

The altimeter measurement h

$$h=|\mathbf{r}-\mathbf{r}_g| \tag{5}$$

is a function of the satellite position $\mathbf{r}$, which in turn is a function of the initial position and velocity vectors $\mathbf{r}_0$, $\dot{\mathbf{r}}_0$, the density values and – in this analysis negligible – of air drag and radiation pressure. In (5) $\mathbf{r}_g$ fixes the position of the subsatellite point on the surface of the geoid and is a function of the unknowns of the gravity field, the density values χ_i. The vector $(\mathbf{r}-\mathbf{r}_g)$ is the normal to the surface of the geoid.

A distance s between the satellite and a tracking station is given by

$$s=|\mathbf{r}-\mathbf{r}_s|. \tag{6}$$

The position vectors $\mathbf{r}_s$ of 34 tracking stations are introduced. They denote a selection of the 41 worldwide distributed stations defined in (Koch, 1974, p. 14).

To evaluate the altimetry- and distance-measurements a least squares adjustment based on a differential correction process is applied. The derivation of the corresponding observation equations and normal equations is published in (Benning, 1975). The orbit is computed by numerical integration methods with a 24-second time step using a 12th order Cowell-Störmer integration for positions, a 10th order Adams-Bashforth predictor and a 10th order Adams-Moulton corrector for the velocities (Witte, 1971). Lagrange's interpolation is applied between time steps of the orbit. To avoid errors in the orbit computation resulting from the numerical integration in (3), the preliminary values of χ_i are set equal to zero.

The determination of the subsatellite point on the reference surface $U=U_0$ is solved iteratively by Lagrange's method (Benning, 1974). The neglected deflection from the vertical amounts on the oceans to a maximum of 10 seconds. The relative error in the computed heights raises beyond $2.5\cdot 10^{-9}$ of the satellite's height in meters.

Assuming that all areas of the earth's surface are covered by a huge amount of data this means for a detailed resolution of the geopotential a division of this

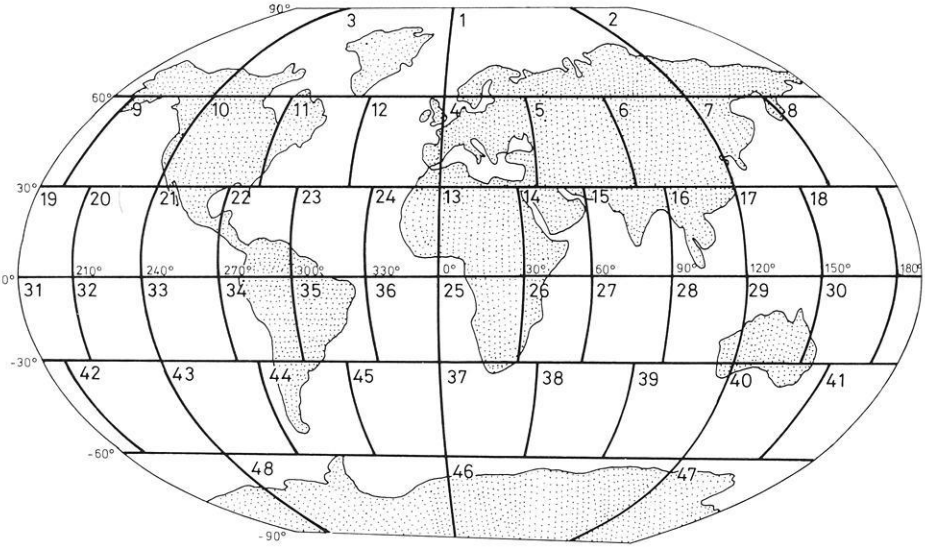

Fig. 1. (30° × 30°) surface elements ΔE_i

surface into small, say 1° × 1°-elements which in turn causes a huge global system of about 40000 normal equations. At present this can neither directly nor iteratively be inverted on computers. Thus in this analysis the number of unknowns is limited to 200. If the reference surface $U = U_0$ is computed by spherical harmonics up to the 15th degree and order the density values and geoid undulations will be very small in comparison to those ones which refer to a reference ellipsoid. Hence the correlations depending on the attraction between the unknown density values decrease nearly exponentially with the increasing distance between the corresponding surface elements. They may be neglected beyond the spherical distance of 20° of the connected surface elements, because they are smaller than |0.04| (Benning, 1974).

Thus for a high geoid resolution the unknown parameters are distributed to a limited, at least (60° × 60°)-area of the earth's surface. Fig. 1 shows a division of the earth's surface into 48 elements which approximate the size of a 30° × 30°-area at the equator. For a locally restricted but fine structured geoid resolution one of these elements, the central one, is defined as the inner zone and is divided into small elements of nearly equal size, *i.e.* 1° × 1°-squares. This inner zone of density values is surrounded by a buffer zone, which according to the maximum number of unknowns is divided into coarse, say 5° × 5°-squares. The densities in the remaining surface elements of Fig. 1 are set equal to zero. For the accurate determination of the densities χ_i at least one observation should be measured to the connected surface element ΔE_i as to avoid a singular system of normal equations.

Now the density values of the inner zone are determined together with those of the buffer zone. While the solution for the inner zone gives the final values, the density values for the buffer zone are discarded. Then the inner zone together with the buffer zone is moved to the next surface element of Fig. 1. This process (= method A) is repeated for all areas which are sufficiently covered with data.

It has been tested by Benning (1975) and gave for the analysis of "errorless" altimetry data small discontinuances between two neighbouring inner-zone-solutions.

Another method to evaluate the data, "method B", consists of a global adjustment to determine coarse structured density values χ_i for all, say $15° \times 15°$-elements ΔE_i of the earth's surface. Hence from this solution new spherical harmonics $\bar{C}_{nm}$ and $\bar{S}_{nm}$ can be computed by (4). The results of this transformation give a better flattening of the best fitting ellipsoid, a corrected value U_0 and a corresponding reference surface $U = U_0$ as well as improved orbital elements.

Now the analysis of all data can be repeated with method A as to determine fine structured density values. According to the accuracy of the recomputed geoid undulations the two methods in question have to be compared. Since at present no real data is available, the numerical tests will be done with simulated altimeter- and distance-measurements.

3. Numerical Results

To examine the stability and accuracy of the formulated two methods from simulated GEOS-C orbit (Nasa, 1972) a data set of 11700 altimeter- and 500 distance-measurements was generated. The altitudes are sequentially collected in a time interval of one measurement per 12 seconds whereas the distances s are continuously distributed in time intervals of 3.6 minutes over the whole time of nearly 87 hours of the satellite-borne altimeter. The data refers to an orbit and reference surface computed by an expansion U into spherical harmonics up to the 15th degree and order ($U = U(n_c \leqq 15)$). Neglecting the topographic heights above sea-level the altitudes are also computed for land areas. The distance measurements were included for the orbit recovery. The altimetry data alone does not give well determined orbits, because the geoid undulations are smooth and the orbits of geodetic satellites do not possess great excentricities.

To save computer time the coordinates of the tracking stations were held fixed and the amount of the whole data was limited to 12200. Errorless data was generated, that means for altimetry data shortest distances between the satellite and the reference surface $U_0 = U$ ($n_c \leqq 15$).

Since the inclination of GEOS-C is 115°, the two pole-caps are without ground tracks beyond $\pm 65°$. With respect to a sufficient data-covering the density values of the correspondent pole-elements are set equal to zero. Furthermore, since nearly all $4° \times 4°$-elements of the remaining surface are covered with data, the distribution of fine structured geoid parameters in method A is limited to 11 elements ΔE_i of Fig. 1, that means to 36 ($5° \times 5°$)-squares of the inner zone and to 90 ($10° \times 10°$)-elements of the buffer zone.

When adjusting a ($15° \times 15°$)-resolution for the density values by evaluating all data the rms discrepancy between geoid heights computed at 10°-intervals is ± 34 cm, the maximum deviation -87 cm. The standard deviations for the density values χ_i lie between ± 0.09 mgal and ± 0.02 mgal and the correlation coefficients for χ_i are less than 0.50.

When evaluating the data with method A detailed density values for two neighbouring inner zones – the elements No. 26, No. 27 of Fig. 1 – were computed.

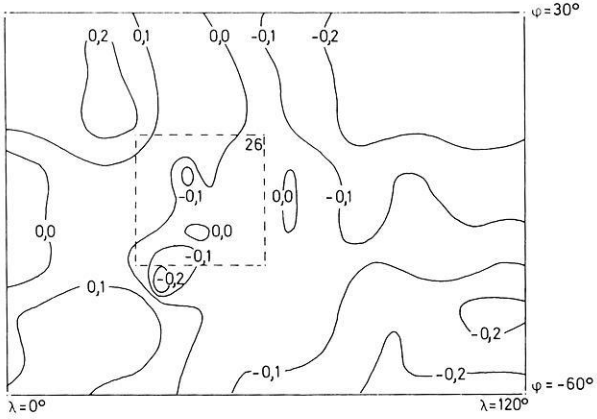

Fig. 2. Geoid Heights (m), referred to $U_0 = U$ ($n_c \leqq 15$), computed for inner zone ΔE_{26} – method A

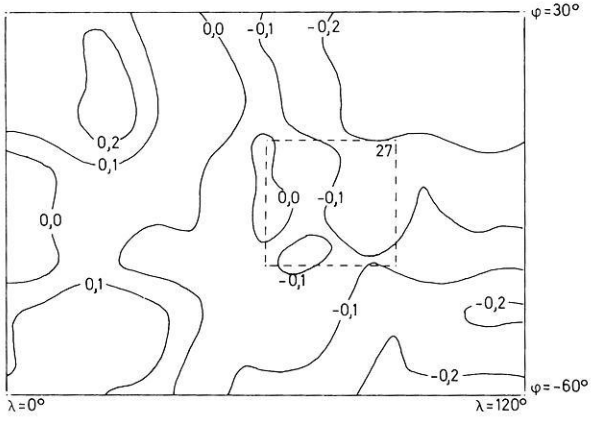

Fig. 3. Geoid Heights (m), referred to $U_0 = U$ ($n_c \leqq 15$), computed for inner zone ΔE_{27} – method A

The iso-contours of the correspondent geoid undulations N are given in Figs. 2 and 3. They show good agreement for all identical areas even for inner zones. In the borders of the two neighbouring inner zones the discontinuances are within the accuracy of ± 15 cm of all computed geoid undulations.

But this result changes if the values N grow.

To proof this the evaluation of the data was done with the identical density-distribution with the examples of Figs. 2 and 3 but with an orbit and reference surface $U_0 = U(n_c \leqq 7)$ which were computed by a spherical expansion U up to the 7th degree and order. Thus the N grow up to $+30$ m and to -21 m respectively.

Nevertheless the geoid heights of identical areas of the buffer zone only differ up to a maximum of ± 2 m to ± 3 m. If we compare the values at the borders of the neighbouring inner zones, they show good conformity within a maximum deviation of ± 1 m till ± 2 m. Thus we may conclude that the analysis of altimetry

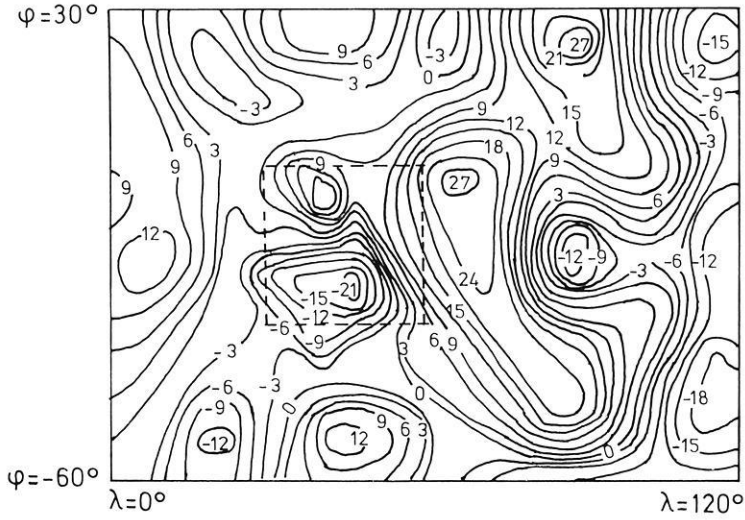

Fig. 4. Geoid Heights (m), referred to $U_0 = U$ ($n_c \leqq 7$), computed for inner zone ΔE_{26} – method A

data for the solution of fine structured density values and geoid undulations with method A gives an accuracy of the recomputed N of at least 10%.

Then the determination of the geoid heights referred to spherical harmonics up to the same degree was repeated with method B, *i.e.* Fig. 6. Hence a global 15°-resolution of 168 density values was applied. Afterwards using the improved spherical harmonics up to the 15th degree and order the detailed resolution with method A was tried. As to compare the methods in question the inner zone was chosen as in the example of Fig. 4.

The discrepancies between correspondent geoid heights of the inner zones in Fig. 4 and 6 reach nearly ±3 m, those in the buffer zones grow up to ±9 m.

When constraining the known spherical harmonics up to the 11th degree and order for the computation of the orbit and reference surface $U_0 = U(n_c \leqq 11)$ and when repeating the evaluation of the data with methods A and B according to Figs. 4, 5, and 6, the results of Figs. 7, 8 and 9 were obtained respectively:

The comparison of the determined neighbouring inner zone values of the Figs. 7 and 8 show discrepancies up to and about ±2 m, whereas the correspondent geoid heights in the buffer zones only differ up to ±1 m. On the other hand the correspondent results of methods A and B represented in Figs. 7 and 9 differ up to ±3 m for the buffer zone and up to ±2 m for the inner zone.

The comparison of these solutions with their directly calculated values in Fig. 10 gives maximum deviations of ±1 m (method A) and ±2 m (method B) for the inner zones and ±2 m resp. ±4 m for the buffer zones. Thus method A yields for somewhat better results than method B.

This indicates deficiencies in the model being applied, for example in the numerical integration methods to compute T in the subsatellite point (Benning and Fröhlich, 1974), in other simplifications or round off errors. Although the worldwide distribution of the tracking stations is good more distance measure-

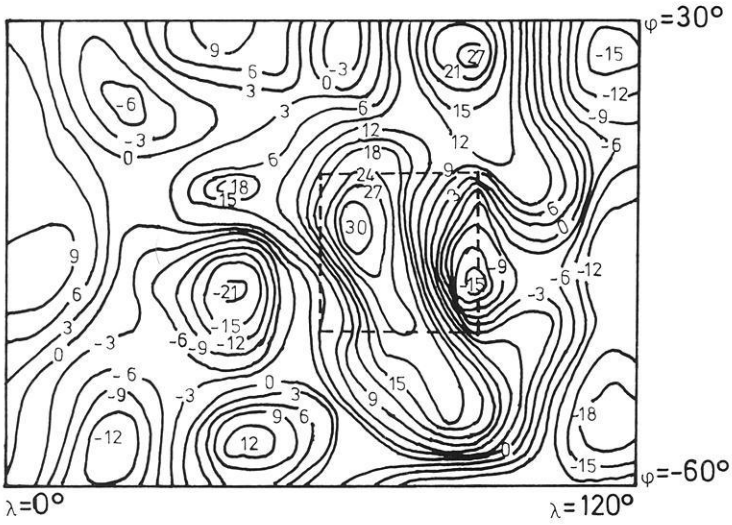

Fig. 5. Geoid Heigths (m), referred to $U_0 = U$ ($n_c \leqq 7$), computed for inner zone ΔE_{27} – method A

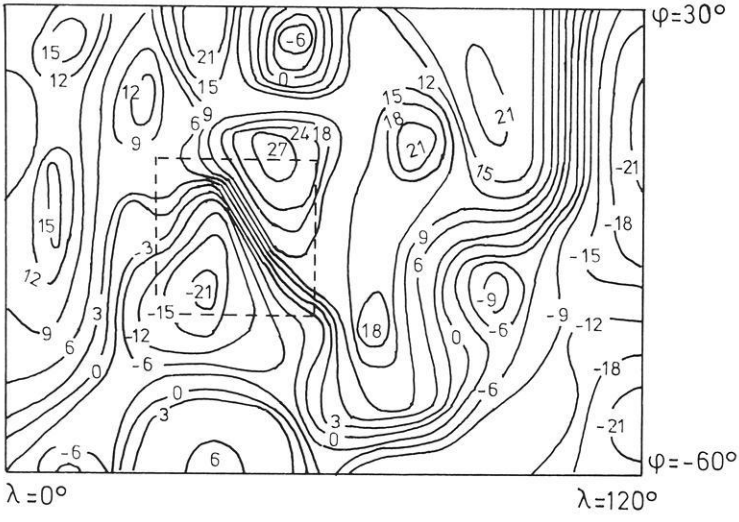

Fig. 6. Geoid Heights (m), referred to $U_0 = U$ ($n_c \leqq 7$), computed for inner zone ΔE_{26} – method B

ments must be included as to improve the estimate and accuracy of the fitted orbit. Data of perhaps 4 or 5 satellites of different inclinations should be available. Furthermore the model of the global force field in method B could be improved by introducing physically relevant information or data for the pole-caps. This would permit a global density-recovery with smaller residuals, an important fact, because the uncertainties of the global density values enter directly the spherical harmonics. Thus they indirectly falsify the recomputed orbit which mainly depends

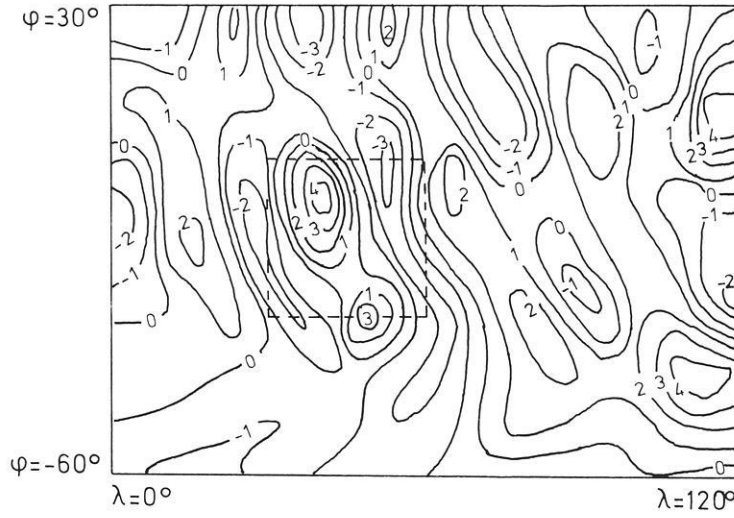

Fig. 7. Geoid Heights (m), referred to $U_0 = U$ ($n_c \leqq 11$), computed for inner zone ΔE_{26} – method A

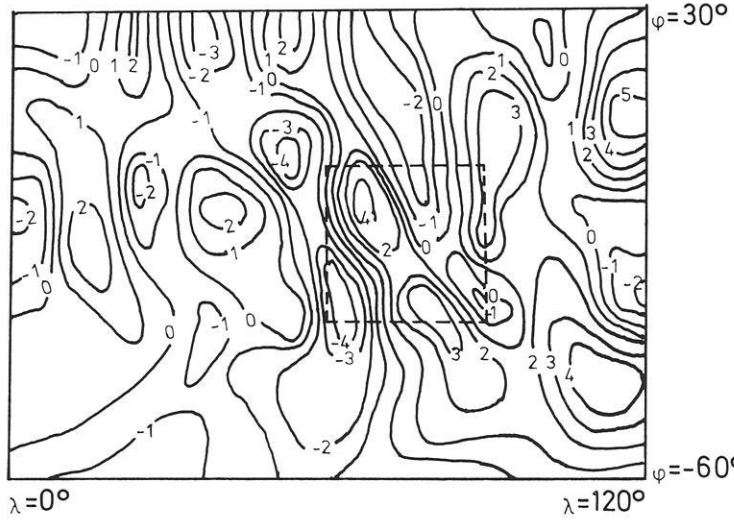

Fig. 8. Geoid Heights (m), referred to $U_0 = U$ ($n_c \leqq 11$), computed for inner zone ΔE_{27} – method A

on the spherical harmonics. The better the orbit the more accurate and the more direct may altimetry data be used for the recovery of the geometry of the oceans.

Concerning to the needed computer time and weighing the obtained accuracies method A, the direct regional resolution of detailed geoid parameters should be preferred.

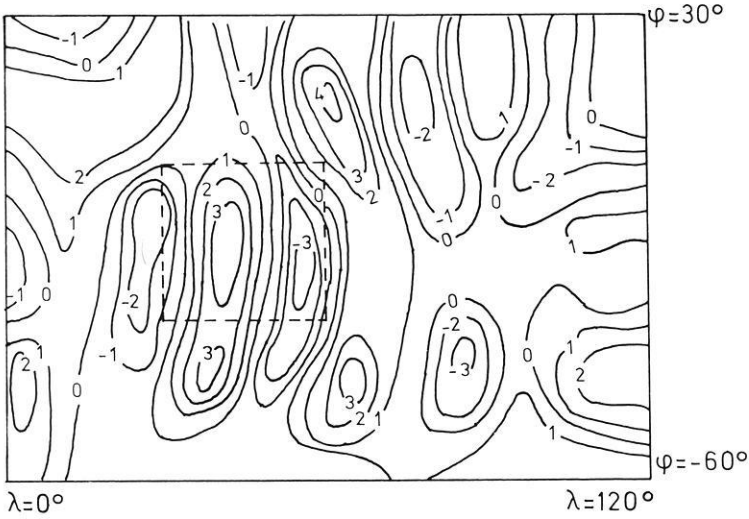

Fig. 9. Geoid Heights (m), referred to $U_0 = U$ ($n_c \leqq 11$), computed for inner zone ΔE_{26} – method B

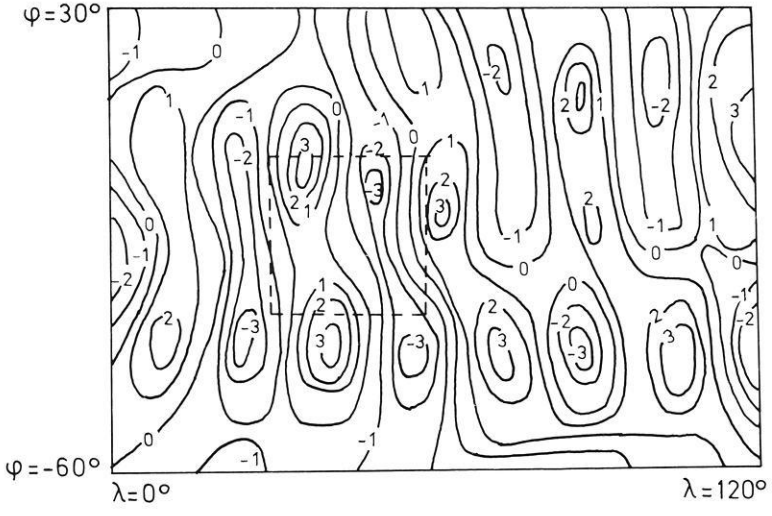

Fig. 10. Directly computed Geoid Heights (m), referred to $U_0 = U$ ($n_c \leqq 11$)

4. Conclusions

Regarding the existing solutions of the gravity field up to spherical harmonics of at least 15th degree and order, the geoid undulations referred to the correspondent reference surface $U = U_0$ will be less than 15 m. Hence, the methods to analyze altimetry data for a detailed knowledge of the earth's gravity field, the methods pointed out here give results of the recomputed geoid undulations with an accuracy of ± 2 m. This result surpasses existing solutions by one order of magnitude.

The feasibility and flexibility of the simple layer model for the geopotential in satellite altimetry is shown by the possibility to limit the unknown parameters to those surface elements which are sufficiently covered with data and which may be fitted to the given data-covering by any mesh size.

As to improve the analytical model for the physical attraction the distribution of the unknown density values may be extended with respect to the technical means (computer storage and -time). This would for example not be possible by means of spherical harmonics, because they denote integrals over the mass distribution of the earth and may not be locally varied nor regionally be limited. Thus the simple layer model is well suited for the analysis of altimetry data with a high resolution and accuracy of the unknowns of the global gravity field. But to strengthen results for the higher order harmonics other worldwide distributed data like gravity anomalies will be introduced into a combined solution.

References

Benning, W.: Auswertung von Altimetermessungen für das Modell der einfachen Schicht des Erdschwerefeldes in der Satellitengeodäsie. Deutsche Geod. Komm. (DGK), München, Series C, No. 200, 1974

Benning, W.: Eine globale Geoidbestimmung aus stückweise regionalen Detaillösungen mit Hilfe von Altimeter- und Entfernungsmessungen in der Satellitengeodäsie. Allg. Verm. Nachr. (AVN) **82**, 12–22, 1975

Benning, W., Fröhlich, H.: Integrationsfehler für das Modell einer einfachen Schicht in der Satellitengeodäsie bei verschwindender Aufpunktshöhe. Mitt. a. d. Inst. f. Theor. Geod. d. Univ. Bonn, No. 29, Bonn, 1974

Koch, K.R.: Alternate representation of the earth's gravitational field for satellite geodesy. Boll. Geofis. Teor. Appl. **10**, 318–325, 1968

Koch, K.R.: Errors of quadrature connected with the simple layer model of the geopotential. NOAA Techn. Report NOS 11, National Ocean Survey, Rockville, Md., 1971

Koch, K.R.: Earth's gravity field and station coordinates from doppler data, satellite triangulation and gravity anomalies. NOAA Techn. Report NOS 62, National Ocean Survey, Rockville, Md., 1974

Nasa: GEOS-C mission. Proposal briefing information. Wallops Island, Virg., 1972

Witte, B.: Berechnungsverfahren für die Bestimmung des Erdschwerepotentials aus Doppler-Beobachtungen mit Hilfe des Modells einer einfachen Schicht. Deutsche Geod. Komm. (DGK), München, Series C, No. 167, 1971

W. Benning
Institut für Theoretische Geodäsie
der Universität
D-5300 Bonn
Nußallee 17
Federal Republic of Germany

Received February 14, 1975

J. Geophys. 41, 513–521, 1975

An Economically Working Method for Computing the Gravimetric Terrain Correction

G. Boedecker

Institut für Theoretische Geodäsie, TU Hannover

Abstract. The described method for the calculation of the terrain correction (deviation of the actual topography from a Bouguer plate) and the entire topographical reduction combines a station-independent orthogonal grid for the outer zones and a station-centered template for the inner zones as subdivision of the topography. This combination seems to have some practical advantages. Furthermore the question of the heights to be used with respect to the curvature of the geoid is discussed. The conventional split of the Bouguer-reduction into terrain reduction and plate reduction seems to be no longer advisable.

Key words: Terrain correction – Bouguer reduction – Simplified digital terrain model.

1. Introduction

To compare measured gravity values at different points of the physical surface of the earth, we first have to eliminate the known gravity-effecting influences, e.g. different heights, geographical latitude, topographical masses, changing densities etc.

The problem of removing the irregularly shaped topographical masses has already brought about a lot of solutions (Ehrismann, 1973). Some of them shall be repeated in a few words.

Most of the authors propose to replace the topography by a sum of mathematically simple bodies, either horizontal layers or vertical prisms, the basal surfaces of which are bounded by cylinder – (α, r) or by parallel (x, y) resp. geographical (φ, λ) coordinates. The upper bound of these prisms may be represented by a plane either horizontal or inclined or by curved surfaces.

It is also possible to approximate the terrain by steady functions for contour lines or vertical profiles or by a mathematically defined surface. Mathematical tools are e.g. polynomials or least squares prediction. Afterwards this artificial topography also may be cut into discrete bodies.

With respect to the practical performance we can distinguish mechanical, graphical and digital methods.

The method described in the following sections may not be the most elegant one from the mathematical point of view, but it has some practical advantages and the formulas and the computer program are quite simple.

Before going into details, we should clarify some basic terms: "Reduction" shall be used in the sense of a computational procedure to get any regularized gravity values from measured gravity data, whereas "correction" really means a correction of a reduction. "Topography" consists of all masses outside the geoid (except atmosphere), whereas "terrain" means the deviation of the actual topography from a plane surface passing through a measuring point P and parallel to the geoid. If any other reference level is used than the geoid, this should be stated by a remark. The terrain correction is therefore a correction to be added to the simple Bouguer reduction (Bouguer plate plus free-air reduction) in order to get the refined Bouguer reduction. The terrain reduction is used as a part of the refined free-air reduction. In this system the topographical reduction denotes the same as Bouguer plate reduction plus terrain correction. Of course we do not need these terms at all; we always can generally talk about shifting of masses or mass reduction and specify these masses.

Originally mostly used was the terrain correction. Therefore it serves as a title of this essay too.

2. The Conception

The topography is subdivided into prisms with horizontal upper surfaces. The subdivision is a combination of a station-independent orthogonal 1 km × 1 km-grid and a station-centered template for the surrounding 4 km × 4 km-area. The template consists of trapezoids, triangles and rectangles, which provide for a connection of orthogonal grid and template without any gaps.

All different types of fields are replaced by ring sectors of the same area, which permits the evaluation of the gravity effect by means of the following wellknown simple formula:

$$\delta g^1 = G\rho\Delta\alpha(r_a - r_i + \sqrt{r_i^2 + h^2} - \sqrt{r_a^2 + h^2}) \tag{2-1}$$

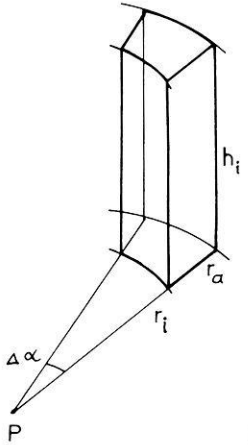

Fig. 1. Variables used in Eq. (2-1) (cf. text)

[1] We shall use the symbol δg for the effect of one compartment as well as for the whole reduction. This will not cause any difficulty.

with:

G gravitational constant 6.67×10^{-8} [$cm^3\ g^{-1}\ s^{-2}$]
ρ density of the prism [$g\ cm^{-3}$].

The other variables are explained by Fig. 1.

The value to be inserted for h depends on the type of the reduction.

2.1. Topographical Reduction

As a part of the complete Bouguer reduction (to obtain Bouguer anomalies) the topographical reduction provides the (computational) removal of all masses outside the geoid or another reference level respectively. The height h always refers to the tangential plane T. Therefore because of the bent surface of the geoid two portions for each prism must be considered: Filling up or removing the terrain to the plane T and afterwards removing down to the geoid G (cf. Fig. 2):

$$\delta g_{\text{Top}} = \delta g'_{\text{Top}} + \delta g''_{\text{Top}} = f(h') + f(h'') = f(|H - H_P - D|) - f(D + H_P). \tag{2-2}$$

In this case we assume that H is not measured rectangular to the geoid or the ellipsoid, but parallel to $\overline{P_0 P}$. This neglection causes at e.g. $r = 100$ km an error of less than 0.02% of the height, i.e. a very small error with respect to the accuracy of height estimation.

D represents the horizon-depression:

$$D \approx \frac{r^2}{2R} \tag{2-3}$$

with:

R mean radius of the earth.

It shall be pointed out, that the topographical reduction no longer is split into the levelling of the terrain at station elevation and the Bouguer-plate reduction. Varying density values easily can be regarded without introducing an artificial "effective Bouguer density".

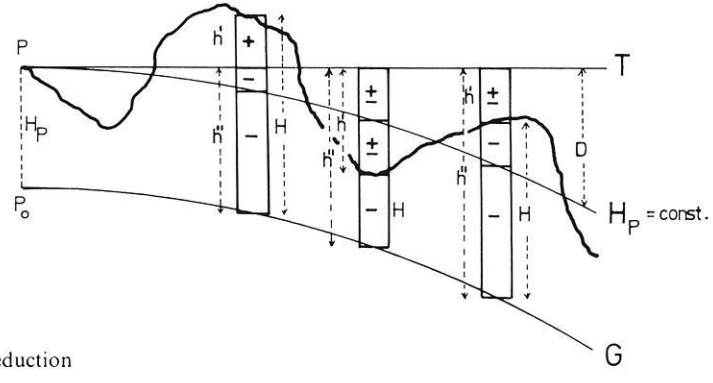

Fig. 2. Topographical reduction

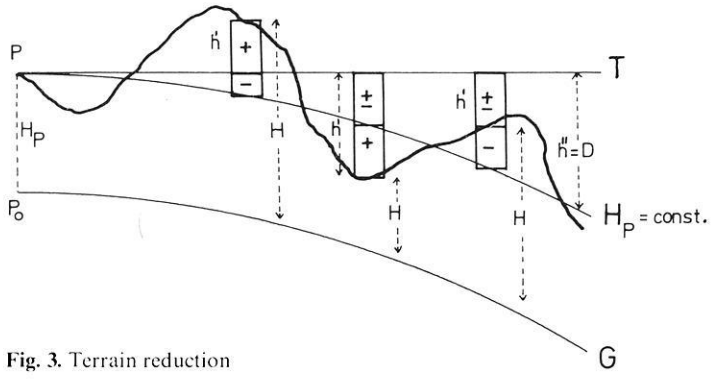

Fig. 3. Terrain reduction

2.2. Terrain Reduction

In order to compute free air anomalies we need as a part of the whole reduction the terrain reduction, which term means the (computational) levelling of the terrain. Corresponding to (2-2) we get:

$$\delta g_{\mathrm{Ter}} = \delta g'_{\mathrm{Ter}} + \delta g''_{\mathrm{Ter}} = f(h') + f(h'') = f(|H - H_P - D|) - f(D). \tag{2-4}$$

The difference between (2-2) and (2-4) consists only of H_P in the expression for h''.

If and only if the density is homogeneous throughout the reduction region we can convert Bouguer anomalies to free-air anomalies and vice versa by applying the Bouguer plate of thickness H_P.

3. Computational Formulas, Outlines of the Program

All computations were carried out by means of a FORTRAN-program with the CDC CYBER 73/76 of the "Regionales Rechenzentrum Niedersachsen" in Hannover. The computation-expenses for one point were less than 1 DM.

3.1. Outer Region

The orthogonal grid for the outer region is constituted by the full-km-values of the ordinary UTM- or Gauss-Krueger-coordinates X, Y. We establish a local coordinates system x, y, so that the center of the extreme south-west square obtains the coordinates ($x = 1$ km, $y = 1$ km), cf. Fig. 4. These local coordinates also represent the indices for the data storage of all heights of the squares $H(x, y)$ in the core memory of a digital computer. This has the great advantage, that for storing x, y, H only one comfortably organizable core-word is necessary. The density values $\rho(x, y)$ are stored in the same manner. The data for the outer region is fed into the computer only once for all stations in the region. Control statements take care of erroneous and missing data. Afterwards an optional num-

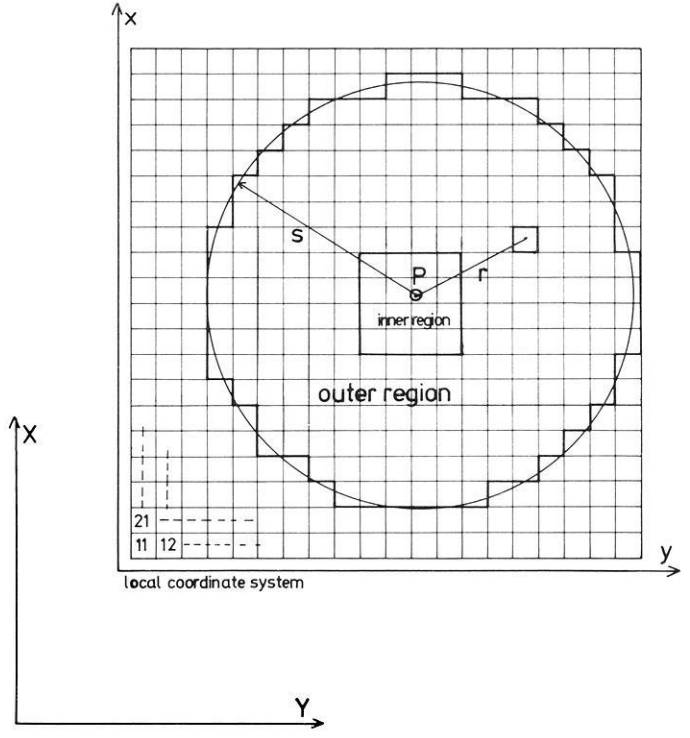

Fig. 4. Outer region

ber of data referring to the stations may be fed in. Then according to a codeword the topographical resp. the terrain reduction is computed.

The data referring to a station consists of point number, coordinates X_P, Y_P, H_P, radius s of reduction area and mean heights for the inner region. The coordinates X_P, Y_P are transformed to x_P, y_P.

For all squares the centers of which are inside the radius s, the gravity effect is evaluated in the following way:

The distance of a square is:

$$r = \sqrt{(x - x_P)^2 + (y - y_P)^2}\,. \tag{3-1}$$

The area of a square is always $F_Q = 1\ [\mathrm{km}^2]$.

Under the condition, that the substitution area also should be of approximately quadratic shape, we obtain:

$$\Delta\alpha = \frac{1}{r}, \qquad r\ [\mathrm{km}] \tag{3-2}$$

and:

$$r_i = r - 500\ \mathrm{m}$$
$$r_a = r + 500\ \mathrm{m}. \tag{3-3}$$

These values are inserted in (2-1). All single gravity effects δg are summed.

3.2. *Inner Region*

The inner region of $4 \times 4\,km^2$ is covered by a template with 44 compartments, centered to the station, and the innermost 100 m zone (cf. Fig. 5). The compartments 1 ... 24 are shaped under the conditions, that on one hand the gravity effect is constant if the terrain has a mean constant inclination and that on the other hand the height-estimation is facilitated. The triangles 25 ... 28 serve for the transfer to the orthogonal grid. The area of the compartments 29 ... 44 is variable according to the position of the station in the grid. When estimating mean heights of these compartments, only the inner parts (cf. Fig. 5) are regarded. All compartments are replaced by areas bounded by polar coordinates.

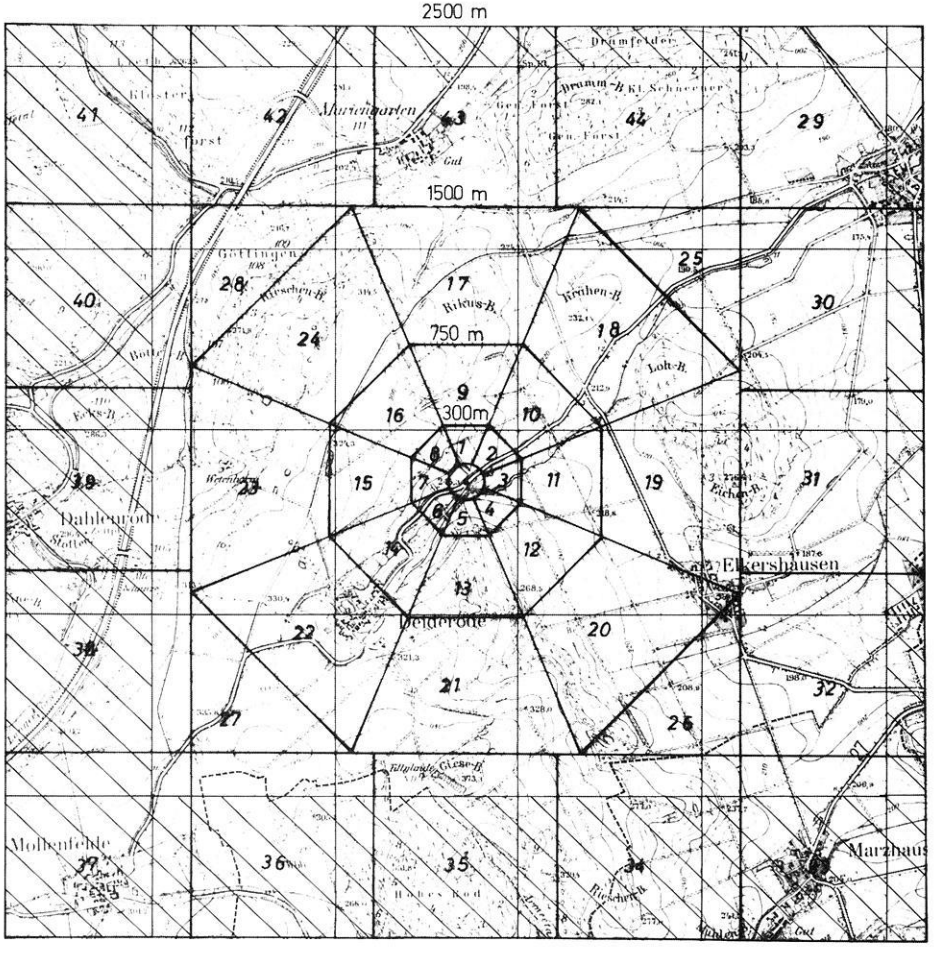

Fig. 5. Inner region (1:25000 map, reduced)

The values to be introduced into (2-1) are:

	$\Delta\alpha$ [R]	r_i [m]	r_a [m]
$i=1 \dots 8$	0.7854	100.00	308.10
$i=9 \dots 16$	0.7854	308.10	770.27
$i=17 \dots 24$	0.7854	770.27	1540.55
$i=25 \dots 28$	0.3537	1446.69	2068.00

$i=29 \dots 44$: Area F and distance r are computed from the station-coordinates within the grid. Setting

$$r_a - r_i = \sqrt{F},$$

we obtain

$$r_a = r + \tfrac{1}{2}\sqrt{F}$$
$$r_i = r - \tfrac{1}{2}\sqrt{F} \tag{3-4}$$

and

$$\Delta\alpha = \frac{\sqrt{F}}{r}. \tag{3-5}$$

For the computer program, only the 44 mean height- and density values are to be fed in.

3.2.1. 100 m-zone. If the inmost surrounding of the station is not approximately horizontal, we may use e.g. the method of a "two-dimensional" mass. The profile in the direction of steepest inclination is recorded on a diagram. The inclination and curvature rectangular to this direction should be negligible. One diagram of this type may be seen in (Jung, 1961, p. 152). We get the terrain reduction by means of this diagram. For the topographical reduction we additionally use (2-1), inserting $r_i = 0$, $r_a = 100$ m, $\rho = \rho_P$ and $h = h'' = H_P$.

4. Error Analysis

We shall estimate the influence of the substitution of the original quadrangles and triangles through ring-sectors. It is not our aim, however, to compare the quality of terrain representation of some conventional templates and our template. The representation always depends on the density of estimated height values. Above all we shall compare our results of some practical computations with those obtained by means of a conventional template.

Inner Region

We divide the inner 1500 m × 1500 m-area into small sectors. If we assume constant height and constant density, we can restrict ourselves to the range $\alpha = 0° \dots 45°$. We use formula (2-1), inserting $r_i = 100$ m, $r_a = \dfrac{1500 \text{ m}}{\cos\alpha_m}$, where α_m is the mean azimuth of the resp. sector.

For $\Delta\alpha$ we take values of $\Delta\alpha = 5°$ decreasing down to $\Delta\alpha = 1°$. This procedure gives us the limit for $\Delta\alpha \to 0$ with a sufficient accuracy. The results differ from our results not more than 1% up to $h = 1000$ m.

Outer Region

The nearest km-square has been subdivided into small sectors like in the inner region with $\Delta\alpha = 1{,}5° \ldots 0{,}5°$. The radii r_i, r_a have been computed according to the boundaries of the square and again we used formula (2-1). The difference to our computation does not exceed 3% ($100\text{ m} \leqq h \leqq 5000$ m, $h = \text{const.}$) and decreases quickly with increasing distance r.

Comparison with a Conventional Template

Computations of the terrain reduction with constant density were carried out for 38 stations in the Harz mountains ($50\text{ m} < H < 1000$ m) using a reduction radius $s = 30000$ m. Mean height estimations and computations were completely independent. Assuming the same accuracy for both methods we get a standard error of

$$m = \pm\sqrt{\frac{[dd]}{2n}} = \pm 0.12 \text{ mgal},$$

whereas the mean reduction amounts to 1.5 mgal. The standard error is less than 10% of the terrain reduction, which according to experience is the presumable error caused by estimation of mean heights.

5. Field of Application

We shall compare the number of squares to be estimated with the number of compartments when using a conventional template. We restrict ourselves to the outer region, because in the inner region our method works with a station-centered template too. Considering the accuracy in the outer region, our new method is better in any case, because the grid is denser than any conventional template.

We assume a quadratic shape of the measuring region. We shall compare the outer region with $2260\text{ m} \leqq r \leqq 29000$ m (cf. Tab. 1). The lower bound corresponds to the region of 4×4 km^2. The number of squares to be estimated is computed after $l = (K + 2 \times 29)^2$. The bounds of r mentioned above fairly correspond with the Hayford zones $G \ldots L$ (resp. $2290\text{ m} \leqq r \leqq 28800$ m) consisting of 108 compartments (Heiskanen/Moritz, 1967, p. 140).

We recognize the growing advantage with growing area and growing station-density. Moreover it is advantageous, that we only need one scale for the inner region, and that the estimation of the mean heights for the outer region is facilitated by the constant shape and size of the squares.

Table 1. Number of compartments to be estimated

Area km^2	Total number of compartments (Hayford)		Number of squares independent of station-distance
$K \times K$	1 station per 5 km^2	1 station per 10 km^2	l
10×10	2160	1080	4624
20×20	8640	4320	6084
30×30	19440	9720	7744
40×40	34560	17280	9604

But it is clear, that this method works favourable only for regional computations, not for global ones because of the distortion of the X, Y-coordinates and because of the great number of squares to be estimated for a great reduction radius.

6. Conclusions

The method reported represents a satisfying compromise of station-centered (inner region) and orthogonal station-independent subdivision of terrain for the gravimetric terrain correction, both terrain reduction for free-air anomalies and topographical reduction for Bouguer anomalies. It is no longer advisable, to split the Bouguerreduction into terrain reduction and Bouguer-plate reduction. It is easy to regard variable density-values.

Acknowledgements. I thank Dipl.-Ing. H. Drewes for leaving the computations of the conventional terrain reduction for the purpose of estimation of accuracy.

This work is part of the research project "Testnetz Westharz", which is sponsored by the "Deutsche Forschungsgemeinschaft" and performed at the "Institut für Theoretische Geodäsie" (Director: Prof. Torge).

References

Ehrismann, W.: Ein allgemeines Verfahren zur digitalen Berechnung der Schwerewirkung von Modellkörpern. Z. Geophys. **39**, 131–166 (1973)

Heiskanen, W.A., Moritz, H.: Physical Geodesy, San Francisco and London: W.H. Freeman and Comp. 1967

Jung, K.: Schwerkraftverfahren in der angewandten Geophysik. Leipzig: Akademische Verlagsgesellschaft Geest & Portig 1961

Dipl.-Ing. Gerd Boedecker
Institut für Theoretische Geodäsie
TUH
D-3000 Hannover
Nienburger Str. 6
Federal Republic of Germany

Received September 2, 1974; Revised Version April 24, 1975

J. Geophys. 41, 523–533, 1975

Pressure Dependence of Elastic Wave Characteristics of Ultramafic Rocks of India *

Y.V. Ramana, M.V.M.S. Rao and B.S. Gogte

National Geophysical Research Institute, Hyderabad

Abstract. Some precambrian ultramafic rocks from peninsular India (pyroxenites, dunites, peridotites, eclogites and serpentinites) are studied using an indigenously developed pressure apparatus. Measurements of velocity and absorption of ultrasonic compressional waves employing a double transducer pulse method up to a hydrostatic pressure of 5.12 kilobars are reported. The changes in velocity due to pressure are concordant to the changes in attenuation decrements in the majority of the rock samples. In general, both velocity and absorption changes are large and tend to be rapid up to a pressure of 1.5 to 2.0 kilobars and are followed by lower gradients up to the peak pressure. Velocity scatter in olivine and pyroxene rich rocks is found to be reduced with increase in stress. Elastic hysteresis loop area is found to bear a nearly linear relationship with the percentage rise in velocity. The chemical and mineralogical studies on these rocks viewed as against the physico-elastic characteristics reveal that the eclogites are formed at intermediate pressures, while dunites are subjected to deutric alteration at shallow depths, presenting a picture of incomplete differentiation of the mantle magma.

Key words: Pressure dependence – Physico-elastic characteristics – Ultrasound velocity – Ultrasound absorption – Ultramafics of India.

1. Introduction

The study of ultramafic rocks in general and olivine rich rocks such as dunites and peridotites in particular, under different conditions of pressure are important, since olivine is a major constituent of the possible mantle rocks. Laboratory experiments on the elastic properties with emphasis on olivine rich rocks are reported by Birch (1960, 1961), Christensen (1966, 1968, 1971, 1974), Christensen and Ramananantoandro (1971), Afanasyev *et al.* (1965), Bajuk *et al.* (1967), Kanamori and Mizutani (1965), Kumazawa *et al.* (1971), Babuska (1972) and others. These laboratory experiments on rocks under different confining pressures also assume importance in view of the recent seismological evidences (Hess, 1964; Keen and Tramontini, 1970). Some results in brief, on the ultramafic

*NGRI/HP–23/74–75.

rocks from the Indian sub-continent are reported by Ramana and Rao (1974) on the compressional velocities at pressures up to five kilobars but in the present study a fuller analysis of the measurements is made to explain the nature of the variation in physical properties noticed in them.

2. Experimental

The experimental arrangement is due to Ramana (1970) and some particulars of the technique are already reported by Ramana and Rao (1973, 1974). Rock samples of 2.54 cm dia. and 4 to 6.5 cm long are specially prepared to have lapped plane parallel faces. Lead zirconium titanate (PZT) ceramic circular discs of 10 mm dia. and 1 MHz natural frequency vibrating in the compressional mode housed in transducer holders of 2.54 cm dia. and about the same length are attached to either end of each rock sample allowing direct contact between the piezo-material and the test sample. The sample together with the PZT housings are enclosed in a heat shrunkable thin transparent tube and sealed at both ends taking care to let out the required electrical leads. The transit time in the sample is measured to the nearest 0.01 micro second (with a HP Pulse Generator on the driving side and a Tektronix preamplifier and fast writing oscilloscope with delay time movable marker facility on the receiving side) while it is subjected to different confining pressures. The velocity measurements are accurate to $\pm 1\%$. The high pressure apparatus is of the piston-cylinder type for the application of all sided fluid pressure with a sealed bottom encasing the shielded electrical leads. Pressure is produced under a hydraulic ram at 27° C and can be read to ± 30 bars.

3. Results and Discussion

3.1. Chemical Data

Partial chemical analyses of the samples are carried out by standard wet and dry chemical methods (Shapiro and Braunock, 1962) and the results are shown in Table 1. The computed values of mean atomic weight (m) vary between 18.76 (serpentinite) and 22.18 (eclogite) and the present results are in agreement with the results reported by Birch (1961). The average value of m for the samples studied is found to be 21.10 and this is close to the average value of 21.00 for ultrabasic nodules in basalts and kimberlite diatremes (Christensen, 1968) whose composition is similar to the uppermost portion of the earth's mantle.

Some details of the petrography and mineral chemistry, in particular, of Sittampundi eclogites are reported by Rao *et al.* (1974), where the dependence of compressional wave velocity on the mineral chemistry of eclogites is discussed presenting the view that the Sittampundi eclogites crystallized in their intermediate pressure granulite facies. Eclogites are found to be showing a lower Mg/Fe ratio (average 1.36) in comparison to the other ultramafic rocks (average 4.41). The mineralogical and chemical characteristics of the present rocks together with

Table 1. Partial chemical analysis of the rock samples

Wt%	Dunite		Pyroxenite		Picrite	Eclogite		Serpentinite
	N-26	34	CH-4	SR-7	541	SC-99	SC-58	BT-13
SiO_2	42.32	39.17	54.17	52.87	40.67	43.16	40.50	40.67
TiO_2	Tr	Tr	2.40	3.20	0.33	Tr	Tr	Tr
Al_2O_3	2.64	1.57	2.57	3.35	10.01	16.30	20.03	2.52
Fe_2O_3	1.69	2.26	1.06	2.49	0.76	3.76	2.20	3.37
FeO	7.80	7.32	5.56	4.40	9.32	6.08	9.52	3.04
CaO	0.67	1.34	2.35	3.14	5.38	14.35	10.99	1.46
MgO	39.57	44.59	30.37	28.56	31.72	13.54	15.44	36.94
K_2O	0.13	0.11	0.29	0.36	0.26	0.11	0.12	0.26
Na_2O	0.95	0.80	0.95	1.05	1.75	2.00	0.62	0.55
Total	95.77	97.16	99.72	99.42	100.20	99.30	99.42	88.81
'm'	20.37	20.83	21.06	21.53	21.95	22.18	22.14	18.76

the existing information on Indian ultramafics (Diwakar Rao *et al.*, 1975) indicate that the original magma was heterogeneous and not completely differentiated and they resemble the peridotite komatiite of South Africa containing high Ca, low Al, with forsterite type of olivine.

3.2. Velocity and Amplitude

The results of compressional velocity measured at intervals of 1 kb are presented in Table 2 for the different samples together with their density and porosity values. Using these results, the extrapolated velocity values at 10 kb are evaluated from the linear relationships between log (dv/dp) and log (p). This has enabled

Table 2. Compressional wave velocities (m/sec) in ultramafic rocks at different pressure

Sample No.	Rock Type	Density gm/cc	Porosity %	Pressure in kilobars						
				0.001	1	2	3	4	5	(10)
CH-4	Pyroxenite	3.279	0.24	7545	7725	7793	7825	7850	7850	(7885)
SR-7	Pyroxenite	3.250	0.71	7227	7500	7576	7606	7626	7645	(7712)
B-9	Pyroxenite	3.251	4.01	6332	7500	7635	7708	7812	7824	(7996)
N-26	Dunite	3.130	0.99	6537	6840	6988	7062	7110	7125	(7209)
34	Dunite	2.750	0.40	6547	6656	6725	6780	6818	6825	(7033)
CH-23	Peridotite	3.168	0.32	6619	6810	6936	7020	7055	7088	(7164)
541	Picrite	3.041	0.28	6664	6820	6885	6930	6953	6962	(7130)
BT-13	Serpentinite	2.746	0.58	5585	5700	5810	5883	5930	5980	(6099)
FS-3	Serpentinite	2.269	6.57	3859	4925	5130	5220	5300	5337	(5454)
SC-99	Eclogite	3.147	0.67	6964	7320	7415	7458	7477	7500	(7604)
SC-58	Eclogite	3.583	1.28	6697	7072	7210	7353	7425	7502	(7819)

Table 3. Comparison of the velocity data (km/sec) at 4 and 10 kb of ultamafic rocks

Rock Type	USA			USSR			Japan			Czechoslovakia			India	
	4	10	Ref.	4	10	Ref.	4	10	Ref.	4	10	Ref.	4	10
Pyroxenite	7.88	8.01	1	7.40–8.00	–	2	–	–		7.40–7.80	–	5	7.63–7.85	(7.71–8.00)
	7.89–7.97	8.00–8.08	9	7.50	–	6	–	–						
Dunite (Partially serpentinized)	6.55 7.41	6.79 7.62	1 4	7.70	7.88	6	7.46	7.65	3	7.34	–	5	6.82–7.12	(7.03–7.21)
Peridotite (Partially serpentinized)	6.05–7.37	6.30–7.62	4	7.70 7.40	– –	2 6	5.90–7.03	6.33–7.16	3	5.83–6.63	–	5	6.95–7.06	(7.13–7.16)
Eclogite	7.57–7.89	7.71–8.01	1	8.04	8.20	6	8.20–8.44	8.48–8.50	3	8.37–8.40	(8.41–8.61)	5	7.44–7.48	(7.60–7.82)
	7.88–8.37	(8.01–8.47)	7				7.98–8.16	(8.10–8.27)	7	8.38	8.45	9		
	8.11–8.38	8.27–8.45	9											
Serpentinite	5.80–6.67	6.00–6.84	1											
	4.91	5.23	4	–	–	–	–	–	–	6.37	–	5	5.30–5.93	(5.45–6.10)
	5.09–5.32	5.45–5.57	8											

Ref.: 1) Birch (1960). 2) Afanasyev' *et al.* (1965). 3) Kanamori & Mizutani (1965). 4) Christensen (1966). 5) Bajuk *et al.* (1967). 6) Volarovich *et al.* (1967). 7) Kumazawa *et al.* (1971). 8) Christensen (1972). 9) Christensen (1974).

comparison of the present results with those of others (see Table 3). In all the samples studied, as expected, the velocity increased and the absorption decreased with increasing pressure, tending to present saturation values at about 1.5 kb. This initial rise in velocity and increase in normalised pulse amplitude which is a measure of the decrease in absorption due to the application of confining pressure is found to depend largely upon the porosity of the specimens and this is well refelcted by the results of Fig. 1. Assuming that the effect of porosity becomes reduced to an appreciable degree at pressures of the order of 1.5 to 2.0 kb, the changes in elastic wave propagation characteristics above 1.5 kb reveal to a large extent the intrinsic properties of the medium. On this basis, the increase in velocity at different pressures (1.5 to 5.0 kb) with respect to that at 1.5 kb is examined and the results are shown in Fig. 2.

The changes in the amplitude of the first received pulse measured as a function of the applied pressure enabled the computation of attenuation decrement of ultrasonic compressional energy at different pressures. This is done on the basis of the relation

$$\Delta\alpha=\alpha_0-\alpha_S=\frac{20\log(A_S/A_0)}{L}\ \text{dB/cm}$$

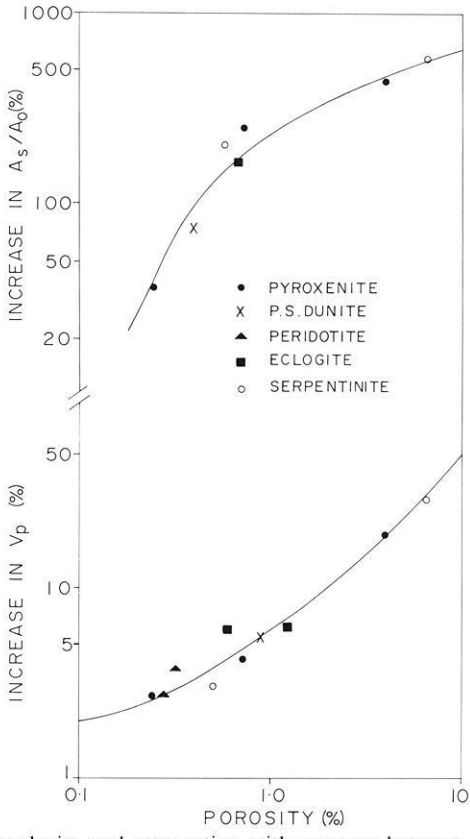

Fig. 1. Effect of porosity on compressional wave velocity and attenuation with pressure between 1 bar and 1.5 kb

where α_0 is the attenuation value at atmospheric pressure, α_S is the attenuation value at the desired pressure, A_S/A_0 is the normalised amplitude of the pulse at the desired pressure, L is the length of the specimen in cm. The amplitude changes are measured in seven specimens and the attenuation decrements computed and plotted against pressure (Fig. 3).

Based on the information available from petrography and chemistry of the rocks studied, variations in the elastic and inelastic properties of individual samples are explained below. Details of textural features and mineral composition of these rocks are reported by Ramana and Rao (1974).

3.3. Pyroxenites

Sample No. B−9 shows, among all samples, the strongest increase in velocity between 1 bar and 1.5 kb and the trend in maintained also up to 5 kb. This is to a certain degree due to its porous nature (porosity 4%). The high porosity of the sample may be explained to be a result of the high degree of uralitization observed in the specimen, especially at the marginal boundaries of the coarse

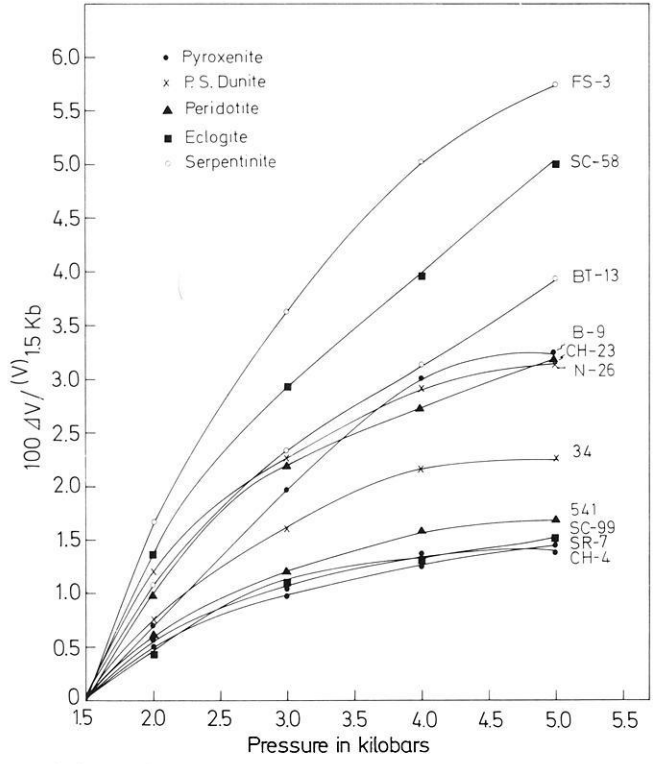

Fig. 2. Change in compressional velocity with pressure normalized to 1.5 kbar

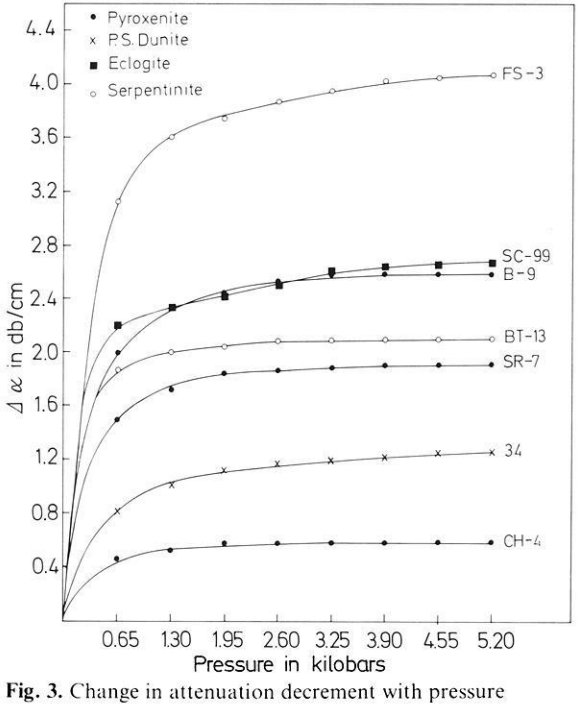

Fig. 3. Change in attenuation decrement with pressure

pyroxene in the groundmass which also contributes to give rise to reduced cohesion between the grains. Pyroxenite from Sukrangi (SR-7) is fairly compact though it has undergone some alteration (serpentine 10%) and does not exhibit a steep rise in velocity in the initial stages. Pyroxenite from Chalk Hills (CH-4) is free from alteration, presenting a strong cohesion in between the grains, and shows small changes in velocity with pressure like the Sukrangi pyroxenite. It is interesting to note that measurements made before and after the pressure tests showed no appreciable change in density and porosity of samples CH-4 and SR-7 while Sample B-9 showed an increase in density by about 2% accounting for a reduction in porosity and these observations are in consonance with the behaviour of the velocity. Also, as seen in Fig. 3, the changes in $\Delta\alpha$ in all the three pyroxenites are truly in accordance with the trend of velocity changes. Since the alteration of pyroxene is not significant, the results obtained are quite comparable to those reported by earlier workers that are presented in Table 3.

3.4. Dunites

The dunite samples collected are from different chromite mines and found to be serpentinized to varying degrees. This explains their low densities and velocities in comparison to the high values of others shown in Table 3. Sample No. 34 is found to be compact and of low porosity (0.4%). This accounts for the small increase in velocity (1.9%) that is observed when the sample is exposed to a pressure of 1.5 kb. The second sample (N-26) presents a large initial increase in velocity (5.7%) which is in accordance with its higher porosity (1%). Appreciable differences in the velocity characteristics are observed in the pressure range 1.5 to 5 kb and 1.5 to 10 kb respectively as seen in Fig. 2 and Table 2. For sample (34) (see Fig. 3), the $\Delta\alpha - P$ gradient is positive beyond 1.5 kb and it is similar to the trend shown by the serpentinite sample (BT-13) and this may be due to its large serpentine content (34%). This improvement in the elastic wave propagation beyond 1.5 kb can be due to the finite compression of the serpentine minerals.

3.5. Peridotite and Picrite

The velocity values at 5 kb (see Table 2) in sample No. N-26 (partially serpentinized dunite) and CH-23 (partially serpentinized peridotite) are comparable and are uniformly higher than the values in sample No. 34 (partially serpentinized dunite) and 541 (picrite) which may be attributed to the higher olivine content of the first two specimens. The velocity values in the Indian peridotitic rocks are comparable with those from other countries at 4 kb.

Changes in velocity characteristics with pressure are found to be nearly identical in both peridotite and picrite despite the presence of plagioclase (19%) and the occurrence of magnetite in negligible quantities in the latter. Initial rise in velocity is in accordance with the porosity value of the peridotite as can be noticed in Fig. 1. Fig. 2 shows that the application of pressure beyond 1.5 kb

yielded a comparatively greater rise in velocity in the peridotitic rock (CH-23) than in the picrite (541) which could be due to the difference in their textural features and the distribution of serpentine in the rock.

3.6. Eclogites

Both eclogite samples are from Sittampundi layered complex containing different amounts of garnet, but having similar textural features. Though the porosity values are slightly different, the change in velocity at 1.5 kb is the same (6%) in both samples and this is in general greater than the percentage rise in velocity values shown by all the other rock types, whose porosity values are comparable to the Sittampundi eclogites. Although the porosity is low (1%), the quality of acoustic transmission is poor at room conditions and it improved only after the application of certain pressure. Fig. 2 shows that the velocity gradient in the case of sample No. SC-58 is higher than that of sample No. SC-99 which could be due to the differences in porosity, greater rim alteration noticed in sample No. SC-58, and due to the differences in the mineral chemistry of the two samples. This has been dealt with in detail recently by Rao *et al.* (1974), while examining the possible causes for lower velocity values of Indian eclogites (Table 3) in comparison to those from Japan and Czechoslovakia.

3.7. Serpentinites

The serpentinite samples studied are collected from the same region where chromite is being mined, but differences are noticed in their composition and physical properties. Chrysotile rich rock (FS-3) is characterized by a lower density, higher porosity and hence a larger and more rapid increase (30.8%) in velocity at 1.5 kb than the antigorite rich rock (BT-13), which showed a rise of 3.0%. Also, the percentage rise in velocity at 5 kb in the chrysotile rich rock is greater than in the antigorite rich rock as illustrated in Fig. 2, with the corresponding differences becoming apparent in the attenuation decrements as well, which may be seen in Fig. 3. Of all the samples studied, FS-3 is found to be the most porous rock and also it exhibits the largest increase in velocity and amplitude due to the application of pressure. Differences in the velocity values at 5 kb in the two serpentinites studied are in accordance with the velocity data in serpentine minerals associated with them. The results on the two serpentinite samples studied are comparable with those reported by earlier workers (Table 3).

3.8. Elastic Hysteresis

Wave velocity is measured with increase in pressure from 1 bar to 5 kb as well as with decrease in pressure from 5 kb to 1 bar for some samples and the results are given in Fig. 4. Velocities obtained with increasing pressure are slightly lower than those found with decreasing pressure which is indicative of the elastic hystere-

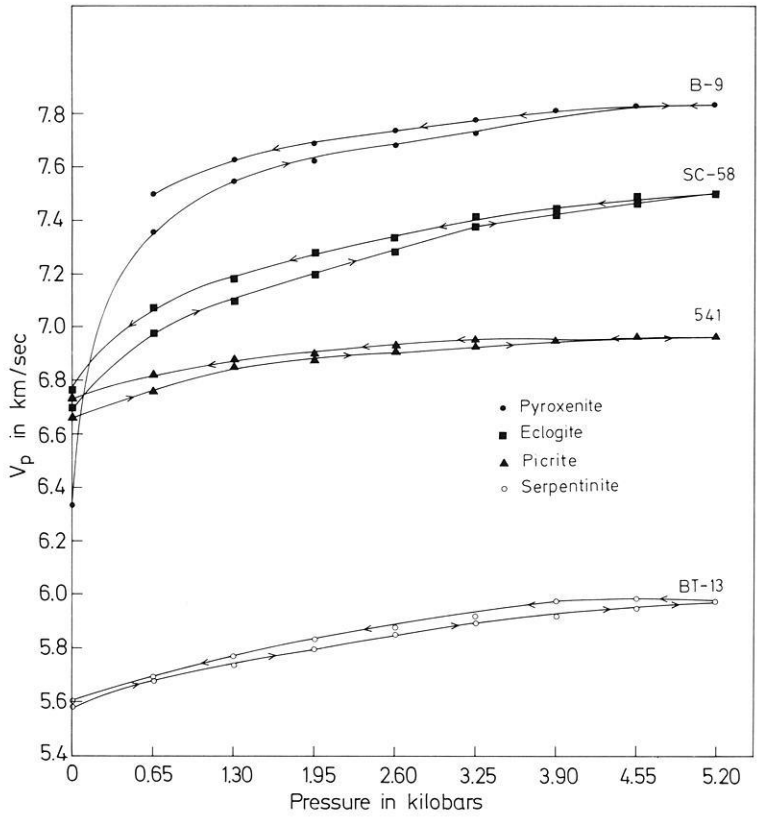

Fig. 4. Pressure hysteresis of compressional wave velocity

sis. Sample Nos. B-9 (Pyroxenite) and SC-58 (Eclogite) are found to exhibit significant hysteresis at pressures below 2 kb, whereas in the fine grained serpentinite (BT-13) and compact picrite (541), departures from the mean curve are low. Fig. 4 enabled the evaluation of individual loop areas (covered between the limits 1 bar and 5 kb) that are a result of the effect of hysteresis in the respective samples. Using these, an interesting relation between the percentage increase in compressional velocity and loop area of the different rock types is drawn in Fig. 5 which assumes a nearly linear relationship. Although hysteresis is attributed primarily to the adjustment of the rock porosity to changes in pressure, it can also indicate to a certain extent the energy dissipated in the sample during a stress cycle.

4. Conclusions

It is clear that the rocks studied are essentially upper mantle rocks having undergone deutric alteration to varying degrees which is reflected by their elastic behaviour under pressure. In general for all the samples, the effect of porosity is

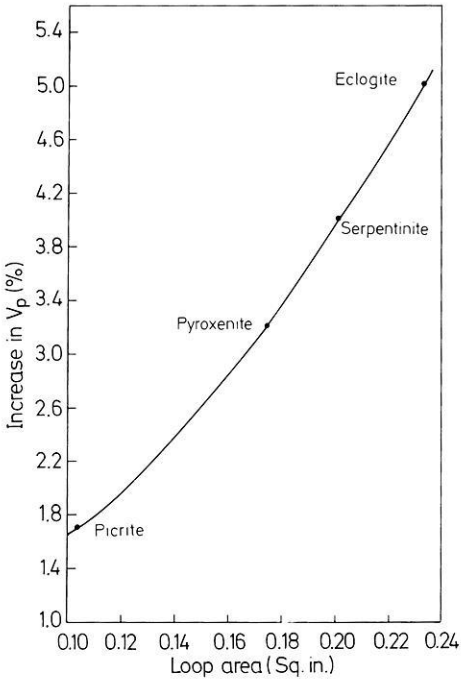

Fig. 5. Dependence of loop area on percentage rise in velocity

prominent up to about 1.5 to 2.0 kb. Variations in elastic wave characteristics beyond 1.5 kb are found to be controlled by the mineralogical composition and texture of rocks. Scatter in velocity values for the group of dunites, pyroxenites, picrite and peridotite is found to be reduced from 8.8% (NTP) to 6.8% (5 kb). The percentage rise in velocity due to the increase of pressure from 1.5 to 5.0 kb is found to bear a linear relation to the loop area of the hysteresis envelope of individual samples.

Acknowledgement. The authors express their thanks to Mr.C. Satyanarayana for assistance in the maintenance of the pressure equipment, Dr. Diwakar Rao for the chemical analysis and to Dr. Hari Narain, Director, N.G.R.I., for encouragement and permission to publish.

References

Afanasyev, G.D., Volarovich, M.P., Bayuk, Ys.I., Galdin, N.Ye.: Investigation of elastic wave velocities in ultrabasic rocks of the Monche-Gorsk pluton under conditions of high multilateral pressure. Dokl. Akad. Nauk SSSR, Earth Sci. **155**, 6–10 (1965)

Babuska, V.: Elasticity and anisotropy of dunite and bronzitite, J. Geophys. Res. **77**, 6955–6965 (1972)

Bajuk, E.I., Volarovich, M.P., Klima, K., Pros, Z., Vanek, J.: Velocity of longitudinal waves in eclogites and ultrabasic rocks at pressures to 4 kilobars. Studia Geophys. geodaet. **11**, 271–280 (1967)

Birch, F.: The velocity of compressional waves in rocks to 10 kilobars Part I. J. Geophys. Res. **65**, 1083–1102 (1960)

Birch, F.: The velocity of compressional waves in rocks to 10 kilobars Part II. J. Geophys. Res. **66**, 2199–2224 (1961)
Christensen, N.I.: Elasticity of ultrabasic rocks. J. Geophys. Res. **71**, 5921–5931 (1966)
Christensen, N.I.: Chemical changes associated with upper mantle structure. Tectonophysics **6**, 331–342 (1968)
Christensen, N.I.: Fabric, Seismic anisotropy and tectonic history of twin-sisters dunite. Bull. Geol. Soc. Am. **82**, 1681–1694 (1971)
Christensen, N.I.: The abundance of serpentinites in the oceanic crust. J. Geol. **80**, 709–719 (1972)
Christensen, N.I.: Compressional wave velocities in possible mantle rocks to pressures of 30 kilobars. J. Geophys. Res. **79**, 407–412 (1974)
Christensen, N.I., Ramananantoandro, R.: The elastic moduli and anisotropy of dunite to 10 kilobars. J. Geophys. Res. **76**, 4003–4010 (1971)
Diwakar Rao, V., Satyanarayana, K., Naqvi, S.M., Hussain, S.M.: Geochemistry of Dharwar ultramafics and the Archaean mantle. Lithos **8**, 77–91 (1975)
Hess, H.H.: Seismic anisotropy of the uppermost mantle under the oceans. Nature **203**, 629–631 (1964)
Kanamori, H., Mizutani, H.: Ultrasonic measurements of elastic constants of rocks under high pressures. Bull. Earthquake Res. Inst. (Tokyo University) **43**, 173–194 (1965)
Keen, C., Tramontini, C.: A seismic refraction survey on the mid-Atlantic ridge. J. Geophys. **20**, 473–491 (1970)
Kumazawa, M., Helmstaedt, H., Masaki, K.: Elastic properties of eclogite xenoliths from diatremes of the East Colorado plateau and their implication to the upper mantle structure. J. Geophys. Res. **76**, 1231–1247 (1971)
Ramana, Y.V.: High pressure test facilities to five kilobars. Annual report of Natl. Geophys. Res. Inst. India, 31–32 (1970)
Ramana, Y.V., Rao, M.V.M.S.: Pressure derivatives of sound velocities in rocks. J. Acoust. Soc. India **1**, 154–157 (1973)
Ramana, Y.V., Rao, M.V.M.S.: Compressional velocities in ultramafic rocks of India at pressures to five kilobars. Geophys. J. Royal Astron. Soc. **37**, 207–212 (1974)
Rao, M.V.M.S., Ramana, Y.V., Gogte, B.S.: Dependence of compressional velocity on the mineral chemistry of eclogites. Earth Planet Sci. Lett. **23**, 15–20 (1974)
Shapiro, L., Braunock, W.W.: Rapid analysis of silicate, carbonate and phosphate rocks. U.S. Geol. Surv. Bull. 1144–A, 56 (1962)
Volarovich, M.P., Kursksev, A.K., Tomashevskaya, L.S., Tuzova, L.L., Urazaov, B.M.: The correlation between the longitudinal wave propagation velocity and rock density at high confining pressures. Bull. (IZV). Acad. Sci. USSR, Phys. Solid Earth **5**, 276–279 (1967)

Dr. Y.V. Ramana
Scientist-in-charge
High Pressure and Rock Mechanics Laboratory
National Geophysical Research Institute
Hyderabad - 500007 India

Received October 29, 1974; Revised Version April 3, 1975

J. Geophys. 41, 535–536, 1975

Short Communications

Paleogravity—A Possible Chance for Determination of Paleo-Geographic North

L. Stegena

Eötvös University, Budapest

Key words: Paleogravity – Paleogeographic north.

As we know since the activities of Eötvös (1848–1919, cf. Eötvös 1953) a Cavendish pendulum with a suspension wire of infinitely small torsion will turn towards and assume its equilibrium along the direction of the minimum curvature of the earth. This direction is, of course, equal to the direction of maximum radius, and is dependent upon the location of the pendulum. In a normal case on the earth (*i.e.* in the absence of an anomaly) this direction is the East-West-direction since

$$\rho_{WE}=\frac{a^2}{(a^2\cos^2\varphi+c^2\sin^2\varphi)^{1/2}} \quad \rho_{NS}=\frac{a^2c^2}{(a^2\cos^2\rho+c^2\sin^2\varphi)^{3/2}}$$

(see *e.g.* Egyed 1969) with ρ being the radius of curvature of the earth, a the equatorial radius, c the polar radius, and φ the geographical latitude.

The R curvature of the gravitational acceleration which is proportional to the driving momentum is very small.

As it is known,

$$R=\sqrt{U_\Delta^2+4U_{xy}^2}$$

where $U_\Delta=U_{yy}-U_{xx}$, being the Northern, y the Eastern direction; and the indices indicating the derivatives of the proper gravitational potential. On the normal Earth:

$$U_{yy}=U_{xx}=0$$

and

$$R=10{,}26\cos^2\varphi \quad \text{eötvös.}$$

If needlelike sediments deposit in the sea water then they – as gravitational compases – during the sedimentation are regulated into in Eastern-Western direction by the driving moment of the curvature of the gravitational acceleration. Therefore the direction-statistics of the needlelike elements of the old sea sediments afford a possibility to the determination of the paleogeographic directions.

However, as it is known from the many Eötvös balance measurements, the earth, on its many points, possesses a considerable local curvature anomaly,

these anomalies being many times greater than the normal value of the curvature. This difficulty perhaps can be solved by many samples obtained from a larger area.

On the other hand it is probable that the magnetic, electrostatic, surface and other forces, besides waterstreams, and subsequent geological recrystallization processes often sweep away the directing effect of the normal curvature. Direction statistics of calcit or silica needles of recent sea sediments perhaps would show how useful the proposed paleogravitational method might be.

References

Eötvös, R.: Gesammelte Werke. Ed.: P. Selényi. Budapest: Akad. Verlag 1953
Egyed, L.: Physik der festen Erde. Budapest: Akad. Verlag 1969

Prof. L. Stegena
Eötvös Loránd Tudományegyetem
Geofizikai Tanszék
Budapest VIII
Kun Béla tér 2
Hungary

Received April 3, 1975

J. Geophys. 41, 537–540, 1975

Electromagnetic Induction at Dili, Portuguese Timor

F.H. Chamalaun and A. White

School of Earth Sciences, Flinders University of South Australia

Key words: Timor – Geomagnetic deep sounding – Electromagnetic induction – Crustal structure.

The island of Timor lies in the Outer Banda Arc, a pronounced physiographic and tectonic feature marking the boundary between the Indian Ocean and Australian plates. The whole Indonesian-Philippine area is of great geophysical complexity and Timor has attracted particular attention because of its structurally complex geology. It has been suggested (Audley-Charles, 1968) that Timor may have been part of the Australian continental margin, at least since the Permian. If Timor formed part of the leading edge of the Australian continent and collided with an island-arc subduction zone in its northward drift from Antarctica it is probable that it now lies just to the south or perhaps over the subduction zone. Alternative hypotheses suggest that the welding between Australia and Eurasia may now be identified by the Timor Trough (Beck and Lehner, 1974; Fitch and Hamilton, 1974). Unfortunately the location of the subduction zone is not easily identified on the basis of seismic activity.

Since there is very little geophysical data available we have initiated a programme involving a variety of geological and geophysical techniques that may assist in defining the actual location of the subduction zone. In this note we present the results of a pilot geomagnetic depth sounding study carried out in August 1973 at Dili, Portuguese Timor. The technique uses natural variations of the geomagnetic field to detect lateral inhomogeneities in the subterranean electrical conductivity structure. The data are commonly displayed as induction "arrows" of length Z/B and having the direction of B, where Z is the vertical component and B is the horizontal component showing the strongest correlation with Z (Schmucker, 1970). At stations near to deep oceans there is nearly always a strong "ocean edge effect" (Parkinson, 1962) but the induction can be strongly influenced by high conductivity zones associated with active tectonic regions, notably in Peru (Schmucker *et al.*, 1966).

In Fig. 1 we reproduce Parkinson's (1964) arrows for Kuyper, Wyndham and Darwin. As expected, the arrow at Kuyper points straight towards the deep

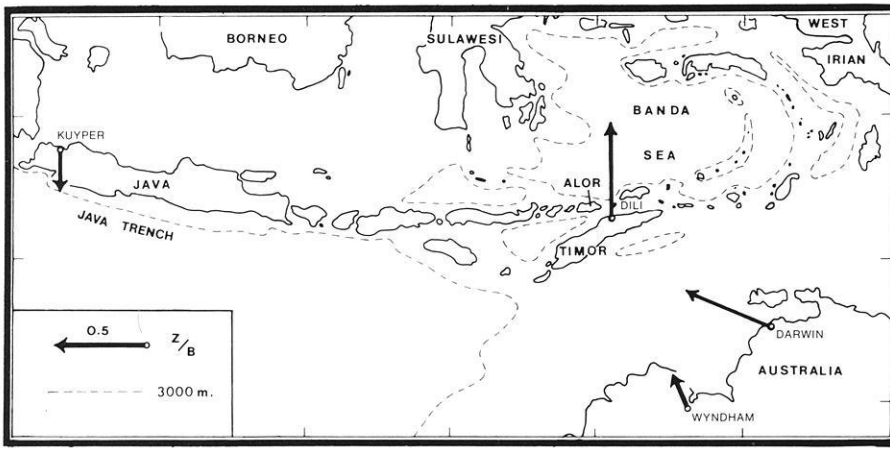

Fig. 1. Map of the Indonesian region. Induction arrows at Kuyper, Wyndham and Darwin from Parkinson (1964). Arrow at Dili is the in-phase arrow for 1 c.p.h.

water of the Java trench which is the site of a northward dipping lithospheric slab in preference to the very shallow water (<200 m) to the north. The arrows at Wyndham and Darwin, though pointing towards the sea, are not strongly correlated with the nearest deep water. Both arrows point to a region south of the island of Timor and the possibility therefore existed that they indicate a zone of high conductivity possibly associated with a subduction zone at or near the Timor Trough. To see if the electromagnetic induction effects in Timor were at all influenced by a zone of high conductivity to the south or by the (extinct) vulcanism to the north, we recorded magnetic variations at Dili on the north coast of Portuguese Timor during August 1973. A three-component fluxgate magnetometer was used, especially developed at Flinders University to be cheap, portable and robust and of low power consumption. To provide thermal stability the magnetometer was buried under a meter of soil. Its performance was checked at Toolangi Geophysical Observatory. The recordings at Dili showed a noticeably strong correlation between the H and Z components. Three 24-hour lengths of data were digitized at 2-minute intervals, the in and out-of-phase components of the transfer functions were obtained in the manner described by Schmucker (1970) and White (1973). Fig. 2 shows the associated induction arrows for a range of periods. The in-phase arrow for 1 c.p.h. is also shown in Fig. 1, for comparison with Parkinson's arrows.

The results show two features, firstly that at the shorter periods the induction arrow is large and points due north, secondly that at longer periods it shortens and swings west. The in-phase ratio Z/B at 1 c.p.h. is 0.625 (± 0.025) which is slightly higher than that at Darwin and more characteristic of coastal stations adjoining deep water. This is most probably caused by the proximity of the Banda Sea which is generally over 3000 m deep. There is no apparent correlation with the Darwin result and we must therefore suppose that the Darwin arrow points to a conductivity structure much closer to Darwin than to Timor.

The fact that the arrow at Dili decreases and swings west for longer period variations is probably explicable in terms of a zone of high conductivity associated

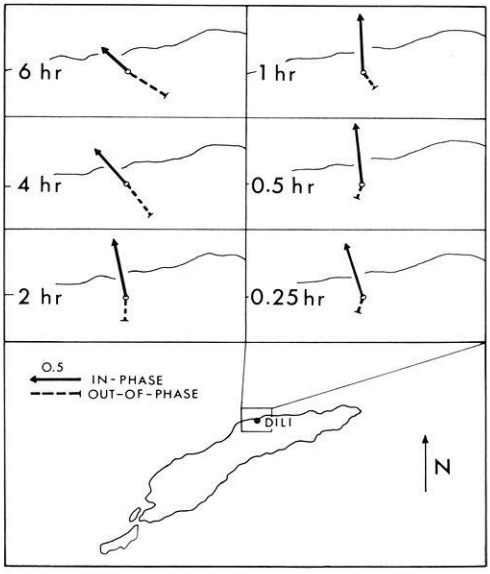

Fig. 2. Induction arrows for a range of periods at Dili, Portuguese Timor

with the still active volcanic inner arc west of Alor. Because of the deeper penetration of longer period variations one would expect this phenomenon to be associated with deep crustal or mantle conductivity contrasts. A longer recording period is desirable to investigate this.

We conclude that the induction arrows at Darwin and Wyndham are not related to a subduction zone south of Timor, but are probably the result of crustal inhomogeneities in the Sahul Shelf. On the other hand, the induction arrow at Dili is more obviously correlated with the Banda Sea. However, the induction effect is unexpectedly large, bearing in mind the relatively restricted nature of the Banda Sea. We therefore suspect that it is not simply due to the coast effect alone but may well in part be related to a subduction zone close to the north coast of Timor.

We are indebted to our colleagues in the Flinders University Outer Banda Arc Project, to Mr. J. Brandwyk for help in designing the magnetometer, and to Mr. and Mrs. Favaro for their hospitality in Dili and the use of the magnetometer site.

References

Audley-Charles, M.G.: The Geology of Portuguese Timor. Geol. Soc. Lond. Mem. **4**, 1–76 (1968)

Beck, R.H., Lehner, P.: Oceans, New Frontier in Exploration. Am. Assoc. Petrol. Geol. Bull. **58**, 376 (1974)

Fitch, T.J., Hamilton, W.: Reply. J. Geophys. Res. **79**, 4893–4895 (1974)

Parkinson, D.W.: The influence of continents and oceans on geomagnetic variations. Geophys. J.R. Astr. Soc. **4**, 441–449 (1962)

Parkinson, D.W.: Conductivity anomalies in Australia and the ocean-effect. J. Geomagn. Geoelectr. **15**, 222–226 (1964)

Schmucker, U., Forbush, S.E., Hartman, O., Giesecke, A.A., Casaverde, M., Castillo, J., Salgueiro, R., del Pozo, S.: Electrical conductivity anomaly under the Andes. Carnegie Institution of Washington, Yearbook **65**, 11–28 (1966)

Schmucker, U.: Anomalies of geomagnetic variations in the south-western United States. Bull. Scripps Inst. Oceanogr. **13**, University of California Press, 1970

White, A.: A geomagnetic variation anomaly across the northern Gulf of California. Geophys. J.R. Astr. Soc. **33**, 1–25 (1973)

Dr. A. White
Dr. F.H. Chamalaun
School of Earth Sciences
The Flinders University of South Australia, Bedford Park, South Australia 5042

Received April 7, 1975

J. Geophys. 41, 541–543, 1975

Preliminary Polar Wander Path of Central Iran

H. Soffel

Institut für Allgemeine und Angewandte Geophysik, München

H. Förster

Institut für Mineralogie und Lagerstättenlehre, Aachen

H. Becker

Institut für Allgemeine und Angewandte Geophysik, München

Key words: Polar wander path – Central Iran – Palaeomagnetism.

In 1973, 1974 and 1975 three palaeomagnetic sampling trips were made in Central Iran including the Lut Block for a determination of the polar wander path of Central Iran. This area is believed to be a fragment of Gondwanaland according to paleogeographic evidence and evidence from reconstruction of the Indian Ocean compiled by Förster (1974, 1975) and also according to various geological aspects summarized by Stöcklin (1974). First palaeomagnetic measurements in Central Iran have been published by Becker, Förster and Soffel (1973) showing that the Infracambrian rocks and iron ores of the Bafq region in Central Iran yield similar virtual geomagnetic pole positions as rocks of comparable age from India.

During the three sampling trips between 1973 and 1975 80 localities have been sampled covering rocks from all formations between Quaternary and Infracambrian. The samples (predominantly magmatic rocks and red sandstones) were taken in areas with well known geology and stratigraphy.

The preliminary results presented here originate exclusively from magmatic rocks fulfilling the following criteria:

a) NRM is well grouped and far away from the present geomagnetic field direction in the sampling area (negligible viscous remanent magnetization due to the present field),

b) very good stability of remanence during alternating field demagnetization,

c) the rocks are fresh, unweathered and unaffected by metamorphism,

d) tectonic corrections are unambiguous.

The results in terms of mean virtual geomagnetic pole (VGP) positions for various formations are shown in Fig. 1 and listed in Table 1 using a scheme of presentation introduced by McElhinny (1973). The polar wander paths of Stable Europe, Russian Platform, Africa, Arabia and India are also shown according to McElhinny (1973). The similarity of the polar wander paths of India

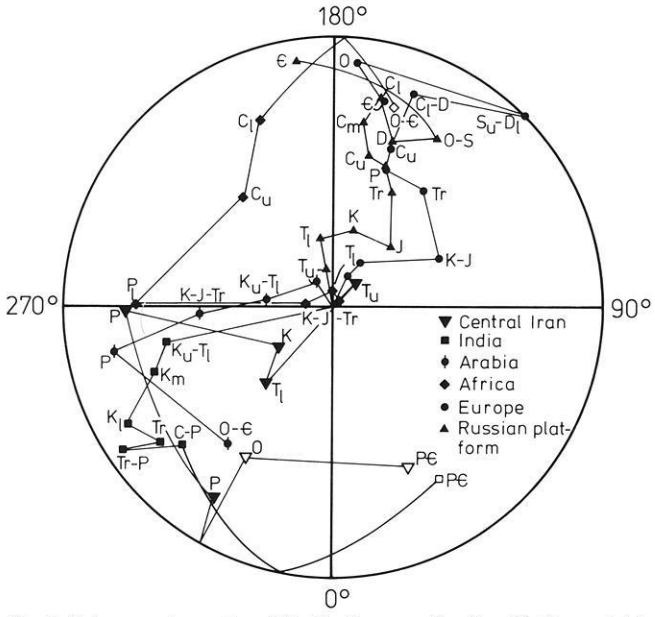

Fig. 1. Polar wander paths of Stable Europe, Russian Platform, Africa, Arabia and India according to McElhinny (1973) together with a preliminary polar wander path of Central Iran (equal area projection)

Table 1. Summary of virtual geomagnetic pole (VGP) positions of Central Iran

Period	N	K	A_{95}	VGP: Lat.	Long.
Upper Tertiary	2	–	–	80.6° N	140.3° E
Lower Tertiary	4	40.4	11.0°	59.5° N	318.9° E
Lower to Upper Cretaceous	3	58.1	10.6°	69.2° N	305.1° E
Permian (possibly Upper Permian)	1	–	–	24.4° N	271.4° E
Permian (possibly Middle and Lower Permian)	2	31.1	17.8°	18.8° N	327.9° E
Ordovician	3	–	–	36.3° S	330.5° E
Infracambrian	11	5.5	22.0°	35.7° S	26.5° E

and Central Iran is obvious. This preliminary palaeomagnetic result therefore supports the idea that Central Iran is a former part of Gondwanaland. The difference for the VGP positions for Lower to Upper Cretaceous and Lower Tertiary between India and Central Iran, both of which are sufficiently well defined, indicates that Central Iran had a much northerly position at that time than India. A former position of Central Iran East of Arabia is compatible with the palaeomagnetic data. The VGP positions for the Mesozoic and Paleozoic of Central Iran are too sparse to allow any detailed reconstructions for these time intervals.

The more complicated palaeomagnetic and rockmagnetic measurements on the remaining samples (red sandstones and other magmatic rocks) in order to improve the Polar Wander Path of Central Iran are presently being made.

The measurements were made in the Institut für Allgemeine und Angewandte Geophysik, Universität München. The sponsorship of the Deutsche Forschungsgemeinschaft is gratefully acknowledged.

References

Becker, H., Förster, H., Soffel, H.: Central Iran, a former part of Gondwanaland? Palaeomagnetic evidence from infra cambrian rocks and iron ores of the Bafq Area, Central Iran. Z. Geophys. **39**, 953–963 (1973)

Förster, H.: Petrologische und metallogenetische Aspekte der Plattentektonik in Iran. In: E. Ehlers, (Ed.): Beiträge zur Physischen Geographie Irans, Marburger Geographische Schriften, 62, S. 7–19. Marburg: 1974

Förster, H.: Continental drift in Iran in relation to the far structures. Afar monograph (Symposium on the Afar region and related rift problems, Bad Bergzabern, April 1974. (Ed. A., Pilger, Clausthal) in press 1975

McElhinny, W.M.: Palaeomagnetism and plate tectonics. Cambridge: University Press, 1973

Stöcklin, J.: Possible ancient continental margins in Iran. In: The geology of continental margins. Ed.: C.A. Burk, C.L. Drake, pp. 873–887. Berlin-Heidelberg-New York: Springer 1974

Prof. Dr. H. Soffel
Dipl.-Geophys. H. Becker
Institut für Allgemeine und Angewandte Geophysik der Universität München
D-8000 München 2
Theresienstraße 41
Federal Republic of Germany

Prof. Dr. H. Förster
Institut für Mineralogie und Lagerstättenlehre der RWTH Aachen
D-5100 Aachen, Wüllnerstr. 2
Federal Republic of Germany

Received June 2, 1975

J. Geophys. 41, 545–547, 1975

Ein astasiertes Vertikalpendel mit tragender Blattfeder*

E. Wielandt
Institut für Geophysik der ETH, Zürich

Astatic Vertical Pendulum Supported by a Leaf Spring

Abstract: A new geometry for medium and long period vertical seismometers or gravimeters has been found where a single, initially flat leaf spring supports the boom in such a way that virtually no restoring force is produced. The free period of the pendulum can be made arbitrarily long, and a maximum of the free period is obtained in the center position. In spite of its extremely simple construction, this pendulum seems to be an alternative to LaCoste systems in many applications.

Key words: Seismometer – Leafspring.

Blattfedern – vor allem flache, nicht vorgespannte – sind viel einfacher und billiger herzustellen als vorgespannte Schraubenzugfedern (Nullängenfedern) für LaCoste-Pendel. Sie werden in verschiedenen Formen in hochfrequenten Geophonen und auch in einigen anspruchsvolleren Seismometerkonstruktionen verwendet (Willmore MKI, Berckhemer FS 60). In langperiodischen Seismometern konnten sie sich bisher nicht durchsetzen, weil keine problemlose Methode zur Astasierung bekannt war[1]. Dabei wären Blattfedern gerade hier, abgesehen von der einfacheren Fertigung, wegen ihrer höheren Eigenresonanz und besseren Wärmeübertragung vorteilhaft (Unterreitmeier, 1973; S. 63). Eine neue, außerordentlich einfache Seismometerkonstruktion mit Blattfeder läßt nun hier einen Fortschritt erhoffen.

Blattfedern können je nach ihrer Form und Einspannung sowohl Kräfte als auch Drehmomente auf den Pendelarm übertragen. Man kann versuchen, beide gegeneinander auszuspielen, um eine Astasierung zu erreichen. Im Gegensatz zum LaCoste-Pendel (LaCoste, 1934) läßt sich aber anscheinend keine einfache Bedingung dafür angeben, aus der man dann die notwendige Federgeometrie berechnen könnte. Um nicht auf reines Experimentieren angewiesen zu sein, haben wir die wirkenden Kräfte und die resultierende Eigenfrequenz des Seismo-

---

* Mitteilung Nr. 117 aus dem Institut für Geophysik der ETH Zürich.

1 Der unseres Wissens einzige Versuch in dieser Richtung soll nicht unerwähnt bleiben. In einem 1966 in den USA patentierten Seismometer ersetzt Willmore die LaCoste-Feder durch einen Faden gleicher Länge, der oben an einer vorgespannten, im Betriebszustand geraden Dreiecks-Blattfeder angelenkt ist. Gerade diese Art Federn bietet jedoch kaum weniger Probleme als Schraubenfedern (Jacoby, 1971; S. 33–36). Auch dürfte Periodenkonstanz schwer zu erreichen sein, weil der obere Aufhängepunkt beweglich ist, was die Vorteile der LaCoste-Geometrie zunichte macht.

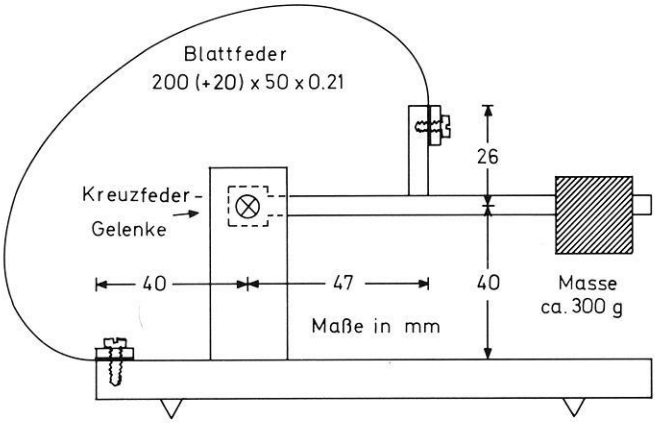

Abb. 1. Versuchsaufbau des Blattfeder-Seismometers

meters mit dem Computer (ETH-Rechenzentrum) berechnet. Folgende Bedingungen waren dabei vorgegeben: Die Blattfeder soll ohne Last, also vor dem Einspannen, eben sein. Sie soll fest, d.h. ohne Gelenke, mit Gestell und Gehänge verbunden werden. In eingespanntem Zustand muß sie überall eine gewisse Mindestkrümmung aufweisen und darf insbesondere keinen Wendepunkt haben, weil sonst leicht der gefürchtete „Knackfrosch-Effekt" eintritt (Umspringen in die entgegengesetzte Krümmung). Allein durch die Anordnung der Feder soll eine beliebig starke Astasierung möglich sein. Natürlich sind auch gewisse Belastungsgrenzen zu beachten.

Nach einigen erfolglosen Vorversuchen schien es zunächst, als seien diese Bedingungen überhaupt nicht gleichzeitig erfüllbar. Eine systematische Suche mit dem Computer ergab jedoch, daß es sogar eine unendliche Anzahl geometrisch recht verschiedener Anordnungen gibt, die das Gewünschte leisten. Man kann dabei nicht nur die Eigenperiode beliebig groß machen, sondern auch noch ein Maximum der Eigenperiode in die Skalenmitte legen, so daß die Periode lokal von der Lage unabhängig ist und das Pendel auch nach beliebig großen Ausschlägen wieder zurückkehrt. (Gerade die letzte Eigenschaft ist, wenn man die Aufgabe rein experimentell angeht, nur sehr schwer zu erreichen.) Wie beim LaCoste-Pendel lassen sich Eigenperiode und Periodenkonstanz durch Verschieben des Einspannpunktes der Feder in zwei Richtungen justieren. Ebensogut läßt sich die Eigenperiode auch durch Kippen des ganzen Instruments um die Drehachse einstellen.

Ein einfaches Versuchsmodell nach Abb. 1 hat die Richtigkeit der numerischen Ergebnisse bestätigt. Es läßt sich mühelos auf 6 sec Eigenperiode einstellen. Eine Grenze ist lediglich durch die Feinheit der Justierung und durch die Präzision der Kreuzfedergelenke gegeben; sie läßt sich zweifellos durch sorgfältigeren Aufbau noch weiter hinausschieben. Die Justierung ist eher weniger kritisch als beim LaCoste-Pendel. Die Astasierung, d.h. die Verkleinerung des rücktreibenden Drehmoments, beträgt etwa 1:100 gegenüber einem gleich großen mathematischen Pendel oder dem FS 60. Die Periode ist innerhalb eines Skalenbereichs

von ± 2 mm auf $\pm 0{,}1$ sec konstant. Das entspricht etwa der üblichen Periodenkonstanz der bekannten langperiodischen Seismometer; freilich können diese wenigstens theoretisch noch weit besser abgeglichen werden (Streckeisen, 1974). Da das Seismometer zur Erweiterung des Frequenzumfangs später mit einer elektronischen Gegenkopplung betrieben werden soll und dadurch praktisch an die Mittellage gefesselt ist, ist die Periodenkonstanz jedenfalls mehr als ausreichend.

Die Feder des Versuchsmodells besteht aus vergütetem NIVAFLEX der Vacuumschmelze Hanau, das uns freundlicherweise vom Institut Dr. Straumann in Waldenburg/Schweiz zur Verfügung gestellt wurde. Dieses Material hat hervorragende elastische Eigenschaften und ist unmagnetisch, aber nicht temperaturkompensiert. Versuche mit temperaturkompensiertem Material sind beabsichtigt. Für Hinweise auf geeignetes Material und vor allem auf Bezugsquellen für Kleinmengen wären wir dankbar. Bei guter Temperaturkompensation und entsprechender Abschirmung müßte sich das neue Pendel auch als Gravimeter eignen.

Danksagung. Ich danke Herrn Dipl.-Geophys. G. Streckeisen für seine Mithilfe.

Literatur

Berckhemer, H.: MARS 66. Z. Geophys. *36*, 501–518 (1970)
Jacoby, H.D.: Die Entwicklung eines kleinen Seismometers mit breitbandigem Ausgangssignal. Diss. Univ. Stuttgart, 72 S., (1971)
LaCoste, L.J.B.: A new type long period seismograph. Physics *5*, 178–180, (1934)
Streckeisen, G.: Untersuchungen zur Meßgenauigkeit langperiodischer Seismometer. Diplomarbeit Inst. f. Geophysik der ETH Zürich, 81 S., 1974
Unterreitmeier, E.: Zur Erhöhung der Störfreiheit langperiodischer Seismographensysteme. Diss. Univ. Jena 1974, Veröff. des ZIPE Potsdam Nr. 25, 199 S., 1973
Willmore, P.L.: Long period vertical seismograph. U.S. Patent Nor. 3292145, (1966)

Erhard Wielandt
Institut für Geophysik der ETH Zürich
CH-8049 Zürich/Schweiz
Postfach 266

Eingegangen am 30. Juni 1975

Book Reviews

M. Båth: **Spectral Analysis in Geophysics**
Developments in Solid Earth Geophysics, Vol. 7. Amsterdam: Elsevier Scientific Publishing Company 1974, 563 Seiten, 101 Abb., gebunden US $ 46.20.

Die Untersuchung von Zeit- und Ortsfunktion nimmt in der gesamten Geophysik einen sehr breiten Raum ein. Bis vor etwa zwei Jahrzehnten beschränkten sich entsprechende Auswertungen häufig auf einige Chrakteristiken des zeitlichen oder räumlichen Verlaufs einer geophysikalischen Größe. Bei Seismogrammen wurden beispielsweise vor allem Einsatzzeit, Richtung der ersten Bodenbewegung und maximale Amplituden verwertet. Der wesentlich größere Teil an Information, den eine Zeitfunktion enthält, bleibt dabei unberücksichtigt. Der Verfasser führt den Leser über eine Betrachtung der Anfänge spektraler Auswertungsmethoden behutsam und pädagogisch geschickt in die mathematischen Grundlagen der Fourier- und „Power"-Spektren ein. Immer wieder werden dabei Phänomene angesprochen, die sich innerhalb der Geophysik besonders für eine spektrale Behandlung eignen. Daß sich bei der praktischen Transformation von Zeitfunktion in den Frequenzbereich nicht nur Vorteile bieten, wird eingehend geschildert. Wenn sich die Behandlung komplizierter Probleme im Frequenzbereich häufig wesentlich einfacher als im Zeitbereich vollzieht, so sollte man sich stets vor Augen halten, daß bei der Transformation in den Frequenzbereich eine ganze Reihe unerwünschter Effekte auftritt, welche eine äußerst kritische Einstellung gegenüber allen Interpretationen erforderlich macht. Nach eingehender Behandlung dieser Fragen wendet sich der Autor dem Schwerpunkt der Darstellung, der Anwendung spektraler Methoden auf seismologische Probleme, zu: Raumwellen, Oberflächenwellen, Eigenschwingungen des Erdkörpers werden genauso berücksichtigt wie die speziellen Fragen der Amplitudenabnahme seismischer Wellen und der Herdmechanik, bei denen sich die Effektivität der spektralen Verfahren besonders deutlich zeigt. Anschließend wendet sich der Verfasser entsprechenden Fragen zu, die bei den Potentialfeldern des Erdkörpers, in der Meteorologie und Ozeanographie auftreten. Die Darstellung schließt mit einem umfassenden Literaturverzeichnis. Der Rezensent bedauert, daß es solche Bücher nicht schon zu seiner Studienzeit gegeben hat.

G. Schneider, Stuttgart

C.B. Officer: **Introduction to Theoretical Geophysics**
Berlin-Heidelberg- New York: Springer 1974, 385 Seiten, 118 Abb., gebunden DM 48.60.

Der Verfasser ist international vor allem durch sein Buch "Introduction to the theory of sound transmission" bekannt geworden. Der dort ausführlich behandelte Themenkreis der Ausbreitung akustischer, im Spezialfall seismischer Wellen in geschichteten Medien, insbesondere innerhalb der Ozeane, nimmt in dieser neuen Darstellung zwei von elf Kapiteln ein. Die Physik der Wasserhülle (Strömungen, Wellen, Gezeiten) einschließlich ihrer thermo- und hydrodynamischer Grundlagen werden in größerer Ausführlichkeit behandelt als der vorher genannte Problemkreis. Den Potentialfeldern des Erdkörpers sind wiederum zwei weitere Kapitel gewidmet. In einem einleitenden Abschnitt rekapituliert der Autor, wie man das häufig in amerikanischen Darstellungen findet, kurz das mathematisch physikalische Rüstzeug für den gesamten Stoffbereich. Am Schluß des Buches wird die Dynamik des Erdkörpers behandelt. Darunter fällt einmal das Verhalten der Erde als rotierender Körper und alle damit zusammenhängenden Fragen. Zum anderen finden die verschiedenen Arten der Deformation Berücksichtigung, die Erdkruste und Erdmantel erleiden.

Der Text ist sehr knapp gehalten. Anordnung, Satz und Symbolik des Formelwerkes sind wohltuend klar.

Am Ende der überwiegenden Zahl der Abschnitte findet der Leser Aufgaben, wobei zur Kontrolle häufig das Endergebnis genannt wird. Die Literaturübersichten am Schluß eines jeden Kapitels verweisen auf bekannte Standardwerke der internationalen Literatur, soweit diese in englischer Sprache erschienen sind. Das Buch wird eine sichere Hilfestellung geben, wenn man es als Lehrbuch zum „Gebrauch neben Vorlesungen", vor allem solchen in theoretischer Geophysik benützt. Für den ausgebildeten Geophysiker ist es ein gutes Nachschlagwerk, das zuverlässige Auskunft über alle wesentlichen theoretischen Grundlagen der Physik des Erdkörpers und seiner Wasserhülle vermittelt.

G. Schneider, Stuttgart

Siegfried J. Bauer: **Physics of Planetary Ionospheres**
Berlin-Heidelberg-New York: Springer 1973.

In contrast to other existing books on aeronomy and ionospheric physics, the present book "concentrates on the fundamental processes in an idealized planetary ionosphere as a general abstraction, with actual planetary ionospheres representing special cases", as the author states in the preface. Therefore the content is organized according to these processes rather than with respect to observed phenomena. It is aimed at introducing graduate students and young research workers into the field. This purpose is served well by the sequence of topics in the monograph: i) the description of the processes, ii) the models and iii) the observed phenomena of planetary ionospheres.

In chapter I, covering about a fifth of the body of the book, the neutral atmospheres are treated, rendering the background for the ionized parts. One third of this chapter is devoted to the description of evaporation in the exosphere, i.e. the escape and capture of particles into and from the interplanetary space, respectively.

Chapters II and IV describe the fundamental chemical processes responsible for gain and loss of ionization. Chapter II covers outer sources of ionization: radiation and meteors. Collisional ionization and loss processes (*e.g.* recombination) are treated in chapter IV.

Heat transport of ionized particles and the resulting temperature distributions are described in chapter III, while the corresponding mass transport is treated in chapter V. Here particular attention is given to ambipolar diffusion, a process long known in the theory of the positive column in low pressure discharges, now found to be responsible for the electron distribution of the topside ionosphere.

Since realistic models of planetary ionsospheres require the simultaneous solution of a set of nonlinear balance equations, the chapter VI on models of planetary ionospheres deals mainly with very simplified models and discusses in more depth the extent of these ionospheres. Here the advantage of the thorough treatment of the various processes in the previous chapters becomes apparent for the reader. Because he was well informed about the complexity of the different processes and their interdependence, he can accept the statement that at present only a computer can take them into account simultaneously, and that the search for an analytic solution of the realistic balance equations seems to be unrealistic at the time being.

The remaining three chapters describe the diagnosis of the ionospheric plasma and the results of the observations. Since the experimental techniques, remote sensing and in situ measurements (Chapter VIII), both use the electromagnetic properties of the plasma, these properties are briefly discussed in Chapter VII, together with plasma instabilities responisble for some of the observed phenomena. These are completely listed in the last chapter IX, subdivided into properties for the ionospheres of the Earth, of Mars, Venus and Jupiter.

The relatively small book of 230 pages containes a wealth of information. Of course, each single topic could only briefly be covered, but the resulting formulas are given as well as the relevant references, the list of which has 260 entries. Thus the interested reader can easily look for more detailed information. Of course, some printing errors and minor flaws can be found in the formulas, e.g. the neglection of the compressibility in Eq. (1–23) and its taking into account in Eq. (1–25). But this should by no means distrack from the value of the book, which lies in the outstanding organization of the diversity of the treated topics. The author, mainly engaged in doing research at the NASA Goddard Space Flight Center, has to be congratulated for his pedagogic capacity. The aim of the book, to give an introduction for the beginner in the field with a good background in general physics, has been met excellently. The specialist will find valuable information about topics not directly on his line of investigations. Thus the book can be recommended for "educated" newcomers as well as for oldtimers.

K. Suchy, Düsseldorf

J. Geophys. 41, 551 – 580, 1975

REVIEW ARTICLE

Wave and Particle Observations by Explorer 45 Pertaining to Wave-Particle Interactions*

T.A. Fritz and D.J. Williams

U.S. Department of Commerce, National Oceanic and Atmospheric Administration
Environmental Research Laboratories, Boulder, Colorado 80302, USA

Abstract. We present a review of results obtained from the NASA Small Scientific Satellite (Explorer 45) concerning wave and particle observations which pertain to wave-particle interactions near the equatorial plane out to radial distances of 5.2 R_E (earth radii). We first outline observations which confirm some preexisting ideas concerning various magnetospheric processes such as the "injection" of particles during substorms, the existence of ELF hiss throughout the region of the plasmasphere, and the role which convection plays in explaining the overall gross motions of the particle dynamics. In the second part of the review we examine observations from Explorer 45 pertaining to magnetospheric processes and mechanisms around which there still exists a good deal of uncertainity. We comment upon the nature of the substorm injection process, and mechanism producing the ELF plasmaspheric hiss, and the role the various competing processes play in the decay of the storm-time ring current.

Key words: Magnetosphere – Wave and Particle Observations – Explorer 45.

I. Introduction and Description of Explorer 45

The subject of wave-particle interactions inside the magnetosphere has become an increasingly active area of research in recent years. We wish to present a short review and compilation of observations made by the NASA Small Scientifice Satellite (S^3), Explorer 45, of waves and particles, near the equatorial plane

* Invited paper presented at the European Geophysical Society Symposium on Plasma Instabilities and Wave Particle Interactions in the Magnetosphere, Trieste, Italy, September 23–25, 1974. The paper is being published as a contribution to a collection honoring Professor G. Pfotzer of the Max-Planck-Institut für Aeronomie, Lindau/Harz, Germany.

in the inner magnetosphere ($L \leqq 5$) which pertain to concepts of wave-particle interactions. Explorer 45 was launched on 15 November 1971 into an elliptical orbit having an apogee of 5.24 earth radii, a perigee of 220 km, a period of 7.82 hours and an inclination of 3.5°. An electrostatic analyzer-channelton instrument plus three separate solid-state detector systems measure proton intensities from 0.73 keV to 2800 keV in 31 differential energy channels and electron intensities from 0.73 to 560 keV in 20 steps. A complete description of the Explorer 45 sattelite and program has been presented by Longanecker and Hoffman (1973).

The satellite spin axis is maintained in the plane of the orbit and pitch angle information is obtained by sectoring the satellite spin (8.451 seconds) into 32 segments. All pitch angles presented here are measured pitch angles using simultaneous data from the on-board 3 axis flux gate magnetometer. Single axis DC electric field measurements are made perpendicular to the spin axis along with AC electric field noise from 0.3 Hz to 100 kHz (19 band pass channels). Two axis search coil magnetometers provide magnetic noise measurements from 1 Hz to 3 kHz in 7 band pass channels. In addition to the band pass measurements both electric and magnetic noise measurements are passed through a broadband (100 Hz to 10 kHz) filter and telemetered separately over a wideband transmitter (Longanecker and Hoffman, 1973). The location of the plasmapause can be identified by using the saturation characteristics of the DC electric fields experiment (Maynard and Cauffman, 1973) and is believed to represent a cold plasma number density of 60 to 100 particles/cm^3 (Maynard, personal communication).

The S^3 concept is unique. The satellite is considered as a single experiment. In keeping with this concept, copies of a single data tape, containing all data, are distributed to each experimenter in the program. With this operational situation and the strong cooperation of the experimenter team members, magnetospheric problems can be viewed and approached with the complete S^3 set of simultaneous data bearing on the problem and the compilation of results can be assembled into review papers such as the present one early in the data analysis program of the satellite.

II. "What We (Think We) Know"

In this section we list some of the reasonably well established features of the behaviour of the waves and particles in the inner magnetosphere near the equatorial plane and attempt to illustrate these features where appropriate with observations from Explorer 45.

1. The magnetospheric particle populations are subject to a decay of existing intensities and to repopulation through processes of "injection" and diffusion.

The sudden appearence of hot plasma in a region not previously populated by such plasma in the magnetosphere is easy to observe so that the concept of "injection" during the onset of each magnetospheric substorm is widely accepted. In Figs. 1–4 we present the relative intensities of electrons and protons

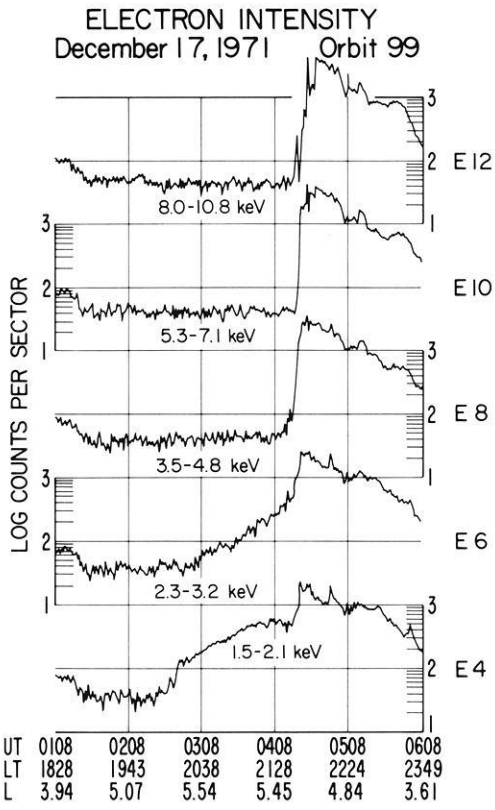

Fig. 1. Intensity of electrons from 1.5 to 10.8 keV recorded by Explorer 45 during orbit 99 near apogee on December 17, 1971 (Barfield and DeForest, 1974)

recorded when S^3 was near apogee on December 17, 1971. It will be noted that there was a sudden increase in the intensity of both electrons and protons near 0420 UT in connection with a substorm observed at about the same time on ground base magnetograms (Fig. 5) (Barfield and DeForest, 1974). This brings us to the next point.

2. During all "injection" events both electrons and protons (ions) appear in the magnetosphere.

Whenever S^3 is outside the high density cold plasma region known as the plasmasphere increases in the intensities of both electrons and ions occur during each magnetospheric substorm. This is similiar to the observations of DeForest and McIlwain (1971) on ATS-5 at $L=6.6$.

3. The inner boundary of the injection process appears to be associated roughly with the plasmapause.

In the example of the injection process given in Figs. 1–4, the satellite crossed the plasmapause at about 0200 UT ($L=4.95$) on the outbound portion of the orbit and then at about 0616 UT ($L=3.4$) on the inbound leg of the orbit according to the DC electric field experiment definition of the plasmapause. In this example the injection process appears to operate entirely outside the plasma-

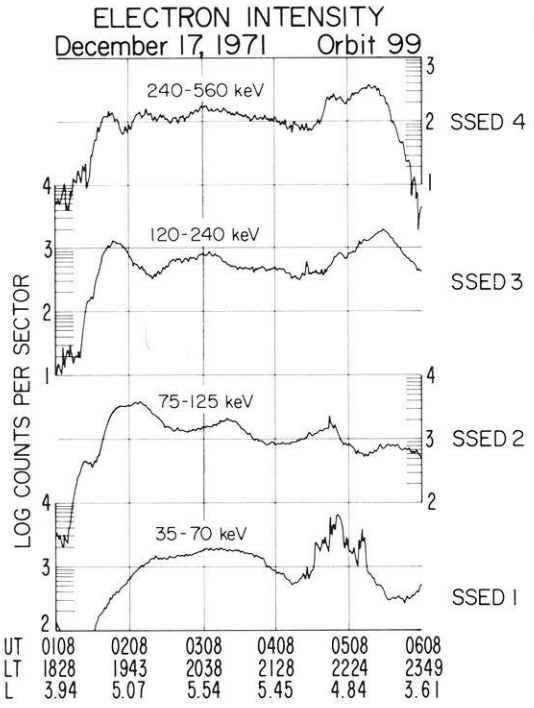

Fig. 2. Continuation of Fig. 1 for electrons from 35 to 560 keV

pause. In Figs. 16 and 17 examples (which we will discuss later) are presented in which energetic protons are injected well into the region of the plasmasphere. The inner boundary of the injected particles can appear at any distance from $L=2.0$ to the apogee of S^3 but the plasmapause is usually no more than 0.5 L away from this inner edge even on the deepest, most intense penetrations of the injection process. There can be overlap but there appears to be a rough association in the position of the two boundaries (Williams and Lyons, 1974a and b; Williams, 1974).

4. After the particles appear as a result of the "injection" process their subsequent motion is consistent with normal drifts in the combined geomagnetic and geoelectric fields present in the magnetosphere

Various features of the injected particle distributions during substorms (Konradi *et al.*, 1973; Williams *et al.*, 1974; Konradi *et al.*, 1975) and during main phase magnetic storms (Smith and Hoffman, 1973; 1974) have been explained in this manner. This is the basic approach employed successfully by McIlwain (1974) in explaining particle variations at ATS-5.

5. Convection does play a dominant role in explaining the overall gross motions of the particle dynamics.

Although other types of electric fields could contribute to the geoelectric field noted in point 4 above, the convection electric field appears sufficient to explain the overall gross motions of the particles. Maynard and Chen (1974)

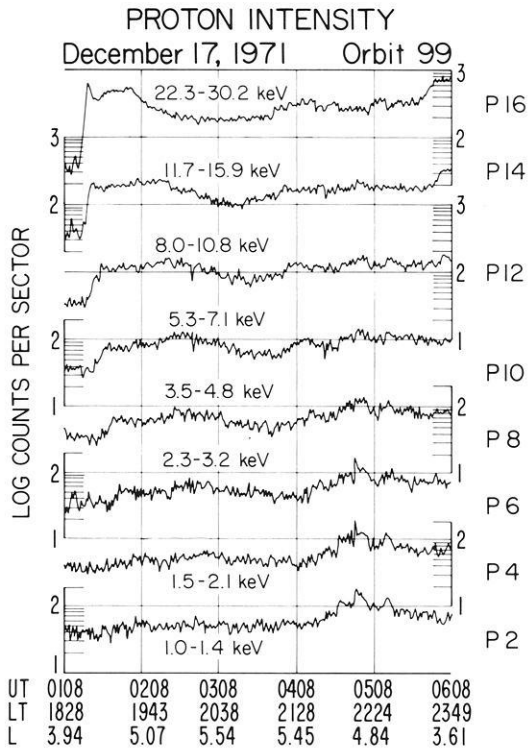

Fig. 3. Continuation of Fig. 1 for protons from 1.0 to 30.2 keV

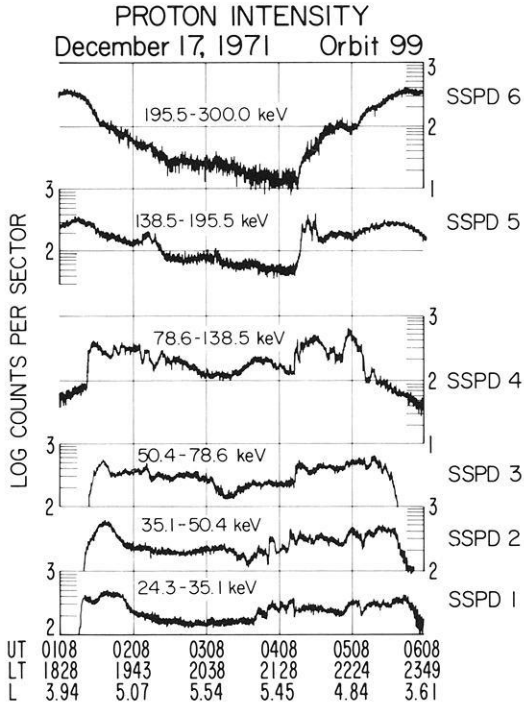

Fig. 4. Continuation of Fig. 1 for protons from 24.3 to 300 keV

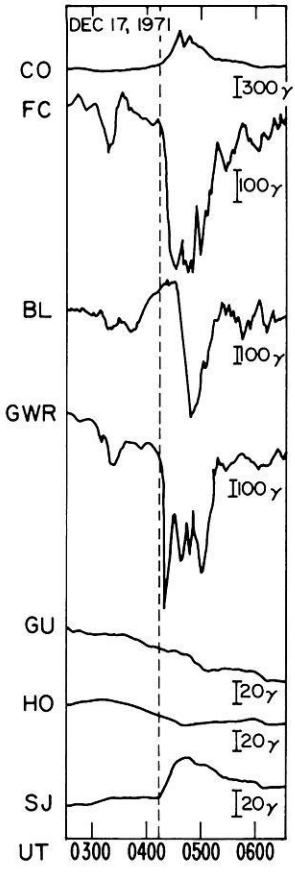

Fig. 5. Magnetograms corresponding to the time period of the Explorer 45 orbit 99 of Figures 1–4 for four high latitude stations, College (*CO*), Fort Churchill (*FC*), Baker Lake (*BL*), and Great Whale River (*GWR*) along with three low latitude stations, Guam (*GU*), Honolulu (*HO*), and San Juan (*SJ*) (Barfield and DeForest, 1974)

have studied the S^3 observations of detached cold plasma regions and confirm that convection is the basic underlying process in the formation of these regions but find that more localized processes are needed to explain the observed detailed structure of these regions. Barfield *et al.* (1975) have studied the development of a single detached cold plasma region and come to similiar conclusions.

6. During intense "injection" events the populations of ions, particularly protons from 10 keV to 100 keV are enhanced to produce a "storm-time" ring current.

Explorer 45 is providing the first total proton energy density measurements in the storm-time ring current region. These observations show that the stormtime ring current is produced by the injection of protons with energies from 1 keV to 140 keV with particles from 10 keV to 60 keV producing the largest increase from the quiet time distribution (Hoffman, 1973; Smith and Hoffman, 1973, 1974; Fritz *et al.*, 1974). An example of the proton spectral changes which occur during an intense proton injection leading to the production of a strom-time ring current is presented in Fig. 6.

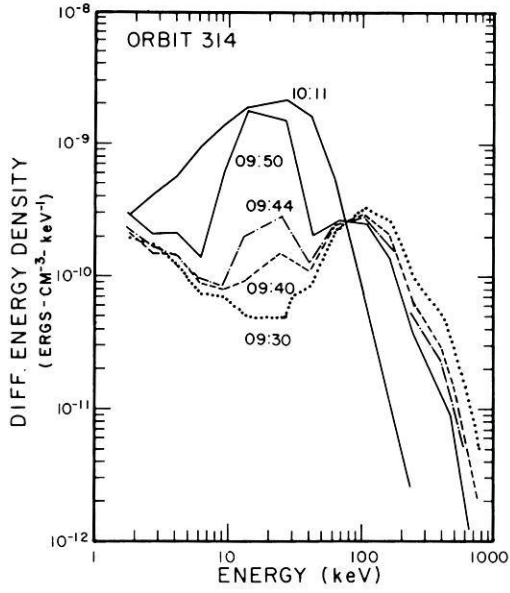

Fig. 6. The evolution of the energy density spectrum of protons as a function of radial distance on the outbound portion of Explorer 45 orbit 314 taken during the period of the main phase decease of the geomagnetic storm beginning on February 24, 1972 (Smith and Hoffman, 1974; Fritz *et al.*, 1974)

7. The plasmasphere is filled with an emission called ELF hiss much of the time. This hiss appears to have been produced at a specific location and then propagates to fill a larger portion of the plasmaspheric volume.

Plasmaspheric hiss has been observed for some time (Russell and Holzer, 1970). An extensive study of the occurrence of this ELF hiss along the S^3 orbit has been performed by Parady *et al.* (1974). Although there are large intensity variations they found hiss in the frequency range from 100 Hz to 1000 Hz on 108 of 112 orbits which they examined. For most orbits the hiss occurred inside the S^3 determination of the plasmapause. There were cases, however, when the hiss definitely extended to radial distances outside of the S^3 plasmapause determination but these could have been cases of a very gradual transitions from the low to high density cold plasma regions. A textbook type of example of the behaviour of this hiss is presented in Fig. 7 (Anderson and Gurnett, 1973). On this inbound S^3 pass electrostatic noise was observed up to the sharp plasmapause crossing at 0615 UT. As the plasmasphere was entered a strong, unstructured hiss emission appeared in the band from 300 Hz to 400 Hz in both the electric and magnetic field wideband data. This transition region is presented in greater detail in Fig. 8. The ELF hiss band was spin modulated and it had the same well defined frequency limits for more than 30 minutes as the satellite moved inward more than one earth radii in distance. By analyzing the spin modulation Anderson and Gurnett (1973) were able to determine that the propagation direction of the hiss was nearly normal to the local magnetic field direction. The invariance of the frequency limits observed and the propagation direction strongly suggest that the hiss was being generated within a localized region and then propagating to other regions of the plasmasphere.

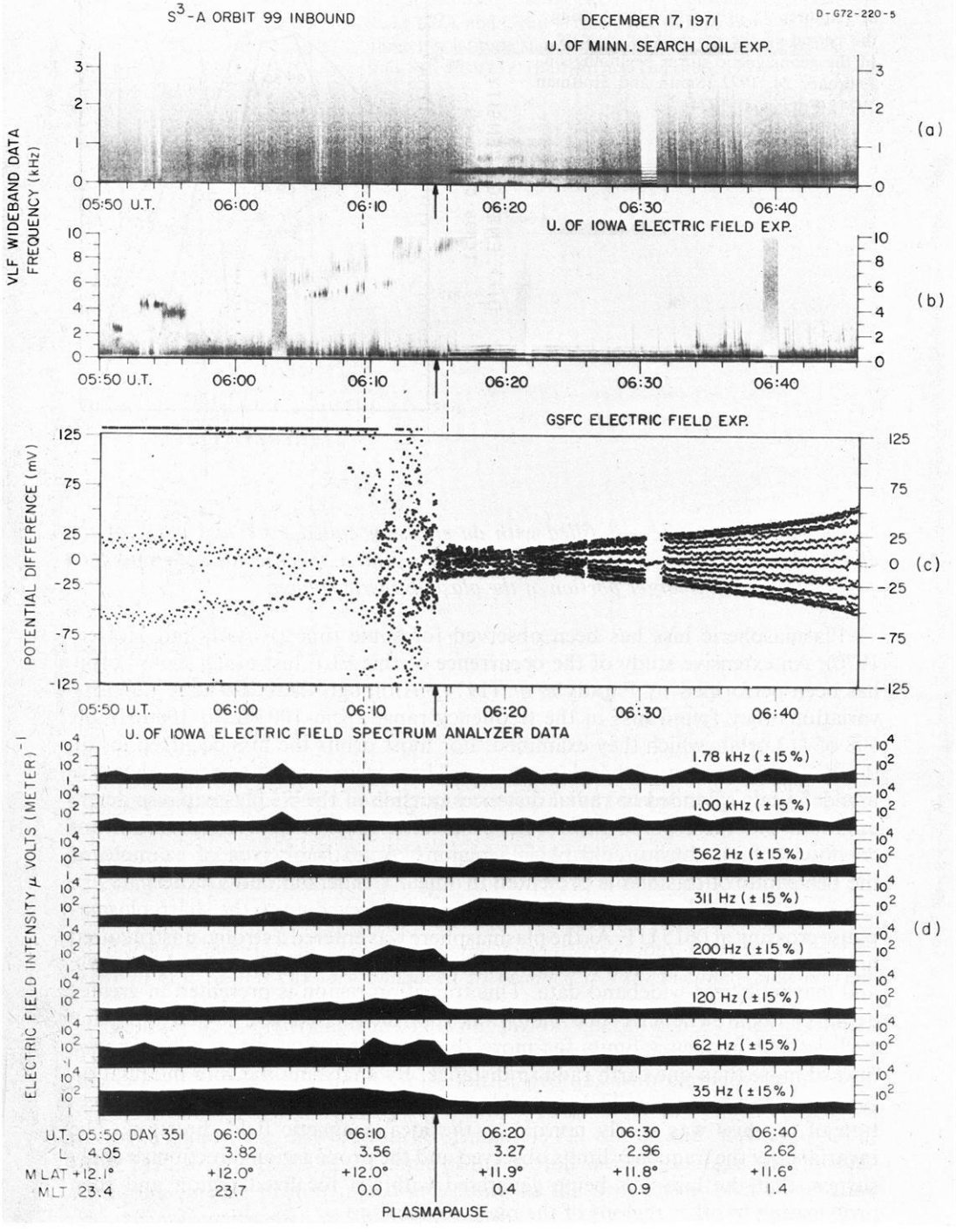
S3-A ORBIT 99 INBOUND
DECEMBER 17, 1971
D-G72-220-5
U. OF MINN. SEARCH COIL EXP.
VLF WIDEBAND DATA FREQUENCY (kHz)
(a)
05:50 U.T.
06:00
06:10
06:20
06:30
06:40
U. OF IOWA ELECTRIC FIELD EXP.
(b)
GSFC ELECTRIC FIELD EXP.
POTENTIAL DIFFERENCE (mV)
(c)
U. OF IOWA ELECTRIC FIELD SPECTRUM ANALYZER DATA
ELECTRIC FIELD INTENSITY μ VOLTS (METER)-1
1.78 kHz (±15%)
1.00 kHz (±15%)
562 Hz (±15%)
311 Hz (±15%)
200 Hz (±15%)
120 Hz (±15%)
62 Hz (±15%)
35 Hz (±15%)
(d)
U.T. 05:50 DAY 351
L 4.05
3.82
3.56
3.27
2.96
2.62
M LAT +12.1°
+12.0°
+12.0°
+11.9°
+11.8°
+11.6°
MLT 23.4
23.7
0.0
0.4
0.9
1.4
PLASMAPAUSE

8. The behaviour of energetic electrons ($E \gtrsim 40$ keV) inside the plasmapause is reasonably well understood. With periodic substorm injections of electrons occurring in the vicinity of the plasmapause, the two-zone structure (inner and outer zone), relative intensities as a function of energy, and pitch-angle distributions of energetic electrons can be explained by balancing radial diffusion with losses from atmospheric coulomb collisions and from pitch-angle diffusion resulting from resonant interactions with the known whistler-mode plasmaspheric hiss noted in point 7.

Rather than attempt a completely self-consistent calculation of wave generation and the resulting particle diffusion, Lyons *et al.* (1972) used a distribution of whistler-mode waves modelled after the observed plasmaspheric hiss spectrum and calculated diffusion coefficients for particle resonances with this spectrum. Examples are shown in Fig. 9 for electrons with three different electron energies at $L=4$. By including all cyclotron harmonic resonances including the Landau (zeroth order) reasonances along with the effects of geomagnetic field gradients, Lyons *et al.* (1972) predicted that the pitch angle distributions of energetic electrons would display a significant bump near 90° equatorial pitch angle due to the relatively slow diffusion rates within the pitch angle range of overlap between the cyclotron and Landau reasonances. The size of this bump should decease with increasing electron energy since the cyclotron resonance extends to increasingly larger pitch angles with increasing electron energy. For a given energy the size of the bump should also decrease with increasing L since the minimum parallel electron energy for which cyclotron resonance can occur decreases with L. Explorer 45 observations of electrons (30 keV to 560 keV) show that such pitch angle distributions (Fig. 10) with the predicted variation with L and energy are a normal feature of the quiet time radiation belts (Lyons and Williams, 1974a). The shape of the pitch angle distributions is greatly perturbed during storm-time injections. Following such injections the Explorer 45 observations show that the quit time pitch angle distributions gradually reform (Lyons and Williams, 1974b).

Lyons and Thorne (1973) were able to calculate the fluxes of electrons as a function of energy and L and to give an explanation for the two-zone, quiet time structure of the radiation belt electrons by balancing pitch angle scattering and coulomb collision losses with inward radial diffusion driven by substorm associated fluctuations of the convection electric field from an average outer zone source. The resulting equilibrium structure is expected to be steady during quiet times except in the outer regions of the plasmasphere where the fluxes vary somewhat during quiet times in response to substorm activity. This is the

◀ **Fig. 7.** Four sets of field observations for inbound Explorer 45 orbit 99 in the vicinity of the plasmapause. All four panels contain data for the same 56 minutes time period from 0550 to 0646 UT on December 17, 1971. Panel (a) is a 0-Hz to 3-kHz frequency-time spectrogram of the magnetic field wideband data. Panel (b) is a 0-Hz to 10-kHz frequency-time spectrogram of the electric field wideband data. Panel (c) is a plot of the dc potential difference between the spheres of the DC electric field experiment (Maynard and Cauffman, 1973). Panel (d) contains plots of the peak amplitudes measured for the eight lowest frequency channels of the University of Iowa's electric field experiment on board spectrum analyzer (Anderson and Gurnett, 1973)

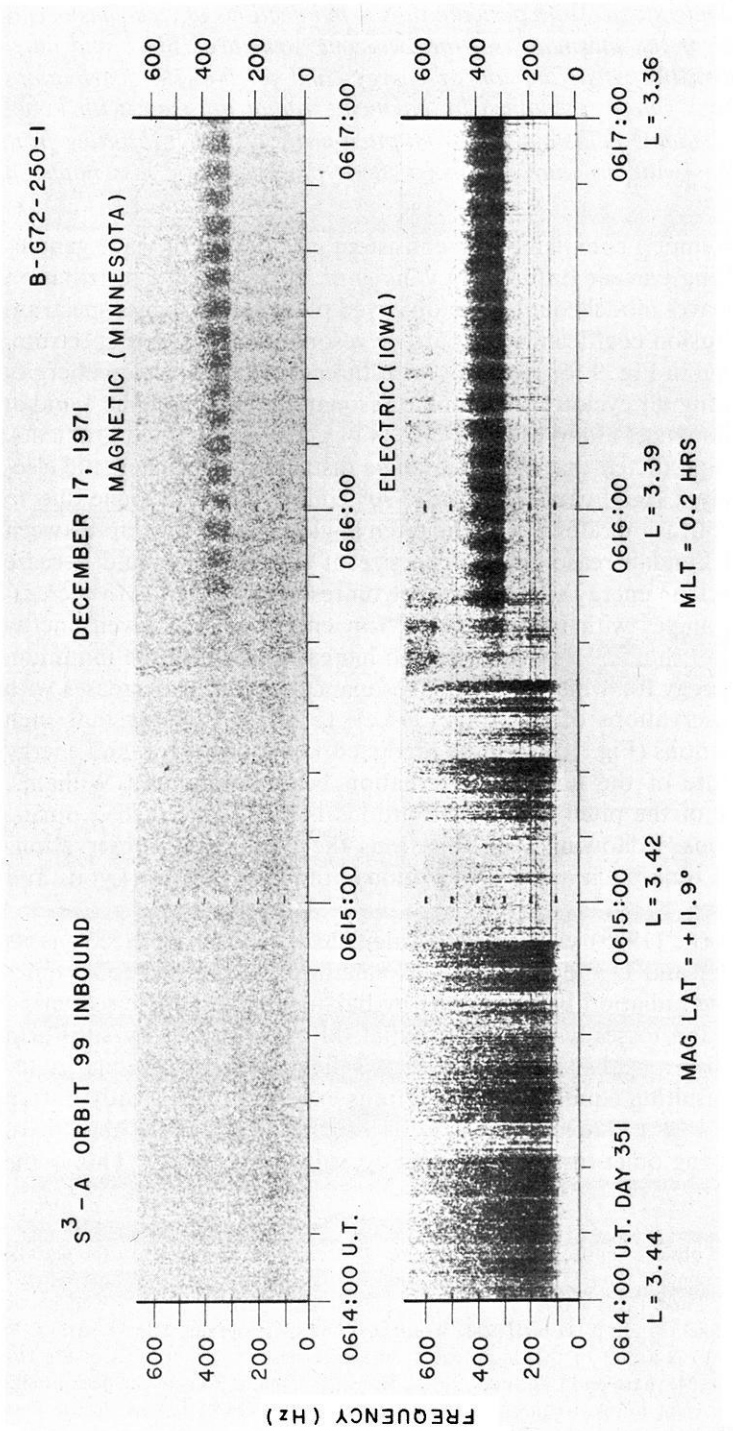

Fig. 8. An expanded portion of Explorer 45 orbit 99 presented in Fig. 7. The upper panel is a 0- to 650-Hz frequenzy-time spectrogram of the magnetic field wideband data. The lower panel is a 0- to 650-Hz frequency-time spectrogram of the electric field wideband data. Both panels are for the same 3-min period near the plasmapause. Note that the intense vertical bursts from 06h14m00s to 06h15m40s UT occur only in the electric field data. The ELF hiss band from about 300 to 420 Hz, which begins at 06h15m37s UT, is present in both the electric and the magnetic field data. Analysis of the spin modulation of the ELF hiss band determined that the hiss is propagating nearly perpendicular to the geomagnetic field. The ELF hiss band has the same well-defined frequency for more than 30 min as the satellite moves inward more than 1 R_E (Anderson and Gurnett, 1973)

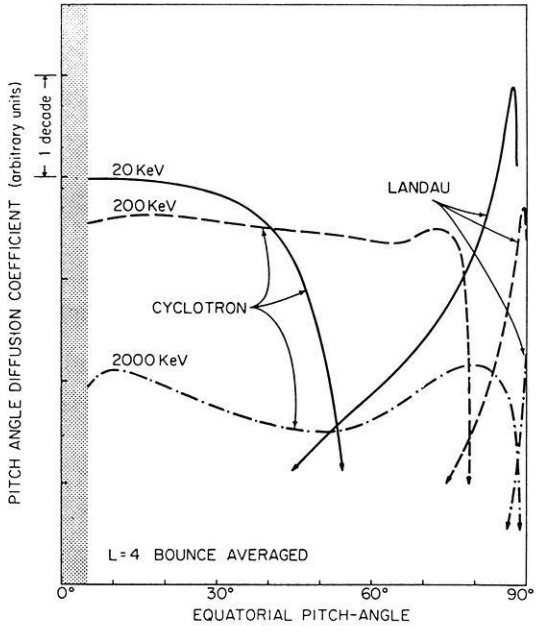

Fig. 9. Bounce orbit averaged cyclotron and Landau resonant pitch angle diffusion coefficients as a function of equatorial pitch-angle at $L=4$ for 20, 200, and 2000 keV electrons. (Lyons *et al.*, 1972)

behaviour shown in Fig. 11 for Explorer 45 observations during quiet times. The theory was able to predict the measured overall structure correctly to about an order of magnitude during the quiet time of December 9–16, 1971 (Fig. 12) which is about the order of agreement expected based on the accuracy and average character of the input parameters required by the theory (Lyons and Williams, 1974a). Following storm-time injections electron fluxes should and do decay slowly back to the pre-storm quiet-time equilibrium structure (Lyons and Williams, 1974b).

III. "What We Do not Know" and Insights Based on S^3 Observations

We now turn to a tabulation of a few of the major topics concerning the behaviour of the waves and particles in the inner magnetosphere about which there is little consensus.

1. What is the nature of the injection process? More specifically, what roles do the processes of in situ acceleration and enhanced convection play in the substorm injection process?

2. What is the actual mechanism producing the plasmaspheric hiss?

3. What roles do the various competing processes play in the decay of the storm-time ring current?

4. What role do the various species of ions play in the magnetospheric processes?

Recent results from the study of Explorer 45 observations have yielded significant insight into each of the questions tabulated above.

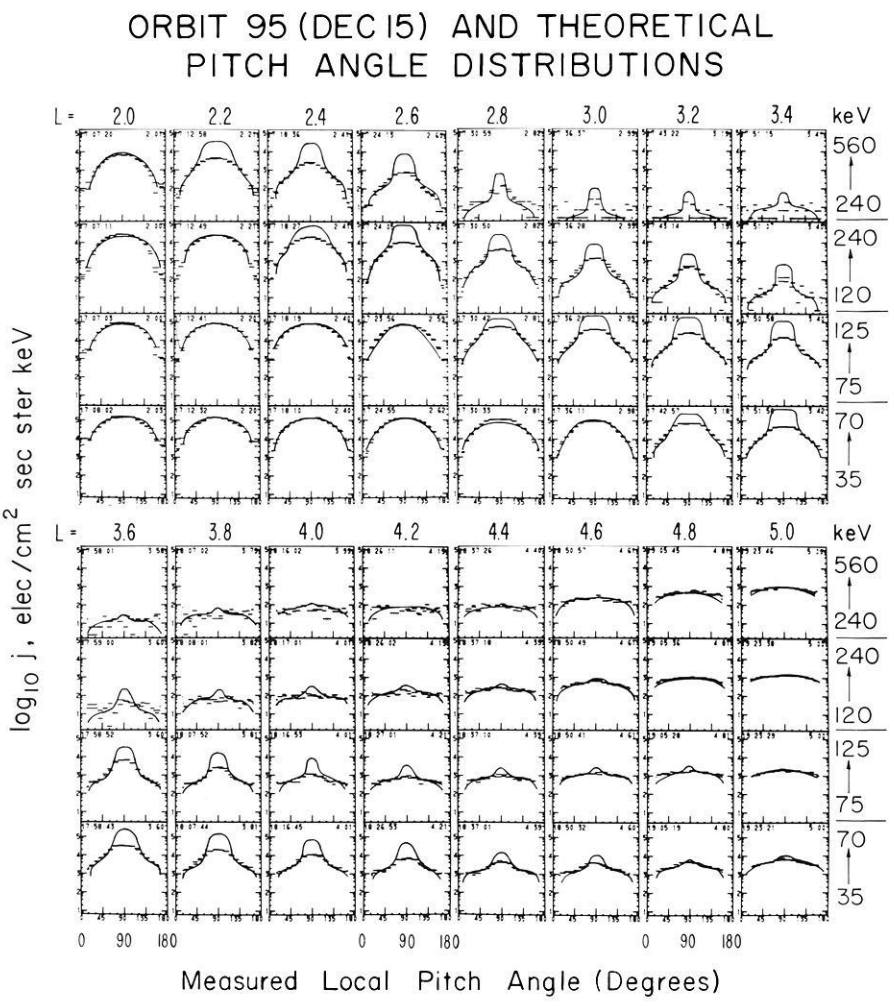

Fig. 10. Equatorial pitch angle distributions observed on Dec. 15, 1971 (orbit 95) and those predicted by Lyons *et al.* (1972) to result from resonant interactions with the plasmaspheric whistler-mode wave band. Distributions are shown every 0.2 in L from $L=2$ to $L=5$, and the four energies are stacked vertically at each L with the lowest energy at the bottom. The dashes give the measured electron flux with their horizontal extend indicating the pitch angle scan for each measurement. The solid curves are the theoretically predicted pitch angle distribution for the geometric mean energy of each energy interval. Diffusion from Coulomb collisons has been added to the theoretical calculations to account for the rounding of the pitch angle distributions within the inner zone. The vertical positionings of the theoretical distributions are arbitrary on a logarithmic scale and have thus been adjusted to best illustrate the comparison with the observations. (Lyons and Williams, 1974a)

The Injection Process

With a single satellite making observations at a single point in space it is difficult to separate effects due to space and/or time in attempting to delineate the features

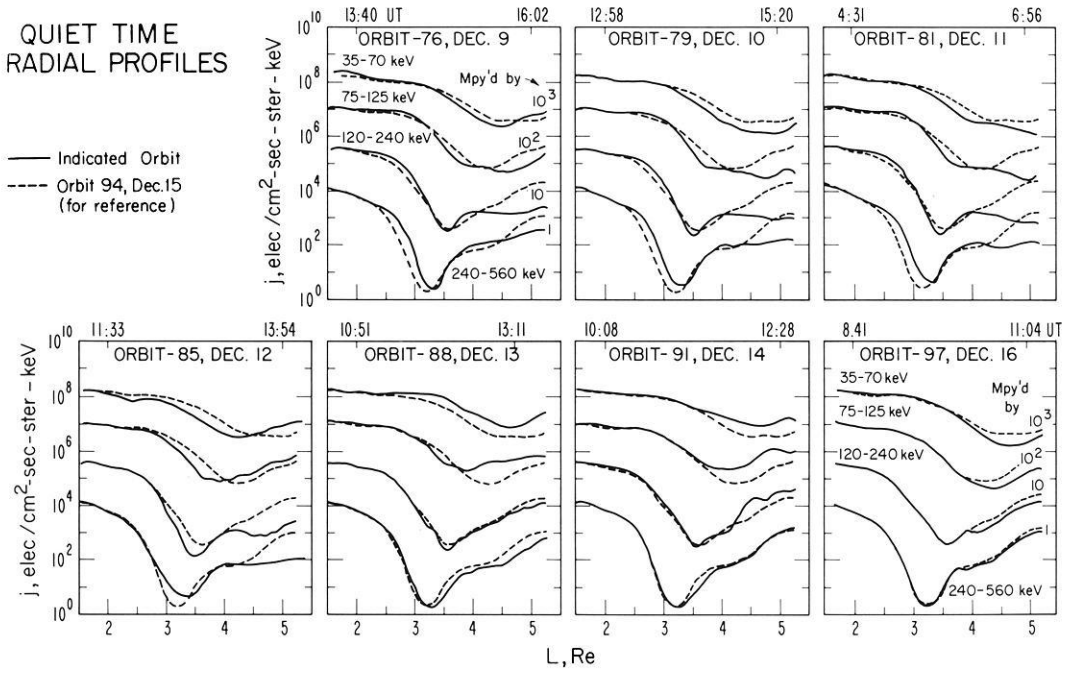

Fig. 11. Radial profiles of the perpendicular (90° local pitch angle) electron flux obtained near the geomagnetic equator, approximately once per day, for the quiet period of Dec. 9–16, 1971. Solid curves give the profiles from the orbit indicated in each panel, while the dashed curves (shown for reference) give the profiles from orbit 94 on December 15, 1971. To clearly display the data, the 120–240 keV, 75–125 keV, and 35–70 keV fluxes have been multiplied by 10^1, 10^2, and 10^3, respectively. (Lyons and Williams, 1974a)

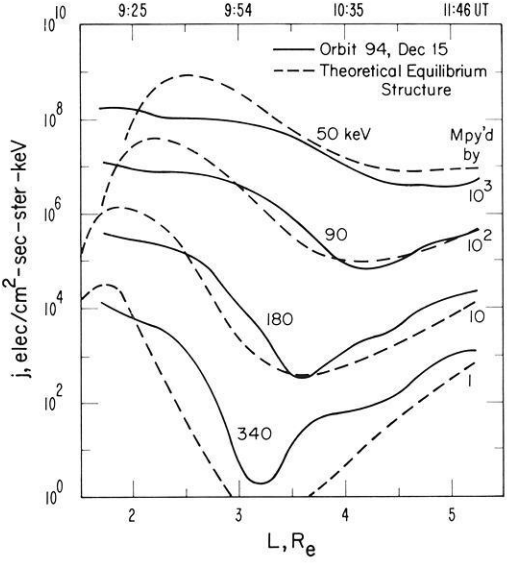

Fig. 12. Comparison between the radial profiles observed on the outbound portion of orbit 94 on Dec. 15, 1971 (solid lines) and the theoretical equilibrium radial profiles (dashed lines) as obtained from the analysis of Lyons and Thorne (1973) using $Bw = 10\,m\gamma$, $E = 0.05\,mV/m$, and an average outer zone electron energy spectrum. The theoretical profiles are for the indicated energies, which are the geometric mean of the four Explorer 45 energy channels. The 180 keV, 90 keV, and 50 keV fluxes have been multiplied by 10^1, 10^2, and 10^3 respectively. (Lyons and Williams, 1974a)

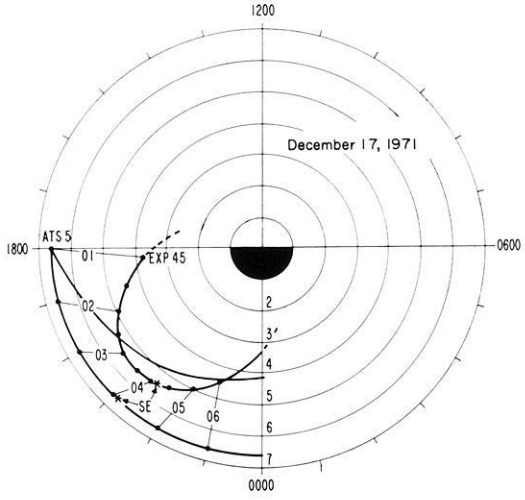

Fig. 13. The trajectories of the ATS-5 and Explorer 45 satellites in an L-value versus local time plot during the period of the substorm injection on December 17,1971 presented in Figs. 1 through 5. (Barfield and DeForest, 1974)

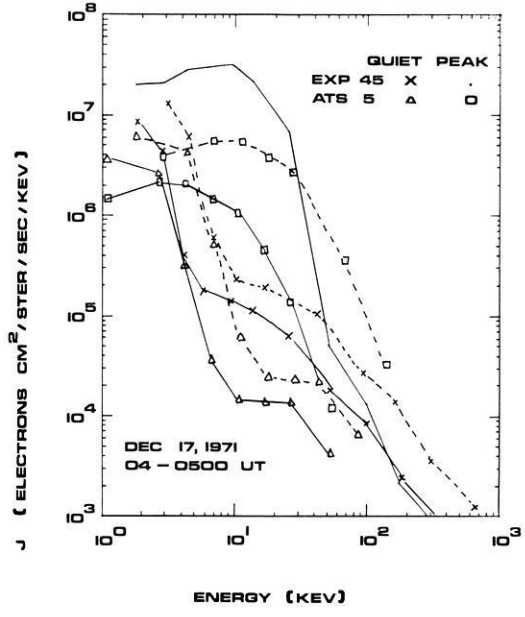

Fig. 14. Energy spectra obtained from the ATS-5 and Explorer 45 satellites during the substorm injection period of December 17, 1971 presented in Fig. 1 through 5. The solid curves represent the actual observations while the dashed curves are representative computed spectra. The dashed "quiet" curves represent the spectra obtained at the position of each sattelite by transforming in phase space from ambient conditions just prior to the substorm to those at the peak epoch. The dashed "peak" ATS-5 curve represents the transformation of the ATS-5 spectrum observed at peak epoch to the position of Explorer 45

of the substorm injection process. During the occurrence of the substorm injection event presented in Figs. 1–5, the ATS-5 satellite at geostationary orbit was in the vicinity of Explorer 45. In Fig. 13 the positions of the two satellites as a function of time are presented. The substorm enhancement (labelled as "SE" in Fig. 13) occurred when the satellites were near their point of closest approach. The "injection boundary" described by Mauk and McIlwain (1974) and by McIlwain (1974) is shown for reference in Fig. 13. Barfield and DeForest (1974)

have attempted to correlate the flux variations at the position of the satellites. In Fig. 14 the electron energy spectrum both before and at the peak of the injection event is presented for the two satellites (solid curves). Barfield and DeForest (1974) have then adiabatically transformed the spectrum recorded at each satellite prior to the event to conditions existing at the peak of the event (dashed curves with "quiet" symbols) using Liouville theorem. It is seen that effects other than those which can be attributed to adiabatic changes occurred at each satellite. In a similiar manner the spectrum recorded at ATS-5 at the peak of the event was transformed to the position of Explorer 45 (dashed spectrum with square symbols). The spectrum at Explorer 45 following the injection (solid curve without symbols) demonstrates a large excess of low energy particles and an absence of higher energy particles from what would be expected on the basis of the measured ATS-5 spectrum transformed to the position of S^3. This result is open to varying interpretations but is strongly suggestive of a non-adiabatic change in the electron distribution function occurring in the vicinity of the satellite in connection with this injection event as opposed to simple enhanced convection "injecting" the particles into the vicinity of the two satellites.

The Source Mechanism for Plasmaspheric Hiss

One of the most promising mechanisms for the production of the plasmaspheric hiss recently proposed by Thorne *et al.* (1974) involves electrons with energies from 10 to 100 keV and is schematically illustrated in Fig. 15. Prior to a substorm, electrons of these energies follow drift paths which are approximately circular (dashed lines). These paths lie outside the plasmapause at dawn but enter the asymmetric bulge of the plasmasphere in the afternoon sector where modest hiss can be produced through the cyclotron resonance mechanism proposed by Kennel and Petschek (1966) due to the enhanced cold plasma density of the plasmasphere. S^3 observations of plasmaspheric hiss during periods of low magnetic activity indicate that there is a maximum in the intensity in the afternoon (Parady *et al.*, 1974). This mechanism is consistent with generation of the hiss at a specific location (Fig. 8) as indicated in Section II (Anderson and Gurnett, 1973) and that the source is in the outer plasmasphere (Parady *et al.*, 1974).

During a substorm intense convection electric fields modify the drift orbits of these medium energy (< 100 keV) electrons (solid lines in Fig. 15) and prevent them from entering the evening plasmasphere thus causing a reduction in hiss intensity at dusk. When the convection electric fields subside electrons again follow circular drift paths and strong hiss is expected near dusk as intense fluxes of substorm-injected electrons drift into the plasmaspheric bulge (Thorne *et al.*, 1974). Using Explorer 45 electron flux observations made in the bulge region of the plasmasphere, Thorne and Barfield (1974) have shown that the medium-energy electron fluxes are depressed during substorms. At substorm subsidence, the electron fluxes return at enhanced flux levels consitent with the drift of the substorm-injected electrons into the bulge. Parady *et al.* (1974) report cases of a complete drop-out of hiss occurring on some passes although they have

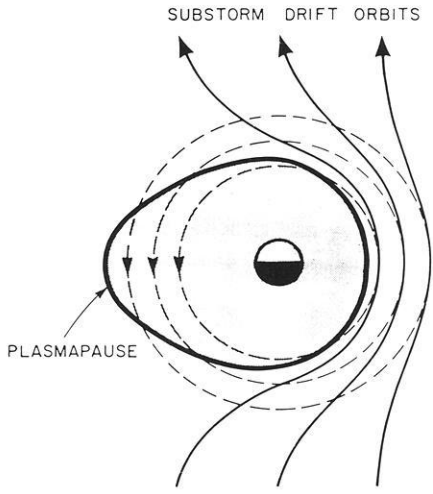

Fig. 15. A model for the generation of ELF emissions during periods of substorm activity. Before the substorm, medium energy electrons (10–100 keV) move on roughly circular (dashed) drift orbits. On entering the high density plasmasphere bulge region, cyclotron resonant energies are lowered, the resonant flux is increased and ELF hiss may be generated. During the substorm, intense convection electric fields modify the electron drift paths (solid lines). Chorus may be generated by the intense flux of injected electrons at dawn but the electrons are forbidden from entering the plasmasphere near dusk thus causing a reduction in hiss intensity. Following the substorm, electrons follow circular drift paths and intense hiss is generated near dusk. (Thorne *et al.*, 1974)

not attempted to correlate this with substorm activity. They also report that the most intense hiss is observed during the recovery phase of magnetic storms near the inner edge of the ring current. In Section II it was indicated that the inner edge of the ring current is roughly associated in position with the plasmapause so this observation is consistent with the intense hiss being produced when the newly injected electron fluxes can again drift into the plasmasphere as the convection electric field subsides. The S^3 experimenters are not in total agreement as to the source of the hiss as Parady, *et al.* (1974) have concluded that protons between 10 and 100 keV appear to be a source for some of the hiss. Parady (1974) has proposed a mechanism in which the protons produced the hiss but this mechanism appears to require anisotrophy factors which are not observed in the proton data (Lyons, personal communication) and appears to be in conflict with the observations of Thorne and Barfield (1974).

The Decay of the Storm-Time Ring Current

There are at least three major mechanisms presently under consideration which lead to the decay of the ring current proton intensities. The ion cyclotron instability as discussed by Cornwall *et al.* (1970, 1971) can operate mainly in the overlap region between the plasmapause and the inner edge of the ring current. The electrostatic loss-cone instability proposed by Coroniti *et al.* (1972) can operate

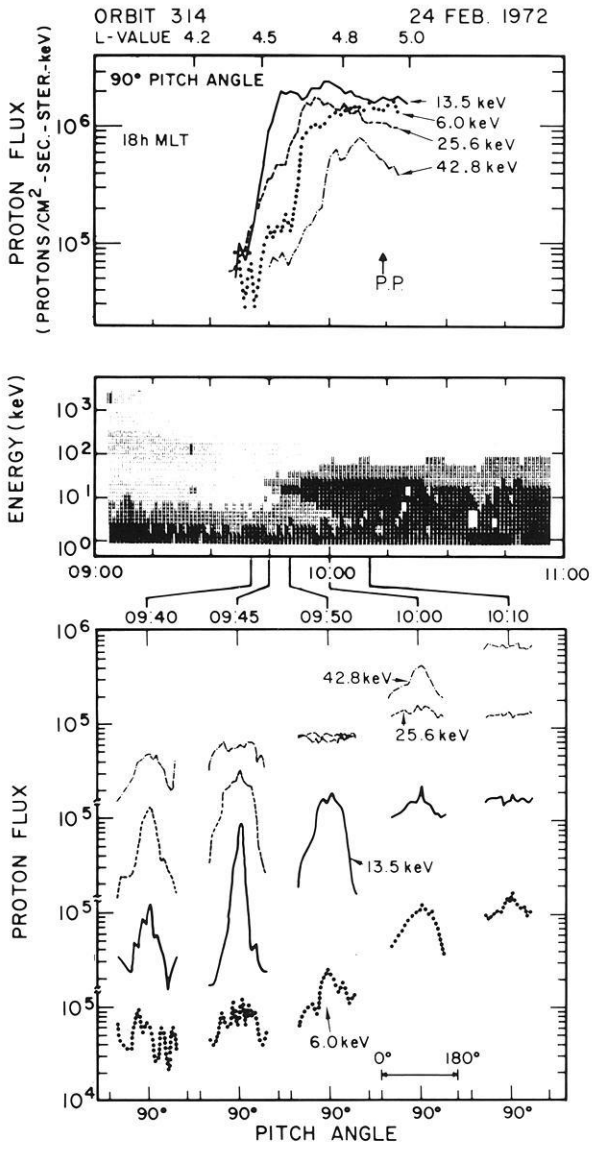

Fig. 16. Details associated with the energy build up which occurred on Explorer 45 orbit 314 presented in Fig. 6. The top panel contains profiles of four energy bands of protons whose widths are about $\pm 15\%$ around the center energies listed. The center panel contains the proton spectrogram which exhibits the nose structure described by Smith and Hoffman (1974). The grey shading is a measure of the flux (in particles/cm^2 sec ster keV) of the equatorially mirroring particles. Black represents the most intense flux. This is an unretouched computer generated plot. The lower panel contains pitch angle distributions for the same four proton energy bands as the top panel at five selected positions in the nose structure. Each pitch angle distribution consists of data from approximately 20 to 160 . (Smith and Hoffman, 1974; Fritz *et al.*, 1974)

most effectively in the region outside the high density plasmasphere. In addition to these two instabilities, charge exchange of the ring current protons with the neutral hydrogen will be ever present during the decay process.

During the injection phase of main phase magnetic storms Smith and Hoffman (1974) have observed a chracteristic of the injected proton distribution which they have named the "nose" event. In Fig. 16 the details of the injection event presented in Fig. 6 are shown. In the top panel the intensity as a function of time (L) is shown for four proton energy passbands. Note that the 13.5 keV passband is the first to increase followed first by the 25.6 keV and then the 6.0 keV passbands. This behaviour is also shown in the energy spectrogram in the middle panel. The particle energies range from 1 keV to 1000 keV and the grey shading is a measure of the intensity of the flux for 90° pitch angle protons in each energy band. The darker the shading the larger the flux. Around 1000 UT the spectrogram appears to contain a projection or "nose" and it is this feature which gives the event its characteristic name (Smith and Hoffman, 1974; Fritz *et al.*, 1974). In the bottom panel of Fig. 16 the pitch angle distributions of the various proton passbands are shown for various points in the evolution of the "nose" event. The general trend in these pitch angle distributions was an initial large increase in the 90° pitch angle intensities followed by an increase in the intensity of the lower pitch angles. Fig. 17 indicates the location along the S^3 orbit where the nose events were observed and their relationship to the plasmapause (PP), the occurrence of the storm sudden commencement (SSC),

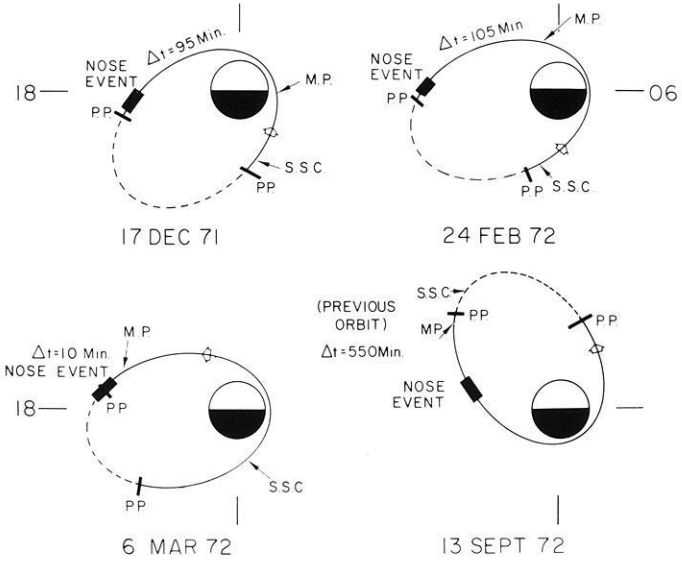

Fig. 17. The Explorer 45 orbit plotted in L and magnetic local time coordinates during four main phase magnetic storms. The positions of the satellite at the times of the storm sudden commencement (*SSC*) and the onset of the main phase decrease (*MP*) are indicated. During the portion of the orbit indicated by a dashed line the satellite was outside the measured plasmapause, indicated by the bars marked PP. The open arrow shows the direction of orbital motion of the satellite. (Smith and Hoffman, 1974; Fritz *et al.*, 1974)

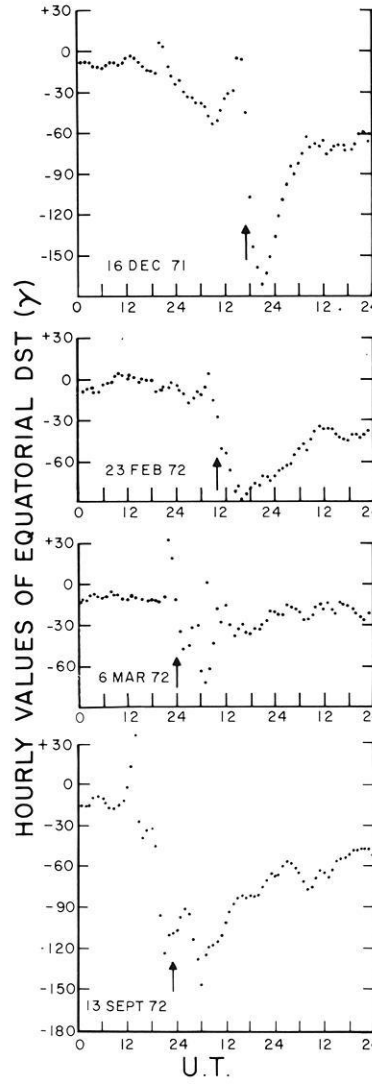

Fig. 18. $D_s t$ for the period of each of the magnetic storms studied in Fig. 17. Times of the nose structures are indicated by the arrows. (Smith and Hoffman, 1974)

and the start of the main phase decrease (MP). The quantity Δt is the time interval between the beginning of the main phase and the observation of the nose event. Fig. 18 presents the temporal relationship with $D_s t$ and shows that each of these events were observed in connection with a major magnetic storm main phase decrease. From Figs. 17 and 18 it is seen that these events (1) occur always just inside the plasmapause, (2) occur only in the local time interval near dusk, (3) occur during main phase magnetic storms but are not strongly time related to the beginning of the main phase decrease or to the sudden commencement, and (4) are independent of direction of the spacecraft being observed on both the inbound and outbound portions of the S^3 orbit.

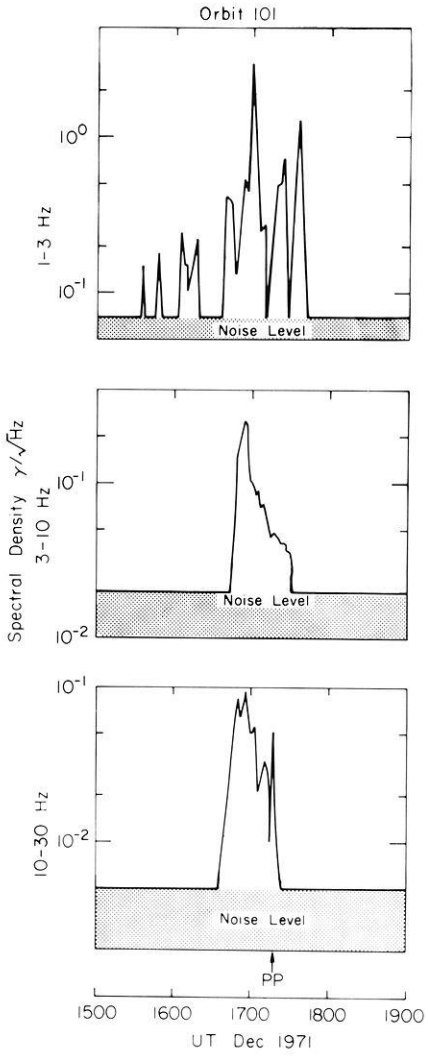

Fig. 19. Spectral densities for magnetic fluctuations in the frequency ranges 1–3 Hz, 3–10 Hz, and 10–30 Hz as measured by Explorer 45 during the outbound portion of orbit 101. The noise levels indicated are for a 30-second peak detector. (Taylor *et al.*, 1974). The plasmapause location marked is that determined by the saturation of the DC electric field experiment (Maynard and Cauffman, 1973). Orbit 101 occurred on December 17, 1971

Smith and Hoffman (1974) have explained the nose structure in the spectrogram in terms of the drift of the protons in a model magnetic and electric field. As pointed out by Roederer and Hones (1974) and more recently by Kivelson and Southwood (1974) small pitch angle particles can penetrate to smaller radial distances from the earth than the 90° pitch angle particles from their source region. The observed pitch angle distribution is just the opposite of that expected indicating that the protons with small pitch angles (large relative parallel energies) are preferentially lost.

The most likely mechanism for such a loss is the ion-cyclotron mechanism noted earlier. Taylor *et al.* (1974) has reported the observation of large amplitude (1–5 γ) waves in the frequency range < 30 Hz. These low frequency events occur very infrequently. Only ten examples were found in over 2000 hours of data. An example of one of these events is shown in Fig. 19. All events were observed

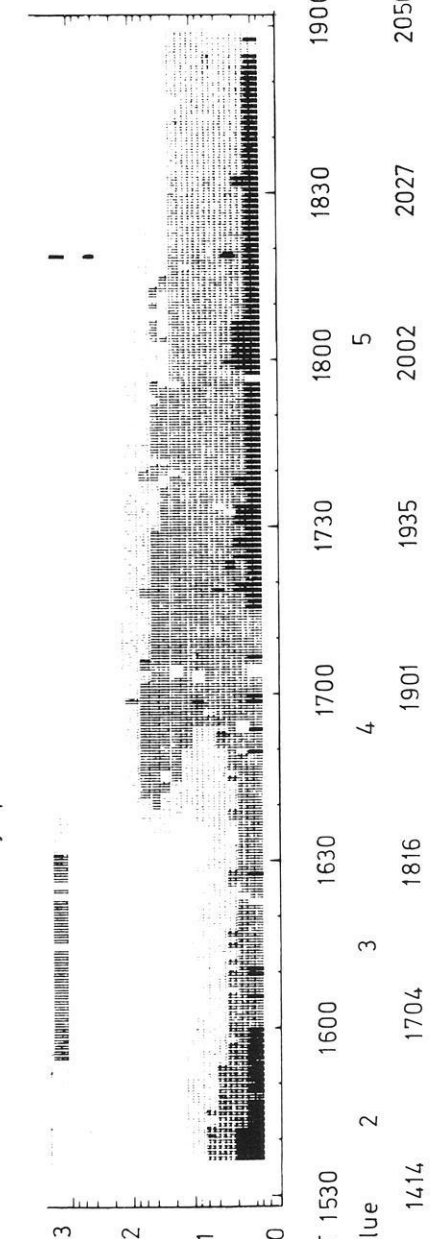

Fig. 20. An unretouched computer generated plot of the proton energy spectrogram for the outbound portion of Explorer 45 orbit 101 showing the position of the nose structure in relation to the occurrence of the 1–3 Hz noise presented in Fig. 19 and the position of the plasmapause (Taylor *et al.*, 1974). (Spectrograms are not corrected for a rate saturation effect which the solid state detectors experiment often suffers in the $2.5 \leqq L \leqq 4.0$ range so that the apparent fluxes of $24.3 \leqq Ep \leqq 201$ keV protons may be too low)

while the satellite was near the plasmapause and in the proton ring current (Taylor *et al.*, 1974).

In Fig. 20 we present another textbook-type example of the ion cyclotron instability in action. In the energy spectrogram a "nose" event is clearly seen extending well inside the plasmapause (PP). Coinciding with this overlap region the ion cyclotron 1–3 Hz noise of Fig. 19 almost perfectly covers the overlap region between the inner edge of the ring current and the plasmapause. To complete the picture developed by Cornwall *et al.* (1970 and 1971), a SAR arc was observed by the Fritz Peak observatory (Hernandez, private communication) during this time period.

In a series of studies (Williams *et al.*, 1973; Williams and Lyons, 1974a and b; Williams, 1974) the concepts of the ion cyclotron instability have been applied to explain the evolution of the proton pitch angle distributions during the recovery phase of a large magnetic storm. An example of this analysis is presented in Fig. 21. The individual plots in each figure show the observed flux versus measured local pitch angle for a particular energy and L value. Plots for all energies are stacked vertically at each L value. Sixteen energies from 1 keV to 390 keV are shown every 0.2 earth radii. Going from low to high altitudes, the pitch angle distributions evolve from rounded distributions peaked at 90° pitch angles to flat distributions, with some energies continuing their evolution to a distribution having a shallow minimum at $\alpha = \pi/2$. This structural evolution generally is seen for all energies $\lesssim 300$ keV. The change from a rounded to a flat distribution often takes place over a small radial distance ($\leqq 0.1$ earth radii) and occurs at increasing radial distances with increasing proton energies. A study of additional recovery phase orbits shows that this pattern moves to higher alititudes with time.

Although no waves < 30 Hz above the threshold of the search coil magnetometers were seen during these recovery phase orbits the transition from the flat-top to the rounded pitch angle distributions appears to result from a depletion of particles with small pitch angles in a manner similar to that described above for the ion-cyclotron instability hypothesis of Cornwall *et al.* (1970). The resonant energy equation describing the cyclotron resonance conditions for protons (Kennel and Petschek, 1966) is:

$$E_{\|,\,\mathrm{res}} = \frac{B^2}{8\pi N} A^{-2}(1+A)^{-1} = \frac{B^2}{8\pi N} F(A)$$

where B is the local magnetic field magnitude and N is the total plasma density. A is a particle anisotropy factor obtained from the pitch angle distribution function and $F(A)$ is a function of order 1 (Williams, 1974). We estimate $E_{\|,\mathrm{res}}$ as a function of altitude by observing the altitude at which the various differential energy channels begin their transition from flat-top to rounded pitch angle distributions.

This measurement of $E_{\|,\mathrm{res}}$ combined with the measured value of B allows a normalized plasma density to be calculated as a function of altitude

$$\frac{N}{F(A)} = \frac{B^2}{8\pi E_{\|,\,\mathrm{res}}} (\mathrm{cm})^{-3}.$$

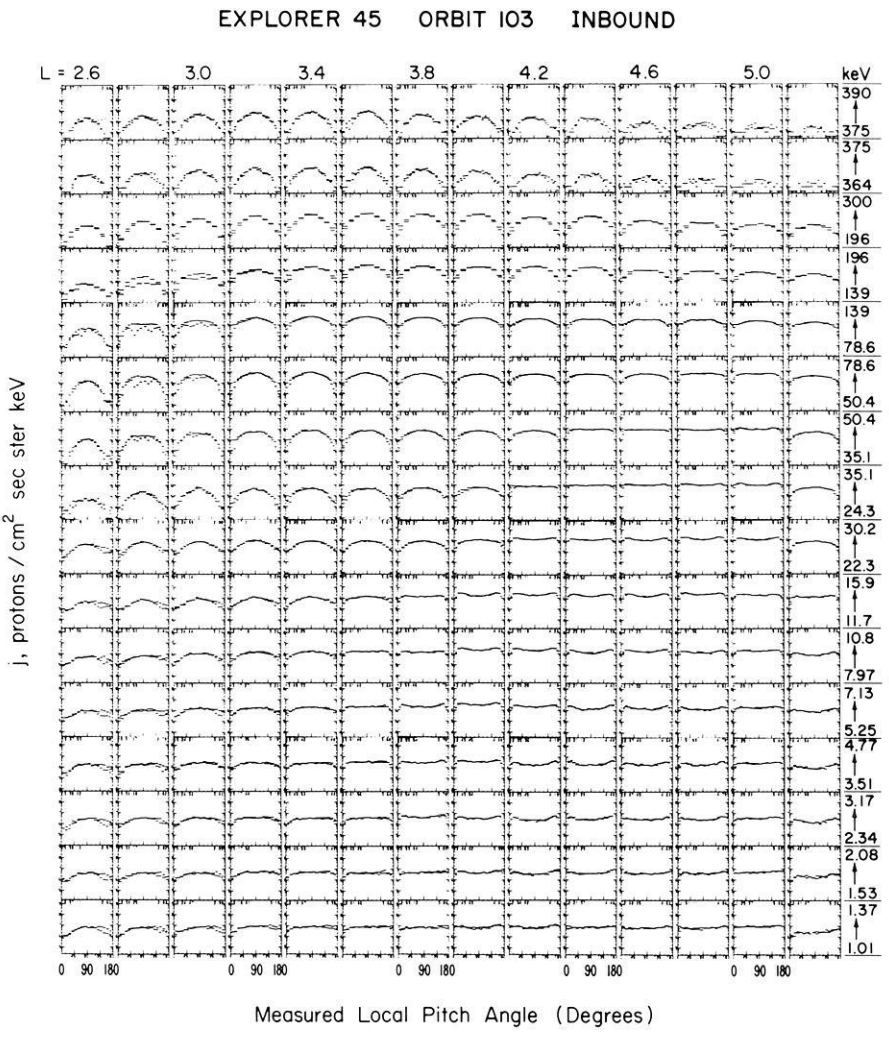

Fig. 21. Proton ring current (hot plasma population) snapshot during the December 18, 1971 storm recovery phase. Note transformation of flat-top (concave-top) pitch angle distributions to rounded pitch angle distributions peaked at 90° with lower energies transforming at lower altitudes. When pitch angle scans in the flat-top distributions reach the loss cone region, intensity decreases are seen implying an empty loss cone. Each individual plot shows $\log_{10}$ differential flux versus measured local pitch angle for a specific energy and L value. Plots for sixteen energies covering 1-390 keV are stacked at a given L value and shown every 0.2 R_E. This is a subset of the full display covering 1-872 keV and every 0.1 R_E which was used for analysis. No data editing has been done. The region where the solid state detector (24.3-300 keV) often suffers a saturation problem (Williams *et al.*, 1973) occurs for $L \lesssim 3.2$. This saturation problem appears as unusual depressions in intensities for pitch angles $90° \pm 45°$. Contamination of the channeltron instrument (1-30.3 keV) by reflected sunlight at near background count rates can be seen during the 90°-180° pitch angle sweep. This problem is related to spin axis orientation, is easily identified, and in the present data does not exist in the 0°-90° pitch angle sweep. Neither of the above effects has any influence on the present study. Data dropouts and telemetry noise effects can also easily be identified (Williams, 1974)

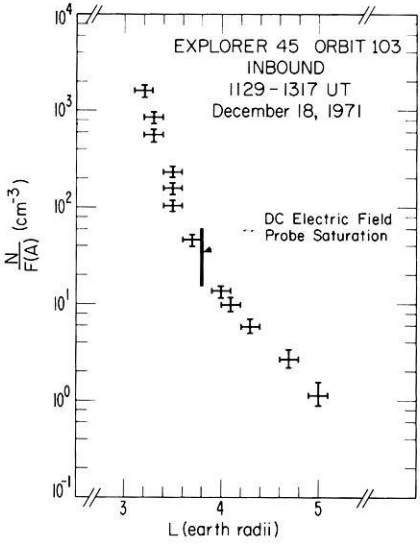

Fig. 22. Plot of $N/F(A)$ versus altitude. Resonant energy equation used to obtain $N/F(A) = B^2/8\,\pi E_{\parallel res}$. Altitude determined as that point where flat top distributions begin their transformation to a rounded distribution. Altitude and density estimate of DC electric field probe saturation is shown. This analysis strongly indicates that the moderate pitch angle diffusion responsible for the rounded pitch angle distribution is due to the amplification of ion-cyclotron waves as the hot ring current plasma interacts with the cold plasmaspheric plasma in the region of the plasmapause (Williams, 1974)

The result of this calculation is shown in Fig. 22 for the orbit presented in Fig. 21. The in situ estimate of the plasma density obtained from the saturation of the DC electric field experiment (Maynard and Cauffman, 1973) is also shown. The agreement is good and the inferred plasmapause shape is quite reasonable.

Additional orbits in this sequence have been analyzed in order to investigate the time behaviour of the $N/F(A)$ boundary. These results are shown in Fig. 23. The apparent outward motion is consistent with average plasmaspheric refilling rates of $\sim 2\times 10^8$ ions/cm^2 sec at $L=3.5$ to $\sim 2.5\times 10^7$ ions/cm^2 sec at $L=4.5$ (Williams, 1974). These refilling rate estimates are in agreement with earlier observations by Chappell *et al.* (1970) and Park (1970) and with the theoretical expectations of Banks (1972).

Therefore we conclude that the ion cyclotron instability as proposed by Cornwall *et al.* (1970) does operate in the vicinity of the plasmapause during main phase magnetic storms.

Low altitude results reported by Hultqvist (Hultqvist, 1974a; Bernstein *et al.*, 1974; Hultqvist, 1974b) indicate that only a small fraction of the total proton precipitation into the atmosphere occurs inside the position of the plasmapuse. This indicates the necessity of requiring a second mechanism such as the electrostatic loss cone instability proposed by Coroniti *et al.* (1972) to operate in the region well outside the region of the plasmapause. Other low altitude observations (Mizera, 1974) indicate that only of the order of 1% of the total proton energy density in the ring current particle distribution is lost in the form of precipitating protons of ring current energies into the atmosphere.

Charge exchange is a loss mechanism which operates throughout the trapping regions. Although the three dimensional density profile for neutral hydrogen to high altitudes around the earth is not well known, results exist showing the importance of charge exchange effects on storm and substorm associated protons (Swisher and Frank, 1969; McIlwain, 1972; Smith *et al.*, 1974). Fig. 24 from

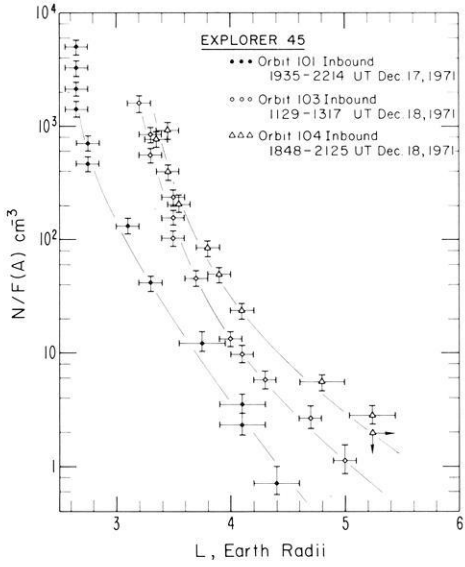

Fig. 23. Same as Fig. 22 with orbits 101 and 104 added. Outward motion of $N/F(A)$ boundary is clearly seen and is consistent with expected plasmaspheric cold plasma refilling rates

Smith *et al.* (1974) shows a comparison of the decay of proton intensities locally mirroring near the equator at various energies with the predictions due to the charge exchange process at $L=4.25$. In this case the agreement between observations and theory is very good.

Williams (1974) has qualitatively illustrated the complimentary nature of the ion cyclotron and charge exchange loss processes for the ring current during recovery phase. This is shown in Fig. 25. The horizontal bar qualitatively shows in relation to the plasmapause region what the relative strengths of charge exchange (CE) and ion cyclotron resonance (IC) losses are. The bar shows the situation for only one energy and pitch angle and will move up and down the figure for other energy-pitch angle combinations. The IC region is extended to overlap the CE region within the plasmasphere because of possible parasitic precipitation effects which may compete with charge exchange time scales (Lyons and Thorne, 1972). The shaded IC region moves left and right in accordance with the time varying plasma density profile in the plasmapause region. No other losses are included.

It is apparent that the hot plasma distribution function is dominated by the ion cyclotron resonance effect in the plasmapause region. However, the specific effects to be observed at altitudes above the plasmapause region will depend critically on the relative values of charge exchange lifetimes and plasmasphere refilling times. Well inside the plasmapause region, the remainder of the hot plasma distribution should be dominated by charge exchange and Coulomb losses. Significant hot plasma intensity exists inside the plasmapause region during recovery phase, presumably because the ion cyclotron interaction initiates only a moderate pitch angle diffusion mode and is relatively inefficient at removing particles near $\alpha \sim \pi/2$. The arrest of the instability at a moderate diffusion level may be due to absorption of wave energy by cold electrons (Cornwall *et al.*,

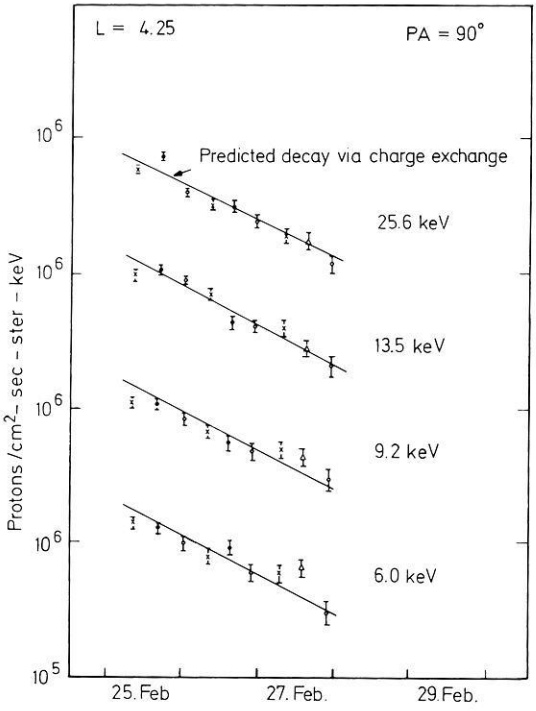

Fig. 24. Proton flux decay for particles mirroring near the equatorial plane at $L=4.25$ and local times around 2000 hours following the magnetic storm of February 24, 1972. Dst for this event is shown in Fig. 18. Fluxes measured at four energies from 6.0 to 25.6 keV are shown. The solid lines have the charge exchange decay slopes (Liemohn, 1961) for these energies at this pitch angle and L-value (Smith *et al.*, 1974)

1971) and by quenching effects due to attainment of large ratios of cold plasma density to hot plasma density (Cuperman and Landau, 1974; Cuperman *et al.*, 1973).

Williams (1974) has also shown data indicating loss rates in excess of charge exchange losses occurring at the beginning of the geomagnetic storm recovery phase. Therefore, it seems that in order to explain initial recovery phase effects as well as the low altitude observations mentioned above, additional loss mechanism have to be invoked. Furthermore, all the considerations concerning losses of the ring current during recovery phase apply to hot plasmas for which $\beta \leqq 1$. The situation for $\beta > 1$ is yet to be experimentally studied in detail and quantitatively explained theoretically.

The Role of Ions ($Z \geqq 2$) in the Magnetosphere

One of the least expected observations made by Explorer 45 was that of an intense flux of energetic ions ($Z \geqq 2$) confined closely to the geomagnetic equatorial

plane (Fritz and Williams, 1973). These ions which appear to be alpha particles, peak in intensity in the vicinity of $L = 3.5$ and could make an appreciable contribution to the "quiet-time" ring current. Recent results obtained by the Lockhead group (Shelly *et al.*, 1974 and references therein) at low altitudes indicate that energetic ions heavier than protons could play a major role in the formation of various current systems flowing in the magnetosphere such as the storm-time ring current. Almost all instrumentation flown aboard satellites in the past has not been designed to differentiate between protons and heavier ions. Very few investigations have attempted to study the potentially important role of ion species other than H^+ in magnetospheric processes. Further studies both those involving instrumentation and those involving theoretical investigations should attempt to investigate the possible role of multiple species of ions which can be involved with wave-particle interactions.

IV. Conclusions

We have attempted to indicate the existence of two wave-particle instabilities in the vicinity of the plasmapause region, the mechanism of Kennel and Petschek (1966) operating in the afternoon hours on tens of keV electrons and the mechanism of Cornwall *et al.* (1970, 1971) operating in the evening hours on tens of keV ring current protons. While these mechanisms appear to modify the distribution function of the particular particles of a given energy participating in the instability, neither mechanism appears to be a dominant loss process for the overall distribution of those particular particles.

The mechanism of Kennel and Petschek (1966) may be responsible for the production of ELF hiss which propagates to fill the region of the plasmaspheric

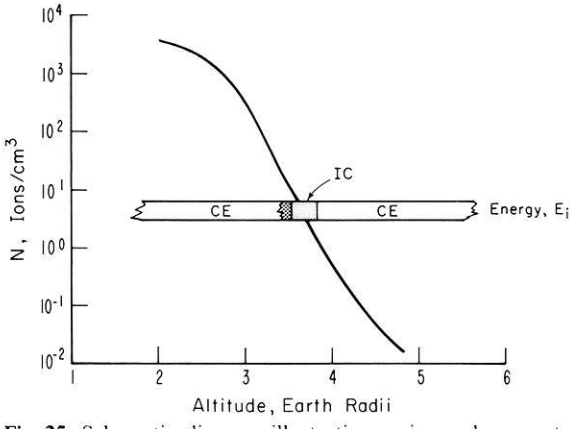

Fig. 25. Schematic diagram illustrating regions where proton flux decay due to charge exchange (*CE*) and ion-cyclotron resonance (*IC*) losses are expected to occur. Situation illustrated for one specific energy, E_i, and pitch angle. Horizontal bar moves up and down (up for lower energies) for other energy-pitch angle combinations. As cold plasma refilling occurs, plasmapause region and shaded IC region move towards higher altitudes. Overlap region illustrates extension of IC region through possible parasitic precipitation effects. No other losses are considered here. (Williams, 1974)

volume. The ELF hiss appears to be present almost all of the time and therefore cannot be acting to precipitate the electrons which produce the hiss on a fast time scale unless the electrons are constantly replenished. The ELF hiss produced in this manner is the dominant loss mechanism for $E > 40$ keV electrons inside the plasmasphere by diffusing these electrons in pitch angle through resonant interactions. With this interaction the properties of electron fluxes throughout the plasmasphere are well understood by balancing sources (radial diffusion) with losses (resonant interactions and atmospheric Coulomb collisions).

The mechanism of Cornwall *et al.* (1970, 1971) is responsible for the production of ion cyclotron waves which produce the effect of creating enhanced electron temperature in the low altitude regions where SAR arcs are produced. The qualitative relationship of this mechanism and charge exchange is shown in Fig. 25.

Energetic proton precipitation at and inside the plasmapause represents a small fraction of the total proton flux precipitating into the atmosphere (Hultqvist, 1974a and b) and this total flux itself represents a small fraction of the total ring current energy density (Mizera, 1974) which must be dissipated in the decay of the ring current. Decay via the charge exchange process appears to be the dominant process in the decay of the storm-time ring current although other wave-particle interactions may be responsible for the precipitation of protons in the region well outside the plasmapause. Whether or not protons which mirror away from the equator (finte $v_{||}$) are affected by charge exchange or ion cyclotron resonance depends on the relative values of charge exchange lifetimes and plasmaspheric refilling times.

Acknowledgements. We would like to acknowledge the use of results from studies using Explorer 45 data, some of which have not reached the final publication phase, of Dr. J.N. Barfield, Dr. L.J. Cahill, Jr., Dr. S.E. DeForest, Dr. D.A. Gurnett, Dr. R.A. Hoffman, Dr. A. Konradi, Dr. L.R. Lyons, Dr. N.C. Maynard, Dr. B. Parady, Dr. P.H. Smith, and Dr. W.W.L. Taylor. We are especially indebted for valuable discussions with Dr. J.N. Barfield, Dr. L.R. Lyons, and Dr. P.H. Smith about various phases of this work.

This paper is intended as a contribution to a collection of papers honoring Professor G. Pfotzer of the Max-Planck-Institut für Aeronomie on his 65th birthday. We would like to express our personal appreciation to Professor Pfotzer for the help he has given in permitting a close cooperation between our respective laboratories and in particular the special arrangements which provided for a year in residence at Lindau for one of us (TAF).

References

Anderson, R.R., Gurnett, D.A.: Plasma wave observations near the plasmapause with the S^3-A satellite. J. Geophys. Res. **78**, 4756–4764 (1973)

Banks, P.M.: Behaviour of thermal plasma in the magnetosphere and topside ionosphere. In: Critical Problems of Magnetospheric Physics, Proceedings of the Joint COSPAR/IAGA/URSI Symposium, Madrid, Spain, May 11–13, 1972, E.R. Dyer, ed., pp. 152–178. Pub. IUCSTP Secretariat, 1972

Barfield, J.N., Burch, J.L., Williams, D.J.: Substorm associated reconfiguration of the duskside equatorial magnetosphere: a possible source mechanism for isolated plasma regions. J. Geophys. Res. **80**, 47–55 (1975)

Barfield, J.N., DeForest, S.E.: Simultaneous observations of magnetospheric particle variations during substorms: Explorer 45 and ATS-5. EOS Trans. Am. Geophys. Union 55, 1016 (1974)

Bernstein, W., Hultqvist, B., Borg, H.: Some implications of low altitude observations of isotropic

precipitation of ring current protons beyond the plasmapause. Planet. Space Sci. **22**, 767–776 (1974)
Chappell, C.R., Harris, K.K., Sharp, G.W.: The morphology of the bulge region of the plasmasphere. J. Geophys. Res. **75**, 3848–3861 (1970)
Cornwall, J.M., Coroniti, F.V., Thorne, R.M.: Turbulent loss of ring current protons. J. Geophys. Res. **75**, 4699–4709 (1970)
Cornwall, J.M., Coroniti, F.V., Thorne, R.M.: Unified theory of SAR arc formation at the plasmapause. J. Geophys. Res. **76**, 4428–4445 (1971)
Coroniti, F.V., Fredricks, R.W., White, R.: Instability of ring current protons beyond the plasmapause during injection events. J. Geophys. Res. **77**, 6243–6248 (1972)
Cuperman, S., Landau, R.W.: On the enhancement of the whistler mode instability in the magnetosphere by cold plasma injection. J. Geophys. Res. **79**, 128–134 (1974)
Cuperman, S., Salu, Y., Bernstein, W., Williams, D.J.: A computer simulation of cold plasma effects on the whistler instability for geostationary orbit parameters. J. Geophys. Res. **78**, 7372–7387 (1973)
DeForest, S.E., McIlwain, C.E.: Plasma clouds in the magnetosphere. J. Geophys. Res. **76**, 3587–3611 (1971)
Fritz, T.A., Williams, D.J.: Initital observations of geomagnetically trapped alpha particle at the equator. J. Geophys. Res. **78**, 4719–4724 (1973)
Fritz, T.A., Smith, P.H., Williams, D.J., Hoffman, R.A., Cahill, L.J.: Initial observations of magnetospheric boundaries by Explorer 45 (S^3). In: Correlated Interplanetary and Magnetospheric Observations, D.E. Page, ed., pp. 485–506. Dordrecht-Holland: D.Reidel 1974
Hoffman, R.A.: Particle and field observations from Explorer 45 during the December 1971 magnetic storm period. J. Geophys. Res. **78**, 4771–4777 (1973)
Hultqvist, B.: Rocket and satellite observations of energetic particle precipitation in relation to optical aurora. Ann. Géophys. (in press) (1974a)
Hultqvist, B.: The ring current and particle precipitation near the plasmapause. Kiruna Geophysical Institute Preprint No. **74**, 304 (1974b)
Kennel, C.F., Petschek, H.E.: Limit on stably trapped particle fluxes. J. Geophys. Res. **71**, 1–28 (1966)
Kivelson, M.G., Southwood, D.J.: Approximations for the study of drift boundaries in the magnetosphere. J. Geophys. Res. (submitted for publ.) (1974)
Konradi, A., Williams, D.J., Fritz, T.A.: Energy spectra and pitch angle distributions of storm-time and substorm injected protons. J. Geophys. Res. **78**, 4739–4744 (1973)
Konradi, A., Semar, C.L., Fritz, T.A.: Substorm injected protons and electrons and the injection boundary model. J. Geophys. Res. **80**, 543–552 (1975)
Liemohn, H.: The lifetime of radiation belt protons with energies between 1 keV and 1 MeV. J. Geophys. Res. **66**, 3593–3595 (1961)
Longanecker, G.W., Hoffman, R.A.: S^3-A spacecraft and experiment description. J. Geophys. Res. **78**, 4711–4717 (1973)
Lyons, L.R., Thorne, R.M.: Parasitic pitch angle diffusion of radiation belt particles by ion cyclotron waves. J. Geophys. Res. **77**, 5608–5616 (1972)
Lyons, L.R., Thorne, R.M., Kennel, C.F.: Pitch angle diffusion of radiation belt electrons within the plasmasphere. J. Geophys. Res. **77**, 3455–3474 (1972)
Lyons, L.R., Thorne, R.M.: Equilibrium structure of radiation belt electrons. J. Geophys. Res. **78**, 2142–2149 (1973)
Lyons, L.R., Williams, D.J.: The quiet-time structure of energetic (35–560 keV) radiation belt electrons. J. Geophys. Res. (submitted for publ.) (1974a)
Lyons, L.R., Williams, D.J.: The storm and post storm evolution of energetic (35–560 keV) radiation belt electron distributions, J. Geophys. Res. (submitted to publ.) (1974b)
Mauk, H., McIlwain, C.E.: Correlation of Kp with substorm-injected plasma boundary. J. Geophys. Res. **79**, 3193–3196 (1974)
Maynard, N.C., Cauffman, D.P.: Double floating probe measurements on S^3-A. J. Geophys. Res. **78**, 4745–4750 (1973)
Maynard, N.C., Chen, A.J.: Isolated cold plasma regions: Observations and their relation to possible production mechanisms. J. Geophys. Res. (submitted for publ.) (1974)
McIlwain, C.E.: Plasma convection in the vicinity of the geostationary orbit. In: Earth's Magnetospheric Processes, B.M. McCormac, ed., pp. 268–279. Dordrecht-Holland: D. Reidel 1972

McIlwain, C.E.: Substorm injection boundaries. In: Magnetospheric Physics, B.M. McCormac, ed., pp. 143–154. Dordrecht-Holland: D. Reidel 1974

Mizera, P.F.: Observations of precipitating protons with ring current energies. J. Geophys. Res. **79**, 581–588 (1974)

Parady, B.: Measurement of low frequency magnetic fluctuations in the magnetosphere. Ph.D. Thesis, 246 pages, University of Minnesota, Minneapolis, Minnesota, March, 1974

Parady, B.K., Eberlein, D.D., Marvin, J.A., Taylor, W.W.L., and Cahill, L.J.: Plasmaspheric hiss observations in the evening and afternoon quadrants. J. Geophys. Res. (submitted for publ.) (1974)

Park, C.G.: Whistler observations of the interchange of ionization between the ionosphere and protonosphere. J. Geophys. Res. **75**, 4249–4260 (1970)

Roederer, J.G., Hones, E.W.: Motion of magnetospheric particle clouds in a time-dependent electric field model. J. Geophys. Res. **79**, 1432–1438 (1974)

Russell, C.T., Holzer, R.E.: AC magnetic field. In: Particles and Fields in the Magnetosphere. B.M. McCormac, ed., pp. 195–212. Dordrecht-Holland: D. Reidel 1970

Shelley, E.G., Sharp, R.D., Johnson, R.G.: The ionosphere as a source of ring current particles, Trans. Am. Geophys. Union **55**, 1015 (1974)

Smith, P.H., Hoffman, R.A.: Ring current particle distributions during the magnetic storm of December 16–18, 1971. J. Geophys. Res. **78**, 4731–4737 (1973)

Smith, P.H., Hoffman, R.A.: Direct observations in the dusk hours of the characteristics of the storm-time ring current particles during the beginning of magnetic storms. J. Geophys. Res. **79**, 966–971 (1974)

Smith, P.H., Hoffman, R.A., Fritz, T.A.: Ring current proton decay by charge exchange. Goddard Space Flight Center Research Report, 1974

Swisher, R.L., Frank, L.A.: Lifetimes for low-energy protons in the outer zone. J. Geophys. Res. **73**, 5665–5672 (1968)

Taylor, W.W.L., Parady, B., Cahill, L.J.: Explorer 45 observations of 1–30 Hz magnetic fields near the plasmapause during magnetic storms. J. Geophys. Res. (submitted for publication) (1974)

Thorne, R.M., Barfield, J.N.: On the origin of plasmaspheric hiss (in preparation) (1974)

Thorne, R.M., Smith, E.J., Fiske, K., Church, S.: Intensity variations of ELF hiss and chorus during isolated substorms. Geophysical Research Letters, **1**, 193–196 (1974)

Williams, D.J., Fritz, T.A., Konradi, A.: Observations of proton spectra ($1.0 \leqq Ep \leqq 300$ keV) and fluxes at the plasmapause. J. Geophys. Res. **78**, 4751–4755 (1973)

Williams, D.J.: Hot-cold plasma interactions in the earth's magnetosphere. Proceedings of the Symposium on the Magnetospheres of Earth and Jupiter, Frascati, Italy, May 28–June 1, 1974

Williams, D.J., Barfield, J.N., Fritz, T.A.: Initial Explorer 45 substorm observations and electric field considerations. J. Geophys. Res. **79**, 554–564 (1974)

Williams, D.J., Lyons, L.R.: The proton ring current and its interaction with the plasmapause: storm recovery phase. J. Geophys. Res. **79**, 4195–4207 (1974a)

Williams, D.J., Lyons, L.R.: Further aspects of the proton ring interaction with the plasmapause: Main and recovery phases. J. Geophys. Res. **79**, 4791–4798 (1974b)

Received October 28, 1974; Revised Version April 7, 1975

J. Geophys. 41, 581–594, 1975

Probability Distribution of Earthquake Accelerations with Applications to Sites in the Northern Rhine Area, Central Europe

L. Ahorner

Erdbebenstation der Universität Köln, D-5060 Bensberg, Vinzenz-Pallotti-Straße 26, Federal Republic of Germany

W. Rosenhauer

INTERATOM, Internationale Atomreaktorbau GmbH, D-5060 Bensberg, Friedrich-Ebert-Straße, Federal Republic of Germany

Abstract. Based on the observed earthquake activity of the period 1750–1970 and the distribution of neotectonic structural activity a regional seismicity model has been established to calculate the earthquake risk for sites in the Northern Rhine area by a computer program. The calculation procedure makes use of Gumbel's extreme value theory and gives the recurrence intervals of various earthquake magnitudes for finite volume elements of seismoactive regions and, in interdependence herewith, the probability distribution of earthquake accelerations at the earth surface as a function of distance from the entirety of finite focal volumes. Numerical calculations were made for 220 sites within an area of 160000 km^2. From the results, earthquake risk maps have been drawn giving isolines of equal probabilities for earthquake accelerations higher than 100 and 300 cm/s^2. The highest earthquake risk has been found in the western part of the Lower Rhine graben between Köln and Aachen, where two seismoactive zones, the Rhenish and Belgian earthquake zones, are intersecting. Methods and results presented are a first step towards an analysis of earthquake risk by probability considerations which is not state of the art in current licensing procedures *e.g.* for nuclear plants.

Key words: Earthquake Risk – Northern Rhine Area – Central Europe.

1. Introduction

As a result of the increasing industrial, commercial and residential developments, which cause the population centers to spread in ever-widening circles, reliable estimations of the local earthquake risk are of interest not only in the main earthquake countries but also in regions with minor seismicity such as Central Europe. This is especially true for sites of nuclear power plants and other industrial objects offering a potential source of environmental danger in regions with dense population.

An appropriate statistical tool to estimate the earthquake risk, i.e. the probability of the occurrence of a strong shock in a given time period, is the Gumbel extreme value theory (1935, 1967), which was applied to earthquake

statistics first by Nordquist (1945) and later by Epstein and Lomnitz (1966), Kárník (1971) and others.

In the present paper the application of Gumbel's extreme value theory to earthquake data of Western Germany will be described. Based on the observed earthquake activity in the period 1750–1970 and the distribution of neotectonic structural activity a regional seismicity model has been established to calculate the probability distribution of earthquake accelerations at given sites by a computer program.

2. Seismicity of the Northern Rhine Area

The object of our study is the Northern Rhine area (4 °E to 10 °E, 49 °N to 52 °N) which covers the western part of Germany (Nordrhein-Westfalen, Hessen, Rheinland-Pfalz) and the adjoining regions of Luxembourg, Belgium and the Netherlands.

The seismicity and seismotectonics of this region have been studied in detail by Ahorner (1968, 1970). Seismicity data are based on historical earthquake catalogues of Sieberg (1940), Sponheuer (1952) and others, and – beginning with shocks later than 1900 – on a re-interpretation of all available macroseismic and microseismic original information. A chronological list has been prepared of earthquakes since 1500 giving for each shock the date of occurrence, the latitude and longitude of the epicenter, the macroseismic intensity I_0 (MSK-scale) near the epicenter, the magnitude M_{loc} (local magnitude according to the original Richter-scale) and an estimate of the focal depth h. No allowance was made of rockbursts and other seismic events of true artificial origin.

Fig. 1 shows the locations of epicenters classified according to magnitude, focal depth and accuracy of epicenter determination. For the period 1500–1749 only shocks with magnitudes $M \geqq 4.5$ were plotted, for 1750–1899 those with $M \geqq 3.5$ and for 1900–1969 those with $M \geqq 2.5$. It is obvious from the distribution of epicenters that nearly all foci being active since 1500 are situated within three zones (bounded by broken lines in the map):

– The Rhenish earthquake zone, which goes from Karlsruhe in the South to Nijmegen in the North, following the neotectonic fracture zones of the Upper Rhine graben, Middle Rhine valley and Lower Rhine graben.

– The Belgian earthquake zone, which trends in a westeastern direction across Belgium and meets the Rhenish zone in the region between Aachen and Köln.

– The Hunsrück earthquake zone, which is of minor importance and covers the south-western border region of the Hercynic Rhenish massif (Rheinisches Schiefergebirge) between Mainz and Luxembourg.

In the western part of the Lower Rhine graben near the intersection point between the Rhenish and Belgian earthquake zone the highest level of seismicity is observed. In this region, the strongest earthquake of the Northern Rhine area took place near Düren 1756 ($M \approx 6$, $I_0 = \text{VIII}$). Another major shock with $M = 5.8$ occurred 1938 in the Belgian zone south-west of Bruxelles. Eight shocks in the last 200 years were of magnitude $M = 5.0 - 5.4$. From magnitude-frequency

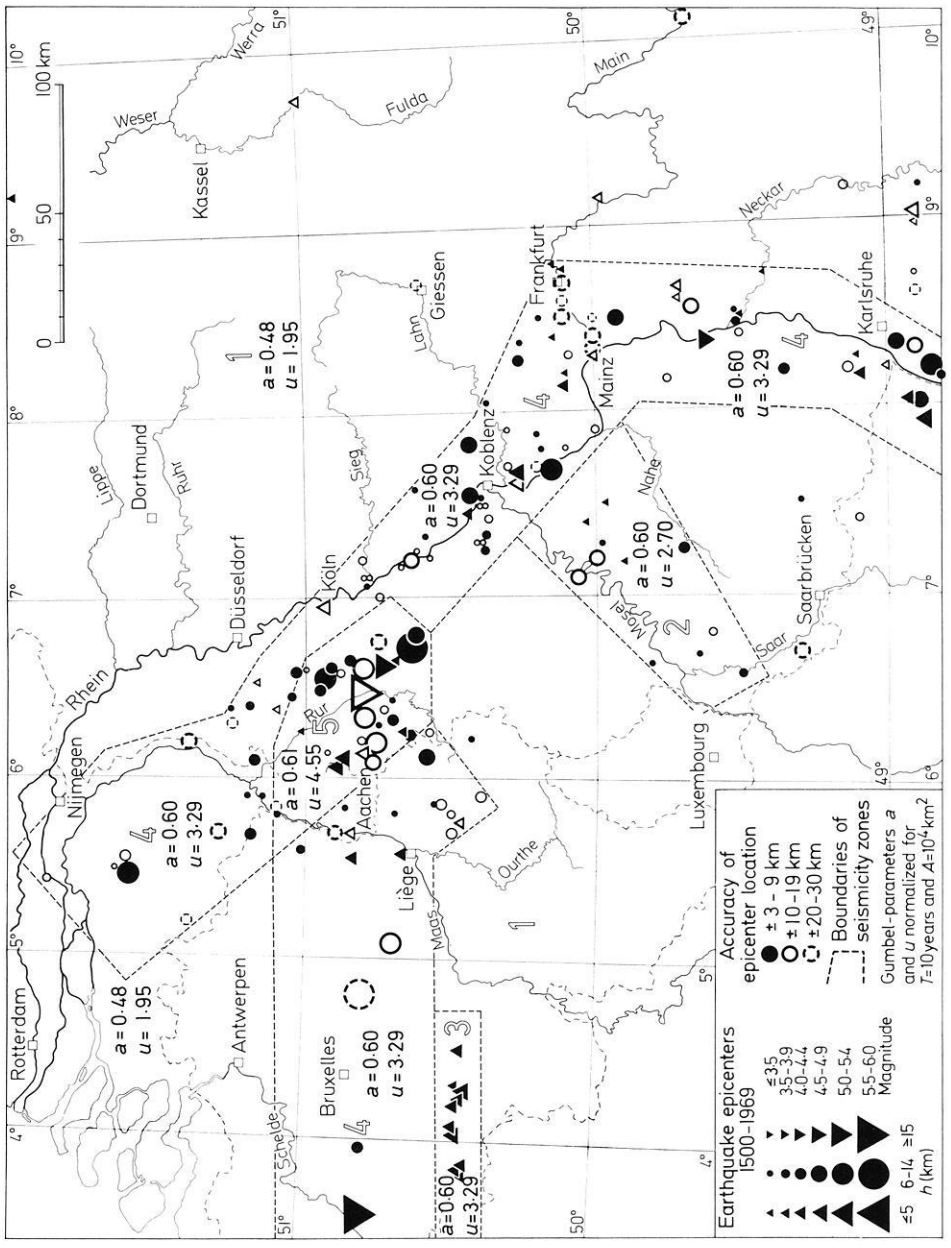

Fig. 1. Seismicity zones and earthquake epicenters of the Northern Rhine area. Normalized Gumbel parameters a and u are given for each region

analysis it becomes clear that the specific seismicity (magnitude frequency per unit area and time) of the Rhenish and Belgian earthquake zone is about one tenth of that of Southern California or the East African rift zone (Ahorner, 1975).

Focal depths of the Northern Rhine area, determined mostly macroseismically, vary between several and 25 km as a maximum. The great majority of shocks is released in the upper part of the crust within the depth range of $h = 6 - 12$ km

(Ahorner, Murawski, Schneider, 1972). Very superficial shocks with $h=1-2$ km are predominant in the Hainaut region south of Bruxelles (Ahorner, 1972). Damaging earthquakes with intensities up to VIII are confined nearly exclusively to the Rhenish and Belgian earthquake zone (Ahorner, Murawski, Schneider, 1970). Outside of these zones only a few earthquakes with local damage have been observed.

In the light of regional seismotectonics the Rhenish and Belgian earthquake zones form together an intra-plate zone of crustal weakness, where – within the Eurasian lithospheric plate – recent block movements are going on with a mean slip rate of a few tenth of a mm per year (Ahorner, 1975). The simple large-scale deformation pattern and the close relationship between seismicity and neotectonic structural activity facilitates the seismic regionalisation of the Northern Rhine area as shown in Fig. 1.

3. Probability Description of Earthquakes

3.1. Conventional Statistics and Extreme Value Theory

Analysing a sample of N earthquakes in a specified region with respect to their Richter magnitudes M one might aim at the cumulative distribution $F(M)$, which is defined by the probability that an earthquake has a magnitude not greater than M:

$$\begin{aligned} &F(M)=P(\text{magnitude}\leqq M)\approx n(M)/N,\\ &n(M)=\text{number of sample members with magnitudes}\leqq M. \end{aligned} \tag{1}$$

$F(M)$ or closely related quantities like the return period $1/[1-F(M)]$ or the probability density $dF(M)/dM$ are not easily applicable to risk estimations because

– reliable probabilities are required for higher values of M at which the small number of occurrences introduces large uncertainties of $F(M)$,

– an extrapolation of $F(M)$ relies upon the completeness of observations at low values of M,

– N ought to be the total number of earthquakes during the observation time; unfortunately, this number is not well defined as it grows with the improvement of the lower detection limit for smaller earthquakes.

The theory of extremes provides an approach avoiding these shortcomings by using a probability picture less detailed than Eq. (1), but still covering enough information for risk applications. Instead of $F(M)$ the cumulative distribution of the largest magnitude within a specified region A and time T is considered:

$$G(M)=P\,(\text{largest magnitude}\leqq M \text{ in } A, T). \tag{2}$$

$G(M)$ could in principle be determined analogously to Eq. (1). Looking only for the earthquakes with the largest magnitudes within certain intervals (e.g. the extremes for $T=5$ years) of the whole observation time one gets:

$$\begin{aligned} &G(M)=ne(M)/Ne,\\ &ne(M)=\text{number of extremes with magnitudes}\leqq M,\\ &Ne=\text{total number of extremes.} \end{aligned} \tag{3}$$

It is obvious that information concerning only the extremes, i.e. the largest earthquakes, is much better for the historical time than the observation material for the whole magnitude spectrum. A complete catalogue of earthquakes down to magnitude $M=4$ has been achieved in Western Germany only since about 1800 and down to $M=3$ only since 1950.

One of the main advantages of Eq. (2) is, however, that it is not necessary to determine the functional shape of $G(M)$, which would require much more data than available. The connection between $G(M)$ and $F(M)$ is easily derived from the fact that the extreme is not higher than M if every single event has magnitude $\leqq M$ and vice versa. The assumption of independence leads to

$$G(M)=[F(M)]^n, \qquad n=\text{total number of earthquakes in } A, T. \tag{4}$$

Investigating the limit $n\to\infty$ it can be proved that for an extensive class of initial distributions $F(M)$ the extreme value distribution $G(M)$ approaches the Gumbel distribution as an asymptote:

$$G(M)\approx\exp\left[-\exp\left(-\frac{M-u}{a}\right)\right], \qquad a=a(F), \quad u=u(n,F). \tag{5}$$

The interpretation of this result is that

– different distributions $F(M)$ lead to the same function $G(M)$ if n is not too small,

– n and the actual shape of $F(M)$ are contained in the numerical values of a and u,

– the knowledge of n and the functionals $a(F)$ and $u(n, F)$ can be dispensed with if the numerical values of a and u are deduced from extreme value observations directly.

As a proof of Eq. (5) the validity of the Gumbel distribution has to be tested against observed extremes.

3.2. Order Statistics and Gumbel Parameters

Using order statistics evaluation methods have been developed particularly suitable to the Gumbel distribution. Numerical results, best fits, tests, uncertainties etc. have been obtained from the INTERATOM program GUMBEL on a CDC 6400.

Let the Ne observed extremes be arranged in increasing order:

$$M_1\leqq M_2\leqq\cdots\leqq M_{Ne}. \tag{6}$$

Looking for the m-th observation counted from the bottom ($m=1, 2, \ldots, Ne$) it is evident that the value expected for it depends on the Gumbel parameters a and u. This dependence is found to be linear, containing a coefficient y_m which obviously has to be interpreted as the expectation of the m-th observation for a Gumbel distribution with $a=1$ and $u=0$:

$$\overline{M}_m=\overline{M}_m(a,u)=a\cdot y_m+u, \qquad y_m=\overline{M}_m(1,0). \tag{7}$$

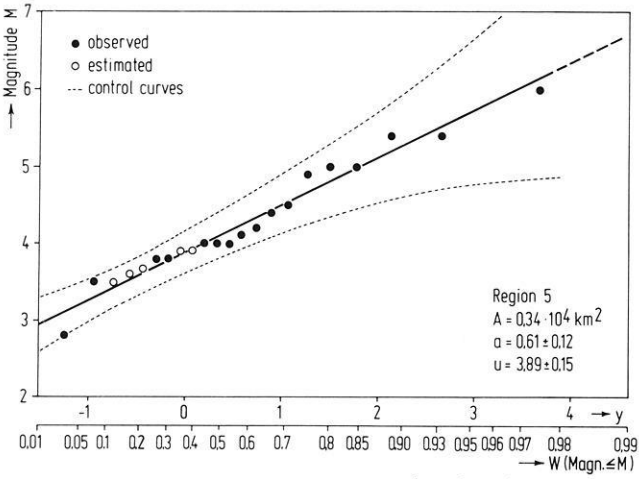

Fig. 2. Gumbel plot of 10-year extremes of earthquake magnitude for the western part of Lower Rhine graben (region 5, observation period 1750 – 1969). Control curves and not normalized parameters a and u calculated by the program GUMBEL are given

The numerical values for y_m are calculated once and for all from explicit formulae or by Monte Carlo simulation in program GUMBEL. Regarding the m-th observation M_m as an estimate of its expectation $\overline{M}_m$ one gets

$$\overline{M}_m \approx M_m, \qquad M_m \approx a \cdot y_m + u. \tag{8}$$

The last equation says that the points (y_m, M_m) scatter about a straight line the parameters of which are the Gumbel parameters wanted.

As an example, Fig. 2 shows the plotted 10-year extremes for the western part of the Lower Rhine graben (see Fig. 1).

The dashed control curves give the range of still acceptable deviations allowing the agreement between Eq. (5) and the observations to be judged by inspection, too. The GUMBEL estimates for a and u are without bias. A simulation subroutine provides the uncertainties of these estimates needed in Section 5.

A Gumbel parameter evaluation (Table 1) has been performed for the seismicity zones described in Section 2. The values a and u (in Table 1 and Fig. 1)

Table 1. Seismological subdivision of the Northern Rhine area

Region		Area $A/10^4$ km^2	Gumbel parameters (normalized)	
			a	u
5	Western part of the Lower Rhine graben (between Aachen and Köln)	0.34	0.61 ± 0.12	4.55 ± 0.20
4	Rhenish and Belgian earthquake zone (except region 5)	3.20	0.60 ± 0.12	3.29 ± 0.21
3	Hainaut zone (shallow shocks)	0.15	0.60 ± 0.12	3.29 ± 0.21
2	Hunsrück zone	0.46	0.60 ± 0.12	2.70 ± 0.18
1	Regions with very low seismicity (outside regions 2–5)	12.8	0.48 ± 0.14	1.95 ± 0.68

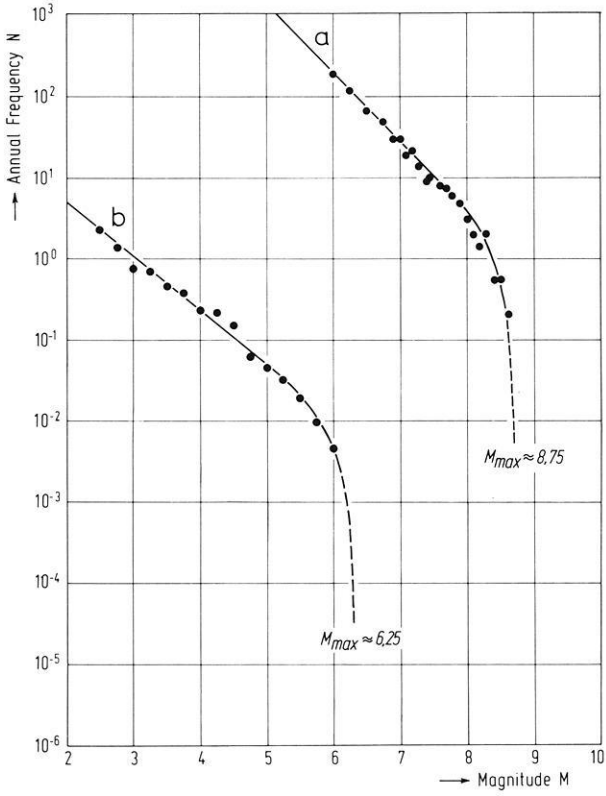

Fig. 3. Mean annual frequency distribution of earthquake magnitudes for the world (curve *a*, from Housner, 1970) and the Northern Rhine area (curve *b*, from Ahorner, 1972). Observed data allow an estimation of the maximum possible magnitude M_{max}

are normalized to $T=10$ years and an area of $A=10^4$ km^2 respectively. The transformation between areas A_0 and A of different size is

$$a_0 = a, \qquad u_0 = u + a \cdot \ln(A_0/A). \tag{9}$$

3.3. Upper Bound for Magnitudes

Observed extremes give an excellent support for the Gumbel distribution up to $M \approx 6$ (see Fig. 2). Without further knowledge one had to accept its validity up to infinite values of M. This, however, is not reasonable because of lithophysical and seismotectonic boundary conditions. Absolute upper bounds seem to exist for the whole world at $M_{max} \approx 8.75$ and for Central Europe at $M_{max} = 6.5 \pm 0.25$ (see Fig. 3 and Housner (1970), Ahorner (1972)).

M_{max} is taken into account by using a conditional probability distribution $G_c(M)$ constructed from Eq. (5) by introducing the condition: M not greater than M_{max}. This means a slight deformation of $G(M)$ in the range of observations and excludes values of M higher than M_{max}:

$$G_c(M) = G(M/M \leqq M_{max}) = \begin{cases} \dfrac{G(M)}{G(M_{max})} & (M \leqq M_{max}) \\ 1 & (M > M_{max}). \end{cases} \tag{10}$$

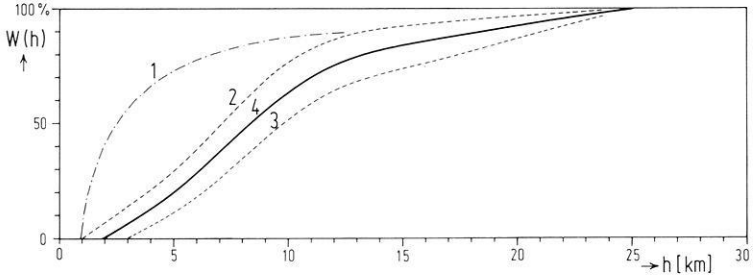

Fig. 4. Focal depth distribution $W(h)$ for different regions and magnitude ranges. Hainaut region: curve *1*. Other regions: curve *2* for $M \leqq 5$, curve *3* for $M > 5$, curve *4* model independent of M

3.4. Depth Distributions

In order to complete the statistical description of earthquakes the focal depth distribution $W(h)$ has to be considered. Several distributions have been found by evaluating observed data (see Fig. 4 and Ahorner, Murawski, Schneider (1972)). For the probability assessment it is sufficient as a first step to use curve *4*, which is the arithmetic mean of curve *2* (earthquakes with $M \leqq 5$) and curve *3* (earthquakes with $M > 5$). Curve *1* is used for the Belgium earthquake region of Hainaut (S of Bruxelles) where the focal depths are especially shallow (Ahorner, 1972).

It is planned to improve the methods by introducing a dependence of the focal depth distribution on magnitude, $W(h, M)$, in order to cover the increasing focal volume for higher magnitudes.

4. Calculation of Site Dependent Distributions for Accelerations

4.1. Transfer Function

The statistical description of earthquakes given in Section 3 is only a first step towards a risk assessment since it describes the causal events in the environs rather than the consequences at a site. A transfer function is needed as a link between causes and consequences, e.g. maximum ground acceleration B at the site.

B depends upon a great number of parameters. For a probability calculation it is justified to neglect a lot of them, e.g. the direction of the focal plane with respect to the site and the differences in the geological transfer medium between focus and site. Important parameters are the magnitude M and the hypocentral distance R between site and focus.

A transfer function of the following shape has been proposed by Esteva (1970) for North America:

$$B = B(M, R) = B_0 \cdot \exp(c\,M) \cdot \left(\frac{R + R_0}{\text{km}}\right)^{-d} \tag{11}$$

with

$$B_0 = 1230\ \text{cm/s}^2, \quad c = 0.8, \quad R_0 = 25\ \text{km}, \quad d = 2.$$

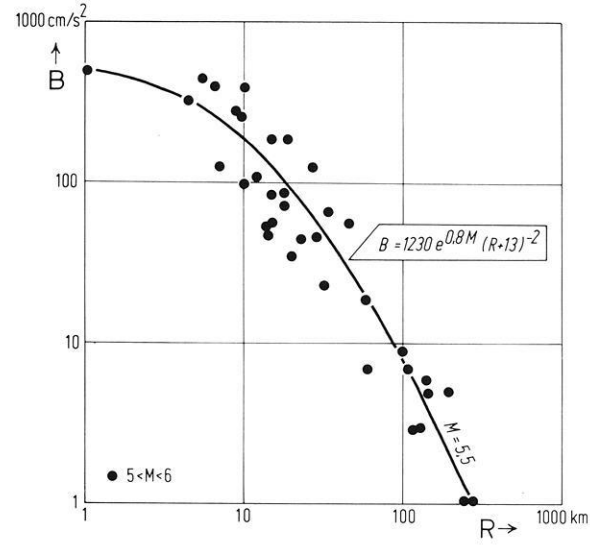

Fig. 5. Maximum ground acceleration B versus hypocentral distance R for earthquakes of magnitude $M=5.5$ calculated from Eqs. (11) and (12). Points give observed accelerations from events with $M=5-6$ after Page *et al.* (1972)

From a comparison with observed accelerations (Fig. 5) in the magnitude range $5<M<6$ given by Page *et al.* (1972) we get the following values and uncertainties which seem more proper for Central Europe:

$$\log\left(\frac{B_0}{\mathrm{cm/s^2}}\right)=3.1\pm0.1, \qquad c=0.80\pm0.05,$$
$$R_0=(13\pm2)\,\mathrm{km}, \qquad d=2.00\pm0.08. \tag{12}$$

Eq. (11) allows one to find the magnitude $M=M(B, R)$ that must not be exceeded in a focal distance R in order to get a maximum acceleration less than B:

$$M=M(B, R)=\frac{1}{c}\left[\ln(B/B_0)+d\cdot\ln\left(\frac{R+R_0}{\mathrm{km}}\right)\right]. \tag{13}$$

4.2. Program WASEW

The computer program WASEW transforms probabilities of earthquakes to probabilities of accelerations at the site.

WASEW subdivides the environs of a site S into elements of volume ΔV small enough to represent their distances to S by a point for each of them (see Fig. 6):

$$R=R(\Delta V, S)=\sqrt{h^2+\Delta^2}. \tag{14}$$

Given a certain value for the maximum acceleration B the quantity wanted is the probability that B is not exceeded at S. This means that M determined by Eqs. (13) and (14) is not exceeded in any ΔV. The corresponding probability is the product of probabilities extended over the environs of S:

$$W(\text{max. acceleration}\leqq B)=\prod W(\text{magnitude}\leqq M \text{ in } \Delta V)$$
$$=\exp\left[\sum \ln W(\text{magnitude}\leqq M \text{ in } \Delta V)\right]. \tag{15}$$

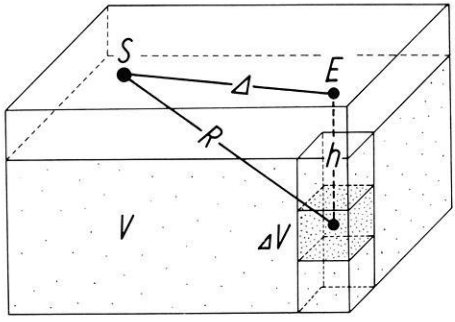

Fig. 6. Scheme to explain WASEW transformation of probabilities of earthquake magnitudes within a given crustal volume V to probabilities of accelerations at the site S. ΔV volume element, h depth of volume element, R distance between volume element and site. E epicenter, Δ epicentral distance

From Eq. (10) one finds that the contribution to the sum is zero for values of $M > M_{\max}$. For $M \leqq M_{\max}$ the probability is required that magnitudes are less than M in ΔV. Analogously to Eq. (10) one gets

$$W(\text{magnitude} \leqq M \text{ in } \Delta V) = \frac{G(M, \Delta V)}{G(M_{\max}, \Delta V)}$$

$$G(M, \Delta V) = \exp\left[-\exp\left(-\frac{M - u(\Delta V)}{a}\right)\right]$$

$$u(\Delta V) = u + a \cdot \ln\left(\frac{\Delta V \cdot W'(h)}{A}\right). \tag{16}$$

The last equation is analogous to Eq. (9) taking into account the depth distribution $W(h)$ (see Section 3.4). Using Eq. (16) one gets

$$\ln W(\text{max. acceleration} \leqq B)$$

$$= \frac{1}{A} \cdot \sum \Delta V \cdot W'(h) \cdot \exp\left(\frac{u}{a}\right) \cdot \left[\exp\left(-\frac{M_{\max}}{a}\right) - \exp\left(\frac{-M}{a}\right)\right]. \tag{17}$$

The sum has to be extended over the elements ΔV in the environs of S with $M \leqq M_{\max}$ determined by Eqs. (13) and (14) and has to take into account the different zones with different areas A and different values for a and u given in Fig. 1.

5. Results

The Northern Rhine area investigated has been covered by a regular net of 220 sites with 25 km grid width. For each site the probability distribution of the maximum ground acceleration has been calculated. The results for two typical sites are given in Fig. 7.

Much care has been devoted to the derivation of uncertainties for the input parameters and to the study of their influence upon the probability results. Monte-Carlo simulation using random numbers was applied to get the variation

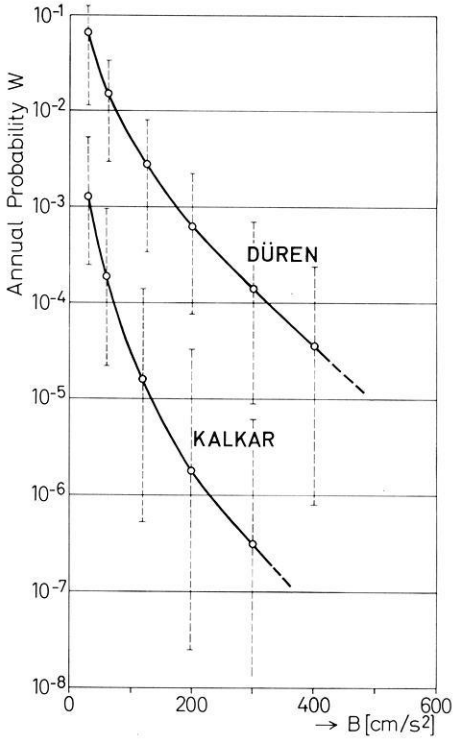

Fig. 7. Annual probability W of exceeding a maximum ground acceleration B at typical localities. Düren is situated in the western part of the Lower Rhine graben (region 5 with high seismicity). Kalkar is situated 40 km SE of Nijmegen (region 1 with very low seismicity, but still influenced by the nearby region 4). The given uncertainties are upper and lower standard deviations

of the resulting probability distribution caused by the uncertainties of the input parameters given in the text. The upper uncertainty of the final result – the probability of exceeding a given maximum ground acceleration at a site – was found to be less than the lower uncertainty (see Fig. 7), e.g. for Düren:

$$W(B > 120\ \mathrm{cm/s^2},\ 1\ \mathrm{year}) = 2.8 \cdot 10^{-3} \begin{cases} \leqq 4.6 \cdot 10^{-3} \\ \geqq 4 \cdot 10^{-4}. \end{cases} \tag{18}$$

The whole set of probability distributions for the 220 sites mentioned above is presented in two maps. Fig. 8 gives numerical results and isolines for the probability that $B = 100\ \mathrm{cm/s^2}$ is exceeded during one year. Fig. 9 shows the same for $B = 300\ \mathrm{cm/s^2}$.

6. Conclusions

A probability picture has been given describing quantitatively the earthquake risk relevant at a site. The numerical results are in good agreement with the more qualitative seismological concepts about earthquake risk which have been used

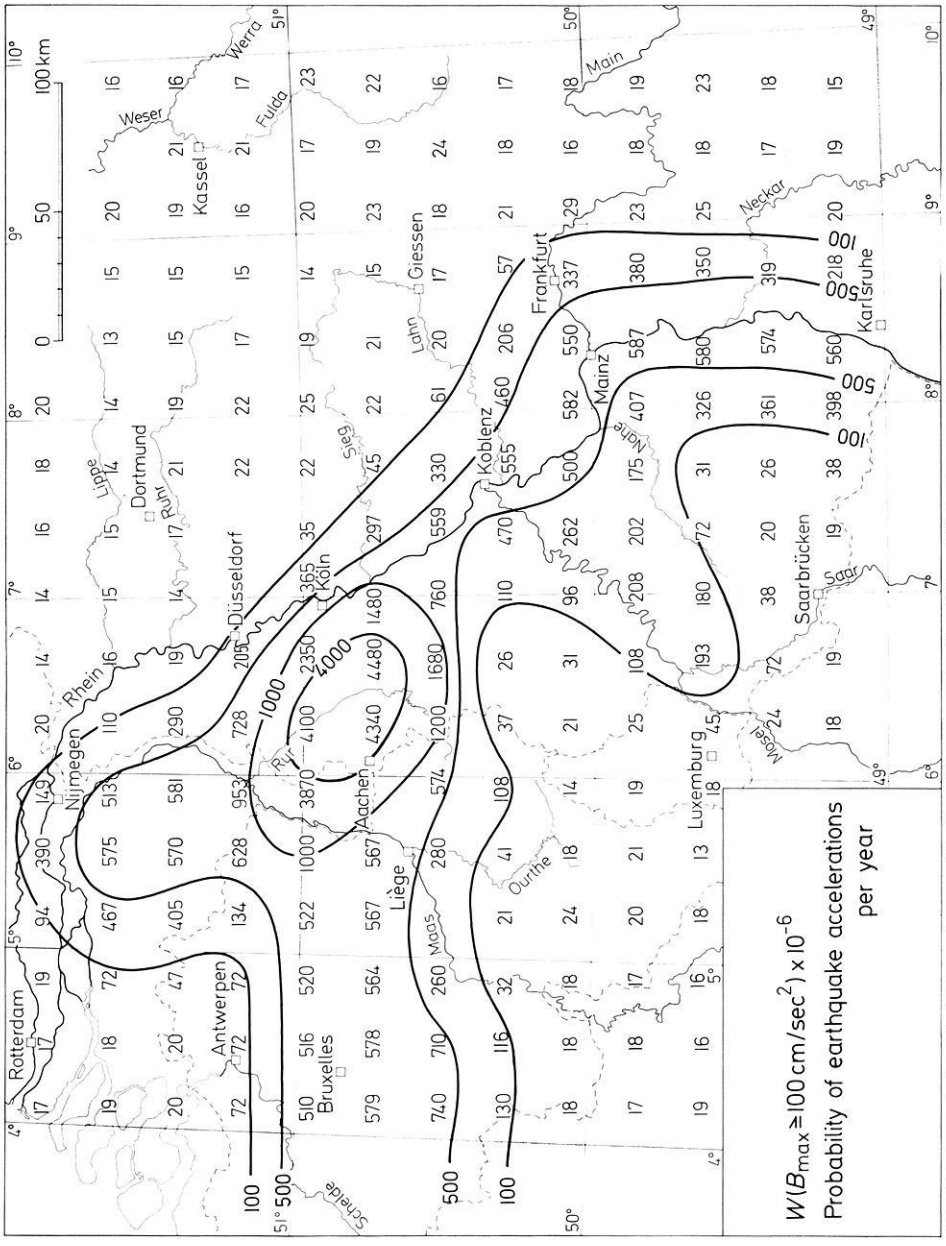

Fig. 8. Numerical probability values and isolines for exceeding $B = 100\ cm/s^2$ during one year

up to now. In spite of considerable uncertainties which have been calculated numerically the presented methods and results will help to improve the earthquake risk analysis on a consistent basis and will make possible comparisons with other risks.

To improve the probability results, further work is required with respect to the following topics:

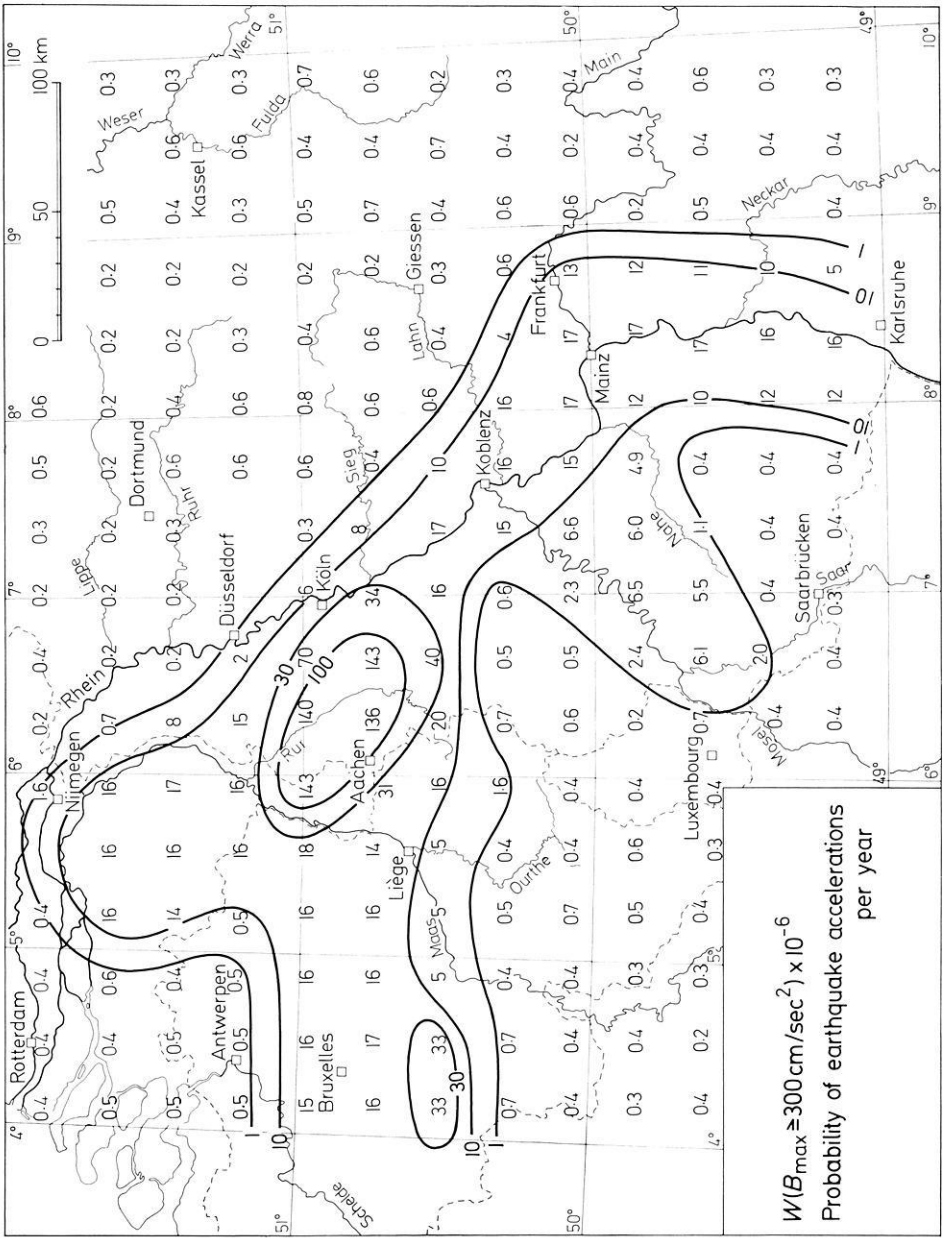

Fig. 9. Numerical probability values and isolines for exceeding $B = 300\ cm/s^2$ during one year

– a more detailed subdivision of seismicity zones based on future seismological and seismotectonic investigation (e.g. micro-earthquake observations),

– inclusion of the focal volume increasing with magnitude (which has conservatively been neglected in the present model),

– derivation of a more exact transfer function for the maximum ground acceleration at sites in Central Europe,

– research concerning statistical models establishing a maximum magnitude in a region,

– expansion of the study to the whole area of the Federal Republic of Germany in order to get a unified treatment of earthquake risk.

References

Ahorner, L.: Seismicity and Quarternary structural activity in the northern Rhine district. Proceedings of the Eights Assembly of the European Seismological Commission, 295–303, Budapest 1968

Ahorner, L.: Seismo-tectonic relations between the graben zones of the Upper and Lower Rhine valley. In: Illies, H. and Müller, St. (ed.): Graben problems, 155–166. Schweizerbart, Stuttgart 1970

Ahorner, L.: Erdbebenchronik für die Rheinlande 1964–1970. Decheniana **125**, 259–283 (1972)

Ahorner, L.: Present-day stress field and seismotectonic block movements along major fracture zones in Central Europe. Tectonophysics (in press) (1975)

Ahorner, L., Murawski, H., Schneider, G.: Die Verbreitung von schadenverursachenden Erdbeben auf dem Gebiet der Bundesrepublik Deutschland. Z. Geophys. **36**, 313–343 (1970)

Ahorner, L., Murawski, H., Schneider, G.: Seismotektonische Traverse von der Nordsee bis zum Apennin. Geol. Rundschau **61**, 915–942 (1972)

Epstein, B., Lomnitz, C.: A model for the occurrence of large earthquakes. Nature **211**, 954–956 (1966)

Esteva, L.: Seismic risk and seismic design decisions. In: Hansen (ed.): Seismic design for nuclear power plants. Cambridge, Mass.: M.I.T. Press 1970

Gumbel, E.J.: Les valeurs extrèmes des distribution statistique. Ann. de l'Institut Henri Poincaré **5**, 115–158 (1935)

Gumbel, E.J.: Statistics of Extremes, 375p. New York and London: Columbia Univsersity Press 1967

Housner, G.W.: Design spectrum. In: Wiegel, R.L. (ed.): Earthquake Engineering, pp. 93–106. Prentice-Hall: Englewood Cliffs, N.J. 1970

Kárník, V.: Seismicity of the European area. Part 2, 218p. Dordrecht-Holland: D. Reidel Publishing Company 1971

Nordquist, J.M.: Theory of largest values applied to earthquake magnitudes. Trans. Am. Geophys. Union **26**, 29–31 (1945)

Page, R.A., Boore, D.M., Joyner, W.B., Coulter, H.W.: Ground motion values for use in the seismic design of the trans-Alaska pipeline system. U.S. Geol. Survey Circular 672, 23p., 1972

Sieberg, A.: Beiträge zum Erdbebenkatalog Deutschlands und der angrenzenden Gebiete für die Jahre 58–1799. Mitt. deutsch. Reichserdbebendienst **2**, 1–111 (1940)

Sponheuer, W.: Erdbebenkatalog Deutschlands und der angrenzenden Gebiete für die Jahre 1800–1899. Mitt. deutsch. Erdbebendienst **3**, 1–195 (1952)

Received April 18, 1975

J. Geophys. 41, 595–613, 1975

P Wave Amplitude Variability at NORSAR

K.A. Berteussen

NTNF/NORSAR, Post Box 51, 2007 Kjeller, Norway

Abstract. A detailed study of *P*-wave amplitude variability within the Norwegian Seismic Array (NORSAR) has revealed that the amplitude pattern is repeatable for events from the same area, but can change rapidly as a function of source region. The difference between the largest and smallest amplitude recorded is on the average 14 dB, with 9.5 and 22 dB as minimum and maximum, respectively. The standard deviation of the amplitudes recorded inside this 110 km aperture array is of the same order as that of a world-wide network. There is no significant variation in noise level inside the array. Because of the large variations in signal amplitudes the performance for a particular region is crucially dependent upon the array configuration. Thus when selecting sites for new installations (single instrument or arrays) care should be taken in order to ensure that the site(s) selected optimizes the event detection performance with respect to the seismic regions of most interest. The rapid amplitude fluctuations observed demonstrate the necessity for adequate spatial sampling prior to inversion of amplitude observations in terms of Earth structure; for NORSAR and LASA (Montana, USA) instrument-to-instrument distances down to 5 to 10 kilometers are required. Currently only models of the random medium type or a block type structure seem able to explain the data satisfactorily.

Key words: Amplitude variations – Amplitude loss – Beamforming – Array configuration – Network density – Spatial sampling.

Introduction

The large scatter in short period *P*-wave amplitude observations has always been problematic for seismologists. In order to reduce this scatter in magnitude determinations using seismograph networks, refined and regionalized versions of the Gutenberg (1945) magnitude formula have been widely used. The statistical aspects of magnitude determinations, such as the problem of relevant sam-

pling, has been studied by Husebye *et al.* (1974), who showed that the magnitude correction for a station may be a function of magnitude. In addition, *P*-wave amplitudes have also been widely exploited in studies of the distribution of anelastic parameters within the earth (*e.g.*, Anderson and Kovach, 1964; Anderson *et al.*, 1965; Kanamori, 1967), as well as studies of local upper mantle and crustal structures (Mereu, 1969; Larner, 1970; Landers, 1971). These studies generally assume that the amplitudes vary slowly and regularly in space. The large seismic arrays provide a valuable opportunity to examine the validity of this assumption.

P-wave amplitude variations are especially important insofar as they bear on the event detection capability of single stations or arrays. A large number of papers have been concerned with the problem of noise suppression, while only few works have drawn attention to the effect of amplitude variations. That this effect can be of considerable importance has recently been shown by Christoffersson and Husebye (1974).

This paper is directed to an analysis of NORSAR *P*-wave amplitude anomalies as a function of event location or seismic regions. In addition, an analysis of the noise level variations within the array aperture is presented. The impact of the results on the array's event detectability is examined. Special attention is given to the problem of deciding which array configuration maximizes the event detectability for different regions. The analysis presented demonstrates that when selecting sites for arrays or single stations, due consideration should be given to relative signal amplitude levels as well as the ambient noise field.

As mentioned previously, the fact that the large seismic arrays provide a dense spatial sampling of earthquake signal amplitudes gives an excellent opportunity to check different geophysical models proposed in order to explain the variations of these amplitudes. For instance, in this paper it will be demonstrated that "aliasing effects" may seriously affect the inversion of amplitude data in terms of earth structures unless the spatial sampling is adequate.

Array Beamforming Theory

The operational principles of seismic arrays are usually based on the assumption that the *P* signals are identical across the array while the noise is Gaussian and approximately uncorrelated from one sensor to another. For a signal/noise model of the above kind, simple delay-and-sum processing (beamforming) provides the optimum signal processing method. The expected gain in SNR is proportional to $\sqrt{N}$ where N is number of sensors in the array. In practice, the above assumptions on noise and signal properties are only approximately valid, resulting in an SNR beamforming gain a few dB less than that corresponding to $\sqrt{N}$. (As a general introduction to array data processing theory, we refer to Birtill and Whiteway (1965).)

An important task of the NORSAR array (for description, see Bungum *et al.*, 1971; Bungum and Husebye, 1974) is seismic surveillance, that is, real-time signal processing for the detection of seismic events. In this application, the simple beamforming technique is preferred on account of its computational simplicity, which is currently a requirement for real-time analysis of array data. In this

section we will give a brief presentation of beamforming theory, emphasizing the gain in SNR when the basic assumption of identical signals is not strictly valid.

Assume we have a spatial arrangement of N sensors, and the output from these is sampled at certain fixed intervals. If the j-th sample from the i-th sensor is denoted a_{ij}, then the power of this sensor may be written

$$A_i^2 = \frac{1}{\mathrm{STA}} \sum_{j=1}^{\mathrm{STA}} a_{ij}^2$$

where STA ("short term average") is number of samples. The power of the sum of the N traces, S_{ab}^2, is the given by

$$S_{ab}^2 = \frac{1}{\mathrm{STA}} \sum_{i=1}^{\mathrm{STA}} (a_{1i} + a_{2i} + \cdots + a_{Ni})^2. \tag{1}$$

It is assumed that proper time delays have been introduced so the signals are in phase or correctly lined up. Performing the squaring operation in Eq. (1) one gets

$$\begin{aligned} S_{ab}^2 = \frac{1}{\mathrm{STA}} \sum_{i=1}^{\mathrm{STA}} (a_{1i}^2 &+ a_{1i} \cdot a_{2i} + \cdots + a_{1i} a_{Ni} + \\ & a_{2i} \cdot a_{1i} + a_{2i}^2 + \cdots + a_{2i} a_{Ni} + \\ & \vdots \\ & a_{Ni} a_{1i} + a_{Ni} a_{2i} + \cdots + a_{Ni}^2). \end{aligned} \tag{2}$$

Performing the summation one gets

$$\begin{aligned} S_{ab}^2 = (A_1^2 &+ A_1 A_2 \rho_{12} + \cdots + A_1 A_N \rho_{1N} + \\ & A_2 A_1 \rho_{21} + A_2^2 + \cdots + A_2 A_N \rho_{2N} + \\ & \vdots \\ & A_N A_1 \rho_{N1} + A_N A_2 \rho_{N2} + \cdots + A_N^2) \end{aligned} \tag{3}$$

where A_i^2 denotes the power of trace i, and ρ_{ij} is the normalized correlation coefficient between sensor i and j. Eq. (3) may be written in matrix form

$$\begin{aligned} S_{ab}^2 &= \{A_1, A_2, \ldots, A_N\} \begin{Bmatrix} 1, \rho_{12}, \ldots, \rho_{1N} \\ \rho_{21}, 1, \ldots, \rho_{2N} \\ \vdots \\ \rho_{N1}, \rho_{N2}, \ldots, 1 \end{Bmatrix} \begin{Bmatrix} A_1 \\ A_2 \\ \vdots \\ A_N \end{Bmatrix} \\ &= A R_S A' \end{aligned} \tag{4}$$

where A is a row vector consisting of the elements A_i, $i=1, N$ and R_S is the signal correlation matrix. A' is the transpose of A. If noise is present, the same formula still applies. For example, letting B be a row vector consisting of N elements where B_i^2 represents noise power for instrument i, and letting R_N be

the noise correlation matrix, we find that the signal-to-noise ratio, SNR, on the summed trace may be calculated from the ratio

$$\mathrm{SNR}^2 = \frac{A \cdot R_S \cdot A'}{B \cdot R_N \cdot B'}. \tag{5}$$

If all elements in A are equal to $\sqrt{\bar{a}^2}$ and $\rho_{ij} = \rho_s$ for $i \neq j$ in the matrix R_S, Eq. (3) gives

$$S_{ab}^2 = \bar{a}^2(N + (N-1) \cdot N \cdot \bar{\rho}_S) = \bar{a}^2 \cdot N(1 + (N-1)\bar{\rho}_S). \tag{6}$$

If the same assumptions are valid also for noise, we get the familiar expression (Denham, 1963)

$$\mathrm{SNR}_{ab}^2 = \frac{\bar{a}^2 \cdot N \cdot (1 + (N-1)\rho_S)}{\bar{n}^2 \cdot N \cdot (1 + (N-1)\rho_N)}. \tag{7}$$

For $\rho_s = 1$ and $\rho_N = 0$, this again reduces to $\mathrm{SNR}_{ab}^2 = \bar{a}^2/\bar{n}^2 \cdot N$; that is, the gain in SNR increases with $\sqrt{N}$.

Example 1. Let us assume we are summing two traces whose signal amplitude is given by A_1 and A_2 respectively. ρ_{12} is assumed equal to one for the signals and zero for the noise, and the noise level is supposed equal to $\bar{n}^2$ on both traces. The signal-to-noise ratio of the summed trace is then found from Eq. (5)

$$\mathrm{SNR}_{ab}^2 = \frac{(A_1 + A_2)^2}{2\bar{n}^2} \tag{8}$$

while the corresponding value for the first trace is $A_1^2/\bar{n}^2$. In order to have a gain in SNR by summing the two traces, one must have

$$\frac{(A_1 + A_2)^2}{2\bar{n}^2} > \frac{A_1^2}{\bar{n}^2} \tag{9}$$

i.e., $A_2 > (\sqrt{2} - 1) \cdot A_1 \approx 0.41 \cdot A_1$. That is, if the amplitude of the second trace is less than 0.41 (7.7 dB) times the amplitude of trace one, adding the two traces does not give a gain in signal-to-noise ratio, even though they have exactly the same signal shape. If $\rho_{12} = 0.7$, which is a reasonable value for P-signals recorded at NORSAR, the criterion is $A_2 > 0.51 \cdot A_1$ in order to have a gain in signal-to-noise ratio by summing the two traces.

Example 2. Let us assume we have already summed 21 traces, all with the same amplitude, $\bar{A}$, and shape. The noise level is as before assumed equal on all traces and completely uncorrelated from one trace to another. The signal-to-noise ratio would then be $\mathrm{SNR}_{21}^2 = \dfrac{\bar{A}^2 \cdot 21 \cdot 21}{n^2 \cdot 21}$.

Adding to this a trace no. 22 of the same shape but with amplitude A_{22} gives:

$$\mathrm{SNR}_{22}^2 = \frac{(\bar{A} \cdot 21 + A_{22})^2}{n^2 \cdot 22}. \tag{10}$$

Requiring SNR_{22} greater than SNR_{21} gives:

$$A_{22} > (\sqrt{22 \cdot 21} - 21) \cdot \bar{A} \approx 0.49 \cdot \bar{A}. \tag{11}$$

That is, in order to have a gain in signal-to-noise ratio, A_{22} must have an amplitude which is not less than 0.49 (6.12 dB) times the amplitude of the other traces.

Example 3. Let us assume that in the above case A_{22} is equal to zero. This gives $SNR_{22} = SNR_{21} \sqrt{21/22}$, that is, the result would be a loss of 0.2 dB in signal-to-noise ratio.

Example 4. Let A_{22} in Ex. 2 be equal to $\bar{A}$, but exactly 180° out of phase; this gives $SNR_{22}^2 = \dfrac{(\bar{A} \cdot 21 - \bar{A})^2}{n^2 \cdot 22}$. That is, the result would be a loss of 0.6 dB in signal-to-noise ratio.

Data

NORSAR is located in southeastern Norway (centered at 60.8° N, 10.83° E) and comprises 22 subarrays each containing three long period (V, NS, EW) and six vertical short period seismometers. The array configuration is shown in (Berteussen, 1975, p. 72). The short period data is searched in real time for earthquake and explosion signals. This is done by first using a recursive bandpass filter and then forming beams steered towards the most active seismic regions and the known underground nuclear test sites. Two types of beamforming (envelope and conventional) are used in order to ensure overall surveillance together with maximum performance in the most interesting regions. Conventional ("coherent") beamforming is the most important of these and involves simple delay-and-sum procedures using all instruments. Totally there are 318 such beams, their deployment in slowness space being shown in Fig. 1.

All *P*-waves recorded at NORSAR during 1972 and 1973 which did not saturate the recording system and had a signal-to-noise ratio (SNR) above 17 dB have been used in the present study. Before calculating the amplitudes the traces were filtered with a 1.2–3.2 Hz 3rd order Butterworth bandpass filter. In total, the data base consists of some 964 events. The computerized method of calculating amplitudes is described in Husebye *et al.* (1974). The data have been grouped according to which of the (coherent) Detection Processor (DP) beam locations (Fig. 1) the events were closest to. No events located more than 0.5 sec/deg (measured in slowness space) from any of the DP beams were used. As was observed by Husebye *et al.* (1974) the amplitude pattern is approximately stationary from one event to the other as long as the events are close enough in slowness and azimuth. This is demonstrated in Table 1, which lists the amplitude loss in dB relative to the best subarray for a set of events detected on DP beam location 188, *i.e.*, events close to the location 37° N, 71° E (Afghanistan-USSR border).

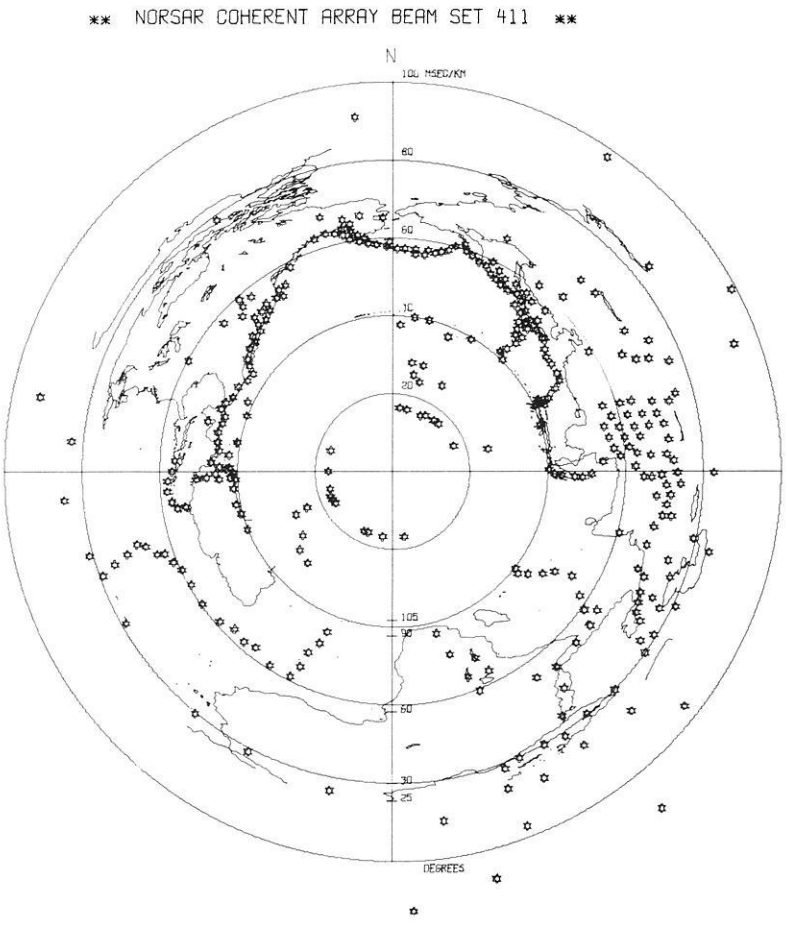

Fig. 1. NORSAR coherent Detector Processor beam deployment. The contours drawn represent the world map as seen in slowness space at NORSAR

The stability of the observed amplitude patterns has been tested using the Kendall coefficient of concordance (Siegel, 1956). Subarray 22 was excluded from analysis, and also those events where any of the other subarrays were out of operation. This Kendall coefficient is equal to 1.0 if the amplitude ranking pattern is reproduced from one event to another, but would be zero if the pattern is completely random. The value obtained was 0.83, while the chance of randomly getting such a large value is less than one in a thousand (0.001). The coefficient has also been calculated for the five DP beam locations where most data was available, namely, 52° N, 160° E; 43° N, 147° E; 11° N, 125° E; 28° S, 177° W; and 32° S, 179° W, respectively. The average value is 0.8 ± 0.1, and for any of the five beams the chance of randomly getting a value as extreme as that obtained is less than 0.001.

Although the amplitude pattern is stable for events coming from approximately the same location, the pattern may change drastically as one moves from

Table 1. Subarray and array beam (AB) amplitude losses in dB for events detected on NORSAR Detection Processor (DP) beam no. 188. This beam is pointed towards 37N, 71E (Afghanistan-USSR border). As seen from the table subarry 11 is best for all events analyzed. The loss values are relative to the best subarray

Event I.D.	Subarray Number																					
	1	2	3	4	5	6	7	8	9	10	11	12	13	14	15	16	17	18	19	20	21	22	AB
40,800	18	6	8	–	16	16	18	11	5	4	0	10	7	18	9	19	21	16	12	5	10	15	11.2
41,530	15	5	8	9	14	14	–	12	4	4	0	10	9	18	9	14	18	16	12	4	10	14	10.4
78,890	16	6	8	10	13	12	22	14	5	1	0	11	7	16	10	15	19	17	12	8	9	13	11.3
17,310	14	6	8	6	12	19	18	11	7	6	0	14	6	17	11	13	14	16	–	6	13	11	11.2
65,000	14	7	7	10	15	14	14	10	4	7	0	14	9	14	9	15	15	13	11	5	11	–	11.8
74,660	13	8	7	4	12	11	18	13	4	5	0	13	7	16	11	9	12	14	13	9	7	15	13.6
49,570	17	6	8	8	16	15	17	11	5	3	0	10	7	16	9	20	18	–	12	4	12	18	10.8
53,910	14	5	8	7	16	18	15	10	4	8	0	8	6	14	9	15	21	15	9	4	7	–	10.0
79,370	14	6	5	9	13	14	13	11	5	7	0	11	9	15	6	13	15	18	12	6	11	13	11.8
2,180	12	6	7	8	13	14	14	10	5	6	0	14	8	18	8	–	18	18	11	6	12	14	12.0
32,550	15	5	6	5	14	11	13	8	2	5	0	11	7	16	2	15	14	15	7	1	12	18	9.3
38,270	18	6	8	9	15	14	17	11	4	5	0	12	7	17	9	17	19	17	13	6	11	16	11.7
79,230	12	6	9	8	–	14	17	10	3	5	0	10	6	13	10	14	17	14	12	8	9	9	11.2
85,910	15	5	7	8	18	14	17	9	4	5	0	11	7	18	7	15	15	15	12	5	11	15	10.7
52,240	11	7	7	7	16	15	17	10	8	8	0	7	7	17	11	13	–	13	9	6	12	11	11.1
17,630	14	9	9	9	18	16	15	12	5	6	0	6	–	17	12	12	18	15	13	5	12	12	12.4
69,380	13	–	9	10	16	15	12	14	6	5	0	9	7	14	11	13	13	17	13	4	12	12	12.7
53,970	14	7	9	10	16	13	15	11	6	3	0	8	6	14	11	13	14	16	11	5	9	–	11.1
58,810	12	4	7	8	16	12	17	11	7	1	0	10	6	14	10	14	20	15	12	5	10	–	11.7

one beam location to the next. This is demonstrated in Fig. 2, where the amplitude pattern for two DP beams steered towards Iran are shown. Both are steered towards a point with distance 35.1 degrees from NORSAR, but with azimuth slightly different, 117.0° and 123.7°, respectively, and as can be seen from the figure, this difference in azimuth has produced two entirely different amplitude populations. Also note that for these beams the difference in amplitude between the best and the poorest subarray is 15 and 19 dB, respectively, *i.e.*, a factor of 6 and 9 in amplitude ratio inside an array of radius 50 km. These are representative values for events coming from east and north, while events from the west usually have somewhat less amplitude differences. This can also be seen from Table 2 where we have listed the average of the observed amplitude values measured in dB down from the best subarray for some selected DP beams. A maximum difference of 22 dB, corresponding to a factor of 13 in ratio between the highest and lowest amplitude, was observed for a beam steered towards the Kirgiz-Sinkiang border region, while the minimum difference of 9 dB, corresponding to a factor of 3, was observed for a PKP beam steered towards South Sanwich Is. region. As an average for all regions there is 14 dB (a factor of 5) in amplitude differences within the array aperture. It should also be mentioned that we here are measuring subarray beam amplitudes. If we measured single sensor amplitudes, the results would be even more extreme. The standard deviation of the amplitude recordings for the different events are (4.4 ± 2.1) dB, corre-

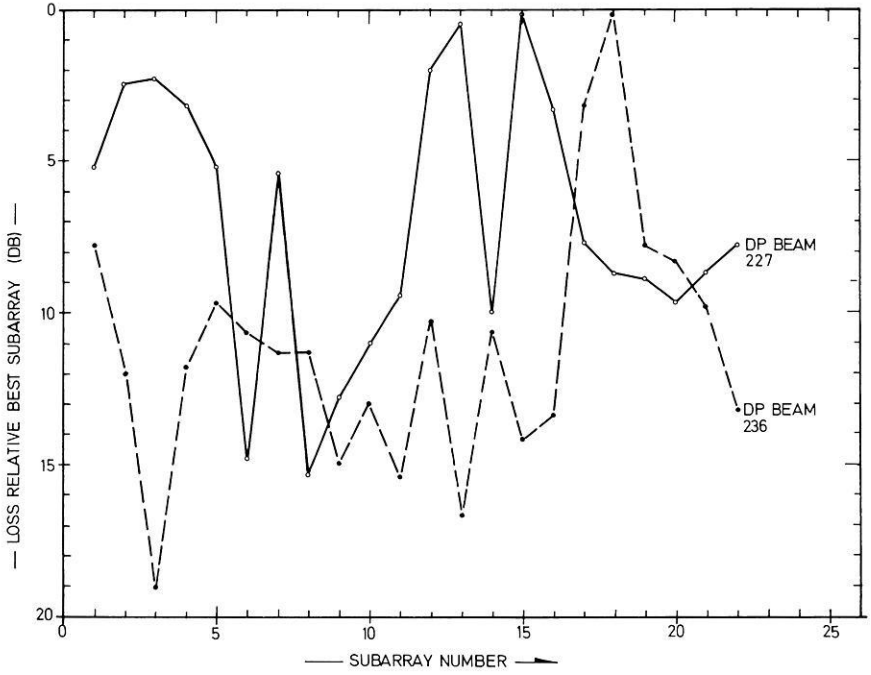

Fig. 2. Average signal amplitude measured in dB down from best subarray for signals coming from two different areas in Iran. DP beams 227 and 236 respectively. ——— DP beam 227, distance = 35.1, Azimuth = 117.0, --------- DP beam 236, distance = 35.1, Azimuth = 123.7

sponding to (0.22 ± 0.11) MB units. Using all instruments Dahle (1975) reports an average standard deviation of 0.4 MB units. These values should be compared with for example the standard deviation of 0.356 MB units Veith and Clawson (1972) found using the amplitudes from different explosions as recorded by a world-wide network of stations. The last row in Table 2 gives the amplitude values of the full array beam relative to the best subarray. As an average the normalized amplitude of the full array beam is 8.8 dB below the best subarray. But because the array beam has a beamforming gain of 13.4 dB (due to noise suppression) it has in average 4.6 dB better SNR than the best subarray beam.

As a further example of the variability of the amplitude pattern, it is found that all the subarrays have at least one DP beam location where it is the best subarray, and also at least one location where it is the poorest subarray. This can be seen from Fig. 3, which is a histogram showing for each subarray how many DP beams it has the maximum and how many it has the minimum amplitude, respectively. Thus, although some of the subarrays are good for most of the seismic regions, there always exists a region where they are the poorest subarrays. In Fig. 4 the amplitude pattern when averaged over all DP beams where any data was available is shown. Because of the variability of the amplitude pattern, the difference between the best-in-average subarray (05C or no. 13) and the poorest (14C or no. 22) is only 5 dB, while the difference between the best and the poorest subarray for single beams was 14 dB on the average.

Table 2. Average subarray and array beam (AB) amplitude losses in dB for some selected DP beams. It should be noted that the beams selected for each region are only one out of several

Beam no.	91	175	195	23	254	13	115	227	236
Region (Flinn and Engdahl)	S. of Honshu	Northern Colombia	Afghanistan	Fox Is. Aleutians	C. Mid-Atlantic	S.E. Alaska	Samar. Philip.	Iran	Western Iran
Distance	81.1	80.8	46.4	66.5	64.6	58.2	91.8	35.1	35.1
Azimuth	44.2	268.0	99.6	358.6	212.3	346.5	63.7	117.0	123.7
01A 1	7	1	17	14	7	3	4	5	8
01B 2	6	1	4	13	4	9	11	3	12
02B 3	5	10	12	7	7	6	9	2	19
03B 4	13	7	12	13	5	13	9	3	12
04B 5	7	4	7	13	13	8	7	5	10
05B 6	13	5	11	15	11	9	9	15	11
06B 7	10	3	15	4	3	9	6	5	11
07B 8	6	6	12	9	7	6	5	15	11
01C 9	2	9	5	7	12	7	3	13	15
02C 10	3	5	7	8	5	8	3	11	13
03C 11	7	10	0	0	2	7	3	9	15
04C 12	2	3	6	3	3	8	3	2	10
05C 13	0	9	3	0	12	5	6	1	17
06C 14	13	7	8	10	10	12	10	10	11
07C 15	11	8	9	8	11	12	5	0	14
08C 16	14	2	10	5	8	7	3	3	13
09C 17	12	11	14	7	7	7	11	8	3
10C 18	11	10	18	8	6	9	3	9	0
11C 19	10	11	11	3	1	8	2	9	8
12C 20	12	8	9	5	9	5	8	10	8
13C 21	14	6	6	9	9	10	3	9	6
14C 22	18	10	16	5	10	0	10	8	14
AB	9	8	10	8	10	9	8	9	13

If one wishes to use Eq. (5) to estimate how the SNR will vary as a function of array configuration, one also needs information about the noise fluctuations across the array, in addition to signal amplitude and correlation information. For approximately half of the events used in this study noise estimates were therefore also obtained. This was done by calculating for each subarray the power inside a $^1/_2$-minute long window, ending 5 seconds before the signal onset. The loss value for each subarray was calculated by subtracting its power (in dB) from the power of the subarray with highest noise level. These values were then averaged over the number of events available and found to range from 0.49 ± 0.30 dB to 0.54 ± 0.31 dB, the maximum difference in noise level across the array is in average only 0.05 dB.

Cultural noise is known to be significant at NORSAR (Bungum and Ringdal, 1974); one could therefore expect that certain subarrays in the neighborhood of towns and major roads could have higher noise levels than the rest at certain

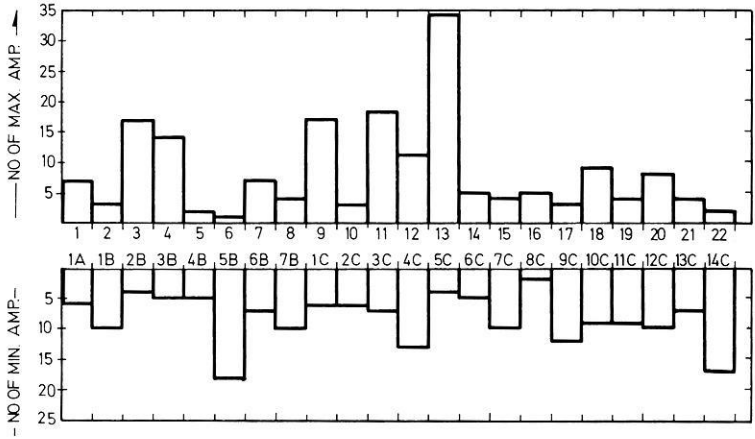

Fig. 3. Histogram showing for how many regions (DP beam locations) a subarray has the highest and for how many it has the lowest amplitude respectively

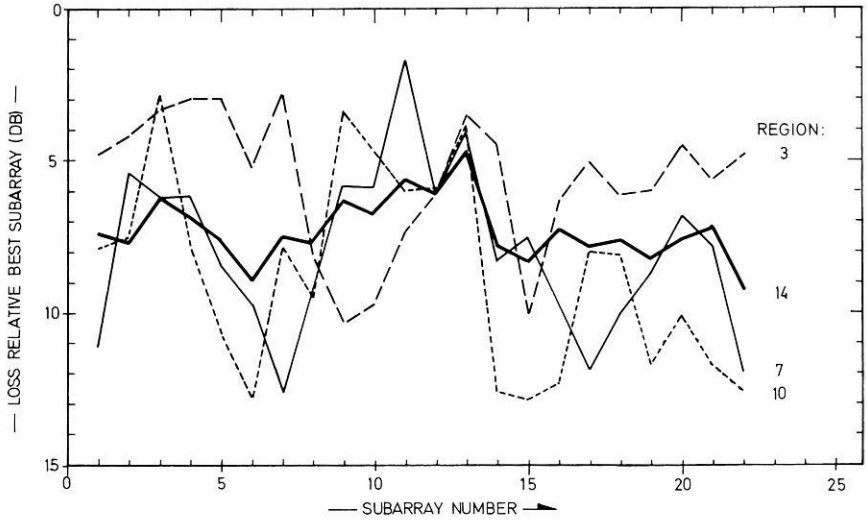

Fig. 4. Average amplitude loss values for some of the regions used in Table 3. The thick line is for Region 14, which covers distance range 30° 180° from NORSAR

times during the day. However, by grouping the noise measurements according to time of day, and then averaging within four hour intervals, no such effect was found. It should here be mentioned that this is bandpass filtered data (1.2–3.2 Hz); if no filter had been applied, the above statement may not have been true. Also subarray 22 (14C) is known to have high noise level due to a neighboring power plant (Hjortenberg and Risbo, 1975). This effect could not be observed; the reason for this is believed to be partly the filter applied and partly that this subarray has been masked in the noisiest periods.

The conclusion is thus that compared with the signal amplitude differences, the effect of the noise level variations across the array safely can be neglected. Thus the vector B in Eq. (5) can be considered to consist of only equal elements. It should be kept in mind that we here have been considering only noise level variations inside the array using filtered data. There are undoubtedly significant variations both in absolute noise level and in the noise spectra as a function of time. These effects are discussed in detail by Bungum and Ringdal (1974) and also Steinert *et al.* (1975).

Event Detectability

As mentioned in the previous section, the array beam amplitude has been calculated and compared with the best (*i.e.*, largest amplitude) subarray. Using Eq. (4) it is possible to calculate the average signal correlation ($\bar{\rho}_s$) between the different subarrays, assuming that the array beam loss is caused solely by imperfect correlation. With the $\bar{\rho}_s$ value known and under the additional assumptions that the noise is uncorrelated from one subarray to another ($\bar{\rho}_n = 0$) and that the noise level is equal at all subarrays, it is possible, by using Eq. (5), to calculate expected SNR loss on the array beam for the case that one or more subarrays are excluded from the beamforming. The procedure has been to calculate the expected SNR for each DP beam when successively more subarrays are excluded, starting with the exclusion of only the smallest amplitude subarray.

In Fig. 5 the expected performance for beam no. 91 (South of Honshu) is shown as a function of number of subarrays, where the subarrays have been ranked according to their amplitudes. For this beam, using only the best subarray (05C), one would have a loss of 4.6 dB relative to the current array beam. Using the 15 best subarrays would give a gain of 0.15 dB. For this beam it is seen from Table 2 that the difference in amplitude between the best subarray (05C) and the poorest one (14C) is as much as 18 dB. In contrast, for beam 175 the difference in amplitude between the best (01A) and the poorest (09C) is only 10 dB. Fig. 6 shows that there is no gain by excluding any of the subarrays in this case.

It has been found that for more than 90% of the DP beams one or more subarrays could be excluded without decreasing the SNR of the array beam signal. For 70% of the beam locations three or more subarrays could be excluded. Only 9% of the beam signals would suffer a loss in SNR by excluding the poorest subarray. As could be expected from the previous discussions (see Examples 2, 3 and 4), there is seldom any significant gain in SNR by deleting subarrays. Only for 2% of the DP beams is it possible to obtain an SNR gain of 0.4 dB or more, while for 18% of the cases a gain of 0.2 dB or more is possible.

Fig. 7 shows the variation in SNR of the array beam signal if a certain number of subarrays are permanently excluded. Because of the small subarray amplitude variations when averaging over all beam locations, a net loss would be observed even by excluding only the very worst subarray.

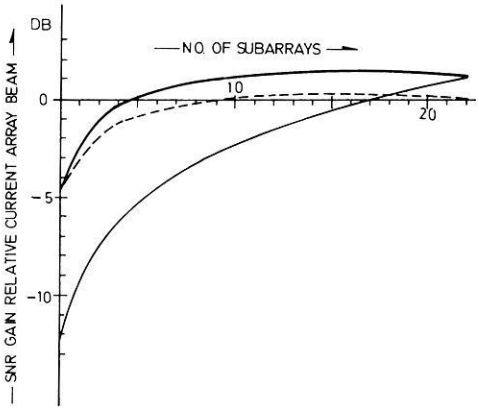

Fig. 5. Expected signal-to-noise ratio as a function of number of subarrays for DP beam 91, pointing towards 29N, 139E (South of Honshu, Japan). The subarrays have been ranked according to their amplitude. The first point on the horizontal axis corresponds to subarray no. 13, which has the highest amplitude in this case. The bottom line shows the theoretical $\sqrt{N}$ performance for the case of identical signals. The relative gain here using all 22 subarrays is 1.2 dB, which implies that the observed array beam signal suffers an average loss of 1.2 dB. The upper line gives the SNR improvement for the case of identical subarray signal shapes, but with the amplitude distribution listed for beam no. 91 in Table 2. The broken line gives the gain in SNR when the signal correlation is in average 0.75

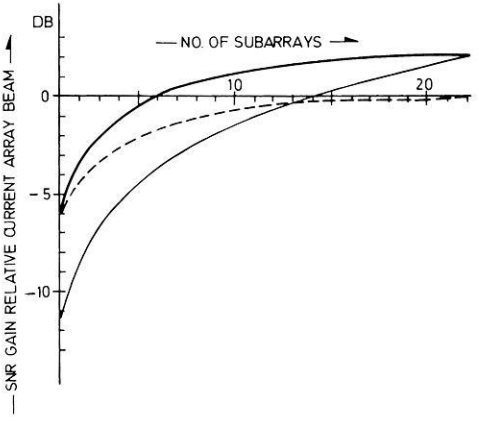

Fig. 6. Same as Fig. 5 for DP beam no. 175 pointing towards 7N, 73W (Northern Colombia). Subarray no. 1, which is best, is 5.9 dB below the array beam. The maximum difference in amplitude between two subarrays is 10 dB. The broken line shows that nothing would be gained by excluding any of the poorest subarrays. The amplitude loss of the currently used array beam is 2.1 dB

Excluding only subarray 14C will, in this case, give a loss of 0.1 dB. If both subarrays 14C and 05B (which has on the average the second smallest amplitude) are excluded, the average loss would be 0.2 dB. Excluding half of the subarrays gives a loss of 2.1 dB on average. For some particular regions, the exclusion of some subarrays would of course be more detrimental.

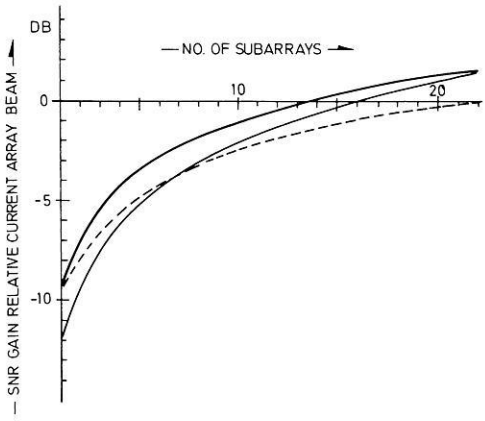

Fig. 7. Same as Fig. 5, but the data has been average over all beam locations. The array beam loss is seen to be 1.6 dB. Subarray no. 13 is best and is 9.3 dB below the full array beam signal. The broken line shows that if only the 11 best subarrays were used, the loss would be 2.1 dB

Table 3. Expected SNR loss for a set of large regions (defined by Bungum and Husebye, 1974) as a fuction of no. of subarrays removed, starting with the on average smallest amplitude subarray. The bottom row gives the corresponding theoretical values

Region	Area of coverage	No. of subarrays removed				
		1	2	5	10	21
1	Aleutians-Alaska	0.22	0.30	0.64	1.12	7.22
2	Western North America	0.15	0.25	0.78	2.44	13.71
3	Central America	0.22	0.44	0.94	2.46	10.12
4	Mid-Atlantic Ridge	0.15	0.23	0.89	2.57	13.62
5	Mediterranean-Middle East	0.22	0.47	0.97	2.03	8.62
6	Iran-Western Russia	0.10	0.24	0.74	2.17	8.72
7	Central Asia	0.04	0.14	0.67	1.53	8.02
8	Southern-Eastern Asia	0.05	0.10	0.78	1.62	7.52
9	Ryukuo-Philippines	0.06	0.09	0.63	1.23	6.72
10	Japan-Kamchatka	0.04	0.06	0.15	1.05	7.82
11	New Guinea-Hebrides	0.09	0.48	1.27	2.90	16.42
12	Fiji-Kermadec	0.12	0.57	1.35	2.61	17.02
13	South America	0.06	0.47	0.95	2.66	11.62
14	Distance range 30°–180°	0.11	0.24	0.75	1.90	9.32
	Theoretical ($1/\sqrt{N}$) loss	0.20	0.41	1.12	2.63	13.42

In Table 3 some of these loss values are listed for a set of larger regions (defined by Bungum and Husebye, 1974). Excluding only subarray 14C would in average give a loss considerable lower than the 0.2 dB expected from the $1/\sqrt{N}$ performance. However, for the Aleutian-Alaska region (1) and the Central American region (3) the loss values are slightly above the theoretical values, because subarray 14C tends to have relatively high amplitudes for these regions. Actually subarray 14C which on average has the smallest amplitudes, has the very highest amplitudes for DP beam nos. 11 and 13 which are both

steered towards southeastern Alaska. Generally it can be seen that excluding from one to twenty-one subarrays starting with the poorest gives loss values below the theoretical values; however, because of the rapid variation in the amplitude pattern, there are always some regions where this is not true. For example, using only the very best subarray, 05C (*i.e.*, masking the other 21), one would for the Western North America, the Mid-Atlantic Ridge, the New Guinea-Hebrides and the Fiji-Kermadec regions (2, 4, 11 and 12) have a performance which is poorer than that expected from the theoretical loss values. Thus, if one were to use only one subarray, and if one were particularly interested in, for example, region 2 (Western North America), this subarray (05C) would not be a good site to choose, even though it in average is the best one.

Discussion

By measuring the subarray and array beam amplitudes of a large number of events, a set of relative amplitude values has been established for most of the NORSAR Detection Processor beams. In addition, these amplitudes have been used to establish those subarrays which could be beneficially masked and the gain in SNR achieved by such masking. Similar results have also been obtained on a regional basis. These results derived depend on the validity of certain simplifying assumptions; these assumptions are examined in turn in the following paragraphs.

The assumptions that the relative subarray amplitudes for a particular beam location were independent of event magnitude is not necessarily true due to the combined effect of the spectrum scaling law (Aki, 1967) and a frequency dependent crust and upper mantle transfer function. For example, Husebye *et al.* (1974) found that the body wave magnitude correction for conventional seismograph stations could vary with event magnitude. To test whether such effects are significant in the amplitude variation across NORSAR, events corresponding to the five most active beam locations were separated in two equally large populations according to their magnitude. The hypothesis that the relative amplitudes for these groups were identical was tested using both the sign test and the Wilcoxon matched-pairs sign-rank test (Siegel, 1956). These tests revealed that this hypothesis had to be rejected at the 0.05 confidence level for all the five samples considered, thus supporting the hypothesis that the relative amplitudes may change as a function of magnitude. The data indicated that the large events had more extreme amplitude differences than the small events. However, by excluding the 3–5 weakest subarrays, we could no longer reject the hypothesis. The latter result seemingly contradicts the first one, but can be explained as follows. For the groups of small magnitude events, the amplitudes of the weakest subarray signals are less than or of the same order as those of interfering noise wavelets, so the observational data for these particular subarray may be erroneous. Thus, when removing the most unreliable observations, the hypothesis of identical relative amplitudes for the two groups cannot be rejected. From

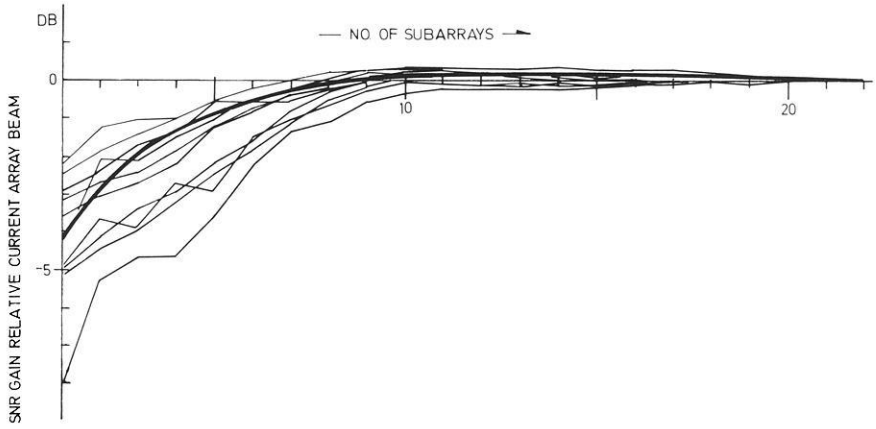

Fig. 8. Expected and obtained performance as a function of number of subarrays for DP beam no. 36. This beam is pointed towards 52N, 160E (off east coast of Kamchatka). The subarrays used have been ranked according to their amplitude. The first one is the one with the highest amplitude, in this case no. 3. The thick line shows the expected performance from the observed amplitude pattern, and corresponds to the dotted line on Figs. 5, 6 and 7. The thin lines give the observed values for 10 different events

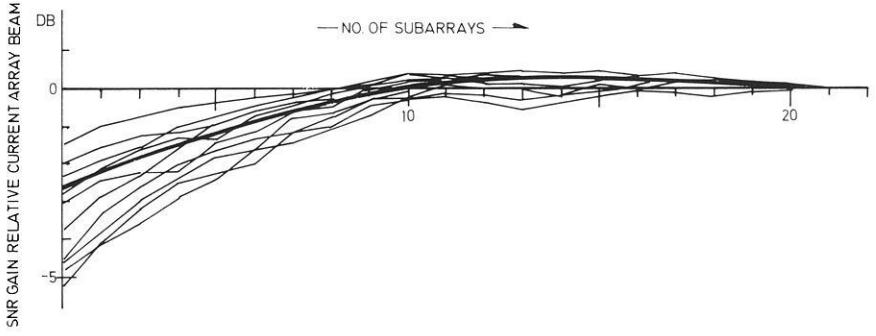

Fig. 9. Same as Fig. 8 for DP beam 63. This beam is pointed towards 43N, 147E (Kurile Islands)

the above results, we concluded that the relative subarray amplitudes do not vary significantly with event magnitude for the type of data considered.

It has also been assumed that all the off-diagonal elements in the matrix R_S in Eq. (4) were equal to the average signal correlation value. This is undoubtedly an oversimplification, as demonstrated in Figs. 8 and 9. The procedure here was first to measure SNR for the best subarray signal, then to add the second best subarray and measure SNR again. The process was repeated until all 22 subarrays were included and thus corresponding to the full array beam. Figs. 8 and 9 show the results obtained for beam locations 36 and 63 using 10 different events in each case. All events are from 1974, *i.e.*, none of them have been used in the previous data collection. The SNR variation is large when less than 10 subarrays are used in the beamforming process, but levels off rapidly as more subarrays are included. For example, the observed SNR variation was

always less than 0.5 dB when the array beam is based on minimum 15 subarrays. The corresponding value for the case of 18 subarrays was 0.3 dB. These results have been interpreted as follows. The signal correlation matrix (Eq. (4)) does not consist of only equal elements in the off-diagonal locations, thus the SNR of the summed traces is not a function of relative amplitude alone but also of the varying correlation between subarrays. When many instruments are used, say 15 or more, the effect of the scatter in the correlation values becomes less important, and for this case the assumption that all off-diagonal elements are equal is acceptable. When all 22 subarrays are used, the two different matrices have the same effect in this context.

Finally, it has been assumed that the noise level is constant across the array, and that the noise is uncorrelated from one subarray to the other. This latest assumption is reasonable in view of previous NORSAR array studies, see for example, Felix *et al.* (1972) and Harley (1972), as well as the noise level measurements made in this study.

So far we have discussed the gain in SNR on the array beam level with respect to a 1/0 (one-zero) subarray weighting scheme. The reason for this is that the beamforming algorithm in the NORSAR on-line Detection Processor is limited to 1/0 weights. However, more flexible models could improve the gain in SNR of the array beam even more. This problem has recently been discussed by Christoffersson and Husebye (1974) who also described different weighting procedures which all are optimal under certain conditions. See also Birtill and Whiteway (1965). For example, using a model based on identical signals except for an unknown amplitude scaling factor, Christoffersson and Husebye (1974) obtained a relative gain in SNR of approx. 2.5 dB for events located in Japan and Central Asia. In order to illustrate this weighting technique, we consider a case with two subarrays having signal amplitudes $A_1=1$ and $A_2=2$. Straight summation of the two traces gives an SNR value of:

$$\mathrm{SNR}_{ab}=\left[\frac{(1+2)^2}{1^2+1^2}\right]^{\frac{1}{2}}=2.12. \tag{12}$$

Assigning weights of 0.45 and 0.89 to the traces gives:

$$\mathrm{SNR}_{wab}=\left[\frac{(0.45\cdot 1+0.89\cdot 2)^2}{0.45^2+0.89^2}\right]^{\frac{1}{2}}=2.24. \tag{13}$$

That is, there is a relative gain in SNR of 0.46 dB by introducing individual subarray weights. These weights have the same general characteristics as the previously discussed 1/0 weights, which means that the gain is largest when the amplitude variations are most extreme. The procedure for calculating such signal amplitude weights is usually too complicated for on-line data processing, but instead we may introduce predetermined subarray amplitude weights. This alternative is not optimum but should still yield a relative gain in SNR; for the single beam locations an average gain of 0.72 dB is to be expected. For several of the areas with large amplitude values this gain can be as large as 1.3 to 1.8 dB. As mentioned above, calculating individual amplitude weights

for each event may give significantly better results, and this more sophisticated version of array beam forming has been implemented in the NORSAR off-line Event Processor.

For several regions the amplitude variations within the NORSAR array are as much as 20 dB, but only exceptionally is a relative gain of more than 0.3 dB obtained in SNR by excluding one or more of the subarrays in beamforming. Moreover, as the subarray amplitude pattern may change drastically within a small seismic region, any type of weighted array beamforming should be a function of the individual beam locations, *i.e.*, different array configurations for different regions. Although some of the subarrays are bad for most of the seismic regions covered by NORSAR, they all have several regions where they contribute positively to the array beam. Therefore, in average there will always be some loss by excluding any of the subarrays consistently. It should be noted that we have been measuring subarray beam amplitudes. If we instead had measured the amplitudes on single sensors, even more drastic variations would have been found. Also, it should be added that there is no good reason to believe that the NORSAR site is unique in regard to the large amplitude variability; data from the LASA array exhibits variations of the same order of magnitude (Berteussen *et al.*, 1975).

When planning the installation of seismic arrays a large effort is invariably devoted to the problem of noise suppression; measurements are generally made of noise correlation as a function of frequency and spatial lag. The array configuration is then made such that maximum noise suppression is achieved when other factors like signal correlation and event location capabilities, etc., also have been considered. However, the fact that signal amplitude variations inside the area of interest may down or upgrade the capabilities of the array significantly are usually not given much attention. Most works show that the short period seismic noise behaves fairly well as expected, *i.e.*, for instruments located more than a specific distance (usually 2–4 km) from each other the $1/\sqrt{N}$ noise reduction is approached. Also, at least for NORSAR, there is not any significant noise level variation across the array. Thus it is reasonable to believe that the noise behavior does not depend much on the exact instrument location, as long as certain instrument-to-instrument distance rules are obeyed. As has been shown, however, this is not so for the teleseismic signals.

Conclusion

It has been found that there may be more than 20 dB amplitude variations inside the NORSAR array, and as much as 10 dB in amplitude difference between instruments located less than 15 km from each other. In order to say something about the signal amplitudes at a certain site, it is thus possible to extrapolate only from very close-by instruments. If one is constructing an array where one of the main concerns is good signal detectability, the problem of finding the particular instrument sites which give best amplitude performance should be investigated. As it turns out, the relative signal amplitude may depend highly on the seismic region. Thus the event detection capability of a station

will vary with region. This pattern may, however, be determined before the array configuration is fixed if careful amplitude studies using a lot of instruments (or by moving them around) are performed. It has been demonstrated that the amplitude pattern is very repeatable from one event to the other for events from the same location. Therefore, each test site would have to be operated just long enough to get a few good signals from the most interesting regions.

As mentioned previously, a large number of papers have been concerned with the investigation of observed *P*-wave amplitudes. Except for a few studies of array data, most of these works have been on data recorded at conventional stations which have had separations much larger than those of the NORSAR subarrays. This is a very important point because this type of sampling may not reveal the true character of the space-variations of the amplitudes. From the data presented herein it is obvious that an amplitude measurement may often not be representative for distances as large as 10–15 km, also the standard deviation of the amplitudes recorded at NORSAR has been found to be of the same order as that of a world-wide seismic network. Thus observations which are inverted, for example to determine Q structures, may be crucially dependent on the density of the observation network. This conclusion is consistent with the results of Aki (1973) (LASA), Capon (1974) (LASA), Dahle (1975) (NORSAR), and Berteussen *et al.* (1975) (NORSAR and LASA). These authors have performed a random medium (Chernov, 1960) analysis for NORSAR and/or LASA and all have reported that the transverse autocorrelation both for amplitude and phase falls to $1/e$ (0.37) of its maximum for a spatial lag of 10 to 20 km. While the random medium interpretation of the results is not necessarily unique, the observational fact that the anomalies are correlated only for distance of 10 to 20 km can, however, not be disputed. If this is taken as the minimum anomaly wavelength one would like to cover, one thus needs a spatial sampling rate of 5 to 10 km to ensure that no aliasing occurs. Finally we remark that only models of the random medium type or a block type structure as proposed by Aki *et al.* (1975) currently seem able to account for the rapid fluctuations of the observed amplitudes.

Acknowledgement. This research was supported by the Advanced Research Projects Agency of the U.S. Department of Defense and was monitored by AFTAC/VSC, Patrick AFB FL 32925, under contract no. F08606-74-C-0049.

Dr. H. Bungum, Dr. E.S. Husebye and Dr. D.W. King are thanked for critically reading the manuscript and for contributing in useful discussions throughout the project.

References

Aki, K.: Scaling law of seismic spectrum. J. Geophys. Res. **72**, 1217–1231, 1967

Aki, K.: Scattering of P-waves under the Montana LASA. J. Geophys. Res. **78**, 1334–1346, 1973

Aki, K., Husebye, E.S., Christoffersson, A.: Three-dimensional seismic velocity anomalies in the earth's crust and upper mantle under NORSAR. In preparation, 1975

Anderson, D.L., Ben-Menahem, A., Archambeau, C.B.: Attenuation of seismic energy in the upper mantle. J. Geophys. Res. **70**, 1441–1448, 1965

Anderson, D.L., Kovach, R.: Attenuation in the mantle and rigidity of the core from multiply reflected core phases. Proc. Nat. Acad. Sci., U.S. **51**, 168–172, 1964

Berteussen, K.A.: Crustal structure and P-wave travel time anomalies at NORSAR. J. Geophys. **41**, 71–84, 1975

Berteussen, K.A., Christoffersson, A., Husebye, E.S., Dahle, A.: Wave scattering theory in analysis of P-wave anomalies at NORSAR and LASA. Geophys. J. in press, 1975

Birtill, J.W., Whiteway, F.E.: The application of phased arrays to the analysis of seismic body waves. Phil. Trans. Roy. Soc. London, Ser. A **258**, 421–493, 1965

Bungum, H., Husebye, E.S.: Analysis of the operational capabilities for detection and location of seismic events at NORSAR. Bull. Seism. Soc. Am. **64**, 637–656, 1974

Bungum, H., Husebye, E.S., Ringdal, F.: The NORSAR array and preliminary results of data analysis. Geophys. J. **25**, 115–126, 1971

Bungum, H., Ringdal, F.: Diurnal variation of seismic noise and its effect on detectability. NORSAR Scientific Rep. No. 5–74/75, NTNF/NORSAR, Kjeller, Norway, 1974

Capon, J.: Characterization of crust and upper mantle structure under LASA as a random medium. Bull. Seism. Soc. Am. **64**, 235–266, 1974

Chernov, L.: Wave propagation in random media, trans. by R.A. Silverman. New York: McGraw-Hill, 1960

Christoffersson, A., Husebye, E.S.: Least squares signal estimation techniques in analysis of seismic array recorded P-waves. Geophys. J. **38**, 525–552, 1974

Dahle, A.: Time and amplitude fluctuations of teleseismic P-signals at NORSAR in view of wave scattering theory. Scientific Report No. 4–74/75, NTNF/NORSAR, Kjeller, Norway, 1975

Denham, D.: The use of geophone groups to improve the signal-to-noise ratio of the first arrival in refraction shooting. Geophys. Prospecting **11**, 389, 1963

Felix, C.P., Gilbert, W.L., Wheeler, S.G.: Preliminary results from the NORSAR system. Proc. Seminar on Seismology and Seismic Arrays, NTNF/NORSAR, Kjeller, Norway, 1972

Gutenberg, B.: Amplitudes of surface waves and magnitudes of shallow earthquakes. Bull. Seism. Soc. Am. **35**, 3–12, 1945

Harley, T.W.: Preliminary evaluation of the NORSAR short period and long period system. Proc. Seminar on Seismology and Seismic Arrays, NTNF/NORSAR, Kjeller, Norway, 1972

Hjortenberg, E., Risbo, T.: Monochromatic components of the seismic noise in the NORSAR area. Geophys. J., in press, 1975

Husebye, E.S., Dahle, A., Berteussen, K.A.: Bias analysis of NORSAR and ISC reported seismic event m_b magnitudes. J. Geophys. Res. **79**, 2967–2978, 1974

Kanamori, H.: Attenuation of P waves in the upper and lower mantle. Bull. Earthquake Res. Inst. **45**, 299–312, 1967

Landers, T.E.: Elastic waves in laterally inhomogeneous media, Ph.D. thesis, Mass. Inst. of Tech., Cambridge, U.S., 1971

Larner, K.L.: Near-receiver scattering of teleseismic body waves in layered crust-mantle models having irregular interfaces, Ph.D. thesis, Mass. Inst. of Tech., Cambridge, U.S., 1970

Mereu, R.F.: Effect of Mohorovicic topography on the amplitudes of seismic P waves. J. Geophys. Res. **74**, 4371–4376, 1969

Siegel, S.: Nonparametric statistics for the behavioral sciences, Int. Stud. Ed., 229–239. New York: McGraw-Hill, 1956

Steinert, O., Husebye, E.S., Gjøystdal, H.: False alarm rate and noise variability at NORSAR. J. Geophys. **41**, 289–302 (1975)

Veith, K.F., Clawson, G.E.: Magnitude from short-period P-wave data. Bull. Seism. Soc. Am. **62**, 435–452 (1972)

Received April 7, 1975; Revised Version September 10, 1975

J. Geophys. 41, 615–632, 1975

Magnetic Hysteresis Loops and Magnetization versus Temperature Curves of Some Basalt Samples Containing Titanomagnetite Ore either Single-Phase or with an Intergrowth of Ilmenite Lamellae

E. Schmidbauer

Institut für Allgemeine und Angewandte Geophysik der Universität,
D-8000 München, Theresienstr. 41, Federal Republic of Germany

Abstract. Measurements of magnetization versus temperature curves, between −185 and 600 °C, and of hysteresis loops, between −205 °C and room temperature, have been performed on six basalt samples from different localities in fields up to 14.5 kOe. Samples containing homogeneous titanomagnetite ore particles show at room temperature a coercive force $H_c < 100$ Oe which increases to 660 Oe on lowering the temperature to −196 °C. The temperature dependence of the saturation remanent magnetization σ_{ro} is also pronounced with relatively high values at low temperatures. Basalts with oxidized titanomagnetite grains and ilmenite exsolution lamellae exhibit rather constant values of H_c and σ_{ro} in the temperature interval mentioned.

The characteristic features of the loops indicate a predominant influence of multi-domain grains, even in the case of oxidized titanomagnetite grains subdivided by ilmenite lamellae down to dimensions of the remaining titanomagnetite that would be expected to show single-domain behaviour. This phenomenon might be interpreted in terms of some kind of cluster effect among these single-domain particles caused by magnetic interaction.

The contribution of the paramagnetic rock matrix to the overall magnetization of the specimens in high magnetic fields is appreciable in most cases. A rough evaluation of the paramagnetic susceptibility deduced at room temperature and at −196 °C gives values consistent with a Curie law for some samples. There are two basalts with hemo-ilmenite grains which contribute presumably to this susceptibility at −196 °C.

Key words: Magnetization of basalts – Hysteresis loops – Paramagnetic susceptibility of the rock matrix.

Introduction

In many investigations on the magnetization of igneous rocks with respect to palaeomagnetism the relationship between the mineralogy of the specimens

and their magnetic properties is discussed to a small extent only. On the other hand, attention has been drawn by a growing number of studies to the problem of stability of the natural remanent magnetization in basalts and its correlation with the type and the chemical state of the magnetic ore grains as well as the grain size distribution. This is in particular relevant to measurements of the palaeointensity of the geomagnetic field. Thus, in recent years interest has concentrated e.g. on the early stage of oxidation in titanomagnetite grains. Magnetic data of these particles reflect clearly a chemical process taking place, although any alteration of the titanomagnetite is hardly detectable on polished sections under the ore microscope.

In general investigations of the magnetization in relation to the mineralogy are based on data deduced from magnetization versus temperature T curves ($\sigma - T$), measurements of thermoremanent and induced magnetization and a.c. demagnetization experiments. From the latter the so called coercivity spectrum is derived, representing for the ensemble of magnetic grains in the respective sample the coercive force distribution with regard to the effective particle size. The coercivity spectrum appears to be a good measure for the stability of the natural remanent magnetization (Larson *et al.*, 1969). A classification of $\sigma - T$ curves for basalts according to the shape and the Curie temperatures, related to the degree of oxidation in the ore grains, a primary or secondary one, has been established in the past by various workers (Wilson and Watkins, 1967; Ade-Hall *et al.*, 1968; Creer and Valencio, 1969; Creer *et al.*, 1970).

Relatively few attempts have been made to date to utilize measurements of magnetic hysteresis loops for this purpose (Nagata, 1961; Radhakrishnamurty *et al.*, 1967–1972; Néel, 1970; Wasilewski, 1973). Studies of basalt specimens including measurements of hysteresis loops at low magnetic fields have been done in order to gain information about single- and multi-domain particles (Radhakrishnamurty *et al.*, 1967–1972). As solely minor loops have been measured, it appears that an interpretation of the results requires very careful analysis because the phenomena related with such loops are extremely complex.

In the following, results of an investigation on the magnetization are presented that has been carried out on a selection of basalts from different localities comprising some samples with non-oxidized titanomagnetite grains and others with particles oxidized to various degrees. Measurements of hysteresis loops and $\sigma - T$ curves were combined with a microscope study including the observation of magnetic domain structures of magnetic ore grains on polished sections of basalt specimens at room temperature. The measurements were extended to low temperatures. As in this temperature range characteristic features of the loops may be more pronounced, there is a greater possibility of being able to separate the magnetization into contributions originating from superparamagnetic, single-domain or multi-domain grains.

Experimental

A translation balance of the Weiss-Forrer type was used for measurements of magnetization σ versus temperature T curves in a range of temperatures

from -185 °C to above the Curie points of the respective basalts. Heating of the samples, fixed in a sample holder, was done in air. To determine hysteresis loops, two vibrating sample magnetometers were available. One, a commercial instrument (PAR), was employed at room temperature up to 14.5 kOe. The other, somewhat less sensitive, could be operated in the temperature interval of -205 °C to room temperature and a maximum field strength of 13 kOe was attained. The Curie points of the samples were determined from $\sigma - T$ curves in a field of 2.5 kOe.

For the magnetic measurements chips were cut from specimens used for polished sections and ground to spheres of 3–4 mm in diameter. The observation of magnetic domains on polished sections was performed with magnetite colloid (Bitter technique) after ion polishing the sample surface with a method developed by Soffel (1968a, b).

The absolute values of magnetization were determined with the commercial vibrating sample magnetometer. In this way the error of measurement could, also for the results on the balance, be kept $< 5\%$. The coercive force H_c and the relative remanent magnetization, quantities derived from the hysteresis loops, are accurate to 5–10%. Values of remanent magnetization have not been corrected for the demagnetizing factor of the ore grains.

The error of the paramagnetic susceptibility deduced from the high field magnetization of the loops may, at -196 °C, amount up to 30% due to possible non saturation of the sample.

Petrographic Data

Six basalt samples were selected for the measurements. In two of them, titanomagnetite grains appear single-phase whereas the remaining four exhibit titanomagnetite oxidized to different extent.

Basalt no. 1 (RK) is a tertiary basalt from the Rauher Kulm, Oberpfalz, Germany. It is characterized by homogeneous titanomagnetite particles, embedded in a rock matrix consisting, in order of decreasing concentration, of pyroxenes, olivine, a glassy matrix and to a lesser extent plagioclase as has been established from a large number of specimens (Refai, 1960; Petersen, 1962, 1966; Soffel, 1968; Creer and Perersen, 1969). The titanomagnetite grains are rather uniformly dispersed in the rock matrix and euhedral to anhedral. Their grain size distribution is illustrated in Fig. 1 for the specimen under investigation. The determination of the ore content in a polished section under the microscope with an integration method yielded 3.5% by volume.

Basalt no. 2 (29/1/1) from Jabal Soda, Libya (Schult and Soffel, 1973) is a tertiary alkali basalt. The grain size distribution of the homogeneous titanomagnetite ore is similar to that of no. 1, the dominating percentage by volume being represented by anhedral particles of 3–30 μ in diameter. A minority of grains shows very faint lamellae of incipient ilmenite exsolution. For this reason it is likely that also a large fraction of the particles, although homogeneous in appearance in reflecting light in polished sections, contain submicroscopic alterations possibly in the form of titanomaghemite and exsolved ilmenite.

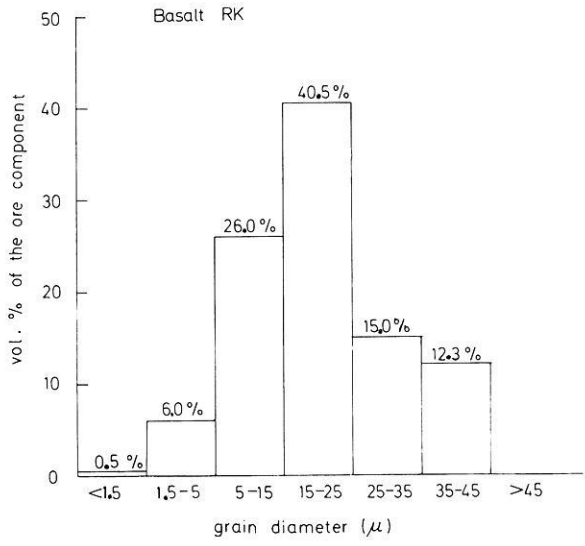

Fig. 1. Grain size distribution of titanomagnetite ore particles in basalt no. 1 (*RK*)

Basalt no. 3 (Fornazzo F4) is from a lava flow of Mount Etna at Fornazzo, Sicily, in 1950/51. The specimen has been drilled from the top of the flow. A detailed description is given by Angenheister *et al.* (1971). The ore grains consist essentially of titanomagnetite grains of 5–80 μ in diameter with clearly developed ilmenite lamellae the amount of the latter being of the order of $\leqq 15$ vol.-% of the grains. There occur also some large grains ($\leqq 200$ μ) with exsolved ilmenite only faintly visible and, hence, the percentage of ilmenite above may not be valid for these particles.

Sample no. 4 (CA-2-AZ,2D) from the Amazon Basin, Brasil, represents a core of a basalt intrusion drilled from a depth of 334 m (Schult, 1970). The ore grains (1.5–100 μ) are on average apparently strongly oxidized titanomagnetite with a dominating intergrowth of ilmenite lamellae the latter representing 60–90 vol.-% of those ore grains. In many of these particles segments of them occur as anisotropic, grey to brownish phase, possibly pseudobrookite. Frequently this phase is also present in the form of well-developed lamellae being occasionally rather broad. The phase is visible also in the form of separate, anhedral grains. By employing the magnetite colloid technique it could be established that this phase is non magnetic whereas a small remainder of original titanomagnetite or titanomaghemite could easily be detected in the grains. The ilmenite lamellae mentioned above are presumably to a large extent decomposed into new, optically not clearly identifiable phases (magnification $\times 1{,}000$ in oil). Such a situation is frequently observed in strongly oxidized basalts where hematite, rutile or anatase and pseudobrookite are encountered as decomposition products.

Basalt no. 5 (SD-1-MT), from the Parana Basin, Brasil, is a specimen of a basalt intrusion, drilled from a depth of 1,453 m (Schult, 1970). A microscopic inspection reveals a complex structure of the ore grains. In principle, three types of grains can be distinguished.

a) Grains (2–150 μ) of titanomagnetite with ilmenite lamellae, the latter amounting up to $\leqq 50$ vol.-% of these particles. Further, rather large segments which may be pseudobrookite as in sample no. 4 of those grains are grey to brownish in appearance; occasionally some kind of granulation seems to occur in these segments (see c).

b) Relatively large (50–200 μ), discrete, euhedral to anhedral and frequently elongate, primary hemoilmenite grains are found revealing to a more or less extent thin grey, anisotropic veinlets. In small segments a granular structure is present peripherally (see c). No magnetization could be detected with the help of the colloid method.

c) In a number of discrete large grains (up to $\leqq 200$ μ) an intimate mixture of a dominating light grey phase and a darker ore occurs, a texture, that has been denoted in the literature as granulation (Ade-Hall *et al.*, 1968). These grains are probably magnetic.

Sample no. 6 (LS-1-PR, 16D) has been drilled in the Parana Basin Brasil, from a basalt intrusion at a depth of 2,350 m (Schult, 1970). This specimen has been taken for the present study because the ore consists predominantly of primary hemoilmenite. It occurs in the form of large (10–250 μ), homogeneous, frequently elongate, euhedral to anhedral and anisotropic grains. In addition, a highly reflecting, anisotropic phase is contained (particles $\leqq 80$ μ) that is $\leqq 10$ vol.-% of the ore and may be pyrrhotite and pyrite. Using the colloid technique, typical parallel patterns are seen in quite a number of cases which point to a hexagonal structure of this phase as is required for pyrrhotite. The hemoilmenite appears to be non-magnetic at room temperature. Possibly, titanomagnetite is present in the form of very small grains.

Some characteristic features of the samples studied are summarized in Table 1.

Results

Basalts with Single-Phase Titanomagnetite Grains

The $\sigma - T$ curve of basalt no. 1 (RK) is presented in Fig. 2a. For the sample used it coincides with analogous measurements carried out previously (Petersen, 1962, 1966; Creer and Petersen, 1969). Hysteresis loops of a virgin sample taken from the same hand sample are shown in Fig. 2b at room temperature and -196 °C. At room temperature one can expect saturation of the titanomagnetite grains in a field $\geqq 5$ kOe whereas at low temperatures higher fields are required. A characteristic feature of the loops is the steadily rising σ up to the maximum fields used. The observation of this linear increase in the high field region could be confirmed up to 14.5 kOe. From the graph a slope of $\Delta\sigma/\Delta H = 2.0 \times 10^{-5}$ (Gcm^3/g) is evaluated at ambient temperature. The ratio σ_{ro}/σ_o (σ_{ro} = isothermal saturation remanent magnetization, σ_o = saturation magnetization, defined as σ that is obtained by extrapolating σ from high fields to $H \to 0$) is relatively low at room temperature, however on lowering T, it is raised steadily up to the maximum value attained at -196 °C. A similar behaviour is established for the coercive force H_c which is much higher at low T. Values for σ_{ro}/σ_o and H_c are listed in Table 2.

Table 1

Specimen number	Locality	Sample specification	Grain size (μ)	Curie points	Opaque mineralogy
1	Rauher Kulm Oberpfalz, West-Germany	RK	1.5–45	180 °C	brown, homogeneous titanomagnetite
2	Libya, Jabal Soda	29/1/1	3–30	300 °C 450 °C	brown titanomagnetite, very rarely beginning exsolution of ilmenite
3	Sicily, Aetna	Fornazzo F4	5–200	525 °C	titanomagnetite with an intergrowth of well developed ilmenite lamellae
4	Brasilia, Amazon	CA-2-AZ, 2D	2–100	520 °C	titanomagnetite with dominating ilmenite exsolution lamellae and decomposition products, primary hemoilmenite grains with a faintly visible net of an exsolved light grey phase
5	Brasilia, Parana	SD-1-Mt, 6D	2–200	530 °C 175 °C	titanomagnetite with well-developed lamellae of ilmenite and its decomposition products, primary homogeneous hemo-ilmenite, granular structure
6	Brasilia, Parana	LS-1-PR, 16	2–250	300 °C	primary, homogeneous hemoilmenite, a bright anisotropic phase probably being pyrrhothite

In order to study the behaviour of minor loops on basalt no. 1 at ambient T, a virgin specimen, previously demagnetized in a tumbler applying a starting field of 2 kOe, was subjected to cycles with the maximum field employed during a cycle increasing from 200 to 8,000 Oe. The results for H_c and σ_r thus obtained are plotted in Fig. 3. As can be seen from the graphs, above about 2 kOe differences relative to the high field values are insignificant.

Although basalt no. 2 (29/1/1) appears to contain largely homogeneous titanomagnetite grains, they must be assumed to be in the first step of oxidation, as mentioned. Evidence for this suggestion is seen from the $\sigma - T$ curve of Fig. 4a which shows on heating a tail with a small hump between 300 and 400 °C (see p. 623). The hysteresis loops (Fig. 4b) between ambient temperature and −196 °C resemble those of basalt no. 1 with the exception that H_c is raised much more on lowering T (Table 2). We must bear in mind that the loops are probably due to two phases.

Basalts with Ilmenite Lamellae in Titanomagnetite Grains

The $\sigma - T$ curves and hysteresis loops for several basalts with an ore mineral composition as described above (see Table 1) are presented in Figs. 5 to 8.

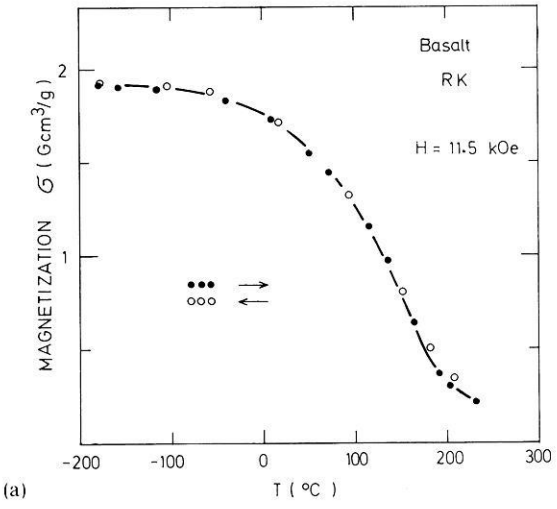

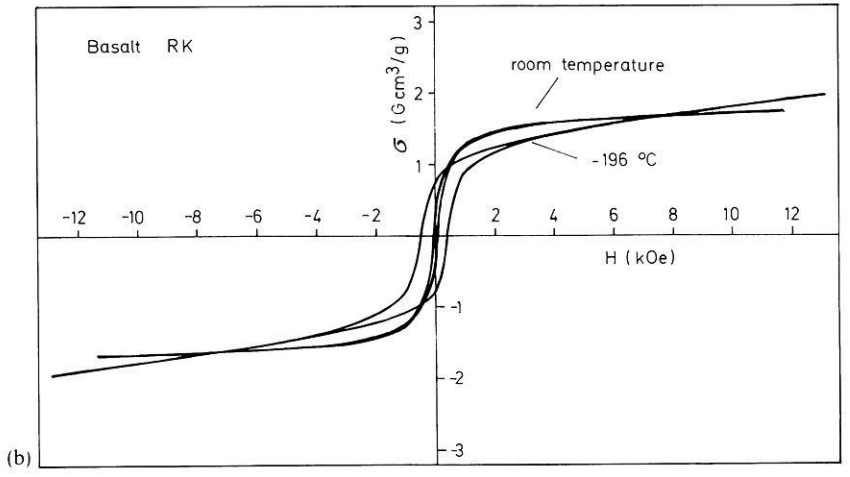

Fig. 2. (a) Magnetization σ versus temperature T curve for basalt no. 1 (*RK*). (b) Hysteresis loops for basalt no. 1 (*RK*)

Basalt no. 3 (Fornazzo F4) is an example of a basalt containing a rather uniform ore grain composition of a small number of ilmenite lamellae in titanomagnetite grains, exhibiting a Curie point of about 525 °C (Fig. 5a). In contrast to the loops of samples no. 1 and 2, H_c remains fairly constant between ambient T and -196 °C. It is also relatively high. σ_{ro}/σ_o does not differ much in the temperature range mentioned. The field strength required to saturate the specimen does not appear to depend appreciably on temperature either. As for the samples presented above, there is an increase in σ with H in a field range where the ore grains can be assumed to be magnetized to saturation. From the form of the low temperature loop in Fig. 5b no indication of an ilmenite contribution can be inferred. For this reason we conclude that the ilmenite, visible under the microscope as lamellae may be paramagnetic down to -196 °C.

Table 2. Basalt

No.		1	2	3	4	5	6
H_c(Oe)	20 °C	52	65	145	115	160	185
	−196 °C	370	660	190	125	280	290
σ_{ro}/σ_o	20 °C	0.17	0.13	0.17	0.13	0.11	0.58
	−196 °C	0.60	0.63	0.20	0.17	0.16	~1.0
$\Delta\sigma/\Delta H \cdot 10^5$	20 °C	2.0	2.0	1.9	1.9	2.3	2.3
(Gcm^3/g)	−196 °C	7.0	7.9	7.4	6.7	9.7	16.2

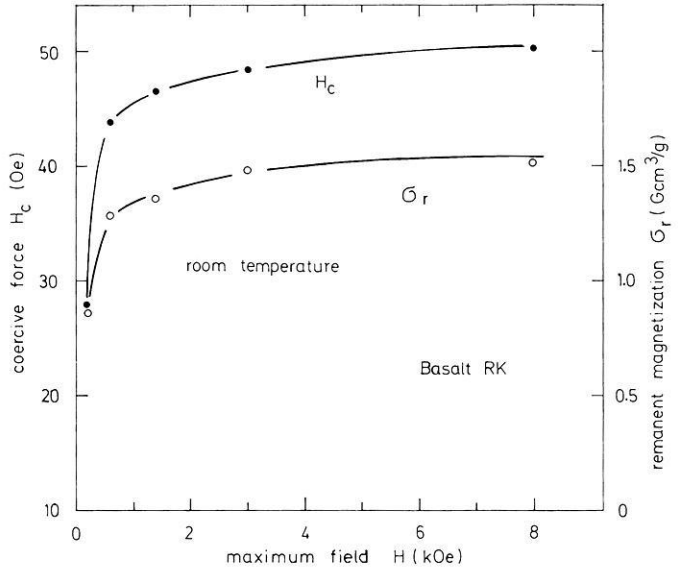

Fig. 3. Dependence of coercive force H_c and isothermal remanent magnetization σ_r on the maximum field strength H, applied during a hysteresis cycle, for basalt no. 1 (*RK*)

We expect the more complex mineralogy of the magnetic ore grains of basalts nos. 4–6 to be reflected in the magnetization data.

Basalt no. 4 (CA-2-AZ) shows a $\sigma - T$ curve with a high temperature Curie point of ~520 °C (Fig. 6a). The course of $\sigma - T$ at low temperatures may be interpreted as the onset of a superposed thermomagnetic curve. However, this point can only be decided by measurements down to 4.2 °K. The hysteresis loops exhibit features similar to those of sample no. 3 (Fig. 6b). H_c and σ_{ro}/σ_o reveal only a slight temperature dependence (Table 2). Although it seems that $\Delta\sigma/\Delta H$ may distinctly differ at −196 °c from that of specimen no. 3, the values listed in Table 2 indicate that there is close conformity; the impression arises merely because of the reduced absolute magnitude of σ for sample no. 4.

For basalt no. 5, however, from the shape of the $\sigma - T$ curve in Fig. 7a, the presence of a second magnetic phase can be inferred with a Curie point at low temperature, besides a phase with a high Curie point. This suggestion is supported by the increase in H_c from ~200 Oe to ~300 Oe at $T \sim -170$ °C

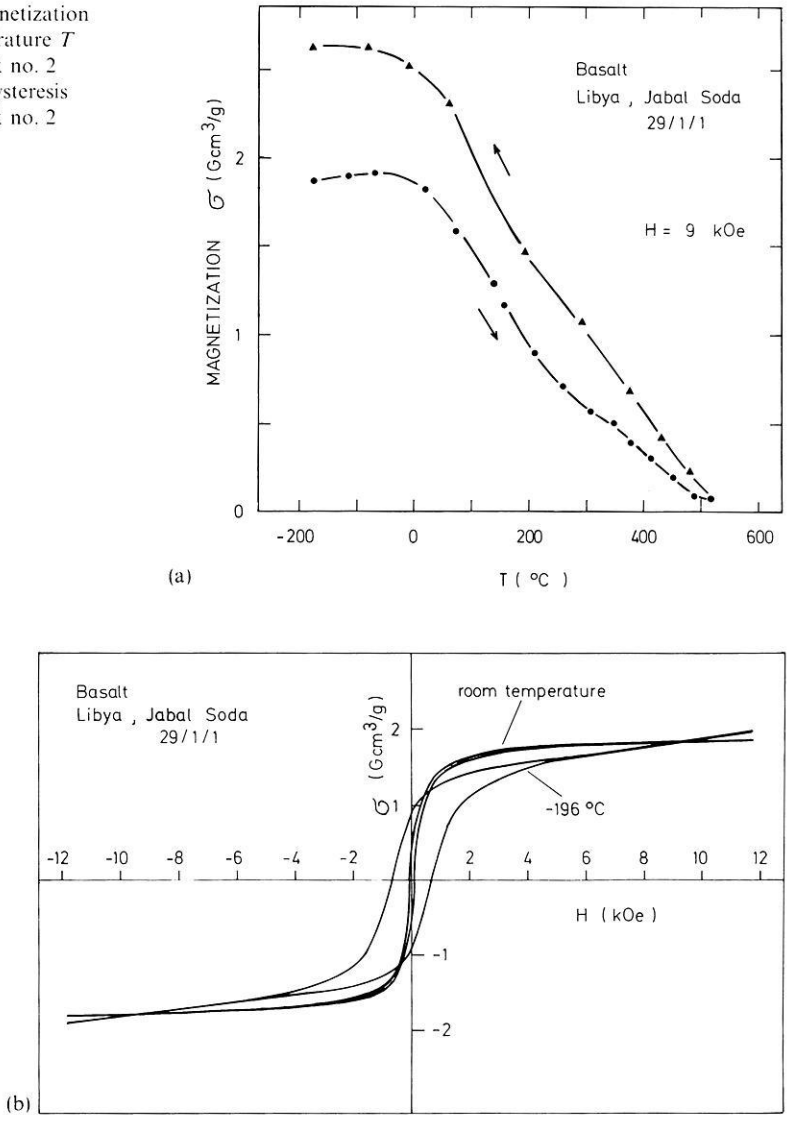

Fig. 4. (a) Magnetization σ versus temperature T curve for basalt no. 2 (29/1/1). (b) Hysteresis loops for basalt no. 2 (29/1/1)

that goes hand in hand with the rise in σ. Also the larger size of the loop in the relevant temperature interval must be attributed to some kind of new phase (Fig. 7b). From Table 2 we see that $\Delta\sigma/\Delta H$ is at -196 °C much higher than for all the basalts so far.

From the ore microscopic results (see p. 619) it is clear that for basalt no. 6 the Curie point at ~ 300 °C as deduced from the σ (T) curve in Fig. 8a originates probably from pyrrhotite. In addition, at low temperatures, a second phase might contribute to σ. The fact that σ_{ro}/σ_o is very high shows that the carrier of σ with $T_c \sim 300$ °C cannot be titanomagnetite or titanomaghemite

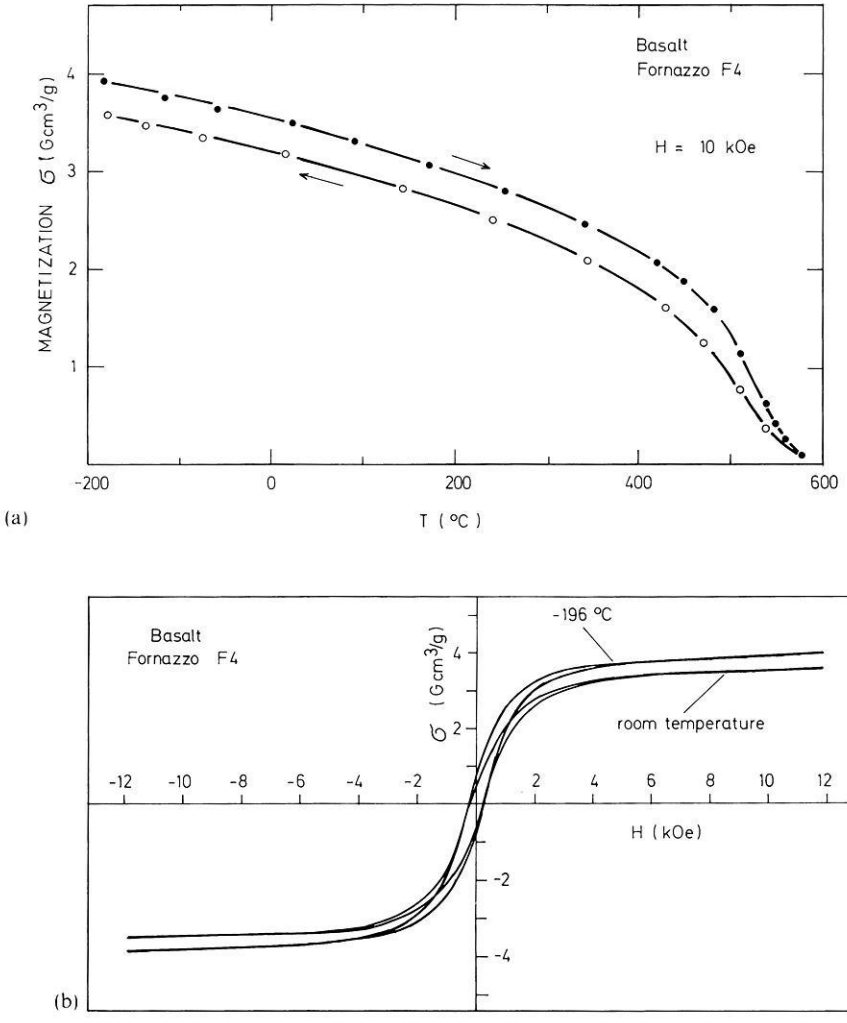

Fig. 5. (a) Magnetization σ versus temperature T curve for basalt no. 3 (Fornazzo F4). (b) Hysteresis loops for basalt no. 3 (Fornazzo F4)

whereas H_c is in the normal order of magnitude (Fig. 8b). Finally, the high magnitude of $\Delta\sigma/\Delta H$ is obviously associated with the low temperature phase (Table 2).

Discussion of Results

Basalts with Single-Phase Titanomagnetite Grains

For basalt no. 1 (RK), an examination of the titanomagnetite ore grains with the microprobe (Creer and Ibbetson, 1970) showed that the titanomagnetite

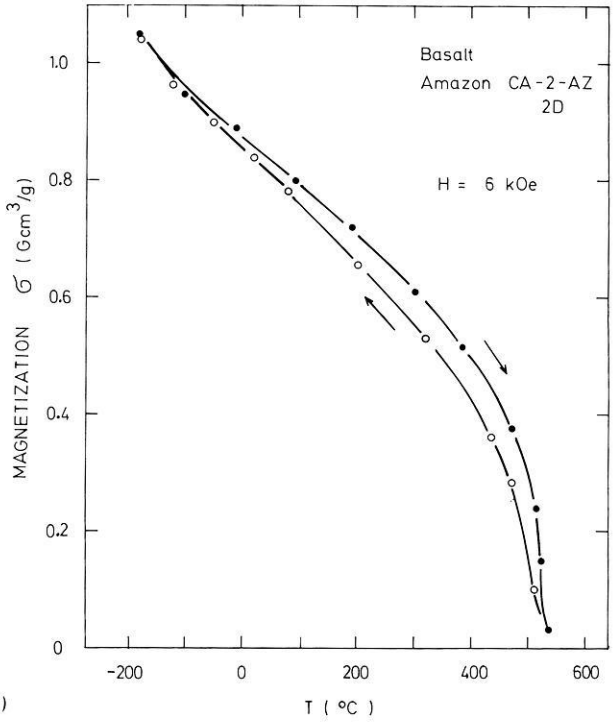

(a)

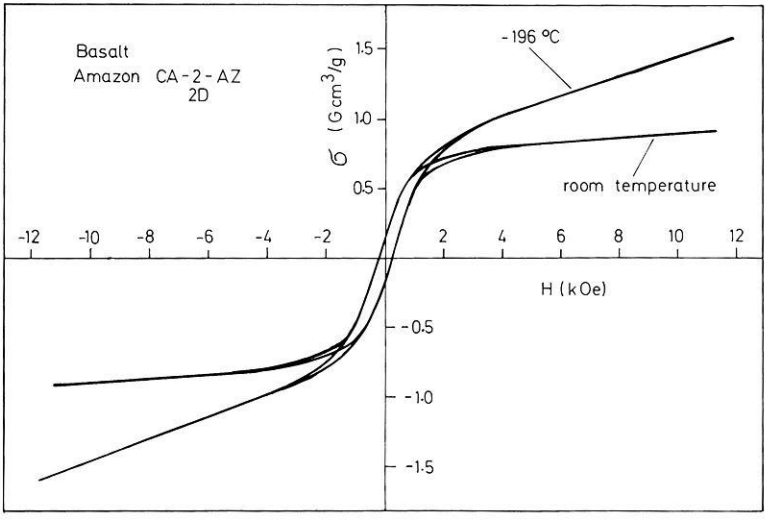

(b)

Fig. 6. (a) Magnetization σ versus temperature T curve for basalt no. 4 (CA-2-AZ, 2D). (b) Hysteresis loops for basalt no. 4 (CA-2-AZ, 2D)

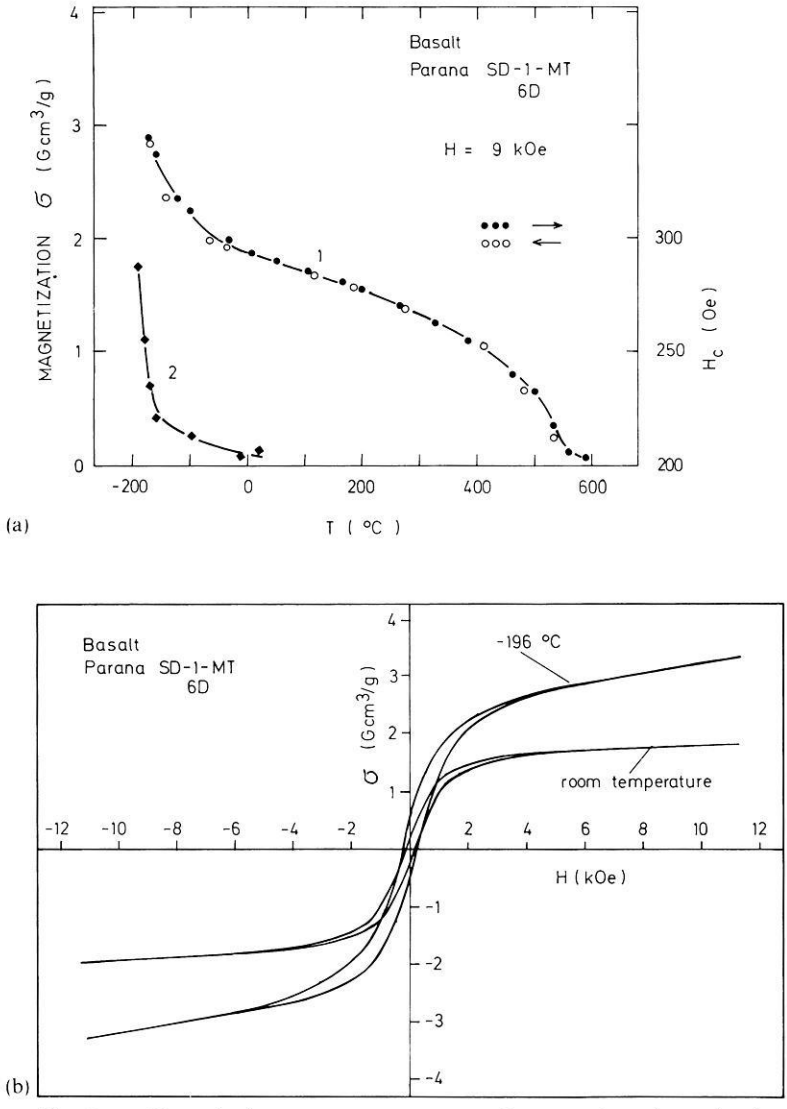

Fig. 7. (a) Magnetization σ versus temperature T curves (*1*) and coercive force H_c (*2*) for basalt no. 5 (SD-1-MT, 6D). (b) Hysteresis loops for basalt no. 5 (SD-1-MT, 6D)

particles may, to a small extent, contain magnesium and aluminum as impurities. Therefore, the salient features of hysteresis loops may not compare completely with those known from the literature for pure, synthetic titanomagnetites, the members of the spinel series Fe_3O_4-Fe_2TiO_4 ($Fe_{3-x}Ti_xO_4$; $0 \leqq x \leqq 1$). On the other hand, the composition of the basalt appears to be notably constant (Refai, 1960; Petersen, 1962, 1966).

The magnitude of H_c and σ_{ro}/σ_o of the RK basalt at -196 °C accords roughly with data measured by O'Reilly (1965) and Banerjee and O'Reilly

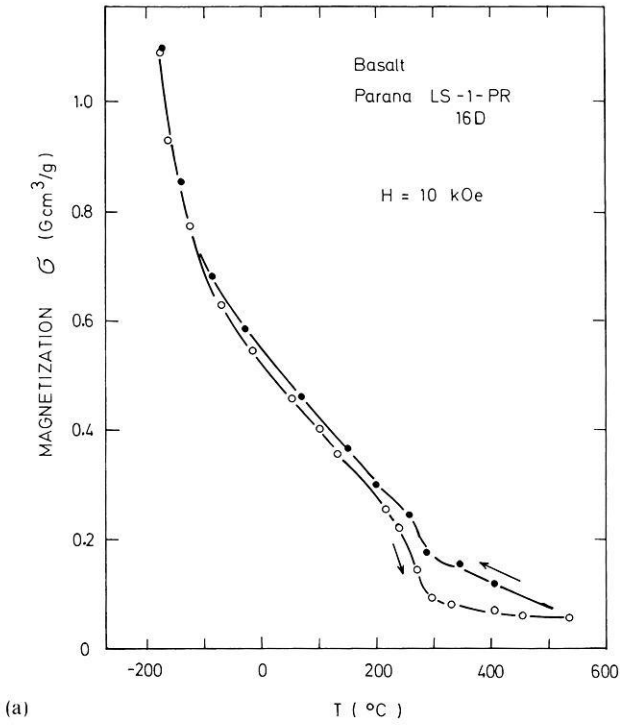

(a)

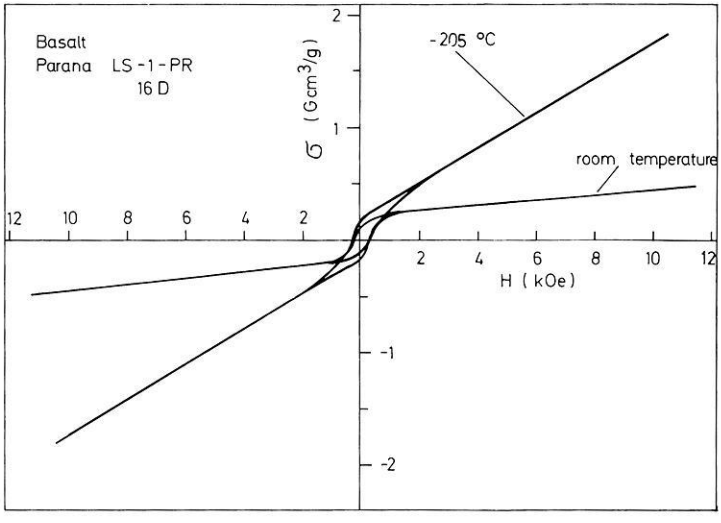

(b)

Fig. 8. (a) Magnetization σ versus temperature T curves for basalt no. 6 (LS-1-PR, 16D). (b) Hysteresis loops for basalt no. 6 (LS-1-PR, 16D)

(1966) on polycrystalline titanomagnetite with $T_c \sim 180$ °C ($x \sim 0.65$). Therefore we assume that in both cases similar mechanisms may be operative determining H_c and σ_{ro}/σ_o. If single-domain particle would be responsible for the loop charac-

teristics at -196 °C, the value $H_c = 370$ Oe found for the RK basalt would be too low. The same applies for the ratio $\sigma_{ro}/\sigma_o = 0.6$ as compared to 0.83 for single-domain particles and $K_1 > 0$. In the synthetic samples the hysteresis loop characteristics at low temperatures are presumably dictated by the high magnetocrystalline anisotropy constant K_1 which is probably due to Fe^{2+} ions on A- and B-sites of the spinel lattice (Syono, 1965). We suppose that also for the RK basalt ore grains K_1 is considerable at low temperatures in spite of the presence of a small amount of Mg and Al in the spinel lattice. Soffel (1971) has demonstrated by observation of domain walls on ore grains of the RK basalt that the critical diameter d_{cr} of the ore grains for the transition from the single-domain to the multi-domain state is < 1.5 μ at room temperature. As dimensions $\leqq 1$ μ cannot be studied using the reflecting light microscope, it is likely that the real d_{cr} is still smaller. It is well known that d_{cr} depends on the crystalline anisotropy constant K_1. Making a rough estimation, Readman and O'Reilly (1972) argue that for titanomagnetites of composition x between 0.4 and 0.7 the critical diameter d_{cr} may be between 0.2 and 1.4 μ, respectively, at $T \sim 80$ °K due to the large K_1 value. Taking these values for the RK sample, we conclude that part of the magnetic grains is likely to be single-domain at low T (see Fig. 1). Although this volume fraction may not be sufficient to raise the coercive force H_c of the RK sample to the values expected for pure single-domain grains, the contribution to the saturation remanent magnetization σ_{ro} may be more pronounced. There must also be considered the fact that a certain percentage of grains which are superparamagnetic at room temperature become single-domain particles at low temperatures and, therefore, carry also remanent magnetization as has been pointed out by Markert and Steigenberger (1971).

The slope $\Delta\sigma/\Delta H$ above technical saturation of the basalt specimen at room temperature arises from the so called paraprocess of the single-domain and multi-domain grains, from superparamagnetic particles, and from the paramagnetism of the rock matrix. ($\Delta\sigma/\Delta H = \chi_{as}$ = specific susceptibility above saturation). In general, the contribution of the paraprocess is small for temperatures well below the Curie temperature of the grains. However, it may become noticeable if major contaminations of non-magnetic ions as Mg and Al are incorporated in the spinel lattice of titanomagnetites. In this case a certain percentage of magnetic ions may be surrounded predominantly by Mg and Al ions and, thus, only a weak or negligible interaction to the magnetic sublattices may occur. For superparamagnetic particles, the Langevin curve, describing σ as a function of H may have a very small curvature within the range of H in question and, hence, the field dependence of σ may hardly be distinguished from a straight line. Commonly, a significant portion of the slope originates from the paramagnetism of pyroxene, olivine, iron-bearing glass etc., being the constituents of the basalt. A determination of σ at -196 °C from Fig. 2b is possible with a reduced accuracy only, on account of the high fields required to saturate the specimen. Assuming that saturation is accomplished at 8–10 kOe, the order of magnitude of χ_{as} at ambient temperature in relation to that at -196 °C is in rough accordance with an assumed Curie law $\chi = C/T$ (C = constant, T = temperature in °K). Therefore the main contribution may arise

from rock paramagnetism. For a more detailed investigation into this problem the maximum magnetic field used in this study may not be sufficient and the temperature range has to be extended down to liquid helium temperature.

From Fig. 2b one infers that σ_0 is lower at -196 °C than at room temperature. Thus, there might be a *P*-type of thermomagnetic curve according to Néels notation. A measurement down to 4.2 °K could decide this problem.

Basalt no. 2 with slightly oxidized titanomagnetite grains, as mentioned, reveals at -196 °C a significantly higher H_c that that discussed above. This finding can be a result of submicroscopic alterations of the ore particles bringing possibly a small-particle effect into play. The other quantities measured do not show salient features. As the composition of the ore grains is unknown, contamination of Al, Mg, Cr etc. may have an influence, too.

Basalts Containing Ilmenite Lamellae in Titanomagnetite Grains

The $\sigma-T$ curve of basalt no. 3 shows a sharp Curie point at 525 °C. The shape in the temperature interval studied is largely what one would expect from a spinel phase rich in Fe with a composition close to magnetite ($T_c=575$ °C). The steady rise at low temperatures may be brought about by rock paramagnetism. For this reason, the contribution of ilmenite can be supposed to be small. This fact implies that ilmenite must be rather pure and cannot contain a significant amount of hematite. Because members of the hematite (Fe_2O_3)–ilmenite ($FeTiO_3$) solid solution series are ferrimagnetic already at low hematite content, ilmenite with $\geqq 5\%$ Fe_2O_3 should give a measurable σ at -196 °C in our case whereas pure ilmenite is antiferromagnetic with a Neel point of ~ 60 °K. Of course, ilmenite contributes also to σ by means of its paramagnetism above the Neel point at -196 °C. Though, the magnitude of σ is distinctly reduced in this case.

As H_c and σ_r/σ_0 are not appreciably variable with temperature, the magnetic anisotropy at low temperatures may be relatively small. On account of the subdivision of titanomagnetite grains by ilmenite lamellae one would derive the existence of single domain particles whence characteristic features of the hysteresis loop may emerge. Such an effect is not obviously recognizable from Fig. 5b. The somewhat increased H_c might be interpreted in terms of some kind of small particle effect, however not being typical for single domain grains. The origin of this discrepancy may lie in a cluster effect of the magnetization of single domain particles. Due to the close neighborhood of titanomagnetite single domain grains in basalt ore particles, subdivided by ilmenite lamellae, they can interact by virtue of their magnetic fields with each other, a phenomenon that must be taken into account in this case. A satisfying theoretical treatment of this problem is still missing. The situation is problematic as well if a mixture of single-domain and multi-domain particle is involved.

The magnitude of χ_{as} deduced from the loops above technical saturation at ambient temperature differs only slightly from that of basalt no. 1 within the accuracy of measurements. The value at -196 °C may be compatible with a Curie law (see Table 2).

The $\sigma-T$ curve of basalt no. 4 (Fig. 6a) is similar to that of basalt no. 3

notwithstanding the complex mineralogical composition of the ore grains. Only in the low temperature range might there be an indication of a second magnetic phase. Thus, the characteristics of the hysteresis loops may originate from quite the same phase as in basalt no. 3.

The relatively low absolute value of σ, inspite of the fact that the ore content in the basalt cannot be considered as low, is due to the high percentage of ilmenite lamellae or their decomposition products in the ore grains. H_c and the shape of the loops are comparable with those of basalt no. 3. The ambiguities inherent in the explanation of the loop behaviour of the latter apply also for basalt no. 4.

Basalt no. 5 gives a $\sigma - T$ curve that shows undoubtedly two magnetic phases (Fig. 7a). Primary hemo-ilmenite grains visible under the microscope may contain so much Fe_2O_3 that a contribution to σ of the correct order of magnitude is possible. A separation of σ at low temperatures into contributions of the various phases is difficult as the magnetization of the hemo-ilmenite compositions in question does not exhibit salient features (Ishikawa and Akimoto, 1957).

As in basalt no. 6 only two ore phases can be detected, σ must be due to these plus paramagnetism at low temperatures. The unusual large linear portion of σ at high fields might in part be associated with primary hemoilmenite particles. This may be possible as hemoilmenites close to ilmenite in composition exhibit $\sigma - T$ curves with tails smeared out towards higher temperatures. Thus, an exact definition of T_c is difficult and, in this temperature region, a linear increase in σ with H might take place in high fields (Ishikawa and Akimoto, 1957).

The magnetic properties of the basalts, presented in the foregoing sections show that the connection between magnetization and the mineralogy is fairly complex, even for basalt no. 1 (RK) the ore grains of which are optically homogeneous. In principle, a more detailed knowledge of this relationship appears to be possible. One of the presuppositions is a careful analysis of the natural specimens with the microprobe and also a chemical analysis in particular of the Fe content would be very useful. On the other hand, a serious barrier that is hindering the aim is a certain lack of data concerning the magnetization of the minerals. A thorough investigation on synthetic single crystal and polycrystalline specimens including the influence of grain dimensions would provide us with data which would assist the study of natural rock samples.

Acknowledgements. The author is grateful to Prof. G. Angenheister, Head of the Inst. f. Allgem. und Angew. Geophysik d. Univ. München, for his support and advice. Thanks are also due to the members of the rock and mineral magnetism group Drs. Petersen, Pohl, Schult, Schweitzer and Prof. Soffel for valuable discussions and supplying samples. It is a pleasure to thank Mr. Lehner and the workshop for the construction of the vibrating sample magnetometer. This work was carried out with financial assistance from the Deutsche Forschungsgemeinschaft.

References

Ade-Hall, J.M., Khan, M.A., Dagley, P., Wilson, R.L.: A detailed opaque petrological and magnetic investigation of a single tertiary lava flow from Sky, Scotland-I Iron-titanium oxide petrology. Geophys. J.R. astr. Soc. **16**, 375–388, 1968

Angenheister, G., Petersen, N., Schweitzer, Chr.: Bestimmung der Intensität des erdmagnetischen Feldes aus Messungen der thermoremanenten Magnetisierung von rezenten Laven des Aetna (Sizilien). Sitzungsber. d. Bayer. Akad. d. Wiss. 51–76, 1971

Banerjee, S.K., O'Reilly, W.: Coercivity of Fe^{2+} in octahedral sites of Fe-Ti spinels. IEEE Trans. Magnetics, Vor. Mag. **2**, 463–467, 1966

Creer, K.M., Ibbetson, J.D.: Electron microprobe analysis and magnetic properties of non-stoichiometric titanomagnetite in basaltic rocks. Geophys. J. R. astr. Soc. **21**, 485–511, 1970

Creer, K.M., Petersen, N.: Thermochemical magnetization in basalts. Z. Geophys. **36**, 501–516, 1969

Creer, K.M., Valencio, D.A.: Palaeomagnetic and rock magnetic studies on Cenozoic basalts from Western Argentina. Geophys. J. R. astr. Soc. **19**, 113–146, 1969

Creer, K.M., Petersen, N., Petherbridge, J.: Partial self-reversal of remanent magnetization and anisotropy of viscous magnetization in basalts. Geophys. J.R. astr. Soc. **21**, 471–483, 1970

Ishikawa, Y., Akimoto, S.: Magnetic properties of the $FeTiO_3-Fe_2O_3$ solid solution series. J. Phys. Soc. Japan **12**, 1083–1098, 1957

Larson, E., Ozima, M., Ozima, M., Nagata, T., Strangway, D.: Stability of remanent magnetization of igneous rocks. Geophys. J.R. astr. Soc. **17**, 263–292, 1969

Markert, H., Steigenberger, N.: On the size distribution of submicroscopic magnetite and titanomagnetite fine particles in basalt. Z. Geophys. **37**, 499–518, 1971

Nagata, T.: Rockmagnetism. Tokyo: Maruzen Company Ltd. 1961

Néel, L.: Interprétation des cycles d'hystérésis « étranglés » de certaine basalts. C.R. Acad. Sc. Paris **270** B, 1125–1130, 1970

O'Reilly, W.: A low temperature study of synthetic titanomagnetites and controlled oxidation products. Thesis, University of Newcastle upon Tyne, 1965

Petersen, N.: Untersuchungen magnetischer Eigenschaften von Titanomagnetiten im Basalt des Rauhen Kulm (Oberpfalz) in Verbindung mit elektronenmikroskopischer Beobachtung. Z. Geophys. **28**, 79–84, 1962

Petersen, N.: Beobachtung einiger mineralogischer und magnetischer Eigenschaften dreier Basaltproben nach unterschiedlicher thermischer Behandlung. J. Geomagn. Geoelectr. **18**, 463–479, 1966

Radhakrishnamurty, C., Likhite, S.D.: Relation between thermal variation of low field susceptibility and magnetic hysteresis of basalts. Earth Planet. Sci. Lett. **9**, 294–298, 1970

Radhakrishnamurty, C., Likhite, S.D., Sahasrabudhe, P.W.: Some curious magnetic properties of rocks. In: Palaeogeophysics (Ed. S.K. Runcorn), pp. 223–234. London: Academic Press 1970

Radhakrishnamurty, C., Raja, P.K.S., Likhite, S.D., Sahasrabudhe, P.W.: Problems concerning the magnetic behavior and determination of Curie points of certain basalts. Pure Appl. Geophys. **93**, 129–140, 1972

Radhakrishnamurty, C., Sahasrabudhe, P.W.: On the magnetic and mineralogical properties of basalts. Pure Appl. Geophys. **66**, 69–76, 1967

Radhakrishnamurty, C., Sastry, N.P.: Low temperature magnetic hysteresis of fine particle aggregates occuring in some natural samples. Phil. Mag. **23**, 503–507, 1971

Readman, P.W., O'Reilly, W.: Magnetic properties of oxidized (cation-deficient) titanomagnetites $(Fe, Ti, \square)_3O_4$. J. Geomagn. Geoelectr. **24**, 69–90, 1972

Refai, E.: Magnetfeld und Magnetisierung der Basaltvorkommen im Raum von Kemnath. Diss. Univ. München, 1960

Schult, A.: Natural magnetization of deep core samples of basaltic rocks from Brazil. Z. Geophys. **36**, 267–286, 1970

Schult, A., Soffel, H.: Palaeomagnetism of tertiary basalts from Libya. Geophys. J.R. astr. Soc. **32**, 373–380, 1973

Soffel, H.: Die Bereichsstrukturen der Titanomagnetite in zwei tertiären Basalten und die Beziehung zu makroskopisch gemessenen magnetischen Eigenschaften dieser Gesteine. Habilitationsschrift, Naturwiss. Fak. Univ. München, 1968a

Soffel, H.: Die Beobachtung von Weiss'schen Bezirken auf einem Titanomagnetitkorn mit einem Durchmesser von 10 Mikron in einem Basalt. Z. Geophys. **34**, 175–181, 1968b

Soffel, H.: The influence of the dislocation density and inclusions on the coercive force of multidomain titanomagnetites of the composition $0.65\ Fe_2TiO_4\ 0.35\ Fe_3O_4$ in basalts as deduced from domain structure observations. Z. Geophys. **36**, 113–124, 1970

Soffel, H.: The single domain-multidomain transition in natural intermediate titanomagnetite. Z. Geophys. **37**, 451–470, 1971

Syono, Y.: Magnetocrystalline anisotropy and magnetostriction of $Fe_3O_4-Fe_2TiO_4$ series with special application to rock magnetism. Jap. J. Geophys. **IV**, 72–143, 1965

Wasilewski, P.J.: Magnetic hysteresis in natural materials. Earth Planet. Sci. Lett. **20**, 67–72, 1973

Wilson, R.L., Watkins, N.D.: Correlation of petrology and natural magnetic polarity in Columbia Plateau basalts. Geophys. J.R. astr. Soc. **12**, 405–424, 1967

Received February 4, 1975; Revised Version July 18, 1975

J. Geophys. 41, 633–639, 1975

The Change of Isothermal Saturation Remanent Magnetization of Basalts as a Result of Cyclic Elastic Deformation

A. Kapička

Geophysical Institute, Czechoslovak Academy of Science,
Boční II, 14131 Praha 4, Czechoslovakia

Abstract. The effect of uni-axial cyclic elastic compression with a constant stress amplitude on the isothermal saturation remanent magnetization of basalts, containing generalized titano-magnetites, was studied. The largest irreversible changes are generated during the first elastic deformations, however, also the subsequent deformation cycles result in a decrease of the remanent magnetization. For the higher values of the cycles ($n > 3$) the linear dependence of the irreversible changes of the remanent magnetization on $\sqrt{\log n}$ is well satisfied. The experimental results are analogous to the results of the cyclic asymmetric overmagnetizing of ferromagnetic substances which are explained by Néel's theory of the reptation effect.

Key words: Rock magnetism – Stress demagnetization – Cyclic elastic deformation.

1. Introduction

As a result of external mechanical stresses the magnetic properties of magnetic minerals and rocks change considerably (*e.g.* Nagata, 1970; Nagata and Carleton, 1968; Ohnaka and Kinoshita, 1968). In a previous paper (Kapička, 1975a) the irreversible changes of the remanent magnetization of some basalts as a result of increasing uni-axial elastic compression were studied, and it was shown that the remanent magnetization varies in a characteristic manner. Fig. 1 shows this dependence for the saturation remanent magnetization as the initial state, measured after unloading. If the initial state is different, the dependence of the irreversible changes of the remanent magnetization on mechanical stress changes qualitatively and quantitatively.

The results of some experiments (Carmichael, 1968; Kapička, 1975b) indicate that if the elastic deformation is repeated under the same stress, a further irreversible change of the remanent magnetization occurs. However, no system-

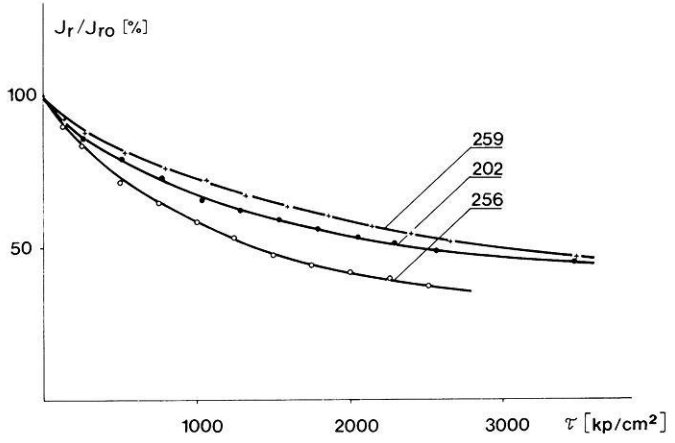

Fig. 1. The normalized remanent magnetization measured after unloading (J_r/J_{ro}) as a function of stress (τ) for the basalts (with sample numbers indicated) under investigation. The initial state of the samples is saturation remanent magnetization

atic observations of this kind with a larger number of deformation cycles have been made nor discussed so far. However, the results of studying the effect of short-term periodic shocks on the remanent magnetization of basalts and magnetite (Shapiro and Ivanov, 1967; Nagata, 1971; Pohl *et al.*, 1975) imply that the overall irreversible change of the remanent magnetization depends on the number and strengh of the mechanical shocks.

The purpose of the present paper is to study the effect of the cyclic uni-axial elastic compression with constant stress amplitude on the remanent magnetization of basalts. The experimental results obtained are compared with some dynamic experiments.

2. Samples and Experimental Procedure

The measurements were taken on basalt samples from the Bohemian Massif, which contain as the magnetic fraction generalized titano-magnetites of different chemical composition (Kropáček and Pokorná, 1974). The volume concentration of the titano-magnetites in the samples was as follows: 13.5% (sample no. 202), 7.8% (256) and 9.1% (259). The granularity of the magnetic fraction: 0.003–0.04 mm (202), 0.01–0.1 mm (256), 0.015–0.05 mm (259). The specific saturation remanent magnetization amounted to 180×10^{-3} Gcm^3/g (202), 197×10^{-3} Gcm^3/g (256) and 99×10^{-3} Gcm^3/g (259). For the purpose of measurement the samples were worked into the shape of a cube with 2 cm sides and their surfaces were ground plane parallel.

The interval of elastic stress deformations of the individual samples was read off the stress-strain curves, obtained with the aid of an electronic deformation machine. The elastic deformation by uni-axial stress was effected in a hydraulic press, between the clams of which and the surface of the samples ground plates of titanium were inserted. The stress direction was parallel to the direction of the remanent magnetization. The rate-of-stress increase in all experiments was approximately constant at 80 kpcm$^{-2}s^{-1}$. The remanent magnetization was measured by an astatic magnetometer. The samples were magneti-

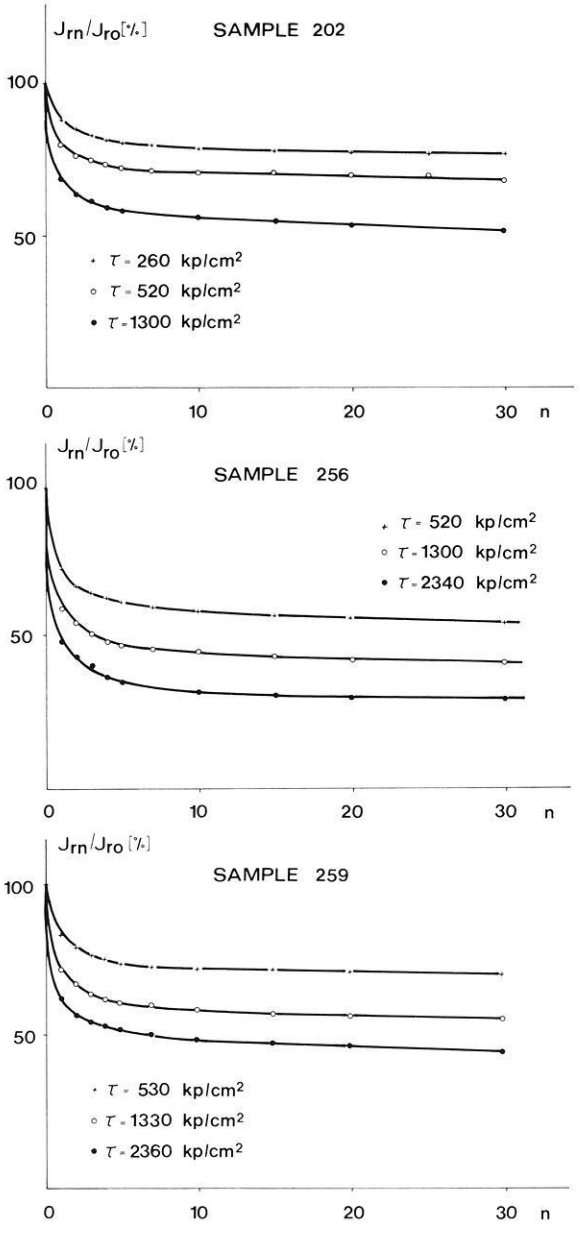

Fig. 2. The normalized saturation remanent magnetization (J_{rn}/J_{ro}) as a function of the number of deformation cycles (n) for various values of the stress

cally saturated with the aid of an electromagnet and their remanent magnetization (J_{ro}) measured. They were then cyclically deformed ($n_{max}=30$) by the chosen stress and, after the individual deformation cycles (n), the remanent magnetization (J_{rn}) was measured in unloaded state. All these measured values were normalized relative to the initial state of the sample. The values of the deformation stress were chosen uniformly within the elastic regions of deformation of the individual samples and ranged from 260 to 2360 kp/cm^2.

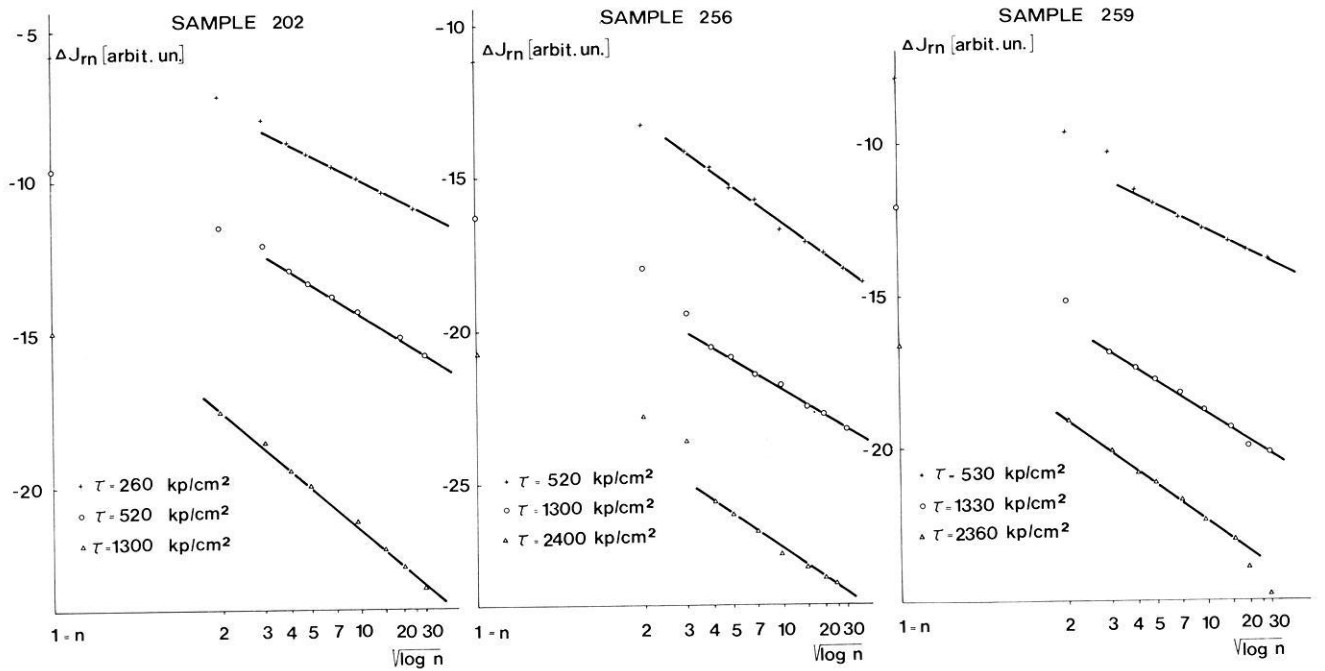

Fig. 3. The changes of the saturation remanent magnetization ΔJ_{rn} as a function of $\sqrt{\log n}$ for various deformation stresses

The observed patterns indicate that the process of cyclic elastic loading of the samples with constant stress results in a gradual irreversible decrease of the saturation remanent magnetization, the pattern of these changes being the same qualitatively for all the basalt samples investigated, as well as for all the values of the stress. The largest decrease of the remanent magnetization occured during the first elastic deformation. Larger changes were also observed in a few subsequent cycles, which agrees well with the dynamic experiments (*e.g.*, Pohl *et al.*, 1975). With increasing n the magnitude of the changes decreases. However, even at the maximum number of deformation cycles ($n=30$) the remanent magnetization displayed a measurable change. The magnitude of the overall decrease is proportional to the magnitude of the applied stress, and the quantitative differences between the individual types of basalts correspond to the observed dependences of the irreversible changes of the remanent magnetization on stress (Fig. 1).

The dependence of the decrease of the remanent magnetization ΔJ_{rn} on $\sqrt{\log n}$, where n is the number of cycles, is plotted in Fig. 3. The change of the remanent magnetization is given as $\Delta J_{rn}=J_{rn}-J_{ro}$, where J_{rn} is the magnitude of the remanent magnetization after the n-th deformation cycle, and J_{ro} is the initial remanent magnetization of the sample. These dependences indicate that a linear relation of ΔJ_{rn} on $\sqrt{\log n}$ is satisfied for higher values of n (in general for $n>3$) for all basalt samples investigated as well as for all applied stresses. The systematic deviation for sample 259 at a stress of $\tau=2{,}360$ kp/cm^2, which is at the limit of elastic deformations, is probably caused for a large number of cycles by the fact that the deformation was no longer purely elastic and that the sample was subject to a slight permanent deformation. The linear dependence of the irreversible changes of the remanent magnetization on $\sqrt{\log n}$ observed for higher values of n, agrees with the paper of Daniel-Szabó and Potocký (1969), in which the effect of the cyclic tensile elastic deformation on the remanent magnetization of metal ferromagnetic samples was studied.

4. Discussion

The experimental results indicate that gradual irreversible changes of the saturation remanent magnetization of basalts occur under cyclic elastic deformation (Fig. 2). The largest decrease is associated with the first elastic deformations. However, also the subsequent deformation cycles result in a slight irreversible decrease of the remanent magnetization. The differences between the individual types of basalts are only in the magnitude of the overall changes of the remanent magnetization. In analysing the dependence of the changes of the remanent magnetization (ΔJ_{rn}) on the number of deformation cycles (n) it comes out that for a higher number of cycles ($n>3$) the linear relation

$$\Delta J_{rn}=K_1-K_2\sqrt{\log n},$$

where K_1 and K_2 are constants, dependent on the magnitude of the stress applied and on the properties of the samples investigated, is satisfied. It can also be seen that this dependence is relatively complicated for small values of n.

The experimental results obtained are analogous to the results of cyclic asymmetric overmagnetizing of ferromagnetic samples between two constant values of the magnetic field H_a and H_b, $H_b \neq -H_a$ (*e.g.*, Dang, 1964; Hajko *et al.*, 1962). According to Néel's phenomenological theory the so-called reptation and bascule-negative effects are responsible for the irreversible changes which occur under cyclic overmagnetizing (Néel, 1957, 1958). The former results in the same $\sqrt{\log n}$ proportional changes of the remanent magnetization at both ends of the overmagnetizing curve, the latter takes effect only in several initial cycles and results in the rotation of the overmagnetization curve. Since our measurements of the changes of the remanent magnetization due to cyclic deformation were only carried out in an unloaded state, which analogously only corresponds to one value of the magnetic field (one usually adopts $H_b=0$), one cannot analyse the pattern of the changes of the remanent magnetization for small values of n according to the analogy mentioned above. However, the dependence found for the higher values of n (Fig. 3) is analogous to the reptation effect.

The direct observations of the domain structure of metal ferromagnetic materials indicate that irreversible motions of the domain walls occur under cyclic asymmetric overmagnetizing (Gengnagel *et al.*, 1962), the magnitude of these changes being proportional to the concentration of the structural defects in the samples. Irreversible changes of the domain structure also occur during cyclic elastic deformations of ferromagnetic samples (Trenkler *et al.*, 1972). These changes are analogous in both cases, because the repeated cycles cause the motion of at least part of the various domain walls, some of which have a tendency to stabilize their position.

The irreversible changes of the domain structure of magnetic minerals, contained in rocks, under elastic deformations can be explained by the change of the internal mechanical microstructure of these minerals (Carmichael, 1968). This change, caused by the external mechanical stress, is mostly associated with the motion of existing structural dislocations. Since the magnitude of the remanent magnetization is a function of n under cyclic elastic deformation, as implied by our experiments, the configuration of the domain walls must differ after the repeated application of the same external stress from that one following the previous deformation cycle. It is probable due to the reversible motion os some structural dislocations (Kapička, 1975b).

The qualitative pattern of the changes of the remanent magnetization under cyclic elastic deformation (Fig. 2) is similar to the results of the demagnetization of basalts due to repeated mechanical chocks (*e.g.*, Pohl *et al.*, 1975). It seems, therefore, that the effect of the cyclic uni-axial elastic compression and the effect of repeated short-term shocks on the remanent magnetization of rocks are closely associated.

References

Carmichael, R.S.: Remanent and transitory effects of elastic deformation of magnetite crystals. Phil. Mag. **17**, 911–927, 1968

Dang van, N.: Reptation des cycles d'hystérésis dissymétriques dont un des champs limites est négatif. Phys. Stat. Sol. **7**, 293–298, 1964

Daniel-Szabó, J., Potocký, L.: Einfluß der zyklischen Belastung auf den remanenten magnetischen Zustand eiserner Drähte. Fyz. čas. SAV **19**, 154–162, 1969

Gengnagel, H., Hajko, V., Daniel-Szabó, J.: Zur Sichtbarmachung von Reptation-Erscheinungen an Rahmeneinkristallen. Czech. J. Phys. B **12**, 714–718, 1962

Hajko, V., Daniel-Szabó, J., Kavečanský, V.: Studium der Reptation- und Bascule-Erscheinungen an polykristallinen Fe-Si-Blechen. Czech. J. Phys. B **12**, 867–869, 1962

Kapička, A.: The effect of uniaxial elastic deformation on the remanent magnetization of basalts. Studia geophys. geodaet. **19**, 1975a (in press)

Kapička, A.: A note on the effect of the elastic pre-deformation on the pressure changes of the remanent magnetization of basalts. Studia geophys. geodaet. **19**, 1975b (in press)

Kropáček, V., Pokorná, Z.: Magnetische Eigenschaften basischer neovulkanischen Gesteine der Böhmischen Masse und ihre Zusammenhänge mit petrologischen Charakteristiken. Travaux Inst. Géophys. Tchécosl. Acad. Sci. Geofyzikální sborník 1973. Praha: Academia 1975 (in press)

Nagata, T.: Basis magnetic properties of rocks under the effects of mechanical stresses. Tectonophysics **9**, 167–195, 1970

Nagata, T.: Introductory notes on shock remanent magnetization and shock demagnetization of igneous rocks. Pageoph **89**, 159–177, 1971

Nagata, T., Carleton, B.J.: Notes on Piezo-remanent magnetization of igneous rocks. J. Geomagn. Geoelectr. **20**, 115–127, 1968

Néel, L.: Essai d'interprétation de la reptation des cycles d'hystérésis. C.R. Acad. Sci. (France) **244**, 2668–2674, 1957

Néel, L.: Sur les effets d'un couplage entre grains ferromagnétiques doués d'hystérésis. C.R. Acad. Sci. (France) **246**, 2313–2319, 1958

Ohnaka, M., Kinoshita, H.: Effect of axial stress upon initial susceptibility of an assemblage of fine grains of $Fe_2TiO_4-Fe_3O_4$ solid solution series. J. Geomagn. Geoelectr. **20**, 107–110, 1968

Pohl, J., Bleil, U., Hornemann, U.: Shock magnetization and demagnetization of basalt by transient stress up to 10 kbar. J. Geophys. **41**, 23–41, 1975

Shapiro, V.A., Ivanov, N.A.: Dynamic remanence and the effect of shocks on the remanence of strongly magnetic rock. Dokl. Akad. Nauk. USSR **173**, 1065–1067, 1967

Trenkler, P., Daniel-Szabó, J., Potocký, L.: Einfluß der zyklischen Belastung auf die Bereichstruktur von Fe-Si Proben im remanenten Zustand. Fyz. čas. SAV **22**, 155–162, 1972

Received April 7, 1975; Revised Version July 25, 1975

J. Geophys. 41, 641–650, 1975

K-Ar-Altersbestimmungen an Vulkaniten bekannter paläomagnetischer Feldrichtung

II. Sachsen

W. Todt und H.J. Lippolt

Laboratorium für Geochronologie der Universität
D-6900 Heidelberg, Berliner Str. 17, Bundesrepublik Deutschland

K-Ar Age Determinations on Volcanics with Known Paleomagnetic Field Parameters

II. Sachsen

Abstract. K-Ar age determinations on whole rock samples of ten volcanic rocks from Saxony have been made. The results are in agreement with the view that the Lausitz volcanism occured during the Upper Oligocene to Lower Miocene. A basalt from the western Erzgebirge yielded also an Upper Oligocene age, whereas another basalt from the Elb-valley eruptive zone showed a considerably younger age (Upper Miocene).

By these age determinations and by paleomagnetic data taken from Nairn and Vollstädt (1967) reversals of the terrestrial magnetic field from reverse to normal at about 27 Ma and at 19 Ma can be inferred.

Key words: Potassium-argon-dating – Upper tertiary volcanics – Paleomagnetism – Saxony.

1. Einführung

Die vorliegende Arbeit schließt an eine frühere Veröffentlichung über die K-Ar-Alter der Vulkanite der Oberpfalz und von Oberfranken an (Todt und Lippolt, 1975). Ziel der vorliegenden Untersuchung war zunächst, einige der von Nairn und Vollstädt (1967) bzw. Vollstädt (1966, 1967, 1972) paläomagnetisch untersuchten vulkanischen Gesteine der Lausitz zu datieren. Zusätzlich sollte durch die vorliegende Datierungsarbeit die Einordnung des Lausitzer Vulkanismus in die Tertiärstratigraphie dieses Gebietes isotopen-geochronologisch gesichert werden. Die über diesen Aspekt hinausgehende Absicht war dabei die zeitliche Festlegung von Umkehrungen des magnetischen Erdfeldes im mittleren Tertiär.

Ein vorläufiges Ergebnis dieser Arbeit wurde bereits früher besprochen (Todt und Lippolt, 1972).

Als weitere Proben wurden zwei Olivin-Nephelinite datiert, von denen der eine aus dem westlichen Erzgebirge (Hirtstein), der andere aus der Elbtalzone (Ascherhübel) stammt. Die Datierung des Olivin-Nephelinits vom Ascherhübel verdient besonderes Interesse (Illies, 1974, persönliche Mitteilung), weil dieses

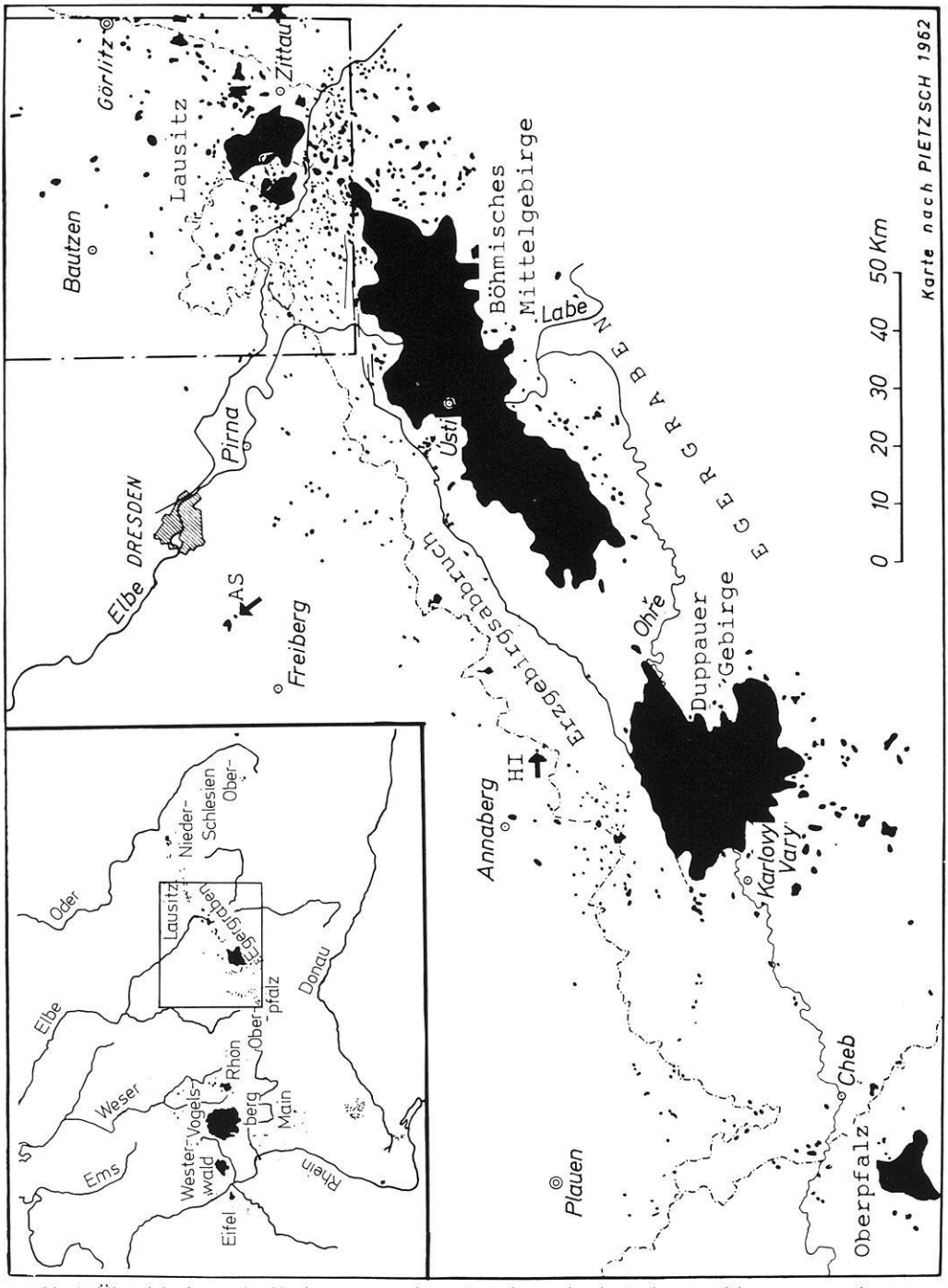

Abb. 1. Übersichtskarte der Vorkommen tertiärer Eruptivgesteine in Sachsen und im angrenzenden Teil von Nordböhmen. Der umrandete Teil im rechten oberen Bildabschnitt ist in Abb. 2 zusammen mit den Lokalitätsangaben vergrößert wiedergegeben. In der linken oberen Bildecke ist eine Übersichtskarte dargestellt, aus der die geographische Lage des Hauptbildes ersichtlich wird. HI und AS (im Hauptbild) bezeichnen die Probenpunkte Hirtstein bzw. Ascherhübel

Vorkommen einer Störung parallel zum Elbtalgraben aufsitzt. Da dieser Graben noch heute aktiv ist, bestand für diese Probe die Aussicht, ein wesentlich jüngeres Alter als das der anderen Proben zu erhalten.

Die Gesteinsproben (jeweils Handstücke) wurden uns von H. Vollstädt/Potsdam bzw. von H. Illies/Karlsruhe überlassen.

2. Geologische Grundlagen

Der tertiäre Vulkanismus Sachsens wurde von Pietzsch (1962, S. 486–512) ausführlich dargestellt. Pietzsch unterteilt ihn regional in die Gebiete Vogtland, Höheres Erzgebirge, Ostererzgebirge und Elbtalzone, Lausitz. Die von uns untersuchten Gesteine stammen aus den letzten drei dieser Gebiete; die Mehrzahl bilden Lausitzer Vorkommen.

Die sächsischen jungvulkanischen Bildungen werden als randliche Eruptionen der südlich des Erzgebirgsabbruchs gelegenen großen Eruptionszentren des Duppauer Gebirges und des Böhmischen Mittelgebirges angesehen. Der Vulkanismus dieser Eruptionszone wird zeitlich an die Grenze Oligozän/Miozän gestellt und ebenso wie der an der Wende Miozän/Pliozän erfogte Erzgebirgsabbruch als Fernwirkung der alpidischen Tektonogenese angesehen (Pietzsch, 1962; S. 501).

Für rein geologische Altersbestimmungen der tertiären Vulkanite Sachsens gibt es nur wenige Beobachtungen (Möbus, 1956). In der Lausitz sind bei Seifhennersdorf basaltische Tuffe in oberoligozäne Polier-Schiefer eingelagert. Diese Schichten werden von basaltischen Decken überlagert, die ihrerseits von phonolithischen Gängen durchbrochen sind, bzw. von phonolithischen Decken überlagert sind. Aus diesem Befund nimmt man für die Haupteruptionszeit Oberoligozän und Untermiozän an. Andererseits wurden auch basaltische Gänge in Phonolithen beobachtet, was eine längere Dauer der vulkanischen Förderung nahelegt.

Im westlichen Erzgebirge wurden basaltische Decken über fluviatilen Sedimenten gefunden. Da diese jedoch fossilleer waren, konnten sie nicht als Altersgrenze für die Basalte verwendet werden. In Analogie zum Böhmischen Mittelgebirge hat man umgekehrt diese Sedimente wegen der Überlagerung durch Basalte als oberoligozän eingestuft.

Auch die anderen vulkanischen Bildungen Sachsens werden als etwa an der Wende Oligozän/Miozän entstanden angesehen. Die von uns in einer früheren Arbeit datierten Basalte der Oberpfalz und Oberfrankens hatten K-Ar-Alter gezeigt, die Unter- bis Mittelmiozän entsprachen (Todt und Lippolt, 1975). Aufgrund der geologischen Einstufung der sächsischen Basalte und Phonolith waren für die vorliegenden Proben Alterswerte zwischen 30 und 20 Ma zu erwarten.

3. Die untersuchten Gesteine

Von den untersuchten Gesteinen der Lausitz gehören vier zu den Olivin-Nepheliniten (i.w.s.), drei zu den Phonolithen und eines zu den Alkali-Olivin-Basalten. Die Elbtalzonen-Probe und die des westlichen Erzgebirges sind jeweils Olivin-Nephelinite.

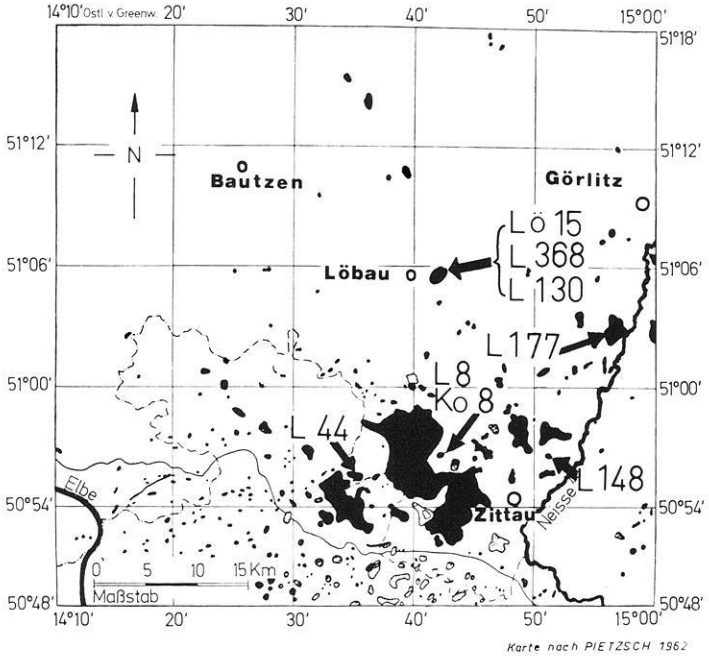

Abb. 2. Übersichtskarte und Probenentnahme in der Lausitz. Probenbezeichnungen nach Nairn und Vollstädt (1967)

Im folgenden sind die datierten Gesteine zusammengestellt. Angegeben sind jeweils Probenbezeichnung (nach Vollstädt, Dissertation 1965), Aufschluß-Nummer nach Nairn und Vollstädt (1967), Lokalität, Gesteinsart (in Anlehnung an die Einteilung von Wimmenauer, 1972) sowie der Erhaltungszustand der Proben nach den Unterscheidungskriterien von Horn *et al.* (1972).

Lausitz:			
Lö 15	NV 7	Löbauer Berg/Löbau	Ol. Nephelinit, frisch
L 368		Löbauer Berg/Löbau	Neph.-Dolerit, frisch
L 130		Löbauer Berg/Löbau	Neph.-Dolerit, frisch
L 177	NV 4	Hofeberg bei Leuba	Ol.-Nephelinit, sehr frisch
KO 8, L 8	NV 18	Koitsche/Zittau	Nosean-Phonolithe, frisch
L 44	NV 26	Windmühlenberg/Seifhennersdorf	Phonolith, frisch
L 148	NV 16	Buchberg/Wittgendorf	Al.-Ol.-Basalt, frisch
Elbtalzone:			
AS		Ascherhübel/Tharandt	Ol.-Nephelinit, unfrisch
Westl. Erzgebirge:			
HI		Hirtstein/Satzung	Ol.-Nephelinit, frisch

Nach Pietzsch (1962) soll es sich bei dem Gestein AS um einen Sonnenbrenner handeln; das uns überlassene Gesteinsstück zeigte jedoch keinerlei Sonnenbrenner-Merkmale.

Die Vorkommen Lö 15, L 368 und L 130 finden sich auf Blatt Löbau (Reinisch, 1925), die Vorkommen L 44, L 148 und KO 8 bzw. L 8 auf Blatt Zittau-Nord (Reinisch, 1930), und das Vorkommen L 177 auf Blatt Ostritz (Hazard, 1896) der Geologischen Karte von Sachsen (1:25000). Das Vorkommen Hirtstein liegt auf Blatt Freital (Pietzsch, 1962), das vom Ascherhübel auf Blatt Kühnhaide (Sauer und Beck, 1914) dieses Kartenwerks.

Der Löbauer Berg wird von einem großen, stockförmigen Olivin-Nephelinit gebildet, aus dem Probe Lö 15 entnommen ist. In ihm kommen einzelne größere Partien eines grobkörnig auskristallisierten Nephelin-Dolerits vor, der das Material für die Proben L 368 und L 130 geliefert hat. Dieser Dolorit stellt das Erstarrungsprodukt des gemeinsamen Magmas in der Tiefe oder im Innern des mächtigen Basalt-Ergusses dar.

Die Olivin-Nephelinit-Probe des westlichen Erzgebirges (Hirtstein) entstammt einem kleinen Steinbruch am Hirtstein bei Satzung südlich von Marienberg, der durch die fächerförmige Abkühlungsstruktur des Basaltes („Palmenwedel") weitbekannt geworden ist.

4. Paläomagnetismus der tertiären sächsischen Vulkanite

Paläomagnetische Untersuchungen an vulkanischen Gesteinen Sachsens wurden von Schulze (1930), Vollstädt (1966, 1967, 1972), Nairn und Vollstädt (1967) und von Rother (1971) veröffentlicht. Aus den Arbeiten von Vollstädt ist die paläomagnetische Richtung von sieben der zehn von uns untersuchten Gesteine bekannt. Die Proben Lö 15 (Nephelinit vom Löbauer Berg), L 148 (Alkali-Olivin-Basalt vom Buchberg), L 177 (Nephelinit vom Hofeberg), L 44 (Phonolith vom Windmühlenberg) haben normale Polarität, die Probe KO 8 (Phonolith-Kuppe Koitsche) und der Nephelin-Dolerit vom Löbauer Berg inverse Polarität.

Die Richtungen der remanenten Magnetisierung dieser Proben sind in Abb. 3 in einem Schmidtschen Netz dargestellt.

5. K-Ar-Alter und Folgerungen

Die zur Datierung verwendeten Verfahren entsprechen den bei Todt und Lippolt (1975) angegebenen Techniken. Von jeder Probe wurden mindestens zwei Kalium-Analysen angefertigt; die Zahl der Argon-Messungen lag zwischen 1 und 5 (s. Tabelle 1, Spalte 6).

Als Argon-Standard wurde die Probe LP6-Bio des US Geological Survey verwendet. Der an ihm bestimmte Mittelwert mehrerer Argon-Bestimmungen ist $4{,}335 \cdot 10^{-5}$ cm^3 STP radiogenes ^{40}Ar pro Gramm Biotit.

Die Ergebnisse der Analysen und die aus ihnen errechneten K-Ar-Modell-Alter sind in Tabelle 1 zusammengestellt. Die gefundenen K-Ar-Gesamtgesteinsalter der Lausitzer Proben liegen zwischen 28 Ma und 19 Ma: von den beiden anderen Proben ist die eine (HI) gleichalt wie die ältesten Lausitz-Proben, die anderen (AS) jedoch deutlich jünger. Bis auf zwei Ergebnisse liegen alle Alters-

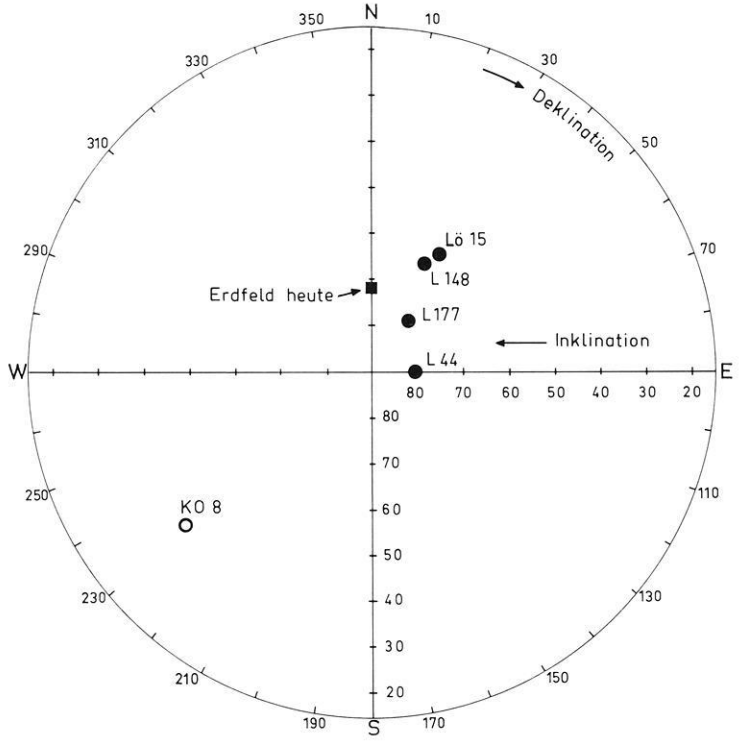

Abb. 3. Richtungen der remanenten Magnetisierung von fünf der datierten Proben nach Messungen von Nairn und Vollstädt (1967). Ausgefüllte Kreise: positive Inklination, offene Kreise: negative Inklination. Flächentreue Projektion in einem Schmidtschen Netz. Die genauen Daten vom Nephelindolerit des Löbauer Berges sind nicht veröffentlicht

werte zwischen 28 und 24 Ma, d.h. die Altersverteilung der sächsischen Vulkanite liegt offensichtlich bei höheren Werten als die der Oberpfälzer und Oberfranken-Vulkanite (Todt und Lippolt, 1975). Daraus kann geschlossen werden, daß der Vulkanismus am Nordostende der Böhmischen Eruptivzone zeitlich vor dem der südwestlichen Ausläufer dieser Zone aktiv war.

Das K-Ar-Modell-Alter des Olivin-Nephelinits vom Löbauer Berg (Lö 15) beträgt $19{,}3 \pm 2{,}0$ Ma. Die beiden Nephelin-Dolerit-Varietäten, die in diesem Olivin-Nephelinit auftreten und entgegengesetzte magnetische Polarität besitzen, weisen übereinstimmende Modell-Alter von $23{,}8 \pm 0{,}7$ Ma (L 368) und $24{,}0 \pm 0{,}6$ Ma (L 130) auf. Dieses Ergebnis ist vereinbar mit der Vorstellung, daß die Dolerite Frühausscheidungen sind, die bei der Eruption des Olivin-Nephelinits mitgerissen worden sind (vgl. Reinisch, 1925, S. 20–26). Der Altersunterschied von 5 Ma könnte in Wirklichkeit noch höher sein, falls die Minerale der Dolerit-Proben bei dem Transport in dem heißen Olivin-Nephelinit radiogenes Argon-40 verloren haben.

Der Alkali-Olivin-Basalt vom Buchberg bei Wittgendorf (L 148) hat ein K-Ar-Alter von $25{,}8 \pm 0{,}8$ Ma, der Olivin-Nephelinit vom Hofeberg bei Leuba ein solches von $26{,}6 \pm 1{,}3$ Ma. Die beiden Phonolith-Proben besitzen die höch-

Tabelle 1. Analysenwerte der datierten Vulkanite. Die einzelnen Argon-Bestimmungen einer Probe wurden innerhalb verschiedener Meß-Serien analysiert. In jeder Serie wurde dabei ein Standard mitgemessen. Die radiogene Argonmenge (Mittelwert) ist in Spalte 4 in cm^3STP/g Material angegeben. Der Anteil des Luftargonbeitrages ist je nach dem Ausheizungsgrad der jeweiligen Aliquote der Probe verschieden; die Extremwerte sind in der Spalte 5 in % angegeben. Die 7. Spalte gibt den quadratisch addierten Fehler der Argon- und Kaliumbestimmungen (1σ-Fehler) an. Die verwendeten Konstanten sind: $\lambda = 0{,}532 \cdot 10^{-9} a^{-1}$; $R = 0{,}123$; $^{40}K = 0{,}0118\%$ des K-gesamt.

Proben-bezeich-nung	Lokalität	Kalium in Gew.-%	^{40}Ar rad in 10^{-6} cm^3 STP/g	Luft-argon-anteil in %	Zahl der Argon-Bestim-mungen	Alter in Ma
1	2	3	4	5	6	7
Lö 15	Löbauer Berg	0,86	0,6587	43–66	3	19,3 ± 2,0
L 368	Löbauer Berg Var. 1	2,11	1,995	11–27	4	23,8 ± 0,7
L 130	Löbauer Berg Var.2	2,42	2,301	19/21	2	24,0 ± 0,6
KO 8	Koitsche bei Zittau	4,72	5,040	8–23	5	26,9 ± 1,0
L 8	gleiche Lokalität wie KO 8	4,68	4,779	14/19	2	25,7 ± 2,0
L 148	Buchberg bei Wittgendorf	0,67	0,6871	30–47	4	25,8 ± 0,8
L 177	Hofeberg bei Leuba	0,77	0,8123	24/27	2	26,6 ± 1,3
L 44	Windmühlenberg bei Seifhennersdorf	4,66	5,187	8–15	3	28,0 ± 0,6
HI	Hirtstein bei Satzung	1,17	1,297	58	1	27,9 ± 1,9
AS	Ascherhübel bei Tharandt	1,39	0,776	61	1	14,1 ± 1,3

sten K-Ar-Alter der untersuchten Gesteine. Zwei verschiedene Proben des Nosean-Phonoliths von Koitsche bei Zittau ergaben Modell-Alter von 25,7 bzw. 26,9 Ma (L 8; KO 8); der Phonolith vom Windmühlenberg bei Seifhennersdorf ergab 28,0 ± 0,6 Ma. Nach diesen K-Ar-Altersbestimmungen zu schließen sollten die Phonolithe die ältesten Vulkanite des Lausitzer Vulkanismus sein. Dem widerspricht jedoch der Geländebefund, nach dem die Eruptionen mit vulkanischen Aschen begannen, sich in basaltischen Ergüssen fortsetzten und mit phonolithischen Gängen und Decken endeten. Es haben jedoch auch Basalte phonolithische Gesteine intrudiert, z.B. hat Siegert (1897) in dem Gebiet des geologischen Blattes Zittau-Süd einen gangförmigen Feldspat-Nephelin-Basalt beschrieben, der einen Phonolithgang durchbricht.

Wir nehmen deshalb an, daß die kleine Zahl von Proben der Lausitz keineswegs repräsentativ für den gesamten Vulkanismus dieses Gebietes ist und daß weitere Messungen an anderen basaltischen Proben Vertreter der älteren Basalte erfassen würden.

Der Olivin-Nephelinit vom Hirtstein (östl. Erzgebirge) ist nach dem K-Ar-Ergebnis ähnlich alt wie die Lausitzer Phonolithe (27,9 ± 1.9 Ma).

Der Olivin-Nephelinit vom Ascherhübel bei Tharandt (Elbtalzone), der zu den nördlichsten Vorkommen jungvulkanischer Gesteine westlich der Elbe gehört, ist mit 14,1 ± 1,3 Ma deutlich jünger als alle anderen datierten Vulkanite. Er besitzt ein obermiozänes K-Ar-Alter. Wir halten diesen Altersunterschied für zuverlässig, da unsere Probe keinerlei Sonnenbrenner-Merkmale zeigte. Auch

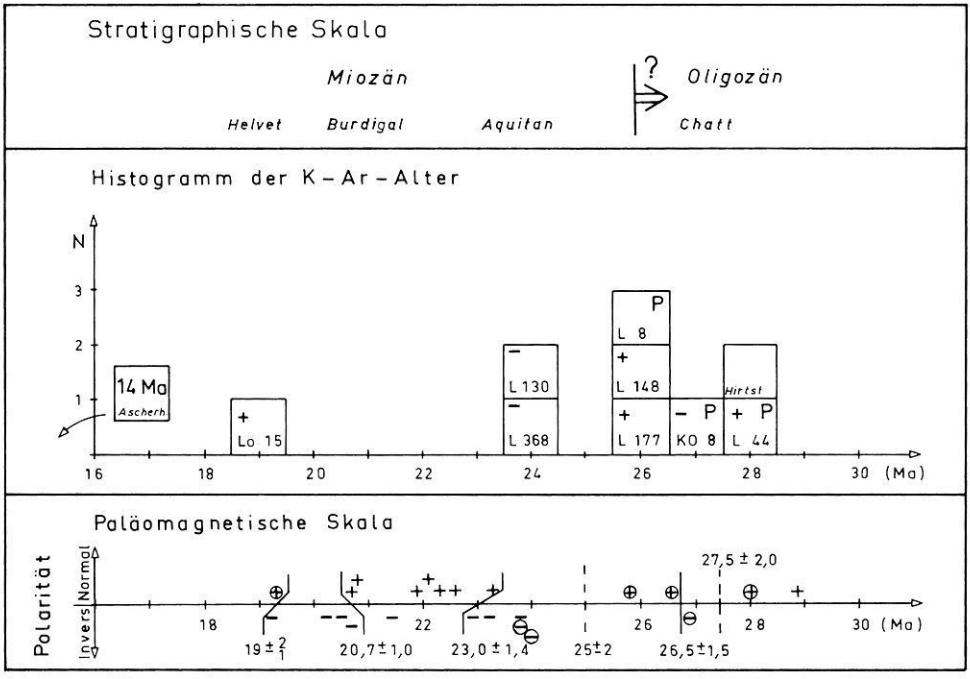

Abb. 4. Zusammenfassung der Ergebnisse: Oben: Stratigraphische Skala nach Funnel 1964. Mitte: Histogramm der K-Ar-Altersergebnisse; − : inverse Polarität, + : normale Polarität. *P*: Phonolithe, alle anderen: Basalte. Unten: Ausschnitt aus der paläomagnetischen Skala nach den Daten dieser Arbeit ⊕, ⊖ und nach Todt und Lippolt (1975) +, −

sind Zusammenhänge zwischen Verwitterung und K-Ar-Modellalter bisher nicht eindeutig nachgewiesen.

In Abb. 4 sind die Ergebnisse dieser Arbeit zusammenfassend dargestellt. Das Histogramm im mittleren Teil der Abbildung zeigt im Vergleich mit der Stratigraphischen Skala (oberer Bildteil, Funnel, 1964), daß der Lausitzer Vulkanismus in Übereinstimmung mit der bisherigen geologischen Einstufung oberoligozänen bis untermiozänen Alters ist. Im Histogramm sind auch die Polaritäten der remanenten Magnetisierung eingetragen. Durch die hier vorgelegten Datierungen kann die von Todt und Lippolt (1975) an den Oberpfälzer Vulkaniten abgeleitete Zeitskala der Polarität des magnetischen Erdfeldes im Oligozän und Miozän erweitert werden: unterer Bildteil. Zu den zwei bereits früher beschriebenen Umkehrungen können zwei weitere in Anlehnung an das Verfahren von Cox und Dalrymple (1967) näher bestimmt und zwei weitere abgeschätzt werden. Es ergeben sich vier Zeitabschnitte mit normaler Polarität zwischen 30 und 20 Ma:

a) ? bis $27{,}5 \pm 2{,}0$
b) $26{,}5 \pm 1{,}5$ bis $25 \pm 2{,}0$
c) $23{,}0 \pm 1{,}4$ bis $20{,}7 \pm 1{,}0$
d) $19\ {}^{+2}_{-1}$ bis ?

Die älteste Feldumkehr (von normal zu invers) wird durch die Alter der Proben L 44 und KO 8 sowie L 8 eingeengt, die nächstjüngere (von invers zu normal) durch die Proben KO 8 sowie L 8 und das Probenpaar L 148 und 177. Aus den Altersunterschieden der Proben L 148 bzw. L 177 einerseits und L 130 sowie L 368 andererseits kann postuliert werden, daß bei 25 ± 2 Ma eine Umkehrung von normaler zu inverser Feldrichtung liegen sollte. Aus der positiven Magnetisierung der Probe Lö 15 und den Oberpfälzer Ergebnissen (Todt und Lippolt, 1975) kann auf eine Feldumkehr von inverser zu normaler Polarität bei 19^{+2}_{-1} Ma geschlossen werden.

Damit sollten in dem genannten Zeitabschnitt wenigstens sechs Umkehrungen der Polarität des Erdmagnetfeldes liegen. Nach der paläomagnetischen Skala von Heirtzler *et al.* (1968) liegen in diesem Zeitraum ca. 30 Feldumkehrungen. Unter der Annahme, daß die Heirtzler-Skala keiner wesentlichen Revision bedarf, sind also zwischen die in den Vulkaniten der Oberpfalz und der Lausitz bezeugten Feldumkehrungen noch weitere einzuordnen.

Literatur

Cox, A., Dalrymple, G.B.: Statistical analysis of geomagnetic reversal data and the precision of potassium-argon dating. J. Geophys. Res. **72**, 2603–2614, 1967

Funnel, B.M.: The tertiary period. The Phanerozoic timescale. A Symposium dedicated to Arthur Holmes. Quart. J. Geol. Soc. (London). **120**, Suppl., 179–191, 1964

Hazard, J.: Erläuterungen zur geologischen Specialkarte des Königreichs Sachsen, Blatt 73 Section Ostritz-Bernstadt, Leipzig 1896

Heirtzler, J.R., Dickson, G.O., Herron, E.M., Pitman III, W.C., Le Pichony, X.: Marine magnetic anomalies, geomagnetic field reversals, and motions of the ocean floor and continents. J. Geophys. Res. **73**, 2119–2136, 1968

Horn, P., Lippolt, H.J., Todt, W.: Kalium-Argon-Altersbestimmungen an tertiären Vulkaniten des Oberrheingrabens. I. Gesamtgesteinsalter. Ecl. Geol. Helv. **65/1**, 131–156, 1972

Möbus, G.: Einführung in die geologische Geschichte der Oberlausitz. Berlin: VEB Deutscher Verlag der Wissenschaften 1956

Nairn, A.E.M., Vollstädt, H.: Paleomagnetic investigations of the tertiary and quarternary igneous rocks: IV. The tertiary volcanics of the Lausitz area, Germany. Geol. Rundschau **57**, 385–402, 1967

Pietzsch, K.: Geologie von Sachsen 486–512. Berlin: VEB Deutscher Verlag der Wissenschaften 1962

Reinisch, R.: Erläuterungen zur geologischen Karte Sachsens, Nr. 72 Blatt Löbau-Hernhut, 2. Aufl. Leipzig 1925

Reinisch, R.: Erläuterungen zur geologischen Karte von Sachsen, Nr. 88 Blatt Zittau-Nord. Leipzig 1930

Rother, K.: Gesteins- und paläomagnetische Untersuchungen an Gesteinsproben vom Territorium der DDR. Veröffentlichung des Zentralinstituts Physik der Erde Nr. 5, Potsdam 1971

Sauer, A., Beck, R.: Erläuterungen zur geologischen Specialkarte des Königreiches Sachsen, Blatt 81 Section Tharandt, S. 107–109, Leipzig 1914

Schulze, E.G.: Magnetische Vermessung einiger tertiärer Eruptivgänge und -Stöcke im sächsischen Elbsandstein-Gebirge. Z. Geophys. **6**, 141–156, 1930

Siegert, Th.: Erläuterungen zur geologischen Specialkarte des Königreichs Sachsen, Section Zittau-Oybin-Lausche (Zittau-Süd) Blatt 107, S. 35, Leipzig 1897

Todt, W., Lippolt, H.J.: Kalium-Argon-Altersbestimmungen an Vulkangesteinen der Lausitz. Fortschr. Mineral. **50**, Beiheft 1, 99, 1972 (Abstrakt)

Todt, W., Lippolt, H.J.: K-Ar-Altersbestimmungen an Vulkaniten bekannter paläomagnetischer Feldrichtung. I. Oberpfalz und Oberfranken. J. Geophys. **41**, 43–61, 1975

Vollstädt, H.: Paläomagnetische Messungen an tertiären Basalten und Phonolithen der DDR. Jb. 1964 Adolf-Schmidt-Observatorium für Erdmagnetismus in Niemegk, S. 145–153. Berlin: Akademie-Verlag 1966

Vollstädt, H.: Gesteinsmagnetische und mineralogische Untersuchungen zur paläomagnetischen Stabilität der natürlich remenanten Magnetisierung von tertiären Basalten und Phonolithen. Freiberger Forschungsh. C 202, 1967

Vollstädt, H.: Über das Inversionsverhalten tertiärer Basalte. Ber. deutsch. Ges. geol. Wiss. B. Miner. Lagerstättenf. 16, 1971, 2, 261–264, Berlin 1972

Wimmenauer, W.: Charakteristische Gesteine des tertiären und quartären Vukanismus in Mitteleuropa. Zitiert von v. Gehlen in: DFG Forschungsbericht: Unternehmen Erdmantel, S. 248, Wiesbaden 1972

Eingegangen am 23. Juni 1975

J. Geophys. 41, 651–658, 1975

An Anomaly of the Upper Mantle below the Rhine Graben, Studied by the Inductive Response of Natural Electromagnetic Fields *

G. Reitmayr **

Institut für Angewandte Geophysik der Universität München

Abstract. The methods of Magnetotellurics (MT) and Geomagnetic Deep Sounding (GDS) have been applied to study the electromagnetic response of the rift structure of the Rhine Graben. The measurements at 17 MT and 7 GDS stations were carried out along a profile running perpendicular across the Graben. Fourier analysis and numerical filters were tried for separation of the frequencies and a least squares technique was applied for data reduction. The thus gained transfer functions can be explained well by two-dimensional models under the following assumption: a well conducting layer at the depth between about 80 and 100 km exists at distances 50 km West and 100 km East of the Rhine Graben. Immediately below the Graben, however, a zone of similar good conductivity lies between about 25 and 45 km depth. The lateral extension of this zone is only some tens of km from the Graben's edges.

Key words: Electromagnetic induction – Magnetotellurics – Geomagnetic deep sounding – Electrical conductivity – Upper mantle – Rift structure – Rhine graben.

Introduction

The aim of geophysical studies of electromagnetic (em) induction is to gain information about the electrical resistivity and its distribution within the earth's interior. Artificial em fields are usually excited in the frequency range of much more than 1 Hz and one gets – because of the skin effect – therefore only insight into the first hundreds of metres of the subsurface. By using slowly, temporally varying natural fields, under favourable circumstances it is possible to extend the estimates down to some hundred kilometres. Not only the physical quantity of the electrical resistivity of the lower crust and the upper mantle itself, however, is of great interest, but of equal importance is its correlation with temperature (an effect of semiconductivity). Further, temperatures within the earth's interior

* This publication is a summary of results of the author's thesis. Details about data analysis and model calculation can be found therein.

** *Address:* Bundesanstalt für Geowissenschaften und Rohstoffe, D-3000 Hannover 23, Postfach 230153, Federal Republic of Germany.

and the associated anomalies connected with tectonically active zones such as faults and rifts are an important aid to understand the origin and development of our earth.

The Scope of Studies

The object of our investigations is the Rhine Graben, the central part of the rifting structure traversing Western Europe in SSW – NNE direction: the Mediterranian – Møsjen Zone. Numerous geophysical and other geoscientific activities in this area have been reported. Among them are the methods of tellurics (Haak *et al.*, 1970), magnetotellurics (Losecke, 1970; Scheelke, 1972) and geomagnetic deep sounding (Winter, 1973), all of which make use of the response of natural em induction. The most complex models applied for interpretation were two-dimensional: a thin sedimentary overburden with a laterally (in one direction) varying resistivity lying over a stratified substratum built up of homogeneous layers, infinite in horizontal directions. The most important finding of the previous investigations was the deduction of a low resistivity layer (resistivity $\varrho \approx 30\ \Omega$m) within the basement ($\varrho \approx 10^3\ \Omega$m) at a relatively shallow depth of 20 or 30 km. The thickness of this layer was found to be 20 to 30 km by Scheelke (1972) and 50 to 90 km by Winter (1973). The extension of it from the Graben's edges could thereby not be determined since those measurements were mainly conducted over the Graben zone itself and in the immediately adjacent areas and, of course, because of the model typ used, which does not admit lateral changes in the deeper structures.

The Measurements and the Applied Interpretation Technique

The locations where we performed our measurements lie on the southern line in Fig. 1, labeled "R II". The time variations of the horizontal components of the electrical field **E** were recorded at 17 stations distributed over a length of approximately 240 km. At two stations the time variations of the horizontal components of the magnetic field **F**, were measured in order to be able to apply the magnetotelluric method (MT). At seven stations of the Eastern part of the profile geomagnetic deep soundings (GDS) were carried out in registering simultaneously the variations of the three components of the magnetic field **F**.

The quantities one usually intends to derive from the recorded time variations in order to compare them with those obtained by model calculations are the so-called transfer functions as a function of period T. In MT they are the apparent resistivity

$$\varrho_a = 2 \cdot T \cdot (E/F)^2$$

(in e.m.u., E and F are horizontal components (orthogonal to each other) of the fields **E** and **F**) and the phase φ. Together they describe the dependence

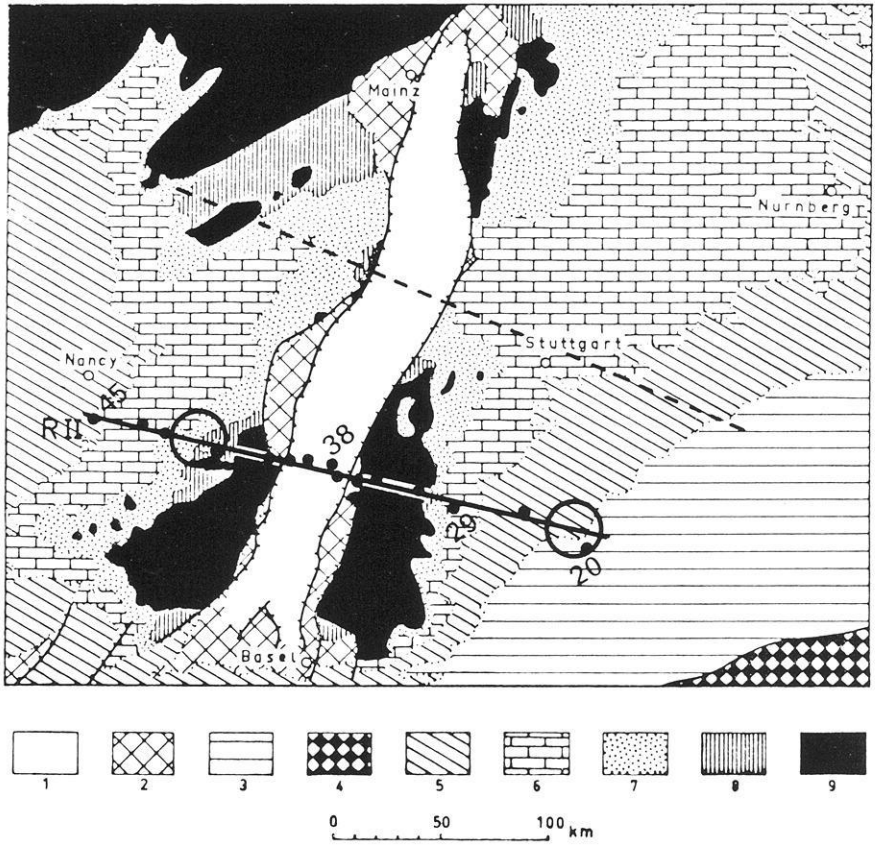

Fig. 1. Generalized geological map of the Rhine Graben area (after Illies, 1967). The lines are profiles on which induction studies have been carried out. On the southern line, labeled "R II", the stations are situated as described in the text. Most of the stations are indicated by dots, a few by numbers. Areas marked with circles represent the zones, where the measurements could be explained with one-dimensional models. *1* Graben trough, *2* Marginal blocks and basins, *3* Molasse trough, *4* Alps, *5* Jurassic, *6* Middle and upper Triassic, *7* Lower triassic, *8* Permian, *9* Prepermian basement

of the horizontal **E**-field components on those of the **F**-field. In GDS they are the geomagnetic induction arrows

$$\mathbf{c} = \mathrm{a} \cdot \mathbf{N} + \mathrm{b}\mathbf{M}$$

(where **N** and **M** are the vectors of unit length in the northern and eastern direction, respectively), as complex quantities, appropriate to express the linear relations between the vertical component Z of the variations of the magnetic field and the horizontal components:

$$Z = a \cdot H + b \cdot D$$

(H is the north component of **F**, D the east component) (Parkinson, 1959; Schmucker, 1970). Model calculations are commonly computed under the

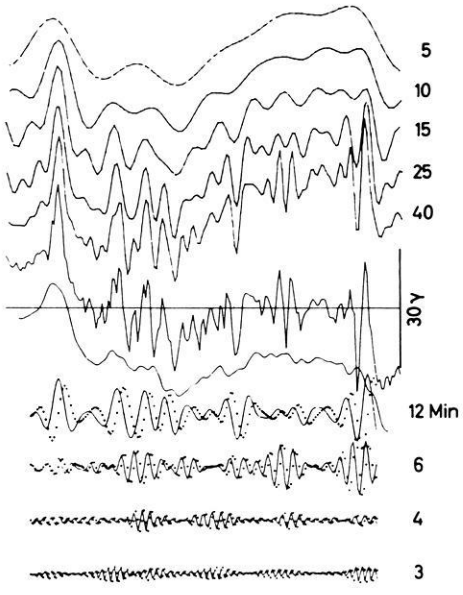

Fig. 2. Around the central line: recorded time variations of the East (D) component of the magnetic field **F** from 7^{20} UT until 10^{30} UT, Dec. 25. 1968 (interval length 190 min), measured at a site near the Eastern border of the Rhine Graben. At the top: after Fourier analysis re-synthetisized variations with different numbers k_{max} of harmonics included (written at the right hand side). Below: results of numerical filtering: continous lines in-phase filter, small crosses out-of-phase filter. The periods of the maximum of the frequency response function in minutes are indicated at the right

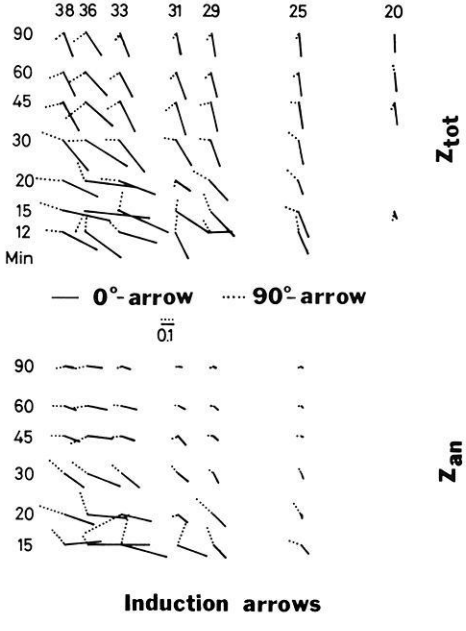

Fig. 3. Induction arrows **c** (after Schmucker, 1970) at measuring sites at the Eastern half of our profile R II across the Rhine Graben (Fig. 1): station 38 is in the middle of the Graben, station 20 at the extreme East is approximately 130 km from it. On the two halves of the figure from top to bottom the results for different periods, written in minutes at the left side, are shown. Upper half: Arrows that have been derived from the variations of the measured total field (Z_{tot}). Lower half: An attempt to use only the part of the vertical component Z (Z_{an}) caused by the anomaly of the Graben itself (*i.e.* the regional Z-variations noticed everywhere in Southern Germany outside the Rhine Graben anomaly have been subtracted). Heavy lines: Real parts of **c**—in-phase or 0^0-arrows. Dotted lines: Imaginary parts—out-of-phase or 90°-arrows

assumption that the fields are harmonically oscillating. Therefore, one has to apply a frequency analysis onto the recorded variations. The periodes T we used were about 10 to $2 \cdot 10^4$ s in the case of MT and $2 \cdot 10^2$ to 10^4 s in the case of GDS. Two different methods for the frequency separations were tried:

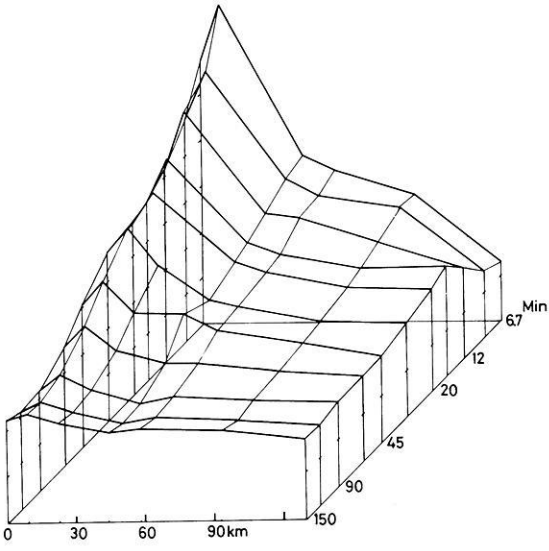

Fig. 4. Length of the empirical induction arrows |c| versus location and period for the Eastern half of the profile R II: at the left side lies the middle of the Graben and at right is the Eastern end of it at a distance of about 130 km: from front to back the periods from 150 to 6.7 min are drawn. At the ordinates the values are marked in a distance of 0.1

the Fourier analysis and application of numerical filters. In Fig. 2 examples are shown. For deduction of the transfer functions the concept of least squares was used. An example of some results thus gained is being shown in Figs. 3 and 4 for the induction arrows.

Another problem in interpreting the field measurements is to compute the transfer functions of model structures in order to be able to compare them with those derived from the measurements: the best fitting model represents the structure existing in nature with highest probability. A two-dimensional model for the Graben structure should represent the real situation quite well. We used two techniques for the model computations:

a method making use of the concept of a thin inhomogeneous layer over an one-dimensional substratum after Schmucker (1971) (who developed some ideas of Price);

the method of finite differences after Jones and Pascoe (1971), improved and programmed by Haak (1974).

Results are shown in Figs. 5 and 6.

Results

In the case of two-dimensional configurations one can choose from a great variety of parameters to find the best fitting model. However, fortunately, one can reduce the troublesome task to define the best model by incorporating knowledge gained from other geoscientific studies and, above all, by trying first simpler models, *i.e.* one-dimensional ones, if such models seem to be appropriate. On our profile we found areas at some distance of the Rhine Graben, about 50 km West and 100 km East (marked by circles in Fig. 1), below which the resistivity

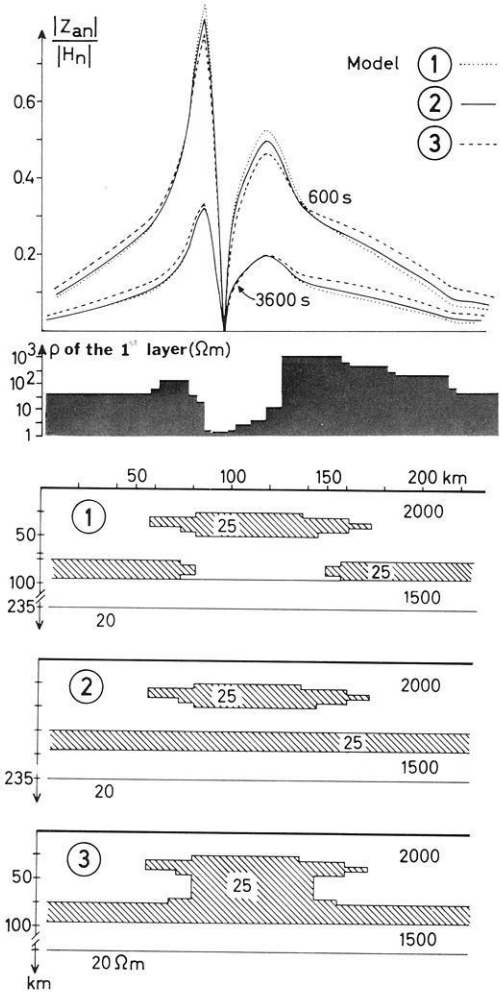

Fig. 5. Above: Length of the induction arrows |c| along profiles for three models, in which only the deeper structures are altered, as results of two-dimensional model calculations. Second diagram from above: Resistivities ϱ in Ωm of the first layer with a thickness of 2 km. Below: The three models of the deeper substratum. The results of calculation are shown for two periods, 10 min and 1 h

distribution can be assumed to be a function of depth only, approximately. In this case the technique of interpretation of the MT data is much less complicate. One can use for example Cagniard's method or the $\varrho^*(z^*)$-inversion-technique of Schmucker (1970). We are confident that the situation in nature at the areas mentioned is not very different from the following model (Haak and Reitmayr, 1974): below the locally varying sedimentary cover the basement has high resistivities $\varrho > 1{,}000$ Ωm. At a depth of approximately 80 km (74–95 km) a low resistivity layer ($\varrho = 10-100$ Ωm) with a thickness of about 20 km (14–25 km) exists. The high resistivities below this conductor do not decrease for several hundred km. A similar distribution has been found in other parts of Southern Germany and around the surrounding areas (Beblo, 1974; Berktold, 1974). Many authors regard this case as a normal continental situation (Fournier *et al.*, 1971).

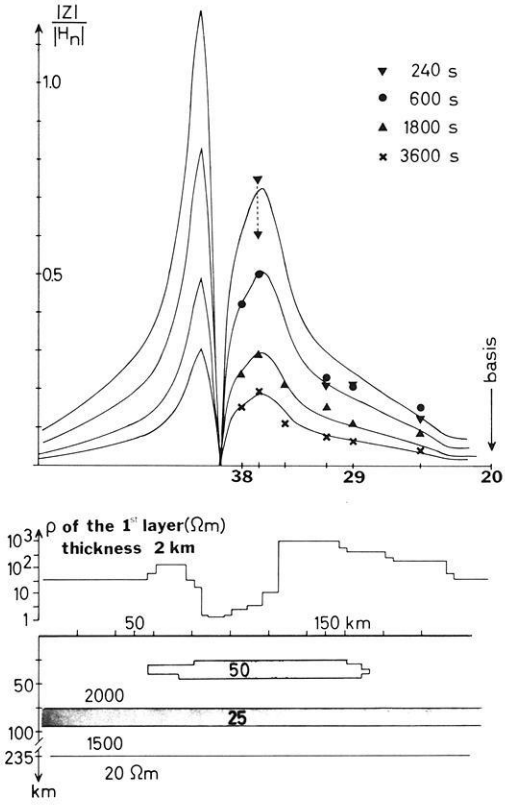

Fig. 6. Length of the induction arrows as derived from our measurements and their explanation by a two-dimensional model. Best fitting with the model shown in which there are two low resistivity zones in the deeper structure: One laterally limited between 25 and 45 km depth below the Rhine Graben (resistivity 50 Ωm) and one running through between 75 and 95 km depth (25 Ωm)

Starting with this knowledge we tried to interpret the local variations of our derived transfer functions by local variations in the sedimentary cover alone; soon, however, there arose difficulties. We noted for instance, that the lengths of the calculated induction arrows do not decrease as slowly as they do in nature when the recording stations are remote from the Graben. This and other results can only be explained by the assumption of deeper situated lateral inhomogenities. Finally we obtained best agreement by introducing in our models a poorly resistant (≈ 50 Ωm) zone, laterally limited to a few tens of km below the Graben, between the depths of 25 to 45 km. The model as well as one of its transfer functions (here the length of the induction arrow) and the corresponding function derived from the measurements can be seen in Fig. 6. An uncertainty, however, remains about the exact geometry (and the resistivities), as demonstrated in Fig. 5.

Above we mentioned our intention to get also information about the distribution of temperature with knowledge of the resistivity within the earth's interior. If one assumes a predominant olivine composition of the upper mantle with approximatley 10% fayalite and a high content of ferric iron (perhaps 0.5% Fe_2O_3) – a composition which is rather probable – a resistivity in the order of 30 Ωm, as found below the Rhine Graben at about 25 km depth and in some distance of it at 80 km, seems to indicate temperatures of roughly 800° C (after

Schult, 1974). Recent investigations, however, suggest that resistivity may be strongly influenced by the content of Fe^{3+}, and so the increase in resistivity below the well conducting layers might be caused by a change in the petrological composition, in the sense that the ferric iron diminishes nearly or totally.

Other authors have tried to interpret those low resistivity layers within the upper mantle by zones of partially melted material (*e.g.* Berdichevsky *et al.*, 1972). Statements concerning the temperatures are then much more uncertain.

Acknowledgements. The author is very grateful to the director of the Institut für Angewandte Geophysik, Munich, Prof. Dr. G. Angenheister for encouragement and support. Great thanks are due to the members of the team "Geoelectrics" at the same institute: Dr. M. Beblo, Dr. A. Berktold, Dr. V. Haak and K. Kemmerle.

References

Beblo, M.: Die elektrische Leitfähigkeit unter den Ostalpen abgeleitet aus magnetotellurischen Messungen längs eines Profiles vom Alpennordrand bis zu den Hohen Tauern. Diss. Geowiss. Fak. Univ. München 1974

Berdichevsky, M.N., Van'yan, L.L., Fel'dman, I.S., Porstendorfer, G.: Conductiong layers in the earth's crust and upper mantle. Gerlands Beitr. Geophys. **71**, 187–196, 1972

Berktold, A.: Erdmagnetische Tiefensondierung in Süddeutschland und in den Alpen. Protokoll DFG-Kolloquium Erdmagn. Tiefensondierung, Grafrath 11.–13.3.1974: Univ. München, pp. 58–70, 1974

Fournier, H., Ádám, A., Miguel, L. de, Sanclement, E.: Proposal for a first upper mantle magnetotelluric E-W profile across Europe. Acta Geodaet. Mont. Hung. **6**, 419–477, 1971

Haak, V.: Berechnung von induzierten elektrischen und magnetischen Feldern in Modellen mit zwei-dimensional verteilter Leitfähigkeit. Protokoll DFG-Kolloquium Erdmagn. Tiefensondierung, Grafrath 11.–13.3.1974: Univ. München, pp. 400–428, 1974

Haak, V., Reitmayr, G.: The distribution of electrical resistivity in the rhinegraben area as determined by telluric and magnetotelluric methods. In: Approaches to taphrogenesis, J.H. Illies and K. Fuchs, ed., pp. 366–369. Stuttgart: Schweitzerbart 1974

Haak, V., Sengpiel, K.-P., Berktold, A., Greinwald, S.: The telluric method: Results of measurements along a profile across the rhinegraben between Stuttgart and Kaiserslautern. In: Graben problems, J.H. Illies and St. Mueller, ed., pp. 235–238. Stuttgart: Schweitzerbart 1970.

Illies, J.H.: Development and tectonic pattern of the rhinegraben. In: The rhinegraben progress report 1967. Abh. Geol. Landesamt Baden-Württemberg **6**, 7–9, 1967

Jones, F.W., Pascoe, L.J.: A general computer program to determine the perturbation of alternating electric currents in a two-dimensional model of a region of uniform conductivity with an embedded inhomogeneity. Geophys. J. **24**, 3–30, 1971

Losecke, W.: Ergebnisse magnetotellurischer Messungen bei Speyer. In: Graben problems, J.H. Illies and St. Mueller, ed., pp. 242–244. Stuttgart: Schweitzerbart 1970

Parkinson, W.D.: Directions of rapid geomagnetic fluctations. Geophys. J. **2**, 1–14, 1959

Reitmayr, G.: Elektromagnetische Induktion im Erdinneren, studiert am Rheingraben. Diss. Geowiss. Fak. Univ. München 1974

Scheelke, I.: Magnetotellurische Messungen im Rheingraben und ihre Deutung mit zweidimensionalen Modellen. Gamma 20, Inst. Geophys. Meteorol. Tech. Univ. Braunschweig, 1972

Schmucker, U.: Anomalies of geomagnetic variations in the Southwestern United States. Bull. Scripps Inst. Oceanogr. Univ. Calif. 13, 1970

Schmucker, U.: Interpretation of induction anomalies above nonuniform surface layers. Geophysics **36**, 156–165, 1971

Schult, A.: The electrical conductivity of minerals and the temperature distribution in the upper mantle. In: Approaches to taphrogenesis, J.H. Illies and K. Fuchs, ed., pp. 376–378. Stuttgart: Schweitzerbart 1974

Winter, R.: Der Oberrheingraben als Anomalie der elektrischen Leitfähigkeit, untersucht mit Methoden der Erdmagnetischen Tiefensondierung. Diss. Math.-Naturwiss. Fak. Univ. Göttingen 1973

Received June 16, 1975

J. Geophys. 41, 659–679, 1975

Some Problems of Large-Scale Gravity Interpretation

E. Groten

Lehrstuhl für astronomische Geodäsie und Satellitengeodäsie der Technischen Hochschule, D-6100 Darmstadt, Petersenstr. 13, Federal Republic of Germany

Abstract. Linear regression and interrelations of mean free air and isostatic gravity anomalies with other geophysical parameters such as upper mantle density variations, depth of M-discontinuity, and heat flow are studied for Germany and Central Europe. In spite of local interdependences large scale correlation is only found for gravity and heat flow values. Gravity data are used in terms of mean anomalies, geoid undulations and single layer density variations (corresponding to a lithosphere of constant thickness).

Key words: Geoid – Gravimetric interpretation – Correlation of gravity with crustal parameters – Gravity field in Germany – Heat flow versus gravity in Europe – Gravity anomaly statistics – Isostatic reduction of gravity.

1. Introduction

Large-scale gravity interpretation has found increasing application since (1) the low harmonics part of gravity became available from satellite orbit analysis, and (2) long range gravity anomalies, as obtained from surface gravimetry, gained more reliability through the application of long-range gravity nets and from filling the existing gaps in the world gravity field. In the present investigation the gravity potential and the corresponding anomalies were considered within limited areas where spherical harmonics of degrees $n \leqq 18$ and mean anomalies of block size $d' \geqq 6$ min of arc are of main concern. The trends are typically given by harmonics of degree $n < 17$.

When absolute values are considered, zero degree terms in the harmonic expansion are of special interest. But in this interpretation mainly variations, *i.e.* relative values, are relevant.

Numerical values for the lower harmonic part are those of the Goddard Earth Model (GEM); additional sources of data information applied in the study are given by Groten and Rummel (1974) and Groten (1974).

It is the aim of the present study to represent the regional gravity field in different ways and to point out problems arising in *regression* studies of gravity with other geophysical parameters and fields.

Correlation being a measure of *linearity* of interpendence has not been used in this study because it is too strongly affected by low harmonics.

Gravity is represented by free air and isostatic anomalies, geoid heights and single layer densities.

In *regional* studies correlation of geoid undulations with other geophysical parameters, like depth of M-discontinuity etc., was previously investigated, *e.g.*, by Durbin (1966), Wolf (1971), Pick and Jabkucova (1972), Groten (1966). Discussion of long-range geoid heights was done, *e.g.*, by Kahle and Talwani (1973).

Statistical regression studies are not hampered by the nonuniqueness resulting from Stokes' theorem which affects the interpretation by *models* deduced from N or Δg. Even though statistical results are less specific than those of model investigations they are good tools in prediction.

In general, methods of *local* gravity interpretation differ from those of *global* interpretation; but the evaluation of appropriate lithospheric models can in both cases be useful in investigating *detailed* distribution of matter; *e.g.* (Watts and Cochran, 1974a, b; Watts and Talwani, 1974a, b). However, statistical inferences as *e.g.* widely applied by Woollard (1972) yield mainly *general* information.

In paragraphs 2 to 4 the gravimetric quantities used in the investigations are defined and described where the reasons for applying isostatic anomalies (according to Airy-Heiskanen) are specificly given. The details of the numerical results shown in paragraph 5 are discussed in paragraph 6.

2. Geoid Computations and Topographic Effects

In large-scale interpretation mean free air anomalies are often used instead of Bouguer anomalies because the correlation of mean free air anomalies of large blocks with topography is smaller than the correlation of mean Bouguer anomalies. In many areas isostatic anomalies are even less related to topographic features. Short period effects of the topography are eliminated or reduced in the potential W, too, particularly in its perturbation part:

$$T = W - U \tag{1}$$

where U is the normal potential. The same is true with geoid heights

$$N = T/\gamma \tag{2}$$

where $\gamma = -\partial U/\partial n$ is normal gravity and n is the surface normal. Using Stoke's integral formula

$$N = \frac{R}{4\pi\gamma} \iint_E \Delta g \, S \, dE \tag{3}$$

(where E = earth's surface,
dE = element of E,
$\Delta g = g - \gamma$ = gravity anomaly,
R = mean radius of the earth,
S = Stoke's function and
$g = -\partial W/\partial n$ = observed gravity).

N is found from gravity anomalies. In the present investigation N as obtained from formula (3) is combined with satellite data using the superposition method given by Groten and Rummel (1974).

When S is considered as a low pass filter function the application of the integral formula (3) might simply be taken as a method for reducing topographic effects of Δg.

In the present investigation it seemed appropriate to rely on a statistical approach which might be summarized by linear and non-linear regression formulas as

$$A = C + \sum_i a_i c_i \,(+\text{non-linear terms}) \tag{4}$$

where A may stand for Δg or N,

a_i are linear regression coefficients,

C is a constant,

$c_1 = h$, topographic height and oceanic depth,

$c_2 = H'$, mantle depth,

$c_3 = v$, mantle velocity,

$c_4 = V$, crustal velocity; the list may be extended by geological and similar parameters.

Since the Bouguer-correction is linear in h and, moreover, the terrain correction as well as the isostatic corrections are to some extent linear in h (Groten and Reinhart, 1968) Eq. (4) in its linear form can be applied in most cases.

The geoid height N as given by Eq. (3) is only a first order approximation. But detailed investigations of the second order approximations as obtained by taking into account Molodensky-type corrections (Brennecke *et al.*, 1975) show that corresponding corrections are always less than 0.4 m and, consequently, do not affect the result given below. This statement holds for the part of the spectrum discussed in the present investigation and should not be generalized because the numerical integration of the correction formula depends strongly on the local statistical behavior of the parameters from which these corrections are evaluated.

3. Single Layer Model

Beside N and Δg gravity has been used in a third way by computing the density of a single layer at the earth surface (Helmert, 1884)

$$\mu' = \frac{1}{2\pi f}\left(\Delta g + \frac{3\gamma N}{2R}\right) \tag{5}$$

in its spherical approximation (where f = Newton's gravitational constant). Further, according to Heiskanen and Moritz (1967),

$$\mu = 2\pi f \mu' = \Delta g + \frac{3T}{2R}. \tag{6}$$

When Eqs. (3) and (6) are combined a formula for $\mu(\Delta g)$ is found; on the other hand, $\mu(N)$ is obtained on inserting the inverse integral formula to Eq. (3) in (6) as shown by Chovitz (1974). Consequently, several formulas for evaluating μ and μ' are available.

If Δg and N are supposed to be produced by density variations ρ within a lithospheric layer of constant thickness H we get from

$$\rho = \mu'/H \tag{7}$$

together with Eq. (5)

$$\rho = \frac{1}{2\pi H f}\left(\Delta g + \frac{3\gamma N}{2R}\right) \tag{8}$$

or, in terms of spherical harmonics, Δg_n,

$$\rho = \sum \rho_n \tag{9}$$

where

$$\rho_n = \frac{\Delta g_n}{2\pi H f}\left(1 + \frac{3}{2(n-1)}\right) \tag{10}$$

and

$$N = \frac{R}{\gamma} \sum \Delta g_n/(n-1). \tag{11}$$

Consequently, for $n > 91$ we get

$$\rho_n \doteq \frac{\Delta g_n}{2\pi f H} \tag{12}$$

neglecting an error of 1.5 percent.

4. Isostatically Reduced Gravity Values

The classical isostatic concepts have undergone several revisions during the last time; see, *e.g.*, MacDonald (1963), Jacoby (1973 b), Artyushkov (1974). They can seriously affect the local geophysical interpretation; detailed isostatic reductions where regional variations of Moho-depth and density as well as deviations from isostatic equilibrium are taken into account, are seldom feasible in large-scale gravimetric interpretation. Consequently, gravity anomalies reduced according to the Airy-Heiskanen method with compensation depth $D = 30$ km have been used in computing geoid heights and the isostatically reduced single layer density. When Moho depth data as given by Giese and Stein (1973) are compared with

the above value of D it is seen that the deviations are not too large. Moreover, it should be kept in mind that in those areas where the depth of the Moho is greater than D, as in the Alps, the mountain roots according to the isostatic concept are at depth $\geqq 40$ km. In the whole, the isostatic reduction is considered as a working concept in order to reduce the numerical values of Δg and to have a model which might largely be independent of topographic effects.

When ρ as given by Eq. (7) is evaluated from isostatic gravity for a lithospheric layer of constant thickness $H = 100$ km with laterally varying density it is supposed to be more appropriate for interpretation in all cases where large-scale topographic effects should be eliminated or, at least, reduced.

In Airys classical isostatic concept the depth of compensation D is chosen in such a fashion that there is zero correlation between isostatic $\Delta g(D)$ and station elevation h. This method is basicly equivalent to Nettleton's well known principle as applied to free air anomalies in density determinations. When this principle is applied the regional regression coefficients of isostatic anomalies $\Delta g(h)$ can be plotted for different D-values. In case of isostatic equilibrium the most probable D is then found for zero correlation.

The necessity of revised concepts with respect to the classical theory becomes evident on inspecting Figs. 1 and 2 where for Holopainen's (1974) isostatic anomalies corresponding linear regression coefficients are shown in revised form for different numerical values of depth of compensation D. The *large-scale* application of Nettleton's principle, *i.e.* zero correlation of topography with reduced gravity, which has previously been critizised (Groten and Reinhart, 1968) with free air anomalies leads to distorted values for the Moho-depth $\leqq D$ if it is applied to these isostatic anomalies with varying depth of compensation D. For it is seen from Figs. 1 and 2 that D found for zero regression coefficients is in most cases incompatible with any reasonable Moho depth values. Discrepancies are only partly explained by deviations from isostatic equilibrium.

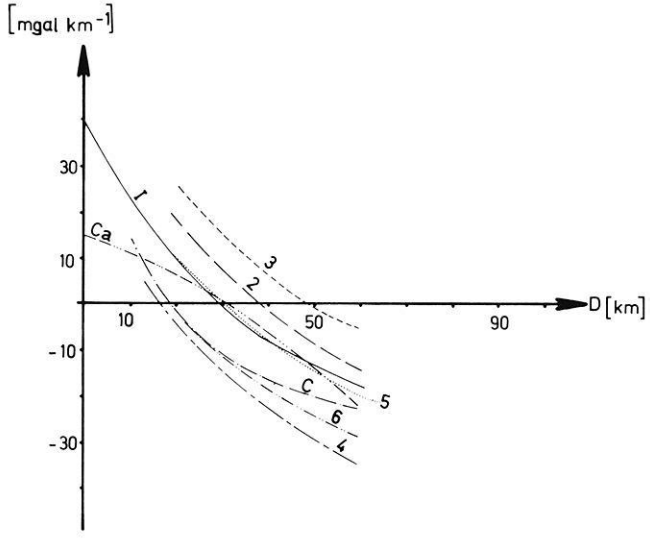

Fig. 1. Regression coefficients (mgal/km) for isostatic anomalies of variable compensation depth (after Airy-Heiskanen) $0 < D < 60$ km; *1*, *2* Northern Italy; *3* Northern Austria, *4*; *Ca* Eastern Alps; *5*, *6* Central part of Austria, *C* Central Alps

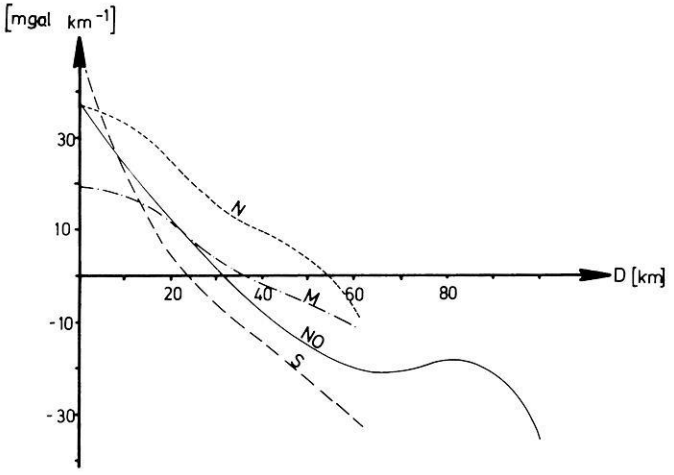

Fig. 2. Regression coefficients (mgal/km) for isostatic anomalies of variable compensation depth (after Airy-Heiskanen) $0 < D < 100$ km; *N* Northern Sweden; *M* Central part of Sweden; *S* Southern part of Sweden; *No* Norway

When isostatic and other anomalies are considered from a statistical view point variances are found to be

$$\text{var(isostatic } \Delta g) = 207 \text{ mgal}^2$$

$$\text{var(free air } \Delta g) = 400 \text{ mgal}^2$$

$$\text{var(Bouguer } -\Delta g) = 835 \text{ mgal}^2$$

for 6′ by 10′ mean values within F.R. of Germany. The autocorrelation function of free air anomalies is not very different from the autocorrelation of isostatic anomalies as seen from Fig. 3.

Together with the variances the autocorrelation functions are considered as a global measure of model truth, *i.e.* the steeper the descent of the autocorrelation function and the smaller the deviations of the covariance (*i.e.* autocorrelation times variance) from zero the better is the model applied in the reduction of Δg.

In case of Bouguer anomalies the large effects of subterranean mass deficits according to the isostatic theory are mainly reflected by the relatively strong autocorrelation within the first few hundred kilometers and, to some extent, by the negative autocorrelation over larger distances.

Whereas free air and isostatic gravity is often equivalent in *continental* regression studies, isostatic gravity values are superior in *regional* comparisons; *e.g.*, Watts and Cochran (1974b) gave a good example for the necessity of eliminating the topographic effect which can distort the interpretation of Δg completely; this fact corroborates the use of isostatic anomalies.

5. Numerical Results

In evaluating Δg, the global part of gravity was only subtracted in form of an ellipsoidal normal potential; additional global trends have not been eliminated. In the computation of the isostatic corrections we did not take into account the

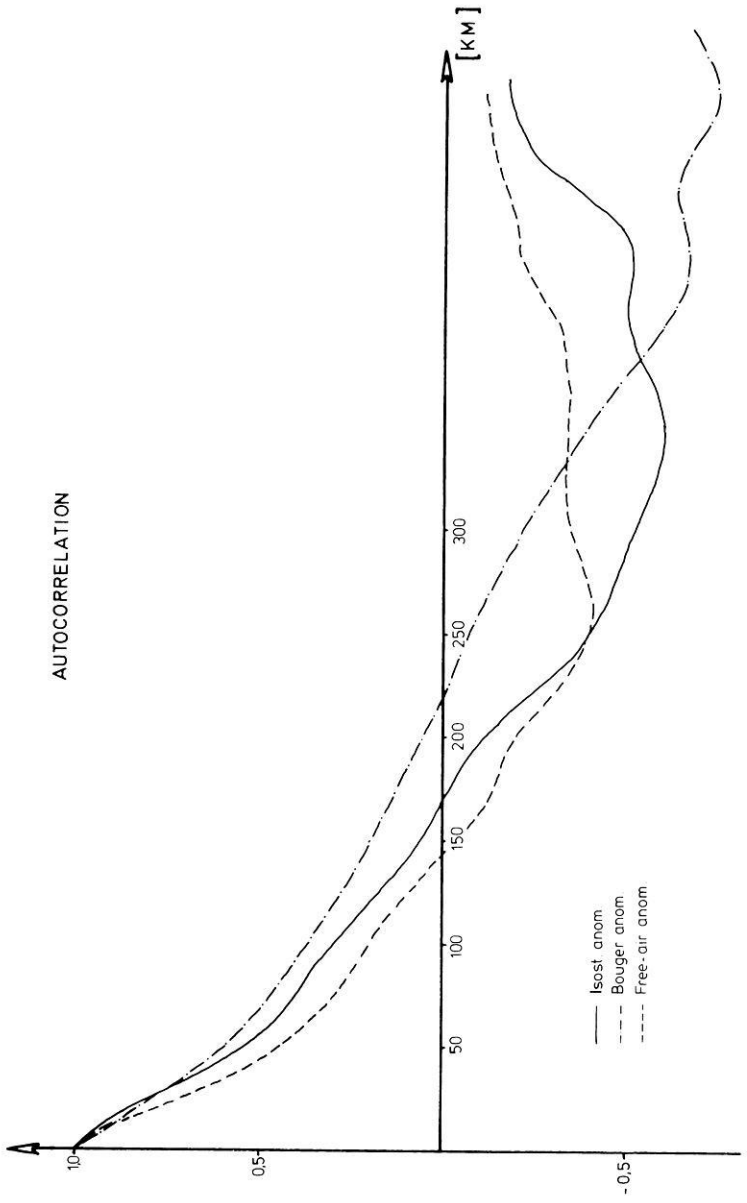

Fig. 3. Autocorrelation functions for mean anomalies (6′ by 10′ blocks) in Germany corresponding to flattening 1:297

global part of this correction, *i.e.* in evaluating the isostatic geoid height the isostatic corrections were, in general, completely ignored for the spherical distances $\psi > 5°$; within $\psi \leqq 5°$ they were everywhere taken into account within the F.R. Germany according to the model of Airy-Heiskanen mentioned before; outside Germany it was only applied in those areas where isostatic compensation really exists. This approach should be more realistic than a complete isostatic correction, including all oceanic areas, as in the Airy-Heiskanen concept. For mean anomalies of large blocks as used in the numerical integration of distant

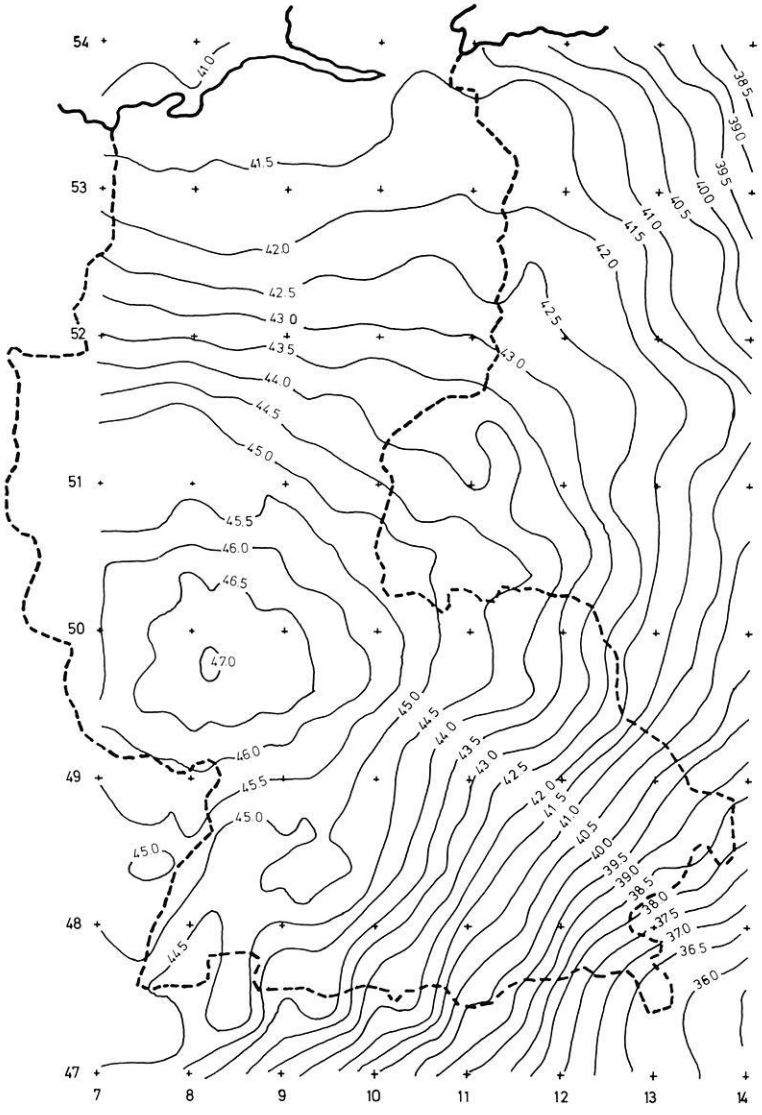

Fig. 4. Isostatic geoid of Germany for flattening 1/298.25; isolines (m) do not contain zero degree term $N_0 = -20$ m

zones in Stokes's formula the isostatic correction is, in any case, not very important. Figs. 4 and 5 show the isostatic geoid and the corresponding lateral distribution of density variations in the lithospheric model, respectively.

Fig. 6 shows the lateral density variations in the lithospheric model corresponding to free air anomalies. According to Eq. (10) the density variations are more dependent on topographic effects than the geoid undulations; when the variations in Fig. 6 are compared with those of the geoid in the same area (Groten and Rummel, 1974) the smoothness of geoid undulations in the northern part

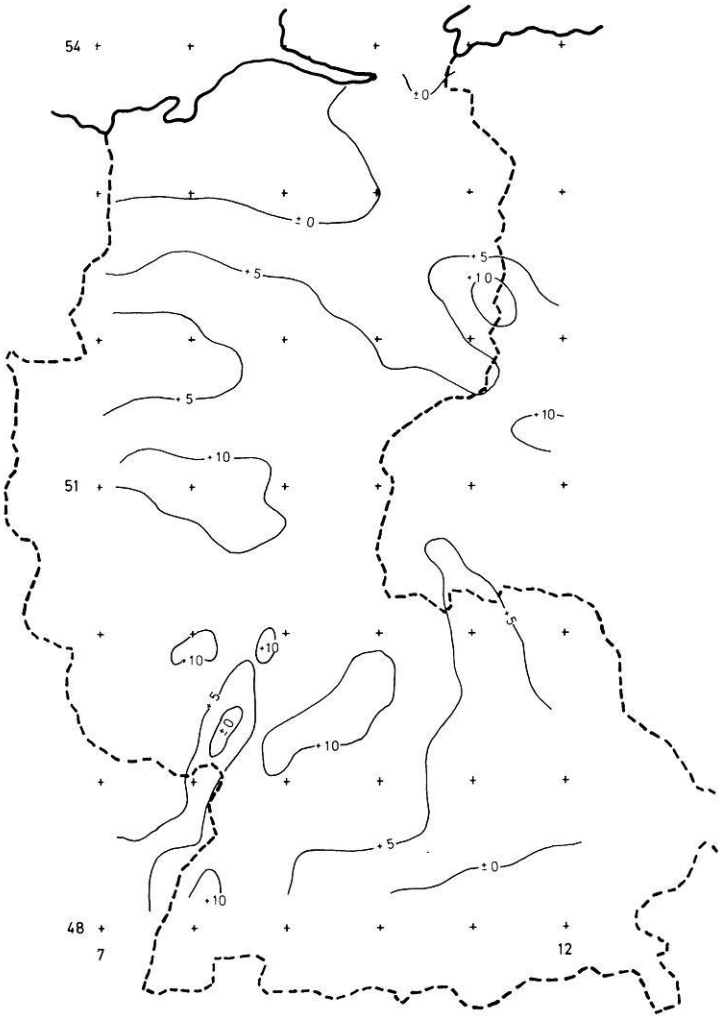

Fig. 5. Lateral density variations (10^{-3} gr/cm^3) in a lithospheric layer of thickness $H = 100$ km corresponding to isostatic anomalies of flattening 1/298.25 in F.R. Germany (for Airy-Heiskanen system with $D = 30$ km)

is in contrast to the detailed structure shown in Fig. 6. The smooth form of the geoid in Northern Germany is surprising and only a very small part of it is explained by lack of sufficient data in some parts of that area.

Let us consider now the correlation between heat flow and geoid undulations: A disadvantage of the results of regression analysis as shown in Figs. 7 to 11 is the lack of data. Therefore strict cross-covariance-analysis had to be replaced by simple regression studies.

Instead of the original heat flow data we used the results of trend analysis as found by Haenel (1971), Haenel and Zoth (1973) and Haenel (1974); in Figs. 8 to 10 they were used together with geoid heights in Europe as given by

Fig. 6. Lateral density variations (10^{-3} gr/cm^3) in a lithospheric layer of thickness $H = 100$ km corresponding to free air anomalies of flattening 1/298.25 in F.R. Germany

Marsh and Vincent (1974). Since the effect of the degree of approximation used in the analysis was remarkable the heat flow values of Haenel (1971) were used in Fig. 8 whereas in Figs. 9 and 10 the data from Haenel (1974) were applied. In Fig. 10 the effects of sedimentation and denudation have been taken into account. On comparing the data in Fig. 7 with those in Figs. 8 to 10 it is realized that there is, in general, only low regional (not local) regression of geoid height with heat flow whereas the *continental* regression is remarkable within the area of investigation. On inspecting details of the free air geoid it is seen that, *e.g.*, in Northern Germany and other areas where the data distribution was insufficient

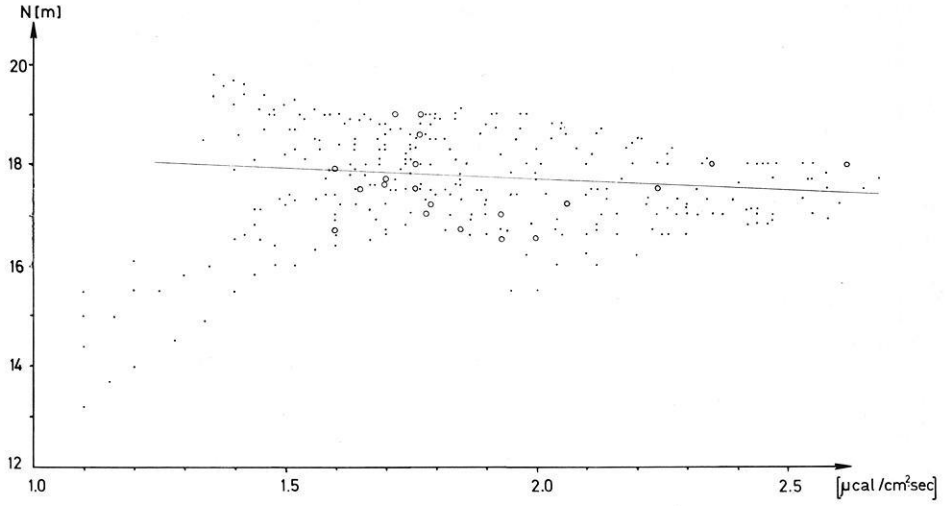

Fig. 7. Regression of (free air) geoid heights in Germany with heat flow values given by Haenel (1971) within $48° \leqq \phi \leqq 52°$ and $7° \leqq \lambda \leqq 12°$ (E) at 0.5° steps

there is apparently a better correlation than in the south where more heat flow data were available. The circles in Figs. 7 to 10 indicate multiple points where the radius is proportional to the number of points represented by the specific circle in the figure.

The meaning of the circles is the same in Fig. 11 where the relatively low regression of Moho depth with free air geoid heights is shown for Germany using the results by Giese *et al.* (1973); Moho depth again is defined as the depth of strongest velocity gradient in the interval 7.2 to 8.4 km/sec. The results are supported by the results of Liebscher (1964). Similarly low correlation is found between geoid heights and large-scale variation of mantle velocity as discussed by Giese and Stein (1971) and Giese *et al.* (1973).

On inspecting the above regression results in Figs. 7 and 11 we may ask for the sources of the regional geoid undulations. The geoid for Southern Germany is shown in Fig. 12 contoured in decimeter intervals. Small-scale variations are evident on this map and it is realized that even there the geoid heights vary only by a few decimeters. There might be local petrological sources of mean gravity anomalies as Kaula (1969) found for larger areas in global interpretation. Correlation of local anomalies with geological structures and Moho depth variations were pointed out, *e.g.*, by Plaumann and Dürbaum (1971) for Siegerland.

Two features of the detailed free air geoid are remarkable; (1) there is no strong anomaly in the area around Basel at the southern end of Rhine Graben; (2) in the "Hessischer Graben" *i.e.* the area around Kassel, north-east of the Rhine-Graben, where Giese *et al.* (1973) found a relative maximum of crustal thickness (in contrast to the relative minimum of crustal thickness in the Rhine-Graben) there is no deformation at all in the free air geoid; see also Groten and Rummel (1974) for an additional geoid section using other gravity data.

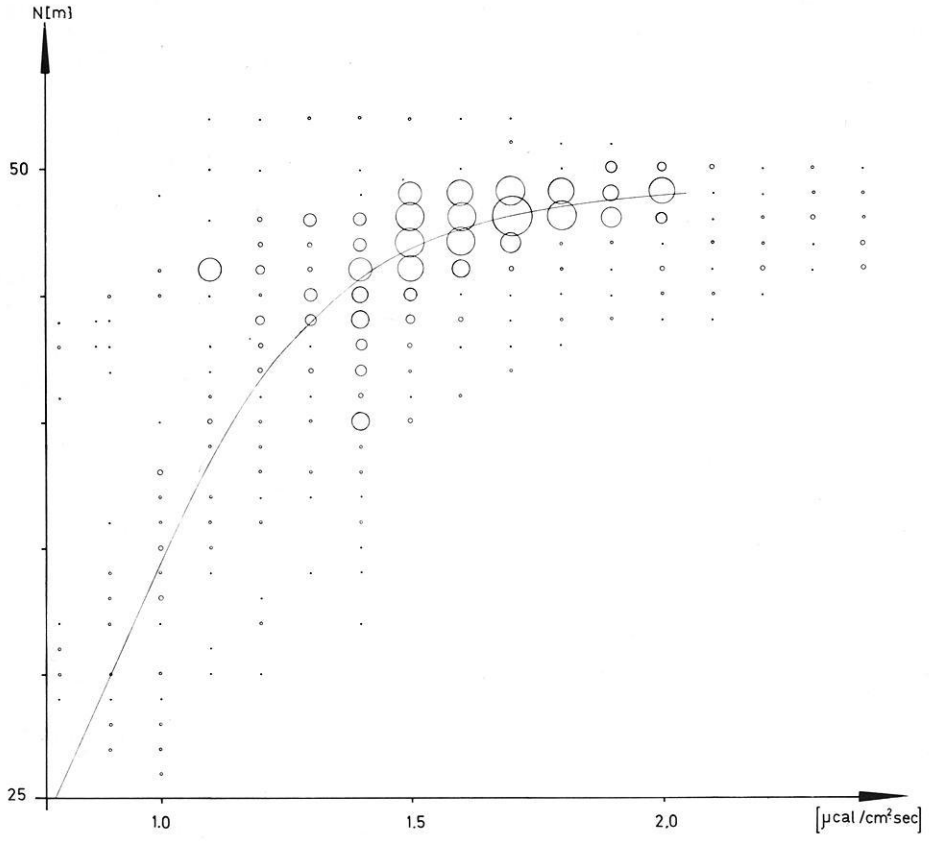

Fig. 8. Regression of (free air) geoid heights in Central Europe ($45° \leqq \phi \leqq 55°$ (N); $5° \leqq \lambda \leqq 25°$($E$)) with heat flow values given by Haenel and Zoth (1973); at 0.5° steps

It seems that such regional features are compensated completely. This assumption is in agreement with very strong *local* regression found in the regression analysis for local data having very different regression coefficients. On the whole, these coefficients might cancel each other in a *regional* survey such that for larger areas of regional extent no remarkable correlation is found. This holds for regression of gravity with crustal thickness, heat flow and other parameters. For instance in the area ($50.25° < \phi < 52.0°$; $9.5° < \lambda < 11.75°$) there is a remarkable negative regression of free air geoid heights with crustal depth which is compensated by a positive regression, *e.g.*, in Bavaria; heat flow in Northern Germany has positive regression with geoid heights in the eastern part and partly negative regression in the western part.

The results given by Woollard (1974) for 1° by 1°-blocks in the United States do not show the strong continental correlation between heat flow and the geoid as evident in Figs. 8 to 10 for central Europe. But a similar regional interdependence of several parameters as discussed above is visible also in Woollard's data. In

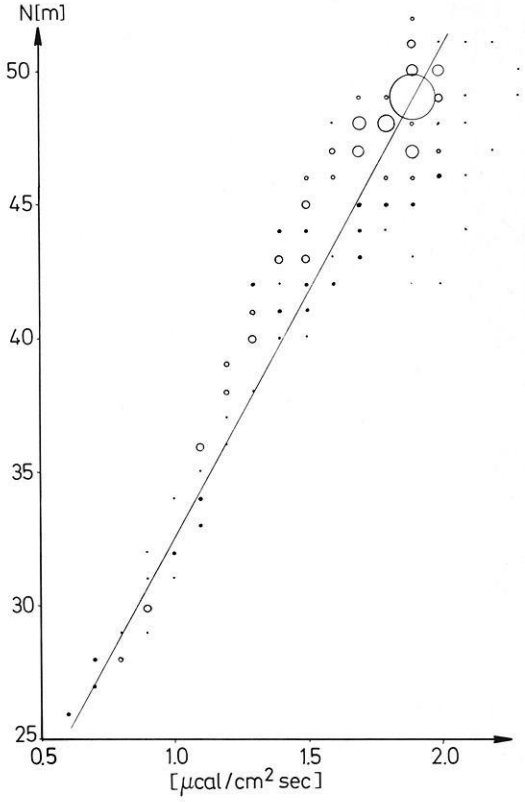

Fig. 9. Regression of (free air) geoid heights in Central Europe ($45° \leqq \phi \leqq 55°$ (N) and $5° \leqq \lambda \leqq 25°$($E$)) with heat flow values given by Haenel (1974); at 0.5° steps without corrections for denudation etc.

contrast to Woollard's results there is no remarkable correlation of mantle velocity and crustal thickness in Germany as is seen by comparing the results of explosion seismology by Giese *et al.* (1973).

On comparing the lithospherical density variations obtained in previous studies with our data it is realized that the lateral density variation models given by Figs. 5 and 6 reflect the velocity variations in Germany as shown by Giese *et al.* (1973). Because of lacking information on the thickness of the lithosphere and since radial density variations are ignored in these models they can, at present, give only crude approximations. This means that for representing *regional* features on continents like the present ones those models are more appropriate than in investigating *global* density distributions including those areas where slabs of lithosphere may locally descend to as much as 700 km depth. But whenever the lithospheric density variations and possibly flow in the asthenosphere are important single layer models seem to be appropriate, even if the thickness of the asthenosphere and the lithosphere are slightly varying. *E.g.*, a decreasing thickness of the asthenosphere as might be expected in central Europe along the north-south direction, *i.e.* towards the Baltic Shield, could yield positive linear regression of heat flow with N.

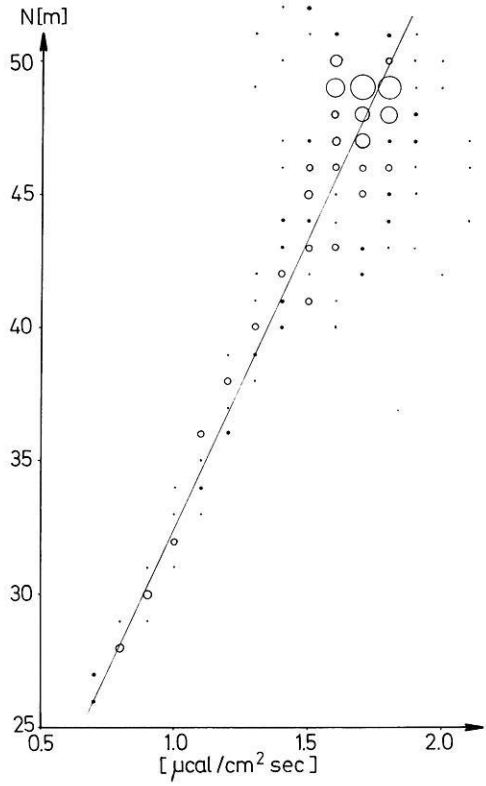

Fig. 10. Regression of (free air) geoid heights in Central Europe ($45° \leqq \phi \leqq 55°$ (N) and $5° \leqq \lambda \leqq 25°(E)$) with heat flow values given by Haenel (1974) corrected for denudation etc.

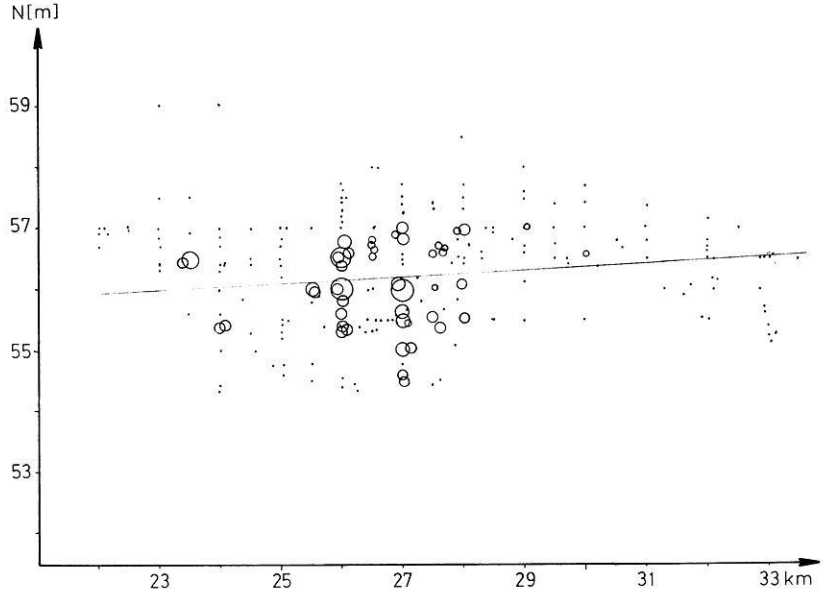

Fig. 11. Regression of Moho depth with geoid heights in Germany $47° \leqq \phi \leqq 52 (N)$; $7° \leqq \lambda \leqq 12°(E)$; data taken at 0.5° steps

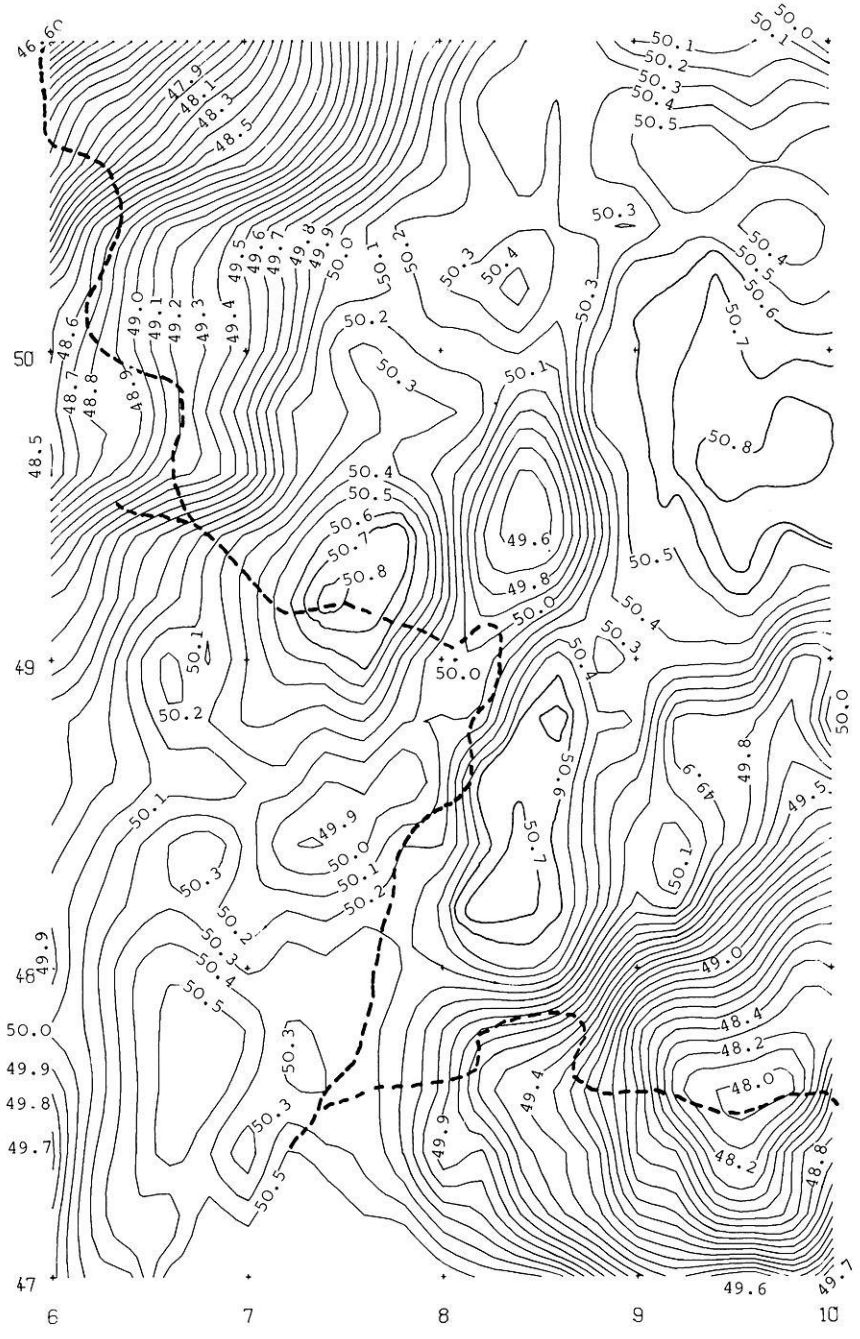

Fig. 12. Very detailed (free air) geoid of the Rhinegraben area for flattening 1/298.25. The broken lines indicate the political borders; N_0 is not included in heights (m) labelled to the isolines

6. Discussion

The Lower Harmonics Part. In Δg, N and μ' different parts of the spectrum are predominant as seen on inspecting Figs. 4, 5, 6 and 12. In any of these cases, the lower harmonics of degree $n<17$ imply trends which are of remarkable interest, even in the regional interpretation. Therefore, the evaluation of the lower harmonics part is briefly discussed.

For several sets of GEM-coefficients as obtained from satellite orbit analysis together with mean surface anomalies of large blocks, differences which would basicly affect the analyses and results have not been found in the gravity harmonics $n \leqq 18$. For the flattening we used

$$f \doteq 1/298.25$$

instead of $f = 1/299.8$ as applied in other investigation as, *e.g.*, by Lambeck (1972). The reason is given by Groten and Rummel (1974).

On the other hand, the low harmonics can seriously affect especially the results of the regression analyses. But the explanation of the sources of the very low harmonics is still problematic. Even though there is probably no interrelation of gravity harmonics for $n \leqq 5$ with heat flow and similar data the low harmonics have not been eliminated from the gravity field used in the present regression analysis. This fact might cause uncertainties but it is difficult to clearly separate those gravity harmonics which could be produced deeply in the lower mantle (Groten, 1968) from those which might affect, *e.g.*, heat flow variations at the earth's surface.

If gravity harmonics for $n \leqq 5$ are produced by variations of the core-mantle boundary or even by an earth's core of slightly variable position (Egyed, 1964), it would be necessary to subtract the harmonics $n \leqq 5$ from the gravity field when regression with heat flow etc. is investigated. However in spite of the strong influence of low harmonics on linear regressions the number of harmonics to be subtracted is uncertain and on corresponding core-mantle models additional information is needed. Consequently, the well justified ellipsoidal normal potential as adopted at the IUGG General Assembly in Moscow 1971 according to Somigliana's theory has been used in the present investigation for evaluating Δg and N.

The residual zero degree term $N_0 = -20$ m in N has been taken from Groten (1974); it is only of secondary interest in our data. Therefore, it is not contained in the isolines of N as given in the above figures of the geoid. Consequently, whenever the geoid heights shown in the present paper are compared with other quantities in *absolute* terms then N_0 has to be added.

Regression of Gravity with Heat Flow. Most of the previous studies on the interrelation between gravity and heat flow have been considered either the very short period part of the spectrum or the low harmonics; so references were necessary in our case to the low harmonics part more than is usually done in regional investigation. A general problem in comparing the gravity field with regional heat flow distribution is the fact that gravity reflects the *present* density distribution whereas heat flow at the surface does not represent the present

thermal field in the earth's interior. A special problem of the present investigation is the lack of data; in the area of Europe where relatively reliable gravity and heat flow data are available there is a remarkable linear trend of both fields in the north-south direction which, in case of the gravity field, is readily modified by simply subtracting different parts of the low harmonics.

On comparing Haenel's (1971, 1974) different heat flow maps with the one compiled by Stegena (1972) the influence of trends depending on the degree of trend analysis in heat flow data processing is evident. In the present study only Haenel's data have been used. Since local topographic effects are not supposed to be directly correlated with heat flow data only geoid heights were used in the regression analysis.

What makes the present study intricate in comparison to previous ones is the possibility of combined effects of convective and radioactive heat flow variations which can exist in the part of the spectrum under investigation.

On inspecting previous statistical investigations of *local* correlations of gravity with heat flow mainly radioactive heat sources have been considered. Moreover, correlation of heat flow with recent crustal movements on the one hand and correlation of free air gravity anomalies with land uplift on the other hand were found; *e.g.*, P. Vyskocil (1974) gave locally varying regression coefficients in Bohemia for the linear interrelation of crustal movements with heat flow. But the sources of both events cannot assumed to be situated in the gabbro layer because for the Moho to be a phase transition gabbro-eclogit a strong positive correlation of temperature gradients with Moho is necessary which has not been found; see, *e.g.*, (Kaula, 1968).

Buntebart (1973 a, b), on the other hand, used Bouguer anomalies in his *model* investigations. Therefore, the question arises what type of gravity anomaly is best related to heat flow data. From our viewpoint, the isostatic anomaly is, in general, best suited because it is less dependent on local topography than other types of anomalies.

Studies of *global* correlation of gravity with heat flow and the interpretations have undergone many revisions since G.J.F. MacDonald, W.H.K. Lee and others started those investigation more than ten years aga (Lee, 1963; MacDonald, 1964; Lee and Uyeda, 1965). The main point was the physical explanation of positive and negative correlation. The question whether gravity is positively or negatively correlated with radiogenic and convective heat flow (McKenzie, 1967; Hagiwara 1971) has meanwhile found plausible explanations; Anderson *et al.* (1973) and others have pointed out that for *convective* heat transfer there is *always positive* correlation of gravity with heat flow for any Rayleigh-coefficient and any source of heat.

Conductive heat transfer was discussed, *e.g.*, by Magnitzkii (1963) and Lambeck (1972) where, however, in Magnitzkii's concept expansion due to temperature variations in any direction differs from Lambeck's concept of radial expansion. The correlation of the spreading rate along oceanic ridges with amplitude and wave lengths of mainly positive free air anomalies of the lower harmonics field $n \leqq 5$ is one of the common points in Lambeck's (1972) and also Anderson's *et al.* (1973) studies.

Kaula's global cross-correlation analysis (see Lee and Uyeda, 1965) of gravity with heat flow gave a slight *negative* correlation at zero degree. At first sight, negative correlation of gravity with heat produced by radioactive decay is straight forward unless mass transport is involved.

On the whole, the positive correlation along ocean ridges could be compensated by overwhelming negative correlation of conductive heat transfer in the oceans. Along ocean ridges the information which is obtained from free air anomalies is mainly due to boundary conditions as discussed, *e.g.*, by Kaula (1973). But corresponding results are not available in the present case and it is not quite clear to what extent the above results can lead to conclusions on the large-scale flow fields in the asthenosphere at central Europe. The simple inference of large-scale or even small-scale dynamic processes in the upper mantle from large-scale mass excess and possible flow in the oceanic part is certainly not justified. Heat transfer together with small-scale mass transport could be present in the Rhine Graben and in the Alps; large or small scale lateral mass transport might also be of interest in other areas of central Europe where it could explain the slight positive correlation of gravity with heat flow values.

Regression of Moho-Depth with Gravity. When the M-discontinuity is defined in the classical sense as the location of steepest gradient of velocity in the area of crust and upper mantle, *i.e.* for $7.2 \leqq v \leqq 8.4$ km/sec, a strong regression of Moho depth with Bouguer anomalies is expected; somewhat smaller regression coefficients are anticipated to exist, in general, for free air and isostatically reduced gravity with Moho depth. On inspecting the above given variances and correlations of Δg it is realized that each type of Δg can, in principle, be chosen for investigating crustal thickness H'; the choice depends on the specific influence of topography. But the various investigations of regional regression of free air anomalies with elevations h (see, *e.g.*, Vyskocil and Koziskova (1966) for small-scale, and Anderson *et al.* (1973) for large-scale studies) as well as the investigations of regional variations of H' (h), show clearly the problems still inherent in the prediction of H' from Δg. *E.g.*, isostatic Δg-values having small variances directly reflect the deviations from the specific crustal model as applied in the isostatic corrections and they are less dependent on topography than other types of Δg. Woollard (1959, 1966a, 1966b, 1970, 1972) and Woollard and Strange (1962) have done most extensive studies of regression of different parameters using free air, Bouguer and isostatic Δg whereas Wolf (1971) and several other authors used free air geoid undulations. Results as summarized by Woollard (1974) reveal general correlation between mean free air anomalies, regional, crustal velocities, mantle velocities, mantle depth and geological age; positive isostatic anomalies are supposed to yield too great Moho depth in comparison to reality whereas negative anomalies may lead to too low Moho depth. Some areas having deviations from isostatic equilibrium associated with positive isostatic anomalies and corresponding variations in H' (h) as well as some of the previous large-scale interpretations have to be revised in view of new lithospheric concepts as, *e.g.*, the correlation of positive and negative Δg with subsiding areas and land uplift. Part of those large-scale features could also be associated with horizontal temperature variations and flow in the asthenosphere as well as with relations between age and crustal thickness

instead of geological sources which were previously supposed to be the reasons for gravity anomalies. For oceanic areas, *e.g.*, Kahle and Werner (1975) give such explanations for gravity regression with heat flow along continental boundaries. Horizontal temperature gradients below the lithosphere are only one further possibility for explaining the relatively strong continental regression of heat flow with gravity data.

7. Conclusions

The presently available data are only useful for rather general statements on the structure in central Europe. Regional variations in the gravity field can be explained by density variations in the upper mantle but presently available data do not give unique and detailed information of sufficient reliability. The mutual compensation of variations of different parameters leading to almost zero regression for regional variations of (1) gravity with Moho depth, (2) gravity with mantle velocity, (3) gravity with heat flow is typical. But especially for the maximum crustal depth in the "Hessischer Graben" no compensating variation of an other geophysical parameter has been found. The linear continental regression of gravity with heat flow could be an apparent one because of the uncertainties in the lower harmonics of gravity. With more data at hand, gravity could, in combination with heat flow and other data, yield additional information about such parameters as density in the upper mantle, especially in the lithosphere and asthenosphere and contribute to solutions of questions on lithospheric motion and asthenospherical flow as discussed by LePichon (1968), Isacks *et al.* (1968), Kaula (1973), Jacoby (1973a), McKenzie (1973), Press (1973) in central Europe.

In southern Germany where heat flow data are more reliable than in the north and vary more strongly, they are much better correlated with isostatic than with free air geoid undulations; this fact corroborates the perturbing influence of topographic effects in regional gravity – heat flow regression and the usefulness of isostatic reduction. The better the model applied in isostatic reduction the more efficient is the use of isostatic anomalies.

The averaging effect of formula (3) was found to be remarkable; small anomalies are completely eliminated. This is best realized by comparing single layer density variations with geoid undulations. Consequently, local regression of gravity with Moho depth etc. cannot be expected to become evident from geoids. But large scale regression should be better detected using geoid heights instead of gravity anomalies.

Acknowledgement. H. Schaab did most of the computer work; Prof. Fuchs gave valuable references; Prof. Woollard provided data prior to publication.

References

Artyushkov, E.V.: Can the earth's crust be in a state of isostasy? J. Geophys. Res. **79**, 741–752, 1974

Anderson, R.N., McKenzie, D., Sclater, J.G.: Gravity, bathymetry and convection in the earth. Earth Planet. Sci. Lett. **18**, 391–407, 1973

Brennecke, J., Groten, E., Rummel, R., Schaab, H.: Variationen zum Geoid in Deutschland. Deutsche Geodät. Komm., München, 1975 (in press)
Buntebarth, G.: Modellberechnungen zur Temperatur-Tiefen-Verteilung im Bereich der Alpen und des Alpenvorlandes. Z. Geophys. **39**, 97–107, 1973a
Buntebarth, G.: Über die Größe der thermisch bedingten Bouguer-Anomalie in den Alpen. Z. Geophys. **39**, 109–114, 1973b
Chovitz, B.H.: Determination of density of a simple layer directly from geoid heights. J. Geophys. Res. **79**, 3026, 1974
Durbin, W.P.: Geophysical correlations, AGU Geophys. Monograph No. **9**, 85–88, 1966
Egyed, L.: The satellite geoid and the structure of the earth. Nature **4940**, 67–69, 1974
Giese, P., Stein, A.: Versuch einer einheitlichen Auswertung tiefenseismischer Daten aus dem Bereich zwischen Nordsee und Alpen. Z. Geophys. **37**, 238–272, 1971
Giese, P., Morelli, C., Steinmetz, L.: Mean features of crustal structure in western and southern Europe based on data of explosion seismology. Tectonophysics **20**, 367–379, 1973
Groten, E.: On linear regression prediction of mean gravity anomalies. AGU Geophys. Monograph No. **9**, 53–57, 1966
Groten, E.: On the masses necessary to produce the anomalous gravitational potential as obtained from satellite observations. Boll. Geofis. Teor. Appl. X, **39**, 235–240, 1968
Groten, E.: Problems related to absolute orientation of geodetic systems. Paper presented at the International Symposium "Redefinition of North American Geodetic Networks", Fredericton/Canada, 1974
Groten, E., Reinhart, E.: Gravity prediction in mountaineous areas. Boll. Geofis. Teor. Appl. X, **37**, 28–43, 1968
Groten, E., Rummel, R.: Improved gravimetric geoid for $7° \leqq \lambda \leqq 12° (E)$ and $47° \leqq \phi \leqq 54° (N)$. Allg. Vermessungsnachrichten **7**, 263–267, 1974
Haenel, R.: Heat flow measurements and a first heat flow map of Germany. Z. Geophys. **37**, 975–992, 1971
Haenel, R., Zoth, G.: Heat flow measurements in Austria and heat flow maps of central Europe. Z. Geophys. **39**, 425–439, 1973
Haenel, R.: Heat flow in northern Italy and heat flow maps of Europe. J. Geophys. **40**, 367–389, 1974
Hagiwara, Y.: Gravity anomaly and mantle convection. J. Geod. Soc. Jap. (Tokyo) **17**, 144–152, 1971
Heiskanen, W.A., Moritz, H.: Physical geodesy. San Francisco: Freeman 1967
Helmert, F.R.: Die Mathematischen und Physikalischen Theorien der Höheren Geodäsie. Leipzig: Teubner 1884
Holopainen, P.E.: On the gravity field and the isostatic structure of the earth's crust in the east Alps. Isostatic Institute of the Intern. Ass. of Geodesy, 1947
Isacks, B., Oliver, J., Sykes, L.R.: Seismology and the new global tectonics. J. Geophys. Res. **73**, 5855–5899, 1968
Jacoby, W.R.: Gravitational instability and plate tectonics. In: Gravity and Tectonics, DeJong and Scholten (Eds.), 17–33. New York: Wiley 1973a
Jacoby, W.R.: Isostasie und Dichteverteilung in Kruste und oberem Mantel. Z. Geophys. **39**, 79–96, 1973b
Kahle, H.G., Talwani, M.: Gravimetric Indian Ocean geoid. Z. Geophys. **39**, 167–187, 1973
Kahle, H.G., Werner, D.: Gravity and temperature anomalies in the wake of drifting continents. Tectonophysics, 1975 (in press)
Kaula, W.M.: Introduction to planetary physics. The terrestrial planets. New York: Wiley 1968
Kaula, W.M.: Tectonic classification of the main features of the earth's gravitational field. J. Geophys. Res. **74**, 4807–4826, 1969
Kaula, W.M.: Global gravity and tectonics. In: Plate tectonics and geomagnetic reversals, Cox (Ed.), 500–501. San Francisco: Freeman 1973
Lambeck, K.: Gravity anomalies over ocean ridges. Geophys. J. **30**, 37–53, 1972
Lee, W.H.K., Uyeda, S.: Review of heat flow data. Terrestrial heat flow. AGU Geophys. Monograph No. **8**, 87–190, 1965
Lee, W.H.K.: Heat flow data analysis. Rev. Geophys. **1**, 449–479, 1963
LePichon, X.: Sea-floor spreading and continental drift. J. Geophys. Res. **73**, 3661–3697, 1968
Liebscher, H.J.: Deutungsversuche für die Struktur der tieferen Erdkruste nach reflexionsseismischen und gravimetrischen Messungen im deutschen Alpenvorland. Z. Geophys. **30**, 51–96, 115–126, 1964

MacDonald, G.J.F.: The deep structure of continents. Rev. Geophys. **1**, 587–665, 1963
MacDonald, G.J.F.: Dependence of the surface heat flow on the radioactivity of the earth. J. Geophys. Res. **69**, 2933–2946, 1964
Magnitskii, V.A.: Interpretation of the main gravity anomalies of the earth. In: Problems of theoretical seismology and physics of the earth's interior, Magnitskii (Ed.), Akademiya Nauk SSSR, 66–71, 1963
Marsh, J.G., Vincent, S.: Global detailed geoid computation and model analysis. Goddard Space Flight Center, Greenbelt, Maryland, 1974
McKenzie, D.P.: Some remarks on heat flow and gravity anomalies. J. Geophys. Res. **72**, 6261–6273, 1967
McKenzie, D.P.: Speculations on the consequences and causes of plate motions. In: Plate tectonics and geomagnetic reversals, Cox (ed.), 447–469. San Francisco: Freeman 1973
Pick, M., Jabkucova, I.: Determination of Mohorovicic discontinuity from deep seismic soundings and the characteristics of the outer earth's gravity field. Bull. Geodesique **106**, 477–486, 1972
Plaumann, S., Dürbaum, H.: Gravimetrie. In: Geologisch-lagerstättenkundliche und geophysikalische Untersuchungen im Siegerländer-Wieder Spateisensteinbezirk, H.D.Lang (Ed.) Beih. geol. Jb. **90**, 65–74, Hannover 1971
Press, F.: The gravitational instability of the lithosphere. In: Gravity and Tectonics, DeJong and Scholten (Eds.), 7–16. New York: Wiley 1973
Stegena, L.: Geothermal map of eastern Europe. Geothermics **1**, 140, 1972
Vyskocil, P.: Recent crustal movements in the Bohemian Massif. Potsdam: Veröff. Zentralinstitut Physik d. Erde **30** (2), 331–345, 1974
Vyskocil, V., Koziskova, M.: Korrelation zwischen den Schwereanomalien und Seehöhen in Mitteleuropa. Travaux Geophys. **XIV**, 75–81, 1966
Watts, A.B., Cochran, J.R.: Gravity anomalies and flexure of the lithosphere along the Hawaiian-Emperor. Seamount chain. Geophys. J. **38**, 119–141, 1974a
Watts, A.B., Cochran, J.R.: Gravity anomaly in the Galapagos Island area. Science **184**, 808–809, 1974b
Watts, A.B., Talwani, M.: Gravity effect of downgoing lithospheric slabs beneath Island Arcs. (Manuscript) (a)
Watts, A.B., Talwani, M.: Gravity anomalies seaward of deep-sea trenches and their tectonic implications. Geophys. J. **36**, 57–90, 1974b
Wolf, H.: Geoid und Mohorovicic-Diskontinuität. Z. Vermessungswesen **96**, 373, 1971
Woollard, G.P.: Crustal structure from gravity and seismic measurements. J. Geophys. Res. **64**, 1521–1544, 1959
Woollard, G.P.: Regional relations in the United States. AGU Geophys. Monograph No. **10**, 557–573, 1966a
Woollard, G.P.: The interrelationship of the crust, the upper mantle and isostatic gravity anomalies in the United States. AGU Geophys. Monograph No. **12**, 312–341, 1966b
Woollard, G.P.: Evaluation of the isostatic mechanism and role of mineralogic transformations from seismic and gravity data. Phys. Earth Planet. Interiors **3**, 484–498, 1970
Woollard, G.P.: A regional analysis of crustal structure in North America and a study of the problems associated with the prediction of gravity in Europe. ACIC-Final Report, St. Louis, Mo., 1972
Woollard, G.P.: *unpublished results presented at the meeting of the International Gravimetric* Commission. Paris, September, 1974
Woollard, G.P., Strange, W.E.: Gravity anomalies and the crust of the earth in the Pacific basin. AGU Geophys. Monograph No. **6**, 60–80, 1962

Received February 12, 1975; Revised Version July 18, 1975

Lothar Sachs: Angewandte Statistik. Planung und Auswertung – Methoden und Modelle. Zugleich vierte, neubearbeitete Auflage der „Statistischen Auswertungsmethoden" mit neuer Bibliographie. 59 Abb. 190 Tabellen, XX 548 Seiten. Preis: DM 58,–.

Berlin, Heidelberg, New York: Springer 1974

Das Buch beschreibt eine große Anzahl von Testmethoden der Statistik. Es ist die erweiterte Neuauflage des Buches „Statistische Auswertungsmethoden" vom gleichen Autor. Der Form nach ist es sowohl als Formelsammlung, als Tabellenwerk (220 Tafeln) und als Lehrbuch zu gebrauchen. Der Inhalt wird in 7 Kapitel unterteilt (in Klammern folgen hier jeweils einige Stichpunkte):

1. Statistische Entscheidungstechnik (Elemente der Wahrscheinlichkeitsrechnung; die Zufallsvariable; Normalverteilung; Wahrscheinlichkeitsnetz; der Weg zum statistischen Test; Student-, χ^2- und F-Verteilungen; diskrete Verteilungen).

2. Die Anwendung statistischer Verfahren in Medizin und Technik.

3. Der Vergleich unabhängiger Stichproben gemessener Werte (Vergleich eines empirischen Mittelwertes mit dem Mittelwert einer normalverteilten Grundgesamtheit; Vergleich einer empirischen Varianz mit ihrem Parameter; Vergleich zweier empirisch ermittelter Varianzen normalverteilter Grundgesamtheiten; Vergleich zweier empirischer Mittelwerte normalverteilter Grundgesamtheiten; verteilungsfreie Verfahren für den Vergleich unabhängiger Stichproben: U-Test von Wilcoxon).

4. Weitere Prüfverfahren (Prüfung verbundener Stichproben mit dem t-Test; die Prüfung von Verteilungen mit dem χ^2-Anpassungstest: Vergleich empirischer Verteilungen mit der Gleichverteilung, mit der Normalverteilung und mit der Poisson-Verteilung; Vertrauensgrenzen einer beobachteten Häufigkeit bei binomialverteilter Grundgesamtheit; der Vertrauensbereich für seltene Ereignisse; Vergleich zweier Häufigkeiten; der exakte Test von Fisher für den Vergleich der Grundwahrscheinlichkeiten zweier Binomialverteilungen).

5. Abhängigkeitsmaße: Korrelation und Regression (Schätzverfahren: Schätzung des Korrelationskoeffizienten, der Regressionsgeraden, einiger Standardabweichungen; Vertrauensgrenzen des Korrelationskoeffizienten; Prüfverfahren: Prüfung des Vorhandenseins einer Korrelation; Prüfung der Linearität einer Regression; Prüfung des Regressionskoeffizienten gegen Null; Vergleich zweier Regressionskoeffizienten; Vertrauensbereiche für die Regressionsgerade; nichtlineare Regression; partielle und multiple Regressionen und Korrelationen).

6. Die Auswertung von Mehrfeldtafeln.

7. Varianzanalytische Methoden (Prüfung der Gleichheit mehrerer Varianzen; varianzanalytischer Vergleich mehrerer Mittelwerte; zweifache und dreifache Varianzanalyse).

Weiterhin enthält das Buch eine Bibliographie und eine 50 Seiten lange Sammlung von Literaturangaben, geordnet nach den 7 Kapiteln.

Zwar werden in einem vorgeschalteten Kapitel Null die Elementarkenntnisse der Buchstabenrechnung auf dem Stand der mittleren Reife erklärt, doch ist dieses Buch keineswegs nur für diesen hiermit angesprochenen Personenkreis zu empfehlen. Gerade die Problematik der Anwendung von Verfahren der Statistik – falsche Fragestellung, falsche Schlußfolgerung aus formal richtig berechneten Zahlen – verlangt eigentlich einen Leser höherer mathematischer Weihen. Der Autor ist sich dieser Gefahr falschen Gebrauchs bewußt und erklärt die Logik statistischer Tests in längeren Abschnitten und bei fast allen speziellen Verfahren sehr anschaulich und präzise. Hierzu diskutiert er bei fast jedem Testverfahren Beispiele und rechnet sie vollständig vor. Am Ende des Buches folgen einige Übungsaufgaben mit ihren Lösungen.

Die große Anzahl der Formeln und Tabellen ist übersichtlich dargestellt. Das Buch ist hervorragend ausgestaltet; es bereitet Vergnügen, es zu studieren. Es kann jedem empfohlen werden, der die Methoden der Statistik anwenden will.

V. Haak, München

G.H. Liljequist: Allgemeine Meteorologie
368 Seiten mit 336 Abb. und 24 Tabellen, zusätzlich 16 Seiten Bildanhang. DM 96,–. Braunschweig: Vieweg 1974.

Über Jahrzehnte fehlte in der deutschsprachigen meteorologischen Literatur ein umfassendes, leicht verständliches Lehrbuch, das man Studenten der Meteorologie oder verwandter Fachgebiete als Einführung empfehlen konnte. Dieser Mangel ist behoben durch die von K. Cehak, Wien vorgenommene Übersetzung eines 1962 in Schweden erschienenen Lehrbuchs. Zusammen mit dem Autor hat der Übersetzer das Buch überarbeitet und insbesondere durch Ersatz oder Ergänzung von Beispielen mehr auf mitteleuropäische Verhältnisse bezogen. Es ist mit seinem großen Format, der klaren, anschaulichen Darstellung und den geringen Ansprüchen an mathematische Vorkenntnisse besonders für Anfänger eine sehr ansprechende Lektüre. In 27 Abschnitten wird das gesamte Gebiet der allgemeinen Meteorologie systematisch behandelt. Die modernen Entwicklungen in der Meteorologie werden nicht besonders betont, dafür aber wird eine solide Grundlage des Fachwissens vermittelt. Der Stoff beginnt mit den Gasgesetzen und der Strahlung, danach folgt die Besprechung der einzelnen meteorologischen Elemente, der bestehenden Zusammenhänge und der Thermodynamik. In besonderen Abschnitten werden die Optik und die Elektrizität der Atmosphäre behandelt, die Radioaktivität wird als Quelle der Ionsisierung kurz angesprochen. Eine Reihe von Abschnitten kann unter dem Begriff Dynamik und Synoptik zusammengefaßt werden, dazu kommt schließlich die gesonderte Behandlung von Stichworten wie „Tropische Meteorologie", „Bodennahe Schicht", „Wechselwirkung Atmosphäre und Meer", „Klimatologie", „Stratosphäre und hohe Atmosphäre".

Der Preis des Buches ist durch den Inhalt und die Aufmachung gerechtfertigt. Es kann deshalb in jeder Beziehung als einführendes Lehrbuch und als zuverlässiges universelles Arbeitsmittel für die angestrebte berufliche Tätigkeit empfohlen werden. K. Höschele, Karlsruhe